Giuseppe Carlo Marano · A.V. Rahul ·
Jiji Antony · G. Unni Kartha ·
P. E. Kavitha · M. Preethi   *Editors*

Proceedings of SECON'22

Structural Engineering and Construction Management

Springer

Lecture Notes in Civil Engineering

Volume 284

Series Editors

Marco di Prisco, Politecnico di Milano, Milano, Italy

Sheng-Hong Chen, School of Water Resources and Hydropower Engineering, Wuhan University, Wuhan, China

Ioannis Vayas, Institute of Steel Structures, National Technical University of Athens, Athens, Greece

Sanjay Kumar Shukla, School of Engineering, Edith Cowan University, Joondalup, WA, Australia

Anuj Sharma, Iowa State University, Ames, IA, USA

Nagesh Kumar, Department of Civil Engineering, Indian Institute of Science Bangalore, Bengaluru, Karnataka, India

Chien Ming Wang, School of Civil Engineering, The University of Queensland, Brisbane, QLD, Australia

Lecture Notes in Civil Engineering (LNCE) publishes the latest developments in Civil Engineering—quickly, informally and in top quality. Though original research reported in proceedings and post-proceedings represents the core of LNCE, edited volumes of exceptionally high quality and interest may also be considered for publication. Volumes published in LNCE embrace all aspects and subfields of, as well as new challenges in, Civil Engineering. Topics in the series include:

- Construction and Structural Mechanics
- Building Materials
- Concrete, Steel and Timber Structures
- Geotechnical Engineering
- Earthquake Engineering
- Coastal Engineering
- Ocean and Offshore Engineering; Ships and Floating Structures
- Hydraulics, Hydrology and Water Resources Engineering
- Environmental Engineering and Sustainability
- Structural Health and Monitoring
- Surveying and Geographical Information Systems
- Indoor Environments
- Transportation and Traffic
- Risk Analysis
- Safety and Security

To submit a proposal or request further information, please contact the appropriate Springer Editor:

- Pierpaolo Riva at pierpaolo.riva@springer.com (Europe and Americas);
- Swati Meherishi at swati.meherishi@springer.com (Asia—except China, Australia, and New Zealand);
- Wayne Hu at wayne.hu@springer.com (China).

All books in the series now indexed by Scopus and EI Compendex database!

Giuseppe Carlo Marano · A. V. Rahul · Jiji Antony ·
G. Unni Kartha · P. E. Kavitha · M. Preethi
Editors

Proceedings of SECON'22

Structural Engineering and Construction
Management

Springer

Editors
Giuseppe Carlo Marano 🄳
DISEG
Politecnico di Torino
Turin, Italy

Jiji Antony
Department of Civil Engineering
Federal Institute of Science and Technology
(FISAT)
Angamaly, Kerala, India

P. E. Kavitha
Department of Civil Engineering
Federal Institute of Science and Technology
(FISAT)
Angamaly, Kerala, India

A. V. Rahul
Department of Civil and Environmental
Engineering
Indian Institute of Technology Tirupati
Tirupati, Andhra Pradesh, India

G. Unni Kartha
Department of Civil Engineering
Federal Institute of Science and Technology
(FISAT)
Angamaly, Kerala, India

M. Preethi
Department of Civil Engineering
Federal Institute of Science and Technology
(FISAT)
Angamaly, Kerala, India

Preface

Green Technology evolves from the concept of sustaining nature's perpetuity. The essentiality of infrastructure development for economic prosperity has deprived the quality of the environment. As the engineer's chore relies not only on the enhancement of the society but also retaining the innards of nature for the future generations, the idea of green engineering technology has been replenished. At the same time, the advancements in the areas of GIS and artificial intelligence have opened up enormous opportunities for civil engineers solving many complexities in the domain. An effective usage of modern technologies had laid the path for the enormous infrastructure projects.

The emphasis of the 3rd International Conference on Structural Engineering and Construction Management (SECON'22) was "Green Technology and Infrastructure Developments" along with the ten tracks, which discuss the advancements and innovations in various streams of Civil Engineering.

This proceedings comprises the papers presented at SECON'22 as chapters in Lecture Notes in Civil Engineering published by Springer. This is the sixth edition and the third international edition of SECON series of conferences organised by Federal Institute of Science and Technology (FISAT), Angamaly, Kerala, India, which has always enjoyed good acceptance and excellent participation from researchers from all across the country. SECON'22 was conducted in a hybrid mode over three days with an overwhelming response from delegates around the globe.

The conference was successful in providing a platform for research scholars, students, academicians and practising engineers for meaningful exchange of ideas and deliberations at an international level. The papers presented spread across current and future technologies, experimental investigations and research findings in the areas related to the conference themes and were presented in 20 parallel sessions spread over the span of three days. We believe that the deliberations of the conference helped us achieve the purpose of dissemination and passing on the innovative methodologies and practices in place globally.

This three-day International Conference on Structural Engineering and Construction Management (SECON'22) had extensive support and participation from across

the world, with papers from five international universities, several national institutions and R&D divisions of industries. More than 400 abstracts were screened and double-blind reviewed to shortlist 100 papers for presentation. The quality of the papers is presented, and almost 75% rejection rate are indicators of the standard the conference was able to accomplish.

On behalf of the organising committee, I express sincere thanks to Mr. Shimith P. R., Chairman, Governing Body—FISAT, Dr. Manoj George, Principal, Dr. C Sheela, Vice-Principal, and Dr. Mini P. R., Dean (Academics), whose constant guidance helped us to organise the conference. I would like to express my gratitude to each and every advisory committee members, reviewers, session chairs and the contributors of research for their constant support and efforts at making the conference a grand success. I extend my sincere gratitude to Prof. Shahria Alam, Prof. Alessandro Palermo, Prof. Moncef L. Nehdi, Dr. MO Kim Hung and Dr. Piyush Chaunsali, for their valuable time and input as the international advisory committee and keynote speakers. Their diligence and enthusiasm to be part of the event helped overcome the challenges of time zones at the peak of the pandemic. The conference also had support from industry and professional organisations both at national and international levels.

I would like to place on record the heartfelt thanks to ISTE-FISAT chapter, ASCE Student Chapter, IEI Kochi Local Centre, ICI Student Chapter and PARADIGM, for the unrelenting support for the conduct of the conference.

I extend my wholehearted thanks to Dr. Jiji Antony, General Convenor, and Head of Department, Department of Civil Engineering, Dr. Unni Kartha G., Co-Convenor, Dr. Kavitha P. E., Publication Chair, Dr. Asha Joseph, Programme Chair, Mr. Jawahar Saud, Publicity Chair, Ms. Rinu J. Achison, Finance Chair, and Mr. Sreerath S., Award and Certificate Chair, of SECON'22, for their constant encouragement and reason of keen interest in the various stages of the planning and execution of the event. I also take this opportunity to thank all our management committee members and executive committee of PTA who have shown great belief in us and urged us towards excellence for the growth of the institute and the students.

Last but not least, I would like to thank the entire team of faculty members, non-teaching staffs and student volunteers for the untiring support for the smooth conduct of the event. This conference would not have been possible without the incredible help and support of all our colleagues and scholars of the department.

Wishing you all very best and looking forward to the next edition of the event.

Angamaly, India   M. Preethi
                                                                          Convenor, SECON'22

Contents

PALFNet: A Soil Erosion Control Geotextile Using Pineapple Leaf Fiber

Darrel Jay Balbin, Dezirre Padilla, Jhann Benard Retamal, Ertie Abana, and Jay Ventura

Abstract Pineapple leaves are agricultural wastes from pineapples that are proliferative in the Philippines. Utilizing this agricultural waste as a renewable resource in the production of natural fiber geotextile instead of synthetic fibers is a step in the right direction both for the environment and the economy. Despite its wide array of applications, the potential of PALF (Pineapple Leaf Fiber) as a soil erosion geotextile is less explored. In this study, a soil blanket called PALFNet was fabricated from PALF. Pineapple Leaf Fibers (PALF) were separated from the leaves by the chemical retting process. The net efficiency or soil loss reduction efficiency that determines the effectiveness of the PALFNet in reducing soil loss during run-off was determined in this study. The fibers were washed and soaked with water then, it was air-dried. Production of a single spline rope was done by twisting two even sections of PALF in the same direction. The weaving of the PALFNet was done through an open-weave pattern by interlocking the single spline rope at a right angle with each other. The PALF rope which was used to create the PALF geotextile had higher tensile strength (6.79 MPa) than the commercially available coco twine. Results of the sediment yield analysis (21.44 g/m^2·h) showed that the PALFNet prevented significant mass runoff from the topsoil during the simulation. It is more efficient than the existing coconut fiber mat, water hyacinth fiber mat, and bamboo fiber mat. The water absorption capacity (163.40%) of the PALFNet reduced the damaging impact of raindrops making it effective in mitigating surface erosion and subsequent slope failure.

Keywords Pineapple leaf fiber · Geotextile · Soil erosion

D. J. Balbin · D. Padilla · J. B. Retamal
School of Graduate Studies and Continual Professional Development, University of Saint Louis, Tuguegarao City, Philippines

E. Abana (✉)
Center for Engineering Research and Technology Innovation, University of Saint Louis, Tuguegarao City, Philippines
e-mail: ertie04@gmail.com

J. Ventura
School of Engineering, Architecture, and Information Technology Education, University of Saint Louis, Tuguegarao City, Philippines

1 Introduction

Soil, just like any other natural resource, is limited. It takes long years to develop. But then, there's the environmental and agricultural concern that is soil erosion. The Intergovernmental Panel on Climate Change (IPCC) found out that soil currently erodes faster than it develops. Vital nutrients for crops are found in the topmost layer of soil called the topsoil. However, soil erosion strips off this significant layer making the soil less fertile. As a result, agricultural output decreases [1]. Meanwhile, sediments washed off from erosion go downstream. These block waterways causing water to inundate. Hence, flooding is more likely to occur. Aside from environmental and agricultural problems, soil erosion also poses economic problems. Because of soil erosion, the world Gross Domestic Product (GDP) is projected to lose eight billion US dollars yearly. It hits food security badly as a decrease in world agri-food production by 33.7 million tons and an increase in agri-food world prices of 0.4–3.5% are anticipated [2].

With more than 50% of the Philippines' land area being Philippine uplands with a slope above eight percent, the soil erosion phenomenon in the country is palpable. The Philippine Council for Agriculture, Aquatic and Natural Resources Research and Development (PCARRD) mentioned that strong rains, inappropriate land use and management, unstable tillage, and road construction make the situation even worse. More than half of the land area is already eroded in thirteen of the country's provinces namely Batangas, Cebu, Ilocos Sur, La Union, Batanes, Bohol, Masbate, Abra, Ilo-ilo, Cavite, Rizal, Capiz and Marinduque.

To reinforce soil and reduce the impact of soil erosions, the use of geotextiles as a protective cover was introduced in construction. Geotextiles are pervious textiles utilized in the soil to improve the engineering performance of soil structure [3]. The utilization of geotextiles in road construction and soil erosion control is not a novel idea. In ancient times, geotextiles made of natural fibers were used to strengthen roads. Geotextiles are either synthetic or natural. Synthetic geotextiles are expensive and non-biodegradable. In the long haul, it can be detrimental to the environment. Whereas, geotextiles fabricated from natural fibers are economical, biodegradable, and eco-friendly. Natural fibers decompose with the passage of time and become organic fertilizers thereby adding nutrients to the soil and enhancing soil fertility.

An example of a natural geotextile is the CocoNet. It is a geotextile made from coconut fibers and widely used for slope protection and soil erosion control. Other natural fibers as soil erosion control geotextiles were investigated in some studies such as bamboo fibers [4], water hyacinth fibers [5], rice straw [6], and pineapple leaf fibers [7]. Leaf fibers are hard fibers extracted from leaves with parallel veins of a monocotyledonous plant [8]. Pineapple leaf fiber (PALF) is used as a raw material for natural fiber composites [9], automotive applications [10], and pulp and paper production [11]. Its promising mechanical properties make it suitable for structural applications. [12] And its high strength-to-low weight ratio, affordability, abundance, and environmental benefits make it desirable for material replacement [8].

Pineapple leaves are agricultural wastes from pineapples that are proliferative in the Philippines. In fact, the country stayed as the second-biggest exporter of fresh pineapples worldwide in 2019. According to the United Nations Food and Agriculture Organization (FAO), it shipped a total of 667,633 MT which is 50% higher than its 447,570 MT shipment in 2018. It contributed 21% to the pineapple trade of the world. Utilizing mere agricultural wastes as renewable resources in the production of natural fiber geotextile instead of synthetic fibers is a step in the right direction both for the environment and the economy. Despite its wide array of applications, the potential of PALF as a soil erosion geotextile is less explored. In [7], the tensile strength of PALF geotextile was evaluated but not its soil reduction efficiency. In this study, a soil blanket called PALFNet will be fabricated from PALF. The blanket will then be subjected to a tensile strength test, water absorption capacity test, and surface run-off simulation to test its performance efficiency in mitigating soil erosion.

2 Materials and Methods

2.1 Soil Testing

Soil used for the surface run-off simulation was gathered from Larion Alto, Tuguegarao City Cagayan. The soil sample was tested in DPWH Regional Office II to identify its properties. The tests performed were MDR (Moisture-Density Relationship) Test, Liquid Limit and Plastic Limit Test and Grading Test.

The moisture-density relationship test defined in AASHTO T 99 Method C [13] (30% or less are retained on the 19 mm (¾ in) sieve was performed to determine the moisture-density relation of the soil using a 2.5 kg (5.5 lb) rammer and a 305 mm (12 in.) drop. The purpose of this laboratory test is to establish the relationship between the moisture content and the dry density of soil for a particular compactive effort. Soil, when placed in a dense state, is compacted to increase shear strength, decrease future settlements, decrease permeability and increase the stability of slopes of embankments.

The liquid limit is defined as the moisture content required to close a distance of 12.7 mm along the bottom of the groove after 25 blows. The plastic limit is defined as the moisture content at which the soil crumbles when rolled into threads of 3.00 mm. If it is wet, it breaks at a smaller diameter. If it is dry, it breaks at a larger diameter. The procedures defined in ASTM Standard D 4318 [14] were performed to determine the liquid limit and plastic limit of the soil.

The grading test of the soil defined in ASTM C 136 and AASHTO T 27 [15] was performed to determine the particle size distribution.

2.2 Fabrication of PALFNet

Pineapple leaves were collected at a pineapple plantation in Allacapan, Cagayan and transported to Tuguegarao City for preparation. The leaves were thoroughly washed to remove impurities before the extraction process as shown in Fig. 1.

Pineapple Leaf Fibers (PALF) were separated from the leaves, as shown in Fig. 2, by chemical retting process using 6% sodium hydroxide (NaOH) solution, soaking it within a 24-h duration [16]. The fibers were extracted by washing the soaked PALF with an ample amount of water to remove the remaining lignin and hemicellulose and to neutralize the NaOH applied to the fibers. Then, the fibers were air-dried to remove the free water content.

After extracting the fibers from the Pineapple leaves, the production of a single spline rope was carried out manually. The process done was twisting two even sections of PALF in the same direction. As the twisting continued, the two sections began to wrap around each other forming a single spline rope. As the tip approached, another set of PALF was attached to overlap the tails of the preceding set and to make them anchored together. This process was repeated until the desired length is attained [5].

The weaving of the PALFNet followed using the traditional open-weave pattern by interlocking the single spline rope at a right angle with each other as shown in Fig. 3. The mesh opening size was 25 × 25 mm to be identical to the sample coconet commercially available. The PALFNet will then be laid on an 850 mm (length) × 450 mm (width) soil for surface run-off simulation.

Fig. 1 Collection and preparation of pineapple leaves

Fig. 2 Extraction of Pineapple Leaf Fibers (PALF)
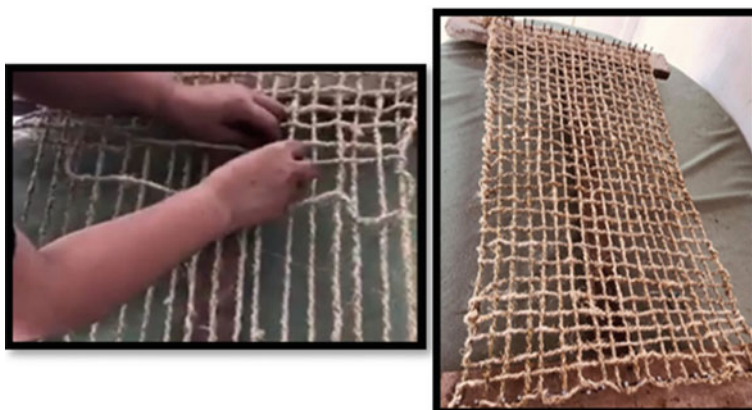
Fig. 3 Fabrication of PALFNet

2.3 Tensile Strength Test

Due to the unavailability of a Universal Testing Machine (UTM) for fiber ropes in the locality, the tensile strength test was done manually. A one-meter fiber rope carrying an empty bucket was tied to a horizontal rod 1.5 m above the ground as shown in Fig. 4. The mass of the empty bucket was recorded beforehand (m_{bucket}). Weights were added to the bucket little by little until the rope broke. The mass of the bucket with the weights at breaking point was recorded (m_{total}). This process was done on five samples PALF ropes and five sample coco twines. The tensile stress ("σ") was computed using Eq. 1 where net weight is computed using Eq. 2.

$$\sigma = \frac{net\ weight}{cross - sectional\ area\ of\ the\ rope} \tag{1}$$

$$net\ weight = (mtotal - mbucket)(9.81) \tag{2}$$

2.4 Water Absorption Capacity Test

The procedure defined in ASTM D570–98 was performed to determine the water absorption capacity of the fiber ropes [17–19]. The dry mass of the fiber rope was recorded (m_{dry}). It was soaked in water for 24 h as shown in Fig. 5. Then, the fiber rope was pat dried with a clean cloth as shown in Fig. 6. Its wet mass was recorded (m_{wet}). This process was done on five samples PALF ropes and five sample coco twines with a length of 700 mm and a diameter of 6 mm. The water absorption capacity (WAC) of the fiber rope was computed as:

Fig. 5 PALF ropes and coco twines soaked in water for 24 h

Fig. 6 PALF ropes and coco twines pat-dried with a clean cloth

$$WAC = \frac{m_{wet} - m_{dry}}{m_{dry}} \times 100\% \qquad (3)$$

2.5 Surface Run-Off Simulation

The average rainfall intensity used in the simulation was computed by measuring the time it took for the shower head to fill up a 152.4-mm container with water. The rainfall intensity from the water source (showerhead) was measured to determine the category of our artificial rainfall. The intensity falls under the category of torrential

Fig. 7 Experimental Test Beds with coconet (left) with PALFNet (middle) and bare soil (right)

rain, the highest category of rainfall intensity as per the Philippine Atmospheric, Geophysical, and Astronomical Services Administration (PAGASA). Torrential rain is more than 30 mm of rain is observed in 1 h and serious flooding is expected in low-lying areas.

Five trials were done on each of the three shower heads. A surface run-off test was done to simulate a run-off scenario on a soil testbed with a 30° slope using water as the principal agent of weathering and erosion [5]. Three soil testbeds were prepared to have a dimension of 850 mm (l) × 450 mm (w). Soil bed A was the soil with coconet, soil bed B was the soil with PALFNet and soil bed C was the bare soil as shown in Fig. 7. The erosion control test was done using an artificial rainfall which was water coming from three shower heads (one for each soil testbed) installed 2 ft. above and perpendicular to the top of the soil testbed. The rainfall intensity was maintained for 30 min.

Surface run-off from the top of the soil flowed through the gutter that was installed at the bottom of the slope, which was directed to a basin that will serve as a catchment. The volume of the run-off in the basins was collected every 5 min [5].

The collected sediments were filtered out using a canvas cloth and sun-dried before their masses (m_{dry}) were measured. The sediment yield was assessed as the rate of sediment removal from the watershed per unit area during a specified period and was calculated using Eq. 4.

$$Sediment\ Yield = \frac{m_{dry}}{surface\ area \times time} \tag{4}$$

The net efficiency or soil reduction efficiency of the PALFNet and coconet in mitigating soil erosion were evaluated using Eq. 5, where $m_{drycovered}$ is the dry weight of the sediments eroded from the geotextile-covered slope and $m_{dryuncovered}$ is the dry weight of the sediments eroded from the uncovered slope.

Table 1 Summary of the soil properties

Property	Value
Liquid limit (%)	39
Plastic limit (%)	27.48
Plasticity index (%)	11.52
Group index	0.24
Group classification	A-2-6 silty or clayey gravel and sand

$$Net\ efficiency = \frac{m_{dry,ncovered} - m_{dry,covered}}{m_{dry,uncovered}} \times 100\% \qquad (5)$$

3 Results and Discussion

3.1 Properties of Soil in Tuguegarao City

The test report on soil from Larion Alto, Tuguegarao City in Table 1 shows the summary of results obtained as per samples submitted.

The result indicates that the soil was identified as subgrade materials (Item 105) and classified as Silty or Clayey Gravel and Sand with an optimum moisture content of 18.86% and a maximum dry density of 1741 kg/m^3. Clayey soil with a high presence of organic matter is more resistant to erosion [20]. Although Silty soils are more prone to erosion, incorporating vegetation such as Vetiver zizanniodes, Leucaena Leucocephala, and Melastoma Malabathricum is effective in improving the factor of safety of slopes against shallow slip failure [21].

3.2 Testing Results

Table 2 presents the result of the tensile strength test done on five samples of 6-mm diameter coco twines and PALF ropes.

Table 2 Result of the tensile strength test on the different samples

Sample no.	Coconet (N)	PALFNet (N)	Coconet (MPa)	PALFNet (MPa)
1	108.40	164.81	3.83	5.83
2	121.15	205.52	4.28	7.27
3	169.71	183.94	6.00	6.51
4	145.68	159.90	5.15	5.66
5	136.36	245.25	4.82	8.67

Table 3 Result of the water absorption capacity test on the different samples

Sample no.	1	2	3	4	5
Coconet, m_{dry} (g)	4.5	4	3.7	3.9	4.7
Coconet, m_{wet} (g)	11.3	8.9	8.9	8.7	10.7
PALFNet, m_{dry} (g)	6.8	5.1	6.8	7.8	4.9
PALFNet, m_{wet} (g)	17.4	12.5	18.2	21.6	13.3
Coconet (%)	151.11	122.50	140.54	123.08	127.66
PALFNet (%)	155.88	145.10	167.65	176.92	171.43

The coco twine was able to carry a mean tensile load of 136.26 N and average tensile stress of 4.82 MPa while the PALF rope was able to carry a mean tensile load of 191.88 N and average tensile stress of 6.79 MPa. This implies that PALF rope is stronger than the coco twine by 55.62 N and 1.97 MPa. The higher tensile strength means it can hold off topsoil better thereby controlling soil loss.

Using Eq. 3, the water absorption capacity of the coco twine and PALF rope was calculated and recorded in Table 3 above.

The result shows that the coco twine has an average water absorption capacity of 132.98% while the PALF rope has average water absorption of 163.40%. This means that the PALF rope can absorb more water than the coco twine by 30.42%. The higher water absorption capacity means it can absorb more water thus reducing the damaging impacts of raindrops such as scouring.

The average rainfall intensity used in the simulation was found to be 45,285 mm/h which falls under the category of torrential rain. Surface run-off simulation was performed to compare erosion rates between bare and geotextile-covered slopes. The first 10 min of the simulation were omitted to allow full saturation of the soil. The mass of sediments washed off from the three testbeds during the simulation is recorded in Table 4.

The results of the sediment yield for the three testbeds are summarized in Table 5 and plotted in Fig. 8. For a torrential rain on silty or clayey gravel and sand-type soil at 30° slope, the results exhibited that coconet has an average sediment yield of 62.17 (g/m²·h), PALFNet has an average of 37.67 (g/m²·h) and the bare soil has an average of 465.01 (g/m²·h). The coconet accumulated 24.50 (g/m²·h) more sediment

Table 4 Mass of the sediments

Rainfall duration (minutes)	Coconet (grams)	PALFNet (grams)	Bare soil (grams)
15	1.9	3.9	65.8
20	7.6	5.2	50.7
25	4.3	7.6	99.9
30	27.2	4.1	28.2

Table 5 Sediment yield

Rainfall duration (minutes)	Coconet (g/m²·h)	PALFNet (g/m²·h)	Bare soil (g/m²·h)
15	19.87	40.78	688.10
20	59.61	40.78	397.65
25	26.98	47.69	626.82
30	142.22	21.44	147.45
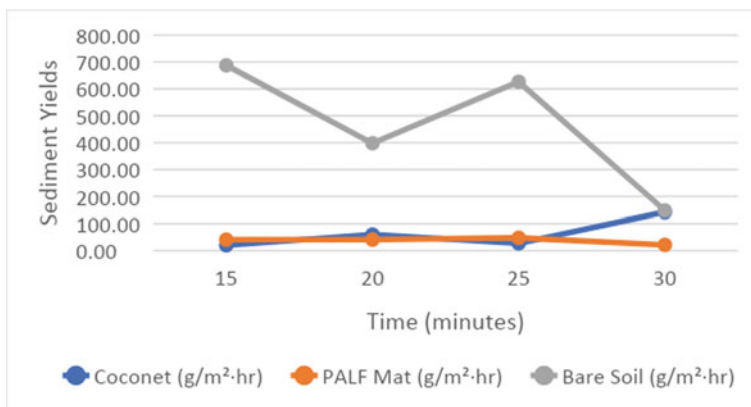
Fig. 8 Visualization of the sediment yield

yield than the PALFNet. The lower the sediment yield, the more controlled the soil erosion. Thus, soil erosion is most controlled in the PALFNet.

It is observed in Fig. 8, that the soils with geotextile cover consistently showed a significant reduction in sediment yield compared to the bare soil testbed. This can be attributed to the water absorption property of the coconet and PALFNet which reduces the raindrop impact on the soil surface layer. However, during the 30th minute of rainfall, the soil with coconet attained its maximum sediment yield of 142.22 (g/m²·h) which was very close to the bare soil which had 147.45 (g/m²·h). This can be associated with scouring of the soil in testbed A. It is during this time also that the soil with PALFNet reached the lowest sediment yield of 21.44 (g/m²·h).

The effectiveness of fiber mat in reducing soil loss during run-off is determined by calculating the net efficiency or soil loss reduction efficiency using formula (5) and the result of 5-min interval rainfall is tabulated in Table 6 and plotted in Fig. 9.

For torrential rain on silty or clayey gravel and sand-type soil at a 30° slope, the results revealed that PALFNet has an average of 90.42% reduction efficiency while coconet has an average of 80.38%. The PALFNet is more efficient than the coconet by 10.04%. Moreover, the net efficiency of PALFNet is higher than that of Water Hyacinth Fiber Mat (WHFM) with a net efficiency of 78.74% for 30° slope [5] and Bambusa Blumeana Fiber Mat with 74.70% for 60° slope [4]. The present

Table 6 Soil loss reduction efficiency

Rainfall duration (minutes)	Coconet (%)	PALFNet (%)
15	97.11	94.07
20	85.01	89.74
25	95.70	92.39
30	3.55	85.46
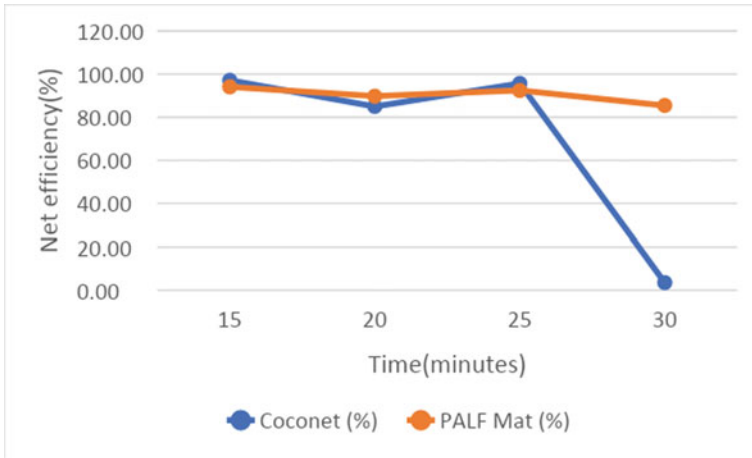
Fig. 9 Visualization of soil loss reduction efficiency

study confirmed the findings in [7] about PALFNet being a feasible replacement of commercially available geotextiles.

4 Conclusion

The performance efficiency of the PALFNet in mitigating soil erosion was investigated in this study in terms of tensile strength, water absorption capacity, and soil loss reduction efficiency using surface run-off simulation or rainfall simulation. PALF rope had higher tensile strength than coco twine. It also absorbed more water than coco twine. Results of the sediment yield analysis showed that the PALFNet prevented significant mass runoff from the topsoil during the simulation. It is more efficient than coconet and even Water Hyacinth Fiber Mat and Bambusa Blumeana Fiber Mat. The water absorption capacity of the PALFNet reduced the damaging impact of raindrops making it effective in mitigating surface erosion and subsequent slope failure. Instead of synthetic geotextile, an effective and eco-friendly soil erosion control geotextile can be made out of Pineapple Leaf Fiber (PALF).

To further validate the results of this study, sediment runoff analysis on actual slopes is recommended. Modifying this study with the consideration of vegetation on soil slopes is also recommended.

References

1. World Resources Institute: The Causes and Effects of Soil Erosion, and How to Prevent It. https://www.wri.org/insights/causes-and-effects-soil-erosion-and-how-prevent-it. Accessed 10 Mar 2022
2. Sartori, M., Philippidis, G., Ferrari, E., Borrelli, P., Lugato, E., Montanarella, L., Panagos, P.: A linkage between the biophysical and the economic: assessing the global market impacts of soil erosion. Land Use Policy **86**, 299–312 (2019)
3. Omar, R.C., Taha, H., Roslan, R., Baharuddin, I.N.Z.: Geotextile from pineapple leaves and bio-grout for slope stabilization and erosion control. Int. J. Geomate **17**(60), 219–224 (2019)
4. Valle, S.B., Albay, R.D., Montilla, A.M.: Bambusa blumeana fiber as erosion control geotextile on steep slopes. IOP Conf. Ser. Mater. Sci. Eng. **513**(1), 1–7 (2019)
5. Chow, M.F., Hashrim, H., Chong, S.T., Ng, Y.J.: Investigating the effectiveness of water hyacinth fiber mat for soil erosion control. IOP Conf. Ser. Mater. Sci. Eng. **551**(1), 1–5 (2019)
6. Deshmukh, A., Sikdar, P., Sahu, A.: A study on erosion control blankets made of rice straw. In: National Conference on Knowledge, Innovation in Technology and Engineering, pp. 408–409 (2015)
7. Celis, O.C.: Viability of pineapple leaves as an alternative natural fiber geotextile. IPTEK J. Proc. **3**(6), 28–32 (2017)
8. Lee, C.H., Khalina, A., Lee, S.H., Padzil, F.N.M., Ainun, Z.M.A.: Physical, morphological, structural, thermal and mechanical properties of pineapple leaf fibers. In: Pineapple Leaf Fibers, pp. 91–121. Springer, Singapore (2020)
9. Cesarino, I., Carnietto, M.B., Bronzato, G.R.F., Leao, A.L.: Fabrication of pineapple leaf fibers reinforced composites. In: Pineapple Leaf Fibers, pp. 265–277. Springer, Singapore (2020)
10. Reddy, B.S., Rajesh, M., Sudhakar, E., Rahaman, A., Kandasamy, J., Sultan, M.T.H.: Pineapple leaf fibres for automotive applications. In: Pineapple Leaf Fibers, pp. 279–296. Springer, Singapore (2020)
11. Praveen Kumar, A.: Pineapple leaf fibers: potential green resources for pulp and paper production. In: Pineapple Leaf Fibers, pp. 297–308. Springer, Singapore (2020)
12. Kayibanda, P., Mang'uriu, G., Onchiri, R.: Inspection of pineapple leaf fibers extraction to be used in construction industry. Environ. Pollut. Prot. **4**(2), 17–24 (2019)
13. GlobalSpec Engineering360: Standard Method of Test for Moisture–Density Relations of Soils Using a 2.5-kg (5.5-lb) Rammer and a 305-mm (12-in.) Drop. https://standards.globalspec.com/std/13399785/AASHTO%20T. Accessed 10 Mar 2022
14. ASTM International: Standard Test Methods for Liquid Limit, Plastic Limit, and Plasticity Index of Soils. https://www.astm.org/Standards/D4318. Accessed 10 Mar 2022
15. Coursehero: Standard Test Method for Sieve Analysis of Fine and Coarse Aggregates. https://www.coursehero.com/file/5967912/Sieve-Analysis/. Accessed 10 Mar 2022
16. Sarah, S., Rahman, W.A.W.A., Majid, R.A., Yahya, W.J., Adrus, N., Hasannuddin, A.K., Low, J.H.: Optimization of pineapple leaf fibre extraction methods and their biodegradabilities for soil cover application. J. Polym. Environ. **26**(1), 319–329 (2018)
17. ASTM International: Standard Test Method for Water Absorption of Plastics. https://www.astm.org/Standards/D570. Accessed 10 Mar 2022
18. Prasad, N., Agarwal, V.K., Sinha, S.: Banana fiber reinforced low-density polyethylene composites: effect of chemical treatment and compatibilizer addition. Iran. Polym. J. **25**(3), 229–241 (2016)

19. Théréné, F., Keita, E., Nael-Redolfi, J., Boustingorry, P., Bonafous, L., Roussel, L.: Water absorption of recycled aggregates: measurements, influence of temperature and practical consequences. Cem. Concr. Res. **137** (2020)
20. Seutloali, K.E., Beckedahl, H.R.: A review of road-related soil erosion: an assessment of causes, evaluation techniques and available control measures. Earth Sci. Res. J. **19**(1), 73–80 (2015)
21. Suhatril, M., Osman, N., Sari, P.A., Shariati, M., Marto, A.: Significance of surface eco-protection techniques for cohesive soils slope in Selangor, Malaysia. Geotech. Geol. Eng. **37**(3), 2007–2014 (2019)

Vulnerability Assessment of a Core Shelter: Basis for Development of a Flood and Wind Map

Rolando Bitagun Jr., Jaime Daliuag, and Ertie Abana

Abstract This study created a flood and wind map based on the findings of a vulnerability assessment conducted in one of Tuguegarao City's most vulnerable regions during a typhoon. Three vulnerability indicators were used for each hazard. The indicators for flood hazards were the presence of the second floor, the raising of the ground floor, and the presence of concrete slab while the indicators for wind hazard were roof shape, overhang, and roof vents. The average of the three-vulnerability factor was used to determine the total flood vulnerability rating and total wind vulnerability rating. Average vulnerability factors of 0.4 to 0.6 were colored with green, 0.6 to 0.8 was colored with yellow, and 0.8 to 1.0 was colored with red, indicating the vulnerability of the structure to the present hazard. The flood map shows that the majority of the households are very vulnerable to flooding. Meanwhile, the wind map shows that few houses can serve as temporary shelters for families that need to be evacuated during the occasion of typhoons.

Keywords Vulnerability assessment · Flood hazard · Wind hazard · Typhoon · Disaster maps

1   Introduction

The Philippines sits in what has been called the Tornado Alley of tropical cyclones which potentially provide freshwater to the country but could cause disaster due to strong winds and heavy rain [1]. Every year, the province of Cagayan in the Northern Philippines is hit by a slew of typhoons, each of which poses a threat to the livelihood, shelter, and, in some cases, life. Strong winds and flooding induced by such occurrences cause major damage to land and structures, as well as a high rate

R. Bitagun Jr. · J. Daliuag
School of Engineering, Architecture, and Information Technology Education, University of Saint Louis, Tuguegarao City, Philippines

E. Abana (✉)
Center for Engineering Research and Technology Innovation, University of Saint Louis, Tuguegarao City, Philippines
e-mail: ertie04@gmail.com

15

of mortality and a significant impact on rural populations. When typhoon Ompong struck the Philippines in September of 2018, Cagayan was battered. Around 182,000 homes were blown from their foundations, killing 6 people and injuring 25 more. The severe typhoon was believed to have caused agricultural damage worth 5 billion pesos and construction damage of around 3.8 million pesos [2].

Natural disasters typically result in significantly larger human and economic losses, particularly in low- and middle-income areas of the Philippines, where effective disaster risk reduction techniques have yet to be integrated or broadly available to communities and individuals [3]. The destructive repercussions of floods are difficult for people to comprehend. Despite receiving flood warnings, it appears that some residents in the community are underestimating the threat, causing them to delay leaving their homes despite the government's order to do so [4].

When the typhoon is strong, roofs are blown off and, in some instances, flash floods wash away structures. With these possible consequences, the urban poor is the most vulnerable ones, so people evacuate during the typhoon [5] and transfer to the evacuation center or neighbor's house where they feel safe. It is but a privilege that most of the time, people are accepted to shelter in their neighbor's homes but the assurance that the people are protected is still in question. This attempted to understand how today's actions and other human processes may influence future adaptive capacity. The response to future climate risks will likely be facilitated by past and present adjustments [6].

In this study, the vulnerability to flood and wind of houses at the Core Shelter in barangay Annafunan East was assessed. This community was identified as a high-risk community to typhoons and flooding by the Regional Disaster Risk Reduction and Management Council (RRDMC). A flood and wind community map, as the outcome, will show typhoon resilient shelters in the community so that people will know where the nearest shelter is to go just in case the roof of their house is blown off or the house is slowly being submerged in floodwater. It will promote the Filipino culture of Bayanihan before or during typhoons, especially for those people who do not want to leave their house despite prior announcements by the local government units. The technique used in the generation of the maps will contribute to the current body of knowledge on using GIS for Disaster Risk Reduction and Management. Most studies only focus on the assessment of shelters but do not apply the results of the assessment on a tangible output that can be presented to the people and concerned government agencies.

2   Methods

This section presents the area where the study was conducted, the data gathering procedure, vulnerability assessment of the different structures in the area, and the process of generating the hazard maps.
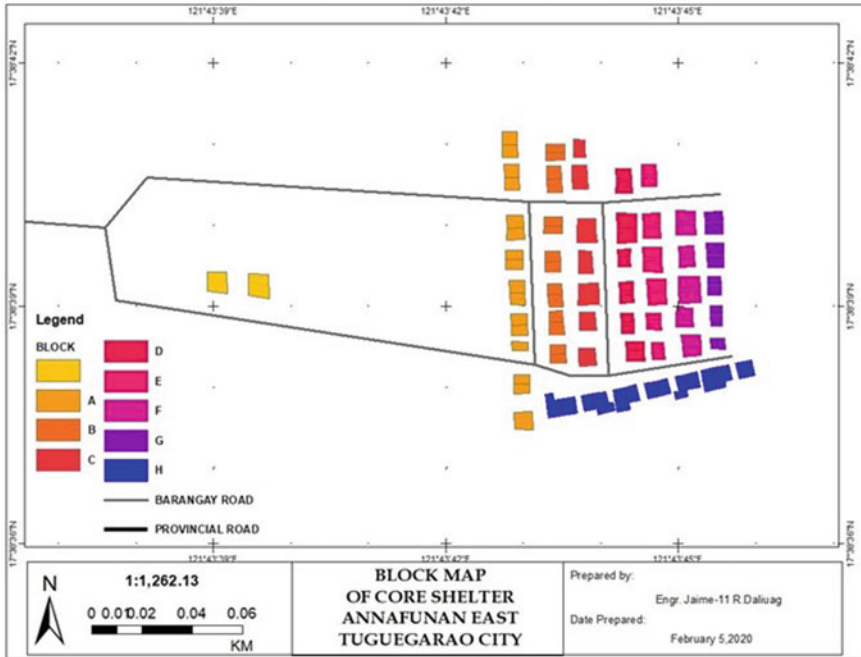
Fig. 1 Block map of Core Shelter, Annafunan East, Tuguegarao City

2.1 Study Area

Information about the Core Shelter in Annafunan East was collected from the barangay and certain government agencies which was analyzed for a better understanding of the current situation and existing conditions of the beneficiaries. There are 102 households currently residing at the Core Shelter which is distributed to different blocks from A to H with 2 adopted buildings as shown in Fig. 1. Buildings in Core Shelter are made of wood, reinforced concrete, and masonry. Most of the structures are duplex houses that shelter two households on a single roof and some houses only shelter a single household.

2.2 Data Gathering

The researchers coordinated first to the barangay before they went for an assessment. The Barangay Chairman allowed the researchers to do the assessment and ordered some of the Barangay Kagawad to assist the researchers in the area. The researchers used the assessment tool shown in Fig. 2 during the vulnerability assessment at the

Fig. 2 Sample assessment tool

Core Shelter. After the assessment, the results were listed in a spreadsheet for easier analysis.

2.3 Vulnerability Assessment

The flood and wind vulnerability of every shelter in the partner community was assessed using the method of [7]. The assessment will solely rely on the use of sight and reasoning based on Table 1. The utilized numeric bands for indicators F2 and W2 were patterned to [7] in order to facilitate speedy visual assessment without the need for a full survey in this study. The data was recorded and analyzed for it to be utilized in the hazard map generation.

After getting the hazard indicator of the households, the vulnerability factor shown in Tables 2 and 3 was used to determine the total vulnerability rating to flood and wind in the household. The average of the three-vulnerability factor was used to determine the total flood vulnerability rating and total wind vulnerability rating. Average vulnerability factors of 0.4 to 0.6 were colored green, 0.6 to 0.8 was colored yellow, and 0.8 to 1.0 was colored red, indicating the vulnerability of the structure towards the present hazard.

Table 1 Description of vulnerability for flood and wind hazards based on the study of [7]

Hazard	Indicator	Indicator no.	Options	Description
Flood	Presence of second story	F1	Yes, No	The presence of a second-level provides a location to keep possessions, minimizing the risk of loss
	Raising of ground floor	F2	0.0–0.25 m, 0.25–0.5 m, 0.5–0.75 m, 0.75–1.0 m	Loss of items is less likely when the ground floor level is raised
	Presence of concrete slab	F3	Yes, No	Floodwater is more likely to sweep away a structure with a slab foundation beneath timber posts
Wind	Roof shape	W1	Gable, Hipped	Wind pressure is better deflected by a hipped roof, which reduces the risk of roof damage
	Overhang	W2	0.0 m, 0.0–0.5 m, >0.5 m	Increased wind pressure at roof level is caused by a larger overhang, which increases the risk of roof damage
	Roof vents	W3	Yes, No	Winds can travel through the building with the presence of roof ventilation, which lowers wind pressure

Table 2 Vulnerability scale for flood hazard based on the study of [7]

Indicator	Options	Vulnerability factor
F1	Yes	0.5
	No	1.0
F2	0.75–1.0 m	0.25
	0.5–0.75 m	0.50
	0.25–0.5 m	0.75
	0.0–0.25 m	1.00
F3	Yes	0.50
	No	1.00

2.4 Hazard Map Generation

A flood hazard map and wind hazard map were generated based on the vulnerability assessment. The map of the Core Shelter that includes the houses was created. Different colors were used to represent the vulnerability of the shelter based on

Table 3 Vulnerability scale for wind hazard based on the study of [7]

Indicator	Options	Vulnerability factor
W1	Hipped Gable	0.5 1.0
W2	0.0 m 0.0–0.5 m >0.5 m	0.33 0.66 1.0
W3	Yes No	0.5 1.0

the indicator number. The map was generated using QGIS. QGIS is a free and open-source cross-platform desktop geographic information system application that supports viewing, editing, and analysis of geospatial data.

3 Results and Discussion

The results of the evaluation by previous studies [7] only show the assessment of surveyed buildings collectively in terms of proportions on the different factors using charts. This way of showing the assessment is less appreciated since this cannot be used by government agencies in identifying the particular structures that need help. On the other hand, the current study created a hazard map to show all the structures assessed with their corresponding vulnerability level using color legends as explained in the methods. This was done because prior studies [7, 8] said that an in-depth analysis of the hazards and impacts of flooding and typhoons on people and their properties was required.

The Core Shelter is at high vulnerability during flood season having most of the houses under high risk as shown in Fig. 3. The houses on the red mark can temporarily shelter in the yellow-colored ones which have a lower vulnerability if the immediate risk is present. Among the households in the area, there were 12 that live in a house that has a second story. However, most of these houses were still vulnerable to flood because their ground floors were not raised, and all are made up of concrete slabs. A concrete floor slab should only have 150 mm minimum thickness, based on laboratory testing [9], to avoid standing water.

Overall, the Core Shelter has low to high vulnerability to winds brought about by typhoons as shown in Fig. 4. Most houses are not that vulnerable to wind as compared with the flood. One reason for this is that houses have roof vents another is that houses have short overhangs or eaves. This indicates that wind forces will have a smaller effect on houses. In comparison to structures with no eaves overhang, the eaves overhang, which is widespread in Philippine detached structures, has a significant impact on the surface pressure coefficient and velocity streamlines [10].

Even though wind hazard is low, this paper doesn't account for the possibility of houses having weak connections of roofs which could potentially be a threat if it is left unaccounted for. The result isn't meant to be a complete substitute for a full
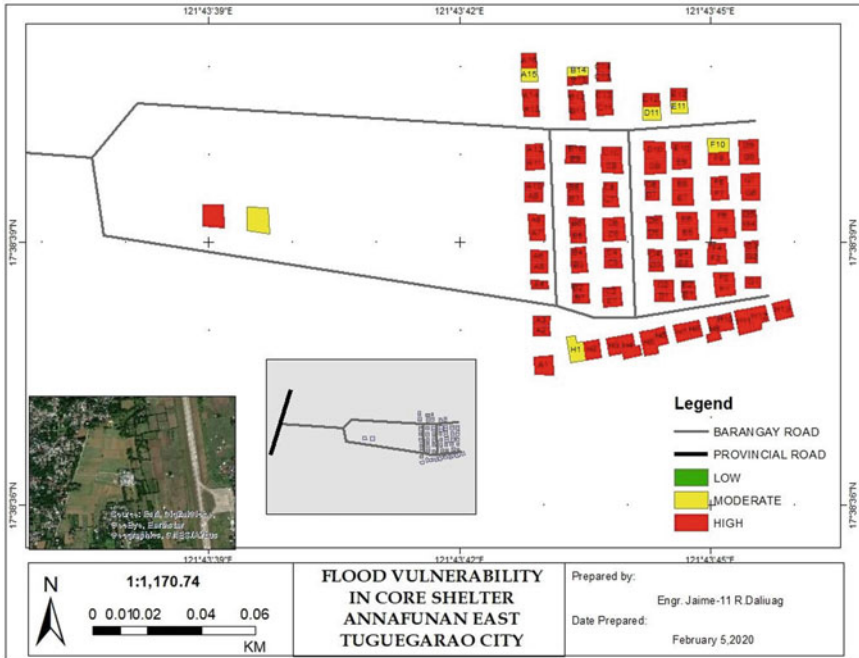
Fig. 3 Flood vulnerability map

mechanical or computational analysis of a structure's response. Rather, the purpose is to begin to grasp the danger presented to structures by taking these first steps toward treating them as vulnerable assets, particularly those in low elevation barangays, using an acceptable and practicable framework.

The assessment used in the study was developed to achieve a disaster-free community [11] which is the primary concern by the researchers. The main beneficiaries of the maps are those people who live in houses that were assessed as non-resilient shelters. The Local Government Unit (LGU) in the selected partner community will also benefit from the results because the map can serve as a basis for crafting policies that will lead to the betterment of the community. Also, the LGU can use the result of the study in identifying what materials can be given to the stakeholders for the community to lessen the effects of typhoons and floods. It can also identify the nearest household they can temporarily transfer.
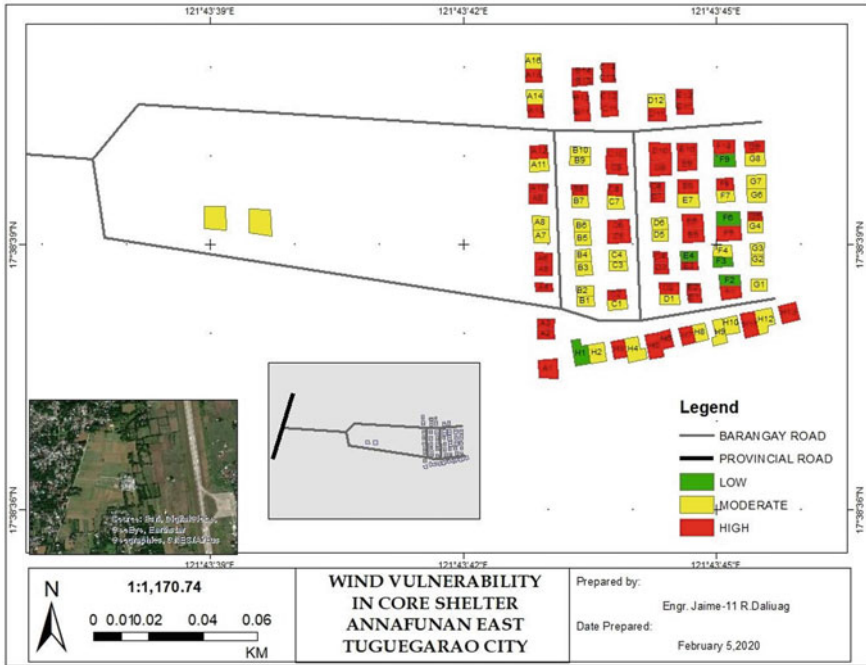
Fig. 4 Wind vulnerability map

4   Conclusion

This study concludes that a flood and wind map can be generated to show the vulnerability to flood and wind during typhoons of every house in a community. These maps show that most of the houses in the study area are vulnerable to floods and strong wind but some houses can serve as temporary shelter for those who need help during the disaster. The maps that were created using the vulnerability assessment can help the local government unit or the disaster management agency to give out materials that can reduce the damage of an incoming typhoon.

With all the findings of the study, it is recommended that the same study should be conducted in other barangay in Tuguegarao, especially those areas that are always affected by flooding and strong winds during a typhoon. The result of the study should be presented to LGU Tuguegarao and the RRDMC of Cagayan for proper validation. Moreover, the results of the assessment can be used as the basis for evacuation plan strategies.

References

1. Kubota, H., Chan, J.C.L.: Interdecadal variability of tropical cyclone landfall in the Philippines from 1902 to 2005. Geophys. Res. Lett. **36**(12), 1–4 (2009)
2. Philippine Atmospheric, Geophysical and Astronomical Services Administration (PAGASA). 2019 Annual Tropical Cyclone Tracks. https://www.pagasa.dost.gov.ph/index.php/tropical-cyclones/annual-tropicalcyclone-tracks. Accessed 08 Mar 2022
3. Jha, S., Martinez, A.Jr., Quising, P., Ardaniel, Z., Wang, L.: Natural disasters, public spending, and creative destruction: a case study of the Philippines (2018)
4. Esteban, M., Valenzuela, V.V., Namyi, Y., Mikami, T., Shibayama, T., Matsumaru, R., Takagi, H., Thao, N.D., de Leon, M., Oyama, T., Nakamura, R.: Typhoon Haiyan 2013 evacuation preparations and awareness. Int. J. Sustain. Future Hum. Secur. **3**(1), 37–45 (2015)
5. Baker, J.: Climate Change, Disaster Risk and the Urban Poor: Cities Building Resilience for a Changing World, 1st edn., Washington, DC (2012)
6. Brooks, N., Adger, W.N.: Assessing and enhancing adaptive capacity. Adaptation policy frameworks for climate change: developing strategies, policies and measures, United Nations development Programme - Global Environment Facility, pp. 165–181 (2005).
7. Stephenson, V., Finlayson, A., Morel, L.M.: A risk-based approach to shelter resilience following flood and typhoon damage in rural Philippines. Geosciences **8**(76), 573–596 (2018)
8. Opella, J.M.A., Hernandez, A.A.: Developing a flood risk assessment using support vector machine and convolutional neural network: a conceptual framework. In: 2019 IEEE 15th International Colloquium on Signal Processing & Its Applications (CSPA), pp. 260–265 (2019).
9. Tagg, A., Laverty, K., Escarameia, M., Garvin, S., Cripps, A., Craig, R., Clutterbuck, A.: A new standard for flood resistance and resilience of buildings: new build and retrofit. In: E3S Web of Conferences, vol. 7, no. 13004 (2016)
10. Enteria, N.A.: CFD evaluation of Philippine detached structure with different roofing designs. Infrastructures **1**(3) (2016)
11. Opella, J.M.A., Hernandez, A.A.: User acceptance of flood risk and hazard mapping system: a field survey in the Philippines. In: 2019 IEEE 9th International Conference on System Engineering and Technology (ICSET), pp. 374–379 (2019)

Effect of Openings in Post-tensioned Shear Wall with External Energy Dissipating Reinforcements Under Cyclic Loading

Sneha Benoy and Asha Joseph

Abstract One of the most recent advancements is the use of post-tensioned tendon in conventional shear walls in order to improve the lateral stiffness and lessen the damage caused by devastating earthquakes. A system of well-designed post-tensioned shear wall can significantly improve the seismic performance of a building. The behaviour of unbonded post-tensioned shear wall under lateral load exhibits a stable and large hysteresis loop, which accounts for good inelastic energy dissipation without much loss in the self-centering behaviour. The purpose of this study is to develop and analyze the performance of post-tensioned hybrid shear walls with energy dissipating reinforcements [EDR] for improving the energy dissipating and self-centering capability of shear wall. EDR in the form of simple mild steel rods is considered for the present study which is placed outside the shear wall to facilitate its easy placement and replacement after an earthquake. The system is expected to withstand earthquakes with less damage and residual drift compared to conventional systems and provides cost effective method to mitigate seismic effects. To understand the behaviour of hybrid shear wall, the structure is modelled in ANSYS software. Non-linear static analysis is carried out and the effect of openings under cyclic loading is analysed. Performance of shear wall under different opening configurations like rectangle, square, circle and diamond are carried out and results are compared with a solid shear wall. The openings are having a constant cross-sectional area and the location of openings is not varied in this present study. Results are analyzed based on the response parameters like base shear, stress and strain concentrations, energy dissipation and stiffness degradation and a suitable opening configuration is suggested based on the obtained results.

Keywords Shear walls · Openings · Energy dissipation · Non-linear analysis · Resilient systems

S. Benoy (✉) · A. Joseph
Federal Institute of Science and Technology, Angamaly 683577, India
e-mail: snehabenoy17@gmail.com

1   Introduction

Developed countries have managed to reduce the number of fatalities lost in recent earthquakes. Having accomplished this, these countries are focusing on reducing the economic damage caused by earthquakes. To that end, efforts are made to reduce building damage during earthquakes. In the last two decades, shear walls have been incorporated in buildings to reduce the effects of lateral forces. Although the use of structural walls limits building damage, ensuring continuous building functionality after earthquakes remains a challenge. The said challenge is a critical component to reduce the loss related to the repair and rehabilitation of the building. To overcome the shortcomings of traditional RC shear walls [1–3] the present study utilizes post-tensioned (PT) tendons. A properly designed system of post-tensioned shear wall in a building can greatly improve its seismic performance. The behaviour of unbonded PT shear wall under lateral load illustrates that the use of PT tendons can provides a stable hysteresis loop, which in turn can enhance its energy dissipation capacity without any appreciable loss in the self-centering behaviour [4, 5].

Recent studies have demonstrated the efficacy of post-tensioned RC shear walls such as improved seismic load carrying capacity, permanent deformation reduction, re-centering potential and higher energy dissipating capability [5–7]. The restoring force provided by the post-tensioning tendons eliminates the permanent deformation after cyclic loading and lowers the displacement demands during a cycle. To enhance the energy dissipation, energy dissipating reinforcements [EDR] in the form of simple mild steel bars is provided outside the shear wall. These bars which crosses the base joint are intended to yield in compression and tension. The energy dissipation is attained through the gap opening/closing behavior at the base of the wall under reversed-cyclic loading. When lateral loads are applied into the nonlinear range, the primary mode of deformation in a system of hybrid shear wall occurs due to a gap opening (as shown in Fig. 1) at the horizontal junction between the foundation and the base panel [8]. When unloaded, the PT steel provides a vertical restoring force (in addition to the gravity loads) to close the gap at the base joint, resulting in a significant reduction in residual (i.e., permanent) lateral displacement of a structure after a severe earthquake. This hybrid system is expected to withstand earthquakes with less damage and residual drift compared to conventional systems and which provides cost effective method to mitigate seismic effects.

Openings in a shear wall can have a significant impact on the structure's overall seismic response. As a result, it is critical to comprehend the impact of openings on shear wall behaviour [9]. A study by Salenikovich et al. [10] on the effect of openings in cold-formed steel composite walls depicted that shear strength and rigidity of the wall with openings were relatively lower than those of the wall without openings, but its ductility was higher than that of the wall without openings. Since in certain circumstances, to meet the functionality, buildings may be perforated with rows of openings.
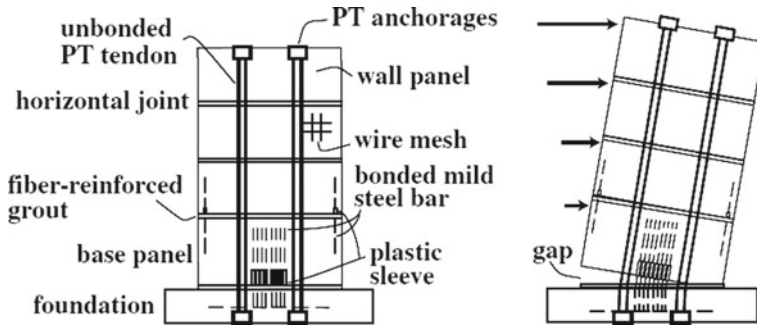
Fig. 1 Displaced position of hybrid wall system under lateral loads [8]

From the literature survey, it has been identified that limited studies have been carried out in this domain and there is a further scope for analysis of behaviour of hybrid shear walls under the effect of openings. Owing to this aspect, an attempt has been made in the current study to understand the behaviour of hybrid shear wall with post-tensioned tendons and external energy dissipating reinforcements (EEDR) under the effect of openings. Numerical study considering different opening configuration is carried out in finite element software ANSYS. Simulation results from the non-linear static analysis such as base shear v/s displacement, stress and strain concentration, energy dissipation and stiffness degradation are used to compare the performance of different shapes of openings and suggest a suitable configuration.

2 Model Configuration

Numerical analysis of post-tensioned shear walls is conducted using ANSYS Workbench 16.0 software. The word "hybrid" refers to the use of a combination of mild reinforcing steel and high-strength unbonded post-tensioning (PT) steel for lateral load resistance across the joints. The adopted shear wall is having a height (hw) of 3.6 m, span (lw) of 2.2 m and 0.1 m thickness (tw). The concrete shear wall rests on the foundation having a dimension of 2400 × 300 × 100 mm, and is modelled as a rigid beam to simulate a strong floor beam. At the bottom portion of the shear wall, energy dissipating reinforcement (EDR) in the form of mild steel bars is provided spanning between an angle section (ISA 75 × 75 × 10) which is attached to the shear wall and a channel section (ISMC 100) which is embedded inside the foundation. The length of EDR is taken as 25 db as per ACI-ITG 5.2 (ACI 2009) [11] with a tapered section having a diameter of 10 mm at the ends and 9 mm at the middle portion.

From preliminary studies, it has been observed that bars of uniform size have the tendency to fail at its threaded portion near the connection. This occurs primarily occurs due to the non-uniform distribution of stresses at lower percentage elongation [12]. Therefore, the weak zone of EDR was shifted from the anchorage end portion to the middle portion by making the diameter at the ends larger than the middle one-third portion to avoid such failure. Model details of EDR connection is shown in Fig. 2. A single band of openings with various shapes like rectangle, square, circular and diamond are contrived. The openings are located at the mid portion of the shear wall and the area of each opening is kept constant as 1×10^5 mm. Detailed geometric details of shear wall with openings are provided in Table 1. Figure 3 provides the configuration details of the openings.
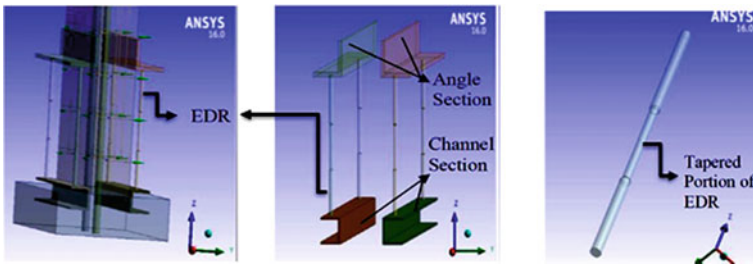
Fig. 2 Connection details of EDR

Table 1 Details of wall specimen with openings

Opening configuration	Dimension (mm)	No. of openings	Total opening (%)
Rectangle	b = 300, h = 500	4	11.12
Square	a = 316.3	5	13.89
Circle	d = 356.82	5	13.89
Diamond	d1 = 500, d2 = 400	4	11.12
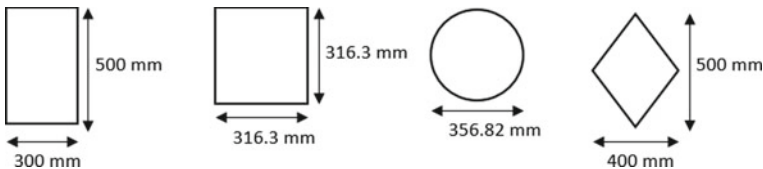
Fig. 3 Geometric details of openings

3 Reinforcement Details

Shear wall is provided with both longitudinal and lateral reinforcements, tie bars and confining reinforcements at boundary. The reinforcements are spaced at 100 mm and each opening is separated by a distance of 300 mm. The wall is provided with 4 # 20 mm ø PT tendons which are embedded inside the shear wall. The wall is provided with 4 # 20 mm ø PT tendons which are embedded inside the concrete shear wall and 4 number of EDR located outside the shear wall. A design force (tensile) of 73.9 kN (0.45 f_{pe}) is applied for each PT tendon as per the analysis done earlier [1]. The number of openings is varied based on the available area for providing the openings. With identical area for each opening (1×10^5 mm^2), the total area of openings is adopted such that it is less than half of the area of the wall panels.

4 Finite Element Modelling

The element library of ANSYS contains several types of elements. ANSYS modelling comprises of providing proper elements, establishing geometry, and assigning appropriate material models. The foundation beam, concrete wall, PT tendons and loading plates are modelled using higher order three-dimensional, twenty-node solid element called SOLID 186 element which exhibits a quadratic displacement behaviour. Each node of these elements has three translational degrees of freedom (DOF). The reinforcing elements (longitudinal, transverse and confining reinforcement) are modelled using three-dimensional two-node beam elements called BEAM 188 with six DOF's in each node. In the model, angle and channel sections are attached to the wall and the foundation beam, respectively. The EDR, channel and angle sections are modelled using the SOLID 186 element as solid elements.

To verify the approach used in this study, a validation was conducted for the hybrid shear wall with post-tensioned tendons and external energy dissipating reinforcements. The paper taken for validation is the work done by Taori et al. [12]. The results from the validation were found to be in good agreement with the numerical model developed by Taori et al. The maximum difference in the base shear of the two models were found to be about 5.86% observed at 2.4% drift [1]. Then the behaviour of hybrid shear wall with and without openings is compared.

5 Material Properties and Boundary Conditions

The behaviour of concrete is characterized using the concrete damaged plasticity model. EDR and reinforcements are modelled using a bilinear curve with strain-hardening, with reference to yield, ultimate stress, and strain values. Table 2 gives

Table 2 Reinforcement properties

Reinforcement type	Diameter (mm)	f_y (MPa)	f_u (MPa)	ε_y	ε_u	E (GPa)
Distribution steel	6	528	622	0.0025	0.15	210
EDR	9	550	650	0.0027	0.14	206
Tie rod	12	502	563	0.0024	0.14	208

Table 3 Concrete and PT tendon properties

Material type	Modulus of elasticity (MPa)	Compressive strength (MPa)	Poisson's ratio	Yield strength (MPa)	Ultimate strength (MPa)
Concrete	31,622	40	0.15	–	–
PT tendons	2×10^5	–	0.3	1650	1850

the properties of reinforcements and Table 3 gives the material properties of concrete and PT tendon used for the study.

To stimulate strong floor behaviour, the bottom end of the foundation is considered as a fixed base. The nodes of the foundation are constrained fully to realize the fixed end. To assure calculation accuracy and save computing time, meshing of elements was done using medium size mesh. Cyclic loads are applied to a loading plate of size 200×100 mm at a height of 2.793 m from the base of foundation. The load is applied in the X-axis direction with Y and Z axes degrees constrained. Figure 4 shows the boundary and loading conditions for shear wall with rectangular opening. The same is applicable for all other shear walls.

6   Loading Protocol

The cyclic load test is conducted on the PT shear walls with opening and a reference shear wall specimen without opening to simulate its behavior under seismic loads. Prior to applying cyclic loads, gravity load and post-tensioning of the tendons is done. A design tensile force of 73.9 kN ($0.45 f_{pe}$) is induced in each PT tendon. The loading protocol for shear wall is shown in Fig. 5.
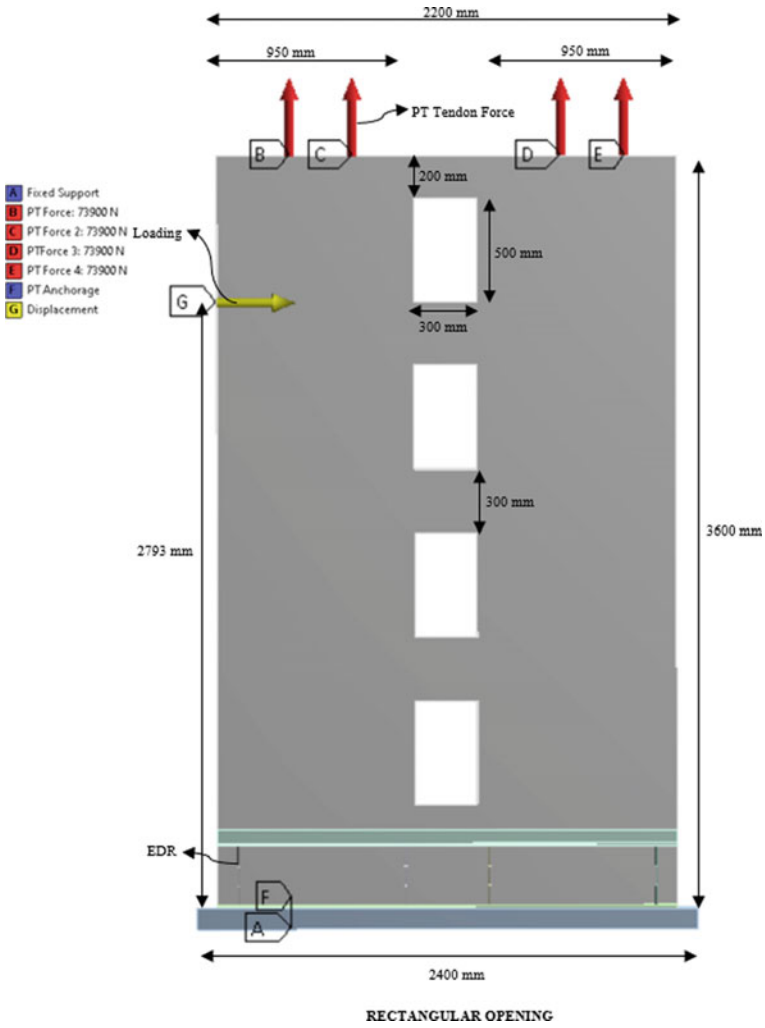
Fig. 4 Modelled hybrid shear walls with loading and boundary conditions
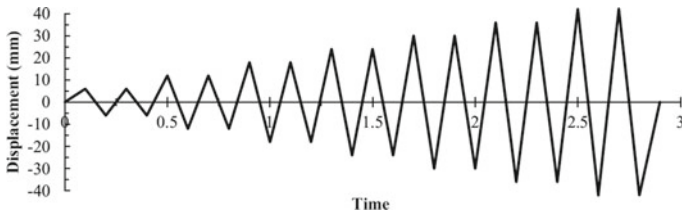
Fig. 5 Cyclic load applied to the numerical models

7   Results and Discussion

The results of the test are obtained in terms of base shear-displacement plots, stress and strain concentration, energy dissipation and stiffness degradation. A conclusive outcome is obtained based on the obtained results.
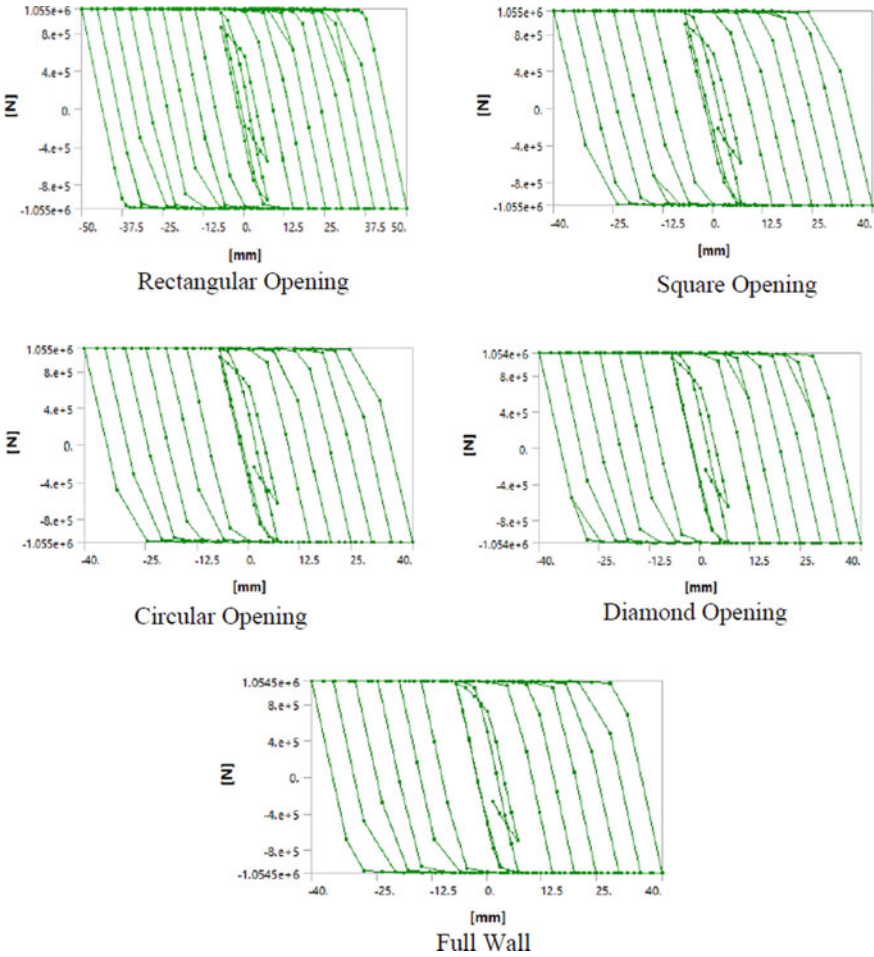
Fig. 6 Base shear-displacement curves of shear wall under cyclic loading

7.1 Base Shear v/s Displacement

The obtained hysteresis curves of the specimen when subjected to cyclic loading was found to exhibit an elasto-plastic model as given in FEMA P440A [13]. These models do not incorporate strength degradation when subjected to repeated cyclic load reversals. Figure 6 shows the lateral load–displacement curves of each specimen under cyclic loading obtained from ANSYS.

Each specimen's lateral load–displacement hysteretic curve shared the following characteristics: the specimen was in an elastic state during the first loading stage, and the relation between lateral force and displacement was essentially linear. The envelope areas of the hysteretic loops were initially small, but when the drift ratios increased, the envelope areas of the hysteretic loops of the specimens gradually increased. This is due to the fact that longitudinal reinforcing bars started to yield beyond the elastic region and the stiffness degradation became gradually more apparent.

7.2 Stress–Strain Concentration

Table 4 gives the stress and strain concentrations of shear walls with and without opening under cyclic displacement loading.

From the equivalent elastic stress contour plots, it was observed that near the openings, stress is concentrating more. The highest stress and strain were measured for square opening during cyclic displacement. Diamond opening experienced a lesser stress when subjected to cyclic loading. In fact, the stresses were less than those felt by complete shear wall. Maximum stress was observed for rectangular openings which was 17.64% higher than that of solid wall without opening. Providing diagonal reinforcements can be considered as an option to reduce the stresses near openings. A detailed study can be carried out on this aspect as well.

Table 4 Maximum stress and strain values under cyclic loading

Opening type	Max equivalent stress (MPa)	Max elastic strain (mm/mm)
Rectangle	396.18	1.35
Square	394.13	0.19
Circle	364.27	0.17
Diamond	331.75	0.19
Reference specimen	336.75	0.14
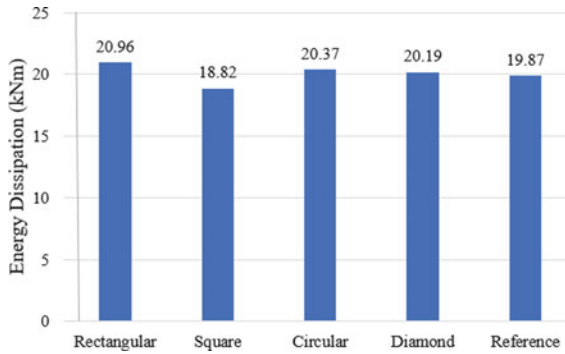
Fig. 7 Energy dissipation capacity of shear walls

7.3 Energy Dissipation

In addition to acceptable drift level, energy dissipation capacity is a desirable attribute in shear wall behaviour. The accumulation of all the energy dissipation cycles is called the cumulative dissipated energy. Although the accumulative dissipated energy when the structure fails is an important parameter, it necessarily does not indicate the level of deformation at which this energy is dissipated [14, 15]. The total area under the load displacement hysteretic loop is typically used to calculate the dissipating energy capacity (ED).

Figure 8 gives the hysteresis loop considered for energy dissipation calculation for each specimen and Fig. 7 is the bar chart representing the energy dissipation capacity of all specimens. The dissipated energy was found to be fairly small for drifts less than 1%. For 1% drift, it was observed that rectangular opening dissipated maximum energy. Except square opening, all other openings dissipated energy higher than solid wall. However, for larger drifts, a nearly linear increase in dissipation capacity was observed.

7.4 Stiffness Degradation

Stiffness degradation is a significant issue in evaluating the seismic performance of shear walls, and the amplitude and rate of stiffness degradation are related to the structures' safety and reliability. Stiffness degradation describes the phenomenon of the mode's secant line stiffness reducing continuously as lateral displacement increases [16].

Figure 9 shows the stiffness degradation curves in the shear wall specimen when subjected to cyclic loading. As loading increases, the stiffness of the walls decreases and secant line degenerates most rapidly in the case of square opening. As expected, the initial stiffness was higher for shear wall without opening. Walls with opening
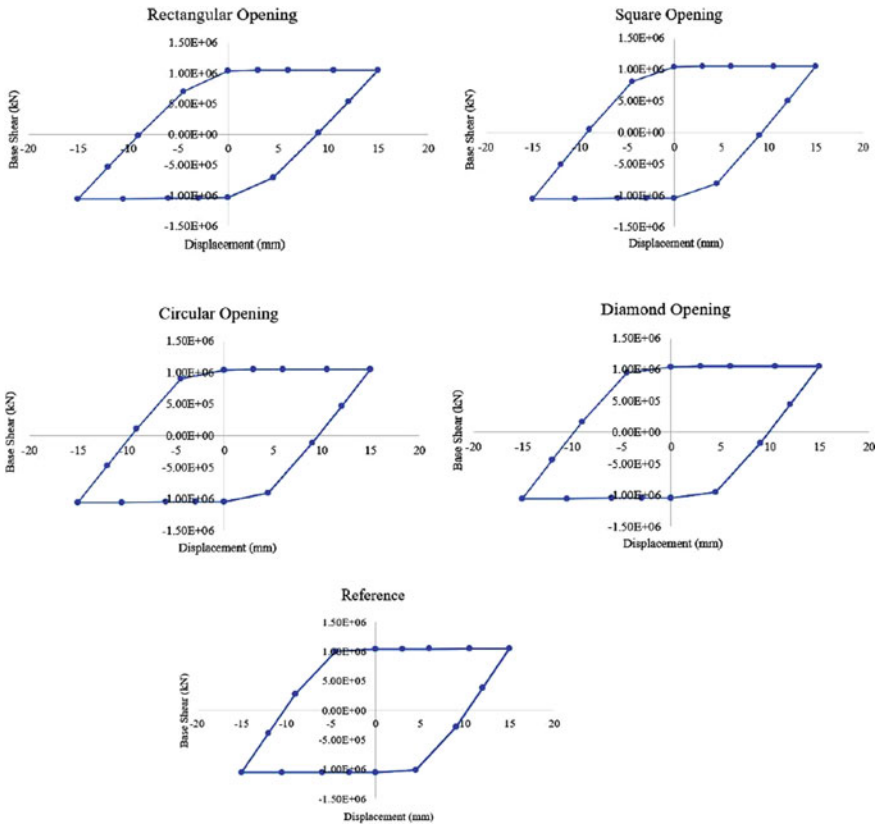
Fig. 8 Hysteresis loop considered for energy dissipation

experienced a reduction in initial stiffness as well as in the stiffness reduction. It was observed from the analysis that square opening had the lowest initial stiffness under cyclic loading. 46% reduction in initial stiffness has been observed in square opening, while rectangular and circular opening experienced a reduction of 32% only. Diamond opening had an initial stiffness of 430 kN/mm and only 14% reduction in initial stiffness has been observed depicting the fact that diamond opening can perform better than the other openings.

When the horizontal displacement was 12 mm, the secant stiffness of solid wall was found to be 65 kN/mm. Except diamond opening, all the shear walls with opening had a stiffness value lesser than that for solid wall at 12 mm. But it was observed that for diamond opening, the stiffness was 101.23 kN/mm, which was 35.78% higher than that for solid wall. The stiffness degradation was found to be gradual in the case of diamond opening.
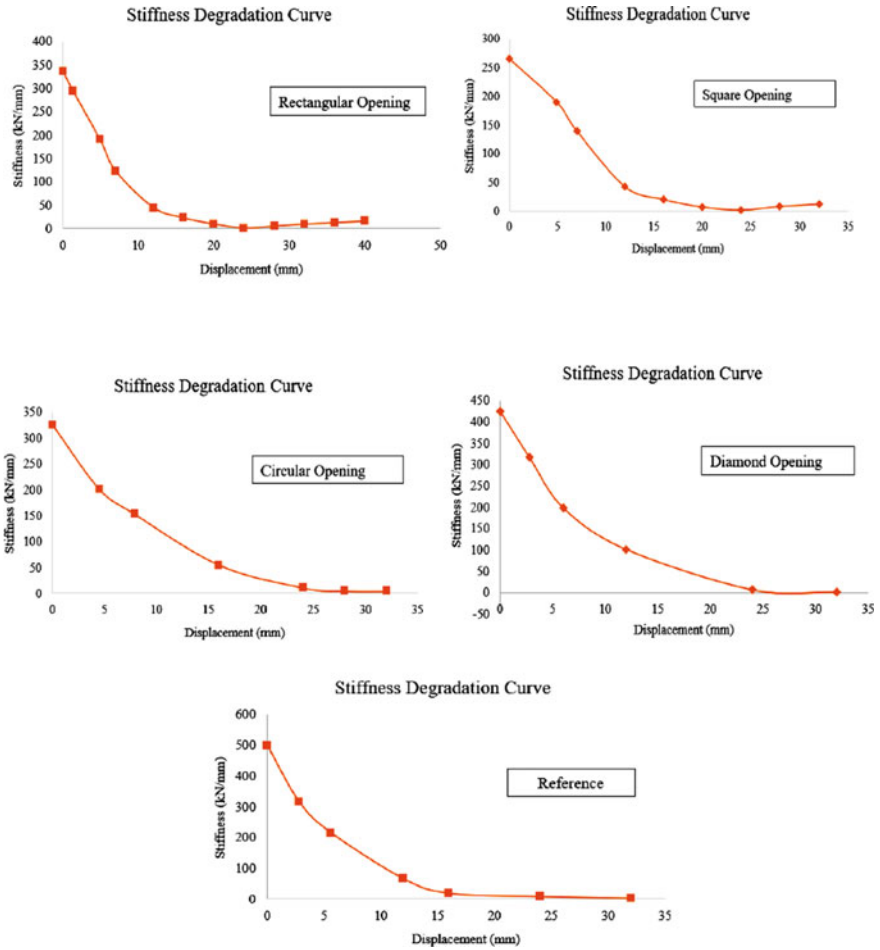
Fig. 9 Stiffness degradation curves of shear walls

8 Conclusion

In recent years, significant amount of research has been conducted on concrete shear wall system for seismically active regions out of which unbonded post-tensioned shear wall system has emerged as a new and resilient system for coping earthquake forces. Recent researches indicate that post-tensioned reinforced concrete shear walls have outstanding characteristics like increased stiffness of walls, strength and stability, damage control and reduced lateral displacements to sustain lateral loads in the aftermath of an earthquake. The present study focuses on hybrid shear wall with post-tensioned tendons and energy dissipating reinforcements in the form of mild steel bars.

A study on the nonlinear behavior of a shear wall with and without opening is performed through the conduct of cyclic load test. The results of shear wall with openings like base shear, stress and strain, energy absorption, and stiffness degradation are compared to shear walls without opening and a suitable opening configuration is suggested based upon the obtained results.

The results of shear wall under cyclic displacement loading shows that:

- Maximum stress was observed for rectangular opening while diamond opening experienced the least stress under cyclic displacements.
- In contrast, the energy dissipation was found higher for rectangular opening by 5.64% while square opening experienced the least energy dissipation than solid wall.
- Each specimen's lateral load–displacement hysteretic curve shared the following characteristics: the specimen was in an elastic condition during the first loading stage, and the relationship between lateral force and displacement was essentially linear.
- Diamond opening experienced lesser stress when it was exposed to cyclic loading. In fact, the stresses were less than those felt by complete shear wall.
- Maximum stress was observed for rectangular openings which was 17.64% higher than that of solid wall without opening.
- 46% reduction in initial stiffness has been observed in square opening, while rectangular and circular opening experienced a reduction of 32% only.
- Diamond opening had an initial stiffness of 430 kN/mm and only 14% reduction in initial stiffness has been observed depicting the fact that diamond opening can perform better than the other openings.

From the present analysis, it has been inferred that providing diamond opening can be considered a possible option as the results proves to be in good agreement with the actual full shear wall without compromising on the structures performance and load carrying ability.

References

1. Benoy, S., Joseph, A.: Numerical investigation and parametric analysis of hybrid shear wall with energy dissipating reinforcements. In: International Conference on Structural Engineering and Construction Management, pp. 191–203. Springer, Cham (2021)
2. Holden, T., Restrepo, J., Mander, J.B.: Seismic performance of precast rein-forced and prestressed concrete walls. J. Struct. Eng. **129**(3), 286–296 (2003)
3. Shatnawi, A., Abdallah, S.G., Tarawneh, B.: Seismic behavior of hybrid post-tensioned cast in place concrete shear walls. Arab. J. Sci. Eng. **44**(5), 4095–4109 (2019)
4. Perez, F.D.J.: Lateral load behavior and design of unbonded post-tensioned precast concrete walls with ductile vertical joint connectors. Thesis and Dissertations (1998)
5. Benoy, S., Joseph, A.: Seismic behaviour of post-tensioned concrete shear wall: a review. Sustain. Agri Food Environ. Res. **10**(1), 1–11 (2022)
6. Erkmen, B., Schultz, A.E.: Self-centering behavior of unbonded, post-tensioned precast concrete shear walls. J. Earthquake Eng. **13**(7), 1047–1064 (2009)

7. Lu, X., Yang, B., Zhao, B.: Shake-table testing of a self-centering precast reinforced concrete frame with shear walls. Earthq. Eng. Eng. Vib. **17**(2), 221–233 (2018)
8. Smith, B.J., Kurama, Y.C., McGinnis, M.J.: Design and measured behavior of a hybrid precast concrete wall specimen for seismic regions. J. Struct. Eng. **137**(10), 1052–1062 (2011)
9. Varma, V.N.K., Kumar, U.P.: Seismic response on multi-storied building having shear walls with and without openings. Mater. Today Proc. **37**, 801–805 (2021)
10. Salenikovich, A.J., Dolan, D.J., Easterling, S.W.: Racking performance of long steel-frame shear walls. In: Proceedings of the 15th International Specialty Conference on Cold-formed Steel Structures, St. Louis, MO, USA (2000)
11. ACI: Requirements for design of a special unbonded post-tensioned precast shear wall satisfying ACI-ITG-5.1 and commentary. ACI-ITG-5.1-09, ACI Committee 93, American Concrete Institute (2009)
12. Taori, P., Dash, S.R., Mondal, G.: Seismic response of post tensioned hybrid shear walls with external energy dissipating reinforcement (EEDR). J. Earthq. Eng., 1–16 (2020)
13. Heintz, J.A.: FEMA P-440a: effects of strength and stiffness degradation on the seismic response of structural systems. In: Improving the Seismic Performance of Existing Buildings and Other Structures, pp. 721–730 (2010)
14. Mohamed, N., Farghaly, A.S., Benmokrane, B., Neale, K.W.: Experimental investigation of concrete shear walls reinforced with glass fiber–reinforced bars under lateral cyclic loading. J. Comp. Constr. **18**(3), A4014001 (2014)
15. Salonikios, T.N., Kappos, A.J., Tegos, I.A., Penelis, G.G.: Cyclic load behavior of low-slenderness reinforced concrete walls: design basis and test results. Struct. J. **96**(4), 649–660 (1999)
16. Zhai, S., Zou, Z., Zhu, Z., Zhang, Z., Liang, W., Cheng, X., Chang, S.: Experimental study on the seismic performance of a partition damped wall-filled frame structure. In: Shock and Vibration 2019 (2019)

Intelligent Modeling for Shear Strength of RC Exterior Beam-Column Joint Subjected to Seismic Loading

B. Swapnil and T. Palanisamy

Abstract RC beam-column joints are subjected to impounding shear demand and bond-slip during the event of an earthquake. Accurate prediction of joint shear strength is necessary to avoid brittle shear failure in design and retrofitting procedures. In this study the accurate shear strength of RC exterior beam-column joints are predicted by providing a contemporary intelligent modeling approach through eXtreme Gradient Boosting regressor (XGBoost), an ensemble learning technique that combines several weak learners to generate a strong predictive model. From the experimental results of diverse publications on exterior beam-column joints, parameters affecting joint shear strength are found through examination of current models, and a vast database is constructed. Eleven such parameters that describe the material property, geometric configuration and bond resistance, are chosen as the inputs, and joint shear strength as the output. The model is then trained, tested and validated on this database. The performance of this model is evaluated by various regression evaluation metrics such as MSE, RMSE, and R^2. Comparison of this model with the existing empirical equation, code provisions, and even with an individual ML algorithm, demonstrated its superiority over all the models in terms of accuracy and computation time. Sensitivity analysis done using predictive power score (PPS) showed that the most important parameter for the estimation of the shear strength of RC exterior beam-column joint is the percentage of beam longitudinal reinforcement.

Keywords Joint shear strength · XGBoost · Sensitivity analysis

1 Introduction

During strong seismic excitations beam-column joints (BCJ) are subjected to impounding shear demand and bond slip which arises when adjoining beams are subjected to plastic moment capacities. Shear failure of BCJ is a complex and brittle phenomenon, thus making it challenging to precisely calculate the shear strength. If

B. Swapnil (✉) · T. Palanisamy
Department of Civil Engineering, National Institute of Technology Karnataka, Surathkal, Mangaluru 575025, Karnataka, India
e-mail: bokadeswapniltrimbak.203st003@nitk.edu.in

BCJs are not designed properly, they can fail catastrophically. The accurate forecasts of the shear strength of RC BCJ are needed to give exact checks in design procedures by avoiding shear failures and implementing appropriate strengthening measures. Soft computing methods are uncommon among existing methodologies and are incapable of accurately predicting joint shear strength. Individual type learning algorithms such as ANN family [1–3], SVM [4] and DT family formed the bulk of ML algorithms produced in prior studies. The datasets employed in prior studies were limited, and the models used to account for complex and non-linear relationship between independent variables and dependent variables were inadequate. Furthermore the downsides of individual type ML algorithms include their instability, which can lead to prediction models with relatively large uncertainties and substantial bias for some ranges of shear strength. Thus to provide a novel approach, this study builds an ensemble model for accurate prediction of the shear strength of RC exterior (BCJ) The overall steps taken in this research on which the new prediction model has been proposed is represented in Fig. 1, these steps are well explained in the methodology and results section.
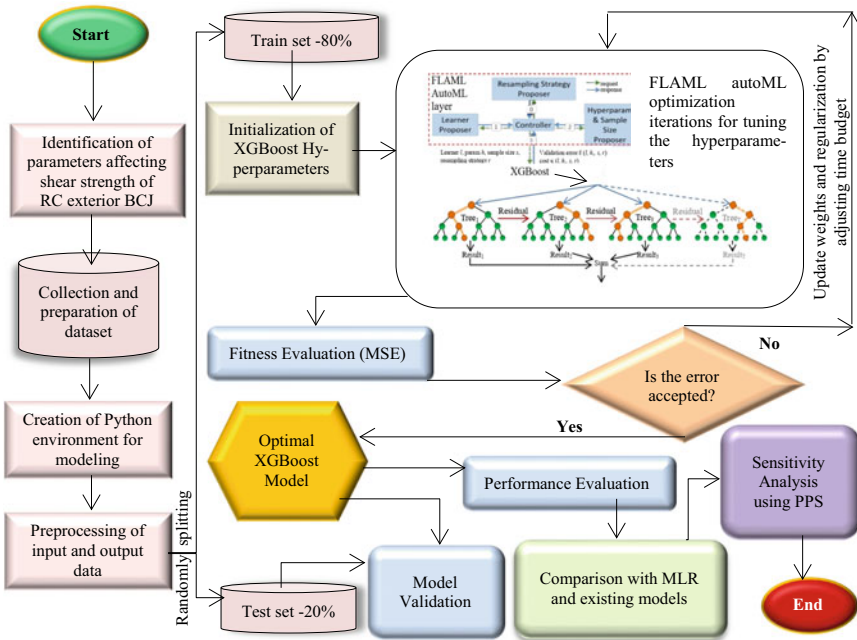
Fig. 1 Research flowchart

2   Methodology

2.1   Preparation of Database

An extensive database of 136 RC exterior BCJs is constructed from the experimental program conducted in various countries [5–12]; such as those schematically shown in Fig. 2, The failure mode of the collected BCJ specimens is joint shear failure and beam-joint failure with no eccentricity between beam and column centerline.

A thorough evaluation of existing empirical equations [7, 13, 14], theoretical models [15, 16] and ACI [17] code provisions resulted in identification of the parameters that affect the shear strength of RC exterior BCJ and taken as the input to the XGBoost and MLR models, which are as follows: (1) cylindrical compressive strength of concrete (f_c), if the dataset has cube strength, then 80% of cube strength is assumed as the cylindrical compressive strength, (2) yield strength of longitudinal reinforcement in beam (f_{yb}), (3) ratio of beam depth to column depth (h_b/h_c), (4) ratio of beam width to column width (b_b/b_c), (5) effective joint width (b_j) as per ACI 352R-2002, (6) Length of beam (L) from joint face to the location where concentrated cyclic load is applied, (7) percentage of top or bottom longitudinal reinforcement in beam (T_{Ast}) or (B_{Ast}) respectively, since, in the entire database percentage of top (T_{Ast}) and bottom (B_{Ast}) longitudinal reinforcement in beam are same, so only either of the two, i.e., T_{Ast} is considered as the input to reduce the statistical overload on the model, (8) column load index (P_y) as per EN 1998-1,
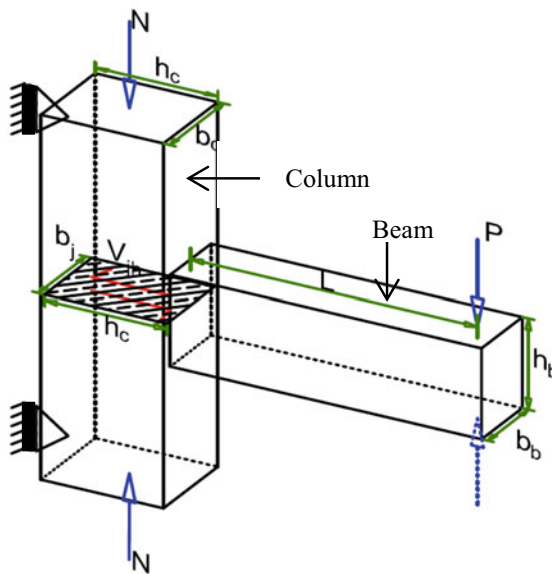
Fig. 2 Geometrical configuration of RC exterior BCJ

$$P_y = \frac{N}{b_j h_c f_c} \tag{1}$$

(9) beam-bar index (x_b) as suggested by [14] to account for the effect of bond resistance on the joint shear strength (Eq. (2)), where n_b is maximum number of either top or bottom beam bars and d_{sb} is the corresponding average beam bar diameter,

$$x_b = \frac{n_b d_{sb}}{b_b}\left(\frac{h_c}{h_b}\right) \tag{2}$$

(10) $\sum$column-to-$\sum$beam flexural moment strength ratio (M_R), (11) joint shear reinforcement index ($\varnothing_s$) as per [14] which are given by Eqs. (3) and (4),

$$\varnothing_v = \frac{A_{sv} f_{yv}}{b_j h_c \sqrt{f_c}}; \varnothing_h = \frac{A_{sh} f_{yh}}{b_j h_c \sqrt{f_c}} \tag{3}$$

$$\varnothing_s = \varnothing_v + \varnothing_h \tag{4}$$

where $\varnothing_v$ and $\varnothing_h$ are the vertical and horizontal joint shear reinforcement index respectively, f_{yv} and f_{yh} are the yield strength of the vertical and horizontal joint shear reinforcement respectively, A_{sv} and A_{sh} are the area of intermediate column reinforcement and horizontal joint shear reinforcement respectively. Sum of the vertical and horizontal joint shear reinforcement factor is known as joint shear reinforcement index $\varnothing_s$. Equation (5) determines the joint shear strength of RC exterior BCJs which is considered as an output (target) data for XGBoost and MLR modeling, where V_{jh} is the maximum horizontal shear force experienced by the specimens in the test.

$$\tau = \frac{V_{jh}}{b_j h_c} \tag{5}$$

Few of the input parameters are shown in Fig. 2 which defines the geometrical configurations of the test specimens. The statistical summary of the collected dataset is shown in Table 1. There is a reasonable amount of variation in the dataset, which is necessary for model to learn the relationship within the data and predict the accurate shear strength, instead of just by heart from monotonous data.

Table 1 Statistical summary of database

Variable	Max	Min	Mean	STD	Unit
f_c	93.800	15.440	40.790	17.749	MPa
f_{yb}	594.000	306.647	479.513	77.522	MPa
h_b/h_c	2.000	0.900	1.287	0.280	–
b_b/b_c	1.000	0.600	0.881	0.107	–
b_j	425.000	100.000	251.523	81.514	mm
L	2250.000	890.000	1296.804	381.299	mm
T_{Ast}	2.000	0.291	1.145	0.452	%
P_y	0.227	−0.052	0.079	0.059	–
x_b	0.503	0.067	0.226	0.089	–
M_R	5.800	0.569	2.172	0.911	–
$\varnothing_s$	2.668	0.000	0.844	0.679	–
τ	9.248	2.094	5.025	1.662	MPa

2.2 Pre-processing of Input and Output Data

Normalization and splitting the data into train and test sets are part of pre-processing step. Data normalization is a necessary step in improving the model training. It boosts learning speed substantially, and the model may be taught in less iterations. Using Eq. (6), input and output data is normalized in the range [0, 1].

$$a_n = \frac{a_i - a_{min}}{a_{max} - a_{min}} \tag{6}$$

The minimum and maximum of the variables are denoted by a_{min} and a_{max} respectively. The normalized data of the variable a_i is a_n. In this study, normalization of data is done by fitting MinMaxScaler() function of scikit-learn library to an object in python 3.7.13 environment and transformed to the normalized input and output data.

Further, the dataset is divided into two groups: training and testing data. 80% (108 samples) of the data is used in training the XGBoost and MLR models, while the remaining 20% (28 samples) of the data is used for testing purpose. A random state of 42 is also defined to randomly shuffle the data. These are achieved using train_test_split command.

The 10-fold cross-validation strategy was devised in this study to reduce the bias associated with random sampling of the training and testing datasets. It divides the entire experimental data into ten subsets, with nine serving as training subsets and one serving as validation subset for each run. It is thought that repeating this process ten times will indicate the prediction model's generalization and reliability.

2.3 XGBoost Modeling

A predictive model may be easily trained with the available database using the supervised family of machine learning techniques. There are several techniques in this area, however in this study, the algorithm being experimented is XGBoost [18], a recently created ML algorithm, which is used by every winner of Kaggle competition and demonstrates high accuracy on small to large datasets of similar regression-like applications [19]. XGBoost is essentially a powerful ensemble learning algorithm. The core principle behind ensemble learning is to create a strong learner from a set of individual weak learning algorithms in an iterative manner. XGBoost transcends into a more advanced variant of the gradient boosted decision tree (GBDT), an ensemble learning approach, with improvements to the loss function and regularization process. It measures the complexity of the trees being built and balances the complexity with respect to training accuracy of the model through regularization process. It relies on parallel and distributed computing on individual decision tree to achieve rapidly much greater performance and results with less computation resources. The mathematical intuition of XGBoost is as follows: Consider the following database with n samples,

$$\{(x_i, y_i)\}_{i=1}^{n} \tag{7}$$

where x_i = column vector of independent variables (input features); y_i = Corresponding target variables (actual value). The entire XGBoost algorithm and its architecture (Fig. 3) can be summarized in the following steps: (1) initialize the weak learner $f(x_i)$; (2) in a for loop, t = (1, … , T), where T refers to the total trees to be built, create a new instance of the model $f_t(x_i)$; (3) this tree is built by greedy grow algorithm in the following steps—(i) start from a tree with depth zero, (ii) for each leaf node, it will try to add a split, (iii) change in objective function, after adding split is calculated using the information gain function as
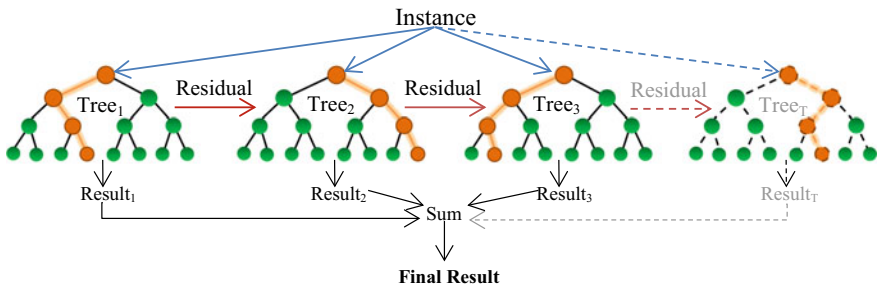
Fig. 3 Architecture of Boost

$$Gain = \frac{1}{2}\left[\frac{G_L^2}{H_L + \lambda} + \frac{G_R^2}{H_R + \lambda} - \frac{(G_L + G_R)^2}{H_L + H_R + \lambda}\right] - \gamma \qquad (8)$$

where G_L, G_R, H_L, and H_R are the first and second gradients of the left and right child after the split, respectively, which have expressions similar to those in Eq. (9), for a sample set of leaf j denoted by I_j, the objective function at at t-th iteration $(Obj^{(t)})$ is

$$(Obj^{(t)}) = \sum_{j=1}^{T}\left[G_j w_j + \frac{1}{2}(H_j + \lambda)w_j^2\right] + \gamma T \qquad (9)$$

where $G_j = \sum_{i \in I_j} g_i$ and $H_j = \sum_{i \in I_j} h_i$, in which, $g_i = \partial_{\widehat{y}_i^{(t-1)}}\left(y_i - \widehat{y}_i^{(t-1)}\right)^2$ and $h_i = \partial_{\widehat{y}_i^{(t-1)}}^2\left(y_i - \widehat{y}_i^{(t-1)}\right)^2$ are the 1st and 2nd order gradients of the squared loss function; $\widehat{y}_i^{(t-1)}$ is the sum of predictions of the previous model (at $t-1$ itration); w_j = leaf scores (or weights); γ and λ = hyperparameters or penalty coefficients for regularization of the model, The above objective function is a sum of T quadratic functions, for each quadratic function; $G_j w_j + \frac{1}{2}(H_j + \lambda)w_j^2$, the optimal weight w_j^* is

$$w_j^* = -\frac{G_j}{H_j + \lambda} \qquad (10)$$

now by substituting this optimal value into Eq. (9), we get min objective function as

$$minObj = -\frac{1}{2}\sum_{j=1}^{T}\frac{G_j^2}{H_j + \lambda} + \gamma T \qquad (11)$$

(iv) the minimal objective function (Eq. (11)) is used in build-up of trees which measures how good is the tree structure, (v) XGBoost stops the split, if the best split have negative gain; (4) all the new models are additively combined (Fig. 3) and the training stops either when T is fixed or when the objective reaches and acceptable level; (5) the final ensemble XGBoost model is given by expressions as below:

$$\widehat{y}_i = \sum_{t=1}^{T}\alpha_t f_t(x_i) \qquad (12)$$

$\widehat{y}_i$ = predicted value of final model; and α_t = learning rate used to avoid overfitting.

In python environment, XGBoost was imported as an object from sklearn library. A set of tuned hyperparameters were given to the XGBoost framework for modeling.

2.4 MLR Modeling

Multivariate linear regression (MLR) is similar to simple linear regression (only one independent and dependent variable), with the exception that it includes two or more independent variables and the relationship between independent and dependent variable is approximately linear. In this study, 11 input parameters are assigned as independent variables and 1 output parameter as dependent variable. In python 3.7.13, MLR was imported as an object named LinearRegression() from sklearn.linear_model module and fitted to the randomly shuffled non-scaled training data. The following regression equation for prediction of joint shear strength (MPa) was obtained

$$
\begin{aligned}
\tau = {} & 0.03868(f_c) + 0.00248(f_{yb}) + 0.28002\left(\frac{h_b}{h_c}\right) + 4.73431\left(\frac{b_b}{b_c}\right) - 0.00160(b_j) \\
& + 0.00056(L) + 2.67287(T_{Ast}) + 5.38956(P_y) + 0.84269(x_b) - 0.14750(M_R) \\
& + 0.46956(\varnothing_s) - 6.34176
\end{aligned}
\tag{13}
$$

2.5 Hyperparameter Tuning of XGBoost Model Using FLAML

In this study, the hyperparameters of the proposed XGBoost model are optimized using fast and light weight automated machine learning (FLAML) algorithm in python framework as suggested by Wang et al. [20]. FLAML tunes the hyperparameters for low computational and temporal resources to find accurate models by integrating several basic however compelling hunt strategies into an adaptive system which significantly outperforms other hyperparameter tuning algorithms and premium AutoML libraries on a large open source AutoML benchmark under equivalent or sometimes smaller magnitudes of budget constraints. The detailed mathematical intuition of FLAML can be found in [20].

From FLAML library AutoML module was imported and XGBoost was fitted to the training data for various instants of tuning run ranging from 10 to 300 s.

The performance evaluation metric used in training the model is MSE. Model RMSE on train (80%) and test (20%) data with respect to various time budgets (from 10 to 300 s of optimization run) for a default max_depth of 6 is shown in Fig. 4(a), and the model RMSE on train and test data with respect to various max_depth for the final tuned model (obtained at 200 s of optimization run), with all the other hyperparameter being constant, is shown in Fig. 4(b).
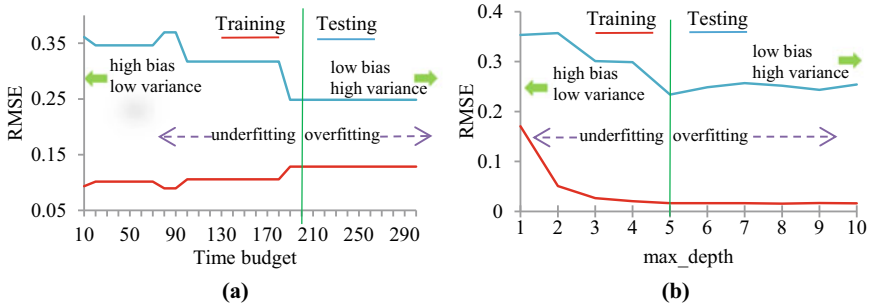
Fig. 4 Hyperparameter tuning in model training through FLAML: **a** RMSE v/s Time budget of optimization run for default max_depth of 6; **b** RMSE v/s max_depth for final tuned model

2.6   Post-processing of Inputs and Output

All the variables which were normalized and fed to the model were brought back into their original form using the inverse_transform function of sklearn library for performance evaluation of model with various evaluation metrics as shown in Table 3.

3   Results

3.1   Performance Evaluation of XGBoost and MLR Models

From Fig. 4(a), it is clear that the preliminary tuned model for a default max_depth = 6 is obtained at least 200 s of optimization iterations, the hyperparameters (other than max_depth) of this preliminary tuned model is then used to study the effects of max_depth on model accuracy (Fig. 4(b)). It is concluded from Fig. 4(b), the final optimal XGBoost model is obtained at max_depth of 5 with all other hyperparameters as shown in Table 2, because the RMSE and their difference between train and test set is lowest and relatively stable at 200 s of tuning operations and max_depth of 5.

Table 2 Hyperparameters of optimal XGBoost model

Hyper-parameter	colsample_ bylevel	colsample_ bynode	colsample_ bytree	learning_ rate	max_delta_ step	gamma
Value	0.68263	1	0.89685	0.32027	0	0
Hyper-parameter	max_leaves	min_child_weight	n_estimators	reg_alpha	subsample	reg_ lambda
Value	5	0.13481	101	0.11025	0.68257	0.07347

Table 3 Performance evaluation metrics

Performance metrics	MAE	MSE	RMSE	R^2	Adjusted R^2
Definition	$\frac{1}{n}\sum_{i=1}^{n}\|A_i - Y_i\|$	$\frac{1}{n}\sum_{i=1}^{n}(A_i - Y_i)^2$	$\sqrt{\frac{1}{n}\sum_{i=1}^{n}(A_i - Y_i)^2}$	$1 - \frac{\sum_{i=1}^{n}(A_i-Y_i)^2}{\sum_{i=1}^{n}(A_i-\overline{A}_i)^2}$	$1 - \frac{(1-R^2)(n-1)}{n-p-1}$

Table 4 Performance Comparison of XGBoost with MLR Model

Model	XGBoost			MLR		
Process	Training	Testing	Overall	Training	Testing	Overall
MAE	0.07833	0.17781	0.09881	0.53474	0.36378	0.49954
MSE	0.01644	0.05471	0.02432	0.46103	0.20942	0.40922
RMSE	**0.12823**	**0.23391**	0.15595	0.67899	0.45762	0.63971
R^2	**0.99430**	**0.97246**	0.99113	0.84020	0.89460	0.85071
Adjusted R^2	0.99365	0.95353	0.99034	0.82189	0.82213	0.83747

Table 3 shows the various performance evaluation metrics used in this study, where A_i, Y_i, and $\overline{A}_i$ are the actual, predicted and mean of the actual values of target variable (joint shear strength) respectively. n is the total number of data points (136) and p is the number of independent variable (11). Once the optimal XGBoost model was fitted to train data, model.predict command was used to predict the output in training and testing phase. For a perfectly mapping model MAE, MSE and RMSE should be nearly equal to zero and R^2 score should be nearly equal to one. The proposed optimal XGBoost model has RMSE and R^2 as 0.12823 and 0.99430 respectively for train set, while test set RMSE and R^2 are 0.233391 and 0.97246 respectively. The overall value of evaluation metrics is obtained by concatenating train and test set. As evident from Table 4 values, the XGBoost model is accurate, relatively stable and is thus a balanced model, neither overfitted nor underfitted and outperforms the traditional individual ML algorithm of multivariate linear regression (MLR).

3.2 Comparison of XGBoost with MLR Model

Figure 5(a) represents actual and predicted joint shear strength of proposed XGBoost model for entire dataset. This graph shows that prediction is almost equal to actual values and there is a very close agreement between actual and predicted joint shear strength obtained from proposed XGBoost model. To emphasis on this, Fig. 5(b) represents error histogram of XGBoost model, which shows that very few, approximately 5 out of 136 data points has residual error (MPa) in the range of −0.75 to

+0.50, while rest are well within −0.25 to +0.25, thus representing an accurate mapping model.

The scatter plots of actual v/s predicted joint shear strength in training and testing phase with a reference 45° line for the proposed XGBoost and MLR model is shown in Fig. 6(a) and (b) respectively. The points closer to 45° line represents a very good fit between actual and predicted joint shear strength. It is evident that XGBoost shows relatively accurate predictions for training as well as test set and supersedes the performance of traditional individual MLR model.
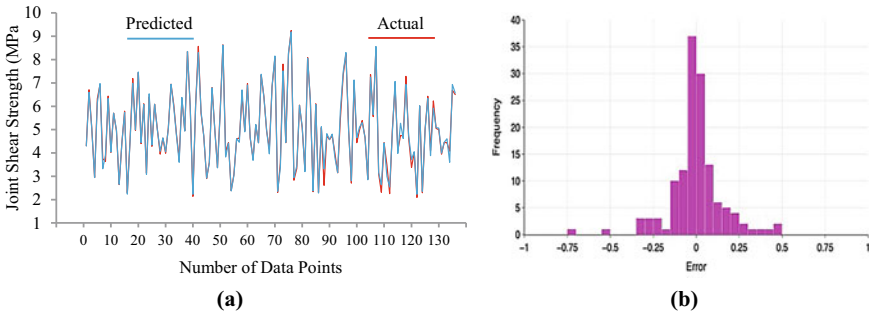
Fig. 5 **a** Actual and predicted joint shear strength of proposed XGBoost model **b** Error histogram of proposed XGBoost model
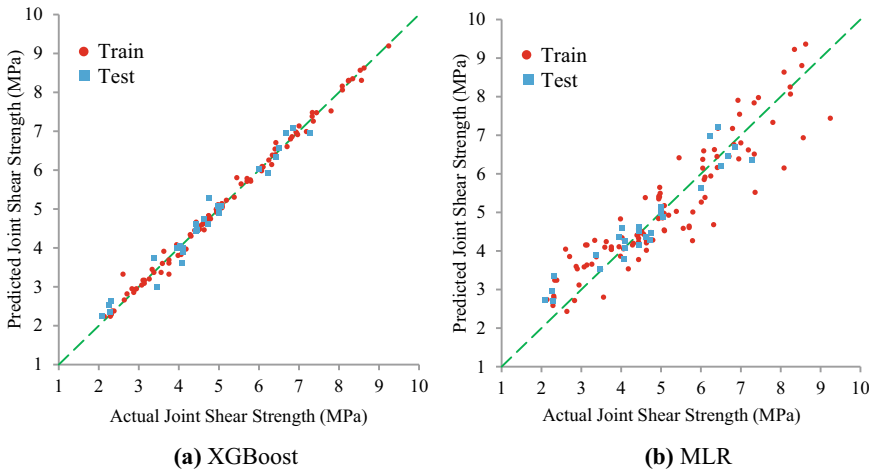
Fig. 6 Predicted v/s actual joint shear strength scatter plot for **a** XGBoost and **b** MLR

Table 5 Performance of design code and an empirical equation

Model	ACI	Tran et al. 2014
Process	Overall	Overall
MAE	1.79586	0.83325
MSE	4.81491	1.15780
RMSE	2.19429	1.07601
R^2	-0.75651	0.57763
Adjusted R^2	-0.91233	0.54016

3.3 Performance Evaluation of Design Code and Empirical Equations

Table 5, shows the performance of ACI 352R-2002 [17] design joint shear strength equation and an empirical equation suggested by Tran et al. [14] respectively. The empirical equation (Tran et al., 2014) is more accurate than design joint shear strength equations of ACI code. Comparison of Table 4 values with that of Table 5 reveals that XGBoost model is relatively accurate and predicts the joint shear strength in close agreement with experimental values, thus depicting most realistic model.

The scatter plots of actual v/s predicted joint shear strength of entire dataset with a reference 45° line for design joint shear strength equation of ACI and Tran et al., 2014 are shown in Fig. 7(a) and (b), respectively. Most of the scatter points in Fig. 7(a), are located on the upper left corner of the reference 45° line, this shows that the design joint shear strength equations recommended by ACI code is overestimating the joint shear strength. Since, predicted values are higher than the actual experimental values, it cannot accurately reflect the actual behavior of exterior BCJs under reversed cyclic loading and demonstrates large variance and substantial bias for some ranges of shear strengths. This is probably due to the inefficiency of the design equation of ACI in incorporating the effect of various parameters (other than f_c) on the joint shear strength of RC exterior BCJ. On the contrary, Fig. 7(b), shows a good fitting model compared with design code equations, but still the predictions are less accurate when compared with the proposed XGBoost model Fig. 6(a). Hence XGBoost model outperforms all the existing models in terms of accuracy, low variance and appropriate bias for the entire dataset.

3.4 Sensitivity Analysis Using PPS

Sensitivity analysis is the process of measuring feature importance in predicting the target variable (joint shear strength). In this study, a new index known as Predictive Power Score (PPS) is used for performing sensitivity analysis. Unlike correlation
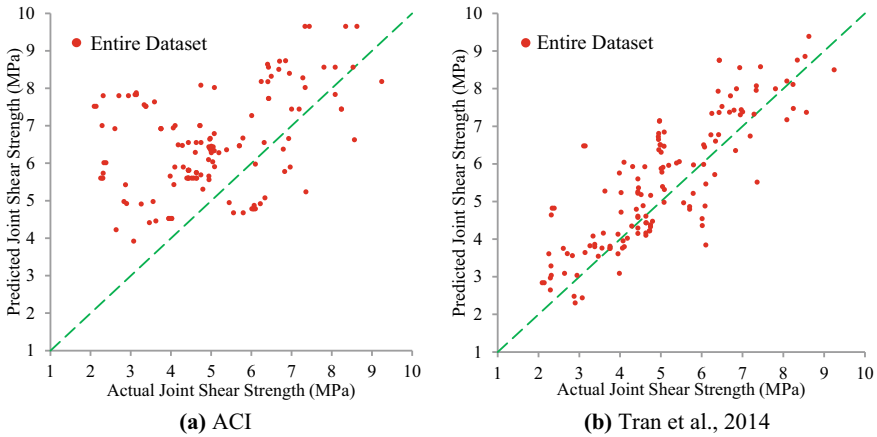
Fig. 7 Predicted v/s actual joint shear strength scatter plot for design shear strength equations of **a** ACI; and **b** Tran et al. 2014

matrix, PPS is an asymmetric and data-type agnostic score that aids in the identification of linear or non-linear relationships between two columns in a database. PPS is calculated using decision tree regressor. In this regression study MAE was used as an evaluation metrics. Then the MAE of naive model is calculated, in which a naive model is an ML algorithm that always predicts the median value in regression task and predicts the common class in classification problems. The MAE of naive model (MAE_{naive}) is used to calculate the PPS as followed:

$$PPS = 1 - \left(\frac{MAE_{model}}{MAE_{naive}} \right) \qquad (14)$$

A PPS value of 1 is considered as good and indicates that a given feature A is alone sufficient to accurately predict the target variable B. 0 value of PPS indicates that the given feature is of no use in prediction of the target, it simply increases the statistical overload on the model. Figure 8 shows PPS for all the 11 parameters affecting the joint shear strength of exterior BCJ. The percentage of top (T_{Ast}) and bottom (B_{Ast}) reinforcement has the highest PPS value of 0.6461, followed by beam bar index (x_b) at 0.5234 and yield strength of beam bars (f_{yb}) at 0.3674. This means that the above three parameters are alone sufficient to predict the joint shear strength of exterior BCJ with reasonable accuracy as they influence joint behavior predominantly. But the most influential parameter for prediction of joint shear strength is percentage of beam longitudinal reinforcement, this fact is in perfect compliance with the results of sensitivity analysis carried out by [21]. Bond resistance also plays an important role as it avoids bond slip or pull out of rebar by developing shear in joint region, this parameter is ignored in most of the code recommendations. The beam longitudinal reinforcement affects its plastic moment capacity during reverse cyclic loading, for a desirable seismic resistance property of strong column weak beam, the beam is
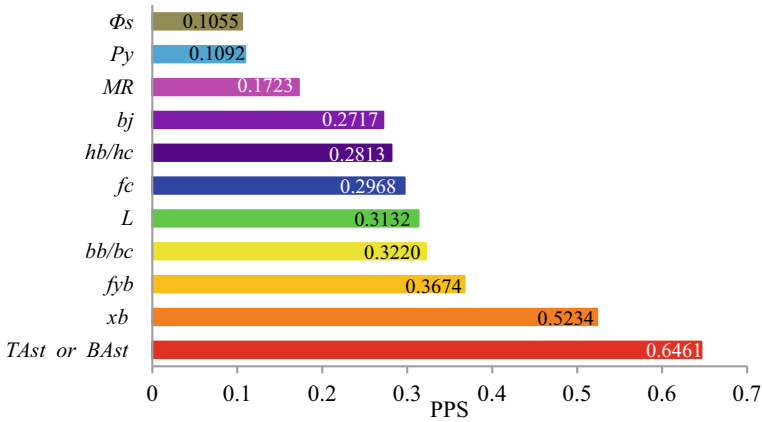
Fig. 8 Variable importance using PPS

made a weaker element. Also, from Fig. 8, it can be inferred that the least important variable, which does not greatly influences shear strength of exterior BCJ are column load index (P_y) and joint shear reinforcement index ($\varnothing_s$). The fact, that $\varnothing_s$ is the least important variable is in close agreement with the sensitivity analysis results carried out by [4], and with the experimental results of [11] by concluding that additional transverse reinforcement does not enhance the behavior of RC exterior BCJ, thus this criteria can be relaxed in code recommendations.

4 Conclusions

The proposed XGBoost model outperforms individual algorithm of MLR, design code equation of ACI and an empirical equation (Tran et al., 2014) in terms of accuracy, less variance and median bias in prediction of joint shear strength. Sensitivity analysis done using PPS showed that the most important parameter for the estimation of the shear strength of RC exterior BCJ is the percentage of beam longitudinal reinforcement. For ready use of this XGBoost model by design engineers, model code is provided open source on GitHub (https://github.com/swapnilbokde/BCJ-Model).

References

1. Alagundi, S., Palanisamy, T.: Neural network prediction of joint shear strength of exterior beam-column joint. Structures **37**, 1002–1018 (2022). https://doi.org/10.1016/j.istruc.2022.01.013

2. Mirrashid, M.: Comparison study of soft computing approaches for estimation of the non-ductile RC joint shear strength. J. Soft Comput. Civ. Eng. **1**(1), 9–25 (2017). https://doi.org/10.22115/scce.2017.46318

3. Kotsovou, G.M., Cotsovos, D.M., Lagaros, N.D.: Assessment of RC exterior beam-column Joints based on artificial neural networks and other methods. Eng. Struct. **144**, 1–18 (2017). https://doi.org/10.1016/j.engstruct.2017.04.048

4. Mangalathu, S., Jeon, J.: Classification of failure mode and prediction of shear strength for reinforced concrete beam-column joints using machine learning techniques. Eng. Struct. **160**, 85–94 (2018). https://doi.org/10.1016/j.engstruct.2018.01.008

5. Kuang, J.S., Wong, H.F.: Effects of beam bar anchorage on beam-column joint behaviour. Proc. Inst. Civ. Eng. Struct. Build. **159**(2), 115–124 (2006). https://doi.org/10.1680/stbu.2006.159.2.115

6. Kaung, J.S., Wong, H.F.: Effectiveness of horizontal stirrups in joint core for exterior beam-column joints with nonseismic design. Procedia Eng. **14**, 3301–3307 (2011). https://doi.org/10.1016/j.proeng.2011.07.417

7. Tsonos, A.G.: Cyclic load behaviour of reinforced concrete beam-column subassemblages of modern structures **81**(1999), 439–449 (2005)

8. Chalioris, C.E., Favvata, M.J., Karayannis, C.G.: Reinforced concrete beam – column joints with crossed inclined bars under cyclic deformations. Earthq. Eng. Struct. Dyn. **37**, 881–897 (2008). https://doi.org/10.1002/eqe.793

9. Karayannis, C.G., Sirkelis, G.M.: Strengthening and rehabilitation of RC beam – column joints using carbon-FRP jacketing and epoxy resin injection. Earthq. Eng. Struct. Dyn. **37**, 769–790 (2008). https://doi.org/10.1002/eqe.785

10. Antonopoulos, C.P., Triantafillou, T.C.: Experimental investigation of FRP-strengthened RC beam-column joints. J. Compos. Constr. **7**(1), 39–49 (2003)

11. Ehsani, M.R., Wight, J.K.: Exterior reinforced concrete beam-to-column connections subjected to earthquake-type loading. ACI Struct. J. **82**(43) (1986)

12. Kaku, T., Asakusa, H.: Ductility estimation of exterior beam-column Subassemhlages in reinforced concrete frames. ACI Struct. J. **SP123**(7) (1991)

13. Bakir, P.G., Bodurog, H.M.: A new design equation for predicting the joint shear strength of monotonically loaded exterior beam-column joints. Eng. Struct. **24**, 1105–1117 (2002)

14. Tran, T.M., Pham, T.M., Hadi, M.N.S.: A new empirical model for shear strength of reinforced concrete beam – column connections. Mag. Concr. Res. **66**(10), 514–530 (2014). https://doi.org/10.1680/macr.13.00310

15. Vecchio, F.J., Collins, M.P.: The modified compression field theory for reinforced concrete elements subjected to shear. ACI Struct. J. **83**(22) (1987)

16. Paulay, T., Preistley, M.J.N.: Seismic Design of Reinforced Concrete and Masonry Buildings, 1st edn. Wiley, Canada (1992)

17. American Concrete Institute: Recommendations for Design of Beam-Column Connections in Monolithic Reinforced Concrete Structures (ACI 352R-02)

18. Chen, T., Guestrin, C.: XGBoost: A Scalable Tree Boosting System. arXiv

19. Zhang, D., Qian, L., Mao, B., Huang, C.A.N., Huang, B.I.N.: A data-driven design for fault detection of wind turbines using random forests and XGboost. IEEE Access **6**, 21020–21031 (2018). https://doi.org/10.1109/ACCESS.2018.2818678

20. Wang, C., Wu, Q., Weimer, M., Zhu, E.: FLAML: A Fast and Lightweight AutoML Library (2019). http://arxiv.org/abs/1911.04706

21. Naderpour, H., Nagai, K.: Shear strength estimation of reinforced concrete beam–column sub-assemblages using multiple soft computing techniques. Struct. Des. Tall Spec. Build. **29**(9), 1–15 (2020)

Prediction of Compressive Strength and Workability Characteristics of Self-compacting Concrete Containing Fly Ash Using Artificial Neural Network

Nitesh Netam and T. Palanisamy

Abstract This study aims to propose an artificial neural network (ANN) model for predicting the properties of self-compacting concrete (SCC). SCC has enhanced properties such as very high workability and it can go through very tight spaces between reinforcements without any application of vibration. To get the desired strength and workability, it is necessary to understand the parameters determining the nature and properties of SCC and the relationships involved among those parameters. In this study binder content, water to binder ratio, fly ash percentage, coarse aggregate, fine aggregate, and superplasticizer content are chosen as input parameters, and output results from the model are slump flow value, L-box ratio, V-funnel time, and compressive strength. An ANN model is constructed and its architecture is selected by evaluating the performance of a network with a different number of neurons for the optimum results. Then this model is trained, tested, and validated through a database of experimental test results gathered from various literature. The accuracy of this model is evaluated by evaluation matrices such as R and MSE. To check the efficiency, the current model comparison was made with an existing data envelopment analysis model (DEA).

Keywords Self-Compacting Concrete · Fly ash · Artificial Neural Network · Compressive strength · Workability

1 Introduction

Self-Compacting Concrete (SCC) mixes can be defined as those mixes which, because of their enhanced flow characteristics, can effectively flow even around the congested reinforcement bars, without leaving any voids and get fully compacted by their own weight, without the need for any external compaction efforts.

N. Netam (✉) · T. Palanisamy
Department of Civil Engineering, National Institute of Technology Karnataka Surathkal, Mangalore, India
e-mail: niteshnetam.202st019@nitk.edu.in

Presently RC structures are designed and constructed to resist earthquake load also, which further results in an increase in the density of reinforcing bar structural members and especially in locations such as beam-column joints. The current construction industry requires to use of such concrete which has sufficient strength and also be able to fill the most complex shapes and places. Thus SCC, which has high fluidity along with enough viscosity to carry aggregates and prevent segregation, has been developed and increasingly used. Construction methods have also been evolved in response to this with wide use of pump pouring of concrete, improvement in pumping capacity, and non-vibrational construction. These methods also reduce the noise generated due to the extensive use of vibrators for construction purposes.

Mineral additions such as fly ash are a very important element of SCC and its significance has increased in the current concrete scenario, as they enhance the concrete properties, especially with its immunity to aggressive environment and the use of such additives is economical too. Also, by increasing the use of mineral additives we making a move towards sustainable development, decreasing the waste of fly ash, reducing the amount of energy consumed in the production of cement, and ultimately helping the environment by reducing the emission of CO_2 [1].

Due to these merits, SCC has gained popularity in the construction industry, but the mix-proportioning and prediction of the workability properties and compressive strength are complex. Various researchers are trying to come up with new and more effective mix proportioning methods which can be used to produce concrete with desired properties [2]. Prediction of properties of SCC, before construction employing artificial intelligence (AI), could help to save cost and time. Thus, by using this method, an initial mix-proportion for desired properties can be obtained, and it will be more effective in optimizing the ingredient proportion from there onwards by various tests.

Various AI methods such as fuzzy logic (FL) system, artificial neural network (ANN) [3], expert systems (ES) along with some other statistical techniques such as least square support vector machine (LSSVM) [4, 5], relevance vector machine (RVM), data envelopment analysis (DEA) [6], etc. are used and popularised by many researchers in the field of civil engineering.

The aim of this study is to propose an ANN model for the prediction of flow properties and compressive strength of SCC.

2   Artificial Neural Network

ANN is a type of artificial intelligence that imitates the way how a human brain works by learning through experiences and utilizing that knowledge in solving future problems. ANN is a nonlinear information processing framework that is built from interconnected computing elements called neurons. Every neuron is linked with the neuron of the next layer by information transmitting channels called connections, and these connections are associated with weights. These weights indicate the influence of each input on the output response. The sum of weighted input signals is then

Table 1 Statistics of the database

Variables	Min	Max	Mean value	STD	Min	Max	Mean value	STD
	The database used for training				The database used for comparison			
Binder (kg/m^3)	400	589	517.7	50.2	431	539	486.875	27.818
Fly ash (kg/m^3)	0	381.88	148.29	82.64	0	60	27.187	19.491
W (kg/m^3)	150	242	194.72	27.88	0.31	0.41	0.36	0.028
FA (kg/m^3)	614.27	1038	852.23	78.26	743	971	875	81.507
CA (kg/m^3)	590	935	755.91	116.62	735	924	817.625	81.507
SP (%)	0.86	17.64	7.4	3.98	3.21	11.8	6.062	2.021
Slump flow (mm)	480	810	673.38	55.13	600	720	684.125	38.767
L-box ratio	0.6	1	0.88	0.09	0.89	0.96	0.93	0.029
V-funnel time (s)	2	34	8.91	4.79	6.1	8.1	7.15	1.1
Compressive strength (MPa)	17	86.8	47.13	15.29	37.2	73.3	58.731	9.2

applied with an activation (or transfer) function to obtain the output response This study consists of ANN modeling which consists of three layers (Input layer, Hidden layer, and output layer). First, the network is trained over several iterations with already available datasets, then it can be used for a dataset that the network has never encountered before.

3 Experimental Database

For the development of the ANN model, 138 datasets containing experimental results of various flow and strength tests are collected from published literature [8–22]. For the effective modeling of the network, only datasets conforming to EFNARC:2005 [7], are used for training. Furthermore, 16 more datasets are taken from the literature of the already existing model to test and compare the efficiency of the proposed ANN model [6]. Statistics of the datasets are presented in Table 1.

4 Parameters Considered for ANN Modeling

For the modeling of the current model contents of Binder (B), Fly ash (F), Water (W), Fine aggregate (FA), Coarse aggregate (CA), and Superplasticizer (SP) are taken as input parameters, and Slump flow diameter (D), L-box ratio (L), V-funnel flow time (V), and Compressive strength (f$_c$) are taken as output parameters. For better performance of the model, all the input parameters are taken in single units i.e.,

kg/m^3. The datasets which differ from this unit system in any literature are converted to kg/m^3 before it was included in datasets used for training. For compressive strength, cube strength is used. If in literature cylindrical compressive strength is measured, then it is converted into cube compressive strength based on assumption that the cube compressive strength is 25% greater than the cylindrical compressive strength.

5 ANN Modeling

MATLAB (R2021a-academic use) is used for developing the ANN model for this research. The architecture of the feed-forward neural network is modeled with one single hidden layer. A single hidden layer neural network is capable of approximating continuous function very effectively. Due to this reason, researchers have adapted the use of a single hidden layer in their studies [3]. The number of neurons in the input layer and output layer is 6 and 4 respectively and the number of neurons in the hidden layer is selected by evaluating the performance of the network with a varying number of hidden neurons, i.e., from 1 to 20 neurons. The performance of the network is evaluated using the correlation coefficient (R) for each network. A graph is plotted taking R-value along the Y-axis and the number of hidden neurons along the X-axis Re (Fig. 1).

The network with 15 neurons showed the best results in comparison to other networks, hence the hidden layer has 15 neurons Re (Fig. 2a). The Levenberg–Marquardt backpropagation algorithm is used for training the network. The activation function used in the hidden layer and output layer is 'tansig' and 'purelin' respectively. Dataset used is randomly divided into three parts. For training of the network 70%, for testing 15%, and for validation 15% of the data are used.

The architecture of ANN obtained from MATLAB is shown in Fig. 2b.
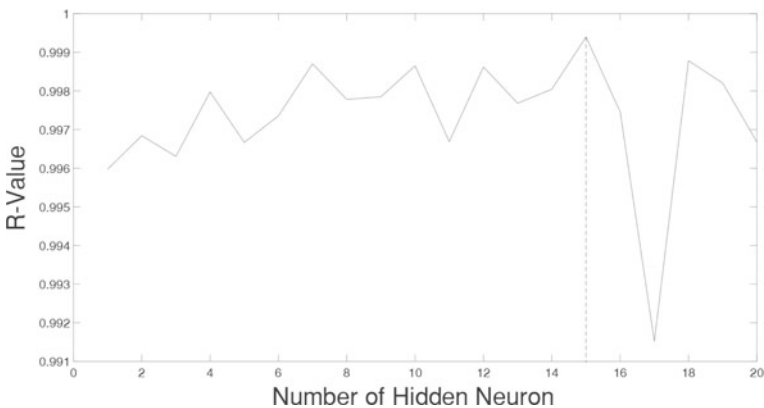
Fig. 1 Finding best architecture for the ANN model
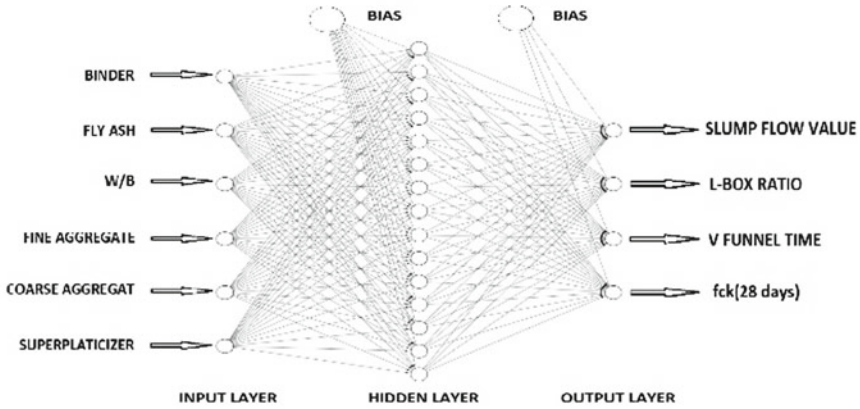
(a)
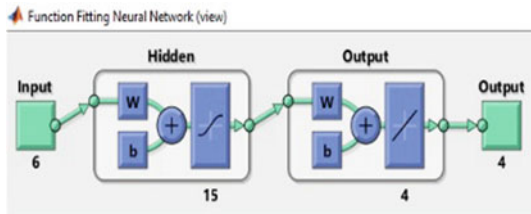
(b)

Fig. 2 The architecture of the ANN model

6 Result and Discussion

Once all the required parameters have been selected, the network is trained by running the MATLAB code. The training continues till the error arising during validation fails to decrease for six iterations or epochs and then validation stops. The maximum number of iterations that can be achieved during the training stage is set to 1000. For our current ANN model, it took 9 iterations or epochs to train the network, and the mean squared error (MSE) for each iteration is shown in Fig. 3. Mean squared error (MSE) is the average squared difference between the output and targets. Lower values are indicative of better results and zero indicates no error. The mean squared error is calculated as per Eq. (1).

$$MSE = \frac{1}{n} \sum_{i=1}^{n} (O_i - P_i)^2 \tag{1}$$
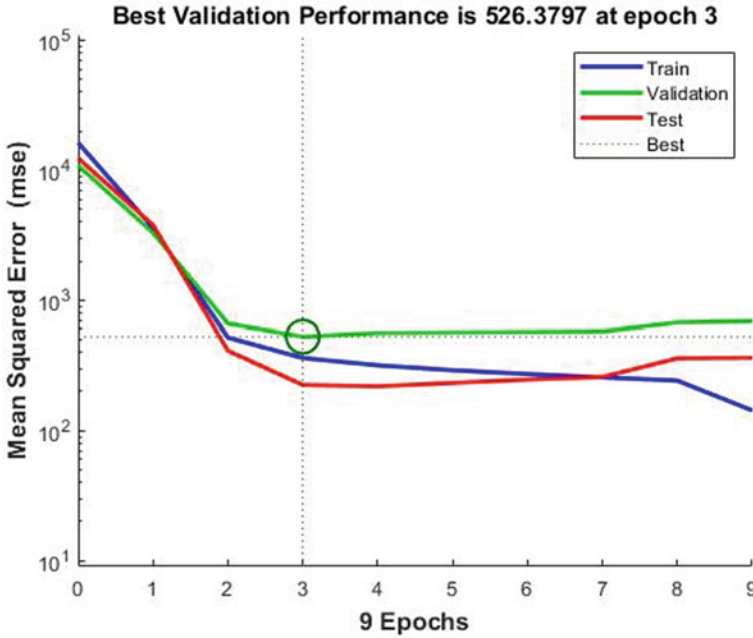
Fig. 3 Performance of network for each iteration

where O_i and P_i are observed and predicted output results respectively.

The performance of the current ANN model is checked by the coefficient of correlation (R) value, during training, testing, validation, and after that for whole datasets. The R-value determines the correlation between the output and targets. An R-value of 1 means a close relationship, and 0 means a random relationship. The R-value is defined as shown in Eq. (2).

$$R = \frac{\sum_{i=1}^{n}(O_i - \overline{O_i})(P_i - \overline{P_i})}{\sqrt{\sum_{i=1}^{n}(O_i - \overline{O_i})^2(P_i - \overline{P_i})^2}} \tag{2}$$

where $\overline{O_i}$ and $\overline{P_i}$ are the mean observed and predicted output values. The R values and regression graphs are plotted with the help of MATLAB. Results obtained from the experiment show that the model achieved a very good predicting capacity for the given dataset. R values for the training, testing, and validation stage are 0.998, 0.99475, and 0.99807 respectively Re (Fig. 4). And the R-value obtained when the model was tested on the whole dataset is 0.99746 which shows the current model can predict output values very close to experimental results Re (Fig. 5).

(a)

(b)

(c)
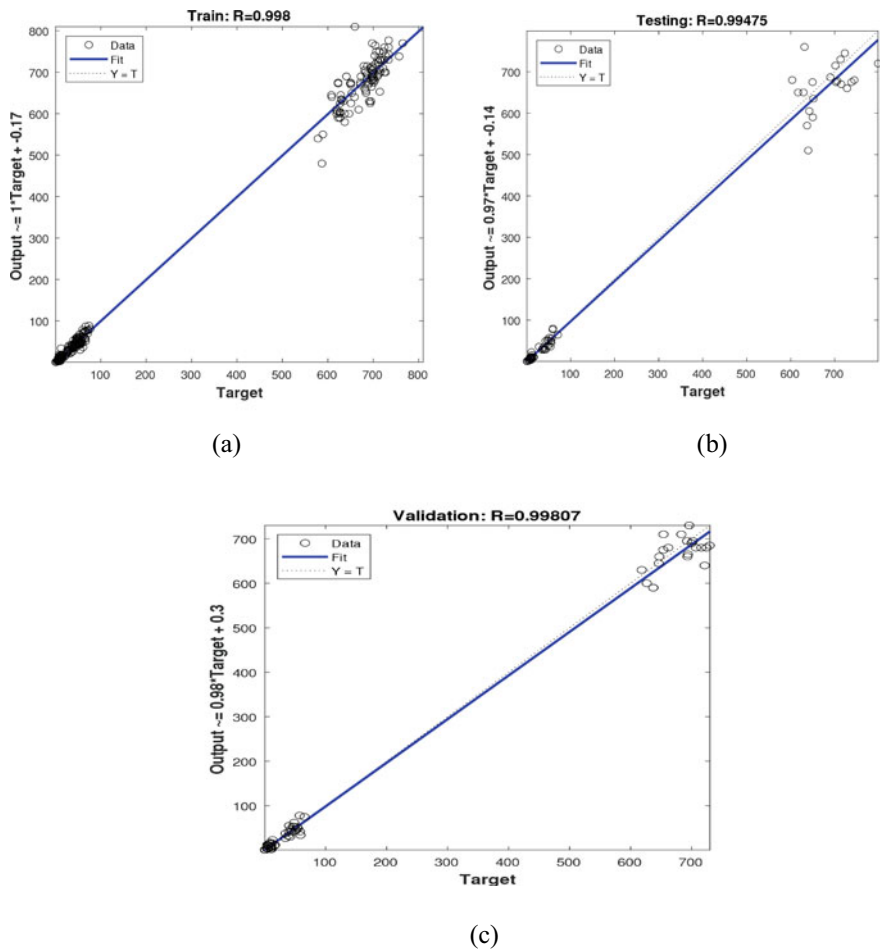
Fig. 4 **a** R plot for training data, **b** R plot for Testing data, **c** R plot for validation data
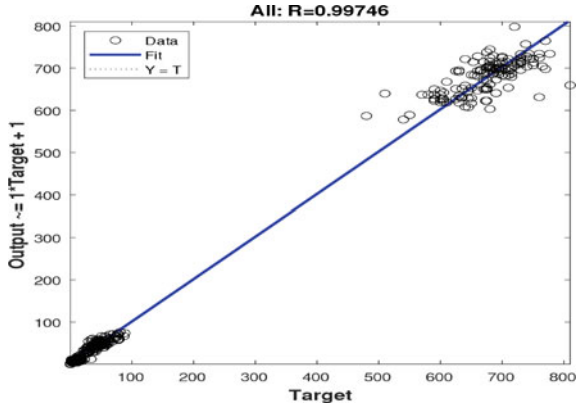
Fig. 5 R plot for actual values and predicted values for all data

7   Comparison with Data Envelopment Analysis (DEA) Model

To validate the actual performance of the proposed ANN model, the network is tested on a dataset that was not used for the training of the network. This dataset is obtained from the literature it is used to check the accuracy of the existing DEA model (Table 2).

Table 2 Comparison between DEA and ANN model with experimental results

N	D (mm)					L-box ratio (H2/H1)					V-funnel (s)					f_ck28 (MPa)				
	EXP	DEA	ANN	E_{DEA} (%)	E_{ANN} (%)	EXP	DEA	ANN	E_{DEA} (%)	E_{ANN} (%)	EXP	DEA	ANN	E_{DEA} (%)	E_{ANN} (%)	EXP	DEA	ANN	E_{DEA} (%)	E_{ANN} (%)
1	600	635.345	644.855	5.7	14.99											66.8	50.245	49.150	24.8	22.84
2	600	621.838	599.266	3.6	17.29											71.3	56.391	56.018	20.9	17.36
3	630	769.799	618.791	22.2	11.12											49.9	49.788	42.265	0.2	22.57
4	679	651.761	701.388	4	11.81											60	69.721	74.464	16.2	17.97
5	686	565.137	737.532	17.6	18.46											62	51.405	56.392	17.1	3.79
6	686	624.382	738.463	9	15.82											60	48.669	52.007	18.9	2.92
7	699	668.269	731.716	4.4	13.34											48	42.958	49.497	10.5	18.17
8	709	661.110	646.678	6.8	1.6	0.89	0.852	0.623	4.3	4.68						57.5	63.722	64.038	10.8	1.17
9	709	755.904	635.890	6.6	2.64	0.91	0.928	1.071	2.0	3.27						53.5	56.856	43.977	6.3	14.83
10	702	765.076	645.566	9	0.48	0.94	0.939	1.148	0.1	0.76						55	56.393	45.742	2.5	20.21
11	705	770.125	658.954	9.2	0.63	0.95	0.936	1.230	1.5	1.35						58	56.030	45.323	3.4	29.46
12	701	770.135	676.178	9.9	0.06	0.96	0.939	1.307	2.2	0.22						59	56.13	44.982	4.9	35.13
13	720	669.880	653.962	7	4.27						8.1	8.894	7.907	9.8	5.48	73.3	78.952	79.916	7.7	2.43
14	700	599.839	686.887	14.3	1.16						8.1	7.316	5.048	9.7	26.87	69.7	60.582	69.847	13.1	4.4
15	705	648.812	741.892	8	5.49						6.1	4.091	0.981	32.9	23.18	58.5	54.529	56.364	6.8	3.92
16	715	641.162	732.431	10.3	8.34						6.3	3.475	4.451	44.8	27.87	37.2	44.303	40.779	19.1	42.38
Mean absolute % error				9.26	7.97				2.0	2.1				24.3	20.85				11.45	16.23

8   Conclusion

1. ANN model is proposed for the prediction of the flow properties and compressive strength of SCCs.
2. The proposed ANN model shows relatively greater accuracy than the already existing DEA model. Hence, the proposed model can be utilized for the prediction of the properties of SCCs.
3. Through the application of ANN time and cost can be saved, which would have been spent on experimental works otherwise.

References

1. Sathyan, D., Anand, K.B.: Influence of superplasticizer family on the durability characteristics of fly ash incorporated cement concrete. Constr. Build. Mater. **204**, 864–874 (2019)
2. Aiyer, B.G., Kim, D., Karingattikkal, N., Samui, P., Rao, P.R.: Prediction of compressive strength of self-compacting concrete using least square support vector machine and relevance vector machine. KSCE J. Civil Eng. **18**(6), 1753–1758 (2014)
3. Koneru, V.S., Ghorpade, V.G.: Assessment of strength characteristics for experimental based workable self-compacting concrete using artificial neural network. Mater. Today **26**, 1238–1244 (2020)
4. Azimi-Pour, M., Eskandari-Naddaf, H., Pakzad, A.: Linear and non-linear SVM prediction for fresh properties and compressive strength of high-volume fly ash self-compacting concrete. Constr. Build. Mater. **230**, 117021 (2020)
5. Sonebi, M., Cevik, A., Grünewald, S., Walraven, J.: Modelling the fresh properties of self-compacting concrete using support vector machine approach. Constr. Build. Mater. **47**, 1217–1224 (2013)
6. Balf, F.R., Kordkheili, H.M., Kordkheili, A.M.: A new method for predicting the ingredients of self-compacting concrete (SCC) including fly ash (FA) using data envelopment analysis (DEA). Arab. J. Sci. Eng. **46**, 4439–4460 (2021)
7. EFNARC: The European guidelines for self-compacting concrete specification, production, and use. European federation of procedures and applicators of specialist products for structures (2005)
8. Dhiyaneshwaran, S., Ramanathan, P., Baskar, I., Venkatasubramani, R.: Study in durability characteristics of self-compacting concrete with fly ash. Jordan J. Civil Eng. **7**(3) (2013)
9. Bingol, A.F., Tohumcu, I.: Effect of different curing regimes on the compressive strength of self-compacting concrete incorporating fly ash and silica fumes. Mater. Des. **51**, 12–18 (2013)
10. Guneyisi, E., Gesoglu, M., Ozbay, E.: Strength and drying shrinkage properties of self-compacting concrete incorporating multi-system blended mineral admixture. Constr. Build. Mater. **24**, 1878–1887 (2010)
11. Krishnapal, P., Yadav, R.K., Rajeev, C.: Strength characteristics of self-compacting concrete containing fly ash. Res. J. Eng. Sci. **2**(6), 1–5 (2013)
12. Mahalingam, B., Nagamani, K.: Effect of processed fly ash on fresh and hardened properties of self-compacting concrete. Int. J. Earth Sci. Eng. **4**(5), 930–940 (2011)

13. Nepomuceno, M.C.S., Pereira-de-Olivera, L.A., Lopes, S.M.R.: Methodology for the mix design of self-compacting concrete using different mineral additions in binary blends of powders. Constr. Build. Mater. **64**, 82–94 (2014)
14. Sahmaran, M., Yaman, I.O., Tokyay, M.: Transport and mechanical properties of self-compacting concrete with high volume fly ash. Cement Concr. Compos. **31**, 99–106 (2009)
15. Siddique, R.: Properties of self-compacting concrete containing class F fly ash. Mater. Des. **32**, 1501–1507 (2011)
16. Siddique, R., Aggarwal, P., Aggarwal, Y.: Influence of water/powder ration on strength properties of self-compacting concrete containing coal fly ash and bottom ash. Constr. Build. Mater. **29**, 73–81 (2012)
17. Uysal, M., Yilmaz, K.: Effect of mineral admixture on properties of self-compacting concrete. Cement Concr. Compos. **33**, 771–776 (2011)
18. Ashtianni, M.S., Scott, A.N., Dhakal, R.P.: Mechanical and fresh properties of high-strength self-compacting concrete containing class C fly ash. Constr. Build. Mater. **47**, 1217–1224 (2013)
19. Jain, A., Gupta, R., Chaudhary, S.: Sustainable development of self-compacting concrete by using granite waste and fly ash. Constr. Build. Mater. **262**, 120516 (2020)
20. de Matos, P.R., Foiato, M., Prudencio, L.R., Jr.: Ecological, fresh state and long-term mechanical properties of high-volume fly ash high-performance self-compacting concrete. Constr. Build. Mater. **203**, 282–293 (2019)
21. Promsawat, P., Chatveera, B., Sua-iam, G.: Properties of self-compacting concrete prepared with ternary portland cement-high volume fly ash-calcium carbonate blends. Case Stud. Constr. Mater. **13**, e00462 (2020)
22. Mustapha, F.A., Sulaiman, A., Mohamed, R.N., Umara, S.A.: The effect of fly ash and silica fume in self-compacting high-performance concrete. Mater. Today Proc. **39**, 965–969 (2021)

Seismic Analysis of a PSC I Girder Bridge Using Nonlinear Static Method

Ambati Vamsi, Basil Baby, and T. Palanisamy

Abstract This paper presents a seismic analysis of three spanned Prestressed Concrete (PSC) I girder bridge, which is known for having a high load-bearing capacity and high flexural resistance. Bridge modeling is done in MIDAS Civil software. MIDAS Civil is a recently developed finite element-based software, exclusively for bridge modeling and well known for its user-friendly interface. A case study was carried on a 36.7 m of three spanned prestressed I girder bridge which consists of 4 numbers of Pre-Cast Post Tensioned-I Girder of 35.7 m long, under seismic Zone-II and is rested on hard soil strata. Loading on the superstructure is assigned as per IRC:6-2017. The entire work is divided into two phases; in the first phase, a three-dimension model of the bridge has been subjected to the linear dynamic method (response spectrum method) to obtain the displacement demand of the bridge. In the second phase, the nonlinear static method (push-over analysis) has been performed as per ACT 40 and FEMA 440. The displacement capacity results from the push-over analysis are used for carrying out seismic performance evaluation of a bridge. After analysis, the seismic response of a bridge is found out in terms of base shear and displacements.

Keywords PSC I girder bridge · Seismic analysis · Nonlinear static method · Response spectrum · Push over analysis · MIDAS civil

1 Introduction

The prestressed concrete was invented for longer spans of concrete bridges or structures and smaller concrete structure sections. Furthermore, the compressive stress in concrete eliminates the cracks in the members, and it results in increases in the structure's stiffness, which affects prestressed concrete deformation. Additionally, prestressed concrete does have some drawbacks. One of the most robust designs requires an engineer to divide the whole process into different stages by considering

A. Vamsi (✉) · B. Baby · T. Palanisamy
National Institute of Technology Karnataka, Surathkal, Mangalore, India
e-mail: ambativamsi.202st003@nitk.edu.in

different structural and load states [1]. RCC girders are uneconomical compared to PSC girders because RCC girders are obtained in reduced sections [2].

The assessment of seismic vulnerability for existing bridges is an essential concern these days [3]. FEMA 440 and ATC-40 present performance-based engineering methods for predicting structural demands using nonlinear static analysis procedures. Both documents' procedures involve the creation of a "pushover" curve to predict the structure's inelastic force–deformation behavior; this technique is used to calculate the inelastic behavior of a structure given different ground motions. The coefficient method is used to estimate the displacement demand by adjusting the elastic forecast of displacement demand in the FEMA 440 document. The ATC-40 document represents the Capacity-Spectrum Method, which determines the displacement demand of a structure by the intersection points at which the capacity curve obtained from the pushover analysis meets the demand curves derived from the response spectrum is the performance point, representing the bridge's actual capacity expressing the design ground motion, modified to account for modal displacement [4].

2 Methodology

2.1 MIDAS

Midas Civil is a finite element software commonly used in civil engineering to analyze structures. Midas Civil can perform both linear and nonlinear structural analyses and can handle various sorts of analyses. The program's quick analysis methods produce extremely flexible and accurate findings, making it ideal for practical design applications. The objective of the present study using Midas software is to perform a nonlinear static analysis over an existing pre-stressed concrete I girder bridge and find out the seismic behavior of that bridge in terms of capacity curve, performance point, hinging patterns, and performance level using Pushover analysis (ATC-40 and FEMA 440).

2.2 Bridge Loading

Loads are considered as per IRC 6-2017 [5]. These are the following loads consider in this case study:

a. Self-weight due to girder, deck slab and diaphragm
b. Super Imposed dead load due to crash barrier
c. Super Imposed dead load due to wearing coat
d. Moving loads due to IRC Class-70R vehicle, IRC-A vehicle loading and their load combinations
e. Wet concrete load from construction stage 1 to construction stage 6

f. Tendon prestressing load
g. Forces due to shrinkage and creep of concrete
h. Forces due to braking of vehicle
i. Forces due to wind load on deck in both longitudinal and transverse direction
j. Forces due to temperature rise and fall
k. Forces due to positive and negative temperature gradient
l. Forces due to water current
m. Forces due to log impact
n. Seismic forces

The load combinations are considered as per IRC 6-2017 [6]. IRC Class-70R loading is generally used for culverts and all types of bridges. Class-70R loading must check for class A loading in the bridge design class (Table 1 and Fig. 1).

Table 1 Moving load details

Lane	Eccentricity (m)	Wheel spacing (m)
Class A lane-1	1.8	1.8
Class A lane-2	5.3	1.8
Class A lane-3	8.8	1.8
Class 70R lane 1 (from right)	3.15	1.93
Class 70R lane 2 (from left)	3.15	1.93
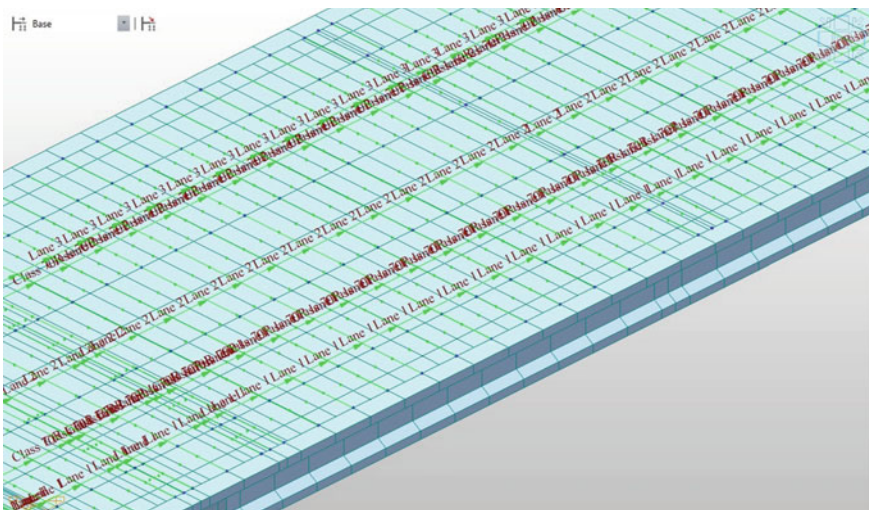
Fig. 1 Moving load on each lane (*source* MIDAS Civil)

3   Analytical Modelling

A model of the bridge was constructed using a three-dimensional finite element software called MIDAS Civil. as shown in Fig. 3. The modeling steps are as follows: defining the material properties, Section properties, assigning the node at origin then extruding and translating in both X and Y direction for girder section, assigning end diaphragm at ends of the span, and intermediate diaphragms at mid-span, assigning pier and pier cap of the bridge, restraints, bearings, etc. And defining several parameters like width of expansion joint, width and depth of bearing, elastic stiffness of a bearing, etc. In the end, the finite element model transformed into a bridge object to create the complete bridge model [7, 8].
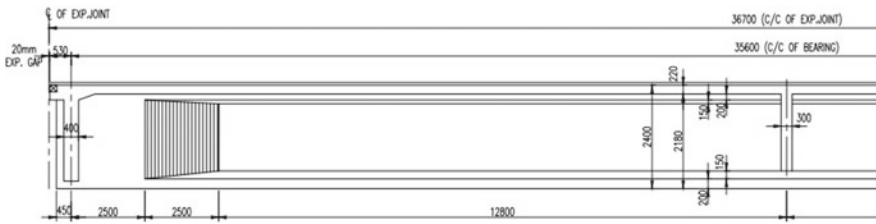
a Sectional Elevation A-A [9]
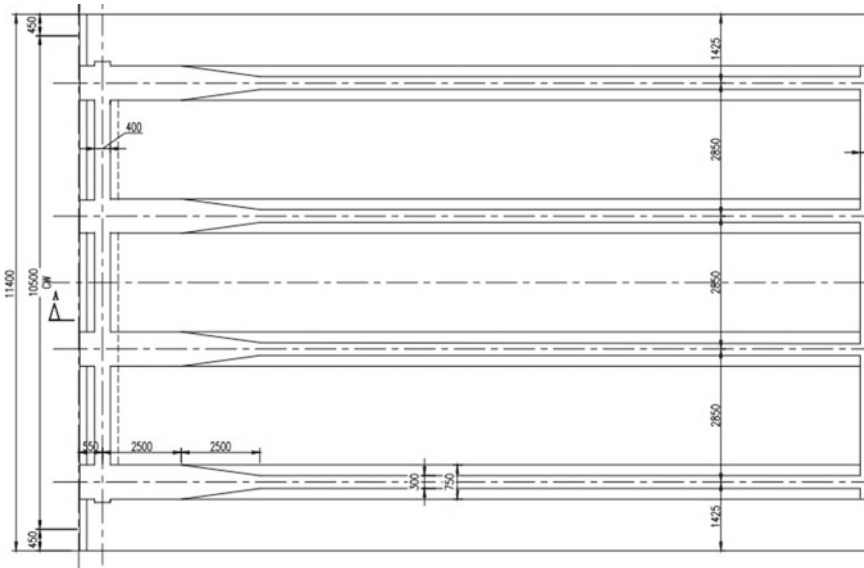
b Plan[9]

Fig. 2 Typical standard plan of a I-girder bridge [9] **a** Sectional elevation A-A [9] **b** Plan [9] **c** Dimensions of pier in transverse direction [9] **d** Dimensions of pier in longitudinal direction [9]
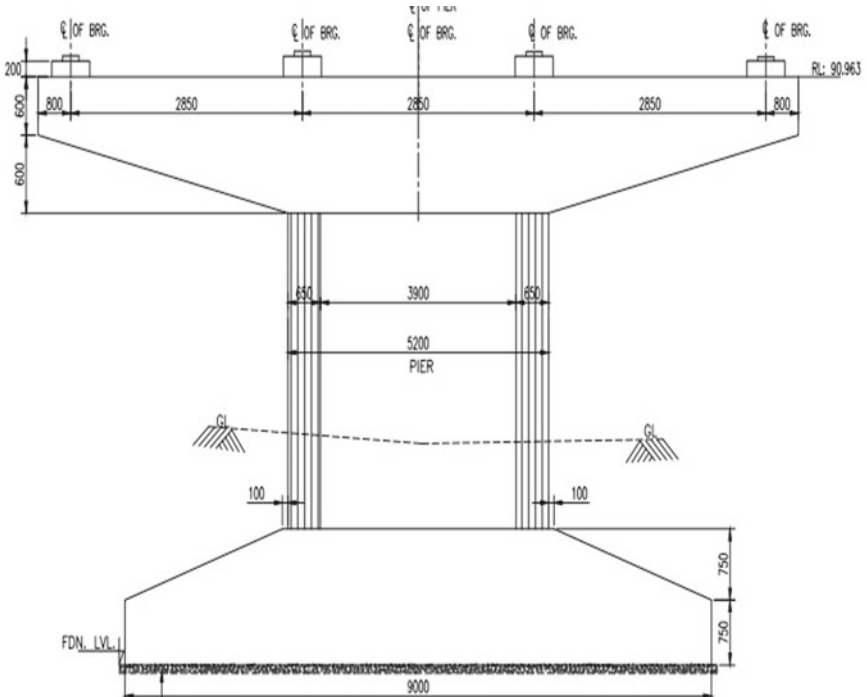
c Dimensions of pier in Transverse Direction[9]
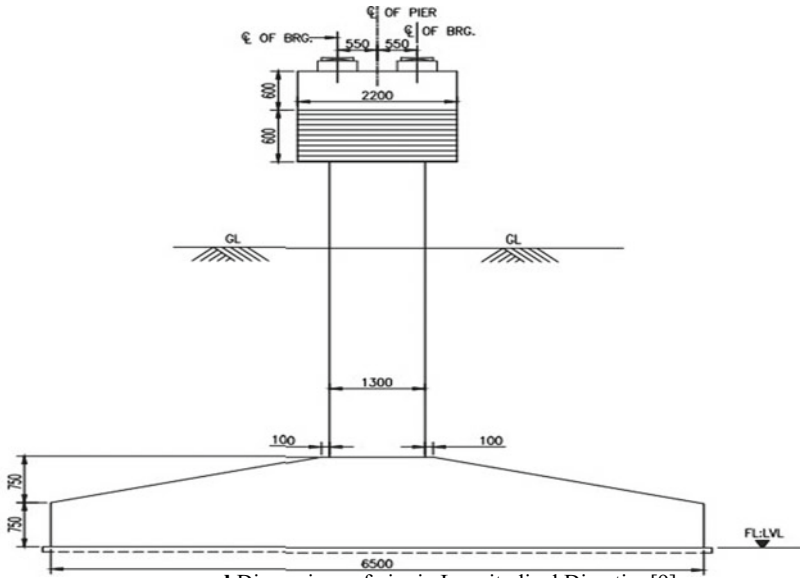
d Dimensions of pier in Longitudinal Direction[9]

Fig. 2 (continued)
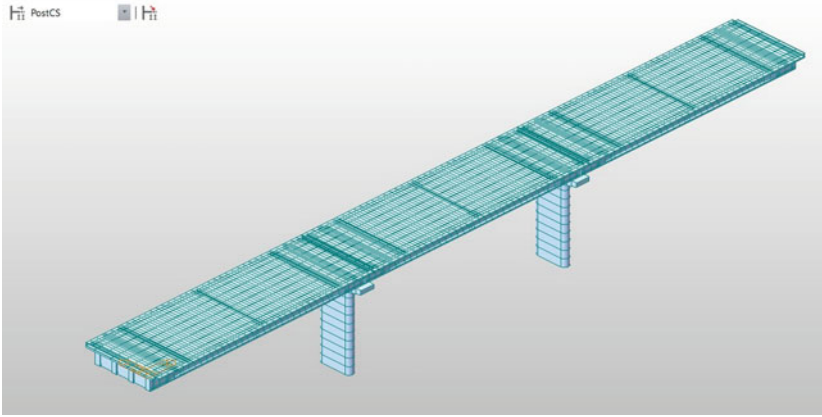
Fig. 3 Finite element model of I-girder bridge in MIDAS civil (*source* MIDAS Civil)

The present bridge deck section was I girder in design, with M40 grade concrete used for construction. The configurations of the deck section change, the thickness of the girder section is diverse parametrically along its length instead of being constant. At the ends it has 2.5 m of T-section then, followed by 2.5 m of the tapered section with linear variation, and the remaining portion is I-section. A cross-section details of the I-girder is shown in Fig. 2c.

3.1 Bridge Description

See Tables 2 and 3.

4 Pushover Analysis

The load in the vertical direction remains constant. In that case, a horizontal lateral force is applied to the structure, gradually increasing so that the design slowly yields from the elastic stage until the failure collapses. This method to determine the structure's seismic performance is defined as the Pushover analysis. It is essentially a nonlinear static analysis of the structure that can approximate dynamic properties. This method can be used to identify the design's weak parts. This method is recorded in the United States FEMA273, ATC-40, and FEMA440 research reports [10].

The two primary assumptions of Pushover analysis methods are as follows. The first-order mode is the primary controller of the structure's response, the influence in other ways can be ignored. During an earthquake, the shape vector governs the deformation of the design along the height and remains constant in the direction

Table 2 Bridge geometry

Sl. no	Bridge component		Specifications
1	Bridge name		Major High-Level Bridge, Sironcha
2	Total length of a bridge		110.1 m
3	Each span length		36.7 m
4	Centre to centre distance of bearings		35.7
5	Dimensions of pier		1.3 × 5.2 m (Solid Track)
6	Total width of bridge		11.40 m
7	Carriage way width		10.50 m
8	Pier cap width	Rectangular part	10.15 m
		Trapezoidal part	5.20 m
9	Pier cap height	Rectangular part	2.20 m
		Trapezoidal part	2.20 m
10	Pier cap length	Rectangular part	0.60 m
		Trapezoidal part	0.60 m
11	Height of pier shaft		11.9 m
12	End diaphragm or cross girder		2.2 × 0.4 m
13	Intermediate diaphragm or cross girder		2.2 × 0.3 m
14	Deck slab depth		0.22 m
15	Girder depth		2.4 m

of the size throughout the earthquake process. Pushover analysis procedure using MIDAS Civil:

Step 1: Define the pushover analysis model
Step 2: Define pushover global control settings
Step 3: Define pushover load cases
Step 4: Define and assign hinge properties
Step 5: Interpretation of the results

A plastic hinge is a section of an element where plastic bending occurs when a section exceeds its elastic capacity and has plastic behavior. Plastic hinges are not proper hinges. They can transfer their plastic moment to adjacent elements, thus maintaining lateral resistance, and can still support dead loads and resulting P-Δ effects. Plastic hinges will still have good lateral resistance but will continue to deform without additional loads. In this model, PMM hinges are used. The primary purpose of PMM hinges is to obtain the nonlinear behavior of a bridge. The reinforcement of a bridge pier is 80 numbers (40 on each face) of 25 mm diameter bars in the Pose 1 zone and 24 numbers of 25 mm diameter bars in the Pose 2 zone. The clear cover is 50 mm. Here Pose 1 indicates reinforcement in the rectangular part of the pier, and Pose 2 means reinforcement in the semicircular portion of the pier.

Table 3 Bridge elastic bearing properties

Span name	Station(m)	Component type	Number of bearings	Bearing property	Stiffness of bearing
Start abutment	0	Abutment	4	POT/POT-PTFE	In longitudinal direction = 519,125.58 kN/m In transverse direction = 34,001.46 kN/m
Span 1	36.7	Pier cap	4	POT/POT-PTFE	In longitudinal direction = 519,125.58 kN/m In transverse direction = 34,001.46 kN/m
Span 2	73.4	Pier cap	4	POT/POT-PTFE	In longitudinal direction = 519,125.58 kN/m In transverse direction = 34,001.46 kN/m
Span 3	110.1	Pier cap	4	POT/POT-PTFE	In longitudinal direction = 519,125.58 kN/m In transverse direction = 34,001.46 kN/m
End abutment	110.1	Abutment	4	POT/POT-PTFE	In longitudinal direction = 519,125.58 kN/m In transverse direction = 34,001.46 kN/m

5 Results and Discussions

5.1 Capacity Curve

The capacity curve represents the performance of a structure when it is subjected to seismic ground motions. A force–displacement curve derived from nonlinear static (pushover) analysis represented the structure's capacity. First, this method assumed distribution for the lateral loads on the frame and increased monotonically. As a result, the elements of a structure yield consecutively, and the structure loses stiffness. Figure 4, from the pushover analysis, shows that the pier's significant yield occurs when the displacement is 15 mm due to the pushover load in the X-direction. For
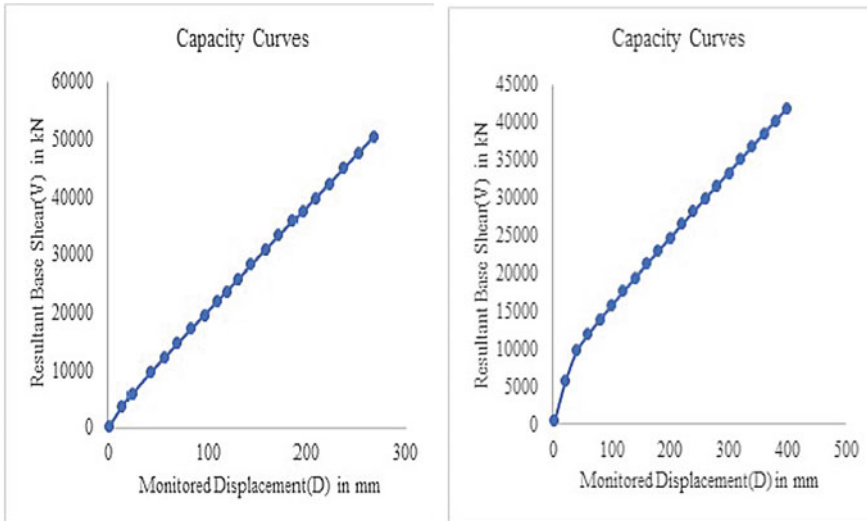
Fig. 4 Capacity curves from pushover load in X & Y directions

pushover load in the Y-direction, yield occurs when the displacement is shifted to 30 mm. The capacity curve shows that the pier could able to withstand a displacement of up to 260 mm in a longitudinal direction and 390 mm in a transverse direction.

5.2 Demand Curve

The design response spectrum is derived from the response spectrum of many individual ground motions. Figure 5 shows the demand spectrum obtained from the code IS 1893(2002) part-1 [5]. The bridge is resting on hard soil. The zone factor is II; the important factor is 1.2, and the response reduction factor is three as per IS 1893(2002) and 5% damping ratio is considered. The design spectrum is drawn between spectral data and the time period in seconds. The demand curve is generated by considering above all parameters.
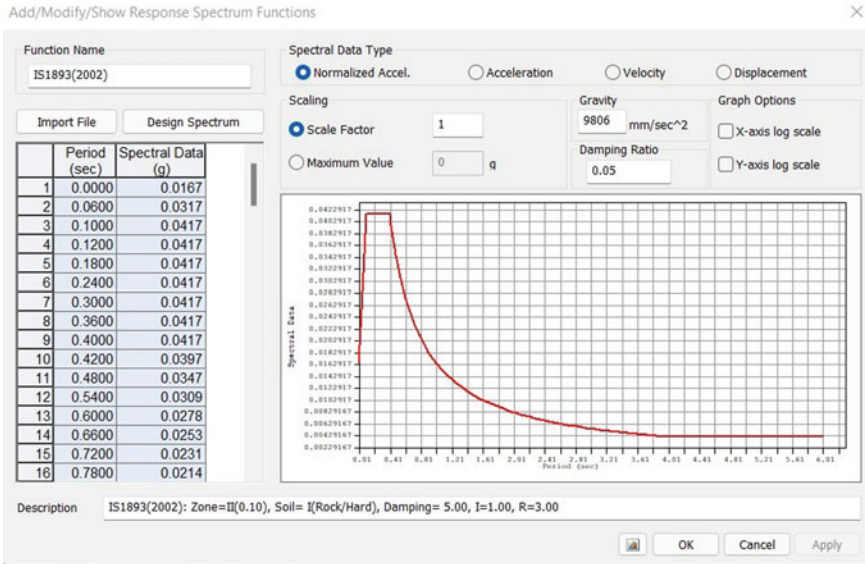
Fig. 5 Design spectrum as per IS 1893:2002 (*source* MIDAS Civil)

5.3 Performance Point

A performance point is a point on the pushover curve corresponding to the likely peak inelastic control node displacement during the ground shaking. In other words, the future earthquake is expected to push the building up to this point. According to IS: 1893:2002, Fig. 6 shows that the red color lines represent the demand spectrum at different damping levels (5, 10, 15, and 20%). The gray color lines represent the constant time period (0.5,1.0,1.5, and 2 s). The intersection points at which the capacity curve meets the demand curves is the performance point, representing the bridge's actual capacity. In Figs. 6 and 7 'V' stands for base shear, and 'D' stands for displacement concerning the performance point. The pushover load pattern is in the form of acceleration, and 20 incremental steps are used in the analysis. The Displacement-based increment method is used, and the maximum translation displacement is 400 mm in both push overload x and y cases. Figure 6 shows that the base shear capacity of a bridge due to push overload in the x-direction is 10410 kN, the corresponding displacement is 46.23 mm, the spectral acceleration is 0.52 g, and the spectral displacement is 33.56 mm. For push overload in the y-direction, the base shear capacity is 9672 kN, the corresponding displacement is 39.27 mm, the spectral acceleration is 0.58 g, and the displacement is 24.31 mm.
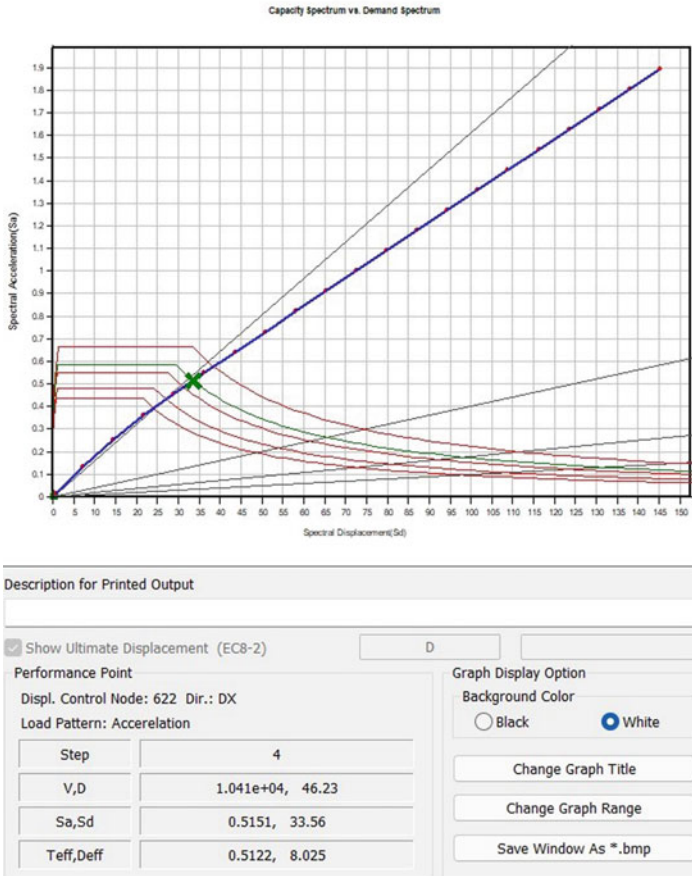
Fig. 6 Performance point w.r.t pushover load in X direction (*source* MIDAS Civil)

5.4 First Yield Point

The Fig. 8 shows that the first yielding occurs at step 3 in the case of Pushover load X and step 4 in the case of Pushover load. Y The blue color indicates the linear hinge, the green color indicates the first yield point, and the red color indicates the collapse.
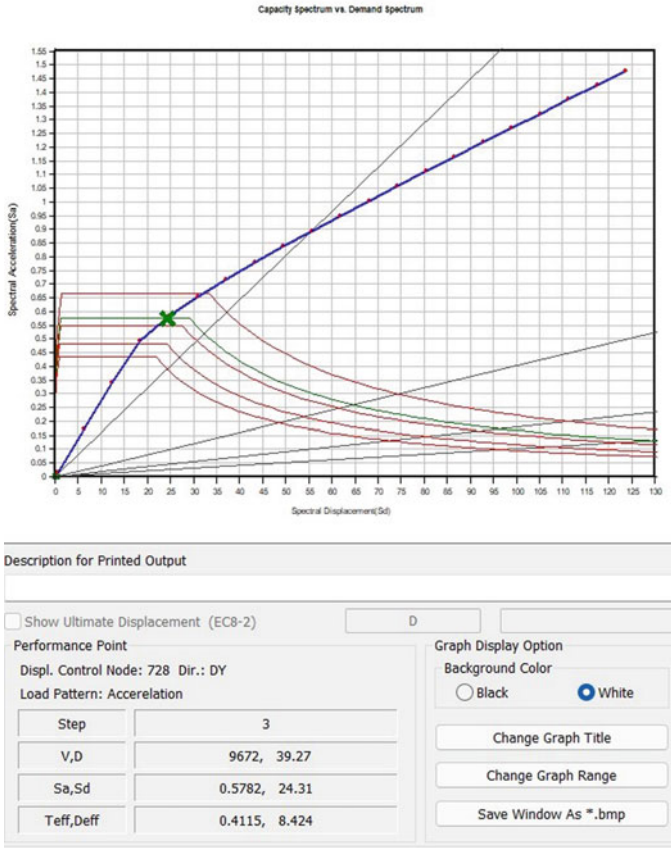
Fig. 7 Performance point w.r.t pushover load in Y direction (*source*: MIDAS Civil)
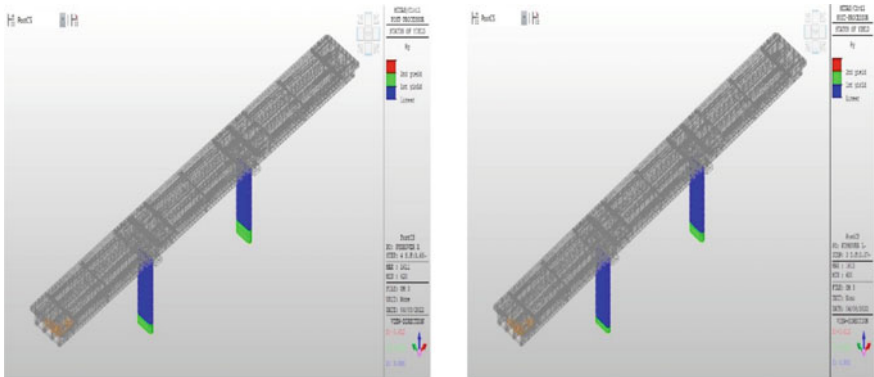
Fig. 8 First Yield point due to pushover load in X & Y directions (*source* MIDAS Civil)

6 Conclusions

The following conclusions are made after performing the analysis:

1. The displacement yield of a bridge due to pushover load X (longitudinal direction) is 46.23 mm and the displacement yield of a bridge due to pushover load Y (transverse direction) is 39.27 mm.
2. The first yielding occurs at step 4 in pushover load X (longitudinal direction) and collapse occurs at step 20.
3. The first yielding occurs at step 3 in Pushover load Y (transverse direction) and collapse occurs at step 14.
4. The value of base shear in the X-direction is 10410 kN, and Y-direction is 9672 kN, So the value of base shear in the X-direction is 7.08% more than Y-direction; hence the bridge is strong in the X-direction.
5. The capacity curve shows that the pier could able to withstand a displacement of up to 260 mm in a longitudinal direction and 390 mm in a transverse direction.

7 Future Scope of the Study

Fragility curves can be generated by using pushover analysis data. The yield displacement and ultimate displacement values are obtained by converting the pushover curve (Base shear vs. displacement) into a bilinear curve (Spectrum acceleration vs. spectral displacement). HAZUS-2003 code is considered for defining the damage states. Standard deviation values can be taken from HAZUS-2003, and damage states will calculate median values. The median values can depend on the damage states. Slight damage can occur where the spectral displacement is at 70% yield displacement; Moderate damage can occur where spectral displacement is equal to the yield displacement etc. The conditional probability can calculate the probability of damage state for a given spectral displacement. Finally, draw a plot fragility curve between the probability and spectral displacement and come to know the probability of damage corresponding to each damage state assessed.

References

1. Kralovanec, J., Moravcík, M., Jost, J.: Analysis of prestressing in precast prestressed concrete beams. Civ. Environ. Eng. **17**, 184–191 (2021). https://doi.org/10.2478/cee-2021-0019
2. Tarafder, N., Meesaraganda, L.V.P.: Seismic endurance of box-girder bridge with different piers. Mater. Today Proc. (2021). https://doi.org/10.1016/j.matpr.2021.11.099
3. Suwal, R., Sharma, B.: Seismic vulnerability evaluation of simply supported multi span RCC bridge pier damage identification of masonry buildings after Gorkha Earthquake. In: 2015 View project Seismic Vulnerability Evaluation of Simply Supported Multi Span RCC Bridge Pier. Www.Ijlemr.Com, 05, pp. 42–48 (2020). www.ijlemr.com

4. FEMA 440: Improvement of Nonlinear Static Seismic Analysis Procedures, FEMA 440, Fed. Emerg. Manag. Agency, Washingt. DC. (2005)
5. T.H.E. Indian, R. Congress, Standard Specifications and Code of Practice for Standard Specifications and Code of Practice for Road Bridges, Irc 21-2000, pp. 1–89 (2000)
6. kupdf.net_irc-06-2017.pdf (n.d.)
7. Shaik, K.A., Chandradhara, G.P.: Soil structure interaction studies on Krishnaraja Sagara Bridge, Mysuru. Mater. Today Proc. **52**, 549–555 (2022). https://doi.org/10.1016/j.matpr.2021.09.496
8. Masrilayanti, R., Kurniawan, R.: Seismic vulnerability assessment of three spans girder bridge in Kuranji - Padang by developing fragility curve. IOP Conf. Ser. Earth Environ. Sci. **708** (2021). https://doi.org/10.1088/1755-1315/708/1/012006
9. D.G. Project: Special Project Division Date (n.d.)
10. Yuan, W., Wang, B., Cheung, P., Cao, X., Rong, Z.: Seismic performance of cable-sliding friction bearing system for isolated bridges. J. Earthq. Eng. Eng. Vib. **11**, 173–183 (2012). https://doi.org/10.1007/sl1803-012-0108-2

Performance Evaluation of Concrete Using Different Additives

Kiran Devi (ORCID)**, Babita Saini, and Paratibha Aggarwal**

Abstract Globalization and urbanization have raised the demand for natural raw materials in the concrete industry. The ongoing depletion of natural resources in the building industry encourages the potential use of various industrial by-products produced by many industries as raw materials. However, the stone processing industry makes a significant contribution to the construction industry along with the generation of waste in huge amounts. Industrial wastes not only contribute to land and water pollution but, also create annoyance. Since the construction industry is under pressure to find cost-effective and long-term alternatives to raw materials; reuse of these wastes could be a possible solution. However, chemical admixtures of accelerating nature are added to concrete mixtures to enhance the early age strength development and setting time. In the present study, calcium nitrate (1%), triethanolamine (0.05%) and stone waste powder (10%) separately and in combination were used in different concrete mixtures to examine the economic and ecological feasibility of additives in different concrete mixtures. The performance index of different mix proportions in terms of strength, cost and ecological analysis was evaluated. It was concluded that the addition of stone waste powder in concrete improved the performance without compromising the cost and environment among all additives. The addition of stone waste powder in concrete reduced the embodied energy and embodied carbon dioxide.

Keywords Concrete · Stone waste powder · Admixtures · Environmental assessment · Performance evaluation

K. Devi (✉) · P. Aggarwal
Department of Civil Engineering, Faculty of Engineering and Technology, Shree Guru Gobind Singh Tricentenary University, Gurugram 122505, Haryana, India
e-mail: kiranbimbhra@gmail.com

K. Devi · B. Saini · P. Aggarwal
Department of Civil Engineering, National Institute of Technology, Kurukshetra, Kurukshetra 136119, India
e-mail: bsaini@nitkkr.ac.in

1   Introduction

Concrete is a versatile construction and offers a number of advantages and disadvantages depending on the environment. Researchers are attempting to make concrete more effective by adding extra elements or admixtures to mitigate the problems of concrete. The adding of extra components to concrete mixes to improve certain qualities is known as admixture. Admixtures improve the qualities of cement-based materials by speeding up or slowing down the setting time, increasing workability without affecting the water content, increasing strength, durability, or resistance to extreme exposure conditions, and increasing impact resistance [1]. Fast construction, which is advantageous to the construction organization, has become a key requirement of the modern era. The formwork can be rented for a limited period of time, and the mould for the precast part can be filled with the following elements early, increasing construction efficiency and speed. Furthermore, under diverse weathering circumstances, particularly at low temperatures, mortar/concrete does not attain sufficient strength [2]. Accelerating admixtures are used to obtain the desired strength and speed up the construction process. By speeding up the hydration process, accelerators can reduce the setting time (ST) and boost the strength of cementitious materials at an early stage. By speeding up the hydration process, accelerators can reduce the setting time and improve the strength of cementitious materials at an early stage. Accelerators enable in the early removal of formworks and, as a result, the early deployment of the structure in service or maintenance, the decrease of hydraulic pressure on formworks and curing time, and partial or complete compensation from the effects of low temperature. Nitrate, nitrite, formate, thiocyanate, amine etc. are used in the mortar and concrete to fulfil the above-mentioned purposes. Calcium nitrate (CN), triisopropanolamine (TIPA) alone and combined increased strength [3]. The addition of triethanolamine (TEA) improved the compressive strength (CS) of Portland cement (PC) paste at 1 day but reduced strength after 3 days. Modified triethanolamine (M-TEA) (0.03 and 0.04%) increased CS at 3 and 28 days [4]. Addition of Ultrafine ground granulated blast furnace slag (GGBS) enhanced CS due to its small size and high specific surface area which caused better cohesive and adhesive bonding. CN improved CS of concrete significantly due to better bonding between constituents in the solid phase [5].

Rajasthan is India's leading stone-producing state. Kota stone is a siliceous limestone variant mined in the Rajasthani city of Kota. Depending on whether the quarrying is done mechanically or manually, the waste from Kota stone manufacturing ranges from 30 to 60%. India produces around 1.2 million tonnes of Kota stone dust waste every year. The waste is slurry-like and is deposited on any accessible ground, degrading the ecosystem. As a result, stone waste will be utilized in the building sector to reduce environmental concerns. The quantity of waste produced by the stone industry is growing, causing ecological damage. Stone slurry as cement replacement (5%) and stone slurry as a sand replacement (50%) increased CS [6, 7]. Marble waste as cement replacement reduced the environmental impact [8, 9].

The purpose of the study was to examine the feasibility or practicality of stone waste powder and chemical admixtures (individual as well as their combinations) in cement concrete specimens in terms of environmental aspects. To study the consequences of accelerating admixtures as cement additive and stone waste powder (SWP) from the stone industries on different properties of concrete mixtures. Performance evaluation of varying concrete mixes was evaluated.

2 Methodology

The ordinary portland cement of 43 grade and potable water was used during all the experimentation. Locally available coarse sand and coarse aggregates of 10 and 20 mm were used as fine and coarse aggregates. Calcium nitrate tetrahydrate purified and Triethanolamine LR was used as an additive of accelerating nature in the present work and procured from the local supplier. SWP from Kota stone has been used as a replacement of cement by 10% in concrete mixtures [10, 11]. Eight different concrete mixes were selected and given in Table 1 [12].

The ecological and economic aspects of concrete can be examined in terms of embodied energy (EE) and embodied carbon dioxide (ECO_2), respectively [12]. Table 2 shows the values of EE and ECO_2 utilized by several researchers for cement, sand, coarse aggregates, water, CN, TEA, and SWP [13] and also includes the cost of all raw ingredients at current market values. Equation 1 was used to calculate the ecological and economical parameters

$$EE/ECO_2/\text{Cost} = \Sigma g_i m_i \qquad (1)$$

where g_i = EE per unit mass of materials and m_i indicate the mass of concrete ingredients i per unit cubic meter.

Table 1 Mix designation of concrete mixtures [11]

Mix no.	Cement, kg/m^3	Fine aggregate, kg/m^3	Coarse aggregate, kg/m^3	Water, kg/m^3	CN, kg/m^3	TEA, kg/m^3	SWP, kg/m^3
N1	390	503.1	1088.1	167.7	0	0	0
N2	360.75	503.1	1088.1	167.7	0	0	29.25
N3	390	503.1	1088.1	167.7	0	0.195	0
N4	390	503.1	1088.1	167.7	3.9	0	0
N5	390	503.1	1088.1	167.7	3.9	0.195	0
N6	360.75	503.1	1088.1	167.7	0	0.195	29.25
N7	360.75	503.1	1088.1	167.7	3.9	0	29.25
N8	360.75	503.1	1088.1	167.7	3.9	0.195	29.25

Table 2 EE, ECO_2, and cost of raw materials [12]

Materials	Cement	Sand	Coarse aggregates	Water	CN	TEA	SWP
EE, MJ/kg	4.8	0.081	0.0083	0.2	0.1368	–	–
ECO_2, $kgCO_2$/kg	0.93	0.0051	0.0008	0.0008	0.481	–	–
Cost, INR/kg	6	1	1.8	0.05	430	1060	–

The performance index (PI) tool encourages the investigation of SWP content in order to create the best combinations that meet the desired performance parameters. The numeric index (Ri) was determined using Eq. 2 with 5.00 being the highest numeric index [12, 14].

$$R_i = \frac{\text{Measured performance for each mixture}}{\text{Best measure performance}} \times 5 \qquad (2)$$

Rather than using qualitative terminology, quantitative analysis may be utilized to characterize the performance of additives in concrete. If the performance of plain concrete is 1.0, then the performance of concrete with additives will be less than or more than 1 in many aspects, indicating poorer or superior performance in comparison to plain mix. Individually, the performance of additives such as SWP, CN, and TEA will be assessed in comparison to a basic concrete mix [12, 15].

3 Results and Discussion

Accelerators individually and in combination increased the strength of concrete due to progress in cement hydration and reduction of porosity due to the formation of more hydration products [10]. Electrical resistivity (ER) increased with the use of CN, TEA and SWP individually but their combination decreased the ER of concrete as compared to plain mix. The combination of accelerators increased the ER of concrete. The combination of accelerators and SSP reduced the ER of concrete [10].

3.1 Environmental Assessment of Concrete

The impact of additives on concrete in terms of ecological and economic aspect was studied and has been given in Table 3. The values of EE, ECO_2 and cost of all the mix proportions varied from 2127.5 to 2339.5 MJ/m^3; 380 to 423.1 kgCO$_2$e/m^3 and 5975 to 8321 INR/m^3 respectively. The value of EE, ECO_2 and cost per unit strength varied from 37.25 to 49.76, 6.65 to 8.93 and 105 to 183.95 for all the mix proportions. The inclusion of SWP reduced EE, ECO_2 and cost of concrete whereas chemical additives increased it all.

Table 3 Ecological and economic analysis of concrete containing additives

Mix no	CN	TEA	SWP	365 D-CS	EE (MJ/m³)	ECO_2 (kg CO_2e/m^3)	Cost (INR/m³)	EE/365 D-CS	ECO_2/365 D-CS	Cost/365 D-CS
H1	0	0	0	52.8	2338.74	420.94	6196	44.32	7.98	117
H2	0	0	10	57.1	2127.54	380.02	5976	37.25	6.65	105
H3	0	0.05	0	55.5	2338.74	420.94	6429	42.13	7.58	116
H4	1	0	0	60.7	2339.34	423.05	8088	38.57	6.98	133
H5	1	0.05	0	55.2	2339.34	423.05	8321	42.35	7.66	151
H6	1	0	10	46.9	2127.54	380.02	6209	45.31	8.09	132
H7	0	0.05	10	42.8	2128.14	382.13	7868	49.76	8.93	184
H8	1	0.05	10	45.7	2128.14	382.13	8101	46.59	8.37	177
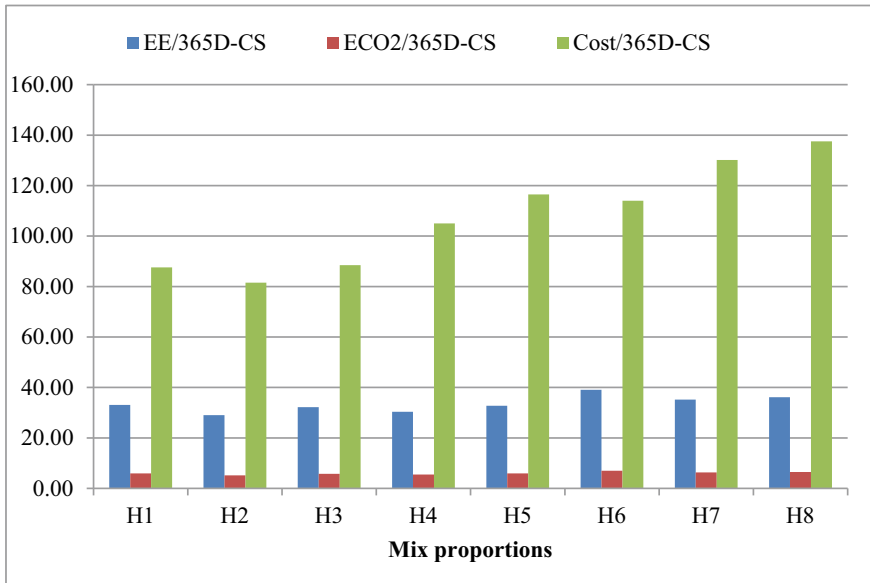
Fig. 1 Variation in EE, ECO$_2$ and cost of concrete

The percentage variation in EE, ECO$_2$ and cost of concrete using various additives and same for per unit strength has been shown in Fig. 1. Figure 1 depicted that use of SWP reduced the EE and ECO$_2$ in concrete mixtures. SWP cut down the cost of concrete; while chemical additives hiked it. The cost per unit strength decreased for H2 and H3 only. The percentage increase in EE and ECO$_2$ were 0.03 and 0.5%, cost varied from 0.2 to 34.30%; and reduction in EE was 9%, ECO$_2$ and cost varied from 9.2 to 9.7 and 3.6% for all the mix proportions. The percentage reduction in EE, ECO$_2$ and cost per unit strength varied from 4.5 to 16%, 4 to 16.6% and 1.3 to 11%; and increase in EE, ECO$_2$ and cost per unit strength varied from 2.2%–12.3%, 1.4%–12% and 12.6%–56.7% respectively for all the mix proportions.

3.2 Performance Evaluation

The performance index of concrete of different mix proportions according to the requirements were evaluated and have been given in Table 4. The highlighted mixes had the best performance according to the individual and combined properties i.e. mechanical strength, ER, resistance against chemical attack at various curing ages. The mix H4 i.e. CN at 1% is the mix which can be preferred in various requirements i.e. where strength and durability is the main concern. But in the case where the economy and environmental concern are the important factors, mix H2 i.e. SWP at

Table 4 Individual performance indices of concrete

Mix No.	365D CS	365D STS	365D ER	EE	ECO$_2$	Cost	EE/365D-CS	ECO$_2$/365D-CS	Cost/365 D-CS
H1	4.54	4.57	4.41	5	4.97	3.59	33.06	5.95	87.58
H2	5	5	5	4.65	4.61	3.48	29.04	5.19	81.57
H3	4.27	4.21	4.23	5	4.97	3.75	32.2	5.79	88.5
H4	4.9	4.64	4.61	5	5	4.85	30.38	5.49	105.02
H5	4.85	4.75	4.73	5	5	5	32.76	5.93	116.54
H6	4.56	4.43	4.49	4.65	4.61	3.64	39.07	6.98	114.03
H7	4.7	4.69	4.77	4.66	4.63	4.74	35.2	6.32	130.15
H8	4.12	3.73	4.26	4.66	4.63	4.89	36.13	6.49	137.53

10% can be preferred and mechanical strength is also better as compared to plain mix.

Table 5 shows the numerical evaluation of the performance index of concrete with additives in comparison to plain mix. The performance of additives in concrete was measured against a control mix and given a score of 1.0. The greater the value of the strength and durability elements, the better the performance, and the lower the value, the worse the performance compared to plain mix. Lower values lead to more cost-effective and environmentally friendly building. In terms of strength and durability, CN had the greatest value among all additions, as shown in Table 4. In addition, as compared to ordinary mix, TEA, SWP, and CN + TEA performed better. SWP was discovered to be a sustainable construction material from both an economic and environmental standpoint. Although CN had higher strength and durability, its addition to concrete increased the cost, energy consumption, and CO_2 emissions. SWP, on the other hand, has high strength and durability (lower than other additives) and also contributes to long-term construction.

Table 5 Performance index of concrete

Mix no.	365 days			EE	ECO$_2$	Cost
	CS	STS	ER			
H1	1.00	1.00	1.00	1.00	1.00	1.00
H2	1.04	1.15	1.07	0.91	0.90	0.96
H3	1.03	1.02	1.06	1.00	1.00	1.04
H4	1.09	1.08	1.12	1.00	1.01	1.31
H5	1.01	1.04	1.02	1.00	1.01	1.34
H6	0.77	0.95	0.78	0.91	0.90	1.00
H7	0.85	0.89	0.83	0.91	0.91	1.27
H8	0.83	0.97	0.78	0.91	0.91	1.31

4   Conclusion

The feasibility of Kota stone slurry powder and admixtures in concrete mixes was investigated in terms of environmental aspects in the current study. As a result, the following findings arrived:

– The incorporation of stone waste powder reduced the EE, ECO$_2$ and cost by 10, 9, and 10% in comparison to control mix. Thereby, SWP in concrete produced stronger, less energy-intensive, lower CO$_2$ emission, and cost-effective final products among all the additives.
– The addition of SWP lowered the energy usage, CO$_2$ emissions, and cost per unit strength by 12%, 13%, and 7%, respectively.
– The performance of various mix proportions was evaluated in comparison to plain mix. SWP has superior performance.

It was discovered that using SWP as stone waste in cement-based products proved effective. The use of SWP in concrete not only increased performance but also promoted long-term sustainability. The difficulty of SWP disposal was overcome by incorporating it into cement. In comparison to the control mix, SWP in concrete generated stronger, less energy-intensive, lower CO$_2$ emission, and cost-effective final products.

References

1. Gambhir, M.L.: Concrete Technology, 4th edn. McGraw –Hill Company, New Delhi (2009)
2. Awasthi, G., Choubey, U.B.: A study of effect of accelerators on compressive and flexural strength of concrete. Int. J. Sci. Technol. Eng. **2**, 78–81 (2005)
3. Aggoun, S., Cheikh-Zouaoui, M., Chikh, N., Duval, R.: Effect of some admixtures on the setting time and strength evolution of cement pastes at early ages. Constr. Build. Mater. **22**, 106–110 (2008)

4. Zhao, J., Wang, D., Wang, X., Liao, S.: Characteristics and mechanism of modified triethanolamine as cement grinding aids. J. Wuhan Univ. Technol.-Mater. Sci. Edn. **30**, 134–141 (2015)

5. Kumar, M.P., Mini, K.M., Rangarajan, M.: Ultrafine GGBS and calcium nitrate as concrete admixtures for improved mechanical properties and corrosion resistance. Constr. Build. Mater. **182**, 249–257 (2018)

6. Almeida, N., Branco, F., Santos Josè, R.: Recycling of stone slurry in industrial activities: application to concrete mixtures. Build. Environ. **42**, 810–819 (2007)

7. Al-Zboon, K., Al-Zou'by, J.: Recycling of stone cutting slurry in concrete mixes. J. Mater. Cycles Waste Manage. **17**, 324–335 (2015)

8. Khodabakhshian, A., de Brito, J., Ghalehnovi, M., Shamsabadi, E.A.: Mechanical, environmental and economic performance of structural concrete containing silica fume and marble industry waste powder. Constr. Build. Mater. **169**, 237–251 (2018)

9. Singh, M., Srivastava, A., Bhunia, D.: Long term strength and durability parameters of hardened concrete on partially replacing cement by dried waste marble powder slurry. Constr. Build. Mater. **198**, 553–569 (2019)

10. Devi, K., Saini, B., Aggarwal, P.: Long term performance of concrete using additives. Int. J. Microstruct. Mater. Prop. (2020). https://doi.org/10.1504/IJMMP.2020.104612

11. Devi, K., Saini, B., Aggarwal, P.: Utilization of Kota stone slurry powder and accelerators in concrete. Comput. Concr. **23**, 189–201 (2019)

12. Devi, K., Saini, B., Aggarwal, P.: Impact of high temperature on mortar mixes containing additives. J. Eng. Res. **10** (2021). https://doi.org/10.36909/jer.10477

13. Flower, D.J.M., Sanjayan, J.G.: Green house gas emissions due to concrete manufacture. Int. J. Life Cycle Assess. **12**, 282 (2007). https://doi.org/10.1065/lca2007.05.327

14. El-Dieb, A.S., Kanaan, D.M.: Ceramic waste powder an alternative cement replacement–characterization and evaluation. Sustain. Mater. Technol. **17**, e00063 (2018)

15. Kayali, O., Ahmed, M.S.: Assessment of high volume replacement fly ash concrete – concept of performance index. Constr. Build. Mater. **39**, 71–76 (2013)

Comparative Study of Site-Specific Response Spectra and IS Code Response Spectra

Shashank Kumar , **M. Abdul Akbar** , **and Neha Bhardwaj**

Abstract Measurement of earthquake excitation through sub-surficial soil layers to site of interest have a prominent role in any structural design. Ground response analysis (GRA) has been carried out to check the effect of earthquake on local soil condition adopting equivalent linear method. Response spectrum is generated using DEEPSOIL for the 16 borehole locations of Jalandhar, Punjab using geotechnical data. Bedrock motion used for this analysis is taken from Jalandhar station. The shear wave velocity is determined empirically by the correlation between standard penetration test value (SPT-N) and shear wave velocity. Average shear wave velocity at 30 m depth is determined and, further 16 borehole sites are classified using NEHRP guidelines. The response spectra are plotted with IS code response spectra and, further the responses are used for determination of the base shear of the building. As per this study, site-specific response spectra is higher for lesser time period, whereas IS code 1893 (Part 1) 2002 response spectra is higher for higher time period. The building used for analysis is already constructed having an orientation of 39° with the north direction. The analysis of the base shear is carried out using STAAD Pro. The base shear results are interpreted by using the different modes of combination and the results are compared between site specific response spectra and IS code response spectra. The average of difference in percentage for SRSS, 10PCT, ABS, CQC is −2.93, 1.24, 0.98, −3.16 respectively.

Keywords Ground response analysis · DEEPSOIL · Shear wave velocity · Response spectra · STAAD pro · Base shear · Modes of combination

S. Kumar (✉) · M. Abdul Akbar · N. Bhardwaj
Department of Civil Engineering, Dr B R Ambedkar National Institute of Technology, G.T. Road, Amritsar Bypass, Jalandhar 144011, Punjab, India
e-mail: shashankk015@gmail.com; shashankk.ce.20@nitj.ac.in

M. Abdul Akbar
e-mail: akbarma@nitj.ac.in

N. Bhardwaj
e-mail: nehab.ce.20@nitj.ac.in

1   Introduction

Earthquake is a natural unpredictable event which cannot be controlled. The majority of the tremors are so small that they cannot be felt, but few of them are strong enough and those events are responsible for property damages all around the world. In India, there is a history of continuous earthquake events because of the Indian plate moving towards the Asian plate, which cause lots of earthquake events every year. Various seismic events such as Loma Prieta earthquake 1989, Kobe earthquake 1995, Michocan earthquake 1985, Northridge earthquake 1994, etc. shows the effects of local geographical and local soil condition on ground responses due to seismic excitation [1]. Behaviour of seismic waves can be seen as they can generally travel several kilometres in rock but very few distance (m) in soil. Sub-surficial layer plays an important role in estimation and determination of ground motion. From previous research works, it is observed that earthquakes originate from the fault resulting in the release of shear waves in the form of energy. These shear waves travel through local soil from the fault to the site of interest, due to which resulting motion at the site felt amplified or de-amplified based on the soil properties, which means ground motion changes with respect to the surficial layers [2].

In India, earthquake resistant structures are designed according to the IS code 1893 (Part 1) named as Criteria for Earthquake Resistant Design of Structures, which has a certain factor of safety. Response spectrum analysis is generally used for determining the peak response parameters such as displacement, velocity, acceleration, stress, etc. of a structure concerning a motion. IS 1893 (Part 1) 2016 has spectra for the static method and for the response spectrum method, which are the plot between design acceleration coefficient (Sa/g) and natural period (T) corresponding to 5% damping. Spectra is depended on the type of soil on which the structure is placed [3]. Analysing the behaviour of any structure with respect to earthquake motion is one of the complex tasks as shown in Fig. 1. One of the most important methods used for dynamic analysis of structure is response spectrum analysis. It is defined as the combination of velocity, acceleration, and displacement where maximum response for all single degree of freedom system, is specified for seismic ground motion corresponding to damping ratio of 5%. Such modes of combination help structural designer in obtaining the maximum responses of the structure. Response spectrum analysis is a type of dynamic analysis in which all final eigen values are used with minimum mass participation value as 90%. For a combination of responses, any of the absolute sum method (ABS), closely spaced modes (CSM) method, and square root of summation of squares method (SRSS) method as well as 10% (10PCT) methods can be used. Base shear estimation plays an important role in earthquake resistant design of structures [4]. Base shear can be explained as it is an estimate of the maximum expected lateral force on the base of the structure due to seismic activity. Value of base shear (V) is completely dependent upon various factors such as seismic zones, sub-surficial soil conditions at site of interest, previous seismic activity data including geological faults, probability of seismic excitation and seismic ground motion, level of ductility and overstrength associated with various structural configurations and total weight,
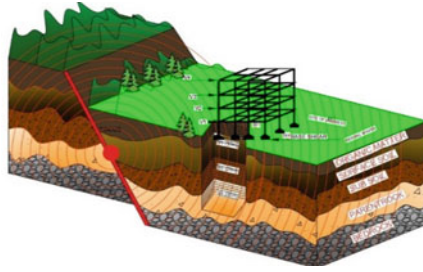
Fig. 1 Distribution of base shear on building due to earthquake

fundamental (natural) period of vibration of the structure when subjected to dynamic loading [5].

There are various softwares used for 1-Dimensional site response analysis, and DEEPSOIL is one of them. In this research analysis of specific sites in Jalandhar, an iterative procedure was done where equivalent linear analysis was carried out and frequency domain solution type was selected. Shear modulus and damping are provided for each layer. In this study, effects of available sub-surficial layers on earthquake motions have been estimated by equivalent linear wave propagation method and obtained results are used for designing of structure. Further, the results were compared with those of a building designed as per IS 1893 (Part-1) 2016.

1.1 Study Area and Geology

Smart City Jalandhar is known to be the third most populated city of Punjab, India. This city is known to be one of the largest city in Doaba region having area of $110 \, km^2$. Jalandhar is known to be the biggest hub of medical cares as there are more than 800 super-specialty, multi-specialty centers, nursing homes and clinics. Jalandhar lies under seismic zone IV which is known as high-risk zone, because of this, it is important to do detailed earthquake motion studies such as ground response analysis. In this study, 4 sites and 16 borehole locations were selected as shown in Fig. 2 for site classification and determination of ground response. The data is collected for the bore holes in Jalandhar from various private and government agencies and Empire Geo technique is one of them. Data is collected for 4 boreholes for each of the 4 sites for ground response analysis (GRA) and design comparisons.

2 Methodology

The collected data of the boreholes is studied and processed, as there is standard penetration test (SPT-N) values corresponding to different depths. The available unit
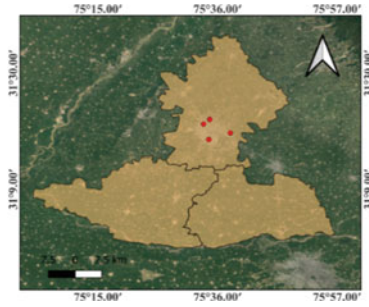
Fig. 2 Location of 16 boreholes

weight, which is estimated by the undisturbed samples taken at different depths for 16 individual boreholes, and standard penetration test values (SPT-N) are used in the study. Ketan Bajaj and P. Anbazhagan studied the spatial variability of shear wave velocity in the Indo-Gangetic basin. They divided the Indo-Gangetic basin into three parts, namely Punjab-Haryana region, Uttar Pradesh region and Bihar region, and derived the correlations for all three regions for corrected and uncorrected SPT-N [6]. Based on the correlation for the Punjab-Haryana region, shear wave velocity is calculated for uncorrected SPT-N values from Eq. (1). Then average shear wave velocity is calculated (as plotted in Fig. 3) for 30 m depth using Eq. (2) to classify the site according to the NEHRP guidelines [7]. The average shear wave velocity of these boreholes lies between 318.02 m/s to 401.29 m/s. Based on the data, 10 borehole sites are classified as C i.e. very dense soil and soft rock, whereas 6 borehole sites are classified as D i.e. stiff soil as shown in Table 1.

$$Vs = 64.23 * N^{0.48} \tag{1}$$
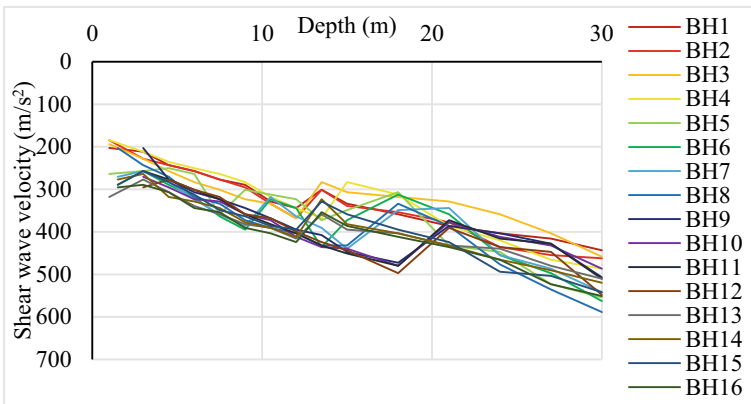
Fig. 3 Average shear wave velocity at 30 m depth for 16 boreholes

Table 1 Classification of site according to NEHRP

Borehole number	Average shear wave velocity at 30 m (m/s)	Site class
BH1	322.88	D
BH2	354.00	D
BH3	359.47	D
BH4	391.90	C
BH5	329.42	D
BH6	318.02	D
BH7	319.92	D
BH8	369.29	C
BH9	369.98	C
BH10	372.27	C
BH11	381.35	C
BH12	376.28	C
BH13	389.66	C
BH14	387.21	C
BH15	383.60	C
BH16	401.29	C

$$V savg 30 = \sum_{i=1}^{i=n} di \Big/ \sum_{i=1}^{i=n} \frac{di}{Vs} \tag{2}$$

Ground response analysis is carried out for all 16 boreholes by the equivalent linear analysis method and frequency domain solution type. The unit weight and shear wave velocity for each layer, of corresponding depths are used for the soil profile development along with 5% minimum damping. Darendeli 2001 reference curve is used. Mehmet Baris Darendeli obtained the 20 soil samples and tested them in the dynamic laboratory to characterize the material. He generated the empirical curves and represented them in the form of empirical equations [8]. These equations are used in DEEPSOIL for further calculations. The shear wave velocity of bedrock used is 760 m/s and the unit weight taken is 24.52 kN/m^2 along with 2% damping [2]. The motion applied on the soil profile is obtained from the PESMOS website run by the department of earthquake engineering, IIT Roorkee [9]. Magnitude of the earthquake is 4.6 having latitude and longitude of 31.7°N and 71.6°E respectively, and the latitude and longitude of the recording station are 31.320°N and 75.594°E respectively, that is Jalandhar station. The maximum acceleration along north–south (NS), east–west (EW) and vertical direction (VT) is −5.33 m/s^2, −3.785 m/s^2 and 10.092 m/s^2 respectively as shown in Fig. 4(a), (b) and (c) respectively.

After running the analysis, the peak spectral acceleration corresponding to time period is obtained for each layer of soil profile. The spectral acceleration obtained is estimated for all three directions of motion (north–south, east–west and vertical direction). The top layers response spectra for all 16 boreholes are further evaluated

(a)   (b)

(c)
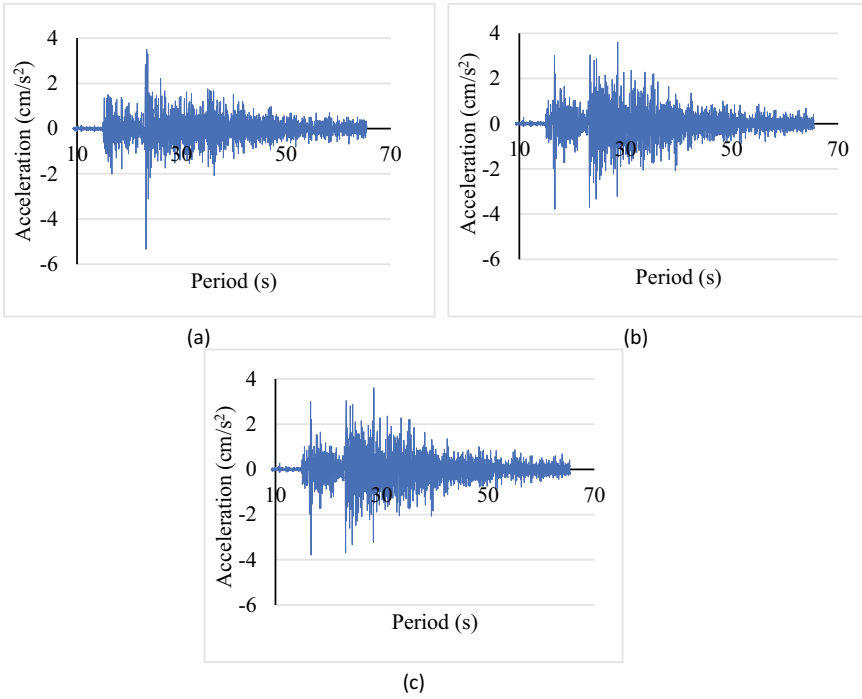
Fig. 4 Acceleration time history in **a** NS direction, **b** EW direction and **c** VT direction

along X, Y, and Z axis from north–south, east–west, and vertical direction by the component method to include the effect of angle. The top layers response spectra are further plotted with respect to IS 1893 (Part 1) 2002 response spectra [10] in the form of spectral acceleration are as shown in Figs. 5, 6 and 7 respectively.
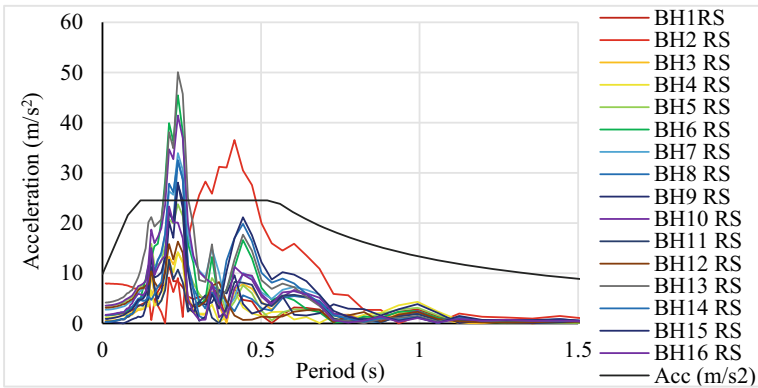
Fig. 5 Acceleration in the X direction after angle effect
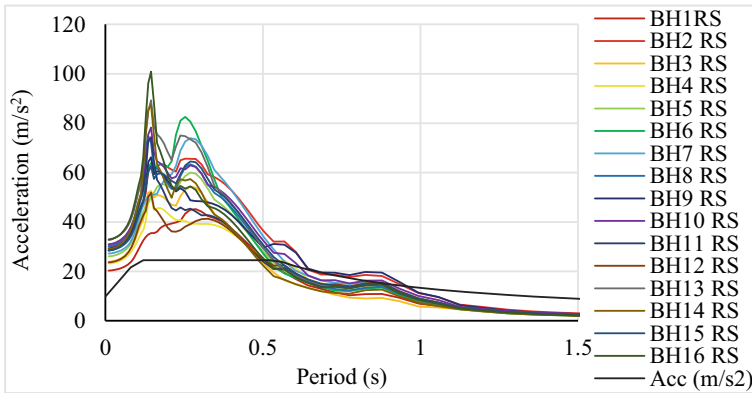
Fig. 6 Acceleration in the Y direction after angle effect
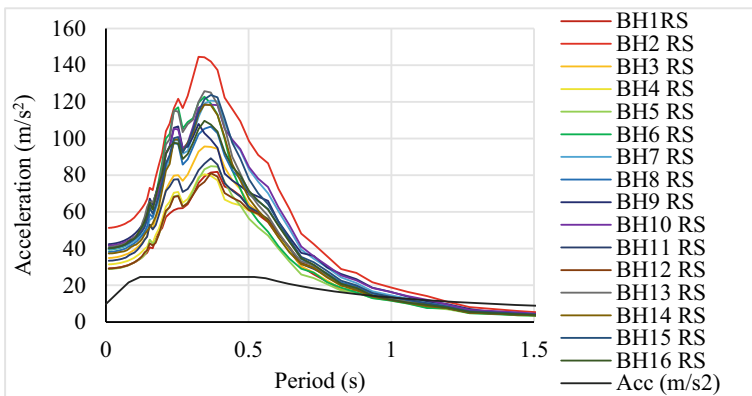
Fig. 7 Acceleration in the Z direction after angle effect

The peak spectral acceleration obtained corresponding to period is further used for the response spectrum analysis. The structure considered for this study is the building of British Olivia School, Rama Mandi, Jalandhar, Punjab, having latitude and longitude of 31.310207°N and 75.635175°E respectively. This building is already constructed. The overall orientation of the building with respect to the motion components are as shown in Fig. 8. The angle between the north–south axis and the structure is 39° as determined using Auto CAD based on the orientation obtained from google map. The components are calculated according to Eqs. (3) and (4). The response spectrum is calculated including the orientation and further used in analysing.

$$EQX = WE * cos\theta - SN * sin\theta \qquad (3)$$

Fig. 8 Angle of building with north axis and components

$$EQZ = SN * cos\theta + WE * sin\theta \tag{4}$$

The analysis is carried out using the existing model of the building in STAAD Pro software. The geometry and 3D rendered view of the structure is shown in Fig. 9. The base shear is estimated corresponding to IS 1893 (Part 1) 2002 including effect of orientation by calculating the components in the form of different modes of combination. All 16 response spectra obtained by analysis in DEEPSOIL are also used to estimate the base shear including effect of orientation by calculating the components of the same. The response spectra are applied to the structure as a response spectrum loading corresponding to the particular direction to analyse the structure. The loading is applied to study the real effects of orientation. The base shear is further obtained in the form of different modes of combination for all 16 boreholes.
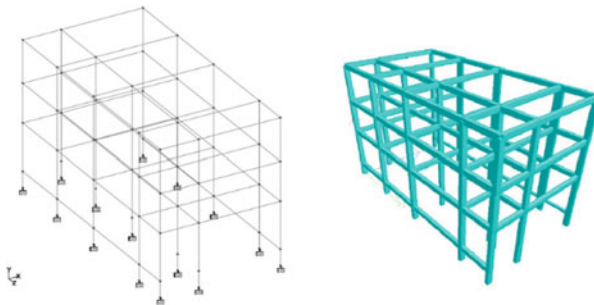
Fig. 9 Geometry and 3D rendered view of structure

3   Results

Using the components method, the response spectrum of code is estimated in the north–south axis and east–west axis corresponding to Z-axis and X-axis respectively. The base shear is estimated according to the magnetic bearing of the earth i.e. north–south direction with the IS 1893 (Part 1) 2002 response spectra with angle is shown in Table 2. The response spectra obtained from DEEPSOIL are used in further analysis. This analysis is taken to obtain the real values, and to check the behaviour of base shear due to past earthquake. In this study, 16 bore hole locations are considered. The response spectra obtained from DEEPSOIL for north–south axis and east–west axis is evaluated according to axis of STAAD Pro by the component method. This analysis is inclusive of the effect of orientation, and hence is realistic as per the earthquake motion. The base shear from DEEPSOIL spectra with angle is as shown in Table 3.

3.1   Comparison

The comparison between base shear obtained from IS 1893 (Part 1) 2002 response spectra with angle and DEEPSOIL response spectra with angle is shown in Table 3. The difference is calculated in percentage for better evaluation.

   After analyzing the difference in percentage between IS code result and DEEP-SOIL result, it is observed that the minimum difference in percentage is −270.48%, −278.77%, −321.23%, −277.41% for X direction, whereas −39.03%, −39.22%, −19.33%, −37.50% for Z direction by SRSS, 10PCT, ABS, CQC respectively. For Y direction (vertical direction), the minimum is 31.04% and maximum is 76.30%. The maximum difference in percentage is 50.70, 99.43%, 46.46%, 50.36% for X direction and in Z direction, it is 17.14%, 17%, 29.91%, 18.18% by SRSS, 10PCT, ABS, CQC respectively. The average of the difference in percentage by mode of combination SRSS, 10PCT, ABS, CQC is −40.44, −27.71, −47.82, −42.55 in X direction and −18.62, 18.84, 0.48, −17.22 in Z direction. The average in Y direction is 50.28 by SRSS, 10PCT, ABS, CQC modes of combination. The average of difference in percentage of particular mode of combination along all direction is close to

Table 2   Base shear from IS 1893 (Part 1) 2002 response spectra in X, Y and Z direction after angle effect

Mode of combination	Total SRSS (kN)	Total 10PCT (kN)	Total ABS (kN)	Total CQC (kN)
X	24.6	25.15	27.97	25.06
Y	194.92	194.92	194.93	194.92
Z	208.64	210.37	295.04	224.42

Table 3 Base shear from DEEPSOIL response spectra in X, Y and Z direction after angle effect and difference in base shear from IS 1893 (Part 1) 2002 response spectra and DEEPSOIL response spectra

Mode of combination		Total (kN)				Difference in percentage (%)			
		SRSS	10PCT	ABS	CQC	SRSS	10PCT	ABS	CQC
BH1	X	32.62	33.1	34.92	32.96	24.59	24.02	19.90	23.97
	Y	282.67	282.67	282.68	282.67	31.04	31.04	31.04	31.04
	Z	162.16	163.3	265.55	176.25	−28.66	−28.82	−11.11	−27.33
BH2	X	12.49	12.49	12.49	12.49	−96.96	−101.36	−123.94	−100.64
	Y	419.62	419.62	419.62	419.62	53.55	53.55	53.55	53.55
	Z	251.79	253.47	420.97	274.28	17.14	17.00	29.91	18.18
BH3	X	27.99	28.35	28.99	28.24	12.11	11.29	3.52	11.26
	Y	333.2	333.2	333.2	333.2	41.50	41.50	41.50	41.50
	Z	166.53	167.66	277.51	180.83	−25.29	−25.47	−6.32	−24.11
BH4	X	49.9	50.68	52.24	50.48	50.70	50.37	46.46	50.36
	Y	323.62	323.62	323.62	323.62	39.77	39.77	39.77	39.77
	Z	180.06	181.33	289.95	195.53	−15.87	−16.02	−1.76	−14.78
BH5	X	36.77	37.39	41.24	37.22	33.10	32.74	32.18	32.67
	Y	363.22	363.22	363.23	363.22	46.34	46.34	46.33	46.34
	Z	150.07	151.11	247.24	163.21	−39.03	−39.22	−19.33	−37.50
BH6	X	29.92	30.41	32.33	30.28	17.78	17.30	13.49	17.24
	Y	397.76	397.76	397.76	397.76	51.00	51.00	50.99	51.00
	Z	155.1	156.1	266.95	168.74	−34.52	−34.77	−10.52	−33.00
BH7	X	13.52	13.52	16.27	13.52	−81.95	−86.02	−71.91	−85.36
	Y	378.52	378.52	378.52	378.52	48.50	48.50	48.50	48.50
	Z	198.21	199.5	335.44	216.84	−5.26	−5.45	12.04	−3.50
BH8	X	22.79	23.02	24.88	22.95	−7.94	−9.25	−12.42	−9.19
	Y	422.76	422.76	422.76	422.76	53.89	53.89	53.89	53.89
	Z	181.76	182.95	305.44	198.22	−14.79	−14.99	3.40	−13.22
BH9	X	43.26	4387	44.42	43.77	43.13	99.43	37.03	42.75
	Y	409.54	409.54	409.55	409.54	52.41	52.41	52.40	52.41
	Z	216.32	217.79	353.16	235.14	3.55	3.41	16.46	4.56
BH10	X	6.64	6.64	6.64	6.64	−270.48	−278.77	−321.23	−277.41
	Y	822.57	822.57	822.58	822.57	76.30	76.30	76.30	76.30
	Z	164.31	164.95	306.09	175.73	−26.98	−27.54	3.61	−27.71
BH11	X	21	21.21	21.78	21.17	−17.14	−18.58	−28.42	−18.38
	Y	398.24	398.24	398.24	398.24	51.05	51.05	51.05	51.05
	Z	168.47	169.56	280.84	183.95	−23.84	−24.07	−5.06	−22.00
BH12	X	26.19	26.51	30.14	26.47	6.07	5.13	7.20	5.33

Table 3 (continued)

Mode of combination		Total (kN)				Difference in percentage (%)			
		SRSS	10PCT	ABS	CQC	SRSS	10PCT	ABS	CQC
	Y	329.98	329.98	329.98	329.98	40.93	40.93	40.93	40.93
	Z	167.38	168.48	275.12	183.06	−24.65	−24.86	−7.24	−22.59
BH13	X	17.26	17.35	21.44	17.32	−42.53	−44.96	−30.46	−44.69
	Y	460.51	460.51	460.51	460.51	57.67	57.67	57.67	57.67
	Z	172.49	173.59	296.31	188.22	−20.96	−21.19	0.43	−19.23
BH14	X	13.39	13.42	13.86	13.41	−83.72	−87.41	−101.80	−86.88
	Y	405.93	405.93	405.93	405.93	51.98	51.98	51.98	51.98
	Z	163.97	165.02	280.49	179.04	−27.24	−27.48	−5.19	−25.35
BH15	X	12.16	121.16	13.27	12.16	−102.3	79.24	−110.78	−106.09
	Y	397.11	397.11	397.11	397.11	50.92	50.92	50.91	50.92
	Z	187.7	188.91	318.96	205.04	−11.16	−11.36	7.50	−9.45
BH16	X	10.63	10.63	12.49	10.63	−131.4	−136.59	−123.94	−135.75
	Y	459.75	459.75	459.76	459.75	57.60	57.60	57.60	57.60
	Z	173.3	174.43	297.67	189.37	−20.35	−20.60	0.88	−18.51

zero. The average of difference in percentage for SRSS, 10PCT, ABS, CQC is −2.93, 1.24, 0.98, −3.16 respectively.

4 Conclusion

Response spectra depend on the type of soil. In this study, an attempt is made to analyse the structure according to the location and real situation using borehole data. The shear wave velocity determined is between 318.02 m/s to 401.29 m/s, i.e. minimum for BH6 and maximum for BH16. Based on the average shear wave velocity, the borehole sites are classified according to NEHRP. Out of 16 boreholes, 6 are classified as stiff soil, whereas 10 are classified as very dense soil and soft rock. The response spectra for the 16 boreholes are determined using equivalent linear method in DEEPSOIL. The analysis done in this study also include the angle effect, which is estimated in the structure (i.e. the building of British Olivia School). The response spectra are plotted after including the effect of angle with response spectra of IS 1893 (Par 1) 2002. For the few boreholes, the response spectra are little higher between time period 0–1 s, whereas after 1 s it is lower than IS 1893 (Part 1) 2002 response spectra. The estimation of base shear from borehole data is done in this study by response spectrum analysis method. The base shear is evaluated according to different modes of combination (SRSS, 10PCT, ABS, CQC) by using STAAD Pro. A comparison between the base shear obtained from IS code and DEEPSOIL spectra is determined in the form of percentage for different modes of combination. As per

this study, there is no uniform pattern obtained for base shear for different boreholes. However, the minimum of difference in percentage is for BH10, BH1 and BH5 along X, Y and Z direction respectively, whereas, the maximum of difference in percentage is for BH10, BH2 along Y and Z direction. Hence, the attempt to determine the base shear for the building using borehole data and region specific motion by response spectrum analysis may be the initiation for further studies.

References

1. Hashash, Y.M.A., Groholski, D.R.: Recent advances in non-linear site response analysis. In: Fifth International Conf. Recent Adv. Geotech. Earthq. Eng. Soil Dyn. Symp. Honor Profr. I.M. Idriss, vol. 29, no. 6, pp. 1–22 (2010). http://scholar.google.com/scholar?hl=en&btnG=Search&q=intitle:Remarks+on+site+response+analysis+by+using+Plaxis+dynamic+module#0
2. Puri, N., Jain, A., Mohanty, P., Bhattacharya, S.: Earthquake response analysis of sites in state of Haryana using DEEPSOIL software. Procedia Comput. Sci. **125**, 357–366 (2018). https://doi.org/10.1016/j.procs.2017.12.047
3. IS 1893 (Part 1): IS 1893 (Criteria for Earthquake resistant design of structures, Part 1: General Provisions and buildings). Bur. Indian Stand. New Delhi, vol. 1893, pp. 1–44 (2016)
4. Soni, P.K., Dubey, S.K., Sangamnerkar, P.: Response quantities of framed buildings under dynamic excitation. Int. J. Innov. Technol. Explor. Eng. **8**(11), 3798–3804 (2019). https://doi.org/10.35940/ijitee.K2192.0981119
5. Khan, M.A.: Seismic design for buildings. Earthquake-Resistant Struct., 283–315 (2013). https://doi.org/10.1016/B978-1-85617-501-2.00010-9
6. Bajaj, K., Anbazhagan, P.: Seismic site classification and correlation between V S and SPT-N for deep soil sites in Indo-Gangetic Basin. J. Appl. Geophys. **163**, 55–72 (2019). https://doi.org/10.1016/j.jappgeo.2019.02.011
7. FEMA 450: NEHRP Recommended Provisions for Seismic Regulations for New Buildings and Other Structures, Part 1, no. Fema 450, p. 338 (2003)
8. Darendeli, M.B.: Development of a new family of normalized modulus reduction and material damping. IEEE Trans. Commun., 1–10 (2001)
9. I.R. Department of earthquake engineering, "pesmos." www.pesmos.in. Accessed 07 Mar 2022
10. Bureau of Indian Standards New Delhi: Criteria for Earthquake Resistant Design of Structures - General Provisions and Buildings Part-1. Bur. Indian Stand. New Delhi, vol. Part 1, pp. 1–39 (2002)

Predicting the Axial Load Carrying Capacity of Columns Reinforced with GFRP Rebars Using ANN Modelling

G. Sumesh Manohar and **T. Palanisamy**

Abstract In recent years most of the concrete structures are getting exposed to environments that are resulting in the corrosion of steel. To eliminate this, studies have been carried out to replace steel in RCC by Glass Fiber Reinforced Polymer (GFRP) rebars. In this paper, several experimental results were considered and the impacts of substituting steel by GFRP rebars were studied. Parameters affecting the load-carrying capacity of columns reinforced with GFRP rebars were identified from various literature and a database has been created. Twelve such parameters describing the material property and geometric configuration are chosen as inputs and the axial load carrying capacity as an output. An ANN model is developed with optimized architecture for predicting the compressive strength of columns reinforced with GFRP rebars. The model is then trained, tested, and validated on this database. The accuracy of the ANN model is evaluated by various regression evaluation metrics such as MSE, RMSE and R^2. Comparison with the existing empirical equations and code provisions showed that the ANN model outperformed all these models. For the purpose of determining the efficiency of ANN model, a subset of the experimental data collected from work done on GFRP reinforced columns is used. Sensitivity analysis is carried out and the results showed that the most important parameters for the estimation of the strength of GFRP reinforced columns are the geometrical dimensions of the column. The results obtained showed that the ANN model is in good agreement with the experimental results.

Keywords Axial load carrying capacity · GFRP rebars · Artificial neural network · Sensitivity analysis

1 Introduction

Concrete is generally reinforced as it is strong in compression but weak in tension, resulting in a homogeneous building material that is strong in both compression and

G. Sumesh Manohar (✉) · T. Palanisamy
Department of Civil Engineering, National Institute of Technology Karnataka Surathkal, Mangalore, India
e-mail: sumeshmanohar.202st011@nitk.edu.in

tension. Steel is commonly used as reinforcement because of its great strength, low cost, and ductility. Governments and asset owners, on the other hand, pay billions of dollars in maintenance expenditures to repair or replace aging infrastructure due to steel's corrosive nature. Corrosion can cause structural failure and even fatality in extreme circumstances. Many additional materials are being used in reinforced concrete in place of steel rebar as a result of advancements in materials technology. Steel or carbon fibers, carbon fiber cables, glass fiber reinforced polymer (GFRP) rebar, and even bamboo are among these materials. GFRP rebar is increasingly being utilised as a substitute for steel reinforcement, as it does not corrode and is lightweight, non-conductive. These properties make it corrosive-resistant, transportable, and quick to install, making it ideal for use in electrical environments like rail constructions.

Fiber-reinforced composites have been used a lot nowadays for internal reinforcement, especially as rebars in prestressed and non-prestressed concrete structures. FRP techniques are successfully adopted in many structural elements like beams [1] and in developing other composite materials such as Kevlar fabrics [2] and some other techniques that are successfully adopted are mentioned in [3]. Many literatures can be seen on bond behavior characteristics [4], dynamic properties [5], and retrofitting techniques [6] which have shown that FRPs can be successfully adopted.

To predict the strength of GFRP columns many methodologies are available, in recent years machine learning gained its importance as many researchers are adopting these techniques due to its complex problem solving capability.

Machine learning techniques are adopted extensively in many fields and depending on the type of data to be analysed there are many different kinds of algorithms available like linear regression, logistic regression, decision tree, Extreme Learning Machine, random forest, Gradient Boosting Algorithm [7]. ANN has shown its dominance for the analysis of regression data in terms of computational time and accuracy.

The following is the outline of the paper. Firstly, a background study of ANN is introduced briefly. Then, the parameters mainly affecting the Axial load carrying capacity were studied. Later the ANN model is developed and its performance is critically evaluated using experimental data sets. A sensitivity analysis is carried out to find out the parameter that is predominantly affecting the axial load carrying capacity. Results and discussions are mentioned before drawing concluding remarks.

2 Research Significance

Previous research has found that using GFRP rebars may significantly enhance the flexural and shear responses of concrete columns. In contrast, no systematic study has shown a strong recommendation for the design of GFRP reinforced concrete columns. Furthermore, the ACI codes forbade the use of longitudinal GFRP rebars due to their unpredictability under compression stress. Furthermore, earlier models in this field were constructed based on a restricted number of experimental data and factors

for GFRP-reinforced concrete columns. Furthermore, some limitations exist in the methodologies used to approximate the performance of GFRP-reinforced concrete columns, such as the tensile and compressive strength of GFRP bars. Furthermore, earlier models' fundamental flaw was linked to the use of regression methods, which resulted in low accuracy when compared to experimental data. In this study, experimental findings from earlier investigations [1–6, 8–11] were utilised to forecast and build a novel model for constructing GFRP reinforced concrete columns using artificial neural networks (ANN). A wide variety of input factors were considered for this purpose, including the geometric parameters of longitudinal rebars and concrete columns, as well as the mechanical properties of concrete and GFRP.

3   Background Study of ANN

A prominent supervised deep learning approach for processing data by a network of decision layers is the Artificial Neural Network (ANN), often known as neural network. The algorithm's structural similarity to the human brain prompted the technique's name. While this does not imply that ANN are a virtual replica of the brain's decision-making process, because we still don't understand how it works and is therefore a black box, there are some broad parallels, mostly in terms of structure. Input, hidden, and output layers make up a conventional neural network design. The input layer receives the data initially and detects features. The input characteristics are then analysed and processed by the hidden layers, with the final findings shown as the output layers. Like human vision, the middle layers process items between the input and output levels invisibly, they are referred to as hidden layers. When a neuron receives an input, it applies weights to the inputs to estimate their values, and then the weighted inputs are sent to the summation function, which calculates the overall sum of the weighted inputs. The weighted total is then supplied into an activation function, which determines whether to fire a neuron output based on a binary value of '0' or '1'. The activation function is triggered and an output is allowed when '1' is used, but not when '0' is used. The difference between the expected output and the actual known output is compared by the activation function to make this choice. The output that has the potential to make a significant difference is set to '0,' disregarded, and returned without being processed by the following layer. Previously developed models for predicting the axial load carrying capacity of GFRP columns are mentioned in Table 1, these equations are further used in the study to validate the ANN model.

Table 1 Existing models for predicting Axial load carrying capacity of GFRP columns

Reference [12]	Predicted model & additional data
CSA S806 − 12	$P_n = \alpha_1 f_c (A_g - A_{FRP}); \alpha_1 = 0.85 - 0.0015 f_c \geq 0.67$
ACI-318-08	$P_n = 0.85 f_c (A_g - A_s) + f_y A_s$
ACI 318-11	$P_n = 0.85 f_c (A_g - A_s)$
CSA S806-02	$P_n = 0.85 f_c (A_g - A_{FRP})$
AS-3600:2018	$P_n = 0.85 f_c (A_g - A_{FRP}) + 0.0025 E_{FRP} A_{FRP}$
Afifi et al.	$P_n = 0.85 f_c (A_g - A_{FRP}) + \alpha_g f_{FRP} A_{FRP}; \alpha_g = 0.35$
Mohamed et al.	$P_n = 0.85 f_c (A_g - A_{FRP}) + \varepsilon_p E_{FRP} A_{FRP}; \varepsilon_p = 0.002$
Mohamed et al.	$P_n = 0.90 f_c (A_g - A_{FRP}) + \varepsilon_{fg} E_{FRP} A_{FRP}; \varepsilon_{fg} = 0.002$
Khan et al.	$P_n = 0.85 f_{cc} (A_g - A_{GFRP}) + \alpha f_{GFRP} A_{GFRP}; \alpha = 0.61$
Hadhood et al.	$P_n = \alpha_1 f_c (A_g - A_{FRP}) + 0.0035 E_{FRP} A_{FRP}; \alpha_1 = 0.85 - 0.0015 f_c$
Tobbi et al.	$P_n = 0.85 f_c (A_g - A_{FRP}) + \varepsilon_{co} E_{FRP} A_{FRP}; \varepsilon_{co} = 0.003$
Samani and Attard	$P_n = 0.85 f_c (A_g - A_{FRP}) + 0.0025 E_{FRP} A_{FRP}$

3.1 General ANN Equations

In general, bias is assumed to be 1 for input values, but the related weight w_0 might be positive or negative. When the sum's weight is positive, bias will try to push the sum to create an output, and when the sum's weight is negative, bias will try to suppress an output.

For two inputs and one output, a general feed forward network with a single hidden layer is used. The position of the layer in which a neuron is found is represented by the superscript, while the numbering from top to bottom is represented by the subscript. The first neuron of the first layer is represented by $a_1^{(1)}$, the second neuron of the second layer is represented by $a_2^{(2)}$, the first neuron of the third layer is represented by $a_1^{(3)}$, and so on. As previously stated, bias is a fixed unit value that is represented by its weight. By using weights, each neuron in the previous layer is linked to each neuron in the following layer. Like $w_{01}^{(1)}, w_{11}^{(1)}, w_{12}^{(1)}, w_{21}^{(1)}, w_{22}^{(1)}$, etc., are the weights of the first layer, and $w_{01}^{(2)}, w_{11}^{(2)}, w_{21}^{(2)}$ are the weights of second layer, so their respective superscripts are 1 and 2. As second neuron of first layer is interconnected with the first neuron of the second layer by weight $w_{21}^{(1)}$, zeroth neuron of the first layer is connected with the first neuron of the second layer by weight $w_{01}^{(1)}$, as depicted in Fig. 1.

The first layer's weighted sum output and bias are passed via an activation function to represent the second layer's first neuron's output, $a_1^{(2)}$. We may assume that each neuron's output is equal to the preceding layer's weighted sum output plus a constant bias and is mentioned in "Eqs. (1), (2), (3) and (4)".

$$a_1^{(2)} = f\left(w_{01}^{(1)} + w_{11}^{(1)} a_1^{(1)} + w_{21}^{(1)} a_2^{(1)} \right) \tag{1}$$
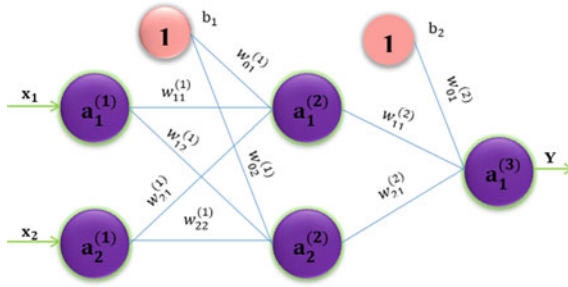
Fig. 1 An ANN for two inputs and single output

$$a_2^{(2)} = f\left(w_{02}^{(1)} + w_{12}^{(1)} a_1^{(1)} + w_{22}^{(1)} a_2^{(1)}\right) \tag{2}$$

$$a_1^{(3)} = f\left(w_{01}^{(2)} + w_{11}^{(2)} a_1^{(2)} + w_{21}^{(2)} a_2^{(2)}\right) \tag{3}$$

$$a = f\left(\sum w_i a_i\right) + b_i \tag{4}$$

Thus the

$$Total number of hyperparameters = \sum [no. of neurons in the next layer \times (no. of neurons in the previously$$

4 Methodology

4.1 Identification and Selection of Parameters Influencing Axial Load Carrying Capacity

The literatures of standard experimental investigations are used to analyse parameters such as column width, depth, concrete compressive strength, percentage of longitudinal reinforcement, tensile strain of GFRP rebars, yield strength of GFRP rebars, Gross area, and load bearing capacity. The inputs and outputs of a supervised learning model must be known and labelled before it can be trained. Thus, except for axial load bearing capacity, all of the characteristics listed above, as well as certain extras like beam eccentricities and slab reinforcement details, will be used as labelled inputs and axial load of column as labelled outputs for trial and error training of a neural network.

4.2 Preparation of Experimental Database

The data that is obtained from various literatures is processed through data scrubbing, feature selection. Normalization is carried out which will help in improving the model accuracy and it rescales the range of values for a given feature into a set range with a prescribed minimum and maximum such as [0, 1] or [−1, 1]. Normalization is given by the formulae

$$X_n = \frac{X - X_{min}}{X_{max} - X_{min}} \tag{5}$$

where X_{max} and X_{min} are the maximum and minimum value of a particular parameter considered in the dataset. X is the considered parameter and X_n is the normalized value for that parameter. Standardization is ignored as it is a regression problem.

4.3 Data Collection

Several literature studies were carried out to collect the input parameters that influence the axial load carrying capacity and these data points are used to train the current model. The parameters that mainly effect the output are Gross column sectional Area (A_g), Column dimensions (B and H), Compressive strength of concrete (f_c), Elastic modulus of FRPs (E_f), Yield strength of FRPs (f_u), The tensile strain of FRPs (ε_u), The total cross-sectional area of FRP longitudinal reinforcement (A_f). The only output parameter for which the ANN model is the axial load carrying capacity (P_u). For the development of ANN model 118 refined data points are used and 10 more existing data experimental data points are used for testing the existing ANN model and is validated with the existing codes and empirical formulas listed in Tables 1 and 2 shows the statistical overview of the obtained dataset.

5 Development of ANN Model

After the dataset has been produced, the next step is to create an ANN model. Which is accomplished using either the licenced MATLAB infrastructure in the Neural Network Toolbox platform or customised sets of programmes. In this paper the work was started with a three-layer feed forward neural network with one input layer, one hidden layer, and one neuron in the output layer. The number of input parameters will be equal to the number of neurons in the input layer. The weights and biases will then be initialised through trial and error once more.

    The ANN model in this study was created using MATLAB (R2021a-academic use). To obtain the best architecture for ANN model various models with varied

Table 2 Database distribution along with their standard deviation and mean

Parameters	Minimum	Maximum	Mean	STD	Priority
B (mm)	150	610	294.72	124.91	2
H (mm)	150	610	310	119.65	1
D (mm)	150	305	272.82	48.887	1
A_g (mm^2)	17,671	372,100	87,689.983	69,678.9611	2
f_c (MPa)	20.8	55.2	36.883	6.474	3
f_u (MPa)	421.3	1662.5	984.2	354.27	7
E_f (GPa)	24.5	134.2	78.3	32.4	7
ε_u (%)	0.95	2.4	1.54	0.32	7
A_f (mm^2)	214.3	4320	2210	1236	4
ρ_l(%)	0.8	5.3	1.955	0.937	4
ρ_t(%)	0.01	4.8	1.294	1.115	6
S (mm)	50	250	14.02	5.24	5
P_u(kN)	114	15,232.2	2185.186	2395.854	-

numbers of hidden layers are investigated, and the results from one of them are presented in this research. The included feed-forward neural network's design consists of two hidden layers, with the number of neurons in the first layer determined through trial and error. In the input and output layers, there are 9 and 1 neurons, respectively, and a neuron for Bias in the hidden and output layers, as illustrated in Fig. 2. The network is trained using the Levenberg–Marquardt backpropagation technique. 'tansig' and 'purelin' are the activation functions used in the hidden and output layers, respectively. The data set is partitioned into three pieces at random. 70% of the data is used for network training, 15% for network testing, and 15% for network validation.

5.1 Performance of ANN Model

The network is trained by executing the MATLAB code once all of the relevant parameters have been specified. The training continues until the validation error does not reduce after '6' iterations or epochs, at which point validation is terminated. During the training stage, the maximum number of iterations that may be obtained is 1000. It took 10 iterations (or epochs) to train our current ANN model, and the mean squared error (MSE) for each iteration is displayed in Fig. 3. The average squared difference between the output and the objectives is known as the mean squared error (MSE). Lower numbers indicate better outcomes, whereas zero indicates no mistake. The performance of the model when checked with code provisions and empirical formulae showed that the ANN model produced more accurate results when compared to existing empirical data.
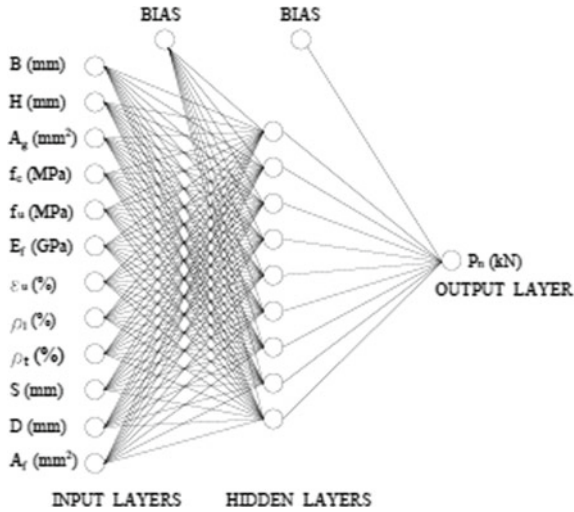
Fig. 2 ANN architecture showing neuron layers, input and output parameters
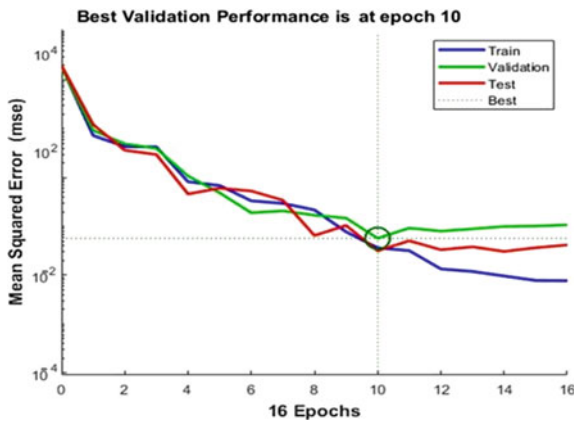
Fig. 3 Network performance vs Iterations

The accuracy of the ANN model is further checked with exiting evaluation metrics and the results are mentioned in Sect. 6.

6 Check for Accuracy of ANN Model

A regression-ML model's performance can be evaluated in a number of ways. CC, MAE, MSE, RMSE, RMSLE, R-square, and modified R-square are the most used

Table 3 Statistical performance evaluation parameters

Evaluation metrics	Definition
Coefficient of correlation	$CC = \dfrac{\sum_{i=1}^{n}(A_i - \overline{A}_i)(Y_i - \overline{Y}_i)}{\sqrt{\sum_{i=1}^{n}(A_i - \overline{A}_i)^2 (Y_i - \overline{Y}_i)^2}}$
Mean absolute error	$\text{MAE} = \frac{1}{n}\sum_{i=1}^{n}|A_i - Y_i|$
Mean square error	$\text{MSE} = \frac{1}{n}\sum_{i=1}^{n}(A_i - Y_i)^2$
Root mean square error	$\text{RMSE} = \sqrt{MSE} = \sqrt{\frac{1}{n}\sum_{i=1}^{n}(A_i - Y_i)^2}$
R^2	$R^2 = 1 - \dfrac{SS_r}{SS_m} = 1 - \dfrac{\sum_{i=1}^{n}(A_i - Y_i)^2}{\sum_{i=1}^{n}(A_i - \overline{A}_i)^2}$

statistical assessment measures. But which of them is best for our model depends on the types of data, and types of machine learning algorithms. Our data will be neither extremely high nor extremely low in magnitude. As a result of the ongoing conversation, we may select/choose CC and RMSE for evaluating the performance of our model, based on the needs of our dataset. Some of the evaluation metrics are listed below in Table 3.

Where, A_i's = actual values, Y_i's = predicted value, $\overline{A}_i$ = mean of actual values, $\overline{Y}_i$ = mean of predicted values, n = Total number of data points, ssr = sum of squared error of regression line, ssm = sum of squared error of mean line.

7 Results and Discussions

In this section, performance evaluation metrics like RMSE, MSE, MAE, R^2 are computed and are tabulated in Table 4. Lesser values represent that the model is good in predicting the required output. RMSE is taken as criteria for selection of model, as the RMSE value obtained is least when model is having 9 number of internal neurons. Therefore, only this model is considered for the further analysis. The RMSE, MSE, R^2 results show the satisfactory behavior of ANN in predicting axial load carrying capacity of GFRP reinforced columns.

Sensitivity analysis was carried out and it is found that the geometrical properties of column are having the highest influence on axial load carrying capacity while

Table 4 Statistical measures

Statistical measures considered	Training	Testing	Validating
RMSE	4.326	6.324	4.965
MSE	0.0749	0.1672	0.0308
MAE	2.909	3.142	1.945
R^2	0.9632	0.9435	0.9214

properties of steel like modulus of elasticity (E_f) and ultimate strength of steel (f_u). The order of priority obtained from sensitivity analysis is mentioned in the last column of Table 2.

Best performance of ANN model in predicting the axial strength of GFRP reinforced columns is observed at 10 epochs and the validation is continued until 16 iterations. As the variation is found to be increasing as the iterations are increasing beyond 10 epochs the validation for further iterations is terminated, and the model is optimized to work only until 10 epochs for any given input. Figure 3 illustrates the afore mentioned details.

Figure 4 shows the difference between the output from ANN model and the experimental results. The values of R for the training, testing, and validation stages are 0.98165, 0.9568, and 0.98042 respectively. The R-value achieved when the model was evaluated on the entire dataset is 0.97734 which can be seen in Fig. 4d, indicating that the present model can accurately predict output values that are very similar to the outcomes of experiments
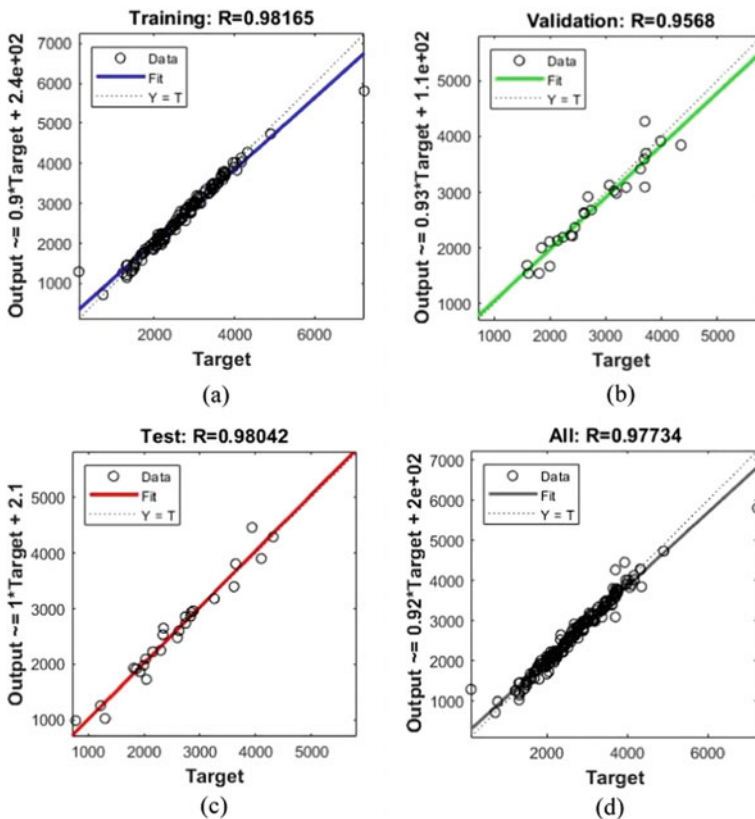
Fig. 4 **a** Regression plot for training, **b** Regression plot for validation, **c** Regression plot for testing data, **d** Regression plot for actual and predicted values of all data

8 Conclusions

In this study, the authors have explored a computer application approach (Machine Learning) using Artificial Neural Network to predict the axial load carrying capacity of columns reinforced with GFRP. The theoretical framework of data collection procedure, development of ANN model and its performance evaluation are presented in this study. This study is found to be cost effective since the computational time required is less when compared to other existing models. The proposed approach is found to be satisfactory since statistical measures are good in agreement with previous literatures. The authors are still working to refine the test data to improve the accuracy of the model without compromising the computational time.

References

1. Nuhu Danraka, M., Mahir Mahmod, H., Job Oluwatosin, O.: Strengthening of reinforced concrete beams using FRP technique: a review. Int. J. Eng. Sci. Comput. **7**(6), 13199–13213 (2017). http://ijesc.org/
2. Dinesh, S., Elanchezhian, C., Vijayaramnath, B., Sathiyanarayanan, K., Adinarayanan, A.: Experimental investigation of banana bract fiber and palm fiber reinforced with epoxy hybrid composites. Mater. Today Proc. **22**(xxxx), 335–341 (2020). https://doi.org/10.1016/j.matpr.2019.06.633
3. Lokesh, P., Surya Kumari, T.S.A., Gopi, R., Loganathan, G.B.: A study on mechanical properties of bamboo fiber reinforced polymer composite. Mater. Today Proc. **22**(xxxx), 897–903 (2020). https://doi.org/10.1016/j.matpr.2019.11.100
4. Lye, H.L., Mohammed, B.S., Liew, M.S., Wahab, M.M.A., Al-Fakih, A.: Bond behaviour of CFRP-strengthened ECC using Response Surface Methodology (RSM). Case Stud. Constr. Mater. **12**, e00327 (2020). https://doi.org/10.1016/j.cscm.2019.e00327
5. Mussa, M.H., Abdulhadi, A.M., Abbood, I.S., Mutalib, A.A., Yaseen, Z.M.: Late age dynamic strength of high-volume fly ash concrete with nano-silica and polypropylene fibres. Crystals **10**(4) (2020). https://doi.org/10.3390/cryst10040243
6. Rahim, N.I., et al.: Strengthening the structural behavior of web openings in RC deep beam using CFRP. Materials (Basel) **13**(12), 1–21 (2020). https://doi.org/10.3390/ma13122804
7. Awad, M., Khanna, R.: Machine learning in action: examples. (2015). https://doi.org/10.1007/978-1-4302-5990-9_11
8. Khorramian, K., Sadeghian, P.: Experimental and analytical behavior of short concrete columns reinforced with GFRP bars under eccentric loading. Eng. Struct. **151**, 761–773 (2017). https://doi.org/10.1016/j.engstruct.2017.08.064
9. Tabatabaei, A., Eslami, A., Mohamed, H.M., Benmokrane, B.: Strength of compression lap-spliced GFRP bars in concrete columns with different splice lengths. Constr. Build. Mater. **182**, 657–669 (2018). https://doi.org/10.1016/j.conbuildmat.2018.06.154
10. Elchalakani, M., Ma, G.: Tests of glass fibre reinforced polymer rectangular concrete columns subjected to concentric and eccentric axial loading. Eng. Struct. **151**, 93–104 (2017). https://doi.org/10.1016/j.engstruct.2017.08.023
11. Afifi, M.Z., Mohamed, H.M., Benmokrane, B.: Axial capacity of circular concrete columns reinforced with GFRP bars and spirals, no. 1995, pp. 1–11 (2014). https://doi.org/10.1061/(ASCE)CC.1943-5614.0000438
12. Karimipour, A., Mohebbi, J., Abad, N., Fasihihour, N.: Predicting the load-carrying capacity of GFRP-reinforced concrete columns using ANN and evolutionary strategy. Compos. Struct. **275**, 114470 (2021). https://doi.org/10.1016/j.compstruct.2021.114470

Maintenance Prioritization of Roads Based on Asset Score Using GIS and AHP

B. G. Sreelekshmi, V. S. Sanjay Kumar, and P. Sabu

Abstract Asset management can be considered as one of the key factors in operation and maintenance of infrastructure. The present paper explains the creation of an Asset Score based upon which prioritisation strategy is arrived for maintenance works for a road network. The road having the highest Asset Score would be given the highest priority for maintenance and likewise will be continued for the remaining roads. Asset Score is created by using a multi-criteria decision-making tool, Analytic Hierarchy Process (AHP). The parameters used for determining the asset score included pavement condition rating, traffic volume (total traffic and number of commercial vehicles), number of access points, crash rate, drainage factor and congestion. The pairwise comparison matrix for AHP is constructed based on experts' opinion acquired through survey. The AHP calculations are carried out in normal method and on Geographic Information System (GIS) environment. The results achieved in two cases were similar. Asset scores gives the prioritization order of road which in turn helps the highway engineers and planners to identify the stretch where the maintenance has to be done, the type of maintenance required and ensure allocation of resources which aids in an effective maintenance. Moreover, the advanced options on GIS software assist to perform analysis which makes the computations easier. GIS can be used not only for mapping but the advanced options enhance the GIS as a powerful tool for analysis.

Keywords Asset score · Pavement maintenance · Analytic Hierarchy Process (AHP) · Geographic Information System (GIS)

B. G. Sreelekshmi
Geoinformatics, Department of Civil Engineering, College of Engineering Trivandrum, Thiruvananthapuram, India

V. S. Sanjay Kumar (✉)
National Transportation Planning and Research Centre, Thiruvananthapuram, India
e-mail: sanjay.natpac@gmail.com

P. Sabu
Department of Civil Engineering, College of Engineering Trivandrum, Thiruvananthapuram, India

1   Introduction

Asset is a useful or valuable thing belongs to person or organization. Infrastructure Asset Management comprises of different procedures which are primarily focused to preserve public infrastructure. Infrastructure assets constitute transportation systems, communication networks, sewage, water and electric system. Among these, prime importance is given to transportation system as the development in transportation sector is considered as the base for the development of all other infrastructures. Road transport has more benefits from other modes of transport because of the flexibility which it provides. As maintenance is the important element in asset management, it is necessary to develop maintenance plan for managing the asset. Prioritization of road network according to its functional or structural parameter is one of the aspects in developing a maintenance plan for road asset management. AHP is a decision support tool which can be used to solve complex decision problems. It uses a multi-level hierarchical structure of objectives, criteria, sub criteria, and alternatives. The pertinent data are derived by using a set of pairwise comparisons. These comparisons are used to obtain the weights of importance of the decision criteria, and the relative performance measures of the alternatives in terms of each individual decision criterion [2]. AHP is a powerful and established prioritizing tool, a mathematical technique, which is used for multi-criteria decision making to help the decision maker in the selection of the best alternative. All roads do not require maintenance at the same time. The order of maintenance for roads can be defined by creating asset score. Asset score is created based on structural and functional parameters of road. Condition of roads can also be evaluated by analyzing the score. Based on asset score we can prioritize the road network for maintenance work. The road with high asset score will be focused first for maintenance. The work is focused to create asset score for road to determine the order of maintenance using GIS. The asset score is developed using AHP. The structural and functional parameters of road is considered for calculating the asset score.

2   Literature Review

The maintenance of road network is important as they are subjected to heavy traffic and also it is primary mode of transportation. All the roads do not have same maintenance period. The roads can be maintained according to its prioritization. Now a days GIS has also been used for the prioritization of roads. Sudipta et al. [5], presents an approach for prioritization of 15 State Highways (SH) in the State of West Bengal. It includes identification of techno economic factors, identification of strategic factors, importance of techno-economic factors in prioritization, importance of causal factors in potential safety hazard and estimation of priority index for each road section. Finally, prioritization of selected SH section was done using scaled priority index. Sarfaraz et al. [4] use AHP to establish relative maintenance

priorities of the pavement sections. The result obtained from AHP is compared with Road Condition Index (RCI). A road condition index is the weighted average of all urgency indexes, product of degree and extent of distress. Pavements with higher RCI should be given higher priority for maintenance.

Akhilesh and Sunil [1] proposes a maintenance plan for low volume rural roads at network level as well as project level. In network level planning, the roads in the network are prioritized for pavement maintenance, depending on pavement conditions and traffic volume. Project level planning consists of a suitable repair and maintenance technique is selected for each road based on the predominant pavement defects, traffic volume, and climatic conditions. In the studies most of the prioritization were worked out by giving importance to pavement condition. AHP was the decision-making tool in the studies. Same type of roads is considered for the studies. The possibility of conducting studies on the combination of different types of roads can also be envisaged. Moreover, the use of GIS was limited with creating data set, creating map and for visualization. The studies are not explored the analysis options available on GIS environment. Since GIS have advanced tools for analysis, the scope of using GIS in calculating the prioritisation of road can be evaluated.

3 Study Network and Data Collection

3.1 Study Area

The study area comprises of six roads in Thrissur district includes one National Highway (NH), three State Highways (SH) and two Major District Roads (MDR). The NH 66 having length of 64 km passing through Thrissur district. SH 75 (Vadanappally-Thrissur VT), SH 61 (Potta-Moonupeedika PM) and SH 51 (Kodakara-Kodungallur KK) are the selected State Highways having length 16 km, 21.3 km and 25 km respectively. The MDRs are Cherpu-Thriprayar (CT) of 14.2 km and Peringotukara-Kaanjany-Chavakkadu (PKC) of 24.7 km length (Figs. 1 and 2).

3.2 Data Used

The primary data required for the work was obtained from National Transport Planning and Research Centre (NATPAC). Three-year data set for each road was collected. The data includes carriageway, Right of Way (RoW), drainage, Pavement Condition Index (PCI). Traffic Volume (PCU), Commercial vehicle per day (CVPD).

The Pavement Condition Index (PCI) indicates the surface condition of pavement. PCI is a numerical rating of the pavement condition based on the type and severity of distress. The PCI value of the pavement condition is represented by a numerical index between 0 and 100, 0 for worst condition and 100 is the best condition. Traffic
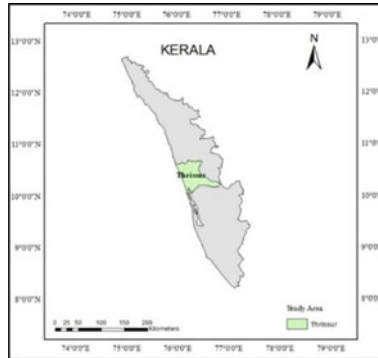
Fig. 1 Study area digitized in GIS
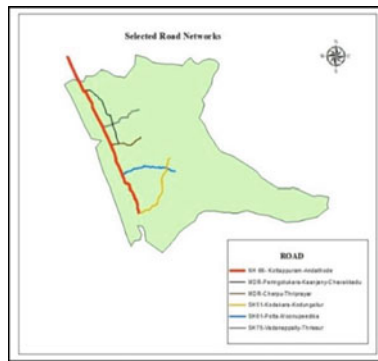
Fig. 2 Road stretches digitized in GIS

volume on pavement is measured in Passenger Car Unit (PCU). The PCU may be considered as a measure of the relative space requirement of vehicle class compared to that of a passenger car under specified set of roadway, traffic and other conditions. The total traffic volume of the mixed traffic flow prevalent on the roads in India is expressed in terms of PCU per hour, PCU per day, PCU/lane/hour. Initial traffic is determined in terms of commercial vehicles per day (CVPD). The traffic analysis and CVPD is very useful to estimate the traffic intensity-based on the actual traffic flow. For the design of pavement or for maintenance programme of future or for economic evaluation.

3.3 Methodology

The various steps involved in the study is depicted as a flowchart shown in Fig. 3. Data set for selected roads constitutes parameters as carriageway, RoW, Traffic Volume, CVPD, PCI, drainage factor, access points, congestion measure and crash rate. The value for parameters such carriageway, RoW, Traffic Volume, CVPD, PCI and drainage were obtained from NATPAC. Access points were determined from google map. Congestion measure is calculated by dividing the traffic volume with the recommended design service volume for two lane roads (15,000 PCU/day) as per IRC 64:1990. The summary of data is provided in Tables 1 and 2.

From the data set seven parameters are identified for creating asset score given in Table 3. The parameters are PCI, Traffic Volume, CVPD, Number of access points, crash rate in year, drainage factor and congestion measure. Number of access points is the number of connecting road to the selected stretch. The total number of access points are divided by the length of road. Based on the length of drainage and condition from the collected dataset, drainage factor is calculated. Rating of 1, 3, 5 is assigned for poor, fair and good condition drainage respectively. The rating is multiplied with the respective length to determine the total drainage rating for the road. Drainage factor is obtained by dividing the total length of drainage with the length of road. Crash rate refers to number of road crashes in a year. The relative importance of each parameter is determined based on the response obtained through google survey. The
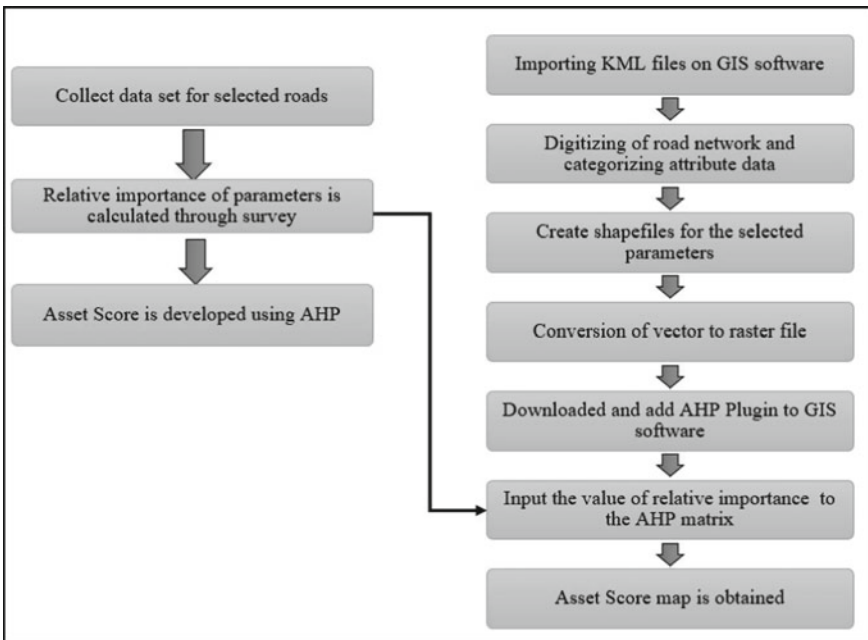
Fig. 3 Flowchart of methodology

Table 1 Data set for selected road network (Source: NATPAC)

Road	Carriageway (m)	Right of Way (RoW) (m)	Traffic volume (PCU/day)	CVPD	PCI
NH 66-Kottappuram-Andathode	5.4–7.4	7.6–30	36,734	4709	64
SH 75-Vadanappally-Thrissur (VT)	5–8.14	7.4–17.2	32,764	3031	66
SH 61-Potta-Moonupeedika (PM)	5.3–7.8	8–14.6	23,538	2877	88
SH 51-Kodakara-Kodungallur (KK)	4.9–8.3	8.8–17	19,588	2227	76
MDR-Peringotukara-Kaanjany-Chavakkadu (PKC)	4.2–6.3	7–13.1	16,317	1295	82
MDR-Cherpu-Thriprayar (CT)	5.3–7.3	9–16.1	19,121	1438	79

Table 2 Data set for selected road network

Road	Access points	Drainage factor
NH 66-Kottappuram-Andathode	506	0.781
SH 75-Vadanappally-Thrissur (VT)	242	1.313
SH 61-Potta-Moonupeedika (PM)	181	0.563
SH 51-Kodakara-Kodungallur (KK)	161	0.520
MDR-Peringotukara-Kaanjany-Chavakkadu (PKC)	245	0.931
MDR-Cherpu-Thriprayar (CT)	116	0.493

pairwise comparison between the seven parameters (PCI, Traffic Volume, CVPD, Number of access points, crash rate in year, drainage factor and congestion measure) was included in the survey form. A questionnaire is circulated among the experts in Transportation Engineering field to collect their opinion based on experience and knowledge. The responses obtained were analysed and asset score was created using AHP.

Table 3 Parameters for creating asset score

Asset score parameters	Unit
Pavement condition rating	PCR or PCI
Traffic volume	PCU/day
Number of commercial vehicles	CVPD
Number of access point	Per km
Crash rate in a year	Crash rate per km
Drainage factor	–
Congestion measure	Volume capacity ratio

4　Results and Discussion

For creating asset score weightage is calculated using AHP in MS excel and in GIS environment. The procedure for calculating the same is described in Sects. 4.1 and 4.2 respectively.

4.1　Calculation of Asset Score Using AHP

The responses obtained from survey were analysed and asset score was created using AHP. A pairwise comparison matrix was created with the selected 7 parameters as rows and columns. The values of the pairwise comparison in the AHP was determined according to the scale introduced by Saaty. The pairwise comparison matrix obtained after the analysis of response is depicted in Table 4.

　The relative weight obtained from the survey is filled in the upper triangular matrix and the inverse values is taken in the lower triangular matrix. The importance of each parameter when they are considered for creating an asset score which can be computed by calculating the principal eigen vector. To calculate the eigen vector first the pairwise comparison matrix is normalised. The average of rows of each parameter in normalised matrix will give principal eigen vector or priority vector value. All these calculations are carried out on Microsoft Excel. After calculating the priority vector, the Consistency Ratio (CR) of judgemental matrix is calculated. CR is obtained as 0.0261. The asset score for each road is created from the relative weight using the Eq. (1)

Table 4　Pairwise comparison based on the response

	Pavement condition	Traffic volume	CVPD	Number of access points	Crash rate in year	Surface drainage	Congestion measure
Pavement condition	1	2	1	3	3	2	2
Traffic volume	1/2	1	1	2	2	1	2
CVPD	1	1	1	3	1	2	2
Number of access points	1/3	1/2	1/3	1	1/2	1	1
Crash rate in year	1/3	1/2	1	2	1	1	2
Surface drainage	1/2	1	1/2	1	1	1	1
Congestion measure	1/2	1/2	1/2	1	1/2	1	1

$$\text{Asset Score} \; = \Sigma \, W_i \, T_i \qquad \text{(Saaty)} \qquad\qquad (1)$$

W_i = Relative weight of ith parameter (1 to 7)
T_i = Values for i^{th} parameter (1 to 7) for the respective stretch

The relative weight obtained from AHP for each parameter is used as the value of W_i and the values are provided in Table 5.

The data set collected for selected road network is normalized and the normalized value of data is provided in the Table 6.

Asset score is developed for each road stretches by solving Eq. (1) using the normalized data and relative weight. While calculating the final set of asset scores the crash rate parameter is discarded due to the non-availability of data.

Asset score is higher for NH 66 (0.1835) followed by SH 75-Vadanappally-Thrissur (VT) (0.1798), SH 61-Potta-Moonupeedika (PM) (0.1472), for MDR-Peringotukara-Kaanjany-Chavakkadu (PKC) (0.1236), SH 51-Kodakara-Kodungallur (KK) (0.1227) and for MDR-Cherpu-Thriprayar (CT) (0.1153). Rank of 1 to 6 is assigned for road stretches based on the asset score to arrange the road from highest asset score to least. Rank 1 is assigned for NH 66 followed by SH 75, SH 61, MDR-PCK, SH 51 and MDR-CT. The significance of rank is to arrange road

Table 5 Relative weights obtained through AHP

Parameters	Relative weights
Pavement condition (PCI)	0.243
CVPD	0.190
Traffic volume	0.161
Crash rate in year	0.129
Drainage factor	0.108
Congestion measure	0.089
No: of access points	0.079

Table 6 Normalized data for road network

Road	Pavement condition (PCI)	Traffic volume (PCU/day)	CVPD	No: of access points	Drainage per length	Congestion measure
NH 66-Kottappuram-Andathode	0.141	0.248	0.302	0.141	0.170	0.248
SH 75-Vadanappally-Thrissur (VT)	0.144	0.221	0.195	0.270	0.285	0.221
SH 61-Potta-Moonupeedika (PM)	0.193	0.159	0.185	0.152	0.122	0.159
SH 51-Kodakara-Kodungallur (KK)	0.168	0.132	0.143	0.115	0.113	0.132
MDR-Cherpu-Thriprayar (CT)	0.181	0.110	0.083	0.177	0.202	0.110
MDR-Peringotukara-Kaanjany-Chavakkadu (PKC)	0.173	0.129	0.092	0.146	0.107	0.129

Table 7 Asset score developed for road stretches

Road	Pavement condition (PCI)	Traffic volume (PCU/day)	CVPD	No: of access points	Drainage per length	Congestion measure	Asset score	Rank
NH 66-Kottappuram-Andathode	0.034	0.040	0.057	0.011	0.018	0.022	0.1835	1
SH 75-Vadanappally-Thrissur (VT)	0.035	0.036	0.037	0.021	0.031	0.020	0.1798	2
SH 61-Potta-Moonupeedika (PM)	0.047	0.026	0.035	0.012	0.013	0.014	0.1470	3
SH 51-Kodakara-Kodungallur (KK)	0.041	0.021	0.027	0.009	0.012	0.012	0.1225	5
MDR-Cherpu-Thriprayar (CT)	0.044	0.018	0.016	0.014	0.022	0.010	0.1232	4
MDR-Peringotukara-Kaanjany-Chavakkadu (PKC)	0.042	0.021	0.018	0.012	0.012	0.012	0.1151	6

based on the decreasing value of asset score. The final asset score and rank based on asset obtained for each road are enumerated in Table 7.

4.2 Creating Asset Score Using GIS

The vector files of roads and attribute data are entered. AHP analysis can directly done on GIS software, for doing the analysis AHP plugin has to be downloaded and installed on GIS software. AHP plugin tool on GIS software is used for raster data. Hence vector files created for selected road is converted to raster files using the conversion tool. Vector files are created for the 7 parameters considered for creating asset score. These files are converted to respective raster files. The raster files for pavement condition parameter are given in Fig. 4. Similarly, raster files are generated for traffic volume, CVPD, access point, drainage factor, and congestion measure. The relative importance of parameters is calculated through the survey is given as input the value of the AHP matrix on the software. The input values are stored as the values of upper triangular matrix. Once the input values are given the consistency ratio and asset score values for each road are obtained automatically. The result of AHP process is obtained in the map shown in Fig. 5.

The consistency ratio obtained for pairwise comparison matrix as 0.026 since the value is less than 0.10 the entries on the comparison matrix are acceptable. The values in pairwise comparison are collected through survey. Relative weights are calculated using AHP the values and asset score for each road is developed from the relative weights. The asset score achieved through normal procedure and GIS software are same.
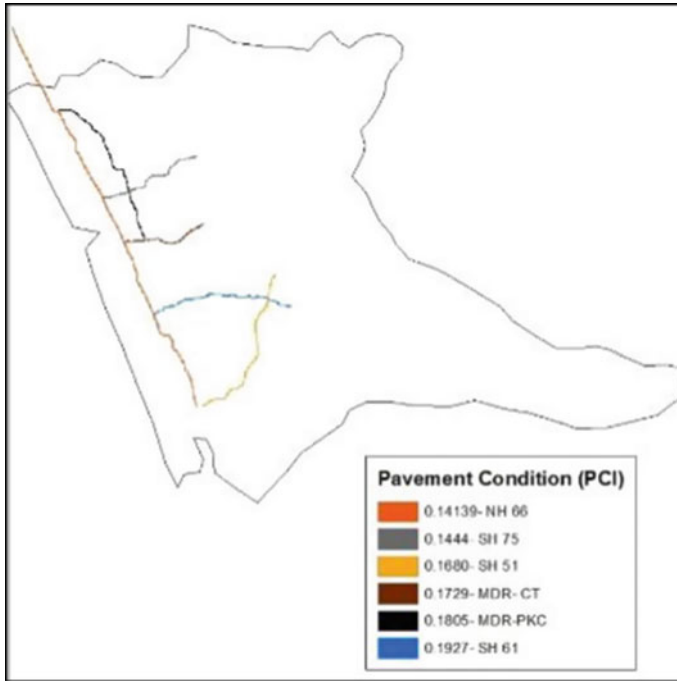
Fig. 4 Raster file for pavement condition

The asset score achieved for the road network are 0.1834 for NH 66-Kottappuram-Andathode, 0.1798 for SH 75-Vadanappally-Thrissur (VT), 0.1472 for SH 61-Potta-Moonupeedika (PM), 0.1236 for MDR-Peringotukara-Kaanjany-Chavakkadu (PKC), 0.1227 for SH 51-Kodakara-Kodungallur (KK), 0.1153 for MDR-Cherpu-Thriprayar (CT). The maintenance prioritization of road can be done using the asset score. The higher value of asset score implies the higher prioritization of the road for maintenance work. Here the higher value of asset score is for NH 66-Kottappuram-Andathode (0.1834) and least for MDR-Cherpu-Thriprayar (CT). The prioritization of maintenance work will be in the order of NH 66-Kottappuram-Andathode, SH 75-Vadanappally-Thrissur, SH 61-Potta-Moonupeedika, MDR-Peringotukara-Kaanjany-Chavakkadu (PKC), SH 51-Kodakara-Kodungallur (KK) followed by MDR-Cherpu-Thriprayar (CT).

Asset Score

🟥	0.1834- NH 66-Kottappuram-Andathode
⬜	0.1798- SH 75- Vadanappally-Thrissur
🟦	0.1472 -SH 61 - Potta-Moonupeedika
⬛	0.1236 -MDR-Peringotukara-Kaanjany-Chavakkadu
🟨	0.1227- SH 51- Kodakara-Kodungallur
🟫	0.1153- MDR-Cherpu-Thriprayar
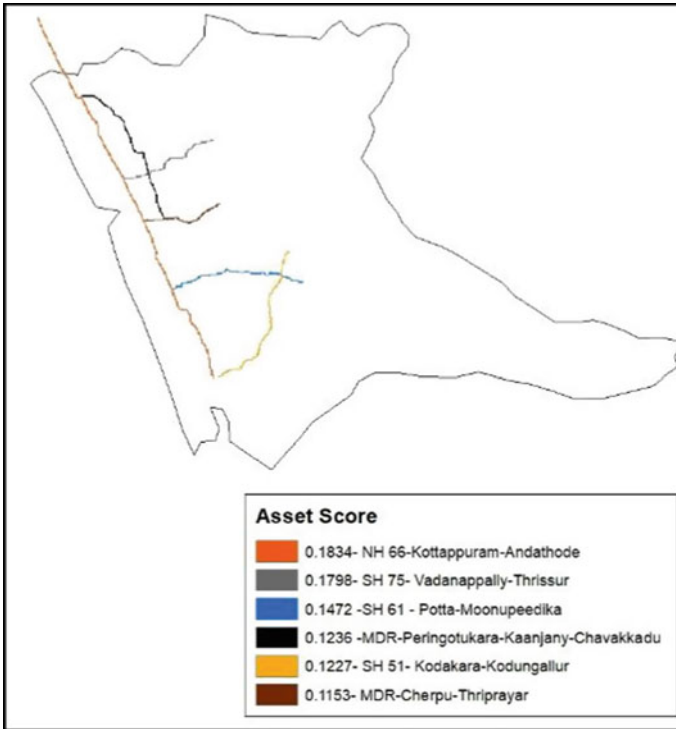
Fig. 5 Asset scores for roads obtained from GIS software

5 Conclusion

This study is focused to prioritize the road network to carried out maintenance activities. For prioritizing road asset score are created. Seven parameters are identified for asset score which consists of Pavement Condition (PCI), Traffic Volume (PCU/day), CVPD, Access Points, Crash rate, Drainage factor and Congestion Measure. Relative weight between the seven variables is worked out by conducting a survey with the experts in Transportation Engineering field. Final weights are assigned after analysing the response. Due to the unavailability of crash rate data, the variable is excluded while determining the asset score. The relative weight among these parameters is determined using multicriteria decision making tool AHP. The calculation is done manually and on GIS environment using GIS software. The result obtained are same in both case. It is noted that the weightage and final asset score are obtained from the software by giving the values of relative importance of asset parameter collected through survey. Rank values from 1 to 6 are given to the road in the decreasing order of asset score. The road having higher asset score is assigned a rank 1 and 6 to road having least asset score. The Asset Score is intended to assist the authorities or facility manager to make decisions regarding resource allocation, funding level, taking care

of assets, to manage risk and carried out maintenance in an effective way. This work also emphasis to use GIS as an analysis tool. More analysis options are available on GIS software further studies regarding asset management can be carried out. As GIS is capable to track real time asset, data compilation, assessing risk, developing maintenance plan etc. GIS can deployed in the field of asset management effectively.

Limitations of the Study

Prioritisation of road for maintenance works is included in the present work. The work is limited to road level prioritisation. Identifications of sections warranting maintenance, type of maintenance required etc. are not included in the scope of the for the present work. The same can included as the future scope of this work and the scope of GIS in maintenance and managing of infrastructure can also be explored.

References

1. Akhilesh, N., Sunil, S.: Condition Based Maintenance Planning of low volume rural roads using GIS. J. Clean. Prod. **312**, 127649 (2021)
2. Triantaphyllou, E., Stuart, H.M.: Using the analytic hierarchy process for decision making in engineering applications: some challenges. Int. J. Ind. Eng. Appl. Pract. **2**, 35–44 (1995)
3. Saaty, R.W.: The analytic hierarchy process-what it is and how it is used. Math. Model. **9**(3–5), 161–176 (1987)
4. Sarfaraz, A., Vedagiri, P., Krishna Rao, K.V.: Prioritization of pavement maintenance sections using objective based analytic hierarchy process. Int. J. Pavement Res. Technol. **10**, 158–170 (2017)
5. Sudipta, P., Bhargab, M., Sarkar, J.R.: An approach for prioritization of state highways and its application. Transp. Dev. Econ. **2**, 2–12 (2016)
6. NATPAC: Road Asset Management for National Highways and State Highways in Kerala, Study Report (2021)
7. IRC 64-1990 Guidelines for Capacity of Roads in Rural areas
8. IRC 130:2020 Guidelines for Road Asset Management System

Seismic Performance of Infilled RC Frames by Pseudo-Optimization Method

G. Priyusha, C. Shreyasvi, and Katta Venkataramana

Abstract In the present situation, most of the structures are made of Reinforced Concrete (RC) because of readily available raw materials, expertise, and most cost-effective construction. Any building/infrastructure located in seismic zone III or higher has to follow the ductile detailing procedure outlined by IS 13920 (2016) to resist the seismic effects. As earthquakes are highly unpredictable, it is the role of the structural engineer to take care of seismic effects while designing a multi-storey building. The main concept behind earthquake resistant design of structures is to utilize the ductile capability of the materials and the structural members. However, the linear behavior cannot capture the performance of the structure beyond its yield limit and hence, nonlinear analysis is commonly used. On the other hand, nonlinear analysis can be computationally expensive and time-consuming. Hence, the objective of the present study is to optimize the analysis and seismic design by applying pseudo optimization technique. The technique makes use of existing linear structural analysis models with some improvements in the design process based on modal energy. The pseudo optimized design is a three-step procedure that is cost-effective and time-saving. It can be easily implemented by practitioners in their structural design without much of a disruption in the existing workflow. In the current research, finite element model based structural analysis software is used to model and analyze the building. To evaluate its seismic performance pushover analysis is done. The study highlights the merits of the pseudo optimization technique through the application of the methodology.

Keywords Practitioner-friendly · Infilled RC frame building · Seismic performance · Modal energy

G. Priyusha (✉) · K. Venkataramana
National Institute of Technology Karnataka, Surathkal, Karnataka 575025, India
e-mail: priyushag.203st006@nitk.edu.in

C. Shreyasvi
Seismic Hazard Scientist, Global Earthquake Model, Pavia, Italy

1 Introduction

Reinforced concrete frame (RCF) buildings are extensively employed all around the world as they're a cost-effective construction system made of readily available materials. RCF has proven to be a good seismic performer in the past. Seismic activities are one of the natural phenomena, which occur in a very unpredictable manner. The sudden slip at the fault and release of linear elastic strain energy stored in the rocks cause the earthquake. Most structural design firms now employ specialized software to carry out their work, which includes using elastic models and analyzing them using equivalent lateral force or response spectrum approaches. Engineers also try to save materials costs and keep the seismic design of most RC structures as close to the minimum code requirements as feasible due to market competition.

Because of the prevalence of RCF, researchers have proposed a variety of design methodologies to develop cost-effective seismic designs that meet or surpass code minimum performance. [1–3] have shown the works on the optimal configuration having varied constraints. To increase the performance of buildings during earthquakes, several strategies like structural optimization and performance-based design were used. Many probabilistic-based algorithms are used, such as evolutionary programming, genetic algorithms, and evolution techniques. Many researchers proposed these strategies, which greatly simplified the analysis [4–6]. Performance-based design (PBD) [7], which is based on FEMA P-58, is another widely utilised method. Buildings under PBD are built to meet specified measured seismic performance criteria. A displacement-based design is the third technique.

The current study presents a design strategy that engineers can apply to improve their infilled RCF designs, which has the following benefits:

(a) It makes use of data from elastic models that are commonly developed in design methods, needing no additional work for developing modeling.
(b) In comparison to conventional design, the building's construction costs are just slightly more.
(c) When compared to the typical design process, the proposed design approach takes only a fraction of the time.

The major objective of this research is to use linear elastic models to apply the pseudo-optimization technique to an infilled RC frame construction for residential applications. The presence of infills increases the frame element's lateral stiffness and strength [8]. As a result, the current study examines the improvement in several parameters as compared to bare RC frame construction. The 3D model has been created using the structural analysis software for bare RC frame and infilled RC frame buildings and analysis is carried out as per Indian standards. To evaluate the seismic performance a non-linear static pushover analysis is studied.

2 Methodology

The proposed design technique aims to deliver a building design strategy that is more seismically resistant than a building constructed using typical design techniques while being less expensive. The conventional seismic design procedure is iterative (Fig. 1 shows the flowchart of the design process in offices).

In this process, two new constraints are adopted. First is developing a linear elastic model which is obvious for the typical design process. As a result, the modeling effort required is not increased. Second, using the software tools accessible in design offices, the design procedure must be simple to implement. The proposed method is claimed as pseudo optimized design since the approach does not make use of any specific tool focussing on optimization yet it fulfills the objective. The models named PSO indicate the pseudo optimized design in the subsequent Sect. 3.

This method is comprised of 3 steps:

Step 1. Apply seismic load patterns in a distribution proportionate to the dominant mode of vibration in each independent (lateral) direction to the building's linear elastic model. The modal energy is calculated straight from the ETABS design software, and it is a measure of the structural element's work while the building can withstand the imposed lateral load. The normalized modal energy (NME) is simply the product of internal force with the corresponding displacement divided by the volume of the element.

Step 2. Based on the visual examination of higher NME values, dimensions have been modified.

(a) For Columns with higher NME values, the cross-sectional area should be increased. Also, it should be noted that the area of the cross-section shall not be increased if it results in a higher cross-section above the lower storey.

(b) For Beams with higher NME values, the depth of the section is increased and it is performed floor-wise for the ease of construction.
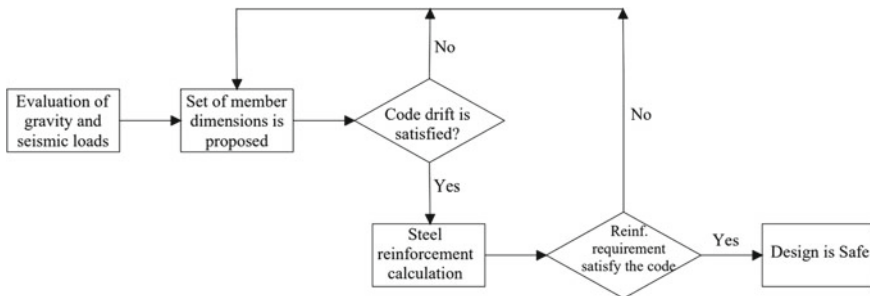
Fig. 1 Typical Design process for an RC-Moment resisting frame in many design offices. (Adapted from [9])

Table 1 Cross-section dimensions and reinforcement - Columns

Column dimension (mm)	Reinforcement ratio (%)
C1 300×380	1.82
C2 300×350	0.97
C3 230×300	1.82

(c)   The higher dimensions of beams and columns are selected as per the thumb rule in the Indian region (for example dimension of 9 inches is subsequently increased to 12 inches). Table 1 lists the dimensions taken into account.

Step 3. Similarly, reinforcement is also increased based on the safe evaluation of the initial RC design of the model. The values considered in this study can be referred to in Table 1.

2.1   *Method of Analysis*

For the regular buildings under zone II and the building height of less than 15 m can be analyzed through the Equivalent static method (Linear static).

If the buildings are exceeding the above norms, the response spectrum method (Linear dynamic) shall be adopted. In this study, both equivalent static method and response spectrum method can be seen since both are required to evaluate scale factor, refer to IS 1893(2016)-part 1 code.

2.2   *Pushover Analysis*

Pushover method is a non-linear static method of analysis that accounts for geometric and material non-linearity. The static pushover analysis method lacks a firm theoretical foundation. It is based on the idea that the initial mode of vibration and mode shape, or the first few modes of vibration, govern the structure's response and this form remains constant throughout the structure's elastic and inelastic response. This lays the groundwork for turning a dynamic situation into a static one. In pushover analysis, we have adopted a displacement-controlled procedure with the specified drift limitations. The non-linear behavior occurs in discrete user-defined hinges. Hinge represents localized force deformation duration member through its elastic and inelastic phases under seismic load. Hinges can be introduced into both frame and vertical wall objects. Generally, for beams and columns flexural and shear hinges shall be assigned. For the strut elements, axial hinges are assigned. [In this study, M3 hinge for beams and PM2M3 hinge for columns are assigned. For strut element axial P hinge is considered, refer Fig. 2b]. The behavior of beam hinges can be studied using the M-θ relationship, refer to Fig. 2a.
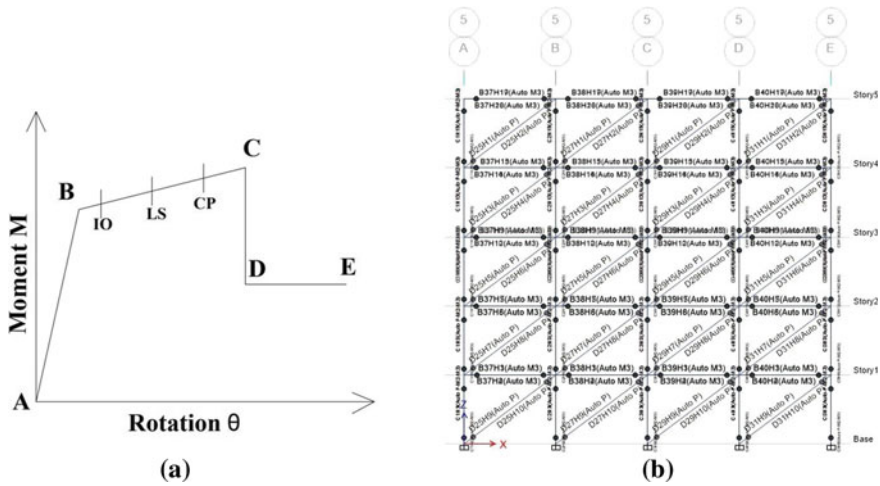
Fig. 2 a M-θ relationship. **b** Assigned hinges to the proposed model

From Fig. 2a AB indicates a linear elastic range from unloaded state A to its effective yield B, followed by an inelastic yet linear response of decreasing (ductile) stiffness from B to C. CD denotes a significant reduction in load resistance, which is followed by a reduction in resistance from D to E, and finally a total loss of resistance from E to F.

3 Modeling Details

For the present study, a five-storied infilled RC residential building lying in seismic zone 3 is considered. The plan and elevation of the building are shown below (Fig. 3a, b). It has 4 bays in each orthogonal direction and the type of soil is medium stiff (Type 2). The superimposed dead load and live loads are 3 and 2 kN/m^2. It is designed and detailed according to IS 1893(Part 1):2016 and IS 13920:2016 respectively.

Three models are considered in this present work:

Model 1: Uniform dimensions of beams and columns are assigned throughout the building.

Beams are 230×300 mm having a top reinforcement of 452 mm^2 and bottom reinforcement of 250 mm^2. Columns are of 300×350 mm with uniform reinforcement on all sides (p$_t = 0.86\%$).

The above model is designed for static and dynamic loads. Equivalent static method and response spectrum method are performed to get the design base shear for the building as it lies in seismic zone III (Z = 0.16). After the analysis is complete, we can get the normalized modal energy values from the software that acts as a source for our optimization process.
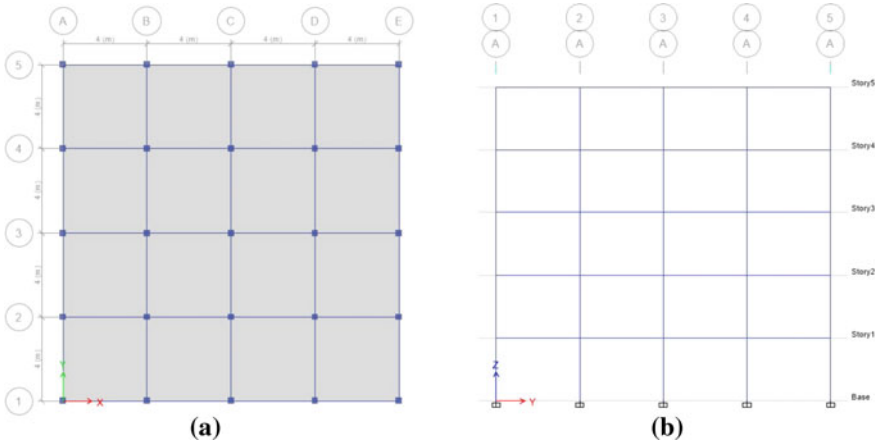
Fig. 3 **a** Plan of the building. **b** Elevation of the building
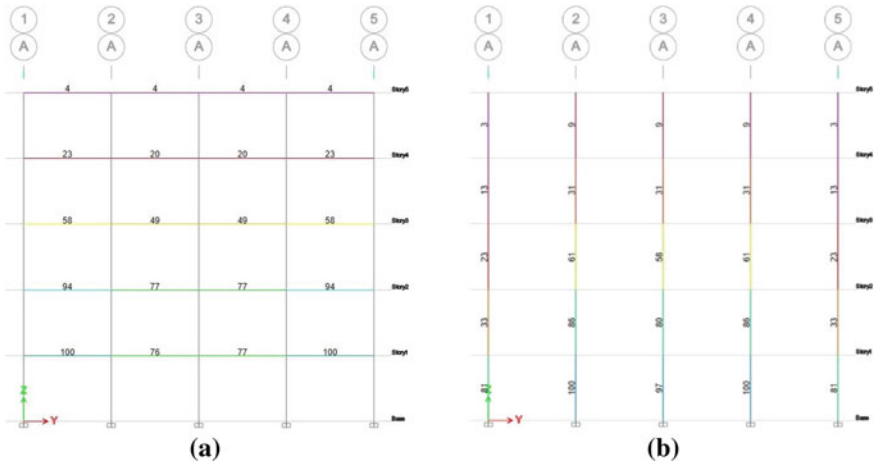
Fig. 4 **a** Normalized modal energies (NME) for beams along axis A. **b** NME for columns along axis A

From Fig. 4b, it is observed that higher NMEs are found in the ground storey and lower NMEs for the top storey in the case of columns. As a result, the ground floor's perimeter columns are given the C1 dimension (refer to Table 1), while the interior columns are given the C2 dimension. C2 columns are assigned to intermediate storeys 2–4, while C3 columns are assigned to the top storey. Similarly, it can be seen from the NME of the beam in frame A that storeys 1 and 2 have higher NME (Fig. 4a) than the other storeys, hence B1 is assigned to these storeys. The B2 beams are assigned to storeys 3 and 4. Since the top storey has lower NME values, B3 beams are designated. The proposed methodology's steps 2 and 3 are now complete.

Table 2 Cross-section dimensions and reinforcement - Beams

Beam dimension (mm)	Top reinforcement (mm^2)	Bottom reinforcement (mm^2)
B1 230 × 350	400	260
B2 230 × 300	380	250
B3 230 × 230	300	230
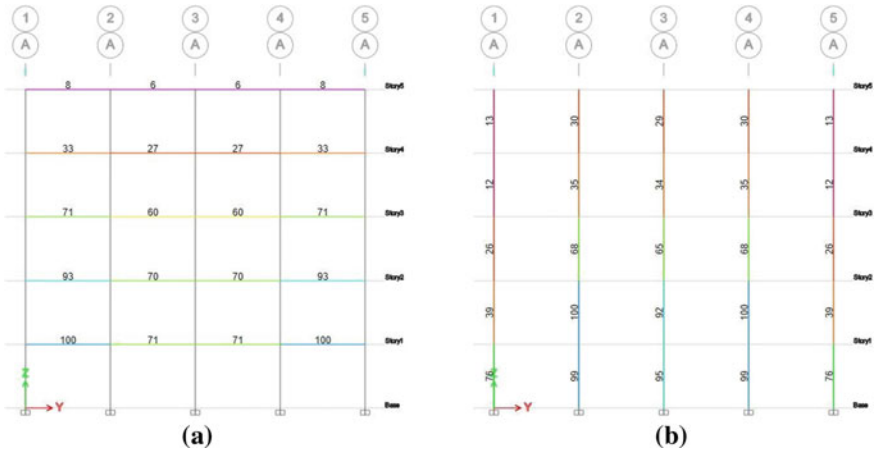
Fig. 5 **a** NME for beams **b** NME for columns of frame axis-A (PSO case)

Model 2: PSO case.

As mentioned in Model 1 the updated dimensions are used here, refer to Table 1 and Table 2.

It is observed that modal energy values (Fig. 5a, b) are been improvised after applying the proposed methodology.

Model 3: PSO case – Braced.

In this model, the steel braces are assigned on the periphery of the entire building and the self-weight of infills is assigned as the uniformly distributed load (UDL) on the peripheral beams. ISMB 175 was best fitted as the steel brace for the particular model.

In this Fig. 6a, b, the NME values are relatively decreased because of the strut action as the Strut element resists the lateral load. We can see from Fig. 6c that NME values on axis A1 are greater than on axis A5, implying that steel braces carry more lateral stress on A1 axis. The NME values for columns on the A5 axis are higher than on the A1 axis, as shown in Fig. 6b. If the bracing carries a less lateral load, the columns are required to resist the lateral load in that direction, resulting in higher modal energy.
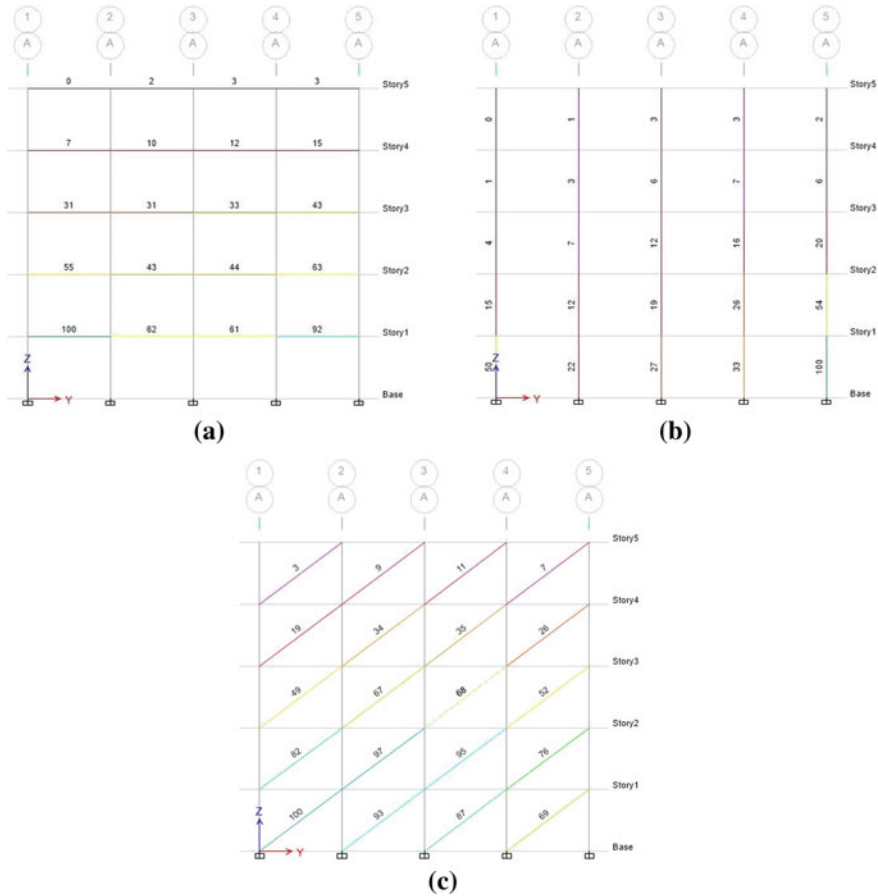
Fig. 6 **a** NME for beams along axis A **b** NME for columns along axis A (PSO case - Braced). **c** NME for steel braces along axis-A

4 Results and Discussions

The proposed design process intends to create safer structures while causing minimal disruption to design offices' current workflow. The paper lays out a step-by-step approach that structural engineers can simply adopt using the structural design software they already have in their offices. All the results worked out have been tabulated in Table 3. Significant changes in drift, stiffness, and base shear are mentioned. For the pushover analysis, 4% of building height is taken as monitored displacement which is 600 mm for all models. The overstrength ratio is additional strength beyond the design strength and is tabulated below. The target displacement is an estimate of the building's top displacement when subjected to seismic excitation, or the highest drift possible without a complete collapse. The displacement ductility ratio is the

Table 3 Comparative results from the above mentioned 3 models

Parameters	Model 1	Model 1 PSO	Model 1 PSO braced
Max story Displacement (mm)	8.83 (X), 9.38 (Y) @ story 5 (S5)	7.1(X), 7.8(Y) @ S5	1.88 (X), 1.95 (Y) @ S5
Max story drift	0.000761(X), 0.000809(Y) @ S2	0.00056(X), 0.000585(Y) @ S3	0.000153(X), 0.000156(Y) @ S2
Story stiffness (kN/m)	163,426 (X), 135,905 (Y) @ S1	203,445 (X), 157,279 (Y) @ S1	710,124 (X), 655,721(Y) @ S1
Design base shear (kN)	246 (X),230 (Y)	212 (X), 195 (Y)	268 (X),268 (Y)
Ductility ratio	1.83	1.84	2.27
Pushover base shear (kN)	2476	3053	7246
Overstrength ratio	10.06	14.40	27.04

Note: X, Y = Parameter measured along X and Y direction respectively

ratio of peak inelastic (target) displacement to elastic (yield) displacement. It gives a better estimate of the ductile capacity of the building.

5   Conclusions

The proposed design process intends to create safer structures while causing minimal disruption to the design office current workflow. Overstrength is a parameter used to quantify the difference between the required and the actual strength of a material, a component, or a structural system. In other words, the overstrength ratio is additional or reserve strength beyond the design strength.

- The maximum storey displacement is reduced by 19% for model 1 PSO and 78% for model 1 PSO braced when compared with model 1. The reason for a drastic reduction in storey displacement is due to the increase in the lateral stiffness in the form of steel braces.
- The maximum story drift for model 1 PSO is reduced by 26% and for model 1 PSO braced case it is reduced by 80% compared to model 1 which is of uniform dimensions.
- The pushover base shear is increased from 2476kN (model1) to 7246kN (model 1 PSO braced) which indicates that the load resisting capacity of the building is more in the non-linear region when it is designed as per the proposed method.
- The overstrength factor for model 1 PSO and model 1 PSO braced are 14.4 and 27.04 indicating the importance of the proposed method in utilizing the reserve strength of the building.

- The displacement ductility ratio for model 1 PSO braced is 2.27 which is 24% more than model 1. It indicates higher ductile capacity of the building in the plastic region.

References

1. Arroyo, O., Gutiérrez, S.: A seismic optimization procedure for reinforced concrete framed buildings based on eigenfrequency optimization. Eng. Optim. **49**(7), 1166–1182 (2017). https://doi.org/10.1080/0305215X.2016.1241779
2. Arroyo, O., Liel, A., Gutiérrez, S.: A performance-based evaluation of a seismic design method for reinforced concrete frames. J. Earthq. Eng. **22**(10), 1900–1917 (2018). https://doi.org/10.1080/13632469.2017.1309605
3. Fragiadakis, M., Lagaros, N.D.: An overview to structural seismic design optimisation frameworks. Comput. Struct. **89**(11–12), 1155–1165 (2011). https://doi.org/10.1016/j.compstruc.2010.10.021
4. Naeim, F.: D. Ph, Chapter 15 Performance Based Seismic Engineering
5. Papavasileiou, G.S., Charmpis, D.C.: Seismic design optimization of multi-storey steel-concrete composite buildings. Comput. Struct. **170**, 49–61 (2016). https://doi.org/10.1016/j.compstruc.2016.03.010
6. Zou, X.K., Chan, C.M., Li, G., Wang, Q.: Multiobjective optimization for performance-based design of reinforced concrete frames. J. Struct. Eng. **133**(10), 1462–1474 (2007). https://doi.org/10.1061/(asce)0733-9445(2007)133:10(1462)
7. Kappos, A.J., Ellul, F.: Seismic design and performance assessment of masonry infilled r/c frames. In: Proceedings of 12th World Conference on Earthquake Engineering, pp. 1–8, Auckland, New Zealand (2000). http://www.iitk.ac.in/nicee/wcee/article/0989.pdf
8. Sukrawa, M.: Earthquake response of RC infilled frame with wall openings in low-rise hotel buildings. Procedia Eng. **125**, 933–939 (2015). https://doi.org/10.1016/j.proeng.2015.11.118
9. Arroyo, O., Liel, A., Gutiérrez, S.: Practitioner-friendly design method to improve the seismic performance of RC frame buildings. Earthq. Spectra **37**(3), 2247–2266 (2021)

Utilization of Sawdust as Sustainable Construction Material

Kiran Devi , **Nana Lida, Taba Teyi, Puyam Bicker Singh, Kaushal Sharma, and Neeraj Saini**

Abstract The large-scale mining of natural materials like sand, for use in infrastructure projects, in emerging countries like India is creating a threat to the environment. As a result, it becomes necessary for researchers to investigate the use of industrial by-products instead of natural materials in order to safeguard the environment. This research looked into the effectiveness of utilizing sawdust to partially substitute river sand in concrete, which could help to minimize both environmental issues and construction costs. Sawdust is a waste product that, when burnt, emits a large amount of carbon dioxide, polluting the environment. The direct dumping of wood waste is damaging to the environment, forcing waste management strategies to be developed. The use of sawdust by replacing fine aggregates can be helpful to the construction industries in terms of economic and environmental aspects. In the present study, sawdust was used as partial substitution to fine aggregates by 0, 5, 10, 15 and 20% to investigate its effect on compressive strength, density, dynamic elastic modulus and water absorption of concrete at different curing ages. The non-destructive tests were also conducted on the concrete specimens. The economic analysis of sawdust was also carried out. The use of saw dust as a sand replacement resulted in inferior performance in several aspects when compared to normal concrete. However, using waste as a sand replacement increased the performance in terms of economic and environmental factors.

Keywords Cement concrete · Sawdust · Compressive strength · Density · Economic analysis

K. Devi (✉) · N. Lida · T. Teyi · P. B. Singh · K. Sharma · N. Saini
Department of Civil Engineering, Faculty of Engineering and Technology, Shree Guru Gobind Singh Tricentenary University, Gurugram, Haryana 122505, India
e-mail: kiranbimbhra@gmail.com

K. Sharma
e-mail: kaushal@sgtuniversity.org

N. Saini
e-mail: drneeraj.fet@sgtuniversity.org

1 Introduction

The most popular building material is concrete. Durability and environmental safety are also essential considerations in the building process. Aggregates are one of the most important ingredients of concrete production, and growing demand of building industry has resulted in rapid depletion of natural resources. Every year, about 11 billion tonnes of natural aggregates are taken from riverbeds all around the world [1]. Several countries have imposed limitations in recent years to prevent the negative environmental impacts of sand mining from rivers. As a result of these rules, researchers and construction companies are looking for alternate aggregate from different industries [1, 2].

Because wood is utilized in so many businesses and is so engrained in our daily lives, there is a huge amount of sawdust and other recovered wood available. The majority of sawdust is produced by timber industries all over the world. Sawdust is a by-product of sawing wood into standard sizes. It's made out of wood chips or loose particles. The particle size is determined by the type of wood used to make sawdust, as well as the size of the saw teeth. During milling procedures, roughly 10 to 13% of the overall content of the log is converted to sawdust, depending on the average width of the blade, the thickness of the timber sawed, and the sawing method [2, 3]. Sawdust is produced in large quantities as industrial waste that must be appropriately disposed of in the environment. Sawdust is primarily disposed of in landfills. Furthermore, open sawdust dumping has the potential to cause serious health problems. When sawdust is burned off, it causes pollution and other environmental problems in developing countries. As a result, proper sawdust use remains a big concern, endangering the ecosystem and environment even more [2, 3]. The substitution of sawdust for sand reduced the workability and hardened density significantly [4–6]. The use of sawdust powder and powdered granulated blast slag in mortar mixtures increased strength while lowering cost [7]. Siddique et al. [6] reported that sawdust powder at 5% has comparable strength afterward strength declined.

The current study investigates the effects of sawdust powder as a fractional substitution to sand on the hardened properties of different concrete mixtures. The correlation between compressive strength and density was derived. The goal of the study was to examine the feasibility of sawdust powder in different concrete mixtures in terms of fresh, hardened, and cost aspects.

2 Materials and Methods

2.1 Material

The ordinary Portland cement of 43 grade, which meets the Indian Standards specification, was used in the concrete mixtures [8]. Table 1 shows the physical parameters of cement. In this study, fine sand and gravel of 10 and 20 mm size were employed,

Table 1 Physical properties of cement

Property	Consistency	IST	FST	Soundness	Specific gravity	Fineness
Value	28.5	175	265	4	3.1	5%

Table 2 Physical properties of aggregates

Property	Aggregates	Type	Fineness modulus	Zone	Specific gravity	Bulk density (loose), kg/m^3	Bulk density (compacted), kg/m^3
Values	Fine aggregates	Natural coarse sand	3.15	II	2.62	1646	1824
	Coarse aggregates (10 mm)	Crushed aggregates	6.0	–	2.67	1480	1700
	Coarse aggregates (20 mm)	Crushed aggregates	6.8	–	2.65	1410	1550

Table 3 Mix designation of concrete mixtures

Sr. No.	1	2	3	4	5
Mix designation	SD0	SD5	SD10	SD15	SD20
Sawdust powder (%)	0	5	10	15	20

and physical aggregate properties are listed in Table 2 [9]. Throughout the trial, only tap water was utilized. Sawdust powder is made from hardwoods and softwoods. It was sun-dried and stored in waterproof bags. Before using in concrete mixtures, sawdust powder was sieved through 1.18 mm sieve. The sawdust powder had a specific gravity of 1.6 and water absorption of 1.6%.

2.2 Mix Proportions

The cement concrete specimens were cast by varying the quantities of sawdust powder and fine aggregate. The mix proportions for different concrete mixtures are detailed in Table 3.

After 28 days of water curing, the cube compressive test on concrete samples was performed in a compressive machine according to IS specification [10]. At 28 days, the density of concrete samples was assessed. The rebound hammer and ultrasonic pulse velocity tests were carried out in accordance with IS:13,311-1992 [11, 12]. The amount of water absorbed by concrete samples was measured.

3 Results and Discussion

3.1 Density

The effect of sawdust powder on the density of hardened concrete has been illustrated in Fig. 1. The density of hardened concrete, on the other hand, gradually falls as the level of sawdust replacement increases, as shown in Fig. 1. The reduction in density of hardened concrete may be due to the lower specific gravity of sawdust particles [2]. At 28 days, sawdust at 5, 10, 15, and 20% reduced density by 7.5, 10.7, 13.7, and 21.2% respectively, as illustrated in Fig. 1(b).
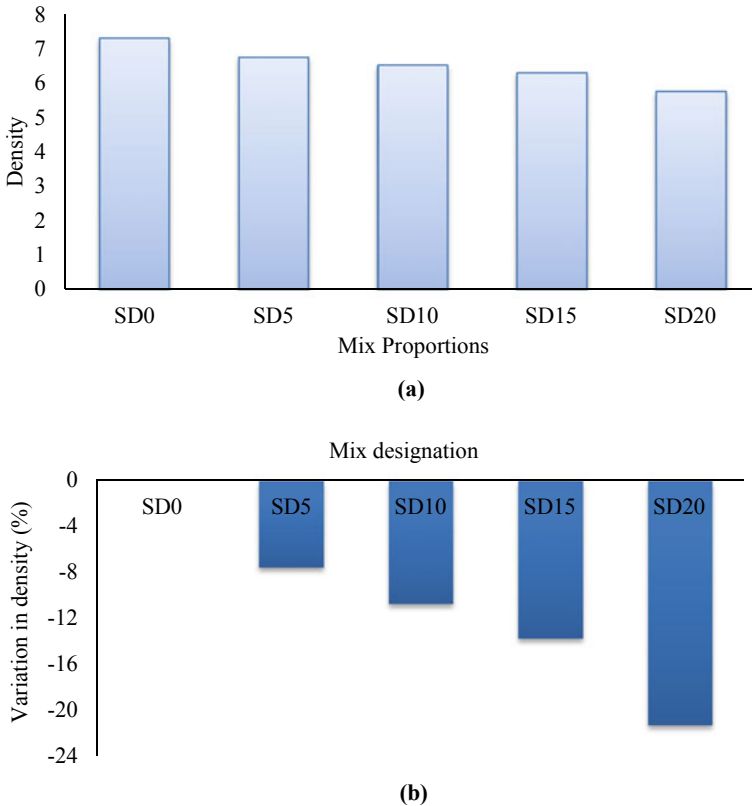
Fig. 1 **a** Variation of density in different concrete mixtures **b** Percent variation in density

3.2 Compressive Strength

The variation in compressive strength of concrete containing substantial quantities of sawdust has been depicted in Fig. 2 (a) and (b). The addition of sawdust to concrete mixes has been demonstrated to lower their strength, as illustrated in Fig. 2(a), maybe due to high porosity and water absorption capacity of sawdust powder which results in insufficient water for the hydration process. The hydration process got delayed in the presence of sawdust powder [13]. The decrease in strength gain with increased sawdust powder may be due to different chemical compositions, consequently leads to poor binding in matrix. The incorporation of sawdust powder reduced strength due
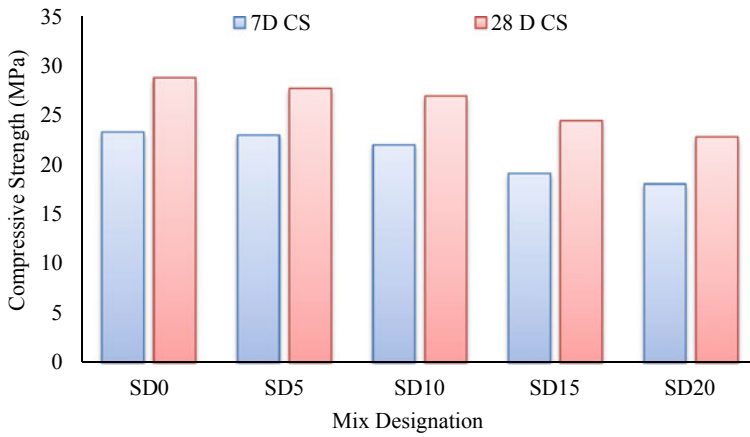
(a)
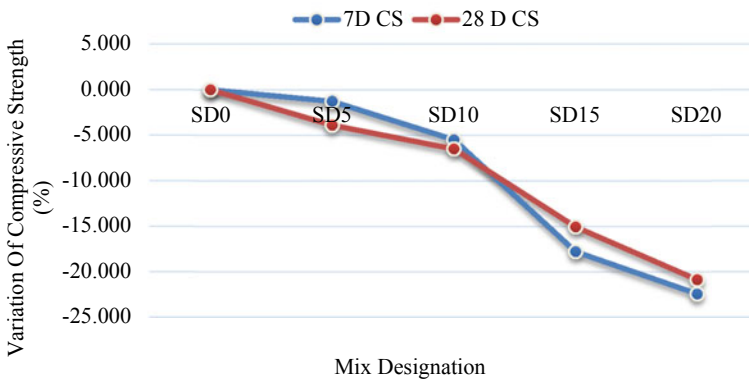
(b)

Fig. 2 a Variation of compressive strength of concrete b Percentage variation of compressive strength of concrete
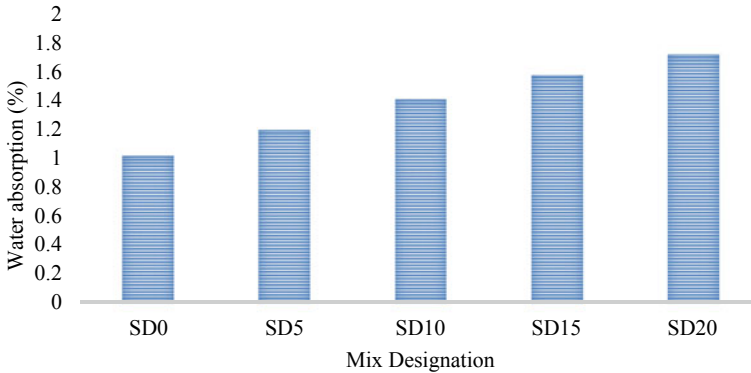
Fig. 3 Variation in water absorption of concrete

to weak interfacial transition zones (ITZ) between aggregates and cement paste [6]. The maximum reduction in compressive strength was 22 & 21% and the minimum reduction was 1 & 4% at 7 and 28 days of water curing as depicted in Fig. 2(b).

3.3 Water Absorption

The addition of sawdust powder in concrete mixtures increased the water absorption as shown in Fig. 3. The increase in water absorption value compared to the reference mix may be due to its high absorption capacity [14]. The maximum water absorption was at 20% substitution.

3.4 Non-destructive Test

The non-destructive testing of different concrete mixtures was carried out using rebound hammer and ultrasonic pulse velocity. The velocity and dynamic elastic modulus of elasticity were increased with the inclusion of sawdust powder as shown in Table 4. The UPV value indicates the good quality of concrete. The compressive strength calculated from the rebound hammer has been illustrated in Fig. 4.

3.5 Correlation Between Compressive Strength and Density

The correlation between compressive strength and density of hardened concrete was derived with a good correlation coefficient as shown in Fig. 5.

Table 4 UPV and dynamic elastic modulus of concrete mixtures

Mix no.	Elastic modulus (GPa)	Ultrasonic pulse velocity (m/sec)
SD0	6.98	3073
SD5	7.31	3214
SD10	7.60	3343
SD15	7.96	3502
SD20	8.55	3763
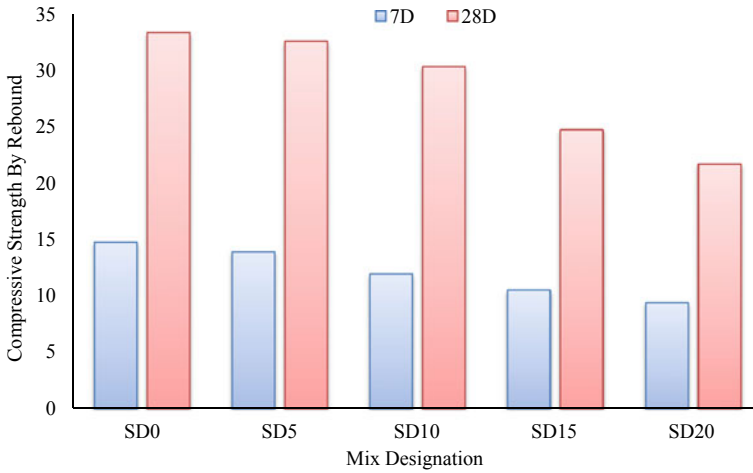
Fig. 4 Variation of compressive strength of concrete by rebound number
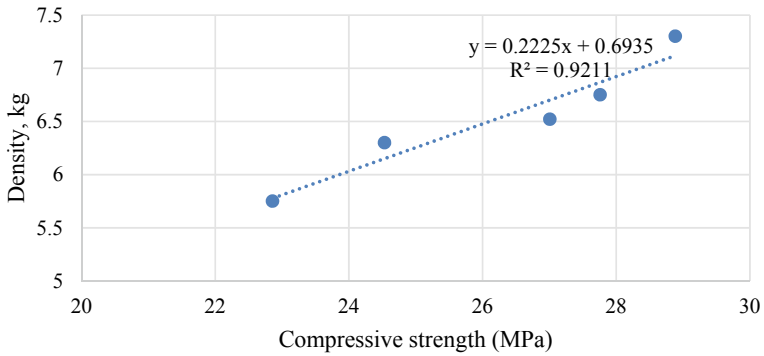
Fig. 5 Correlation between strength and density
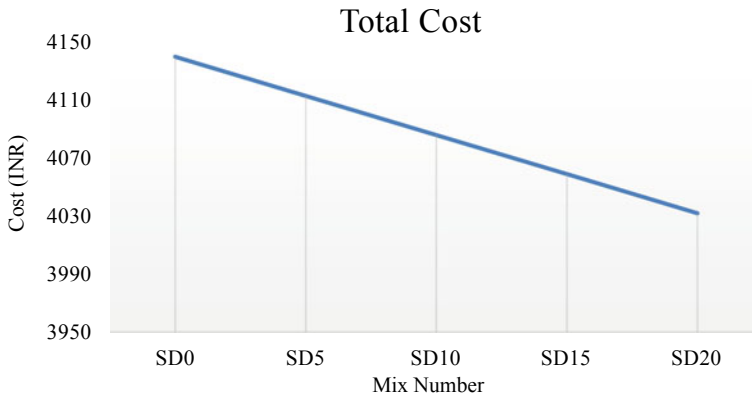
Fig. 6 Cost analysis of concrete mixtures

3.6 Cost

Figure 6 depicts the cost analysis of several sawdust-based concrete compositions. The addition of sawdust powder to concrete mixtures lowered construction costs. The cost of the production of concrete specimens incorporating sawdust at 0, 5, 10, 15, and 20% was INR 4140, INR 4113, INR 4086, INR 4059, and INR 4032, respectively. With 20% sawdust powder, the greatest cost reduction of 3% was obtained.

The cost of cement, sand, and aggregates were all considered while computing the total cost of concrete. Because sawdust was acquired as a free resource from a sawmill and used as a better alternative to landfilling or utilizing it as a cooking fuel in rural regions, the cost of sawdust has no bearing on this cost estimate. By restricting the use of natural resources, minimizing the volume of waste material, and lowering CO_2 emissions, proper sawdust utilization in concrete can help to save the environment.

4 Conclusion

In the present study, sawdust powder was utilized in the different concrete mixtures to investigate its effect on the different properties. The incorporation of sawdust powder in concrete reduced the density, strength, and cost of concrete. The reduction in density, compressive strength, and cost varied from 7–21, 4–22, and 3% with the different percentages of sawdust powder. The maximum increase in water absorption was at 20% sawdust powder. A good correlation between compressive strength and density was derived with a high correlation of 0.92. The sawdust concrete has lower strength that can be used where lower strength is required. Since sawdust concrete has a lower density, therefore it can be used where a lower structural load is required.

Since sawdust is a waste product with no other purpose or resale value, its new application as a construction material has the potential to remove a large volume of industrial waste from landfills.

References

1. Devi, K., Saini, B., Aggarwal, P.: Utilization of Kota stone slurry powder and accelerators in concrete. Comput. Concr. **23**, 189–201 (2019)
2. Batool, F., Islam, K., Cakiroglu, C., Shahriar, A.: Effectiveness of wood waste sawdust to produce medium to low-strength concrete materials. J. Build. Eng. **44**, 103237 (2021). https://doi.org/10.1016/j.jobe.2021.103237
3. Osei, D., Jackson, E.: Compressive strength of concrete using sawdust as aggregate. Int. J. Sci. Eng. Res. **7**, 1349–1353 (2016)
4. Cheng, Y., You, W., Zhang, C., Li, H., Hu, J.: The implementation of waste sawdust in concrete. Engineering **5**, 943–947 (2013)
5. Ahmed, W., Khushnood, R., Memon, S., Ahmad, S., Baloch, W., Usman, M.: Effective use of sawdust for the production of eco-friendly and thermal-energy efficient normal weight and lightweight concretes with tailored fracture properties. J. Clean. Prod. **184**, 1016–1027 (2018)
6. Siddique, R., Singh, M., Mehta, S., Belarbi, R.: Utilization of treated saw dust in concrete as partial replacement of natural sand. J. Clean. Prod. **261**, 121226 (2020)
7. Shanmuga Priya, D., Sakthieswaran, N., Ganesh Babu, O.: Experimental study on mortar as partial replacement using sawdust powder and GGBS. Mater. Today Proc. **37**, 1051–1055 (2021)
8. IS 8112 (1989) Specification for 43-grade ordinary Portland cement. Bureau of Indian Standard, New Delhi, India
9. IS 383 (2016) Indian Standard Specification for Coarse and Fine Aggregates from Natural Sources for Concrete. Bureau of Indian Standard, New Delhi, India
10. IS 516 (1959) Methods of Tests for Strength of Concrete. Bureau of Indian Standard, New Delhi, India
11. IS 13311 (1992) (Part-1: Ultrasonic Pulse Velocity) Non-destructive testing of concrete-Methods of test. Bureau of Indian Standard, New Delhi, India
12. IS 13311 (1992) (Part-2: Rebound Hammer) Non-destructive testing of concrete-Methods of test. Bureau of Indian Standard, New Delhi, India
13. Vaickelionis, G., Vaickelionene, R.: Cement hydration in the presence of wood extractives and pozzolan mineral additives. Ceramics **50**(2), 115–122 (2006)
14. Aigbomian, E.P., Fan, M.: Development of wood-crete from treated sawdust. Constr. Build. Mater. **52**, 353–360 (2014)

Assessment of Soil-Pile-Structure Interaction Influencing Earthquake Response of Building in Layered Soils

T. S. Shilpa, Muttana S. Balreddy, and S. V. Dinesh

Abstract Pile foundations are the deep foundations provided for the structures resting on soft or weak soil. The pile foundation design is done in such a way that it should withstand the structural loads along with seismic forces. The process in which response of the soil influences the motion of the structure and the motion of the structure influences the response of the soil is known as soil-structure-interaction. Neglecting the effect of SSI leads to the unsafe design for the structures resting on weak soil. In the present study the behaviour of the building with SSI interaction under the action of seismic forces is undertaken using SAP2000 software. When the seismic waves travel through different soil profiles, there is an alteration in the earthquake waves due to the variation of soil properties. The deep soil software is used to model the ground response. The earthquake data at the surface level and at the bedrock level from the DEEPSOIL is used to study the dynamic behaviour of the structure with fixed base condition and with SSPSI condition under the action of vertical and lateral load through time history analysis using SAP2000. The input earthquakes considered in the present work are Chi-Chi, Kobe and Imperial valley. The two different conditions were considered and it includes three layers of soil (SCS-NEVADA-SCS) with end bearing pile and three layers of soil (SCS-NEVADA-SCS) with floating piles. The results include that the PGA (Peak Ground Acceleration) at the surface level is reduced compared with the bedrock data because of the liquefaction. In SSPSI model there is a maximum displacement and inter-storey drift values compared to fixed base model which are unsafe in condition and leads to failure of the building. The mode shapes of both SSPSI model and fixed base model were shown. The bending moment and shear force in SSPSI model increases compared to fixed base model. Acceleration amplification ratio for Kobe earthquake is maximum compared

T. S. Shilpa · M. S. Balreddy (✉) · S. V. Dinesh (✉)
Department of Civil Engineering, Siddaganga Institute of Technology, B. H. Road, Tumkur, Karnataka, India
e-mail: msb@sit.ac.in

S. V. Dinesh
e-mail: dinesh@sit.ac.in

T. S. Shilpa
e-mail: shilpats@sit.ac.in

to other two earthquakes. In SSPSI model, floating pile foundation contributes for lesser displacement and inter-storey drift of structure compared to end-bearing pile foundation.

Keywords DEEPSOIL · SAP2000 · End bearing piles · Floating piles

1 Introduction

Natural disasters are unavoidable and it is not possible to control them. It includes floods, cyclones, earthquakes and volcanic eruption at various intervals of times. It is not only disturbing the normal life pattern but also causes the huge amount of damage to life and property and also interrupt the development process. With the help of advanced technology, man tried to overcome from these natural disasters by adopting the preventive measures. Earthquake is one of the disasters for which magnitude, time, location and intensity cannot be predicted accurately. The design of the structures subjected to earthquake loading depends on the understanding of soil-foundation-superstructure interaction during the seismic action. Pile foundations are the deep foundations adopted for the structures where the foundations are resting on soft or weak soil. The pile foundation design is done in such a way that it should withstand the structural loads along with the seismic forces, because it affects durability and efficiency of structures. The pile foundations provided in seismically active region helps to improve the bearing capacity of the soil and reduces the total and differential settlement. The presence of the liquefiable soil influences the response of the foundation in the complex way. During earthquake due to shaking, the soil reduces the strength and stiffness, and the material starts behaving from solid to liquid. One dimensional ground response analysis and identification of liquefiable strata of Guwahati city was studied Sharma et al. (2019). The vulnerability of land due to future earthquakes was explained in Guwahati city. In this work the one-dimensional equivalent linear method was used to perform the ground response analysis using Deepsoil software. It concludes that soft soil deposits cause amplification of seismic motions and the presence of deeper sandy soils causes the less amplification. Hazzar et al., (2017) investigated the influence of vertical loads on lateral response of pile foundations. The results were obtained for the different load cases for pile response in the sandy and clayey soil under the lateral and vertical loads. In case of sandy soil, the lateral resistance was not influenced by vertical loads. The presence of vertical loads reduces the lateral load capacity by 20% and the bending moment by 30% in the clayey soil.

The previous studies on soil-pile-structure interaction influencing earthquake response of building in layered soil including 1/3rd of liquified sand along with the water table are limited. There are also limited studies on the effect of fixed and flexible base foundation with end-bearing and floating pile condition on structural response. In the present study, finite element based numerical techniques were carried

out to analyse the building resting on group of piles subjected to various earthquake loadings in liquified soil deposits by varying the end conditions.

2 Methodology

Five bay five storey building supported by the pile foundation resting on the 3-layer soil profile is modelled in SAP2000 by consideration of the different pile group configurations. For the superstructure modelling, frame elements were used. The two conditions were considered for the analysis, fixed base and flexible base with floating and end bearing condition. By using the concept of Equivalent area of circular piles the rectangular area of cross-section was used with reinforced concrete sections. The soil type is sandy soil (SCS-Nevada-SCS) having a dimension of $(60 \times 60 \times 10)$ m. Pile groups of 2×2 and 2×1 of both end bearing condition and frictional piles of the proper cross-sections were used while modelling. The material properties were defined for the pile, pile-cap, soil model and superstructure and they are assigned to the respective elements in the model. The details of the building considered for the study are, five number of stories with each storey height of 3 m, five number of bays in X direction, five number of bays in Y direction, bay width in both directions are 4 m, column dimension of (0.45×0.45) m, beam dimension of (0.3×0.45) m, slab thickness of 0.15 m, concrete grade in superstructure is M30 and for substructure is M25, concrete density of $25\,kN/m^3$, Poisson's ratio of the concrete is 0.2, live load applied for both floor and roof of $3.5\ kN/m^3$ and damping ration of 5%. Four groups were made from the obtained base reactions based on the symmetry in the structure. Based on the obtained axial load from the structure, a group of piles were designed with (2×1) and (2×2) patterns. Figure 1 shows the 3D view of the building.

The dead load is calculated as per IS 875 1987 (part 1) and it is depending on the materials used in the structure and also the dimension of the structure. The self-weight is calculated automatically by the software. The live load as per IS 875 1987 (part 2). The live load is applied to both the roof and the floor and is about $3.5\ kN/m^2$. The super dead load of about $1\ kN/m^2$ is applied to both the roof and the floor. The time history analysis is done by applying earthquake loads as lateral load EQX and
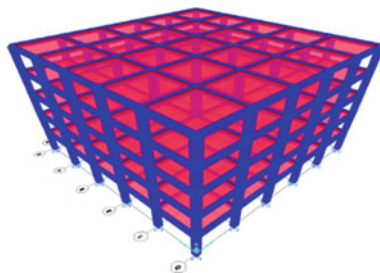
Fig. 1 3D view of the five-storey building

Table 1 Bedrock properties [Abdoun et al. (2003) and Bowles (1997)]

Properties	Density (kN/m^3)	Damping ratio (%)	Modular rigidity (kPa)
Bedrock motion	24.51	2	5,625,000

Table 2 Soil and pile properties [Abdoun et al. (2003) and Bowles (1997)]

Properties	Types of soil		Pile
	Nevada sand layer	Slightly cemented sand layer	
Youngs modulus [E] (MPa)	10	60	1260
Poisson's ratio [μ]	0.25	0.30	0.36
Relative density [%]	40	70	–
Maximum void ratio, e_{max}	0.887	–	–
Minimum void ratio, e_{max}	0.511	–	–
Cohesion [c_u] (kPa)	–	5.1	–
Density (kg/m^3)	1800	1900	1270
Friction [Ø] (º)	30	34.5	–
Coefficient of permeability [k] (m/s)	6.61×10^{-5}	1×10^{-10}	–
Modular rigidity (kPa)	4000	23,076	

EQY in both directions. Axial load from the superstructure (P KN), Factor of safety (2.5) and Bearing capacity factors are the main data used for the design of pile. The pile cap design is done by the bending theory. As the pile cap transfers the load to the pile. As per BS:8110 part 1 the design is done and it is checked for bending and local shear. There is significant modification in the behaviour of the seismic waves when they travel through the different layers of soil. One-dimensional ground response analysis can be performed by using DEEPSOIL software. The earthquake data input which consisting of PGA and PSA (Peak Spectral Acceleration) values taken from the time history plots. Table 1 shows the input bedrock Properties and Table 2 shows the soil and pile properties. The software has processor to record the earthquake response at each different layers of soil. In the present work, DEEPSOIL software is used to model the ground response under earthquake conditions.

3   Time History Analysis

In the present study, five bay five storey building was considered for the analysis. The time history analysis was carried out for Chi-Chi, Kobe and Imperial valley earthquake data using the DEEPSOIL software. The Chi-Chi earthquake is having PGA of 0.055 g, Kobe having a PGA of 0.065 g and Imperial valley is having a PGA of 0.031 g. As there is an attenuation of the PGA taken place because of the

a. 3D model of 3-layer soil profile   **b.** Building resting on pile with pile-cap
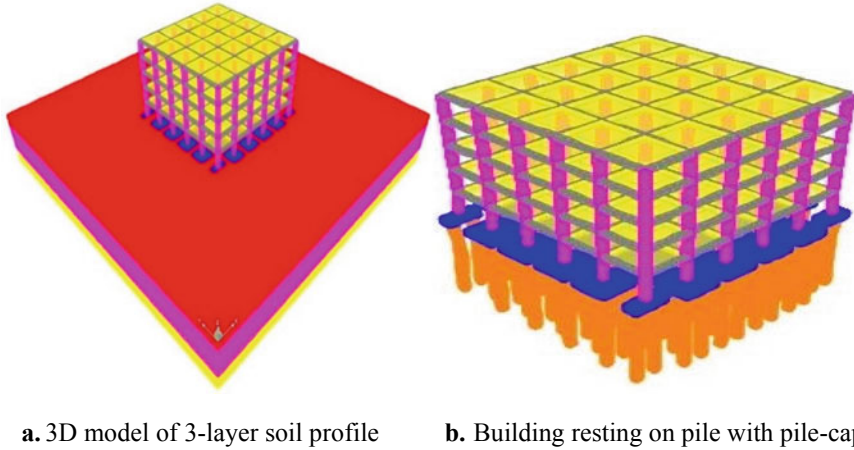
Fig. 2 Five bay five storey building resting on group of pile foundation

presence of the liquefiable layer and it also mentioned by Guillermo et al., (2018). The bedrock data of Chi-Chi, Kobe and Imperial valley earthquake are 0.169, 0.82 and 0.169 g. All three earthquake data were given as input data for SSPSI model. The time history analysis is also carried out by considering same three soil layers but the length of the pile is of 7 m and its end is in contact with liquified sand. Figure 2 shows five bay five storey building resting on group of pile foundation.

4 Results and Discussions

4.1 Storey Displacements and Inter-Storey Drifts

The time history analysis is carried out for Chi-Chi, Kobe and Imperial valley earthquake. In the case of fixed base model, for the Kobe earthquake there is a maximum displacement and inter-storey drift compared to other two earthquakes. Inter-storey drift values are less than $0.004 \times$ storey height as per IS 1893 (part 1): 2002 cl. 7.11.1. The fundamental frequencies of vibration of the structure are 0.216, 0.188 and 0.241 Hz when subject to Chi-Chi, Kobe and Imperial valley earthquakes respectively.

In the fixed base model, there is no displacement at the base because of the fixity at the base. Figure 3a shows the variation of the storey displacement at each of the storey height as it goes on increases from base to 15 m and it reaches a maximum displacement of 19.77 mm for Chi-Chi, 24.03 mm for Kobe and 15.54 mm for Imperial valley at the top 15 m height for the time history loading. Figure 3b shows

a. Storey displacement　　　　　　　**b.** Inter-storey drift
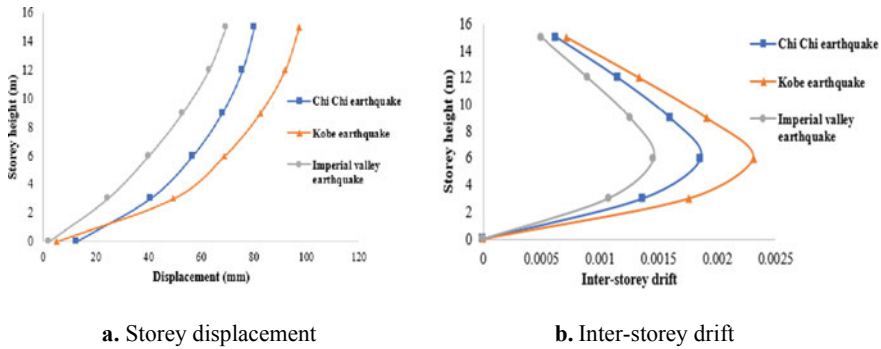
Fig. 3 Fixed base model

the Inter-storey drift at each of the storey height as it is maximum at 6 m height about 0.001859 for Chi-Chi, 0.002304 for Kobe and 0.00146 for Imperial valley.

Figure 4a shows a maximum displacement of 80.31 mm at the top 15 m height for the time history loading. In the SSPSI model there is displacement at the base about 12.69 mm because of the flexibility at the base. For Kobe it reaches a maximum displacement of 97.26 mm at the top 15 m and 5.191 mm at the base. For imperial valley it reaches a maximum displacement of 69.53 and 2.119 mm at the base. Figure 4b shows the Inter-storey drift at each of the storey height as it is maximum at 3 m height about 0.009336 for Chi-Chi, 0.0147 for Kobe and 0.007437 for Imperial valley. In the case of Chi-Chi earthquake there is a maximum displacement of 69.87 mm at 15 m height and minimum displacement of 3.37 mm at the base. For the Kobe earthquake maximum displacement is 80.03 mm and the minimum is 3.146 mm.

For imperial valley earthquake the maximum displacement is 57.66 mm and minimum is 1.21 mm as shown in Fig. 5a. In the case of Chi-Chi earthquake there

a. Storey displacement　　　　　　　**b.** Inter-storey drift

Fig. 4 SSPSI model with end-bearing pile

a. Storey displacement   **b.** Inter-storey drift
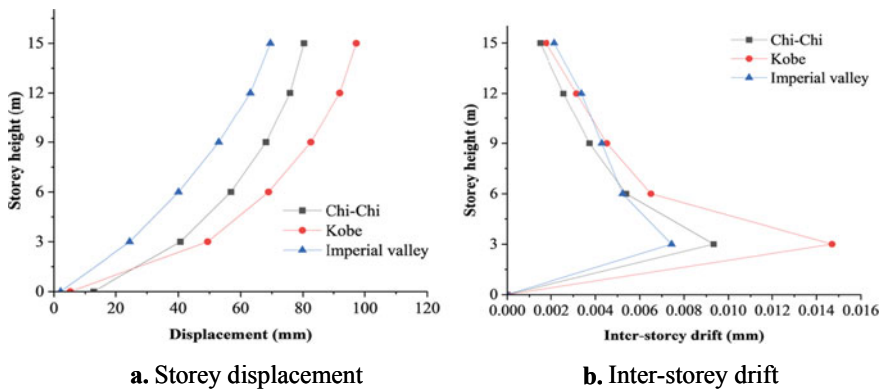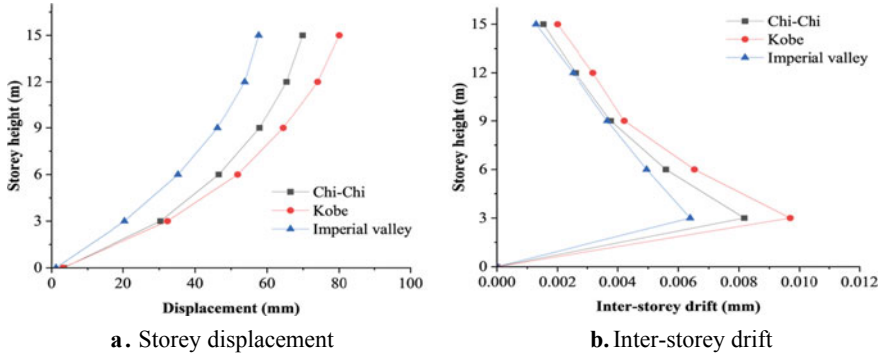
Fig. 5 SSPSI model with floating pile

is a maximum inter-storey drift of 0.0090 at 3 m height and decrease as the building height increases. For the Kobe earthquake maximum inter-storey drift of 0.009724 and for imperial valley earthquake the maximum inter-storey drift of 0.00639 as shown in Fig. 5b.

Compared to the fixed based model there is an increase in the displacement and inter-storey drift in SSPSI model with end-bearing piles and floating piles. In the case of floating pile foundation, for kobe earthquake there is a maximum displacement of 80.03 mm and the minimum of 3.37 mm at the base. Compared to the end-bearing pile foundation in the case of floating pile foundation there is a decrease in the inter-storey drift of the building. Inter-storey drift values are greater than $0.004 \times$ storey height as per IS 1893 (part 1): 2002 cl. 7.11.1 for both end-bearing and floating pile conditions.

The storey drift in any storey due to the minimum specified design lateral force, with partial load factor of 1.0, should not exceed 0.004 times the storey height. All the other parameters like bending moment, acceleration amplification ratio and spectral accelerations were recorded and found good results for fixed base model, SSPSI model with end-bearing and floating condition.

5   Conclusions

Ground response analysis in DEEPSOIL has been carried out by considering bedrock at 10 m depth and the profile was considered to consists of three layers with liquifiable layer in the middle. The ground response analysis for the above cases was determined and the acceleration time history at the top surface is taken as input at the base of the structure and the seismic analysis of the frame structure was carried for fixed base model and SSPSI model. From the study the following conclusions were drawn.

1. The presence of water table attenuates the ground motion in the case of three layer soil surface with liquified soil in the middle. The attenuation varies from 69 to 82% in 3 layers deposit for the considered bedrock motion.
2. In SSPSI model, floating pile foundation contributes lesser displacement and inter-storey drift of the structure compared to end bearing pile foundation.
3. In fixed base model, as the PGA of the acceleration time history increases both the displacement and inter-storey drift increases in all the cases.
4. Compared to the fixed base model, shear force and bending moment in SSPSI model increases and varies from 50 to 60%.
5. Acceleration amplification ratio is maximum for the end bearing piles compared to the floating piles.
6. From the spectral accelaration data collected from deep soil software, it is noticed that bedrock spectral accelaration is higher compared to spectral accelaration when it reaches at the top surface after passing three layers of soil. It is because of the presence of liquefiable layer where the energy attenuation takes place.

References

1. Abdoun, T., Dobry, R., O'Rourke, T.D., Goh, S.H.: Pile foundation response to lateral spreads: centrifuge modelling. J. Geotech. Geo Environ. Eng. ASCE **129**(10), 869–878 (2003)
2. Hokmabadi, A.S., Fatahi, B., Samali, B.: Assessment of soil-pile-structure interaction influencing seismic response of mid-rise building sitting on floating pile foundation. Comput. Geotech. **55**, 172–186. Elsevier (2014)
3. Dehghanpoor Sichani, A., Thambiratnam, D., Chan, T.: A review of seismic soil-pile-superstructure interaction methods. In: Earthquake Geotectnical Engineering, ResearchGate (2017)
4. Sharma, B., Siddique, A.F., Medhi, B.J.: One dimensional ground response analysis and identification of liquefiable Strata of Guwahati City. In: Barman, M., Zaman, M., Chang, J.R. (eds.) Transportation and Geotechniques: Materials, Sustainability and Climate. GeoChina 2018. Sustainable Civil Infrastructures, pp. 146–162. Springer, Cham (2019). https://doi.org/10.1007/978-3-319-95768-5_13
5. Guillermo, A., López Jiménez, G.A., Dias, D., Jenck, O.: Effect of the soil-pile-structure interaction in seismic analysis: case of liquefiable soils. Acta Geotech. 1–17. Springer (2018)
6. IS 2911–1–1 (2010): Design and Construction of Pile Foundations-Code of Practice, Part 1: Concrete Piles, Section 1: Driven Cast In-situ Concrete Piles [CED 43: Soil and Foundation Engineering]
7. IS: 456–2000: Code of Practice for Plain and Reinforced Concrete. Bureau of Indian Standards Manak Bhavan, 9 Bahadur Shah Zafar Marg New Delhi-110002
8. IS-875 (Part 1)–1987: Code of Practice for Design Loads (other than earthquake) for buildings and structures–Unit weights of buildings materials and stored material. Bureau of Indian Standards Manak Bhavan, 9 Bahadur Shah Zafar Marg New Delhi-110002
9. IS-875 (Part 2)–1987: Code of Practice for Design Loads (other than earthquake) for buildings and structures–Imposed loads. Bureau of Indian Standards Manak Bhavan, 9 Bahadur Shah Zafar Marg New Delhi-110002
10. IS-875 (Part 5)–1987: Code of Practice for Design Loads (other than earthquake) for buildings and structures–Special loads and load combinations. Bureau of Indian Standards Manak Bhavan, 9 Bahadur Shah Zafar Marg New Delhi-110002

11. IS-1893 (Part 1)–2002: Criteria for earthquake resistant design of structures. Bureau of Indian Standards Manak Bhavan, 9 Bahadur Shah Zafar Marg New Delhi-110002
12. Hazzar, L., Hussien, M.N., Karray, M.: Influence of vertical loads on lateral response of pile foundations in sands and clays. J. Rock Mech. Geotech. Eng. **9**, 291–304 (2017)
13. Matinmanesh, H., Saleh Asheghabadi, M.: Seismic analysis on soil-structure interaction of buildings over sandy soil. Procedia Eng. **14**, 1737–1743. Elsevier (2011)
14. Bagheri, M., Jamkhaneh, M.E., Samali, B.: Effect of soil-structure-interaction on mid and high-rise building resting on a group of pile foundation. Int. J. Geomech. ASCE **18**(9), 1–27 (2018)
15. Van Nguyen, Q., Fatahi, B., Hokmabadi, A.S.: Influence of size and load bearing mechanism of piles on seismic performance of buildings considering soil-pile-structure interaction. Int. J. Geomech. ASCE **1**(1), 1–22 (2017)
16. Han, Y., Wang, S.-T.: Soil-Pile-Structure interaction in earthquake engineering. In: IACGE, ASCE, pp. 557–566 (2013)

Municipal Solid Waste Management in Kakkanad by Bin Allocation Using Arcgis

S. Divya, Aleena Shyjo, Aleena Sajan Abbas, Akhil K. Ajith, and Jawahar S. Saud

Abstract Waste management is one of the world's most challenging issues, irrespective of whether a country is developed or developing. The lack of garbage bins in needed areas, as well as the overflow of already existing bins at public locations prior to the start of the next cleaning process, is a major problem in waste management. This, in turn, causes different threats to that location, such as bad odor and ugliness, which may be the root cause of the spread of various diseases. This project is based on a smart waste management system to avoid any potentially dangerous scenarios and to maintain public cleanliness and health. This project proposes an IoT-based smart waste management system that uses sensor devices to monitor the waste level in the bins. When the bin fills up to 80%, the system detects it and immediately alerts the appropriate authorities, who then organize garbage pickup. A smartphone application is being created to monitor and integrate this, as well as to make it easier for citizens to locate the bins. This project reviews the use of Geographic Information System (GIS) in the field of MSWM in Kakkanad. Kakkanad is located in the eastern part of the Ernakulam district. Kakkanad is the major industrial and residential region in the city of Kochi thus making it one of the most critical areas of waste generation. Using ArcGIS software mapping of the area is done and the points for bin allocation are identified.

1 Introduction

Waste management issues are coming to the forefront of the global environmental agenda at an increasing frequency, as population and consumption growth results in increasing quantities of waste. India generates 6.2 million tons of waste each year. The manual analysis of urban solid waste management is very tedious as it involves

S. Divya (✉) · A. Shyjo · A. S. Abbas · A. K. Ajith · J. S. Saud
Department of Civil Engineering, FISAT, Angamaly, Kerala, India
e-mail: sdivz330@gmail.com

huge data and statistics. The lack of garbage bins in needed areas, as well as the overflow of already existing bins at public locations prior to the start of the next cleaning process, is a major problem in waste management.

2 Study Area

The selected area is Kakkanad, a suburb in Thrikkakara municipality. The latitude for **Kakkanad, Kochi, Kerala, India** is: 10.011104 and the longitude is: 76.343877. Kakkanad is located in the eastern part of the Ernakulam district. Kakkanad is the major industrial and residential region in the city of Kochi thus making it one of the most critical areas of waste generation. Using ArcGIS software, mapping of the area is done and the points for bin allocation are identified and could be replicated in residential zones all over Kerala.

2.1 Data Collection

An **interview** was conducted by visiting GCDA (Greater Cochin Development Authority) and later Thrikkakara municipality. The Health inspector affiliated to the Health Department, Thrikkakara municipality provided us with the required data regarding the project. It was found that the population of Kakkanad is 77319 persons, the area is 2816 sq km and the waste produced is 300 g/head. The current collection plan of Kakkanad is the Bio Bin. A questionnaire survey was taken in the study area among citizens and officials (Figs. 2 and 3).

3 Results

The survey was taken in residential areas and flats. It was analyzed that most of the flats in Kakkanad suburbs have a proper waste treatment plan and wastes are collected on a daily basis. The collection godown of kakkanad at Thrikkakara was visited. It was learned that waste management systems like CREDAI, and HITECH are being used in flats in the Kakkanad area for waste treatment. The number of waste bins in public areas is very less.

Are the disposal methods being followed as per Municipal Solid Waste Management Rules of 2016?
8 responses
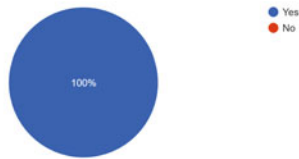
Are there training/awareness programs for residents , educating them about MSWM ?
8 responses
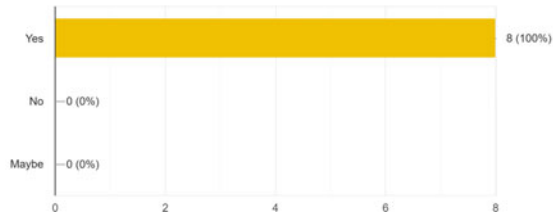
What type of solid waste comes out from households mostly ?
8 responses
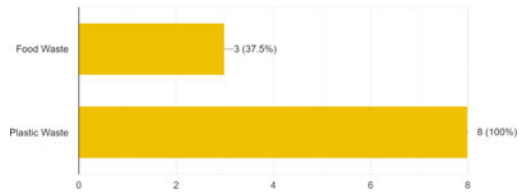
In what type of container waste is collected ?
8 responses
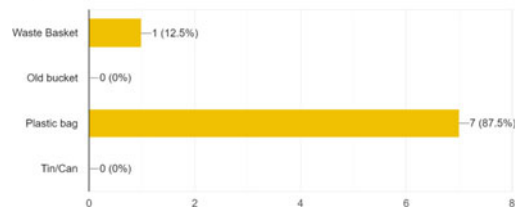
How often is the waste container emptied?

8 responses

Once a day	1 (12.5%)
Once in three days	6 (75%)
Once a week	4 (50%)
Once a month	0 (0%)
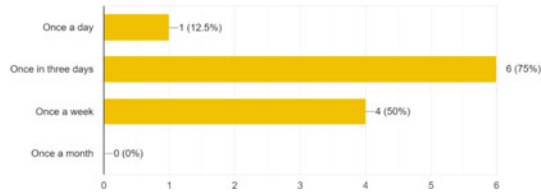
Where do you usually put away collected wastes?

8 responses

In the public bin	0 (0%)
In the itinerant waste van	0 (0%)
By the valley/lake side/river	0 (0%)
By the road or street side	0 (0%)
On an open space	4 (50%)
In a hole in own compound	1 (12.5%)
Other	5 (62.5%)
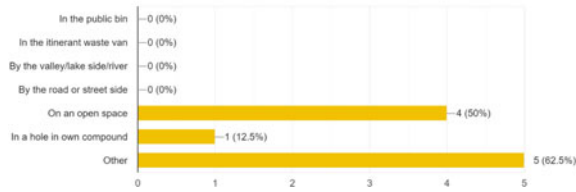
Are there sufficient public bins in the area ?

8 responses

Yes	3 (37.5%)
No	5 (62.5%)
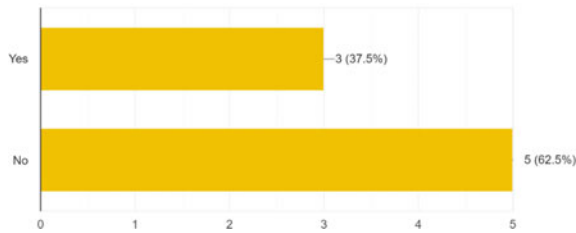
Do you think the waste disposal method is a problem in this locality ?

6 responses

Yes	5 (83.3%)
No	1 (16.7%)
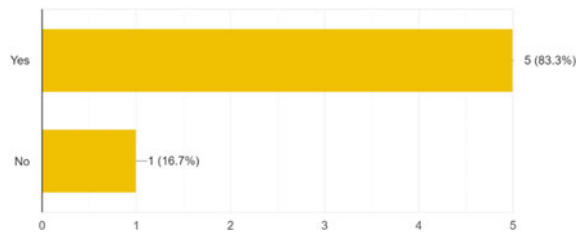
How often are the nearest public bins emptied?
2 responses

Once a week	0 (0%)
Twice a week	0 (0%)
Thrice a week	1 (50%)
Everyday	2 (100%)
Don't know	0 (0%)
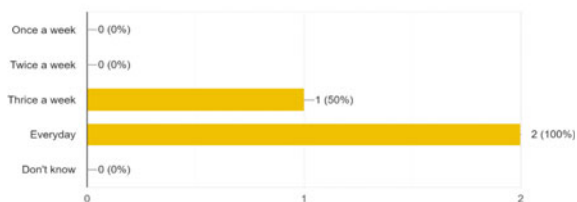
How can you describe the state of the public bins ?
2 responses

Rusting rotting	0 (0%)
Not in a good condition	0 (0%)
Adequate size	1 (50%)
Inadequate	0 (0%)
Don't know	0 (0%)
NOT A PUBLIC BIN	1 (50%)
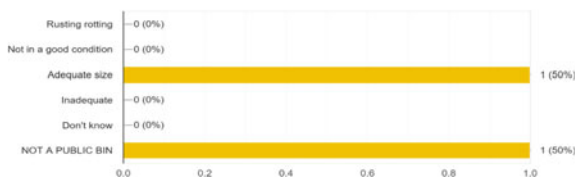
Are people concerned about these issues

Concerned   Not concerned

How concerned are people about environmental pollution?   How concerned are people about sustainable development?
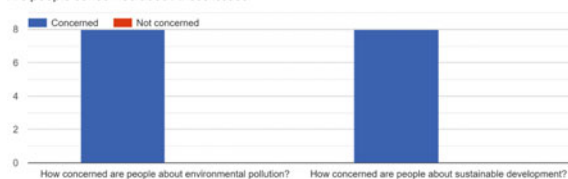
Is there presence of the following in and around public waste bin or dumping land?
8 responses

Dark flowing water	1 (12.5%)
Odour	8 (100%)
Mosquitoes and coackroches	8 (100%)
Fire	0 (0%)
Domestic Animals	3 (37.5%)
Rats and scavengers	5 (62.5%)
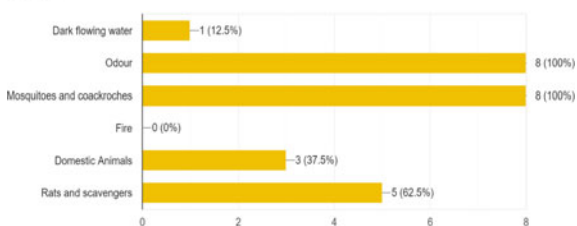
Is there a waste management center for Kakkand

8 responses

Yes	8 (100%)
No	0 (0%)
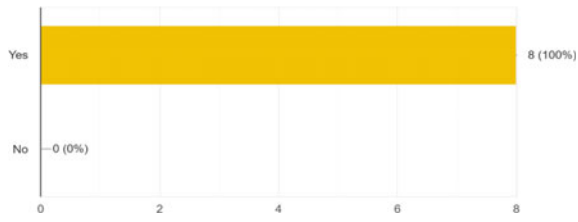
Are you satisfied with the waste management processes of Kakkand

8 responses

Yes	7 (87.5%)
No	1 (12.5%)
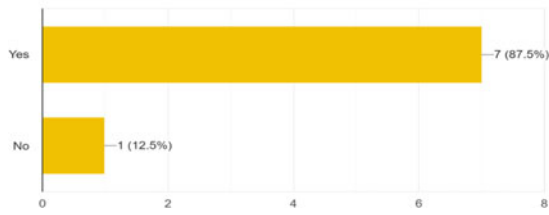
Is the moisture content in the collected waste more or less ?

7 responses

Yes	7 (100%)
No	0 (0%)
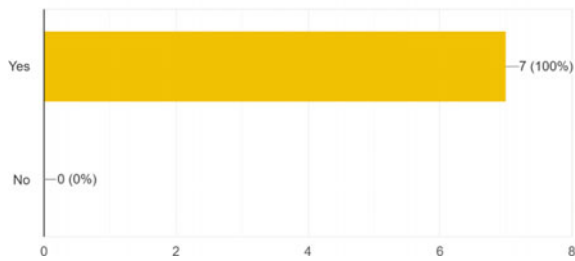
Does the waste in land , water resources , and waste burning in open areas create health issues in people living nearby ? Is it common ?

8 responses

Yes	7 (87.5%)
No	1 (12.5%)
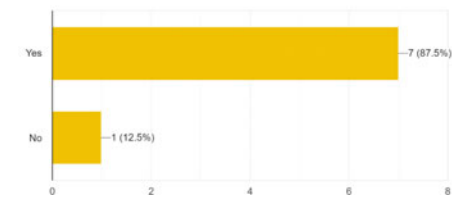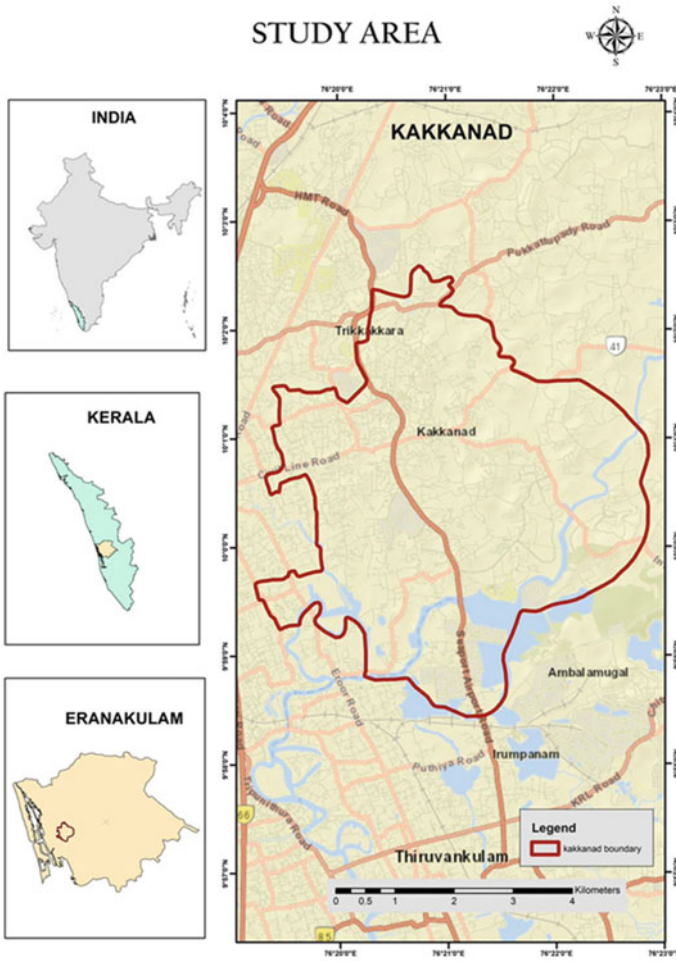
Fig. 1 Kakkanad-study area

3.1 App Development

3.1.1 Importance of Mobile Apps in Solid Waste Management

Solid waste needs to be properly stored, collected, transferred, treated and disposed of. The main effort was to minimize the impact on the environment and health. Thus, the engineering and logistics tools were sufficient to plan and implement waste management systems. Resource management and social behavior are an integral part of all waste management systems, increasing the need to develop mobile applications for the sector. Mobile technology could start to change the way solid waste and recycling companies do business. New tools enable business owners and the average

Fig. 2 Survey collection

consumer of waste and recycling to take advantage of access to information on services, planning, etc., while helping them make smarter decisions about results (Figs. 4 and 5).

3.1.2 Bin Hub

It's a page that will be displayed once the user or the authority login to the application where it will display the status of the bin whether it is 80% filled. If yes, the trash can is full, then it will be notified in the application (Figs. 6, 7, 8 and 9).

3.2 Mapping

3.3 Proposal for IoT Based Bins

The proposed system, which involves setting up trash cans linked with the GIS system that transmits the location to the server. This transmitted data is updated to the database from which the information on the trash can be accessed through the smartphone.

This proposed system is developed in order to solve the problems faced by the people with respect to waste management by taking it to the next level where it can be applied to the use in cities. By doing this, major problems faced by urban areas can be checked. Whenever the trash can gets filled to the threshold level then the

Fig. 3 Survey Collection from a waste collection point of Kakkanad

message is received by the authority responsible to get it cleaned up through the means of an android application in order to get the job done by the authority. Usually the overflowing trash cans bring out the pollution of nearby roads and pedestrians and also cause a foul smell. The proposed system brings in the reduction of the overflowing trash cans, maintains a clean and sanitary environment, and also reduces the workload. This system can be reliable 96% of the time. The application is reliable 100% of the time, and the user can access it 24×7 365 days of the year.

3.3.1 Collection Method in IoT System

Smart collection bin works with the combination of sensors namely weight sensor and an Infrastructure Red (IR) sensor that indicates its weight and different levels respectively. The IR sensors will show us the various levels of garbage in the dust-bins and also the weight sensor gets activated to send its output ahead when its threshold level is crossed. The microcontroller used was an ARM LPC2148 and the controller gives all details to the transmitter module (Wi-Fi module). At the receiver section a mobile handset is needed to be connected to the Wi-Fi router so the details of the garbage bin are displayed onto the HTML page in the web browser of the mobile handset. This system ensures the cleaning of dustbins soon when the garbage level reaches its maximum. This reduces the total number of trips of garbage collection vehicles and hence reduces the overall expenditure associated with the garbage
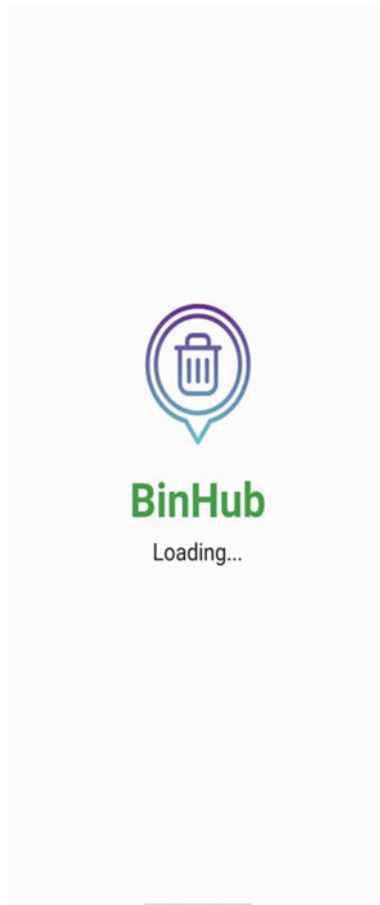
Fig. 4 App interface

collection. It ultimately helps to keep cleanliness in the society. Therefore, the smart garbage management system makes the garbage collection more efficient.

3.4 Data Flow Diagram

In the data flow diagram, the trash can is a system and is bidirectional to the user and the database. Where the trash can features sending a message, indicating the level, and tracing the location (Figs. 10 and 11).
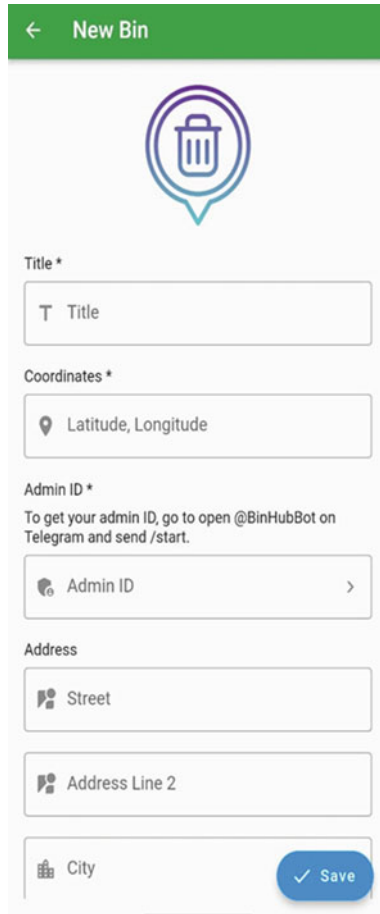
Fig. 5 App admin interface

3.5 Sequence Diagram

In the sequence diagram, the user throws the garbage in the trash can. When the trash can senses the garbage at the threshold level then there is information stored in the database like time, location, and efficiency of the bins. And when it is filled then there is a message sent to the particular authorities to empty it. When the trash can is emptied then the details of being emptied are stored in the database and this process continues for the same.
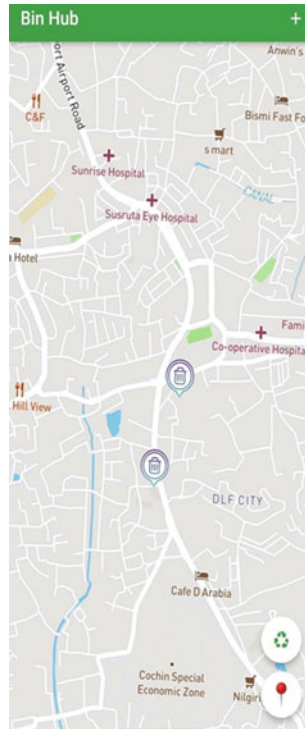
Fig. 6 User interface

4 Discussion

As a result of rapid increase in population, solid waste management is being an unavoidable factor in urban areas. The lifestyle and living conditions of people a result in a high level of solid waste generation. The manual analysis of urban solid waste management is tedious, hence computerization of systems is necessary. The project aims in developing waste management in a city where population and the production of waste is high. We analyzed the points of locations where the presence of waste bins are important for waste management in that area. We develop a mobile application termed "BIN HUB" to help locals to identify the nearest location of disposal bins. We create a system where the mobile application notify the crew once bin is filled to ensure that the bins are cleared as soon as the fixed levels are reached.

5 Conclusions

The study area was covered with 43 wards. The study area was highlighted on the map as presented in Fig. 1. Municipal Solid Waste Management (MSWM) The bodies were unable to prove a 100% efficient system and even were not able to reach the efficiency of 80%. So, we couldn't expect 100% efficient SWM practice in urban areas. But appropriate SWM could raise the SWM efficiency to a substantial limit. The SWM practice in the study area was moderate. Door to-Door (DTD) waste collection, initiated by the local community and supported by DCC, was observed. But in some areas, the SWM practice was not so maintained recurrently resulting in jumbled waste disposal. In most parts of the study area, there were no bins or containers for the dumping of solid wastes. Waste collecting bodies had no such bin or container at that site. Community-based SW collection vans had collected wastes rarely (once or twice a week) from that site. Emerging facilities (BioBin, CREDAI, etc.) in that part of the study area need proper SWM with considering future population projection and rapid urbanization. The southern part of the study area was a fully residential area and BioBin waste collection was practiced. The unprivileged people had a lack of proper sanitation, drinking water, and solid waste dumping facilities, and only wastes are collected at night from the adjacent containers. In local areas, local waste-collecting bodies were inactive and need proper SWM practices. In areas that comprise a huge number of people, SWM practice was not so good. Except for one location, no major illegal dumping was seen in that part of the study area. From the questionnaire survey, it was found that most of the waste generated was food waste and plastic waste. During the rainy season, the scenario was quite bad with the flooding of the wastes to the roads with rain. Comparatively, DTD waste collection helps to minimize the SW problem of the study area, but the crevice and timing of waste collection from households by the local SW collecting bodies were hectic. As the residential area was highly over-populated, people threw their wastes beside the playground, along the roadside, and in the open spaces as well. Thus, the importance of bins was noticed.

In the present study, important parameters for solid waste disposal were chosen and based on different kinds of literature and map studies, their ranks and weights were assigned that can help in making vital decisions in bin location, as a result the impacts due to unscientific waste disposal can be avoided. The geological studies in GIS and application development play a vital role in the detection of bins using satellites hence, the combination study with GIS, App development, and route optimisation will be a powerful weapon to study the solid waste management and helps the government to detect some places where the waste management can be carried successfully Combined with remote sensing technologies, the geographic information system became the most appropriate method to tackle spatial aspect questions, such as identifying a good place for bins. GIS as an analysis resource has helped to collect knowledge and geomorphological evidence on recent land usage. Our administrators may solve other problems with further analyzes of the results, such as

Fig. 7 Waste deposit points
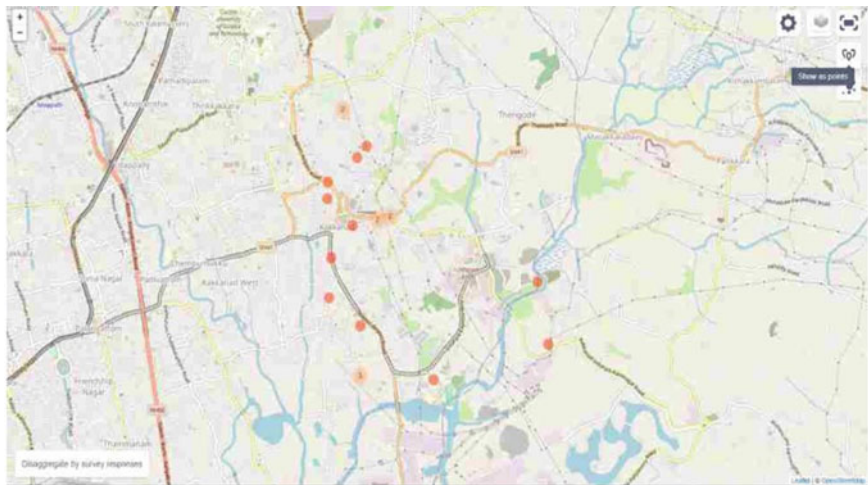
Fig. 8 Critical points

finding an appropriate waste disposal location. Therefore, the usage of these urban waste control systems would no longer create an issue for city officials.
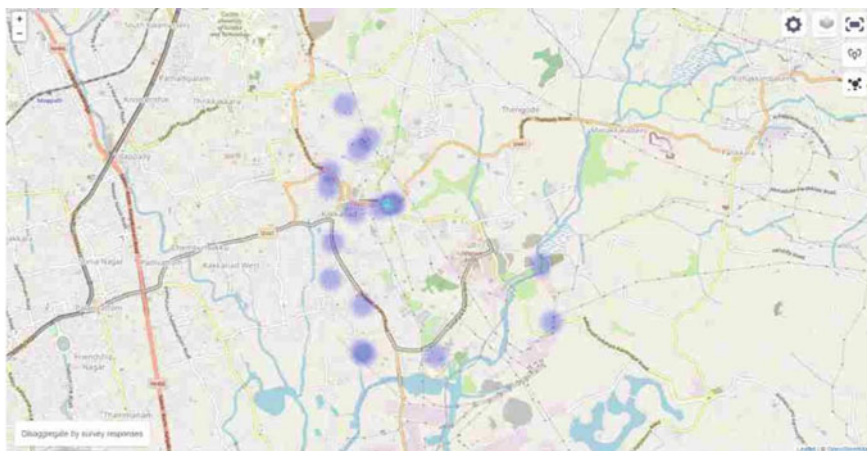
Fig. 9 Hotspots
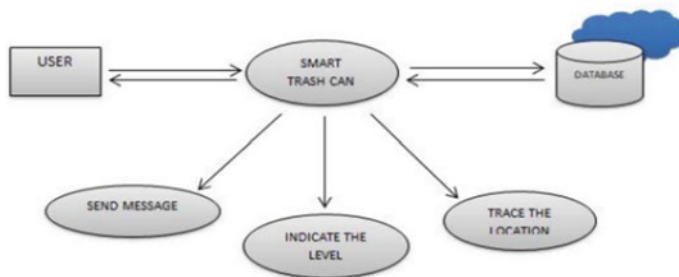
Fig. 10 Data flow diagram
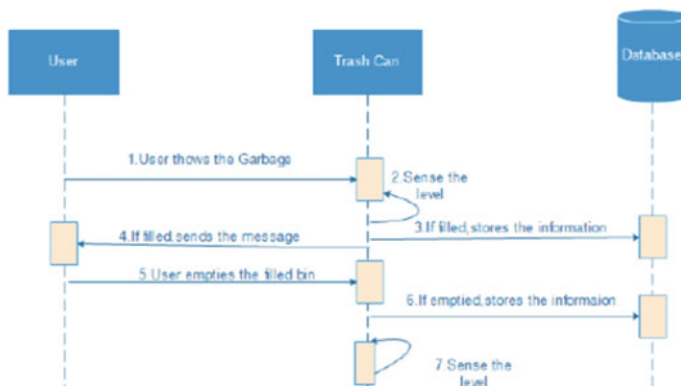
Fig. 11 Sequence diagram

References

1. Kahraman, C., et al.: Intuitionistic fuzzy EDAS method: an application to solid waste disposal site selection. J. Environ. Eng. Landsc. Manag. **25**(1), 1–12 (2017)
2. Mussa, A., Suryabhagavan. K.V.: Solid waste dumping site selection using GIS-based multi-criteria spatial modeling: a case study in Logia town, Afar region, Ethiopia. Geol. Ecol. Landsc. **5**(3), 186–198 (2021)
3. Nõlvak, H., et al.: Microbial community changes in TNT spiked soil bioremediation trial using biostimulation, phytoremediation and bioaugmentation. J. Environ. Eng. Landsc. Manag. **21**(3), 153–162
4. Radha, R., Stanis, A., Mary, A.: Pentapartitioned Neutrosophic Pythagorean Soft set. Infinite Study (2021)
5. Sumathi, V.R., Natesan, U., Sarkar, C.: GIS-based approach for optimized siting of municipal solid waste landfill. Waste Manag. **28**(11), 2146–2160 (2008)
6. Verma, A., Bhonde, B.K.: Optimisation of municipal solid waste management of Indore City using GIS. Int. J. Emerg. Technol. **5**(1), 194 (2014)
7. Monika, K.A., Rao, N., Prapulla, S.B., Shobha, G.: Smart dustbin-an efficient garbage monitoring system. Int. J. Eng. Sci. Comput. **6**(6), 7113–7116 (2016)
8. Parkash, P.V.: IoT based waste management for smart city. Int. J. Innov. Res. Comput. Commun. Eng. **4**(2), 1267–12744 (2016)
9. Chaware, S.M., Dighe, S., Joshi, A., Namrata, B., Korke, R.: Smart garbage monitoring system using internet of things (IOT). Int. J. Innov. Res. Electr. Electron. Instrum. Control Eng. (IJIREEICE) **5**(1), 74–77 (2017). UNEP (United Nations Environment Programme) (2005) Solid Waste Management. Vol. 1, ISBN: 92-807-676-5
10. Minghua, Z., et al.: Municipal solid waste management in Pudong New Area, China. Waste Manag. **29**, 1227–1233 (2009)
11. Simelane, T., Mohee, R.: Future directions of municipality solid waste management in Africa Pretoria (2012)
12. Adekunle, I.M., Adebola, A.A., Aderonke, K.A., Pius, O.A., Toyin, A.A.: Recycling of organic wastes through composting for land applications: a Nigerian experience. Waste Manag. Res. **29**, 582–593 (2011)
13. Jalil, A.: Sustainable development in Malaysia: a case study on household waste management. J. Sustain. Dev. **3**, 91–102 (2010)
14. Sharholy, M., Ahmad, K., Mahmood, G., Trivedi, R.C.: Municipal solid waste management in Indian cities—a review. Waste Manag. **28**, 459–467 (2008)
15. Aremu, A.S.: Optimization and assessment of waste bin locations using geographic information system. In: Proceedings of the 3rd Annual Civil Engineering Conference, University of Ilorin, Ilorin, pp. 231–236 (2011)
16. Verma, A., Bhonde, B.K.: Optimisation of municipal solid waste management of Indore City using GIS. Int. J. Emerg. Technol. **5**, 194–200 (2014)
17. Chalkias, C., Lasaridi, K.: A GIS Based Model for the Optimization of Municipal Solid Waste Collection: The Case Study of Nikea, Athens. Harokopeio University of Athens, Athens, Greece (2009)
18. Purkayastha, D., Majumder, M., Chakrabarti, S.: Collection and recycle bin location-allocation problem in solid waste management: a review. Pollution **1**, 175–191 (2015)
19. Vijay, R., Gautam, A., Kalamdhad, A., Gupta, A., Devotta, S.: GIS based locational analysis of collection bins in municipal solid waste management system. J. Environ. Eng. Sci. **7**, 39–43 (2008)
20. Sumedh, D., Kashid, D.B., Nalawade, A.D., Nagne, R.K., Dhumal, K.V.K.: Solid waste and waste bin management by using RS & GIS: A review. Int. J. Sci. Eng. Res. **6**, 554–557 (2015)

21. ESRI (Environmental Systems Research Institute) (2015)
22. UNDP (United Nations Development Programme) (2012) Feasibility Study and Detailed Design for Solid Waste Management in the Gaza Strip. DHV ENFRA TECC
23. PCBS (Palestinian Central Bureau of Statistics) (2018) Localities in Deir al Balah Governorate by Type of Locality and Population Estimates, 2007–2016

Comparative Analysis of Bracing Configuration for Retrofitting of Existing Structures on Hill Slopes

Yaman Hooda and **Pradeep K. Goyal**

Abstract The seismic vulnerability of the structures depends upon their typological and topographical nature. Structures built on planar regions are less seismic vulnerable to the structures built in hill regions due to irregularity in nature in both vertical and horizontal profile in latter case. Because of the economic growth and speedy urbanisation, the rate of construction of structures on hill slopes are increasing subsequently as the rate of population increases. While experiencing an earthquake event, the existing structures, without any or older codal regulations, are worst affected. This study deals with the seismic vulnerability analysis of existing structures located on the hill slopes; with both structural configurations of Set – Back Configuration and Step – Back Configuration. Etabs 2018 is taken as an analytical tool, under the consideration of Pushover Analysis and revised codal provisions of IS 1893: 2016. Retrofitting is provided for the structural elements falls under the category of "Structurally unfit" from the results of Building Performance Level analysis. Bracing is considered to the best retrofitting technique for the frame structures, especially for the structures located on hill slopes. The retrofitting method of bracing is compared with two different contemplations: 1. Bracing with different sections and 2. Bracing with different configurations. The various factors considered for the comparative analysis included Maximum Storey Displacement, Maximum Storey Drift, Time Period, Circular Frequency and Base Reaction. After this analysis, the best possible bracing section and bracing configuration can be decided as a retrofitting method for the existing structures on hill slopes.

Keywords Seismic vulnerability · Hill slopes · Retrofitting · Bracing · Irregularity

Y. Hooda (✉) · P. K. Goyal
Department of Civil Engineering, Delhi Technological University, New Delhi, India
e-mail: yamanhooda@gmail.com

P. K. Goyal
e-mail: pkgoyal@dtu.ac.in

Y. Hooda
Department of Civil Engineering, Manav Rachna International Institute of Research and Studies, Faridabad, Haryana, India

1 Introduction

As per the latest data received from The World Economic Forum, the rate of the occurrence of Geo – Physical disasters is increasing rapidly in past 70 decades. One of the most prominent disasters comes under the category of Geo – Physical disasters is Earthquakes. Earthquakes, like any other disasters, causes a widespread loss to both the lives and property in a society. And its effects are even worse if the structures are located on the hill slopes. The structures already existing (constructed before the provision of earthquake in the designing) on the hill slopes are more prone to the seismic waves as compared to the newly constructed structures as the later involved the inclusion of the guidelines related to the effect of seismic waves on the structures. Furthermore, with more development and occurrence of the earthquakes in different parts of the world, the guidelines changes and thus, designing and analysis has to be done as per the revisions in the codal provisions. When the existing structures are being analysed with the latest provision, these structures are proved to be vulnerable towards the seismic waves. Thus, it will become a mandate to retrofit the existing structures. Bracing is considered to be one of the most effective retrofitting techniques when the structure is located on the hill slopes due to its load transfer mechanism. There are different ways in which bracing can be adopted as a retrofitting method. This study will be focusing on the study of effect of providing the bracing as a retrofitting method on the property of maximum displacement and maximum storey drift, being considering the two profiles of the structures found on the hill slopes: Set – Back Configuration and Step – Back Configuration. In Set – Back Configuration, there are ono changes in the stories above the ground level; but the length of the column increases as sloping surface increases (Fig. 1). Whereas in case of Step – Back Configuration, a "stepped" structures is built; may providing the same after every bay, with increase column height on a sloping surface (Fig. 2).

The behaviours of the structures located on the hill slopes under the cation of seismic forces are analysed analytically to determine the dynamic response of the structures [1]. While considering the existing structures located on the hill slopes, one of the most important parameters while designing the structure is the slope angle. The slope angle may vary from zero to 60°, the observation being made that the structures located on the steep slopes experiences more damage as compared to the

(a)   (b)
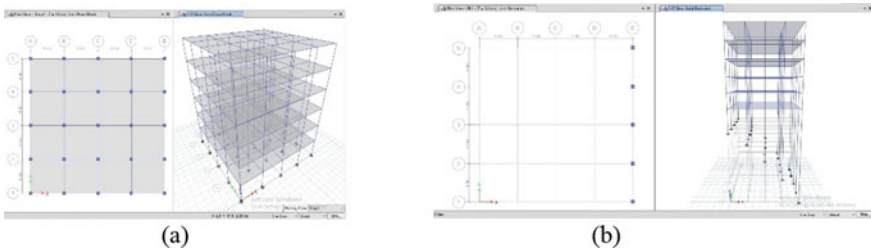
Fig. 1 Set – back configuration with zero and 15° slope angle
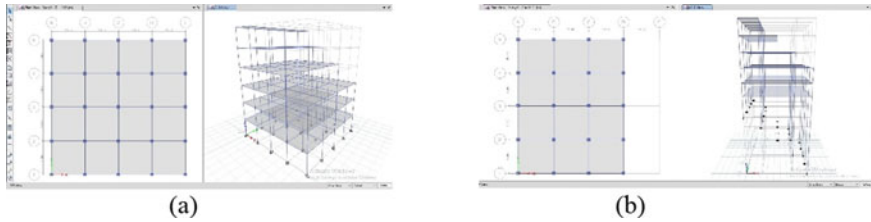
Fig. 2 Step – back configuration with zero and 15° slope angle

one which are locating on the flat ground [2]. Most of the research conducted on the determination of the behaviour of the structures located on the hill slopes uses different analytical methods such as SAP 2000, STAAD Pro and ETABS [3–5]. With the irregularities of the building typology on the hill slopes of set – back configuration and step – back configuration, the main criteria of the analysis of the structures to determine their seismic response is maximum storey displacement and maximum storey drift [6–9]. When the structure is being analysed to determine its building performance level under seismic analysis, plastic hinges are formed which thereby, determine the actual nature of the structure when experiences seismic activity. If the structure falls under the category of "severe damage", the same needs to be retrofitted. Retrofitting is a technique to re – gain the strength the existing structure by adding/ modifying one or all of the structural components of the affected building. Retrofitting can be done by various methods such as jacketing, bracing, replacing the existing structural member, etc. For the structures located on the hill slopes, the best retrofitting technique is bracing due to its load transferring mechanism [10, 11].

2 Methodology and Analysis

To conduct the seismic analysis of the existing structure on hill slope, one existing structure of set – back configuration and other step – back configuration is considered. For comparing the results, the slope to ground angle is kept constant as zero and 15°. The overall area of the structure is 256 km^2. The structures are G + 5 storey structure, with M 30 being the grade of concrete for beams and columns; and M 25 for slabs. Etabs is considered as analytical tool for the study.

Since the existing structures are being located on the hill slopes, as per the codal provisions of IS 1893: 2016 [12], the seismic zone is "Zone V" and the type of soil is considered as "Hard". Also, since the structure is a framed structure (SMRF), the Reduction Factor is taken as 5 and Importance Factor is 1. The first phase of the analysis considered the analysis of the structures under the basic types of loads including Dead Load, Live Load and SuperDead Load (special case of loading in ETABS which consists the load from floors, i.e., slab loads. The advanced phase of the analysis including the seismic analysis as per the criteria of Pushover Analysis, followed by formation of hinges in both prime structural members: beams and
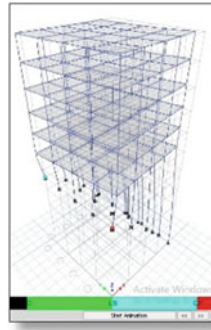
Fig. 3 Building performance level for 15° slope angle

columns. While doing the analysis, P – Delta was being performed by considering Mass Iteration Factor, value of which is being determined by considering the factor of 1.5 (DL) and 1.2 each (LL and SDL). The effect of pushover analysis was considered by considering the mass source, having safety factor of 1 (DL and SDL) and 0.25 (LL) [13].

After performing the analysis, the Building Performance Level of the structures considered had been determined by classifying it under the categories of LS (Life Safety), IO (Immediate Occupancy) and CP (Collapse Prevention). The structural elements fall under the category *"Above CP Level"* are of primary concern. For example, Fig. 3 represents Building Performance Level for the model considered for Set – Back Configuration for 15° sloping angle, having column members falling under the category of "Above CP Level"; which often termed as "unfit" elements; defined as those structural members which are worst affected under the action of seismic forces, and thus needs retrofitting.

These structurally "unfit" elements need to be re – strengthen and this study focused on the retrofitting these structures by providing different configurations of bracing. The different configuration used in this study is 1. Single Bracing (connection with upper beam – column junction), 2. Single Bracing (connection with lower beam – column junction) and 3. X – Bracing.

3 Results and Discussions

The two of the most important characteristics that are considered for understanding the behaviour of the structures under seismic action are 1. Maximum Storey Drift and 2. Maximum Storey Displacement. The structures are being analyzed and following results are obtained after performing Pushover Analysis (Table 1):

Table 1 Maximum storey displacement and maximum storey drift

Type of structure	Maximum displacement (X – Direction)	Maximum displacement (Y – Direction)	Maximum storey drift
0° Slope Angle (Set Back)	10 mm at Top Storey	31 mm at Top Storey	0.0003 at Storey 2
15° Slope Angle (Set Back)	38.23 mm at Top Storey	56.02 mm at Top Storey	0.006 at Storey 1
0° Slope Angle (Step Back)	25 mm at Top Storey	61 mm at Top Storey	0.002 at Storey 2
15° Slope Angle (Step Back)	34.35 mm at Top Storey	57.15 mm at Top Storey	0.0062 at Storey 1
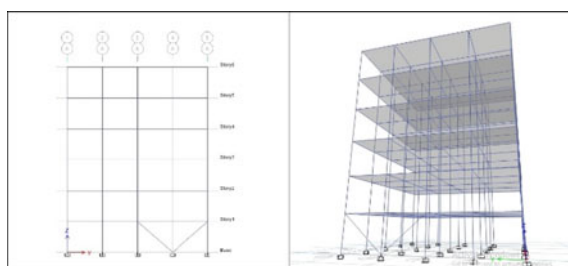
Fig. 4 Bracing connecting with bottom beam – column junction of structurally "Weak" column for 0° angle slope

The analysis showed that the maximum displacement in all the model configurations was observed at the top storey, whereas a different behaviour was observed in case of storey drift. The maximum drift was observed at storey level 1 in case of 15° slope angle and storey level 2 in case of 0° slope angle. After determining the *Building Performance Level,* it had been observed that two columns in 15° angle slope and 1 column in 0° angle slope were found to be "structurally weak" and thus needs to be retrofitted.

3.1 Retrofitting

The structurally unfit columns were retrofitted and four different types of bracing techniques are adopted. To perform the comparative analysis, the structural element of the bracing is kept constant as ISA 150 × 100 mm, with a thickness of 12 mm (Figs. 4, 5 and 6, Table 2).

The comparative results obtained can be summarized in the following table:
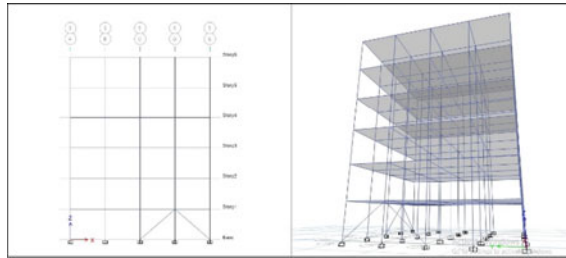
Fig. 5 Bracing connecting with top beam – column junction of structurally "Weak" column for 0° angle slope
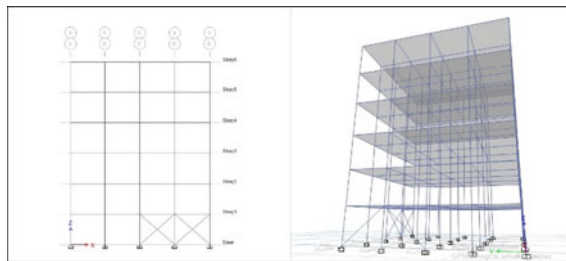
Fig. 6 X – Bracing with 0° angle slope

Table 2 Maximum percentage decrease after retrofitting of structural element

Type of structure	Decrease in maximum displacement (X – Direction)	Maximum displacement (Y – Direction)	Decrease in maximum storey drift
0° Slope Angle (Set Back)	52% with X - Bracing	47% with X - Bracing	34% with X – Bracing
15° Slope Angle (Set Back)	50% with Bracing connecting with top beam–column junction	45% with X - Bracing connecting with bottom beam–column junction	32% with X – Bracing
0° Slope Angle (Step Back)	45% with X - Bracing	38% with X – Bracing	32% with X – Bracing
15° Slope Angle (Step Back)	47% with Bracing connecting with top beam–column junction	44% with Bracing connecting with bottom beam–column junction	33% with X – Bracing

The result shows that the maximum decrease in both x and y direction for both the configurations in 0° Slope Angle was observed in X – Bracing, where as in case of 15°, maximum percentage was observed with Bracing connecting with top beam – column junction in x – direction and Bracing connecting with bottom beam – column junction for y – direction. The results for maximum storey drift was quite similar as in all the considered scenarios, maximum decrease was found in X – bracing.

4 Conclusion

After performing the Pushover Analysis, the following observations were recorded:
  For 0 – Degrees Slope:

- Maximum Storey Displacement (X – Direction) was observed as 25 mm at Top Storey in Step – Back Configuration and 10 mm at Top Storey in Set – Back Configuration.
- Maximum Storey Displacement (Y – Direction) was observed as 61 mm at Top Storey in Step – Back Configuration and 31 mm at Top Storey in Set – Back Configuration.
- Maximum Storey Drift was 0.0003 and 0.002 at Storey 2 for both Set and Step – Back Configuration respectively.

  For 15 – Degrees Slope:

- Maximum Storey Displacement (X – Direction) was observed as 34.35 mm at Top Storey in Step – Back Configuration and 38.23 mm at Top Storey in Set – Back Configuration.
- Maximum Storey Displacement (Y – Direction) was observed as 57.15 mm at Top Storey in Step – Back Configuration and 56.02 mm at Top Storey in Set – Back Configuration.
- Maximum Storey Drift was 0.006 and 0.0062 at Storey 2 for both Set and Step – Back Configuration respectively.

  After performing the retrofitting analysis, the following observations were made:

- For 0° Slope Angle for Set – Back configuration, decrease in maximum displacement in x and y direction was observed to be 52 and 47% with X – Bracing, with 34% reduction in storey drift.
- For 0° Slope Angle for Step – Back configuration, decrease in maximum displacement in x and y direction was observed to be 45 and 38% with X – Bracing, with 32% reduction in storey drift.
- For 15° Slope Angle for Set – Back configuration, decrease in maximum displacement in x and y direction was observed to be 50% and 45% with Bracing connecting with top beam – column junction and Bracing connecting with bottom beam – column junction respectively, with 32% reduction in storey drift.

- For 15° Slope Angle for Step – Back configuration, decrease in maximum displacement in x and y direction was observed to be 47% and 44% with Bracing connecting with top beam – column junction and Bracing connecting with bottom beam – column junction respectively, with 33% reduction in storey drift.

Thus, one can use X – Bracing system for structurally retrofit the structure with 0° Slope Angle and for 15° Slope Angle, both the bracing systems with Bracing connecting with top beam – column junction and Bracing connecting with bottom beam – column junction can be considered.

The analysis of the existing structures is of primary concern as they were not being constructed as per the revised codal provisions, which made them unsafe in times of seismic activity. After determining the structurally weak elements, the same must be re – strengthen.

References

1. Singh, Y., Gade, P.: Seismic behaviour of buildings located on slopes–an analytical study and some observations from Sikkim earthquake of 18 September 2011–15WCEE, LISBOA 2012
2. Kumar, A., et al.: Earthquake behavior of reinforced concrete framed buildings on hill slopes. In: International Symposium on New Technologies for Urban Safety of Mega Cities in Asia (USMCA 2013) Report No: IIIT/TR/2013/-1
3. Thombre, P., Makarande, S.G.: Seismic analysis of building resting on sloping ground. JETIR **3**(6) (2016). (ISSN-2349-5162)
4. Rajeswari, D., et al.: Analysis of multi store symmetrical building in zone-ii on flat and sloping ground up to failure by using ETABS. Int. J. Appl. Res. **3**(5), 575–580 (2017)
5. Rajavelu, K., Saravanan, K.: Seismic analysis of RC structure in hill slope area. Int. J. Res. Appl. Sci. Eng. Technol. (IJRASET) **5**(XI) (2017). ISSN: 2321-9653
6. Vinod, N., Swarup, A.: Study of seismic behaviour of multi-storied R.C.C. buildings resting on sloping ground and bracing system. IJARIIE **3**(4) (2017). ISSN(O)-2395-4396
7. Kavya, G.S., et al.: Seismic performance of step-back and step back- set back building resting on a hill slope. Int. Res. J. Eng. Technol. (IRJET) **05**(09) (2018). e-ISSN: 2395-0056
8. Desai, M., et al.: Free vibration and seismic analysis on sloping ground considering different structural system. J. Eng. Technol. **8**(1), 70–83 (2019). (ISSN. 0747-9964)
9. Surana, M., et al.: Analytical evaluation of damage probability matrices for hill-side RC buildings using different seismic intensity measures. Eng. Struct. **207**, 110254 (2020). (ISSN. 18737323)
10. Yaman, H., Pradeep, G.K.: Seismic assessment of a hospital building: a case study. In: IOP Conference Series: Earth and Environmental Science, vol. 796, p. 012006 (2021)
11. Zaidi, S.A., et al.: Study on the effects of seismic soil-structure interaction of concrete buildings resting on hill slopes. Mater. Today Proc. **43**, 2250–2254 (2021). Part 2, (ISSN. 22147853)
12. IS 1893-2016 (Part-1), Criteria for Earthquake resistant design of structures, General provisions and buildings, Bureau of Indian Standards, New Delhi 110002
13. Jammula, D., et al.: Seismic analysis of G + 9 framed structures made of reinforced concrete resting on hill slopes. Materials Today: Proceedings (ISSN. 22147853)–In Press

Finite Element Analysis of Steel Beam with Trapezoidal Corrugated Web

Niranjan Dilip Patil

Abstract Corrugated web beams in which the web is formed with corrugation such as sinusoidal or trapezoidal has been generally used in industrial buildings like warehouses and bridge girder construction. In steel structure applications, the web gives more resistance to the compressive stress and transmits shear in the beam while the flanges support the major external loads. Therefore, web is considered for nonlinear analysis study by comparing the parameters like thickness and shape. It will reduces the cost of materials without failure for the load-carrying capacity of the beam. In this paper an attempt is made to study the behavior of trapezoidal corrugated web beam (TCWB) under loading for different corrugation angles of web in I-steel sections. In order to simulate the structural behavior of the trapezoidal corrugated web beams, the model is developed by using the finite element analysis software ANSYS. The parameters consider in the study are change in web corrugation angles of 30° and 45°. The comparison has been made by comparing the load vs mid span deflection behaviour and stress distribution within the web of the beam.

Keywords Corrugated web beam · Corrugation angle · Non-linear analysis · ANSYS

1 Introduction

Industrial buildings, some commercial buildings like warehouses, some public buildings like stadiums, transport terminals, bridges of railway lines, various towers are constructed with steel materials. Now a days pre-engineered steel building is more popular in all countries. In a pre-engineered building, various components are manufactured in a factory and are erected at a site of construction by which building can be completed very quickly. In the recent years many advanced materials are to be introduced in steel structures. This steel structures have many advantages as

N. D. Patil (✉)
Mahatma Gandhi Missions College of Engineering and Technology, Kamothe, Navi Mumbai 410209, India
e-mail: niranjanpatil0@gmail.com

compare to other structures such as the better satisfaction with the flexible architectural, durability, strength, design, low inclusive cost and environmental protect as steel is manufacture to precise and uniform shapes. One of the developments in structural steel during the past few years has been the availability of corrugated web I-beams. The use of corrugated webs is a possible way of achieving adequate out-of-plane stiffness without using stiffeners. A steel structures is an assemblage of a group members or elements expected to carry their applied forces and transform them safely to the ground applied forces may be axial forces, bending or torsion or a combination of those and it depends on orientation of the member.

In many steel structures of beam-to-beam connection or beam to column connections the web is usually carry most of the compressive stress and transmits shear in the beam while flanges support the major external loads. Therefore, web is usually investigated by comparing the thickness and the shape. It can decrease the cost and materials without weakening the load-carrying capability of the beam. In this report, web is considered for nonlinear analysis study by comparing the parameters like thickness and shape. It will reduce the cost of materials without failure for the load-carrying capacity of the beam. There are various type of corrugated web were stated such as the horizontal corrugated web of one arc corrugation or two arcs corrugation and vertically corrugated web. In this study of vertically corrugated web beam, trapezoidal corrugated web beam studied over the ordinary plane web beams and this non-linear analysis, stress analysis results to develop the benchmark result.

The Corrugated beam provided with web opening throughout its translational web is mostly adopted where large web openings are provided throughout the web beams. In modern buildings, the application of large ducts and pipes made by I-shaped beams and girders of structural steel acquired in building structure may lead to unacceptably for large constructions which are in-depth between the story. The use of corrugated web beam with opening can be adopted when it makes ducting and services work much more adorable for steel structure. Despite of many usefulness, the introduction of opening throughout the web may reduce the strength and shear capacity of the beam if there is no proper design of such beams. The opening shape should depend on the shape of the duct present into the web such as normal plane web or triangular corrugation.

In vertical corrugated beam there are several types of profiles can be designed for various purposes and decorative with the same capability normal web beam can achieve. Trapezoidal and sinusoidal corrugations in web beams are generally used corrugated web beams in recent day steel constructions.

In the last 3 decades use of corrugated plates rapidly increased applications in structural engineering, civil engineering, in aerospace engineering, marine engineering and building construction industry.

In the period of 1960 to 1980 the trapezoidal corrugated web beam has been used for steel buildings and for highway bridges in Europe and Japan.

Generally trapezoidal corrugated web steel I-beam is buildup of two steel top and bottom flanges welded trapezoidal profiled corrugated web plate as shown in Fig. 1. The major components of trapezoidal corrugated steel beam are web and flanges can be made from different type of steel grade and size depending on design requirement
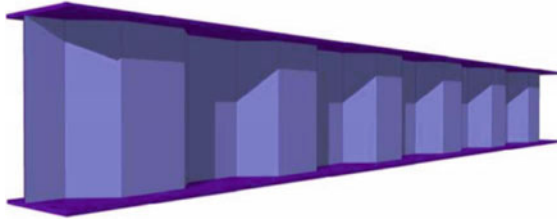
Fig. 1 Typical trapezoidal corrugated web beam
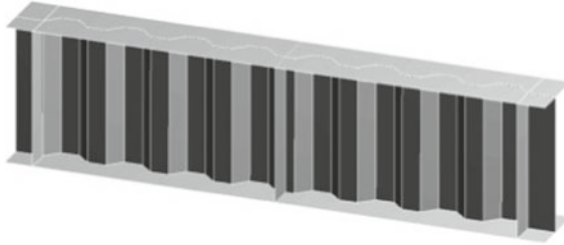
Fig. 2 Types of corrugated web beams

of steel structures. To avoid fatigue failure, two types of web corrugation profiles are adopted in web I-beams, which are the trapezoidal profile and sinusoidal profile as shown in Fig. 2 respectively. This trapezoidal corrugated beam gives more shear stability and better fatigue resistance as comparing to normal plane web beams. It gives better aesthetics and architectural view due to the corrugated thin plates presents in its web. Such types of Trapezoidal corrugated web beam also eliminate the use of stiffeners for web stability which leads to cost reduction in fabrication of steel beams. In this study the behaviors of trapezoidal corrugated steel web beam investigated to ensure the structural safety with structural dimensions of beams.

When compared with normal plane web beam this corrugated steel web I-beam gives 9 to 13% less weight than current traditionally stiffened girders with plane webs with stiffeners. The thinner web plates provided into the corrugated web beam eliminate the stiffeners which are mostly adopted in normal flat webs for I-beams.

1.1 Beams with Corrugated Webs

This beams with corrugated web beams can be easily fabricated and erected by the process of welding. The different materials of thin plates are to be used for flange plate and corrugation thinner web plate.

The web of the girders can be corrugated using different profiles like rectangular corrugated web, trapezoidally corrugated web, sinusoidal corrugated web, semicircular corrugated web and cell formed corrugated web. The aesthetics of the different configurations is totally different, but also the fabrication, the mechanical behaviour and the costs of the different types have to be taken in account when making a choice for one of them. The thinner trapezoidally corrugated web beam section provides a higher resistance against bending and higher load carrying capacity besides more cost economical when compared with other types. Extensive research has been done on the performance of hot-rolled steel beams with trapezoidally corrugated web. The research on cold-formed steel beams with corrugated web is limited. Hence, the present study deals with the behaviour of cold-formed steel beams with trapezoidally corrugated web [5,13].

1.2 Advantages of Trapezoidal Corrugated Web Beam (TCWB)

- This trapezoidal corrugated web beam gives better stability for local buckling as compare to normal plane web
- Such type of TCWB results in less cost and higher load carrying capacity.
- The high strength-to-weight ratio is achieved in trapezoidal corrugated web steel beam.
- The erection cost of trapezoidal corrugated web beam is less in economy also it gives more resistance for bending about the weak axis in respective beam.

1.3 Problem Statement

The aims of this report are to study analytical response of trapezoidal corrugated webs from the prebuckling stage until ultimate failure in ANSYS code of simulation, to review existing analytical models for the estimation of various characteristics of trapezoidal corrugated web beams under the loading conditions and verify their performance when compared to the new test results. After the analytical study the preferred beam can be considered for better stability of steel structure.

- By considering the previous literature published for the such analytical models in different code for its strength and capacity, the investigation is necessary to examine closed behaviors of trapezoidal corrugated steel beam.
- To carry out the modelling in ANSYS code for the different parameters selected as web thickness and shape.
- To carry out Nonlinear finite element analysis using ANSYS to study the various stress distribution occurs at the corrugated web panels on various loading stages for selected geometry.

- To conclude the analytical results comparing the Trapezoidal corrugated web beam with normal plane web beam.

1.4 Objectives

The objectives of this studies are:

- To adopt the geometry of selected design of steel beam.
- To perform linear/non-linear buckling analysis by using ANSYS software.
- In FE analysis variables/parameters studied are load deflection behaviour/ von misses stresses distribution.

1.5 Motivation for the Study

Research on the behaviour of corrugated steel beams spans are of approximately fifty years. Even today, in spite of many investigations of last three decades one cannot suggest the better suitability of steel beam for various depth of beams. The developments in steel industry are rapidly changes the way in which traditional structures are designed and built and hence make possible the economic use of materials.

As India is the third-largest steel producer in the world. In 2015, India produced 91.46 million tons (MT) of finished steel thereof steel industry growth is decreased in recent years. In construction industry traditional sections and materials are used so it very needful to study various steel designs that can replace the traditional one which can be used in various sectors like infrastructure, automobile, industries etc.

2 Previous Investigations and Literature Review

Current chapter is focused on different studies carried out by different researchers on various aspects of trapezoidal corrugated web beam, Scope of studies, methodology adopted and their findings are discussed in detail.

C.L. Chan, Y.A. Khalid, B.B. Sahari, A.M.S. Hamouda (2001) The paper published in Journal of Constructional Steel Research entitled with "Finite element analysis of corrugated web beams under bending" shows the different sections of corrugated web beam and its FEA solution. Also studied the effect of web corrugation on the bending capacity of the beam using finite element method. Beams with plain web, horizontally corrugated web and vertically corrugated web were studied. In this research it is concluded that corrugated web beams with larger corrugation radius, could sustain higher bending moment and there is 10.6% reduction in weight ratio when compared with the beam with normal plane web. Also, the other various

profiles are also studied for comparing purposes to adopt the beams in better strength in buckling [1].

Richard Sause, Hassan H. Abbas, Wagdy G. Wassef, Robert G. Driver, and Mohamed Elgaaly (2003) Report entitled with "Corrugated Web Girder Shape and Strength Criteria" submitted to Department of Transportation describes work conducted to investigate design criteria for the shear and flexural strength of corrugated web in girders, and the recommendation is made for the corrugation shape for the girders on the demonstration bridge. The report summarizes prior shear strength theory and test results for corrugated web girders worked in experimental study [10].

Y.A. Khalid, C.L. Chan, B.B. Sahari, A.M.S. Hamouda (2004) The paper entitled with "Bending behaviour of corrugated web beams" gives the idea about a non-linear analysis performed. The effect of web corrugation on the beam's strength is presented in this paper. The LUSAS package is adopted for nonlinear analysis done on various specimen considered for experimental as well as analytical study. It was concluded that the vertical-corrugated web beam could carry between 13.3 and 32.8% higher moment compared to the plain and horizontal-corrugated web beams. It was also established that the web corrugation in the vertical direction (along the length) gives higher bending capacity compared to the horizontal direction (in the cross-section plane) and also the beam weight could be reduced by 13.6% by using vertically corrugated web with the maximum size of corrugation radius [2].

Ezzeldin Yazeed Sayed-Ahmed (2007) The paper entitled with "Design aspects of steel I-girders with corrugated steel web" shows the numerical and analytical studies are performed to establish the buckling modes of the corrugated web, verify the validity of the proposed equation and establish the post-buckling strength of corrugated web girders.The hot rolled steel corrugated web beam are fabricated in this study. The numerical model was taken for study to determine the critical moment causing lateral instability for corrugated web girders compared to normal plane web. It was concluded that the resistance to lateral- torsional buckling of such girders is 12 to 37% higher than that of plate girders with plain web [11].

Fatimah Denan, Mohd. Hanim Osman and Sariffuddin Saad (2010) the paper entitled with "The study of lateral torsional buckling behaviour of beam with trapezoid web steel section by experimental and finite element analysis" presents the experimental and numerical study on lateral torsional buckling behaviour of steel section with trapezoid web. The experimental and numerical study on the lateral-torsional buckling behaviour of steel section with trapezoidal web and plan web are investigated in this literature. Comparison was made with conventional beams with flat web. The result showed that corrugation thickness affects on the resistance to lateral- torsional buckling and its shear capacity [6].

Richard Sause, Thomas N. Braxtan (2010) The paper entitled with "shear strength of trapezoidal corrugated steel webs" gives brief study on the shear strength of trapezoidal corrugated steel web beam for different parameters of depth and shape. The formula for calculating the shear strength are summarized in this study. It concludes that the corrugated webs are provided to increase the shear stability of the steel webs of such beams and girders and also elimination of the transverse stiffeners can be done [14].

Chung Jia Jiunn (2010) The thesis entitled with "Finite Element Analysis of Corrugated Web Beam with openings", gives the brief idea about corrugated web beam. They also stated that in various steel construction industry, the web resist most of the compressive stress and transmits shear in the beam while flanges support the major external loads. Therefore, web is considered for the various investigations for stress distribution by comparing the thickness and the shape [3].

M.F. Hassanein, O.F. Kharoob (2013) The paper entitled with "Behaviour of bridge girders with corrugated webs: (II) Shear strength and design" The current paper gives more details about the shear strength of bridge girders which are made by corrugated webs (BGCWs) where the realistic initial imperfection amplitudes are studied. The ABAQUS software package is used to construct a nonlinear finite element analysis which includes geometric and material nonlinearities for full-scale Bridge girders of corrugated webs failing by shear [12].

B. Jáger, L. Dunai, B. Kövesdi (2016) The paper entitled with "Experimental investigation of the M-V-F interaction behaviour of girders with trapezoidally corrugated web" shows the steel girder can be subjected by the combination of bending (M), shear (V) and transverse forces (F) which result in a complex stress field and a coupled instability phenomenon may occur [4].

Moussa Leblouba, M. Talha Junaid, Samer Barakat, Salah Altoubat, Mohamed Maalej (2017) The paper entitled with "Shear buckling and stress distribution in trapezoidal web corrugated steel beams" This paper presents the results of laboratory tests on a series of stocky trapezoidal corrugated web steel beams to investigate their behaviour under shear loading. Due to their lightweight and superior load carrying capacity, corrugated web steel beams (CWSBs) have gained popularity in the last few decades. CWSBs are known to fail at much higher loads compared to stiffened flat web beams. To understand their shear response, a series of three-point load tests were performed on five shear-critical trapezoidal corrugated web beams [9].

R. Divahar, P. S. Joanna (2018) The paper entitled with Joanna "Numerical simulation and experimental investigation on static behavior of cold formed steel beam with trapezoidally corrugated web by varying depth-thickness ratio" gives mid-span deflection result on trapezoidal corrugated web beam with various aspects [15].

Literature Gap

Many researchers done the study on trapezoidal corrugated web beam, as listing out the major gaps in overall literature is about the corrugation angle effect on trapezoidal corrugated web beam which affect on the strength of the beam and in its stress distribution. Also, by changing the depth of web of beam with change in corrugation angle need to study in structural behaviour of trapezoidal corrugated web beam.

3 Parametric Study—Parameters

In order to optimize the various design parameters for I-section with trapezoidal corrugated web, parametric study was carried out varying various parameters like height of the web, width of the flange, corrugation angle, aspect ratio of the web panel and length.

In order to fix the range of parameter, parameters were initially varied in wide range and the maximum ranges for which the results are optimum are obtained.

The various parameters need to studied were:

1. Aspect ratio.
2. Angle of Corrugation.
3. h_w/t_w Ratio.
4. Web stiffener

The parametric study of trapezoidal corrugated web beam includes various geometrical properties of the section as shown in Fig. 3 (Fig. 4).

The selected parameters for the study are as below.
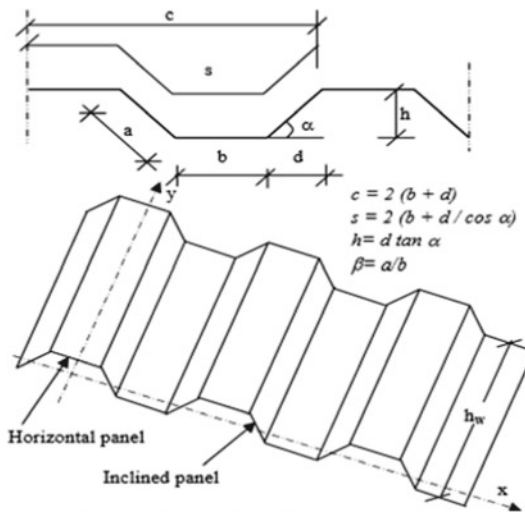
Fig. 3 Trapezoidal profile of corrugated web [3]
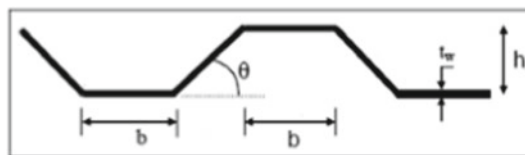
Fig. 4 Geometrical nominations of trapezoidal web [3]

1. Web thickness (t_w) – 4 mm.
2. Corrugation angle (θ) – 0, 30°, 45°.
3. Corrugation plate length (b) – 50 mm.
4. Corrugation web width (h) – 50, 35.35 mm.
5. Corrugation web depth (h_w) – 250, 300 mm.

4 Finite Element Analysis and Modelling

In the previous analytical studies, the model of beam with flanges and different size and shape of web is adopted henceforth the stiffened beam and unstiffened beam is to be taken for the study of shear behavior of webs in trapezoidal corrugated web beams. However, it is usually difficult to make pure trapezoidal corrugated steel web which give exactly behaviors for its shear when such a numerical model is used. Thus, in this paper, only a pure trapezoidal corrugated steel web is modeled or different parameters like different shape of web profile with corrugation angle and stiffeners are provided with simple support boundary condition for the conservative consideration. Figure 1 shows a finite element model of the trapezoidal corrugated steel web based on the general Finite Element program ANSYS 12.0 package [7]. In this model, the out-of-plane freedoms of all the edge nodes are constrained as shown in Fig. 5.

4.1 Element Type

The element type used to generate the model, because of its features, is named by the program SHELL 181 [16].

SHELL 181 is suitable for analysing thin to moderately-thick shell structures. It is a 4-node element with six degrees of freedom at each node: translations in the x, y, and z directions, and rotations about the x, y, and z axes.
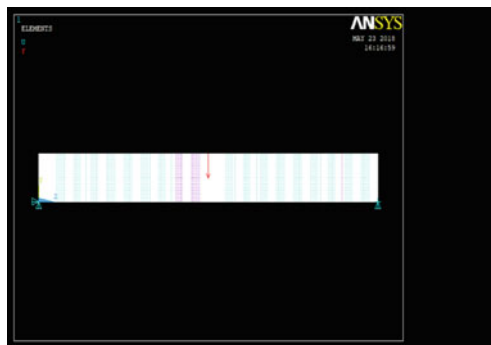
Fig. 5 Finite element model

4.2 Material Properties

For the selection of material, the same steel properties are adopted for the both web and flange plates whereas in this steel with a yield strength of 250 N/mm^2. The properties are defined as temperature independent, and the behaviour of the material is set as multilinear isotropic, with strain hardening.

The set of properties are as the following:

- Yield stress: 250 N/m^2
- Modulus of elasticity €: 2.1×10^5 N/mm^2
- Tangent modulus (G): 5% of modulus of elasticity $= 5000$
- Poisson's ratio: 0.3

4.3 Geometry

In the selection of geometry of trapezoidal section modelling is done using keypoints. The keypoints are taken in active coordinate system in form of X, Y, Z plane. Then keypoints are joined by straight line so as to form trapezoidal section. Areas are created by selecting lines for the web as well as flanges respectively. Meshing is done by selecting the same length of lines and dividing the lines in number of elements. By using mesh tool, the areas are meshed (Fig. 6).

5 Result and Discussion

This chapter presents the analytical results on the structural behaviour of steel beams with plain web, trapezoidal corrugated web with various aspects. Data presented include the load versus deflection curves, shear stress distribution; von misses stress
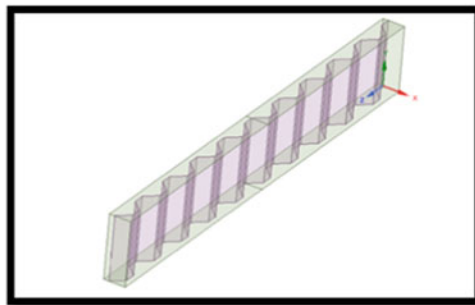
Fig. 6 Geometry of trapezoidal section

distribution. Also, the comparative study is done with web stiffener and web without web stiffener.

5.1 Mid Span Deflection Behaviour Using FEA Models

The Mid span deflection is the important factor to evaluate the behaviour of the simply supported beams. Loads were applied at mid-point distance from the supports at a uniform rate till the ultimate failure of the specimens occurred. The mid span deflection is to be taken as the displacement of span along y direction after applying the load of 400 KN on both plain web beam and trapezoidal corrugated web beam with 45° and 30° corrugation angles. Below Figs. 7, 8, 9 and 10 shows the displacement of both plain web beam and trapezoidal corrugated web beam with 45° and 30° corrugation angles with same loading condition. The results are considered with beam with web stiffener and without web stiffener for the different depth of 250 and 300 mm respectively.

5.1.1 Steel Beams with Web Stiffener Provided Specimens with depth = 250 mm

The results of beams having the depth of 250 mm with web stiffener provided are shown in Fig. 7. They are classified according to corrugation angle of plain web (i.e. 0°), trapezoidal corrugated web (i.e. 45° and 30°). The analytical mid span deflection of steel beams with plain webs and trapezoidal corrugated webs are shown in Fig. 7(a)–(c). The specimens with Plain web PWB 0° failed at load step of 58 with a central deflection of 49.524 mm. The other specimens TCWB 30° and TCWB 45° failed at load step of 30 and 31 with the corresponding average deflections of 6.46 and 4.471 mm respectively. It is observed that the beam with 45° corrugated webs has less deflection and higher load carrying capacity when compared with all other specimens.

Specimens with depth = 300 mm
The results of beams having the depth of 300 mm with web stiffener provided are shown in below Fig. 8(a)–(c). They are classified according to corrugation angle of plain web (i.e. 0°), Trapezoidal corrugated web (i.e. 45° and 30°). The analytical mid span deflection of steel beams with plain webs and corrugated webs are shown in Fig. 8(a)–(c). The specimens with Plain web PWB 0° failed at load step of 74 with a central deflection of 46.659 mm. The other specimens TCWB 30° and TCWB 45° failed at load step of 37 with the corresponding average deflections of 4.246 and 3.65 mm respectively. It is observed that the beam with 45° corrugated webs has less deflection and higher load carrying capacity when compared with all other specimens.

a) Plain web θ = 0⁰

b) TCWB θ = 30⁰

c) TCWB θ = 45⁰
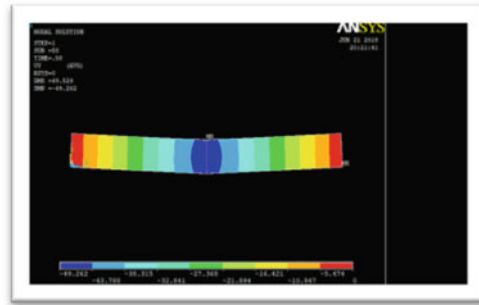
Fig. 7 a–c Mid Span deflection behaviour with web stiffener (D = 250 mm)

5.1.2 Steel Beams Without Web Stiffener Provided Specimens with depth = 250 mm

The results of beams having depth of 250 mm without web stiffener provided are shown in below Fig. 9(a)–(c). They are classified according to corrugation angle of plain web (i.e. 0°), Trapezoidal corrugated web (i.e. 45° and 30°). The analytical mid span deflection of steel beams with plain webs and corrugated webs are shown in Fig. 9(a)–(c). The specimens with Plain web PWB 0° failed at a central deflection

a) Plain web θ = 0^0

b) TCWB θ = 30^0
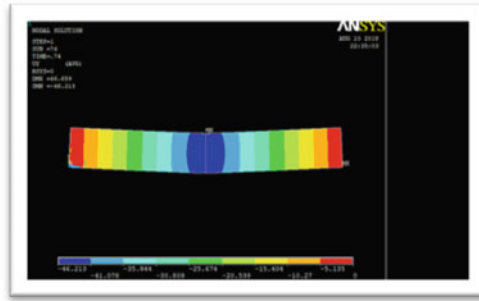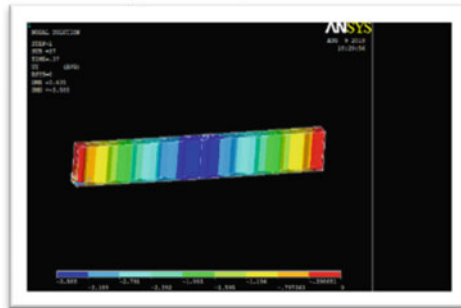
c) TCWB θ = 45^0

Fig. 8 a–c Mid Span deflection behaviour with web stiffener (D = 300 mm)

of 21.89 mm. The other specimens TCWB 30° and TCWB 45° failed at average deflections of 9.73 and 10.49 mm respectively. It is observed that the beam with 45° corrugated webs has less deflection and higher load carrying capacity when compared with all other specimens.

Specimens with depth = 300 mm

The results of beams having depth of 300 mm without web stiffener provided are shown in below Fig. 10(a)–(c). They are classified according to corrugation angle of

a) Plain web θ = 0⁰

b) TCWB θ = 30⁰

c) TCWB θ = 45⁰
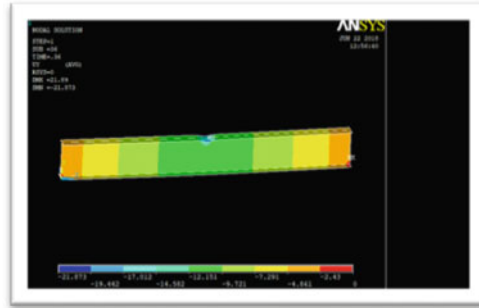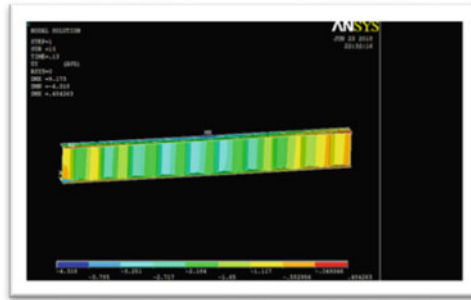
Fig. 9 a–c Mid span deflection behaviour without web stiffener (D = 250 mm)

plain web (i.e. 0°), Trapezoidal corrugated web (i.e. 45° and 30°). The analytical mid span deflection of steel beams with plain webs and corrugated webs are shown in Fig. 10(a)–(c). The specimens with Plain web PWB 0° failed at a central deflection of 13.54 mm. The other specimens TCWB 30° and TCWB 45° failed at average deflections of 12.45 and 10.48 mm respectively. It is observed that the beam with 45° corrugated webs has less deflection and higher load carrying capacity when compared with all other specimens.

a) Plain web θ = 0⁰

b) TCWB θ = 30⁰

c) TCWB θ = 45⁰
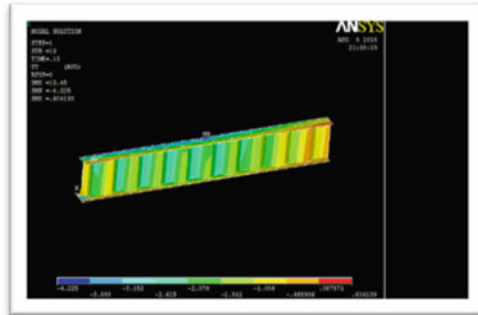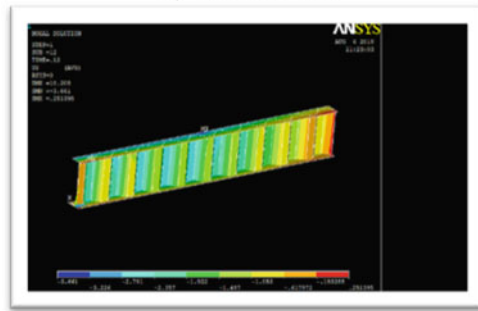
Fig. 10 a–c Mid span deflection behaviour without web stiffener (D = 300 mm)

5.2 Shear Stress Distribution Using FEA Models

Shear stress distribution is shown in below Figs. 11, 12, 13 and 14 with the same loading and boundary conditions. As result showed the shear stress distribution is less in the trapezoidal corrugated web beam compared to the plain web. Figures 11, 12, 13 and 14 shows the distribution of shear stress along the beam's length at different loading stages. Prior to buckling, the shear stress is uniformly distributed throughout the web and it increases linearly until buckling takes places [13]. At the onset of

buckling, the shear stress reaches its maximum values which are shown in Figs. 11, 12, 13 and 14. The shear stress distribution is considered with beam with web stiffener and without web stiffener for the different depth of 250 and 300 mm respectively.

a) Plain web θ = 0⁰

b) TCWB θ = 30⁰

c) TCWB θ = 45⁰

Fig. 11 a–c Shear stress distribution behaviour with web stiffener (D = 250 mm)

a) Plain web θ = 0⁰

b) TCWB θ = 30⁰

c) TCWB θ = 45⁰
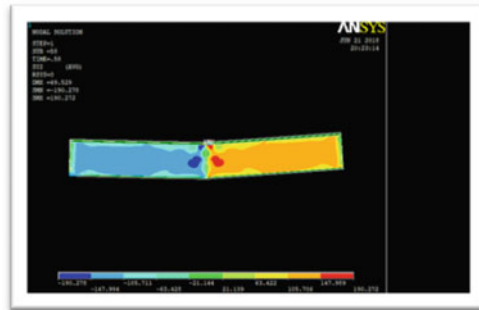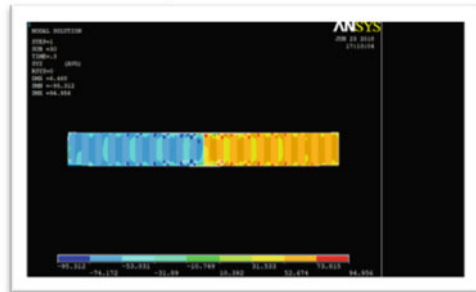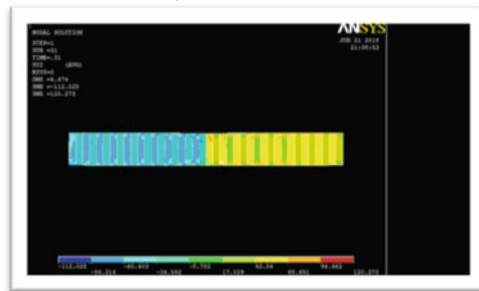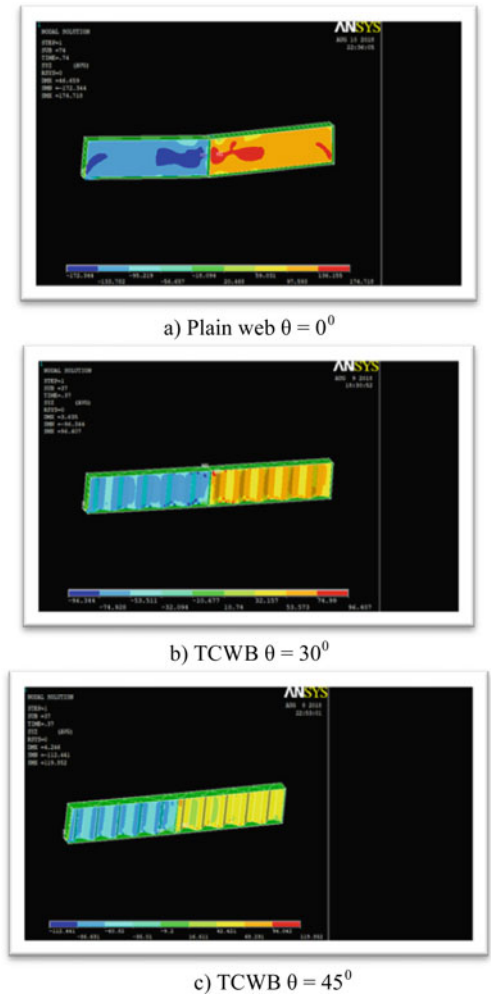
Fig. 12 **a–c** Shear stress distribution behaviour with web stiffener (D = 300 mm)

5.2.1 Steel Beams with Web Stiffener Provided Specimens with depth = 250 mm

The results of beams having depth of 250 mm with web stiffener provided are shown in below Fig. 11(a)–(c). They are classified according to corrugation angle of plain web (i.e. 0°), Trapezoidal corrugated web (i.e. 45° and 30°). The analytical shear stress distribution of steel beams with plain webs and corrugated webs are shown in Fig. 11(a)–(c). The specimens with Plain web PWB 0° shows the maximum shear stress distribution of 190.278 mm displacement. The other specimens TCWB 30° and TCWB 45° shows the maximum shear stress distribution with the corresponding

a) Plain web θ = 0⁰

b) TCWB θ = 30⁰

c) TCWB θ = 45⁰
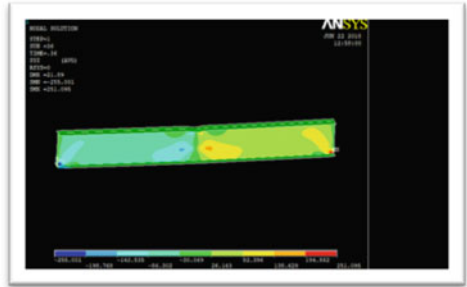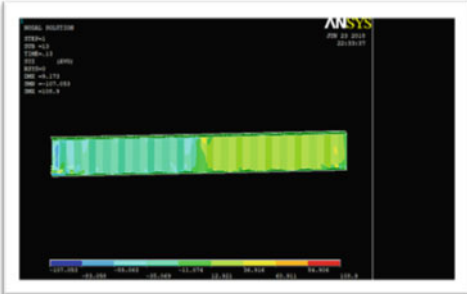
Fig. 13 a–c Shear stress distribution behaviour without web stiffener (D = 250 mm)

average deflections of 94.96 and 120.273 mm respectively. It is observed that the beam with 45° corrugated webs has less maximum shear stress distribution with corresponding load carrying capacity when compared with all other specimens.

Specimens with depth = 300 mm

The results of beams having depth of 300 mm with web stiffener provided are shown in below Fig. 12(a)–(c). They are classified according to corrugation angle of plain web (i.e. 0°), Trapezoidal corrugated web (i.e. 45° and 30°). The analytical shear stress distribution of steel beams with plain webs and corrugated webs are shown in Fig. 12(a)–(c). The specimens with Plain web PWB 0° shows the maximum shear
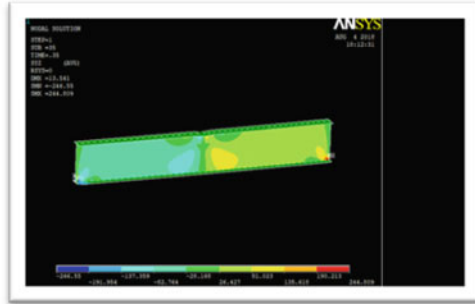
a) Plain web $\theta = 0^0$
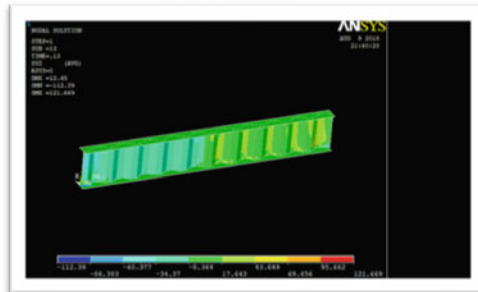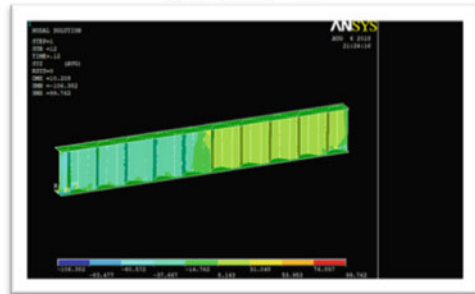
b) TCWB $\theta = 30^0$

c) TCWB $\theta = 45^0$

Fig. 14 a–c Shear stress distribution behaviour without web stiffener (D = 300 mm)

stress distribution of 174.718 mm displacement. The other specimens TCWB 30° and TCWB 45° shows the maximum shear stress distribution with the corresponding average displacement of 96.344 and 119.52 mm respectively. It is observed that the beam with 45° corrugated webs has less maximum shear stress distribution with corresponding load carrying capacity when compared with all other specimens.

5.2.2 Steel Beams Without Web Stiffener Provided Specimens with depth = 250 mm

The results of beams having depth of 250 mm without web stiffener provided are shown in below Fig. 13(a)–(c). They are classified according to corrugation angle of plain web (i.e. 0°), Trapezoidal corrugated web (i.e. 45° and 30°). The analytical shear stress distribution of steel beams with plain webs and corrugated webs are shown in Fig. 13(a)–(c). The specimens with Plain web PWB 0° shows the maximum shear stress distribution of 255.01 mm displacement. The other specimens TCWB 30° and TCWB 45° shows the maximum shear stress distribution with the corresponding average deflections of 109.873 and 109.05 mm respectively. It is observed that the beam with 45° corrugated webs has less maximum shear stress distribution with corresponding load carrying capacity when compared with all other specimens.

Specimens with depth = 300 mm

The results of beams having depth of 300 mm without web stiffener provided are shown in below Fig. 14(a)–(c). They are classified according to corrugation angle of plain web (i.e. 0°), Trapezoidal corrugated web (i.e. 45° and 30°). The analytical shear stress distribution of steel beams with plain webs and corrugated webs are shown in Fig. 14(a)–(c). The specimens with Plain web PWB 0° shows the maximum shear stress distribution of 244.809 mm displacement. The other specimens TCWB 30° and TCWB 45° shows the maximum shear stress distribution with the corresponding average deflections of 121.669 and 106.382 mm respectively. It is observed that the beam with 45° corrugated webs has less maximum shear stress distribution with corresponding load carrying capacity when compared with all other specimens.

5.3 Von Misses Stress Distribution Using FEA Models

Von misses stress distribution is shown in below Figs. 15, 16, 17 and 18 for the same loading and boundary condition. Von misses stress is a yield criterion for the failure of beam which is also known as maximum distortion energy criteria suggest that yielding of ductile material begins when the second deviatoric stress invariant reaches its critical value. Trapezoidal corrugated web gives better von misses stress distribution in the web which conclude that the web of trapezoidal corrugated web has more strength in web compared to plain web [8]. The von misses stress distribution is considered with beam with web stiffener and without web stiffener for the different depth of 250 and 300 mm respectively.

a) Plain web θ = 0⁰

b) TCWB θ = 30⁰

c) TCWB θ = 45⁰
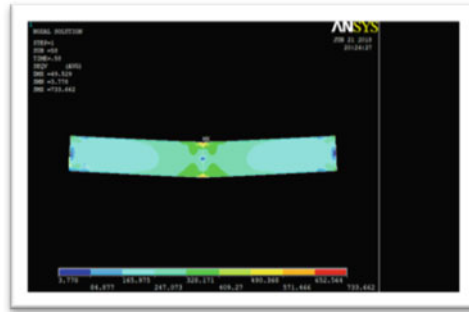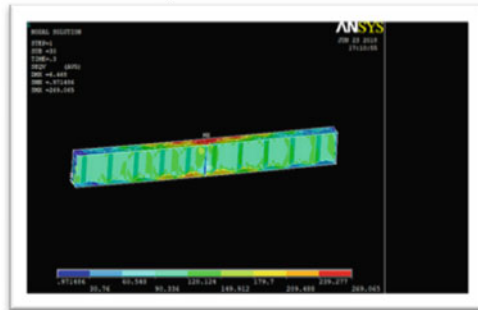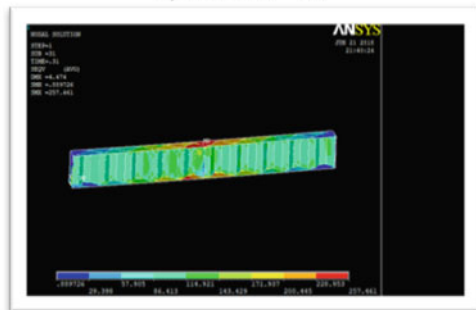
Fig. 15 a–c Von misses stress distribution behaviour with web stiffener (D = 250 mm)

5.3.1 Steel Beams with Web Stiffener Provided Specimens with depth = 250 mm

The results of beams having the depth of 250 mm with web stiffener provided are shown in below Fig. 15(a)–(c). They are classified according to corrugation angle of plain web (i.e. 0°), Trapezoidal corrugated web (i.e. 45° and 30°). The analytical von misses stress distribution of steel beams with plain webs and corrugated webs are shown in Fig. 15(a)–(c). The specimens with Plain web PWB 0° shows the maximum
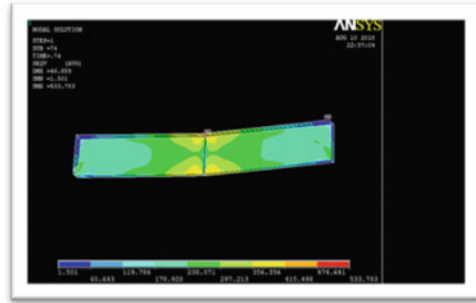
a) Plain web $\theta = 0^0$
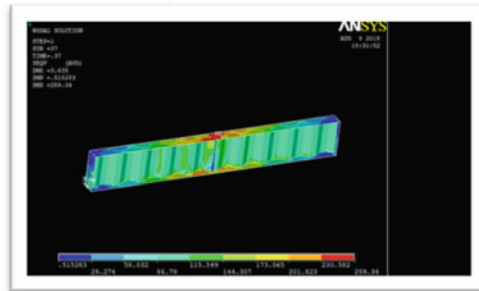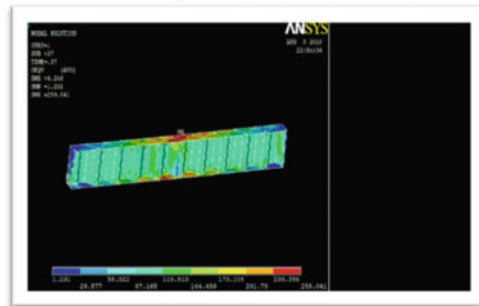
b) TCWB $\theta = 30^0$

c) TCWB $\theta = 45^0$

Fig. 16 a–c Von misses stress distribution behaviour with web stiffener (D = 300 mm)

von misses stress distribution of 733.64 N/mm². The other specimens TCWB 30° and TCWB 45° shows the maximum von misses stress distribution with the corresponding average distribution of 269.45 N/mm² and 257.46 N/mm² respectively. It is observed that the beam with 45° corrugated webs has less maximum shear stress distribution with corresponding load carrying capacity when compared with all other specimens.
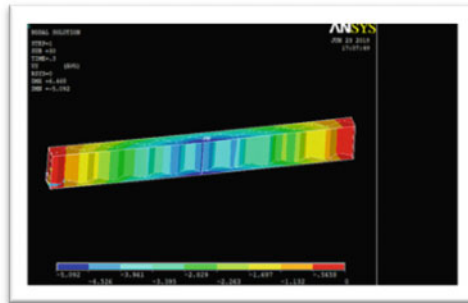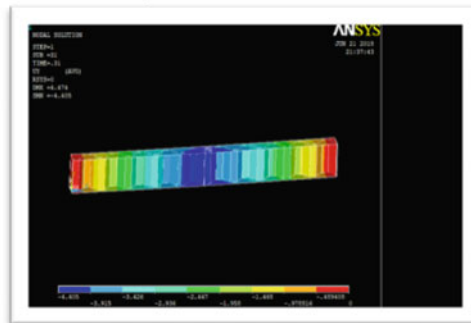
Specimens with depth = 300 mm

The results of beams having the depth of 300 mm with web stiffener provided are shown in below Fig. 16(a)–(c). They are classified according to corrugation angle of plain web (i.e. 0°), Trapezoidal corrugated web (i.e. 45° and 30°). The analytical von

a) Plain web θ = 0⁰

b) TCWB θ = 30⁰

c) TCWB θ = 45⁰
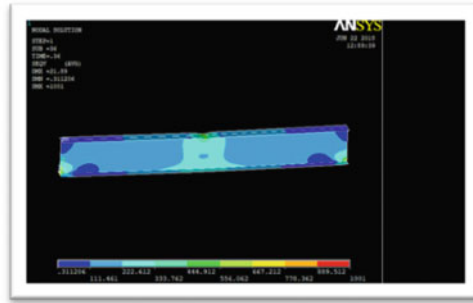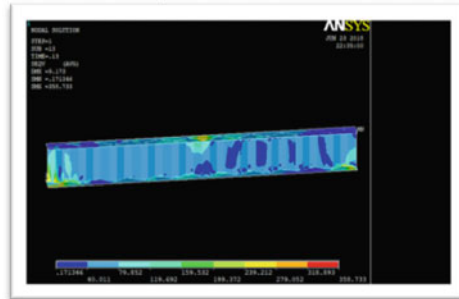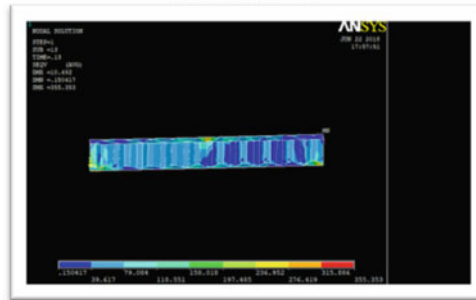
Fig. 17 **a–c** Von misses stress distribution behaviour without web stiffener (D = 250 mm)

misses stress distribution of steel beams with plain webs and corrugated webs are shown in Fig. 16(a)–(c). The specimens with Plain web PWB 0° shows the maximum von misses stress distribution of 533.783 N/mm². The other specimens TCWB 30° and TCWB 45° shows the maximum von misses stress distribution with the corresponding average distribution of 259.345 N/mm² and 259.041 N/mm² respectively. It is observed that the beam with 45° corrugated webs has less maximum shear stress distribution with corresponding load carrying capacity when compared with all other specimens.
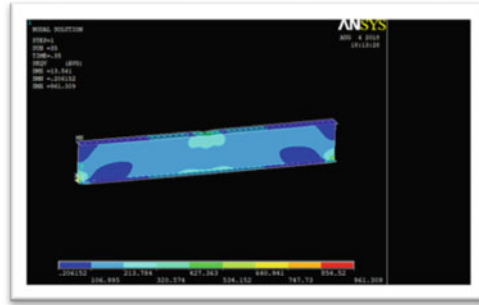
a) Plain web $\theta = 0^0$
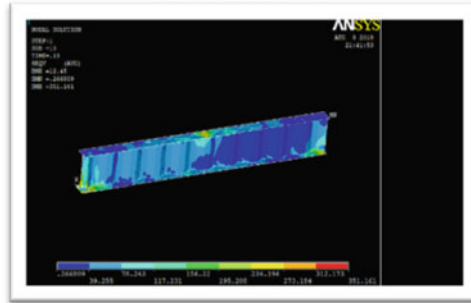
b) TCWB $\theta = 30^0$
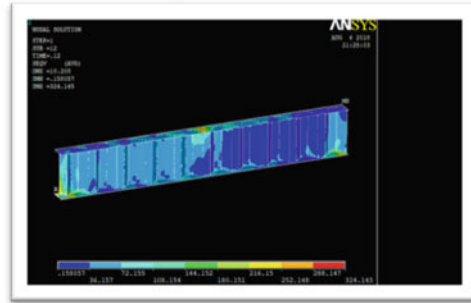
c) TCWB $\theta = 45^0$

Fig. 18 a–c Von misses stress distribution behaviour without web stiffener (D = 300 mm)

5.3.2 Steel Beams Without Web Stiffener Provided Specimens with Depth = 250 mm

The results of beams without web stiffener provided are shown in below Fig. 17(a)–(c). They are classified according to corrugation angle of plain web (i.e. 0°), Trapezoidal corrugated web (i.e. 45° and 30°). The analytical von misses stress distribution of steel beams with plain webs and corrugated webs are shown in Fig. 17(a)–(c). The specimens with Plain web PWB 0° shows the maximum von misses stress distribution of 1001 N/mm². The other specimens TCWB 30° and TCWB 45° shows the

maximum von misses stress distribution with the corresponding average distribution of 358.73 N/mm^2 and 355.35 N/mm^2 respectively. It is observed that the beam with 45° corrugated webs has less maximum shear stress distribution with corresponding load carrying capacity when compared with all other specimens.

Specimens with depth = 300 mm

The results of beams without web stiffener provided are shown in below Fig. 18(a)–(c). They are classified according to corrugation angle of plain web (i.e. 0°), Trapezoidal corrugated web (i.e. 45° and 30°). The analytical von misses stress distribution of steel beams with plain webs and corrugated webs are shown in Fig. 18(a)–(c). The specimens with Plain web PWB 0° shows the maximum von misses stress distribution of 961.309 N/mm^2. The other specimens TCWB 30° and TCWB 45° shows the maximum von misses stress distribution with the corresponding average distribution of 351.161 N/mm^2 and 324.145 N/mm^2 respectively. It is observed that the beam with 45° corrugated webs has less maximum shear stress distribution with corresponding load carrying capacity when compared with all other specimens.

5.4 Load Deflection Curve

The Load–deflection curve is the important factor to evaluate the behaviour of the simply supported beams. Loads were applied at central distance from the supports at a uniform rate till the ultimate failure of the specimens occurred. Below Figs. 19, 20, 21 and 22 shows the comparison of the load deflection curves obtained using ANSYS for steel beams with 250 and 300 mm depth of plain webs, trapezoidal corrugated web with 45 and 30° corrugation angle. The load deflection curve is to be taken at the displacement of span along y direction after applying the load of 400 KN on both plain web and trapezoidal corrugated web with 45 and 30° corrugation angles. The results are considered with beam with web stiffener and without web stiffener for the depth of 250 and 300 mm respectively.

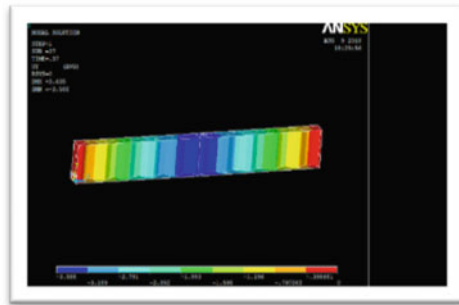### 5.4.1 Steel Beams with Web Stiffener Provided Specimens with depth = 250 mm

The results of beams having depth of 250 mm with web stiffener provided are shown in below Fig. 19(a)–(c). They are classified according to corrugation angle of plain web (i.e. 0°), Trapezoidal corrugated web (i.e. 45° and 30°). The analytical load–deflection curve of steel beams with plain webs and corrugated webs are shown in Fig. 19(a)–(c). The specimens with Plain web PWB 0° failed at load of 232 kN with a central deflection of 48.2478 mm. The other specimens TCWB 30° and TCWB 45° failed at same load of 236 kN with the corresponding average deflections of 44.066 and 44.051 mm respectively. It is observed that the beam with 45° corrugated webs

a) Plain web θ = 0⁰

b) TCWB θ = 30⁰

c) TCWB θ = 45⁰
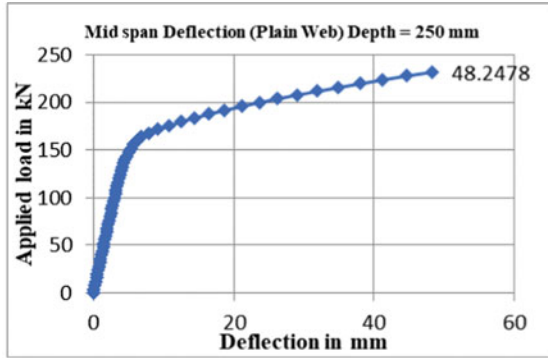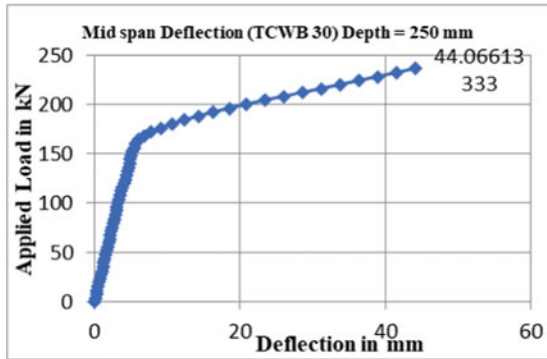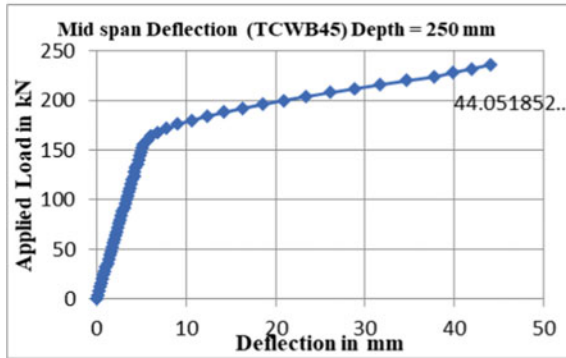
Fig. 19 a–c Load deflection behavior with web stiffener (D = 250 mm)

a) Plain web θ = 0⁰

b) TCWB θ = 30⁰

c) TCWB θ = 45⁰
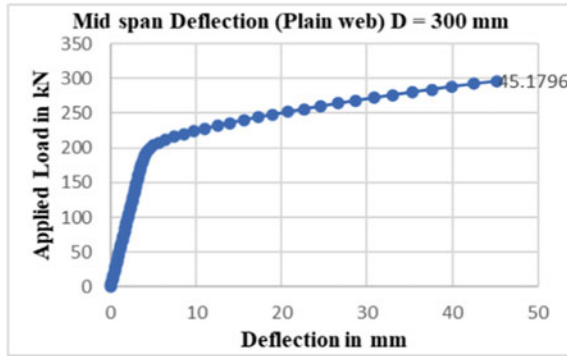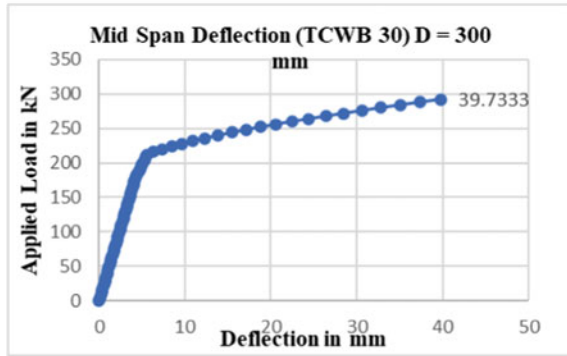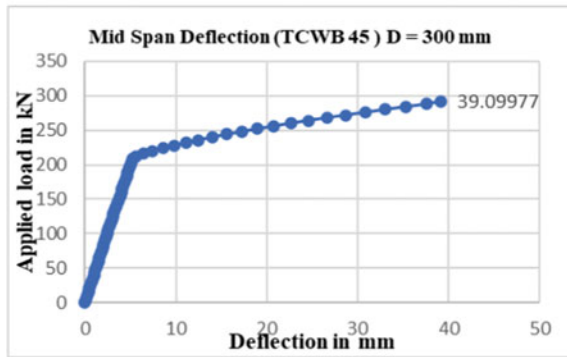
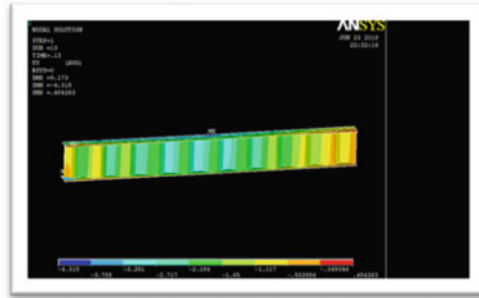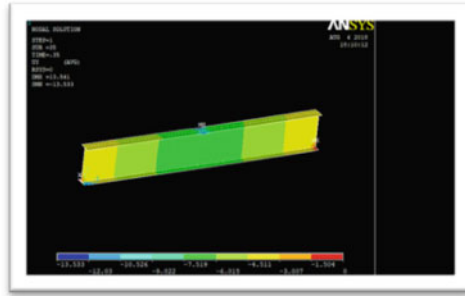**Fig. 20 a–c** Load deflection behaviour with web stiffener (D = 300 mm)

a) Plain web θ = 0⁰

b) TCWB θ = 30⁰

c) TCWB θ = 45⁰
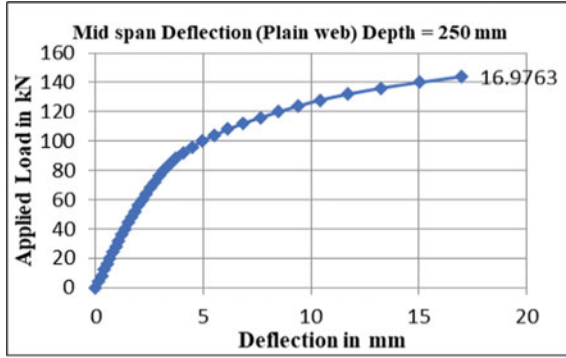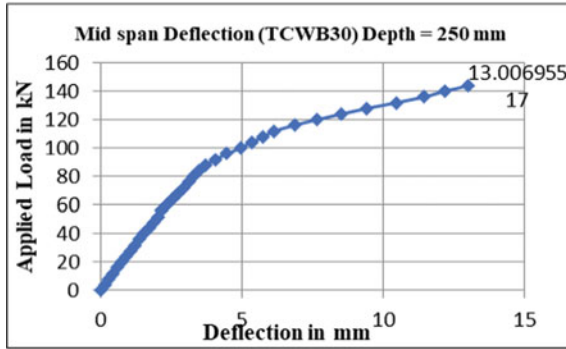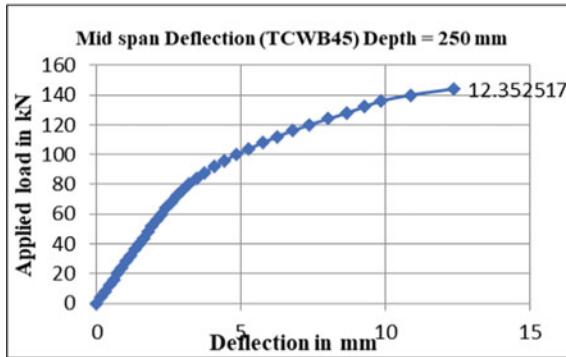
Fig. 21 a–c Load deflection behaviour without web stiffener (D = 250 mm)

a) Plain web θ = 0⁰

b) TCWB θ = 30⁰

c) TCWB θ = 45⁰
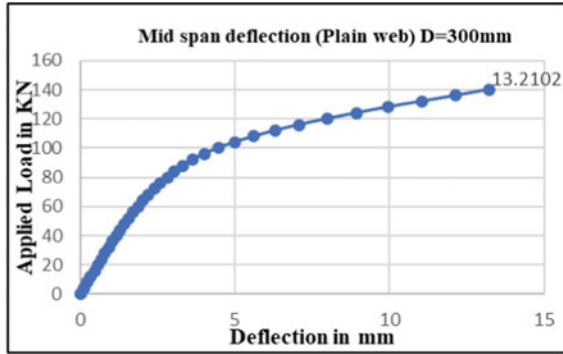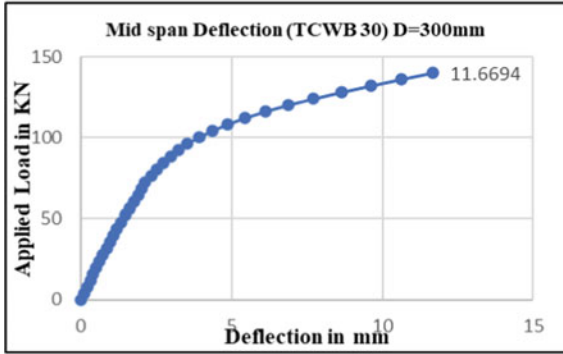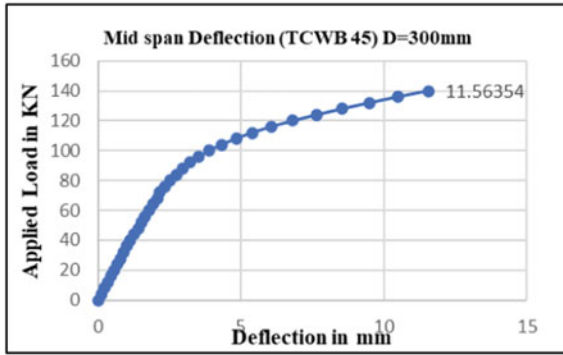
Fig. 22 a–c Load deflection behaviour without web stiffener (D = 300 mm)

has slightly less deflection and higher load carrying capacity when compared with all other specimens.

Specimens with depth = 300 mm

The results of beams having depth of 300 mm with web stiffener provided are shown in below Fig. 20(a)–(c). They are classified according to corrugation angle of plain web (i.e. 0°), Trapezoidal corrugated web (i.e. 45° and 30°). The analytical load–deflection curve of steel beams with plain webs and corrugated webs are shown in Fig. 20(a)–(c). The specimens with Plain web PWB 0° failed at load of 296 kN with a central deflection of 45.1796 mm. The other specimens TCWB 30° and TCWB 45° failed at same load of 292 kN with the corresponding average deflections of 39.7333 and 39.0997 mm respectively. It is observed that the beam with 45° corrugated webs has slightly less deflection and higher load carrying capacity when compared with all other specimens.

5.4.2 Steel Beams Without Web Stiffener Provided Specimens with depth = 250 mm
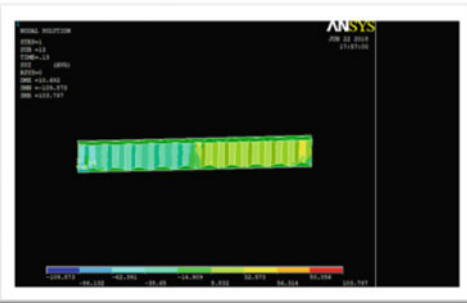
The results of steel beams having depth of 250 mm without web stiffener provided are shown in below Fig. 21(a)–(c). They are classified according to corrugation angle of plain web (i.e. 0°), Trapezoidal corrugated web (i.e. 45° and 30°). The analytical Load–deflection curve of steel beams with plain webs and corrugated webs are shown in Fig. 21(a)–(c). The specimens with Plain web PWB 0° failed at load of 144 kN with a central deflection of 16.976 mm. The other specimens TCWB 30° and TCWB 45° failed at same load of 144 kN with the corresponding average deflections of 13.00 and 12.35 mm respectively. It is observed that the beam with 45° corrugated webs has slightly less deflection and higher load carrying capacity when compared with all other specimens.

Specimens with depth = 300 mm

The results of steel beams having depth of 300 mm without web stiffener provided are shown in below Fig. 22(a)–(c). They are classified according to corrugation angle of plain web (i.e. 0°), Trapezoidal corrugated web (i.e. 45° and 30°). The analytical Load–deflection curve of steel beams with plain webs and corrugated webs are shown in Fig. 22(a)–(c). The specimens with Plain web PWB 0° failed at load of 140 kN with a central deflection of 13.2102 mm. The other specimens TCWB 30° and TCWB 45° failed at same load of 140 kN with the corresponding average deflections of 11.66 and 11.56 mm respectively. It is observed that the beam with 45° corrugated webs has slightly less deflection and higher load carrying capacity when compared with all other specimens.

5.5 *Discussion*

The analytical investigation of results was discussed in this chapter. The comparative study on the performance of beams with plain web, trapezoidally corrugated web with various aspects. Specimens with various methodologies have been carried out considering the load carrying capacity, shear stress distribution and von misses stress distribution along the web. It is observed that the beams with trapezoidally corrugated web gives better performance based on the load carrying capacity, shear stress distribution and von misses stress distribution along the web. A result obtained from ANSYS Finite Element Analysis was compared with the previous studies to outcome the results for validation purpose. It is observed that the ANSYS Finite Element Analysis results very nearly coincide with the previous studies to outcome the results.

5.5.1 Comparative Study of Steel Beams with Web Stiffener Provided (D = 250 mm)

The Ultimate load and maximum deflection of steel beams with plain and corrugated web are given in Table 1. From the analytical results, it is observed that the beam with 45° corrugated webs has less deflection and higher load carrying capacity when compared with all the other specimens.

Figure 23 shows the ultimate load versus central deflection of the all the three specimens with plain and corrugated web. For the specimens with 250 mm depth (dw/tw = 62.5), the load carrying capacity of the beams having 45° corrugated web is 1.02% higher than the specimens having 30° corrugated web and it is 1.11% more than the specimens having plain web. So, it can be concluded that trapezoidal corrugated web beam has more load carrying capacity than other specimens.

Table 1 Percentage increase in deflection with web stiffener (Depth = 250 mm)

Sr. no.	Type of beam (corrugation angle)	Ultimate load (kN)	Mid span deflection in mm	Percentage increase in deflection (%)
01	Plain web θ = 0°	232	48.2478	1.11
02	TCWB θ = 30°	236	41.9218	1.02
03	TCWB θ = 45°	236	41.0937	–
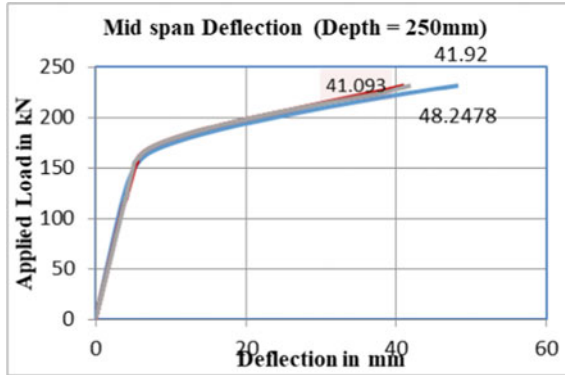
Fig. 23 Comparative study of load deflection curve with web stiffener (Depth = 250 mm)

5.5.2 Comparative Study of Steel Beams with Web Stiffener Provided (D = 300 mm)

The Ultimate load and maximum deflection of steel beams with plain and corrugated web are given in Table 2. From the analytical results, it is observed that the beam with 45° corrugated webs has less deflection and higher load carrying capacity when compared with all the other specimens.

Figure 24 shows the ultimate load versus central deflection of the all the three specimens with plain and corrugated web. For the specimens with 300 mm depth (dw/tw = 75), the load carrying capacity of the beams having 45° corrugated web is 1.016% higher than the specimens having 30° corrugated web and it is 1.155% more than the specimens having plain web. So, it can be concluded that trapezoidal corrugated web beam has more load carrying capacity than other specimens.

Table 2 Percentage increase in deflection with web stiffener (Depth = 300 mm)

Sr. no.	Type of beam (corrugation angle)	Ultimate load (kN)	Mid span deflection in mm	Percentage increase in deflection (%)
01	Plain web $\theta = 0°$	296	45.1796	1.155
02	TCWB $\theta = 30°$	292	39.7333	1.016
03	TCWB $\theta = 45°$	292	39.09977	–
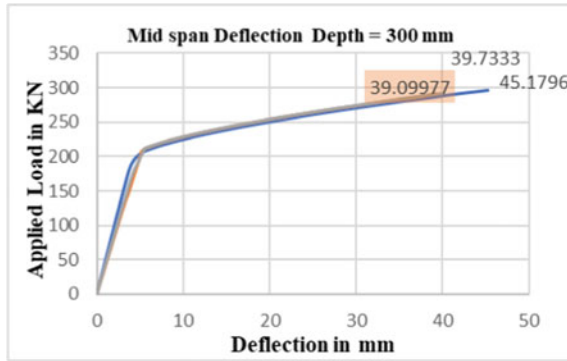
Fig. 24 Comparative study of load deflection curve with web stiffener (Depth = 300 mm)

5.5.3 Comparative Study of Steel Beams Without Web Stiffener Provided (D = 250 mm)

The Ultimate load and maximum deflection of steel beams with plain and corrugated web without stiffener are given in Table 3. From the analytical results, it is observed that the beam with 45° corrugated webs has less deflection and higher load carrying capacity when compared with all the other specimens.

Figure 25 shows the ultimate load versus central deflection of the all the three specimens with plain and corrugated web. For the specimens with 250 mm depth (dw/tw = 62.5), the load carrying capacity of the beams having 45° corrugated web is 1.05% higher than the specimens having 30° corrugated web and it is 1.22% more than the specimens having plain web. So it can be concluded that trapezoidal corrugated web beam has more load carrying capacity than other specimens.

Table 3 Percentage increase in deflection without web stiffener (Depth = 250 mm)

Sr. no.	Type of beam (corrugation angle)	Ultimate load (kN)	Mid span deflection in mm	Percentage increase in deflection (%)
01	Plain web $\theta = 0°$	144	15.030	1.22
02	TCWB $\theta = 30°$	144	13.01	1.05
03	TCWB $\theta = 45°$	144	12.35	–
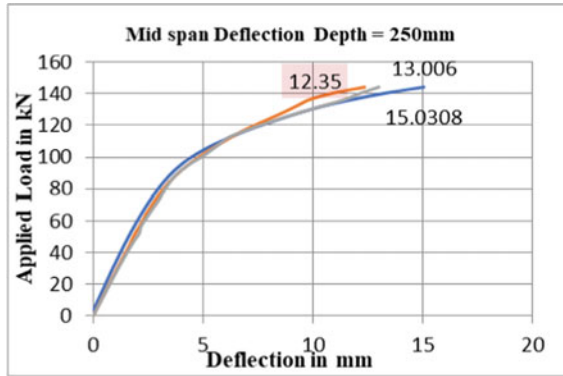
Fig. 25 Comparative study of load deflection without web stiffener (Depth = 250 mm)

5.5.4 Comparative Study of Steel Beams Without Web Stiffener Provided (D = 300 mm)

The Ultimate load and maximum deflection of steel beams with plain and corrugated web without stiffener are given in Table 4. From the analytical results, it is observed that the beam with 45° corrugated webs has less deflection and higher load carrying capacity when compared with all the other specimens.

Also Fig. 26 shows the ultimate load versus central deflection of the all the three specimens with plain and corrugated web.

For the specimens with 300 mm depth (dw/tw = 75), the load carrying capacity of the beams having 45° corrugated web is 1.009% higher than the specimens having 30° corrugated web and it is 1.1427% more than the specimens having plain web. So, it can be concluded that trapezoidal corrugated web beam has more load carrying capacity than other specimens.

Table 4 Percentage increase in deflection without web stiffener (Depth = 300 mm)

Sr. no.	Type of beam (corrugation angle)	Ultimate load (kN)	Mid span deflection in mm	Percentage increase in deflection (%)
01	Plain web $\theta = 0°$	140	13.2102	1.1427
02	TCWB $\theta = 30°$	140	11.6694	1.009
03	TCWB $\theta = 45°$	140	11.56	–
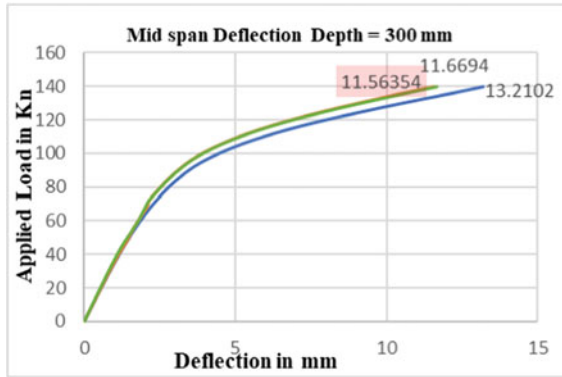
Fig. 26 Comparative study of load deflection without web stiffener (Depth = 300 mm)

6 Conclusion

From the analytical investigation conducted using nonlinear Finite Element Analysis (FEA) and based on the prediction of load bearing capacity of I-beam with trapezoidal corrugated web using various standards, the following conclusions are drawn within the limit of the present investigation.

- The load carrying capacity is more with trapezoidal corrugated web beam when compared to plain web beam.
- The trapezoidally corrugated web with 45° corrugation angle gives better performance based on the load carrying capacity, shear stress distribution and von misses stress distribution along the web comparing to plain webs.
- It is concluded that the load carrying capacity of the beam can be increased by using corrugation in the web of beam which also less uses of the material of web which is useful for the application for many constructions of steel constructions. The strength analysis and modal analysis of such corrugated I-section beam will be carried out for its application.
- Steel beam with trapezoidally corrugated web having 45° corrugation angles has performed well when compared to the beams having plain web and 30° corrugated webs. But, in the load deflection behaviour of the beams with trapezoidal corrugated web with 45° is slightly more than the beams with trapezoidal corrugated web with 30° corrugation angles.
- The finite element modelling using ANSYS software is sufficiently accurate in predicting the load carrying capacity and behaviour of the I-beam with trapezoidal corrugated web.

References

1. Chan, C.L., et al.: Finite element analysis of corrugated web beams under bending. J. Constr. Steel Res. **58**(3December2001), 1391–1406 (2001)
2. Khalid, Y.A., et al.: Bending behaviour of corrugated web beams. J. Mater. Process. Technol. **150**(3), 242–254 (2004)
3. Chung, J.J.: Finite element analysis of corrugated web beam with openings, A thesis submitted in University Malaysia Pahang, November 2010
4. Jáger, B., Dunai, L., Kövesdi, B.: Experimental investigation of the M-V-F interaction behavior of girders with trapezoidally corrugated web. Eng. Struct. **133**, 49–58 (2017)
5. Divahar, R., et al.: Lateral Buckling of cold formed steel beam with trapezoidal corrugated web. Int. J. Civ. Eng. Technol. **5**(3), 217–225 (2014)
6. Denan, F., et al.: The study of lateral torsional buckling behavior of beam with trapezoid web steel section by experimental and finite element analysis. IJRRAS **2**(3), 232–240 (2010)
7. ANSYS User's Manual (version 12). Houston: Swanson Analysis Systems Inc. (2006)
8. Elgaaly, M., Seshadri, A., Hamilton, R.W.: Bending strength of steel beams with trapezoid corrugated webs. ASCE J. Struct. Eng. **123,** 772–782 (1997). https://doi.org/10.1061/(ASCE)0733-9445(1997)123:6(772)
9. Leblouba, M., Junaid, M.T., Barakat, S., Altoubat, S., Maalej, M.: Shear buckling and stress distribution in trapezoidal web corrugated steel beams. Thin–Walled Struct. **113**, 13–26 (2017)
10. Sause, R., Abbas, H., Wassef, W., Driver, R.G., Elgaaly, M.: Corrugated web girder shape and strength criteria (2003). http://preserve.lehigh.edu/cgi/viewcontent.cgiArticle=1244&contextengr-civil-environmental-atlss-reports
11. Sayed-Ahmed, E.Y.: Design aspects of steel I-girders with corrugated steel webs. Electron. J. Struct. Eng. **7**, 27–40 (2007)
12. Hassanein, M.F., Kharoob, O.F.: Behavior of bridge girders with corrugated webs: (ii) shear strength and design. Eng. Struct. **57**, 544–553 (2013). https://doi.org/10.1016/j.engstruct.2013.04.015
13. Nie, J.G., Zhu, L., Tao, M.X., Tang, L.: Shear strength of trapezoidal corrugated steel webs. J. Constr. Steel Res. **85**, 105–115 (2013). https://doi.org/10.1016/j.jcsr.2013.02.012
14. Sause, R., Braxtan, T.N.: Shear strength of trapezoidal corrugated steel webs. J. Constr Steel Res. **67**, 223–236 (2011). https://doi.org/10.1016/j.jcsr.2010.08.004
15. Divahar, R., Joanna, P.S.: Numerical simulation and experimental investigation on static behavior of cold formed steel beam with trapezoidally corrugated web by varying depth-thickness ratio. Asian J. Civ. Eng. https://doi.org/10.1007/s42107-018-0012-9
16. Eurocode 3–Design of steel structures–Part 1–5: Plated structural elements, Annex D, European committee for standardization CEN (2006)

Comparative Study on Position of Floating Column for RCC Multistorey Building Subjected to Seismic Forces

Varsha Kakatkar, Nikhil Jambhale, Veerendrakumar C. Khed, and Shivanand Mendigeri

Abstract Nowadays, aesthetic and functional considerations frequently demand irregularity so a Floating column is another sort of irregularity that changes the structure's load pathway. Presence of Floating column in a building is highly dangerous in seismically active areas. In the present study, G + 14 RC building is modeled and analyzed for dynamic loadings using ETABS. The objective of present work is to study the seismic response of building with and without floating column having floating column on different floor levels i.e. at Ground floor, 5th floor, 10th floor and 15th floor. The building with critical position of Floating column is found out and Lateral resisting systems are provided. Results are compared with respect to max storey displacement, storey drift, time period etc. The building is considered to be located in Zone IV with medium soil as per IS1893:2016. The study shows that structure having FC at bottom storey on the outer periphery and at corner of exterior frame is more crucial and seismic performance of building is improved by providing bracings and shear wall.

Keywords Floating column · Bracings · Shear wall · ETABS

1 Introduction

In metropolitan regions, rapid civilization prompts development of thousands of structures. Nowadays, in several urban areas multi-storey RC framed structures are common and due to the prerequisite and ease of use of building, construction of such buildings are turning out to be more complicated [1]. Structures in metropolitan urban communities are covering the utmost conceivable region on a plot and also the structures are extending upward because of thickly populated metropolitan areas.

V. Kakatkar (✉) · N. Jambhale · V. C. Khed · S. Mendigeri
Department of Civil Engineering, KLE Technological University's Dr. M. S Sheshgiri College of Engineering and Technology, Belagavi 590008, Karnataka, India
e-mail: varsha.kakatkar21@gmail.com

N. Jambhale
e-mail: nikhil_jambhale@klescet.ac.in

V. C. Khed
e-mail: vchkhed@gmail.com
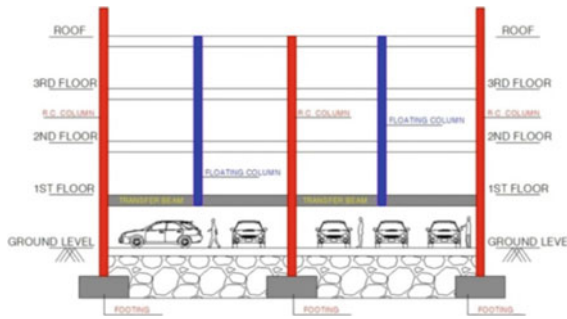
Fig. 1 Floating column building

Aesthetic and functional considerations frequently demand irregularity; a floating column is another sort of irregularity that changes the structure's load pathway [2]. As the position of column will cause a problem, accommodation of such frames is becoming difficult so in that case Floating column will come into picture. The impact of vertical irregularity in buildings created because of parking, reception lobbies or by other means is taken into consideration (Fig. 1).

Generally in building load transfer occurs from horizontal members to vertical members which transfer the load to foundation. So an ordinary column is a vertical member transferring the load directly to the foundation level [3]. But nowadays few of the columns are planned such that they do not extend to the ground due to a variety of architectural factors or site conditions. In such instance, columns transfer above loads to a beam below them as a point load, this beam is known as "Transfer Girder" [4] and from overhanging sections takes a redirection and travel to the nearest column until it reaches to the foundation. The name "Floating column" applies to this type of column [5]. In such circumstances, the point load ascends to high bending moment on the beam, necessitating the use of additional steel [5]. The overall seismic base shear that a building suffers during an EQ is governed by its natural period, and the seismic force distribution is caused by the stiffness and mass distribution along the height [6].

To limit lateral deflection, the building with lateral bracings or a shear wall is used in the current study. Bracing systems are used to withstand horizontal forces like seismic action, wind load, as well as carry those forces to the foundation [9]. When the braces are installed in a structure it becomes more stable as a result of the load being transferred sideways and it also helps to reduce deflection of the structure [7].

A large amount of strength and stiffness is provided by shear wall in the direction of their orientation and this minimizes lateral deflection as a result restricts structural damage. To resist lateral stresses also to minimize shear and moment loads on beams, shear wall are oriented vertically [8].

Sushil sharma et al. [2], this paper highlights the response of G + 10 high rise regular and vertically irregular building with and without presence of FC subjected to earthquake force in zone V. The critical position of FC has been studied for different locations around the periphery columns. They observed that drift is maximum for

model with highest irregularity and when FC is present at outer periphery of the structure. Parveen Hamza et al. [7], for earthquake zones IV and V, a G + 9 storey building is examined statically and dynamically with exterior floating columns. Results are compared and worst case scenario is identified in this study of seismic analysis. They observed that, by introducing the bracings i.e. strengthening method gives much lower storey displacement and storey drift and is within permissible limit and it can be made safe but this can vary when floating column is introduced at different positions. Abhishek Kumar, Vikrant Dubey [3], this research is carried out to check, the seismic effect of bracings in a structure having Floating column. From this analytical study they seen that, the storey displacement is more for the building with floating column and it reduces with provision of bracing in the floating column structures. The reaction of the structure increases because of bracing system with respect to floating column structures. Mohammed Irfan, C S Shashi Kumar et al. [6], in this study they have considered 3 height different buildings G + 3, G + 10 and G + 15 consisting floating columns at different positions in plan and analysed by Time History Analysis. FEM codes are developed for the analysis of structure under various seismic excitations. They observed that when there is increment in the mass of structure, the stiffness and natural period also increases in turn Base shear increases. Natural period and lateral stiffness can significantly change acceleration demand. They found that column at corner of exterior column is critical than at interior frame. Udaygowda M L, Karthik S [10], in this paper analysis of G + 30 storey building with different position of floating column is studied by Time History method and Construction sequence analysis. They recommended that buildings having floating column are avoided in higher seismic zone. They concluded that the overall response of structure depends on method of analysis used, type and position of floating column, seismic zone. Allacheruvu Raghavendra et al. [11] in this paper analysis of G + 9 building with and without FC is carried out in zone III and zone IV and also how to minimize the risk factor of seismic forces by strengthening the building having FC with bracings is studied. From this study they observed that there is increment in deflection values for model with FC than normal building due to presence of FC. By using bracings for the building with FC these values are reduced. FC having bracings at centre gives higher performance level.

Therefore present work is aimed to study seismic behavior of multistorey building with vertical stiffness irregularity in the form of Floating columns by changing the position on different floor levels and identifying the structure with critical position of Floating column to provide suitable strengthening to the building to resist lateral forces.

2   Methodology

In this present work, the seismic response of multistorey buildings with Floating column has been studied for Equivalent static method and Response spectrum method and assumed to be in zone IV as per IS1893:2016 [13]. The study is carried out on

vertical irregularity in the form of Floating columns. G + 14 storey frame models are analyzed using ETABS. The seismic response of Building with and without floating columns on different floor levels i.e. at Ground floor, 5th floor, 10th floor and 15th floor is studied to find the critical position of Floating column. For all models Equivalent static analysis is performed for determining base shear, which is then used to calculate the dynamic scale factor. The results of analysis are tabulated, discussed and conclusions are made. Also the building with critical position has been found out and Lateral resisting systems are provided. The structure is as per IS1893:2016.

2.1 Modelling and Analysis

The structure considered in present study is G + 14 storied RC Framed building having plan dimension 20 × 30 m with bay length 5 m in each directions which consist of 7 models and these models are modelled and analysed in Etabs software (Table 1).

Input Parameters used for modeling of building [12]*:*

Table 1 General properties

Material properties	
Design parameter	Value
Concrete density	25 kN/m^3
Density of masonry	19 kN/m^3
Characteristic strength of concrete (f_{ck})	30 MPa
Steel grade (f_y)	500 MPa
E_f	27,386.128 MPa
E_S	2×10^5 MPa
Details of a building and sectional properties	
Properties	Value
Plan dimension	20 × 30 m
Number of storeys	15
Height of the floors	3 m
Bay length in x and y direction	5 × 5 m
Size of beam	750 × 400 mm 600 × 350 mm
Size of column	750 × 750 mm 500 × 500 mm
Slab thickness	150 mm
External wall	230 mm
Internal wall thickness	150 mm
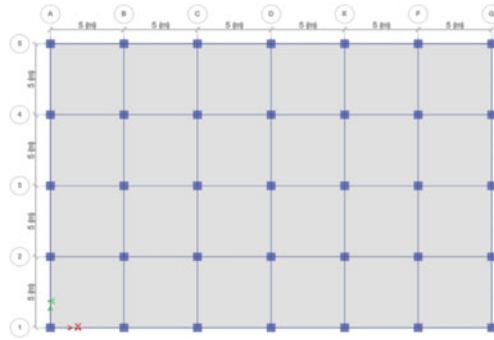
Fig. 2 Plan of building without FC

2.2 Etabs Model Details

The present study consists of 7 models. Model 1 indicates the building without Floating column; Model 2 is building with Floating Column type 1. Floating columns are provided in 5th grid i.e. grid 5A, 5B, 5C, 5D, 5E, 5F, 5G. Model 2 with Floating column is analyzed for different cases such as FC at storey 1, FC at storey 5, FC at storey 10, FC at storey 15. Model with critical position of FC is found out and based on preliminary analysis suitable type of bracings i.e. eccentric and X bracings of size ISMB 200 are provided and shear wall having thickness of 300 mm is provided at a particular location to minimise the deflection of the building. Following flow chart shows the types of models in detail (Figs. 2, 3 and 4);
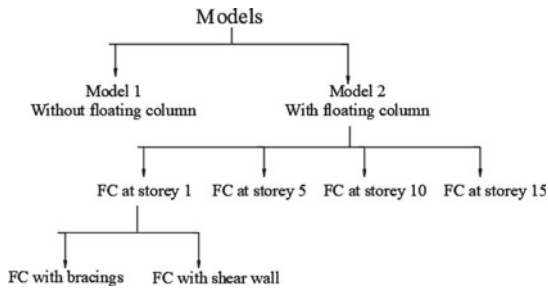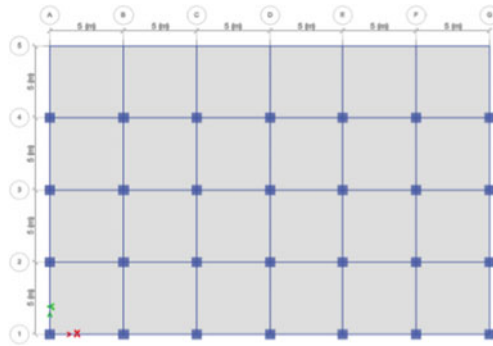
Fig. 3 Plan of building with FC type 1
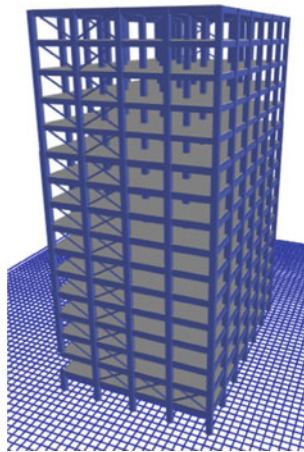
Fig. 4 Isometric view of building with type 1 FC and with bracings

2.3 Loadings on Structure

The loads considered for analysis of RC structure as per IS 875–1987 [12] (Part 1 and 2) (Table 2).

Seismic Loading: The effect of this load is considered along both the axes of building. The loads are computed based on clause of IS 1893:2016.
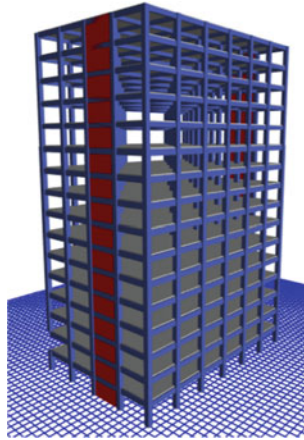
Fig. 5 Isometric view of building with type 1 FC and with shear wall

Table 2 Loadings on structure

Type of load	Load calculation
Dead load	
External wall load	14.7 kN/m
Internal wall load	3.3 kN/m
Parapet load	4.9 kN/m
Live load	
LL on Floors	4 kN/m^2
Roof live	1.5 kN/m^2
Floor finish	1.0 kN/m^2

2.4 Seismic Parameters

By referring IS 1893:2016, following parameters are considered (Table 3);

Table 3 Seismic details of a building (as per IS 1893:2016) [13]

Seismic specifications	Value
Zone	IV
Z	0.24
Soil type	Medium soil (type II)
Response reduction factor (R)	5
I	1
Damping	5%

2.5 Load Combinations

Load combinations for RCC Structures are given in accordance with IS standards

$$1.5(DL + LL)$$
$$1.2(DL + LL \pm EL)$$
$$1.5(DL \pm EL)$$
$$0.9DL \pm 1.5EL$$

3 Results and Discussion

3.1 Displacements

When a structure is subjected to lateral loads, lateral displacement is defined as, "the maximum horizontal displacement of the structure with respect to the base". At the bottom level, lateral displacement will be minimal and at the roof level of the top storey, it will be maximal. As per IS 1893:2016, the maximum permissible displacement value is H/250 (Figs. 6 and 7).

It is observed that storey displacement is 3.37 times more in building with FC to that of building without FC and it is more than permissible limits i.e. 187.28 mm, where the maximum permissible limit is 180 mm. Storey displacement reduces when FC are shifted towards upper floors by 12.31, 36.48, 63.42% at storey 5, storey 10, storey 15 respectively. FC provided at storey1 causes displacement which is more than permissible limit. In order to minimise storey displacement and to enhance seismic performance of the building, lateral load resisting system like bracings and shear wall are employed. So by adopting bracing system and shear wall, displacement is reduced and it is within the permissible limit. The displacement of building having FC at storey1 is decreased by 18% after providing bracings and 37.26% after providing shear wall.
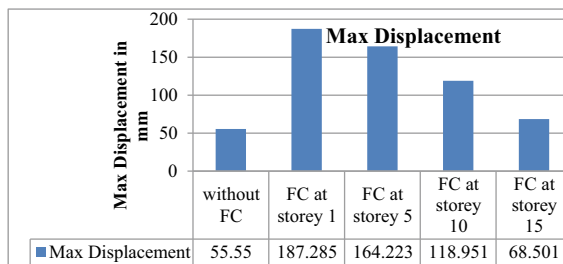
Fig. 6 Variation in max storey displacement at different floor levels for all types of models
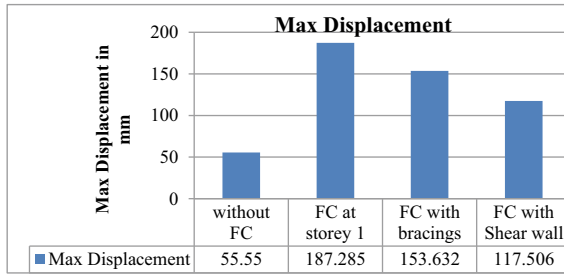
Fig. 7 Variation in max storey displacement for type 1FC building with bracings and shear wall

3.2 Storey Drift

Storey drift is defined as, "the maximum displacement within a storey or displacement of one storey relative to the subsequent storey above or below caused by effect of seismic loads." As per clause 7.11.1 of IS standards, due to the maximum specified design lateral force, the storey drift in any storey with a partial load factor of 1.0 shall not be exceed 0.004 times the storey height (Figs. 8 and 9).

The permissible storey drift is 0.012 and for all models storey drift values are within maximum permissible limit. Building without FC has less drift than building
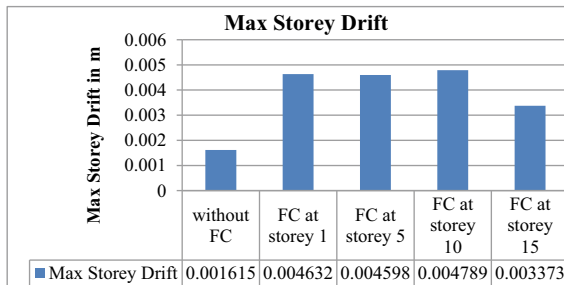
Fig. 8 Variation in max storey drift at different floor levels for all types of models
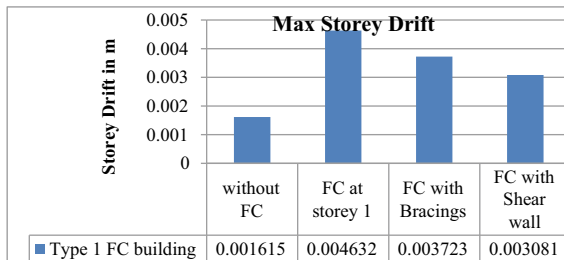
Fig. 9 Variation in storey drift for type 1FC building with bracings and shear wall

with FC and it is maximum when FC are provided at storey 10 i.e. compare to building without FC, storey drift for type 1 FC is increased by 2.96 times. Compare to FC provided at storey 10, storey drift is lesser by 3.27, 3.98, 29.56% when FC are provided at storey 1, storey 5, storey 15 respectively. Storey drift is maximum at soft storey for all models. By providing bracings to the type 1 having FC at storey 1, Storey drift in type 1 having FC at storey1 is decreased by 19.62% after providing bracings 33.5% after providing shear wall.

3.3 Time Period

"The fundamental natural period is a feature of building that can be defined as the time required for completing one cycle of oscillation". The presence of floating column has a considerable impact on natural period, which is a function of mass and stiffness, according to literature study (Figs. 10 and 11).

From above graph it is observed that, the time period for building without FC is shorter than building with FC. Time period is more when the FC is provided at storey 1.i.e. time period for type 1 FC is increased by 13.53%. Time period decreases when FC shifts towards upper floors i.e. compare to FC at storey 1, it reduces by 4.42, 10.15, 11.96% when FC are provided at storey 5, storey 10, storey 15 respectively. Time period of building decreases as the stiffness of the structure increases. By providing

	without FC	FC at storey 1	FC at storey 5	FC at storey 10	FC at storey 15
Time period	2.29	2.6	2.485	2.336	2.289
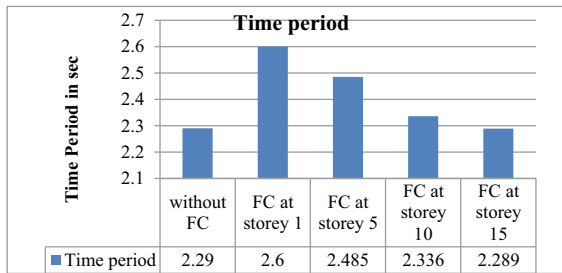
Fig. 10 Variation in time period for all types of models at different floor levels

	without FC	FC at storey 1	FC with bracings	FC with Shear wall
Time Period	2.29	2.6	2.252	2.265
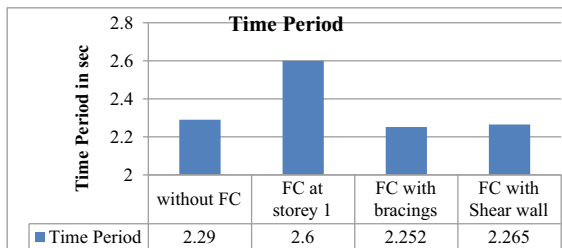
Fig. 11 Variation in time period for type 1FC building with bracings and shear wall

bracings to the type 1 having FC at storey 1, time period reduces by 13.4% and by providing shear wall it is reduces by 12.9%.

4 Conclusion

- Storey displacement is 3.37 times more in building with FC to that of building without FC and it is more than permissible limits. The location of shear wall shown in Fig. 5 found effective in reducing the displacement and to increase seismic performance also the type of bracing system adopted is found suitable to maintain the discontinuity in load path affected by presence of floating column. By providing bracings and shear wall to the building displacement is reduced by 18 and 37.26% respectively.
- For type 1 FC storey drift is maximum at soft storey for all models. Consequently the variability of storey drift has been found depending on location of FC.
- Time period of building decreases when FC shifts towards upper floors and it is less for building without FC than building with FC and it decreases as the stiffness of the structure increases.
- The position of FC has a considerable effect on the building. However, it is difficult to predict which position is best for all types of building analytically hence it is necessary to carry out careful analysis.
- FC provided near ground storey is more flexible than provided at top floors and when FC provided at top floor, seismic performance of a building is nearly same as building without FC. Provision of lateral resisting system to the type 1 FC, seismic performance is improved and the building with shear wall shows better results in terms of displacement.

References

1. Pandey, G., Jamle, S.: Optimum location of floating column in multistorey building with seismic loading. Int. Res. J. Eng. Technol. **5**(10), 971–976 (2018)
2. Sharma, S., Pastariya, S.: Effect of floating column on seismic response of multi-storey building. Int. J. Adv. Sci. Res. Eng. Trends **5**(12), 111–120 (2020)
3. Kumar, A., Dubey, V.: A study on effect of bracing system on floating column structure under earthquake forces. Int. J. All Res. Educ. Sci. Methods **8**(9), 480–484 (2020)
4. Meena, V.K., et al.: Seismic response evaluation of RC frame building with floating column. Int. J. Eng. Manag. Res. **2**(6), 429–432 (2016)
5. Hemanth, G., Bhanupriya, B., et al.: Earthqake analysis of multi-storied buildings with floating columns, vol. 4, Issue11, pp. 1127–1132 (2017)
6. Mohammed Irfan, C.S., Kumar, S., et al.: Seismic analysis of multi-storey building with and without floating columns. Int. Res. J. Eng. 5(11), 1324–1330 (2018)
7. Waykule, S.B., Kadam, S.S., et al.: Study of behaviour of floating column for seismic analysis of multistorey building. Int. Res. J. Eng. Technol. **3**(6), 70–83 (2016)

8. Gaddad, K., Vijapur, V.: Comparative study of multi storey building with and without floating columns and shear walls, vol. 5, Issue 7, pp. 108–104, July 2018
9. Parveen, H., et al.: Seismic performance & structural stability analysis of floating column building. Int. J. Sci. Eng. Res. **11**(1), 91–98 (2020)
10. Udaygowda, M.L., Karthik, S.: Effect of floating column position on multi storied RCC structure subjected to dynamic load. Int. J. Recent Trends Eng. Res. **4**(6), 162–171 (2018)
11. Raghavendra, A., Reddy, T.A., et al.: Comparative seismic study on strengthening of floating column building using bracings, vol. 3, issue 6, pp. 65–71 (2016)
12. IS 456:2000 Code of Practice for Plain and Reinforced Concrete, Bureau of Indian Standards, New Delhi, India
13. IS 1893 (Part 1):2016 Criteria for Earthquake Resistant Design of Structures, Bureau of Indian Standards, New Delhi 110002
14. IS 875(Part-2):1987 Code of Practice for Design Loads for Buildings and Structures, Bureau of Indian Standards, New Delhi, India

Deflection Surface Analysis of Thin Plate Structures Using Regression Technique

Vishal Singh and M. H. Prashanth

Abstract Deflection analysis of any structure is of common interest while designing the structure. Analysis for deflection in thin plate structures is generally done with the help of Kirchhoff's plate theory, also known as classical plate theory. Kirchhoff's plate theory helps in developing a fourth-order partial deflection equation relating the deflection of a plate to the loading condition on the plate and the material or bending rigidity of the plate. The present study focuses on the analysis of a simply supported thin concrete plate that is subject to uniform loading over the entire plate area. The deflection surface of the plate is developed using Navier's double trigonometric Fourier series. Regression analysis is done to understand how various plate parameters like material rigidity, loading on the plate, and area of the plate could affect the magnitude of deflection of the plate. Also, the effect of the mentioned plate parameters on the magnitude of bending moments, twisting moments, and shear forces acting on the plate is studied. Regression modelling is used to achieve the same. Statistical metrics like R-squared error, Root Mean Square Error (RMSE), and Mean Absolute Percentage Error (MAPE) are used to check the efficiency of regression analysis. In the present study, the regression modelling technique is also used to solve the fourth-order partial differential equation.

Keywords Kirchhoff's plate theory · Partial differential equations · Navier's Fourier series · Regression analysis

1   Introduction

The thickness of a plate plays an important role in the purpose of performing bending analysis of the plate. Depending on the thickness of the plate, plates are classified as either thin plates or thick plates. Plates having a thickness of less than five percent of their least lateral dimension are considered thin plates. When the deflection of plates is less than one-fifth of their thickness, the deflection is considered a small

V. Singh (✉) · M. H. Prashanth
National Institute of Technology Karnataka, Surathkal 575025, India
e-mail: singhvishaldineshshashi.203st007@nitk.edu.in

deflection. For thin plates with small deflection, Kirchhoff's Plate Theory, also known as Classical Plate Theory, is most commonly used. This theory has assumptions similar to those of Euler's beam theory, which is used for the bending analysis of beams.

Classical Plate Theory helps to develop a fourth-order partial differential equation (refer "Eq. 1") relating the deflection of the plate to the imposed loading on the plate and the material or bending rigidity of the plate.

$$\frac{\partial^4 w(x,y)}{\partial x^4} + 2\frac{\partial^4 w(x,y)}{\partial x^2 \partial y^2} + \frac{\partial^4 w(x,y)}{\partial y^4} = \frac{P_z(x,y)}{D} \tag{1}$$

where, $D = \frac{Et^3}{12(1-\vartheta^2)}$

E = Modulus of Elasticity of the plate material.

t = thickness of the plate.

ϑ = Poisson's ratio of the plate material.

In "Eq. 1," $w(x,y)$ is the deflection of the plate in the z-direction when the plate is subjected to a transverse load of $P_z(x,y)$, which is perpendicular to the x–y plane and parallel to the z-axis. The plate is positioned such that the dominant lengths of the plate are along the x and y axes and the thickness of the plate is along the z-axis. "D" denotes the material rigidity or the bending rigidity of the plate.

1.1 Navier's Solution Technique

In order to solve the problem of a thin plate simply supported on all sides, Navier's double trigonometric Fourier series is the most commonly adopted analytical solution technique. Consider a simply supported thin slab as shown in "Fig. 1". The dimensions of the plate along the x–y axes are *a* and *b*, respectively. The plate's origin is fixed at the top left corner. The solution of deflection function w (x, y) for such a plate is written as shown in "Eq. 2".

$$w(x, y) = \frac{1}{\pi^4 D} \sum_{m=1}^{\infty} \sum_{n=1}^{\infty} \frac{P_{mn}}{\left[\left(\frac{m}{a}\right)^2 + \left(\frac{n}{b}\right)^2\right]^2} \sin\frac{m\pi x}{a} \sin\frac{m\pi y}{b} \tag{2}$$

$$P_{mn} = \frac{4}{ab} \int_0^a \int_0^b p(x, y) \sin\frac{m\pi x}{a} \sin\frac{m\pi y}{b} \, dx \, dy \tag{3}$$

$p(x, y) = Po;$ Uniformly Loaded plate along x = a and y = b

$= Po\, (x/a);$ Uniformly varying load along x = a

$= Po \sin(\pi x/a).\sin(\pi y/b);$ Sinusoidal loading along x = a and y = b

Po is the maximum intensity of the loading.
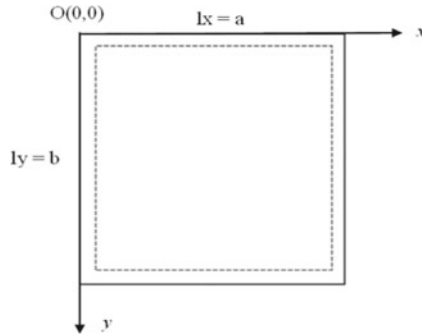
Fig. 1 Simply supported plate

1.2 Regression Analysis

Regression analysis involves predicting the value of a response variable with the help of one or many predictor variables. Regression analysis is the mathematical modeling of available data in an equation form. Regression modelling can be imagined as fitting a best-fit line or curve to the given set of data points. The Least Square Method is the most commonly used method for performing regression analysis. It helps in minimising the mean squared error values between the predicted and actual variables.

There are many types of regression modeling, such as linear regression, multivariate linear regression, and polynomial regression. Linear and polynomial regression correspond to using one input variable to calculate the desired output variable. Multivariate linear regression involves using more than one input variable for the prediction of an output variable. The output in multivariate linear regression is expressed as a linear combination of input variables with coefficients attached to it.

If "y" is the output variable and "x" is the input variable, then "Eq. 4 and 5" represent the equations for linear and polynomial regression, respectively.

$$y = c_0 + c_1 x \tag{4}$$

$$y = c_0 + c_2 x^2 + c_3 x^3 + \ldots\ldots + c_n x^n \tag{5}$$

A more generic form for the above equations ("Eq. 4 and 5") can be written as follows:

$$y = \sum_{i=0}^{n} c_i x^i \tag{6}$$

In the above "Eq. 6", c_i represents the coefficient attached to the power terms of an input variable. It is indicative of the contribution of the attached power term to the calculation of the output variable. In regression analysis, the values of these

coefficients are found using various methods. However, in this study, we will restrict the use of the least square method for finding these coefficients.

Various statistical metrics are used in order to measure the accuracy of the fitness of the line or curve formed from the regression modelling of the data. Some of them used in this study are R-squared (R^2) error, Root Mean Square Error (RMSE), and Mean Absolute Percentage Error (MAPE). The value of R-squared error close to 1 implies the goodness of fit of the model. Similarly, the value of RMSE and MAPE close to 0 indicates most of the data points are either close enough to the fitted line or curve or lie exactly on it if the value is exactly zero. Thus, the above parameters help in understanding the overall nature of the fitted line or curve to the given data set.

2 Literature Review

Various energy methods [1–6] like the Ritz method, Glarkin-Vlasov method, and more are used for solving the thin plate PDE for different boundary and loading conditions. New mathematical methods like the symplectic geometric approach [7] and the Boundary Distributed Source method [8] are also used for the bending analysis of the Kirchhoff plate. A deep neural network model [9] was developed in order to predict the deflection surface of square and circular plates with different boundary conditions. The maximum deflection values of these surfaces were then matched with the values from some other available methods. Good accuracy was achieved with the neural network model developed.

A regression model was developed to predict the productivity of a concrete pour system [10]. Polynomial regression was used to establish a mathematical model between strains in three particular directions at a particular drilling depth [11]. The performance of the Neural Network model, Regression Model, and Case-Based Reasoning for estimating the cost of construction projects is discussed in [12]. [13] gives a review of the use of linear regression and polynomial regression by authors in different areas of research. The paper highlights the feasibility of use and limitations of regression modelling. Thus, we see some useful practical applications of regression modeling in field of civil engineering.

Various methods were developed or modified in order to solve the differential equation developed by Kirchhoff's plate theory for thin plates. However, no attempt has been made until now to use regression modelling for solving the differential equation. At the same time, use it to understand how the parameters like loading, material constant, and area of the plate could possibly affect the deflection, bending moments, twisting moments, and shear forces developed in the thin isotropic rectangular plate.

3   Objective and Methodology

The present study focuses on understanding how variations in parameters like the loading condition, material rigidity, and area of the plate would affect the magnitude of deflection, bending moments, twisting moments, and shear forces. The effect of independent parameters on the dependent parameters is studied by varying one independent parameter at a time with respect to the dependent parameter and keeping other independent parameters constant.

In order to achieve the above objective, a thin, simply supported isotropic rectangular plate is used for data generation and analysis. For such a plate, the values of deflection at various points are achieved using Navier's Solution technique. Values for moments and shear forces are developed from differential equations relating deflection to these moments and shear forces. Python is used as a programming language for generating the above data required and then performing regression analysis on the same.

The regression technique is used to solve the partial differential equation at the end of the study. It involves the use of computer programming to achieve the same.

4   Results

The independent parameters are divided into three categories:

k = Po / D; Po = maximum loading intensity and D = bending or material rigidity.

A = area of the plate.

r = aspect ratio of the plate.

The values of the above parameters with respect to the dependent parameters will be generally compared at the mid-point of the simply supported thin rectangular plate loaded uniformly throughout the plate. If any other location is chosen, it will be specified.

In the present study, we will also deal with a different coordinate system, viz. relative positional coordinates (rpc) denoted as (x/lx, y/ly). It helps in understanding the point under consideration on a plate of any size or aspect ratio. The aspect ratio (lx/ly) will always have a value less than or equal to one. This implies that the shorter dimension will always be placed along the x-axis.

4.1   k (Po/D) v/s Deflection(w)

Herein we vary "k" w.r.t deflection "w" at rpc (0.5,0.5). The area and aspect ratio are constant. We vary "Po" value and the thickness (t) of the plate in order to vary the "D" value of the plate.
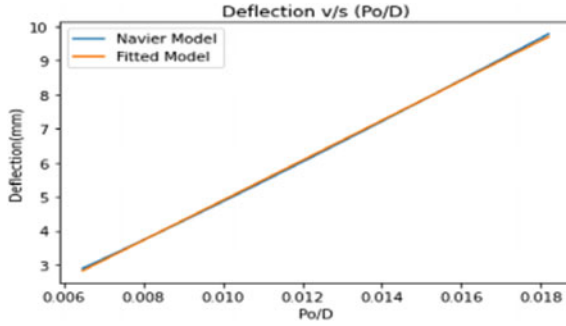
Fig. 2 Deflection v/s (Po/D)

$lx = 3\,m$, $ly = 4\,m$, $t(m) = [0.1, \ldots, 0.5]_{20 \times 1}$, $Po\left(kN/m^2\right) = [50, \ldots, 60]_{20 \times 1}$; $E = 30 \times 10^9\,N/m^2$; $\nu = 0.3$

A linear relationship was found between the two parameters. The following equation ("Eq. 7") was obtained using the least square method.

$$w = 548.9\ k - 0.9536 \tag{7}$$

For the above fitted model to the dataset obtained by the Navier's model, the values of R-squared error, RMSE, and MAPE are 0.9996, 0.0381, and 0.0068 respectively. In "Eq. 7", we can neglect the constant term due to its small magnitude in comparison to the variable term. Thus, we can in general say that w at rpc (0.5, 0.5) is proportional to "k" by neglecting the constant term.

From "Fig. 2", we can visually inspect the predicted model. However, by testing more test cases at different rpc coordinates, it was observed that:

$$w\left(\frac{x}{lx}, \frac{y}{ly}\right) \alpha\, k \tag{8}$$

4.2   Area(A) v/s Deflection(w)

Herein we vary "A" w.r.t deflection "w" at rpc (0.5,0.5). k (Po/D) and aspect ratio is constant.

$t = 0.15\,m$, $Po = 50\,kN/m^2$, $ly(m) = [1, \ldots, 12]_{20 \times 1}$; $lx(m) = [0.75, \ldots, 9]_{20 \times 1}$; $E = 30 \times 10^9\,N/m^2$; $\nu = 0.3$
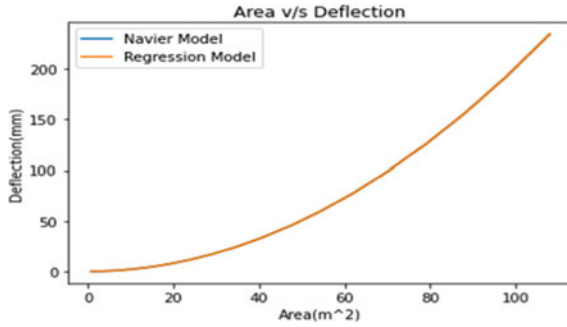
Fig. 3 Deflection v/s area

A higher-order relation of degree two was found between the two parameters. The following equation ("Eq. 9") was obtained using the least square method.

$$w = 0.02011 \times A^2 \tag{9}$$

For the above-fitted model to the dataset obtained by Navier's model, the values of R-squared error, RMSE, and MAPE are 1, 0, and 0 respectively. Thus, we can in general say that w at rpc (0.5, 0.5) is proportional to the square of the area of the thin plate.

From "Fig. 3", we can visually inspect the predicted model. After verifying more test cases at different rpc coordinates following a similar procedure, it was observed that:

$$w\left(\frac{x}{lx}, \frac{y}{ly}\right) \propto A^2 \tag{10}$$

Thus, relations established in "Eqs. (8) and (10)" can be assembled together as follows:

$$w\left(\frac{x}{lx}, \frac{y}{ly}\right) \propto A^2 \times k \tag{11}$$

$$w_2\left(\frac{x}{lx}, \frac{y}{ly}\right) = \left(\frac{k_2}{k_1}\right) \times \left(\frac{A_2}{A_1}\right)^2 \times w_1\left(\frac{x}{lx}, \frac{y}{ly}\right) \tag{12}$$

"Equations (11) and (12)" are valid provided the aspect ratio of the plate is constant.

4.3 *Moments and Shear Forces*

Bending moments (Mxx, Myy), twisting moments (Mxy = Myx) and shear forces (Qx, Qy) are represented by the following differential equations ("Eqs. (13), (14), (15), (16) and (17)"):

$$Mxx = -D\left(\frac{\partial^2 w}{\partial x^2} + v\frac{\partial^2 w}{\partial y^2}\right) \tag{13}$$

$$Myy = -D\left(\frac{\partial^2 w}{\partial y^2} + v\frac{\partial^2 w}{\partial x^2}\right) \tag{14}$$

$$Mxy = -D(1-v)\left(\frac{\partial^2 w}{\partial x \partial y}\right) \tag{15}$$

$$Qx = -D\left(\frac{\partial^3 w}{\partial x^3} + \frac{\partial^3 w}{\partial x \partial y^2}\right) \tag{16}$$

$$Qy = -D\left(\frac{\partial^3 w}{\partial y^3} + \frac{\partial^3 w}{\partial y \partial x^2}\right) \tag{17}$$

Also, the moments are related to the loading condition $P_z(x, y)$ as shown in the differential equation ("Eq. 18"):

$$\frac{\partial^2 Mxx}{\partial x^2} + 2\frac{\partial^2 Mxy}{\partial x \partial y} + \frac{\partial^2 Myy}{\partial y^2} = -P_z(x,y) \tag{18}$$

Following similar process as earlier with deflection for bending moments at rpc (0.5,0.5) and twisting moments at rpc (0.4,0.6) as at rpc (0.5,0.5) the twisting moments have near about zero magnitude we get following relation models:

$$Mxx_2\left(\frac{x}{lx}, \frac{y}{ly}\right) = \left(\frac{P_2}{P_1}\right) \times \left(\frac{A_2}{A_1}\right) \times Mxx_1\left(\frac{x}{lx}, \frac{y}{ly}\right) \tag{19}$$

$$Myy_2\left(\frac{x}{lx}, \frac{y}{ly}\right) = \left(\frac{P_2}{P_1}\right) \times \left(\frac{A_2}{A_1}\right) \times Myy_1\left(\frac{x}{lx}, \frac{y}{ly}\right) \tag{20}$$

$$Mxy_2\left(\frac{x}{lx}, \frac{y}{ly}\right) = \left(\frac{P_2}{P_1}\right) \times \left(\frac{A_2}{A_1}\right) \times Mxy_1\left(\frac{x}{lx}, \frac{y}{ly}\right) \tag{21}$$

$$Myx_2\left(\frac{x}{lx}, \frac{y}{ly}\right) = \left(\frac{P_2}{P_1}\right) \times \left(\frac{A_2}{A_1}\right) \times Myx_1\left(\frac{x}{lx}, \frac{y}{ly}\right) \tag{22}$$

The above relation for bending and twisting moments was tested on a 3 × 4 m plate loaded with udl 50 kN/m², t = 0.15 m and a 6 × 8 m plate loaded with udl 100 kN/m², t = 0.25 m. Plates were meshed along 20 nodal points along the x and

y axes, respectively. The values were calculated and matched on these 400 points for both the plates using Navier's solution technique and the relation model in "Eqs. (19), (20), (21) and (22)". The R-squared error value, RMSE, and MAPE had values 1,0,0 respectively for all the bending and twisting moment relational models.

In a similar manner shear forces Qx and Qy are varied at rpc (0.4, 0.3) as shear forces have zero magnitude at rpc (0.5,0.5). The following relation models were obtained:

$$Qx_2\left(\frac{x}{lx}, \frac{y}{ly}\right) = \left(\frac{P_2}{P_1}\right) \times Qx_1\left(\frac{x}{lx}, \frac{y}{ly}\right) \tag{23}$$

$$Qy_2\left(\frac{x}{lx}, \frac{y}{ly}\right) = \left(\frac{P_2}{P_1}\right) \times Qy_1\left(\frac{x}{lx}, \frac{y}{ly}\right) \tag{24}$$

The above relations for shear forces was tested on a 3×4 m plate loaded with udl $50 \, kN/m^2$, $t = 0.15$ m, and for a 3×4 m plate loaded with udl $100 \, kN/m^2$, $t = 0.25$ m. Plates were meshed along 20 nodal points along the x and y axes, respectively. The values were calculated and matched on these 400 points for both the plates using Navier's solution technique and the relation model in "Eqs. (23) and (24)". The R-squared error value, RMSE, and MAPE had values of 1,0,0, respectively. Thus, validating the above shear force models. No straightforward polynomial relation was seen between area of the plate and shear forces like that for moments and deflections.

4.4 Validation of Results on a Clamped Square Plate

The deflection equation for thin plate clamped from all the sides as used in [3] is given below in "Eq. 25".

$$w(x, y) = c \ x^2 y^2 (a - x)^2 (y - b)^2 \tag{25}$$

where, $c = 0.3411 \times (Po/Db^4)$; for square plates.

Consider a 4×4 m square plate and 3.5×3.5 m square plate with following specifications:

$$t = 0.15 \, m, \ Po = 50 \, kN/m^2, \ E = 30 \times 10^9 \, N/m^2, \ \nu = 0.3$$

Calculating w (1,2) for 4×4 m square plate using "Eq. 25" we get a value of 1.034 mm. The above coordinates in rpc system is (0.25, 0.5). These rpc coordinates in normal coordinate system for 3.5×3.5 m plate is (0.25 × 3.5, 0.5 × 3.5). The value of w (0.875, 1.75) calculated for 3.5×3.5 m plate using relation model in "Eq. 12" is 0.6061 mm. This value when calculated using "Eq. 25" comes out to be 0.6065 mm. Thus, it can be seen that the values are almost an exact match. Similarly, other relational models of moments and shear forces were validated. The results were

also an exact match. It can thus be concluded that the relational models developed for deflection, moments, and shear forces are valid for all types of boundary conditions and loading types. It is an attribute of the governing differential equation.

4.5 Using Regression Technique to Solve Kirchhoff's PDE

The solution of deflection function in the fourth order partial differential equation is in the following form:

$$w(x, y) = f(x).f(y) \tag{26}$$

Consider an example of a simply supported thin plate. The deflection function is written in the following form as per Navier's Solution technique.

$$w(x, y) = \sum_{m=1}^{\infty} \sum_{n=1}^{\infty} C_{mn} \sin\left(\frac{m \pi x}{a}\right) \sin\left(\frac{n \pi y}{b}\right) \tag{27}$$

"Equation 27" can also be written in matrix form as follows:

$$w = [S]\{C\} \tag{28}$$

where [S] = shape function matrix (row matrix).

= $[X_m(x). Y_n(y)]_{1 \times t}$; t = total no. of coefficients to find.

m, n = 1,2,....t

{C} = column matrix of coefficients of the order t × 1.

"Equation 28" when substituted in the partial differential equation can be written as follows:

$$[S]''''\{C\} = \{P_z(x, y)/D\} \tag{29}$$

Substituting values of (x, y) coordinates in "Eq. 29", it can be solved for the values of coefficients in the column matrix "C" using the least square method.

Assume a 3 × 4 m plate of 150 mm thickness, $E = 30 \times 10^9$ N/m², subjected to a 50 kN/m² intensity udl load. Poisson's ratio is 0.3. Simply supported on all sides. Deflection, moments, and shear forces will be found out using the regression method and Navier's method. A comparison will be made between both the methods.

The coefficients are considered upto 9 terms. This implies m, n = 1, 3, 5.

$$w(x, y) = C_{11} \sin\left(\frac{\pi x}{a}\right) \sin\left(\frac{\pi y}{b}\right) + C_{13} \sin\left(\frac{\pi x}{a}\right) \sin\left(\frac{3\pi y}{b}\right)$$
$$+ C_{15} \sin\left(\frac{\pi x}{a}\right) \sin\left(\frac{5\pi y}{b}\right) + C_{31} \sin\left(\frac{3\pi x}{a}\right) \sin\left(\frac{\pi y}{b}\right)$$

Table 1 Statistical metrics comparision for different set of values of collocation points

7 × 7 10 × 10 20 × 20	w(x,y) (mm)	Mxx (kNm)	Myy (kNm)	Mxy (kNm)	Qx (kN)	Qy (kN)
R^2	0.9945 0.9987 0.9997	0.9926 0.9984 0.9997	0.9986 0.9973 0.9993	0.9972 0.0994 0.9999	0.9913 0.9972 0.9987	0.9843 0.9943 0.9969
RMSE	6.5e-5 3.1e-5 1.4e-5	0.8717 0.4023 0.1496	0.7822 0.3803 0.1942	0.4471 0.2042 0.0607	2.4099 1.3681 0.9323	2.5164 1.5107 1.1155
MAPE	0.0471 0.0245 0.0114	0.0818 0.0404 0.0163	0.0892 0.0452 0.0233	0.0346 0.0152 0.0056	0.0838 0.0945 0.1080	0.2075 0.2775 0.3317

$$+ C_{33} \sin\left(\frac{3\pi x}{a}\right)\sin\left(\frac{3\pi y}{b}\right) + C_{35} \sin\left(\frac{3\pi x}{a}\right)\sin\left(\frac{5\pi y}{b}\right)$$

$$+ C_{51} \sin\left(\frac{5\pi x}{a}\right)\sin\left(\frac{\pi y}{b}\right) + C_{53} \sin\left(\frac{5\pi x}{a}\right)\sin\left(\frac{3\pi y}{b}\right)$$

$$+ C_{55} \sin\left(\frac{5\pi x}{a}\right)\sin\left(\frac{5\pi y}{b}\right) \tag{30}$$

The values of the 9 coefficients in "Eq. 30" as calculated by regression technique for 20 × 20 collocation points on the plate are 2.9640208e-03, 6.4424703e-05, 2.5894828e-05, 6.0252573e-06, 2.0920067e-06, 8.40991446e-07, 4.94941828e-07, 3.91800948e-06, 1.69238072e-07. The coefficients are listed sequentially as shown in "Eq. 30". "Table 1" shows the comparison of statistical metrics for different values of collocation points along the plates.

From "Table 1" it is evident that increasing the number of collocation points on the plate increases the accuracy. However, after a certain extent the increase may not be much and hence can be restricted to a desired range by trial and error. As in the above case 20 × 20 points give the desired accuracy in comparison with the Navier's model.

Solving for the value of "c" in the "Eq. 25" with 20 × 20 collocation points on a square clamped plate of dimensions 4 × 4 m, t = 0.15 m, Po = 50 kN/m², E = 30 × 10^9 N/m², and ν = 0.3, using the least square method, we get a value of 5.09477e-6. The value of "c" as obtained from using the formula suggested in [3] is 7.1853e-6. The value of "c" increases to about 5.78e-6 with 200 × 200 collocation points and to 5.92e-6 with 500 × 500 collocation points. Thus, with an increase in the density of collocation points on the plate, the rate of increase in the value of the constant slows down significantly.

Consider a simply supported rectangular plate of 4 × 4 m, t = 0.15 m, E = 30 × 10^9 N/m², and ν = 0.3. It is subjected to a uniform loading of 50 kN/m² in a rectangular patch of an area of 2 × 2 m at the centre of the plate. Solving this problem with Navier's solution technique and the regression technique (20 × 20 points) for

up to the first four coefficients, i.e., for m and n = 1, 3 we get R-squared error and RMSE values of 0.97 and 0.000122 respectively. Increasing the collocation points up to 100 × 100, we get R-squared error and RMSE values of 0.99 and 3.45e-5 respectively. The deflection function for the above rectangular patch load problem is shown in "Eq. 31".

$$w(x,y) = C_{11} \sin\left(\frac{\pi x}{a}\right)\sin\left(\frac{\pi y}{b}\right) + C_{13} \sin\left(\frac{\pi x}{a}\right)\sin\left(\frac{3\pi y}{b}\right)$$
$$+ C_{31} \sin\left(\frac{3\pi x}{a}\right)\sin\left(\frac{\pi y}{b}\right) + C_{33} \sin\left(\frac{3\pi x}{a}\right)\sin\left(\frac{3\pi y}{b}\right) \qquad (31)$$

The values of coefficients $C_{11}, C_{13}, C_{31}, C_{33}$ calculated using the regression technique with 100 × 100 points on the plate are 2.91770373e-03, −3.76809053e-05, −3.76809053e-05, 3.75488349e-06 respectively.

Consider a simply supported rectangular plate of 4 × 4 m, t = 0.15 m, E = 30 × 10^9 N/m^2, and ν = 0.3. It is subjected to a uniform loading of 50 kN/m^2 in a circular patch of radius 2 m, having it's centre coincide with the centre of the plate. This problem cannot be solved with Navier's method. It is however possible to find the coefficients of "Eq. 31" for the circular loading with help of regression modelling. The coefficients $C_{11}, C_{13}, C_{31}, C_{33}$ for 100 × 100 points on the plate are 5.53611459e-03, 5.77005821e-05, 5.77005821e-05, −4.58416547e-06 respectively.

4.6 Findings from the Study

Relational models have been developed in the present study which relates moments, deflection, shear forces to loading intensity, plate rigidity and area of the plate. The deflection magnitude is directly proportional to the square of the area of the plate, and that of the moments to the area of the plate. Correspondingly, the partial differential equation of deflection is of fourth order and that of the moments is of second order. Also, a linear relationship exists between the quantities on left-hand side and right-hand side of the differential equations, for both, deflection and moments. These points can be considered as attributes of the differential equation under consideration.

The present study also helps us explore the use of regression modelling for solving the fourth order partial differential equation developed by Classical Plate Theory.

5 Conclusion

The relational models developed for deflection, moments, and shear forces help us to understand the variations in their magnitude with changes in the magnitude of loading, material properties, and area of the plate, provided the aspect ratio of the

plate is constant for the same boundary condition and similar loading condition. It helps in saving manual and computational effort while designing such thin plate structures.

The use of the regression method in order to solve the fourth-order partial differential equation can be used as a new alternative to the commonly used traditional methods like the Ritz method, the Galerkin method, and the Navier's method. The major advantage this method offers over the available traditional methods is that it can provide a solution for any irregular shaped transverse loading on a thin rectangular plate wherein it becomes impossible to solve using the traditional methods mentioned above. For such cases in regression modelling, it would involve using logic in implementation of code in any programming language using conditional formatting for assembling the matrix at different collocation points throughout the plate to cover the irregularity of the loading sufficiently enough to get the desired results. At present, only numerical methods offer such flexibility. However, regression modelling is much easier to understand and implement. The dependability of regression modelling on a predefined function satisfying the boundary conditions is a major limitation faced by this method, unlike the numerical methods used for solving the differential equations.

References

1. Nwoji, C.U., Onah, H.N., Mama, B.O., Ike, C.C.: Ritz variational method for bending of rectangular Kirchhoff plate under transverse hydrostatic load distribution. Math. Model. Eng. Probl. **5**(1), 1–10 (2018). https://doi.org/10.18280/mmep.050101
2. Ike, C.C.: Flexural analysis of rectangular Kirchhoff plate on Winkler foundation using Galerkin-Vlasov variational method. Math. Model. Eng. Problems **5**(2), 83–92 (2018). https://doi.org/10.18280/mmep.050205
3. Khan, Y., Tiwari, P., Ali, R.: Application of variational methods to a rectangular clamped plate problem. Comput. Math. Appl. **63**(4), 862–869 (2012). https://doi.org/10.1016/j.camwa.2011.11.051
4. Okafor, F., Udeh, O.: Direct method of analysis of an isotropic rectangular plate using characteristic orthogonal polynomials. Niger. J. Technol. **34**(2), 232 (2015). https://doi.org/10.4314/njt.v34i2.3
5. Zerfu, K., Ekaputri, J.J.: An approximate deflection function for simply supported quadrilateral thin plate by variational approach. In: AIP Conference Proceedings, vol. 1867, no. August (2017). https://doi.org/10.1063/1.4994417
6. Oba, E.C., Anyadiegwu, P.C., George, A.G.T., Nwadike, E.C.: Pure bending analysis of isotropic thin rectangular plates using third-order energy functional. Int. J. Sci. Res. Publ. (IJSRP) **8**(3), 254–262 (2018). https://doi.org/10.29322/ijsrp.8.3.2018.p7537
7. Liu, Y., Li, R.: Accurate bending analysis of rectangular plates with two adjacent edges free and the others clamped or simply supported based on new symplectic approach. Appl. Math. Model. **34**(4), 856–865 (2010). https://doi.org/10.1016/j.apm.2009.07.003
8. Markous, N.A.: Boundary mesh free method with distributed sources for Kirchhoff plate bending problems. Appl. Math. Model. **94**, 139–151 (2021). https://doi.org/10.1016/j.apm.2021.01.015
9. Guo, H., Zhuang, X., Rabczuk, T.: A deep collocation method for the bending analysis of Kirchhoff plate, February 2021. https://doi.org/10.32604/cmc.2019.06660

10. Dunlop, P., Smith, S.: Estimating key characteristics of the concrete delivery and placement process using linear regression analysis. Civ. Eng. Environ. Syst. **20**(4), 273–290 (2003). https://doi.org/10.1080/1028660031000091599
11. Ostertagová, E.: Modelling using polynomial regression. Procedia Eng. **48**, 500–506 (2012). https://doi.org/10.1016/j.proeng.2012.09.545
12. Kim, G.H., An, S.H., Kang, K.I.: Comparison of construction cost estimating models based on regression analysis, neural networks, and case-based reasoning. Build. Environ. **39**(10), 1235–1242 (2004). https://doi.org/10.1016/j.buildenv.2004.02.013
13. Maulud, D., Abdulazeez, A.M.: A review on linear regression comprehensive in machine learning. J. Appl. Sci. Technol. Trends **1**(4), 140–147 (2020). https://doi.org/10.38094/jastt1457

Underwater Strengthening of Tubular Joints of Fixed Offshore Steel Platform Using Grouted Clamps

Shikha Singh and Nirender Dev

Abstract Majority of offshore steel platforms in Mumbai High Field in Arabian Sea as well as around the world are about to reach their design life. To continue to operate the platforms after their design life, existing offshore platforms requires re-certification in every five years. Underwater & topside surveys are carried out to collect sufficient information for their engineering assessment. Platform is then analysed as per code API RP 2A criteria's for life extension. Mitigation for overstressed joints/members based on above analyses is performed and then recertification is provided to continue operation. Mitigation of underwater tubular joint is especially a major concern. Available standards/codes do not provide a detailed guideline for their strengthening measures.

This paper reviews the development of grouted clamp method for strengthening of overstressed joints without removal of existing member. Grouted clamps are bolted underwater with grout infilled in gap with structural member. In this proposed framework, In-place analysis of jacket structure is performed using SACS software to identify overstressed joints with environmental loads in present condition. Finite Element Analysis (FEA) software, ABAQUS, was used to build the computational model of the tubular joint with clamp which provides detailed stress distribution for the joints. The results from the investigation are discussed and conclusions are drawn about the applicability of the proposed framework for the strengthening of tubular joints.

Keywords Offshore steel platforms · Life extension · Finite Element Analysis · API RP 2A · Grouted clamp · Re-certification

S. Singh (✉)
Delhi Technological University, Delhi, India
e-mail: shikha.sgsits@gmail.com

N. Dev
Department of Civil Engineering, Delhi Technological University, Delhi, India
e-mail: nirendradev@dce.ac.in

1 Introduction

For oil & gas extraction, fixed offshore steel platforms are the most common type of structure installed at sea having shallow water depths, it comprises of mainly three parts, Jacket (Underwater structure), Deck (Above water topside structure) & foundation. Oldest platforms installations have reached their design life and therefore require life extension assessment through re-certification in every five years. Requalification of platform is performed as per API RP 2A design criteria [1], with additional loading of new facilities at top and considering any damages in underwater structure. Assessment may result into the requirement of strengthening or modifications for the requalification of platform.

Under water structure, jacket is the portion which is most difficult to repair on damage. Damages like hole, crack, dent, etc. due to incident like drop of any item, excessive corrosion or sometime jacket members get overstressed due to excessive increase in topside loading which happen due to modification at top during the life of the platform. This paper intend is to provide strengthening of the overstressed underwater tubular joint using grouted clamp method in a Jacket structure of the fixed offshore steel platform that is located in the in Mumbai High Field in Arabian Sea.

Grouted clamp is provided at the location of Member/Joint, which requires strengthening. The annular space created by the clamp is filled with grout. Bolts are fully tightened prior to injection of grout into the annular space between the sleeve and the existing tubular member, the grout/steel interface is not therefore stressed. Using grout allows for larger annular tolerances, along member imperfections, enabling even load transfer along the repair. The means of load transfer is via bond and interlock between the grout/steel interface [8].

2 Analysis of Jacket Structure for Requalification

2.1 General

Assessment of existing fixed offshore steel platform is carried out in SACS software as per criteria of API-RP-2A [1] in three stages. First stage involves In-Place analysis which is carried out to simulate the behaviour of the structure as close as possible to give the response of the structure during its service and it is performed with 85% of environmental load at design level and overstressed Joints/Members are identified from the analysis. Further in second stage, these overstressed members & joints are to be checked in In-place analysis with 100% of environmental load at ultimate level. In the final stage overstressed joints and members identified in ultimate level check are further assessed by performing Non linear analysis in SACS, where incremental environmental loading is applied on the structure till it collapses and reserve strength of the structure is achieved. RSR is defined as the ratio of a platform's ultimate lateral

load carrying capacity to its 100-year environmental condition lateral loading [7]. If RSR of the structure is less than the desired criteria of API RP 2A, then strengthening of overstressed members & joints identified during ultimate analysis is provided to achieve the desire Reserve strength ratio (RSR).

2.2 Structural Model

The Jacket structure analysed is comprised of a 4-legged Well platform in Mumbai high field. It is located in a water depth of 76.00 m. An In-place analysis of the jacket using SACS computer programme has been carried out in order to evaluate the structural adequacy of the jacket in accordance with API-RP2A. Overall view of Offshore Platform is shown in Fig. 1.

2.3 Design Environmental Conditions

The analysis has been carried out for both (100- years return period) extreme storm and (1-year return period) operating storm condition with wave, current and wind from 8 directions with all topside deck dead loads and live loads. The environmental loadings were applied to approach angles from 0 to 315° at 45° intervals as shown in Fig. 2. Still water depth has been taken as (CD) + (LAT) + (50% of Astronomical Tide) + (Storm Surge) for Storm Environment. Metocean data used for the in-place analysis of jacket structure are as shown in Tables 1 and 2 [6].

2.4 Requalification Analysis Results

The result of the design level analysis shows that Joint 1934 is overstressed & has high Joint UC of 2.05. In order to requalify the platform, it is proposed to strengthen the overstressed joint as shown in Fig. 3 through infilling the chord and X-joint grouted clamps. To simulate the clamp in analysis, the members are modelled as concentric tubular at the clamp location with axial, torsional and bending stiffness properties modified, considering the grouted clamp and infill grout stiffness.

Fig. 1 Overall view of offshore platform
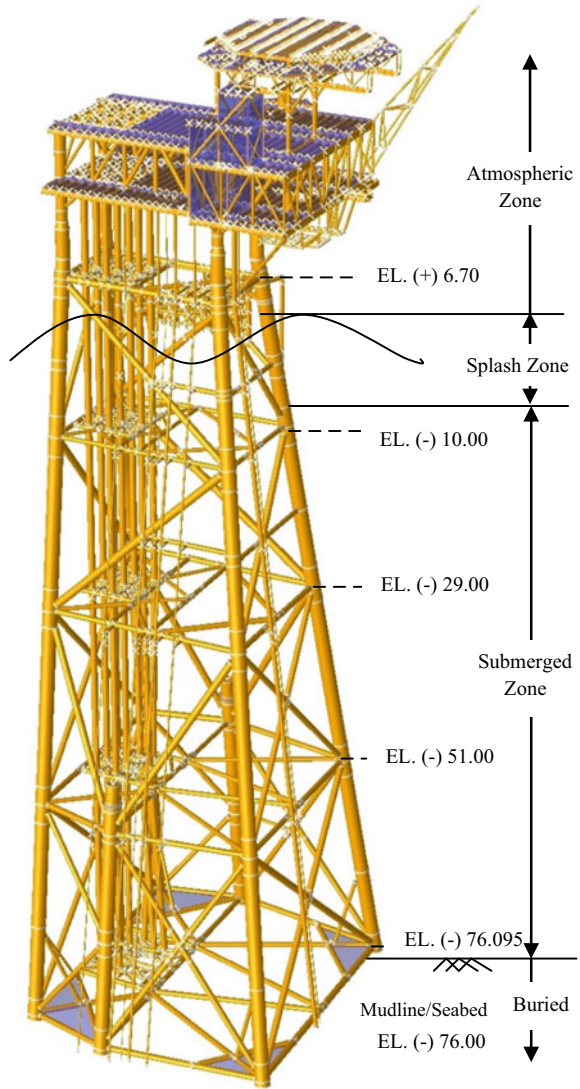
3 Platform Anomalies Based on Requalification Analysis

The following are descriptions of the area that require repair based on In-Place analysis are shown in Table 3. We aim to solve this problem by using grouted clamps as described below.
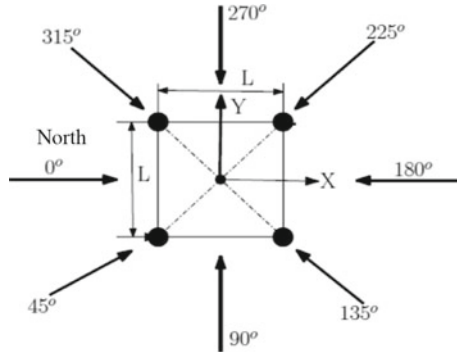
Fig. 2 Wave approach directions

Table 1 100-year wave and wind data

Wave/Wind approach direction								
	0	45	90	135	180	225	270	315
100 Year Wave Maximum Height (m)	15.09	16.77	17.07	17.68	18.00	14.48	13.26	16.00
100 Year Wave Period (Sec)	13.00	13.70	13.90	14.20	14.40	12.50	11.80	13.80
Still Water Depth (m)	78.26	78.44	78.56	78.81	78.81	78.26	78.26	78.26
1-h wind speed (km/h)	187	179	176	182	192	192	192	192

Table 2 100-year current profile

Elevation	Current Speed (m/s)							
	Approach direction							
	0	45	90	135	180	225	270	315
100-Year Current								
Bottom	0.51	0.31	0.213	0.27	0.37	0.31	0.25	0.25
Y-1/4	0.97	0.69	0.609	0.66	0.81	0.72	0.65	0.65
Y-1/2	1.19	0.86	0.75	0.82	1.02	1.20	0.83	0.82
Y-3/4	1.40	1.02	0.90	0.99	1.21	1.08	0.95	0.98
Surface	1.64	1.23	1.09	1.18	1.45	1.27	1.16	1.22

4 Description of Grouted Clamps

4.1 General

The overstressed joints are strengthened by infilled of the chord and joint clamp. Grouted clamp alone at joint is not enough to reduce the joint UC < 1.0, hence

Fig. 3 Proposed
strengthening (Row A)
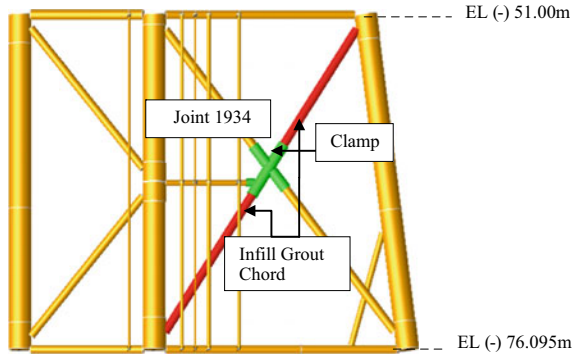
Table 3 Description of area to be strengthened at platform

No.	Description
1	Joint 1934 to be strengthened (UC = 2.05)
	X-Joint no.1934 on Row-A between El (-) 51.00 m and El (-) 76.095 m

Table 4 Material properties

Steel	Grout	Bolt
Elastic Modulus = 200 Gpa Yield Strength = 345 MPa for clamp/248 for existing member	Elastic Modulus = 53 GPa Compressive strength = 140 MPa	ASTM A193 B7 and compatible ASTM A194 nuts and ASTM F436 washers

additional strengthening in the chord member at X –brace location is provided by infill grout. The infilled grout will help reduced the chord ovalization that reduced the joint stress. Moreover, the chord grouting reduces the brace member forces, that in turn reduces the joint stress. There is one infilled chord and one grouted clamp in this jacket. The length of the grouted clamp is designed to avoid the clashing adjacent members, but also provide sufficient encasement. The grouted clamp is designed with 20 mm thickness, the similar steel thickness of the jacket joint-can of 25 mm. The advantage of using a grouted clamp for this application is that it allows the installation and construction tolerance of 75 mm, which is grout thickness. Example of grouted clamp is shown below in Fig. 4.
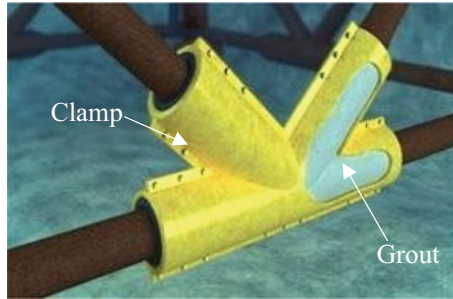
Fig. 4 Grouted clamp (Foundocean)

4.2 Clamp Details

The clamps sections shall be bolted together to form full circle clamp around existing members. The bolts in the grouted clamps have been selected based on requirements in AISC, RCSC "Specification for Structural Joints Using ASTM A325 or A490 Bolts" [5]. After all the bolts are fully tightened to the designed torque levels, the annulus gap shall be fully grouted with ultra-high strength grout. The bond strength between the grout and steel is calculated based on the design guidelines Sect. 2.2 of HSE Offshore Technology Report OTO 2001/016 on Pile/Sleeve Connection [3].

The overall installation sequence is outline as below:

i.   Clean the jacket member in the area intended for clamp installation.
ii. Installed the clamp and new member.
iii. Bolts are then pre-tensioned to the desired torque; no additional tightening is required after the design torque level is achieved.
iv. Adjust the centralizers to ensure that a uniform grout thickness not less than 50 mm is achieved.
v.   Install the cover plates and rubber seals at the bottom and top of clamp.
vi. Fill the annulus with grout.

5 Finite Element Analysis for Strengthening of Jacket Structure

Member forces and moments are extracted from Re-qualification analysis are utilised to design the grouted clamps by using finite element method. These clamps are then modelled in the SACS file to check the actual redistribution of forces based on strengthening provided to joints and connected members with following analysis criteria's.

5.1 Analysis Criteria

The detail stresses in the grouted clamp sections is analysed using finite element analysis in conjunction with member UC checks using SACS software. Multipurpose finite element analysis software ABAQUS 6.14 is used for this aspect of the analysis. The FEA analysis provides the detailed stress distribution and the bolt load checking. The modelling strategy has been derived based on the below criteria:

1. Member forces and moments are extracted from SACS analysis and applied to the FEA model. Loads are applied at discreet points employing the same coordinate nomenclature as the SACS model.
2. In FEA modelling, steel members and clamps are modelled as Shell Elements S4R, whilst grout is modelled as Solid elements C3D8R. Maximum mesh is 80 mm in size. For the clamp arm, bolt holes and stiffeners, the mesh size is approximately 50 mm.
3. Steel is modelled as an elastic material. Grout is modelled by using Damage Plasticity material model considering crushing and cracking of the grout.
4. The interface between grout and steel is modelled using Surface to Surface (master–slave) contact interaction. In this interaction, there are two interfaces; the vertical and tangential interfaces. The vertical interface is modelled as "hard contact", and tangential interface is modelled as frictional contact. In the hard contact, there will be a "contact pressure" between two surfaces as a function of the "overclosure". Depending on the contact pressure and frictional coefficient, there will be Coulomb frictional stress between the two surfaces. In tangential interface, there is also cohesive bond between steel and grout. The cohesive bond strength is according to Sect. 2.2 of HSE Offshore Technology Report OTO 2001/016 on Pile/Sleeve Connection [3]. Similar interface between steel and steel, but there is no bonding.
5. Bolts are modelled individually and tied to two faces of the half clamps.
6. The analysis enables assessment of the detailed stress distribution in the member, clamps, grout and bolts.

5.2 Material Properties

Material properties used for the finite element analysis are as follows (Table 4):
   Interface between Steel and Grout:

Friction coefficient (steel-steel)   = 0.40 (DNVGL-ST-0126) [9]
Friction coefficient (steel-grout)   = 0.70 (DNVGL-ST-0126) [9]
Behaviours   = Hard contact, allow for separation.
Bond strength   = 0.19 MPa (Plain bond).

5.3 Design Strength

5.3.1 Steel Strength

Steel allowable stresses are calculated based on API RP2A-WSD [1] Clause 4.3.2; Fy/FS = 0.625Fy, using FS = factor of safety = 1.60. One-third increase in the allowable stresses is applied for 100-year extreme storm condition as per API RP 2A-WSD Clause 3.1.2.

$$\text{Allowable stress} = S = 1.33 \times 0.625$$
$$Fy = 288\,\text{MPa(for Fy} = 345\,\text{MPa, New steel for Clamp)}$$
$$= 240\,\text{MPa(for Fy} = 289\,\text{MPa, existing member)}$$
$$= 207\,\text{MPa(for Fy} = 248\,\text{MPa, existing member)}$$

Member stress: Overall member stress = S = 288 MPa.

Local stress: Due to localized effect = 1.5 × S = 431 MPa.

Peak stress: = 2.0 Fy or 3 S = 690 MPa.

The stress due to the global axial and bending is classified as the member stress, which is the typical UC check in SACS is used. The element may have additional stress due to the local bending, the combined stress of the member/membrane stress with the local bending stress are to be checked with local stress. Additionally, there will be peak stress at the load concentration location. The peak stresses have to be within the small localized zone. Peak stress zones should not be more than Sqrt (Rt) for tubular member, i.e. 80 mm for tubular member of the member 660 mm diameter is 19 mm thickness. The peak stress and local stress is partially due to nature of FEA analysis and will not have a bearing on the overall integrity of the structure.

5.3.2 Grout Strength

The grout stress is checked by ISO 19902 [2] and DNVGL-ST-0126 [9] as below.

Mean compressive strength : fcm = 140 MPa.

Standard deviation : θ = 5 MPa.

Characteristic compressive strength : fck = fcm - 1.64 θ = 131.8 MPa (ISO19902 Eq. 19.6–20) [2]

Characteristic in-situ compressive strength : fcN = 0.85 fck (1-(0.85fck)/600).
= 91.1 MPa (DNVGL-ST-0126 Cl 6.3.2.3) [9]

Material safety factor : γm = 1.5 (DNVGL-ST-0126 Cl 6.3.2.6) [9]

Design compressive strength : fcd = fcN/ γm = 60.7 MPa.

Design Elastic Modulus $= 1.1 \times 22\ (91.1/10)0.3$
$$= 46.95\ \text{GPa (EN 1992 3.1.3) [2]}$$

5.3.3 Bolt Loads

High strength hexagonal A193 B7 bolts are to be used for connecting the clamp sections. Bolts with 1-inch in diameter are used. AISC bolt design is followed.

Diameter of bolt $= 25.4$ mm (1" bolt).
Nominal strength $= 645$ Pa (A193 B7 bolts) (Table J.3.2 AISC 360) [4]
Bolt capacity $= 327$ kN (Tension) | 196 kN (Shear).
Factor of safety $= 2.0 / 1.333 = 1.5$ (AISC 360, J3-1) [4]
Allowable load $= 218$ kN (Tension) | 130 kN (Shear).
Bolt Pretension value $= 229$ kN (Table J3.1 AISC 360) [4]

5.4 Description of Finite Element Model

The sub-model for the grouted clamp is modelled as shown in Fig. 5. The clamp is encased to the jacket members by two halves sections. Each arm of clamp is designed to have sufficient length to encase the member, it is about the 2.5 times the member diameter, 2.0 m from the joint centre. The members are modelled 1.0 m extended from the clamp end, that to have sufficient structural discontinuity. Individual parts are modelled such as brace members, the two clamp sections, the grout in the clamp, the infilled grout and bolts. Figure 5 shows the individual part in difference colours. The two clamp sections are assembled by using high strength bolts which are modelled individually and tied to two faces of the half clamps as shown in Fig. 6. The bolts are designed as 1-inch in diameter. The maximum mesh size is 80 mm as shown in Fig. 7.
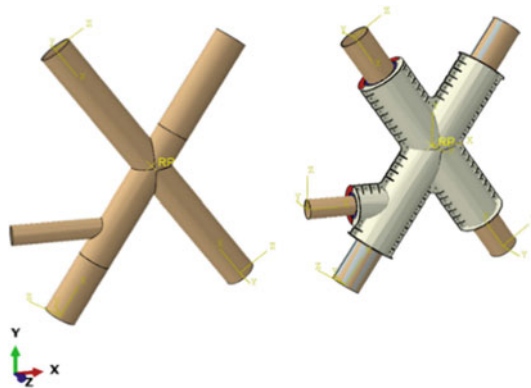
Fig. 5 FEA Model
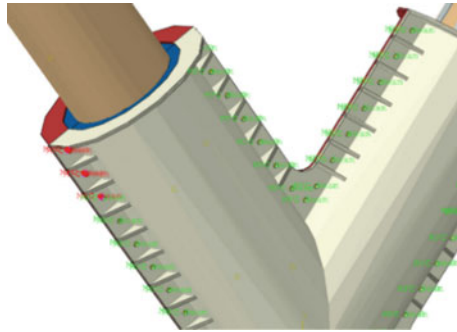
Fig. 6 Detail of Bolt in the model; tied to the two half faces of clamp in the model
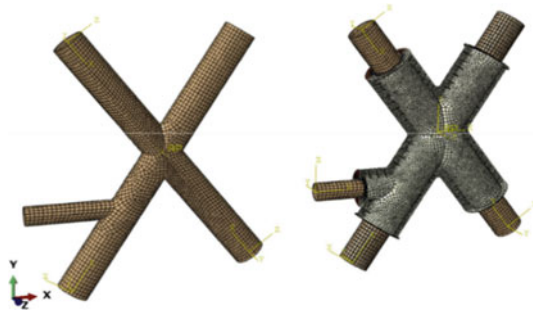
Fig. 7 Mesh in the model

5.5 Loading and Boundary Conditions

The load extracted from the SACS analysis applied to the finite element model were as shown in Table 5. The bottom edge of the chord is fixed as shown in Fig. 8. The loads are applied at respective arm with their local coordinate system.

5.6 Finite Element Analysis Results

5.6.1 Analysis Results in Original Condition

The stresses induced in the jacket member and joint are shown in Fig. 9. The maximum stress is 440.1 MPa in the mid-plane on the brace side. The member is with a yield strength of 248 MPa and allowable stress is 207 MPa. SACS provided the joint UC of 2.05 for this joint. When accounting for local bending due to the chord ovalization, the maximum stress is 885.8 MPa on the joint, Fig. 10. The stress plotted is MisesMax which is the maximum Von Mises stress out of all layers (planes)

Table 5 Load extracted from SACS and Applied on the Joint 1934 model

SACS member	Member	Case	Forces (kN)			Moment (kN-m)		
			Fx	Fy	Fz	Mx	My	Mz
0474-1934	Brace-1	Original	5580.2	36.4	−34.1	1.0	−255.4	228.3
		Strengthened	4084.6	31.0	−51.3	0.3	349.1	206.1
0473-1934	Brace-2	Original	6078.7	−34.9	−59.1	-17.5	−212.6	−256.7
		Strengthened	4846.5	−28.6	−72.3	-17.9	−302.5	−207.4
0421-1945	Brace-3	Original	437.2	18.0	−28.1	1.7	−82.9	76.2
		Strengthened	751.9	10.8	−40.3	0.9	−118.4	61.2
1934-0448	Chord-1	Original	−4829.9	−41.7	−60.6	37.5	350.5	270.1
		Strengthened	−6773.1	−53.8	−67.5	61.5	591.0	352.9
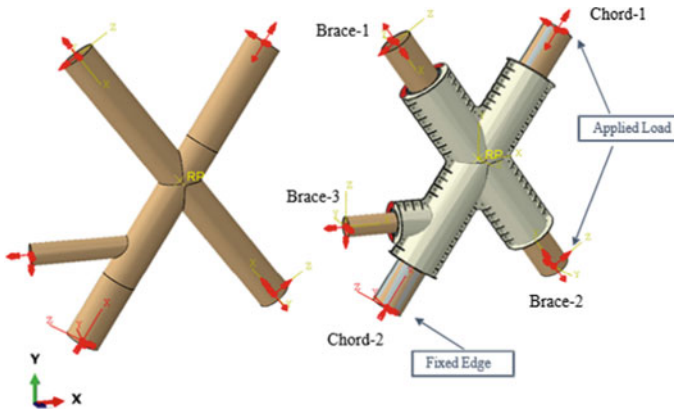
Fig. 8 Load and Boundary conditions applied in the model

through the steel shell thickness. That chord section with a yield strength of 289 MPa, allowable stress is S = 240 MPa and 1.5 S = 360 MPa.

Figure 11 show the stress area that is higher than 360 MPa in grey. The overstressed zone is extended for about 600 mm, that is much more than allowable peak stress zone of 90 mm. This Original joint stress level is not compliance to the design requirement.

5.6.2 Analysis Results in Strengthened Condition

The maximum stresses induced in the jacket member after strengthening are shown in Fig. 12 and Fig. 13 for mid plane stress and MisesMax stress respectively. There is not significant difference in term of the two stresses levels since the member stress is dominant and localized stress are largely arrested. The maximum stress is 198.1 MPa
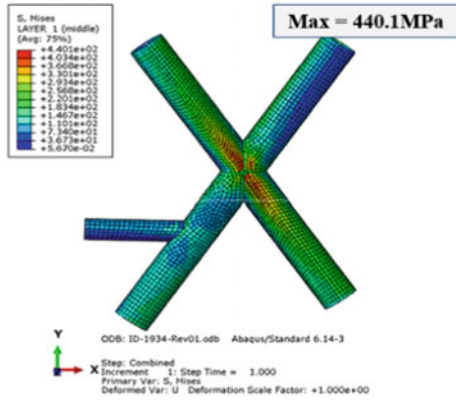
Fig. 9 Stresses in the joint 1934 in Original condition (Mid-plane stress)
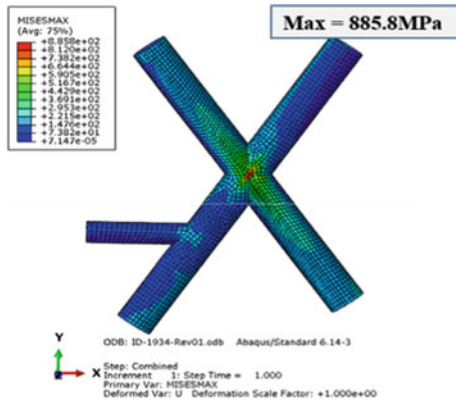
Fig. 10 Stresses in the joint 1934 in Original condition (Mises Max)
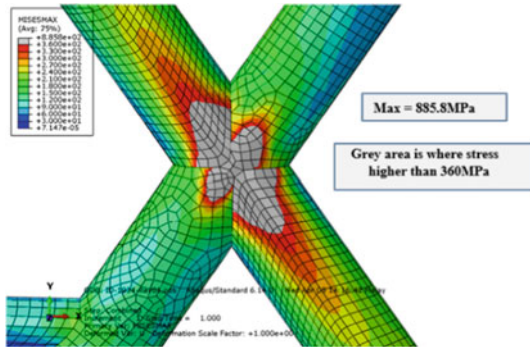
Fig. 11 Stresses in the joint 1934 in Original condition (MisesMax) Stress limited to 360 MPa (1.5S)

in the Brace-2, the brace UC in FEA is 0.96 by taking allowable stress of 207 MPa. SACS provided this member UC = 0.89 before reaching into the clamp.

The stress in the joint is shown in Fig. 14. The mid-plane stress is 154.2 MPa & MisesMax is 199.3 MPa. The stress in the chord of the joint is shown in Fig. 15. The mid-plane stress is 146.6 MPa & MisesMax is 185.2 MPa. All of them are within the allowable stress level of 1.0S. UC of the joint in the brace could be translated to 0.74. SACS reported as 0.95.

The stress in the clamp of Joint-1934 is shown in Fig. 16, the maximum stress is 105.7 MPa in the clamp, which is well within the design allowable stress of 288 MPa, the translated UC to be 0.37.

There are 74 numbers of 1" in diameter bolt in the clamp. The bolt load distribution in the clamp is shown in Fig. 17. The maximum bolt load is 52.1 kN (Tension) and 6.5 kN (shear); that is at the corner edge of the clamp. They are within the respective allowable bolt load of 218 and 130 kN.
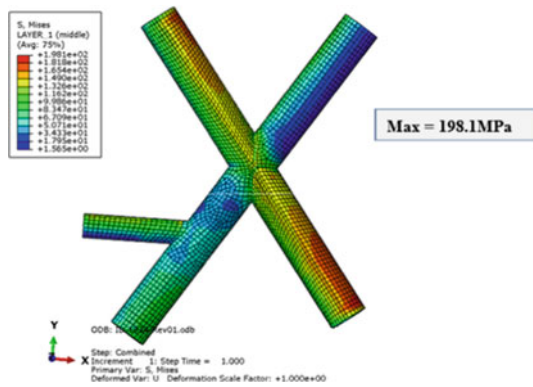
Fig. 12 Stresses in the joint 1934 after strengthening (Mid-plane stress)
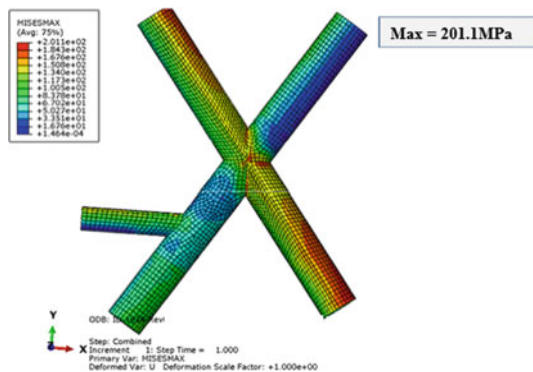
Fig. 13 Stresses in the joint 1934 after strengthening (Mises Max)
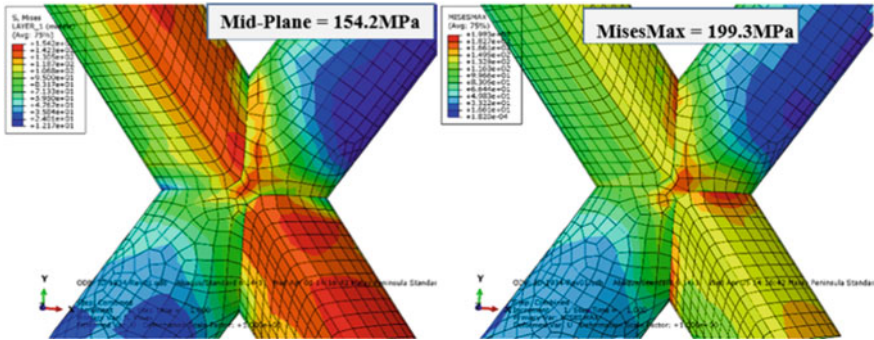
Fig. 14 Stresses in the joint 1934 after strengthening (Mid-plane vs MisesMax)
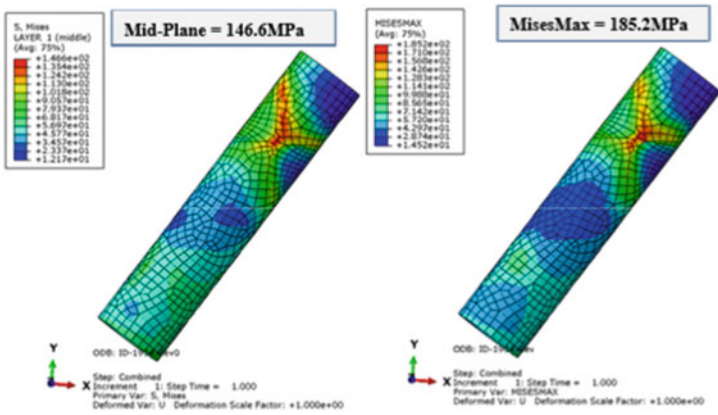
Fig. 15 Stresses in the Chord of Joint 1934 after strengthening (Mid-plane vs MisesMax)
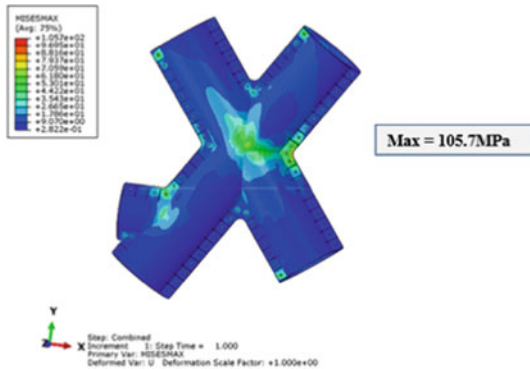
Fig. 16 Stresses in the clamp of Joint 1934
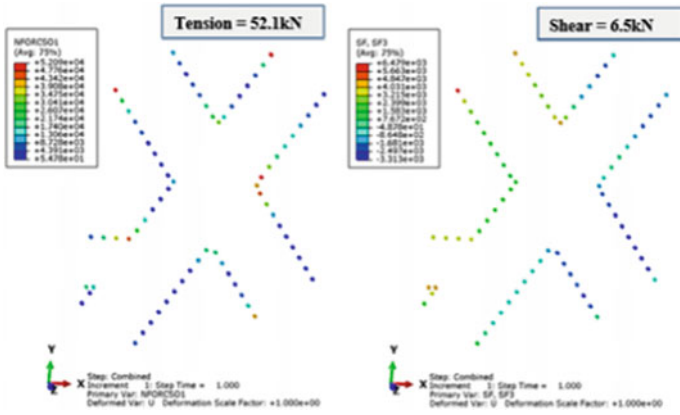
Fig. 17 Bolt Loads in the Clamp at Joint 1934
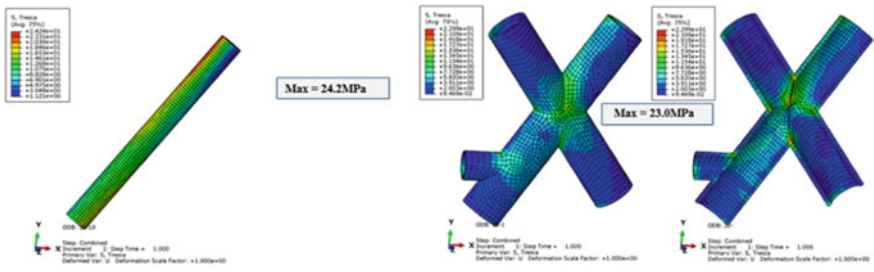
Fig. 18 Stresses in the Grouts at Joint 1934

Table 6 Summary of results for joint 1934

Item	Maximum	Allowable
Joint Stress (brace)	154.2 MPa	207 MPa
Joint Stress (chord)	146.6 MPa	240 MPa
Steel Clamp	105.7 MPa	288 MPa
Grout	24.2 MPa	60.7 MPa
Bolt	52.1 kN	218 kN

The maximum stress in the grout are 24.2 MPa and 23.0 MPa at the infilled grout and the clamp grout respectively as shown in Fig. 18. It is within the allowable stress of 60.7 MPa.

The joints and the clamps are within their permitted allowable stress levels, as well the grout and bolts. Summary of the results are tabulated in Table 6.

6 Results and Conclusions

Member code check were done in accordance to API RP 2A [1]. Infill grouted member was code check in accordance to ISO 19902:2007 [2] as there is no provision in API RP 2A for this. The overstressed joints have been strengthened to have them compliance to the design requirement. Table 7 lists the joint UC for joint 1934 in original and strengthened Condition from that it is observed that UC for the Joint 1934 is less than 1.00 in strengthened condition.

Based on the analysis, it is also learned that critical member UC for the X-brace members at joint 1934 was reduced. Infill grouted the chord member has significantly reduced the member UC > 1.00 to UC below 0.80. Stiffness of the chord member increased, causing more load attraction and at the same time reducing the brace member loading. It is shown that the member capacity in axial compression and bending increased after infill grouting and all design loading (Original and strengthened condition) are within the member capacity. Summary of the member UC's of adjacent members to the Joint 1934 are tabulated in Table 8.

Table 7 Joint UC for Joint 1934 and Joint 1948 (Original and Strengthened condition)

Joint	Chord	Brace	Chord		Brace		Maximum Joint UC	
			Dia. (mm)	WT (mm)	Dia. (mm)	WT (mm)	Original	Strengthened
1934	1945	0473	660.0	25.0	660.0	19.0	2.05	0.95
	0448	0474	660.0	25.0	660.0	19.0	1.88	0.80

Table 8 Summary of member UC for X-brace at Joint 1934

Member	Condition	Member Size	UC
0420-1945	Original	Ø660 × 19 mm	1.00
	Strengthened	Ø660 × 19 mm/Ø850 × 20 mm + Infill Grout	0.57
1945-1934	Original	Ø660 × 25 mm	0.83
	Strengthened	Ø660 × 25 mm/Ø850 × 20 mm + Infill Grout	0.64
1934-0448	Original	Ø660 × 25 mm	0.77
	Strengthened	Ø660 × 25 mm/Ø850 × 20 mm + Infill Grout	0.66
0448-0472	Original	Ø660 × 19 mm	1.12
	Strengthened	Ø660 × 19 mm/Ø850 × 20 mm + Infill Grout	0.73
0473-1934	Original	Ø660 × 19 mm	1.03
	Strengthened	Ø660 × 19 mm/Ø850 × 20 mm	0.37
0474-1934	Original	Ø660 × 19 mm	0.97
	Strengthened	Ø660 × 19 mm/Ø850 × 20 mm	0.34
0421-1945	Original	Ø406 × 12.7 mm	0.44
	Strengthened	Ø406 × 12.7 mm/Ø596 × 20 mm	0.16

Based on the above results it can be concluded that, Overstressed joint of the jacket structure can be strengthened with the proposed grouted clamp arrangement and Re-qualification analysis with this strengthening shall be acceptable for re-certification to continue operation of the platform after its design life.

References

The following codes, specifications, standards and references were used in the analysis for structural strengthening of the platform.

1. API Recommended Practice for Planning, Designing and Constructing Fixed Offshore Platforms–Working Stress Design, API RP 2A-WSD, 21st Edition
2. ISO/BS-EN 19902: Petroleum and natural gas industries–Fixed steel offshore structures
3. HSE Offshore Technology Report OTO 2001/016 on Pile/Sleeve Connection (2002)
4. AISC 360-10 American Institute of Steel Construction, Specification for Structural Steel Buildings, Allowable Stress Design and Plastic Design, 22 June 2010
5. AISC, RCSC: Specification for Structural Joints Using ASTM A325 or A490 Bolts (2004)
6. Environmental data based on document Notice Inviting Expression of Interest (EOI) for Hiring of Mobile Offshore Production Unit (MOPU) in Kutch Offshore, 29 August 2017
7. Chakrabarti, S.: Handbook of Offshore Engineering. Elserveir Ltd. (2005)
8. Life Extension Solutions for Offshore Structures and Pipelines, Foundocean
9. DNVGL-ST-0126: Support structures for wind turbines

Finite Element Analysis and Parametric Study of Concrete Beams Under Impact Loading

Arya Sajith and Shilpa Pal

Abstract The focus of the present study is to do a finite element analysis of concrete beams under impact loading. For this, velocity impact simulations have been done in ANSYS Explicit dynamics module and the behaviour of the concrete beams have been studied from the deformation and stress response so obtained. Detailed parametric study has been done by focusing on the height of the impact, shape of the impactor, material of the impactor, position of the impact and grade of concrete. It is found from the results that as the height of impact increases the residual strength of the beam decreases. Higher grade of concrete has more strength against deformation and that the box impactor and central position of impact increase the deformation of the beam. From the study it can also be inferred that Finite Element Modelling can be used in accurately determining the behaviour of concrete beams under impact load at an early design stage itself.

Keywords Velocity impact · Finite element analysis · Explicit dynamics

1   Introduction

Impact load analysis has a wide range of application in Civil Engineering. Many researchers have been exploring the behaviour of concrete structures under extreme loads like impact, earthquake etc. using Finite element modelling (FEM). Impact load analysis helps in understanding the impact resistance of a structure which is the ability to absorb and dissipate energy without causing damage to the structure due to an impulsive dynamic load which occurs in a short time. Impact load arises in various situation such as a structure when is hit by a vehicle, a marine structure subjected to ice load as an impact, aircraft crashes, accidental drop weights and terrorism attacks [2, 7]. ANSYS is an important tool of FEM package which can be used to simulate impact load in a structure to understand its behavior and the impact resistance of it [4].

A. Sajith (✉) · S. Pal
Delhi Technological University, Shahabad Daulatpur, Main Bawana Road, Delhi, India
e-mail: aryasajith@gmail.com

Abdel-Kader and Fouda performed the projectile impact test on concrete slab made with reinforcements arranged in different alignment to observe the influence of the ratio and type of reinforcement on the performance of concrete [1]. Anil et al. studied the effect of variation of the support conditions on the behaviour of slabs subjected to impact loads. Experimental study and numerical study was done by varying support type and support layout [2]. Singh et al. focused on low and high-velocity impact simulations on reinforced concrete beam and slab to study the impact resistance of geopolymer reinforced concrete. The study concluded that geopolymer concrete has better impact resistance compared to conventional concrete [9]. Very few studies have been carried out to understand the behaviour of plain concrete beams under impact load. This paper focuses on studying the effect of impact load under various parametric conditions to analyse how the strength of the beam is affected.

2 Specimen Configuration and Parameters

To analyse the effect of impact load on concrete beams, a concrete beam of size 150 × 150 mm with a clear span of 700 mm was modelled in commercially available ANSYS software. The important parameters considered for the parametric study were the effect of grade of the concrete beam, position of impact, shape of the impactor, height of the impact and material of the impactor.

2.1 Properties of the Beam and the Impactor for the Parametric Study

Three different grades of concrete (M25, M30 and M40 grade) have been used to compare the effect of impact load on different grades of concrete. The detailed properties of both the grades are mentioned in Table 1 [2, 6, 9].

Three different positions of impact have also been used to study how and where the maximum deformation happens after impact. For this, the impact position used were centre, 1/3rd distance from the right and 1/3rd distance from the left (Fig. 1).

Table 1 Properties of different grades of concrete

Properties	M40 grade	M30 grade	M25 grade
Density	2400 kg/m^3	2340 kg/m^3	2314 kg/m^3
Poisson's ratio	0.15	0.2	0.18
Young's modulus	31.62 GPa	30.91 GPa	26.432 GPa
Shear modulus	13,749 MPa	12,879 MPa	11,200 MPa
Bulk modulus	15,058 MPa	17,172 MPa	13,767 MPa
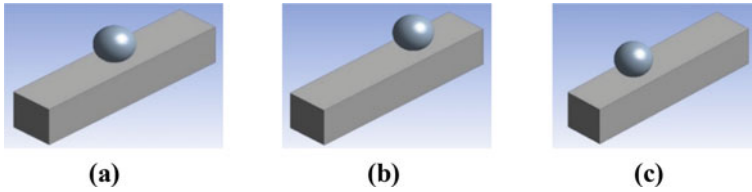
Fig. 1 **a** Centre impact **b** 1/3rd from right **c** 1/3rd from left

Table 2 Properties of the impactor

Properties	Steel	Copper alloy	Gray Cast Iron
Density	7850 kg/m^3	8300 kg/m^3	7200 kg/m^3
Poisson's ratio	0.3	0.34	0.28
Young's Modulus	200 GPa	110 GPa	110 GPa
Shear modulus	166,670 MPa	114,580 MPa	83,333 MPa
Bulk modulus	76,923 MPa	41,045 MPa	42,969 MPa

The default shape used for the study was a spherical ball [3]. The dimension of the ball taken was 13 cm in diameter and 5 kg in weight. This size of the impactor was taken in accordance with the ACI code drop weight test. In order to study the effect of different shape of the impactor, a box type hammer impact was also used in analysis. The dimension of the box impactor used is 6 × 6 × 32 cm. The beam was also fixed on opposite sides along the length to do a comparison on how impact load affects for different boundary conditions.

In order to analyse the effect of impact load from different heights of impact on the residual strength of the beam, three different heights (3, 2.5, 2 m) of impact have been considered [5]. For the purpose of the parametric study on material of the impactor, different materials like steel, copper and cast iron balls were also used. The general properties of the materials used as impactor is given in Table 2.

3 Finite Element Modelling of Impact Load

Finite element analysis can solve structural problems and evaluate the capability for service, failure analysis, fatigue life or performance design optimization. In the present study, FEM has been done using the explicit dynamics module in ANSYS software. Explicit dynamics is a system component of the ANSYS workbench. It can be used to simulate responses of highly transient, nonlinear physical phenomena
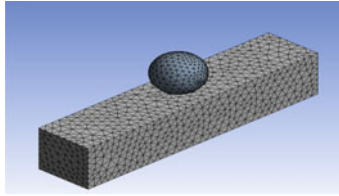
Fig. 2 Meshing

like drop test and high speed impact. The steps involved in finite element modelling in ANSYS are:

- Adding material properties and creating the model geometry
- Create meshing and body interaction
- Analysis and data collection

3.1 Meshing of the Model

After the geometry of the model was created, the next step is to assign the materials to the elements and create meshing. Meshing is the process of dividing a geometric shape into thousands of little pieces to properly define the shape of the object and to give a more accurate analysis and result. For this, a meshing of 20 mm was done for the model as shown in Fig. 2 as per the mesh convergence study.

3.2 Body Interaction

The body interaction folder under connections is used to define a global connection option for explicit dynamics. They are used to give surface to surface contact between two different materials [4]. They body interactions available are mainly bonded, frictional, frictionless and reinforcement. In the present study, frictional body interaction has been assigned to the model.

3.3 Velocity

The two main values important in creating an impact load in ANSYS is velocity and end time. Impact testing are divided into two types based on velocity namely, low velocity impact by a large mass and high velocity impact by a small mass [8]. Here low velocity impact (drop weight test) is used. Once the meshing and body interaction has been assigned, end time is provided under the initial analysis option. In this study,the

Table 3 Effect on grade of concrete due to impact

Grade of concrete	Deformation in mm	Stress in MPa
M25	1.2248	317.77
M30	1.1004	251.79
M40	1.0686	238.00

end time given was 0.35 milli-s. This value was chosen as the maximum deformation for the impact was obtained during this end time. The velocity determines the force of impact. To find the velocity, Eq. (1) was used.

$$v = \sqrt{2gh} \tag{1}$$

where h is the height of impact. Hence, 7672, 7003 and 6264 mm/sec were used as the velocities.

4 Results and Discussions

The powerful FEM tool ANSYS has been used to study the behaviour of plain concrete beam under impact load for different parameters to know the effect of it on the beam. Total deformation and equivalent stress have been used to study the behaviour of beam. The results obtained after analysis are shown below.

4.1 Effect of Grade of Concrete

Grade of concrete is referring to the strength of concrete used during construction. It is very important as it plays an important role in ensuring the efficiency of a structure. It helps in preventing collapse by ensuring the strength required. Three grades of concrete namely M25, M30 and M40 have been used to compare its effect on the beam under ball impact load. It is observed that there is a 10% decrease in total deformation for M30 and 13.6% decrease for M40 which showed that the total deformation decreases when grade of concrete is increased (Table 3).

4.2 Effect of Different Position of Ball Impactor

A spherical steel ball of 5 kg when dropped to a M30 grade concrete beam from 3 m height, three different positions of impact has been analysed. It can be concluded that in a structural element the effect of damage due to impact is more when the impact

Table 4 Effect of position of impact

Position of ball impact	Deformation in mm	Stress in MPa
Centre	1.1004	251.79
1/3rd from left	0.96842	191.15
1/3rd from right	0.99902	241.39

Table 5 Effect of boundary condition

Boundary condition	Deformation in mm	Stress in MPa
Fixed on opposite sides along the length	0.85428	578.22
Free on all sides	1.1004	251.79

load is applied on the centre (12 to 16%) as compared to the impact applied on the ends (Tables 4 and 5).

4.3   Effect of Shape of Impactor

The shape of impactor used for the study was a spherical ball. In order to compare the effect of shape, a box type impactor has been used. For comparison, the volume of both the impactors have been kept same. It was observed that the box type impactor damages the concrete beam more than the ball impactor (Fig. 3).

4.4   Effect of Boundary Condition

Different boundary conditions can be assigned to a beam to analyse the extend of deformation. In this study, the boundary condition used is fixing the beam on its opposite sides along the length. It can be concluded that the deformation reduces upto 25% when opposite sides are fixed.

4.5   Effect of Height of Impact

Height of impact plays a major role in the strength of the structure. Height of impact determines the velocity with which the impact falls on the member, which affects the force of impact.

It can be observed from the numerical study that for every half meter increase in height of dropping the ball impactor, the total deformation is increasing by 10–11%
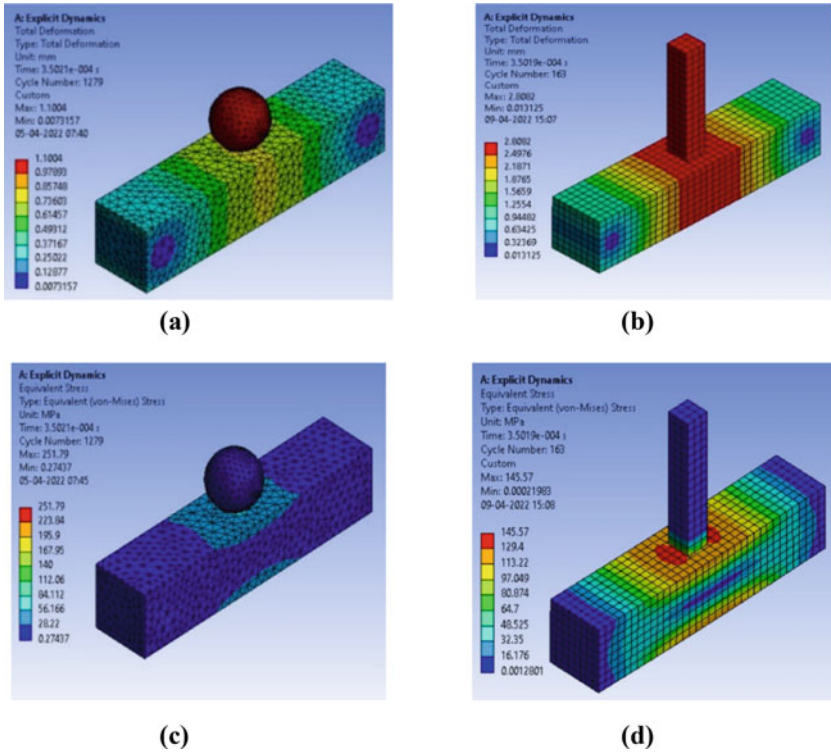
Fig. 3 **a** Deformation of ball impactor **b** Deformation of box impactor **c** Stress of ball impactor **d** Stress of box impactor

thereby indicating a decrease in the residual strength of the beam. Max deformation is observed at 3 m height with a velocity of impact to be 7672 mm/sec (Fig. 4).

4.6 Effect of Material of Impactor

Copper alloy being the densest material compared to the other two material considered, namely Gray cast iron and steel, shows maximum deformation effect in the concrete beam under ball drop impact load around 13–16% higher. Hence, copper alloy impactor creates more damage to the concrete beam (Fig. 5).

(a)   **(b)**
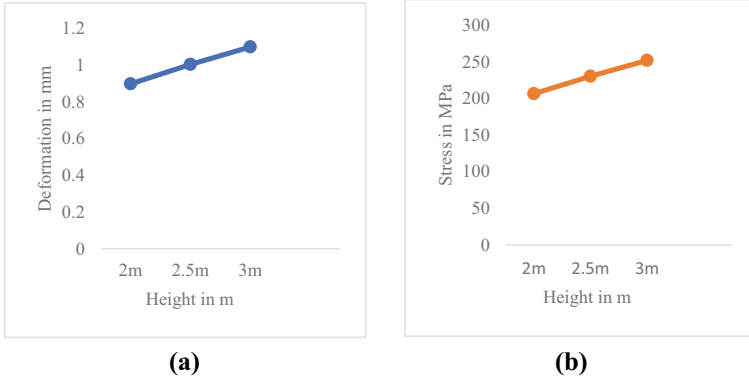
Fig. 4 **a** Deformation **b** Stress
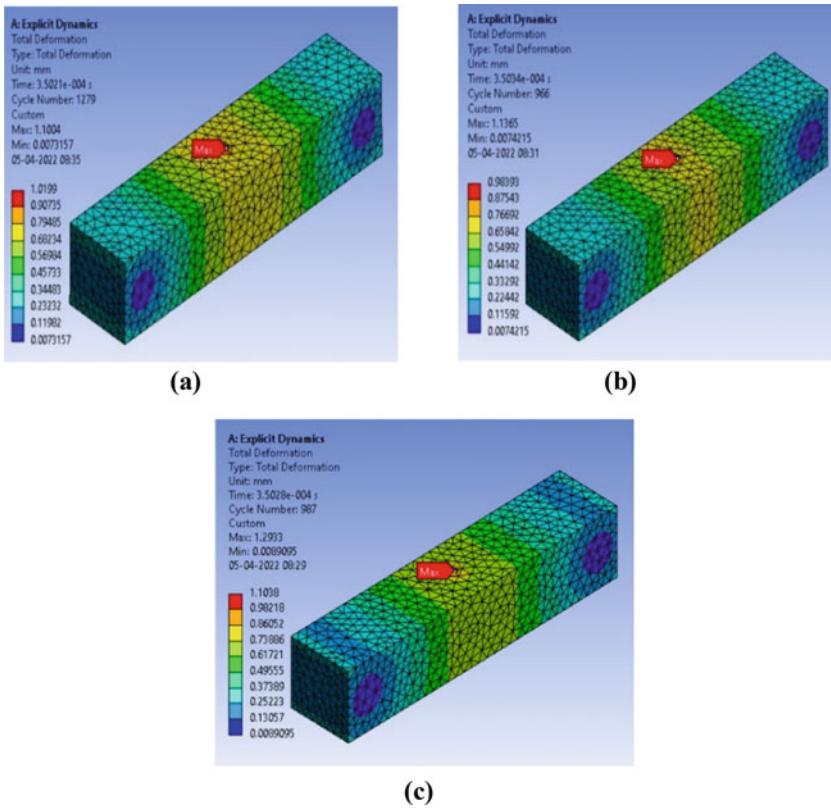
Fig. 5 **a** Steel impactor **b** Gray cast iron impactor **c** copper alloy impactor

5 Conclusion

A detailed parametric study was done for impact load on plain concrete beam using the finite element software ANSYS. Various parameters like height, shape, position etc. was discussed to study how the strength of the beam gets affected and what will be the extend of damage.

The height of the impact plays an imprtant role in deformation of the beams. Higher the height, greater the velocity of impact, greater is the damage. It was also observed that effect of impact is more when the impact occurs on the centre. Higher grade of concrete gives more resistance to damage and can protect the occurrence of failure to the member to a great extend. From the parameters considered, material of impactor and the position of impact have brought the maximum change in deformation in comparison.

It is evident from the study that Finite Element analysis is one of the best tools that can be used to accurately determine the behaviour of concrete beams under impact load. It gives an early indication of the extent of damage and failure at the design stage itself. This can help in saving cost and time during construction phase by calculating and analyzing the structural member using FEM at the design stage. This will help to modify and include the necessary changes in order to utilize the maximum strength of the beam and avoid future collapse of the structure.

References

1. Abdel-Kader, M., Fouda, A.: Effect of reinforcement on the response of concrete panels to impact of hard projectiles. Int. J. Impact Eng. **63**, 1–17 (2014)
2. Anil, O., Kantar, E., Yilmaz, M.C.: Low velocity impact behaviour of RC slabs with different support types. Constr. Build. Mater. **93**, 1078–1088 (2015)
3. Elavarasi, D., Mohan, K.S.R.: On low-velocity impact response of SIFCON slabs under drop hammer impact loading. Constr. Build. Mater. **160**, 127–135 (2018)
4. Ganesan, P., Kumar, S.V.S.: FE modelling of low velocity impact on RC and prestressed RC slabs: Struct. Eng. Mech. **5**(2019), 515–524 (2020)
5. Kumar, V., Iqbal, M.A., Mittal, A.K.: Experimental investigation of prestressed and reinforced concrete plates under falling weight impactor. Thin Walled Struct. **126**, 106–116 (2018)
6. Nachiar, S.S., Satyanarayanan, K.S., Lakshmipathy, M., Sai Pavithra, S.: Study on behaviour of compression members based on concept of biomimics. Mater. Today Proc. **34**, 518–524 (2021)
7. Ong, K.C.G., Basheerkhan, M., Paramasivam, P.: Resistance of fibre concrete slabs to low velocity projectile impact. Cement Concr. Compos. **21**(5–6), 391–401 (1999)
8. Pham, T.M., Hao, H.: Review of concrete structures strengthened with FRP against impact loading. Structures **7**, 59–70 (2016)
9. Singh, I., Dev, N., Pal, S., Visalakshi, T.: Finite element analysis of impact load on reinforced concrete. In: Ha-Minh, C., Tang, A.M., Bui, T.Q., Vu, X.H., Huynh, D.V.K. (eds.) CIGOS 2021, Emerging Technologies and Applications for Green Infrastructure. LNCE, vol. 203. Springer, Singapore (2022). https://doi.org/10.1007/978-981-16-7160-9_26

Condition Assessment and Restoration of Gas Turbine Generator Foundation of 1 × 370 MW Combined Cycle Power Plant

Ganapati Waddar

Abstract Combined cycle power plant involves a large variety of Civil Structures, which involves more complex and challenging designs and construction. The gas turbine is supported by three reinforced concrete Pedestals namely exhaust diffuser support, adiabatic flame temperature (AFT) support & turbine base anchor support. The entire gas turbine generator is covered with compartment with galvanized iron sheets. The chamber is covered with CO_2 cooling system. This paper comprises of case study on condition assessment and restoration of gas turbine foundation which was affected due to fire in the Gas turbine chamber during operation. The duration of fire was around two hours. Assessment was done to know the extent of damage in the concrete pedestals and appropriate remedial measures were suggested. The extent of damage is assessed by carrying out non-destructive tests, differential thermal analysis and restoration method which was very challenging. The suggested method is technically, economically viable, and easy from constructional aspects. The method has been implemented successfully at site and the system has been restored. The methodologies discussed in this paper can be used to supplement the conventional method, gain confidence, and mitigate the potential risks associated with long-term plant operability.

Keywords Gas turbine · Non-destructive tests · Differential thermal analysis · Cover meter · Restoration

1   Introduction

The gas turbine generator (GTG) foundation is a machine foundation which hosts the turbine, generator and exhaust diffuser supported by reinforced cement concrete (RCC) pedestals over the block foundation. The gas turbine compresses air and mixes it with fuel that is heated to a very high temperature. The hot air–fuel mixture moves through the gas turbine blades, making them spin. The fast-spinning turbine

G. Waddar (✉)
Karnataka Power Corporation Ltd, Bengaluru 560 001, India
e-mail: atgsganesh1987@gmail.com
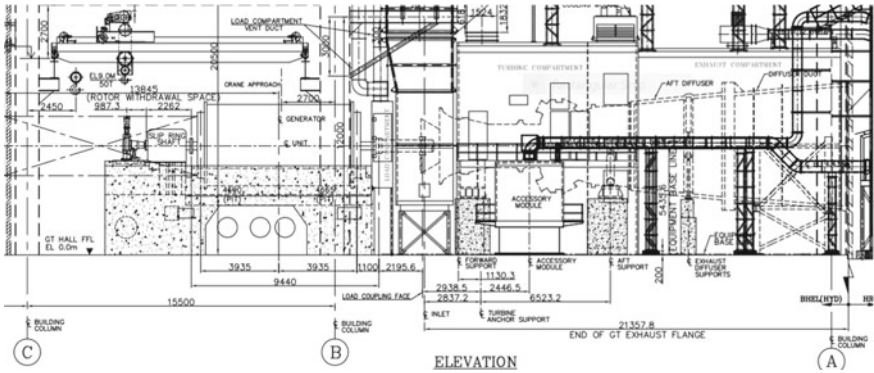
Fig. 1 Part elevation of General arrangement of GTG equipment

drives a generator that converts a portion of the spinning energy into electricity. During commissioning of 1×370 MW combined cycle power plant in the month of October 2020, a fire broke out in the Gas Turbine chamber. The duration of fire was reported to be around two hours. The fire was extinguished completely after two to three hours. A fire in the gas turbine chamber has caused damage and distress in the RCC pedestals of GTG foundation. The extent of damage in the concrete pedestals generally depends upon the intensity and duration of fire. Condition assessment was done to know the extent of damage. Generally, the principal types of damages due to fire are discoloration, reduction in concrete strength, cracking and spalling of concrete, deformation of members and other miscellaneous functional failures etc. Though, concrete is not a refractory material, it has a good fire resistance property. In case of RCC structures, the fire resistance is not only dependent upon the type of concrete, but also the thickness of cover to reinforcement. Figure 1 shows part elevation of general arrangement of GTG equipment.

Fire introduces high temperature gradients and because of it, the surface layers that is, cover concrete tends to separate and spall off from the cooler interior. The effect of increase in temperature on the concrete strength is not much upto 250 °C but above 300 °C, definite loss of strength take place [3].

2 Condition Assessment

2.1 Physical Observations

Following are the observations were made consequent to detailed inspection of exhaust diffuser support, AFT support, and Turbine Base Anchor support of the GTG foundation.
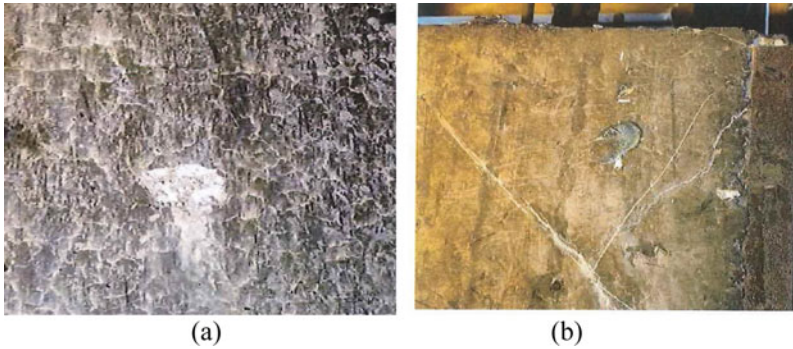
Fig. 2 **a** Deposition of black soot and typical view of web cracks in RC pedestals, **b** Typical view of cracks in pedestals
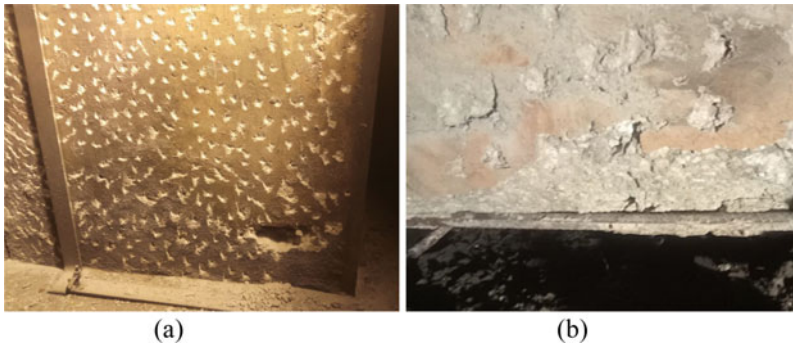
Fig. 3 **a** Spalling of concrete, **b** Exposed rebars in RC pedestal

a. Deposition of black soot was observed on RC pedestals at various locations (see Fig. 2a).
b. Minor cracks, Web cracks were observed in RC pedestals at few locations (see Fig. 2a and b).
c. Minor surface honeycomb was observed in RC pedestals at few locations.
d. Spalling of cover concrete and exposure of rebars was observed in RC pedestals at few locations (see Fig. 3a and b).

2.2 Investigative Tests

The extent of damage due to fire in GTG concrete pedestals is ascertained with the following investigative studies.

Table 1 Cover meter test results showing concrete cover in RC Pedestals

Sl. No	Pedestal description	Cover to rebars (in range) mm
1	Exhaust diffuser support	36–53
2	Aadiabatic flame temperature (AFT) support	34–55
3	Turbine base anchor support	36–53

Dimensional Measurements of Structural Members. A detailed physical measurement was carried out to obtain the dimensions of RC pedestals. The dimensions of RC pedestals were physically measured, recorded for verification & same has been verified with the furnished structural drawings. From the dimensional measurement/verification it was evident that the dimensions are in conformity with the GA drawings furnished.

Cover Meter Studies to Assess the Thickness of Cover Concrete Provided to the Rebars in RC Pedestals. Cover meter studies were carried out randomly on fire affected regions and unaffected regions of RC pedestals in order to assess the thickness of cover concrete provided to the rebars & loss of thickness of cover concrete in the fire affected region. The tests were conducted using Profometer-5+ equipment of make M/s. Proceq, Switzerland as per the guidelines furnished by the manufacturer's manual. The results of the tests tabulated in Table 1 indicates that the thickness of cover concrete provided to the rebar in the tested RC pedestals.

Differential Thermal Analysis (DTA) Tests on Concrete Samples Extracted from the Fire Affected Region of RC members. Differential Thermal Analysis (DTA) was conducted on severely fire affected regions RC Pedestal by extracting concrete sample in order to assess the temperature of exposure through physical and chemical changes occurring due to fire. A concrete sample extracted from identified maximum fire affected regions were subjected to heating in DTA, shows peak variation at different temperatures where chemical reaction takes place. Absence of such peaks indicates that the concrete is already exposed to that temperature. Based on this, the reduction in properties of concrete can be arrived at.

Test Description- Nitrogen of 50 ml/min was used while testing. For TGA& DTA temperature test, operating range adopted was around 10 to 900 °C @ 50 ml/min. and for DSC temperature test, the operating range was adopted 10 to 600 °C @ 50 ml/min.

Results- Concrete sample exposed to fire affected area of the structure is subject to Thermo Gravimetric Analysis (TGA), Differential Thermal Analysis (DTA) and Differential Scanning Calorimetry (DSC). The main difference between TGA, DTA and DSC is the method of measuring the changes in samples that are caused by heat. In TGA, the change in mass of the sample is measured with the increasing temperature while, in DTA, the temperature difference that builds up between the sample and a reference is measured and in DSC, the heat released during a chemical

process is measured. It was also noticed that, upon fire damage, there is a minor change in physico – chemical behavior of concrete such as gypsum with moisture dissolution (Ca (OH)$_2$) along with nominal mass loss at lower temperature ranges (about 90 to 210 °C) and alkali dissolution with conversion of alpha quartz to Beta form (between about 460– 580 °C) was observed. It is also evident from the combined micrograph that, de-carbonation of calcium carbonate during expose to air was found in temperature range of 590 to 760 °C. In ordered to assess the actual behavior of concrete on the fire affected areas, it was strongly suggested to test the concrete specimens for compressive strength studies for also further conclusions. The test results are shown in the Figs. 4, 5 and 6. From the DTA results, it can be inferred that the concrete near the fire affected region was exposed to temperature and the same is tabulated in Table 2. It is also indicates that loss of strength and cover concrete has affected due to fire exposure.

Non-destructive Tests to Assess the Quality of Concrete/Strength of Concrete

Ultrasonic Pulse Velocity (UPV) Test on RC Pedestals. Ultrasonic Pulse Velocity test was conducted on RC Pedestals at random on fire affected regions and unaffected regions at accessible regions by forming uniform grids, in order to assess the quality of concrete. The test was conducted using Portable Ultrasonic Non-destructive Digital Indicating Tester (PUNDIT) Lab + equipment of make M/s. Proceq, Switzerland as per the guidelines in Indian Standard IS: 13,311(Part 1):1992-(Reaffirmed in 2013). Direct, In-direct & Semi-direct methods of test was adopted at site. The results of the tests indicates that the quality of concrete in the tested RCC pedestals namely Exhaust Diffuser Support, AFT support and Turbine Base Anchor Support were found to be in the range of "Doubtful to Good Concrete" in case of pre-restoration and "Medium to Excellent Concrete" in case of post-restoration respectively. Table 3 indicates the Dynamic Young's Modulus of Elasticity (Ed) values calculated as per the Eq. (1) for
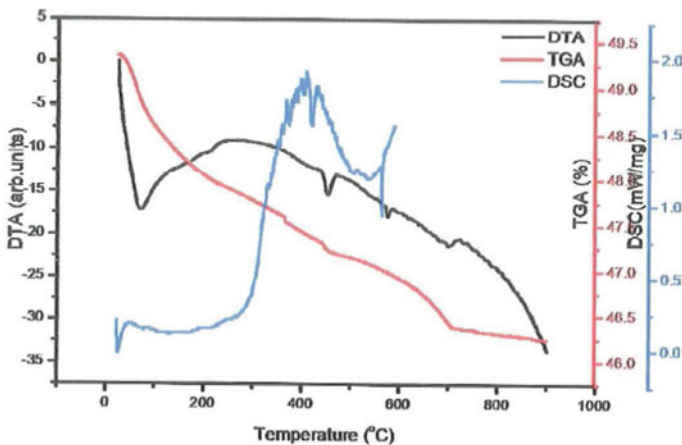
Fig. 4 Micrograph view on combined TGA, DTA & DSC analysis of fire affected concrete specimen for Exhaust Diffuser Support
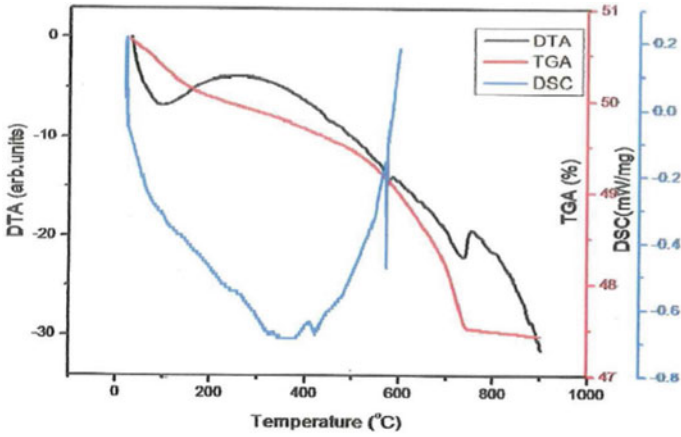
Fig. 5 Micrograph view on combined TGA, DTA & DSC analysis of fire affected concrete specimen for Turbine Base Anchor Support
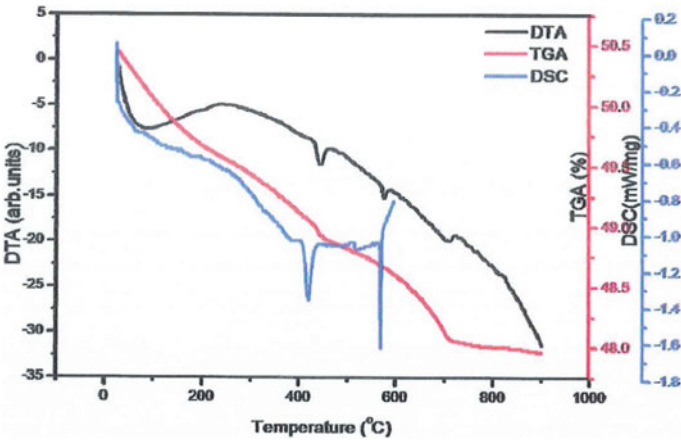
Fig. 6 Micrograph view on combined TGA, DTA & DSC analysis of fire affected concrete specimen for AFT support

pre-restoration of the concrete pedestals using UPV Test Measurements [5].

$$\text{Dynamic Young's modulus of elasticity (Ed)} = \frac{\rho(1 + \mu) * (1 - 2\mu)V^2}{(1 - \mu)} \quad (1)$$

where, ρ= concrete density in kg/m3 (assumed 2400 Kg/m^3)
E = Dynamic Young's modulus of elasticity in MPa or N/sq.mm.
V= Pulse velocity in km/s.
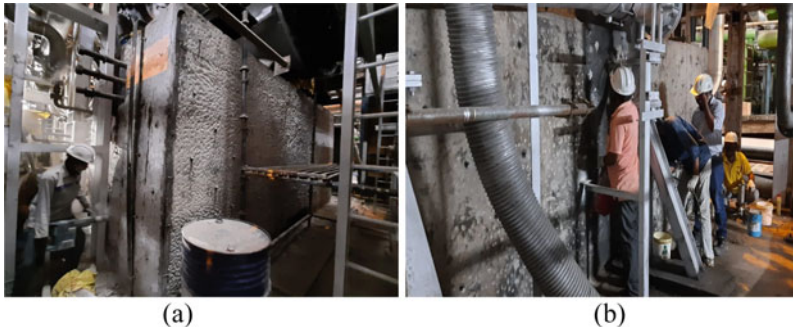
Fig. 7 **a** Drilling of holes for fixing nozzles, **b** Injection grouting in progress

Table 2 DTA test results showing temperature near fire affected area in RC Pedestals

Sl. No	Pedestal description	Pre-restoration results
		Temperature (°C)
1	Exhaust diffuser support	460–510
2	Adiabatic flame temperature (AFT) support	560–600
3	Turbine base anchor support	400–460

Table 3 Dynamic Young's Modulus of Elasticity (Ed), GPa before pre-restoration of Pedestals

Sl no.	Pedestal description	Designed			Pre-restoration	
		Grade of concrete	Static modulus of elasticity (Ed), Gpa	Dynamic modulus of elasticity (Ed), Gpa	Mean velocity (km/s)	Dynamic MODULUS of Elasticity (Ed), Gpa
1	Exhaust diffuser support	M30	27.386	34.10	3.40	23.12
2	Adiabatic flame tem-perature (AFT) support	M30	27.386	34.10	3.60	25.12
3	Turbine base anchor support	M30	27.386	34.10	3.10	19.22

μ = Poisons ratio (assumed 0.25 for M 30 grade concrete)

Rebound Hammer Test on RC Pedestals. Rebound Hammer test was carried out on RC pedestals on fire affected regions and unaffected regions in an accessible area in order to assess the surface estimated strength of concrete nearer to surface. The tests were conducted using Schmidt Rebound Hammer of make M/s. Proceq, Switzerland

Table 4 Rebound Hammer test results showing Compressive Strength before restoration

Sl .no	Pedestal description	Grade of concrete	Pre-restoration
			Compressive strength N/mm^2
1	Exhaust diffuser support	M30	29–46
2	Adiabatic flame temperature (aft) support	M30	29–40
3	Turbine base anchor support	M30	29–41

as per the guidelines in Indian Standards IS 13311 (Part 2):1992 and IS: 516(Part-5/Sec-4):2020. The test results tabulated in the Table 4 indicates that the assessed minimum and maximum compressive strength of concrete nearer to the surface in the tested RC pedestals [6].

3 Inference

Following are the discussions made from the results of detailed tests:

1. From the results of Ultrasonic Pulse Velocity Test as per Table 2 of IS: 13,311(Part 1):1992-(Reaffirmed in 2013), it is inferred that the quality of concrete in the tested RC pedestals in the fire affected regions falls under the category of "Doubtful to Good concrete" in case of pre-restoration [5].
2. From the results of Rebound hammer test, it is revealed that the strength of concrete in the tested RC pedestals in the fire affected regions is found to be satisfactory [6].
3. From the results of the cover meter test, it is revealed that cover concrete provided to the rebars in the tested RC pedestals in the fire affected region is found to be satisfactory.
4. From the results of TGA, DTA and DSC tests, it is inferred that, the extent of fire affected on surface to inner core of structure is estimated to about maximum of about 460 to 540 °C in case of Exhaust diffuser support, 560 to 600 °C in case of AFT support and 400 to 460 °C in case of Turbine anchor base support pedestals. It is also noticed, upon fire damage, there is some minor changes in Physico-Chemical behavior of concrete such as gypsum and moisture dissolution with mass loss at lower temperature (90–210 °C) and alkali dissolution with conversion of Alpha quartz to Beta form (Between 460–580 °C) was observed. The distress/damaged regions calls for appropriate recommended measures to render it to normal.

4 Restoration Measures

Based on the detailed investigation and results of investigative tests, the following recommendations, restoration measures are suggested for damaged/distressed RC pedestals of Exhaust Diffuser Support, AFT Support & Turbine Base Anchor Support.

a. Existing de-bonded cover concrete/loose concrete shall be removed completely by gentle chipping until hard and sound concrete is exposed.
b. The exposed concrete surface shall be cleaned thoroughly with air and water jet to remove sooth, loose & dust particles.
c. Low viscosity epoxy injection/grouting treatment shall be carried out as per the methodology given below (see Fig. 7a and b).

- 12 mm diameter holes with 75 mm deep shall be drilled at 600 c/c staggered to fix PVC nozzles for grouting
- 10 mm diameter PVC nozzles shall be fixed into the drilled holes using anchor grout as per specifications.
- Low viscosity epoxy grouting shall be carried out at a pressure not less than 3 to 4 kg/Sq.cm until refusal is reached, as per specification.
- PVC nozzles shall be cut in flush with the adjacent surface as per standard practice.

d. The exposed bars shall be cleaned with buffing wheel/wire brush/emery to remove the soot/corrosion scales/rust (if any) followed by two coats of anti-corrosive chemicals as per specification.
e. 75 mm deep holes of 10 mm diameter shall be drilled for fixing of shear connectors. The drilled holes shall be thoroughly cleaned to remove dust particles using air & water jet. 8 mm diameter shear connectors shall be fixed in drilled holes using polyester resin anchor grout.
f. 14 mm diameter holes of 100 mm deep shall be drilled to fix the proposed reinforcement (12Y at 250 C/C) shall be fabricated, placed in position & tack welded to shear connectors (see Fig 8a and b). The bars shall be fixed using polyester resin anchor grout as per manufacturer specifications.
g. 75 mm thick (minimum), free flow concrete encasement shall be provided using 6 mm down size aggregates, with slurry tight shuttering as per specification enclosed.
h. The encased micro concrete shall be cured for a minimum period of 14 days as per standard practice (since micro concrete is having good bonding capability, bonding agent is not required).
i. For treatment of Honeycomb concrete region of RC pedestals, the loose concrete shall be removed by gentle chipping and cleaned thoroughly. The chipped portion shall be filled with polymer modified mortar and finished in level with surrounding concrete surface [1, 2].

Table 5 Dynamic Young's Modulus of Elasticity (Ed), GPa after post-restoration of Pedestals

Sl no.	Pedestal description	Designed			Post-restoration	
		Grade of concrete	Static modulus of elasticity (Ed), Gpa	Dynamic modulus of elasticity (Ed), Gpa	Mean velocity (km/s)	Dynamic modulus of elasticity (Ed), Gpa
1	Exhaust diffuser support	M30	27.386	34.10	4.00	32.00
2	Adiabatic flame temperature (AFT) support	M30	27.386	34.10	3.60	25.92
3	Turbine base anchor support	M30	27.386	34.10	3.70	27.30

Once again, UPV test was performed after completion of restoration work to ascertain the achievement of required strength gain, homogeneity and dynamic young's modulus of concrete. From the results of Ultrasonic Pulse Velocity Test as per Table 2 of IS: 13,311(Part 1):1992-(Reaffirmed in 2013), it is inferred that the quality of concrete in the tested RC pedestals falls under the category of "Medium to Excellent Concrete" after post-restoration of pedestals. Table 5 indicates the Dynamic Young's Modulus of Elasticity (Ed) values for post-restoration of concrete pedestals using UPV Test Measurements [5] (Tables 6, 7 and 8).

Table 6 Specifications for anchor grout [4]

Connecting material	Fe-415/Fe-500/Fe-500D grade steel
Diameter of holes to be grouted in concrete and depth of grout	10 mm diameter and 75 mm deep
Anchoring medium	Quick setting polyester resin anchor grout
Curing time	24 h minimum (air curing)
Source of resin grout available	Masterflow 93, M/s BASF India Ltd., Bangalore Dr. Fixit Anchorfix P&S" M/s. Pidilite Industries Ltd., Lokfix S/L/P" from M/s. Fosroc Dhemicals (India) Pvt. Ltd.,EP310, M/s ARDEX Endura or any other equivalent
Compressive strength of anchor grout	20 N/Sq.mm in 5 h. @30^0C 75 N/Sq.mm in 7 days

(continued)

Table 6 (continued)

Type of equipment for drilling	Rotary-cum-Hammering action Electrically operated drilling machine with masonry drill bits
Source of equipment for drilling in concrete	Electrix (India) Pvt., Ltd., BOSCH Ltd., HILTI India Ltd., or any equivalent

Table 7 Specifications for epoxy anchor grout [4]

Reference	ASTM-881–87 Type I, Grade I, Class B or C
Type of Epoxy	Low viscosity solvent free prepacked resign and hardener, free flow epoxy system after mixing
Viscosity	Mix viscosity 800 mPa.s maximum at 25 °C
Pot life	Not less than 45 min
Compressive strength after 7 days curing at 25^0C	Not less than 75 N/Sq. mm
Injection equipment	Electrically operated or compressed air driven injection pump with suitable syringe system, fitted with suitable pressure gauge
Operating pressure	3–4 kg/Sq.cm
Available sources	MasterInject 1315, M/s. BASF India Ltd., Dr. Fixit Epoxy Injection Grout, M/s. Pidilite Industries Ltd Quickmast 231, M/s. Don Construction Chemicals India Ltd., Conbextra EP10, M/s. Fosroc Chemicals (India) Ltd., KP 250 M/s. Krishna Conchem Products Pvt. Ltd., Sikadur 52, M/s. Sika Qualcrete Pvt Ltd., Or any equivalent

Table 8 Specifications for free flow micro-concrete [4]

Description and source	General purpose, Dual Shrinkage compensated free flow cementitious micro concrete of higher strength
Material requirement	a. Ready to use free- flow micro- flow concrete b. Coarse aggregate - 5 to 12 mm downsize coarse aggregates dust free and washed conforming to IS 383–1970 c. Water- conforming to IS 456:200

Table 8 (continued)

Mix proportion	1: 0.5 to 0.75: 0.16 (1 Bag -30, 15 to 22.5 kg CA, 4.8 L of water)
Surface Preparation	Plaster on the surface shall be removed completely
Formwork	Marine ply-wood to dimensions with slurry tight joints coated with form release agents
Concrete Compaction	Self-Compaction with 72 h minimum stripping time
Period of Curing	14 days min
Fresh Wet Density	Approx. 2200 kg/m^3
Flexural Strength	5.0 N/mm^2–28Days
Compressive Strength	1 day- not less than 10 N/mm^2 3 days- not less than 30 N/mm^2 7 days- not less than 40 N/mm^2 (Conforming to BS:4511–80)
Mould releasing agents And free flow micro concrete material source	Master Finish 202 & WB 249 and Master Emaco S346, M/s. BASF India Ltd. Dr. Fixit Deshuttering Oil and Dr. Fixit Micro Concrete, M/s. Pidilite Industries Ltd., Reebol Emulsion & Renderoc RG, M/s. Fosroc Chemicals (India) Ltd., "C10" (1:3 dilution) "C10 PM" (no dilution is required), M/s ARDEX EnduraSeparol, Sika microcrete 1 or 2, M/s. Sika India Pvt. Ltd or any equivalent and Sika

Fig. 8 a Fixing of rebars using anchor grout, **b** Reinforcement jacketing (typical)

5 Conclusions

From the outcome of detailed study of the fire affected GT concrete pedestals, it was concluded that loss of strength was observed in RC pedestals at most of the locations. The considerable effect of fire was observed in AFT support pedestal. Whereas in Exhaust Diffuser Support it is moderately affected and in Turbine Base Anchor Support pedestal, the fire effect is minimal.

However, the loss in strength due to fire on RC pedestals calls for appropriate restoration measure as recommended above. After carrying out the above recommended restoration measures effectively by an experienced agency under the guidance of experienced technical personnel, the fire affected regions/RC pedestals were restored to normal.

In case of post–restoration, based on the results of field tests conducted, it was concluded that the quality of restored/strengthened concrete in all the RC pedestals supporting Gas Turbine structure is found to be satisfactory. Further, it is needless to emphasize the periodic maintenance of the structure should be strictly adhered to for effective functioning and life enhancement of the structure.

References

1. Alcocer, S.M., Jirsa, J.O.: Strength of reinforced concrete frame connections rehabilitated by jacketing. ACI Struct. J. **90**(3), 249–261 (1993)
2. Dritsos, S.E.: Jacket retrofitting of reinforced concrete columns. Constr. Repair **11**(4), 35–40 (1997)
3. Vidivelli, B.: Rehabilitation of Concrete Structures, 1st edn. Standard Publishers Distributors, Delhi (2007)
4. Handbook on Repairs and Rehabilitation of RCC Structures- Director General (Works) CPWD, New Delhi, India
5. IS 13311 (Part 1):1992, Non-Destructive Testing of Concrete Methods of Test- Part 1 Ultrasonic Pulse Velocity
6. IS 13311 (Part 2):1992, Non-Destructive Testing of Concrete Methods of Test- Part 1 Rebound Hammer

Finite Element Model of Smart Composite Steel Plate Shear Walls

A Case Study of Distance Between Shear Studs

Hadee Mohammed Najm, Saber Kouadri, and Manahel Shahath Khalaf

Abstract The composite shear wall is having various merits over the traditional reinforced concrete walls. As a result of this, several experimental studies have been reported in the literature in order to study the seismic behavior of composite shear walls. On the other hand, very, few numerical investigations found in the previous literature because of the involvement of complexities at the interaction behavior of steel and concrete. Therefore, the objective of the present paper is to present a numerical study on Smart composite shear walls which is having an infilled steel plate and concrete. The study is carried out using the ANSYS software. The mechanical mechanisms between the web plate and concrete have been investigated thoroughly. The results obtained from the FE analysis shows very good agreement with the test results, in terms of the hysteresis curves, failure behavior, ultimate strength, initial stiffness, and ductility. The present numerical investigations were focused on the effects of the gap and the distance between the shear stud on the CSPSW behavior. The results indicate that increasing the gap between steel plate and concrete wall from 0 to 4% from the width improved the stiffness by 18% as compared with the reference model, which led to delay failures of this model. Changing the distance between shear studs from (20 to 25%) from width enhanced the ductility and energy absorption with ratios (66, 32%), respectively, compared with the reference model.

Keywords Composite steel plate shear wall · Hysteresis curves · Ductility · Energy absorption · Finite element model

H. M. Najm (✉)
Civil Engineering Department, Aligarh Muslim University (AMU) Aligarh, Aligarh, UP, India
e-mail: gk4071@myamu.ac.in

S. Kouadri
Department of Civil Engineering and Hydraulics, Faculty of Applied Science, Kasdi Merbah University Ouargla, Ouargla, Algeria

M. S. Khalaf
Department of Civil Engineering, College of Engineering, University of Diyala, 32001 Diyala, Iraq

1 Introduction

The components of composite steel plate shear walls (CSPSW) are consists of web plates, infill steel plates, concrete, and shear studs. The composite steel plate shear wall proves to excellent over reinforced concrete walls in terms of ultimate strength, stiffness, ductility and energy dissipation [1].

The previous researchers have shown a lot interest towards the used of composite steel plate shear walls in buildings [2–4]. The appropriate provisions for composite shear walls, such as seismic various seismic of composite shear walls are ASCE 7–10 and AISC 341–10 [5, 6], has been prepared by allowing the use of CSPSW systems in earthquake zones. The researchers have conducted many experimental tests in order to study the behavior of composite shear walls in the absence of boundary walls. Nie et al. [7], Mydin [8], Wright [9], and Wang [10] depict that a composite shear walls not only have a very high ultimate strength but also have a very excellent ductile behavior. The local buckling of web and fracture failure of corners of the wall are the observed failure modes. Zhang et al. [11] and Zhang et al. [12] showed that more channels lead to reduce the ultimate strength and stiffness of the wall but observed good improvement in the ductile and energy dissipation behavior. Finally, to calculate the ultimate strength and initial stiffness has been proposed. But all the necessary variables are not included in the proposed equation which leads to the conservative results and therefore this will create a strong demand to perform an exhaustive numerical analysis of composite shear wall [13, 14].

Many researchers have suggested the equation-based FE analysis for composite shear walls. Nguyen et al. [15], Epackachi et al. [16], and Rafiei et al. [17] established the finite element models and check their accuracy. The parametric analysis of the connector in the wall shows that increase in number of connectors could improve the bearing capacity of the steel plate and that change in spacing of the connector could affect the failure mode of the steel plate. Wei et al. [18] studied the axial compression performance of composite shear walls. The effect of distance-to-thickness ratios on the failure mode was studied, and a formula to calculate the axial compression of a composite shear wall has been suggested. The higher axial compression ratio of the wall is beneficial to restrain the internal concrete and improve the compressive strength of the concrete, so the energy dissipation capacity of the composite shear wall is enhanced [19, 20]. Increasing the thickness of the steel plate can increase the stiffness and ultimate bearing capacity of the wall, as the hysteretic curve of the wall is plumper [21–24]. Epackachi et al. [25] simulated shear walls with different aspect ratios. When the aspect ratio was between 0.6 and 3.0, the coupling effect of the moment and shear force was obvious. The specifications [6, 26–28] define the formula for the shear capacity of composite shear walls. The formulas for the shear and flexural capacity were given, but the formula for estimating the flexural-shear coupling was not provided [29].

In summary, the seismic performance of the CSPSW is usually affected by various factors such as the thickness of the infill steel plate, the thickness of the concrete wall, the distance between the shear stud, the ratio of reinforcement, concrete strength, steel

yield strength and layout of the shear stud [30]. The previous researchers Rahai, A. and Hatami, F. [31] investigated experimentally the performance of composite shear wall and established the base for the research on the seismic behavior. Although few analyses have suggested the formulas for calculation of lateral stiffness, ductility and energy dissipation, they are all based on the test results. The predictive effect with other parameters is unknown. In addition, the previous studies mainly focused on the behaviour of traditional CSPSW, while this investigation is regarding not only to study the behavior of the smart CSPSW under cyclic load but also to study the effect of many parameters on this new type of CSPSW.

2 Smart Structures Technology

The research on how to maintain the integrity of humans inside the buildings is an important issue of concern in modern times, as buildings with the low-security level pose a threat to the human spirit. Smart structures technology is the latest building and structure control system and notes own condition, detect impending failure, monitors the damage and adapts to changing environments [32, 33]. The smart technology of composite steel plate shear wall is installed by adding a gap between the steel frame and concrete wall; this gap is provided to improve the performance of CSPSW. The most important benefits of this gap are improvement in stiffness, ductility and energy absorption of all the systems [34].

A smart composite shear wall system consists of an infill steel plate, boundary frame (beam and column) and concrete wall attached on one side of the infill steel plate or both side (in this research, the steel plated is attached on one side only). The reinforced concrete wall in mediating contact with the boundary steel frame, because there is a gap in between [35]. The difference between the traditional and smart CSPSW is through a change in the behavior of concrete wall under cyclic loading, where in the traditional CSPSW the concrete wall work in conjunction with steel plate, whereas in smart CSPSW, due to the gap between the steel frame and concrete wall, RC will not work and resisting lateral load until the inter-story drift has reached the certain value. Figure 1 shows the structural components of the newly developed shear walls [36–38].
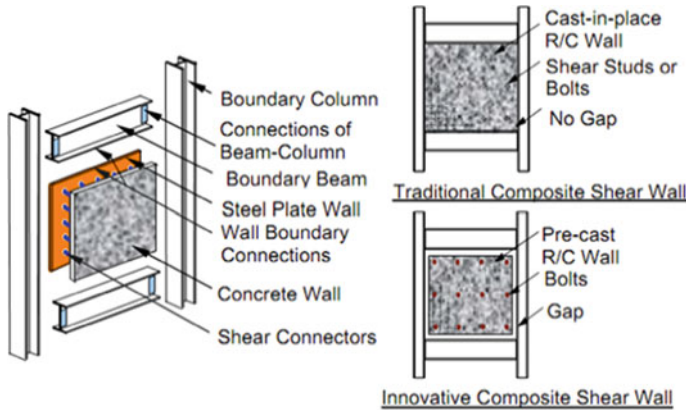
Fig. 1 Traditional and innovative composite steel plate shear wall

3 Experimental Test

3.1 Sample Design

The experimental work conducted on CSPSW was carried out by Rahai and Hatami [31] to study the behavior of composite shear walls made of concrete and steel. The details of experimental work of CSPSW are as shown in Fig. 2.

The length of the frame span, which is a center to center distance between the columns, is 2 m and the height of the frame is 1 m, which is a center to center distance between the top and bottom beams. The double IPE200 section strengthened with flange cover plate (150 * 12) is used for both columns and beams. Steel plate inscribed
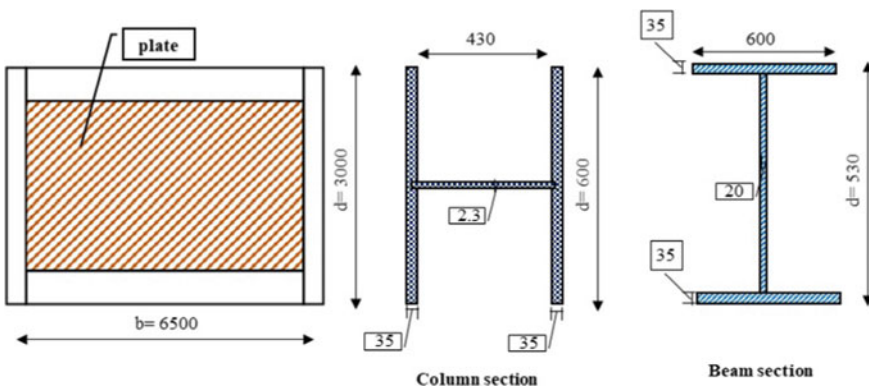
Fig. 2 Experimental specimen dimensions

Table 1 Details of the experimental specimens and its mechanical properties

Group no.	Group name	SW	Gap	Thickness of steel	Thickness of concrete	Distance between Shear stud	Ratio Of reinforce-ment	Compressive strength	Yield strength	Layout of shear stud (H*V)
1	Gap between steel frame and concrete wall	SW-G0mm	0	3	50	200	1%	45	240	3*8
		SW-G30mm	30	3	50	200	1%	45	240	3*8
		SW-G40mm(R)	40	3	50	200	1%	45	240	3*8
		SW-G50mm	50	3	50	200	1%	45	240	3*8
2	Distance between shear stud	SW-D200mm(R)	40	3	50	200	1%	45	240	3*8
		SW-D210mm	40	3	50	210	1%	45	240	3*8
		SW-D220mm	40	3	50	220	1%	45	240	3*8
		SW-D230mm	40	3	50	230	1%	45	240	3*8
		SW-D240mm	40	3	50	240	1%	45	240	3*8
		SW-D250mm	40	3	50	250	1%	45	240	3*8

inside the boundary beams and columns is 1776 * 776 long and 1776 * 1776 mm wide. The thickness of plate and concrete cover are 3 mm and 50 mm respectively.

The provision of 30 mm gap is provided between the concrete cover and the boundary elements. A bolt of 7 mm diameter and 100 long is used to connect the 50 mm concrete cover to a steel plate.

Table 1 shows the characteristics strength of steel that is used in all models St37 with yield stress 240 MPa and ultimate stress 370 MPa. The behavior of steel is considered as bilinear elastic–plastic curve for modelling. The compressive strength of concrete at 28 day's cylindrical core sample is 45 MPa, and its tensile strength is equivalent to 3 MPa.

3.2 Loading programme and Test Setup

Horizontal loading was controlled by force [31]. In the force loading phase, the horizontal forces were 600 kN, and loading was cyclically loaded with 1/60 Hz frequency. The experimental load characteristics are as shown in Table 2. The loading history is illustrated in Fig. 3.

Table 2 Cyclic loading time history

Time (second)		Max. load (KN)	Loading shape	Frequencies (Hz.)
Start	End			
0.0	71	0.0	Cyclic	0.0
72	180	300	Cyclic	1/60
181	360	500	Cyclic	1/60
361	540	600	Cyclic	1/60
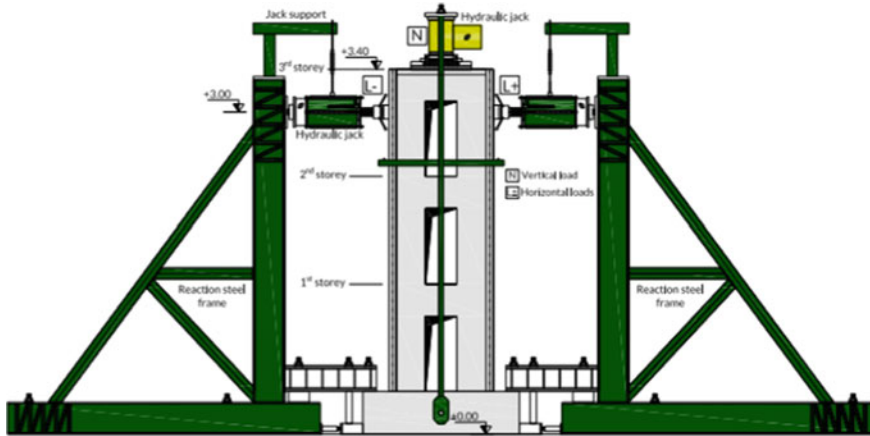
Fig. 3 Cyclic loading arrangement

4   Finite Element Model (FEM)

4.1   Model Overview

The numerical study is performed by finite element analysis using ANSYS. The finite element model is consisting of five parts, like the infilled steel plate, shear studs, outer steel frame, reinforced concrete wall and reinforcement. The outer steel frame is consisting of a web and flange plate.

The four nodded shell 181 element from ANSYS element library is used to model the outer steel frame, infilled plate, web and flange plate. The element is having six degree of freedom at each node. The change of stress in the thickness direction cannot be ignored in shear stud and concrete walls because the sizes in the three directions have little difference. So, the element choice to represent the shear stud and reinforcement was a link 180. The element used to represent the concrete wall was 3D solid65. In the test, the shear studs were welded on the web plate. Thus, the shear studs are tied to the steel plate in the FE model. In the test, the reinforcement and the steel studs were fixed in the concrete. The friction contact model has been
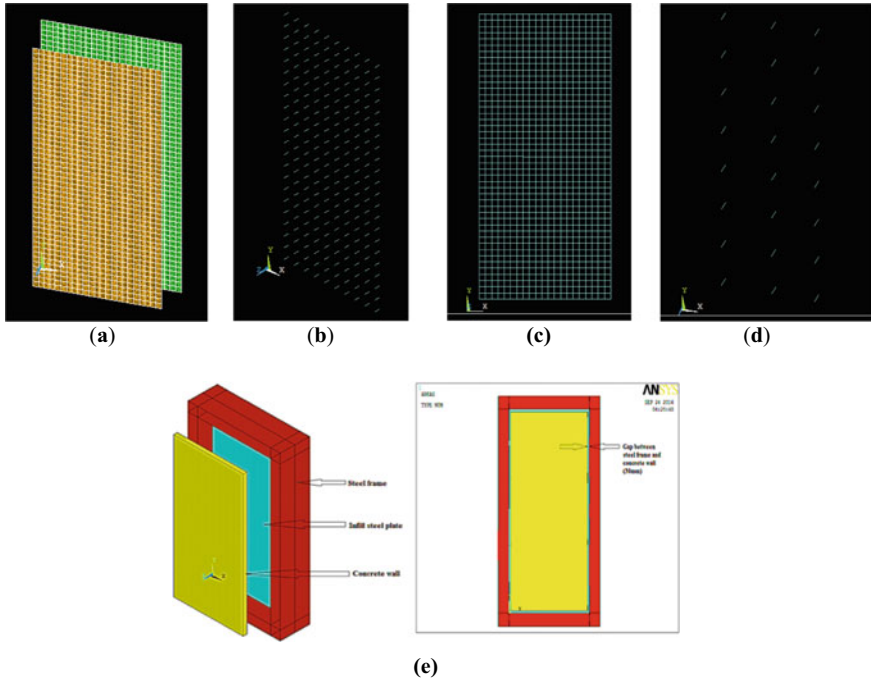
Fig. 4 Contact between different elements: **a** Interface surface; **b** Load slip; **c** reinforcement; **d** shear stud; **e** assembled FEM

used between the steel plate and concrete. The tangential friction coefficient is 0.6 [35], as shown in Fig. 4a. Interface surface between infill steel plate and concrete wall represented by targe170 and contact 174. Finally, the load slip action is representing by comb39, as shown in Fig. 4. The assembled FE model is shown in Fig. 4e.

4.2 Validation of Finite Element Model

Before performing an actual parametric study, the validation of FE model is performed. The results of hysteretic curves obtained from FE analysis and test results have been compared and are as shown in Fig. 5. It is observed that FE results are closely matches with test results. Therefore, it is concluded that the FE model can simulate the hysteretic curves of the composite steel plate shear wall in a better way.

In the test loading process, the steel plate experienced severe local buckling at different positions with increasing horizontal displacement. The FE model could simulate the local buckling phenomenon as shown in Fig. 6.

The results obtained during the last cyclic loading from the ANSYS output are presented in Figs. 7 & 8, which shows the comparison of out-of-plane deflection
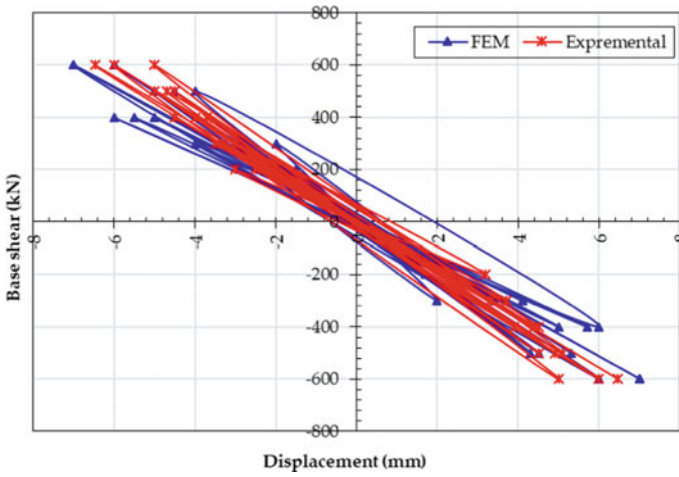
Fig. 5 Comparison of deformation-load in the numerical and experimental model for CSPSW
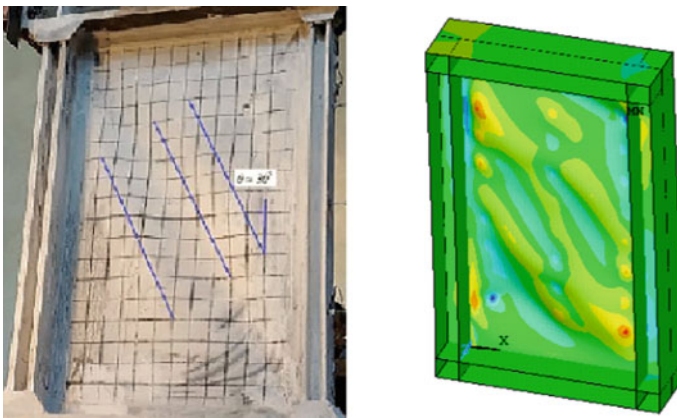
Fig. 6 Local buckling for experimental and numerical

and crack formation in composite shear wall in different experimental and numerical specimens. The lateral displacement found to be 6.47 mm and 7 mm in case of numerical and experimental test respectively.
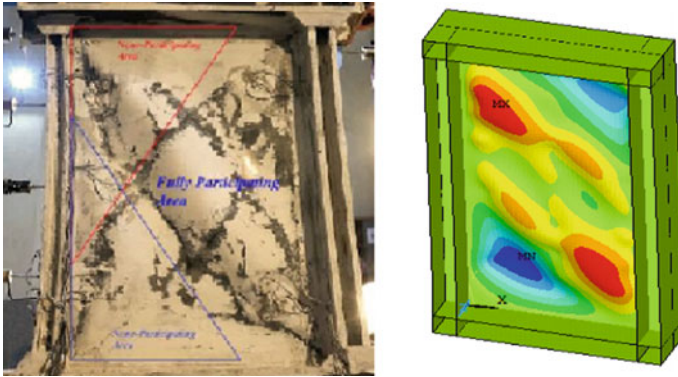
Fig. 7 Out-of-plane deflection
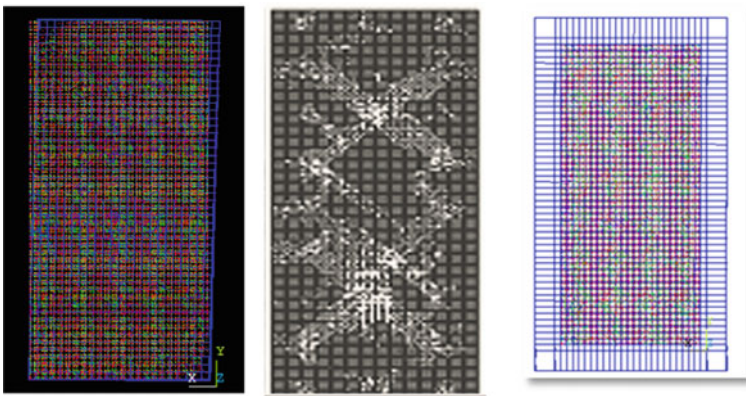
Fig. 8 Crack deformations of concrete wall

5   Parametric Analysis

For optimization of shear wall parameters in tall structures, the parametric study has been performed by varying the section size and design guidelines have been suggested [31]. The effects of various variables have been critically studied on stiffness, ductility and energy dissipation of the composite shear wall. In order to study the hysteric behavior of the model in parametric analysis, the cyclic load is applied to the wall. The boundary conditions in the model are consistent with the test.

The variables consist the gap between the concrete wall and steel frame and layout of a shear stud. The standard model parameters are chosen as follows: the gap between the concrete wall and steel frame is 40 mm, concrete wall thickness is 50 mm, the steel ratio is 1%, infill steel plate thickness is 3 mm, the distance between shear stud is 200 mm, the axial compressive strength of the concrete is 45 MPa, the

yield strength of the infill steel plate is 240 MPa, Layout of Shear Stud (H * V) (3 * 8).

In the parametric analysis, the gap ranges from (0–30–40–50) mm, the distance between the shear stud ranges from (200–210–220–230-240–250) mm.

5.1 Influence Rules of the Parameters

The influence rules of key design parameters are studied by including material displacement, stiffness, ductility and energy dissipation. The structural behavior of the composite steel plate shear wall when subjected to cyclic load is characterized by four different stages with increasing the applied load; these stages are:

- The initial elastic stiffness phase
- The shear yielding stiffness phase
- Post yielding stiffness phase
- The Pre-failure stiffness phase

While the smart CSPSW, at first loading, shows a linear elastic response where the steel frame and infill steel plate, beams and columns, undergo inelastic deformations.

After that, the interaction between the infill steel plate and the reinforced concrete panel in the compression field is extra efficient. While the lateraling loading is more raised, the infill steel plate responsible is immaterially and geometrically nonlinearity; moreover, the laterally shear stiffness of the wall drops significantly owing to the shear yield of the infill steel plate.

During the third phase, with the excess of lateraling unloading, the pure shear yield transpires pending the fully shear yield appearing in the infill steel plate, and the lateral stiffness reduce gradually at this phase.

While the lateral load surpasses the shear yield capacity of the infill steel plate, the material and geometric nonlinearity responsible for steel frame and boundary elements be massive. At this phase, the frame supplies the utmost laterally stiffness.

The test results appear that increasing the model thickness (infill steel plate and concrete wall) worked to increase the structural strength capacity and the model's ability to absorb and dissipate energy which led to delay the model failure; at the same time, it prevented the rapid drop for the loads carrying capacity.

Also, increasing the distance and layout of the shear stud (certified number of shear studs) increased the structural strength capacity and enhanced the ability of the model to absorb energy and the model ductility.

Also, when increased the properties of smart CSPSW the structural strength capacity and model ability to absorb and dissipate energy would be enhanced.

5.1.1 The First Group Models (Influence of Gap Between Concrete Wall and Steel Frame)

Lateral displacement

When loading the first group models SW-G0mm, SW-G30mm, SW-40MM(R) and SW-G50mm gradually, it can be noted the model was passed in a four-phase as explained below. Also, lateral displacement of group 1 at each phase can be seen in Fig. 9.

Phase A

In this phase, the applied load causes linear relation between the horizontal unload and the resulting displacement. This relationship for the models SW-G0mm, SW-G30mm, SW-40MM (R) and SW-G50mm continued until it was reached to yield deflection.

In this phase, the lateral displacement of models SW-G30mm, SW-40MM (R) and SW-G50mm was larger by (12, 17 and 28)%, respectively, as compared with the reference model SW-G0mm. By increasing the lateral load, the first yield will occur in the steel plate defined. The out of plane displacement of group 1 for 0, 30, 40, and 40 mm gaps are shown in Fig. 10.

It is worth mentioning that, in this stage, all the models of traditional and smart composite steel plates with a gap (30, 40, 50) mm, respectively, were symmetric in their behavior until they reached the shear yield zone.

Phase B

This phase began at the shear yield zone, which represents the first point of the transformation curve to a flat line that owns a high incline as a result of the high increase in the specimen deflection.

When increasing the gap between the steel frame and concrete wall, the interaction between the reinforced concrete panel and infill steel plate in the compression zone
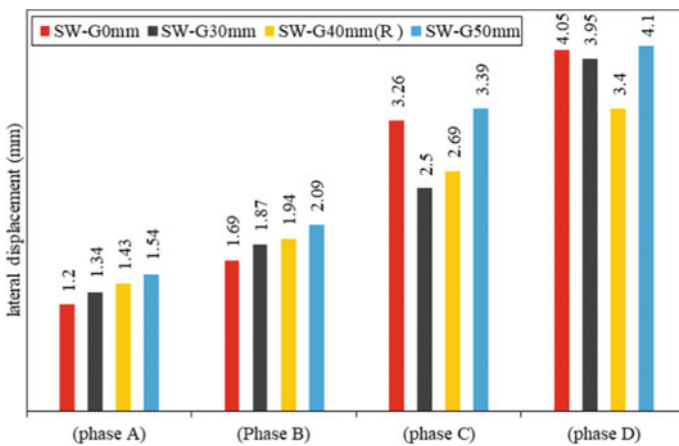
Fig. 9 Lateral displacement of Group 1
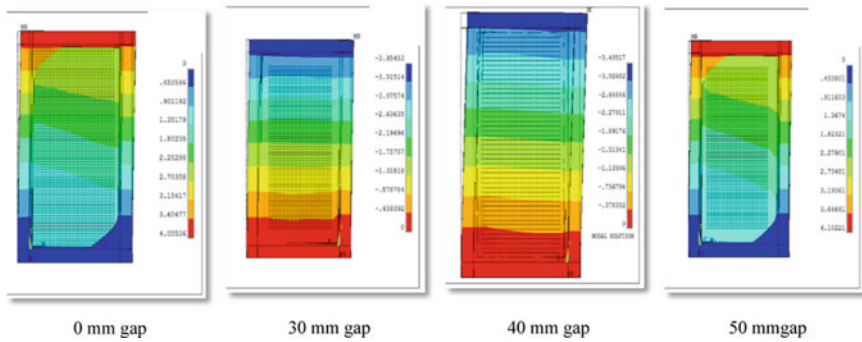
Fig. 10 Out of plane displacement for various gap between steel frame and concrete wall

became more active, which caused a decrease in the lateral shear stiffness for this model. The shear yield zone of the model SW-G30mm, SW-40MM (R) and SW-G50mm are found to be larger than by (11, 15 and 24)% as compared to the reference model SW-G0mm.

Phase C

During this phase, when laterally load increases, the shear yield spreads until the fully shear yield occurs in the infill steel plate, and the models with gaps gave good results under increased lateral load.

For models with a gap (30 and 40) mm, the lateral displacement was lower than that of the model without a gap of SW-G0mm by (23 and 20)%. However, this displacement for models with a gap (50) mm was larger than that of reference model SW-G0mm by 4%.

Phase D

This phase refers to the pre-failure of the models. In CSPSW, the infill steel plate of CSPSW resistance lateral load by pure shear yield, as a reinforced concrete panel prevent inelastic buckling.

In this phase and in the same cycle loading (600 KN), the deflection of SW-G50MM is larger by 14% as compared with the reference model SW-G0MM. While for the rest model (SW-G30mm and SW-G40mm(R)) at the same cycle loading, the deflection was lower by (2, 16%) respectively.

In this phase, all the models submit a nonlinear inelastic reaction of the steel frame, and the lateral stiffens are supplied by steel boundary elements. It is worth mentioning that in this stage, the behavior of SW-G50MM symmetry to the behavior of SPSW, the large gap between the steel frame and concrete wall led to the formation of cracks in the concrete before getting contact between them; also, the system loses the idea of smart composite steel plate shear wall which depends basically on concrete contribution delay to work with steel frame.

Stiffness

Stiffness is the ratio of load vs deformation and can be used to describe either the elastic or plastic (after yield) range. It can be seen from the load–deflection curve
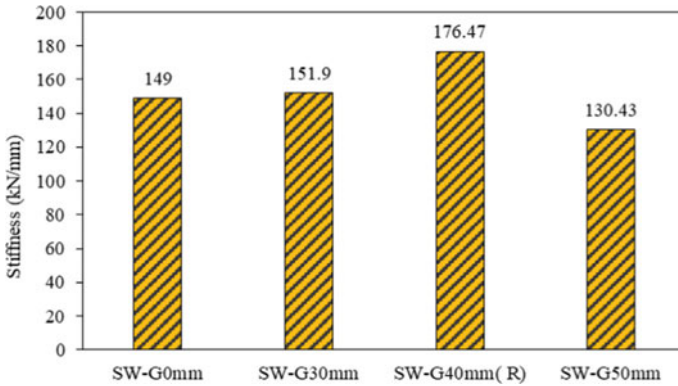
Fig. 11 Stiffness of group 1

that the stiffness refers to the slop of the curve at any point along the curve. Figure 11 presents the initial elastic stiffness (K_e) and proportion of the initial elastic stiffness of SPSW to CSPSW (K_{ec}/K_{es}) (Rahai and Hatami, 2009).

Figure 11 shows the stiffness for all group one models. From this result, it can be noted that when increasing the gap (30 and 40) mm for SW-G30MM and SW-40MM (R), the stiffness was increased by (2, 18%) respectively, as compared with the reference model SW-G0MM and thus worked to increase the model resistance deformations. However, in the model of gap (50) mm, its stiffness decreased significantly by 13% as compared with the reference model SW-G0mm, where the specimen was resistant to lateral load. SW-40 mm (R) has good stiffness among all the models of the first group, where its stiffness is equal to 176.47 kN/mm.

Ductility
Ductility is referred to the deformation that a material can undergo after it has yielded or exceeded its elastic range. From the load–deflection curve, it is concluded that the ductility refers to the length of the curve after the yield point to failure. The ductility ratio is calculated as the ratio of the maximum displacement to the yield displacement ($\mu = \delta_{max}/\delta_y$). The yield point displacement (δ_y) is calculated through the notion of equal plastic energy so that the area bounded by the perfect elastic–plastic curve is equal to that of the actual push-over curve [30] (Shafaei et al., 2016).

The results of Fig. 12 show that the model SW-G50mm has a low ductility up to 1.71 as a result of the high value of the deflection at the ultimate load, and this caused sudden buckling and rapid drop in the load-carrying capacity when it was access to the ultimate load.

The great ductility of models with little gap was because of the high estimation of the lateral displacement at an ultimate load contrasted and the lateral displacement value at the yield load and, in this manner, brought on a gradual failure in the model load capacity.

From this, it appears that there was a proportional relationship between the ductility and the gap between the steel frame and concrete wall; therefore, increasing
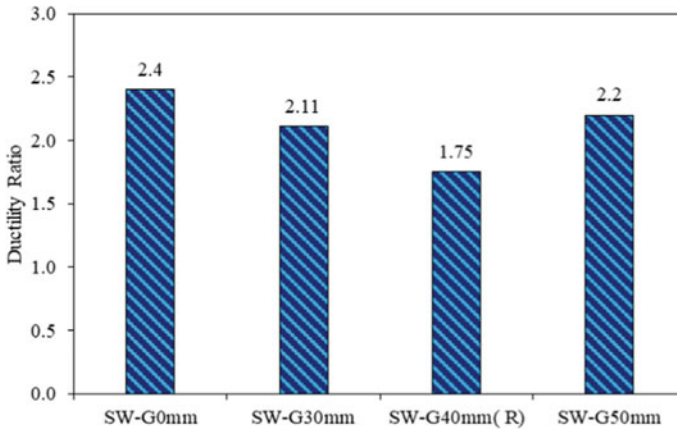
Fig. 12 Ductility ratio of group 1

the gap was caused a decrease in the ductility because the moment of inertia was decreased when the gap was increased, so was affected on the ability of the shear wall to resist the lateral load.

Energy Absorption

Energy absorption ability is a critical indicator of model's resilience to loading. Models with high energy absorption ability are typically found to have high imperviousness to impact and crash loading and hence are valuable for high-performance structures.

The absorbed energy by a shear wall in a half-cycle can be objectively accepted as the zone under (shear load–displacement), from which the region of recoverable elastic is not subtracted. It is assumed that the unloading and the elastic moduli are approximately the same. For example, when the max cycle load of the reference model is equal to (600 kN), displacement is equal to (4.01 mm), and its curved takes a parabola shape. So, energy absorption is equal to (1/3*displacement*load), where the former law represents the area of parabola shape [30] (Shafaei et al., 2016).

The results of Fig. 13 show the energy absorption of each model through each phase. Through the phase, B can be noticed that increase in the gap between the steel frame and concrete wall increased the energy absorption by (2, 34, 35)% for SW-G30mm, SW-G40mm (R) and SW-G50MM, respectively, as compared with reference model SW-G0mm.

Models with the gap (SW-G30mm, SW-G40mm (R) and SW-G50mm) had good energy absorption, and it was due to the high area under the curve of load-deformation, and it was referred to increase the resistance of the model to the deformation.

In the phase, D can be noticed that the energy absorption of the models SW-G30mm, SW-G40mm (R), and SW-G50mm was larger than by (10, 6 and 12)% as compared to the model SW-G0mm.
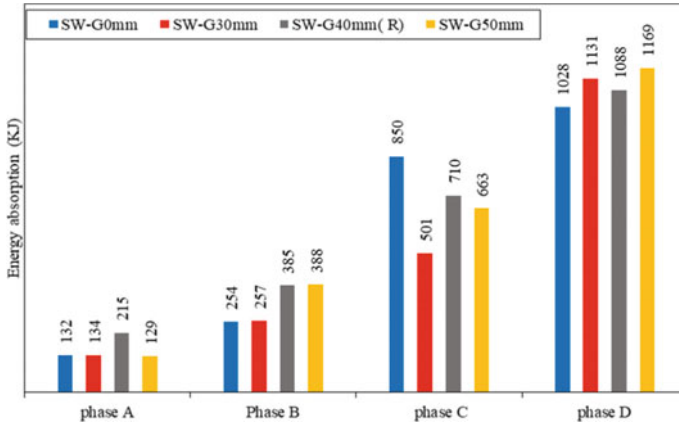
Fig. 13 Energy Absorption of Group 1

From the results of the phases above and the calculation of stiffness, ductility and energy absorption, it is noticed that the gap between the steel frame and concrete wall should be limited by a specific value (4% of the width) because this value gives a good result which results in delay the failures of the model and in the other hand this model economical in the amount of concrete. So, the other groups of smart CSPSW can use SW-G40mm (R) as a reference model.

5.1.2 The Second Group Models (Influence of Distance Between Shear Stud)

1. Lateral displacement

From the Fig. 14, it can be seen that the models SW-D210mm, SW-D220mm, SW-D230mm, SW-D240mm and SW-D250mm go through the same phase as the reference model SW-D200mm(R), when loaded gradually and which are as follows:

Phase A
For the models SW-D210mm, SW-D220mm, SW-D230mm, SW-D240mm and SW-D250mm, the elastic phase starts from the beginning of loading to the yield displacement. The lateral displacement value of the models SW-D210mm, SW-D220mm, SW-D230mm, SW-D240mm and SW-D250MM were lower by (20, 30, 58, 59, 60)% as compared with the reference model SW-D200mm(R) at the same load as a result of decreasing of the distance between shear stud of smart CSPSW which causes decrease the yield displacement and increase the yield load values that leads to increase the elastic stage for all the models as compared to reference model SW-D200mm(R).
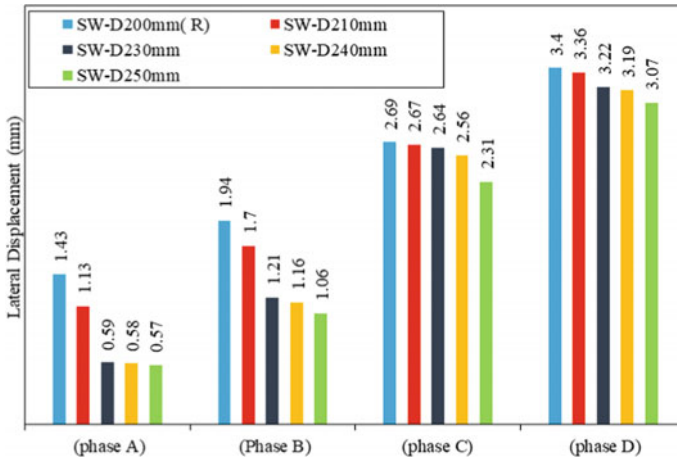
Fig. 14 Lateral displacement of group 2

From this, it can be noted that a decreased distance between shear studs in all the models has a large effect on the elastic stage for these models.

Phase B

The strength capacity of the models SW-D210mm, SW-D220mm, SW-D230mm, SW-D240mm and SW-D250mm, were governed by the plastic deformation which occurred as a result of the moment capacity and the shear force at the shear studs. This moment capacity of the models decreases due to a decrease in distance between shear studs (increased number of shear studs) as a result of the occurrence of a high reduction in the moment contribution of these models. So, the lateral displacement of the models SW-D210mm, SW-D220mm, SW-D230mm, SW-D240mm and SW-D250mm was lower than (12, 24, 37, 40, and 45)% as compared to the reference model SW-D200mm(R). From this, it can be noted that the presence of increased distance between shear studs effected significantly on the shear yield phase through the escalation of strain hardening capacity that lead to a significant in the escalation models' stresses redistribution compared with the reference model SW-D200mm(R).

Phase C

In this phase, all models of the second group have very similar behaviour with very close values of the yield load and yield displacement. It is also observed that the increased distance between shear studs in the CSPSW models didn't have a large effect on the Post shear yielding phase for these models. In this phase, when there is a variation in the distance between shear stud from (200–250) mm for SW-D210mm, SW-D220MM, SW-D230MM, SW-D240MM and SW-D250MM, the lateral displacement was lower by (0.74, 0.74, 1.86, 4, 14)% as compared with the reference model SW-D200mm(R).

Phase D

This phase begins when the model reached the ultimate load by exposure of all model elements that are situated above and below the shear stud to high stresses. The collapse of the reference model SW-D200mm(R) began with the occurrence of buckling in the infill steel plate as a result of using a large number of shear studs. In other words, the small distance between the shear studs leads to high plastification around shear studs as a result of exposure to a high compression which leads to global buckling failure mode.

After the comparison of the result in this phase at the same cycle of loading, it is noticed that the lateral displacement of SW-D210mm, SW-D220mm, SW-D230mm, SW-D240mm and SW-D250mm is lower by (1, 2, 5, 6, 9)% as compared with the reference model SW-D200mm(R).

Overall, it has been observed that the distance of shear stud has a slight effect on the term of lateral displacement, as shown in Fig. 15.
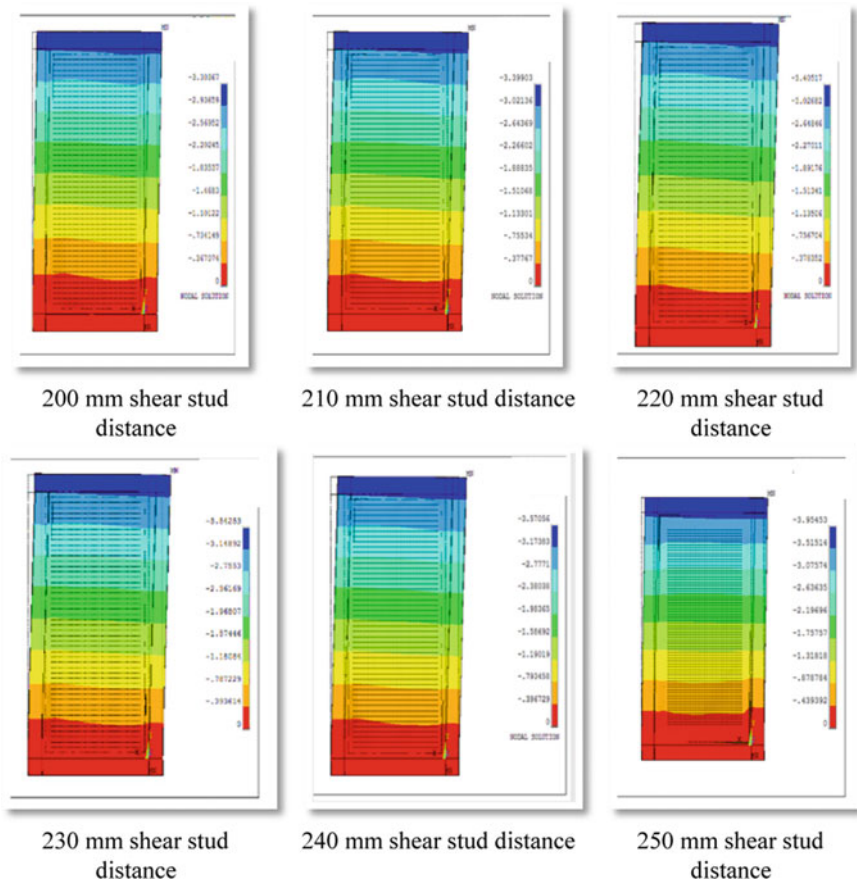
Fig. 15 Out of plane displacement of group 2 for various shear stud distance
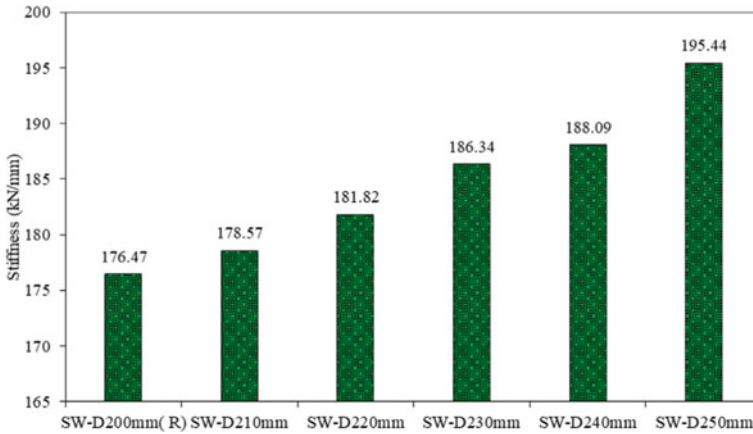
Fig. 16 Stiffness of group 2

1. Stiffness
   Figure 16 gives the values of the stiffness for the second group models. Figure 16 shows that increased distance between shear studs in the models SW-D210mm, SW-D220mm, SW-D230mm, SW-D240mm and SW-D250mm enhance their stiffness by 1, 3, 5, 6 and 10% respectively compared with the reference model SW-D200mm as a result of the small lateral displacement of these models. From these stiffness values, it can be seen that the distance between shear studs has very little effect on the model stiffness.

2. Ductility
   Figure 17 shows the ductility values of the second group models SW-D210mm, SW-D220mm, SW-D230mm, SW-D240mm and SW-D250mm. From Fig. 17, it can be concluded that the increased distance between shear studs in the models SW-D210mm, SW-D220mm, SW-D230mm, SW-D240mm and SW-D250mm enhanced their ductility significantly by 12, 22, 34, 37 and 40% respectively compared with the reference model SW-D200mm (R).

   It was observed a gradual drop in the load-carrying capacity of these models when they reached the ultimate load compared with the sudden and rapid drop of the reference model SW-D200mm (R).

3. Energy Absorption
   The results of Fig. 18 show the energy absorption of each model through each phase. For SW-D210mm, SW-D220mm, SW-D230mm, SW-D240mm and SW-D250mm in phase C, when the increasing the distance between shear studs then, the energy absorption increases by (14, 23, 32, 33, 30)% as compared with reference model SW-D200mm(R). While through the phase D, it can be seen that increased distance between shear studs increased the energy absorption by (9, 15, 20, 22, 24)% for SW-D210mm, SW-D220mm, SW-D230mm, SW-D240mm and
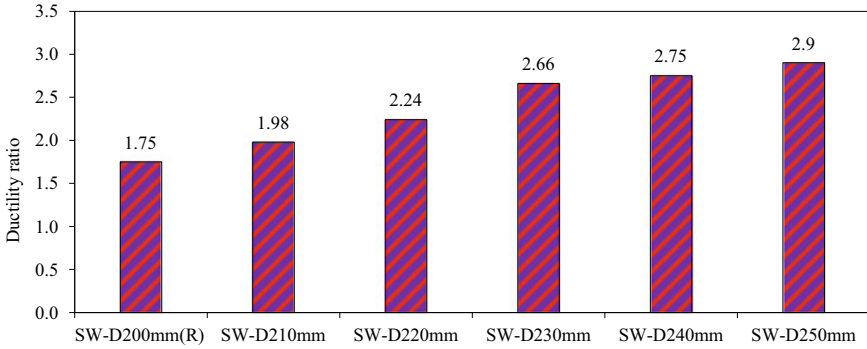
Fig. 17 Ductility ratio of group 2

SW-D250mm as compared with reference model SW-D200mm (R). The models with a large distance (SW-D250mm) have good energy absorption, and it was due to the high area under the curve of load–deflection, and it is referring to the increased resistance of the model to the deformation.

From the results of the phases above and calculation of stiffness, ductility and energy absorption, it is noticed that the distance between shear stud for (2000 * 1000) mm (length*width) specimen dimensions should be limited by a specific value (250 mm) because of large distances will cause widespread buckling of the steel plate in free sub-panels between shear stud and would result in no improvement, so the best range for the distance between shear stud was between (200–250) mm.
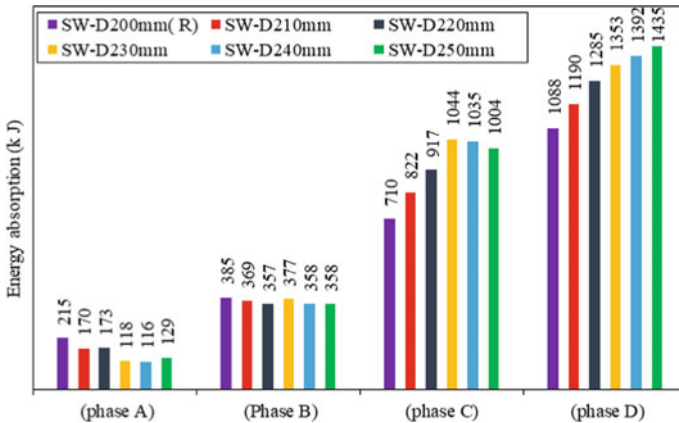
Fig. 18 Energy absorption of group 2

6 Conclusions

Based on the numerical results conducted in this study, the conclusion marks have been drawn as follows:

Increasing the gap between the steel frame and concrete wall has an effect on the sequences of yielding of components, where yielding showing in the beam and infill steel plate first. At the end of the test, the columns showed yielding at the base but didn't buckle. The gap between the steel frame and the concrete wall should be limited by a specific value (4% of the width) because this value gives a good result in delay failures of the model. On the other hand, this model is economical in terms of the amount of concrete.

The distance between shear stud for (2000 * 1000) mm (length * width) specimen dimensions should be limited by a specific value (250 mm) because large distances will cause widespread buckling of the steel plate in free sub-panels between shear stud and would result in no improvement, so the best range for the distance between shear stud was between (200–250) mm.

References

1. Ramesh, S.: Behavior and Design of Earthquake-Resistant Dual-Plate Composite Shear Wall Systems. Purdue University, West Lafayette (2013)
2. Bruneau, M., Alzeni, Y., Fouché, P.: Seismic behavior of concrete-filled steel sandwich walls and concrete-filled steel tube columns. In: Steel Innovations Conference 2013 (2013)
3. Yan, J.B., Yan, Y.Y., Wang, T.: Cyclic tests on novel steel-concrete-steel sandwich shear walls with boundary CFST columns. J. Constr. Steel Res. **164**, 105760 (2020). https://doi.org/10.1016/j.jcsr.2019.105760
4. Liu, Y., Zhou, Z., Cao, W., Wei, L.: Study on seismic performance of the masonry wall with lightweight concrete filled steel tube core column and thermal-insulation sandwich. J. Earthquake Eng. Eng. Vib. **15** (2016). https://doi.org/10.13197/j.eeev.2015.01.223.liuy.027
5. ASCE 7 Minimum Design Loads for Buildings and Other Structures (2022)
6. AISC American Institute of Steel Construction - Seismic Provisions for Structural Steel Buildings. Seismic Provisions for Structural Steel Buildings (2010)
7. Nie, X., Wang, J.J., Tao, M.X., Fan, J.S., Bu, F.M.: Experimental study of flexural critical reinforced concrete filled composite plate shear walls. Eng. Struct. **197**, 109439 (2019). https://doi.org/10.1016/j.engstruct.2019.109439
8. Othuman Mydin, M.A., Wang, Y.C.: Structural performance of lightweight steel-foamed concretesteel composite walling system under compression. Thin-Walled Struct. **49**, 66–76 (2011). https://doi.org/10.1016/j.tws.2010.08.007
9. Wright, H.: Axial and bending behavior of composite walls. J. Struct. Eng. **124**, 758–764 (1998). https://doi.org/10.1061/(asce)0733-9445(1998)124:7(758)
10. Wang, M.Z., Guo, Y.L., Zhu, J.S., Yang, X.: Flexural-torsional buckling and design recommendations of axially loaded concrete-infilled double steel corrugated-plate walls with T-section. Eng. Struct. **208**, 110345 (2020). https://doi.org/10.1016/j.engstruct.2020.110345
11. Zhang, X., Qin, Y., Chen, Z.: Experimental seismic behavior of innovative composite shear walls. J. Constr. Steel Res. **116**, 218–232 (2016). https://doi.org/10.1016/j.jcsr.2015.09.015
12. Zhang, W., Wang, K., Chen, Y., Ding, Y.: Experimental study on the seismic behaviour of composite shear walls with stiffened steel plates and infilled concrete. Thin-Walled Struct. **144**, 106279 (2019). https://doi.org/10.1016/j.tws.2019.106279

13. Najem, M.H.: Influence of concrete strength on the cycle performance of composite steel plate shear walls. DJES **11**, 1–7 (2018). https://doi.org/10.24237/djes.2018.11401
14. Najem, M.H.: The effect of infill steel plate thickness on the cycle behavior of steel plate shear walls. DJES **11**, 1–6 (2018). https://doi.org/10.24237/djes.2018.11301
15. Nguyen, N.H.; Whittaker, A.S. Numerical modelling of steel-plate concrete composite shear walls. Eng. Struct. **2017**, 150 (2017). https://doi.org/10.1016/j.engstruct.2017.06.030.
16. Epackachi, S., Whittaker, A.S., Varma, A.H., Kurt, E.G.: Finite element modeling of steel-plate concrete composite wall piers. Eng. Struct. **100** (2015). https://doi.org/10.1016/j.engstruct.2015.06.023
17. Rafiei, S., Hossain, K.M.A. Lachemi, M., Behdinan, K., Anwar, M.S.: Finite element modeling of double skin profiled composite shear wall system under in-plane loadings. Eng. Struct. **56** (2013). https://doi.org/10.1016/j.engstruct.2013.04.014
18. Wei, F.F., Zheng, Z.J., Yu, J., Wang, Y.Q.: Computational method for axial compression capacity of double steel-concrete composite shear walls with consideration of buckling. Gongcheng Lixue/Eng. Mech. **36** (2019). https://doi.org/10.6052/j.issn.1000-4750.2017.12.0938.
19. Guo, L. Wang, Y., Zhang, S.: Experimental study of rectangular multi-partition steel-concrete composite shear walls. Thin-Walled Struct. **130** (2018). https://doi.org/10.1016/j.tws.2018.06.011
20. Wang, M.Z., Guo, Y.L., Zhu, J.S., Yang, X.: Flexural buckling of axially loaded concrete-infilled double steel corrugated-plate walls with T-section. J. Constr. Steel Res. **166** (2020)
21. Shafaei, S., Ayazi, A., Farahbod, F.: The effect of concrete panel thickness upon composite steel plate shear walls. J. Constr. Steel Res. **117**, 81–90 (2016) . https://doi.org/10.1016/j.jcsr.2015.10.006.
22. Qin, Y., Shu, G.P., Zhou, G.G., Han, J.H.: Compressive behavior of double skin composite wall with different plate thicknesses. J. Constr. Steel Res. **157**, 297–313 (2019). https://doi.org/10.1016/j.jcsr.2019.02.023
23. Huang, Z., Liew, J.Y.R.: Structural behaviour of steel-concrete-steel sandwich composite wall subjected to compression and end moment. Thin-Walled Struct. **98**, 592–606 (2018). https://doi.org/10.1016/j.tws.2015.10.013
24. Li, X., Li, X.: Steel plates and concrete filled composite shear walls related nuclear structural engineering: experimental study for out-of-plane cyclic loading. Nucl. Eng. Design **315**, 144–154 (2017). https://doi.org/10.1016/j.nucengdes.2017.02.019
25. Epackachi, S., Nguyen, N.H., Kurt, E.G., Whittaker, A.S., Varma, A.H.: In-plane seismic behavior of rectangular steel-plate composite wall piers. J. Struct. Eng. **141** (2015). https://doi.org/10.1061/(asce)st.1943-541x.0001148.
26. JGJ/T 380 Technical specification for steel plate shear walls. Ministry of Housing and Urban-Rural Development, Beijing (2015)
27. ACI committee 318 building code requirements for structural concrete and commentary (ACI 318M-11) (2011)
28. ANSI/AISC N690–18 Specification for safety-related steel structures for nuclear facilities. Am. instit. Steel Constr. (2018)
29. Epackachi, S., Nguyen, N., Kurt, E.G., Whittaker, A., Varma, A.H.: An experimental study of the in-plane response of steel-concrete composite walls. In: Proceedings of the 22nd International Conference on Structural Mechanics in Reactor Technology (SMiRT-22), San Francisco, California, USA, 18 August 2013 (2013)
30. Yan, J.B., Liew, J.Y.R., Zhang, M.H., Sohel, K.M.A.: Experimental and analytical study on ultimate strength behavior of steel–concrete–steel sandwich composite beam structures. Mater. Struct./Materiaux et Constructions **48** (2015). https://doi.org/10.1617/s11527-014-0252-4.
31. Rahai, A., Hatami, F.: Evaluation of composite shear wall behavior under cyclic loadings. J. Constr. Steel Res. **65**, 1528–1537 (2009). https://doi.org/10.1016/j.jcsr.2009.03.011
32. Li, Q., He, Y., Zhou, K., Han, X., He, Y., Shu, Z.: Structural health monitoring for a 600 m high skyscraper. Struct. Des. Tall Spec. Build. **27** (2018). https://doi.org/10.1002/tal.1490.
33. Wang, R., Cao, W.L., Yin, F., Dong, H.Y.: Experimental and numerical study regarding a fabricated CFST frame composite wall structure. J. Constr. Steel Res. **162**, 105718 (2019). https://doi.org/10.1016/j.jcsr.2019.105718

34. Tong, J.Z., Yu, C.Q., Zhang, L.: Sectional strength and design of double-skin composite walls withre-entrant profiled faceplates. Thin-Walled Struct. **158** (2021). https://doi.org/10.1016/j.tws.2020.107196

35. Zhao, Q., Astaneh-Asl, A.: Cyclic behavior of traditional and innovative composite shear walls. J. Struct. Eng. **130** (2004). https://doi.org/10.1061/(asce)0733-9445(2004)130:2(271).

36. Luo, Y., Guo, X., Li, J., Xiong, Z., Meng, L., Dong, N., Zhang, J.: Experimental research on seismic behaviour of the concrete-filled double-steel-plate composite wall. Adv. Struct. Eng. **18**, 1845–1858 (2015). https://doi.org/10.1260/1369-4332.18.11.1845

37. Huang, S.T., Huang, Y.S., He, A., Tang, X.L., Chen, Q.J., Liu, X., Cai, J.: Experimental study on seismic behaviour of an innovative composite shear wall. J. Constr. Steel Res. **148**, 165–179 (2018). https://doi.org/10.1016/j.jcsr.2018.05.003

38. Nie, J.G., Hu, H.S., Fan, J.S., Tao, M.X., Li, S.Y., Liu, F.J.: Experimental study on seismic behavior of high-strength concrete filled double-steel-plate composite walls. J. Constr. Steel Res. **88**, 206–219 (2013). https://doi.org/10.1016/j.jcsr.2013.05.001

Strength Evaluation and Retrofitting of Deteriorated Corrugated Girder

Akshaya Jayaprakash, J. Bharati Raj, and Keerthy M. Simon

Abstract Girders are horizontal structural supports that carry greater loads and are responsible for load transfer over longer spans. A structurally deficient girder may lead to the complete failure of structure. Corrosion is one of the major reasons for deterioration of the girder strength. Replacement of such girders is not possible and hence alternate strengthening methods have to be proposed. In this paper, performance degradation of corrugated steel girder in shear buckling under various damage scenarios have been discussed. An attempt has been made to analyse the strength of corrugated girder by imparting corrosion in three forms of surface corrosion. Also, the effect of retrofitting methods using fibre reinforced polymers (FRPs) on the strength of damaged corrugated girders has been studied using nonlinear static analysis in ANSYS Workbench 2021 R2 Software. The results indicate that the thickness loss governs the failure of steel girder and corrugation helps in better corrosion resistance. Also, it was found that the strength of the deteriorated girder could be enhanced by retrofit using carbon fibre reinforced polymer.

Keywords Corrugated girder · Local corrosion · Shear buckling failure · Stiffened corrugated steel web

1 Introduction

Girders are large deep beams used in construction, typically for longer lengths and is capable of carrying loads heavier than normal beams and is used as a horizontal main support for small beams in bridges. The performance of steel bridges under corrosion is strongly associated with the environmental conditions. Corrosion can

A. Jayaprakash (✉) · J. B. Raj · K. M. Simon
Department of Civil Engineering, NSS College of Engineering, Palakkad, Kerala, India
e-mail: akshayajayaprakash198@gmail.com

J. B. Raj
e-mail: bharatiraj@nssce.ac.in

K. M. Simon
e-mail: keerthymsimon@nssce.ac.in
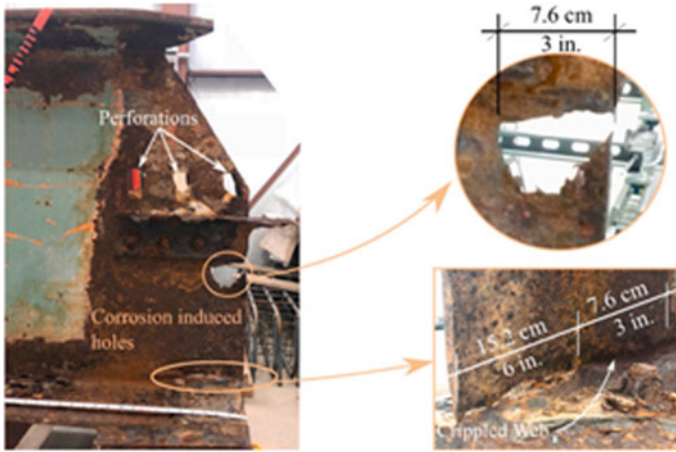
Fig. 1 Typical steel girder corrosion at web and flange [4]

be produced due to several reasons and its severity depends on the type and extend of corrosion [6].

Excessive corrosion over the years leads to the disconnection of the girder web from the flanges and causes structural deficiency of girders. Figure 1 represents a typical steel girder corrosion at web and flange.

Various studies have been conducted to address the extent of corrosion and the associated strength loss in girders [2]. Most studies have focussed on the torsional, shear, and flexural behaviour of the girders [1]. From past studies, it has been seen that corrugated webs provide high shear stability and eliminate the need for stiffeners [8]. The use of corrugated webs is not only economical but also increases the buckling strength, out of plane stiffness and aesthetics. In spite of these advantages, limited studies have been conducted on the effect of surface corrosion on the strength deterioration of corrugated girders. Hence, an attempt has been made to analyse the strength loss of a corrugated girder under corrosion and study the shear buckling behaviour of the girder. Also, a study on the effect of retrofitting on the strength of damaged corrugated girders has also been carried out using nonlinear static analysis in ANSYS Software, based on parameters like ultimate deflection, ultimate load, stress distribution, buckling failure mode and load–deflection curves.

2 Model Validation

The material properties and model dimensions for the validation was taken from the work by Georgios Tzortzinis et al (2021) in which the effect of deterioration of girders was carried out experimentally, analytically and numerically [4]. The analytical model was validated with specimen 1 (properties as shown in Table 1).

Table 1 Details of specimen 1 [4]

Properties	Steel components	
	Web	Flanges
Thickness (mm)	14.5	20.4
Depth (mm)	838.2	292.1
Yield stress (MPa)	317	262
Young's modulus (GPa)	200	200
Poisson's ratio	0.2	0.2

Flanges and plates were modelled using solid 186 and web by using shell 188. Mesh size was 20 mm. For the experimental configuration, the load was applied downwards at the top flange through a 460 mm long plate. At 1520 mm interval, restraint braces were placed. At each end, the beam was supported by bearing plates. In the analytical model, load was applied as a uniform pressure covering the entire flange width and was extended to 460 mm along the top flange. At the location of lateral torsional buckling (LTB) supports, out of plane displacement was restricted.

The two fixed steel bearing plates were used to support the bottom flange of the girder. Figure 2 shows the ANSYS model of the deteriorated girder.

The ultimate load carrying capacity of corroded girder obtained from literature was 596.5 kN and that obtained from the validation model was 570.45kN with a vertical displacement of 10.5 mm. The percentage error was found to be 4.3% (less than 5%), and hence could be validated.
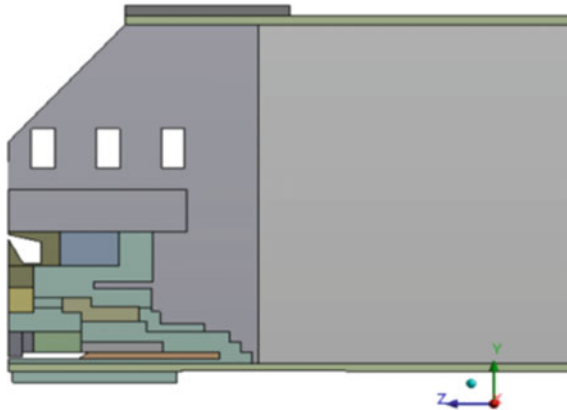
Fig. 2 Validation model

Table 2 Mechanical properties of steel components [9]

Properties	Steel components	
	Web	Flanges
Thickness (mm)	3	25
Depth (mm)	1200	25
Yield stress (MPa)	400	427
Young's Modulus (GPa)	203	202
Ultimate stress (MPa)	524	546

3 Analytical Programme

3.1 Material Properties

The material properties and dimensions of corrugated steel girder were taken form Sihao Wang et al. (2019) [9]. The girder of span 4400 mm and web depth 1200 mm was modelled. The material properties of the components are given in Table 2.

3.2 Parametric Study

The loss of thickness is a major concern for strength reduction in girders. For the present study on corrugated steel girders, corrosion has been imparted in the analytical models as varying percentage of surface corrosion. Corrosion initiates on support area or corner area and gradually extends throughout the girder. Location of corroded area was fixed based on literature reviews [4]. The models were designated as shown in Table 3. As per the literature reviews it was clear that the corrosion can be modelled as thickness loss [4] and in addition to this, corrosion is associated with different corrosion dimension along with the thickness loss. Case 1, 2 and 3 corresponds to thickness reduction of 25, 50 and 75% respectively. Seven models (S1 to S7) were considered for each case by varying the corrosion length and corrosion height dimensions. Each of these models have been compared with the normal corrugated girder (NCG) of dimension 1200 × 4400 mm. S1 means that 25% of height and 25% of width got reduced and accordingly for S2, S3, S4, S5, S6 and S7.

3.3 Modelling

Figure 3(a) shows the design dimensions of corrugated steel web. The corrugations were provided in a trapezoidal manner [5]. The width of parallel and inclined folds was 110 mm and 90 mm respectively. The depth of corrugation was 55 mm.

Table 3 Specimen designations & dimensions

Cases	T (mm)	S1 H25 × W25	S2 H25 × W50	S3 H25 × W75	S4 H25 × W100	S5 H50 × W25	S6 H75 × W25	S7 H100 × W25
Case 1	2.25	300 × 1100	300 × 2200	300 × 3300	300 × 4400	600 × 1100	900 × 1100	1200 × 1100
Case 2	1.5							
Case 3	0.75							
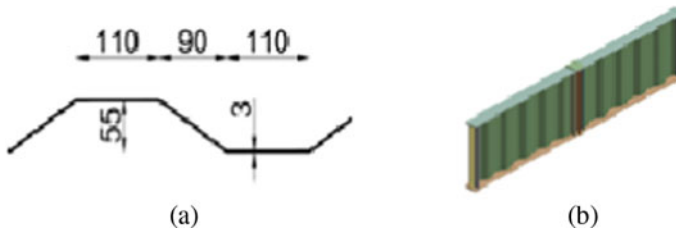
Fig. 3 **a** Corrugation pattern **b** Model of corrugated steel girder

Figure 3(b) indicates the model of the NCG steel girder of span 4400 mm, web depth of 1200 mm and web thickness 3 mm [9]. The three cases were modelled by reducing the web thickness to 2.25 mm, 1.5 mm and 0.75 mm corresponding to corrosion of 25%, 50% and 75% respectively.

Figure 4 shows the models of girders under various corrosion patterns (S1–S7) modelled using ANSYS Software. The elements were modelled using Solid 186 with a mesh size of 45 mm. The specimen was simply supported with concentrated load at centre. Similar modes were generated for case 2 and case 3 also.

4 Retrofitting of Deteriorated Corrugated Girder

The retrofitting of corrugated corroded girder can be done using several methods like post-tensioning, extended end plates and the use of fibre reinforced polymers (FRPs) [3]. In this study, the effect of retrofitting the corroded girders using carbon fibre reinforced polymer (CFRP) has been evaluated. Table 4 gives the mechanical properties of CFRP laminates used in modelling [7]. The yield strength of CFRP (1240 MPa) is higher than that of steel and CFRP has a low modulus of elasticity of 91.7 MPa. The deteriorated girder S1 with a thickness loss of 25% was selected for retrofitting. The model of the retrofitted girder is shown in Fig. 5. CFRP laminates were provided above the corroded portion only. Mesh size of 35 mm was adopted and the loading conditions were kept unaltered. Contact between CFRP and girder were modelled using the bonded connections in ANSYS Workbench.
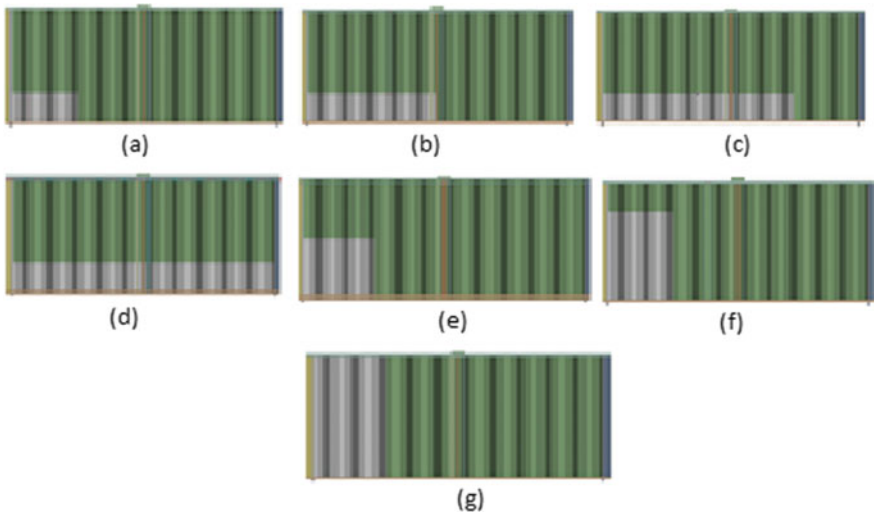
Fig. 4 Corroded girder specimens **a** S1 **b** S2 **c** S3 **d** S4 **e** S5 **f** S6 **g** S7

Table 4 Mechanical properties of CFRP [7]

Properties	CFRP
Thickness	1.27 mm
Modulus of elasticity	91.7 GPa
Bulk Modulus	76.4 GPa
Shear Modulus	35.26 GPa
Yield Strength	1240 MPa
Poisson's ratio	0.3

Fig. 5 Retrofitted girder (S1)

5 Results and Discussion

The corrugated girders were modelled and tested under displacement-controlled loading in ANYSIS software. All the seven specimens were modelled and analysed for corrosion of 25, 50 and 75% and was compared with the non-corroded corrugated girder (NCG).

5.1 Non Corroded Girder

The ultimate load of non-corroded steel girder was observed to be 1683 kN with a deformation of 10.93 mm. The load versus deflection curves were plotted for each case and compared with non-corroded specimen.

5.2 Corrosion Scenarios

The load–deflection curves for various cases were plotted and compared with NCG. Damage scenarios were simulated by varying the extent of corrosion in web depth and girder span. Figure 6(a) shows the combined load deflection curve for Case 1 (25% corrosion) and were compared with the load deflection curve of NCG. The ultimate load of non-corroded girder was 1683kN. The corrosion patterns are differed by their length and width and caused an average decrease of 24.7% in the strength of the girder. Figure 6(b) shows the combined load deflection curve for Case2 (50% corrosion). The results show that the strength of girder deteriorated by an average of 49.67%. Figure 6(c) illustrates the load deflection curve of Case 3 (75% corrosion). There was an average reduction of 75.34% in ultimate load. It could be noted that there was a drastic reduction in the strength of girders under corrosion in comparison with the non-corroded one. The percentage reduction in strength was nearly equal to the percentage of reduction applied on the web thickness. Stresses diagrams of case 1 are illustrated below in the Fig. 7. Case 2 and case 3 show similar pattern of results.

The deflection values of three cases were illustrated in the Table 5. There is not much variation in the defection values of S7 for case 2 and case 3 and this might be due to the simultaneous increase in corrosion length along with the thickness loss of 50% and 75%. Figure 8(A) And (B) illustrates the bar chart showing the variation of ultimate load and deflections of each specimen with respect to those of NCG. The stiffness of non-corroded and deteriorated girders was different but there was no significant change in the effective stiffness within the corroded specimens. The deflection of deteriorated girders decreased by an average of 23.68, 45.28 and 63.86% when compared with NCG for 25, 50 and 75% corrosion respectively. Figure 9 shows the diagram showing deflection of seven specimens for case 1. Case 2 and case 3 shows similar pattern of results.
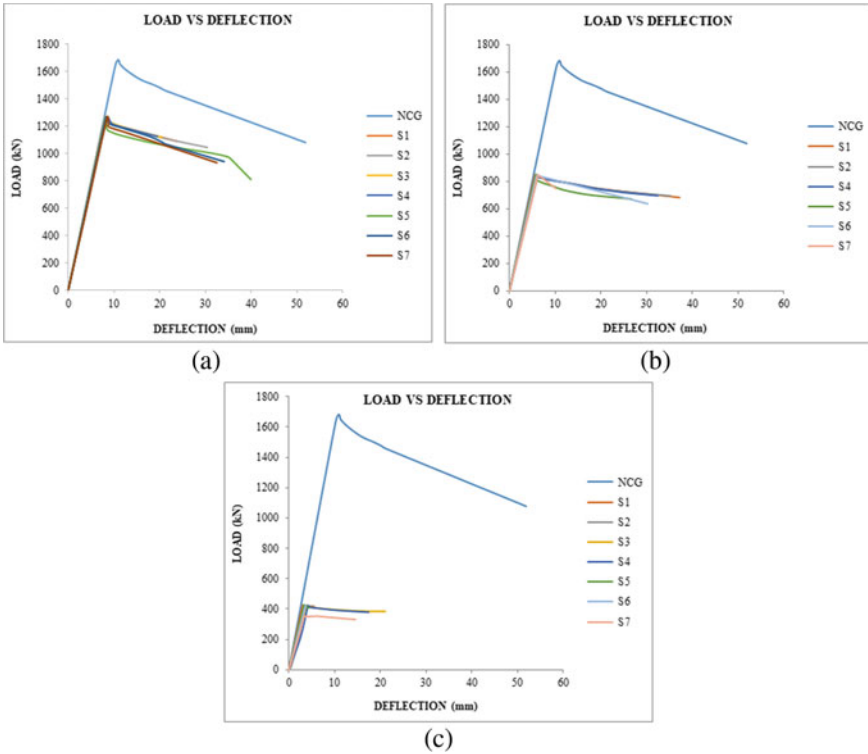
Fig. 6 Combined load deflection curve for Case 1, Case 2 and Case 3

It could be seen that irrespective of the corrosion length and width, the percentage reduction of load and deflections remained the same.

5.3 Retrofitting Using CFRP

The deteriorated girders were retrofitted by CFRP and the effect on the strength was analysed. The model S1 with 25% of thickness loss was chosen for retrofitting. Retrofitting was given in the corroded portion only for better economy. Figure 10(a) shows the deformed shape of the specimen. The results showed that the corroded portion failed by local buckling. When the model was retrofitted by using CFRP, there was a reduction in the buckling of the girder. Figure 10(b) shows the deformed shape of the retrofitted model. The ultimate load of the deteriorated specimen was initially 1267.3 kN with a corresponding deflection of 8.15 mm. Compared to NCG, there was a reduction of 24.7% in the strength of the specimen. On retrofitting, the strength was increased to 1634.8 kN with a deflection of 10.512 mm. This indicates that the strength of deteriorated girder was increased by 28.99% on retrofitting.
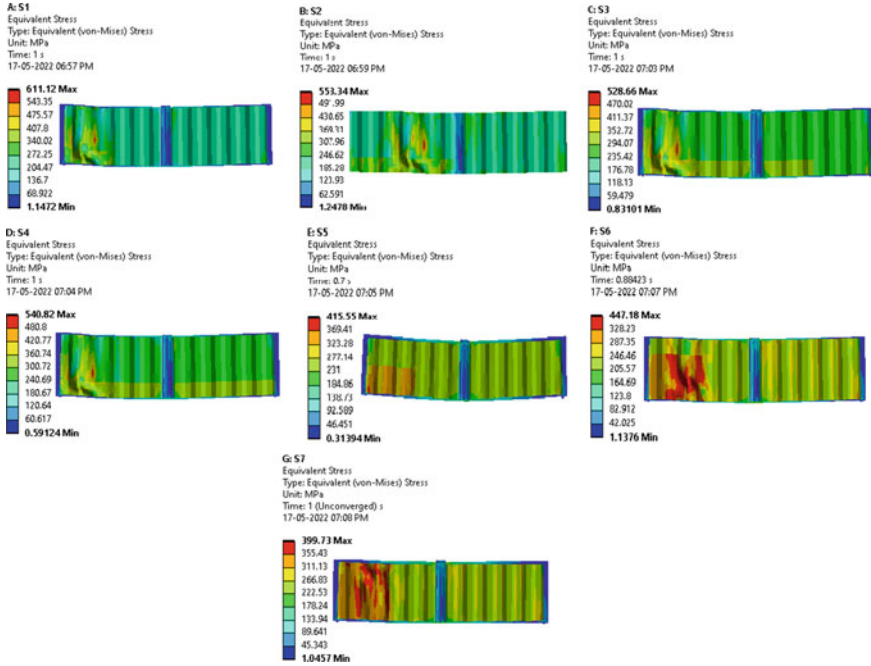
Fig. 7 Stress diagram for case 1

Table 5 Deflection of specimens in mm

T_{loss} (%)	S1	S2	S3	S4	S5	S6	S7
25	8.146	8.164	8.454	8.622	8.169	8.430	8.464
50	5.588	5.910	6.082	6.319	5.812	5.961	6.227
75	3.080	3.390	3.824	4.205	3.335	3.644	6.198
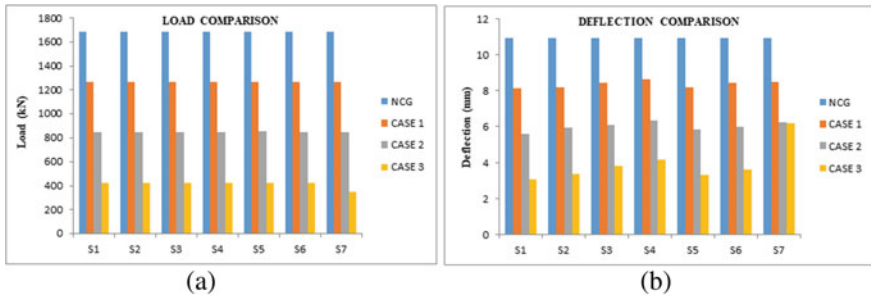
Fig. 8 **a** Load comparison **b** Deflection comparison
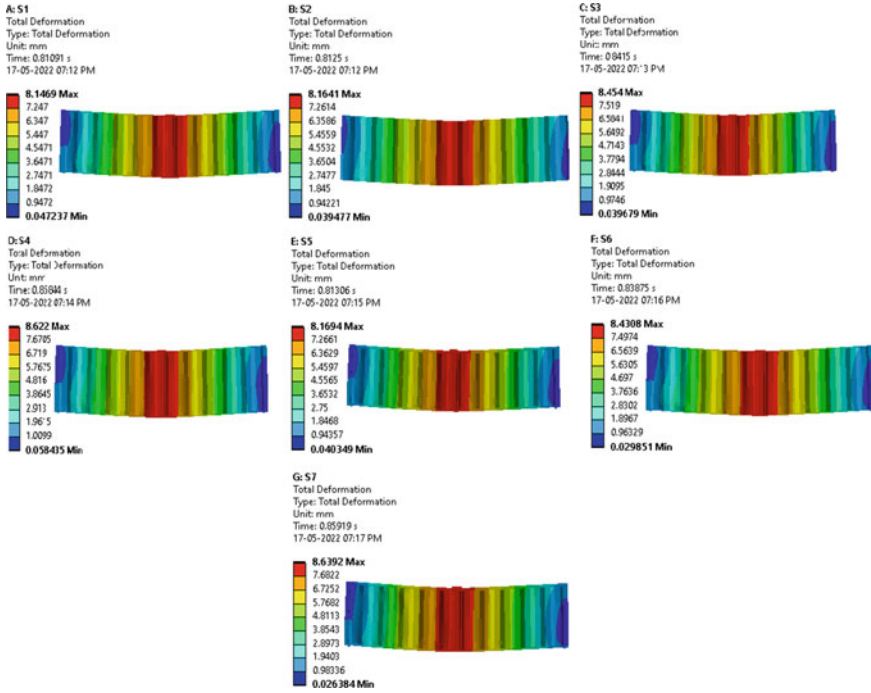
Fig. 9 Deflection diagram for case 1
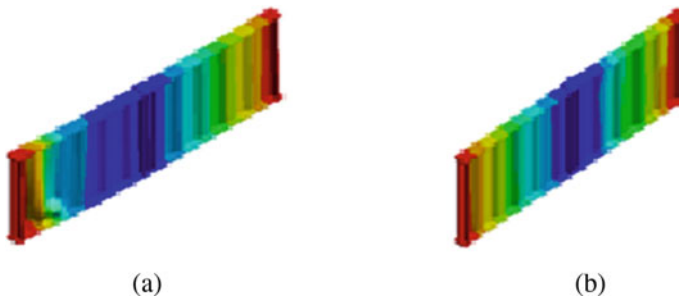
Fig. 10 Vertical deformation of **a** Deteriorated girder (S1) **b** Retrofitted girder

The combined load deflection curves of deteriorated and retrofitted models are shown in Fig. 11 The failure modes of deteriorated and retrofitted models are shown in Fig. 12(a) and (b) respectively.

As there is no significant variation of load among seven specimens, effect of retrofitting will be assumed to be same for the rest six specimens of case 1, and it can be predicted that retrofitting increases the strength for remaining cases also. Hence,
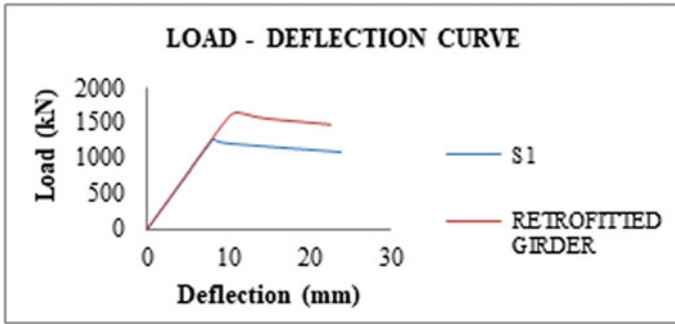
Fig. 11 Load – Deflection graph of retrofitted girder
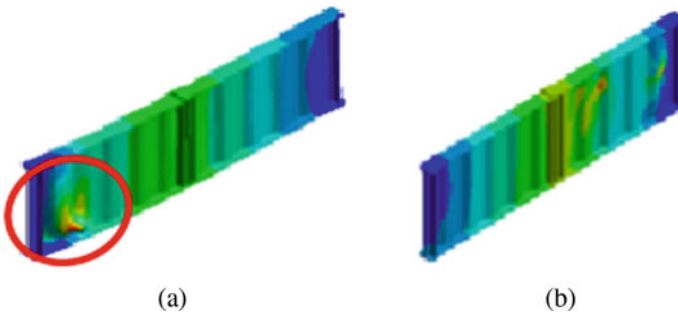
Fig. 12 Failure mode of **a** Deteriorated girder (S1) **b** Retrofitted girder

the retrofitting could be restricted to the corroded portion and not applied for the entire span, which would be an economical design option.

6 Conclusions

In this study, the strength of corroded corrugated girders was evaluated by nonlinear static analysis using ANSYS Workbench 2021 R2. The effect of retrofitting of the deteriorated girders using CFRP was also studied. The corrosion was initially induced at the bottom left corner and was spread along the full length and width of the web. The corrosion extent was considered as 25, 50 and 75% by applying a reduction in the web thickness. The load deflection responses of the specimens were compared with the non-corroded corrugated girder (NCG) and the following conclusions were arrived.

1. The thickness reduction in the web and flange is a major factor affecting the loss of strength in deteriorated girders. Also, the deformed shape of corroded beams is affected by the corrosion zone dimensions.

2. The ultimate load of deteriorated girders decreased by an average of 24.7%, 49.66% and 75.3% for a thickness loss of 25%, 50% and 75% respectively, which indicated that the percentage reduction in strength is nearly equal to the percentage loss of thickness in the girder.
3. The deflection of deteriorated girders reduced by 23.68%, 45.28% and 63.86% for 25%, 50% and 75% thickness loss respectively.
4. The effect of corrosion concentrated at bottom left portion is same as that of fully corroded specimen, so there is no significant variation in ultimate load and deflection for a given thickness loss along the length and width of web.
5. Retrofitting of deteriorated girder using CFRP increased the ultimate load by 28.99% and reduction in local buckling was observed. Hence, it could be concluded that retrofitting of the corroded girder by using CFRP laminates could be considered as an effective and economical method for enhancing the strength of corroded corrugated girders.

References

1. Biscaya, A., Pedro, J.J.O.: Experimental behaviour of longitudinally stiffened steel plate girders under combined bending, shear and compression. J. Eng. Struct. **238**, 112139 (2021)
2. Gong, C., Frangopol, D.M.: Reliability of steel girder bridges with dependent corrosion growth. J. Eng. Struct. **224**, 111125 (2020)
3. Xu, C., Xiao, H., Fu, J.: Fatigue behavior of steel fiber reinforced concrete composite girder under high cycle negative bending action. J. Eng. Struct. **241**, 112432 (2021)
4. Tzortzinis, G., Knickle, B.T., Bardow, A., Brena, S.F.: Strength evaluation of deteriorated girder ends II: numerical study on corroded I beams. J. Thin Walled Struct. **159**, 107216 (2021)
5. Kot, H.G., Toham, S.A., Saddek, A.B.: Shear buckling strength of plate girder with trapezoidal corrugated steel web. J. Eng. Technol. **35** (2016)
6. McMullen, K.F., Zaghi, A.E.: An accelerated repair method for steel girders with severe end corrosion damage. J. Eng. Struct. **251**, 113493 (2021)
7. L. Structural Group. V-Wrap™ C200-H: High strength carbon fiber fabric in strengthening solutions, ed. U.S.A: Structural Technologies LLC 2016, p. 2 (2016)
8. Dabaon, M.A., Boghdadi, M.H., Hadidy, A.M.: Nonlinear finite element modelling of plate girders with zigzag corrugated webs. In: International Conference on Advances in Structural and Geotechnical Engineering, ICASGE 2015 (2015)
9. Wang, S., He, J., Liu, Y.: Shear behavior of steel I-girder with stiffened corrugated web, part I: experimental study. J. Thin Walled Struct. **140**, 248–262 (2019)

Experimental Study to Compare the Behaviour of Drilling Fluids as a Borehole Stabilizer

Sneha Raju, V. Veena, and Liji Anna Mathew

Abstract Drilling Fluids or supporting fluids are used for the stabilization of boreholes. The most commonly used drilling fluids are bentonite slurry and polymer slurry. This paper presents the study on the effect of drilling fluids on the frictional resistance of bored piles in clayey sand. In this study sodium-based bentonite and cationic polyacrylamide were used. The rheological properties such as fluid density, viscosity and pH of the slurry, and optimum percentage of both the drilling fluids were determined. Apparent viscosity of the drilling fluids was found out using Marsh Funnel Apparatus. The percentage of bentonite was varied from 0 to 9%, whereas for polymer 0 to 0.2% was varied. By considering apparent viscosity and pH, the optimum percentage of bentonite and polymer slurries was found to be 8 and 0.05% respectively. A series of direct shear tests was conducted to determine the frictional resistance at soil - concrete interface with and without using drilling fluids. The results indicate that there is a reduction in the frictional resistance with the application of drilling fluids at soil-pile interface. The frictional resistance is more in the case of polymer slurry than bentonite slurry.

Keywords Drilling fluids · Frictional resistance · Rheological properties · Stabilization

1 Introduction

In India, tall buildings are becoming essential due to the growth in population and scarcity of land. In order to transfer heavy loads from these buildings to the soil, pile foundation is mainly preferred. But in the case of bored in-situ piles, there will be collapse of trenches in the sidewall of the borehole due to low adequate strength to bear heavy loads [6]. Drilling fluids are used as a borehole stabilizer [1]. The most commonly used drilling fluid is Bentonite slurry. During bentonite slurry circulation in the borehole, the slurry gets penetrated to the wall, which forms a layer of filter

S. Raju (✉) · V. Veena · L. A. Mathew
Department of Civil Engineering, Albertian Institute of Science and Technology, Kalamassery, Kochi, India
e-mail: rajubsneha92@gmail.com

cake which acts as an interfacial layer between the soil and the concrete. It effects the load bearing capacity of the pile [6]. Therefore, synthetic polymer-based slurry has been used as an alternative for bentonite [2, 3]. In the case of polymer slurry, there will be no filter cake formation [5, 6]. During excavation, polymer fluid will flow into the surrounding soil due to the difference in pressure head between the drilling fluid and ground water [5]. On permeation, the voids get occupied and a gel substance is formed which bonds the particles together [6]. It is non-pollutant and not harmful to the environment with less consumption quality as comparing it with bentonite [8]. The rheological properties determine the characteristics of the drilling fluid [6, 7]. By the usage of drilling fluids there will be effect on the frictional resistance of the piles.

2 Materials Used

2.1 Bentonite

Bentonite slurry is the mainly used drilling fluid due to its high swelling value and thixotropic nature [6]. It has high gel strength ang high montmorillonite content [1]. Mainly sodium-based or calcium-based bentonite are commonly used in the sites [4]. In this study sodium-based bentonite powder brought from Van Bent minerals was used with initial water content 19.4%. It has a liquid limit of 531% and pH of 9.77 which satisfies the criteria for selection as a drilling fluid given in IS 2911(part 1/sec 2) 2010. It has a free swell index of 514% and plasticity index of 475%.

2.2 Polymer

Sodium form of acrylamide polymer is mainly used. It is a chemically cationic polyacrylamide in the form of white granules which are completely soluble in water.

2.3 Clayey Sand

Clayey sand collected from a local site at Kochi was used in the study. Table 1 shows the physical properties of the soil. By particle size distribution it is found that the soil contains 78% of sand, 16% of silt and 6% of clay.

Table 1 Physical properties of Clayey sand

Property	Results
Colour	Black
Natural moisture content (%)	29
Specific gravity	2.66
Liquid limit (%)	25
Plastic limit (%)	Non-plastic
Cohesion (kPa)	17
Angle of internal friction (degrees)	34
Maximum dry density (kN/m^3)	18.7
Optimum moisture content (%)	12
Classification	SC

3 Rheological Properties

The term 'Rheology' deals with the study of flow and deformation of materials under applied forces [7]. To be an effective stabilizer, drilling fluids should satisfy certain parameters such as fluid density, pH and apparent viscosity [6].

3.1 Fluid Density

It represents the quantity of materials present in the drilling fluid. It can be found out by using Mud balance or Calibrated hydrometer.

3.2 pH

pH is a measure of the acidity or alkalinity of the slurry. Slurry that becomes acidic will fail to perform its necessary functions and become thin and watery. Therefore, the pH of the slurries should be alkaline and measures should be taken to keep it within the range.

3.3 Apparent Viscosity

It is defined as a substance's resistance to flow. It effects the load bearing capacity as it will not allow the soil particles to settle in the advancement of drilling of bore hole [6]. If the viscosity increases then the slurry will become thick and if the viscosity

decreases the slurry will be thin. It is measured by using Marsh funnel viscometer as per ASTM code D 6910.

4 Experimental Findings and Discussions

4.1 Rheological Properties for Drilling Fluids

Variation in Viscosity with Concentration. Different percentage of bentonite was added to 1500 ml of water and mixed for 10 min in a mechanical stirrer, and the time required was recorded. The time required to collect one quart of a litre or 946 ml of bentonite or polymer slurry from the marsh funnel cone is taken as the apparent viscosity. The time in seconds is recorded as a measure of the viscosity. The higher the viscosity, the fluid resistance is more. The optimum percentage is taken when viscosity has reached near to 60 s. For Bentonite the percentage added was varied from 0 to 9% and for polymer 0 to 0.2% was varied. From Tables 2 and 3 it is clear that there is an increase in the viscosity as the percentage of concentration increases. Table 2 shows that for bentonite slurry from 8% onwards the viscosity has reached near to 60 s. Table 3 shows that for polymer slurry from 0.05% onwards the viscosity has reached near to 60 s.

Variation in pH with Concentration. The pH value of the slurry was noted by using an electronic pH meter. First of all, the electrode has to be cleared by using distilled water. And mainly two buffer solutions are used for calibration. The two buffers are of pH 4 and 9.2. Then, both bentonite and polymer slurries were prepared by varying concentration. After that, pH values were found out by pH meter. Tables 4 and 5 shows the variation in pH value with varying concentration of slurries.

Table 2 Variation in viscosity with bentonite concentration

Percentage of bentonite added (%)	Viscosity (secs)
0	28
1	32
2	33
3	34
4	35
5	37
6	41
7	48
8	56
9	72

Table 3 Variation in viscosity with polymer concentration

Percentage of polymer added (%)	Viscosity (secs)
0	32
0.05	58
0.1	122
0.2	243

Table 4 Variation in pH with bentonite concentration

Percentage of bentonite added (%)	pH value
0	7.1
1	9.35
2	9.39
3	9.43
4	9.46
5	9.51
6	9.54
7	9.63
8	9.63

Table 5 Variation in pH with polymer concentration

Percentage of polymer added (%)	pH value
0	7.1
0.05	9.8
0.1	10
0.2	10

From Table 4 it is clear that there is an increase in pH value from 1 to 8% and the value is between the range of 9–11.5 as per IS 2911. Table 5 shows the variation in pH with polymer concentration and all mix satisfies the pH value range of 9–11.5. Therefore, by considering viscosity and pH value, 8% bentonite slurry and 0.05% polymer slurry taken as the optimum values.

Fluid Density. By using Calibrated hydrometer, the fluid density of 8% bentonite slurry and 0.05% polymer slurry were measured out. It was found to be 1.03 and 1.01 g/cc for bentonite and polymer respectively.

Optimum Values. The optimum values of drilling fluids that have to be used for finding out the frictional resistance are given below in Table 6.

Table 6 Optimum values of drilling fluids

Parameters	Bentonite slurry	Polymer slurry
Optimum percentage	8%	0.05%
Apparent viscosity	56 s	58 s
pH	9.63	9.8
Fluid density	1.03 g/cc	1.01 g/cc

4.2 Frictional Resistance at Soil-Concrete Interface with and Without Drilling Fluid

A series of direct shear tests were performed to study the effect of drilling fluid on the frictional resistance of soil. To obtain frictional resistance at soil-concrete interface, angle of internal friction and cohesion were measured using direct shear test. A fixed pre-failure plane was assumed to obtain frictional resistance, when a layer of drilling fluid was placed on that plane and sample was sheared. To represent a concrete pile, a cement mortar block of CM 1:2 was created with a block size of $6 \times 6 \times 1.6$ cm and it was placed in the lower portion of the direct shear mould. During the test the mortar block was kept at the lower half portion of DST mould and then the drilling fluid with optimum values was prepared and spread over the mortar block and kept for 15–30 min without being disturbed and then the upper half was filled with clayey sand with density as 1.87 g/cc. Three direct shear tests were conducted, one without any drilling fluid, next with 8% bentonite slurry and last one with 0.05% polymer slurry.

Figure 1a, b, c shows the photographs of test samples prepared without drilling fluid, with 8% bentonite slurry and with 0.05% polymer slurry respectively. Figure 2a, b, c shows the variation in shear stress with normal stress for samples prepared without drilling fluid, with 8% bentonite slurry and 0.05% polymer slurry. The shear parameters obtained from the direct shear tests are as given in Table 7. The results indicate that there is reduction in the values of cohesion and angle of internal friction while using drilling fluids at soil-concrete interface.

(a) Without drilling fluid   (b) With 8%bentonite slurry   (c) With 0.05% polymer slurry

Fig. 1 Photographs of direct shear test samples prepared with and without drilling fluids at soil–concrete interface

4.3 Effect of Drilling Fluids on Pile Capacity

As per IS 2911(part 1/sec2), the frictional resistance of pile in clayey sand can be calculated by Eq. (1) stated below.

$$\Sigma_{i=1}^{n}(A_{si}\alpha_i C_i + K_i P_{Di}\tan\delta_i A_{si}) \tag{1}$$

Here, coefficient for earth pressure for ith layer is assumed to be 1.5 for bored piles. Adhesion factor for i^{th} layer is considered as 1. The diameter and length of the test pile were assumed as 500 mm and 45 m respectively. Table 8 shown below gives the pile capacity due to frictional resistance under different conditions.

From Table 8, it is clear that by the use of polymer slurry the pile capacity due to frictional resistance reduced by 11.1% and in case of bentonite slurry the percentage reduction is 23.4%.
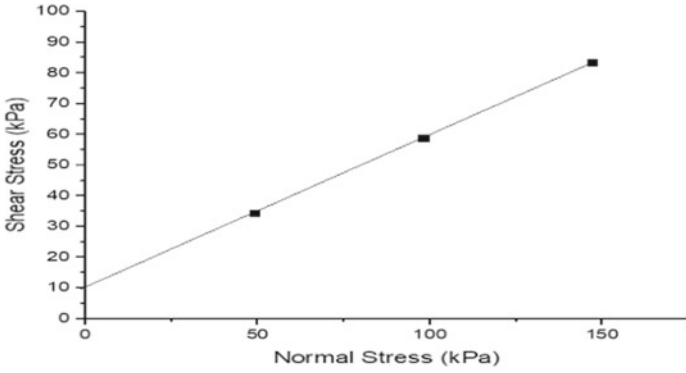
(a)   Without drilling fluid
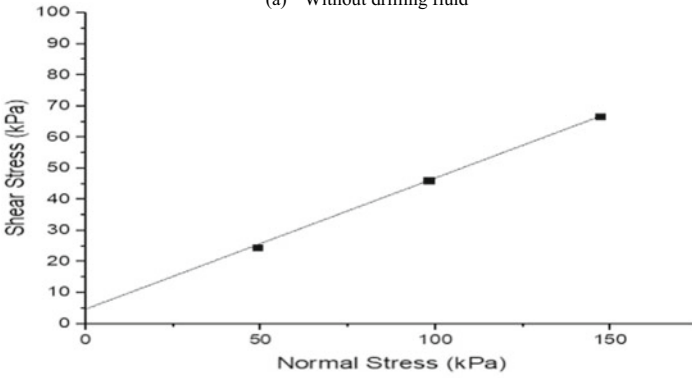
(b) With 8% bentonite slurry
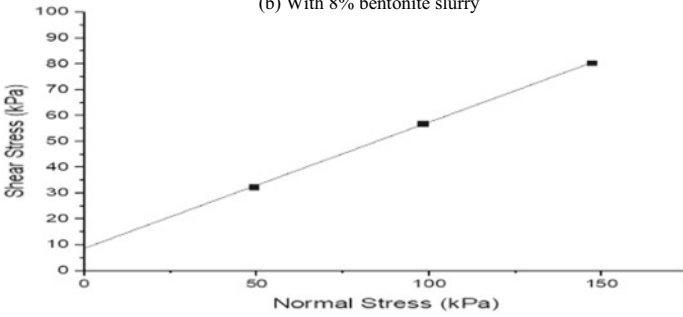
(c) With 0.05% polymer slurry

Fig. 2 Normal stress v/s shear stress for samples with and without drilling fluids at soil–concrete interface

Table 7 Shear strength parameters of soil with and without drilling fluids

Sample	Cohesion (kPa)	Angle of internal friction (degrees)
Without drilling fluid	10	27
With 0.05% polymer slurry	9.5	24
With 8% bentonite slurry	5	22

Table 8 Pile capacity due to frictional resistance under different conditions

Sample	Frictional resistance (kN)	Percentage reduction (%)
Without drilling fluid	5735	0
With 0.05% polymer slurry	5100	11.1
With 8% bentonite slurry	4391	23.4

5   Conclusions

The conclusions which are obtained from the study are mentioned below:

(1)   The optimum percentage of polymer and bentonite which was used for preparing the slurry was found to be 0.05% and 8% respectively.
(2)   A series of direct shear tests were performed on samples prepared with and without drilling fluid at soil–concrete interface. The results indicate that there is a reduction in angle of internal friction while using drilling fluids.
(3)   The angle of internal friction reduced from 27 to 24° when polymer slurry was used whereas with bentonite slurry it reduced to 22°.
(4)   Pile capacity due to frictional resistance at soil-concrete interface was calculated, and there is a reduction in the value of frictional resistance when drilling fluids are used as a borehole stabilizer. The use of polymer slurry reduced pile capacity due to frictional resistance by 11.1% due to the formation of thin polymer layer at the interface. The use of bentonite slurry reduced the pile capacity due by 23.4%, due to the formation of filter-cake at the soil-pile interface.

References

1. Alcheikh, I., Ghosh, B.: A comprehensive review on the advancement of non-damaging drilling fluids. Int. J. Petrochem. Res. **1**(1), 61–72 (2017)
2. Lam, C., Jefferis, S.A.: Performance of bored piles constructed using polymer fluids: lessons from European experience. J. Perform. Constr. Facil. **30**(2), 04015024 (2016)
3. Lam, C., Jefferis, S.A., Suckling, T.P.: Construction techniques for bored piling in sand using polymer fluids. Proc. Inst. Civil Engineers Geotech. Eng. **167**(6), 565–573 (2014)
4. Lam, C., Jefferis, S.A., Suckling, T.P., Troughton, V.M.: Effects of polymer and bentonite support fluids on the performance of bored piles. Soils Found. **55**(6), 1487–1500 (2015)
5. Lam, C., Martin, P.J., Jefferis, S.A.: Rheological properties of PHPA polymer support fluids. J. Mater. Civ. Eng. **27**(11), 04015021 (2015)

6. Ilamparuthi, K., Kumar,V.K.: Effect of filtercake on interfacial friction-an experimental study. In Proceedings of Indian Geotechnical Conference, pp. 183–186. Springer Nature, Singapore (2011).
7. Shrivastava, A.K., Jain, D., Vishwakarma, S.: Frictional resistance of drilling fluids as a borehole stabilizers. Int. J. Geo-Eng. **7**(1), 1–15 (2016)
8. Thasnanipan, N., Aye, Z.Z., Subaneewong, C., Teparaksa, W.: Performance of wet-process bored piles constructed with polymer-based slurry in Bangkok subsoil. In: Deep Foundations 2002: An International Perspective on Theory, Design, Construction, and Performance, pp. 143–157. ASCElibrary (2002)

Influence of DDBD Approach in Seismic Assessment of Vertically Irregular RC Buildings

Anurag Sharma, R. K. Tripathi, and Govardhan Bhatt

Abstract In recent years, the direct-displacement based design (DDBD) method has come up as an alternative to the traditional force-based design (FBD) method. Although several DDBD methods have been developed and used in the last few years, however in the context of open-ground storey (OGS) buildings, DDBD has received comparatively less attention from researchers. The most prevalent type of vertically irregular reinforced concrete building has been the OGS buildings, which have irregularity at the ground storey. The present numerical study investigates the applicability of the DDBD method for low-rise OGS buildings situated in Zone-V of Indian seismic regions. Different structural configurations buildings are adopted, having the same plan area but with different plan-aspect ratios. The non-linear static and time history analyses are performed under seven different spectrum compatible ground motions. The overall results of the study indicate the ability of DDBD to achieve the desired performance level for low-rise OGS buildings, except for a few cases. The plan-aspect ratio is also found to have a substantial impact on the seismic performance of OGS buildings during earthquakes.

Keywords Direct-displacement based design · Vertically irregular buildings · Static analysis · Dynamic analysis · Inter-storey drift

1 Introduction

The forced-based design (FBD) method is the traditional seismic design practice using either the modal response spectrum method or the equivalent lateral force method for the design of structures [1]. Most of the current national seismic design

A. Sharma (✉) · R. K. Tripathi · G. Bhatt
Department of Civil Engineering, National Institute of Technology Raipur, Raipur 492010, India
e-mail: asharma.phd2017.civil@nitrr.ac.in

R. K. Tripathi
e-mail: rktripathi.ce@nitrr.ac.in

G. Bhatt
e-mail: gov.ce@nitrr.ac.in

codes have been proposed based on the FBD method. But in recent years, it has been found that in FBD method, the inelastic seismic behaviour of structures cannot be estimated precisely. Therefore, to overcome the drawbacks of FBD method, Performance-based design (PBD) approach has been considered by the researchers. The main goal of PBD is to attain preferable performance level under the specific hazard level [2, 3]. Priestley [4] proposed the direct-displacement-based design (DDBD) method, which is one of the most prominent PBD methods. In the past decade, notable attempts have been made to develop the DDBD approach for several structural systems such as reinforced concrete frames, steel structures, masonry and isolation systems [5–8]. However, Open-ground storey (OGS) buildings have received comparatively less attention within the context of DDBD method. OGS are those buildings where masonry infill walls are given in all the stories except the ground storey. Sharma et al. [9] studied the applicability of DDBD method for low-rise RC buildings situated in Indian seismic regions. But, their studied where limited to bare frames. Varughese et al. [10] focused on OGS designed using DDBD method and suggested some modification by proposing a new-lateral load distribution pattern. Giannakouras and Zeris [11] investigates the DDBD approach for irregular RC frames emphasising on higher modes and second order ($P - \delta$) effects.

In this investigation, an attempt is made to explore the applicability of the DDBD approach on vertically irregular RC buildings (OGS) with different plan-aspect ratios, but with the same plan area and storey height. Buildings are assumed to be located in Zone-V (0.36 g) of India seismic region. To evaluate the seismic behavior of OGS frames, non-linear static pushover (NSA) and non-linear time history (NTHA) analyses are conducted. The buildings have been analysed in SAP2000 software [12]. As performance level criteria, a target drift of 1.5% representing the life-safety standard as defined by FEMA-356 [13] is used.

2   Basics of DDBD Approach

All the RC frame buildings are outlined using DDBD approach adopted from Priestley et al. [14]. To have a basic understanding of DDBD, a brief layout is explained through Fig. 1. The DDBD procedure is based on the transition of multi-degree of freedom (MDOF) system into an equivalent single degree of freedom (E-SDOF). The (E-SDOF) system is characterised by the effective stiffness at the desired design displacement. Equivalent viscous damping (EVD) for a specific design ductility is estimated based on the hysteretic behaviour. Then based on the design displacement and EVD, the effective period can be measured. As suggested by Priestley et al. [14], the aim of DDBD approach "is to obtain a pre-defined performance objective of a structure for a given intensity of ground motion through determination of required strength of structure". Mostly, performance objectives are expressed in terms of deformations (displacement, drifts etc.).
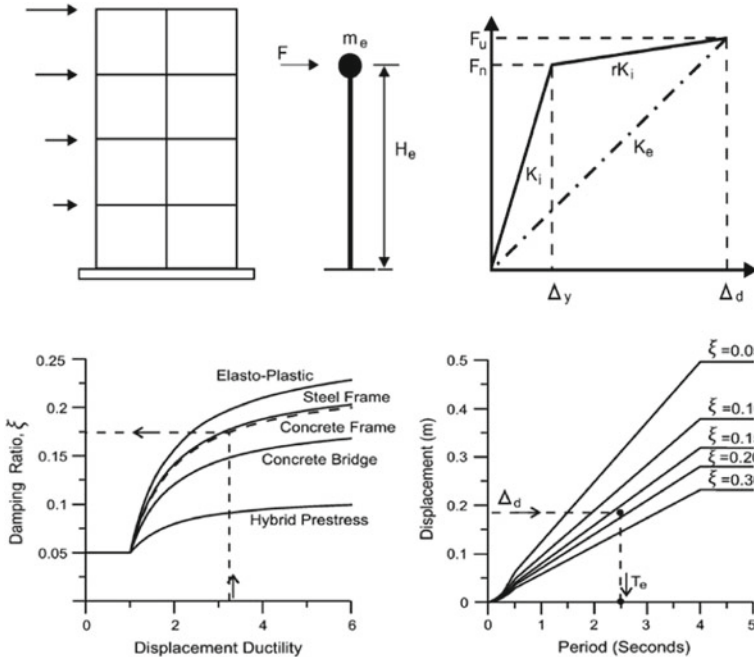
Fig. 1 Fundamentals of DDBD approach [14]

3 Building Design Consideration

Three vertically irregular RC buildings representing the different levels of plan-aspect ratios are considered shown in Fig. 2. Plan 1 (X4-Y4), Plan 2 (X4.8-Y5) and plan 3 (X6-Y4) have the plan-aspect ratios of 1, 1.5 and 2, respectively. For instance, plan 1 (X4-Y4) consists of a uniform span of 4 m in both X and Y directions, while plan 2 (X4.8-Y5) and plan 3 (X6-Y4) have three bays in longitudinal direction with span length of 4.8 and 6 m. Whereas, in transverse direction plan 2 and plan 3 have two bays with span length of 5 and 4 m. The plan area is kept constant at 144 m^2 and the storey height of all the plans is kept similar to 3 m each. As a result, the overall height of four-story buildings representing low-rise RC buildings is 12 m. Cross-section details of beam and columns obtained from DDBD procedure is provided in Table 1. Beam and columns are modelled considering non-linearity as per FEMA-356 [13]. The hinges are assigned at the end of beam (unidirectional moment -M3) and column (axial load and bidirectional moment -P-M2-M3). The cross-section of beams and columns are proportioned in such a manner that it fulfills the strong-column weak-beam theory. The masonry infills are modelled as equivalent compression struts. The macro-modelling approach is adopted as per Indian standard IS 1893 [15]. As a performance level, a target drift of 1.5% representing life-safety performance criteria as defined by FEMA-356 [13] is chosen.

(a)   Plan 1   (b)   Plan 2   (c)   Plan 3
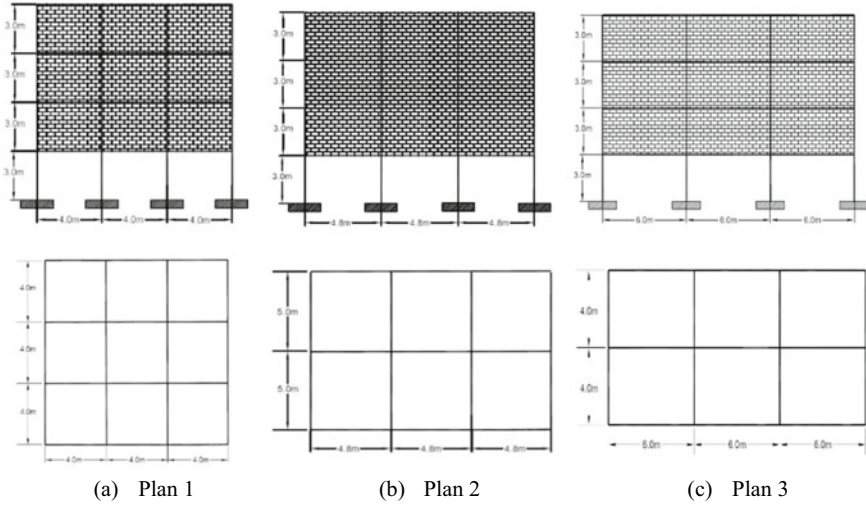
Fig. 2 Elevation and plan view of **a** Plan 1, **b** Plan 2, and **c** Plan 3 Four-Storied Buildings

Table. 1 Sections and reinforcement details

Plans	Section (m)	
	Beam	Column
Plan 1 (X4-Y4)	0.35×0.4	0.5×0.5
Plan 2 (X4.8-Y5)	0.35×0.4	0.5×0.5
Plan 3 (X6-Y4)	0.35×0.4	0.5×0.55

4   Seismic Performance of OGS Buildings

To estimate the seismic behaviour of selected OGS buildings designed using DDBD approach, non-linear static and dynamic analyses are performed using SAP2000 software [12]. Note that the P-delta effects are taken into consideration in both the analyses.

4.1   Non-linear Static Pushover Analysis (NSA)

Non-linear static pushover (NSA) analysis is an approach "in which the magnitude of the structural loading or displacement is incrementally increased in a certain predefined pattern which grossly identifies the weak links in the structure, strength, and ductility of the structure under monotonic loads" [16]. The results of the NSA are generally shown in the form of capacity curves. Figure 4 represents the capacity
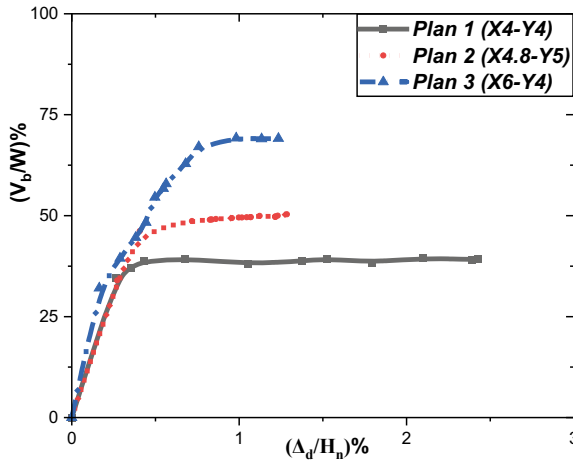
Fig. 3 Non-linear capacity curves of the OGS models

curves of all the selected OGS models. The Y-axis of the normalised pushover curves is the base-shear coefficient defined as the ratio of base-shear (V_b) to the seismic weight of the frame (W). Whereas, the X-axis represents the ratio of lateral displacement (Δ_d) to total height of the frame (H_n). The capacity curves show linear behaviour up to base shear of 38%, corresponding to plans 1, 2 and 3. At the same time, the lateral strength of plan 1 is found to be about 40% seismic weight at about 2.42% lateral drift. Similarly, for plan 2 and 3 the lateral strength is about 51 and 69% at about 1.28% and 1.23%, respectively. Because of the absence of infills and the existence of infill walls as an equivalent diagonal strut in the upper floors of OGS models, the majority of the lateral deformation is observed in the ground storey [17]. It is also noticed that as the plan-aspect ratio increases, there is a significant increase in stiffness resulting in higher base-shear values (Fig. 3).

4.2 Non-linear Static Time-History Analysis (NTHA)

Non-linear time history (NTHA) analysis is used to examine the seismic performance of the selected OGS frames. NTHA is carried out utilising seven historical ground motions selected from the CESMD website's strong motion database [18] and summarised in Table 2. Using SeismoMatch software [19], the GMs records are then changed to fit the target spectrum of Indian Standard IS 1893 [15]. Figure 4 depicts the compatible response spectrum of all seven ground motions with the Indian Standard target spectrum [15].

Inter-storey drift ratio (ISDR) is one of the key parameters in analysing the structural performance of buildings [20, 21]. The inter-storey drift ratio (ISDR) for the selected OGS frames is presented in Fig. 5. Time-history results of plan 1, plan 2
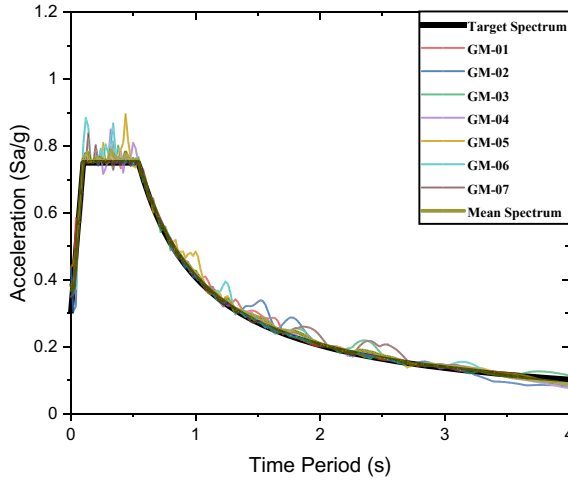
Fig. 4 Spectrum compatible ground motions

Table. 2 Earthquake ground motions

GMs	Event	Station	Year	PGA (g)
GM-01	Northeast - India	Saitsama	1986	0.460
GM-02	Uttarkashi	Tehri	1991	0.459
GM-03	India-Burma Border	Diphu	1995	0.488
GM-04	India-Burma Border	Doloo	1997	0.509
GM-05	India-Burma Border	Silchar	1997	0.537
GM-06	Chamoli	Ghansiali	1999	0.530
GM-07	Chamoli	Joshimath	1999	0.503

and plan 3 are presented in Fig. 5(a), (b) and (c), respectively. Whereas, mean values of ISDR of all study frames is shown in Fig. 5(d). It is noted that for plan 1, the maximum drift can be found in forIndian-Burma Border (IBB) Diphu earthquake at around 1.60% and mean drift of all seven earthquakes at 1.32%. Whereas, for plan 2 the maximum drift can be found for Indian-Burma Border (IBB) Diphu earthquake at 1.67% and average drift at 1.48% which is just 1.05% lower than the target drift of 1.5%. Similarly, for plan 3 having the plan-aspect ratio of 2, the maximum drift can be observed for Indian-Burma Border (IBB) Doloo at 1.81% and mean drift at 1.61% respectively. From Fig. 5(d) it can be noted that, the mean drift of all the plans is around 1.47%, which marginally satisfies the performance criteria of 1.5% drift level. Also, it can be seen that all selected models were able to satisfy the target drift, except for plan 3 model. Overall, for any ground motions, the OGS frame exhibits a very high ISDR response in the ground floor as compared to upper floors. Due to the
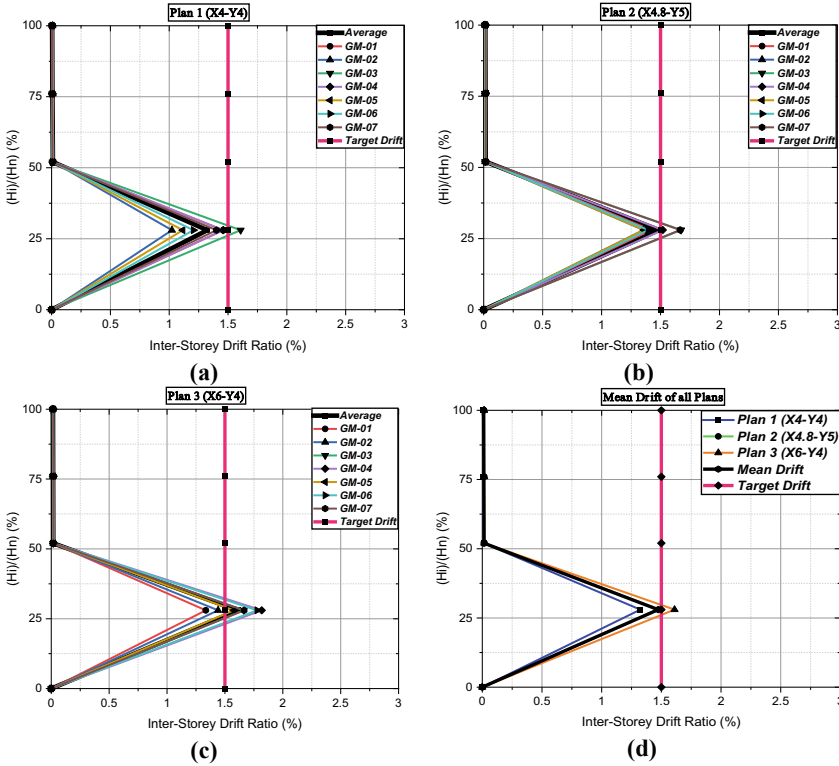
Fig. 5 Inter-Storey Drift Ratio (ISDR): **a** plan 1, **b** plan 2, **c** plan 3, **d** Mean

presence of infills in upper stories of OGS, there is very less relative displacement in upper stories resulting in very less ISDR response in upper floor levels [22].

5 Conclusions

The seismic performance of low-rise OGS buildings is assessed in this study using non-linear static and dynamic analyses. All the OGS buildings are designed using DDBD approach. Three different plans are selected, having different plan-aspect ratios of 1, 1.5 and 2. From non-linear static (NSA) results, it is concluded that as the plan-aspect ratio increses, there is significant increase in the lateral capacity of the OGS frame buildings. Also, from non-linear time history (NTHA) results, it is found that plan 1 and plan 2 were able to fulfill the target objective of 1.5% drift level. In contrast, plan 3 with plan-aspect ratio of 2 exceeds the target drift level by 6.84% making the building vulnerable to earthquake excitations. Therefore, it can be stated that the plan-aspect ratio has a significant contribution in the behaviour

of OGS buildings. Overall, it can be noted that the DDBD method is significant in designing OGS buildings, but with a scope of improvement in the design process to get much more desirable results.

References

1. Shakeri, K., Dadkhah, H.: Development of DDBD for steel MRFs using inelastic response-based seismic lateral force distribution. J. Build. Eng. **43**, 103063 (2021). https://doi.org/10.1016/j.jobe.2021.103063

2. Sharma, R.K.A., Tripathi, G.B.: Comparative performance evaluation of RC frame structures using direct displacement-based design method and force-based design method. Asian J. Civil Eng. **21**(3), 381–394 (2020). https://doi.org/10.1007/s42107-019-00198-y

3. Alehojjat, S.B., Bahar, O., Yakhchalian, M.: Improvements in the direct displacement-based design procedure for mid-rise steel MRFs equipped with viscous dampers. Structures. **34**, 1636–1650 (2021). https://doi.org/10.1016/j.istruc.2021.08.047

4. Kowalsky, M.J., Priestley, M.J.N., MacRae, G.A.: Displacement-based design of RC bridge columns in seismic regions. Earthq. Eng. Struct. Dyn. **24**, 1623–1643 (1995). https://doi.org/10.1002/eqe.4290241206

5. Priestley, M.J.N., Kowalsky, M.J.: Direct displacement-based seismic design of concrete buildings. Bull. New Zeal. Soc. Earthq. Eng. **33**, 421–444 (2000)

6. Pettinga, J.D., Priestley, M.J.N.: Dynamic behaviour of reinforced concrete frames designed with direct displacement-based design. J. Earthq. Eng. **9**, 309–330 (2005). https://doi.org/10.1142/S1363246905002419

7. Sahoo, D.R., Prakash, A.: Seismic behavior of concentrically braced frames designed using direct displacement-based method. Int. J. Steel Struct. **19**, 96–109 (2019). https://doi.org/10.1007/s13296-018-0092-0

8. Cardone, D., Palermo, G., Dolce, M.: Direct displacement-based design of buildings with different seismic isolation systems. J. Earthq. Eng. **14**, 163–191 (2010). https://doi.org/10.1080/13632460903086036

9. Sharma, A., Tripathi, R.K., Bhat, G.: Applicability of DDBD approach on low-rise RC buildings situated in Indian seismic regions. Arch. Struct. Constr. **1**, 193–205 (2021). https://doi.org/10.1007/s44150-021-00005-w

10. Varughese, J.A., Menon, A.D., Prasad, M.: Displacement-based seismic design of open ground storey buildings. Struct. Eng. Mech. **54**(1), 19–33 (2015). https://doi.org/10.12989/sem.2015.54.1.019

11. Giannakouras, P., Zeris, C.: Seismic performance of irregular RC frames designed according to the DDBD approach. Eng. Struct. **182**, 427–445 (2019). https://doi.org/10.1016/j.engstruct.2018.12.058

12. CSI and SAP2000. Integrated Software for Structural Analysis and Design. Berkeley, California: Computer and Structures Inc. (2020)

13. FEMA:356: FEMA - Federal Emergency Management Agency. Prestandard and commentary for the seismic rehabilitation of buildings. Washington, D.C. (2000)

14. Priestley, M., Calvi, G.M., Kowalsky, M.J.: Displacement-Based Seismic Design of Structures. IUSS Press (2007). https://doi.org/10.1193/1.2932170

15. Bureau of Indian Standard(BIS): IS: 1893-Part 1: Criteria for earthquake resistant design of structures, part-1 general provisions and building sixth revision. New Delhi (2016)

16. Kumbhar, O.G., Kumar, R., Noroozinejad Farsangi, E.: Investigating the efficiency of DDBD approaches for RC buildings. Structures. **27**, 1501–1520 (2020). https://doi.org/10.1016/j.istruc.2020.07.015

17. Kaushik, H.B., Rai, D.C., Jain, S.K.: Effectiveness of some strengthening options for masonry-infilled RC frames with open first story. J. Struct. Eng. **135**, 925–937 (2009). https://doi.org/10.1061/(ASCE)0733-9445(2009)135:8(925)
18. Center for Engineering Strong Motion Data. https://strongmotioncenter.org/
19. SeismoMatch: A computer program for an application capable of adjusting earthquake records (2020). www.seismosoft.com
20. Sharma, A., Tripathi, R.K., Bhat, G.: Seismic assessment of RC building frames using direct-displacement-based and force-based approaches. Innov. Infrastruct. Solut. **5**, 115 (2020). https://doi.org/10.1007/s41062-020-00364-1
21. Sharma, A., Tripathi, R.K., Bhat, G.: Direct-displacement and force-based seismic assessment of RC frame structures. J. Build. Pathol. Rehabil. **7**, 1–16 (2022). https://doi.org/10.1007/s41024-021-00160-z
22. Choudhury, T., Kaushik, H.B.: Component level fragility estimation for vertically irregular reinforced concrete frames. J. Earthq. Eng. **24**, 947–971 (2020). https://doi.org/10.1080/13632469.2018.1453413

Study on the Properties of Alccofine-1203 Based Self Compacting Concrete

A. A. Ruksana and S. Sreerath

Abstract Self Compacting Concrete (SCC) is a significant advancement in the concrete industry that has the ability to flow uniformly into formwork without vibration, segregation, or bleeding, and to create a good working environment without the need of vibration. However, the main ingredient, cement, has a huge carbon footprint owing to its manufacture and transport. The primary mitigation measure to counteract that would be reducing the use of cement. Supplementary Cementitious Materials (SCMs) can help to achieve that. Another key ingredient in the manufacture of SCC would be admixtures. The choice will depend on the compatibility. Alccofine-1203 is a mineral admixture of ultra-fine particle size and with great pozzolanic reactivity achieved through the method of controlled granulation. This study aims to investigate the partial replacement of cement with Alccofine-1203 in SCC. The fresh properties and compressive strength of SCC mixes prepared with varying doses of Alccofine-1203 content were studied. The fresh properties were assessed by slump flow, V-funnel & L-box tests and compressive strength test is also done as it is the key mechanical property. The results show that the utilization of Alccofine-1203 in SCC has great influence on engineering as a promisable construction material.

Keywords SCC (SCC) · Alccofine-1203 · Strength · Fresh properties · Compressive Strength

1 Introduction

Self Compacting Concrete (SCC) is an important invention for overcoming the problem of compaction in densely reinforced concrete constructions. Due to its unique qualities of flowability, SCC has shown to be a perfect alternative to traditional concrete in the construction industry over the years without vibrators. SCC has a similar composition as that of the traditional concrete, but with a higher amount of sand. Cement, fine aggregates, and a superplasticizer are used for its production.

A. A. Ruksana (✉) · S. Sreerath
Department of Civil Engineering, Federal Institute of Science and Technology (FISAT), Ernakulam 683577, India
e-mail: ruksanaabdulkareem@gmail.com

One of the main disadvantages of SCC is its high cost, which was because of the use of large quantities of cement and chemical admixtures. Hence, there comes a need to decrease this high consumption of cement in SCC by resorting to any other kinds of cementitious materials.

Meanwhile, cement production in the whole world accounts for around 7% of worldwide Green House Gas (GHG) emissions. When compared to other GHGs in the energy sector, CO_2 has a very high proportion. The percentage of CO_2 emissions not only demonstrates the negative influence on the ecosystem, but it also increases the GHG effect, producing global warming. Despite the fact that cement production emits GHGs as a byproduct, there is still a great need for this material in the global infrastructure construction. If this continues, the natural resources available for cement manufacture will get depleted, producing significantly furthermore environmental impacts and loss of natural resources. These two conditions necessitate the use of other cementitious materials that can totally or partially replace cement; these materials are known as Supplementary Cementitious Materials (SCMs). The addition of a few alternative pozzolanic elements to concrete has improved its strength, durability, workability and permeability.

Ambuja Cements has established the production of Alccofine-1203, a micro fine cementitious material produced from the industrial by-product of GGBS produced in a controlled manner. Alccofine-1203 is a specially treated product of slag with high amount of glass content and high range of pozzolanic reactivity prepared by the method of controlled granulation [5]. Available literatures have a common observation: due to higher specific surface area and high pozzolanic activity nature of Alccofine-1203, mechanical properties of SCC can be improved with the incorporation of Alccofine-1203 blended with other mineral admixtures. It has been also seen that the usage of SCMs instead of cement helps in the reduction of cement, also making SCC environmental friendly [1–4].

In the current study, a research was done on the possibility of creating an SCC by the replacement of cement with Alccofine-1203 alone, as a mineral admixture. Fresh properties and compressive strength studies of SCC mixtures were conducted. In all the mixes, Alccofine-1203 was replaced in varying proportions: 0, 6, 8, 10, 12 and 15% by weight of cement. Fresh concrete tests such as slump flow, V-funnel and L-box tests were conducted to confirm self compactability parameters. This study looks at how SCC can be combined with SCM to improve workability and compressive strength, resulting in a high-strength, cost-effective, and environment friendly concrete mix.

Table 1 Physical properties of cement

Experiment	Result	Standard method as per Indian Standard Code
Fineness	6.5%	IS:4031(Part-IV)-1988
Specific gravity	2.69	IS:4031(Part-XI)-1988
Initial setting time	85 min	IS:1489(Part 1)-1991
Consistency	33%	IS:4031(Part-IV)-1988

Table 2 Physical properties of fine aggregates

Sl. No	Properties	Test results
1	Specific gravity	2.75
2	Water absorption	1.31%
3	Fineness modulus	2.83

2 Experimental Investigation

2.1 Materials

2.1.1 Cement

Portland Pozzolana Cement (PPC) of Grade 53 conforming to IS:1489 (Part 1)-1991 is used for the preparation of various mixes. The physical properties of the used cement are listed in Table 1.

2.1.2 Fine Aggregate

M-Sand is used as fine aggregate and are tested as per IS:2386 (Part III)-1963. Physical properties of the used fine aggregates are tabulated in Table 2. Gradation of fine aggregates done by sieve analysis conformed to Zone-II as per IS:383–2016 and the gradation curve is shown in Fig. 1. M-sand of average particle size passing through 4.75 mm sieve is used in this study.
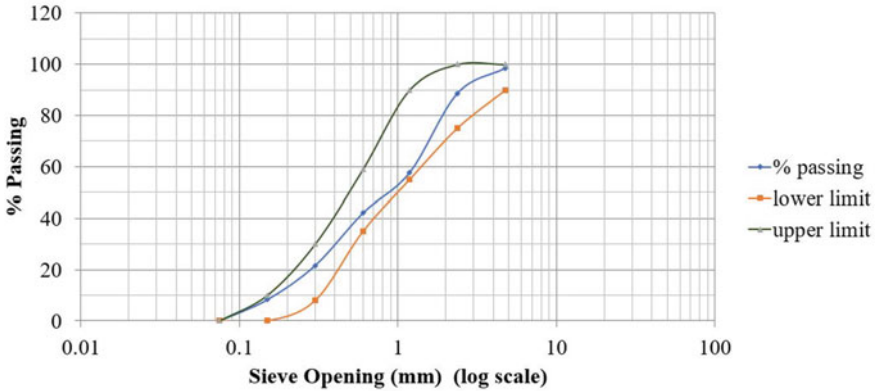
Fig. 1 Gradation curve of M-Sand

Table 3 Physical properties of coarse aggregates

Sl. No	Properties	Test results
1	Specific gravity	2.85
2	Water absorption	0.101%
3	Bulk density	1.33 kg/L

2.1.3 Coarse Aggregate

Crushed granite angular aggregates were available from a local source had a maximum size of 12.5 mm, is used for the present study. Tests on coarse aggregate are conducted according to IS:2386 (Part III)-1963. Physical properties of the used coarse aggregates are shown in Table 3.

2.1.4 Alccofine-1203

Alccofine-1203 was procured from Ambuja Cement Ltd., Goa, and was used throughout the investigation in accordance with ASTM C989-1999. Figure 2 shows a sample of the Alccofine-1203 material. Table 4 lists the physical and chemical properties of ALC.

Fig. 2 Alccofine-1203

Table 4 Physical and chemical properties of Alccofine-1203

Physical Properties of Alccofine-1203 *					
Fineness (cm^2/gm)	Specific gravity	Bulk density (kg/m^3)	Particle size distribution		
			D10	D50	D90
>12,000	2.9	700–900	1.5 micron	5 micron	9 micron
Chemical Properties of Alccofine-1203 *					
CaO	SO_3	SiO_2	Al_2O_3	Fe_2O_3	MgO
61–64%	2–2.4%	21–23%	5–5.6%	3.8–4.4%	0.8–1.4%

* As per manufacture's booklet

2.1.5 Polycarboxylate Ether Superplasticizer

Conflo-LN is a superplasticizer made from polycarboxylate ethers. With a relatively low dosage (0.3–0.4% by cement weight) they enable a water reduction up to 30%, due to their chemical structure which enables good particle dispersion. They increase the efficiency of cement by improving the workability of the cement mix. Table 5 lists the characteristics of Conflo-LN.

2.1.6 Water

The specimens are mixed and cured with potable water, as suggested by IS:456–2000. The presence of any kind of sulphates & salts can reduce the concrete strength and have to be avoided.

Table 5 Physical properties of Conflo-LN

Property	Value
Colour	Brown liquid
Consistency	Low viscosity
Specific gravity	1.19–1.20
Air entrainment	1–2% depending on sand grading & water content
Chloride content	Nil
Nitrate content	Nil

Table 6 Designation of specimens prepared with Alccofine-1203

Mix ID	Proportion of binding materials
CM	100% Cement
ALC6	94% Cement + 6% Alccofine-1203
ALC8	92% Cement + 8% Alccofine-1203
ALC10	90% Cement + 10% Alccofine-1203
ALC12	88% Cement + 12% Alccofine-1203
ALC15	85% Cement + 15% Alccofine-1203

2.2 Mix Proportions

SCC does not have a precise mix design. M30 grade concrete is developed in this study according to IS:10,262–2019 and EFNARC 2005 [9]. After varying between different dosages supplied by the manufacturer, a water binder ratio of 0.42 and 0.4 percent superplasticizer is finally adopted for all combinations. Control Mix (CM) was prepared without adding any kind of mineral admixtures in SCC as per the referred literatures. Five different SCC mixes were then casted, cured and tested to examine the influence of Alccofine-1203 on SCC, where PPC was replaced with Alccofine-1203 at 0, 6, 8, 10, 12 and 15% by weight of cement content.

The cement content taken is on the higher side of the generally adopted values. There are chances for shrinkage cracks with high percentage of fine content. No such cracks were seen in the casted specimens. If such cracks have formed internally, that would have reduce the strength of the specimen. In the present work, no such reduction in strength was observed. Hence the present mix design is adopted. The presence of shrinkage cracks and their effects is out of scope of this work. Tables 6 and 7 list the mix designations as well as the proportions of each blend.

Table 7 Mix proportions of SCC specimens

Mix ID	w/b	SP (%)	Water (kg/m³)	Cement (kg/m³)	Alccofine-1203 (kg/m³)	Fine aggregate (kg/m³)	Coarse aggregate (kg/m³)
CM	0.42	0.4	210	500	0	1125	515.85
ALC6	0.42	0.4	210	470	30	1125	515.85
ALC8	0.42	0.4	210	460	40	1125	515.85
ALC10	0.42	0.4	210	450	50	1125	515.85
ALC12	0.42	0.4	210	440	60	1125	515.85
ALC15	0.42	0.4	210	425	75	1125	515.85

Table 8 Fresh stage properties of different mix

Test	CM	ALC6	ALC8	ALC10	ALC12	ALC15
Slump Flow (mm)	690	698	705	718	710	680
V-Funnel (s)	9.27	10.02	9.1	8.65	11.2	11.85
L-Box	0.83	0.78	0.82	0.89	0.75	0.8

2.3 Testing of Specimens

Slump flow, V-funnel, and L-box tests were used to evaluate the workability properties of the mixes, according to EFNARC specifications and are summarized in Table 8. Compressive strength test conducted at the 7th day and 28th day of curing was performed according to IS:516–1959. Concrete cubes of size $150 \times 150 \times 150$ mm were prepared for the compressive strength test. The casted samples were kept in their moulds covered with a damp cloth at room temperature for 24 h. The specimens were removed from the moulds after 24 h and transported to the curing tank & is kept submerged for the respective time periods.

3 Results and Discussions

3.1 Fresh Properties

The workability properties of SCC were determined using slump flow, L-box and V-funnel tests to determine filling and passing ability. Table 8 shows the results of various workability tests of SCC blends.

Fig. 3 Slump flow test

3.1.1 Slump Flow Test

Slump flow test was conducted to determine the SCC's flow ability in terms of mean spread diameter and is shown in Fig. 3. According to IS:10,262–2019, the acceptable range for slump flow of class SF2 is 660–750 mm. All the test results lied within the range. It was observed that SCC mix containing 10% Alccofine-1203 had the highest slump value. This is because of the presence of high glass content and less water demand of Alccofine-1203.

3.1.2 V-Funnel Test

The flowability and stability of SCC mixes were determined using the V-funnel test. Figure 4 indicates the test setup for V-funnel setup. According to IS:10,262–2019, the acceptable range for flow time of SCC is 8–12 s. The results of V-funnel test are listed in Table 8. Shorter time indicated the greater flow ability. It was observed that the ALC10 mix showed the greatest flow among all the mixes.

3.1.3 L-Box Test

The L-box ratio (H2/H1) indicates the filling and passing ability of each mixture. Blocking is more common in L-box test than in other tests. Figure 5 indicates the test setup for L-box setup and Table 8 lists out the results of the test. As per IS:10,262–2019, the L-box blocking ratio (BR) must be less than 0.8 and shall not exceed 1. Higher values of BR represent lesser blockage of aggregates. It was observed that the combination containing 10% Alccofine-1203 had the highest BR value.

Fig. 4 V-funnel test setup

Fig. 5 L-box test setup

Fig. 6 Crack propagation pattern of cube sample at failure

3.2 Compressive Strength

Figure 6 shows the crack pattern of the failed cube sample. The compressive strength test revealed considerable performance differences, with the ALC10 series achieving the highest compressive strength. The compressive strength at different ages of ALC6 found to be decreasing than the control mix. The 7th day compressive strength of the mixes ALC8 and ALC10 was improved by 1.65 and 13.62% respectively, with respect to the control mix & the 28th day compressive strength of the mixes ALC8 and ALC10 was increased by 2.82 and 11.34% in comparison to control mix. The remaining mixes ALC6, ALC12 and ALC15 exhibited a decreasing pattern for the compressive strength in comparison to the control mix. i.e., beyond 10% replacement levels, it has resulted in the decrease in strength of ALC series.

Figure 7 indicates the compressive strength of normal SCC and Alccofine-based SCC mixes [10]. According to the results, the SCC mix created with 10% Alc-cofine-1203 had the highest compressive strength of all the mixes. This could be attributed to Alccofine-1203's ultra-fine nature and its physical characteristic of better packing. Compressive strength has been reduced for higher substitutions of Alccofine-1203 than 10%. It is attributed to the reason that at these addition levels, Alccofine-1203 being very finer than cement will increase the water demand for workable mixes leading to reduction in pore bonding strength; acts just as an SCM filling the pores, without getting involved in the hydration process.
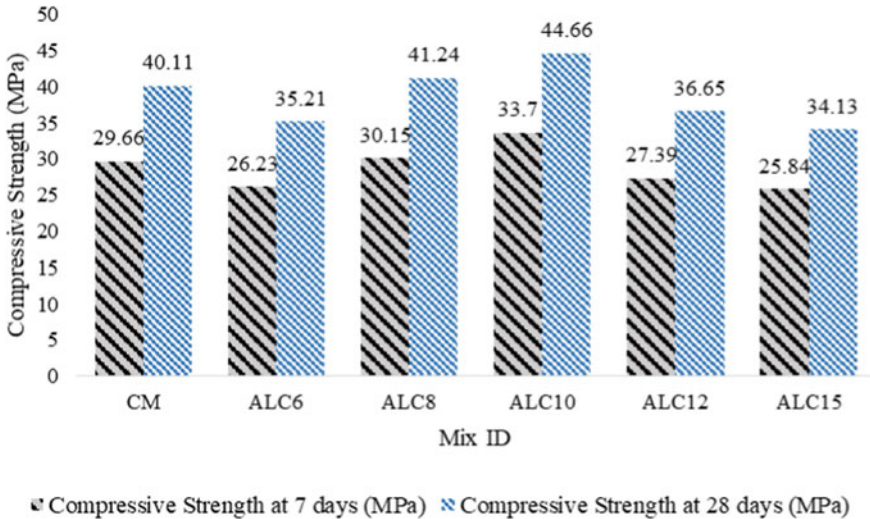
Fig. 7   7th and 28th day Compressive Strength (MPa) of SCC mixes

4   Conclusions

The purpose of the study is intended to analyze the fresh properties and compressive strength of Alccofine-1203-based SCC made with partial replacement of cement with Alccofine-1203. Following conclusions were drawn from the findings of the study:

1. The incorporation of Alccofine-1203 as an SCM enhanced the fresh and hardened properties of the SCC mixes because it has got high amount of silica content with great pozzolanic activity. As a result, more C–S–H gel is produced, resulting in an increase in compressive strength.
2. All the SCC mixes showed good workability properties with high flow ability and segregation resistance.
3. The optimum dose of Alccofine-1203 was found to be 10% by means of compressive strength test. The reason was the optimized size, ultrafine nature, unique chemical composition and high glassy nature of Alccofine-1203.
4. As a result, the Alccofine-1203 based SCC with 10% Alccofine-1203 content outperforms the target strength. Thus, it can be successfully replaced with cement.

References

1. Sai Srinath, B.L.N., Patnaikuni, C.K., Balaji, K.V.G.D., Santhosh Kumar, B., Manjunatha, M.: A prospective review of alccofine as supplementary cementitious material. Mater. Today: Proc. **47**, 3953–3959 (2021). https://doi.org/10.1016/j.matpr.2021.03.719

2. Kavyateja, B.V., Sashidhar, C., Sashidhar, C.: Effectiveness of Alccofine-1203 and fly ash on mechanical properties of ternary blended Self Compacting Concrete. Mater. Today: Proc. **33**(1), 73–79 (2020)
3. Khatana, R.S., Aggarwal, P., Aggarwal, Y.: Effect of Alccofine-1203 on fresh and hardened properties of self compacting concrete. In: National Conference on Technological Innovations for Sustainable Infrastructure (2015)
4. Mohan, A., Mini, K.M.: Strength and durability studies of SCC incorporating silica fume and ultra fine GGBS. Constr. Build. Mater. **171**, 919–928 (2018)
5. Sagar, B., Sivakumar, M.V.N.: Use of Alccofine-1203 in concrete: review on mechanical and durability properties. Int. J. Sustainable Eng. **14**(6), 2060–2073 (2021)
6. IS:4031(Part 1)-1996, Portland Pozzolana Cement -Specification, New Delhi, India
7. IS:383–2016 - Specification for Coarse and Fine Aggregates from Natural Sources for Concrete, New Delhi, India
8. IS:2386(Part 3)-1963 - Methods of test for aggregates for concrete: Specific gravity, density, voids, absorption and bulking
9. IS:10262–2019 Concrete Mix Proportioning—Guidelines." Bureau of Indian Standards, New Delhi, India
10. IS:516–1959 - Methods of Tests for Strength of Concrete, New Delhi, India

Value Engineering in Controlling Cost Overrun in Residential Building Projects

Riya Ann Varghese, Reshma Kassim, and Sinu Philip Varghese

Abstract On comparing with other industries, construction industry requires a huge effort to balance factors such as cost, quality and time. Cost overrun is a major factor that diminishes the value of construction projects. Saving money without compromising quality is an idea that everyone can promote. Value Engineering (VE) is a systematic approach that can be used to attain better balance between cost, quality and function of a product or facility. The main aim of this research is to identify the awareness level of VE in the construction sector and to compare the value generation for the client in terms of money before and after applying VE principles. In this research, a case study of residential building project is considered and focused on selecting best value-adding material for masonry work using VE phases. Questionnaire surveys are used to identify the awareness level about VE in construction sector and the responses are analyzed using SPSS software. To manage cost overrun in residential projects, this study focuses on recommending alternative proposals for building blocks that add value to the work at low cost without compromising the functional quality. Selection of best alternative is based on parameters such as cost, quality and availability, and material ranking using weighted decision matrix. The findings from the study showed that about 4% cost saving is possible by the application of VE in masonry work of residential project and also suitable recommendations are made based on the data collected.

Keywords Cost overrun · Poor value · Value Engineering · Weighted decision matrix

R. A. Varghese (✉) · R. Kassim
Saintgits College of Engineering (Autonomous), Kottayam, Kerala, India
e-mail: riyaa.secm2022@saintgits.org

S. P. Varghese
Nael General Contracting Group, Abu Dhabi, United Arab Emirates

353

1 Introduction

In the construction industry, it requires a huge effort to maintain the balance between factors such as cost, time, and quality. In order to achieve the value of construction projects, certain modern techniques can be easily adapted to stabilize the factors such as money, time, and quality. Value can define as a ratio of function to cost [5, 6]. Therefore, the value can be enhanced by either improving the function or minimizing the cost. Value Engineering (VE) is an efficient modern technique that can improve construction quality with an aim of low cost. According to the Society of American Value Engineers, VE is defined as a systematic application of accepted techniques that pick out the function of a product or service and deliver the required function efficiently at the lowest cost without compromising the functional quality. VE is not a cost reduction method but it is an approach to improve the value of service by modifying and enhancing functions [9].

1.1 Cost Overruns in Residential Projects

In the construction aspect, the expression 'Project cost' is defined as the financial sum needed to complete the production of construction items. From the literature study [3], it was identified that 9 out of 10 residential projects have passed previously set estimations. So, cost overrun is a serious issue that needs to be addressed. The term "Cost Overrun" is defined as the stage when the final project cost exceeds the original estimates. Poor quality material selection plays a vital role in controlling the overall project cost in residential building projects. There are many different methods to control cost overrun in construction projects, but any of these methods does not include an examination in terms of the "value". It can seen that many buildings were constructed at high costs, but the desired functions were not provided. In order to add value to the work, it is very necessary to maintain a balance between cost, time, and quality. A better balance between these three factors are possible by the application of VE concepts. VE mainly focuses on eliminating unnecessary costs [2] from the project, thereby increasing the value of that building and ensuring that resources like money, material, and workforce are not wasted.

1.2 Objectives of Study

1. To study and apply Value Engineering in construction industry.
2. To identify the awareness level of VE in construction sector in Kerala.
3. To compare the value generation of client in terms of money before and after applying the principles of Value Engineering in masonry works of residential building projects.

Table 1 Sample for the study

Site	Area of building	Project cost
Thiruvalla, Kerala	1920 SQFT	₹ 3,500,000

2 Application of Value Engineering on Residential Building Project

In this study, Value Engineering was applied on a residential building, especially on the masonry work using a proper VE job plan. The phases of VE include:

- Information phase
- Functional phase
- Creativity phase
- Evaluation phase
- Presentation phase

2.1 Information Phase

Information phase is the initial phase of VE. All necessary information and required data regarding the project were collected to find the issue to be solved and gather information regarding the function and requirement of the project [4]. As a part of this information phase, a residential building project at Thiruvalla, Kerala was taken as a sample for this study and the details are shown in Table 1.

2.2 Functional Phase

Functional analysis phase is the second phase of VE, which is used to identify the intended function of the specific project [1]. To eliminate unnecessary costs, project function have to be identified. The main function of a residential building project is to provide a structurally sound and secure accomodation for the occupants. In this study, poor functional value areas are considered as the areas where cost overrun is expected. So, poor functional value areas are identified by conducting pilot study which includes meeting with contractors and specialist in construction sector. Also, questionnaire surveys are conducted to get more responses regarding areas of poor functional value.

Pilot Study
Pilot study was conducted to identify potential problem areas and deficiency in research problem. This study was conducted with the purpose to identify the areas of

Table 2 Framework of questionnaire

Section	Details of questionnaire	Question type
1	Biographical information of respondents	Closed-ended
2	To identify the awareness level about VE	Closed-ended
3	To study cost overrun in residential projects	Closed-ended
4	Material study of alternative building blocks	Closed-ended
5	Ranking of masonry block	Closed-ended

poor value, thereby applying VE in the identified poor value area. It included interview with experienced professionals in constuction industry and obtained feedback regarding the possibility of cost overrun in residential buildings. From the feedback, it was identified that about 20 to 30% of total cost consist of cost for masonry work and most of them have experienced cost overrun in the residential building project. Using this preliminary information, masonry work was considered in this study to apply VE principles. Also, alternative proposals for masonry work (wall construction materials) were identified for further study.

Questionnaire Survey

Based on the information collected from the pilot study, questions are prepared. Questions are prepared according to the objectives of the study. The questionnaire survey helped to collect detailed information regarding the study from experienced professionals in the construction sector. The questionnaire consists of five sections and the format is represented in Table 2. The first four sections were used to add data to the functional phase of VE job plan. The last section of the questionnaire survey was used to collect information regarding the creativity phase of VE job plan. The responses are collected from architects, contractors, sub-contractors, structural engineers, and site engineers. The response rate was 51%, which shows the fact that it's little challenging to get a huge response rate upon conducting the questionnaire survey in the construction industry in this Covid 19 pandemic.

2.3 Creativity Phase

Creativity phase is the most challenging phase of VE job plan. The purpose of this phase is to generate a number of alternatives to accomplish the same function. Using the pilot study, masonry work is considered as a poor value area as we can expect the possibility of cost overrun due to poor material selection. So, the alternative materials considered for wall construction are brick, concrete block, AAC block, laterite block, fly ash brick, interlocking brick, hollow bricks and GFRG (Glass Fiber Reinforced Gypsum) panels. The last section of questionnaire survey was used to collect maximum information regarding the performance of alternative proposals of materials for masonry work. First part of this section includes questions regarding

Table 3 Weightage of criteria for selection of wall construction materials

Preference level	Score
Major preference	3
Average preference	2
Least preference	1

the preference level of factors such as cost, quality and availability during material selection for wall construction. Three preference levels are provided: major preference, average preference and least preference. The score of preference level is as shown in Table 3. The mean value of this score is considered as the weightage of each of these factors and used to calculate the weighted decision matrix to find out the best value adding material.

The second part of questionnaire survey focuses on identifying the cost effectiveness, quality, availability of building blocks such as brick, concrete block, AAC block, laterite block, fly ash brick, interlocking brick, hollow bricks and GFRG panels. These materials were ranked based on its cost effectiveness, quality and availability using four point Likert scale.

2.4 Evaluation Phase

The main purpose of the evaluation phase is to evaluate the obtained ideas and understand their advantages and disadvantages. Then it is reduce to a short list of ideas with greater potential to improve the project [7, 8]. The shortlisted ideas are presented in the final presentaion phase of VE job plan. The properties of alternative masonry materials considered are listed in Table 4.

There are so many tools to evaluate alternative proposals. In this study, tools like cost comparison, analysis using SPSS and weighted decision matrix were used to finalize an effective material that add value to the masonry work of residential building project at minimum cost without compromising the functional quality which is discussed in detail in Sect. 3, result and discussions.

3 Result and Discussions

3.1 Cost Analysis

The total quantity of brick, concrete block, AAC block, laterite block, fly ash brick, interlocking brick and hollow bricks for the sample residential building of 1920 SQFT and the corresponding cost was calculated. Quantity survey of the material

Table 4 Properties of masonry blocks

Alternative materials	Properties
Brick	Made from clay, compressive strength is in the range 3.5 to 35 N/mm^2, higher mortar consumption, required in more quantity, overall construction cost is high, requires more time to construct the wall
Concrete block	Made from cement and fine aggregates, less mortar consumption than brick, better strength, durable
AAC block	Lightweight construction block, reduce dead weight on structure, available in large size, faster laying is possible, price of individual block is higher but total construction cost is lower compared to bricks
Laterite block	Heavy building blocks, load bearing masonry block, available in Malabar region of Kerala, difficult to handle due to large size
Interlocking brick	Locked brick units, excellent seismic resistance, cost effective, plastering is not required, requires skilled labours, can be reused
Fly ash brick	Made from fly ash, sand, cement, lime and gypsum, flat and uniform surfaces, less mortar consumption, less chance for breakage
Hollow brick	Block with cavities, commonly used for compound wall construction, low cost blocks
GFRG panels	Modern building technique, light weight panels, faster construction, offer better strength, energy efficient, no need of plastering, saves construction time

was done using long wall - short wall method and the cost comparison is as shown in Table 5.

Table 5 Cost comparison of alternative proposals

SL. No.	Material	Size (cm)	Total quantity required	Price per piece (₹)	Total material cost (₹)
1	Brick	21 × 10 × 7.5	34,000	10	339,500
2	Concrete block	30 × 20 × 15	5941	36	213,876
3	AAC block	60 × 20 × 20	2230	85	189,550
4	Laterite block	35 × 20 × 20	3820	50	191,000
5	Interlocking brick	30 × 15 × 15	7921	35	277,235
6	Fly ash brick	60 × 20 × 15	2971	55	163,405
7	Hollow brick	30 × 20 × 15	5941	30	178,230
8	GFRG panel	–	–	1120 Rs/m^2	199,775

3.2 Analysis Using Statistical Package for Social Science (SPSS)

Data collected through questionnaire survey was analysed using SPSS software version 28. The rate of response to the questionnaire survey was 51%. The year of experience of the respondents is as shown in Fig. 1.

Reliability Analysis
In this study, the internal consistency was measured using Cronbach's alpha coefficient. It is most commonly used when we have multiple Likert questions in a questionnaire that form a scale and we wish to determine if the scale is reliable. When the average inter-item correlation increases, Cronbach's alpha also increases. The result of reliability analysis using SPSS is shown in Fig. 2.

From the analysis it was found that Cronbach's alpha value of the questionnaire of 41 items is 0.852, which indicate a very good level of internal consistency.

Awareness Level of VE
Awareness level of VE based on responses from questionnaire survey is as shown in Fig. 3.

From the frequency analysis of awareness level of VE, it was found that among the respondents the level of awareness of VE is only 62%. 39% of the respondents
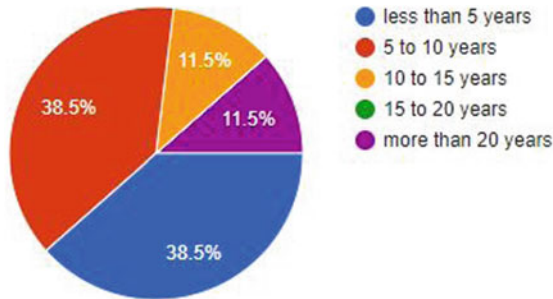
Fig. 1 Year of experience of the respondents

Fig. 2 Result of reliability statistics
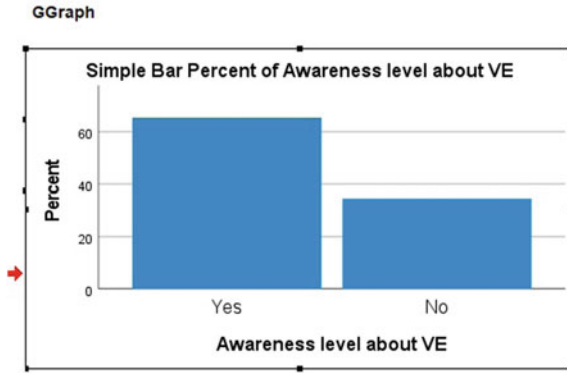
Fig. 3 Awareness level about VE

have year of experience in between 5 and 10 years and 12% of the respondents have year of experience above 20 years. The result indicate that the level of awareness is average.

Frequency Analysis of Cost Overrun in Residential Project

Bar chart of cost overrun in residential building is as shown in Fig. 4. Result of frequency analysis of percentage of cost overrun in residential building based on questionnaire survey is shown in Fig. 5.

From the frequency analysis of cost overrun in residential building project, the result and discussions are as follows:
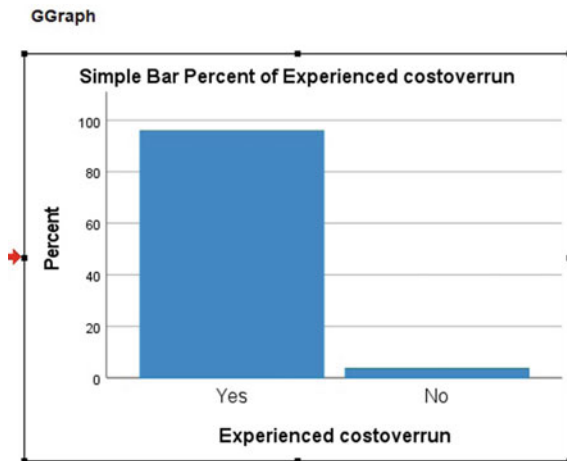
Fig. 4 Bar chart showing percentage of respondents experienced cost overrun in residential building projects. (SPSS result)

percentage of cost overrun in residential building projects				
		Frequency	Percent	Valid Percent	Cumulative Percent
Valid	5 to 10%	16	61.5	61.5	61.5
	11 to 20%	9	34.6	34.6	96.2
	above 30%	1	3.8	3.8	100.0
	Total	26	100.0	100.0	
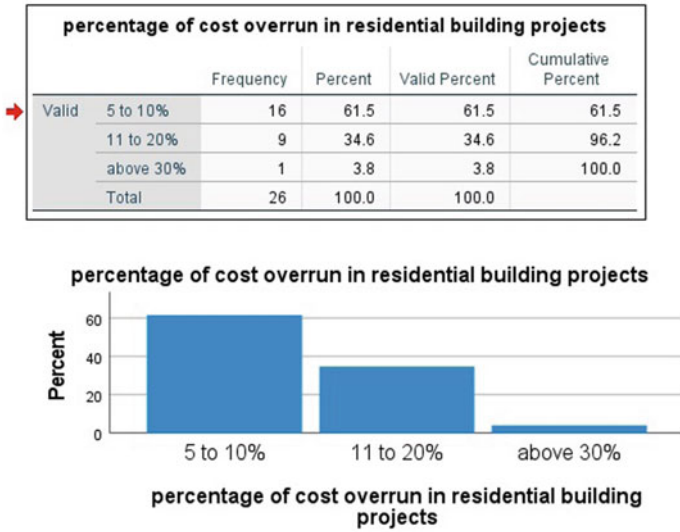
Fig. 5 Frequency table and bar chart showing the percentage of cost overrun in residential building projects. (SPSS result)

96% of the respondents experienced cost overrun in residential building projects. This is a clear indication that the level of awareness about VE in construction sector is average. 62% of the respondents experienced 5 to 10% cost overrun in the residential project that they are associated with. 35% of the respondents agreed that they have experienced 11 to 20% cost overrun in residential projects. It clearly indicated that the concepts of VE and awareness about VE are not utilized in a proper way.

From these findings, it was understood that there are some barriers in implementing VE in construction projects. Using the literature study, it was identified that lack of good knowledge, lack of support from top authority, lack of ability to take risk, and inadequate training are some of the factors that obstruct the application of VE. Also, the major problem is that, in most of the residential projects, traditional methods and materials are used. There is a reluctance in accepting new materials and methods which causes difficulties in implementing VE.

3.3 Weighted Decision Matrix

The weighted decision matrix is a powerful decision-making technique that can be used to evaluate a set of choices against a set of criteria. In this study, weighted decision matrix is used to find out the value adding material for wall construction. Material selection is based on the three criteria; cost, quality and availability. Weightage of these criteria was obtained from frequency analysis as shown in Fig. 6. Weightage

Frequencies

		Weightage of cost	Weightage of quality and performance	Weightage of availability
N	Valid	26	26	26
	Missing	0	0	0
Mean		2.38	2.92	2.58
Sum		62	76	67
Percentiles	80	3.00	3.00	3.00

Fig. 6 Weightage of cost, quality and availability (SPSS result)

Table 6 Material score

Material	Cost-effectiveness	Quality	Availability
Brick	2.31	3.42	3.19
Concrete block	3.04	2.96	3.65
AAC block	2.42	2.58	2.58
Fly ash brick	2.35	2.58	2.35
Laterite block	2.5	3.15	2.42
Interlocking brick	2.38	2.69	2.42
Hollow brick	2.65	2.04	2.96
GFRG Panels	2.77	2.12	2.96

of cost is 2 and for quality and availability, weightage is 3 (3- high preference, 2-average preference) and material score based on cost effectiveness, quality and availability is as shown in Table 6. Using this material score and weightage of criteria the best value-adding material is selected.

Using the weightage of cost, quality and availability and based on the material score weighted decision matrix of the alternative proposals was calculated and is shown in Table 7.

Most of the construction experts give high preference to quality and availability(weightage 3) and for criteria cost, average preference (weightage 2) is given. Using these weightage and score of each material based on cost effectiveness, quality and availability, the best alternative material can be choosen. Here, concrete block got high score 25.91 ≈ 26, as most of the respondents rank it as a highly cost effective, good quality and easily available material. In this study, for the selected sample 4% overall cost saving is possible by the use of concrete block. For brick, it has greater acceptance in terms of quality and availability, but in terms of cost effectiveness, brick has got least score. On comparing with other materials, large quantity of brick is required for masonry work. So, it results in a rise in the project cost, which does

Table 7 Weighted decision matrix

Criteria	Cost		Quality		Availability		Total score
Weightage	2		3		3		
Material	Score	Total	Score	Total	Score	Total	
Brick	2.31	4.62	3.42	10.62	3.19	9.57	24.45
Concrete block	3.04	6.08	2.96	8.88	3.65	10.95	25.91
AAC block	2.42	4.84	2.58	7.74	2.58	7.74	20.32
Fly ash brick	2.35	4.7	2.58	7.74	2.35	7.05	19.49
Laterite block	2.5	5	3.15	9.45	2.42	7.26	21.71
Interlocking brick	2.38	4.76	2.69	8.07	2.42	7.26	20.09
Hollow brick	2.65	5.3	2.04	6.12	2.96	8.88	20.3
GFRG panel	2.77	5.54	2.12	6.36	2.96	8.88	20.78

not meet the principles of VE. In case of AAC block, quality and availability wise the material is good, but it is not good as brick and cement block. On considering laterite block, it has got an acceptable score (21.71). But this material is highly available in malabar side of kerala. In this study, the sample selected was a residential building at Thiruvalla, where the availability of laterite block is very rare. Its transportation charge will add extra charges. Quality wise most of the construction experts do not prefer hollow blocks for residential projects. Also, availability wise interlocking brick does not have much acceptance. GFRG panels and fly ash brick have less acceptance in terms of quality. So, value of a project can be achieved only by using materials that have acceptance in terms of cost, quality and availability.

4 Conclusions

VE is an effective approach to manage cost overrun in residential building project without sacrificing the functional quality of the project. From this study, it was found that around 4% of cost saving (value generation) is possible by applying VE in masonry work in residential building of 1920 SQFT. Concrete block is identified as the best value adding masonry block. On comparing with brick, 37% material cost saving in masonry work is possible by using concrete block as a masonry block. Quality, cost-effectiveness and availability of materials have equal importance in selecting the best alternative using VE creativity phases.

Lack of knowledge, inadequate training, wrong belief, lack of risk-taking ability and lack of support from experts are the major obstacles for applying VE. Proper awareness programs and seminar about the importance of VE is necessary in order to enrich the knowledge of construction specialist and to improve the value of building projects. Proper education is necessary for clients and contractors to build a faith in applying VE principles. Based on the findings, the study recommends conducting

workshops and seminars about VE, which can improve the knowledge of the practitioners, improve awareness, and promote a positive impact on the construction industry projects.

References

1. Abdelfatah, S., Abdel-Hamid, M., Ahmed, A.A.: Applying value engineering technique using building information modelling at underground metro station. Int. J. Eng. Res. Technol. **13**(7), 0974–3154 (2020)
2. Al-Fadhli, S.K.I.: Value engineering and constructability assessment relating infrastructure projects. In: IOP Conference Series: Materials Science and Engineering, vol. 737, no. 1, p. 012040. IOP Publishing (2020)
3. Khodeir, L.M., El Ghandour, A.: Examining the role of value management in controlling cost overrun [application on residential construction projects in Egypt]. Ain Shams Eng. J. **10**(3), 471–479 (2019)
4. Mahadhik, U.A.: Value engineering for cost reduction and sustainability in construction project. IOSR J. Mech. Civil Eng. (IOSR-JMCE), 2278–1684 (2020)
5. Patil, S.D., Jadhav, S.S.: Implementation of VE for commercial and residential project. IJARIIE, 2395–4396 (2019)
6. Poornima, K.J., Chitra, G.: Application of value engineering for an institutional building. J. Adv. Civil Eng. Manag. **3**(1, 2) (2020)
7. Rad, K.M., Yamini, O.A.: The methodology of using value engineering in construction projects management. Civil Eng. J. **2**(6), 262 (2016)
8. Sharma, P., Srikonda, R.: Application of value engineering in affordable housing in India. Int. J. Eng. Technol. Manag. Res **8**(2), 29–40 (2021)
9. Ilayaraja, K., Zafar Eqyaabal, M.D.: Value engineering in construction. Indian J. Sci. Technol. **8**(32) (2016). https://doi.org/10.17485/ijst/2015/v8i32/87285

Wind Load Effect on Square and Helical Buildings

Himanshu Tonk, Ajay Pratap, Neelam Rani, and Vinayak Gautam

Abstract With the advancements in construction technologies, conventional shaped buildings have paved the way for the construction of buildings with unconventional designs that meet the aesthetic demands of modern times as well as counter the effects of wind more effectively. These aerodynamic modifications could be embedded in the basic structural design of the building, or these could be implemented by bringing about minor changes in the exterior of the conventional building. In this paper, numerical investigation is conducted on a square and 180° twisted square (helical) building model based on the wind tunnel experiment study. ANSYS FLUENT software is used for numerical simulation. Velocity profile inside wind tunnel and mean pressure coefficient on the faces of helical building for 0° wind direction is numerically validated with experimental result. Further, wind force coefficients evaluated on different faces of helical and square building are compared with each other under wind incidence angle of 0, 15, 30 and 45°. It was observed that the magnitude of force coefficient decreases for helical building when compared with square building.

Keywords Wind force coefficient · Mean wind speed · CFD · Turbulence intensity · Square building

1 Introduction

Over the years, Compuational Fluid Dynamics (CFD) has grown as an alternative over traditional methods of analyzing the effects of wind on the buildings, such as

H. Tonk (✉) · A. Pratap · N. Rani · V. Gautam
Dr. B R Ambedkar National Institute of Technology, Jalandhar, India
e-mail: himanshut.ce.20@nitj.ac.in

A. Pratap
e-mail: ajayp.ce.19@nitj.ac.in

N. Rani
e-mail: ranin@nitj.ac.in

V. Gautam
e-mail: vinayakg.ce.20@nitj.ac.in

Wind Tunnels owing to the several advantages it provides over wind tunnel studies. Mittal et al. [1] carried out CFD simulation using a feasible k–ε model that fairly matches experimental results for high wind conditions, whereas the modified SKE model performs better for simulating the flow in low wind speed regions. Revuz et al. [2] investigated a series of steady-state solutions in which the only parameter changed was the domain size, while the mesh resolution in the building/wake region remained constant. Liu and Niu [3] concluded that the effects of computational variables, such as grid resolution for all cases and discretization time step and non-dimensional sampling time for the Large Eddy Simulation (LES) and Detached Eddy Simulation (DES) cases, were investigated. Rajasekarababu et al. [4] conducted a logical assessment using the Improved Delayed Detached Eddy Simulation (IDDES) turbulence model in CFD to predict wind pressure coefficients and flow features on and around a 1:300 scaled setback tall building model at 0 and 90° AOI (Angle of Incidence) under open terrain conditions. Tanaka et al. [5] conducted wind tunnel experiments to determine aerodynamic forces and wind pressures acting on square-plan tall building models with various configurations such as corner cut, setbacks, helical, and so on.

In this research, this paper aims to validate the pressure coefficients on the experimental square building used in the wind tunnel experiments performed by Tanaka et al. [5] and then obtaining pressure coefficients for this building as well a single-sided helical building based on this square building having the same height by changing the Wind Incidence Angle (WIA) from 0–45° at every 15° interval.

2   Model Specification

Tanaka et al. [5] performed a wind tunnel study on square based models for the purpose of force and pressure measurements.

Two scaled models from the experimental paper are chosen for the purpose of this study, a basic square model (SQ) having dimensions Length (L) = 50 mm, Breadth (B) = 50 mm and Height (H) = 400 mm and a square based 180° helical model (HE) having similar plan dimensions. Figure 1 shows the two models. The height of both the models is same, i.e., H = 400 mm, thus L/B = 1 and H/L = 8. The length scale was 1/1000. For this paper, CFD study is performed on these models by varying Wind Incidence Angle (WIA) from 0 to 45° at every 15° interval. (WIA) parallel to X axis is 0° and it is varied upto 45° in anti-clockwise direction at 15° intervals. Faces of both the models have been named Face-A, Face-B, Face-C and Face-D in clockwise manner as shown in the figure. Roofs have been named Roof R-1 and Roof R-2 for square and helical model respectively. Figure 1 shows both the models.
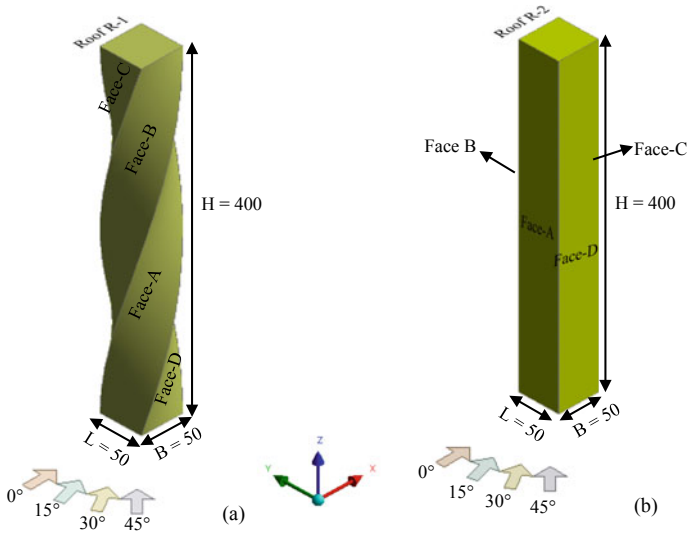
Fig. 1 **a** 180° helical model **b** Basic square model (all dimensions are in mm)

3 Computational Domain and Meshing

The fluid domain is created around the building model based on the guidelines of Franke et al. [6] (Fig. 2).

The inlet is placed at 5H from the windward face of the building, the outlet is placed at 15H from the leeward face of the building. Top and sides of the domain are also distanced at 5H from the building. The distance between inlet and building
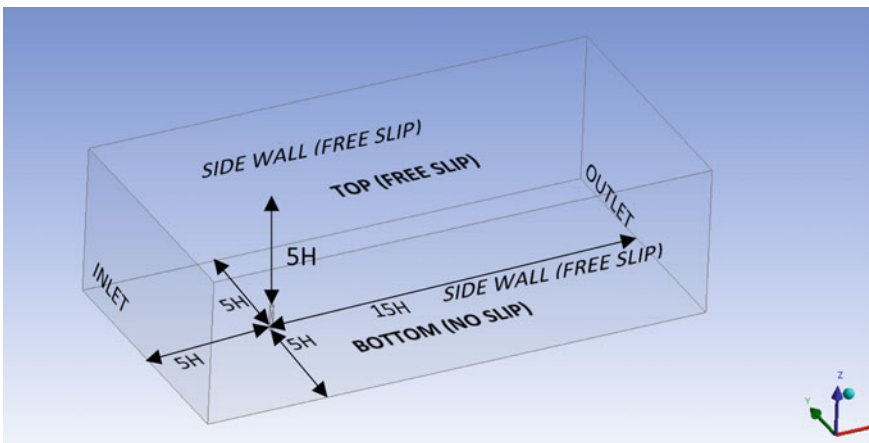
Fig. 2 Domain created for study
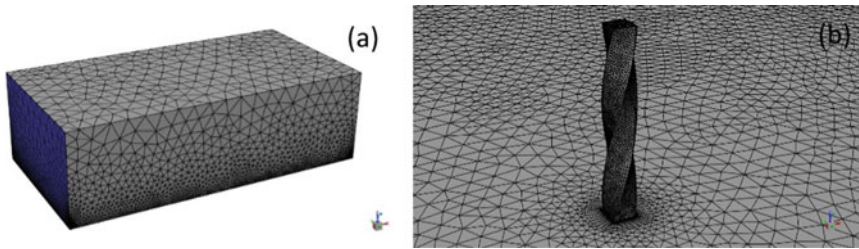
Fig. 3 a Meshed view of domain **b** 180° helical Meshing

corresponds to the area upwind of the building [7]. The top boundary is kept at 5H from the building to prevent artificial acceleration of the flow over the building and the total height of the computational domain should be set to correspond to the boundary layer height determined by the terrain category of surroundings [6]. The lateral distances of the domain from the building should ensure that the blockage ratio is less than the value of 3% [6, 8]. Unstructured meshing is adopted based on the recommendation of Tominaga et al. [7]. ANSYS Meshing software was adopted for tetra meshing of building model and fluid domain.

15 number of Inflation layers are provided around building models to capture boundary layer. A total of 557,572 elements are created in the meshing of 180° helical building model and fluid domain. Figure 3 shows the tetrahedral mesh created.

4 Boundary Conditions and Solver Setting

The inlet is designated as velocity-inlet, and the outlet is designated as pressure-outlet with a relative pressure of 0 Pa. [7, 8]. The side and top walls of the domain were specified as free slip and bottom, or ground was specified as no slip and rough. The building walls are specified as no slip and smooth. Power-law velocity profile has been specified as per the wind tunnel experiment [10]. Realizable k-ε turbulence model [11] is used, which is a modification of the Standard k-ε model. The k-ε turbulence models solve transport equations for turbulent kinetic energy (k) and dissipation rate (ε). Realizable k- ε model is a variant of the Standard k-model. Shih et al. [11] proposed some modifications to the standard k-ε model.

The ANSYS Fluent solver has been used to simulate the results. ANSYS Fluent employs the control-volume technique, first integrating governing equations for each discrete volume obtained by meshing the domain during the pre-processing or meshing stage, to formulate algebraic equations for dependent variables, and then linearizing those discretized equations to solve them. For incompressible flow, a "pressure-based" solver type has been chosen, and the simulation is steady state. The pressure–velocity coupling method is SIMPLE, and for pressure, momentum, and turbulence equations, second order differencing is used. For convergence, the residual value is set to 0.0001. Force coefficients, in addition to residuals, have

been used to monitor convergence. The initialization is Hybrid, and the number of iterations is set to 1000.

5   Result and Discussion

The velocity profile obtained from CFD simulation at the domain's inlet is validated with the velocity profile used in wind tunnel experiment of Tanaka et al. [5]. This is followed by the validation of the contours of mean pressure coefficients on the surface of the helical building model at 0° WIA against the contours obtained by wind tunnel experiment performed on the 180° helical model for the pressure measurement study.

5.1   Validation Study

Figure 4 shows the comparison of velocity profile obtained at the centerline of the computational domain's inlet by simulation against the experimental velocity profile used in the pressure measurement during the wind tunnel study of Tanaka et al. [5]. The figure shows that the CFD velocity profile is closely following the experimental profile thus confirming the accuracy of mesh and flow parameters that have been input for the simulation.

Figure 5 shows the comparison of mean pressure coefficient contours on the surfaces of 180° helical building given in experimental paper (Fig. 5(b)) [5] with the contours obtained from CFD simulation of this building model at 0° wind incidence angle (Fig. 5(a)). For the front view, the experimental mean pressure coefficient range varies from around 0.6 towards the upper region of the face till -0.6 towards the bottom, upon comparison with CFD contour of front view. The CFD contour is in good agreement with the experimental contour for that region of the right view which constitutes of Face-B, however the face, which is in the middle portion of right
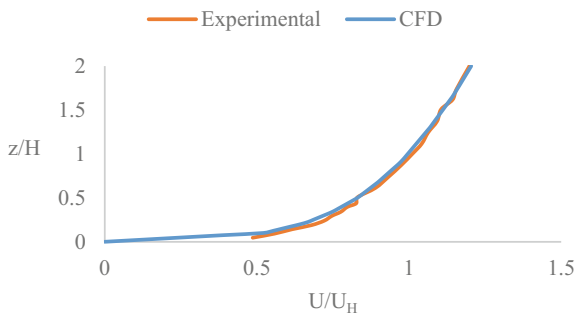
Fig. 4 Comparison of experimental and CFD velocity profiles
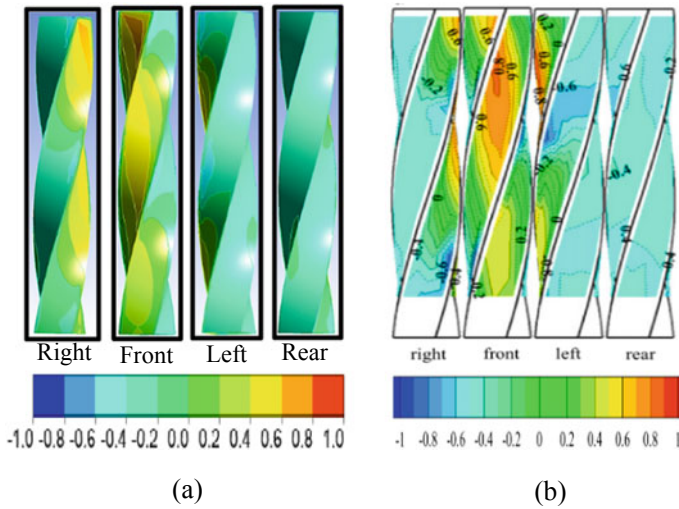
Fig. 5 a Mean pressure coefficient (C_P) contours on the faces of CFD 180° helical model at 0° WIA **b** Mean pressure coefficient (C_P) contours on the faces of experimental 180° helical model 0° WIA

view, i.e., Face-A has slight variation from that of the experimental contour. The contour of the front view is almost similar to the experimental contour except for the minor variation in top right region, where the values are more negative (light bluish) compared to the experimental contour (light greenish). The left and rear contours have minimal variations and are closest to the experimental contour. However, these minor variations can be justified from the fact that the results produced by CFD simulations cannot exactly reproduce the results of the wind tunnels as some variation in the wind flow characteristics can be expected to occur while replicating the conditions of wind tunnel flow on software.

5.2 Force Coefficient

A comparison of force (or facet average pressure) coefficients of the faces of basic square building model (SQ) and the corresponding faces of 180° helical model (HE) is presented in this section. Figure 6 shows the comparison of facet average pressure coefficients for the faces of basic square (SQ) and corresponding faces of 180° helical (HE) models for the wind incidence angles of 0, 15, 30 and 45°. For Face-A, the facet-average pressure coefficient values of square model remain positive throughout all the angles whereas for the helical model, the values remain negative throughout. For square model, the maximum facet average value is observed at the WIA's of 0 and 15° (same value) and the minimum facet average value was observed at the angle of 45° WIA. For helical model's Face-A, opposite trend has been observed. The maximum
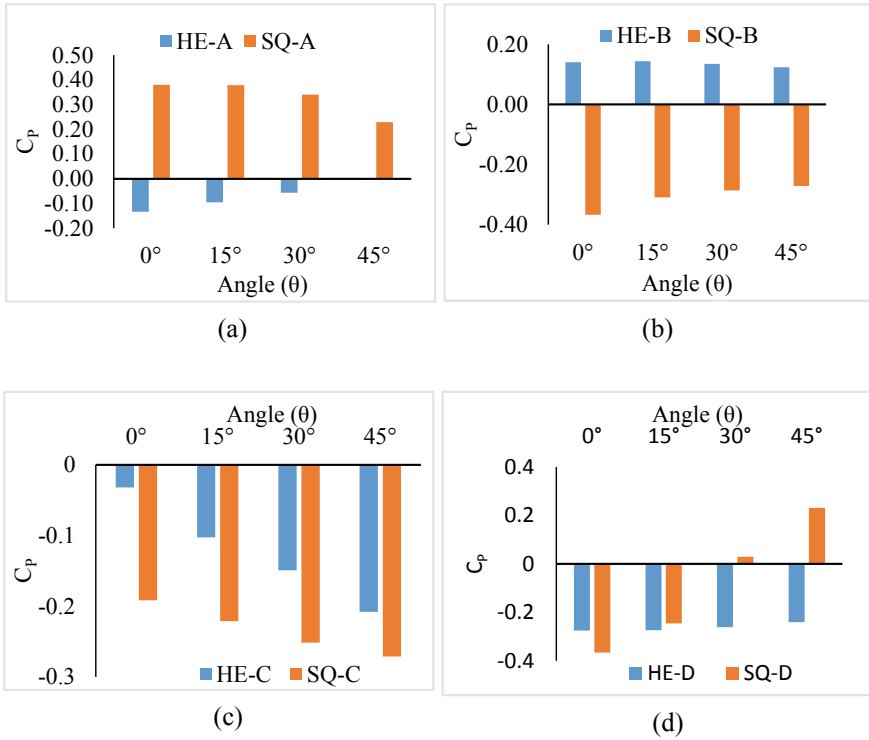
Fig. 6 Facet average pressure coefficient values for **a** Face-A **b** Face-B **c** Face-C **d** Face-D

value is observed at 45° WIA whereas the minimum (highest suction) is observed at 0° WIA and the values can be seen consistently increasing (more positive) from 0° to 45° WIA.

For Face-B of the square model, the facet average values remain negative (suction) throughout. The maximum negative value is observed at the WIA of 0° as Face-B of square model acts as side face at this angle which attains greatest suction, however when WIA starts increasing, the negative values on Face-B start decreasing (in magnitude) and the minimum negative value (in magnitude) is observed at the maximum WIA of 45°. The facet-average pressure coefficient values for Face-B of helical model remained positive throughout with values showing increment when WIA changed from 0 to 15° (2.64% increase over value at 0° WIA); maximum facet-average value is observed at the angle of 15°. The values then decreased as angle changed from 15 to 30° (6.03% decrease over value at 15° WIA) and a further decrement has been observed when angle changed from 30 to 45° (8.22% decrease over value at 30° WIA), with minimum positive facet-average value observed at the WIA of 45°.

For Face-C of square model, the values consistently became more negative as WIA increased from 0 to 45° with minimum negative facet-average value observed

at WIA of 0° and maximum negative facet-average value for 45° WIA. Face-C of helical model showed similar trend as the Face-C of the square model with facet-average values showing consistent decrement as WIA changed from 0° to 45° with minimum negative facet-average having been observed at 0° WIA and maximum negative having been observed at 45° WIA.

For Face-D of square model, a reverse trend has been observed as compared to Face-C. The values on Face-D of square model consistently became less negative as WIA changed from 0 to 45° with maximum negative facet-value observed at 0° WIA and minimum negative facet-average value observed at 45° WIA. The Face-D of helical model followed a similar trend as Face-D of square model with values consistently becoming less negative with increment in WIA.

The maximum positive facet-average value of square model is observed at 0° WIA on Face-A (0.38) whereas the maximum negative facet-average value is observed at 0° WIA on Face-B (−0.36). The maximum positive facet-average value of helical model was observed at 15° WIA on Face-B (0.14) whereas the maximum negative facet-average value has been observed at 0° WIA on Face-D (−0.28).

6 Conclusions

CFD analysis of an isolated 180° helical model and an isolated square model based on the experimental models was carried out in this paper. The comparison of facet-average pressure coefficients of the corresponding faces of square and helical model yielded some key observations. Face-A of both the models showed opposing trends; while the facet average values of square model decreased with increase in WIA, those of the helical models increased with increase in WIA. 15° WIA was found to be critical for Face-B of the helical model as the facet-average pressure coefficient value initially increased up to 15° but then showed consistent decrease beyond this WIA. The Face-C of both square and helical models showed consistent increase in suction as the WIA's changed from 0 to 45° whereas Face-D of both the models showed consistent decrease in suction with the increase in WIA's from 0 to 45°. 15° WIA again emerged as a critical angle for Face-D of square model as the facet-averaged pressure coefficient transitioned from negative to positive at this angle. The maximum positive facet average pressure coefficient values for square and helical models were observed at 0° WIA (Face-A) and 15° WIA (Face-B) respectively, however the maximum positive facet-average value of square model (0.38) was significantly higher than of the helical model (0.14). The maximum negative facet average pressure coefficient values for both square and helical models were observed at 0° WIA (Face-B and Face-D respectively). However, the maximum negative facet-average value (maximum suction) observed at Face-B of square (−0.36) was greater than the maximum negative facet-average value observed at Face-D of helical model (−0.28).

References

1. Mittal, H., Sharma, A., Gairola, A.: Numerical simulation of pedestrian level wind flow around buildings : effect of corner modification and orientation. J. Build. Eng. **22**, 314–326 (2019)
2. Revuz, J., Hargreaves, D.M., Owen, J.S.: On the domain size for the steady-state CFD modelling of a tall building. Wind Struct **15**(4), 313–329 (2012)
3. Liu, J., Niu, J.: CFD simulation of the wind environment around an isolated high-rise building : An evaluation of SRANS, LES and DES models. Build. Environ. **96**, 91–106 (2016)
4. Rajasekarababu, K.B., Vinayagamurthy, G., Selvi Rajan, S.: Experimental and computational investigation of outdoor wind flow around a setback building. Build. Simul. **12**(5), 891–904 (2019)
5. Tanaka, H., Tamura, Y., Ohtake, K., Nakai, M., Kim, Y.C.: Experimental investigation of aerodynamic forces and wind pressures acting on tall buildings with various unconventional configurations. J. Wind Eng. Ind. Aerodyn. **107–108**, 179–191 (2012). https://doi.org/10.1016/j.jweia.2012.04.014
6. Franke, J., et al.: Recommendations on the use of CFD in wind engineering. In: COST Action C14 Impact Wind Storm City Life Urban Environment, no. January (2004)
7. Tominaga, Y., et al.: AIJ guidelines for practical applications of CFD to pedestrian wind environment around buildings. J. Wind Eng. Ind. Aerodyn. **96**(10–11), 1749–1761 (2008)
8. Baetke, Frank, Werner, Heinrich, Wengle, Hans: Numerical simulation of turbulent flow over surface-mounted obstacles with sharp edges and corners. J. Wind Eng. Ind. Aerodyn. **35**, 129–147 (1990)
9. Roy, K., Bairagi, A.K., Water, K.M., Authority, S., Bengal, W.: ABL airflow through CFD simulation on tall building of square plan shape. Asian J. Civ. Eng. **17** (2016)
10. A. I. of Japan, AIJ Recommendations for Loads on Buildings. Architectural Institute of Japan 2019 (2015)
11. Shih, T., Liou, W., Shabbir, A., Yang, Z., Zhu, J.: A new k-ϵ eddy viscosity model for high reynolds number turbulent flows. Comput. Fluids **24**(3), 227–238 (1995)

Modeling Delay Mitigation Strategies and Their Driving Relationships for Road Projects

Harish L. Reddy and M. S. Nagakumar

Abstract This article identifies and examines the important mitigation strategies currently followed across road projects in India. A hierarchical model is developed using the interdependency relations among the factors and their influence in the mitigation of project delays. The literature review identified 18 key factors responsible for causing delay in projects. These were framed into an open-ended questionnaire survey and responses were collected from project professionals. The survey asked the respondents to state from their experience, the best way to mitigate the stated delays in projects. The responses collectively yielded thirteen mitigation strategies. A focus group made up of six experts (four from industry and two from academia) was formed to ascertain the interrelationship among these thirteen mitigation strategies. The driving factors and dependent factors were identified. The interpretive structural modeling (ISM) technique was applied to develop the model and develop a hierarchy among the mitigation strategies. The mitigation strategies were grouped into three levels of hierarchy based on the ISM model. The findings suggest that the *'use of adequate and competent personnel on-site'*; and *'proactive approach from all stakeholders'* would resolve most of the delay problems in projects. These two were at level III – higher influence on mitigation. These were followed by *'regular meetings, discussions, and feedback'*; *'active stakeholder engagement'*; *'quality in work'*; and *'good communication and coordination'*. These were placed at level II – moderate influence on mitigation in the hierarchy. These were followed by *'proper planning'*, *'good resource management'*, *'proper site management'*, *'regular monitoring and control of work'*, *'identifying and resolving root causes'*, *'performing regular audits and design checks'*, and *'good contract documents'* placed at the level I – lower influence on mitigation.

Keywords Delay mitigation · Interpretive structural model · Project management · Project success

H. L. Reddy (✉)
NICMAR, Pune, India
e-mail: msg2harish@gmail.com

M. S. Nagakumar
R V College of Engineering, Bengaluru, India

1 Introduction

Delay can be defined as the "time overrun either beyond completion date specified in a contract or beyond the date that the parties agreed upon for delivery of a project" [1]. Flash report published by the Infrastructure and Project Monitoring Division [2] shows that a large number of central sector-sponsored infra projects will not be able to meet their deadlines. An analysis of 1737 central sector infra projects (costing Rs. 150cr and above) revealed that only 11 projects were ahead of schedule and 213 projects reported to be on schedule. Nearly, 525 projects are delayed beyond their original schedules and nearly 90 have reported extended delays beyond their revised completion times. The anticipated cost overrun amounts to nearly 4,38,031.24 Cr which is nearly 19.61% of the anticipated cost of projects. There are reportedly 106 projects suffering a delay between 1 and 12 months, 123 projects suffering delay between 13–24 months, 179 projects suffering a delay between 25–60 months, and nearly 117 projects suffering delay beyond 60 months [2].

The report mentions causes of delays to include reasons such as land acquisition, approvals from forest departments, lack of infra support and linkages, delay in a tie-up of project finances, delays in scope finalization, and detailed engineering among others [2]. The task force report on project and program management lists delays such as uncertainty in land acquisition, delay in regulatory approvals, lack of comprehensive upfront planning and risk management, and low maturity of project management processes among others [3]. Numerous studies have been carried out to identify the causes of delays in projects. According to the current literature review of peer-reviewed publications, 18 factors that are mainly responsible for delays in projects have been identified. These are listed below and the order of appearance does not imply importance.

1. Poor crisis management
2. Problems with the use of specialized machinery
3. Site obstructions
4. Unfair practices toward stakeholders
5. Disputes and conflicts between stakeholders
6. Strict rules and system bureaucracy
7. Site accessibility problems
8. Poor supervision of works
9. Communication and coordination problems
10. Biased and ambiguous contract documents
11. Delay in issue for GFC drawings
12. Reworks, errors, and mistakes
13. Untrained personnel on work
14. Cash flow and fund management problems
15. Arbitrations and litigations
16. Increases in prices
17. External influences
18. Poor project planning and control

Source: [4–21]

It was also found that only a small piece of literature exists on how to effectively mitigate these delays. Also, the interrelationships among the mitigation strategies are not identified. Such investigation will identify the most common and key mitigation strategies to be used by the industry as well as the hierarchy in which they have to be implemented.

H Abdul Rahman [22] carried out a questionnaire survey and interview technique to gather data for recommending delay mitigation. Frequency analysis of data revealed increasing productivity, request for extension of time, site meetings with functional groups, and more executive authorities to project manager, changing construction methods or technology as the suggested mitigation measures. Chang sar chai [23] used a questionnaire survey and principal component analysis to identify 17 mitigation measures and categorized them into three groups namely predictive, preventive, organization, or corrective measures. Among the three preventive measures were found to be more influential in mitigating delays, The preventive measures included the following: preparing comprehensive contract documents, competent project team, effective strategic planning, clear information and communication channels, timely delivery of materials, availability of resources, competent consultant and reliable contractor.

Edwin Thomas banobi [24] interviewed experts from the owner side and contractor side to identify the mitigation measures and agreement among the two stakeholders towards the results. It was found that measures such as close project supervision, capacity building training, and proper logistic management were in agreement with client and contractor groups. Whereas top management support and timely procurement were favored by the client group. Timely payments and complete designs on time were favored by the contractor group. Prasad K V [25] with the help of a questionnaire survey and statistical tests found the causes of delays in projects. Later using semi-structured in-depth interviews arrived at 34 mitigation strategies for the delays. These were categorized into preventive, corrective, and organization groups similar to Chang sar chai [23] and in addition assigned the responsibility of the mitigation measure to the stakeholder group involving client, contractor, and engineer. It was found that some mitigation measures can be implemented by one stakeholder while others needed active participation by two or all three stakeholders to ensure success in delay mitigation.

Amilcar arantes [26] carried out a questionnaire survey and exploratory factor analysis to identify the predominant six causes of delay. This was followed by focus group sessions to arrive at mitigation measures for these delays. For each delay cause, a set of mitigation measures (3–6) were identified. The prominent mitigation measures include the following: ensuring the right engineering and project management skills, preparation of realistic plans and contract awards, mechanisms to manage financial issues, competent site managers, most appropriate site conditions, and information management systems. Yiannis Vacanas [27] used integrated statistical methodology and workflow to identify causes of delay as well as common practices to mitigate them. A realistic program of works, a contractual requirement to update the program and dissemination to all stakeholders, periodic updates of the

work program, complete design and construction details before tendering, frequent progress meetings, and use of smart technologies were the identified key mitigation strategies. These studies have used qualitative techniques to identify the key mitigation measures and mostly rely on expert opinion in identification. The studies however do not establish any hierarchy or interdependency among the mitigation strategies. This is vital to project success as the implementation of one strategy might not be successful without the implementation of another strategy and might not yield expected results to the project. In addition, implementing mitigation measures requires a sufficient budget by the organization. When the funds are limited, organizations need to implement selected mitigation measures that yield maximum benefit to the project and the organization. The present paper attempts to fill this gap of knowledge by trying to understand the interrelations among the mitigation strategies and developing a hierarchy model among the mitigation strategies.

2   Objectives of the Study

Considering the gap in knowledge mentioned in the previous section, the objectives of this paper are as follows:

1. To identify the common and key measures to mitigate delays in projects from the perception of all stakeholders.
2. To identify the driving, dependent and interdependent relations among the identified mitigation measures using expert opinion.
3. To develop a hierarchical model of identified mitigation measures using interpretive structural equation modeling.

3   Methodology

The authors identified 18 key delay factors based on the literature review. A questionnaire was formed using these 18 factors and sent to professionals for their feedback on an effective mitigation strategy. An open-ended questionnaire was used and a snowball method of sampling was adopted. The respondents were presented with each delay causing factor and were asked to write in their own words about the mitigation strategy. A short paragraph section was provided to record their response. In addition, their professional information was also collected. They were asked to mention their role in the project, years of experience, names, and contact details. A total of more than 500 survey forms were circulated online and further, they were requested to forward these forms to their known associates. Over four months, a total of 44 responses were received. The profile of the respondents is shown in Fig. 1.

12.8% of the respondents belonged to the client group, 34% belonged to the design group, 17% belonged to the project management consultant group, 12.8% belonged to the contractor group, and the remaining 23.4% contained a mix of other stakeholder
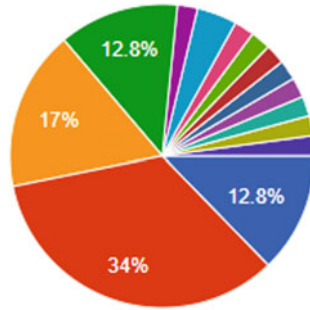
Fig. 1 Respondents' profile

groups in projects. The average experience of all the respondents combined was more than 15 years in project management.

The responses were read and the keyword in the response was coded. The keywords were then grouped to reveal 13 popular delay mitigation strategies. The 13 delay mitigation strategies are listed below.

1. Proper planning
2. Regular meetings, discussions, and feedback
3. Active stakeholder engagement
4. Good communication and coordination
5. A proactive approach from all stakeholders
6. Use adequate and competent personnel
7. Good resource management
8. Regular monitoring and control of work
9. Proper site management
10. Identifying and resolving root causes
11. Performing regular audits and design checks
12. Good contract documents
13. Quality in work

Source: Compiled by authors

To study the interrelationship amongst variables quantitative techniques such as interpretive structural modeling, cognitive mapping, word frequency analysis, and fuzzy cognitive maps are available. In this study, interpretive structural modeling was used for analysis and model development.

A focus group was formed with the help of 6 experts (4 from industry and 2 from academia) having an average experience of more than 15 years. The expert group was given the above-listed 13 mitigation strategies and were asked to discuss among themselves to define the interrelationships, driving, and dependent delay mitigation strategies. They were also asked to highlight any mitigation measure which was missed out from the list. The existence of a relationship between any two strategies (i and j) and the associated direction was investigated. The methodology adopted by Shrivas and Singla [28] was used as a reference. A matrix was developed with the

strategies listed both on the X-axis and Y-axis. The expert group would mark "Y" if the strategy listed in a row drives the strategy listed in the column. If it does not drive, then they would indicate "N" in the cell. The cells were filled only after an agreement among the experts. If the row and column of 'i' and 'j' strategies were "Y", then it would indicate interdependency between them while an "N" in both cells would indicate an independent relationship. Once the matrix was completed, the interpretive structural modeling (ISM) approach was used to study the relationship between mitigation strategies and to develop levels of hierarchy for implementation in projects.

4 Application of ISM

ISM is an excellent technique that will help in the transformation of unclear and poorly articulated ideas into a visible and well-defined model system [29]. It combines the use of keywords, diagrammatic representation, and mathematical inputs to prepare models [30]. ISM uses the practical experiences of experts to develop and construct a multilevel structural model [31]. The completed matrix based on inputs from the focus group is shown in Table 1.

The list of driving and dependent relations among the strategies is shown in Table 2. The driving relations are named as the reachability set and dependent relations are named as the antecedent set as indicated by Shrivas and Singla [28]. The reachability set contains a list of strategies that are being driven by the strategy listed in the first column.

Table 1 Final relationship matrix

Strategy	1	2	3	4	5	6	7	8	9	10	11	12	13
1	–	N	Y	Y	N	N	Y	Y	Y	N	Y	Y	N
2	Y	–	Y	N	Y	N	Y	Y	Y	Y	N	N	N
3	Y	Y	–	Y	Y	Y	Y	Y	Y	Y	N	Y	Y
4	Y	Y	Y	–	Y	N	Y	Y	Y	Y	Y	Y	N
5	Y	Y	N	Y	–	N	Y	Y	Y	Y	Y	Y	N
6	Y	Y	Y	Y	Y	–	Y	Y	Y	Y	Y	Y	Y
7	N	N	N	N	N	N	–	Y	Y	N	Y	N	N
8	N	Y	Y	Y	N	N	N	–	Y	Y	Y	Y	N
9	Y	N	N	N	N	N	Y	Y	–	Y	N	N	N
10	Y	N	Y	N	N	N	N	N	N	–	N	N	N
11	Y	N	N	N	N	N	Y	N	Y	Y	–	N	N
12	Y	N	Y	Y	N	Y	N	Y	N	N	Y	–	Y
13	N	N	N	Y	Y	N	N	N	N	N	N	N	–

Source: Compiled by authors

Table 2 Driving and dependent relations matrix

Strategy	Driving strategies (Reachability Set)	Dependent Strategies (Antecedent Set)
1	3,4,7,8,9,11,12	2,3,4,5,6,9,10,11,12
2	1,3,5,7,8,9,10	3,4,5,6,8
3	1,2,4,6,8,10,12	1,3,4,5,6,7,8,9,10,12,13
4	1,2,3,5,7,8,9,10,11,12	1,3,5,6,8,12,13
5	1,2,4,7,8,9,10,11,12	2,3,4,6,13
6	1,2,3,4,5,7,8,9,10,11,12,13	3,12
7	8,9,11	1,2,3,4,5,6,9,12
8	2,3,4,9,10,11,12	1,2,3,4,5,6,7,9,12
9	1,7,9,10	1,2,3,4,5,6,7,8,,11
10	1,,3	2,3,4,5,6,8,9,11
11	1,7,9,10,	1,4,5,6,7,8,12
12	1,3,4,6,8,11	1,3,4,5,6,8
13	4,5	3,6,12

Source: Compiled by authors

To determine the hierarchy among strategies, an intersection set is found [32]. If the intersection set is the same as the reachability set, then the strategy will be placed at the top. These are then removed from the list and the process is repeated for the remaining strategies to find the highest match between reachability and intersection matrix. Total three levels of hierarchy are identified as shown in Tables 3, 4 and 5. The strategies having greater dependency and interrelations are placed at level I. The strategies which are the driving forces and have minimum dependency are placed at level III. Figure 2 shows a diagrammatic representation of the driving relationships among the mitigation strategies.

According to Fig. 2, the use of adequate and competent personnel on-site is being chosen as the critical delay mitigation strategy for projects. This is closely followed by a proactive approach from all stakeholders. These two are found to be the main driving forces to mitigate delays in projects and hence are placed in level III – Higher influence on mitigation. Regular meetings, discussions, and feedback; active stakeholder engagement; and good communication and coordination; quality of work are placed at level II – Moderate influence on mitigation. The remaining strategies i.e., proper planning; good resource management; regular monitoring and control of work; proper site management; identifying and resolving root causes; performing regular audits and design checks; good contract documents are placed in level I – Lower influence on mitigation.

A cross-impact matrix multiplication applied to classification analysis (MICMAC) is used to represent the factors into four clusters [33], namely autonomous, dependent, linkage, and driving clusters. Table 6 shows the total driving and dependent relations between each strategy.

Table 3 Hierarchy among strategies (Level I)

	Reachability set	Intersection set	Level
1	3,4,7,8,9,11,12	3,4,9,11,12	I
2	1,3,5,7,8,9,10	3,5,8	
3	1,2,4,6,8,10,12	1,4,6,8,10,12	
4	1,2,3,5,7,8,9,10,11,12	1,3,5,,12	
5	1,2,4,7,8,9,10,11,12	2,4	
6	1,2,3,4,5,7,8,9,10,11,12,13	3,12	
7	8,9,11	9	I
8	2,3,4,9,10,11,12	2,3,4,9,12	I
9	1,7,9,10	1,9	I
10	1,,3	3	I
11	1,7,9,10,	1,7	I
12	1,3,4,6,8,11	1,3,4,6,8	I
13	4,5	0	

Source: Compiled by authors

Table 4 Hierarchy among strategies (Level II)

	Reachability set	Intersection set	Level
2	1,3,5,7,8,9,10	3,5,8	II
3	1,2,4,6,8,10,12	1,4,6,8,10,12	II
4	1,2,3,5,7,8,9,10,11,12	1,3,5,,12	II
5	1,2,4,7,8,9,10,11,12	2,4	
6	1,2,3,4,5,7,8,9,10,11,12,13	3,12	
13	4,5	0	II

Source: Compiled by authors

Table 5 Hierarchy among strategies (Level III)

	Reachability set	Intersection set	Level
5	1,2,4,7,8,9,10,11,12	2,4	III
6	1,2,3,4,5,7,8,9,10,11,12,13	3,12	III

Based on Table 6, a MICMAC matrix is formed as shown in Fig. 3. Cluster I includes autonomous variables with weak driving power and weak dependencies. Quality in work is placed here. Cluster II includes variables that have strong dependencies. Good resource management, Proper site management, Identifying and resolving root causes, Performing regular audits, and design checks are placed in this cluster. Cluster III includes variables that are strongly interrelated with other variables. Proper planning, Active stakeholder engagement, good communication

LEVEL I – LOWER INFLUENCE

IDENTIFYING AND RESOLVING ROOT CAUSES

REGULAR MONITORING AND CONTROL OF WORK

PERFORMING REGULAR AUDITS AND DESIGN CHECKS

PROPER PLANNING

GOOD RESOURCE MANAGEMENT

GOOD CONTRACT DOCUMENTS

PROPER SITE MANAGEMENT

LEVEL II – MODERATE INFLUENCE

REGULAR MEETINGS, DISCUSSIONS AND FEEDBACK

ACTIVE STAKEHOLDER ENGAGEMENT

GOOD COMMUNICATION AND COORDINATION

QUALITY IN WORK

LEVEL III - HIGHER INFLUENCE

USE OF ADEQUATE AND COMPETENT PERSONNEL

PROACTIVE APPROACH FROM ALL STAKEHOLDERS

Fig. 2 Model depicting hierarchy among delay mitigation strategies

Table 6 Total driving and dependent relations

Strategy	Driving relations	Dependent relations
1	7	9
2	7	5
3	11	7
4	10	7
5	9	5
6	12	2
7	3	8
8	7	9
9	4	9
10	2	8
11	4	7
12	7	6
13	2	3
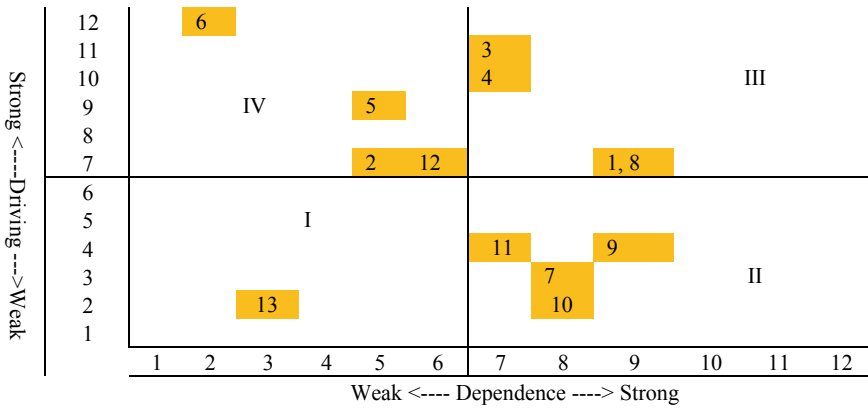
Fig. 3 Graph of MICMAC analysis

and coordination, regular monitoring, and control of work are placed in this cluster. Cluster IV includes variables that have strong driving power and are less dependent on other variables. Regular meetings, discussions, and feedback, a proactive approach from all stakeholders, the use of adequate and competent personnel, and good contract documents are placed in this cluster.

5   Discussions and Conclusions

The article started with a literature review and identified 18 key factors causing a delay in projects. An open-ended questionnaire survey was carried out to identify the best mitigation measures for handling these delays. The analysis of responses resulted in 13 mitigation strategies. A focus group made of experts was formed to reveal the underlying dependencies and relationships among the identified mitigation strategies. The responses from the focus group were used to develop the ISM model and the MICMAC matrix. The study revealed that the use of adequate and competent personnel on projects is the main driving force for ensuring success in projects and it also drives the success of other mitigation strategies. This factor was not dependent on any other strategy. Along with this, a proactive approach from all stakeholders was placed at the same level. This was the second driving force for mitigating delays. It was dependent on the use of adequate and competent personnel and was the driving force for level II and level I variables. Regular meetings, discussions, and feedback; active stakeholder engagement; and good communication and coordination; quality of work are placed in level II which indicates that these have strong driving power but also are dependent on other variables. Quality in work is placed in cluster I in the MICMAC matrix which indicates weak driving and dependency power for mitigating delay. This needs to be looked at from the perspective that quality is a compulsory requirement of projects and needs to be ensured irrespective of the project being

completed on time or delayed. Proper planning; good resource management; regular monitoring and control of work; proper site management; identifying and resolving root causes; performing regular audits and design checks; good contract documents are placed in Level I. These are dependent on the implementation of strategies listed in level II and level III for their effectiveness to be realized in mitigation of delays.

This article provides an insight into the strategies to be adopted for mitigating delays in projects and the relations between them. The study helps practitioners and professionals in project management, to identify the key strategies and the direction towards mitigating delays to ensure success in projects. The methodology helps to identify the underlying interrelationships, driving, and dependent relations among different mitigation strategies. The study primarily targeted to mitigate delays in the construction industry and provides findings suitable to other areas of industry and project management in general.

Disclosure Statement No potential conflict of interest was reported by the author(s).

References

1. Shahsavand, P., Marefat, A., Parchamijalal, M.: Causes of delays in construction industry and comparative delay analysis techniques with SCL protocol. Eng. Constr. Archit. Manag. **25**(4), 497–533 (2018). https://doi.org/10.1108/ECAM-10-2016-0220
2. Infrastructure and Project Monitoring Division. 425th Flash report on Central sector projects. Ministry of Statistics and Programme Implementation, Government of India (2021). http://www.cspm.gov.in/english/flr/FR_Apr_2021.pdf
3. Niti Aayog. Report of the task force on project and program management. Government of India (2019). http://www.niti.gov.in/node/706
4. Elawi, G., Alghatany, M., Kashiwagi, D.: Owners' perspective of factors contributing to project delay: case studies of road and bridge projects in Saudi Arabia. Procedia Eng. **145**, 1402–1409 (2016). https://doi.org/10.1016/j.proeng.2016.04.176
5. Kog, Y.C.: Major construction delay factors in Portugal, the UK, and the US. Pract. Period. Struct. Des. Constr. **23**(4), 04018024 (2018). https://doi.org/10.1061/(ASCE)SC.1943-5576.0000389
6. Asiedu, R., Alfen, H.: Understanding the underlying reasons behind time overruns of government building projects in Ghana. KSCE J. Civ. Eng. **20**(6), 2103–2111 (2015). https://doi.org/10.1007/s12205-015-0544-4
7. Kavuma, A., Ock, J., Jang, H.: Factors influencing time and cost overruns on freeform construction projects. KSCE J. Civ. Eng. **23**(4), 1442–1450 (2019). https://doi.org/10.1007/s12205-019-0447-x
8. Larsen, J., Shen, G., Lindhard, S., Brunoe, T.: Factors affecting schedule delay, cost overrun, and quality level in public construction projects. J. Manag. Eng. **32**(1), 04015032 (2016). https://doi.org/10.1061/(asce)me.1943-5479.0000391
9. Kog, Y.C.: Project management and delay factors of public housing construction. Pract. Period. Struct. Des. Constr. **23**(1), 04017028 (2018). https://doi.org/10.1061/(asce)sc.1943-5576.0000350
10. Tengan, C., Aigbavboa, C.: Level of stakeholder engagement and in monitoring and evaluation of construction projects in Ghana. Procedia Eng. **196**, 630–637 (2017). https://doi.org/10.1016/j.proeng.2017.08.051
11. Kim, S., Tuan, K., Luu, V.: Delay factor analysis for hospital projects in Vietnam. KSCE J. Civ. Eng. **20**(2), 519–529 (2015). https://doi.org/10.1007/s12205-015-0316-1

12. Ökmen, Ö.: Risk assessment for determining best design alternative in a state-owned irrigation project in Turkey. KSCE J. Civ. Eng. **20**, 109–120 (2016). https://doi.org/10.1007/s12205-015-0397-x

13. Mittal, Y., Paul, V., Rostami, A., Riley, M., Sawhney, A.: Delay factors in construction of healthcare infrastructure projects: a comparison amongst developing countries. Asian J. Civil Eng. **21**(4), 649–661 (2020). https://doi.org/10.1007/s42107-020-00227-1

14. Abbasi, O., Noorzai, E., Gharouni, J.K., Golabchi, M.: Exploring the causes of delays in construction industry using a cause-and-effect diagram: case study for Iran. J. Archit. Eng. **26**(3), 05020008 (2020). https://doi.org/10.1061/(asce)ae.1943-5568.0000431

15. Ruqaishi, M., Bashir, H.: Causes of delay in construction projects in the oil and gas industry in the Gulf cooperation council countries: a case study. J. Manag. Eng. **31**(3), 05014017 (2015). https://doi.org/10.1061/(asce)me.1943-5479.0000248

16. Gunduz, M., Nielsen, Y., Ozdemir, M.: Fuzzy assessment model to estimate the probability of delay in Turkish construction projects. J. Manag. Eng. **31**(4), 04014055 (2015). https://doi.org/10.1061/(asce)me.1943-5479.0000261

17. Bagaya, O., Song, J.: Empirical study of factors influencing schedule delays of public construction projects in Burkina Faso. J. Manag. Eng. **32**(5), 05016014 (2016). https://doi.org/10.1061/(asce)me.1943-5479.0000443

18. Kog, Y.C.: Construction delays in Indonesia, Malaysia, Thailand, and Vietnam. Pract. Period. Struct. Des. Constr. **24**(3), 04019013 (2019). https://doi.org/10.1061/(asce)sc.1943-5576.0000434

19. Niazi, G., Painting, N.: Significant factors causing cost overruns in the construction industry in Afghanistan. Procedia Eng. **182**, 510–517 (2017). https://doi.org/10.1016/j.proeng.2017.03.145

20. Yaseen, Z.M., Ali, Z.H., Salih, S.Q., Al-Ansari, N.: Prediction of risk delay in construction projects using a hybrid artificial intelligence model. Sustainability **12**(4), 1514 (2020). https://doi.org/10.3390/su12041514

21. Sanni-Anibire, M., Mohamad Zin, R., Olatunji, S.: Causes of delay in the global construction industry: a meta analytical review. Int. J. Constr. Manag. **22**, 1395–1407 (2020). https://doi.org/10.1080/15623599.2020.1716132

22. Abdul-Rahman, H., Berawi, M.A., Mohamed, O., Othman, M., Yahya, I.A.: Delay mitigation in the Malaysian construction industry. J. Constr. Eng. Manag. **2006**(132), 125–133 (2006)

23. Chai, C.S., Yusaf, A.M., Habil, H.: Delay mitigation in the Malaysian housing industry: a structural equation modeling approach. J. Constr. Dev. Countries **20**(1), 65–83 (2015)

24. Banobi, E.T., Jung, W.: Causes and mitigation strategies of delay in power construction projects: Gaps between owners and contractors in successful and unsuccessful projects. Sustainability **11**, 5973 (2019). https://doi.org/10.3390/su11215973

25. Prasad, K.V., Vasugi, V., Venkatesan, R., Bhat, N.: Analysis of causes of delay in Indian construction projects and mitigation measures. J. Finan. Manag. Property Constr. (2019). https://doi.org/10.1108/JFMPC-04-2018-0020

26. Arantes, A., Luis Miguel, D.F.: A methodology for the development of delay mitigation measures in construction projects. Prod. Plan. Control (2020). https://doi.org/10.1080/09537287.2020.1725169

27. Vacanas, Y., Danezis, C.: Determination of effective delay avoidance practices in construction projects. J. Leg. Aff. Dispute Resolut. Eng. Constr. **13**(1), 04520039 (2021)

28. Shrivas, A., Singla, H.K.: Analysis of interaction among the factors affecting delay in construction projects using interpretive structural equation modeling approach. Int. J. Constr. Manag. **22**, 1455–1463 (2020). https://doi.org/10.1080/15623599.2020.1728486

29. Sushil, S.: Interpreting the interpretive structural model. Global J Flexi Syst Manag. **13**(2), 87–106 (2012)

30. Agarwal, A., Shankar, R., Tiwari, M.K.: Modeling agility of supply chain. Indu Market Manag. **36**(4), 443–457 (2007)

31. Sage, A.: Interpretive Structural Modelling: Methodology for Large Scale Systems. McGraw-Hill, New York (1977)

32. Digalwar, A.K., Giridhar, G.: Interpretive structural modeling approach for development of electric vehicle market in India. Proc. CIRP **36**, 40–45 (2015)
33. Jena, J., Sidharth, S., Thakur, L.S., Pathak, D.K., Pandey, V.C.: Total interpretive structural modeling(TISM): approach and applications. J. Adv. Manag. Res. **14**(2), 162–224 (2017). https://doi.org/10.1108/JAMR-10-2016-0087

Structural Behaviour of Concrete Column Confined with Basalt Textile Reinforced ECC

H. S. Athira and Sajitha R. Nair

Abstract Concrete columns can be confined in a variety of ways, including fibre reinforced polymers (FRP), steel jacketing, and textile reinforced mortar (TRM). The load carrying capability of RC columns was increased using these ways. However, a few problems have been found for these confinement approaches in recent years such as brittleness, premature failure and poor performance in high temperatures. Using the ABAQUS programme, this study examines the structural behaviour of concrete columns constrained by basalt fibre textile and Engineered Cementitious Composites (ECC) under axial loading. The structural behaviour of short column confined with basalt textile reinforced ECC and unreinforced column was validated using the finite element software ABAQUS.

Keywords Basalt fibre textile · Engineered cementitious composites · Axial loading

1 Introduction

Structures which are subjected to axial compressive forces are known as compression members. They are most typically found as columns in reinforced concrete structures, where they are used to support the vertical framing system. If the effective length of a member is greater than thrice the least lateral dimension, then it is said to be a column, according to IS codal provisions. Column helps in transmitting the load from the structure to the foundation. Depending upon the slenderness ratios these members are divided into short columns and slender columns. If the slenderness ratio is greater than 12, then it is a long column, else short column.

The load carrying capacity of reinforced concrete columns can be improved by the provision of confinement. Some of the effective methods for improving the load carrying capacity includes fibre reinforced polymers (FRP) confinement and steel

---

H. S. Athira (✉) · S. R. Nair
Department of Civil Engineering, NSS College of Engineering, Palakkad, Kerala, India
e-mail: 20m041@nssce.ac.in

(a) Cross-sections

Effectively confined concrete

(b) Elevation
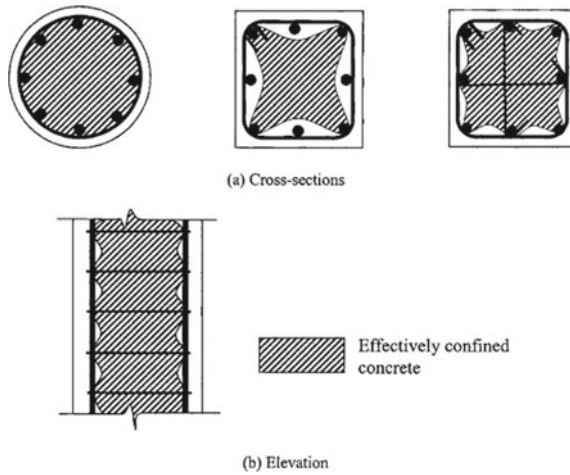
Fig. 1 Confinement of concrete columns [11]

jacketing. Steel jacketing enhances the durability of the member and plastic deformation is also improved. FRP is a jacketing material that contains organic resin which improves the strength of structural members. FRP is widely used for construction than steel jacketing and it possess less self-weight. The compressive strength and energy absorption for RC columns strengthened with FRP are enhanced. But there are some disadvantages to FRP that include poor performance in elevated temperatures and in moist conditions. The confinement of concrete columns is shown in Fig. 1.

Another alternative method for enhancing structural confinement is a textile-reinforced mortar (TRM). Among the textile fibers available, this study concentrates on the basalt textile. From previous studies, it was found that the basalt textile was effective and compatible with TRM jacketing because it is more stable and performance is good in elevated temperatures. The failure in the bond between fiber and mortar is observed because of the less tensile strength of mortar and the results of confinement provided are not as good as FRP confinement. Hence a proper study about the strengthening of columns is required to enhance the load-carrying capacity of columns. Properly designed and detailed confinement helps in preventing buckling of longitudinal bars and thereby avoiding shear failure and providing sufficient ductility. In this study, a new strengthening system i.e., confining the concrete columns with basalt textile reinforced engineering cementitious composites (ECC) to enhance the structural behavior of slender column is studied.
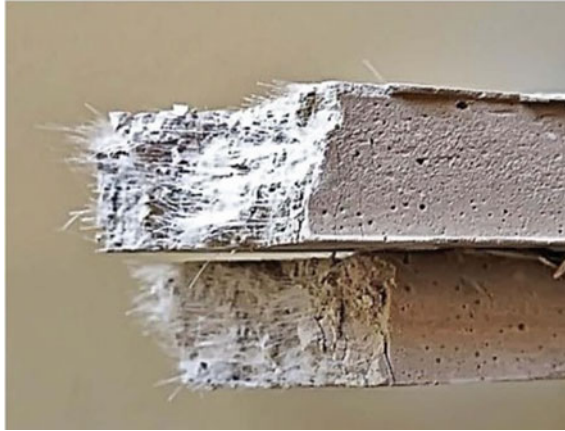
Fig. 2 Fibre reinforced – ECC [5]

1.1 Engineered Cementitious Composites

Engineered Cementitious Composites, commonly known as ECC are high-performing engineered cementitious composites that have strain hardening behaviour in tension. Due to this property, greater stress should be applied in order to cause a small variation in strain. The ultimate tensile strain of ECC ranges from 2 to 8% due to the implication of fibers [8]. Poly-vinyl Alcohol (PVA) fibers are generally added to the mix to obtain the cementitious composite. Due to this tensile capacity, it is used as an enhancement material in several structural members. So, when ECC is combined with concrete the composite structure can withstand greater stress and enhancement of load-carrying capacity of the columns is acheived. Yuan et al. [9] studied the structural behaviour of beam-column joint with the application of ECC suggests that the ECC reinforced beam-column joint shows larger load-carrying capacity of ECC reinforced beam-column joint is greater than normal RC beam-column joint, Likewise the ductility and energy disscpiation also increased. So, this study attempts to enhance the mechanical properties of column based on the characteristics of ECC A fibre reinforced – ECC matrix is shown in Fig. 2.

1.2 Textile Reinforced Concrete

Textile reinforced concrete (TRC) is a high-performance cement-based composite that has evolved in recent years. Textiles can greatly improve the mechanical behaviour of cement matrices under static and dynamic loading, as well as provide higher tensile strength, toughness, ductility, energy absorption, and environmental

protection. Fabric and yarn shape can be controlled by the flexibility of fabric production methods. This, combined with the ability to add a variety of yarns of various types and performances, as well as cement matrix alterations, allows the composite to be designed to a wide range of requirements. Textile reinforced concrete (TRC) strengthening systems are becoming more popular for enhancing the performance of unreinforced masonry or reinforced concrete structures. Generally, the use of fiber reinforced polymer has some disadvantages that include the use of organic epoxy resin, such as poor performance in elevated temperature and poor bonding behaviour on moist surface (FRP). TRC has been invented to overcome these constraints by the replacement of biological matrix with inorganic mortar or fine-grained concrete. The inorganic mortar or concrete is preferred for masonry structures since it is more compatible with masonry substrate.

Basalt fibre textiles are employed to limit the concrete columns in this investigation. Basalt is a type of natural rock that forms deep under the surface of the earth as molten magma. This type of rock is driven to the surface as a solid with a high melting point of 1400 °C and possesses great alkali resistance. Basalt may be woven into a grid and possess great chemical and mechanical properties, that includes good resistance against cold and fire, a greater Young's modulus than glass fibre, and good endurance. Some studies looked into using bidirectional basalt fibres injected with an inorganic-based matrix to restrict existing concrete columns. Studies related to basalt fibre which is used as environmentally friendly grids to enhance the strength of inorganic matrix. Concrete cylinders were reinforced with basalt textile combined with different types of mortar to improve the strength of concrete cylinders. There are different kinds of fibres available such as carbon, glass, basalt, etc. as shown in Fig. 3a, b and c.

2 Literature Review

Tong Li et al. (2021) [2] evaluated the experimental study on compressive behaviour of masonry piers using TRC composites and PVA fibers. This jacketing system lead to the formation of only thin cracks on the surface. By using carbon fiber textile in this jacketing system, the compressive strength of the pier was improved. **Xuan Chen et al. (2021)** [1] conducted both experimental and numerical studies on compressive behaviour of concrete columns. The jacketing system used was a mixture of basalt fiber textile and ECC and the ultimate load carrying capacity of the columns was improved. **Ali N. Al-Gemeel et al. (2019)** [4] studied the feasibility of a new strengthening system using basalt textile and ECC mortar. The failure mechanism, energy absorption, etc. were compared with conventional mortar composite. **Ali N. Al-Gemeel et al. (2019)** [3] evaluated basalt fibre textile reinforced ECC for the confinement of concrete columns. The bond strength between ECC and textile was studied. **Ali N. Al-Gemeel et al. (2018)** [6] presented a feasibility study on basalt fiber textile and ECC for the confinement of square concrete columns. The ductility and the ultimate strength of the columns was improved. **Dan Meng et al. (2017)**
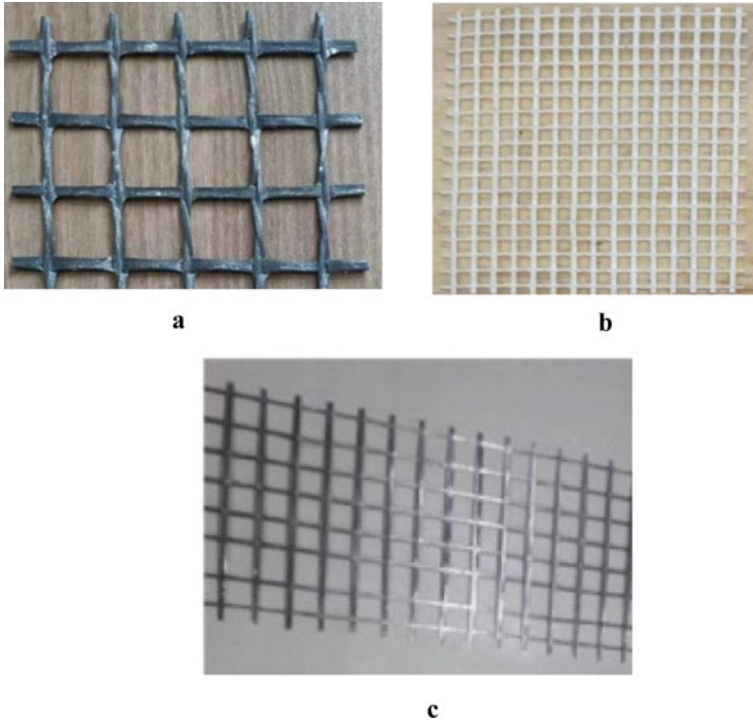
Fig. 3 **a** Carbon textile [2] **b** Glass textile [2] **c** Basalt textile [1]

[7] studied about the tensile strain capacity of polyvinyl alcohol fibre reinforced engineered cementitious composite (PVA-ECC). Experimental and numerical studies were conducted on PVA-ECC beams.

3 Finite Element Simulation

This paper deals with the finite element study on the structural behaviour of short column subjected to uniaxial loading. The strain development characteristics of fibre textile impregnated with ECC matrix were obtained from the simulation. This helps to understand the failure mechanisms of textile reinforced concrete columns.

3.1 Constitutive Model

The behavior of concrete is non-linear under compression and tension (Fig. 4). The non-linear behavior of concrete is modeled using the concrete damage plasticity (CDP) model which is represented by Eq. (1):

$$\sigma = (1 - d)E_0\big(E - E^{pl}\big) \tag{1}$$

where ε and σ are the total strain and stress; ε_{pl} is the plastic strain; E0 is the initial elastic stiffness; d is the damage factor which indicates the loss of elastic stiffness and its values ranges between 0 which is undamaged to 1 which indicates damaged.

Zhou et al. developed a constitutive relationship which is utilized in the presnt simulation analysis for the Polyvinyl Alcohol-Engineered Cementitious Composites (PVA-ECC) material as shown in Fig. 5 [7]. The compressive behaviour for the proposed model were defined by Eqs. (2) and (3).

$$\left.\begin{array}{ll} \sigma_c = E_0\mathcal{E} & 0 < \mathcal{E} \le \mathcal{E}_{0.4} \\ \sigma_c = E_0\mathcal{E}(1 - \alpha) & \mathcal{E}_{0.4} < \mathcal{E} \le \mathcal{E}_0 \\ \sigma_c = m(\mathcal{E} - \mathcal{E}_0) + f'_{cr} & \mathcal{E}_0 < \mathcal{E} \le \mathcal{E}_1 \\ \sigma_c = n(\mathcal{E} - \mathcal{E}_1) + \sigma_1 & \mathcal{E}_1 < \mathcal{E} \le \mathcal{E}_{max} \end{array}\right\} \tag{2}$$

where E_0 is the modulus of elasticity of ECC; ε_0 is the strain at the peak load; $\varepsilon_{0.4}$ is the strain at 40% of the peak load, α is the reduction factor for elastic modulus, defined in Eq. (3); m and n are the slope of the bilinear curve; f'_{cr} is the stress at the peak load; ε_1 and σ_1 are the strain and stress at the inflection point, respectively. The value of ε_1 is taken as 1.5 ε_0, which is obtained for the past study.
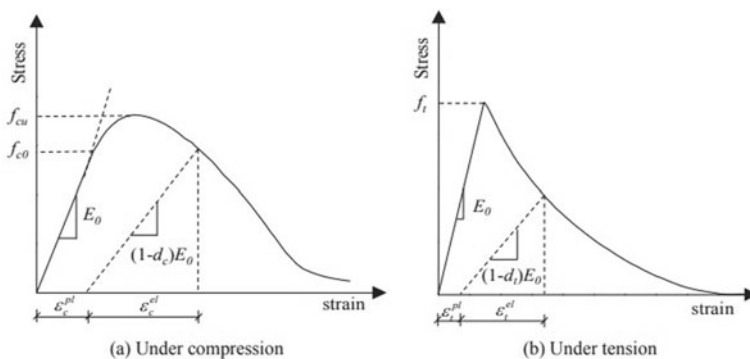
Fig. 4 Constitutive models for concrete [9]
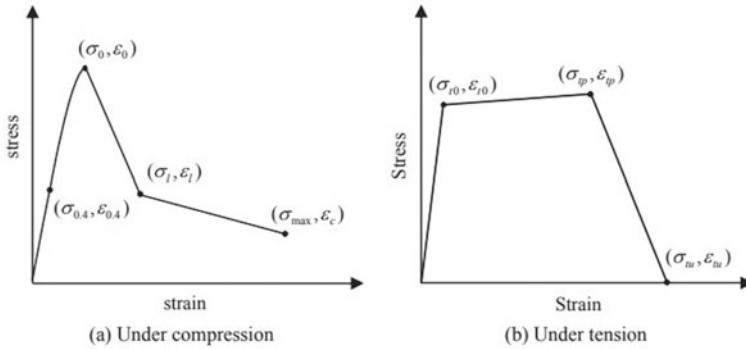
Fig. 5 Constitutive models for ECC [7]

$$\alpha = \alpha \frac{E_0 E}{f'_{cr}} - b \tag{3}$$

where a and b are computed by the slope of the equivalent hardening line. A trilinear curve is preferred for the constitutive relationship for the tensile behaviour of ECC. The relationship for the tensile behaviour is defined in Eq. (4).

$$\left. \begin{aligned} \sigma_t &= E_0 \mathcal{E} & 0 \leq \mathcal{E} \leq \mathcal{E}_{t0} \\ \sigma_t &= \sigma_{t0} + \left(\sigma_{tp} - \sigma_{t0}\right)\left(\frac{\mathcal{E}-\mathcal{E}_{t0}}{\mathcal{E}_{tp}-\mathcal{E}_{t0}}\right) & \mathcal{E}_{t0} \leq \mathcal{E} \leq \mathcal{E}_{tp} \\ \sigma_t &= \sigma_{tp}\left(1 - \frac{\mathcal{E}-\mathcal{E}_{tp}}{\mathcal{E}_{tu}-\mathcal{E}_{tp}}\right) & \mathcal{E}_{tp} \leq \mathcal{E} \leq \mathcal{E}_{tu} \\ \sigma_t &= 0 & \mathcal{E}_{tu} \leq \mathcal{E} \end{aligned} \right\} \tag{4}$$

where σ_{t0} and ε_{t0} are the first crack tensile stress and strain; σ_{tp} and ε_{tp} are the ultimate tensile stress and strain; ε_{tu} is the ultimate tensile strain.

Until the rupture happens, the basalt fibre textile showed a linear behaviour and compressive resistance was observed. Hence, basalt textile was assumed to be an elastic material, and experimental results gives the value of Youngs Modulus [10]. The linear curve represents constitutive relationship of the basalt textile and it shows that basalt textile was elastic until the failure, as shown in Fig. 6 [1].

The parameters for the CDP provided is shown in Table 1 [7].

3.2 Validation of the Finite Element Model

Using Abaqus software, a finite element study was conducted in combination with static analysis. The validation is done according to Xuan Chen's investigations [1]. The columns are validated in two conditions, failure modes and stress–strain curves.
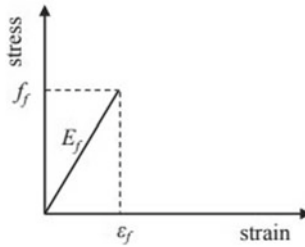
Fig. 6 Constitutive model for basalt fiber textile [1]

Table 1 CDP parameters

Dilation angle	Eccentricity	$\frac{f_{b0}}{f_{c0}}$	K	Viscosity parameter
35°	0.1	1.16	0.667	0.001

Test Specimens. Three column specimens with core strength of 34.7 MPa was modelled, an unreinforced column (C), column strengthened with basalt textile reinforced mortar (MT-C) and a column strengthened with basalt textile reinforced ECC (ET-C). A diameter of 110 mm and a height of 220 mm are provided for the column core. The confinement thickness for the composite column was 20 mm whereas the height is same as that of the column core. Basalt fiber textile with spacing of 25 × 25 mm was used. The confined column is shown in Fig. 7 [1]. The details of specimen provided are shown in Table 2.

Material Properties. Compressive strength and density for concrete, mortar and ECC provided are 34.7 MPa and 2578 kg/m^3, 46 MPa and 2096.3 kg/m^3, and 65 MPa and 2107 kg/m^3 respectively. For the basalt fiber textile, a spacing of 25 × 25 mm and density of 120 g/m^2 are provided.

Numerical Modelling. The concrete core and Polyvinyl Alcohol-Engineered Cementitious Composites (PVA-ECC) matrix were simulated using ABAQUS software. C3D8R element type was adopted for meshing. It consists of 8 noded 3D
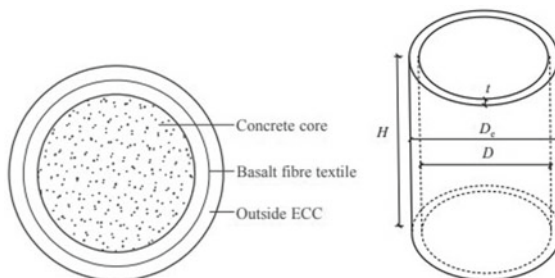
Fig. 7 Confined column [1]

Table 2 Test specimen details

Specimen	D_e (mm)	H (mm)	t (mm)	s (mm)
C	110	220	0	–
MT-C	150	220	20	25×25
ET-C	150	220	20	25×25

where H is the height, D_e is the outer diameter, D is core diameter, t represents confinement thickness and s, the spacing of basalt textile.

stress element with reduced integration. This method is well suited for nonlinear analysis which involves significant deformations. The concrete core and PVA-ECC contact surfaces were established as tie contacts. For the basalt textile fibers, S4R were adopted as element type. These are shell elements and the interface between ECC and basalt fiber textile was set us rigid body [11]. The core, ECC jacketing matrix and basalt fiber textile are shown in Fig. 8a, b and c respectively.

The foundation of the column specimens was provided as fixed condition. The concrete core was subjected to loading with a maximum capacity of 100 kN at 0.2 MPa/s loading rate. The load was given as vertical displacement at the top face of the core column and stresses, strains and deformations were recorded.

Failure Modes. The failure modes for the unreinforced column (C), column strengthened with basalt textile reinforced mortar (MT-C) and column strengthened with basalt textile reinforced ECC (ET-C) are shown in Fig. 9a, b and c respectively. It was seen that the major damage has occurred at the mid region of the column for the unreinforced specimen whereas for MT-C, cracks were developed from the loading point and it propagated to the middle part. The textile reinforcement retarded the occurrence of damage in core portion. But when it reached the middle portion
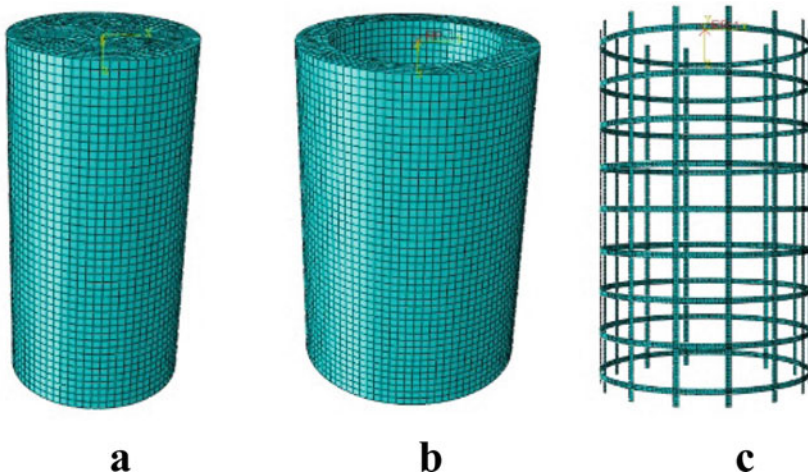
Fig. 8 a Concrete core **b** ECC jacketing matrix **c** Basalt fiber textile

the column failed. For the ET-C specimen a major damage was occurred only at the top portion of the column. The failure modes for the columns in Xuan Chen's investigations are shown in Fig. 10a, b and c respectively. It was noted that the crack development and damage distribution were same for both the cases. The maximum value for the equivalent plastic strain (PEEQ) for the unreinforced specimen, MT-C specimen and ET-C specimen are 0.004359, 0.007859 and 0.0101 respectively and from Xuan Chen's investigations it was 0.004752, 0.008679 and 0.010295 respectively. So, from these results, a percentage error of about 8.27, 9.45 and 1.89% was obtained for the unreinforced and the mortar and ECC confined specimens respectively, shown in Table 3, and thus validated.

Axial Stress–Strain Curve. The stress–strain graph for the unreinforced column, shown in Fig. 11a, was compared with the axial stress–strain curve from Xuan Chen's investigation [1], shown in Fig. 11b. It was seen that the slope of the curve obtained from both are nearly the same. It is observed that the plot of stress–strain follows three stages. At first, a linear pattern is seen for all the columns. This indicated that this stage is connected with the core strength. After this stage, a non-linear pattern was
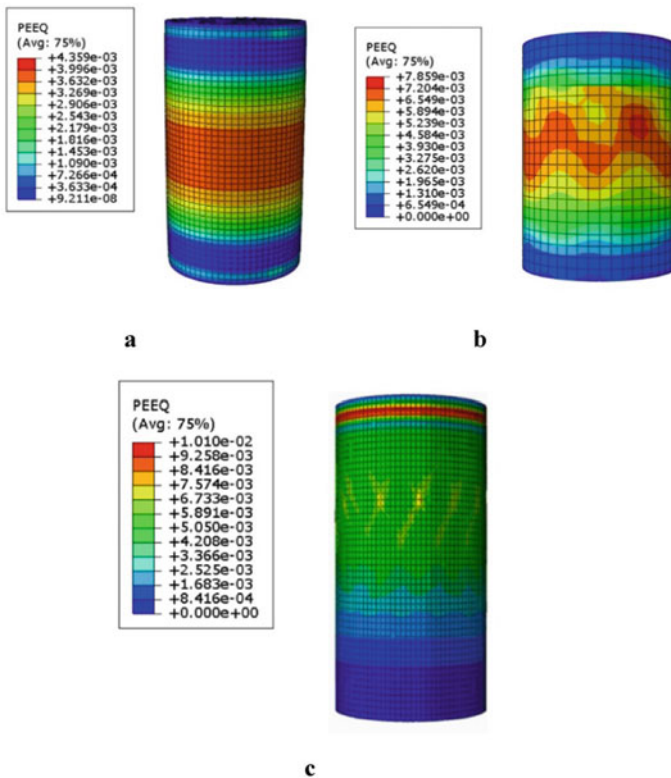
Fig. 9 **a** Failure mode of C **b** Failure mode of MT-C **c** Failure mode of ET-C
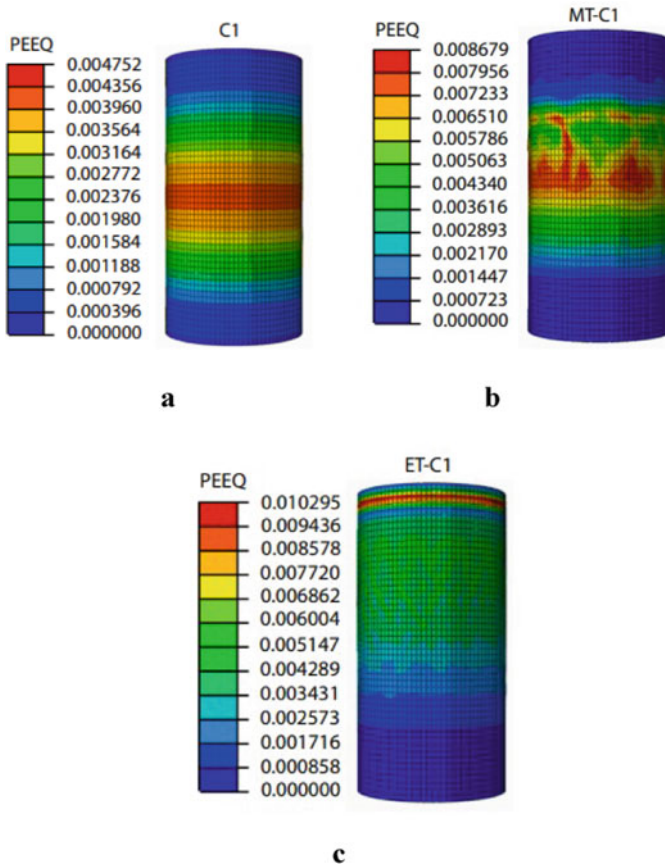
Fig. 10 **a** Failure mode of C [1] **b** Failure mode of MT-C [1] **c** Failure mode of ET-C [1]

Table 3 Comparison of Equivalent plastic strain between Journal and software results

Specimen	Equivalent plastic strain (PEEQ)		Percentage error (%)
	Journal [1]	ABAQUS	
C	0.004752	0.004359	8.27
MT-C	0.008679	0.007859	9.45
ET-C	0.010295	0.0101	1.89

observed, which indicates that the load gets transferred to the confinement provided. Among the columns, ET-C showed a greater slope. This pattern is followed up to the point of peak strength. Then the third stage was seen, i.e., the decreasing pattern of the curve. ET-C column showed a slower decreasing curve compared to other specimens.
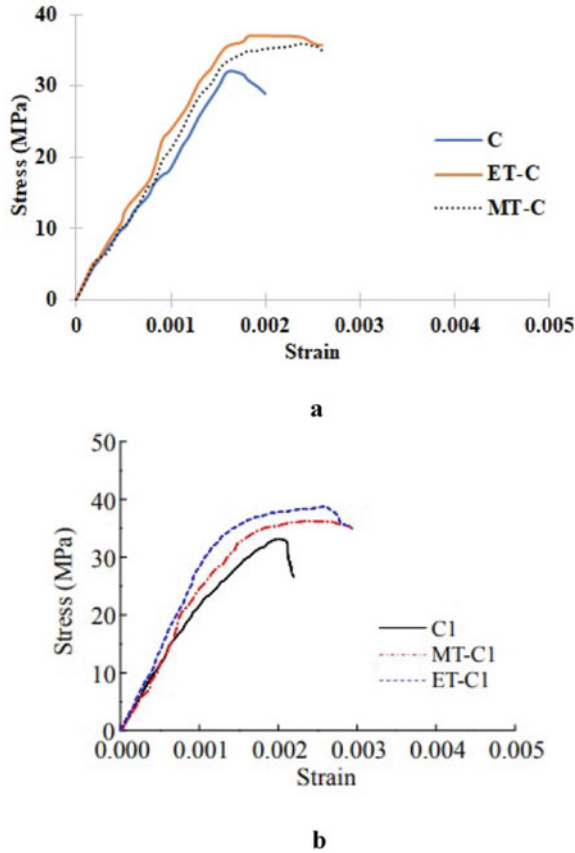
Fig. 11 **a** Stress–Strain curve **b** Stress–Strain graph [1]

4 Results

After validating the model in ABAQUS, column strengthened with basalt textile reinforced ECC was found to possess better compressive strength. An equivalent plastic strain (PEEQ) of 0.0101 was obtained for the basalt-ECC confined column. The error percentage was found to be 1.89% compared with Xuan Chen's investigation [1].

5 Discussions

The addition of ECC composite to the column provided a better bonding strength between concrete core and confinement layer. The ultimate load carrying capacity of textile and ECC strengthened column and textile-mortar strengthened column was

increased by 20% and 14% compared with the unreinforced column. Therefore, this new confining technique was found to be an effective method for enhancing the load carrying capacity of the concrete columns.

References

1. Chen, X., Zhuge, Y., Al-Gemeel, A.N., Xiong, Z.: Compressive behaviour of concrete column confined with basalt textile reinforced ECC. Eng. Struct. **243**, 112651 (2021)
2. Li, T., Deng, M., Jin, M., Dong, Z., Zhang, Y.: Performance of axially loaded masonry columns confined using textile reinforced concrete (TRC) added with short fibers. Constr. Build. Mater. **279**, 122413 (2021)
3. Al-Gemeel, A.N., Zhuge, Y.: Using textile reinforced engineered cementitious composite for concrete columns confinement. Compos. Struct. **210**, 695–706 (2019)
4. Al-Gemeel, A.N., Zhuge, Y., Youssf, O.: Experimental investigation of basalt textile reinforced engineered cementitious composite under apparent hoop tensile loading. J. Build. Eng. **23**, 270–279 (2019)
5. Guo, Y., Yu, J., Luo, Y.: Development and mechanical performance of fire-resistive engineered cementitious composites. J. Mater. Civil Eng. **31**(5), 04019035 (2019)
6. Al-Gemeel, A.N., Zhuge, Y.: Experimental investigation of textile reinforced engineered cementitious composite (ECC) for square concrete column confinement. Constr. Build. Mater. **174**, 594–602 (2018)
7. Meng, D., Huang, Y.X.T., Zhang, C.K.L.: Mechanical behaviour of a polyvinyl alcohol fibre reinforced engineered cementitious composite (PVA-ECC) using local ingredients. Constr. Build. Mater. **141**, 259–270 (2017)
8. Dehghani, A., Nateghi-Alahi, F., Fischer, G.: Engineered cementitious composites for strengthening masonry infilled reinforced concrete frames. Eng. Struct. **105**, 197–208 (2015)
9. Tao, Y., Chen, J.F.: Concrete damage plasticity model for modeling FRP-to-concrete bond behavior. J. Compos. Constr. **19**, 04014026 (2015)
10. Larrinaga, P., Chastre, C., Biscaia, H.C., San-Jose, J.T.: Experimental and numerical modeling of basalt textile reinforced mortar behavior under uniaxial tensile stress. Mater. Des. **55**, 66–74 (2014)
11. Tabsh, S.W.: Stress-strain model for high-strength concrete confined by welded wire fabric. J. Mater. Civ. Eng. **19**(4), 286–294 (2007)

Seismic Response Prediction of RC Buildings Using Artificial Neural Network

U. Abhijit Menon and Deepthy S. Nair

Abstract The study presented in this work deals with the seismic response of reinforced concrete (RC) structures subjected to earthquake motion using an Artificial Neural Network (ANN). The strong ground motion may lead to catastrophic failure of buildings or their components. Therefore, it is necessary to analyze the structure with seismic loads and to predict the damaged state of buildings. Here, an RC structure with different heights is subjected to a wide range of earthquake motions, and time history analysis is carried out to obtain the structure's seismic response, which is further used as the dataset in training ANN. Then ANN is constructed using MATLAB software from the dataset collected. The architecture of ANN is composed of three layers—the input layer, hidden layer, and output layer. The input layer consists of structural parameters such as structural configuration, the height of the structure, etc., and seismic parameters such as duration, Peak Ground Acceleration (PGA), Peak Ground Velocity (PGV), epicentral distance, etc. The maximum story drift ratio and maximum displacement are the output layers of ANN. The optimum input parameters which give the least error and maximum accuracy were identified to predict the dynamic response of the RC multistoried buildings.

Keywords Neural network · Seismic response · Drift ratio · Story displacement · ANN · Prediction using ANN

1 Introduction

An earthquake is the shaking of the ground generated by seismic waves passing through the surface of the earth. Earthquake damage to man-made structures is mostly caused by ground shaking. When the energy in the earth's crust is released, seismic waves are generated, usually when the masses of rock move against each other making fracture and slide. These rock masses create geological fault or narrow zones which are more prone to earthquakes. The Earth's crust is made of tectonic plates

U. A. Menon (✉) · D. S. Nair
Department of Civil Engineering, NSS College of Engineering, Palakkad, Kerala, India
e-mail: 20m037@nssce.ac.in

in which the fault lines run along the edge. The elastic rebound theory is used to explain tectonic earthquakes. According to the hypothesis, a tectonic earthquake occurs when the strain in rock masses exceeds the strength of rock, and the chance of rupture is higher. The fracture propagates through the earth's masses in the same direction or passes long distance through the weak zones. Earthquakes have caused major disasters to buildings and killed many people throughout history. Depending upon the magnitude of the earthquake, it can cause buildings and bridges to slide over, and the burst of pipelines due to the phenomenon caused by earthquake that includes tsunami, landslide, soil liquefaction, etc.

Seismic analysis is a part of structural analysis and is used to calculate the seismic response of the structure. During the analysis and design of multi-storied structures, the response of the structure is obtained for structural assessment and retrofitting process when the place is prone to earthquake. The seismic analysis is classified basically into two types: static analysis and dynamic analysis. The static analysis is used for buildings with limited height. The dynamic analysis is further classified into response spectrum analysis and time history analysis. Time history analysis is used to find the response of a structure using ground motion data and non-linear time history analysis provides the actual behavior of the structure considering the elastoplastic deformation of the structure.

In recent years, soft computation methods are developed based on artificial intelligence. The basic concept of soft computing is learning from experimental data and hence complex mathematical solutions are not necessary. It helps in solving problems with the appropriate result rather than conventional or analytical methods. It includes Fuzzy logic, genetic algorithms, machine learning, ANN, and expert system. ANN is a popular tool to predict the seismic response of the structure.

2 Artificial Neural Network

ANNs are inspired by human biological functions that are capable of solving problems through memory and training. The problems such as pattern reorganization, classification, pattern completion, function approximation, optimization, control, and data mining can be solved by the neural network system. The classification-based problem on seismic response of ductile frames [1] was investigated by Bilal Ahmed et al. [1]. The deep learning tool was used to detect the damage of slope systems subjected to earthquakes [2] in a previous study. Myoungsu Shin et al. (2021) developed machine learning models to predict the seismic drift responses of planar steel planes [3]. Hyo Seon Park et al. (2020) developed an ANN model to predict the seismic response of buildings based on the correlation between the earthquake and building characteristics [4]. Different types of ANN include Single-layer NN, Multi feedforward NN, Temporal NN, Self-organizing NN, Combined feedforward and self-organizing NNs, such as the radial basis function networks that can be used with help of computer-aided algorithms. However past studies [5] proved that Multi feedforward perceptron NN is effective in predicting the seismic response of the structure.
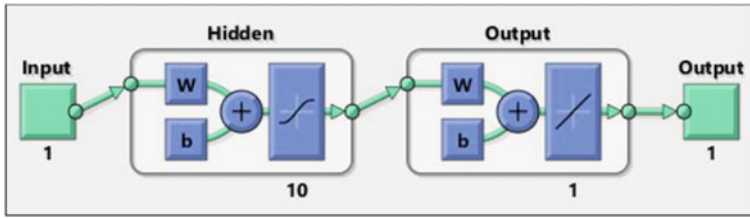
Fig. 1 Feedforward perceptron

Mohammed Rachedi et al. (2021) used multi feedforward perceptron type of ANN to predict the seismic behavior and structural assessment of existing bridge structure [6] and Jiuk Shin et al. used multi feedforward perceptron type of ANN to predict the seismic assessment and mitigation for RC framed buildings [7]. The neural network consists of interconnected neurons connected through synapses. As shown in Fig. 1, the architecture of Multi feedforward NN consists of three layers—an input layer, hidden layer, and an output layer. The input layers receive the input data and the neurons contain their own weight. This data is transformed to the next layer through synapses with the help of adders and activation function and finally passed to output layers. The purpose of the activation function is to introduce non-linearity in the network because the real problem will not be linear always. As the basic function of ANN is memory and training, the successful prediction of results will be achieved through the training of the network with significant data collection as memory. The training of ANN requires training algorithms that produce output with more accuracy. The training algorithm detects the synaptic weights from the input and hidden layer to minimize the error in the output layer. The dataset for ANN for the training algorithm requires the input data and the corresponding output data called target data. So, the trained ANN with a significant amount of dataset detects the optimum synaptic weights which give the latest error. A test data which is not included in the trained ANN can provide the output with the least error called generalized ability [5]. The generalization ability of ANN was studied for the seismic response of a viaduct in past studies [6]. The generalization ability can be improved by re-training with an increased dataset and a wide range of parameters [8].

2.1 Scope of the Work

This paper focuses on the symmetrical building of fixed length and breadth with varied heights. Reinforced concrete buildings are considered for this study and the output is limited to drift and displacement of the building. This study can be extended to unsymmetrical and irregular buildings with a wide range of input parameters. Different output parameters can be analyzed for further study.

Table 1 Range of ground motion data

Parameters	Values
Magnitude	5–7.36
Hypocentre distance (km)	0–13.8
Epicenter distance (km)	8.71–226.98
Duration (s)	11.7–70
PGD (cm)	0.01–0.17
PGV (cm/s)	0.65–10.05
PGA (g)	0.06–3.91

3   Collection of Dataset

The input data and the target data should be obtained for the construction and training of ANN. The dataset contains information that is stored in ANN in terms of weights and biases. The weights and biases play a significant role in predicting the output value.

3.1   Selection of RC Multi-storied Building

A symmetrical building with four different heights was selected for input data and a Non-linear Time History analysis is performed for this selected building to obtain target data which is used in ANN. The length and width of the building are 15 m. The height of the buildings is 12, 15, 18 and 24 m.

3.2   Selection of Ground Motion

The earthquake data was collected from PEER (Pacific Earthquake Engineering Research) ground motion database [9]. A total of 10 earthquakes with a wide range of significant data were considered. Table 1 shows the selected range of parameters which is considered as input data in the architecture of ANN and to perform time history analysis.

3.3   Modelling of RC Building

The modeling of RC buildings was carried out in ETABS software [10]. The selected symmetrical is modeled in the software with the base dimension of 15 m × 15 m. The
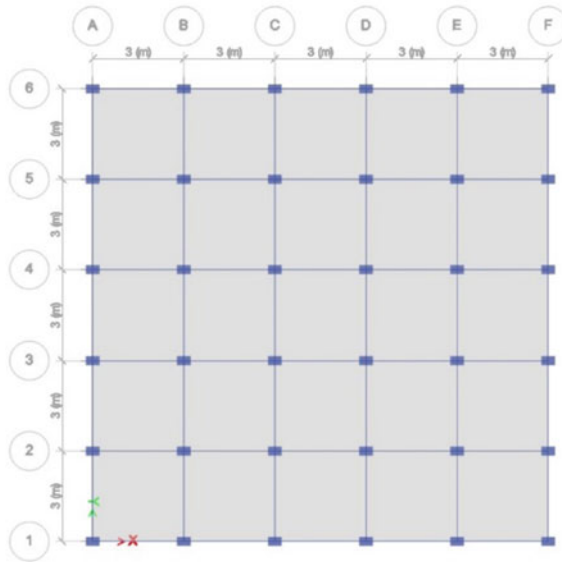
Fig. 2 Plan view of the building

height of the building varies with four different heights and four building models with different height was modeled. The grade of concrete and steel was M30 and Fe500 respectively. Self-weight is applied as dead load. Wall load is applied as 12.42 kN/m. Live load and floor finish load is applied as 2 and 1 kN/m^2 respectively. Earthquake load was applied to the buildings using the data obtained from peer earthquake database. Figure 2 shows the plan view of the building and Fig. 3 shows 3d view of selected buildings.

3.4 Nonlinear Time History Analysis

Each building is subjected to 10 selected ground motions to obtain the required target data. A total of 40 analyses are performed since 4 buildings and 10 earthquakes are considered. Time history is defined in ETABS and Non-Linear Time history direct integration method was adopted for analysis. For each analysis, the maximum story drift and the maximum displacement were collected for the dataset. The displacement and story drift was found to be maximum for the seismic load case in every building. Table 2 shows the member size obtained after analysis.
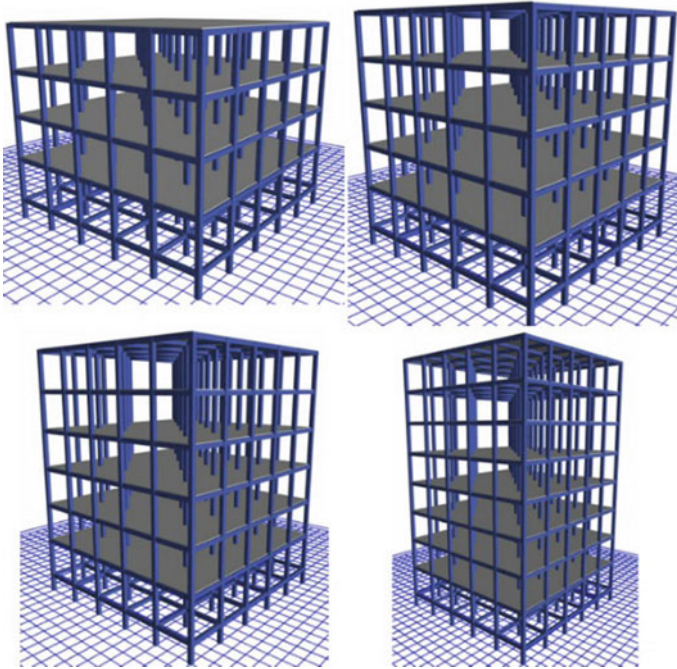
Fig. 3 3d view of selected building

Table 2 Member sizes of selected buildings

Member designation	12 m high building	15 m high building	18 m high building	24 m high building
Beam size (m)	0.23 × 0.3	0.23 × 0.3	0.3 × 0.35	0.3 × 0.4
Column size (m)	0.3 × 0.3	0.3 × 0.3	0.35 × 0.35	0.4 × 0.4

4 Neural Network

From the data collected, Artificial Neural Network was created with help of a tool in MATLAB. Multi feedforward perceptron is used for ANN which is proven to be effective in previous studies [5]. In the architecture of ANN, 10 hidden neurons were used in a hidden layer which was found by the trial-and-error method. The sigmoid function (login) activation function was used which was found by the trial-and-error method.
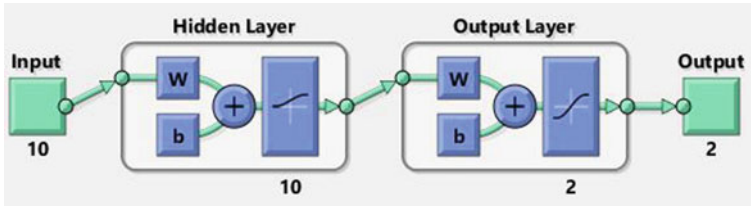
Fig. 4 Architecture of Artificial Neural Network

4.1 Problem Formulation

The input layer of the neural network consists of structural parameters and seismic parameters. In this paper, 3 structural parameters were considered which pertain to the shape of the building and 7 seismic parameters were considered. The input parameters of ANN include.

- Length of the building
- Breadth of the building
- Total height of the building
- Duration of earthquake
- Magnitude of earthquake
- Epicentral distance
- Hypocentral distance
- Peak Ground Displacement (PGD)
- Peak Ground Velocity (PGV)
- Peak Ground Acceleration (PGA)

The output parameters formulated in the neural network are maximum story drift and maximum displacement. The target data are the same which is obtained from Non-Linear Time History Analysis. As shown in Fig. 4, the architecture of ANN consists of 10 input layers, 1 hidden layer, and 2 output layers with the collected 40 datasets. The input layer is displayed in green colour and it transfers data to hidden layer through weights and biases.

4.2 Training of Dataset

The dataset provided was divided into 70% for the training dataset, 15% for the testing dataset, and 15% for the validation dataset. The test, validation, and training set were chosen randomly by the software.

4.3 Performance Evaluation

The results are evaluated by two performance evaluation parameters i.e., Mean squared error (MSE) and Regression value (R). The Mean squared error is defined as the mean or average of the squared differences between the predicted dataset and the target dataset. Regression value is a method that predicts the seismic response from target data based on the predicted values.

Performance graph The best validation performance is 0.38687 found at epoch 5. Figure 5 shows that the MSE value is decreasing and the value is closer to zero at the best performance. The green line denotes the validation dataset, red denotes the test dataset and blue denotes the trained dataset. The best performance from this total dataset is noted. So, the MSE is minimum for this neural network and can be used as the best-performed network.

Regression graph The equation of the line is obtained from the output data and compared to the target data. The green line denotes the validation dataset, red denotes the test dataset and blue denotes the trained dataset. From Fig. 6, the R values are 0.95998 for training, 0.99206 for the validation dataset, and 0.99683 for the testing data set. So, the overall R-value combining the three data set is 0.96832 which is nearly equal to 1. Hence the neural network created is found to be more accruable.
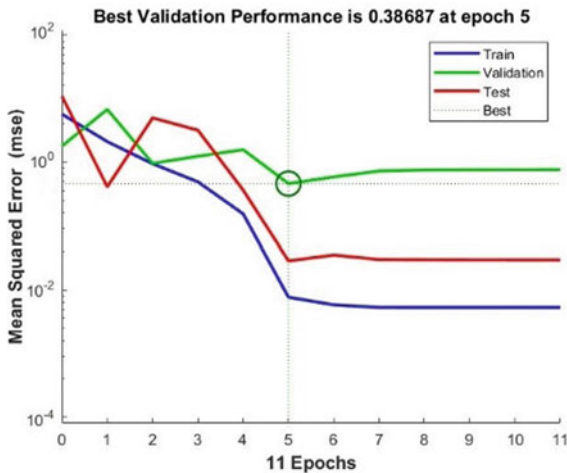
Fig. 5 Performance graph
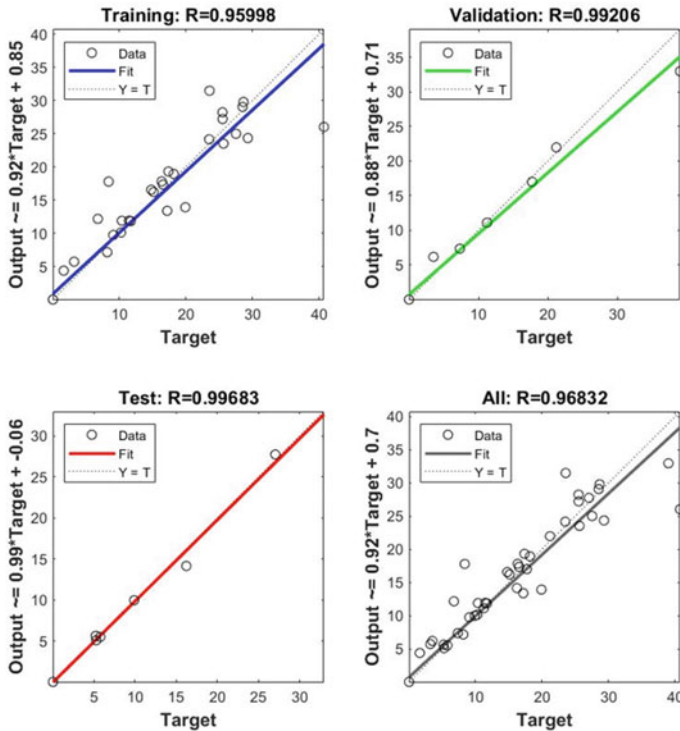
Fig. 6 Regression graph

5 Comparison of Results

A test building was selected with a height of 21 m which is out of range from the structural input parameters. And one test earthquake data that is out of range of input seismic parameters was selected. The generalization capability of ANN is identified with the test building and the test earthquake. Table 3 shows the values of selected ground motion.

The test building is modeled in ETABS and Non-Linear Time History Analysis is performed with the test earthquake. Figure 7a and b shows the maximum story drift and maximum displacement for the same building.

The data of the test building and test earthquake is given as input parameter in the trained ANN and the output was stimulated. The maximum displacement and maximum story drift ratio predicted by ANN are 33.15 and 0.002195 respectively. The blue and red line denotes the global x-axis and global y-axis respectively. Table 4 shows the error percentage of results from ETABS and trained ANN.

Table 3 Test ground motion data

Parameters	Values
Magnitude	6.50
Hypocentre distance (km)	55.62
Epicentre distance (km)	55.860
Duration (s)	16.858
PGD (cm)	0.0295
PGV (cm/s)	1.8151
PGA (g)	0.9718
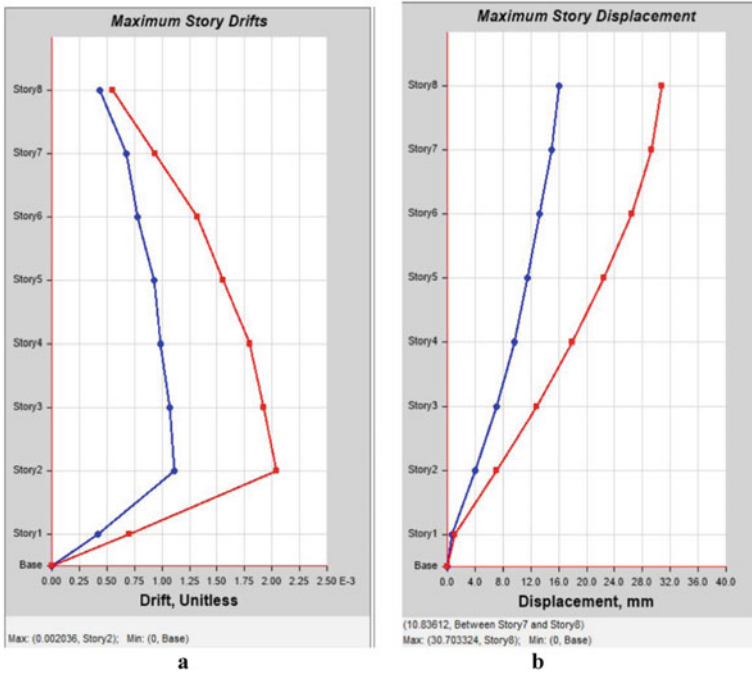
Fig. 7 **a** Maximum story drift. **b** Maximum displacement

Table 4 Error percentage

	Maximum story drift ratio	Maximum displacement (mm)
ETABS	0.002036	30.703
Trained ANN	0.002195	33.15
Error %	7.8	8.0

6 Results

After creating the neural network in MATLAB, the best-performed network was identified. The MSE value is 0.38687 and the R-value is 0.9683. This trained ANN predicts the response of the test building with the test earthquake and the error percentage was found to be 7.8% for maximum drift ratio and 8% for maximum displacement.

7 Discussions

The MSE value is closer to zero, the difference between the target data and output data is very minimal and hence the error is very minimum. The R-value is nearly equal to one, which means the curve fitting line of target data and output data are close to each other and considerable accuracy is achieved. Therefore, ANN can be used for predicting the seismic response of the RC building with a considerable amount of accuracy. This study can be extended to a wider range of data and more significant parameters can be included to improve the accuracy.

References

1. Ahmed, B., Manglathu, S., Jeon, J.S.: Seismic damage state predictions of reinforced concrete structures using stacked long short-term memory neural networks. J. Build. Eng. **46**, 103737 (2021)
2. Huang, Y., Han, X., Zhao, L.: Recurrent neural networks for complicated seismic dynamic response prediction of a slope system. Eng. Geol. **289**, 106198 (2020)
3. Nguyen, H.D., Dao, N.D., Shin, M.: Prediction of seismic drift responses of planar steel moment frames using artificial neural network and extreme gradient boosting. Eng. Struct. **242**, 112518 (2021)
4. Oh, B.K., Glisic, B., Park, S.W., Park, H.S.: Neural network-based seismic response prediction model for building structures using artificial earthquakes. J. Sound Vib. **468**, 115109 (2020)
5. Morfidisa, K., Kostinakis, K.: Approaches to the rapid seismic damage prediction of r/c buildings using artificial neural networks. Eng. Struct. **165**, 120–141 (2018)
6. Rachedi, M., Matallah, M., Kotronis, P.: Seismic behavior & risk assessment of an existing bridge considering soil-structure interaction using artificial neural networks. Eng. Struct. **232**, 111800 (2021)
7. Shin, J., Scott, D.W., Stewart, L.K., Jeon, J.-S.: Multihazard assessment and mitigation for seismically-deficient RC building frames using artificial neural network models. Eng. Struct. **207**, 110204 (2020)
8. Stefanini, L., Badini, L., Mochi, G., Predari, G., Ferrante, A.: Neural networks for the rapid seismic assessment of existing moment frame RC buildings. Int. J. Disaster Risk Reduct. **67**, 102677 (2021)
9. PEER (Pacific Earthquake Engineering Research Centre): Strong motion database. https://ngawest2.berkeley.edu (2013)
10. Divya, R., Murali, K.: Comparitive study on design of steel structure and RCC frame structure based on column span. Mater. Today Proc. **46**, 8848–8853 (2021)

A Simple Negative Stiffness Device for Passive Control of Structures

P. Fasna and A. S. Sajith

Abstract The concept of structural weakening and damping is commonly used for the response mitigation of structures subjected to seismic forces. As after an earthquake, this method results in permanent deformation in the structure and eventually losing its functionality, the idea of 'Apparent weakening' has been found to be effective in passive seismic response control in recent research. Apparent weakening implies the softening of the structure's apparent stiffness by assisting the displacement (inducing flexibility) of the structure during seismic events. This is achieved by adding a negative stiffness device parallel to the structural stiffness and making the overall system more flexible but ensuring stability at large displacements. This has led to much research in the area of configuring negative stiffness devices of different geometry, complexity and effectiveness. In this study, a new model demonstrating negative stiffness is developed for a single degree of freedom (SDOF) shear building and analyzed in MATLAB. The proposed device set-up is simple and also does not involve complex theoretical background in terms of design. The numerical analysis in MATLAB showed that the proposed model could easily demonstrate the concept of apparent weakening as it is found to be effective in reducing the base shear and displacement response of the SDOF model.

Keywords Apparent weakening · Negative stiffness device · Base shear

1   Introduction

As a result of earthquakes and wind loads, structures may experience lateral displacements and considerable vibrations on structural and non-structural elements, as well as occupant discomfort. So, in order to improve the wind and seismic performance of

P. Fasna (✉) · A. S. Sajith
Department of Civil Engineering, National Institute of Technology Calicut, Kozhikode, India
e-mail: fasnapoyili@gmail.com

A. S. Sajith
e-mail: sajithas@nitc.ac.in

buildings, it is important to reduce or control structural vibrations in naturally occurring hazardous situations. Structural vibration control involves altering the structure's stiffness, mass, damping, and shape, as well as supplying a certain amount of passive or active reaction forces, to regulate the structure's vibration during earthquakes and wind.

Seismic vibration control refers to techniques for reducing seismic effects in buildings and structures, thereby reducing damage due to earthquake. Active, semi-active, and passive controls are the three basic types of seismic vibration control. From the standpoint of fulfilling various design goals as well as in terms of cost-effectiveness, these three methods have both advantages and limitations. Active vibration control systems continuously measure incoming vibrations and cancel them out with the help of actuators. A control algorithm and sensor feedback are used to calculate the force exerted by the actuator in real-time. Although this approach is more effective than passive control, its applications are limited due to the high power need and continual measurement of the feedback signal. Passive control approach enhances the energy dissipation capacity of a structure through localized supplemental energy dissipation systems which are the devices installed inside a seismic isolation system. Semi-active control systems utilize the best aspects of active and passive control systems. Semi-active systems run on battery power, which is crucial during earthquakes once the structure's main power supply may fail. Local feedback is inevitable even under semi-active control.

The idea of weakening of structures (lowering the stiffness) while adding supplementary viscous damping to simultaneously minimize total accelerations and inter-story drifts was introduced by Reinhorn in 2005 [1]. However, the weakening of structures causes the structural system to yield early, leading to damage and permanent deformation. Owing to the shortcomings of weakening, a new concept termed apparent weakening has emerged, in which the structure imitates yielding without changing its original structural properties [2]. This is achieved by adding negative stiffness to the structure before the yield point, and then its combination with the structure's positive stiffness. This is achieved by adding negative stiffness to the structure before the yield point, which then combines with the structure's positive stiffness to accomplish apparent weakening. A true negative stiffness implies that the force must help motion rather than oppose it, as it does in a positive stiffness spring. Seismic response control of structures using apparent weakening by introducing an adaptive negative stiffness system (ANSS) was first proposed by Pasala et al. in 2013 [3]. An adaptive system is composed of adaptive stiffness and/or damping devices that can alter their stiffness and/or damping depending on the amplitude of the displacement [4]. ANSS is composed of a negative stiffness device (NSD) and a passive damper. The NSD reduced base shear and floor acceleration responses of the structure but it increased the floor displacements. A passive damper was used to control the excessive displacements so that both base shear and floor displacement can be reduced simultaneously. Figure 1 shows the configuration of NSD employed by Pasala et al. in their research.

The present study intends to demonstrate the idea of apparent weakening using a simple configuration of negative stiffness device on a single degree of freedom shear
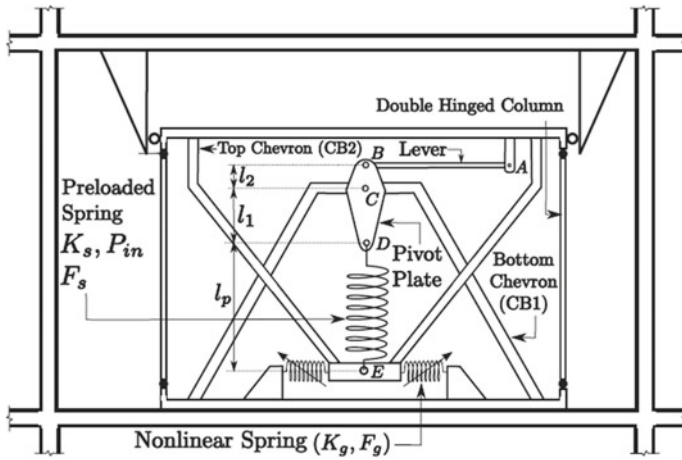
Fig. 1 Negative stiffness device (Pasala 2013)

building model and analyze the base shear and floor displacement response using MATLAB. Also, the use of a linear DVA for reducing the vibration amplitude of the floor is presented.

2 Negative Stiffness Systems in Elastic Structures: Basic Principle

NSD is a device that generates a force in the same direction as the induced displacement, therefore the name 'Negative Stiffness'. Consider a linear single degree of freedom (SDOF) structure with stiffness K_e (not considering damping), NSD of stiffness K_n, as well as a passive damper with damping coefficient C. Figure 2a depicts the force–displacement diagrams [3]. Beyond the displacement u_y', the combined stiffness is reduced to $K_e - K_n$ (assembly stiffness K_a) by the addition of NSD to the structure as shown in Fig. 2b. If the maximum displacement and maximum restoring force of a linear system are u_2 and F_2, then the maximum displacement and maximum restoring force of the combined system are u_3 and F_3, respectively, given the same load. Although the base shear is reduced, the maximum displacement of this adaptive system is now increased in comparison to an elastic system.

As shown in Fig. 2c, the deformation of the assembly can be decreased by adding a passive damping device in parallel with the NSD. The base shear of the system is not much increased by attaching a damper to the structure + NSD assembly.
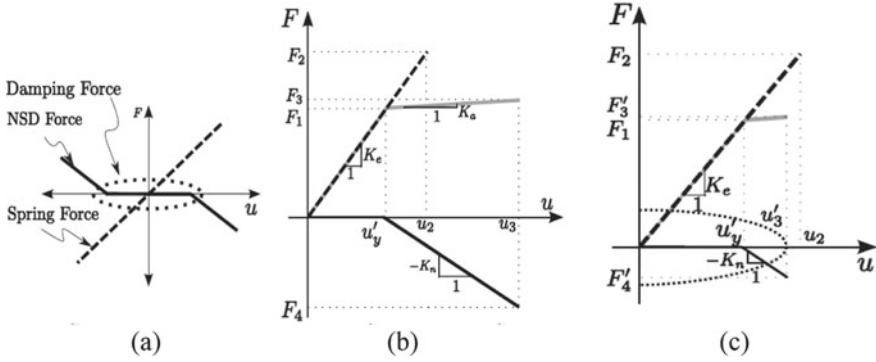
Fig. 2 Principle of negative stiffness system (Pasala 2013) **a.** component forces **b.** structure + NSD **c.** structure + NSD + damper (dashed black line—base structure; solid black line—NSD; grey line—assembly; dotted black line—viscous damper)

3 Working of NSD

Pasala et al. were the first to develop an actual device working on the concept of negative stiffness for the passive seismic response control. The schematic diagram of the developed device is shown in Fig. 1. The device configuration consists of a pre-compressed vertical spring between the two chevron braces and has an elastic bilinear spring placed horizontally [3]. The pivot plate and pre-loaded spring motion, as well as the spring characteristics, define the NSD behaviour. The pre-compressed spring rotates due to the kinematics of its top and bottom pins. Because the spring is pre-compressed and rotated in the opposite direction of the induced displacement, it assists rather than opposing the motion, resulting in negative stiffness.

4 Present Study

4.1 Modelling of a New NSD

The effectiveness of the configuration of the NSD developed by Pasala et al. in reducing the base shear response of the structure by apparent weakening can be understood from the literature. However, the experimental set-up of this NSD requires many additional components such as actuators, guiding frames, supporting frames etc. which makes the configuration complicated. This gives the scope to an alternative simple configuration of structure with negative stiffness model.

A schematic diagram of the proposed experimental setup of a single-storied structure demonstrating apparent weakening is shown in Fig. 3. A single storied shear building model is considered for the analysis. A buckling member with fixed supports at one end and hinged support at the other end is connected to the building model

using a rigid bar. The rigid bar helps in transmitting the load coming on the building from the ground to the buckling member. The buckling member is pre-loaded with a load that is less than its critical load and it assists the lateral movement of the structure under external loading and thereby bringing weakening in the structure.

To the proposed structure + NSD assembly a passive dynamic vibration absorber is set up to reduce the deformations of the system as shown schematically in Fig. 4.

The mathematical models of the systems in Figs. 3 and 4 are shown in Fig. 5a and b, respectively.
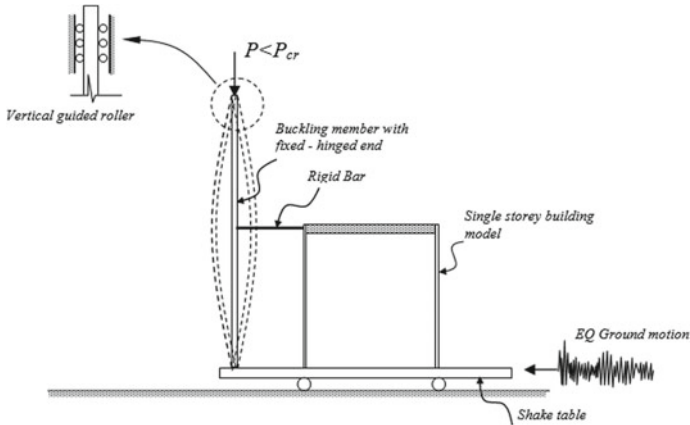
Fig. 3 Schematic diagram of structure + NSD assembly
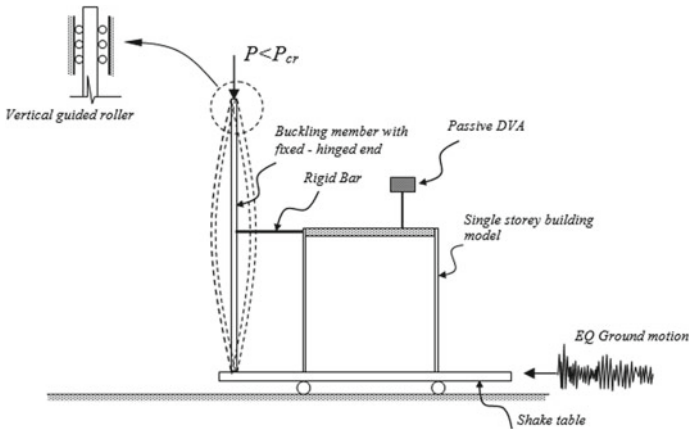
Fig. 4 Schematic diagram of structure + NSD + DVA assembly
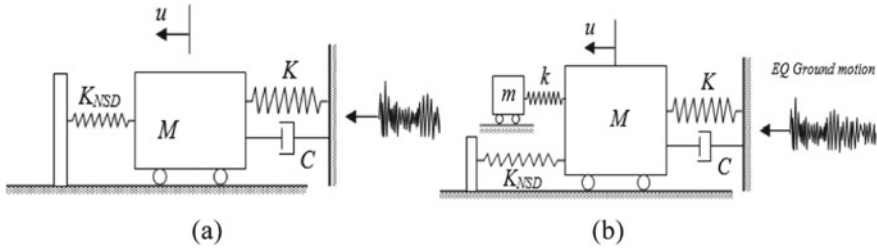
Fig. 5 Mathematical model of **a.** Structure + NSD. **b.** Structure + NSD + DVA

4.2 Mathematical Interpretation of the System

A uniform, axially loaded (a load less than its critical load) fixed-hinged column is connected using a rigid bar to the structural model. The column motion synchronised with the structure illustrates the working of the system with reduced stiffness. This is in fact a nonlinear problem. By assuming small deflection theory, this problem is mathematically developed as a linear model.

The fixed-hinged beam-column(BC) is connected to the SDOF structural model using a rigid arm. The beam-column is preloaded with a load P, which is less than its critical load. Since this is a fixed-hinged column, the critical load is taken as.

$$P = \frac{2\pi^2 EI}{l^2} \tag{1}$$

Due to the ground excitations, the SDOF model undergoes acceleration and this acts as a central concentrated load (at each instant of excitation) on BC through the rigid arm. So the case can be taken as a fixed-hinged BC with a central concentrated load. This is schematically shown in Fig. 6. From Fig. 6, compatibility condition is taken as:

$$\theta_B = \theta_{B1} + \theta_{B2} = 0 \tag{2}$$

For Fig. 6a, from the theory of BC, the deflection at the mid-point is the maximum deflection and can be expressed as:

$$y_{max} = \frac{Q}{2Pk}\left(tan(\frac{kl}{2}) - \frac{kl}{2}\right) \tag{3}$$

where, $k^2 = (P/EI)$, and for Fig. 6b, the deflection at the midpoint is:

$$y(x) = \frac{M_B}{P}\left(\frac{\sin\left(k\frac{l}{2}\right)}{\sin(kl)} - \frac{1}{2}\right) \tag{4}$$
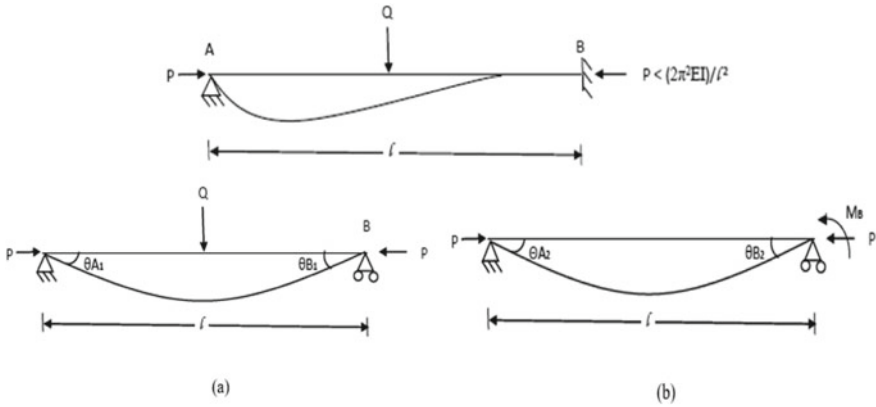
Fig. 6 Loads acting on the beam-column

From the compatibility condition and basic theories of BC, M_B can be determined. Then, the total deflection at the midpoint of the BC can be determined as the sum of the deflections in Eqs. (3) and (4). From the deflection and load acting on the BC, the lateral stiffness of the BC can be worked out. From the analysis, it is found that the lateral stiffness of the BC depends only on the critical load for the BC and is given:

$$K_{bc} = \frac{1}{\left(\frac{\tan u - u}{2Pk}\right) + \left(\frac{-3l}{16P}\frac{\lambda(u)}{\psi(u)}\right)\left(\frac{\sin u}{\sin 2u} - 0.5\right)} \tag{5}$$

where, $u = (kl/2)$ and,

$$\psi(u) = \frac{3}{2u}\left(\frac{1}{2u} - \frac{1}{\tan(2u)}\right), \lambda(u) = \frac{2(1 - \cos u)}{u^2 \cos u} \tag{6}$$

4.3 Numerical Analysis

The governing equation of motion of the generalized model for base excitation problems is:

$$[M]\{\ddot{u}\} + [C]\{\dot{u}\} + [K]\{u\} = -[M]\{\ddot{u}_g\} \tag{7}$$

where, $[M]$, $[C]$ and $[K]$ are the mass, damping and stiffness matrices of structure and $\ddot{u}_g$ is the ground acceleration corresponding to the seismic loading. With the addition of the BC model, the assembly stiffness reduces to $K_{assembly} = K_{stru} - K_{bc}$.

The modified system is represented as:

$$M\{\ddot{u}\} + C\{\dot{u}\} + K_{\text{assembly}}\{u\} = -M\{\ddot{u}_g\} \tag{8}$$

The present study uses a SDOF primary system and the parameters of this system has been adopted form lab model available at the Structural engineering lab of Department of Civil Engineering, NIT Calicut. The slab plate is steel with dimensions 300 × 200 × 8 mm and the columns are made of aluminium flats with cross-sectional dimensions of 25.4 × 3 mm. The storey height is 400 mm. MATLAB code is developed to find the response of base SDOF assembly under seismic excitation using Newmark's-β method. The analysis is done on the structural model assuming that it is excited by a single component of earthquake ground motion considered. The earthquake ground motion component used in the study is the Elcentro earthquake component (1940) of Imperial Valley ELC 180 [5]. Since the structural parameters are those of a small scale laboratory model, a scale factor of 0.1 is used for the input excitation.

For the base structure model, the Peak value of the floor displacement obtained is 1.0 mm and the maximum base shear is 2.9786 N. The RMS value of the floor displacement is 0.257 mm and the RMS base shear is 0.5521 N. For the initial trial, a fixed-hinged BC with twice the height of the structure and made of aluminium flat is chosen and the cross sectional dimensions are taken as same as that of the dimensions of the columns in the SDOF model. Critical load of BC is found using Eq. (1) and stiffness of the BC is obtained as $K_{bc} = 1.9296$ kN/m with the help of Eq. (5). From the numerical analysis, for the SDOF + BC model, the Peak value of the floor displacement obtained is 1.4 mm and the maximum base shear is 1.603 N. The RMS value of the floor displacement is 0.262 mm and the RMS base shear is 0.5425 N. The base shear and floor displacement responses of the structure + BC model are as shown in Fig. 7.
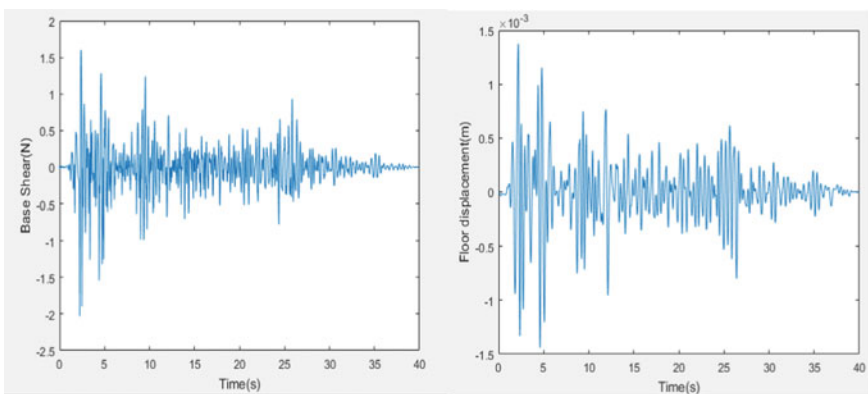
Fig. 7 Responses of the structure + BC model for the El centro excitation

Table 1 Response comparison of SDOF with beam columns of varying stiffness

Stiffness of beamcolumn (N/m) ($\times 10^3$)	Peak floor displacement (mm)	Maximum base shear (N)
1.1396	1.1	1.9957
1.2155	1.1	1.9615
1.5194	1.1	1.7975
1.6713	1.1	1.7176
1.8233	1.2	1.6429
1.9296	1.4	1.6032
1.9752	1.5	1.5925
2.0512	1.6	1.5721
2.1272	1.8	1.5457
2.2791	2.2	1.4494
2.4311	2.6	1.2374
2.6590	2.7	1.1156
2.8869	3.0	1.1072
2.9628	2.2	1.1524

Finding the Optimal Beam-Column for the SDOF Model

Since the initial trial model of the BC succeeded in giving apparent weakening (with reduced baseshear) to the structure, the next step is to find the optimal BC model for the response reduction of base structure. Since the stiffness of the BC depends only on the pre-load applied to it, which is actually a function of the cross sectional dimension of the BC, by varying it's cross sectional dimension and hence the lateral stiffness, a range of stiffness values of the BC is found out to which the apparent weakening principle is working and the optimum stiffness value of the BC is determined (Table 1).

From the analysis, the maximum base shear reduction is observed for the SDOF + BC model with the stiffness of the BC as 2.8869×10^3 N/m. The corresponding cross-sectional dimensions of the BC are 38×3 mm.

The structure connected with the BC model provides a decreased base shear and increased floor displacement on applying earthquake excitations. In order to reduce the increased displacements, a passive DVA (dynamic vibration absorber) model, a sample tuned mass damper is attached on top of the shear building model (as shown in Fig. 5b). For the structure with the optimum BC model obtained from the previous analysis, a tuned mass damper is attached with 2% tuning mass.

The structure + BC + DVA assembly is then analyzed using MATLAB for the Elcentro earthquake component. The Peak value of the floor displacement obtained is 0.5 mm and the maximum base shear is 2.36 N. The rms value of the floor displacement obtained is 0.239 mm and the rms base shear is 0.52273 N. The base shear and floor displacement responses of the model are as shown in Fig. 8.
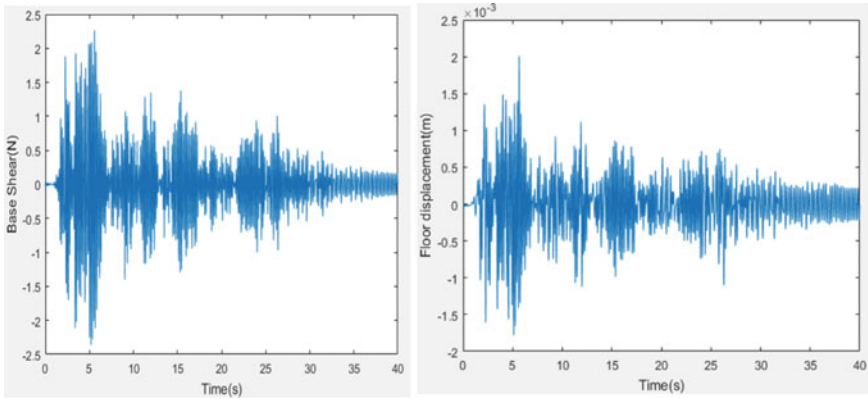
Fig. 8 Responses of the structure + BC + DVA model for the El centro excitation

Table 2 Response comparison of structure + optimum BC + DVA with the base structure

	Base structure model	Structure + BC + DVA model
Peak floor displacement (mm)	1.000	0.500
Maximum base shear (N)	2.979	2.360
RMS floor displacement (mm)	0.257	0.239
RMS base shear (N)	0.552	0.523
(%) difference in peak displacement		50.000
(%) difference in max. Base shear		20.800
(%) difference in RMS displacement		7.000
(%) difference in RMS displacement		5.320

The responses of base structure and structure + BC + DVA are interpreted in Table 2.

The proposed structure + BC + DVA model could reduce the maximum base shear response by 21% for the El Centro earthquake component considered. The model also reduced the peak floor displacement by 50%.

5 Conclusions

In this study, a simple alternate configuration of the negative stiffness device is proposed for a single degree of freedom structure. The combined structure + beam-column + DVA model is found to be effective in reducing the peak floor displacement to 50% and maximum base shear to 21%. This simple set-up could easily demonstrate the concept of 'Apparent weakening' of structures. Also, it does not involve complex theoretical background in terms of design. Because of its simple nature, it

can be easily implemented in structures. However, its practical implementation will require further studies on feasibility.

References

1. Reinhorn, A.M., Viti, S., Cimellaro, G.P.: Retrofit of structures: strength reduction with damping enhancement. In: Proceedings of the 37th Joint Meeting of U.S.-Japan Panel on Wind and Seismic Effects, UJNR, pp. 16–21. Public Works Research Institute, Tsukuba, Japan (2005)
2. Nagarajaiah, S., Reinhorn, A.M., Constantinou, M.C., Taylor, D., Pasala, D.T.R., Sarlis, A.A.: True adaptive negative stiffness: a new structural modification approach for seismic protection. In: Proceedings of the 5th World Conference on Structural Control and Monitoring (2010)
3. Pasala, D.T., Sarlis, A.A., Nagarajaiah, S., Reinhorn, A.M., Constantinou, M.C., Taylor, D.: Adaptive negative stiffness: new structural modification approach for seismic protection. J. Struct. Eng. **139**(7), 1112–1123 (2013)
4. Fenz, D.M., Constantinou, M.C.: Spherical sliding isolation bearings with adaptive behaviour: theory. Earthquake Eng. Struct. Dynam. **37**(2), 163–183 (2008)
5. Gisha, M.M., Asim, Q., Jangid, R.S.: Optimal placement of negative stiffness damping system. In: Proceedings of the ASME Conference on Smart Materials Adaptive Structures and Intelligent Systems, Colorado Spring, USA (2015)

Effect of Strongback System on Progressive Collapse Response of Concentrically Braced Steel Frames

Namitha A. Nambiar and V. N. Krishnachandran

Abstract Progressive collapse happens when reasonably small damage in structural elements triggers a cascade of failures that are more excessive than the initial damage, causing the structure to collapse as a whole or a part of it. Strongback bracing system (SBS) is a seismic force resisting system that integrates the characteristics of a conventional inelastic braced system with a substantially elastic steel truss. This paper scrutinizes the effect of strongback system on progressive collapse resistance of concentrically braced steel frames, through which an appropriate design may be developed that results in structurally sound construction, that can withstand both progressive collapse loads and seismic stresses. The progressive collapse performance of structural models is assessed by nonlinear static alternate path method specified in the Unified Facilities Criteria standard. A SBS prototype is designed and analysed considering five major damage scenarios, and are then compared with the responses of a conventional inverted V braced system. Results of the pushdown analysis are presented to demonstrate differences in responses of the braced frame systems with and without strongback. This study showed that the moment frames retrofitted with strongback spine were more resistant to progressive collapse when susceptible to column loss. However, this was reduced when the corner column was removed. Retrofitting the moment frame with strongback spine led to an increase in the cross-section of structural elements owing to its higher progressive collapse resistance.

Keywords Concentrically braced frames · Nonlinear static analysis · Progressive collapse · Alternate path method · Strongback system · Column loss

N. A. Nambiar (✉) · V. N. Krishnachandran
Department of Civil Engineering, NSS College of Engineering, Palakkad, Kerala, India
e-mail: namithaanil97@gmail.com

V. N. Krishnachandran
e-mail: vnkrishnachandran@nssce.ac.in

1   Introduction

Hurricanes, tsunamis, earthquakes, explosions, car strikes, fires, construction errors, as well as terrorist attacks, can cause extreme disasters to any structure. Localized structural damage to buildings is common in such incidents, which can lead to complete destruction. Because of the attention paid to such recent collapses, it is now widely understood that robust buildings are required that can withstand local damage without succumbing to excessive collapse. As it is difficult to foresee the likelihood and size of these severe occurrences, it is neither viable nor possible to construct a structure to withstand them using typical load-bearing methods. Collapse resistance refers to a structure's insensitivity to anomalous events.

In a comparison of progressive collapse analyses, [8] found that dynamic analytic approaches produce more accurate results. According to [10], seismically designed structures performed better under progressive collapse loads. The lateral system with cross bracings, according to [6], is not vulnerable to progressive collapse. Salmasi and Sheidaii [11] demonstrated the resistance of eccentrically braced frames to disproportionate stresses. [4] focused on collapse performance-based optimization of concentrically braced frame structures. Naji and Zadeh [2] used the alternate load path approach to investigate the response of concentrically and eccentrically braced frames in several column loss scenarios. Musavi-Z and Sheidaii [9] discussed the effect of seismic force resistance capacity of moment-resisting frames on progressive collapse response of dual systems to identify the best suitable and economic approach to distributing the earthquake loads.

This study looks at the effect of a hybrid strongback system that combines zipper frames, tied eccentrically braced frames, and an elastic truss system. Vertical tie bars are introduced over the majority of the height of a chevron braced bay in the system illustrated. These connect the intersection points of diagonal braces along the span of the beams. The augmented braced bay segments are dimensioned to form a continuous vertical truss that is expected to stay essentially elastic during levels of excitation as shown in Fig. 1. [5] presented the numerical and experimental studies of strongback system as a modified braced frame to delay weak-storey behaviour. Toorani et al. [1] studied the design approach and nonlinear dynamic behaviour of structures using strongback systems (SBS).

Figure 2 depicts several alternative bracing arrangements and strongback spines. The engineer can have more versatility in positioning or aligning the yielding braces if the strongback mast system is properly sized. Other essentially elastic structures, such as shear walls, huge plate girders, etc. may be utilised as the strongback mast instead of vertical trusses.

There have been many studies on the effects of earthquake resistant design thresholds on progressive collapse performance and also several research works have been centered on strongback systems. As per [7], the synergy underlying seismic and progressive collapse designs is a significant objective that must be explored in coming researches on progressive collapses. The progressive collapse resistance capacity of dual systems with specific steel moment frames and special concentric
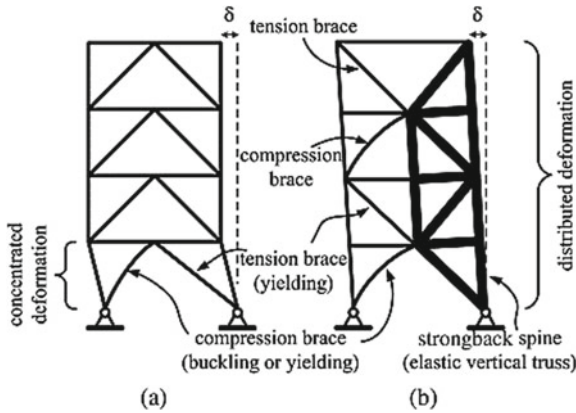
Fig. 1 Frame drifts with and without strongback: **a** conventional braced frame; **b** strongback braced frame [1]
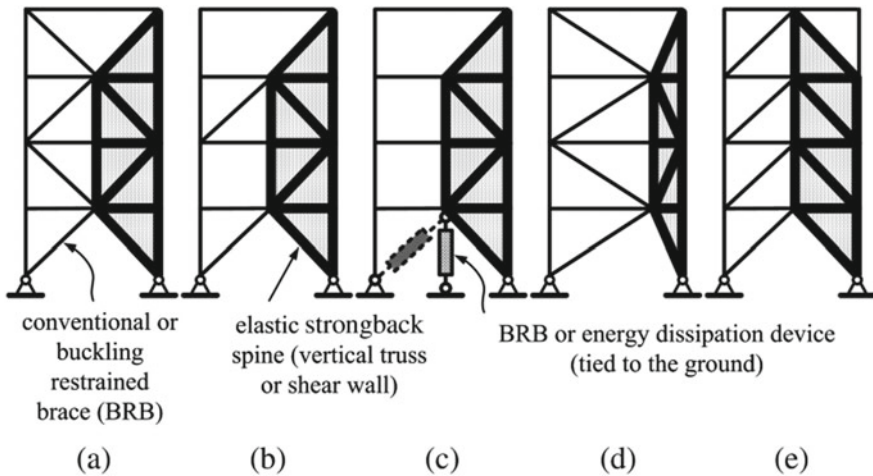
Fig. 2 Various configurations: **a** double-story X; **b** intermittent inverted-V; **c** tied-to-ground; **d** shifted double-story X; **e** Inverted-V [1]

bracing, retrofitted with strongback system was evaluated for this purpose, using nonlinear static APM as indicated in the UFC [12] guideline. To study the responses, five damage scenarios depicted by column and brace loss are analysed in the SBS prototype and is then compared with the response of a conventional chevron braced frame under similar conditions.

2 Structural Modelling

Two-dimensional models were developed in SAP2000 [9]. The structure is a six-storeyed residential building with four bays and 24 m × 24 m plan dimensions with storey height of 3.2 m and a span length of 6 m, as shown in Fig. 3 and Table 1. Inverted V bracing is used as the bracing configuration. 6.5 and 2.0 kN/m² were the design dead and live loads, respectively. To account for wall loads, perimeter beams were subjected to a dead load of 4.0 kN/m. Wide-flange sections of ASTM A992 steel were used for the beams and columns, while Hollow Steel Sections (HSS) constructed of A500 steel were used for the braces. As shown in Table 2, ten building models are being studied.
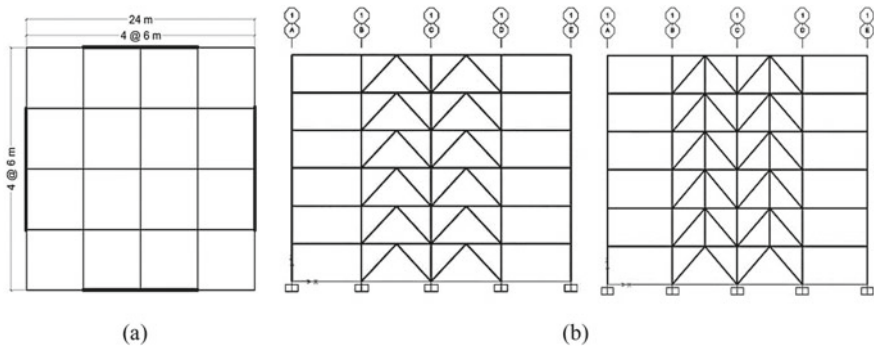
Fig. 3 **a** Plan. **b** Elevation – dual systems with inverted V braces and strongback braced frame

Table 1 Member sizes of the models

Storey	Columns		Beams		Brace	Struts
	Internal	External	Internal	External		
1	W 12 × 136	W 12 × 136	W 12 × 35	W 12 × 22	HSS 6 × 6 × 3/8	–
2	W 12 × 136	W 12 × 136	W 12 × 35	W 12 × 22	HSS 6 × 6 × 3/8	HSS 10 × 10 × 3/8
3	W 12 × 120	W 12 × 136	W 12 × 35	W 12 × 22	HSS 6 × 6 × 3/8	HSS 10 × 10 × 3/8
4	W 12 × 120	W 12 × 136	W 12 × 35	W 12 × 22	HSS 5 × 5 × 5/16	HSS 8 × 8 × 5/16
5	W 12 × 96	W 12 × 136	W 12 × 35	W 12 × 22	HSS 5 × 5 × 5/16	HSS 8 × 8 × 5/16
6	W 12 × 96	W 12 × 136	W 12 × 19	W 12 × 19	HSS 5 × 5 × 5/16	HSS 8 × 8 × 5/16

Table 2 Model details

Building models	Descriptions
Model 1	Inverted V braced frame with corner column (A1) removal
Model 2	Strongback braced frame with corner column (A1) removal
Model 3	Inverted V braced frame with second perimeter column (B1) removal
Model 4	Strongback braced frame with second perimeter column (B1) removal
Model 5	Inverted V braced frame with second perimeter column (B1) and associated brace removal
Model 6	Strongback braced frame with second perimeter column (B1) and associated brace removal
Model 7	Inverted V braced frame with middle column (C1) removal
Model 8	Strongback braced frame with middle column (C1) removal
Model 9	Inverted V braced frame with middle column (C1) and associated braces removal
Model 10	Strongback braced frame with middle column (C1) and associated braces removal

3 Progressive Collapse Analysis

As previously stated, nonlinear static APM, as per UFC [12], has been employed for progressive collapse analysis. In framed buildings, the location of the first damage (column loss) determines the impacted region after local failure. For the site of the deficit column in the first storey, the following five potential instances were analysed (Fig. 4):

1. Corner Column (A1)
2. Second perimeter column (B1)
3. Second perimeter with brace
4. Middle column (C1)
5. Middle column with braces
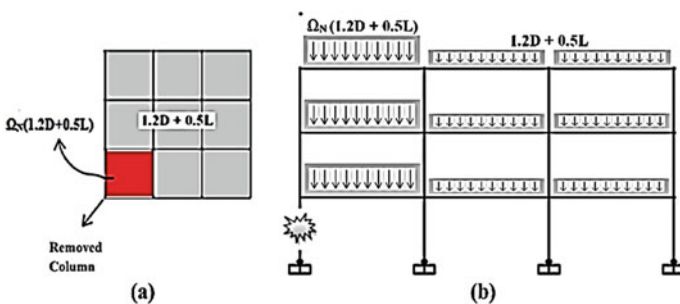
Fig. 4 Loading conditions for pushdown analyses: **a** plan; **b** elevation [9]

Plastic hinges were defined as per ASCE 41 [3]. The load combination imposed to bays in proximity of the lost column at every floor beyond that level, in compliance with the UFC standard is "Ω_N (1.2D + 0.5L)". The remaining bays were assigned with gravity load combination "(1.2D + 0.5L)" with D and L representing dead and live loads, respectively. Equation (1) was used to compute the dynamic increase factor in nonlinear static analysis of steel constructions [12], where plastic rotation angle and yield rotation is denoted by θ_{pra} and θ_y respectively, as per ASCE41 [3].

$$\Omega_N = 1.08 + 0.76 / \left(\frac{\theta pra}{\theta y} + 0.83 \right) \tag{1}$$

With parameters a, b, and c, Fig. 5 depicts a generalised force–displacement relationship for steel. Beams, columns, and braces were provided with plastic hinges. Table 3 shows the type and position of the allocated hinges. Nonlinear acceptance criteria for structural steel columns and beams must meet the life safety, and collapse prevention limit states [12].
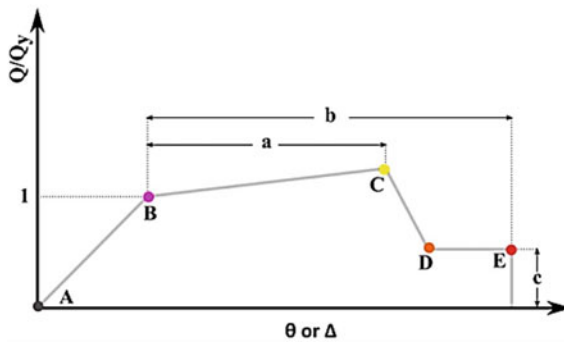
Fig. 5 Force–displacement relation for steel [9]

Table 3 Details of given hinges

Member	Hinge	Position
Column	Axial-flexural (P–M2–M3)	Ends of columns
Beam	Flexural (M3)	Ends of beams
Brace	Axial (P)	Middle of brace
Struts	Axial-flexural (P–M2–M3)	Middle of strut

4 Results and Discussions

4.1 Push Down Analysis

To determine the progressive collapse response, the overview of the pushdown analysis is summarized as load factor–displacement plots. The load factor is formulated as the ratio of imposed load at pushdown analysis steps to total progressive collapse loads. The vertical displacement of the joint above the column loss site is depicted as displacement. Progressive collapse resistance is characterised as the greatest load factor that meets UFC acceptance standards. Table 4 summarizes the outcomes of the pushdown analysis of the considered failure instances.

Corner Column Removal. Figure 6(a) shows the responses of models subjected to corner column (A1) loss. There was no noticeable increase in progressive collapse resistance, when retrofitted with strongback spine. Thus, the load factor- displacement curve superposes. The effect of progressive collapse does not propagate throughout the structure since the corner column is far away from majority of the key structural components, only affects the bay adjacent to the column removed position.

Second Column Removal. Figure 6(b) demonstrates the impact of removing the second column(B1) from the models. For strongback braced frame model, there was an increase in the structure's progressive collapse resistance accounted by an increase in the load factor of strongback braced frame by 55.15%.

The plastic hinge deformation of this case in both models is depicted in Fig. 7. The effect of providing strongback spine can be accounted with a decrease in the percentage of members above E range from 6.41% in conventional braced system to 0% in strongback braced system, henceforth, the mitigation of collapse and ultimate crushing of braces is possible. Strongback retrofitted system has no primary structural member in C to D range. Thus, it is inferred that alternate load paths have been created through adjacent columns, depicted by the yielding of columns.

Table 4 Pushdown analysis results

Scenario	Without SBS		With SBS	
	Progressive collapse resistance	Displacement (cm)	Progressive collapse resistance	Displacement (cm)
Corner Column Loss (A1)	1.0138	56.34	1.0129	56.35
Second column loss (B1)	1.8880	5.1585	4.2101	9.9839
B1 + brace loss	1.8871	5.1578	2.4929	5.9525
Middle column loss (C1)	3.1762	5.2626	4.1190	1.992
C1 + braces loss	2.8161	5.8446	3.9285	2.0046
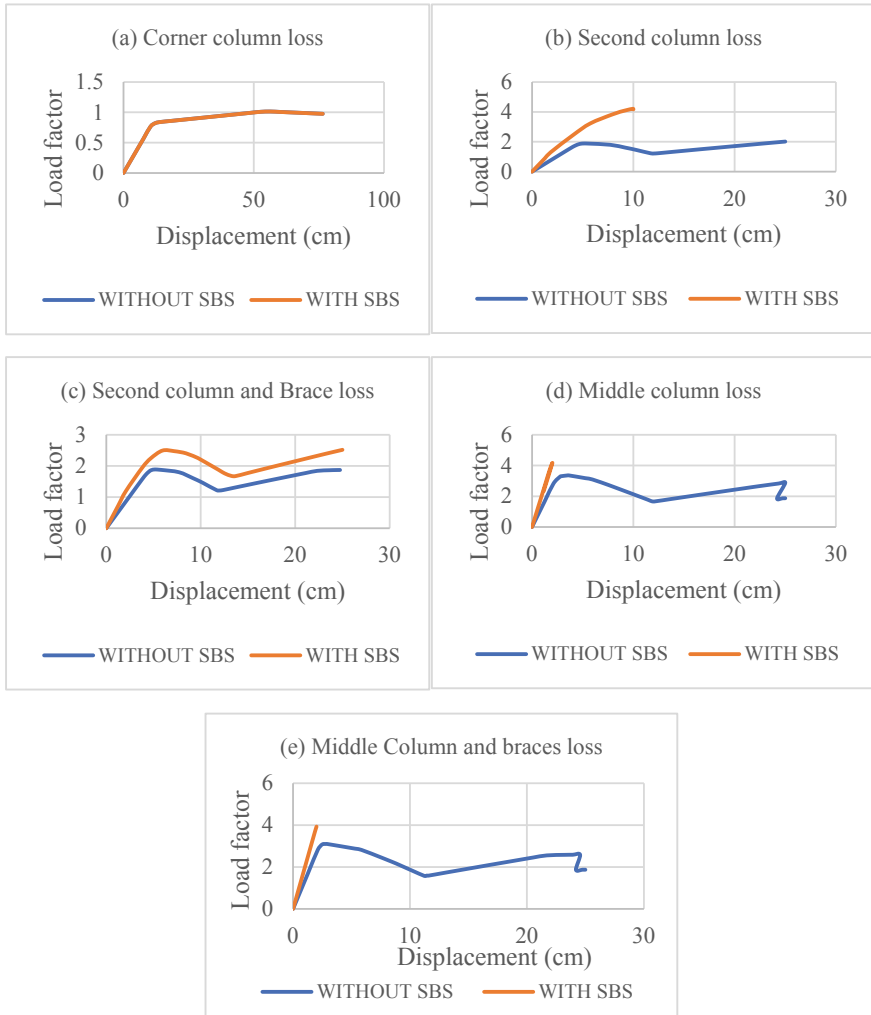
Fig. 6 Load factor–displacement plots of the five damage scenarios

Second Column and Brace Removal. The responses of models subjected to a loss of the second perimeter column (B1) and its associated brace are as shown in Fig. 6(c). An increase of progressive collapse resistance by a percentage of 24.3 in a strongback retrofitted frame demonstrated a good performance of the structure to progressive loads, even after the loss of a primary and a secondary structural member.

The plastic hinge formation patterns of discussed damage scenario are depicted in Fig. 8. It is evident that the damage level of the braces has been reduced from 6.41% to 2.56%. Strongback retrofitted system has no primary structural member in C to D state. All the hinges formed in the primary structural members are IO,
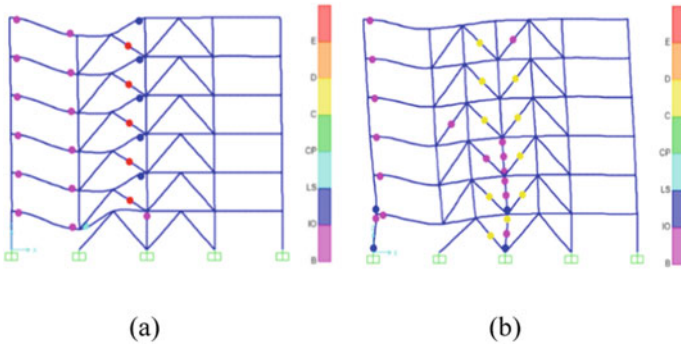
Fig. 7 Hinge formation patterns for **a** model 3 and **b** model 4
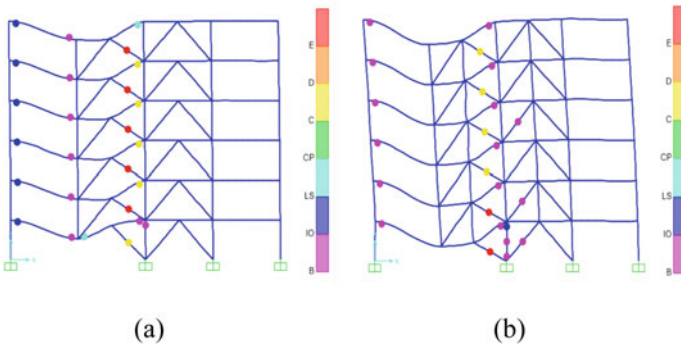
Fig. 8 Hinge formation patterns for **a** model 5 and **b** model 6

representing only yielding. Whereas, compared to second perimeter column loss, progressive collapse resistance decreased when the brace associating the column is removed, both for conventional braced system and strongback braced system.

Middle Column Removal. Figure 6(d) shows the responses of models subjected to middle column (C1) loss. Compared with conventional steel frame with chevron bracing, the progressive collapse resistance of strongback braced frame is found to be 22.88% more at a decreased displacement of 1.992 cm. It is observed that the curve is linear for strongback braced frame, implying its resistance to the effect of progressive collapse.

It is illustrated in Fig. 9(a) and (b), that when strongback spine is provided, none of the structural members reached the collapse limit, unlike the conventional model. No hinges beyond LS are formed, demonstrating zero failure happening in the structure, which can be measured as a decrease in hinges beyond C from 28.2% to 0%.

Middle Column and Braces Removal. An increase of progressive collapse resistance by 28.31% in a strongback retrofitted frame demonstrated a good performance
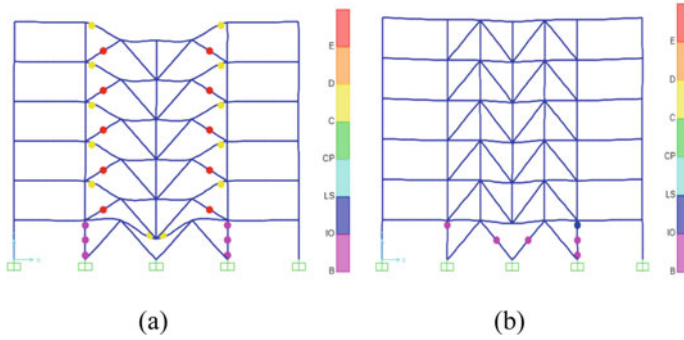
Fig. 9 Hinge formation patterns for **a** model 7 and **b** model 8
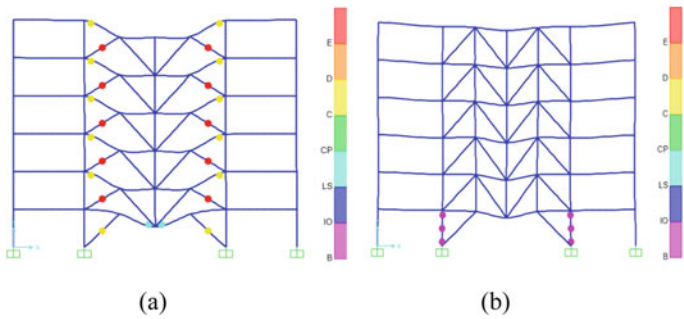
Fig. 10 Hinge formation patterns for **a** model 9 and **b** model 10

of the structure to progressive loads, even after the loss of primary and two secondary structural members, as shown in Fig. 6(e). This case is the most critical damage scenario in the conventional braced system, and the effectiveness of SBS is evident.

Damage caused by progressive loading in this scenario is completely prevented by retrofitting the system with a strongback spine. There is a reduction of hinges from 28.2 to 0% which are loaded beyond C, when the structure is strongback braced. The system stays completely elastic through all the steps (Fig. 10).

4.2 Modal Analysis

Figure 11 depicts the time period for the initial mode of various models. It is observed that the models retrofitted with strongback spine have a larger time period in all the damage scenarios considered.

In corner column loss scenario, strongback braced frame has 1.77% increase in time period than conventional braced frame. For model 4, time period is 1.62% more than model 3, whereas, for model 6, time period is 1.65% more than model
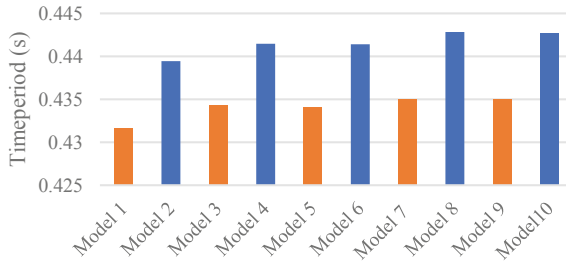
Fig. 11 Time period of building models

5. For middle column removal and, middle column and associated braces removal, the increase in time periods of strongback braced frames are respectively 1.75 and 1.73%. The occurrence of higher natural frequencies is desired. Furthermore, the structure can resonate more easily at low natural frequencies, resulting in amplification. Thus, the increase in time period ensures that the retrofitted structure has decreased vibrations than conventional inverted V braced frames.

5 Conclusions

The effects of strongback system in an inverted V braced steel structure was evaluated in this study under various damage scenarios, which led to an enhanced response to progressive collapse loads in the structure. In accordance with UFC [12] requirements, a nonlinear static alternate path technique was utilised to investigate the progressive collapse response of six storey steel buildings with similar characteristics, with and without strongback spine. The findings of five different damage scenarios were compared to those of a standard braced frame. The following conclusions were drawn from the analytical analysis undertaken in this study:

1. The pushdown analysis shows that, with the exception of the corner column removal scenario, models with strongback spine have a significant increase in progressive collapse resistance. Thus, with increasing span from the spine, the effect of strongback in resisting collapse is thought to decrease.
2. When the models were retrofitted with a strongback system and exposed to a second perimeter column loss, the progressive collapse resistance increased by 55.15 percent. The damage level of braces has been lowered, and no key structural members have been found to be beyond the collapse prevention level.
3. When the retrofitted model was subjected to the loss of the second perimeter column and a brace connected with it, progressive collapse resistance increased by 24.3 percent, indicating that the structure performed better even after the loss of a primary and secondary structural element. It is inferred that there were only braces above the collapse prevention level, henceforth, the safety of primary structural members is ensured.

4. The progressive collapse resistance of a strongback braced frame is shown to be 22.88 percent higher than a conventional braced frame subjected to middle column loss at a decreased displacement of 1.992 cm. The plastic hinge pattern illustrated that none of the structural members is collapsed.

5. Even after the loss of the middle column and two braces associated with it, the progressive collapse resistance of strongback braced frame is 28.13% more than the conventional one. Damage, in this case, is completely prevented and the system stays completely elastic throughout all the steps.

6. The removal of the central column and braces had the greatest impact on the traditional inverted V braced structure, but the strongback spine was able to effectively mitigate the damage.

7. In all of the damage scenarios evaluated, the models retrofitted with strongback spine have a longer time period. For a strongback braced frame, the time period for middle column removal is the longest and the shortest for corner column removal.

References

1. Toorani, A., Gholhaki, M., Vahdani, R.: The investigation into the effect of consecutive earthquakes on the strongback bracing system. Structures **24** (2020)
2. Naji, A., Zadeh, M.K.: Progressive Collapse Analysis of Steel Braced Frames, Practice Periodical on Structural Design and Construction. ISSN 1084-0680 (2019).
3. ASCE 7: Minimum Design Loads for Buildings and Other Structures. American Society of Civil Engineers, New York (2017)
4. Hassanzadeh, A., Gholizadeh, S.: Collapse-performance-aided design optimization of steel concentrically braced frame. Eng. Struct. **197** (2019)
5. Barbara, G.S., Mahin, S.A.: Experimental and numerical investigation of Strongback braced frame system to mitigate weak story behavior. J. Struct. Eng. **144**(2), 04017211 (2018)
6. Fu, F.: 3-D nonlinear dynamic progressive collapse analysis of multi-storey steel composite frame buildings-parametric study. Eng. Struct. **32**(12) (2010)
7. Kiakojouri, F., Sheidaii, M.R.: Effects of finite element modelling and analysis techniques on response of steel moment-resisting frame in dynamic column removal scenarios. Asian J. Civil Eng. **19**, 295–307 (2018)
8. Marjanishvili, S., Agnew, E.: Comparison of various procedures for progressive collapse analysis. J. Perform. Construct. Facilities **20**(4) (2006)
9. Musavi-Z.M., Sheidaii, M.R.: Effect of seismic resistance capacity of moment frames on progressive collapse response of concentrically braced dual systems. Asian J. Civil Eng. **22**: 23 (2020)
10. Park, J., Kim, J.: Fragility analysis of steel moment frames with various seismic connections subjected to sudden loss of a column. Eng. Struct. **32**(6) (2010)
11. Salmasi, A.C., Sheidaii, M.R.: Assessment of eccentrically braced frames strength against progressive collapse. Int. J. Steel Struct. **17**(2) (2017)
12. UFC Guidelines: Design of Buildings to Resist Progressive Collapse. Unified Facilities Criteria, Washington, DC (2016)

Seismic Performance of Composite Structure Assembled with Cold Form Self-Defending Frame

T. S. Fathima and S. Sreerath

Abstract In recent decades, Cold Form Steel systems are considered as one of the most feasible approaches for constructing residential and commercial low-rise and mid-rise buildings because it has numerous benefits such as environmentally friendly, recyclable materials, light weightness, high performance, cost effectiveness, dimensional modularity, stability and more convenience for construction (Niari, S.E., Rafezy, B., Abedi, K.: Seismic behaviour of steel sheathed cold-form steel shear wall: experimental investigation and numerical modeling. Thin-Walled Struct. **96**, 337–347 (2015)). Due to these reasons, Cold Form Steel can be integrated effectively with other materials for instance, concrete to create Composite systems. This study proposes a steel frame assembled with CFS self-defending frame, which acts as a first line of defence thereby preventing the collapse of structures when earthquake strikes. In the present work, an effort was made to study the influence of self-defending CFS structures as an assembled seismic member to improve the seismic performance of steel frame structures (Cao, W.-L., Wang, R.-W., Yin, F., Dong, H.-Y.: Seismic performance of a steel frame assembled with a CFST-bordered composite wall structure. Eng. Struct. **219**, 110853 (2019)). The pushover analysis is carried on a bare frame with and without a self-defending frame using ANSYS Workbench R22. Lateral loading is carried on a model with CFS alone and its performance is studied by conducting various parametric changes in optimising the performance by number of horizontal members in self-defending frames and alignment. The analytical results indicate that the seismic performance of bare frame structure was greatly enhanced by introducing assembled Cold Form Steel self-defending frame in structures.

Keywords Steel frame structures · CFS-combined composite wall · Inclined braces · Lateral loading · Cyclic loading · ANSYS

T. S. Fathima (✉) · S. Sreerath
Department of Civil Engineering, FISAT, Angamaly, India
e-mail: nfszfathima786@gmail.com

1   Introduction

Compared with other forms of structures made of steel, steel frames commonly used nowadays in construction projects have outstanding features such as large architectural spaces, flexible layouts, quick construction and standardised production [3]. Due to this, the use of Cold Formed Steel (CFS) systems is significantly increasing in the countries where traditional structural solutions have always dominated the construction sector. This is due to recognized technical, structural and economic competitiveness of such systems. These members provide several advantages such as lightness of structural systems, high quality of end products, and flexibility due to wide variety of shapes, sectional dimensions, short execution period and minimization of environmental impacts [2]. Among them, the features of being light-weight and having good ductility have made cold formed steel framing system an attractive structural system in seismic regions where mid-rise buildings traditionally have relied on heavier construction materials.

In this work, a fabricated frame-infill structure which can be used for low to mid rise buildings is proposed. The frame was made using a square CFS column and an H-shaped steel beam using semi-rigid connection. The in filled structure is a CFS self-defending frame which is connected to the upper and lower beams of frame. Here, the frame column is capable of carrying vertical load and some of lateral load while CFS frame in infill structure can also bear the loads coming on the structure [3]. When the CFS defending frame which serves as the first line of defence is damaged, the frame can continue bearing the vertical load in order to avoid the collapse of structure as the second line of defence.

2   Literature Review

Many scholars have studied structures made of steel elements. Shirin Esmaeili Nair studied the steel sheathed CFS shear wall panels. The steel sheathing thickness and the number of the layers of sheathings are the parameters, considered for determining maximum lateral load capacity and failure modes. Also, Non-linear Finite Element Analyses have been performed in order to investigate the seismic behaviour of steel sheathed CFS shear wall panels [1].

Recent research was carried out by M. Gerami and M. Lotfi on 112 frames with different bracing arrangements and different dimensional ratios with different thickness of sheathing plates under cyclic and monotonic loading using Finite Element Nonlinear due to ductility for all specimens. Test samples were braced walls with crossed straps and shear wall panels with the sheathings. The type of lateral loading analysis of the wall is a nonlinear pushover analysis. The cyclic loading regime that has been used in the study is based on Method B of ASTM Standard [2].

Amol V. Gowardhan carried out static linear analysis for high rise steel frame building with different patterns of bracing systems. The shear capacity of the structure can be increased by introducing Steel bracings in the structural system [4]. Bert Van Lancker investigated the Lateral stiffness of cold-formed steel shear wall panels braced with glass panel by changing the parameters like the width-to-height ratio of the panel, the thickness of the adhesive layer, the thickness of the frame members, the glass thickness and the type of section used for the frame. The results show that increasing the adhesive thickness causes decrease in lateral stiffness and a decrease in composite behaviour, while an increase in section thickness, section height and section width resulted in an increase in horizontal stiffness and relative displacements between the glass panel and the frame [5].

Ioannis Papargyriou investigated new connection configurations which engage the flanges in the connection behaviour by optimising the parameters, including the beam thickness and the gusset plate shape and thickness on the moment–rotation behaviour of the connections to determine ductility, energy dissipation and damping coefficient. The results shows that a rounded T-shaped gusset plate delivers an advantageous combination of bending moment capacity, rotation capacity and stiffness and creates a minimal obtrusion when installing the floor system [6]. Also, the lateral cyclic behaviour of six full-scale hybrid wall panels with truss structural design was carried out by Nima Usefi to investigate and characterise the seismic performance of new CFS solutions [7]. Omit pourabdollah investigated the performance of light weight K-braced cold formed steel (CFS) shear panels under cyclic loading and the results shows that use of gusset plate in the braced to stud connection of the K- braced CFS shear panels significantly increase their shear strength, energy dissipation and ductility capacities in comparison to the CFS shear panels with regular connections [8].

3 Model Configuration

The steel frame assembled with CFS self-defending frame consists of two parts-the CFS self-defending frame and steel frame which were connected by bolts [3]. Here, different model of specimen was presented including one bare frame for comparison and other frames assembled with CFS self-defending frame by changing the model with different aspect ratios and by changing the number of horizontal members in self-defending frame were used. All the model has same constructions and outer dimensions, in which H-shaped steel beams and steel tube were connected with bolts.

Table 1 Dimensional properties of elements

Elements	Specification	Thickness
Steel tube	150 mm × 150 mm	6 mm
H shaped Steel beam	194 mm × 150 mm	Flange:9 mm Web:6 mm
CFS frame	100 mm × 100 mm	2 mm
Stiffener plate	–	8 mm
Bolt	14 dia	–

Table 2 Model descriptions

Models	Description
SF-pushover	Bare frame
SF-CF-1500	CFS self-defending Frame with aspect ratio-1.85
SF-CF-2000	CFS self-defending Frame with aspect ratio-1.39
SF-CF-2500	CFS self-defending Frame with aspect ratio-1.11
SF-1500-4B	Steel frame with 4 no. of beam element
SF-1500-5B	Steel frame with 5 no. of beam element
SF-1500-6B	Steel frame with 6 no. of beam element
SF-1500-7B	Steel frame with 7 no. of beam element
SF-1500-8B	Steel frame with 8 no. of beam element

The dimensional properties of elements are shown in Table 1.

The bare frame specimen is referred to as SF. The other specimen according to different aspect ratios and construction of different number of horizontal members in self-defending frame are shown in Table 2.

The structure is modelled and analysed in ANSYS Workbench R22.

3.1 Material Property

A bilinear curve with strain hardening with reference to the yield, ultimate stress, and strain values was assumed for modelling the component the material properties of various components like steel tube, H-shaped steel beam, and CFS self-defending frame are given in Table 3.

Table 3 Details of specimen

Properties	Concrete	Steel tube	H-Shaped steel beam	Cold form steel	Bolt
Density (kg/m^3)	2400	-	-		-
Poisson's ratio	0.2	0.3	0.3	0.3	0.3
Young's modulus (Pa)	32,275	2×10^5	2×10^5	2×10^5	2×10^5
Yield Strength (MPa)	4.2	300	284	350	940
Biaxial Compressive strength (MPa)	55.8	–	–		–
Uniaxial Compressive strength (MPa)	46.5	–	–		–
Uniaxial Tensile strength (MPa)	4.2	–	–		–

3.2 Finite Element Modelling

The H-shaped steel beam, steel tube, CFS column and CFS beam are modelled using higher order three-dimensional twenty-node solid elements exhibiting quadratic displacement behaviour (SOLID186) are available in ANSYS Workbench R22. Each node of these elements has three translational degrees of freedom. The bolts are modelled using three dimensional two-node beam elements (BEAM188) with six DOFs in each node. The mesh size adopted was 20 mm and the shape of meshing is Hexahedron.

3.3 Boundary Conditions and Loading

The specimen was modelled in the YZ plane in which the column foot of the specimen was provided with fixed support by preventing translation and rotation along all directions. In order to determine the structural behaviour, non-linear static pushover analysis is to be performed. It is carried out to find out lateral loading capacity. Non-linear cyclic analysis is carried out to find the hysteresis behaviour. A lateral displacement of 85 mm was provided at the left interface in the form of load which was obtained by the trial-and-error method.

4 Results and Discussion

4.1 Effect of Bare Frame with and Without CFS Self-Defending Frame

To analyse the effect of bare frame with and without CFS self-defending frame, a non-linear pushover analysis is performed under monotonic loading. A bare frame is modelled with steel tube as column member and H-shaped steel beam as beam element that are assembled by bolt connections. The bare frame specimen is referred to as SF-pushover. The SF-pushover specimen is compared with steel frame assembled with CFS self-defending frame to obtain the lateral performance of the model.

The force reaction and corresponding deformation were noted for bare frame with and without CFS self-defending frame and load deformation curve were plotted for the same. The deformation pattern of bare frame with and without CFS self-defending frame is shown in Fig. 1. The bare frame without CFS had a higher deformation of 92.348 mm, while the steel frame with CFS self-defending frame had a lower deformation of 72.755 mm.
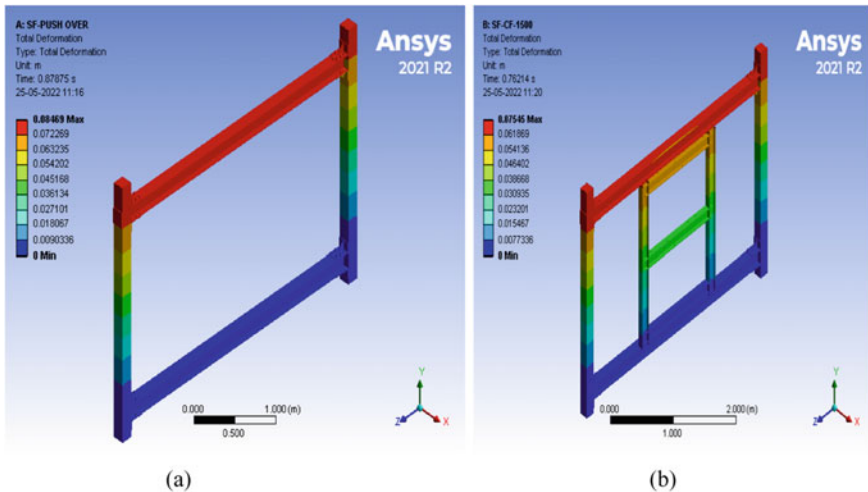
Fig. 1 Deformation of **a** bare frame **b** steel frame with CFS

LOAD V/S DEFLECTION
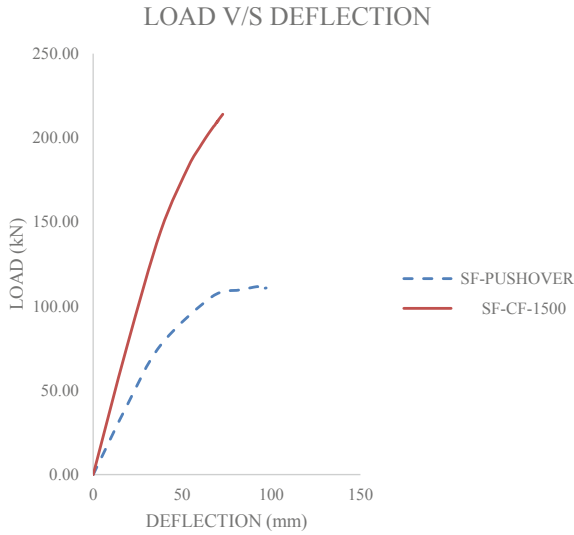
Fig. 2 Load vs deformation curve

Figure 2 indicates the load vs deformation curve obtained from the analysis. The graph clearly indicates that the model with lower deformation value i.e., steel frame with CFS self-defending frame has higher load carrying capacity compared to bare frame without CFS.

4.2 Effect of Aspect Ratio

The aspect ratio (height to length ratio) has been found to have a significant impact on the performance of the CFS self-defence frame. To understand the influence of aspect ratio better, finite element models of CFS self-defending frames with varying aspect ratios were conducted. The different models made are SF-CF-1500 (Cold form self-defending frame having aspect ratio of 1.85), SF-CF-2000 (Cold form self-defending frame having aspect ratio of 1.39). SF-CF-2500 (Cold form self-defending frame having aspect ratio of 1.11). For aspect ratio of 1.85, the specimen used is having a height 2783 mm and length of 1500 mm, for aspect ratio of 1.39, the specimen used is having height of 2783 mm and length of 2000 mm and for the specimen having the aspect ratio of 1.11, the height and length adopted are 2783 and 2500 mm.

The force reaction and corresponding deformation were noted for the finite element models of CFS self-defending frames with varying aspect ratios were plotted in Fig. 3.It can be inferred that when aspect ratio increases, the load-carrying capacity of the beam increases and hence deflection decreases. So, it can be noted
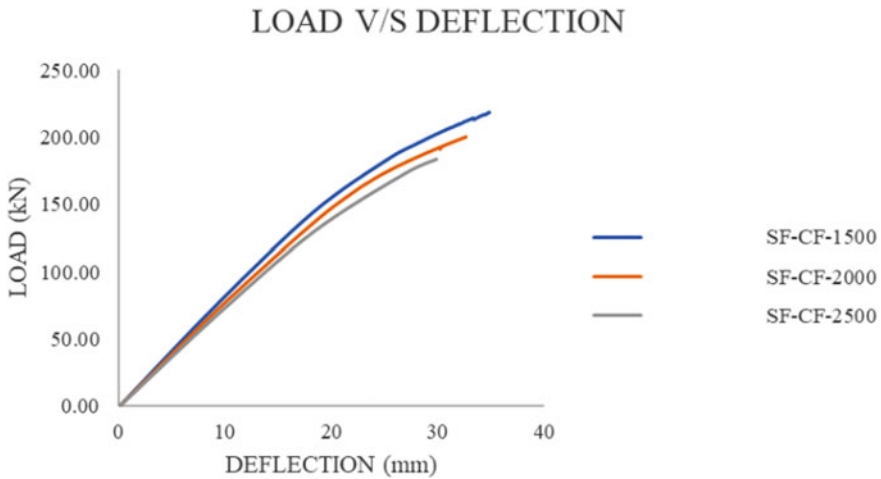
Fig. 3 Load vs deformation curve of models with different aspect ratios

that SF-CF-1500 having aspect ratio of 1.85 has higher load carrying capacity of 213.99 kN

4.3 Effect of CFS Self-defending Frames by Optimizing the Performance by Changing the Number of Horizontal Members in Self-defending Frames

It has been noted that CFS self-defending frame with aspect ratio of 1.85 is used as the base model for optimizing the performance of CFS self-defending frame by changing the number of horizontal members in self-defending frame. The model such as SF-1500-4B (steel frame with 4 No. of CFS beam element), SF-1500-5B (steel frame with 5 no, of CFS beam element), SF-1500-6B (steel frame with 6 no. of CFS beam element), SF-1500-7B (steel frame with 7 No. of CFS beam element), SF-1500-8B (steel frame with 8 No. of CFS beam element) are made using Ansys Workbench R22 and is shown in Fig. 4.

For determining the structural behaviour, non- linear static pushover analysis is performed on different models and the load vs deformation curve is plotted as shown in Fig. 5.

The graph clearly indicates that the model with higher load carrying capacity i.e, SF-1500-8B compared to other models having lower load carrying capacity. The load carrying capacity obtained for the SF-1500-8B is 341.83 kN.

The load comparison Chart shown in Fig. 6 indicates that the load carrying capacity of SF-1500-8B is 59.74% more than SF-CF-1500.

(a) SF-1500-4B

(b) SF-CF-5B

(c) SF-1500-6B

(d) SF-1500-7B

(e) SF-1500-8B
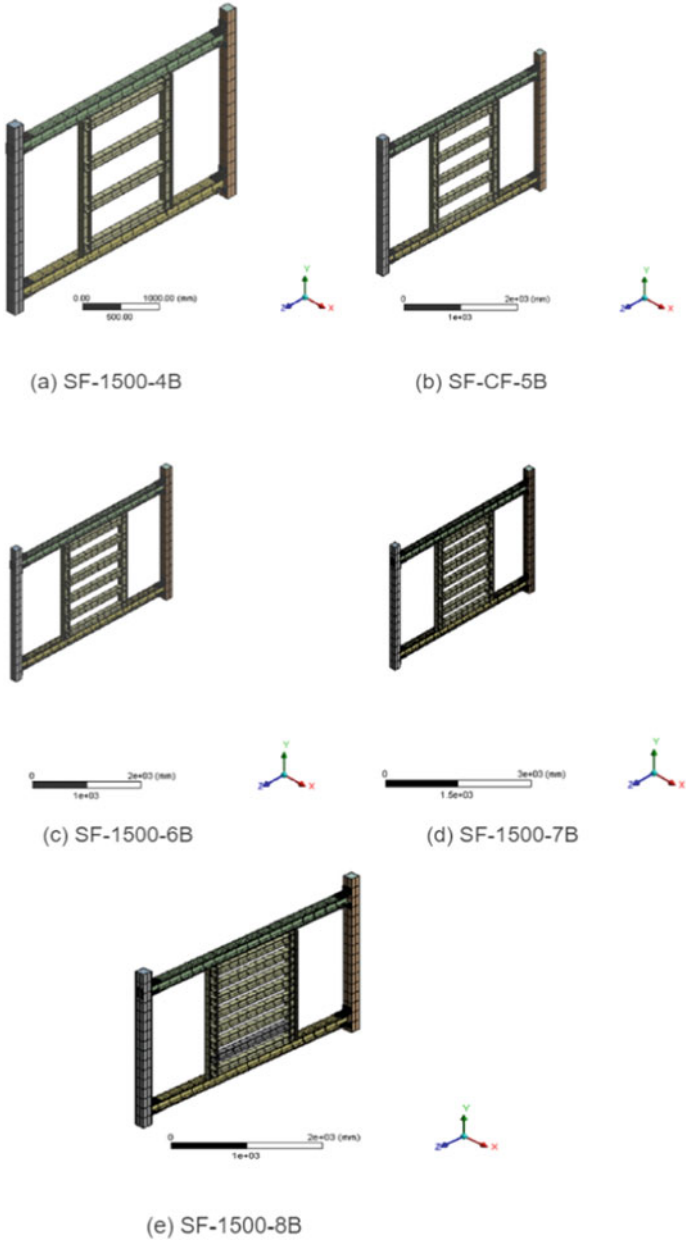
Fig. 4 Different models for parametric study

LOAD V/S DEFLECTION

Fig. 5 Load vs deflection curve

LOAD-COMPARISON

	SF-CF-1500	SF-1500-4B	SF-1500-5B	SF-1500-6B	SF-1500-7B	SF-1500-8B
load(kN)	213.99	273.32	283.47	291.76	327.62	341.83
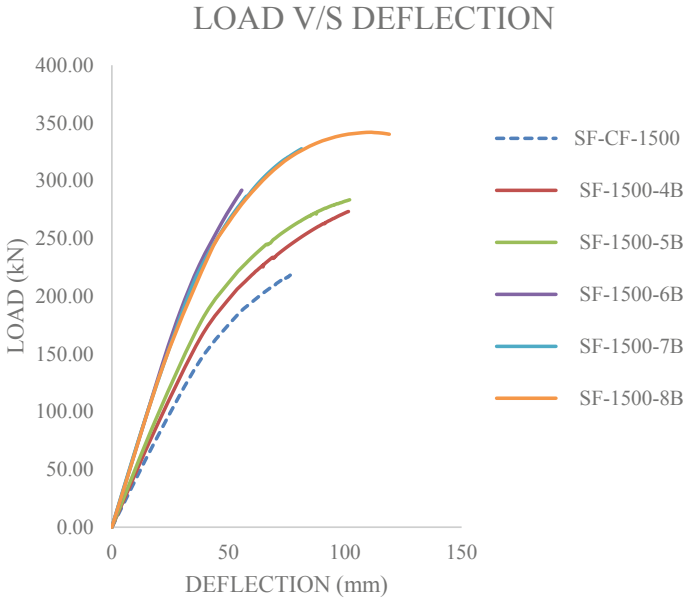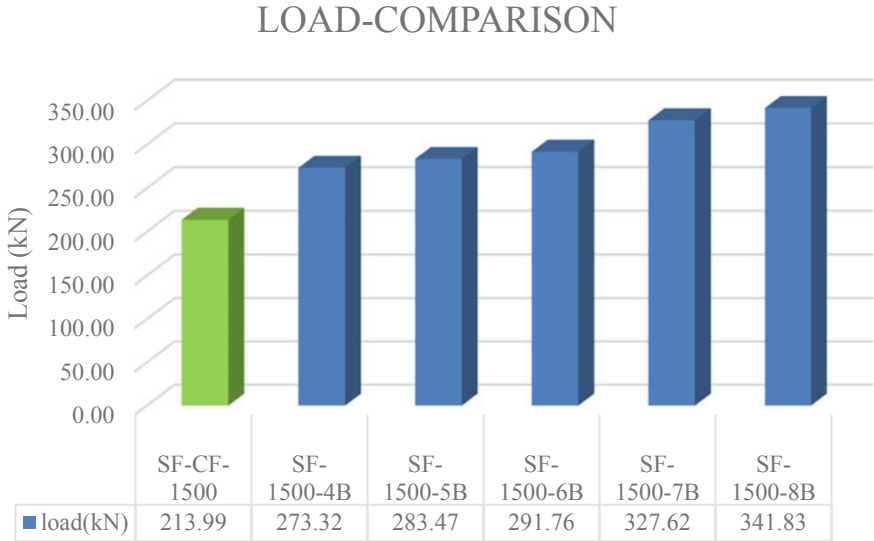
Fig. 6 Load comparison chart

5 Conclusion

This work studied the comparisons of the performance of bare frame with and without CFS self-defending frame were analysed using non-linear static pushover analysis. Also, comparison of the behaviour of CFS self-defending frames having different aspect ratios were also conducted. Lateral loading is carried on a model with CFS alone and its performance was studied by conducting various parametric changes in optimising the performance by number of horizontal members in self-defending frames and alignment.

The main conclusions are as follows:

1. The addition of a CFS self-defending frame to standard steel constructions can significantly enhance the structural parameters, notably, axial load carrying capacity.
2. The aspect ratio has a direct influence on the load carrying capacity. ie, as aspect ratio (depth to breadth ratio) increases, the load-carrying capacity of the beam increases and the deflection decreases.
3. The improvement in axial load carrying capacity in conjugation with aspect ratio may be attributed to the fact that the increase in moment of inertia with the increase in depth.
4. The incorporation of more CFS beam elements to the steel structures can significantly increase the load carrying capacity of structures.

References

1. Niari, S.E., Rafezy, B., Abedi, K.: Seismic behaviour of steel sheathed cold-form steel shear wall: experimental investigation and numerical modeling. Thin-Walled Struct. **96**, 337–347 (2015)
2. Gerami, M., Lotfi, M.: Analytical Analysis of Seismic Behaviour of Cold-Formed Steel Frames with Strap Brace and Sheathings Plates. Hindawi (2014)
3. Cao, W.-L., Wang, R.-W., Yin, F., Dong, H.-Y.: Seismic performance of a steel frame assembled with a CFST-bordered composite wall structure. Eng. Struct. **219**, 110853 (2019)
4. Gowardhan, A.V., Dhawale, G. D., Shende, N.P.: A comparative seismic analysis of steel frame with and without bracings using software Sap-2000. Int. J. Eng. Res. Technol. **4** (2016)
5. Lancker, B.V., Sonck, D., De Corte, W., Belis, J.: Lateral stiffness of cold-formed steel shear wall panels braced with glass panes: A numerical study. In Proceedings of the Structural Stability Research Council Annual Stability Conference, pp. 23–26 (2015)
6. Papargyriou, I., Mojtabaei, S.M., Hajirasouliha, I., Becque, J., Pilakoutas, K.: Cold-formed steel beam-to-column bolted connections for seismic applications. Thin-Walled Struct. (2022)
7. Usefi, N., Ronagh, H.: Seismic characteristics of hybrid cold-formed steel wall panels. Thin-Walled Struct. **27**, 718–731 (2020)
8. Pourabdollah, O., Farahbod, F., Rofooei, F.: The seismic performance of K-braced cold-formed steel shear wall panels with improved connections. J. Construct. Steel Res. (2017)

Embodied Energy Analysis of Engineered Wooden Flooring

T. Anirudh and K. B. Anand

Abstract The construction industry's use of building materials and energy has risen dramatically in recent years. GHG (greenhouse gas) emissions, global warming, resource depletion, pollution, and ecological imbalance are linked to energy consumption. It is important to assess existing construction processes, methods, techniques, and materials and choose the one that uses the least amount of energy. The total of all the energy required to produce any goods or services is referred to as embodied energy. Research on the embodied energy of building materials will drive towards the manufacture of low embodied energy materials; their selection by the structural designers and constructors, thereby reducing energy consumption and carbon dioxide emissions. The primary objective of this study is to determine the total embodied energy of engineered wood flooring. The system boundary considered in this study includes the energy and material inputs from raw material extraction, transportation, and plant production process. The data obtained from a production unit is used to determine the amount of energy consumed at each production stage of engineered wooden floors. Finally, the product embodied energy of engineered wooden floors is compared with the reported values of other types of flooring materials.

Keywords Embodied energy · Engineered wooden flooring · Plant process energy

1 Introduction

Embodied energy analysis is a tool or accounting approach for calculating the total energy consumed during various phases of a product's or service's life cycle. The embodied energy (EE) comprises the energy consumed during the extraction and processing of raw materials, transportation of raw materials to the manufacturing plant or site, manufacturing of building materials from these raw materials (plant process energy), transporting building materials to the construction site and energy

T. Anirudh · K. B. Anand (✉)
Department of Civil Engineering, Amrita School of Engineering, Coimbatore, Amrita Vishwa Vidyapeetham, Coimbatore, India
e-mail: kb_anand@amrita.edu

use for the various process during the construction and demolition of building components [1]. Initial embodied energy and recurring energy are two forms of embodied energy. The calculation of a structure's embodied energy considers numerous on-site and off-site procedures that use direct energy, such as building, prefabrication, and transportation. In contrast, most indirect energy is utilized in manufacturing building materials, renovation, refurbishment, and demolition [2]. A basic understanding of the embodied energy contents of building materials would drive the manufacture of low embodied energy materials and their selection by designers to reduce energy consumption and carbon dioxide emissions [3]. Because the building materials manufacturing industry accounts for 20% of worldwide fuel consumption, embodied energy data are crucial for national and global energy strategic objectives. Embodied energy makes up a reasonable percentage of overall life cycle energy [4]. The quantity of energy consumed in the making of a building depends on the materials and construction method. Adoption of alternative materials and construction practices can bring down EE of buildings and their environmental impact [5–8]. In recent years, studies have been conducted to evaluate the environmental impact of construction materials used for floor covering [9].

The objective of the present study is to determine the total embodied energy of engineered wood flooring. Engineered wood, also known as composite wood or manufactured board, is a wood product made by binding strands or particles together with adhesives or other means [10, 11]. The data obtained from the wood industry is used to determine the amount of energy consumed at each stage of production and identify the most energy-consuming stage in the production. Finally, the total EE of engineered wood flooring is compared with the reported values of other types of flooring materials.

2 Methodology

The energy corresponding to each production stage of engineered wooden floors is calculated from cradle to gate. The amount of energy and material inputs are observed in an industry in northern Kerala, India. It includes the energy corresponding to raw material extraction, transportation, and plant process.

2.1 Production Stages of Engineered Wooden Flooring

The raw materials used to produce engineered wooden floors are wood (red cedar, eucalyptus, or pine for the base veneers; teak, padauk, mahogany, rosewood for face veneers), glue (Phenol formaldehyde), and PU-UV insulated coating. Production stages of engineered wooden flooring are shown in Fig. 1.

The preparation stage of the production process includes the extraction of raw materials from their source, storing the wooden logs in the log yard, converting logs

PREPARATION STAGE			
LOG YARD	CROSS CUTTING	BOILING	DEBARKING

EXTRACTION STAGE			
PEELING	CLIPPING	DRYING	EDGING

FIXING STAGE			
GLUE SPREADING	ASSEMBLING	PRE-PRESSING	HOT PRESSING

FINISHING STAGE		
CONDITIONING	TRIMMING	SANDING

FLOOR FINISHING STAGE			
GROOVE MAKING	INSULATING	FILLING	FINISHING
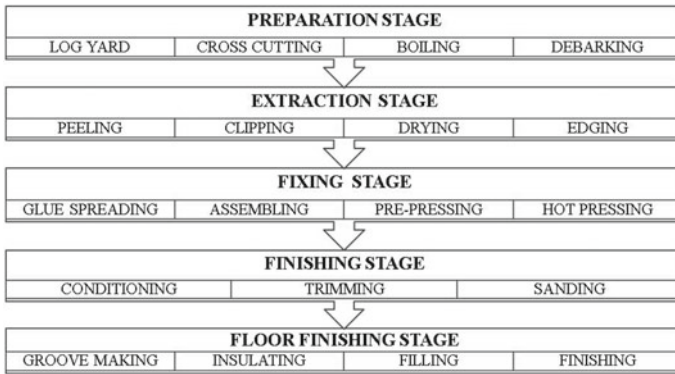
Fig. 1 Production stages of engineered wooden floors

into required sizes, and preparing it for the further stages of production. The wooden logs are cut into desired sizes ranging from 3 to 8 feet as per the requirement. A cross-cutting machine having a chain saw is used for this. The process of extraction of material in the required form from the raw materials collected is called as extraction stage. It includes peeling, clipping, edging, and drying. After the preparation stage, wooden logs are peeled using the peeling machine. The output obtained from the peeling machine is called veneers. Face veneers and core veneers are two kinds of veneers. The type of veneer obtained depends upon the species of wooden logs used. The thickness of the veneer ranges from 0.4 to 2.8 mm. The clipping is a process of converting the veneers into the required sizes. It involves the removal of defective parts. Drying is done to maintain the required moisture content. Generally, the initial moisture content of veneers will be 35 to 45%, and this will be reduced to 6% after drying. The temperature at which the drying happens is around 90 to 120˚C.

Moreover, the drying time required for each veneer is 20 min. In contrast, edging is the process of straightening the edges of veneers. An edge cutting machine is used for this. Gummed tape is used for joining. The fixing stage of production includes spreading the adhesives over veneers, assembling those veneers one above the other, and pressing the assembly to obtain the required thickness. Glue spreading is the process of spreading the adhesives over the veneers using rotating rollers. Adhesives used are urea-formaldehyde and phenol-formaldehyde. Assembling is the process of placing core and face veneers accordingly. The number of layers that should be placed depends upon the thickness required for the engineered wood product. A minimum of 3 layers of veneers are required for assembling. In pre-pressing, compressing the veneer assembly to attain the panel with the required size is done. Hot pressing is also carried out. The duration of one press may vary from 20 to 30 min. After attaining the required thickness for the panels, the final finishing needs to be done. It includes trimming and sanding. Trimming of sides of wooden panels is done to obtain the required sizes. A panel sizing machine is used for trimming. After the finishing stage, there is a distinct floor finishing step, where groove making, insulating, filling, and

Table 1 Materials used for the production of 1 m^2 of engineered wooden floors (12 mm thick)

Raw materials	Quantity (kg)
Wood	10.81
Glue– Phenol formaldehyde	0.19 to 0.27
PU-UV insulation coating	0.01
Anti-scratch topcoat	0.015
UV filler	0.05
UV sealer	0.045

finishing are done. Along the thickness of the panels, tongue and groove are made on both sides. This helps in the easier installation of wooden flooring by interlocking mechanism. Also, it avoids the use of glue for installation. PU UV insulated coating is provided for the wooden panels. The UV sealers, fillers, and anti-scratch topcoat are used as the High-performance floor coating system. Then the entire panels are passed under UV lamps. Finally, sanding is done for smoothening. The quantity of raw materials required for the production of 1 m^2 engineered wooden flooring is shown in Table 1.

2.2 Data Collection

The data required for this research is collected from the engineered wood floors manufacturing industry. The data collection is done through plant observation, oral enquiry with plant personnel, and also by collecting the relevant documents from the industry. The consolidated datasheet is noted in Table 3. The Production Audit report from the industry, which details the production and yield of a particular day, is collected. The input and output quantity at each production stage is calculated from the collected information. The machinery specification report, which details the total power of individual machines, is also collected from the industry. By considering the machines' idling time and efficient working time, the equivalent power is found. The equivalent power of the respective machines is shown in Table 2.

3   Result Analysis and Discussions

The total energy involved in producing engineered wooden flooring comprises the initial embodied energy of raw materials, material transportation energy and plant process energy utilized for the production of engineered wood.

Table 2 Total Equivalent power of each machine

Machinery	Equivalent power (kW)
Cross-cutting machine	44.049
Peeler	5.478
Dryer	10.921
Edge cutting machine	1.902
Glue spreader	2.97
Press	47.07
Boiler	20.51
Panel sizer	15.656
Floor finishing	256.75

Assumptions—transit distance for wood = 100 km; transit distance for other materials = 1000 km

Table 3 Consolidated datasheet

Location of manufacturing plant	Kannur district, Kerala
The area from where raw materials are collected	Around 100 km radius
Transit: Mileage and capacity of the truck	7 km/l, 2.7 t
Distance for transporting glue and insulation coating	1000 km
Transit: Mileage and capacity of the truck	14 km/l,750 kg
Fuel used	Diesel
The calorific value of fuel	45.5 MJ/kg
EE coefficient of Wood	Not applicable since it is a natural material
EE coefficient of glue- Phenol formaldehyde	87 MJ/kg
EE coefficient of PU-UV insulation coating	80 MJ/kg
Number of workers	53
Dimension of the floor panel	1.208 m × 0.198 m × 12 mm
Layers of veneer required for 12 mm floor panel	7
Thickness of veneers	2 mm
Average daily production	629.303 m^2
Working hours for dryer and boiler	24 h
Working hours for floor finishing plant	8 h
Working hours for other machines	12 h
Waste management	Wood wastes produced are used in boilers as fuel for producing steam for drying and hot pressing stage

Table 4 Embodied energy of raw materials

Description	Wood	Glue	PU UV Insulation	Topcoat	UV filler	UV sealer
EE coefficient of materials (MJ/kg)	0	87	80	65	65	65
Total EE of materials (MJ/m^2)	0	20.60	0.80	0.98	3.25	2.93

Table 5 Transportation energy

Description	Wood	Others (Glue, PU UV, Topcoat, UV filler, UV sealer)
Fuel used (l)	28.57	71.5
Correction factor	1	0.373
Transportation energy (MJ/m^2)	1.72	1.61

Assumptions—specific gravity of diesel fuel is 0.832, and the calorific value is 45.5 MJ/kg

3.1 Embodied Energy of Raw Materials

Since wood is a natural material, initial embodied energy or the extraction energy is negligible, and the embodied energy of other raw materials is taken from the databases [12–14]. The embodied energy of raw materials is shown in Table 4.

3.2 Transportation Energy

Transportation energy is calculated from the distance of transportation, capacity, and mileage of trucks that carry materials by assuming the specific gravity of fuel and its calorific value [15].The correction factor is calculated using the actual and used capacity of trucks. Finally, transportation energy is obtained from the product of the correction factor, quantity of fuel used and its calorific value. The transportation energy of raw materials is shown in Table 5.

3.3 Plant Process Energy

The plant process energy comprises the total energy consumed in the form of electricity for the machinery used to produce engineered wooden floors. The energy consumption in each production stage is calculated from the equivalent power of machines used and their total working hours in that stage. The total energy corresponding to all these stages gives the plant process energy. Figure 2 depicts the stage-wise energy split-up of plant process energy. The most energy-intensive part
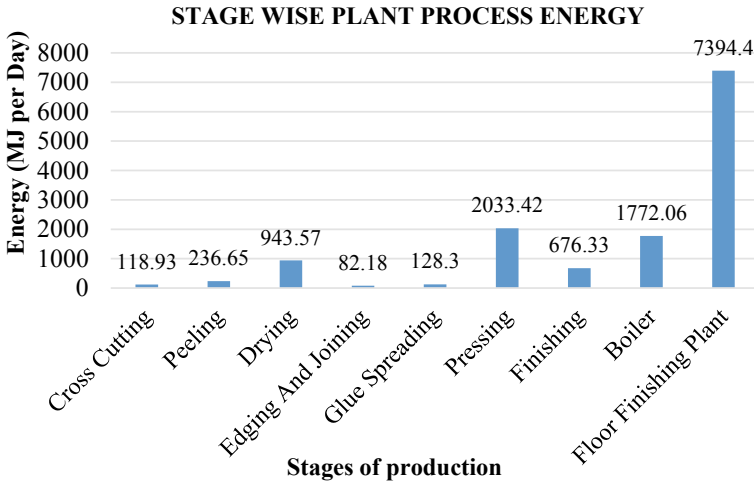
Fig. 2 Stage wise energy consumption in the production process

of the production process is the floor finishing stage. It consumes around 55% of total plant process energy. It is found that 13,385.84 MJ of energy is used in a day for the entire plant process. The total energy consumed during the plant production process for 1 m^2 of engineered wooden flooring is found.

$$\text{Total plant process energy} = \frac{13385.84 \text{ MJ}}{629.3 \text{ m}^2} = 21.274 \text{ MJ/m}^2$$

The total embodied energy of engineered wooden floors from cradle to gate is 53.16 MJ/m^2. Figure 3 depicts the total embodied energy of engineered wood flooring. Compared to plant process energy and transportation energy, the Initial Embodied energy of raw materials has the highest energy consumption value. The initial embodied energy of raw materials alone is 28.56 MJ/m^2. As the production of engineered wooden flooring involves the use of energy intensive raw materials like adhesives and resins, initial embodied energy of raw materials consumes around 53% of total embodied energy consumption from cradle to gate.

4 Comparison with Other Types of Flooring

A wide variety of hard surface flooring materials are available in the market. It includes ceramic tile flooring, engineered wooden flooring, stone tile flooring, and terrazzo flooring. The comparison of energy consumption of these floorings is of technical and commercial interest as well as from a sustainability angle. The result obtained from this study shows that the total embodied energy of engineered wooden

TOTAL EMBODIED ENERGY (MJ/m^2)

■ EE of materials ■ Plant process energy ■ Transportation energy
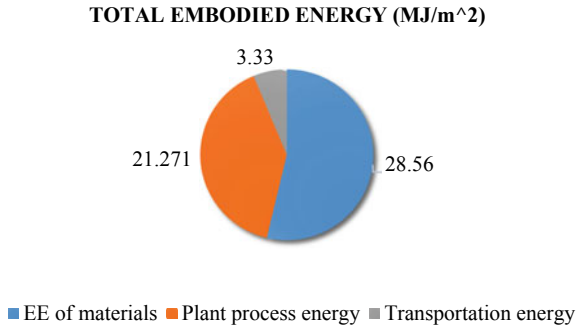
Fig. 3 Total embodied energy (cradle to gate)
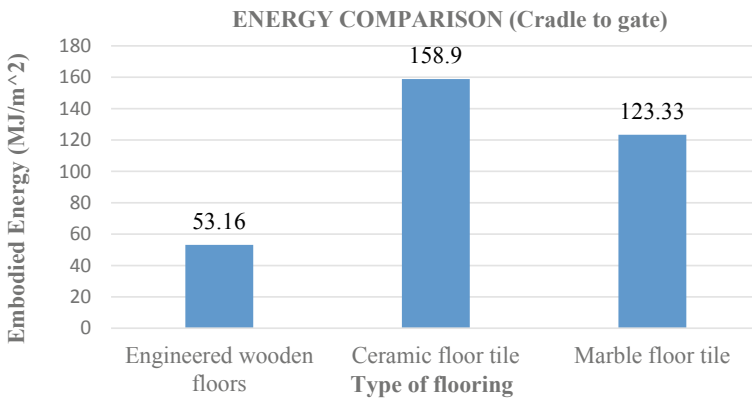
Fig. 4 EE comparison of alternative flooring materials (data from [16])

floors from cradle to gate is 53.16 MJ/m^2. Figure 4 shows the comparison of the present study's embodied energy value (cradle to gate) with that reported by Giuseppe M. Nicoletti. et al. [16]. It is noted that the total embodied energy value reported from cradle to gate for ceramic tile and marble tile is much higher than the values obtained for engineered wooden floors. The energy corresponding to raw material extraction, transportation to the plant, and plant production energy is compared. With respect to plant production energy, engineered wooden flooring has a value of 21.271 MJ/m^2, marble tile production has a value of 59.61 MJ/m^2 and ceramic tile production has a value of 129.78 MJ/m^2.

The lesser embodied energy value for engineered wooden floors gives it an edge over the other two hard surface flooring. Even though these floors are not directly comparable, replacing them with engineered wooden floors in all possible ways accounts for sustainability [17, 18].

5 Conclusion

The result of the study shows that the total embodied energy of engineered wooden floors from cradle to gate is 53.16 MJ/m^2. It is found that the floor finishing stage constitutes a significant portion of plant process energy. Also, compared to plant process energy and transportation energy, the Initial Embodied energy of raw materials has the highest energy consumption value. In comparison with other types of flooring from previous literature, it is noted that the engineered wood floors consume lesser energy during their production. Engineered wooden floors have material energy of 28.56 MJ/m^2, whereas ceramic tile and marble tile have material energies of 22.89 and 56.32 MJ/m^2. Also, engineered wooden floors have need much lesser plant process energy (21.27 MJ/m^2), compared to 129.78 MJ/m^2 and 59.61 MJ/m^2 for ceramic tile and marble tile, respectively.

References

1. Dixit, M.K., Fernández-Solís, J.L., Lavy, S., Culp, C.H.: Identification of parameters for embodied energy measurement: a literature review. Energy Build. **42**(8), 1238–1247 (2010)
2. Dixit, M.K.: Embodied energy calculation: method and guidelines for a building and its constituent materials. PhD Diss., Texas A&M Univ., USA, December (2013)
3. Gustavsson, L., Joelsson, A., Sathre, R.: Life cycle primary energy use and carbon emission of an eight-storey wood-framed apartment building. Energy Build. **42**(2), 230–242 (2010)
4. Praseeda, K.I., Reddy, B.V.V., Mani, M.: Embodied and operational energy of urban residential buildings in India. Energy Build. **110**, 211–219 (2016)
5. Abey, S.T., Anand, K.B.: Embodied energy comparison of prefabricated and conventional building construction. J. Inst. Eng. Ser. A **100**(4), 777–790 (2019)
6. Chandni, T.J., Anand, K.B.: Utilization of recycled waste as filler in foam concrete. J. Build. Eng. **19**(April), 154–160 (2018)
7. Menon, S.U., Anand, K.B., Sharma, A.K.: Performance evaluation of alkali-activated coal-ash aggregate in concrete. Proc. Inst. Civ. Eng. Waste Resour. Manage. **171**(1), 4–13 (2018)
8. Viswanath, A.K., Anand, K.B.: Lifecycle assessment of alkali activated cement concrete. J. Phys. Conf. Ser. **2070**(1) (2021)
9. Ros-Dosdá, T., Celades, I., Vilalta, L., Fullana-i-Palmer, P., Monfort, E.: Environmental comparison of indoor floor coverings. Sci. Total Environ. **693** (2019)
10. Markström, E., Kuzman, M.K., Bystedt, A., Sandberg, D., Fredriksson, M.: Swedish architects view of engineered wood products in buildings. J. Clean. Prod. **181**, 33–41 (2018)
11. Balasbaneh, A.T., Sher, W.: Comparative sustainability evaluation of two engineered wood-based construction materials: Life cycle analysis of CLT versus GLT. Build. Environ. **204**, 108112 (2021)
12. Geoff, H., Craig, J.: Inventory of Carbon and Energy. University of Bath (2008)
13. International Finance Corporation: India Construction Materials Database of Embodied Energy and Global Environmental Indicators for Materials Warming Potential Methodology & Results Version 1.0 METHODOLOGY REPORT, pp. 1–100 (2017)
14. Alcorn, A.: Embodied energy and CO_2 coefficients for NZ building materials. Report Series Centre for Building Performance Research Report, March (2003)
15. Fuel and Oil: Report on fuels and combustion. BEA, 1–26
16. Nicoletti, G.M., Notarnicola, B., Tassielli, G.: Comparative LCA: ceramic vs marble tiles. J. Clean. Prod. **10**, 283–296 (2002)

17. Tikul, N.: Assessing environmental impact of small and medium ceramic tile manufacturing enterprises in Thailand. J. Manuf. Syst. **33**(1), 1–6 (2014)
18. Türkmen, B.A., Özbilen, Ş.K., Duhbacı, T.B.: Improving the sustainability of ceramic tile production in Turkey. Sustain. Prod. Consum. **27**, 2193–2207 (2021)

Structural Performance of Composite Walls Composed of Profiled Steel Skin and Rubberized Concrete

Aaron D. Poruthur and Neeraja Nair

Abstract Composite materials have long been used in a variety of sectors. The non-residential multi-story building industry is dominated by composite construction. For more than two decades, this has been the situation. Its success can be attributed to the strength and stiffness that can be achieved with minimal materials and widely accepted prefabricated structural systems. One of them is the Profiled Double Skin Composite Walls (PDSC's). It is made up of two contoured steel plates with concrete filling the area between them. Studies have shown that the composite effects of steel plates and infilled concrete can improve composite wall axial bearing capacity. The global buckling performance of slender PDSCWs under axial compression has been studied by a number of researchers. The lateral loading conditions, on the other hand, were not thoroughly investigated. The profiled steel plates can be used as permanent formwork for infilled concrete, and they can also be employed in basement walls and shear walls for improved impact resistance and delayed failure. The best configuration for strength achievement is done and best designs are suggested.

The analysis of composite walls made up of profiled steel skin plate and rubberized concrete for various profile forms, strength parameters, and the application of composite walls as shear walls are explored statically and dynamically using ANSYS software in this work.

Keywords Composite · Prefabricated · Bearing capacity · Shear walls · Modelling · ANSYS

1 Introduction

Throughout the past two decades, composite construction has dominated the non-residential multi-story building industry, with developments over time. The strength and rigidity that may be achieved with little materials is the key to this achievement. Concrete is good in compression, while steel is good in tension, which is

A. D. Poruthur (✉) · N. Nair
Department of Civil Engineering, FISAT, Angamaly, Kerala, India
e-mail: aarondp9898@gmail.com

why composite construction is typically so good. These qualities can be leveraged by structurally connecting the two materials together, resulting in a highly efficient and lightweight design. The reduced self-weight of composite elements reduces the forces in the elements that support them, particularly the foundations. Composite systems also provide advantages in terms of building speed. Floor depth reductions realised by composite construction can save money on services and improve the building envelope.

Composite beams, composite slabs, composite columns, and composite connections are all covered in this article. While beams and slabs are prevalent in UK construction, and there are several basic varieties of composite beam, composite columns, and composite connectors are not.

The plastic stress distribution in a typical downstand beam acting compositely with a composite slab. The relative proportions of the steel section and slab mean that, as is commonly the case, the plastic neutral axis lies within the concrete. All the steel is therefore in tension. Concrete is a material that works well in compression but has negligible resistance in tension. Hence for structural purposes it traditionally relies on steel reinforcement to carry any tensile forces (this is the role played by the steel part of a composite cross section, which is effectively external reinforcement), or must be pre-stressed so that even when subject to tension, an element is in net compression.

Vertical flatdek decking, deck welded shear plate of steel, edge welded, and rubber concrete are all composite wall components. The two materials must be structurally connected together for the concrete part (within the so-called effective width) of a cross section to carry compression and the steel part to carry tension. This is accomplished with headed shear studs affixed to the steel beam's upper flange for the composite walls. Through deck, welding is commonly used to achieve this attachment. The profiled metal decking that serves as the foundation for the composite walls is sandwiched between the stud's base and the top flange, and all three are joined together by welding. The presence of galvanizing on the decking has no bearing on the quality of the welds.

Single span lengths of decking (which butt up to rows of studs welded directly to the top flange in the fabrication shop) or drilling holes in the decking so that it can be dropped over the shop welded studs are used in extreme instances to prevent through deck welding. Other shear connections, such as bigger diameter studs and shot-fired connectors, are available; although 19 mm diameter headed studs are by far the most frequent option for buildings.

One of the advantages of welded studs is that they are ductile, which means that the shear connection can be built using plastic principles (without regard to fatigue) since force can be redistributed between neighboring studs. This simplifies the design process significantly.

A composite wall can be made out of hollow steel sheets filled with concrete or open steel sections encased in concrete. The benefit of structurally connecting the steel and concrete together is to raise the resistance to failure by a factor of two. The rigidity could grow by up to three times. As the size of the wall increases in relation to the height, the relative benefits diminish.

The components of a composite wall are discussed above, but composite slabs and composite columns follow the same concepts. Force is conveyed via embossments and certain characteristics of the deck geometry in a slab that replaces a steel section with profiled steel decking (rather than discrete shear studs). A composite column can be either a concrete-filled hollow section steel tube or an open steel section encased in concrete. Friction and discrete mechanical connectors, such as shear studs that can be affixed to an implanted steel piece, are used to transfer force between the two materials. It is critical for the designer to remember the building stage in all types of composite construction. Assuming no temporary propping, the steel portion of a composite cross section must withstand self-weight and other building loads on its own, as the concrete is ineffective at that stage. Not only is there less resistance, but there is also the possibility of instability. The steel beam is restrained laterally when acting compositely, but lateral torsional buckling (LTB) can lower the effective resistance during construction; only when the decking runs transversely and is securely secured can LTB be avoided.

Engineers have a duty and responsibility to develop some unique methods of fast construction as the construction business grows. Due to their nature, composite shear walls, which are largely precast, are best used in an ongoing project and can also be added to an existing structure. In this work, the height to width ratios are investigated, as well as the lateral loading circumstances and the drift values generated from the deformation produced.

The aim of the study is to compare the effect of slenderness ratio of a typical composite wall incorporating rubber concrete by performing a linear static analysis and conducting the lateral loading capacity for checking the suitability of using it as a shear wall [1–7].

2 Finite Element Formulation

2.1 Geometry of the Component

The width of the PDSC's was 600 mm and one end of the specimen is fixed. The details of the specimen are illustrated in Table 1. It consist of rubberized concrete encased in reentrant profiled steel plate for different slenderness ratio. Figures 1 and 2 shows the specimen details.

2.2 Material Properties

The material properties used for the study is shown in Tables 2, 3, and 4. The modulus of elasticity for the steel used in PDSCW's is 2E + 05 MPa. The yield stress of the steel used in PDSCW's is 235 MPa.

Table 1 Details of specimen

Specimen	Dimension (mm)	Slenderness ratio
PDSCW 1	1000 × 600	1.6667
PDSCW 2	2000 × 600	3.333
PDSCW 3	3000 × 600	5
PDSCW 4	4000 × 600	6.6667
PDSCW 5	5000 × 600	8.333
PDSCW 6	6000 × 600	10
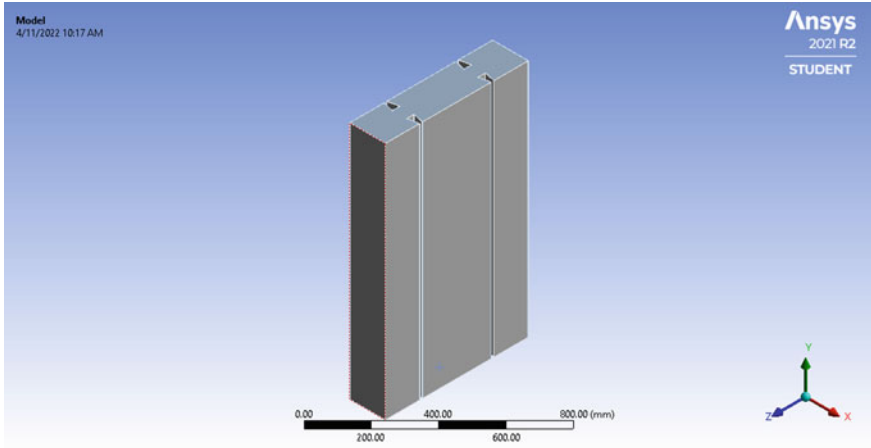
Fig. 1 Geometry of the specimen [1]
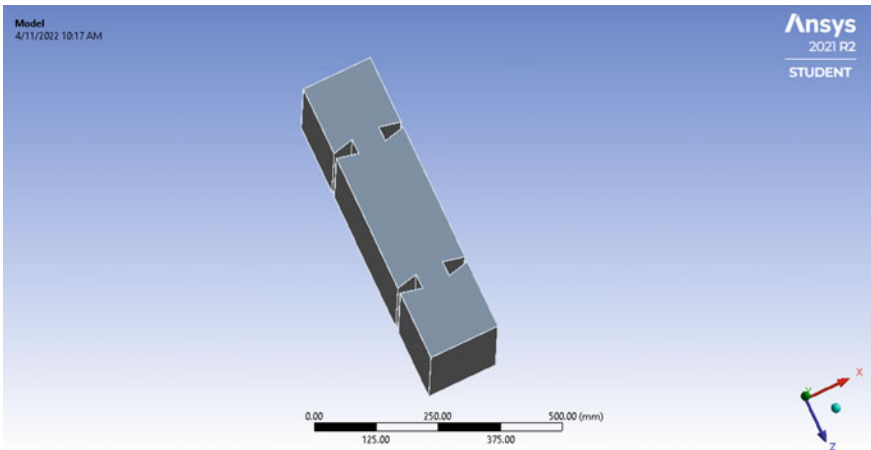
Fig. 2 Geometry of the specimen

Table 2 Material properties of steel

Width of specimen	600 mm
Thickness of plate	1 mm
Yield stress	235 MPa
Young's modulus	2E + 05
Poisson's ratio	0.2
Material	Structural steel
Height	1 m, 2 m, 3 m, 4 m, 5 m, 6 m

Table 3 Material properties of concrete

Width of specimen	600 mm
Thickness of wall	150 mm
Uniaxial compressive strength	40 MPa
Uniaxial tensile strength	3.9 MPa
Biaxial compressive strength	30 MPa
Dilatancy angle	5°
Young's modulus	30,186
Poisson's ratio	0.2

Table 4 Material properties of rubberized concrete

Width of specimen	600 mm
Thickness of wall	150 mm
Uniaxial compressive strength	28.9 MPa
Uniaxial tensile strength	3.7 MPa
Biaxial compressive strength	30 MPa
Dilatancy angle	6°
Young's modulus	1.45E + 04
Poisson's ratio	0.2
Material	Rubberized concrete

2.3 Finite Element Modeling

The analytical study of the PDSCW's were done to study load carrying capacity and corresponding deflection of the component. Six Finite element models were developed to evaluate the influence of various slenderness ratios of profiled reentrant walls and evaluate the optimum slenderness ratio for PDSCW's. The elements were modeled using SOLID 186 element. SOLID 186 is a 20 noded solid element that exhibits the quadratic displacement behavior. 20 nodes having three degree of
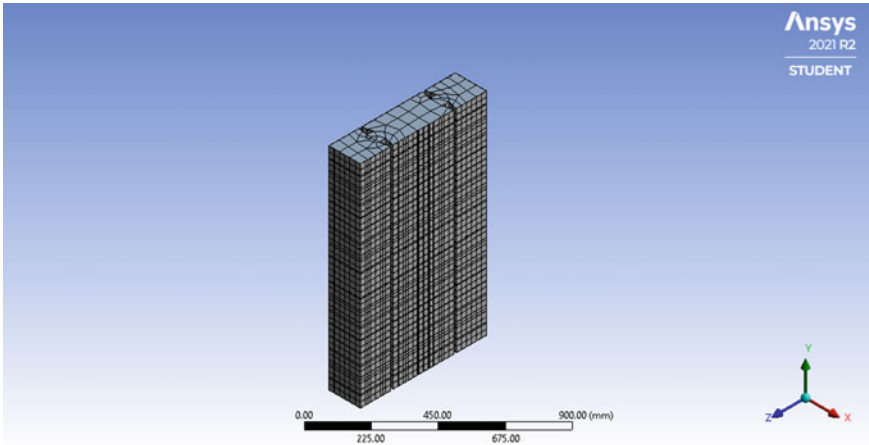
Fig. 3 Meshed diagram

freedom per node define the element: translations in nodal XYZ direction. Mesh size adopted was 50 mm and the shape of meshing was hexahedron (Fig. 3).

2.3.1 Support Condition and Loading

One end of the PDSCW's is fixed and an axial loading is provided at the top interface in the form of load. Displacement value is provided by trial and error method. The support condition and loading of the PDSCW's is as shown in the Fig. 4
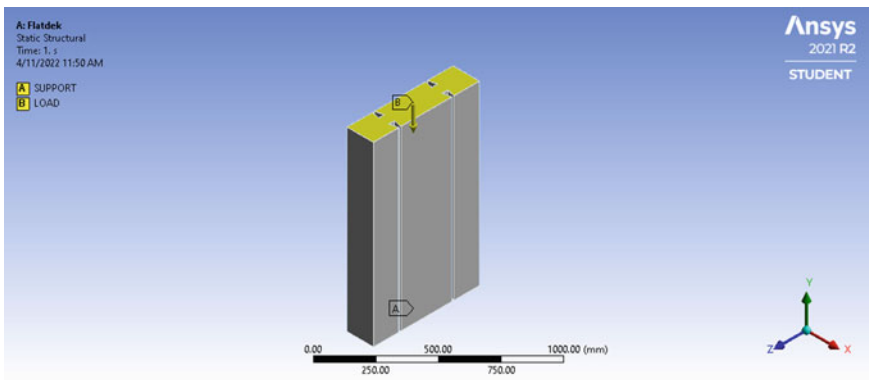
Fig. 4 Boundary condition of PDSCW's
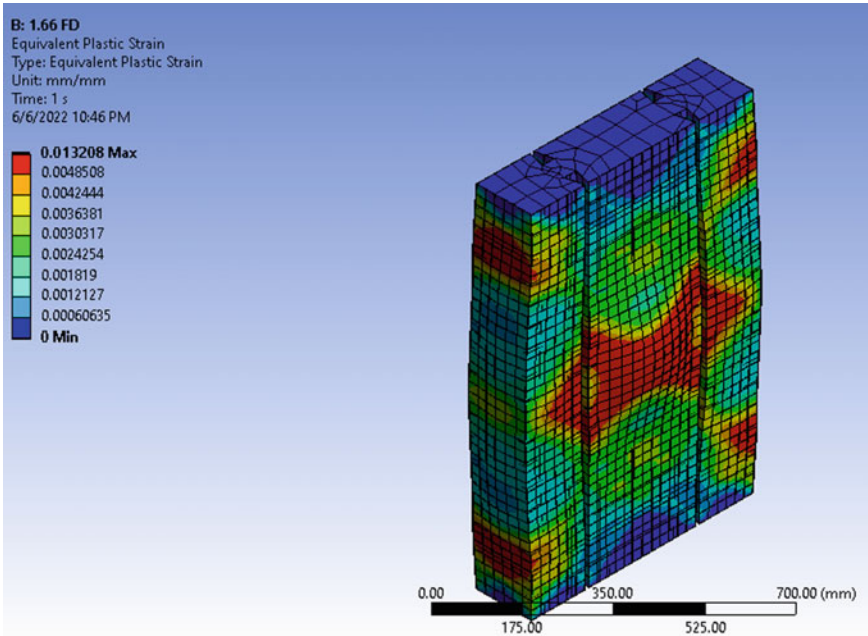
Fig. 5 Plastic strain of model 1.667 slenderness ratio

3   Results and Discussion

The models with various slenderness ratios are analyzed. Failure patterns were obtained for all the models. Force reaction and corresponding deformations were obtained for all the models. Load deformation curves were also plotted for the same. The deformation pattern of the model under loading is as shown in the Fig. 5, 6, 7, 8, 9 and 10.

Figure 11 indicates load vs deflection curve obtained from the analysis. Graph clearly indicates that the model with slenderness ratio 3.333 has more load carrying capacity and optimum deflection. Figure 13 shows the load comparison cure and Fig. 12 shows the deflection comparison. Figure 14 indicates that the rubcrete wall have better ultimate load carrying capacity compared to the control wall with normal concrete.
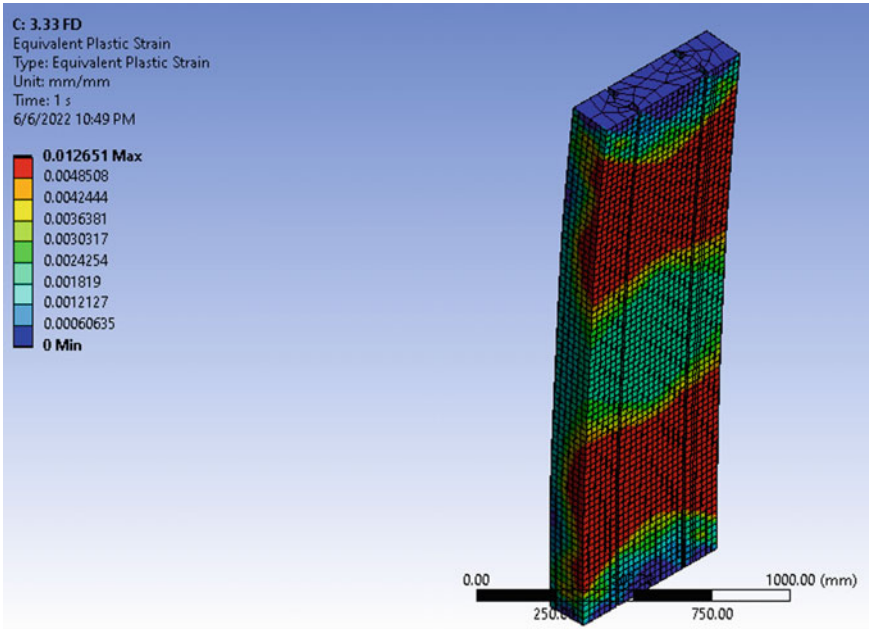
Fig. 6 Plastic strain of model 3.33 slenderness ratio
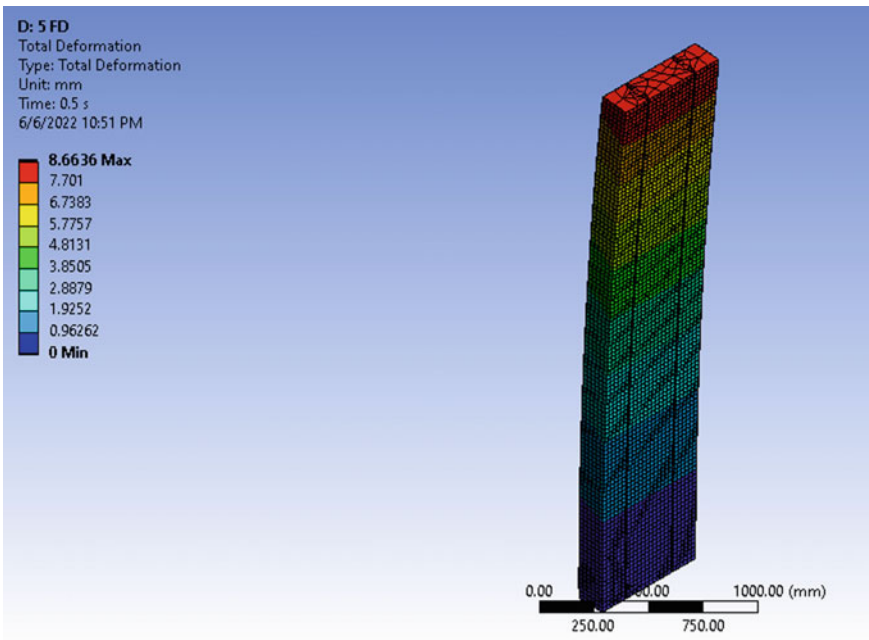
Fig. 7 Plastic strain of model 5.0 slenderness ratio
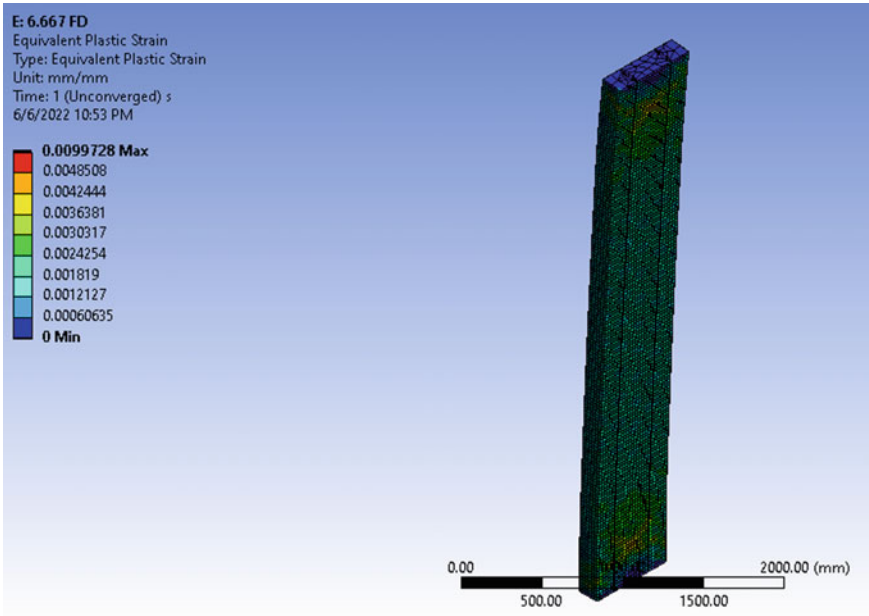
Fig. 8 Plastic strain of model 6.667 slenderness ratio
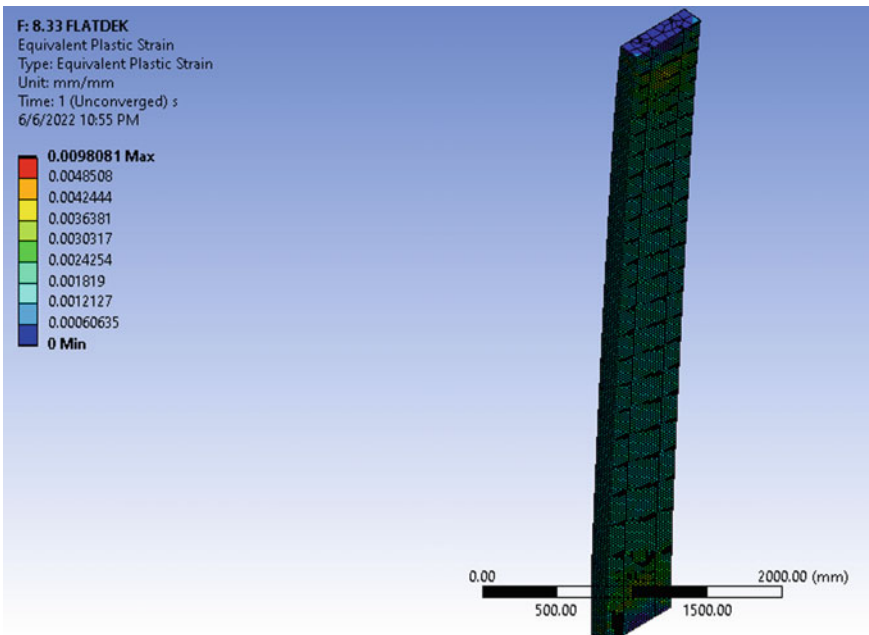
Fig. 9 Plastic strain of model 8.33 slenderness ratio
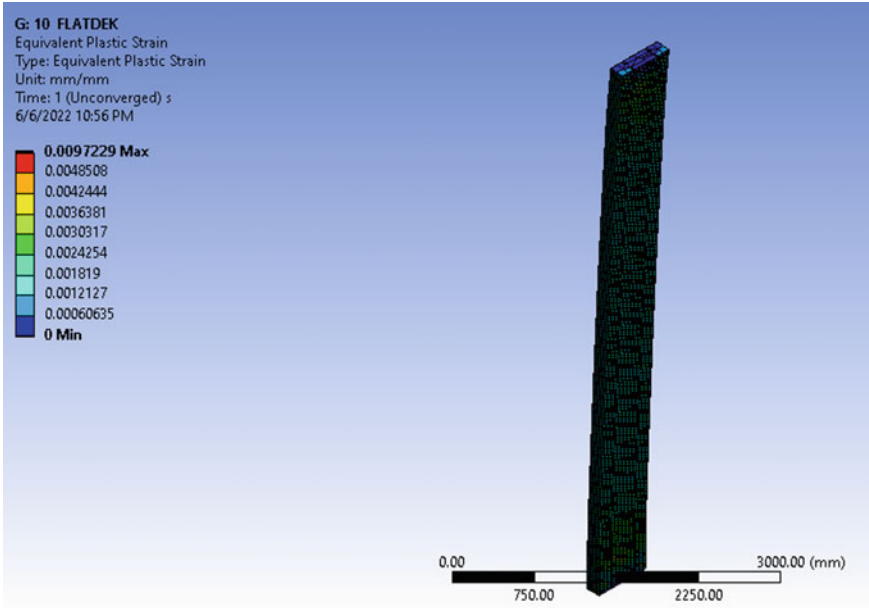
Fig. 10 Plastic strain of model 10.0 slenderness ratio

Fig. 11 Load vs Deflection

DEFLECTION COMPARISON

	1.66 FD RUBCRETE -4	3.33 FD RUBCRETE -8	5 FD RUBCRETE - 10	6.667 FD RUBCRETE - 14	8.33 FD RUBCRETE - 18	10 FD RUBCRETE - 18
DEFLECTION (mm)	3.9106	6.4033	18.418	38.525	52.044	71.051

Fig. 12 Deflection comparison

LOAD COMPARISON

	1.66 FD RUBCRETE -4	3.33 FD RUBCRETE -8	5 FD RUBCRETE -10	6.667 FD RUBCRETE -14	8.33 FD RUBCRETE -18	10 FD RUBCRETE -18
LOAD (kN)	2848.2	3107.3	2819	2829.6	2801.8	2801.8
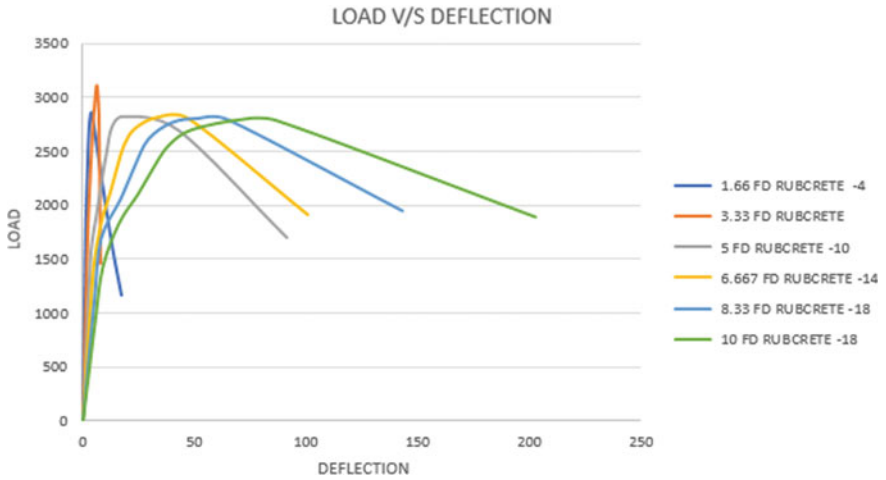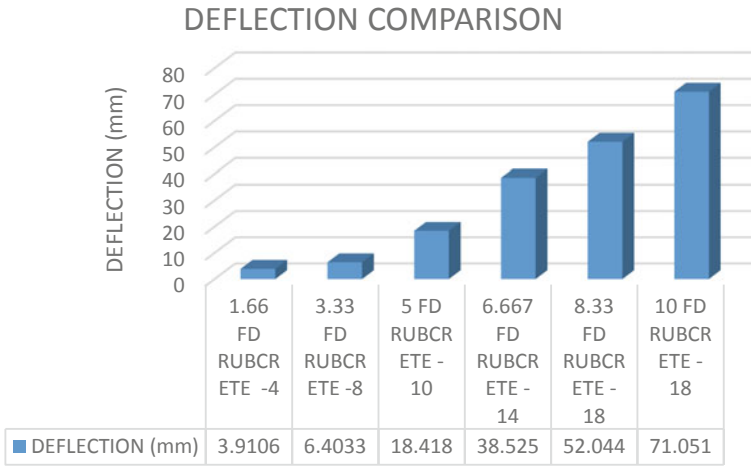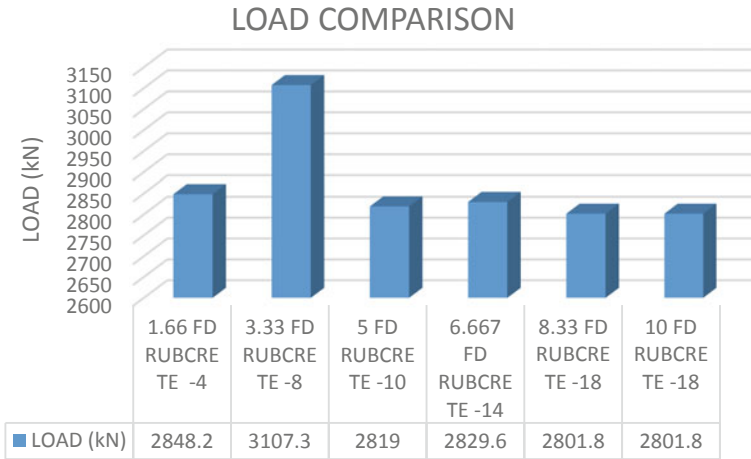
Fig. 13 Load comparison
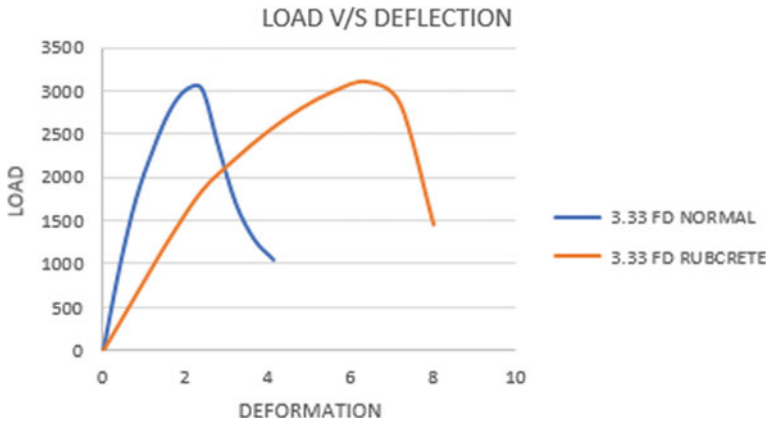
Fig. 14 Ultimate load comparison of control specimen and rubcrete specimen

4 Conclusion

In this study, the static structural analysis of PDSCW's was conducted

(a) For various slenderness ratios weres carried out and it is evident that by using rubberized concrete, the failure is delayed compared to the normal concrete specimen.
(b) By varying the slenderness ratio the change in displacement is obtained.
(c) Model with a slenderness ratio of 3.333 shows greater load carrying capacity and has less deflection. Model with a slenderness ratio of 10 is taking the maximum deflection. The maximum load carrying capacity is 3090 kN
(d) Rubcrete wall of slenderness ratio 3.33 is having higher ultimate load carrying capacity compared to the control wall with normal concrete.Indicating delayed failure.

References

1. Tong, J.-Z., Yu, C.-Q., Zhang, L.: Sectional strength and design of double-skin composite walls with re-entrant profiled faceplates. Thin-Walled Struct. **158**, 107196 (2021)
2. Yu, C.-Q., Tong, J.Z.: Compressive behavior of slender profiled double-skin composite walls. J. Constr. Steel Res. **182**, 1066557 (2021)
3. Wang, M.-Z., Guo, Y.-L., Zhu, J.-S., Yang, X.: Flexural-torsional buckling and design recommendations of axially loaded concrete infilled double steel corrugated-plate walls with T-section. Eng. Struct. **208**, 110345 (2020)
4. Tong, J.-Z., Pan, W.-H., Shen, M.-H.: Performance of double-skin composite walls with re-entrant profiled faceplates under eccentric compression. J. Build. Eng. **28**, 101010 (2020)
5. Tong, J.-Z., Yu, C.-Q., Zhang, L.: Sectional strength and design of double-skin composite walls with re-entrant profiled faceplates. Thin-Walled Struct. **158**, 1071966 (2021)

6. Hilo, S.J., Badaruzzaman, W.H.W., Osman, S.A., Al-Zand, A.W., Samir, M., Hasan, Q.A.: A state-of-the-art review on double-skinned composite wall systems, Thin-Walled Struct. **97**, 74–100 (2015)s
7. Wright, H.D., Gallocher, S.C.: The behaviour of composite walling under construction and service loading. J. Constr. Steel Res. **35**, 257–273 (1995)

Structural Performance of Pre-twisted Composite Column

Hiba Fazly and P. E. Kavitha

Abstract Pre-twisted structural members are widely in the construction industry due to the development of designs, elegance and as an innovative concept from both engineers and architects. Buckling is a type of failure that occurs in compression members due to structural instability. When a natural pre twist is induced along the length of a column section, the resistance of the column varies at every point along its centroidal axis. A pre-twisted column in 3D-space has its strong flexural plane weakened and its weak flexural plane strengthened, resulting a net favorable effect on the buckling strength of the pre-twisted column. Untwisted rectangular column has a weaker and stronger axis depending on the depth. The axis along the greater depth is stiffer and have more load carrying capacity compared to weaker axis. By pre-twisting the rectangular column to an optimum angle, both axis stronger and thus the column will be stiffer in both directions to withstand earthquake load in any direction. Since the direction of earthquake is unpredictable, both axis of the column should be strong to withstand the earthquake load. This work focuses on the analytical study of a simplified model of pre-twisted rectangular composite column under lateral loading condition which is equivalent to quasi static earthquake load for different angle ratios to find the influence of twisting angle. The rectangular pre-twisted column is also compared with equivalent square pre-twisted column. The optimum angle of pre-twisting is obtained in the range of 120°–150°. At the optimum pre-twisting angle, both axis of the rectangular composite column is strengthened leading to a better lateral load carrying capacity.

Keywords Pre-twisted · Lateral load · Buckling · Composite column · Optimum angle

H. Fazly (✉) · P. E. Kavitha
Department of Civil Engineering, FISAT, Angamaly, India
e-mail: hibafazly@gmail.com

P. E. Kavitha
e-mail: kavithape@fisat.ac.in

1   Introduction

Composite structures are used in modern constructions due to their faster construction, light weight, high strength and lower labour intensiveness. Steel is a recyclable material which leaves minimum waste under demolition, proving to be a sustainable construction material and concrete is a widely used economic construction material. Hence the combination of these two materials provides increased structural stability, speed of construction and more economical sections. Buckling is a type of failure that occurs in compression members due to structural instability. The strength of compression can be increased by increasing the moment of inertia of the cross section as strength depends on their slenderness ratio. The buckling of the plate elements in the cross section under compression or shear may take place before the overall column buckling by lateral buckling or yielding called local buckling. Local buckling imposes a reduced effect on the load carrying capacity of columns due to the reduction in the stiffness and strength of locally buckled plate elements. Thin columns mostly buckle along the plane of least resistance. When the section of column is permanently pre-twisted, the column resistance varies at each point along its centroidal axis [2].

A structural member with a natural twist about its longitudinal axis is known as a pre-twisted member. The axial strength and the static performance of the column may be influenced by this pre buckling twist, which, in turn, may vary in any arbitrary manner along with the length of the member. Previous research has shown that with the increase in the angle of twist, the buckling strength of the column increases and pre-twisting can be considered as a simple method to strengthen thin columns subjected to axial loads or making thinner, lighter and more economical columns with the same strength. When a natural pre twist is induced along the length of a column section, the resistance of the column varies at every point along its centroidal axis. The column usually buckles around the weak axis, but with pre twisting, the buckling mode of the column may no longer be perpendicular to the weak axis. Pre-twisting induce a coupling effect on the weak and strong flexural planes of a column. As a result, a pre-twisted column in 3D-space has its strong flexural plane weakened and its weak flexural plane strengthened, resulting in a net favorable effect on the buckling strength of the pre-twisted column. Pre-twisted structural members are widely used in the construction industry due to the development of designs, elegance and as an innovative concept from both engineers and architects [3, 5].

Since the direction of earthquake is unpredictable, both axis of the column should be strong to withstand the earthquake load. Untwisted rectangular column has a weaker and stronger axis depending on the depth. The axis along the greater depth is stiffer and have more load carrying capacity compared to weaker axis. By pre-twisting the rectangular column to an optimum angle, both axis can be made stronger and thus the column will be stiffer in both directions to withstand earthquake load in any direction. This work focuses on the analytical study of a simplified model of pre-twisted rectangular composite column under lateral loading condition which is equivalent to quasi static earthquake load for different angle ratios to find the

influence of twisting angle and comparing it with an equivalent pre-twisted square column.

2 Literature Review

Feng Zhou et al. conducted experimental and numerical investigations on pre-twisted steel box-section columns to investigate the effects of pre-twisted angle ratio on the compressive behavior of steel box-section columns. Pre-twisted angle ratios had little effect on the axial capacity, initial stiffness and lateral deformation capacity of shorter columns that failed by plastic yielding and pre-twisting is more effective in improving the elastic buckling of long columns as elastic buckling is influenced by the section's inertia compared to inelastic buckling which is affected by material yielding. The lateral deformations at the mid-height of the columns were reduced while the ultimate loads were increased [3]. Farid H. Abed et. al. studies show buckling capacity of fixed-ended pre-twisted columns were improved up to 50% [1]. Nivin Philip et. al. found pre-twisting was effective in increasing the buckling capacity of an unboxed column up to 51% having an optimal pre-twist angle of 135° and 15% increase for boxed columns having an optimal angle of 155° [4]. Farid H. Abed et. al. found a sharp increase in buckling capacity up to 90% improvement as compared with non-twisted columns at an angle of pre-twists between 120° and 150° [2].

3 Influence of Flexural Rigidity on Pre-twisting

By comparing moment of inertia of regular rectangle and pre-twisted column cross section of cross Section 280 × 100 mm, it can be seen that when the column is pre-twisted the weaker axis becomes more stiffer when the cross section is rotated and the stronger axis became weaker (Fig. 1).

The moment of inertia of rectangular section is given by:

$I_{xx} = \frac{BD^3}{12}$ and $I_{YY} = \frac{DB^3}{12}$, where B is breadth and D is the depth of the column (Fig. 2).

The moment of inertia of pre twisted rectangular section is given by:

$I_{XX'} = I_{xx}\cos^2\theta + I_{YY}\sin^2\theta$ and $I_{YY'} = I_{xx}\sin^2\theta + I_{YY}\cos^2\theta$, where θ is the angle of pre-twist (Table 1).

From above calculation, it can be concluded that a weaker axis becomes more stiffer when the cross section is rotated and the stronger axis became weaker [3] i.e., Pre-twisting strengthen a weaker axis. It is also seen that after pre-twisting angle 180° the results are complimentary, similar to the previous twisting angle 0°–180°.
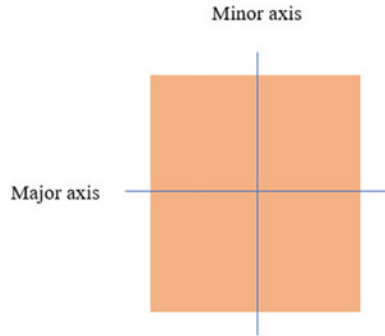
Fig. 1 Regular column
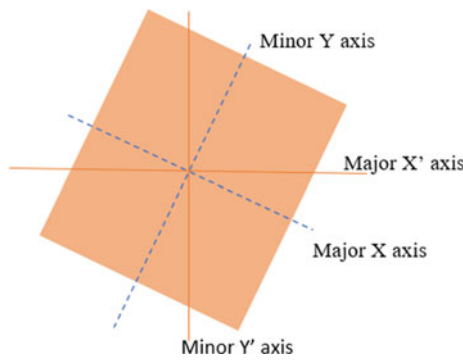
Fig. 2 Pre-twisted column

Table 1 Moment of inertia of pre-twisted column along X and Y axis

Pre twisting angle (°)	$I_{XX'}(m^4)$	$I_{YY'}(m^4)$
0	18.29×10^{-7}	2.33×10^{-7}
30	14.3×10^{-7}	6.32×10^{-7}
60	6.32×10^{-7}	14.3×10^{-7}
90	2.33×10^{-7}	18.29×10^{-7}
120	6.32×10^{-7}	14.3×10^{-7}
150	14.3×10^{-7}	6.32×10^{-7}
180	18.29×10^{-7}	2.33×10^{-7}
210	14.3×10^{-7}	6.32×10^{-7}
240	6.32×10^{-7}	14.3×10^{-7}
270	2.33×10^{-7}	18.29×10^{-7}
300	6.32×10^{-7}	14.3×10^{-7}
330	14.3×10^{-7}	6.32×10^{-7}
360	18.29×10^{-7}	2.33×10^{-7}

4 Parametric Study

In order to investigate the lateral deformation of pre-twisted composite columns at different angles, three-dimensional finite element analyses have been performed using ANSYS workbench 2021 R2.

4.1 Geometric Description and Material Properties

The dimension of the composite pre-twisted column taken for the study is 280 × 100 × 10 × 16 mm (h × b × t_w × t_f), where h is the overall web depth, b is the overall flange width, t_w and t_f are the thickness of the web plate and flange plate, respectively, filled with concrete. M30 and Fe 235 are the grades of concrete and steel used for modelling respectively. The length of the column adopted is 1.5 m as shown in the Fig. 3. In this study the column is pre-twisted at angle from 0° to 360° at an interval of 30°. The pre-twisting effect is obtained using the option "Twisting Specifications-Turns", where turns is ratio of pre-twisting angle to 360°. The material properties of 10- and 16-mm steel sheets are shown in Table 2 (Figs. 4 and 5).
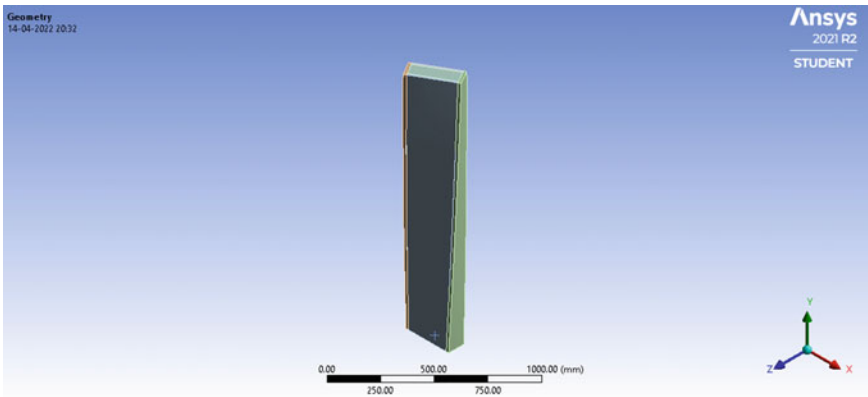
Fig. 3 Pre-twisted column at 30°

Table 2 Material properties of steel sheets

Thickness (mm)	E (GPa)	f_y (MPa)	f_u (MPa)	ε_u (%)	ε_f (%)
10	196	284.9	440	23.3	33.1
16	196	272.1	433.2	24.3	38.3
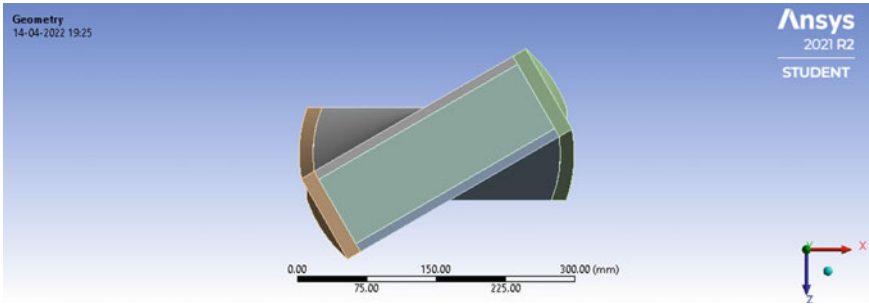
Fig. 4 Top view of pre-twisted column at 30°
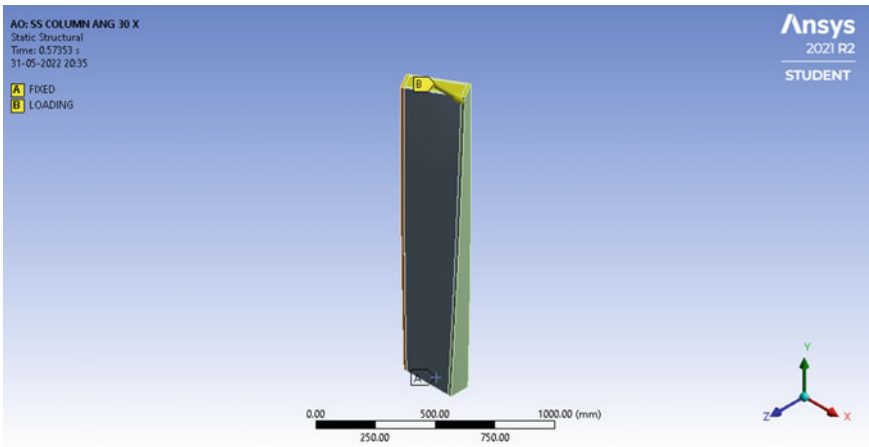
Fig. 5 Boundary condition of pre twisted column at 30°

4.2 Boundary Condition

In all the analytical models, the bottom end of the pre-twisted column is fixed and top end is free along the loading direction. The load is applied on the free end of the column. The load was applied through displacement control. Lateral loads in both X and Z axis are provided in the free end to study the influence of pre twisting angle in resisting the laterals loads.

4.3 Finite Element Modelling

Modelling in ANSYS includes providing appropriate elements, defining geometry and assigning suitable material models. The model is of 1.5 m long twisted at different

angles, modelled using SOLID 185 element. The paper taken for validation is the work done by Feng Zhou, Yancheng Cai, Yu Chen. "Experimental and numerical investigations on pre twisted steel box section columns". Pre-twisting angle is provided to column using the option "twist – turns", where turns is the ratio of pre-twisting angle to 360°. Meshing size provided is 50 mm.

4.4 Result and Discussion

4.4.1 Influence of Pre-twisting Angle

The influence of pre-twisting angle from 0° to 360° is studied at an interval of 30°. Angle 0° represents the column without pre-twisting. Figures 6 and 7 shows total deformation of pre twisted column at 30° along Z and X axis, respectively. Figures 8 and 9 illustrates the ultimate load-deformation curves for rectangular composite pre-twisted column for length 1.5 m along X and Z axis, respectively. In each figure, the curves for columns with different values of ϕ were included (Figs. 10 and 11).

Table 3 shows ultimate load and corresponding deformation to the ultimate load at various pre-twisting angle along both axis. When the column is pre-twisted at an angle between 120° and 150°, the lateral load capacity is increased along both the X and Z axis. A load greater than 300 kN is obtained on both axis. Since the column fails along the weaker axis, by pre-twisting at an optimum angle the column can be strengthened on both axis making the column withstand lateral load in any direction.
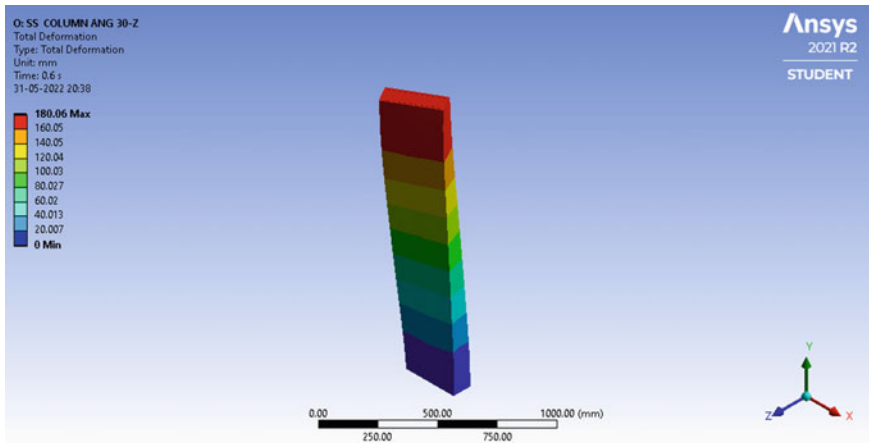
Fig. 6 Total deformation of pre-twisted column at 30° along Z axis
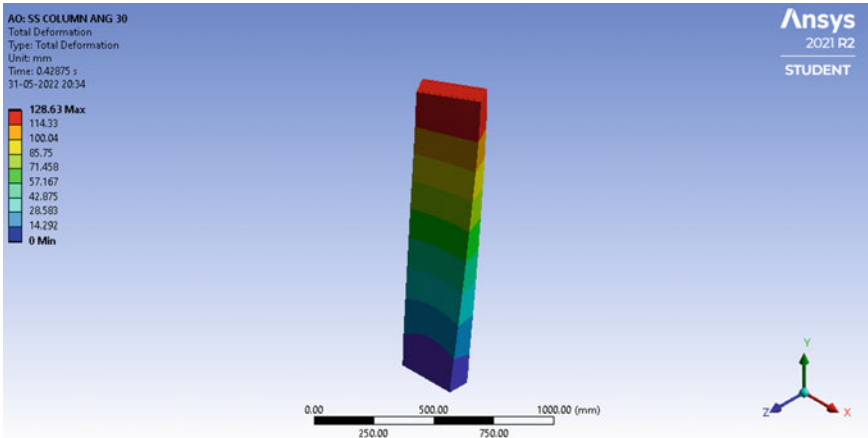
Fig. 7 Total deformation of pre-twisted column at 30° along X axis
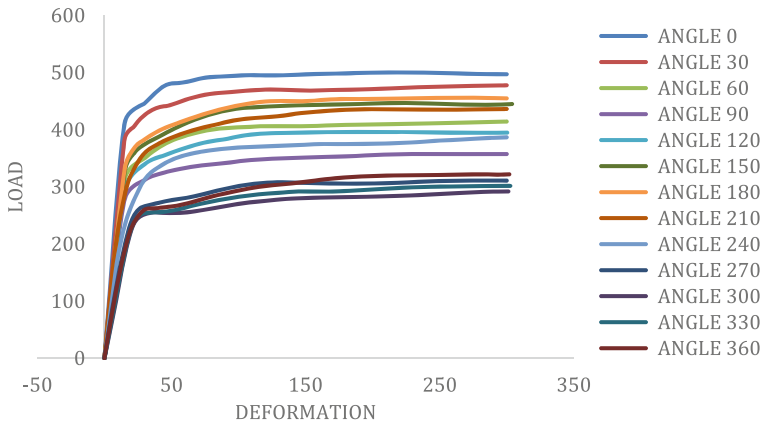
Fig. 8 Load v/s deformation along X axis

4.4.2 Comparison of Rectangular and Square Twisted Columns

Rectangular composite pre-twisted columns were compared with equivalent square twisted columns for optimum angles. The equivalent square column was obtained taking square root of area of rectangular column, i.e., sqrt of 280 × 100 mm = 168 × 168 mm. Angle 120° and 150° were taken to compare, as for rectangular column, in both axis a load greater than 300 kN is obtained. The result shows square pre-twisted columns lateral load carrying capacity is lesser compared to rectangular column as shown in Table 4. Figures 12 and 13 shows comparison of rectangular and square columns along X axis and Z axis respectively.
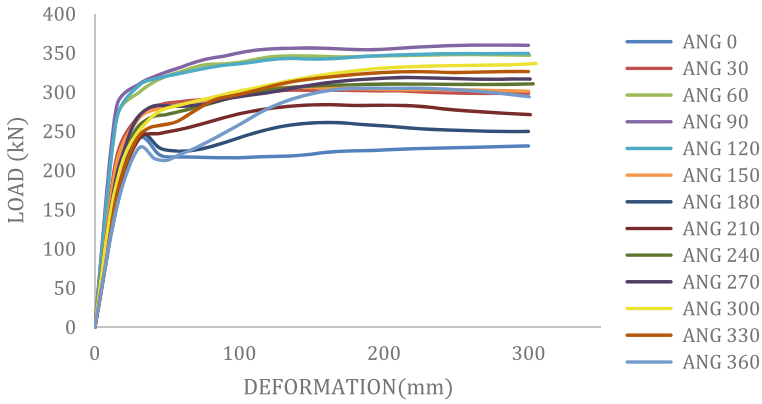
Fig. 9 Load v/s deformation along Z axis
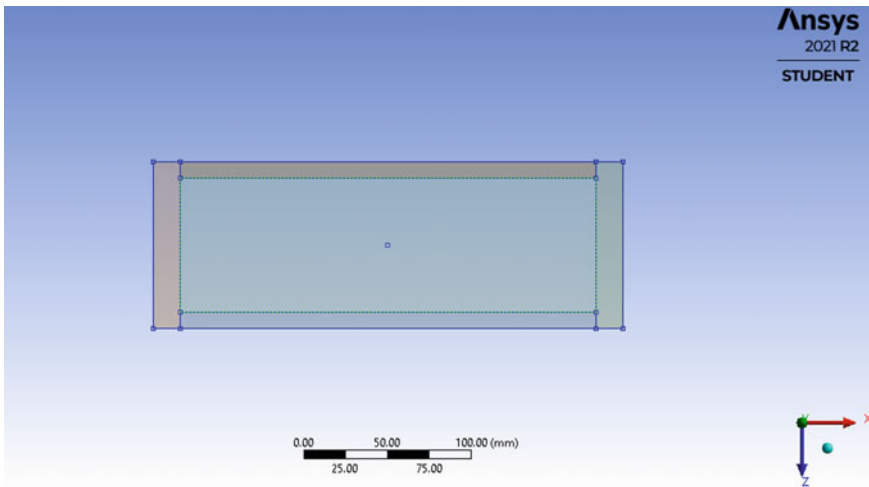
Fig. 10 Top view of un twisted rectangular column

In un twisted rectangular column, along X axis the ultimate load carrying capacity is 239.94 kN and along Z axis is 500.24 kN i.e., in the direction of greater depth, the moment of inertia is more and hence greater load carrying capacity. By pre twisting, both axis can be made stronger and thus more load carrying capacity in both axis. In case untwisted column, one axis is stronger and other is weaker. if the earthquake load is acting along weaker axis, the column may fail, it can be avoided pre twisting.

A square column is equally resistant to lateral load in both axis. But when a pre-twisted rectangular column is compared with a pre-twisted square column, the lateral load carrying capacity of square column is reduced drastically as the value of moment of inertia is reduced. Comparing a pre twisted rectangular and square, the
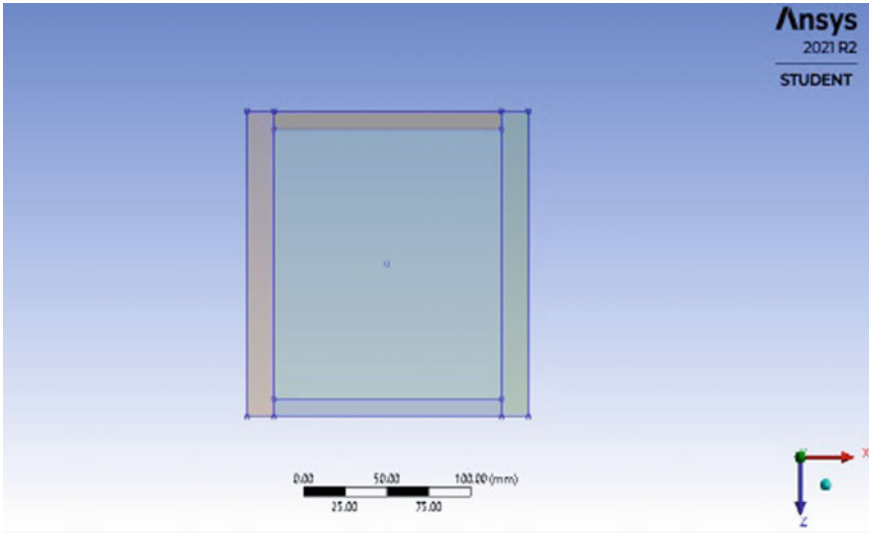
Fig. 11 Top view of un twisted square column

Table 3 Influence of pre-twisting angle of rectangular twisted columns along both axis

| | Z AXIS | | X AXIS | |
	DEFORMATION (mm)	LOAD (kN)	DEFORMATION (mm)	LOAD (kN)
ANG 0	30	239.94	225	500.24
ANG 30	180.06	302.32	128.63	470.28
ANG 60	255.64	348.09	120	406.39
ANG 90	165	355.82	240	357.75
ANG 120	135	343.15	225.32	396.07
ANG 150	135	306.35	221.56	446.75
ANG 180	45	228.81	266.25	455.89
ANG 210	165.88	283.97	187.5	435.79
ANG 240	257.82	310.09	175.03	374.87
ANG 270	61.735	282.07	271.41	310.89
ANG 300	324.19	337.26	256.02	288.09
ANG 330	217.5	326.32	296.03	301.69
ANG 360	30.014	227.75	285.43	321.72

Table 4 Comparison of rectangular and square twisted columns along both axis

	Z axis				X axis			
	Deformation (mm)		Load (kN)		Deformation (mm)		Load (kN)	
	Rect	Square	Rect	Square	Rect	Square	Rect	Square
ANG 0	30	90	239.94	339.11	225	90	500.24	336.22
ANG 120	135	165.75	343.15	202.12	225.32	195	396.07	345.15
ANG 150	135	180.82	306.35	196.00	221.56	180	446.75	331.87

Fig. 12 Comparison of rectangular and square columns along x axis

	Rect. Ang 0	Rect. Ang 120	Rect. Ang 150	Square Ang 0	Square Ang 120	Square Ang 150
Ultimate Load (kN)	239.94	343.15	306.35	339.11	202.12	196.00
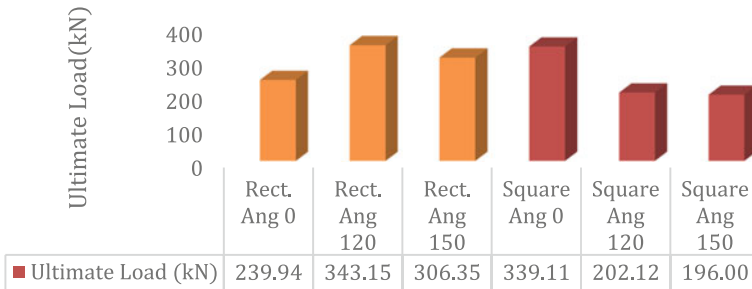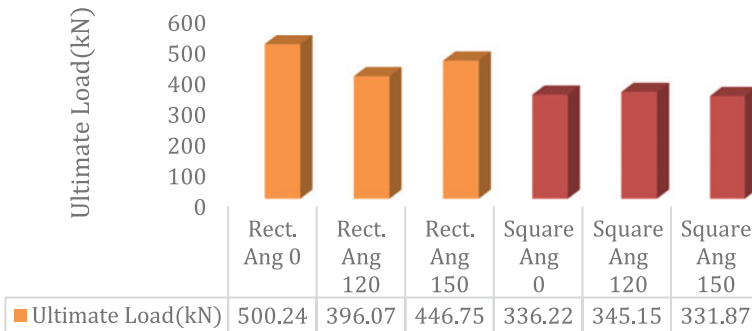
Fig. 13 Comparison of rectangular and square columns along z axis

	Rect. Ang 0	Rect. Ang 120	Rect. Ang 150	Square Ang 0	Square Ang 120	Square Ang 150
Ultimate Load(kN)	500.24	396.07	446.75	336.22	345.15	331.87

rectangular pre twisted column have more load carrying capacity as shown in Table 4. So, replacing a rectangular column with a square column is not a good approach.

5 Conclusion

A non-linear finite element model (FEM) was developed and a series of lateral load tests conducted on pre-twisted composite columns. A pre-twisted composite column was obtained in ANSYS using the option "Twisting Specification – Turns". A simplified approach is followed in the present study by analyzing pre-twisted columns with boundary conditions one end fixed and the other end free subjected to lateral load at the top of the column. The rectangular composite columns were of dimension 280 × 100 mm, with a length of 1.5 m. The grade of steel plate is Q235 with the nominal yield stresses of 235 MPa. The pre-twisted angle ratios included in the study is from 0° to 180° at an interval of 30°. Findings from the numerical analysis are summarized in the following:

- Pre-twisting of rectangular column causes the weaker axis to be stiffer and the stronger axis to be weaker. It is observed that at an optimum angle between 120° and 150° each axis becomes equally stiffer.
- When the column is twisted at an angle between 120° and 150°, the lateral load capacity is increased along both the x and z axis. In the present study an ultimate load greater than 300 kN is obtained in both directions. Since the column fails along the weaker axis, by twisting at an optimum angle the column can be strengthened on both axis making the column withstand lateral load in any direction. It is highly recommended to construct a column stronger in both axis since the direction of earthquake is always unpredictable.
- When a pre twisted rectangular column is compared with a pre twisted square column, the lateral load carrying capacity of square column is reduced drastically as the value of moment of inertia of the square column is much less than that of rectangular column. So, replacing a rectangular column with a square column is not a good approach.

References

1. Abed, F.H., Megahed, M., Al, R.A.: On the improvement of buckling of pre twisted universal steel columns. Structures **5**, 152–160 (2016)
2. Abed, F.H., Megahed, M.: Experimental investigation of buckling response of pre twisted structural steel columns. Structures **27**(2232), 2244 (2020)
3. Zhou, F., Cai, Y., Chen, Y.: Experimental and numerical investigations on pre-twisted steel box section columns. Eng. Struct. **246**, 112996 (2021)
4. Philip, N., Paul, T.: Blast load analysis of pre-twisted steel columns. J. Inst. Eng. (India): Series A **100**, 261–273 (2019)
5. Paul, T., Philip, N.: Influence of pre twisting angle on the buckling capacity of steel columns: a review. Int. J. Civil Eng., 1–10 (2016)

Structural Performance of Special Case S-RC-SRC Beam Column Connection Joint

Jinu V. Rajan and Gayathri Krishnakumar

Abstract In a structural member, the beam column joint is considered as the most critical part during an earthquake since they are the dominant position in transferring force between members. Their properties are significant in safeguarding the structure under an earthquake. S-RC-SRC beam column joint represents Steel-Reinforced Concrete-Steel Reinforced Concrete connection joint. These joints could be used for extension of structures, constructing composite floors and also used in high-rise buildings, large span bridges and transmission towers. Unequal span frames are used to meet the architectural demand and other special detailing requirements. Unequal depth beam column joint can satisfy different moment and shear demand. From various related studies, it is concluded that S-RC-SRC joints can meet the requirements of high bearing capacity, aesthetic requirements of buildings, better ductility and strong energy dissipation capacity. This work focus on the analytical study of structural behaviour of special case S-RC-SRC beam column connection joint by varying parameters with irregularity conditions such as unequal depth, varying beam material etc. subjected to lateral loading.

Keywords S-RC-SRC · Composite · Ductility · Energy dissipation · Lateral loading

1 Introduction

1.1 General

During an earthquake, the most critical position in a structural member is the beam-column joint. A beam-column joint refers to the portions of beam framing into the column. From a structural point of view, they connect main structural members and

J. V. Rajan (✉) · G. Krishnakumar
Department of Civil Engineering, FISAT, Angamaly, India
e-mail: mailmeatjinumariam@gmail.com

G. Krishnakumar
e-mail: gayathrikrishnakumar@fisat.ac.in

are the most complicated components as the forces and moments from adjacent beams and columns are transferred through the joint. Composite structures with unequal spans are common in engineering applications such as in long-span space and high-rise buildings to meet the architectural demand and other special detailing requirements. Unequal Depth Beam Column (UDBC) joints satisfy different moment and shear demands. Recent earthquake studies have shown that the integrity of the whole structure is failed if the joints to which these members are connected fails even though the beams and columns in a frame remain intact. Therefore, ductility and energy absorption capacity of the beam-column joints are of great significance in the seismic resistance of structures.

Steel frame structure, Reinforced Concrete structure and Steel Reinforced Concrete structure are considered as a typical structural form of building. All these structural forms have distinguishing characteristics and good points of the structural form can be combined to make an ideal and economical structural form. S-RC-SRC composite frame consists of upper steel-beam-to-column and lower RC-beam-to-SRC-column. They are commonly used for the construction of composite buildings i.e.; if floors are also to be constructed as composite and also for the extension of buildings. From various related studies, it is concluded that the structure can meet the requirements of high bearing capacity, better ductility and strong energy dissipation capacity and also satisfy aesthetic requirements of buildings.

1.2 Literature Review

Bin Rong et al. [1] conducted experimental and numerical investigation on seismic performance of H-shaped steel column-RC beam-SRC column (S-RC-SRC) composite joint and concluded that the enlargement of steel size could reduce the ultimate bearing capacity slightly. Bin Rong et al. [2] conducted experimental and numerical research on seismic performance of S-RC-SRC composite frame and found that the increase of the strength grade of concrete had few contributions to the overall horizontal ultimate load-carrying capacity of the specimen. The increase of axial compression load and decrease of slenderness ratio load had great impact on the overall horizontal ultimate load-carrying capacity of the specimen. Ben Mou *et. al* [3] conducted numerical investigation and design method of bolted beam-column joint panel with eccentricity in beam depth and the results demonstrated that due to the T-shape connector, the beam depth ratio has a limited effect on the shear performance. Wei-hui Zhong et al. [4] conducted a research on collapse resistance of composite beam-column assemblies with unequal spans under an internal column-removal scenario and found that decreasing the beam span resulted in a larger resistance under both mechanisms, whereas increasing the beam height increased the resistance under the flexural mechanism. Guang-Yong Wang et al. [5] carried out an experimental study to investigate the post-fire seismic performance of SRC beam to SRC column frames and found that after fire exposure, SRC frames showed good energy dissipation capacity. Isaac Montava et al. [6] conducted an experimental

study on SRC joints and concluded that steel embedded sections have greater energy absorption capacity. Qin Gao et al. [7] conducted test on interior precast SRC beam-column joints and found that better seismic performance is exhibited by joints with slab than that without slab. SuJian Yu et al. [8] conducted experimental and numerical study to rate the effect of different beam end connections on the seismic performance of SRC column to steel beam joint. Wei Huang et al. [9] studied the characteristics of analytical deformation and shear capacity of SRC-RC transfer columns. Wei-hui Zhong et al. [10] studied the collapse resistance of joints with unequal spans and found that larger resistance was obtained when the beam span was decreased.

This paper is intended on the analytical study of the structural behaviour of special case S-RC-SRC beam column connection joint by varying parameters with irregularity conditions such as unequal depth, varying beam material etc. subjected to lateral loading.

2 Analytical Program

To conduct the analytical study on structural behaviour of S-RC-SRC beam column joint, finite element model of the connection joint is developed using Ansys 16.0 software.

2.1 Geometric Model

The base model (Specimen 1) consists of S-RC-SRC frame with RC beams on both sides having a sectional area of 150 mm × 300 mm as shown in Fig. 1a. The height of the upper column is 1300 mm while that of the lower column is 1500 mm.

Other models are developed by varying beam material such as left steel beam and right RC beam. The dimensions of the rest of the models are mentioned in Table 1. The RC beam is kept fixed with a dimension of 150 mm × 300 mm.

A simplified geometric model of other specimens is shown in Fig. 1b. The only change is in the dimension of the steel section of the left beam.

2.2 Material Properties

Concrete having a compressive strength (f_c) of 32.3 MPa, tensile strength (f_t) of 2.95 MPa and elastic modulus (E_c) of 30,245 MPa is chosen. C30 concrete is taken. Axial compression ratio of 0.2 is considered. Steel is having an elastic modulus (E_s) of 201 GPa.
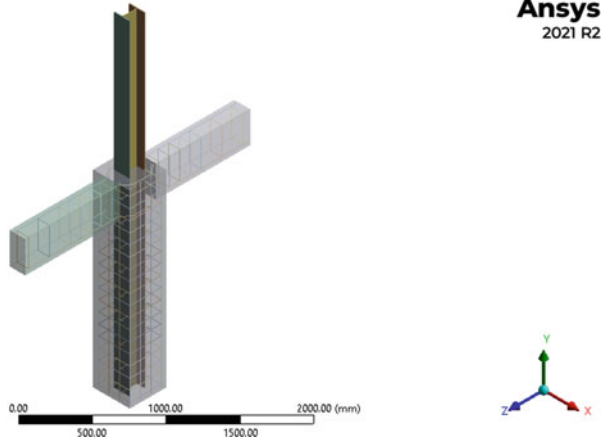
Fig. 1a Model of specimen 1

Table 1 Dimensions of steel beams

Models	Steel section (mm)
Specimen 2	$300 \times 150 \times 6.5 \times 9$
Specimen 3	$300 \times 150 \times 4.5 \times 6$
Specimen 4	$280 \times 125 \times 6 \times 9$
Specimen 5	$250 \times 125 \times 6 \times 9$
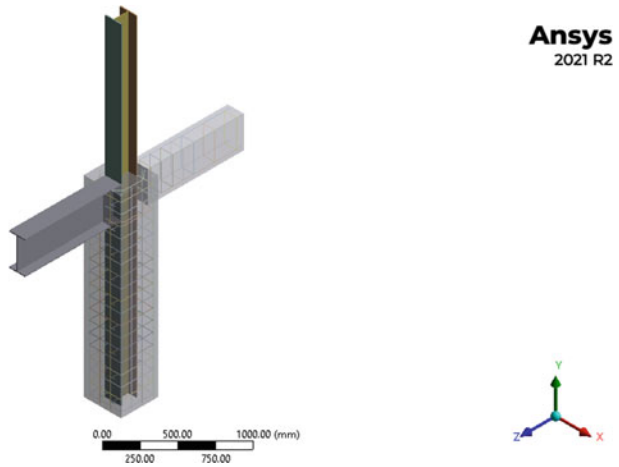
Fig. 1b Model of other specimens

2.3 Finite Element Modelling

Five element models were developed to determine the structural behaviour of S-RC-SRC joint by varying beam material and varying depth. The model consists of an upper steel column, lower SRC column, RC and steel beams. The element type used is SOLID 185 for steel and concrete. It is defined by eight nodes having three degrees of freedom at each node; translations in nodal x, y, z directions. For shear stud and rebar, REINF 264 is used. Meshing is done using adaptive size control. Figure 2a shows the meshed model of joint with both RC beams (Specimen 1). Figure 2b shows the simplified meshed model of other four specimens.
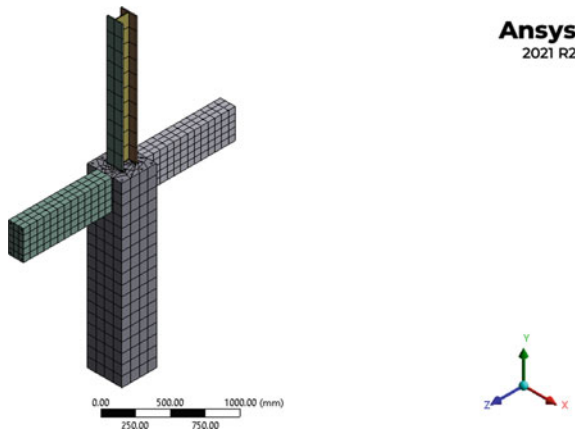
Fig. 2a Meshed model of specimen 1
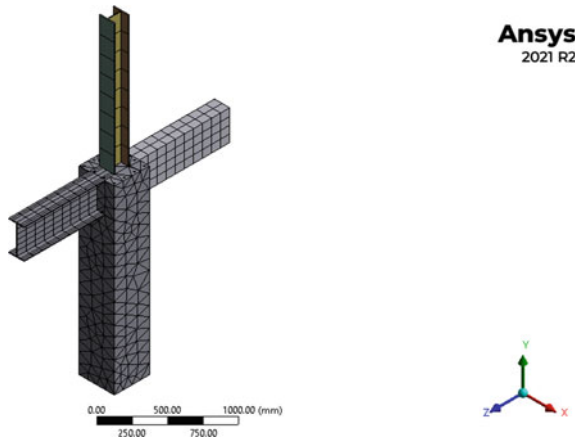
Fig. 2b Meshed model of other specimens

2.4 Loading and Boundary Conditions

The bottom of the column is hinged while top of the column is kept fixed. Cyclic loading is applied on both beams. Boundary conditions and loading are shown in Figs. 3a and 3b. Displacement control method is used to apply load where load in the form of displacement is applied to find the load carrying capacity of the specimen until failure.
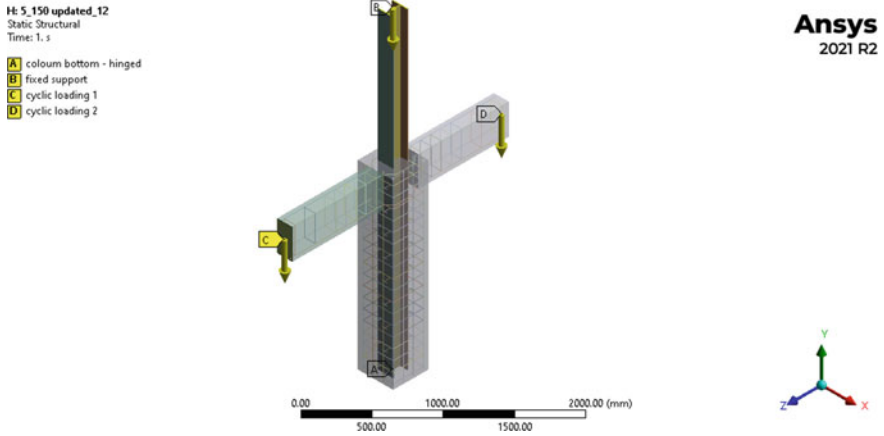
Fig. 3a Loading and Boundary conditions of specimen 1
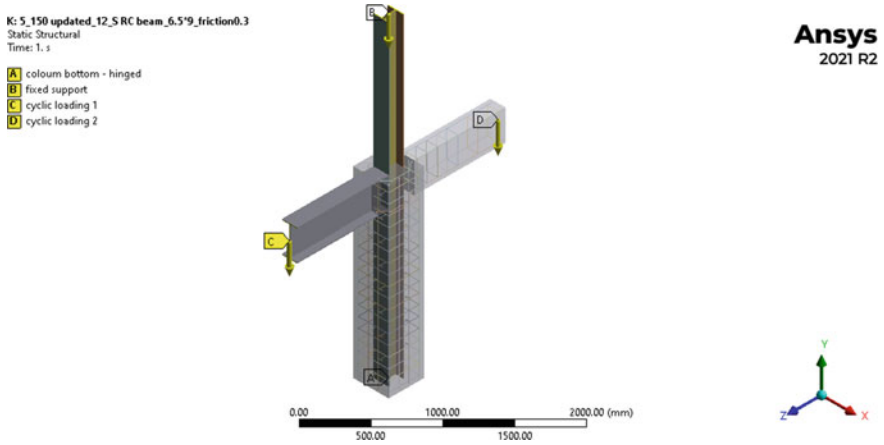
Fig. 3b Loading and Boundary conditions of other specimen

3   Results and Discussions

Detailed 3D finite element modelling is conducted for evaluating the structural performance of special case S-RC-SRC beam column joint with varying beam depth and beam material.

Figure 4a shows the total deformation of specimen 1 and Fig. 4b shows the total deformation of specimen 2.

The ultimate load and ultimate deflection of all the specimens has been summarized in Table 2.
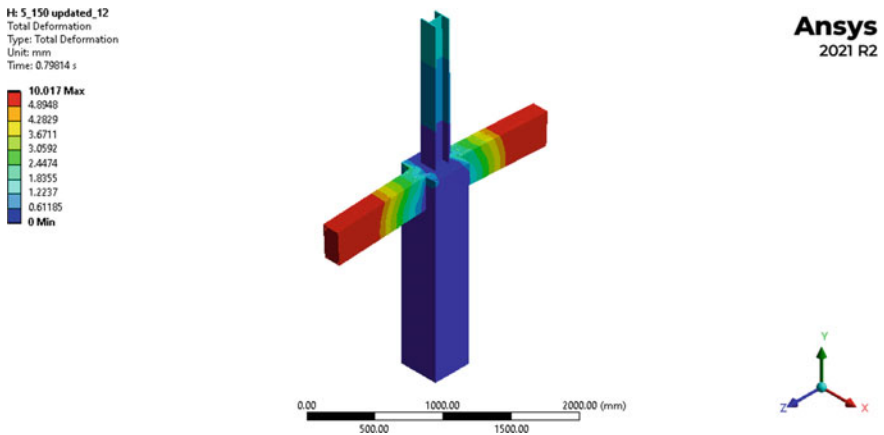
Fig. 4a   Total deformation of specimen 1
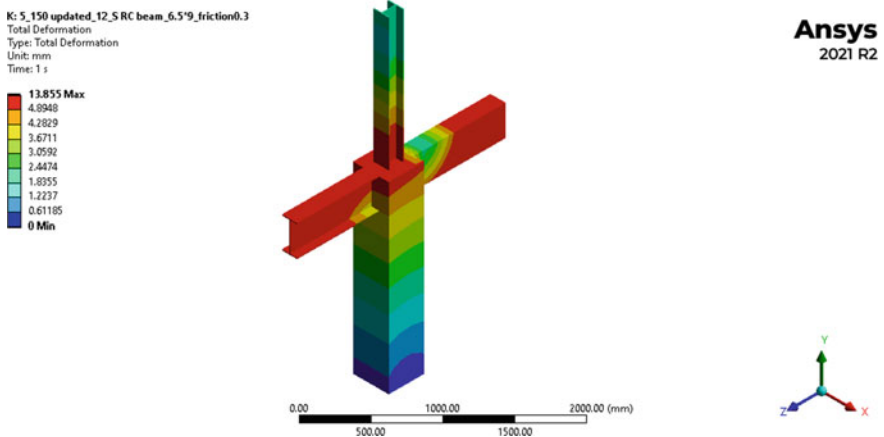
Fig. 4b   Total deformation of specimen 2

Table 2 Comparison of ultimate load and deflection of specimens

Models	LB		RB	
	UD (mm)	UL (KN)	UD (mm)	UL (KN)
Specimen 1 (H)	8.2286	50.697	10.017	50.822
Specimen 2 (K)	13.855	135.68	10.389	54.933
Specimen 3 (N)	16.395	113.68	7.2086	55.4
Specimen 4 (O)	7.708	114.3	7.3563	61.372
Specimen 5 (P)	7.7008	114.3	7.356	61.347

LOAD COMPARISON

	H	K	N	O	P
LB	50.697	135.68	113.68	114.3	114.3
RB	50.822	54.933	55.4	61.372	61.347
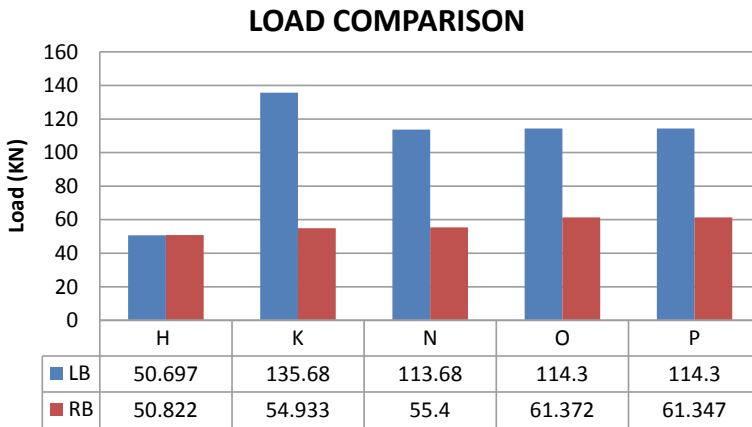
Fig. 5a Load comparison of specimens

Figure 5a shows the comparison of load and Fig. 5b shows the comparison of deflection of all specimens.

From the comparison chart, it can be seen that the steel beam has more load carrying capacity than RC beam. From Fig. 5a shows that specimen 2 has a better load carrying capacity than other specimens. So, by increasing the depth of the steel beam, the load carrying capacity increases.

Figure 6a shows the effect of Steel beam on the equivalent plastic strain of the SRC column and Fig. 6b shows the effect of RC beam on the equivalent plastic strain of the SRC column.

From the above chart, it can be obtained that RC beam has a great influence on the plastic strain of SRC column than steel column. At the beginning of the steel beam, the maximum strain value is obtained for specimen with least steel size (specimen 5).

Figure 7a shows the effect of Steel beam on the equivalent plastic strain of the steel column. Figure 7b shows the effect of RC beam on the equivalent plastic strain of the steel column.

DEFLECTION COMPARISON

	H	K	N	O	P
LB	8.2286	13.855	16.395	7.708	7.7008
RB	10.017	10.389	7.2086	7.3563	7.356
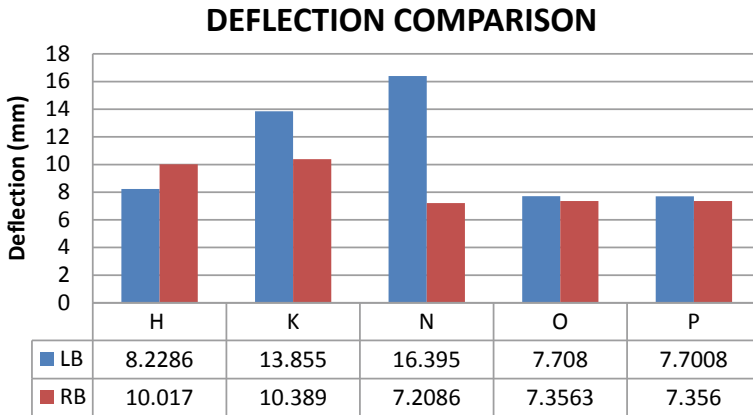
Fig. 5b Deflection comparison of specimens

LB

S and RC beam (P)
15mm (250*125*6*9)

S and RC beam (O)
15mm (280*125*6*9)

S and RC beam (N)
15mm
(300*150*4.5*6)

S and RC beam (K)
12mm
(300*150*6.5*9)
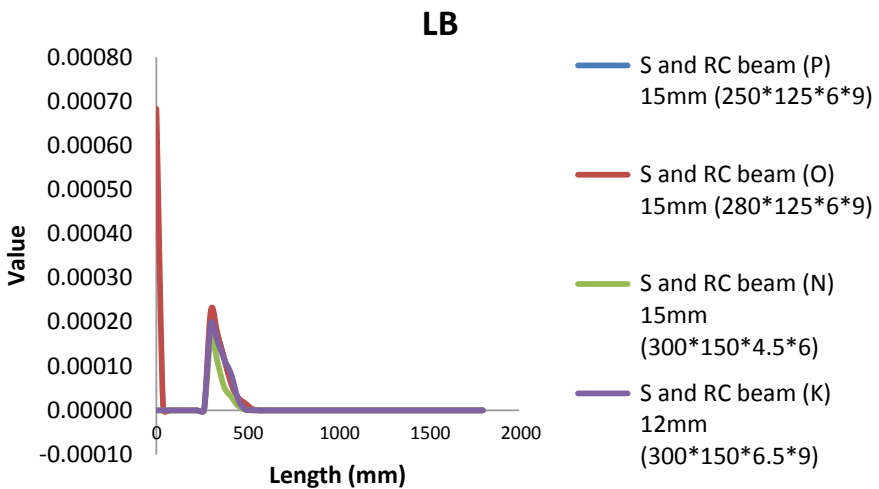
Fig. 6a Effect of steel beam on equivalent plastic strain of SRC column

From the above chart, it can be seen that the effect of steel beam on the equivalent plastic strain of steel column is maximum at the starting of the beam. It abruptly decreases as the beam meets the joint. But for RC beam, the effect is maximum when the beam reaches a length greater than 1000 mm.

Figs. 8a and 8b shows the equivalent strain on left steel beam and right RC beam respectively.

From the above chart, it is evident that steel beam with greater beam depth has more equivalent strain value than other specimens. But for RC beam, the equivalent strain on RC beam of specimen 5 is more.
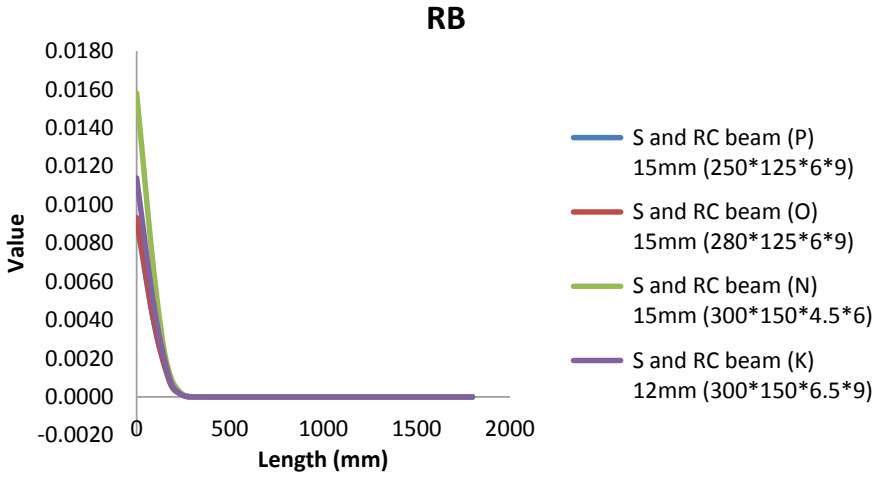
Fig. 6b Effect of RC beam on equivalent plastic strain of SRC column
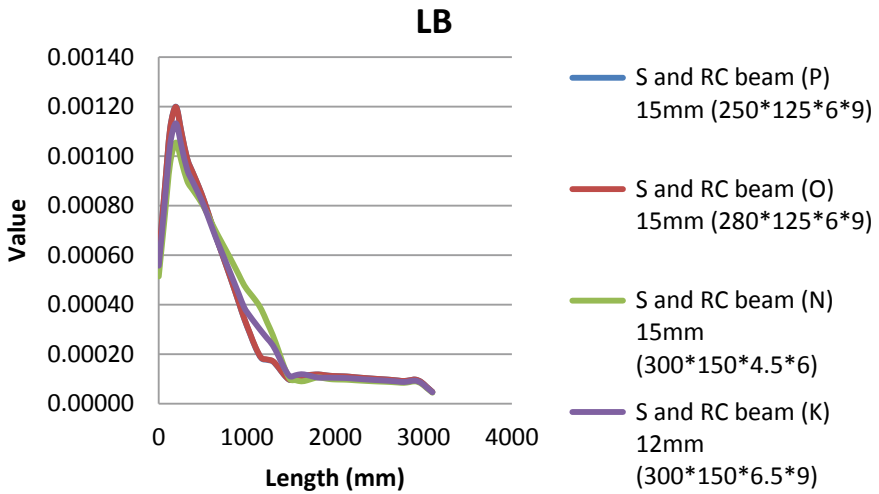
Fig. 7a Effect of steel beam on equivalent plastic strain of steel column
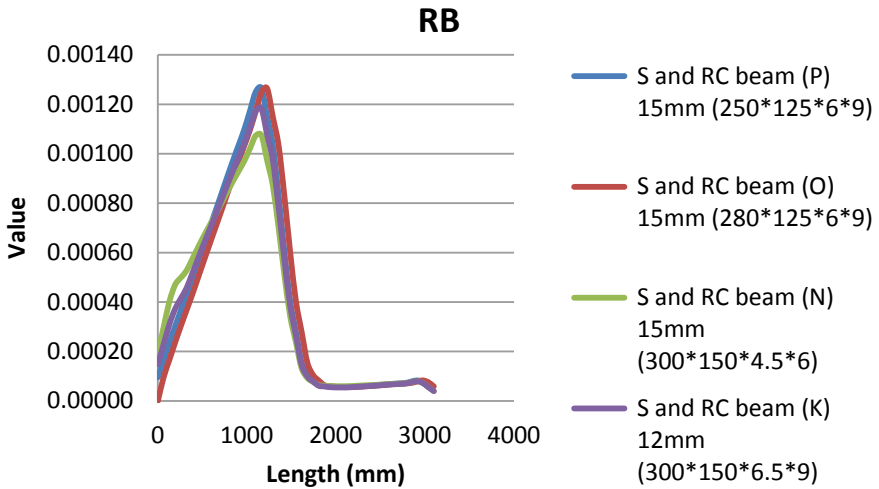
Fig. 7b Effect of RC beam on equivalent plastic strain of steel column
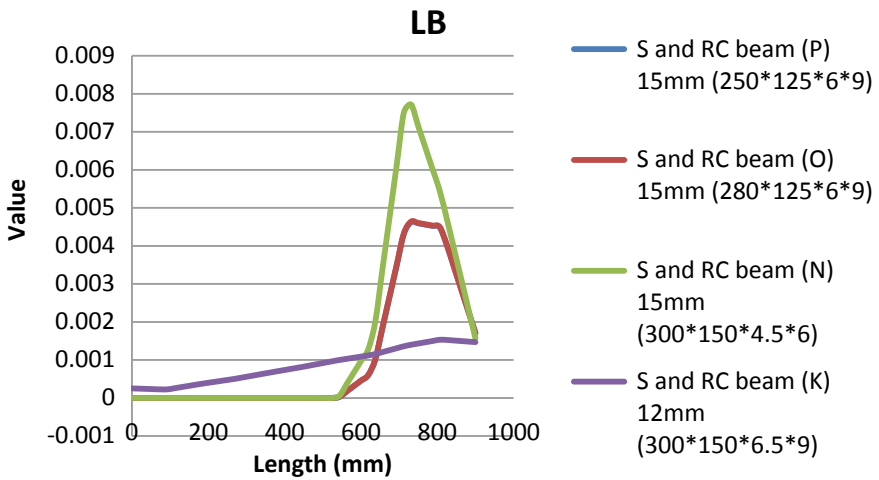
Fig. 8a Equivalent strain on Steel beam

RB
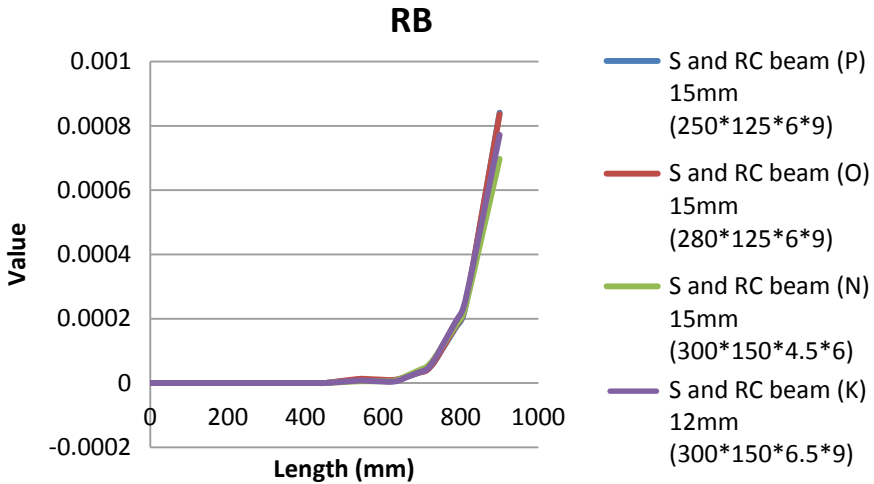
Fig. 8b Equivalent strain on RC beam

4 Conclusions

The steel beam has more load carrying capacity than RC beam. Similarly, the deflection is more for steel beam than RC. Specimen 2 has a better load carrying capacity than other specimens. So, by increasing the depth of the steel beam, the load carrying capacity increases. The enlargement of steel size could reduce the ultimate bearing capacity slightly. RC beam has a great influence on the plastic strain of SRC column than steel column. At the beginning of the steel beam, the maximum strain value is obtained for specimen with least steel size (specimen 5). The effect of steel beam on the equivalent plastic strain of steel column is maximum at the starting of the beam. It abruptly decreases as the beam meets the joint. Steel beam with greater beam depth has more equivalent strain value than other specimens.

References

1. Rong, B., Sun, J., Xu, M., Zhang, R., Sun, Y., Zhang, W., Zhang, W.: Experimental and numerical investigation on seismic performance of S-RC-SRC composite joint. J. Build. Eng. **43**, 103079 (2021)
2. Rong, B., Sun, J., Xu, M., Zhang, R., Sun, Y., Zhang, W., Zhang, W.: Experimental and numerical research on seismic performance of S-RC-SRC composite frame. J. Build. Eng. **43**, 103119 (2021)

3. Mou, B., Liu, Y., Wei, P., Zhao, F., Chenglong, W., Ning, N.: Numerical investigation and design method of bolted beam-column joint panel with eccentricity in beam depths. J. Constr. Steel Res. **180**, 106568 (2021)
4. Xu, C., Peng, S., Wang, C., Ma, Z.: Influence of the degree of damage and confinement materials on the seismic behavior of RC beam-SRC column composite joints. Compos. Struct. **231**, 111002 (2020)
5. Wang, G.Y., Zhang, C., Xu, J., Zhang, D.M.: June). Post-fire seismic performance of SRC beam to SRC column frames. Structures **25**, 323–334 (2020)
6. Montava, I., Irles, R., Pomares, J.C., Gonzalez, A.: Experimental study of steel reinforced concrete (SRC) joints. Appl. Sci. **9**(8), 1528 (2019)
7. Gao, Q., Li, J.H., Qiu, Z.J., Hwang, H.J.: Cyclic loading test for interior precast SRC beam-column joints with and without slab. Eng. Struct. **182**, 1–12 (2019)
8. Yu, S., Wu, C., Zhou, F., Wang, P., Zhao, K., Liu, J.: Experimental study and numerical simulation of a new prefabricated SRC column to steel beam composite joint. Structures **27**, 999–1010 (2020)
9. Huang, W., Zhou, Z., Liu, J.: Analytical deformation characteristics and shear capacity of SRC-RC transfer columns. J. Constr. Steel Res. **138**, 692–700 (2017)
10. Zhong, W.H., Tan, Z., Tian, L.M., Meng, B., Song, X.Y., Zheng, Y.H.: Collapse resistance of composite beam-column assemblies with unequal spans under an internal column-removal scenario. Eng. Struct. **206**, 110143 (2020)

A Review on T-stub to Square Hollow Section Bolted Connections

M. C. Yadupriya and **Rajeevan Bavukkatt**

Abstract Connections are an integral part of a structure, as it transfers the load from one member to another. This paper provides a review of T-stub to square hollow section bolted connections. The failure criteria of bolted beam-column connections vary on the strength and mechanical properties of the individual components. Steel hollow sections are superior to equivalent solid sections in bending stiffness and torsional rigidity. The combination of square hollow and T stub sections under tension are subjected to prying action. When prying force exceeds the applied load, failure of the connection occurs. The typical failure modes observed in this connection are bolt fracture and flange yielding. A critical review of the effect of the types of bolts, bolt pre-tensioning, component thickness, and changes in failure mode are presented. The review provides a summarised collection of past and current research on this type of connection.

Keywords T-stub · Tension · SHS · Bolt · Stiffness · Stainless steel

1 Introduction

Connections are the critical element of any steel structure, and their design is more complex than individual members. Since most cost of the structural steel comprises connections, the design of connections should be prioritized for structural safety and economy.

Bolted connections are the most prevalent type of connection. This connection provides flexibility in constructing and disassembling portions of the structure whenever required. Members subjected to shear, tension, or both shear and tension might benefit from this form of connection type. Welding is another common method adopted for connecting two members. Bolted connections add flexibility to joining the members and reduce the stresses. On the other hand, welded connections are

M. C. Yadupriya (✉) · R. Bavukkatt
Department of Civil Engineering, Government College of Engineering Kannur, Kannur 670563, India
e-mail: 20m714@gcek.ac.in

rigid types of connections and do not allow any movement. In addition, the fusion of the two metals results in the temperature stresses in welded connections.

2 Bolted Connections

Many studies exist on a beam to column bolted connections using a T stub. Satisfactory performance was obtained in strength, yielding, and ductility. Blind bolted connections can substitute bolted connections to connect the beam to column. Studies on this connection showed that the loading was mainly subdivided into monotonic tensile and cyclic loading. Failure at the column face, failure of bolts, yielding of flanges, and combined failure were commonly observed.

2.1 Cyclic Loading

Saberi et al. [1] conducted experimental and numerical investigation on beam to column connection with stiffened and unstiffened endplates under cyclic loading. The sensitivity of the T- stub connection to the component thickness was more than the end plate connection. When comparing a stiffened endplate of reduced thickness to an unstiffened endplate, the stiffened end plate's moment capacity was higher and occurred at a larger rotation.

On the hourglass T stub model, a new approach was introduced to reduce the energy dissipation capacity of the damper by Latour et al. [2]. The model was subjected to cyclic loads. When the T stub was connected to a fixed base, considerable shear was developed in the bolt. However, it was negligible when connected through the flanges of the T stub. Low cycle fatigue curves developed can be used to design dissipative connections. The partially restrained bolted connections were modelled using finite element methods by Brunesi et al. [3].

2.2 Tensile Loading

Lee et al. [4] performed experimental and numerical studies on hollow square sections and T-section connected by blind bolts to evaluate the flexural performance. The study concluded that under serviceability loading conditions given by the International Institute of Welding (IIW) and Eurocode 3 standards, it was acted as a semirigid connection. The bolt sleeves were found to reduce the bending, and hence stiffness of the connections was increased. It was recommended to tighten the bolt hole and sleeve tolerance for efficient connection. The endplate of thickness up to 20 mm was suitable to increase the stiffness. The overall thickness of the connection was taken as 80% initial stiffness of the tension specimen. Under tension, the total stiffness

of the joint was calculated using the equation of individual components given by
Eurocode 3. Based on the study, the T stub connection under compression had an
initial stiffness five times higher than that of the stiffness of a T stub under tension.

Experiments conducted by Ozkılıc et al. [5] on unstiffened T-stubs utilized large
bolt size and smaller plate thickness for developing the flange failure. The ductility
and capacity were improved. The distance between the T-stub web to the bolt center
line affected the plastic capacity. The standards like EN1993-1-8 and AISC 358-16
predicted the capacities on the conservative side. The effect of throat thickness of weld
was considered in the study by Girao Coelho et al. [6]. As the weld size increased,
the stiffness of the connections was also increased. But the deformation capacity
showed a decreasing trend. Zhao et al. [7] conducted tensile tests on structural steels
of different varieties. Experimental test data were validated against the Eurocode 3
equations and the yield line analytical method.

Various researchers proposed different prying models to predict the capacity of
T stub connections. James et al. [8, 9] explained the stiffness modelling of compo-
nents of T stub connection. In this modelling, three types of mechanisms in the T
stub connection contributing to the failure were considered. Load Resistance Factor
Design (LRFD) strength models conservatively estimated the capacity of T stub
components like flange and bolt. A T-stub connected to the rigid base was experi-
mentally and numerically analyzed by Bezerra et al. [10], and their resistance capacity
was compared with the AISC and Eurocode standards. The prying action was domi-
nant in the case of flexible T stub connection. The rigid T stub connection was not
affected by the prying action. The reaction force R on the bolt was obtained as the
combination of prying force Q and applied force P, as shown in Fig. 1.

The effect of pretension on bolted stiffened T stub was experimentally studied
by Zhang et al. [11]. The application of pre-tensioning increased the load-carrying

Fig. 1 Prying action in T
stub connection
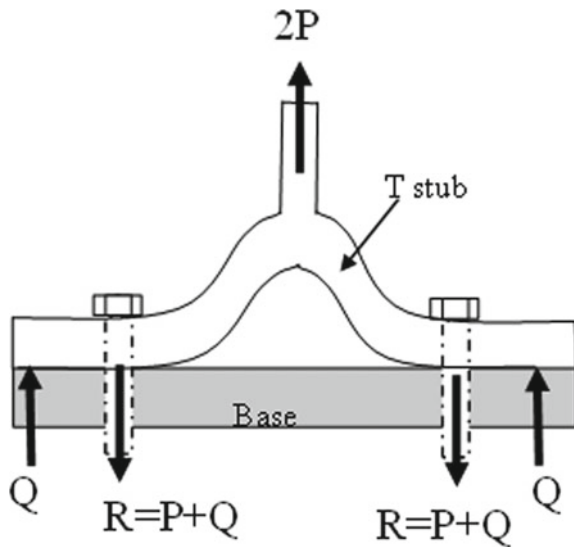
capacity, yield strength, and initial stiffness. The significance of bolt preloading on the connection stiffness was experimentally tested by Faella et al. [12].

2.3 Blind Bolted Connections

Debnath et al. [13] explained the modelling aspects of blind bolts, such as contact surfaces and the method of applying preload. The slip-critical blind bolt developed by Gao et al. [14] was an innovation in blind bolt connections. When this connection was subjected to tension and shear, slip resistance was observed to be increasing. Jiao et al. [15] also performed experiments on connections using slip-critical blind bolts subjected to cyclic loading.

Sun et al. [16] suggested a T-shaped one-sided bolt. Regarding yield bending moment, initial stiffness, and ultimate bending moment, the T shaped one side bolted connection (TOBC) having vertical slotted bolt holes excelled with the TOBC in the horizontal direction. Similar studies on T- stubs with square-necked TOBC were performed by Wang et al. [17]. The observed failure modes were bolt fracture, flange yielding, column wall yielding, and bolt hole shearing. In addition to the commonly seen failure modes in T stub connection, Liu et al. [18] recently identified two failure modes-failure of bolt thread and combined failure of bolt thread and flange of T stub.

Tahir et al. [19] found that the beam size and endplate thickness appreciably affect the moment capacity and rotational stiffness of blind bolted endplate connection. Lacey et al. [20] did a detailed review on inter-module connections. After a rigorous analysis, the most appropriate methods were suggested to calculate stiffness values.

2.4 Concrete Filled Bolted Connections

The strength and stiffness of the connection could be considerably increased by pouring concrete into hollow sectional columns. Wang et al. [21] assessed a set of studies using extended end plate blind bolted connections for a concrete-filled column under monotonic loading. Some measures were suggested in the panel region, like local thickening of the tube wall to increase the initial stiffness. Also, the anchorage length of the bolt was extended to improve the tensile performance. But it has no significant effect on the moment capacity. An anchorage length ratio of 0.25 was proposed for the design.

Experiments and finite element studies on the extended hollow bolts were reviewed by Cabrera et al. [22] under tensile loading. One modified blind bolt, known as an extended hollow bolt (EHB), can be used for the moment-resisting connections. As an extension to the Lindapter Hollow bolt, Tizani and Ridley-Elis developed the EHB. These bolts have an anchorage effect due to nuts and extended shafts. In addition, the concrete can be infilled into the hollow section to increase the stiffness of the connection. The three modes of failures observed in concrete-filled
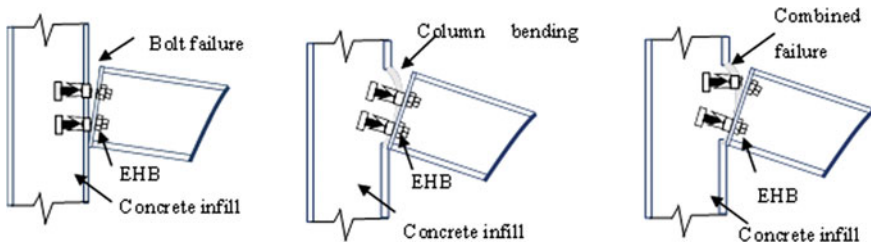
Fig. 2 Different types of failure modes in extended hollow bolt connections

hollow columns connected with EHB were bolt failure, column bending failure, and combined failure, as indicated in Fig. 2.

Similar studies were performed by Jiao et al. [15], Wang et al. [23], and Guo et al. [24] on the seismic performance of bolted concrete filled steel tubular (CFST) columns. Guo et al. [24] conducted experiments to analyze the seismic performance of blind bolted concrete-filled circular column to beam joints. The connection was ductile and had better energy dissipation capabilities. In addition to the commonly seen failure modes, welding seam fractures occurred in the connections. Yao et al. [25] conducted tensile and cyclic tests on T stub connection. In addition to the commonly provided components, a cogged extension to the bolts and a curved endplate were incorporated into the study. Pull-out tests were conducted to determine the effect of anchorage of bolts. The cogged extension provided additional benefit to the tensile behaviour of the connection.

To determine the initial rotational stiffness of the CFST column to beam connection, an analytical approach was provided by Zhou et al. [26]. Endplate thickness and bolt diameter were identified as key parameters controlling the behaviour. The analytical model developed can be used for the design of semirigid connections. Pokharel et al. [27] investigated the double-headed anchored blind bolt on the concrete-filled hollow tube. A set of parameters were considered under cyclic and monotonic loading. The flange thickness had an appreciable effect on the stiffness of the connection.

In the study of Hantouche et al. [28], built-up T stub section with a thick flange made of complete joint penetration weld was numerically and experimentally studied. The bolt's force was increased to accommodate the prying effect. The design considered the prying effect by proposing a larger bolt size. An equation was proposed for calculating the applied force.

2.5 Stainless Steel Bolted Connections

Stainless steel's structural performance differs from carbon steel because it lacks a distinct yield point and exhibits an early deviation from linear elastic behaviour with severe strain hardening. The studies on stainless steel bolted connections were

limited when compared to structural steel. The code of practice available was also minimal on the stainless-steel connections. AISC 370 code can be used to design stainless steel connections [29].

The double shear tests under tension were conducted on stainless steel staggered bolted connections by Santos et al. [30]. The strength and net section fracture of stainless-steel connection with three grades were considered. Three failure modes were observed in the bolted connection subjected to shear[31]. They were bolt failure, bearing failure, and plate failure at the net section. The experimental studies were conducted by Li et al. [32] on connections with normal bolts and blind bolts. The study was later extended [33] to the concrete infilled stainless steel blind bolted connections. Stainless steel would be suitable in aggressive environments like contact with seawater due to its robustness and less maintenance. Furthermore, due to the presence of concrete, a boundary condition similar to a fixed case exists between the face of the hollow section.

Similarly, inward bending of the side face of the hollow section was prevented to some extent. The initial stiffness and capacity were significantly improved. The friction coefficient cannot be directly measured [34]. Instead, some lubricants were applied to get the friction coefficient and preload effect.

Eladly et al. [35] conducted numerical studies on stainless steel beam to column connections with excellent ductility properties. The stiffeners were found to reduce the stresses on connecting elements, and hence ultimate moment capacity and energy dissipation capacity were improved. Endplate stiffeners can be considered as another type of protection in extended endplate connections. Their application developed plastic strains on the stiffeners themselves, reducing strains and stresses on other connection components.

2.6 Critical Review

The bolted T stub connections subjected to tensile loading were reviewed, and it has been identified that the action of prying force was significant under tension. In addition, the concrete infill into the bolted connections helps to improve their strength and stiffness. Studies were conducted on the steel connections extensively, but stainless-steel connections need further parametric studies.

3 Conclusions

A detailed review was conducted on the bolted T stub connections to understand their behaviour and failure patterns. In addition, further studies on the structural performance of stainless-steel T stub connections were suggested to improve knowledge and enable the development of relevant theoretical models. The important conclusions that were derived from this review are summarised below.

- The T stub beam-column connections were effective under compressive, tensile and cyclic loading. The component method can be used to determine the stiffness of the whole connection.
- The strength and stiffness of the bolted connection using a hollow sectional column can be increased by concrete infill. The grade of concrete and anchorage of bolts were the key parameters affecting the behaviour of concrete infilled columns.
- The prying force commonly seen in the T stub has an important role in the bolt force. Prying force, preloading, and applied loading constitute the forces acting on the bolt. The load-carrying capacity, initial stiffness, and yield strength were increased under the application of pre-tensioning.
- The prying action increased with the distance from the bolt centreline to the stem of the T stub.

References

1. Saberi, V., Gerami, M., Kheyroddin, A.: Comparison of bolted end plate and T-stub connection sensitivity to component thickness. J. Constr. Steel Res. **98**, 134–145 (2014). https://doi.org/10.1016/j.jcsr.2014.02.012
2. Latour, M., Rizzano, G.: Experimental behavior and mechanical modeling of dissipative T-stub connections. J. Struct. Eng. **138**(2), 170–182 (2012). https://doi.org/10.1061/(asce)st.1943-541x.0000435
3. Brunesi, E., Nascimbene, R., Rassati, G.A.: Evaluation of the response of partially restrained bolted beam-to-column connection subjected to cyclic pseudo-static loads. In Structures Congress, pp. 2–4 (2013)
4. Lee, J., Goldsworthy, H.M., Gad, E.F.: Blind bolted T-stub connections to unfilled hollow section columns in low rise structures. J. Constr. Steel Res. **66**(8–9), 981–992 (2010). https://doi.org/10.1016/j.jcsr.2010.03.016
5. Ozkılıc, Y.O.: The capacities of unstiffened T-stubs with thin plates and large bolts. J. Constr. Steel Res. **186**, 106908 (2021). https://doi.org/10.1016/j.jcsr.2021.106908
6. Girão Coelho, A.M., Simões da Silva, L., Bijlaard, F.S.: Finite-element modeling of the nonlinear behavior of bolted T-stub connections. J. Struct. Eng. **132**(6), 918–928 (2006). https://doi.org/10.1061/ASCE0733-94452006132:6918
7. Zhao, M.S., Lee, C.K., Chiew, S.P.: Tensile behavior of high performance structural steel T-stub joints. J. Constr. Steel Res. **122**, 316–325 (2016). https://doi.org/10.1016/j.jcsr.2016.04.001
8. James Swanson, B.A., Member, A., Leon, R.T.: Stiffness modeling of bolted t-stub connection components. J. Struct. Eng. **127**(5), 498–505 (2001). https://doi.org/10.1061/(ASCE)0733-9445
9. James Swanson, B.A., Leon, R.T.: Bolted steel connections: tests on t-stub components. J. Struct. Eng. **126**(1), 50–56 (2000). https://doi.org/10.1061/(ASCE)0733-9445(2000)126:1(50)
10. Bezerra, L.M., Bonilla, J., Silva, W.A., Matias, W.T.: Experimental and numerical studies of bolted T-stub steel connection with different flange thicknesses connected to a rigid base. Eng. Struct. **218**, 110770 (2020). https://doi.org/10.1016/j.engstruct.2020.110770
11. Zhang, Y., Gao, S., Guo, L., Fu, F., Wang, S.: Ultimate tensile behavior of bolted stiffened T-stub connections in progressive collapse resistance. J. Constr. Steel Res. **189**, 107111 (2022). https://doi.org/10.1016/j.jcsr.2021.107111
12. Faella, C., Piluso, V., Rizzano, G.: Experimental analysis of bolted connections: snug versus preloaded bolts. J. Struct. Eng. **124**(7), 765–774 (1998). https://doi.org/10.1061/(ASCE)0733-9445

13. Debnath, P.P., Chan, T.M.: A comprehensive numerical approach for modelling blind-bolted CFST connections. Structures **33**, 2208–2225 (2021). https://doi.org/10.1016/j.istruc.2021.05.052

14. Gao, X., Wang, W., Teh, L.H., Zhuang, L.: A novel slip-critical blind bolt: experimental studies on shear, tensile and combined tensile–shear resistances. Thin-Walled Struct. **170**, 108630 (2022). https://doi.org/10.1016/j.tws.2021.108630

15. Jiao, W., Wang, W., Chen, Y., Teh, L.H.: Seismic performance of concrete-filled SHS column-to-beam connections with slip-critical blind bolts. J. Constr. Steel Res. **170**, 106075 (2020). https://doi.org/10.1016/j.jcsr.2020.106075

16. Sun, L., et al.: Studies on T-shaped one-side bolted connection to hollow section column under bending. J. Constr. Steel Res. **175**, 106359 (2020). https://doi.org/10.1016/j.jcsr.2020.106359

17. Wang, P., Sun, L., Zhang, B., Yang, X., Liu, F., Han, Z.: Experimental studies on T-stub to hollow section column connection bolted by T-head square-neck one-side bolts under tension. J. Constr. Steel Res. **178**, 106493 (2021). https://doi.org/10.1016/j.jcsr.2020.106493

18. Liu, M., Zhu, X., Wang, P., Tuoya, W., Hu, S.: Tension strength and design method for thread-fixed one-side bolted T-stub. Eng. Struct. **150**, 918–933 (2017). https://doi.org/10.1016/j.engstruct.2017.07.093

19. Tahir, M.M., Mohammadhosseini, H., Ngian, S.P., Effendi, M.K.: I-beam to square hollow column blind bolted moment connection: experimental and numerical study. J. Constr. Steel Res. **148**, 383–398 (2018). https://doi.org/10.1016/j.jcsr.2018.06.012

20. Lacey, A.W., Chen, W., Hao, H., Bi, K.: Review of bolted inter-module connections in modular steel buildings. J. Build. Eng. **23**, 207–219 (2019). https://doi.org/10.1016/j.jobe.2019.01.035

21. Wang, J., Zhang, N., Guo, S.: Experimental and numerical analysis of blind bolted moment joints to CFTST columns. Thin-Walled Struct. **109**, 185–201 (2016). https://doi.org/10.1016/j.tws.2016.07.017

22. Cabrera, M., Tizani, W., Ninic, J.: A review and analysis of testing and modeling practice of extended Hollo-Bolt blind bolt connections. J. Constr. Steel Res. **183**, 106763 (2021). https://doi.org/10.1016/j.jcsr.2021.106763

23. Wang, J., Zhang, H.: Seismic performance assessment of blind bolted steel-concrete composite joints based on pseudo-dynamic testing. Eng. Struct. **131**, 192–206 (2017). https://doi.org/10.1016/j.engstruct.2016.11.011

24. Guo, L., Wang, J., Wu, S., Zhong, L.: Experimental investigation and analytical modelling of blind bolted flush or extended end plate connections to circular CFDST columns. Eng. Struct. **192**, 233–253 (2019). https://doi.org/10.1016/j.engstruct.2019.04.053

25. Yao, H., Goldsworthy, H., Gad, E.: Experimental and numerical investigation of the tensile behavior of blind-bolted T-stub connections to concrete-filled circular columns. J. Struct. Eng. **134**(2), 198–208 (2008). https://doi.org/10.1061/ASCE0733-94452008134:2198

26. Zhou, G., An, Y., Wu, Z., Li, D., Ou, J.: Analytical model for initial rotational stiffness of steel beam to concrete-filled steel tube column connections with bidirectional bolts. J. Struct. Eng. **144**(11), 04018199 (2018). https://doi.org/10.1061/(asce)st.1943-541x.0002187

27. Pokharel, T., Goldsworthy, H.M., Gad, E.F.: Tensile behavior of groups of double-headed anchored blind bolts within concrete-filled square hollow sections under cyclic loading. J. Struct. Eng. **147**(3), 04020349 (2021). https://doi.org/10.1061/(asce)st.1943-541x.0002929

28. Hantouche, E.G., Kukreti, A.R., Rassati, G.A., Swanson, J.A.: Prying models for strength in thick-flange built-up T-stubs with complete joint penetration and fillet welds. J. Struct. Eng. **141**(2), 04014102 (2015). https://doi.org/10.1061/(asce)st.1943-541x.0001051

29. Jiang, K., Zhao, O.: Experimental and numerical studies of stainless steel angle-to-plate connections. Thin-Walled Struct. **173**, 109026 (2022). https://doi.org/10.1016/j.tws.2022.109026

30. dos Santos, J., et al.: Testing and design of stainless steel staggered bolted connections. Eng. Struct. **231**, 111707 (2021). https://doi.org/10.1016/j.engstruct.2020.111707

31. Salih, E.L., Gardner, L., Nethercot, D.A.: Bearing failure in stainless steel bolted connections. Eng. Struct. **33**(2), 549–562 (2011). https://doi.org/10.1016/j.engstruct.2010.11.013

32. Li, Y.L., Zhao, X.L.: Experimental study on stainless steel blind bolted T-stub to square hollow section connections. Thin-Walled Struct. **167**, 108259 (2021). https://doi.org/10.1016/j.tws.2021.108259

33. Li, Y.-L., Zhao, X.-L.: Study on stainless steel blind bolted T-stub to concrete-filled stainless steel tube connections. Eng. Struct. **257**, 114107 (2022). https://doi.org/10.1016/j.engstruct.2022.114107

34. Zheng, B., Wang, J., Gu, Y., Shu, G., Xie, J., Jiang, Q.: Experimental study on stainless steel high-strength bolted slip-resistant connections. Eng. Struct. **231**, 111778 (2021). https://doi.org/10.1016/j.engstruct.2020.111778

35. Eladly, M.M., Schafer, B.W.: Numerical and analytical study of stainless steel beam-to-column extended endplate connections. Eng. Struct. **240**, 112392 (2021). doi: https://doi.org/10.1016/j.engstruct.2021.112392

Thermal and Structural Behavior of Precast Concrete Sandwich Panels

P. U. Jithin and Asha Joseph

Abstract Precast concrete sandwich panel (PCSP) is a specific type of precast cladding that consists of an internal wythe of insulation sandwiched between two external wythes of concrete connected using a shear connector. PCSP walls and slabs are energy efficient which may serve the dual function of transferring load as well as insulation against heat. These panels are economical, attractive and energy-efficient that are provided in many structures including residential buildings, offices, schools, hospitals and industrial buildings. A Finite Element Model was developed to determine the thermal performance of PCSP under standard conditions. Thermal analysis of PCSP is conducted with different thicknesses of internal wythe. The thickness of insulation varied from 80 mm to 160 mm and fire performance has improved with increased thickness of internal wythe. The thermal performance of the panel was quantified by the thermal transmittance (U-value) for varying insulation materials. In this study, Expanded Polystyrene (EPS), Extruded Polystyrene (XPS), Phenolic Foam (PF), and Polyisocyanurate foam (PIR) were selected as alternative materials for insulation. By comparing the U values, PF has been found to have better thermal performance. The U-value of $0.053\ Wm^{-2}K^{-1}$ for PCSP with EPS insulation is about 75.9% less than PCSP with EPS insulation.

Keywords Precast concrete · Sandwich panels · Shear connector · Insulation material · Thermal transmittance

1 Introduction

A Precast Concrete Sandwich Panel is a specific sandwich panel that comprises an internal layer of insulation sandwiched between two external wythes of thin concrete connected using a shear connector. Reinforcement in external wythes is provided in

P. U. Jithin (✉) · A. Joseph
Department of Civil Engineering, FISAT, Angamaly, India
e-mail: jithinunnikrishnan333@gmail.com

A. Joseph
e-mail: ashameledath@fisat.ac.in

the form of conventional reinforcement or welded wire mesh. Benefits of using PCSP over other types of claddings include its long-term viability and flexibility, thermal insulation, economical, attractiveness, quick installation, lightweight, and high structural performance. These panels can be used as walls and slabs that are found in many structures including residential buildings, industrial buildings, schools, and hospitals.

Depending on the shear connector's distribution and type, PCSPs can be constructed as either composite or partially composite or non-composite. Hou et al. [1] used diagonal steel bars as the shear connector. From the perspective of energy efficiency, the higher thermal conductance of steel and concrete connectors makes them unattractive. NU tie (truss-shaped glass fiber–reinforced polymer ties), which has magnificent thermo-mechanical properties was used for this study [2]. Gara et al. [3] studied the flexural behavior of PCSP under four-point bending through various numerical simulations as well as through experiments. They had proposed panel designs with different core thicknesses. Wire mesh was used to reinforce concrete and non-shear connectors were used to link the wythes. The authors concluded that, increasing panel thickness was requisite for increasing load-carrying capacity.

Upasiri et al. [4] conducted parametric studies to determine the fire performance of Composite Sandwich Panels (CSP) wall panels of varying thicknesses with Foamed Concrete (FC) and Autoclaved Aerated Concrete (AAC) under standard and hydrocarbon fire conditions. The FE results be revealed that composite sandwich panels with AAC core have improved 9%–92% insulation fire rating compared to AAC Plain Concrete Panel (PCP) for varying thicknesses.

This study mainly focuses on investigating the thermal performance of sandwich panels. A 3 m panel with Expanded Polystyrene (EPS) insulation was initially taken for the analysis. Then a parametric study was concluded by changing the thickness of the internal wythe from 80 to 160 mm. The next intention was to investigate the panel with different insulation materials. From the analysis results, the best insulation material which performs more efficiently in terms of thermal transmittance was evaluated.

2 Development of Finite Element Model

The finite Element Model was developed using ANSYS software to investigate the thermal performance of PCSP. A transient thermal analysis is conducted by changing the thickness of the insulation panel and the one with the highest thermal efficiency was adopted. Subsequently, analysis is carried out by changing the insulation materials with optimum thickness from the previous analysis. This section explains the development of FE model and validation of the FE model with published results.
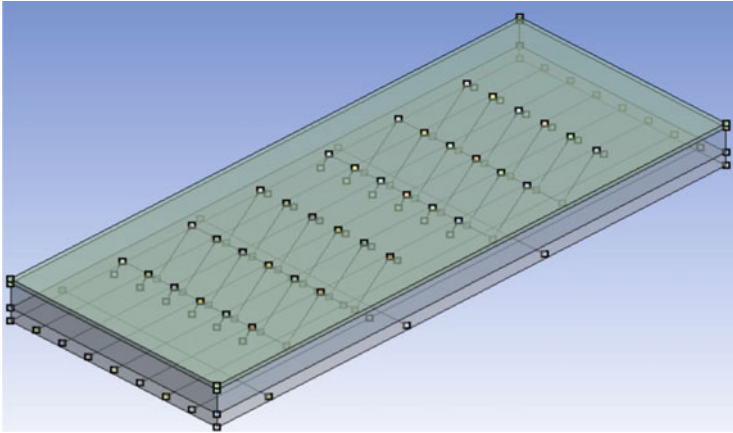
Fig. 1 Geometry of PCSP

2.1 Geometry

PCSP panel was designed for 3-m-long, 1.22-m-wide and 200-mm-thick. The panel was longitudinally pre-tensioned using seven number of Grade 1860 low-relaxation prestressing strands of 15-mm diameter. 12 numbers of NU ties (truss-shaped GFRP ties) are uniformly distributed along the panel to resist horizontal shear and to control the deflection of the panel. The geometry of the proposed panel is shown in Fig. 1.

2.2 Material Specifications and Engineering Properties

In order to get more precise temperature results density, thermal conductivity and specific heat was given as temperature dependent properties. The heat loss due to convection and radiation from exposed and unexposed surfaces were also assigned. The list of thermal properties used for various materials used for this study is shown in Table 1.

Table 1 Engineering data for thermal analysis

Material	Density (Kgm^{-3})	Thermal conductivity $(Wm^{-1}K^{-1})$	Specific heat $(JKg^{-1}K^{-1})$
Concrete [7]	2400	2.25	880
GFRP tie [8]	1870	0.35	640
EPS [8]	15	0.034	1300
Structural steel [8]	7850	60.5	434

2.3   *Validation*

Prior to the conduct of the thermal analysis, the FE model was validated by comparing the results published by Heninet et al. [2] through their experimental work. The model consists of PCSP panel with 7.9 m-long, 1.22 m-wide and 200 mm-thick, connected by 24 numbers of NU ties. The geometry of the panel for validation is shown in Fig. 2 and material properties are same as that given in Table 1.

Static structural analysis was performed the resultant load–deflection curve from present study is shown in Fig. 3.

The maximum ultimate load obtained from the study of Henin et al. was 48.93 kN and from the present study, the load-carrying capacity of PCSP is founded to be 51.05 kN, as shown in Table 2 where the variation from the published value is 7.29% only.
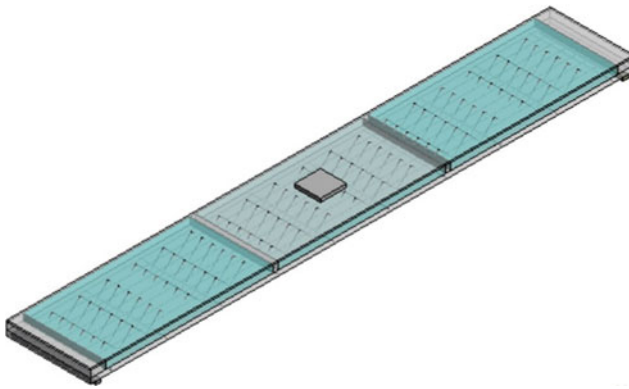
Fig. 2   Isometric view of PCSP panel
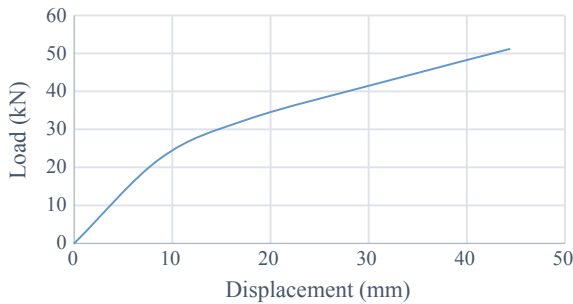
Fig. 3   Load–deflection response curve plotted based on the result obtained from ANSYS

Table 2 Comparison of results

Parameter	Load (kN)	Displacement (mm)
Henin et al. [2]	48.93	45.12
The value obtained from the present study	51.50	44.35

2.4 Simulations of Temperature Field

A nonlinear heat transfer analysis was first conducted for each of the PCSP specimens taken for the study and thermal load is applied. Thermal load is applied with the help of ISO 834 fire cure, in which the fire could be represented as a time–temperature history. Standard fire curves are used to compare the structural fire performance [5]. Figure 4 shows the time–temperature variation of the ISO 834 Standard fire curve. The PCSP was assumed to be only exposed to fire from the lower surface along its entire length, since PCSP was modelled as a slab member. Discretised model of the PCSP is given in Fig. 5. SOLID279 element was used for modelling of panel wythes, which have 20 nodes with a temperature degree of freedom at each node. Transient thermal analysis was performed with the initial temperature as the room temperature (20 °C), and the applied temperature load was set by ISO 834 fire curve for a duration of 180 min.

3 Thermal Performance of PCSP

To evaluate the thermal performance of each specimen, 4 thermocouples were located in the cross-section as shown in Fig. 6. This configuration allows for an comprehensive analysis of the temperature progression of each cross-section: (i) middle of
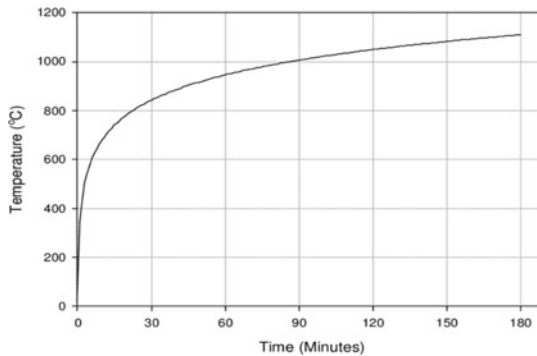
Fig. 4 Time–temperature variation of standard fire curve from ISO 834 [5]
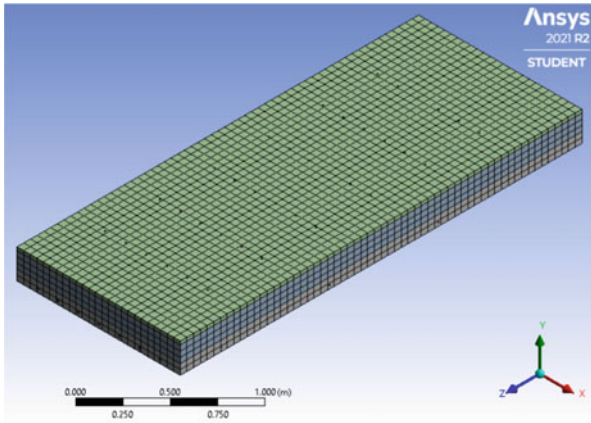
Fig. 5 Finite element model of PCSP
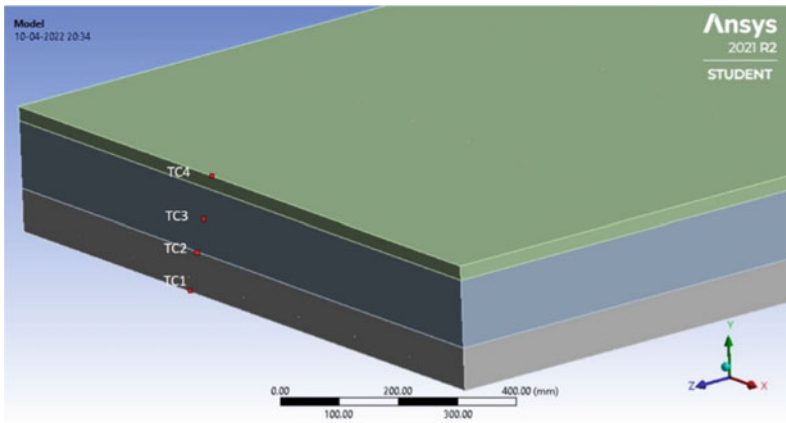
Fig. 6 Thermocouple locations in panel

bottom concrete wythe, (ii) the bottom of insulation wythe, (iii) middle of insula-
tion, and (iv) at the top of topping of the panel and these thermocouple locations
TC1, TC2, TC3, and TC4 are depicted in Fig. 6.

3.1 Varying Thickness of Insulation Wythe

The fire performance of PCSP with different insulation thicknesses; 80 mm, 100 mm,
120 mm, 140 mm, and 160 mm with EPS insulation (EPS80, EPS100, EPS120,
EPS140 and EPS160) were studied under standard fire conditions. The maximum

thickness of insulation is limited to 160 mm [6]. The variation in temperature field and heat flux values at different panel locations were noted for varying thicknesses of insulation.

The thermal performance of the panel is usually quantified by the thermal transmittance, U-value ($Wm^{-2}K^{-1}$) in Europe, and the thermal resistance, R-value (m^2KW^{-1}) in the US. The U-value in $Wm^{-2}K^{-1}$ is used in this study for the comparison of the thermal performance of insulating materials with different thicknesses. From the maximum values of heat flux, Q (Wm^{-2}), and temperature at the hot, T_h (K), and cold surfaces T_c (K) of the panel, the thermal transmittance through the wall, U ($Wm^{-2}K^{-1}$) were calculated.

$$U = \frac{Q}{T_h - T_c} \tag{1}$$

The higher the U-value the greater will be the heat loss for a given temperature difference [7].

After performing transient thermal analysis the maximum temperature values were recorded in various thermocouple locations for EPS80, EPS100, EPS120, EPS140, and EPS160. Figure 7(a) and (b) shows the maximum temperature obtained at each of the thermocouple locations for EPS80 and EPS160 respectively. In all FE models, an ambient temperature of 20 °C was considered. A maximum temperature of 27.08 °C was obtained for EPS80 and a minimum temperature of 23.37 °C for EPS160. The heat flux values for each EPS thickness obtained after analysis are also shown in Fig. 8. PCSP with EPS120, a maximum heat flux value of 219.86 Wm^{-2} was obtained which is shown in Fig. 9. From the heat flux values and temperature at cold and hot surfaces, the U-value was calculated as per Eq. (1) for 180 min. A minimum U-value of 0.22 $Wm^{-2}K^{-1}$ was obtained for EPS160 and a maximum of 0.52 $Wm^{-2}K^{-1}$ was calculated for EPS80. The maximum temperature and U-values is listed in Table 3. Thus from the analysis result, it is found to be EPS160 shows the lowest thermal transmittance, hence this model was used for further study.

3.2 Varying Materials of Insulation Wythe

After fixing the appropriate thickness from the above parametric study, the next intention was to change the insulation material of the internal wythe of the sandwich panel. Apart from EPS, Extruded Polystyrene (XPS), Phenolic Foam (PF), and Polyisocyanurate foam (PIR) were used as rigid foam insulation in this study. EPS is a tough and rigid, closed-cell foam made from pre-expanded polystyrene beads, whereas XPS is relatively stronger and denser. PF insulation comprising of phenolic resins and other additives and PIR is a thermoset plastic almost identical to Polyurethane (PUR) foam. The conductivity values of these insulation materials are presented in Table 4. From the result of transient thermal analysis, the most thermally efficient material is determined.
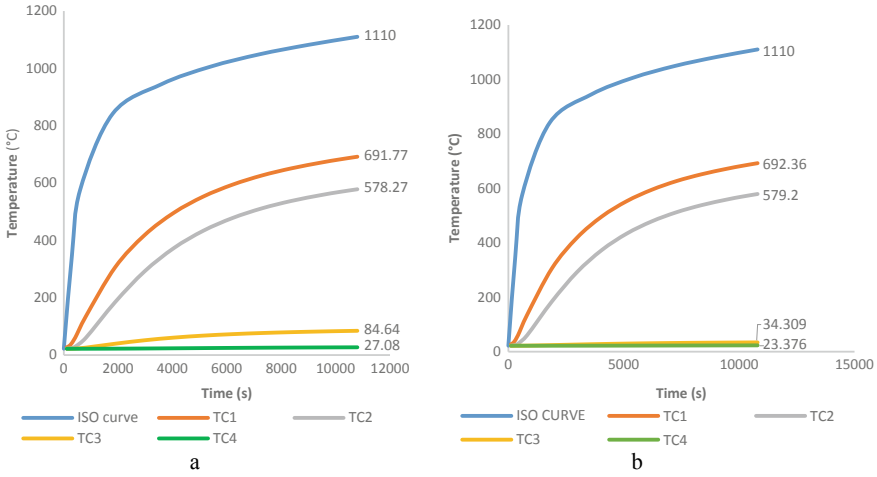
Fig. 7 Variation of temperature with time of **a** EPS80 and **b** EPS160
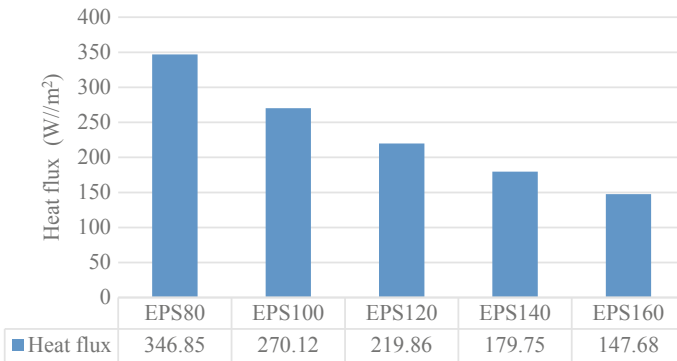
Fig. 8 Heat flux values of EPS with varying thickness

The thermal performance of different insulation materials of 160 mm insulation thickness was compared based on thermal transmittance (U value) and is given in Table 5. The maximum temperature is shown in Figs. 10, 11 and 12 and heat flux values obtained at the top surface of panel were shown in Fig. 13 for different insulating materials. By comparing thermal transmittance values, it is observed that PF has the lowest U-value. There is an increase in U value by 75.9%, 62.1% and 42.4% for EPS, XPS and PIR respectively in comparison to PF. Hence PF is recommended for the construction as the most thermally efficient insulating material for PCSP panel design.

In order to achieve a target thermal transmittance of 0.185 $Wm^{-2}K^{-1}$, the thickness required for PCSP with different insulation was shown in Fig. 14 from the FE results.
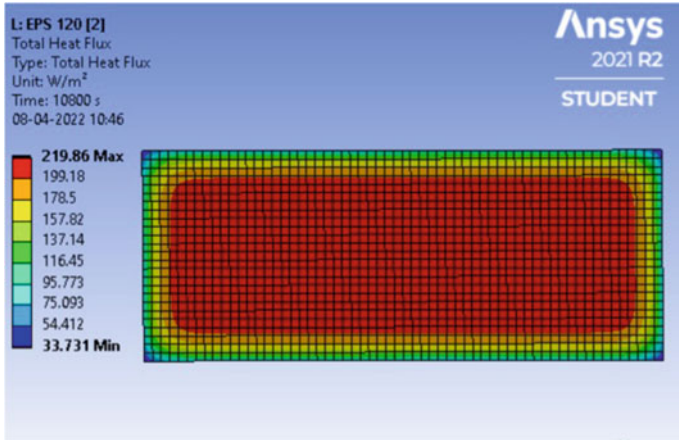
Fig. 9 Heat flux results of FE model EPS120 configuration at the top surface

Table 3 Maximum temperature and U-values of EPS with varying thickness

Insulation	Maximum temperature at top surface of panel (°C)	U-value ($Wm^{-2}K^{-1}$)
EPS80	27.08	0.520
EPS100	25.98	0.406
EPS120	24.42	0.329
EPS140	23.85	0.269
EPS160	23.37	0.220

Table 4 Density and conductivity values of insulation types

Material	Density (Kgm^{-3})	Thermal conductivity ($Wm^{-1}K^{-1}$)
XPS [8]	38	0.035
PF [8]	35	0.021
PIR [8]	30	0.025

Table 5 The U-values of the panel with varying materials at 160 mm thickness

Insulation	U-value ($Wm^{-2}K^{-1}$)
EPS	0.220
XPS	0.140
PF	0.053
PIR	0.092
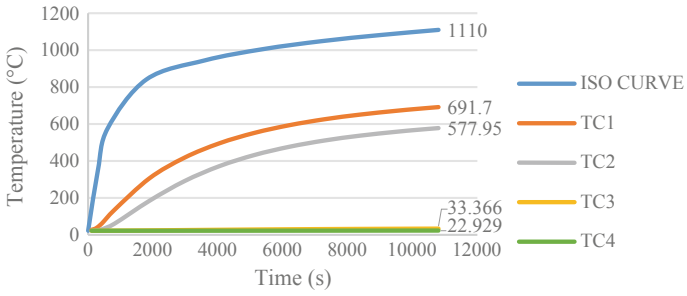
Fig. 10 Variation of temperature with time of XPS panel
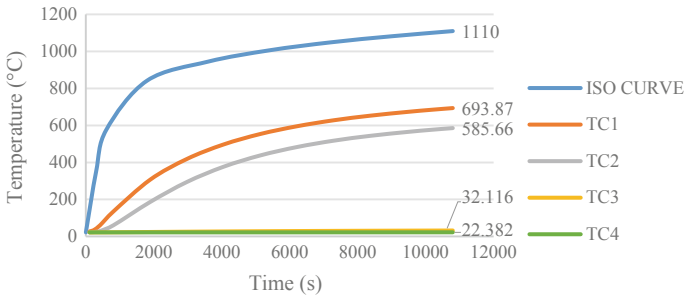
Fig. 11 Variation of temperature with time of PF panel
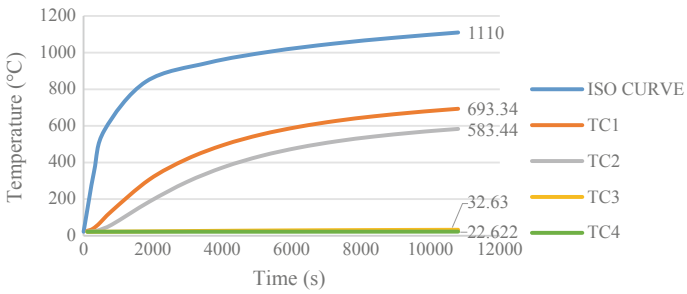
Fig. 12 Variation of temperature with time of PIR panel
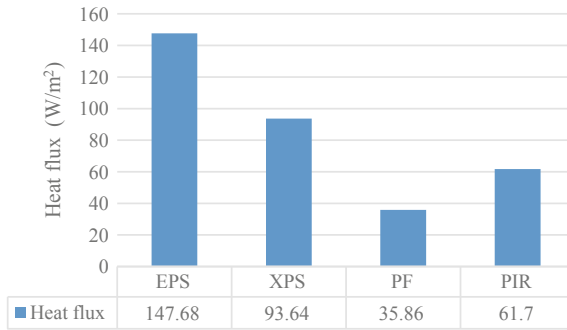
Fig. 13 Heat flux values of different insulation materials

	EPS	XPS	PF	PIR
■ Heat flux	147.68	93.64	35.86	61.7
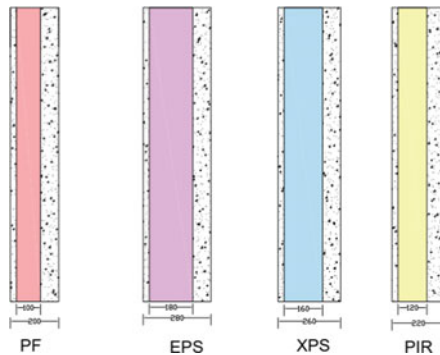
Fig. 14 Required insulation thickness for a PCSP to meet a U-value of 0.185 $Wm^{-2}K^{-1}$ using different materials

4 Conclusions

Transient thermal analyses of PCSP with different core thicknesses were carried out to study the fire performance of PCSP and to select the optimum thickness of PCSP. Also, the thermal performance of varying insulating materials such as EPS, XPS, PF and PIR have also undergone the investigation and the best thermally efficient material was based on thermal transmittance. From the finite element analysis, the following conclusions are drawn.

- Fire performance improvement was observed when the thickness of insulation wythe is increased. The maximum thickness of insulation was limited to 160 mm since increasing thickness further contributes comparatively a little increase in thermal performance.
- The lowest U-value of 0.22 $Wm^{-2}K^{-1}$ was obtained for EPS160 as compared to EPS insulation with other thicknesses.

- In this study, four different types of insulation materials were selected as internal wythe in PCSP. The analytical study demonstrated that the Phenolic Foam insulation had a better thermal performance as compared to other insulation types. The U-value calculated for PF was equal to 0.053 $Wm^{-2}K^{-1}$, which is 75.9% lesser value as compared to PCSP with EPS insulation.
- PF was identified as the best thermal resistant insulating core wythe for a PCSP with 160 mm thickness. By adopting this model, the building can ensure thermally cool, lightweight and economical. Since PF is 60% less costly as compared to EPS per square meter, as well as PF is cheaper as compared to other two insulations also.\

References

1. Hou, H., Ji, K., Wang, W., Bing, Q., Fang, M., Qiu, C.: Flexural behavior of precast insulated sandwich wall panels: full-scale tests and design implications. Eng. Struct. **180**, 750–761 (2019)
2. Henin, E., Morcous, G., Tadros M.K.: Precast/prestressed concrete sandwich panels for thermally efficient floor/roof applications. Pract. Period. Struct. Des. Constr. **19**(3) (2014).
3. Gara, F., Ragni, L., Roia, D., Dezi, L.: Experimental tests and numerical analysis of floor sandwich panels. Eng. Struct. **36**, 258–260 (2012)
4. Upasiri, I.R., Konthesigha, K.M.C., Nanayakkara, S.M.A., Poologanathan, K., Gatheeshgar, P., Nuwanthika, D.: Finite element analysis of lightweight composite sandwich panels exposed to fire. J. Build. Eng. **40**, 1–15 (2021)
5. Ariyanayagam, A.D., Mahendran, M.: Development of realistic design fire time–temperature curves for the testing of cold-formed steel wall systems. Front. Struct. Civ. Eng. **8**(4), 427–447 (2014)
6. Shams, A., Horstmann, M., Hegger, J.: Experimental investigations on textile-reinforced concrete (TRC) sandwich sections. Compos. Struct. **118**, 643–653 (2014)
7. O'Hegarty, R., Kinnane, O.: Review of precast concrete sandwich panels and their innovations. Constr. Build. Mater. **233**, 1–19 (2020)
8. O'Hegarty, R., Reilly, A., West, R., Kinnane, O.: Thermal investigation of thin precast concrete sandwich panels. J. Build. Eng. **27**, 1–11 (2020)

Study on Steel Slit Shear Walls with Different Characteristics of Hysteretic Behavior

Aleena Babu and Gayathri Krishnakumar

Abstract Energy dissipation devices are usually used to absorb or consume a portion of input energy from earthquake or wind, for reducing the structural response and to protect structural members. Steel Slit Shear Wall SSSW is one type of metallic damper having advantages of better ductility, easier installation and repair and higher energy dissipation. It is an excellent yield type energy dissipation device which doesn't require any welding. It could be used in structures as energy dissipation fuses. This work focus on the development of economic shear wall with high yielding capacity without buckling failure to ensure the shear resistance of the building by varying the parameters like slit spacing and slit gap and are tested under the quasi static cyclic loading condition.

Keywords Steel slit shear wall · Seismic resilience · Energy dissipation · Metallic damper · Ductility

1 Introduction

Several energy dissipation devices have been developed in recent years to attain seismic resilience. The most popular devices are those that disperse energy by yielding materials such as steel plates, steel bars, steel strips, and other similar materials. The plastic energy dissipation is concentrated in certain regions to reduce the structure's damage.

Steel slit shear walls (SSSW), which are made up of rows of vertical connections, are extremely important in resisting seismic loads as a horizontal load carrying member. It can be very useful in the design and retrofit of structures because it is an outstanding energy dissipative device. Furthermore, the wall's steady mechanical

A. Babu (✉) · G. Krishnakumar
Department of Civil Engineering, FISAT, Angamaly, India
e-mail: aleenababu88@gmail.com

G. Krishnakumar
e-mail: gayathrikrishnakumar@fisat.ac.in

behaviour, as well as its production and installation flexibility, make it a viable structural option. Strength and stiffness are commonly used as major criteria for evaluating the wall's properties. However, because to the complicated technique used to solve several geometric variables, no universal design principles are achieved. Furthermore, in terms of energy dissipation, simply measuring stiffness and strength will not fully reflect seismic behaviour of the wall, and a comprehensive measure to analyse seismic behaviour will be lacking.

The contributing factors for the hysteretic behaviour of the steel slit shear wall (SSSW) were investigated by Haifeng Bu, Liusheng He, and Huanjun Jiang. Four SSSW specimens were designed, with design parameters of link configuration (flat and twisted) and steel property (mild carbon steel and low yield steel). The structural responses are compared in terms of maximum inter-story drift, residual inter-story drift, and story shear force distribution. Toko Hitaka and Chiaki Matsui investigated a novel type of earthquake-resistant element: A steel plate shear wall with vertical slits. According to the test results, restricting the width-to-thickness ratio in the flexural linkages to less than 20 ensures that the walls can withstand around 3% drift without significant hysteretic degradation. K. Ke and Y.Y. Chen presented When a wall is subjected to lateral stresses, the calculation method for energy dissipation of links, as well as steel plate shear walls with slits, can accurately forecast the energy dissipation of the wall. When the dimension of the plate is validated, it is discovered that the energy dissipation capacity is dictated by the aspect ratio of flexural connections, despite the fact that plastic buckling reduces energy absorption. G. Cortés, J. Liu investigated that Steel Slit Panel Frames (SSPFs) are a lateral force resisting system (LFRS) created to resist seismic loads in buildings. The energy in the system is dissipated by the Steel Slit Panels (SSPs). This paper first introduces the system; it then discusses three different SSPs that may be used for the system. Muhammed Gürbüz and İlker Kazaz studied the relationship between the collapse behaviors of steel plate shear walls (SPSW). Using design parameters, a formula is created to estimate the ultimate drift ratio of SPSWs. The infill plate-frame interaction is explored, and it is discovered that for acceptable seismic behaviour of SPSWs, 25% of the total shear force resisted by the frame component is required.

This paper is intended to come up with an economic shear wall with high yielding capacity without buckling failure to ensure the shear resistance of the building by varying the parameters like slit spacing and slit gap and tested under quasi static cyclic loading.

2 Finite Element Formulation

2.1 Geometry of the Component

The height of the SSSW component was 1000 mm and the one end of the specimen is fixed. The details of the specimen are illustrated in Table 1. It consists of steel plate with number of slits with different spacing and slit size. Dimension of the shear panel adopted was 480 × 420 mm. The stiffening ribs were arranged in such a way

Table 1 Details of specimen

Specimen	Dimension of shear pannel	Slit size (mm)	Number of slits
SSSW-1	1150 × 1720	2	0
SSSW-2	1150 × 1720	2	1
SSSW-3	1150 × 1720	2	3
SSSW-4	1150 × 1720	2	5
SSSW-5	1150 × 1720	2	7

that ribs are equally spaced in horizontal and vertical direction. Figure 1 and 2 shows the specimen details. Specimen was made of low yield steel which is having a plate thickness of 9, 4.6 and 3 mm and has a yield stress of 100 Mpa. The specimen was installed with rotation of 90°.

2.2 Material Properties

A bilinear stress strain curve was assumed for modelling the component. The material properties used for the study is as shown in Table 2. The modulus of elasticity E for the steel used in shear panel 2×105 MPa. The yield stress of the steel slit shear wall is 100 Mpa.

2.3 Finite Element Modeling

The analytical study of the SSSW components were done to study the post buckling behavior and the load carrying capacity under push over analysis. 16 finite element models were developed to evaluate influence of the various slit spacing and slit size on the seismic performance of steel shear walls. The model consists of a shear panel and slits which increase the yielding capacity as shown in figure. The elements were modelled using SOLID 186 element. The 20-node solid element SOLID 186 has quadratic displacement behavior. The element is made up of 20 nodes, each with three degrees of freedom: Translations in the x, y, and z dimensions. The mesh size used was 20 mm, and the meshing shape was Hexahedron.

2.3.1 Arrangement of Slits

In order to study the influence of the slits on the load carrying capacity 16 models were developed as shown in Tables 1 and 3. The material properties of the slits was kept constant and the spacing and slit size of the shear plates were varied for each of the model.
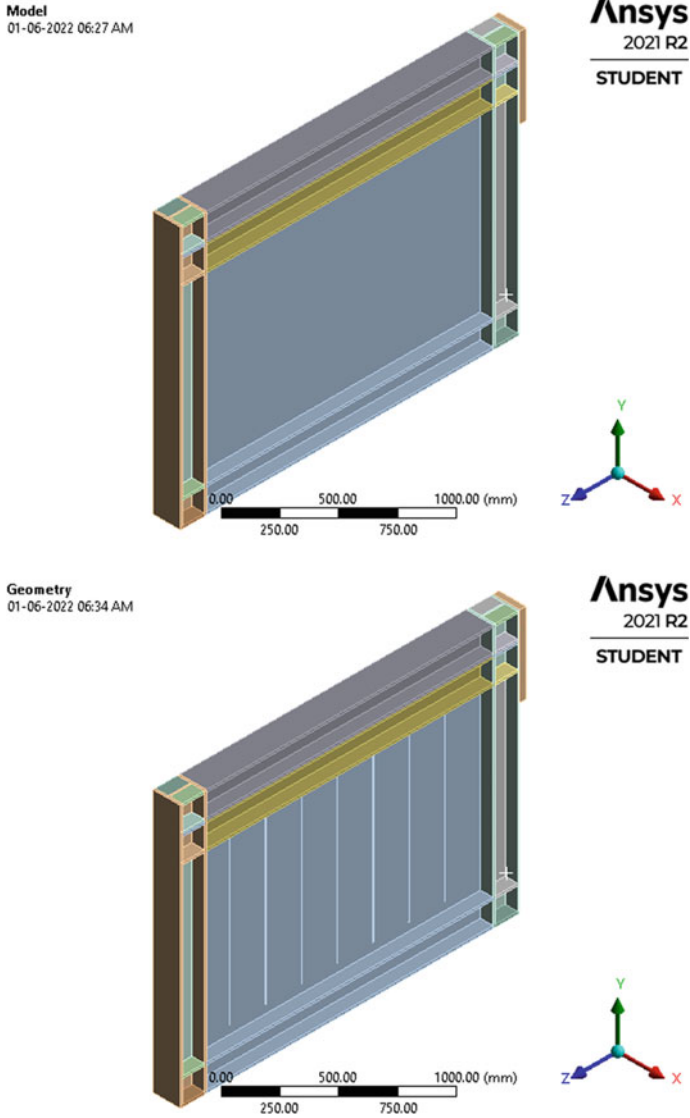
Fig. 1 Geometry of the specimen

2.3.2 Support Condition and Loading

One end of the steel slit shear wall is fixed and a lateral displacement is provided at the top interface in the form of load. The displacement value is provided by trial and error method. The support condition and loading of the steel slit shear wall is as shown in the Fig. 2.
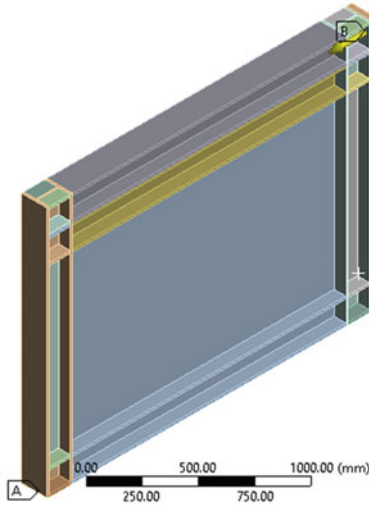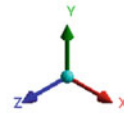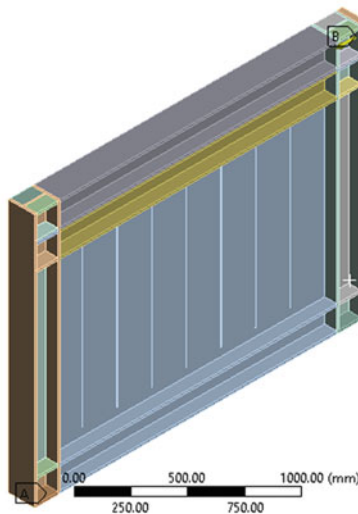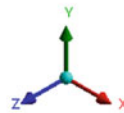
Fig. 2 Boundary condition of slitted shear wall specimen

Table 2 Material properties

Dimension of shear wall (mm)	420 × 360 mm
Thickness of plate	9, 4.3, 2 mm
Yield stress	100 Mpa
Slit gap	2, 10, 20 mm
Height	1.5 m
Material	Low yield stress

Table 3 Comparison of ultimate load and deflection of specimen

Specimen	Deflection (mm)	Load (kN)	Ductility
Without slits	5.58	1043.1	0.18
With 1 slit	14.59	1072.1	1.06
With 3 slits	22.49	715.68	1.20
With 5 slits	35.38	676.17	1.76
With 7 slits	83.50	665.76	3.67

3 Results and Discussion

The models with various slit configurations were analyzed. Failure patterns were obtained for all the models. Force reaction and corresponding deformation were obtained for all the models. Load-deformation curves were also plotted for the same. The Deformation pattern of the model under loading is as shown in Fig. 3.
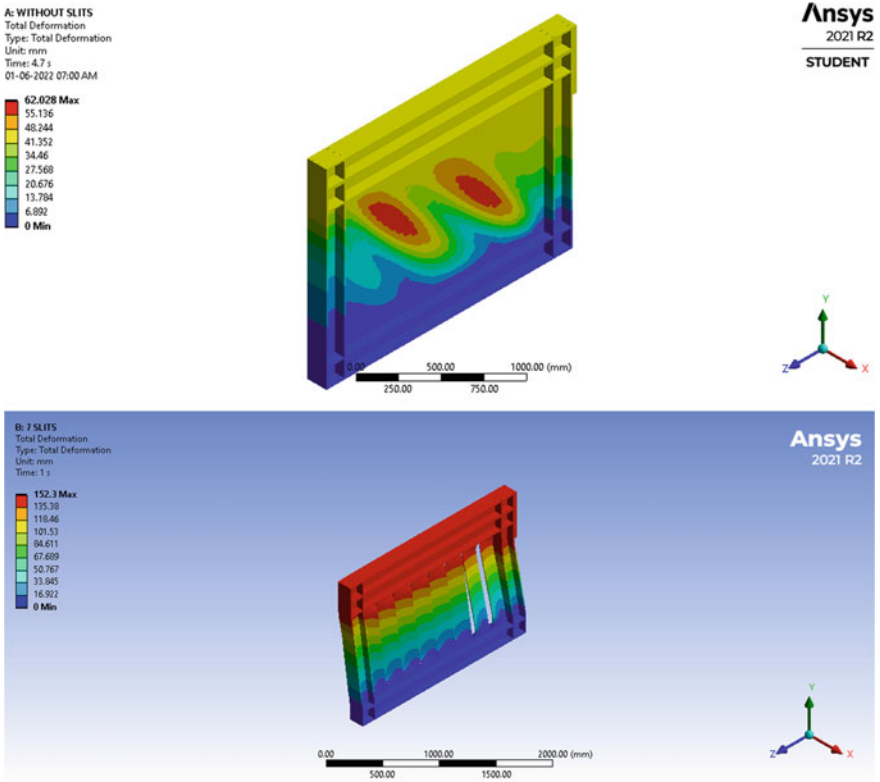
Fig. 3 Deformed specimen
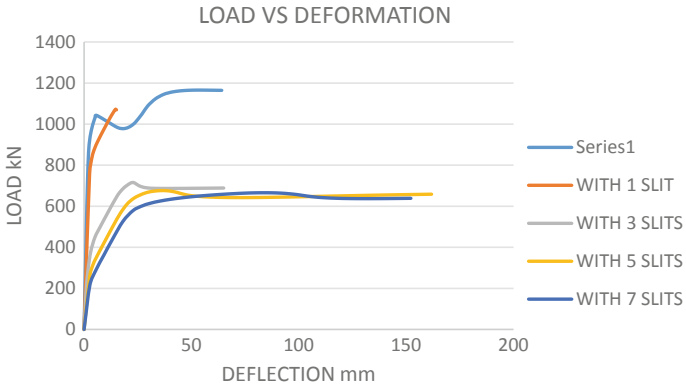
Fig. 4 Load v\s deformation curve
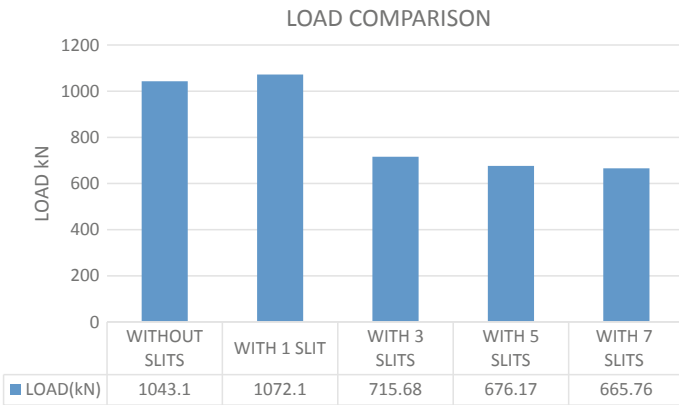
Fig. 5 Load comparison

Figure 4 indicates load v/s deformation curve obtained from the analysis. Graph clearly indicates that model with more number of slits and with more slit size i.e. SSSW 14, SSSW 15, SSSW 16 has higher load carrying capacity (Figs. 5 and 6).

DEFLECTION COMPARISON

	WITHOUT SLITS	WITH 1 SLIT	WITH 3 SLITS	WITH 5 SLITS	WITH 7 SLITS
■ DEFLECTION(mm)	5.5846	14.599	22.496	35.388	83.5
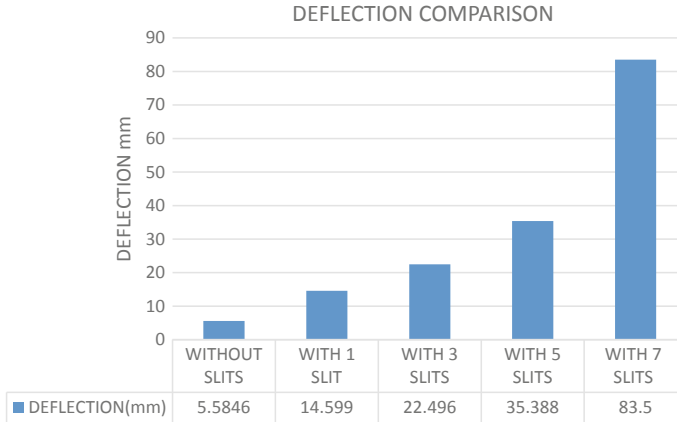
Fig. 6 Deflection comparison

4 Conclusion

SSSW component exhibits excellent lateral load-resisting capacity for newly built steel structures or damaged reinforced concrete structures. They also provide sufficient lateral stiffness to limit the lateral inter-story drift. Slits were introduced of the same material properties but varying slit spacing and slit size. Nonlinear static analysis was carried out for each of the SSSW specimen to determine the influence of various slit configuration on the load carrying capacity of the steel slit shear wall. The results of the analysis showed that SSSW specimen with slits exhibits better seismic performance. The test results of the study showed that the model with more number of slits exhibited better yielding capacity and can take more deflection. By providing the slits over entire shear panel, the buckling of the panel can be reduced and thus load carrying capacity can also be increased.

References

1. Formisano, L., Lombardi, F.M.: Mazzolani, Full and perforated metal plate shear walls as bracing systems for seismic upgrading of existing RC buildings. Ingegneria Sismica **33**(1–2), 16–34 (2016)
2. Ahmadi, H.M., Sheidaii, M., Tariverdilo, S., Formisano, A., De Matteis, G.: Experimental and numerical study of perforated steel plate shear panels. Int. J. Eng. Trans. A: Basics **33**(4), 520–529 (2020)
3. Sun, G., Zhu, Y.: Cyclic testing of an innovative self-centering X-braced ductile shear panel. Eng. Struct. **244**, 112732 (2021)
4. Mateus, J.A.S., Tagawa, H., Chen, X.: Buckling-restrained steel bar damper for spine frame system. Eng. Struct. **229**, 111593 (2021)
5. Jiang, H., Bu, H., He, L.: Study of a new type of self-centering beam–column joint in steel frame structures. Struct. Des. Tall Spec. Build. **29**, e1779 (2020)

6. Hitaka, T., Matsui, C., Imanura, T., Hatado, T.: Elastic–plastic behavior of steel bearing walls with slits. J. Struct. Constr. Eng. AIJ **519**, 111–117 (1999)
7. Hitaka, T., Matsui, C.: Experimental study on steel shear wall with slits. J. Struct. Eng. **129**(5), 586–595 (2003)

Strength Optimization of Litzka Type Welded Beams by Varying Angle of Castellations

Swathy and Asha Joseph

Abstract Castellated steel beams are the members which are crafted from hot rolled I-section steel beams by cutting the web in a zigzag pattern and re-welding the generated two halves in order to form a castellated steel beam with hexagonal openings so that the depth of section can be increased. Generally, hexagonal shaped openings are provided in the web of the steel beam; however, the provision of spacer plate can lead to octagonal shape of web openings which leads to an increase the depth of beam. Nowadays, castellated beams are very popular in the field of building construction due to their ease of service provision, strength and low cost. There are various advantages for castellated steel beams compared to solid web beam. Castellated Steel Beam can reduce the floor height of buildings by allowing the service pipes, wires and ventilation ducts to pass through web openings. The use of castellated beams can efficiently reduce usage of steel in the structures. The study focuses on the effect of varying angle of castellation on the Litzka type beams and to determine the optimum angle giving maximum strength. Nonlinear analysis is performed on the Litzka type castellated beams with welded connections using ANSYS software. The maximum load carrying capacity was observed for angle of castellation of 55° with 100 mm spacer plate and it was found that larger depth of spacer plates can be provided for beams of larger angle of castellation.

Keywords Castellated steel beams · I-Section · Litzka type beams · Octagonal openings · Varying angles

Swathy (✉) · A. Joseph
Department of Civil Engineering, Federal Institute of Science and Technology, Angamaly, Kerala, India
e-mail: swathyasokan035@gmail.com

1 Introduction

The idea of creating single web openings in wide-flange steel beams in order to pass service lines through the beam stems back to the early use of steel sections. Castellated beams are defined as expanded I-section steel beams with hexagonal openings in the web [1]. Cellular beams are defined as expanded steel sections with circular openings in the web section. Castellated steel beams with repeating web openings and expanded web sections were introduced in 1910 by the Chicago Bridge and Iron Works (Das and Srimani, 1984) [1]. This idea of expanded sections with web openings was also developed independently by Boyd in Argentina in 1935 and was later patented in the United Kingdom (Knowles, 1991) [1].

Various efforts were put forward by the structural engineers for improving the behaviour of the materials used for construction and their geometrical shapes. These efforts mainly focused on obtaining lighter weight, higher strength and cheaper materials for the construction of steel structures. Castellated steel beams were developed as an improvement in built-up structural members, during the Second World War, to modified hot rolled I-section steel beams by increasing their stiffness and strength [2].

The fabrication process of castellated steel beam involves cutting wide flange standard I-sections steel beam along its centreline and re-joining the generated two halves using welded connection. This results in an increase of the overall I-section depth by a maximum of 50% and significantly enhances the flexural strength of the beam [2]. The increase in the overall depth of the beam, which is attained as a result of the fabrication process, modifies the stiffness and strength of castellated steel beam compared to the hot rolled parent section. The addition of steel plates in between the two halves of the tee sections can lead to a further increase in the overall depth of the section. These incremental plates are known as "Spacer Plates" [2]. The redistribution of the stresses within the members are encountered due to the presence of openings in the web of the castellated beams and this leads to a decrease in the stiffness of the beams, resulting in larger deflection. As a result local web distortions are more likely to accompany the lateral torsional buckling deformation leading to the occurrence of lateral distortional buckling mode. Stiffness can be increased and the moment resistance of the steel plates can be strengthened by providing stiffeners along longitudinal and transverse directions and also along the edge of opening. The buckling strength of the web can be increased by providing these stiffeners [2].

Numerous studies were conducted to study the performance of castellated beams under different geometric conditions. Castellated beams with circular, hexagonal, octagonal, rectangular and diamond shaped openings are studied. Listiyono Budi (2016) [3] conducted a optimization study of the size and distance of hexagonal holes in castellated beams using finite element analysis. The optimum angle size and hole distance was found out in this study. Morkhade et al. (2021) [4] studied the effect of varying eccentricity on castellated beams. A parametric study was carried out by varying openings eccentricity. It was concluded that the provision of eccentricity can reduce the strength by 9 to 16%. Bhat (2020) et al. [5] analytically studied the

behaviour of hybrid steel beams with web openings. The hybrid beam considered for the study have higher steel grade for flange than that of web. Hybrid beams finds application when the design requirement is not satisfied by hot rolled sections or homogeneous built-up sections. An optimum ratio of spacing and width of opening was found in the study. A research work was carried out by Prabhakaran et al. (2021) [6] to achieve a cold formed castellated steel beam with openings of diamond shape which is more economical and have limited buckling. Different buckling modes and load carrying capacity of the beams were studied through numerical analysis and experimental investigations. Mei Liu (2020) [7] conducted a numerical investigation on the behaviour of a Bolted Castellated Steel Beam (BCSB) with web openings of octagonal shape. The residual stresses developed in the web post due to welding can be avoided using high strength bolted connections. However, this can lead to a reduction in the strength of the castellated beam. A new web opening shape was proposed by Mehetre et al. (2020) [8]. He proposed a castellated beam with sinusoidal openings to avoid the failure of the beam due to shear stress concentration at the corners of other shapes of openings. The maximum moment carrying capacity and deflection of the castellated steel beams was studied. The results gave best fillet radii for maximum moment carrying capacity.

This paper aims at studying the effect of introduction of spacer plates into castellated beams of different angle of castellation and finding an optimum depth of the spacer plate from the consideration of maximum strength.

2 Analytical Program

2.1 Material Properties

Standard I-section beam of mild steel material is considered for this analysis. The average value of yield stress (σ_y) of the steel considered for the study is 233.3 MPa, the Young's modulus (E) is 210 GPa and Poison's ratio is 0.3. The density of the steel is 7850 kg/m^3.

2.2 Geometrical Parameters

Standard I-section beam, ISMB150, was used as the parent section for the analysis. Castellated beams of different angles were produced from the parent I-section to increase the depth of the section which in turn increases the strength of the section. Spacer plates of various depths are inserted for further modification of strength. In the present study, a castellated beam with twelve hexagonal openings were considered over a span of 3.1 m. This was further modified into octagonal openings by the introduction of spacer plates.

Table 1 Dimensions of ISMB150

1	Width of flange (b_f)	75 mm
2	Thickness of flange (t_f)	8 mm
3	Depth of web (d_w)	134 mm
4	Thickness of web (t_w)	5 mm
5	Overall depth (h)	150 mm

The geometrical parameters of the parent section (ISMB150) considered for this study is given in Table 1. The geometry of castellated beams with and without spacer plates is shown in Table 2 and the Fig. 1 depicts the geometry of the castellated beam in which b is the horizontal projection distance of the hypotenuse of hexagonal hole, e is the horizontal distance between adjacent castellation holes, n is the number of hexagonal holes in the castellated steel beam and φ is the angle of castellation of the hexagonal holes.

2.3 Modelling and Analysis of Castellated Beam

For the study proposed in this paper, different models were created for performing static analysis. In this study, the development of the finite element models and the analysis was done in the software ANSYS 2022 R2 version. Each beam had a span of 3.1 m with twelve number of castellation's. The geometry of the beams are given in Table 2. The beams were modelled using solid 186 element which is defined a twenty-node structural 3D element with 3° of freedom per node. The beams were provided with hinged support at both the ends and subjected to two-point loading. The load was provided using displacement controlled method. Concentrated loads are applied on the flange in order to distribute the load through the flange width so that the local failure of the beam due to load application can be prevented. This provides a realistic method for applying the load on the beam.

The parametric study is conducted by considering two parameters. The parameters considered are angle of the castellation and the depth of the spacer plates. The angles considered for this study are 45, 50, 55, 60 and 65° and the depth of the spacer plates provided are 25, 50, 75 and 100 mm.

Table 2 Geometry of castellated beams with and without spacer plates

Specimen	Ø (degree)	b (mm)	e (mm)	n	Spacer plate (mm)
CB45	45	75	50	12	0
LB45-25	45	75	50	12	25
LB45-50	45	75	50	12	50
LB45-75	45	75	50	12	75
LB45-100	45	75	50	12	100
CB50	50	63	62	12	0
LB50-25	50	63	62	12	25
LB50-50	50	63	62	12	50
LB50-75	50	63	62	12	75
LB50-100	50	63	62	12	100
CB55	55	52.5	72.5	12	0
LB55-25	55	52.5	72.5	12	25
LB55-50	55	52.5	72.5	12	50
LB55-75	55	52.5	72.5	12	75
LB55-100	55	52.5	72.5	12	100
CB60	60	43.5	81.5	12	0
LB60-25	60	43.5	81.5	12	25
LB60-50	60	43.5	81.5	12	50
LB60-75	60	43.5	81.5	12	75
LB60-100	60	43.5	81.5	12	100
CB65	65	34.5	90.5	12	0
LB65-25	65	34.5	90.5	12	25
LB65-50	65	34.5	90.5	12	50
LB65-75	65	34.5	90.5	12	75
LB65-100	65	34.5	90.5	12	100
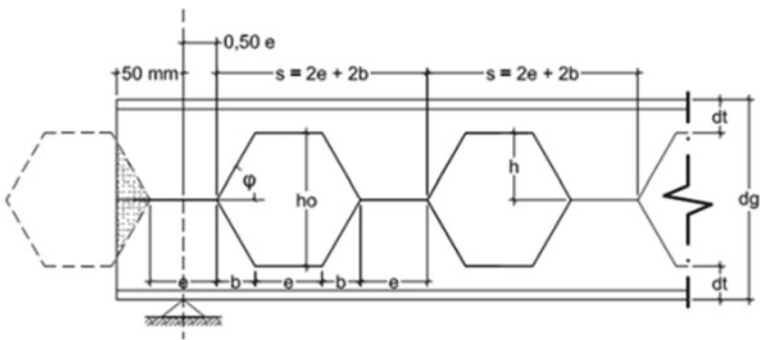
Fig. 1 Geometry of castellated beam

Table 3 Maximum load carrying capacity of the castellated beam with and without spacer plates

Specimen	Angle (degree)	Spacer plate (mm)	Load (kN)
CB45	45	0	68.613
LB45-25		25	64.76
LB45-50		50	62.39
LB45-75		75	57.58
LB45-100		100	51.046
CB50	50	0	67.35
LB50-25		25	72.59
LB50-50		50	74.058
LB50-75		75	70.42
LB50-100		100	64.64
CB55	55	0	65.9
LB55-25		25	70.96
LB55-50		50	74.73
LB55-75		75	77.48
LB55-100		100	78.2
CB60	60	0	64.105
LB60-25		25	68.58
LB60-50		50	71.962
LB60-75		75	74.689
LB60-100		100	76.935
CB65	65	0	62.45
LB65-25		25	66.34
LB65-50		50	69.351
LB65-75		75	71.93
LB65-100		100	74.018

3 Results and Discussions

The effect of varying the angle of castellation and depth of spacer plate were investigated by comparing the maximum load capacity of the section obtained from the static structural analysis of the beam. The results of the study is given in Table 3.

The load-deformation curve of Litzka beam provided with a spacer plate of 25 mm thickness and varying angle of castellation is shown in Figs. 2, 3 and 4.
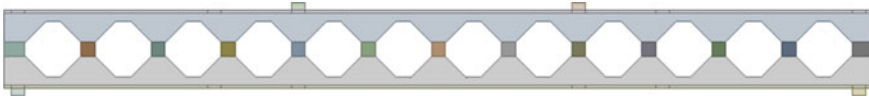
Fig. 2 Finite element model of castellated beam
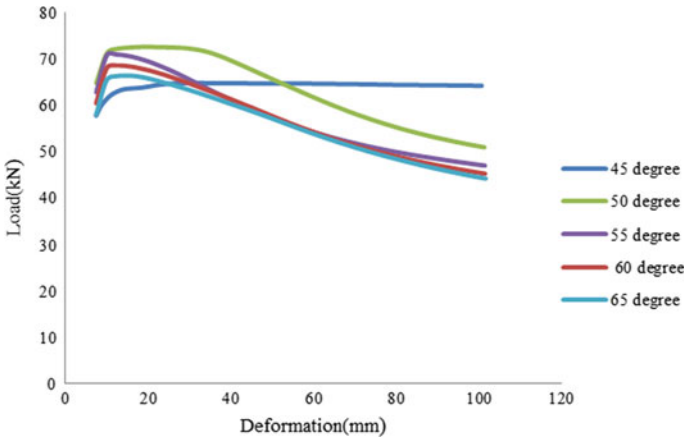
Fig. 3 Load-deformation curve of Litzka beam with 25 mm spacer plates

The results from the parametric study shows that the maximum load carrying capacity for an angle of castellation of 45° is 68.613 kN and is observed for the model without spacer plate. For an angle of castellation of 50° the maximum load capacity is 74.058 kN for castellated beam of 50 mm spacer plate depth with an increase in strength by 9.95%. An increase in load carrying capacity of 18.66% was observed for castellated beam of 55° angle of castellation with a load of 78.2 kN. For an angle of castellation of 60 and 65° there was a load increment of 20.01 and 18.52% respectively with loads of 76.935 and 74.018 kN.
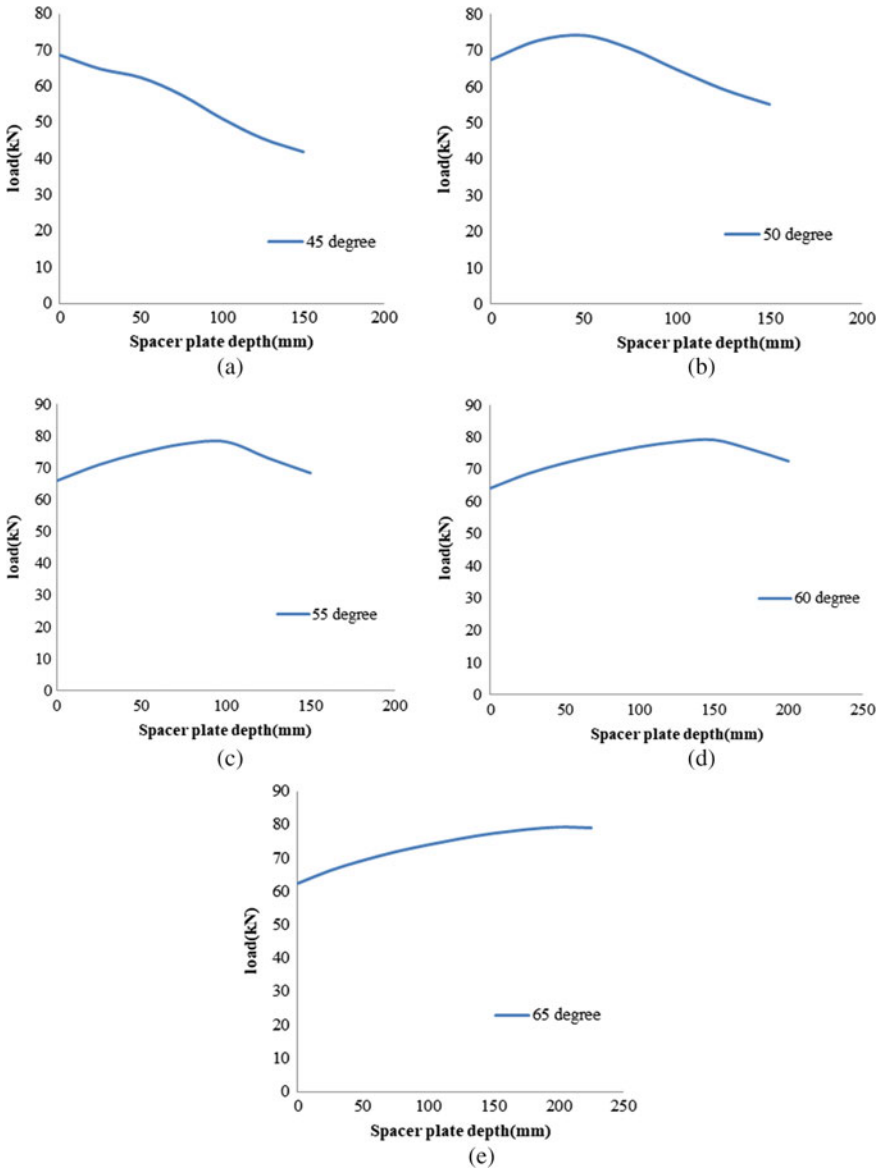
Fig. 4 Load v/s spacer plate depth graph for: **a** 45° **b** 50° **c** 55° **d** 60° e 65°

4 Conclusions

The behaviour of Litzka beam with octagonal openings formed as a result of providing spacer plates in castellated beams of hexagonal openings under two-point loading

was analytically investigated in the present study. Parametric study was conducted by varying angle of castellation and the depth of the spacer plates. The aim of the work was to develop a Litzka beam with better strength performance. The optimum depth of the spacer plate for each angle of castellation was found out. The main conclusions of the study are listed below:

- A continuous decrease in load carrying capacity is observed while inserting and increasing the depth of the spacer plates in a castellated beam with an angle of castellation of 45°
- For an angle of castellation of 50° maximum load carrying capacity is observed for litzka beam with 50 mm spacer plates with an increase in the strength by 9.95% compared to normal castellated beam.
- Similarly for the angle of castellation of 55, 60 and 65° an increment in load carrying capacity of 18.66, 20.01 and 18.52% respectively is observed for a spacer plate depth of 100 mm.
- Maximum load carrying capacity was observed for angle of castellation of 55° with 100 mm spacer plate.
- Larger depth of spacer plates can be provided for beams of larger angle of castellation.

References

1. Sameer, S., Fares, F., John Coulson, S., David, W., Dinehart, T.: Steel Design Guide 31, Castellated and Cellular Beam Design, AISC, United States of America (2016)
2. Hayder Wafi Ali Al-Thabhawee, F., Muslim Abdul-Ameer Al-Kannoon, S.: Improving behavior of castellated beam by adding spacer plat and steel rings. J. Univ. Babylon Pure Appl. Sci. **26**(4), 331–344 (2018)
3. Listiyono Budi, F., Sukamta, S., Partono, W.: Optimization analysis of size and distance of hexagonal hole in castellated steel beams. Procedia Eng. **171**, 1092–1099 (2017)
4. Samadhan, G., Morkhade, F.: Experimental and analytical investigation of castellated steel beams with varying openings eccentricity. J. Inst. Eng. (India) Ser. A **102**(2), 479–488 (2021)
5. Bhat, R.A.F., Gupta, L.M.: Behaviour of hybrid steel beams with closely spaced web openings. Asian J. Civ. Eng. **22**(1), 93–100 (2021). https://doi.org/10.1007/s42107-020-00300-9
6. Prabhakaran, S.F., Maboob, S.A.S.: Numerical analysis and experimental investigation on behavior of cold-formed steel castellated beam with diamond castellation. Int. J. Steel Struct. **21**(3), 1082–1091 (2021)
7. Mei Liu, F.: Web-post buckling of bolted castellated steel beam with octagonal web openings. J. Constr. Steel Res. **164**, 105794 (2020)
8. Mehetre, A.J.F., Talikoti, R.S.S.: Effect of fillet radii on moment carrying capacity of sinusoidal web opening castellated steel beams in comparison with hexagonal web openings. Iran. J. Sci. Technol. Trans. Civ. Eng. **44**(1), 151–161 (2020)
9. Ehab Ellobody, F.: Interaction of buckling modes in castellated steel beams. J. Constr. Steel Res. **67**(5), 814–825 (2011)
10. Sameer Fares, F., Coulson, J.S., Dinehart, S.D.: Castellated and cellular beam design. American Institute of Steel Construction (2016)
11. Richard Frans, F.: Numerical modelling of hexagonal castellated beam under monotonic loading. Procedia Eng. **171**, 781–788 (2017)

12. Soltani, M.R., Boucha¨ır, A.F., Mimoune, M.S.: Nonlinear FE analysis of the ultimate behavior of steel castellated beams. J. Constr. Steel Res. **70**, 101–114 (2012)
13. Peijun Wang, F.: Shear buckling strengths of web-posts in a castellated steel beam with hexagonal web openings. J. Constr. Steel Res. **121**, 173–184 (2016)
14. Cyril Thomas, A., Baskar, K.: Assessment of load carrying capacity of thin-webbed castellated beam. In: Rao, A., Ramanjaneyulu, K. (eds.) Recent Advances in Structural Engineering, Volume 1. LNCE, vol. 11, pp. 339–350. Springer, Singapore. https://doi.org/10.1007/978-981-13-0362-3_27
15. Walid Zaarour, F., Richard Redwood, S.: Web buckling in thin webbed castellated beams. J. Struct. Eng. **122**, 860–866 (1996)

Computerized Waste Guidance System

Sam Franklin Nadar, Maitrey Patel, Steffi Stephen, and P. Ashwini

Abstract In today's world, with the rapid increase in population and urbanization, the need for efficient solid waste management has increased substantially. If the solid waste management program of the society does not keep up with the current pace of urbanization, it will result in the procurement of more land for landfills, which in turn will serve as grounds for the breeding of mosquitoes and other flies that are carriers of various diseases. In this study, a single bin with two partitions for dry and wet waste was developed that segregates the waste at the source itself. The three main components used by the bin were- a Logitech camera for recognizing the waste; IR sensors for checking the filled level of the bin and a raspberry pi which works as the CPU of the machine. This technology will reduce the need for manual segregation of waste and also improves community hygiene, quality of life, and environment. It will be a prime leap towards the future of solid waste management in an integrated smart city and will have a major role in the conservation of carbon footprint for the upcoming generation.

Keywords SWM · Environment · Segregation · Sensors · Landfills · Smart bin · Management

1 Introduction

In many countries, the waste collected is either incinerated or disposed off in the landfills or water bodies. The world generates 2.01 billion tons of municipal solid waste annually out of which 69.6% is disposed off in landfills and only 19% is used for composting or recycling. (Source: datatopics.worldbank.org) In the third world countries, the situation is even worse as the landfills are overfilling with waste and the water bodies are getting polluted with non-degradable plastic waste, leading to

S. F. Nadar · M. Patel · S. Stephen (✉) · P. Ashwini
Pillai HOC College of Engineering and Technology, Rasayani, India
e-mail: steffistephen5492@gmail.com

P. Ashwini
e-mail: ashwininairp@gmail.com

the creation of a toxic environment around it. In India, 80% of 1.5 lakh metric ton daily garbage remains exposed or untreated. (Source: indiatoday.in) Many studies have addressed the drawbacks of the conventional solid waste management system practiced in different parts of the world. [1] the SWM system in Pudong, China fails to achieve the maximum degree of recycling and reuse of resources [2] assessment of MSW in Puducherry shows the shortcomings of the MSWM system and problems caused due to dump yards and landfills. The harmful effects of landfills ground-water contamination in Mexico, evidence of leachate in groundwater, air pollution caused due to GHG emissions from landfills in Chennai and air pollution caused by greenhouse gas emissions from the landfills [3–5], and [6].

Many studies also point out how increasing recycling and reusing solid waste can help to generate money [7] pointed out that by scientific management of solid waste Mumbai can generate revenue of Rs. 33 lakhs (approx. $44,000) per day; the plastic waste generation and its potential recycling of the solid waste [8] and how municipal solid wet waste can be used for composting. [9] Due to the lack of proper ways for segregation at the source level, major portion of the waste generated in the world is not recycled. This in turn leads to many problems like the accumulation of waste, formation of toxic gases, contamination of recyclable dry waste, creation of breeding grounds for vector carrying diseases, etc. To minimize the consequences solid waste management now-a-days focuses on source level segregation that increases the rate of recycling and decreases the need for landfills. This paper illustrates the working of automated smart bins which helps in segregation at the source level thereby increasing the rate of recycling, composting, etc. This bin makes use of the technology Internet of Things (IoT) to classify the waste into dry and wet category. The dry waste segregated can hence be send for recycling and the wet waste for composting and biochar.

2 Methodology

2.1 Integrated Monitoring and Control System

By using the application of IoT on waste generation, segregation, collection, and recycling, an integrated system is developed. This developed computerized waste guidance or management system can manage all the facilities simultaneously (see Fig. 1) for proposed CWGS or CWMS. The whole system is connected to the IoT platform with the help of a Wi-Fi module ESP8266 or the Wi-Fi of R-pie, through which real-time monitoring of generation and recycling happens.
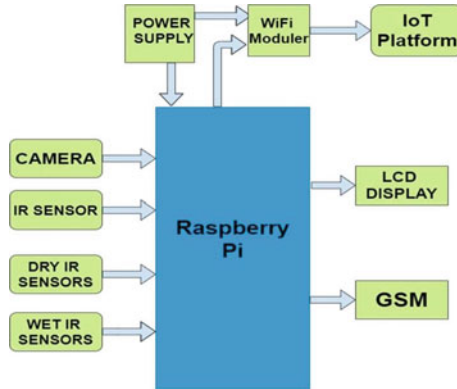
Fig. 1 Block diagram for the proposed computerized waste guidance system

2.2 Integrated Monitoring System

The proposed CWGS consists of a waste generation monitoring system, waste segregation system, waste collection monitoring system, and waste recycling monitoring system. These systems are connected with the individual sensors and camera for waste generation system monitoring. IR sensors are used along with the camera for the detection and segregation of waste. Two IR sensors are used for the waste collection system and for the recycling monitoring system of waste management. The camera and sensors are interfaced with raspberry pi, which works as a microcontroller. The data sent by the various systems are analyzed and monitored in raspberry pi. The raspberry pi is interfaced with LCD, GSM, and the IoT platform. The output result data from the raspberry pi is transferred into the IoT platform "Thingspeak" using the Wi-Fi module.

2.3 Waste Generation and Waste Segregation System

The generation of waste increases every year in the world with an increase in population. The generation of waste cannot be in a specific cycle or pattern it will always be generated in a non-uniform manner. The generation mainly depends upon the time, season, and lifestyle of the people living in the place. The time influences the waste generation pattern, like in day time the waste is generated more than in the night time. Whereas during any vacation or festive season the waste generated in a day can be generated within an hour by a community. The lifestyle of people also plays an important role in the generation of waste. The waste in metro cities, which run 24 * 7, cannot be estimated by just the time and seasons. So all these factors make waste generation monitoring a difficult process. For efficient solid waste management, real-time monitoring of waste is required. Furthermore, the waste generation

is collected together and transported to the dump- yard for sorting of waste. Here majority of times the waste stacks up to the height of an 18–20 store building due to its mismanagement. Moreover, for the sorting of waste in the dump yards the weaker economic class section of the society is exploited. They are compromised not only in terms of their wages but also in their health and safety. Then the waste is later landfilled or is disposed in the seas, which eventually adds to the pollution of land, air, and water. Due to the mixing of different types of waste at the landfills they make the air, land, and waste around them toxic. Thus, the need for the sorting of waste at the source level itself is very crucial, but studies suggest that sorting of waste cannot be done by laymen.

2.4 Architecture of Bin

The system consists of a bin that has an IR sensor for the detection of waste. The waste is detected as soon as the waste falls on the flap of the bin. IR sensors then send the message to R-pi and then it starts the camera to recognize the waste. This detected data is sent to the Thing speak IoT platform which makes graphs and analytic data in MATLAB. This MATLAB data can be collected and stored and used for further studies and improvising the system of waste management for different types of areas. After the camera recognizes the nature of waste using the given dataset, sorting of waste into the wet and dry category is done. Based on the data recognized the flap in the bin rotates for a 60–70° angle clockwise for wet waste and counter clockwise for dry waste. By doing so the waste is sorted at the source level itself and can be collected in separate compartments of the smart bin (Fig. 2).

2.5 Waste Collection and Waste Recycling Systems

The waste collection becomes a challenge when the waste generation increases randomly as discussed above. The collection of waste has problems, if not collected timely it creates a nuisance in the surroundings. Most, of the time due to mismanagement of the waste the bin overflows. This alarms the need to change the conventional collection system and makes the monitoring of waste collection important. And many times, waste bins are not properly filled and the collection vehicle comes for collection, this causes fuel idling and eventually increases the management cost. The bin is designed and programmed for overcoming all these problems efficiently, furthermore, the collected wet waste can be carried directly to the composting, biochar, and RDF centers and dry waste to the MRF centers. This can lead to an increase in the recycling of waste and revenue can be generated by recycling waste.

Fig. 2 Flow chart for proposed generation and segregation system

2.6 Proposed Management System

The bin system consists of a two-level sensor on both the wet and dry compartments to indicate the corporation whether the bin is filled for collection. If the wet compartment is filled and the dry isn't then it will send an individual message to the registered corporation mobile number through the GSM module or Wi-Fi to the Thingspeak IoT platform. This would eventually reduce the number of sorties for the cooperation vehicle and the collected wet waste will be taken to the manure production plants and the dry waste to the MRF center directly. So, reducing the fuel costs and monitoring the waste collection system properly is ensured. The collection volume of both the wet and dry waste data will be collected from the IoT platform. This can help us to increase the rate of recycling and composting processes by studying the patterns, graphs, and analytics given from the Thingspeak platform. So, the management can improve its efficiency and thereby reducing the pollution and nuisances caused by the disposal of waste into landfills (Fig. 3).

Fig. 3 Flow chart for the proposed collection and recycling system

2.7 Assembling and Operations of the Bin

The bin is made up of a stainless-steel frame. A partition is provided to separate the wet and dry waste. The bin comes with a hood in which the camera is mounted along with the IR sensor. The hood will protect the camera and sensor from the natural elements like moisture and heat and will also avoid theft of the components. The electronic and the electrical system is concealed within it. The full bin and the components along with everything will be coated with a hydrophobic coating. A stepper motor is used to turn the flap to 70° on both sides (i.e. dry and wet side compartment of the bin). The flap has a central axis connected to the stepper motor gear for turning to either side. The flap is lined on the edges with rubber for tight and secure closing and opening to avoid leaking of bad odour and breeding of insects. A separate compartment is provided for housing the R-pi and other circuits. The separate compartment is concealed within the walls of the bin and not visible from outside. Two-level sensors are placed on each compartment for sensing the level of the waste collected which is also coated fully with a hydrophobic coating. These coating will protect the bin from wear and tear and also from the weather. To decant the waste collected from the bin two open flaps are provided below the bin which opens the other way for both the compartment hinged to a central axis on the bottom side of the bin (Fig. 4).
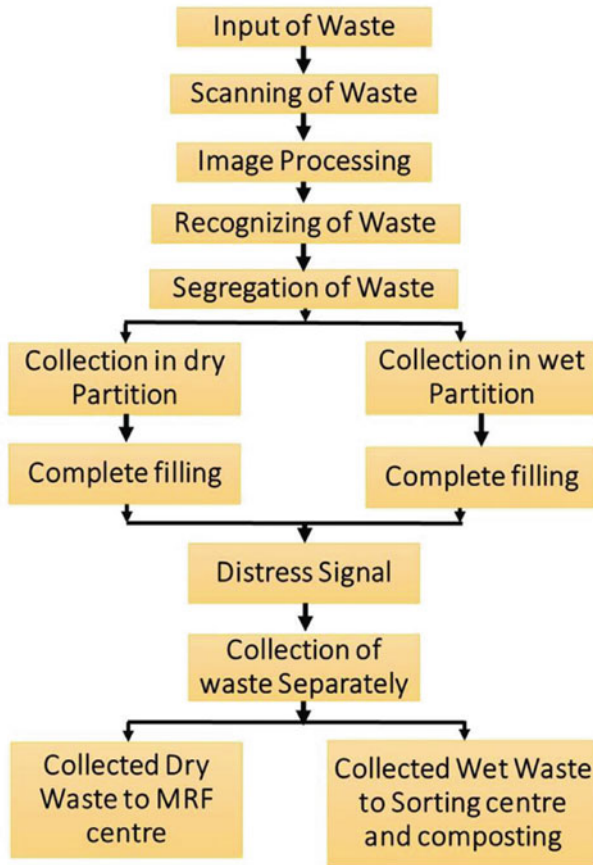
Fig. 4 Flow chart for the proposed collection and recycling system

3 Case Study

To predict the efficiency of our computerized waste guidance system, we conducted a study in the New Panvel East area, Navi Mumbai, India. The study shows the financial benefits of our waste guidance system if we provided smart bins in this area.

3.1 New Panvel Cost Estimate

New Panvel is a residential, commercial, and educational node of Navi Mumbai in Panvel city. It has an area of 24 km^2. In 2005, the population of New Panvel was about 350,000 (source: Wikipedia). If we consider 4 people in every family then the

total number of families in New Panvel would be 87,500. If we assume there are approx. 100,000 homes or families in New Panvel. Now the number of bins required in the streets of New Panvel will be about 220 (Fig. 5). So the total number of bins required in New Panvel will be equal to 1,00,220.If we consider the cost of mass manufacturing of each bin as Rs. 4000/- ($54) then the total cost of providing the bins in New Panvel is 40,08,80,000 /- ($5,345,067). Let the total cost of setting up

Fig. 5 Street light map of New Panvel area

the guidance system in New Panvel City be 45 Cores ($6,000,000), including the maintenance cost of the bins for the next five years.

3.2   Waste Generation in New Panvel

Per capita per day waste generation of big cities in India is around 0.5 kg/per person/day. Consider New Panvel waste generation per day is equal to 0.5 kg/per person/day * 350,000 = 175,000 kg/day. For the whole year the waste generation in New Panvel = 175,000 * 365 = 63,875,000 kg. Total waste produced for five years = 319,375,000 kg.

3.3   Market Estimation

The detailed calculation on expected returns from implementing the proposed system is shown in Table 1. The total amount generated by selling biodegradable, paper, plastic, metal, and glass waste would be equal to Rs. 1,89,22,33,000 ($25,229,773).

Table 1 Returns expected from the system

Type of waste	Composition (%)	Waste generated in Panvel in 5 years (Kg)	Recycling value of waste per Kg (Rs.)	Total returns (Rs.)
Biodegradable	52.32	167,097,000	5	835,485,000
Paper	13.8	44,073,750	12	528,885,000
Plastic	7.89	25,198,687.50	15	377,980,312.50
Metal	1.49	4,758,687.50	29	138,001,937.50
Glass	0.93	2,970,187.50	4	11,880,750
Inert	22.57	72,082,937.50	–	–
Others	1.00	3,193,750	–	–
Total		**31,93,75,000**		**1,89,22,33,000**

4   Result

The immediate segregation of the public waste can help in the efficient recycling of dry waste like plastic, paper, metal, etc. and the wet waste can be used for composting and biochar, etc. This system can reduce the load on landfills exponentially, which is

very harmful to the environment also the waste left after treatment would be significantly less and could be easily disposed of without causing harm to the environment. The smart bin shows up to 70–80% of accuracy in waste segregation. The bin can also provide general statistics of the type of waste generated in an area, time of maximum waste generation, etc. This can help us to increase the efficiency of the bin for different places. Overfilling of bins can be avoided since the bin notifies the corporation when it is about to be filled. Also, the amount of fuel idling caused because of the corporation vehicles can be avoided.

5   Conclusion

If the above waste guidance system is to be implemented it can not only help in reducing the harmful effects of the conventional waste management system but can also help in generating revenue. The statistical data provided by the bin can be used to improve or update the waste guidance system to its maximum efficiency. The smart bin can be modified for different places like hospitals and industries to segregate harmful toxic waste. Finally, all the information is uploading into a cloud platform that can be monitored by the users from anywhere, critical conditions are detected and monitored rapidly over the old- styled system which requires a huge quantity of time and effort. In the present century such a convenient, smart, and intelligent waste management system is certainly required.

References

1. Zhu, M., et al.: Municipal solid waste management in Pudong new area, China. Waste Manage. **29**, 1227–1233 (2009)
2. Pattnaik, S., Reddy, M.V.: Assessment of municipal solid waste management in Puducherry (Pondicherry), India. Resour. Conserv. Recycl. **54**, 512–520 (2010)
3. Reyes-López, J.A., Ramírez-Hernández, J., Lázaro-Mancilla, O., Carreón-Diazconti, C., Martín-Loeches Garrido, M.: Assessment of groundwater contamination by landfill leachate: a case in México. Waste Manage. **28**, S33–S39 (2008)
4. Rapti-Caputo, D., Vaccaro, C.: Geochemical evidences of landfill leachate in groundwater. Eng. Geol. **85**, 111–121 (2006)
5. Jha, A.K., Sharma, C., Singh, N., Ramesh, R., Purvaja, R., Gupta, P.K.: Greenhouse gas emissions from municipal solid waste management in Indian mega-cities: a case study of Chennai landfill sites. Chemosphere **71**, 750–758 (2008)
6. Zhang, C., Xu, T., Feng, H., Chen, S.: Greenhouse gas emissions from landfills: a review and bibliometric analysis. Sustainability **11**, 2282 (2019)
7. Kumar, S., Sil, A.: Challenges and opportunities in SWM in India: a perspective. In: Dev, S., Yedla, S. (eds.) Cities and Sustainability. SPBE. Springer, New Delhi. https://doi.org/10.1007/978-81-322-2310-8_10
8. Thanh, N.P., Matsui, Y., Fujiwara, T.: Assessment of plastic waste generation and its potential recycling of household solid waste in Can Tho City, Vietnam. Environ. Monit. Assess. **175**, 23–35 (2011)

9. Petric, I., Helic, A., Avdic, E.A.: Evolution of process parameters and determination of kinetics for co-composting of organic fraction of municipal solid waste with poultry manure. Bio Resour. Technol. **117**, 107–116 (2012)
10. Aazam, M., St-Hilaire, M., Lung, C.-H., Lambadaris, I.: Cloud-based Smart Waste Management for Smart Cities. IEEE (2016)
11. Ramachandra, T.V., Bharatha, H.A.: Gouri Kulkarni, Sun Sheng Hand, 2017, Municipal solid waste: Generation, composition and GHG emissions in Bangalore, India. Renew. Sustain. Energy Rev. **82**, 1122–1136 (2018)
12. Marshall, R.E., Farahbakhsh, K.: Systems approaches to integrated solid waste management in developing countries. Waste Manage. **33**, 988–1003 (2013)
13. Cui, L., Chen, L.R., Li, Y.P., Huang, G.H., Li, W., Xie, Y.L.: An interval-based regret-analysis method for identifying long- term municipal solid waste management policy under uncertainty. J. Environ. Manage. **92**, 1484–1494 (2011)
14. Mohammad Sujauddin, S.M.S., Huda, A.T.M., Hoque, R.: Household solid waste characteristics and management in Chittagong, Bangladesh. Waste Manage. **28**, 1688–1695 (2008)

Static Investigation of Plants Inspired Bio-Mimic Column Structures

Dalvinet K. Varghese and S. Sreerath

Abstract Bio-inspired engineering design has drawn considerable attention in recent years for its great structural and mechanical features. Tubular sections are considered as the most common shape utilized in energy absorption due to their high strength, high stiffness, inexpensiveness, versatility, ease of manufacture as well as high energy absorption capacity. Mimicking the natural structures could lead to design efficient structures with improved performance. Most of the studies focused on crashworthiness and energy absorption capacity of lightweight tubular structures. In this study, inspiration of microstructure of the novel bionic-bamboo tube (BBT) structure is developed as steel columns and investigated for their static performance in compression under axial load. Complete analytical evaluation using nonlinear static structural analysis is done in ANSYS finite element (FE) simulation software. This research discovered that the adoption of ribs in a structure has a significant impact on the load bearing capability of bionic bamboo column structures (BBC).

Keywords Mimic · Bamboo structure · Bionic design · Steel column · FEA

1 Introduction

Through millions of years of evolution in nature created living things with extraordinary features. This evolution aims to protect plants and animals from drastic climate and predators. These extraordinary and unique properties were mimicked by researchers to implement high performance structures and materials. Nature employs a range of forms and design strategies to enhance structural efficiency and decrease material consumption. Mimicking these forms and design leads to structurally optimized systems [1]. Biomimicry (from the Greek bios, which means "life," and mimesis, which means "to imitate") is the discipline of observing nature and mimicking natural forms, systems, and processes in order to create more effective designs, products and service systems [2]. Bio-inspired light weight structures

D. K. Varghese (✉) · S. Sreerath
Department of Civil Engineering, FISAT, Angamaly, India
e-mail: dalvinetvarghese@gmail.com

have been used in the construction of energy-absorbing structures in recent years and have a great application in many industries, such as aerospace, architecture, military, and automotive [3, 4].

Plants are the highly evolved species in nature due to millions of years of evolution and natural selection [5]. Due to unique structural features of plants such as bamboo, reed, straw, cattail and horsetail grass are able to withstand severe environment loads such as gravity, wind and snow pressure. Highly evolved bamboo shows high crashworthiness due to the presence of vascular bundles in their structure [4, 6, 7]. Bamboo is a material with good mechanical properties in nature. Research has shown that the gradient distribution of vascular bundles and the organic combination between vascular bundles and parenchyma cells contribute excellent mechanical properties to bamboo.

All the previous studies were focused on development of thin walled tubular structure by the influence of bamboo [4, 6, 8–11]. This underlines the need to investigate the effect of ribs in thick walls, hence the focus of this research. Moreover, in this work bamboo inspired structures were developed into steel columns and investigated the performance of these steel columns under axial static loading.

2   Model Setup

Available literature has a common opinion that bamboo can withstand harsh environmental loads such as wind, snow and gravity due to their extraordinary tubular structure [6]. Vascular bundles in the bamboo structure have a great influence in the load carrying capacity of bamboo. A series of parenchyma cells are present inside the vascular bundle of a bamboo. These parenchyma cells with different rib shapes create axial mechanical properties to the thin walled structures [4, 7]. Jie fu et al. found that construction of thin wall structure with ribs has a remarkable effect on its crashworthiness [6]. In this study, five cross-sectional configurations of double skinned bionic bamboo columns were compared to conventional bamboo columns. The layout of the adopted sections are shown in Fig. 1. Geometric parameters for the adopted bionic bamboo columns are shown in Table 1. Hot rolled steel is used as the base material for conventional and bionic bamboo columns. Heavy steel of 8 mm thickness was used for conventional steel column. All bionic bamboo columns and conventional column had the same axial length of 3000 mm. Table 2 shows the mechanical properties of the hot rolled steel used.
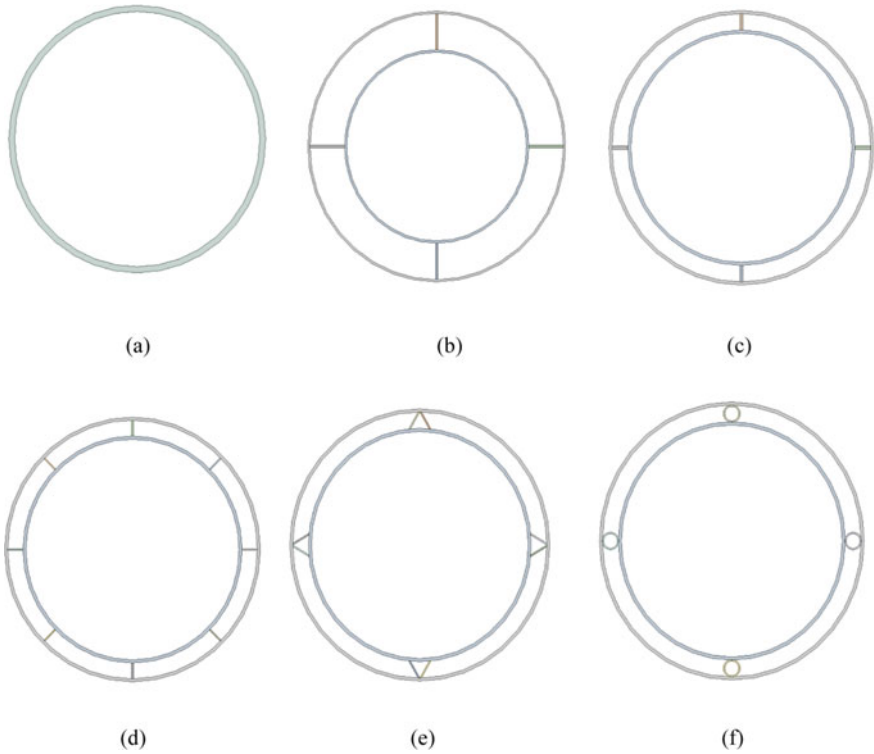
Fig. 1 **a** C1: Conventional column, **b** C2: Bionic column with I shaped ribs of 3 mm thickness, **c** C3: Bionic column with I shaped ribs of 4 mm thickness, **d** C4: Bionic column with I shaped ribs of 2 mm thickness, **e** C5: Bionic column with v shaped ribs, **f** C6: Bionic column with round shaped ribs

Table 1 Geometric parameters for conventional and bionic bamboo columns

Type	Rib shape	Rib number	Rib thickness	Column thickness	Outer diameter	Inner diameter
			mm	Mm	mm	mm
C1	–	–	–	8	355.6	–
C2	I	4	3	3	350	250
C3	I	4	4	4	350	300
C4	I	8	2	4	350	300
C5	V	4	2	4	350	300
C6	O	4	2	4	350	300

Table 2 Mechanical properties of hot rolled steel

Property	Steel
Density, ρ	7850 (kg/m^3)
Poisson's ratio,μ	0.3
Elastic modulus, E	2×10^5 (MPa)
Yield stress, σ_y	345 (MPa)

3   Numerical Analysis

In this study, the finite element models were developed to analyze the axial load carrying capacity of bionic bamboo column (BBC) structures using ANSYS software. Here the displacement control method is used to apply load on both conventional and bionic bamboo columns. Conventional column and bionic bamboo columns were crushed axially up to a final displacement of 8 and 6 mm respectively. It is found that the suitable element size is 50 mm, which gives computational efficiency and numerical accuracy. The bottom and top end of the column is pinned. There were two plates in which one was attached to top and other to the bottom of the steel column. Axial load is applied on the top plate as displacement.

4   Result and Discussion

Table 3 depicts the load, deformation, and weight of steel columns following axial loading, while Fig. 2 depicts the load–deflection curve of conventional and bionic bamboo columns.

Table 3 Characteristics of bionic bamboo columns

Type	Load	Deformation	Weight
	kN	mm	kg
C1	2880.80	6	304.38
C2	2015.70	5.69	243.77
C3	2757.80	5.56	296.55
C4	2751.40	5.84	296.55
C5	2745.50	5.87	296.04
C6	2829.00	5.80	300.59
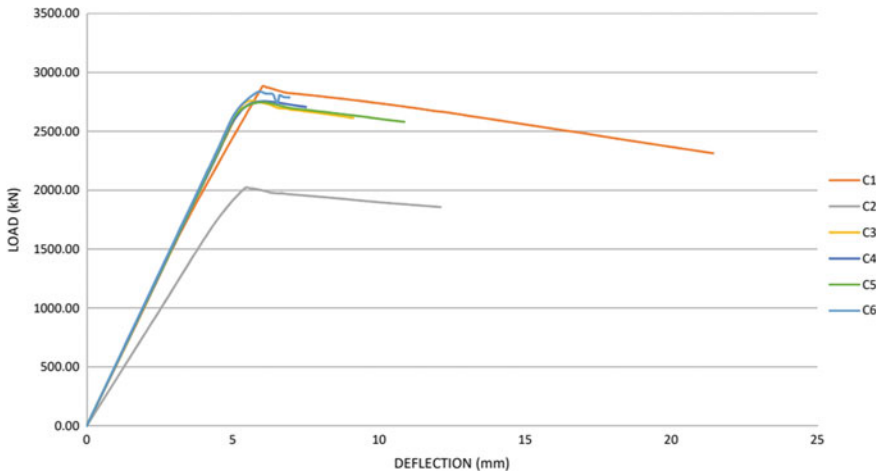
Fig. 2 Plot between load and deflection for the adopted specimen

4.1 Effect of Ribs

The load carrying capacity of a steel column is enhanced when ribs are added to it. In this study, addition of ribs in BBCs decreased the dead weight of BBCs.

4.2 Effect of Rib Number

From the present study, increasing the number of ribs hasn't given a much better result. When comparing load bearing capacity of C3 (2757.80 kN) and C4 (2751.40 kN), C3 gave maximum load bearing capacity. Increasing the number of ribs causes an increase in the dead weight of the member, while load bearing capacity is not enhanced. So, it can be inferred that there is an optimum number for ribs in the point of view of axial load carrying capacity. Its effect in other characteristics is however, out of the scope of present work.

4.3 Effect of Rib Shape and Thickness

C4, C5 and C6 have a rib thickness of 2 mm. When comparing these three types, C6 has a high load bearing capacity than C4 and C5 has less load bearing capacity than C4. From this comparison it is clear that the shape of ribs have a great effect on the load bearing capacity. C2 and C3 have a rib thickness of 3 and 4 mm respectively, in which, C3 yielded at a higher axial load. Load carrying capacity of C6 is more when

compared with C3, which implies that shape of rib has more effect on load bearing capacity than the thickness of the ribs.

4.4 Effect of Column Thickness

Column thickness of C2 is 3 mm and other bionic bamboo columns have a thickness of 4 mm. According to the findings, C6 has a better axial load bearing capacity than other BBCs. Conventional column (C1) has a thickness of 8 mm. All the columns in the study show similar load bearing capacity, hence by using BBCs can reduce the dead weight of the conventional columns. The study's major goal was to keep the deadweight close to equal. As a result, we are unable to reach any conclusions on the effect of column thickness on axial load carrying capacity at this time. We don't have enough evidence to comment on the variation in load carrying capacity from the exclusive column thickness standpoint because we're more focused on the point of ribs.

4.5 Weight of Column

It is clear from the current work that employing ribs to reduce the dead weight of the structure even for greater loads, more accurately using it as a mimic of nature.

5 Conclusions

In this study, the bionic bamboo columns were developed by imitating bamboo structure, was investigated under axial loading. Five bionic bamboo columns with different cross-sectional configurations were investigated using a nonlinear finite element method. From the static analysis under axial loading following results were found.

- From the current study, it is found that the Conventional column and bionic bamboo columns have similar axial load carrying capacity.
- Although all models show almost the same load carrying capacity, there was 1.25 to 19.91% decrease in dead weight of bionic bamboo columns (BBCs) when compared with conventional column.
- The current study found that the shape of ribs has an effect on the axial load carrying capacity of bionic bamboo columns (BBCs).
- In case of load bearing capacity C6 (2829 kN) shows high performance among the BBCs and in case of dead weight C2 (243.77 kg) is better than other types of columns.

- In terms of axial load carrying capacity, there is an optimum arrangement of ribs, at least for the same rib geometry.
- By using a ribbed structure, the axial load carrying capacity of a column can be slightly increased while keeping the dead weight of the column lowered. This emphasises why ribbed arrangements are seen in nature rather than solid or cylindrical arrangements in column-like structures.

References

1. Sindhu Nachiar, S., Satyanarayanan, K.S., Lakshmipathy, M., Sai Pavithra, S.: Study on behaviour of compression members based on concept of biomimics. Mater. Today Proc. **34**(2), 518–524 (2021). ISSN 2214-7853

2. du Plessis, A., et al.: Beautiful and functional: a review of biomimetic design in additive manufacturing, additive manufacturing, vol. 27, pp. 408–427 (2019). ISSN 2214-8604

3. Badarnah, L., Kadri, U.: A methodology for the generation of biomimetic design concepts. Archit. Sci. Rev. **58**, 120–133 (2015)

4. Palombini, F.L., de Araujo Mariath, J.E., de Oliveira, B.F.: Bionic design of thin-walled structure based on the geometry of the vascular bundles of bamboo. Thin Walled Struct. **155**, 106936 (2020). ISSN 0263-8231

5. Gong, C., Bai, Z., Lv, J., Zhang, L.: Crashworthiness analysis of bionic thin-walled tubes inspired by the evolution laws of plant stems, Thin Walled Struct. **157**, 107081 (2020). ISSN 0263-8231

6. Fu, J., Liu, Q., Liufu, K., Deng, Y., Fang, J., Li, Q.: Design of bionic-bamboo thin-walled structures for energy absorption. Thin Walled Struct. **135**, 400–413 (2019). ISSN 0263-8231

7. Song, J.F., Xu, S.C., Wang, H.X., Wu, X.Q., Zou, M.: Bionic design and multi-objective optimization for variable wall thickness tube inspired bamboo structures. Thin Walled Struct. **125**, 76–88 (2018). ISSN 0263-8231

8. Zou, M., Xu, S., Wei, C., Wang, H., Liu, Z.: A bionic method for the crashworthiness design of thin-walled structures inspired by bamboo. Thin Walled Struct. **101**, 222–230 (2016). ISSN 0263-8231

9. Liu, S., Tong, Z., Tang, Z., Liu, Y., Zhang, Z.: Bionic design modification of non-convex multi-corner thin-walled columns for improving energy absorption through adding bulkheads. Thin Walled Struct. **88**, 70–81 (2015). ISSN 0263-8231

10. Xu, T., Liu, N., Yu, Z., Xu, T., Zou, M.: Crashworthiness design for bionic bumper structures inspired by cattail and bamboo. Appl. Bionics Biomech. **2017**, 1–9 (2017). https://doi.org/10.1155/2017/5894938

11. Song, J., Xu, S., Zhou, J., Huang, H., Zou, M.: Experiment and numerical simulation study on the bionic tubes with gradient thickness under oblique loading. Thin Walled Struct. **163**, 107624 (2021). ISSN 0263-8231

Structural Performance of Innovative Connection Between Concrete Flat Slab and Steel Column

Alka Anna Abey and M. Preethi

Abstract Steel-concrete composite structures are widely used in bridge and building construction. Flat slab system is commonly used in construction industry due to structural and architectural merits. Due to its easiness in construction and use, they are used in medium height residential buildings, offices, parking garages etc. Conventionally RC columns and RC slabs are used for construction practices. In this paper RC columns are replaced with steel tubular column. This owes to many advantages like faster construction, reduced size and superior structural performance. Punching shear failure at slab-column connection is a major cause of structural damage due to the smooth external finish of steel column. Punching shear resistance can be enhanced by providing shear connectors in the steel concrete interface. Shear connectors such as steel plates and steel sections are provided between steel column and flat slab, which is made of steel and is welded to the column and integrated into the flat slab. The work focuses on punching shear performance of column to slab connection using various shear connectors like steel plates, sections. This study presents comparison of different shear connectors that includes vertical plates, various cross-sections such as H, I, U, C, T in composite structures. Punching shear behaviour is studied by changing cross-section shapes. The composite structure is modelled and analysed using ANSYS software. The analytical results are investigated to study punching shear behaviour of the composite structure. The comparative study shows that the steel column-flat slab system using inverted C-shaped cross-section have higher punching shear capacity compared to various cross-sections.

Keywords Composite · Shear connector · Punching shear resistance · ANSYS

A. A. Abey (✉) · M. Preethi
Federal Institute of Science and Technology, Angamaly, Ernakulam, India
e-mail: alkaanna.12@gmail.com

1 Introduction

1.1 General

Flat slabs are constructed without beams and are supported over columns with or without caps. It has many advantages such as aesthetically pleasing appearance, accommodation of building services and lower construction cost. Flat slab construction is widely adopted for residential buildings and office buildings. In current flat slab construction, reinforced concrete is used to make slabs and columns. Reinforced concrete column can be replaced by steel tubular column. It has many advantages when compared to reinforced concrete columns which includes, structural efficiency, fire resistance and seismic resistance. The main disadvantage that prevents steel tubes to be used in flat slab construction is because of the absence of punching shear resistance, due to its smooth external surface. Punching shear resistance can be improved by using shear connectors, to connect the steel tubular column to flat slab.

1.2 Shear Connector

Shear connector is the component that helps in shear transfer between steel profile and concrete slab in steel-concrete composite construction. According to the distribution of shear forces and functional dependency between strength and deformations, shear connectors can be of rigid and flexible.

Rigid shear connectors help in resisting shear forces through the front side by shearing. Rigid shear connectors produce stronger concentrated stress around concrete that will lead to either in failure of concrete or in failure of weld. These consist of bars, angles, horseshoes or tees welded to the flange of the steel fabricated units.

Flexible shear connectors help in resisting shear forces by bending, tension or shearing in the root, at the connection point of steel beam. The manner of failure of flexible shear connector is more ductile and is not prompt. These consist of studs, plates and channel connectors.

2 Analytical Work

2.1 Finite Element Modeling

Finite element model was developed using ANSYS 16.2. Solid 185 elements were used to model slab, steel plates and steel sections. The model and its configurations

are chosen as per the details provided in prior research paper. Beam 188 elements were used to model reinforcement. Meshing size provided is 50 mm.

2.2 Geometry and Mechanical Properties

Size of slab is 1300 × 1300 mm and has a thickness of 150 mm. The steel column, which was positioned in one of the slab corners of size 200 × 200 × 12 mm.

M 40 and Fe 355 are the grades of concrete and steel used for modeling respectively. The mechanical properties adopted for the different elements in analysis are given in Table 1.

A composite section is modelled in ANSYS with shear connectors of various cross-sections that include vertical plates and various cross-sections of shape I, C, U, H and T. A model is made by keeping a steel section as a shear connector welded to the column and integrated into the flat slab. The shear connectors are positioned centrally to the slab in all models. Figure 3 shows the modeling of shear connectors with various cross-sections. The various cross-sections of shear connectors modelled in ANSYS are;

i.   Vertical plates

Three Steel plates of size 185 × 92 mm each having 5 mm thickness with a spacing of 50 mm are selected for modelling Fig. 1(a).

ii.   H-shaped cross-section

Steel H-shaped cross-sections of size 95 × 90 × 5 mm of 5 mm thickness are selected for modeling as shown in Fig. 1(b).

iii.   I-shaped cross-section

Steel I-shaped cross-sections of size 90 × 95 × 5 mm are selected for modeling as shown in Fig. 1(c).

iv.   C-shaped cross-section

Steel C-shaped cross-section of size 105 × 90 mm of 5 mm thickness are selected for modeling as shown in Fig. 1(d).

v.   U-shaped cross-section

Table 1 Mechanical properties of specimens used in modeling

Material	Poisson's Ratio	Young's modulus of Elasticity (N/mm^2)
Steel Column	0.3	200,000
Steel cross sections	0.3	200,000
Rebar	0.3	200,000
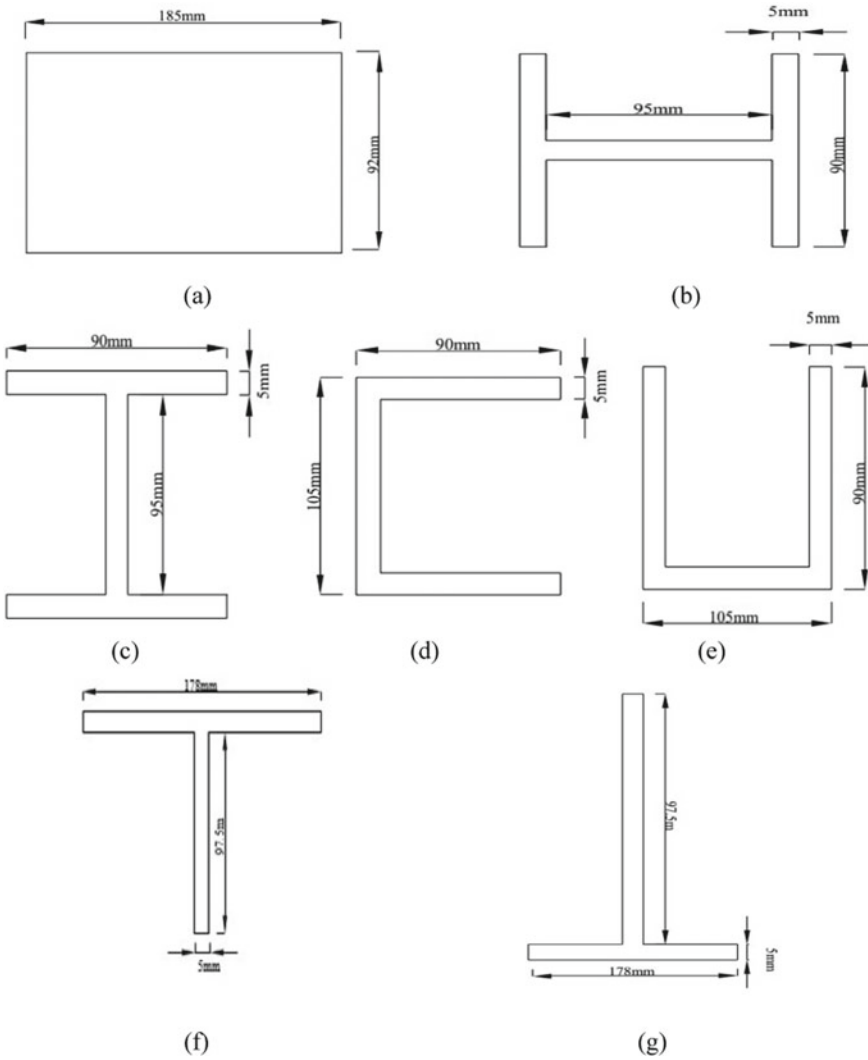
Fig. 1 Details of shear connectors used in modeling: **a** Vertical plate; **b** H-shaped cross-section; **c** I-shaped cross-section; **d** C-shaped cross-section; **e** U-shaped cross-section; **f** and **g** T-shaped cross-section

Size of 90 × 105 mm of 5 mm thickness are used for modeling as shown in Fig. 1(e).

vi. T-shaped cross-section (T1 and T2)

Two models of T-shaped cross-sections are used for modeling with different alignment of size 178 × 97.5 × 5 mm as shown in Fig. 1(f) and (g).
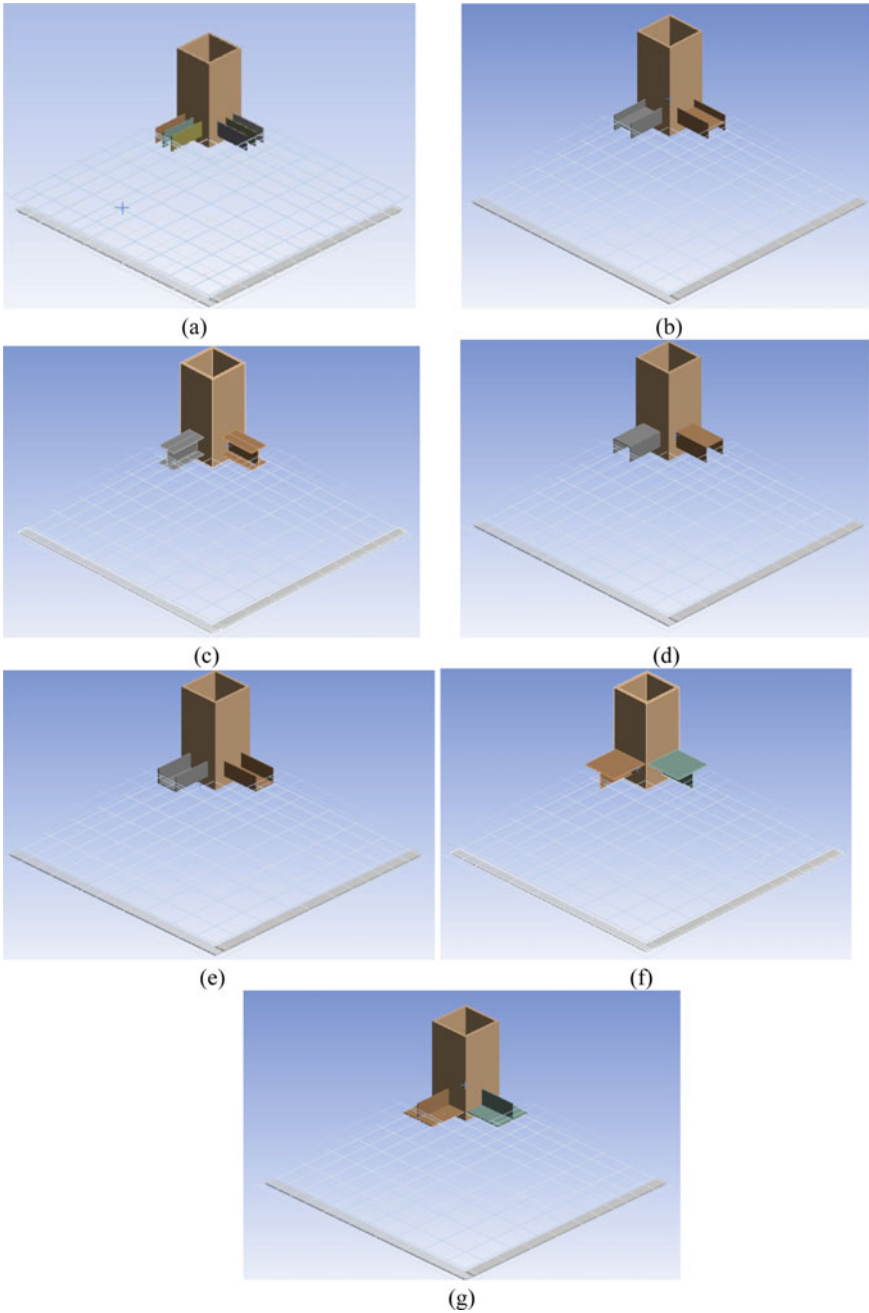
Fig. 2 Modeling of Shear connectors: **a** Vertical plate; **b** H-shaped cross-section; **c** I-shaped cross-section; **d** C-shaped cross-section; **e** U-shaped cross-section; **f** and **g** T-shaped cross-section
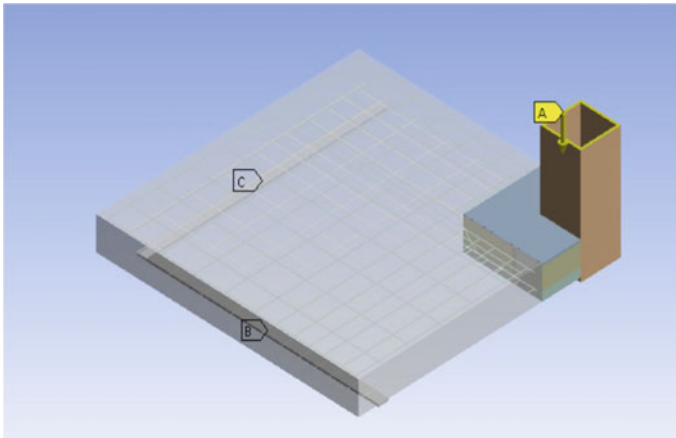
Fig. 3 Boundary condition of steel column-flat slab system with vertical plate and various cross-section shear connectors

2.3 Boundary Condition

In all the analytical models, both exterior end of slab is fixed and the load is applied gradually from the top of the column. The load was applied through displacement control option. Bottom of column was constrained in three (X, Y, and Z) displacement directions; in addition, rotation about Y-axis was constrained. For steel column-flat slab system with shear connectors vertical plates and various cross-sections same boundary condition is applied. Figure 3, shows the boundary condition of steel column-flat slab with shear connector.

2.4 Analytical Results and Discussions

Columns are axially loaded. Displacement controlled forces were given in analysis. Total deformation diagrams of connections with vertical plates and various cross-sections are shown in Fig. 4. Damages occurred mainly in the tensile surface of the concrete slab. Horizontal plates with welded shear studs are taken as the benchmark specimen as per the research paper. Total deformation and punching shear capacity of the validation model are 14.05 mm and 97.5 kN respectively. The total deformation obtained for connection with T-shaped cross-section of 5 mm thickness is 105.33 mm, which was greater among all other shear connectors of various cross-sections and it has punching shear capacity of 72.18 kN shown in Fig. 4(e). The minimum total deformation was obtained for the shear connection system having I-shaped cross-section is 37.62 mm with punching shear capacity of 139.87 kN shown in Fig. 4(b).
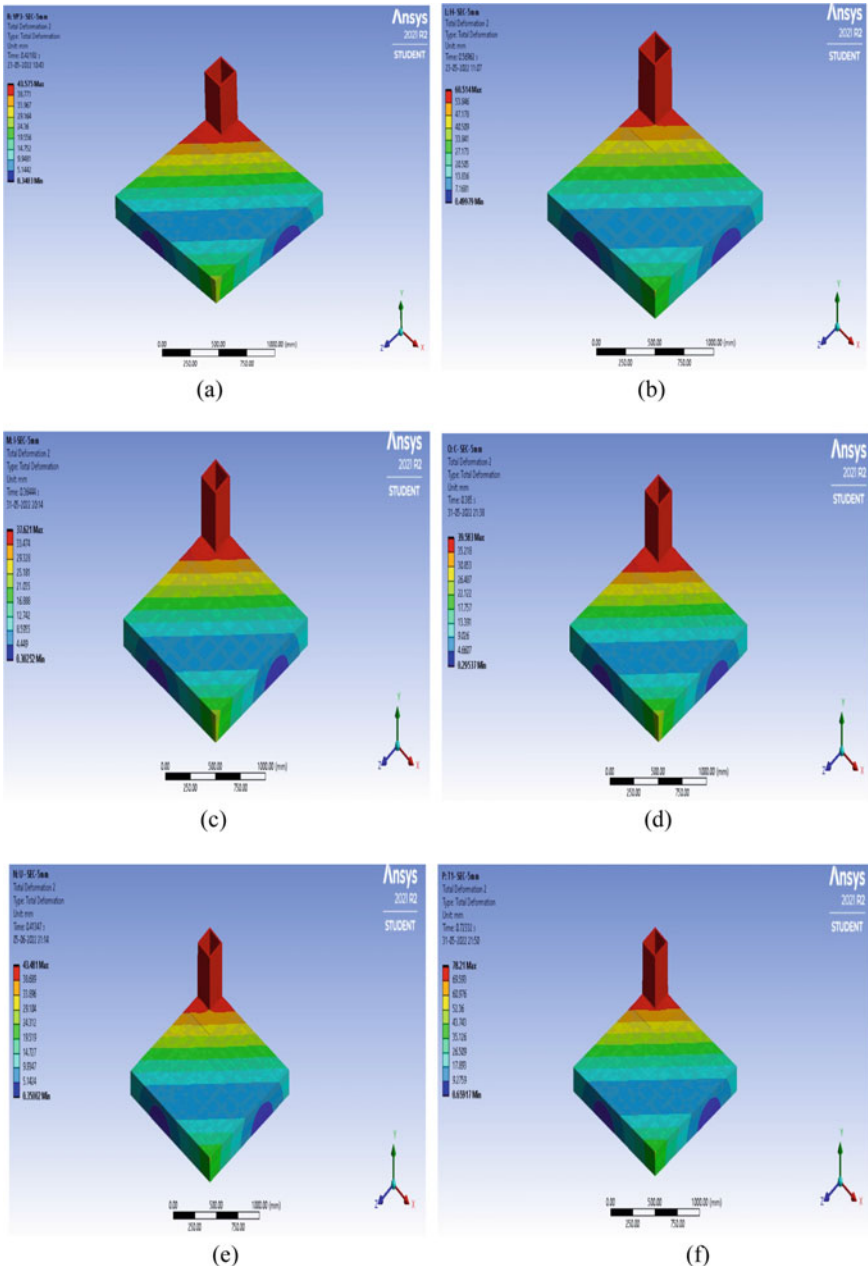
Fig. 4 Total deformation of steel tubular-flat slab system with various cross-section of shear connector: **a** Vertical plate (5 mm thickness); **b** H-shaped cross-section; **c** I-shaped cross-section; **d** C-shaped cross-section; **e** U-shaped cross-section; **f** and **g** T-shaped cross-section

Fig. 4 (continued)

(g)
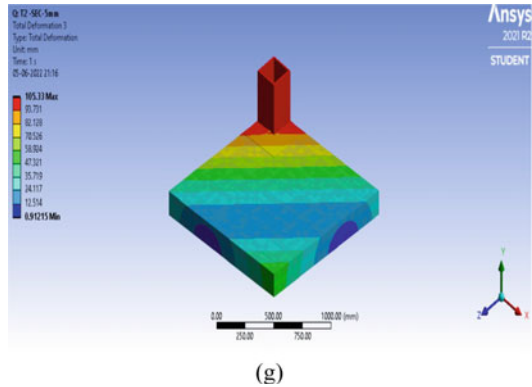
Table 2 Punching shear capacity and corresponding maximum deformations of shear connectors

Shear connectors	Deformation (mm)	Punching shear capacity (kN)
Horizontal plates with studs	14.05	97.5
Vertical plates-5 mm	43.575	133.5
H-section	60.514	102.61
I-section	37.621	139.87
C-section	39.583	142.88
U-section	43.481	96.783
T1-section	78.21	136.61
T2-section	105.33	72.18

Steel tubular column-flat slab system with various cross-sections of shear connections are compared first. Table 2 shows, Punching shear capacity and corresponding Maximum deformations of shear connectors.

The load-displacement curve of seven specimens is shown in Fig. 5. It is clear that, system having connection with C-shaped cross-section has better performance than other connections. It has greater punching shear resistance compared to all other shear connectors of various cross-sections. The punching shear capacity of triple vertical plates of thickness 5 mm is 133.5 kN, and punching shear capacity of H, I, C, U, T1 and T2 cross-sections is observed as 102.61 kN, 139.87 kN, 142.88 kN, 96.78 kN, 136.61 kN and 72.18 kN respectively. At the peak load, the slab was able to sustain the load. After reaching the peak load there is a prolonged branch which shows the ductile behavior of the system.
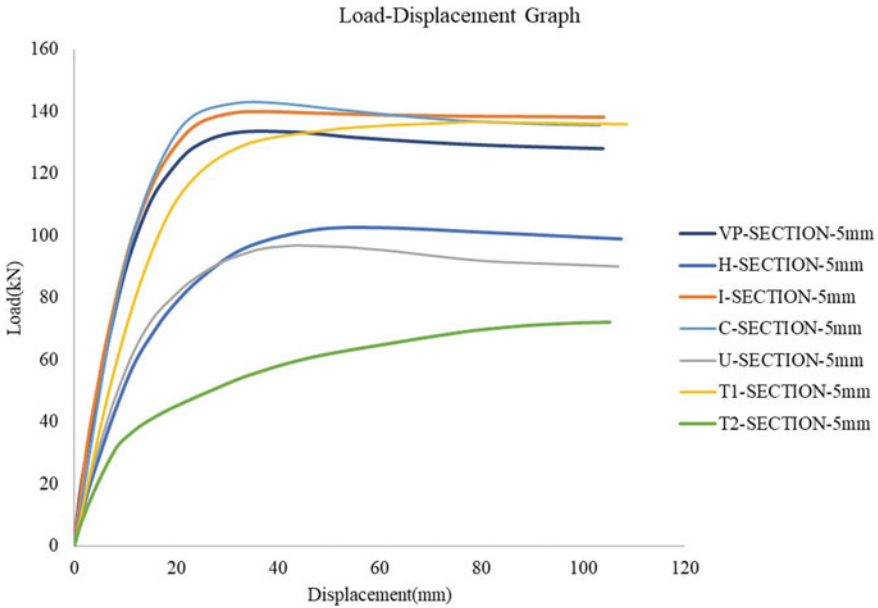
Fig. 5 Load-displacement curve of steel column-flat slab system using shear connectors

Figure 6 shows comparison of Load carrying capacity of various cross-sections of shear connectors. Punching capacity is maximum for C-shaped cross-section of 5 mm thickness and is about 142.88 kN. The punching capacity of steel column-flat slab connection with triple vertical plate of thickness 5 mm increased by 26.9% when compared to validation model. Punching shear capacity of steel column-flat slab with H, I, C, and T1 shaped shear connector increased by 5.05%, 30.3%, 31.8% and 28.6% when compared to validation model. Punching shear capacity of steel column-flat slab with U and T2 shaped shear connector decreased by 0.7%, and 24.6% when compared to validation model. Figure 7, shows comparison of Deformation in various cross-sections of shear connectors. The deformation is maximum for T-shaped cross-section and is about 105.33 mm. The deformation is minimum for I-section of 37.62 mm. Deformation of steel column-flat slab with various cross-sections including vertical plates, H, I, C, U, T1, and T2 shaped shear connectors increased by 67.7%, 76.7%, 62.6%, 64.5%, 67.6%, 82% and 86.6% when compared to horizontal plates with welded studs.
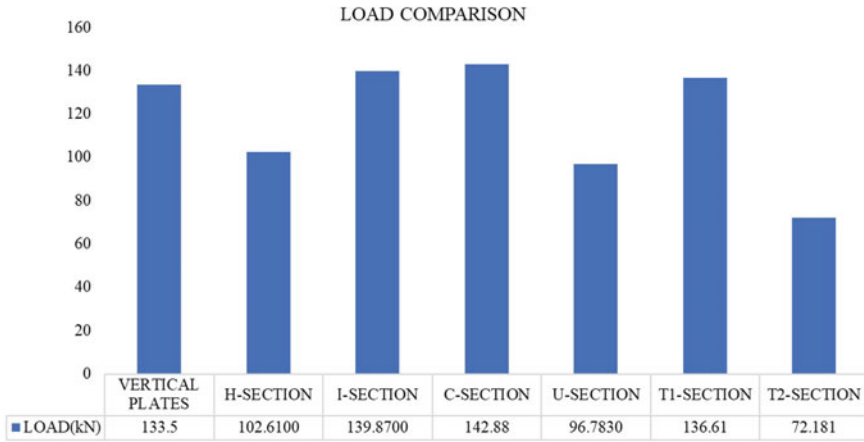
Fig. 6 Comparison of load carrying capacity of vertical plates and various cross-sections of shear connectors
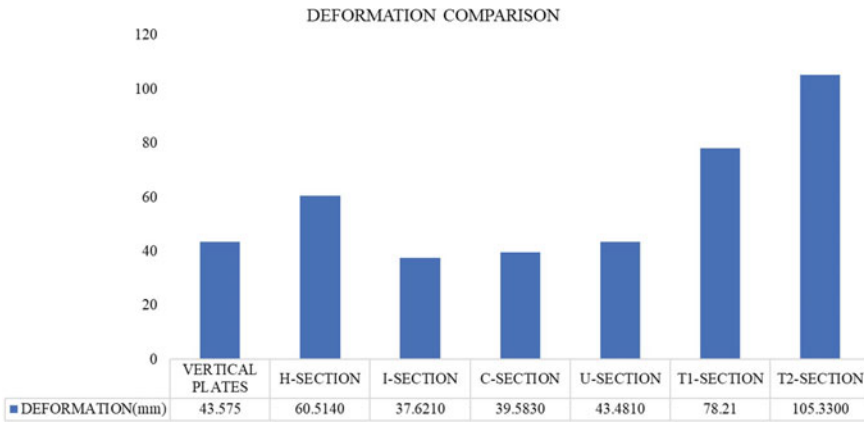
Fig. 7 Comparison of deformation in vertical plates and various cross-sections of shear connectors

3 Conclusion

The results show that the connections with various geometry can reduce punching shear failure and must be added to improve the safety and integrity of flat slab. In this study comparison of shear connection system with triple vertical plates and various cross-sections were done. The steel tubular column-flat slab system with shear connectors of cross-sections including vertical plates, H, I, C and T has more punching shear capacity compared to the validation model. C-shaped cross-section of 5 mm thickness model have greater Punching shear capacity of 142.88 kN and are suitable for resisting punching shear. The punching capacity of steel column-flat

slab connection with C-shaped cross-section, increased by 31.8% when compared to validation model. Thus, the cross-sections can be used as a shear connector for improved punching shear resistance and there by punching shear failure can be reduced.

References

1. Bompa, D.V., Elghazouli, A.Y.: Structural performance of RC flat slabs connected to steel columns with shear heads. Eng. Struct. **117**, 161–183 (2016)
2. Eder, M.A., Vollum, R.L., Elghazouli, A.Y.: Performance of ductile RC flat slab to steel column connections under cyclic loading. Eng. Struct. **36**, 239–257 (2012)
3. Eder, M.A., et al.: Modelling and experimental assessment of punching shear in flat slabs with shear heads. Eng. Struct. **32**(12), 3911–3924 (2010)
4. Lee, C.-H., Kim, J.-W., Song, J.-G.: Punching shear strength and post-punching behavior of CFT column to RC flat plate connections. J. Constr. Steel Res. **64**(4), 418–428 (2008)
5. Yan, P.Y., Wang, Y.C.: Hybrid steel tubular column/flat slab construction—Development of a shear head system to improve punching shear resistance. J. Constr. Steel Res. **119**, 154–168 (2016)
6. Yu, J.L., Wang, Y.C.: Punching shear behavior and design of an innovative connection from steel tubular column to flat concrete slab. J. Struct. Eng. **144**(9), 04018144 (2018)
7. Yu, J.L., Wang, Y.C.: Punching shear behavior and design of an innovative connection from steel tubular column to flat concrete slab. J. Struct. Eng. **144**(9), 04018144 (2020)

Improving Collapse Performance of Steel Frame with Efficient Design of Reduced Beam Sections

N. J. Anumol and Nincy Jose

Abstract Steel moment frames with welded connections have shown brittle fractures at beam to column joint during earthquakes. In order to improve the ductility of the steel connections, Reduced Beam Sections (RBS) is introduced. This mitigation measure helps in the relocation of plastic hinges to the reduced beam section provided on the beam, which eventually improve the ductility of steel connections. This work focuses on the study of progressive collapse analysis with and without RBS in beam column frames using ANSYS software. This work also helps to improve the collapse performance of steel frame with welded connection with the effective design modification in RBS like Tubular Web RBS (TRBS). The efficient design modifications are implemented instead of weakening the section to stiffening the section. At the position of the plastic hinge a portion of beam web is replaced with steel tube in order to provide TRBS. This technique helps to delay the progressive collapse at the joint. Non-linear static analysis is carried out to evaluate the performance depending on the vertical displacement, plastic hinge, moment capacity of the beam to identify the most suitable location for incorporating the RBS in the frame.

Keywords RBS · Ductility · Progressive collapse · Steel moment frame

1 Introduction

The Northridge earthquake which occurred in 1994 and the Kobe earthquake in 1995 caused certain failures in the beam column frame with welded connection, because of the high ductility demands which results in tension concentration and welded connection which are vulnerable. In order to improve the ductility performance, reduced beam sections (RBS) is implemented to reduce imposed demands on the beam-column connections. The provision of RBS delays the failure at the beam

---

N. J. Anumol (✉) · N. Jose
Department of Civil Engineering, FISAT, Angamaly, India
e-mail: anumolnj713@gmail.com

N. Jose
e-mail: nincyjose12@gmail.com

column joint. This is due to the relocation of the plastic hinge from beam column joint to the position of the RBS. This leads to an increase in the displacement and load. Hence the collapse is delayed.

Progressive collapse is defined as local structural failure which leads to the failure of the adjacent members resulting in the total structural failure. Progressive collapse is initiated by loss of one or more vertical load carrying members like columns. After one or more column fail, the load is transferred to other structural elements usually beams.

The uniform load is represented as q in the Fig. 1. After the sudden removal of column at the center, the spans connected to the removed column referred to as failed spans exhibited maximum deformation. These spans were selected to investigate the collapse resistance of the remaining steel frame structure. In this study progressive collapse criteria is considered as column removal scenario as per the base journal [1]. In this study the central column between two bays of beams is pushed down by displacement controlled method and the load is applied gradually until failure. According to the base journal considered for the study the internal force and deflection were anti symmetric at both failed spans and the inflection points were close to the beam mid span. Therefore a substructure with half span beams and a column was considered for the study. Because both ends of the substructure were obtained from the inflection points, the substructure boundary was connected to the surrounding support by a hinge to allow rotation.

Researchers have conducted various investigations on different types of RBS connections with reduced section of flange and web. Huiyun Qiao et al. investigated a reduced beam section (RBS) connection with beam flange containing radius cuts and beam web with circular opening. He concluded that RBS connections may increase structural deflection and crack width in the steel frame structure under large deformations [1]. Aboozar Saleh et al. studied a novel reduced beam section called Tubular Web RBS connection (TW-RBS). In TW-RBS, the failure is transferred to a position on the beam flange in front of the tubular web or at the connection of the tubular web to the beam flange without any damage detection at center line of the accordion web [2]. Bao Meng et al. investigated the study of RBS connection with "V"-type plates to the reduced section of the upper and lower flanges of a beam. As a result the maximum resistance and displacement can be increased by 52.9 and 34.9% [6].
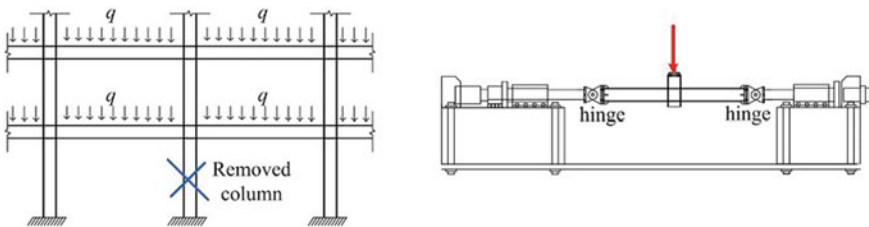
Fig. 1 Steel frame structure [1]

The present study consists of RBS with flange reduction (RBS FC) and Tubular web RBS having different diameter for the steel tubes with varying thickness. A comparative study is carried out between the specimen with and without RBS to find the improvement in the performance. The parametric study is carried out by changing the distance of center of tube to the column face (a) and the diameter of tube for TRBS (D). Vertical loading is applied and the load carrying capacity and the deformation is analysed for each model.

2 Design Considerations

The flange reduced section (RBS FC) is having the length and width of which were selected as per the ANSI/AISC 341-16 recommendations. In case of the Tubular Web RBS (TRBS) the distance of center of tube to the column face and the diameter of tube are illustrated in the Table 1. By considering the allowed range for e, the diameter of the tube can be determined from the equation given below.

$$D = 2(e - a) \tag{1}$$

According to AISC seismic provisions the RBS connections are designed based on the parameters like the distance from the column face to the beginning of RBS (a) and to the center of the corrugated region (e) is calculated. According to this, the distance to the reduced region (a) is 50–75% of the beam flange width (b_f) and reduced region length (b) is 65–85% of the beam depth (d_b). The acceptable ranges of parameters a and e ($e = a + \frac{b}{2}$), based on the above values can be depicted as follows:

$$0.5b_f \leq a \leq 0.75b_f \tag{2}$$

$$0.5d_b \leq e \leq d_b \tag{3}$$

The diameter of the steel tube used for the TRBS is chosen from the IS code (IS1167-1998), from which the values obtained for minimum and maximum diameters 43.5 and 89 mm respectively. The diameter available within this range is selected for the study. The dimensional parameters of reduced sections of TRBS shown in the Table 1.

The rotation of the beam, $\theta = \frac{w}{l}$, where w is the displacement and l is the beam length. The moment developed at the beam column joint was determined manually by multiplying the applied load with the span of the beam considered.

Table 1 Reduced section dimensional parameters

Section	Nominal Diameter as per IS CODE (mm)	Thickness (mm)	Diameter (1) (mm)	Allowed range of "e" (mm)	Allowed range of " a" (mm)
TRBS-60.3 X 4.5—A75	50	4.5	60.3	105.15	75
TRBS-60.3 X 2.9—A75	50	2.9	60.3	105.15	75
TRBS-76.1 X 4.5—A75	65	4.5	76.1	113.05	75
TRBS-76.1 X 3.2—A75	65	3.2	76.1	113.05	75
TRBS-88.9 X 4.8—A75	80	4.8	88.9	119.45	75
TRBS-88.9 X 3.2—A75	80	3.2	88.9	119.45	75
TRBS-60.3 X 4.5—A69.85	50	4.5	60.3	100	69.85
TRBS-60.3 X 2.9—A69.85	50	2.9	60.3	100	69.85
TRBS-76.1 X 4.5—A61.95	65	4.5	76.1	100	61.95
TRBS-76.1 X 3.2—A61.95	65	3.2	76.1	100	61.95
TRBS-88.9 X 4.8—A55.55	80	4.8	88.9	100	55.55
TRBS-88.9 X 3.2—A55.55	80	3.2	88.9	100	55.55

3 Finite Element Formulation

The finite element model was developed using ANSYS software to investigate the performance of RBS on column beam connections. A comparative study is conducted between the model with and without RBS. The TRBS is also developed and a parametric study is performed by varying the parameters like diameter, thickness and distance of RBS from the column face. This section explains the finite element formulation of the model.

3.1 Geometry of the Model

For modeling the beam column connection, ISMB 200 and ISHB 250 is used for beam and column. The beam length is taken as 1315 mm [1]. The beam and column specifications are shown in the Table 2. The beams of all specimens are connected to the column by welding. Welded connection is modeled as bonded connection between the members in ANSYS software. Figure 2 shows the geometry of the model.

Table 2 Beam and column specifications

Section	Depth of beam (d_b) (mm)	Width of flange (b_f) (mm)	Thickness of flange (t_f) (mm)	Thickness of web (t_w) (mm)
Beam	200	100	10.8	5.7
Column	250	250	9.7	6.9

(a) RBS0

(b) RBSFC

(c) TRBS
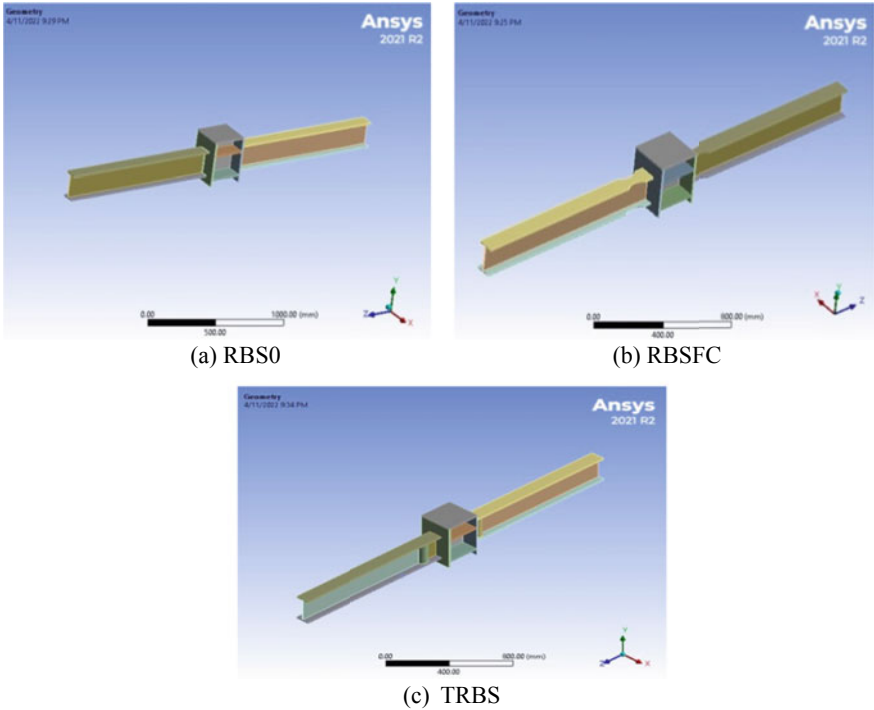
Fig. 2 Geometry of model

3.2   Material Properties

Table 3 shows the material properties for beam and column used for the study. The density of steel is 7850 kg/m^3. Stiffeners are not provided at the beam column joint. Instead plates are provided within the column for proper load distribution over the column and to prevent warping of the column as per the journal [1].

3.3   Finite Element Modeling

The analytical study on beam column joint with and without RBS is carried out to study the improvement on the collapse performance. RBS with flange reduction is modeled as per the ANSI/AISC recommendations. Tubular web RBS is also modeled and a parametric study is carried out by changing the distance of center of tube to the column face and the diameter of tube. The model mainly consists of a beam and column with flange reduction of the beam for the RBS FC model and the web is reduced and steel tube is introduced for the TRBS model. The elements were modeled using SOLID 186 element. Solid 186 is a 20 node solid element that exhibits quadratic displacement behavior. The element is defined by 20 nodes having 3 degrees of freedom per node: Translations in the nodal x, y and z directions. Mesh size adopted was 25 mm and shape of the meshing was Hexahedron. Figure 3 shows the meshing diagram.

Table 3 Material properties

Youngs modulus (Mpa)	2×10^5
Yield strength, f_y (Mpa)	345
Poissons ratio	0.3

Fig. 3 Meshing
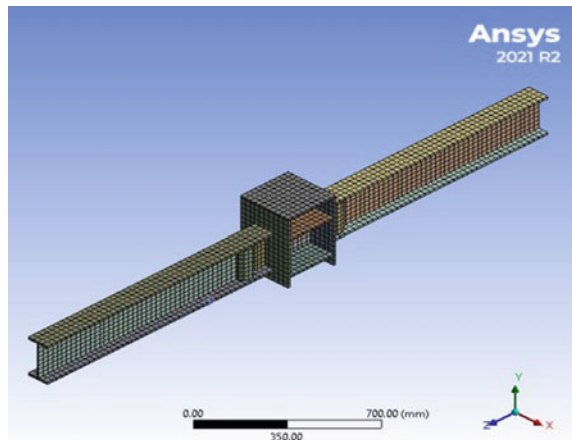
Fig. 4 Boundary condition
of TRBS
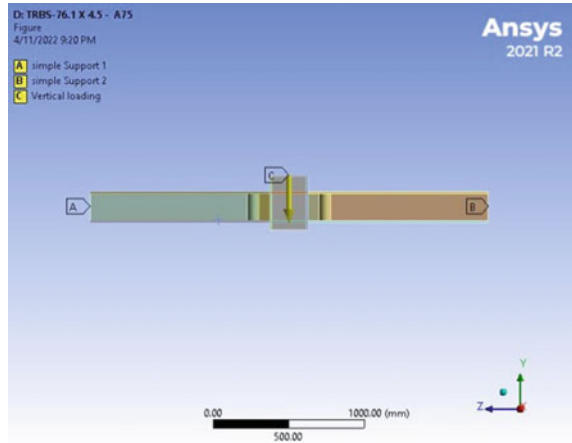
3.4 Support Condition and Loading

The two ends of the beam were provided with pinned support by preventing translation and permitting rotation along Z direction as shown in the figure. A vertical displacement of 500 mm was provided at the column in the form of load. The displacement value provided is obtained by trial and error method. Figure 4 shows the support and loading conditions.

4   Results and Discussion

The specimens with different RBS connections were analysed. Failure pattern for all the specimens were obtained. Force reaction and the corresponding deformation were obtained for all models. From the obtained results load deformation curves were plotted. The deformation pattern for a model is depicted in the Fig. 5. Figure 6 indicates the load v/s deformation curve obtained from the analysis. A comparative study is carried out between beam column joint with and without RBS. It is observed from the graph that the RBS with flange reduced specimen is taken the greater load than the without RBS section (Table 4).

Fig. 5 Deformation of
TRBS
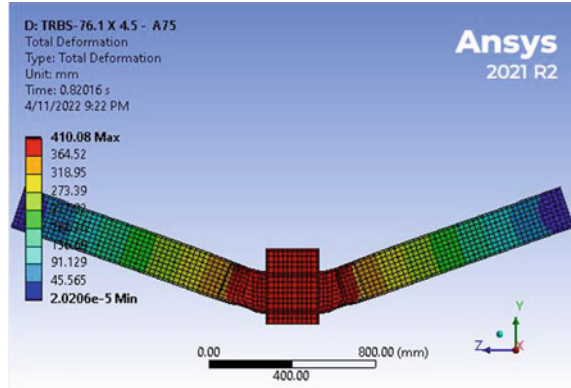
Fig. 6 Load vs deformation
curve of model with and
without RBS
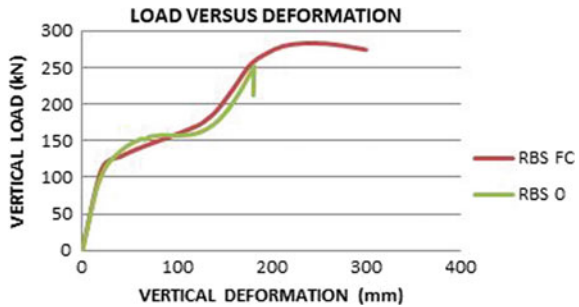
4.1 Parametric Study

Parametric study is carried out in the Tubular Web RBS by varying the distance from
the column face to the start (parameter a) and the diameter of the steel tube (D).
The graph is plotted between the vertical deformation and vertical load. The result
shows that with increase in the diameter and the thickness of the steel tube increases
the load carrying capacity of the beam. With increase in the parameter a shows a
decrease in the load.

Figure 7 shows that with increase in diameter of the steel tube the load carrying
capacity is also increased. And the model with maximum load carrying capacity is
taken to depict the effect of thickness on the load depicted in Fig. 8. Figure 9 indicates
the minimum a value for different diameters chosen. Figure 10 shows with increase
in "a" value load carrying capacity is decreased and vice versa.

Table 4 Mechanical properties

Section	w_{max} (mm)	P_{max} (kN)	θ_{max} (rad)	M_{max} (kNm)	Yield point (mm)	Ductility
W RBS	86.076	158.04	0.12	207.82	14.40	5.98
RBS-FC	233.18	283.18	0.22	372.38	42.04	5.55
TRBS-60.3 X 4.5—A75	346.72	575.83	0.44	757.22	70.07	4.95
TRBS-60.3 X 2.9—A75	336.06	526.28	0.40	692.06	70.07	4.80
TRBS-76.1 X 4.5—A75	378.45	638.66	0.49	839.84	70.07	5.40
TRBS-76.1 X 3.2—A75	350.97	641.17	0.49	843.14	35.06	10.01
TRBS-88.9 X 4.8—A75	417.84	694.02	0.53	912.64	70.07	5.96
TRBS-88.9 X 3.2—A75	386.06	595.99	0.45	783.73	70.07	5.51
TRBS-60.3 X 4.5—A69.85	359.14	593.23	0.45	780.10	31.56	11.38
TRBS-60.3 X 2.9—A69.85	339.4	520.23	0.40	684.10	70.07	4.84
TRBS-76.1 X 4.5—A61.95	358.57	646.3	0.49	849.88	28.06	12.78
TRBS-76.1 X 3.2—A61.95	374.39	668.77	0.51	879.43	35.06	10.68
TRBS-88.9 X 4.8—A55.55	409.85	691.42	0.53	909.22	70.07	5.85
TRBS-88.9 X 3.2—A55.55	390.35	592.06	0.45	778.56	31.56	12.37

Fig. 7 Parametric study of diameter with constant "a" value
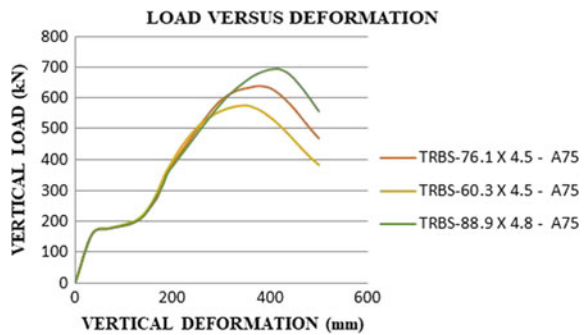
Fig. 8 Parametric study on thickness
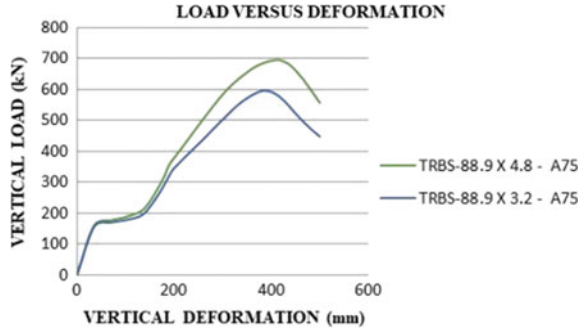
Fig. 9 Parametric study varying a value for different diameters
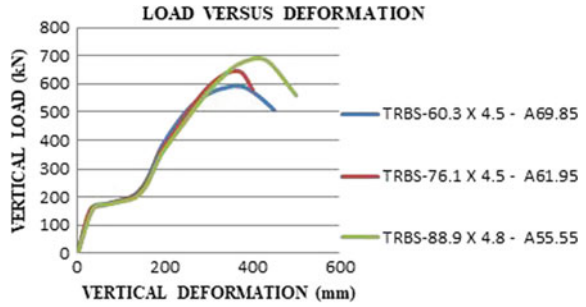
Fig. 10 Parametric study on varying value on TRBS
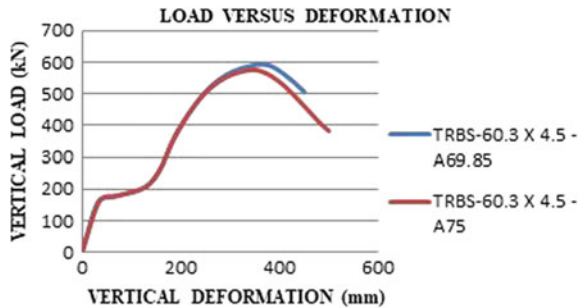
Figure 11 shows the ductility comparison. From the graph the TRBS 76.1 X4.5—A61.45 shows better ductile behaviour.

Ductility comparison
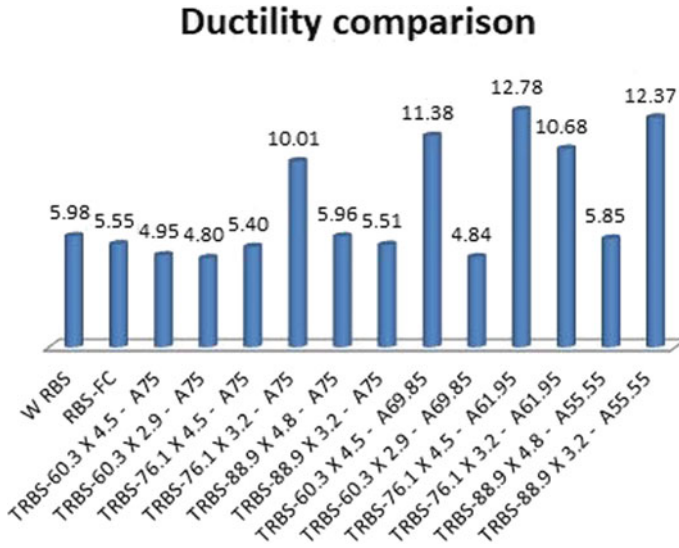
Fig. 11 Ductility comparison

5 Conclusions

Reduced beam section shows transformation of stress concentration from face of the column to the beam section. By comparing the results obtained from this study it can be concluded as follows:

- RBS shifts the plastic hinge formation away from the beam column face.
- The conventional type RBS, that is the RBS with flange cut is taking a load of 283.18 kN which is greater than the beam column frame without RBS 158.04 kN. The percentage increase in the load value is about 44.19%.
- The enhanced RBS technique like Tubular Web RBS (TRBS) has been made through cutting continuous web and replacing that part with a tube at the desired location of the plastic hinge. The steel tube dimensions are determined as per the IS code provisions.
- The parametric study on the diameter of the steel tube used for the TRBS shows an increase in the load values. That is with increase in the diameter the load value increases. The thickness of the steel tube is also varied and the results shows increasing the thickness also shows increase in load values.
- The increase in the parameter a, the distance from the column face to the RBS shows a decrease in the load carrying capacity.

References

1. Qiao, H., Chen, Y., Wang, J., Chen, C.: Experimental study on beam-to-column connections with reduced beam section against progressive collapse. J. Constr. Steel Res. **175**, 106358 (2020)
2. Saleh, A., Mirghaderi, S.R., Zahrai, S.M.: Cyclic testing of tubular web RBS connections in deep beams. J. Constr. Steel Res. **117**, 214–226 (2016)
3. Mirghaderi, S.R., Torabian, S., Imanpour, A.: Seismic performance of the Accordion-Web RBS connection. J. Constr. Steel Res. **66**(2), 277–288 (2010)
4. Swati, A.K., Gaurang, V.: Study of steel moment connection with and without reduced beam section. Case Stud. Struct. Eng. **1**, 26–31 (2014)
5. Chen, C., Qiao, H., Wang, J., Chen, Y.: Progressive collapse behavior of joints in steel moment frames involving reduced beam section. Eng. Struct. **225**, 111297 (2020)
6. Meng, B., Zhong, W., Hao, J., Song, X.: Improving anti-collapse performance of steel frame with RBS connection. J. Constr. Steel Res. **170**, 106119 (2020)
7. Wang, W.D., Han, L.H., Uy, B.: Experimental behaviour of steel reduced beam section to concrete-filled circular hollow section column connections. J. Constr. Steel Res. **64**(5), 493–504 (2008)

Review of Various Microbial Immobilization Methods Towards Self-healing Application

Check for updates

Basil Baby, T. Palanisamy, and S. Arjun

Abstract Crack development and propagation in concrete structures, associated with internal and external stresses possess a severe threat to the performance and durability. Repair works of such concrete structures impart an immense financial toll. Self-healing mortar and concrete are developed with a view to provide a solution to address the aforementioned problem. The viability and performance of calcite precipitating microbes inside the concrete, in the long term, is always a concern when it comes to self-healing application. Among different methods to introduce such bacteria inside, immobilisation is considered to yield better results having the advantage of lesser impact from the adverse environment. This paper reviews the available immobilisation and encapsulation methods for microbial transport into the mortar or concrete, which makes use of porous media, hydrogels, polymeric coatings, etc., and its effectiveness in making a resilient building material. The current practices and the challenges associated with encapsulation methods to make a viable bio-mortar is critically reviewed and presented. The interaction of microbial colonies with the transporting medium and crack healing efficiency is compared based on different encapsulation methods. An experimental study was conducted to determine the impact of nutrients on the compressive strength of cement mortar was also conducted to identify the impact on strength parameters. The nutrients like calcium lactate, calcium nitrate, urea, calcium formate, and yeast extract in different dosages were analysed to achieve the optimum dosage value. It was observed nutrients other than urea and yeast extract, improved the compressive strength of bio-mortar at respective optimum dosages.

Keywords Bio-mortar · Bio-concrete · Self-healing · Resilient building material · Immobilization · Encapsulation

B. Baby (✉) · T. Palanisamy · S. Arjun
Department of Civil Engineering, National Institute of Technology Karnataka, Mangaluru, India
e-mail: basilpisharathu@gmail.com

1 Introduction

Even though have unique feature, immobilization and encapsulation are words used with identical meanings by most researchers when it comes to self-healing concrete. The term immobilization in bio concrete is the process by which the motility of microbes is inhibited by constraining them inside a protective coating so that they can revive once the ambient environment is available. On the other hand, encapsulation is the method adopted to contain the microbe inside a porous media which acts as a carrier, to regenerate their calcite precipitating action once it comes in contact with nutrients. Concrete is a material widely used around the world to meet construction needs, is more prone to cracks subjected to various physical as well as chemical aspects [17]. The network of cracks developed results in deterioration of concrete, but incurs huge investment for repair and rehabilitation works, with the aid of conventional means [30]. In this prospect, calcium carbonate precipitation of non-pathogenic bacteria can be used as an effective tool in densifying the microstructure and sealing the micro-cracks in concrete volume. In comparison with chemical applications for repair activities, microbially induced calcite precipitation (MICP) is recognized as conducive to the environment [1]. But the bacteria used for MICP should be alkalophilic and tolerant to temperatures up to which hydration temperature may go up [13]. Different types of mechanisms are available for inducing calcium carbonate precipitation and various methods can be employed in achieving the process inside the concrete. This paper reviews various mechanisms for induced crack healing by bacteria and the potential of different immobilization techniques in achieving better crack healing.

1.1 Mechanism for Microbially Induced Calcite Precipitation

Microbially induced calcite precipitation mechanisms are illustrated in Fig. 1 and bacteria that can exhibit respective mechanisms are given in Table 1, and it is achieved in the following ways:

Photosynthesis
Cyanobacteria are one of the major carriers of photosynthetic activity in calcite precipitation [2]. These bacteria will assimilate CO_2 and will react with water to produce bicarbonate and hydroxyl ion. This bicarbonate will combine with positively charged calcium ions adhered on the bacterial walls and will precipitate calcium carbonate [7].

Ureolysis
Bacteria such as Sporosarcina pasteurii can produce urease enzyme that hydrolysis urea to produce carbamate and ammonia. Ammonia reacts with water to form hydroxyl ion and carbamate is readily reduced to carbonic acid which react together
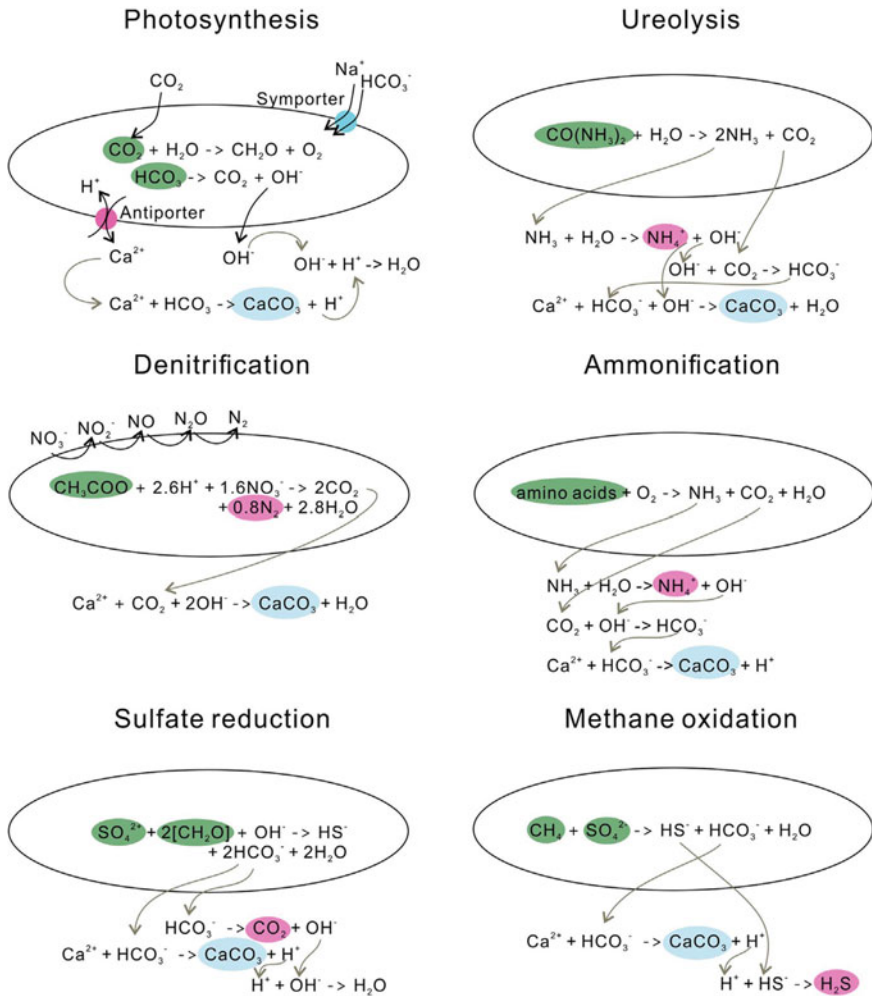
Fig. 1 Mechanisms for MICP (Courtsey: Zhu T et al.,) [36]

to give carbonate ion. Positively charged calcium ions will adhere to the bacterial surface to produce calcium carbonate [22].

Denitrification

Anaerobic bacteria like Diaphorobacter, Denitrobacillus, etc., will reduce nitrate ions to nitrogen gas and carbon dioxide. In the presence of moisture, the carbon dioxide will react with calcium ions to give calcium carbonate [22].

Table 1 Various mechanisms of calcite precipitation exhibited by bacteria

Metabolic pathway	Bacterial strain	Reference
Photosyntheis	Cyanobacteria Synechococcus PCC8806	[3]
	Greensulphur bacteria	[11]
Ureolysis	Sporosarcina pasteurii	[19]
	Bacillus subtilis	[18]
	Bacillus cereus	[16]
	Bacillus sphericus	[9]
Denitrification	Pseudomonas aeruginosa	
	Diaphorobacter nitroreducens	[5]
Ammonification	Myxobacteria	[10]
Sulfate reduction	Desulfovibrio vilgaris	[23]
	Desulfovibrio desulfuricans	
Methane oxidation	Methanogens	[20]

Ammonification

Bacteria from Myxococcus species metabolise amino acids to produce bicarbonate ion and ammonia [10]. This ammonia will further hydrolyse to form hydroxyl ions and will adhere to calcium ions to produce calcium carbonate [36].

Sulfate Reduction

The sulfate-reducing microbes will reduce compounds like calcium sulphide from calcium sulfate and its hydrolysis results in the formation of calcium hydroxide. This in turn will react with carbonic acid to give calcium carbonate. An increase in pH will result in the optimum precipitation of $CaCO_3$ [3].

Methane Oxidation

In the anaerobic oxidation of methane, first, it is converted into carbonate ions, and sulfate is converted to HS^- ions. It will combine with carbonate ions to give calcium carbonate, as the bacterial surface is ashered with positively charged Calcium ions [20].

2 Immobilisation of Bacterial Spores in Concrete

Organic as well as inorganic porous material with sufficient pore size to house the bacterial spores can be used as carrier material for the immobilisation of MICP bacteria. In addition to that, artificial microcapsules are also used as encapsulation material to take the microbial spore inside the concrete. The effectiveness in healing the crack width by MICP microbes is illustrated in Table 1. The most common method employed to encapsulate bacteria is by vacuum impregnation method. Thereafter the

material encapsulated with microbial spores is then coated with a protective coating to safeguard it during mixing and placing. Different encapsulation materials employed in the research of self-healing concrete are as follows:

2.1 *Expanded Perlite*

Expanded perlite (EP) is of volcanic origin, has size in the range of fine aggregate fraction, and comprises a porous structure. The pore structure of size up to 0.15 mm is found which can easily accommodate bacterial spores. It can protect the spores from the pH of concrete and increases the flexural strength of concrete [25]. The large porous network and higher absorption capacity make EP a first-choice material for encapsulating bacteria. These pores can facilitate the oxygen pockets for spores to germinate. With this immobilisation technique, crack widths of 0.79 mm were healed [35]. The average market rate lies in the range of of Rs. 50–55/kg.

2.2 *Expanded Clay*

Expanded clay is a lightweight aggregate with a size in the range of 1–4 mm. The average price of expanded clay in Indian market is Rs. 63/kg. The Using Bacillus cohnii Jonkers et al., were able to obtain the maximum width of crack healed like 0.15 mm whereas Zhang et al. were able to seal a crack width of size up to 0.45 mm. As a partial replacement, Expanded clay immobilized spores can be used in place of fine aggregate fraction.

2.3 *Biochar*

Biochar made from pyrolysis of wood can reduce greenhouse gas as it sequesters stable carbon from within, and have properties that make it conducive as a construction material viz its inferior thermal conductivity, less inflammable, and high chemical stability. It comprises pore sizes ranging from 2 nm to 20 μm. [26]. The maximum crack width healed observed was 0.70 mm [15]. Manufactured biochar costs around Rs. 13/kg.

2.4 Hydrogel and Microcapsule

Microcapsules/Hydrogel can be organic/inorganic composites composed of polymers. These microcapsules can isolate the bacteria from the surrounding environment [33]. Inert spore will become active, once the encapsulated capsule is broken on loading. Also, it won't affect the water absorption and hydration properties of mortar, as the nutrients and microbial spores are perfectly encapsulated but are costlier than other methods. Hydrogel encapsulated spores were able to arrest cracks of 0.5 mm [32]. The synthetic hydrogel is priced around Rs. 550/kg.

2.5 Diatomaceous Earth

Diatomaceous earth (DE) particles are also highly porous in nature and have a good surface absorption capacity. These materials are priced around Rs. 50/kg in Indian market. These materials when used as carriers produce a better micro-environment for enhanced urease activity of bacterial spores. DE immobilized spores resulted in the closure of fissures with the width of 0.17 mm [28].

2.6 Recycled Aggregate

The oven-dried recycled aggregates are often more porous than natural aggregates due to the prolonged stresses it was subjected to. The bacterial spores immobilized in recycled aggregate resulted in the sealing of fissures with widths of 0.7 mm [14]. The average price of recycled aggregate is around Rs. 12/kg.

From Table 2, crack widths from size 0.20 to 1.2 mm were healed. The lightweight aggregate Expanded Perlite and Microcapsules exhibited better healing ratios. Nanoparticle encapsulated spores also showed increased healing capacity, but the cost-effectiveness will be less. The type of bacteria, enzymatic activity, bacterial cell concentration can also have an impact on the crack width healed, despite of the type of carrier material. It is also evident that the type of nutrient used in initiating metabolic activity of encapsulated/ immobilised spores also plays a vital role in effective crack healing. Hence further investigation on the effect of nutrients on compressive strength of mortar cube specimens were also investigated.

Table 2 Self-healing by MICP bacteria using various immobilization techniques

Bacterial strain	Method	Crack width healed (mm)	Reference
Bacillus pseudofirmus	Encapsulation in calcium alginate chitosan hydrogel	1	[8]
Bacillus cohnii	Immobilizing in expanded clay	0.15	[12]
Bacillus sphaericus	Melamine-based microcapsule	0.97	[29]
Bacillus sphaericus	Encapsulation in hydrogel	0.5	[31]
Sporosarcina pasteurii	Encapsulation in calcium sulphoaluminate cement	0.417	[34]
Bacillus cohnii	Immobilizing in perlite	0.79	[35]
Bacillus cohnii	Immobilizing in expanded clay	0.45	[35]
Bacillus sphaericus	Immobilizing in biochar	0.55–0.70	[15]
Bacillus sphaericus	Encapsulation in chitosan-based hydrogel	0.20-0.30	[29]
Bacillus alkalinitrilicus	Immobilizing in expanded clay	0.46	[28]
Bacillus subtilis	Immobilizing in iron-oxide nano-particle	1.2	[24]
Bacillus subtilis	Immobilizing in bentonite	0.2	[24]
Bacillus subtilis	Immobilizing in recycled coarse	0.7	[14]

3 Effect of Nutrient Dosage on Compressive Strength of Mortar

In order to obtain a better performing MICP material, it is necessary to add suitable nutrient agent to the composites core. Many kinds of research were conducted to assess the efficiency of healing system, encapsulation methods and interaction between nutrients and bacteria, the prospect of the interaction of nutrients with composite matrix should be investigated. this in turn will bring more quality control and better performance of the mortar or concrete system incorporated with MICP spores via encapsulation. Thus it will bring a better understanding on the impact of nutrients on various parameters of composite system.

3.1 Mix Proportion and Sample Preparation

Based on the literature review, following nutrients commonly adopted for MICP were selected: calcium lactate ($C_6H_{10}CaO_6$) in dosage of 3, 2.5 and 2%, calcium

nitrate $(Ca(NO_3)_2)$ in dosage of 2, 2.5 and 3%, and calcium formate $(Ca(HCOO)_2)$ in dosages 1, 2 and 3%, yeast extract at 0.15, 0.3 and 0.60% to cement weight, and urea at a concentration of 0.15, 0.3 and 0.60%, as additive replacing cement, in case of a MICP bacteria with Ureolytic mechanism. Ordinary Portland Cement 53 grade was used and mixed in the proportion cement: sand as 1:3, with w/c as 0.45.

3.2 Results and Discussions

The results obtained from the tests on compressive strength are tabulated in Table 3.

Calcium lactate is often used for biocalcification and has a positive impact on the compressive strength of the specimen. Calcium formate and calcium nitrate are provided as additives to boost the hydration, a steadily inclined growth of the compressive strength was anticipated, and the results obtained underlined the fact. Also, unlike calcium nitrate, the mortar provided with calcium formate as a nutrient additive reached a value tad higher in terms of the compressive strength when compared to the control specimens. The addition of yeast extract in the dose of 0.6% replacing cement resulted in a sudden drop on the performance in terms of compression tests results, attributed to the formation of air pockets inside. From the results, it can be concluded that the optimum dosage of calcium lactate, calcium formate, calcium nitrate, and urea are 2.5, 1, 2.5 and 0.15% respectively.

Table 3 Dosage of nutrients and 28 day compressive strength

Nutrient	Dosage (% of cement weight)	Avg compressive strength at 28 days	Percentage change in strength
CS	0	8.03	100
Calcium lactate	2	8.83	110
	2.5	10.28	128
	3	9.23	115
Calcium formate	1	9.64	120
	2	8.51	106
	3	8.11	101
Calcium nitrate	2	6.10	76
	2.5	8.60	107
	3	6.58	82
Urea	0.15	8.11	101
	0.3	7.31	91
	0.6	6.50	81
Yeast extract	0.15	6.26	78
	0.3	6.42	80
	0.6	5.78	72

4   Conclusion

Microbially Induced Calcite Precipitation is an effective way of producing sustainable and durable concrete or mortar. As a repair mortar, the role of MICP bacteria in reducing repair costs in long term is of great importance. From the study following conclusions can be drawn out:

- Using MICP bacteria in mortar or concrete can save costs in terms of repair and rehabilitation expenses. This is a proven technology in terms of crack healing and is efficient in densifying the microstructure of the composite.
- Usage of carriers led to higher crack healing efficiency compared to conventional methods of direct addition. Crack widths up to 1.2 mm were healed using the encapsulation technique.
- Even though the price of encapsulation materials varies from Rs. 12/kg to Rs. 550/kg, the factors like the capacity of the material to safeguard the bacterial spores, the application scenario, and the easiness with which the same can be synthesized should be considered while choosing the encapsulation technique rather than considering financial constraints alone.
- Immobilisation/encapsulation forms a viable tool in protecting the microbial spores from the unfavorable environment. Thus, the longevity of microbial spores is ensured.
- Melamine based capsules are more effective in crack healing, compared to other polymer types and the wall thickness of capsules is an important parameter determining the performance of the respective immobilization technique.
- Apart from the bacterial concentration the choice of nutrients also forms an important parameter in delivering a mortar/concrete with better mechanical characteristics. Among the commonly used nutrients, calcium lactate, calcium formate, and calcium nitrate had a positive impact on the mechanical performance of the composite.

References

1. Achal, V., Mukherjee, A., Goyal, S., et al.: Corrosion prevention of reinforced concrete with microbial calcite precipitation. ACI Mater. J. **109**(2), 157–164 (2012)
2. Altermann, W., Kazmierczak, J., Oren, A., Wright, D.T.: Cyanobacterial calcification and its rock-building potential during 3.5 billion years of earth history. Geobiology **4**, 147–166 (2006)
3. Baumgartner, L.K., Reid, R.P., Dupraz, C., Decho, A.W., Buckley, D., Spear, J., et al.: Sulfate-reducing bacteria in microbial mats: changing paradigms, new discoveries. Sediment. Geol. **185**, 131–145 (2006)
4. Chen, H., Qian, C., Huang, H.: Self-healing cementitious materials based on bacteria and nutrients immobilized respectively. Constr. Build. Mater. **126**, 297–303 (2016)
5. Erşan, Y.C., Da Silva, F.B., Boon, N., et al.: Screening of bacteria and concrete protection materials. Constr. Build. Mater. **88**, 196–203 (2015)

6. Erşan, Y.Ç., De Belie, N., Boon, N.: Microbially induced CaCO3 precipitation through denitri-fication: an optimization study in minimal nutrient environment. Biochem. Eng. J. **101**, 108–118 (2015)

7. Hammes, F., Verstraete, W.: Key roles of pH and calcium metabolism in microbial carbonate precipitation. Rev. Environ. Sci. Bio/Technol. **1**, 3–7 (2002)

8. Gao, M., Guo, J., Cao, H., et al.: Immobilized bacteria with pH-response hydrogel for self-healing of concrete. J. Environ. Manag. **261**, 110225 (2020)

9. Gavimath, C., Mali, B., Hooli, V., et al.: application of bacteria to improve the strength of cement concrete. J. Adv. Biotechnol. Res. **1**, 541–544 (2012)

10. González-Muñoz, M.T., Rodriguez-Navarro, C., Martínez-Ruiz, F., Arias, J.M., Merroun, M.L., Rodriguez-Gallego, M.: Bacterial biomineralization: new insights from Myxococcus-induced mineral precipitation. Geol. Soc. Spec. Publ. **336**, 31–50 (2010)

11. Peretó, J.: Anoxygenic Photosyntheis, Encyclopedia of Astrobiology,p. 46. Springer, Heidel-berg (2011)

12. Jonkers, H.M.: Bacteria-based self-healing concrete. Heron. **56**, 1–12 (2011)

13. Kiranmaye, B.R., Dutta, J.R., Kar, A., et al.: Optimization of culture parameters of Pseu-domonas alcaligenes for crack healing in concrete. Mater. Today: Proc. **28**, 713–716 (2020)

14. Khushnood, R.A., Qureshi, Z.A., Shaheen, N., et al.: Bio-mineralized self-healing recycled aggregate concrete for sustainable infrastructure. Sci. Total Environ. **703**, 135007 (2020)

15. Kua, H.W., Gupta, S., Aday, A.N., et al.: Biochar-immobilized bacteria and superabsorbent polymers enable self-healing of fiber-reinforced concrete after multiple damage cycles. Cem. Concr. Compos. **100**, 35–52 (2019)

16. Maheswaran, S., Dasuru, S., Murthy, A.R.C., et al.: Strength improvement studies using new type wild strain Bacillus cereus on cement mortar. Science **106**, 50–57 (2014)

17. Mindess, S., Young, F., Darwin, D.: Concrete. 2nd ed. Technical Documents (2003)

18. Pei, R., Liu, J., Wang, S., et al.: Use of bacterial cell walls to improve the mechanical performance of concrete. Cem. Concr. Compos. **39**, 122–130 (2013)

19. Ramachandran, S.K., Ramakrishnan, V., Bang, S.S.: Remediation of concreteusing micro-organisms. ACI Mater. J. Am. Concr. Inst. **98**(1), 3–9 (2001)

20. Reeburgh, W.S.: Oceanic methane biogeochemistry. Chem. Rev. **107**, 486–513 (2007)

21. Jakubovskis, R., Jankutė, A., Urbonavičius, J., Gribniak, V.: Analysis of mechanical perfor-mance and durability of self-healing biological concrete. Constr. Build. Mater. **260**, 11982 (2020)

22. Mondal, S., Ghosh, A.D.: Investigation into the optimal bacterial concentration for compressive strength enhancement of microbial concrete. Constr. Build. Mater. **183**, 202–214 (2018)

23. Seifan, M., Samani, A.K., Berenjian, A.: Bioconcrete: next generation of selfhealing concrete. Appl. Microbiol. Biotechnol. **100**(6), 2591–2602 (2016)

24. Shaheen, N., Khushnood, R.A., Khaliq, W., et al.: Synthesis and characterization of bio-immobilized nano/micro inert and reactive additives for feasibility investigation in self-healing concrete. Constr Build Mater. **226**, 492–506 (2019)

25. Shen, L., Yu, W., Li, L., Zhang, T., Abshir, I.Y., Luo, P., Liu, Z.: Microorganism, carriers, and immobilization methods of the microbial self-healing cement-based composites: a review. Materials (Basel) **14**(17), 5116 (2021)

26. Gupta, S., Kua, H.W., Pang, S.D.: Healing cement mortar by immobilization of bacteria in biochar: an integrated approach of self-healing and carbon sequestration. Cem. Concr. Compos. **86**, 238–254 (2018)

27. Zhu, T., Paulo, C., Merroun, M.L., Dittrich, M.: Potential application of biomineralization by Synechococcus PCC8806 for concrete restoration Ecol. Eng. **82**, 459–468 (2015)

28. Wang, J.-Y., De Belie, N., Verstraete, W.: Diatomaceous earth as a protective vehicle for bacteria applied for self-healing concrete. J. Ind. Microbiol. Biotechnol. **39**(4), 567–577 (2012)

29. Wang, J., Mignon, A., Trenson, G., et al.: A chitosan-based pH-responsive hydrogel for encapsulation of bacteria for self-healing concrete. Cem. Concr. Compos. **93**, 309–322 (2018)

30. Wang, J., Soens, H., Verstraete, W., et al.: Self-healing concrete by use of microencapsulated bacterial spores. Cem. Concr. Res. **56**, 139–152 (2014)
31. Wang, J., Snoeck, D., Van Vlierberghe, S., et al.: Application of hydrogel encapsulated carbonate precipitating bacteria for approaching a realistic self-healing in concrete. Constr. Build. Mater. **68**, 110–119 (2014)
32. Wang, J., Van Tittelboom, K., De Belie, N., et al.: Use of silica gel or polyurethane immobilized bacteria for self-healing concrete. Constr. Build. Mater. **26**(1), 532–540 (2012)
33. White, S.R., Sottos, N.R., Geubelle, P.H., Moore, J.S., Kessler, M.R., Sriram, S.R., Brown, E.N., Viswanathan, S.: Autonomic healing of polymer composites. Nat. Int. Wkly. J. Sci. **409**, 794–797 (2001)
34. Xu, J., Wang, X.: Self-healing of concrete cracks by use of bacteria-containing low alkali cementitious material. Constr. Build. Mater. **167**, 1–14 (2018)
35. Zhang, J., Liu, Y., Feng, T., et al.: Immobilizing bacteria in expanded perlite for the crack self-healing in concrete. Constr. Build. Mater. **148**, 610–617 (2017)
36. Zhu, T., Dittrich, M.: Carbonate precipitation through microbial activities in natural environment, and their potential in biotechnology: a review. Front. Bioeng. Biotechnol. **4**, 4 (2016)

Punching Shear Strengthening of RC Light Weight Flat Slab Using Embedded Through Section Technique

T. P. Arathi and K. I. Praseeda

Abstract Flat slabs are concrete plates propped on column, without the existence of beams. Punching shear failure is a local mechanism, that arises when a concentrated load is applied to a small area of the slab. This abrupt failure hence reduces the load-bearing capacity of the slab and can potentially results in the progressive collapse of the entire structure. To enhance the performance of flat slab against failure due to punching and deflection, additional reinforcement should be provided in the column region. This study focuses on strengthening of flat slab by Embedded Through Section (ETS) to overcome the punching shear failure. Objective is the strength analysis of flat slab column connection by imparting different cases. The complete analytical model has been carried out using non-linear static analysis in ANSYS Software.

Keywords Flat slab · Punching shear · Embedded through section

1 Introduction

1.1 General Background

Flat slab can be defined as a reinforced concrete structural element, which carries horizontal and vertical load and directly transfers to the columns, without any beams or girders [5]. Nowadays, flat-slab structural system is much popular in the design of multi-storeyed buildings, due to the many advantages offered by the system in terms of its shorter construction time, depth, flexibility in design layout and architectural convenience [1]. Flat slabs are mainly classified to 3 types:—Simple flat slab, flat slab with drop panel, and flat slab with column capital. Drop panel is the local thickening of the slab in the region of column. Column capital is a flared portion of the column at the top, where the slab is being supported. However, the main problem associated with the flat slabs is the brittle punching shear failure. Punching shear failure in

T. P. Arathi (✉) · K. I. Praseeda
Department of Civil Engineering, NSS College of Engineering, Palakkad, Kerala, India
e-mail: 20m052@nssce.ac.in
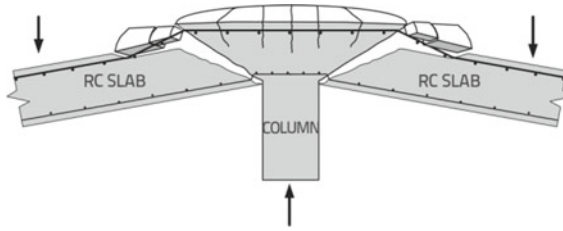
Fig. 1 Punching shear failure (*Source* https://encrypted-tbn0.gstatic.com/images?q=tbn:)

flat slab is caused by the unbalanced moment and vertical shear borne by the flat slab-column connection, which makes it a weak link in the whole flat slab-column, and then leading it to serious damage or even collapse of the structure. Unbalanced moments in buildings with flat slabs is caused by loading on either side of the column or of unequal spans. Usually, in flat slab constructions, the punching shear failure as in Fig. 1 could occur abruptly even without any warning signs leading to many devastating loses [3]. Punching shear failure is a local failure mechanism, which is associated with the formation of truncated cone shape [5]. This failure may be attributed to construction errors, inadequate structural design or change in the use of the current structure along with the higher floor loads. Due to the increase in the applied loads and deficiencies faced during design or construction stage, currently a number of existing flat slabs require strengthening for safety reasons against punching shear.

1.2   Strengthening Methods

To overcome the punching shear failure, following strengthening methods can be used:

a.   Strengthening the tension reinforcement

It improves the flexural stiffness, flexural strength, and shear capacity of connections. This technique includes embedded through section and are irreplaceable after implementation. It is cost-effective and durable. Here, the main materials used in shear strengthening are: Steel, CFRP and GFRP. The installation of shear reinforcement enhances the punching strength.

b.   Enlargement of support

Another category is a conventional way by enlarging the supporting area which, in principle, leads to an increase of critical section around the column. This geometrical change would result in enhancement of flexural capacity of the slab. The enlargement of the support could be improved by widening the column, casting a concrete capital or post-installing a steel capital.

iii.   Post-installation technique

Post-installation technique is achieved by post installed screws, external steel shear bolts and inclined shear reinforcement installed through slab thickness. Shear strength and ductility increased for slab strengthened with post-installed shear reinforcement. Use of steel bolts as shear reinforcement helps in strengthening slabs against punching failure is effective in preventing sudden punching shear failure in flat slabs [4]. This is one of the methods, which are replaceable, even after retrofitting.

Generally, all the strengthening techniques showed an enhancement in the punching shear capacity of the flat slab-column connection. ETS technique is observed to be the cost effective with easiness in fabrication and advancement in technology.

Embedded Through Section

Embedded through-section (ETS) is a technique which is developed to increase the punching shear capacity of the reinforced concrete flat slab-column connection using fibre-reinforced polymer (FRP) rods. Here, the strengthening bars are inserted into the pre-drilled holes of the core of concrete [2]. By doing so, they are protected from environmental aggressive agents, fire and vandalism acts. The ETS method represents several advantages over the other existing methods, such as in externally bonded FRP sheets and near-surface mounted FRP rods [6]. In the ETS technique, FRP lies on the concrete core of the RC beam, and it provides a greater confinement and though it improves the bonding performance [6]. This method consumes less time, only less adhesive are required, and no need of surface preparation or does not require skilled workers to install [6]. Moreover, the application of using FRP rods (instead of steel rods) prevents possible corrosion of the strengthening rods. The flat slabs including such method undergo a significant reduction in the punching shear capacity.

2   Analytical Programme

2.1   Material Properties

Light weight concrete and rebar are mainly used for the preparation of RC light weight flat slab. Properties of concrete and rebar assigned for the analysis is tabulated in Tables 1 and 2. 10 mmø bars were used in the slab while 16 mmø and 8 mmø were used as main reinforcement and stirrups in column respectively.

Table 1 Mechanical properties of concrete

	Modulus of elasticity (MPa)	Poisson ratio	Uniaxial compressive strength (MPa)	Uniaxial tensile strength (MPa)
Concrete	26,999	0.12	33	1.9

Table 2 Mechanical properties of steel bars

Size of bar (mm)	Young's modulus (MPa)	Poisson ratio	Yield strength (MPa)
16	2×10^5	0.3	460
10	2×10^5	0.3	342
8	2×10^5	0.3	350

2.2 Modelling and Analysis

Based on the studies, various models of flat slab-column connections are created for the undertaking of static analysis using ANSYS software package. Each model has dimensions for the flat slab as 2000 × 2000 mm with thickness 140 mm and that of column is 250 × 250 mm, which is having a depth of 1500 and 400 mm to the top and bottom of the slab respectively. Rebars are modelled as bilinear isotropic hardening and plasticity for the concrete is modelled by Menetary-William method. Element type used for concrete is SOLID 185 and for rebar is REINF 264. Unstrengthened model is depicted in Fig. 2.

(a)   (b)
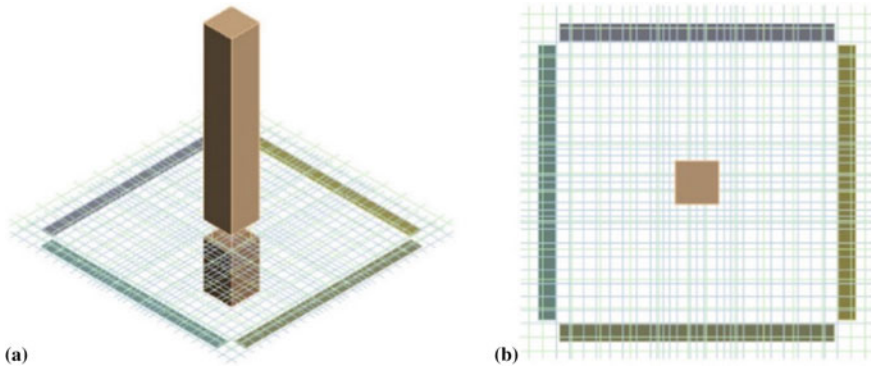
Fig. 2 Unstrengthened model: **a** isometric view, **b** top view
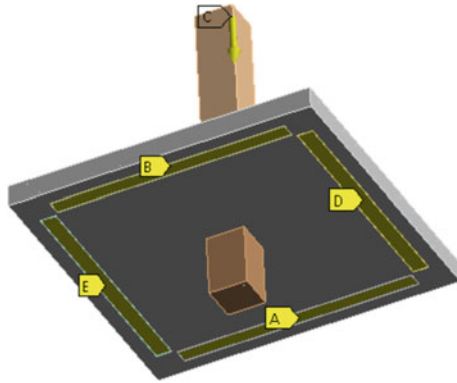
Fig. 3 Boundary condition

2.3　Boundary Condition

The flat slab is simply supported at an in-plane distance of 1700×1700 mm and is subjected to concentrated load at the centre of the top face of column as in Fig. 3.

2.4　Parametric Study

Punching shear is a major concern in the strength reduction of flat slab-column system. Embedded Through Section (ETS) technique is imparted for strengthening. Effect of strengthening is determined by varying the parameters like diameter of bars (16, 12, 10 mm) and with the number of rows (1 row and 2 rows) in two types of arrangements such as rectangular (RA) in Fig. 4 and circular arrangement (CA) in Fig. 5. Table 3 illustrates the model configurations.
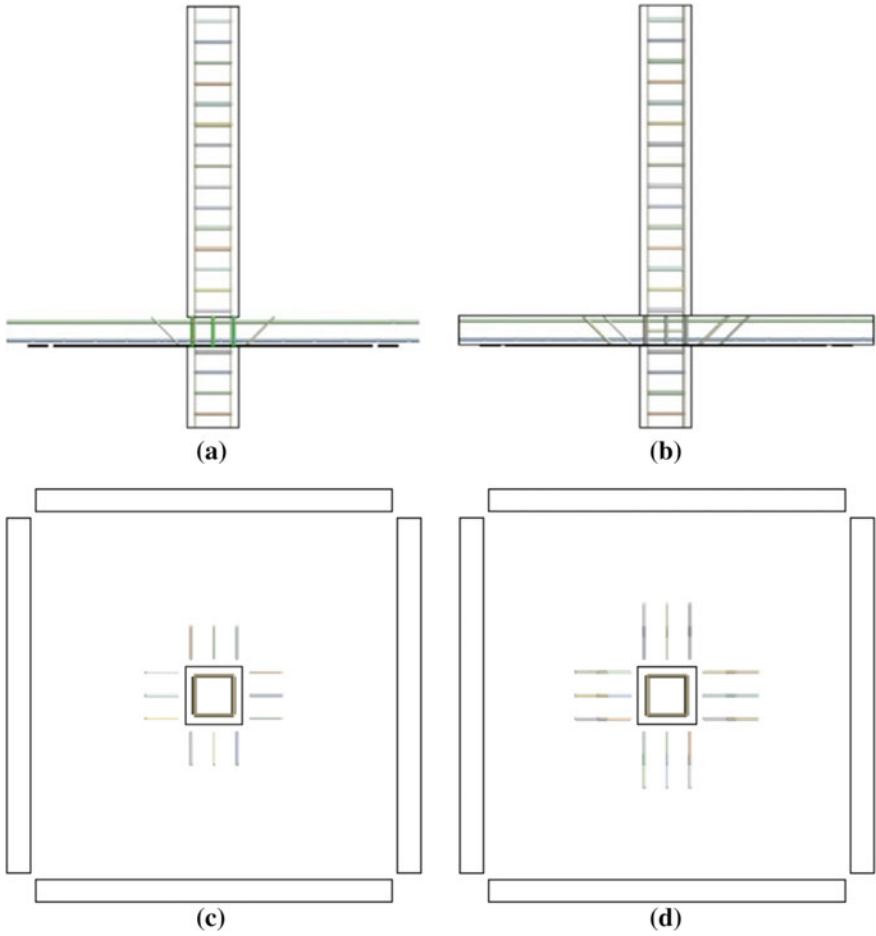
Fig. 4 Rectangular arrangement: **a** 1R sectional view, **b** 2R sectional view, **c** 1R top view, **d** 2R top view
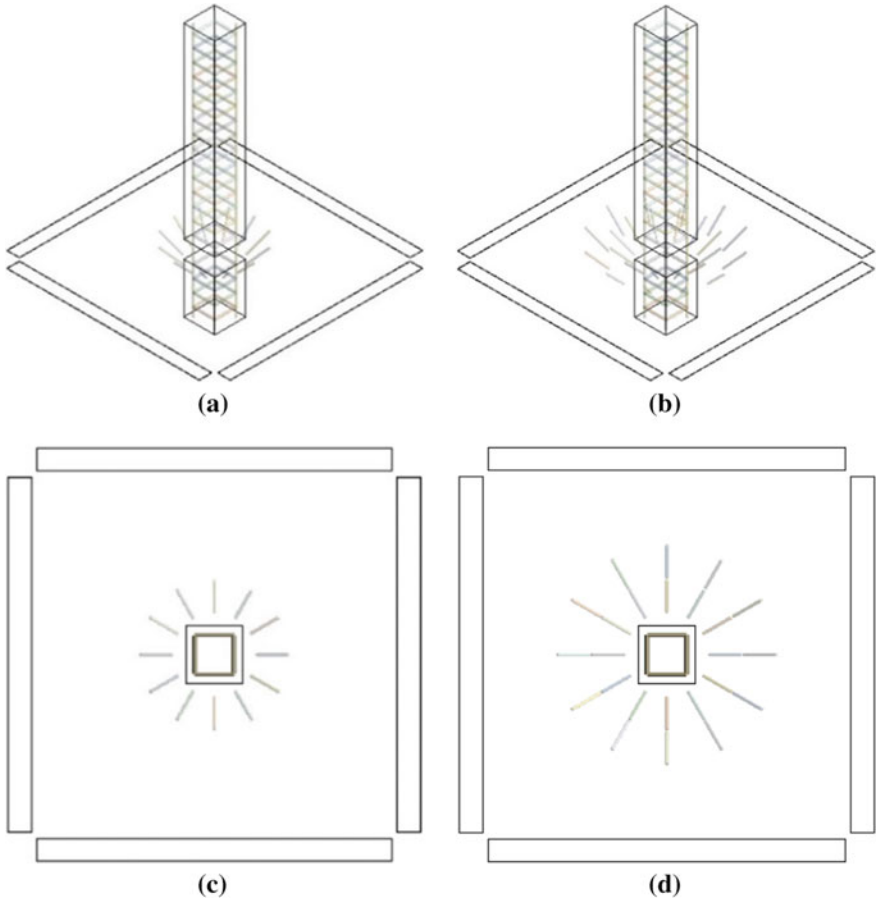
Fig. 5 Circular arrangement: **a** 1R sectional view, **b** 2R sectional view, **c** 1R top view, **d** 2R top view

Table 3 Model configurations

Models	Material	ETS arrangement	Diameter of bar (mm)	Number of rows
Model 1	Unstrengthened	–	–	–
Model 2	Steel	RA	16	1
Model 3			12	
Model 4			10	
Model 5			16	2
Model 6			12	
Model 7			10	
Model 8		CA	16	1
Model 9			12	
Model 10			10	
Model 11			16	2
Model 12			12	
Model 13			10	
Model 14	GFRP	RA	16	1
Model 15			12	
Model 16			10	
Model 17			16	2
Model 18			12	
Model 19			10	
Model 20		CA	16	1
Model 21			12	
Model 22			10	
Model 23			16	2
Model 24			12	
Model 25			10	

3   Results

The ETS technique of flat slab-column is modelled and tested under displacement-controlled loading in ANSYS software. Specimens with different parameters were analysed and compared with unstrengthened model. Load versus deflection curves were plotted in Fig. 6 and compared. Figure 7 and 8 depicts the load and deflection comparison of each case respectively. Table 4 shows the percentage increase in load for each model. Plastic strain and distribution of damage is shown in Fig. 9.
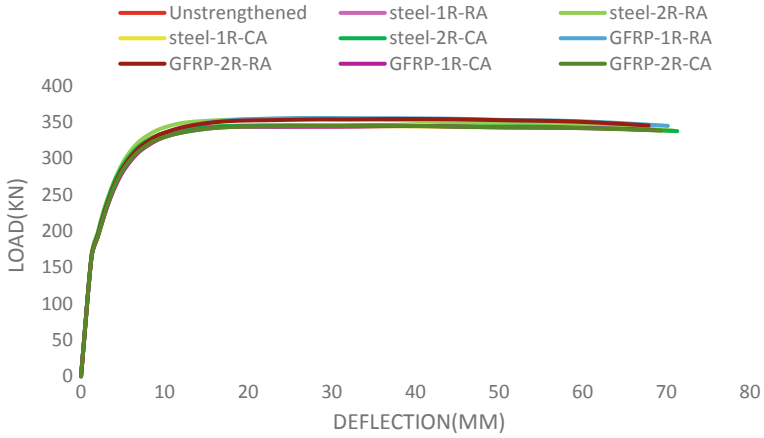
Fig. 6 Load-deflection plot
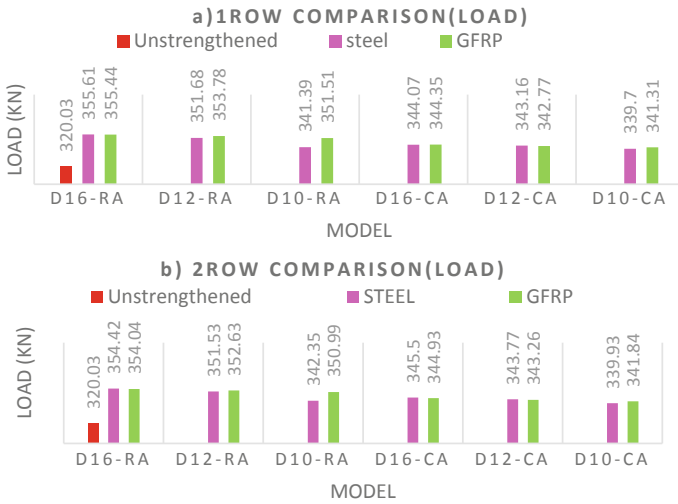
Fig. 7 Load comparison of **a** 1 row, **b** 2 row
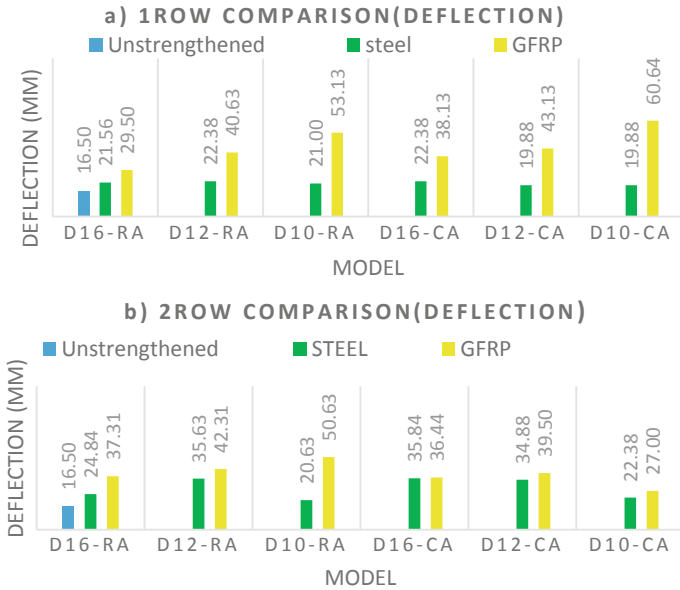
Fig. 8 Deflection comparison of **a** 1 row, **b** 2 row

Table 4 Percentage increase in load

Models	Deflection (mm)	Load (kN)	Increase in load (%)
Unstrengthened	16.5	320.03	1
ETS-D16-1R-RA-steel	21.56	355.61	11.1
ETS-D12-1R-RA-steel	22.38	351.68	9.9
ETS-D10-1R-RA-steel	21.00	341.39	6.7
ETS-D16-2R-RA-steel	35.84	345.5	7.9
ETS-D12-2R-RA-steel	34.88	343.77	7.4
ETS-D10-2R-RA-steel	22.38	339.93	6.2
ETS-D16-1R-CA-steel	22.38	344.07	7.5
ETS-D12-1R-CA-steel	19.88	343.16	7.2
ETS-D10-1R-CA-steel	19.88	339.7	6.1
ETS-D16-2R-CA-steel	35.84	345.5	8.0
ETS-D12-2R-CA-steel	34.88	343.77	7.4
ETS-D10-2R-CA-steel	22.38	339.93	6.2
ETS-D16-1R-RA-GFRP	29.50	355.44	11
ETS-D12-1R-RA-GFRP	40.63	353.78	10.5

(continued)

Table 4 (continued)

Models	Deflection (mm)	Load (kN)	Increase in load (%)
ETS-D10-1R-RA-GFRP	53.13	351.51	9.8
ETS-D16-2R-RA-GFRP	37.31	354.04	10.6
ETS-D12-2R-RA-GFRP	42.31	352.63	10.2
ETS-D10-2R-RA-GFRP	50.63	350.99	9.7
ETS-D16-1R-CA-GFRP	38.13	344.35	7.6
ETS-D12-1R-CA-GFRP	43.13	342.77	7.1
ETS-D10-1R-CA-GFRP	60.64	341.31	6.6
ETS-D16-2R-CA-GFRP	36.44	344.93	7.8
ETS-D12-2R-CA-GFRP	39.50	343.26	7.3
ETS-D10-2R-CA-GFRP	27.00	341.84	6.8
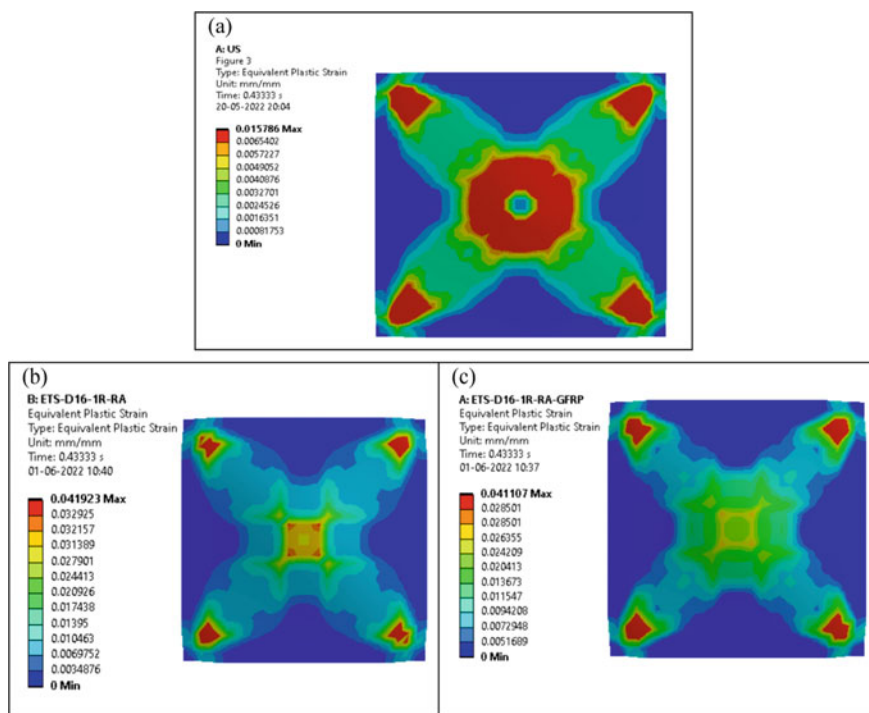
Fig. 9 Typical figures of plastic strain: **a** unstrengthened, **b** Steel-1R-RA, **c** GFRP-1R-RA

4   Conclusions

Strength evaluation of flat slab-column with ETS technique by non-linear static analysis is carried out for different cases. Responses obtained for each case is then compared with the conventional unstrengthened flat slab-column. Following conclusions are derived from the analytical study:

1. Punching shear strength is improved by using ETS bars.
2. Based on the study, strength performance of ETS using steel and GFRP are comparable. It is noted that for steel rods, an increment in the strength by 11.1% and GFRP rods with 11% are observed from conventional model.
3. Deflection capacity is increased from 16.5 mm (unstrengthened model) to 60.64 mm for GFRP bars and to 35.84 mm with steel bar.
4. Rectangular (orthogonal) arrangement of bars in single row shows better results than circular (radial) arrangement.
5. Considering the cost aspect, GFRP is more economical over steel.

References

1. Zhou, L., Huang, Y., Chen, B.: Punching shear behavior of slab-column connections embedded with steel skeletons. Structures **33**, 2879–2892 (2021)
2. Bui, L.V.H., Stitmannaithum, B., Jongvivatsakul, P.: Comprehensive investigation on bond mechanism of embedded through-section fiber-reinforced polymer bars to concrete for structural analysis. J. Build. Eng. **29**, 101180 (2020)
3. Deifalla, A.: Strength and ductility of lightweight reinforced concrete slabs under punching shear. Structures **27**, 2329–2345 (2020)
4. Said, M., Adam, M.A., Arafa, A.E., Moatasem, A.: Improvement of punching shear strength of reinforced lightweight concrete flat slab using different strengthening techniques. J. Build. Eng. **32**, 101749 (2020)
5. Lapi, M., Ramos, A.P., Orlando, M.: Flat slab strengthening techniques against punching-shear. Eng. Struct. **180**, 160–180 (2019)
6. Chaallal, O., Mofidi, A., Benmokrane, B., Neale, K.: Embedded through-section FRP rod method for shear strengthening of RC beams: performance and comparison with existing techniques. J. Compos. Constr. **15**(3), 374–383 (2011)

Construction Resource Wastage Optimization and Green Ideologies – An Insight on Literature

HA. Nishaant and J. Sudhakumar

Abstract This research aims to compile and evaluate the existing studies on construction resources, construction wastes, and green concepts. Following a descriptive assessment of the collection of literature, future research options are discussed. Critical Success Factors (CSFs) are derived from studies published between 2015 and 2021 on the issue of construction wastes, construction resources, and green construction ideologies. In addition, this paper discusses the constraints behind construction waste optimization and green implementation. The results of this study can be utilized to aid decision-making in the context of construction resource wastage optimization. This is a novel attempt to collect CSFs relevant to the construction sector. It might be used for more research and development to assure the quality and success of the project. A bibliographic analysis is adopted based on citation and country origin of publications. The partial identification of CSFs limits this research. Despite an intensive search, the returned CSFs may not be all of the published ones. On the other hand, more extensive search approaches can be used to improve this task. Future studies in this area should focus on the real-time strategy.

Keywords Construction waste · Green ideology · Construction resource · Critical success factors

1 Introduction

Construction companies are faced with the task of completing frequently difficult projects on time, on budget, and with a healthy profit margin. Proper usage of construction resources leads to effective construction management from a different perspective regarding the overall project's time, cost, and quality. Any detritus from the construction process is construction waste or debris. Construction waste has already been a major environmental issue in many nations worldwide, leading to

HA. Nishaant (✉) · J. Sudhakumar
Department of Civil Engineering, National Institute of Technology, Calicut, India
e-mail: nishaant_p180003ce@nitc.ac.in

construction resource inefficiency. Hence, construction resource wastage optimization leads to overcoming several obstacles in the construction industry. Meanwhile, waste reduction is one of the components of green construction concepts, and Waste management is an important part of sustainable construction. From this perspective, waste management is avoiding waste where possible, decreasing waste where feasible, and recycling/reusing resources that would otherwise be discarded. Hence these three major terminologies: Construction resources, construction wastes, and green construction, should be discussed as combinable for effective construction practices. Therefore, this study gathers information regarding construction resources, construction wastes, and green concepts. The detailed systematic analyses are as follows,

1.1 Construction Resources and their Factors

The construction process is quite fragmented. Process integration can boost measurable performance indicators [1]. 'Empowerment/Training' might considerably increase the performance of Human Resources (HR) in projects. 'Quality Assessment' has a significant influence on the concepts in the HR-planning framework.

Additionally, the following consequential concepts for effectual HR management practices are 'Networking Management,' 'Delegating,' and 'Reward/Compensation' [2]. One of the most difficult challenges for construction project planners is analyzing the time-cost-resources variation trade-off [3]. To be effective, current construction projects need adequate planning and resource management. Tasks that keep the schedule are considered core concerns [4]. Four-dimensional (4D) modeling provides a lot of potential for enhancing the design and planning of building processes. It has been demonstrated that combining a three-dimensional model with scheduling data allows for the practical identification of design and planning problems in the construction project [5]. Building information modeling (BIM) has been identified as an information technology that can significantly alter the Architecture, Engineering, and Construction (AEC) business and has attracted the interest of a number of construction experts. Despite earlier studies' reports of BIM progress, the widespread adoption of BIM has yet to attain its full potential [6]. The use of computer vision (CV) in the construction industry is increasing. Many CV-based research projects have as their goals the monitoring of productivity and project progress and the tracking of equipment for safety reasons [7]. More information on construction and demolition wastage creation and handling, the concentration, and emissions of hazardous compounds are needed [8]. In advanced building component manufacturing, process integration and the utilization of multi-skilled resources increase production network flexibility in response to changes in demand and resource availability [9]. The availability of resources in construction works may restrict the execution of optimal schedules. Conventional resource-constrained project scheduling problem (RCPSP)

models struggled to efficiently distribute resource consumption, especially when recurring tasks are involved.

On the other hand, real models give local optimum remedies and do not at all include activity acceleration algorithms [10]. Natural resource extraction is rising at a breakneck pace, and the challenges it has created demand immediate attention and action. Technological innovation makes extensive use of natural resources in order to satisfy human desires [11]. On the other hand, serious accidents in mobile vehicles or heavy equipment have been one of the most likely reasons for fatal and nonfatal injuries among construction workers [12]. Hence, proper utilization and optimization of resources are highly recommended in construction projects. Technical issues should be resolved while reusing recycled materials through present evidence formulations and a series of items investigations [13]. In response to the various network sizes, distinct distributions exist for the various cost components [14]. The RCPSP issue has been researched for decades as an essential subject in construction management; nevertheless, an integrated information model that completely supports the RCPSP solution technique is quite inadequate [15].

1.2 Construction Wastes and Management

Waste minimization design is a crucial method for efficiently reducing the generation of waste early on. However, it appears that no acceptable procedures exist for evaluating the impact of different design approaches on waste minimization while taking into consideration the interrelationships of alternative design approaches [16]. The waste generation rate (WGR) is a standard metric for evaluating and improving construction waste management (CWM) performance over time [17]. There are very few design decision-making technologies to allow efficient assessment and deployment of construction waste reduction across all design stages [18]. In urban centers and emerging countries, construction waste disposal is intimately linked to rapid economic expansion [19]. Many instances show that utilizing building information modeling (BIM) to validate design is an effective strategy to reduce construction waste, which is mostly caused by poor design and unplanned changes throughout the design and construction stages [20]. Previous studies comparing CWM performance have struggled due to a lack of high-quality data, leaving the CWM performance discrepancy topic largely unresolved [21]. A large volume of construction waste has been created as a result of an increased range of construction operations than in the past, which has profound environmental consequences if not adequately handled. As a result, appropriate construction waste management is critical for long-term sustainability [22]. The construction sector has recently been under compulsion to do dramatic measures to reduce waste. Waste awareness advocates for waste management techniques that are implemented after the waste has been generated [23]. Managing the project construction or expanding urbanisation, waste soil landfill site selection, and safety have become significant issues [24]. Legislation and fiscal policies have always been the primary drivers of construction sector viability

[25]. The need to use BIM to reduce Construction and Demolition Waste (CDW) is widely acknowledged; however, most CDW management technologies available at the moment lack BIM capabilities [26]. The high amount of construction trash has a severe environmental impact [27]. Construction debris and agricultural wastes are two of the world's most serious environmental issues. Construction waste takes up nearly a quarter of all landfill space worldwide [28]. Only a small amount of study has been done to cover both the design and construction stages, allowing for a thorough assessment of the entire construction waste reduction outcome [29]. Construction waste reduction (CWR) corresponds to lowering the quantity of harmful waste created during the construction process to the smallest amount possible, hence diminishing trash's environmental effect and enhancing the construction industry's long-term sustainability. Currently, many nations' CWR management systems do not place sufficient focus on a proper incentive strategy in their reduction management initiatives. CWR is influenced by a variety of circumstances. Thus, it's critical to identify and investigate the most relevant ones [30].

So to maintain sustainability and to eliminate waste, green construction and ideologies will be the better option. Green building is one that reduces or eliminates negative impacts on our environment and natural surroundings while simultaneously having the potential to create positive ones through its design, construction, or operation.

1.3 Green Construction Ideologies

Green construction aids in the conservation of natural resources while also increasing our quality of life. In general, the long-term profitability of the cement and concrete industries is vital for the planet's health and human growth [31]. Through the strategies used in sustainable projects, the construction sector seems to have a considerable potential to reduce total energy usage [32] significantly. Green buildings, also known as Environmentally Friendly Buildings (EFBs), address conservation concerns and make better use of important resources than conventional structures [33]. The competence of a project manager is a critical aspect in determining the project's success. Green buildings have developed as a reaction to the degradation of the environment. Green buildings confront more complicated concerns during construction than regular structures, and project managers are faced with additional hurdles [34]. The phase of construction on-site has been seen as crucial in implementing a green construction strategy [35]. Industrial wastes may be used to make building materials on a big scale, diverting enormous volumes of industrial by-products from landfills and boosting the infrastructure system's sustainability and profitability [36]. The construction industry has long been regarded as the leading source of CO_2 emissions in the industrial sector [37]. The pipeline network is one of the most common routes of energy transportation for transferring gas, oil, and by-products across several sorts of locations and generating impacts that are typically continental in scope. Typically, the construction of a cross-country pipeline has significant environmental and social

consequences that must be researched and controlled [38]. The construction process is critical to the environment's long-term sustainability. Some nations have established green construction standards to increase the criteria throughout the construction process since the idea of sustainable construction has gained traction around the world [39]. Because of its influence on various elements of human life experiences and conditions, the construction industry is a significant business [40]. Hence, sustainability should maintain adequately. According to studies, project managers' work fulfilment has a considerable impact on their performance. Project managers' job satisfaction in green construction has received little attention [41]. Aside from rising urbanization and massive energy use, the release of hazardous substances becomes a significant source of frustration [42]. In nations that rely heavily on coal resources, fly ash (FA) is general solid waste. The use of FA as a partial alternative for cement concrete has the potential to minimize land usage pressure while also protecting the environment [43]. The foundation of green building design is a thorough understanding of the site's beauty and complexity. Designers may employ some characteristics to re-create particular ecosystems. In order to accommodate new sorts of living spaces, buildings in metropolitan areas must be altered [44]. The green construction supply chain is one of the topics that has recently been researched in relation to supply chain fundamentals, notably in the construction supply chain. A project network with several concurrent projects, in particular, is handled with the purpose of reducing not only project delays, but also logistical costs such as procurement, ordering, and transportation, as well as vehicular pollution levels [45]. Hence, this study tries to get the information and recommendations from literature to improve the efficiency of construction resource wastages and green ideologies, to maintain an effective, sustainable environment.

2 Methodology

2.1 Collection of Literature

Papers published between 2015 and 2021 are reviewed as the first step in this systematic research and arrangement of relevant material, as the goal of this work is to examine the published literature under three different topics, "Construction Resources," "Construction Wastes," and "Green Construction."

This article aims to determine the breadth of construction resource wastage and green ideologies, as well as the present state of their development and assessment in terms of critical success factors (i.e., the focused area, respectively). The search of the papers is further limited to 15 nos. from each topic, i.e., a total of 45 articles are analyzed in this study. Limitations of the documents are based on the maximum nos. of citations. Further, some of the papers are excluded in terms of different scope, which is done based on a thorough analysis. Web of Science [46] library is used
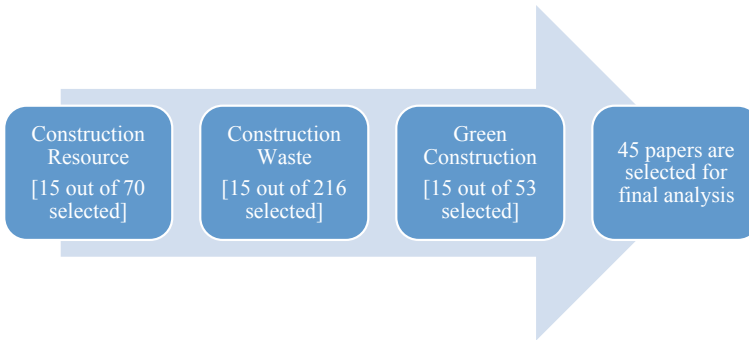
Fig. 1 Selection of literature

for the study. The codes used for the examination in a web of science portal are as follows,

1. "Construction Resource*" (Topic) AND 2015–2021 (Year Published),
2. "Construction Waste*" (Title) AND 2015–2021 (Year Published)
3. "Green Construction" (Title) AND 2015–2021 (Year Published)

Figure 1 illustrates the selection of literature for the study.

2.2 Bibliographic Analysis

The following figures show the graphical representation of the citation and publication reports with respect to the year of publication. 2015 to 2021 literature is analyzed. Figures 2, 3, and 4 illustrate the data related to construction resources, construction wastes, and green construction, respectively. These graphical data are based on the codes mentioned in Sect. 2.1. Based on which top 15 papers are selected respectively.

Literature data of construction resources, construction wastes, and green construction based on the same codes are analyzed cumulatively in terms of country origin, and the treemap data gathered from the web of science portal is shown in Fig. 5.

3 Results and Discussion

Several studies are performed worldwide with respect to construction resources, construction wastes, and green construction respectively. But the combination of these three ideologies is limited across the world. The main idea of this study is to analyze these topics cumulatively. The prime reason behind this analysis is to achieve a systematic approach to these studies. The aim is to achieve construction resource wastage optimization with the idea of green concepts. The following tables illustrate
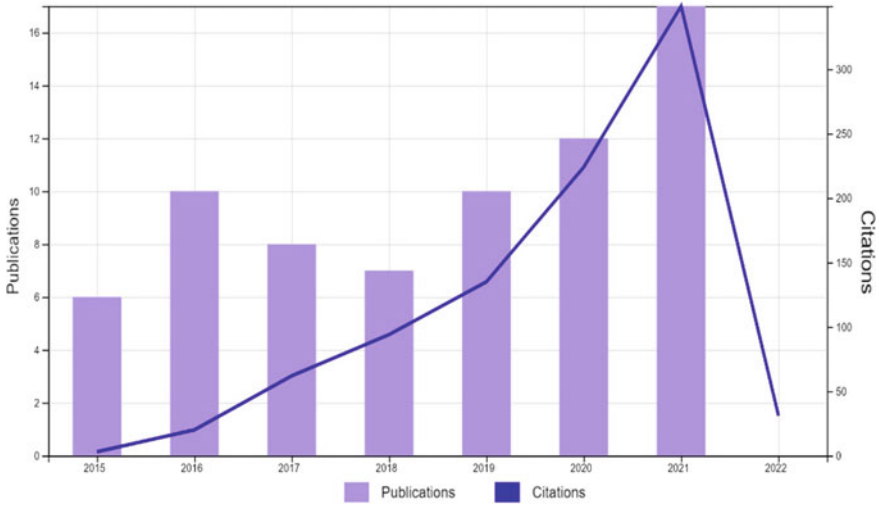
Fig. 2 Year-wise literature analysis related to construction resources
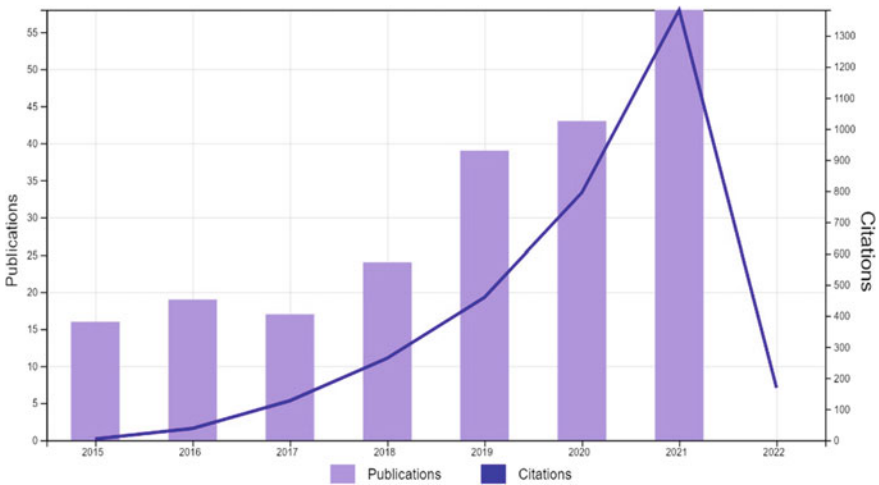
Fig. 3 Year-wise literature analysis related to construction wastes

the area (critical success factors) and findings at which these literature are addressed. These kinds of analyses will be helpful for gathering information on recent trends as well as giving future research scope. Construction resources, construction wastes, and green construction CSFs are discussed in Tables 1, 2, and 3, respectively.
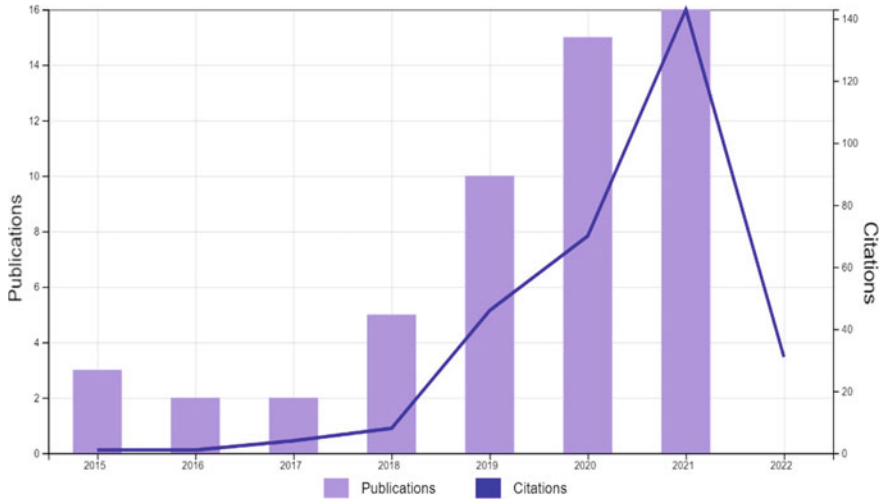
Fig. 4 Year-wise literature analysis related to green construction
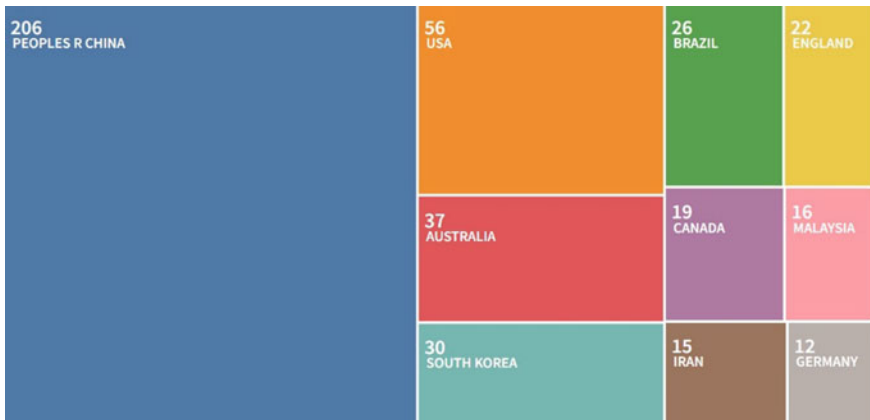
Fig. 5 Literature classification based on countries

4 Conclusions

In terms of construction resources, construction wastes, and green construction, several factors are analyzed in the previous studies. The main aim of exploring the most cited papers (i.e., 15 from each, a total of 45 articles) from each specified topic is to find out the primary area requirement for the implications and development with respect to efficient management of projects. On the other hand, these three areas are discussed separately in most of the cases previously. But the cumulative analysis is limited. This will lead to effective construction resource wastage optimization and

Table 1 Construction resources CSFs and approaches

Sl. No	CSFs	Approaches/Findings	Reference
1	Multi-skilled resource utilization in off-site construction	Optimal process integration architecture	[1]
2	Human resources (HR) issues	HR planning framework	[2]
3	Time-cost-resource optimization problems	The shuffled frog-leaping model is adopted	[3]
4	Temporary resources tracking	Vision-based sensing technology	[4]
5	Resource allocation	Relevance 4D modelling	[5]
6	Resource constraints in scheduling	Integrated BIM-based scheduling approach	[6]
7	Construction resources recognition	An automated method for creating and annotating synthetic images	[7]
8	Resource management	Effectiveness of European Recovery and improvement ideologies	[8]
9	Resource planning in prefabrication networks	Formulation of probabilistic constraints is required to optimize	[9]
10	Repetitive activities	Multimode resource-constrained project scheduling problem	[10]
11	Resource efficiency	Recycling of marble waste	[11]
12	Struck-by accidents due to a mobile vehicle or equipment	Unmanned Aerial Vehicle (UAV)-assisted visual monitoring method	[12]
13	Construction and demolition waste management (Resource recovery)	Circular construction (reuse, recycle, and recovery of materials)	[13]
14	Supply chain network design	Optimal integration of the facility location problem	[14]
15	Resource-constrained scheduling	Work package-based information model	[15]

implementation of green ideologies for sustainable development. Tables 1, 2, and 3 illustrate the overall picture of the requirement of critical success factors worldwide. The findings of the study are as follows,

The necessity of construction resource-related studies, ideologies, and requirement factors are addressed in Table 1. Resource allocation and resource leveling play a vital role in resource management studies. Multi-constrained multi-site resource allocation in a real-time environment is a challenging task in substantial construction projects. There is no proper approach available. Many heuristic decision-making concepts based on experience are followed to overcome several uncertainties in terms of construction resource allocation problems. Construction and resource wastages on the other hand, can be overcome by proper planning and implementation of activities, in addition, recycle and reusing of resources. Based on the type of issue, the remedial measures may vary. Table 2 elaborates on some of the ideologies

Table 2 Construction wastes CSFs and approaches

Sl. No	CSFs	Approaches/Findings	Reference
1	Construction waste minimization	Utility tool for the dynamic assessment	[16]
2	Construction waste management	Big data analysis	[17]
3	Construction waste minimization	Decision making framework using BIM	[18]
4	Wood timber formwork wastages	Can be recycled into value-added particleboards	[19]
5	Construction wastes due to design errors	BIM Validation could prevent 4.3–15.2% of design errors	[20]
6	Comparison of construction waste management performance between public and private projects	Big data analysis	[21]
7	Construction waste reduction management	System dynamic model	[22]
8	Construction waste analytics	Big Data architecture	[23]
9	Landslide of the construction waste landfill	Numerical simulation and analysis	[24]
10	Construction waste management	Suggesting waste management legislation	[25]
11	Construction and demolition management	BIM technology	[26]
12	Construction waste reduction	A hypothetical model developed	[27]
13	Agricultural and construction wastes	ANN model analysis	[28]
14	Construction waste reduction management	A system dynamics-based environmental benefit assessment model	[29]
15	Construction waste reduction factors	Structural equation modeling	[30]

regarding construction waste optimization practices and construction waste management. Waste management is one of the critical factors of green construction. That is why this study considered green ideologies also. Table 3 illustrates the different approaches to green construction and ideas in the current scenario. A sustainable environment is one of the prime requirements. Several proofs are there to explain the toxicity of construction processes. Hence, green construction will be one of the possible remedies as well as it will also help to overcome construction wastes. Moreover, previous literature addressed constraints and struggles behind construction waste optimization and green implementation concerning different scenarios. The real-time strategy should be the emphasis of future research in this area.

Table 3 Green construction CSFs and approaches

Sl. No	CSFs	Approaches/Findings	Reference
1	Eco-friendly green construction	Nanosilver–silica modified geopolymer mortar's antimicrobial efficacy	[31]
2	Risks associated with green projects	This study intended to raise construction professionals' awareness of legal risks	[32]
3	Eco-friendly buildings (EFBs)	Analysis of architects' and consumers' perspectives towards EFBs	[33]
4	Project Manager competency on green construction	Project managers' emotional intelligence, leadership and organization, and target management are all regarded as crucial elements	[34]
5	Awareness on green construction	There are significant gaps between awareness and activity identified	[35]
6	Green construction materials	The ternary blend of combustion ashes to produce hydraulic binders	[36]
7	Green construction of reinforced concrete two-way slabs	Design model and comprehensive investigation of embodied carbon emissions	[37]
8	Green construction	Alternative pipeline water crossing construction reduces the environmental effect	[38]
9	Green construction code checking	Deployment and validation of automated checking procedures	[39]
10	Evaluation and selection of green suppliers	Framework is proposed	[40]
11	Job satisfaction in green construction projects	A literature review and questionnaire survey are conducted	[41]
12	Adoption of green construction site practices	Contractors should be flexible when implementing green practices	[42]
13	Sustainable green construction materials	Sustainable utilization of fly-ash in construction materials used in a severe cold region	[43]
14	Green construction and sustainable development	Conceptualizing state of the art in cooperative social responsibility	[44]
15	Green construction supply chains under uncertainty	Combined scheduling of multi-project activities and suppliers	[45]

References

1. Arashpour, M., Wakefield, R., Blismas, N., Minas, J.: Optimization of process integration and multi-skilled resource utilization in off-site construction. Autom. Constr. **50**, 72–80 (2015)
2. Pournader, M., Tabassi, A.A., Baloh, P.: A three-step design science approach to develop a novel human resource-planning framework in projects: the cases of construction projects in USA, Europe, and Iran. Int. J. Project Manage. **33**(2), 419–434 (2015)
3. Ashuri, B., Tavakolan, M.: Shuffled frog-leaping model for solving time-cost-resource optimization problems in construction project planning. J. Comput. Civ. Eng. **29**(1), 04014026 (2015)
4. Teizer, J.: Status quo and open challenges in vision-based sensing and tracking of temporary resources on infrastructure construction sites. Adv. Eng. Inform. **29**(2), 225–238 (2015)
5. Zhou, Y., Ding, L., Wang, X., Truijens, M., Luo, H.: Applicability of 4D modeling for resource allocation in mega liquefied natural gas plant construction. Autom. Constr. **50**, 50–63 (2015)
6. Liu, H., Al-Hussein, M., Lu, M.: BIM-based integrated approach for detailed construction scheduling under resource constraints. Autom. Constr. **53**, 29–43 (2015)
7. Soltani, M.M., Zhu, Z., Hammad, A.: Automated annotation for visual recognition of construction resources using synthetic images. Autom. Constr. **62**, 14–23 (2016)
8. Arm, M., Wik, O., Engelsen, C.J., Erlandsson, M., Hjelmar, O., Wahlström, M.: How does the European recovery target for construction and demolition waste affect resource management? Waste Biomass Valorization **8**(5), 1491–1504 (2017)
9. Arashpour, M., Kamat, V., Bai, Y., Wakefield, R., Abbasi, B.: Optimization modeling of multi-skilled resources in prefabrication: theorizing cost analysis of process integration in off-site construction. Autom. Constr. **95**, 1–9 (2018)
10. García-Nieves, J.D., Ponz-Tienda, J.L., Salcedo-Bernal, A., Pellicer, E.: The multimode resource-constrained project scheduling problem for repetitive activities in construction projects. Comput. Aided Civ. Infrastruct. Eng. **33**(8), 655–671 (2018)
11. Thakur, A.K., Pappu, A., Thakur, V.K.: Resource efficiency impact on marble waste recycling towards sustainable green construction materials. Curr. Opin. Green Sustain. Chem. **13**, 91–101 (2018)
12. Kim, D., Liu, M., Lee, S., Kamat, V.R.: Remote proximity monitoring between mobile construction resources using camera-mounted UAVs. Autom. Constr. **99**, 168–182 (2019)
13. Ghaffar, S.H., Burman, M., Braimah, N.: Pathways to circular construction: an integrated management of construction and demolition waste for resource recovery. J. Clean. Prod. **244**, 118710 (2020)
14. Golpîra, H.: Optimal integration of the facility location problem into the multi-project multi-supplier multi-resource construction supply chain network design under the vendor managed inventory strategy. Expert Syst. Appl. **139**, 112841 (2020)
15. Wang, H.W., Lin, J.R., Zhang, J.P.: Work package-based information modeling for resource-constrained scheduling of construction projects. Autom. Constr. **109**, 102958 (2020)
16. Wang, J., Li, Z., Tam, V.W.: Identifying best design strategies for construction waste minimization. J. Clean. Prod. **92**, 237–247 (2015)
17. Lu, W., Chen, X., Peng, Y., Shen, L.: Benchmarking construction waste management performance using big data. Resour. Conserv. Recycl. **105**, 49–58 (2015)
18. Liu, Z., Osmani, M., Demian, P., Baldwin, A.: A BIM-aided construction waste minimisation framework. Autom. Constr. **59**, 1–23 (2015)
19. Wang, L., Chen, S.S., Tsang, D.C., Poon, C.S., Shih, K.: Value-added recycling of construction waste wood into noise and thermal insulating cement-bonded particleboards. Constr. Build. Mater. **125**, 316–325 (2016)
20. Won, J., Cheng, J.C., Lee, G.: Quantification of construction waste prevented by BIM-based design validation: case studies in South Korea. Waste Manage. **49**, 170–180 (2016)
21. Lu, W., Chen, X., Ho, D.C., Wang, H.: Analysis of the construction waste management performance in Hong Kong: the public and private sectors compared using big data. J. Clean. Prod. **112**, 521–531 (2016)

22. Ding, Z., Yi, G., Tam, V.W., Huang, T.: A system dynamics-based environmental performance simulation of construction waste reduction management in China. Waste Manage. **51**, 130–141 (2016)
23. Bilal, M., et al.: Big data architecture for construction waste analytics (CWA): a conceptual framework. J. Build. Eng. **6**, 144–156 (2016)
24. Ouyang, C., et al.: Dynamic analysis and numerical modeling of the 2015 catastrophic landslide of the construction waste landfill at Guangming, Shenzhen, China. Landslides **14**(2), 705–718 (2017)
25. Ajayi, S.O., Oyedele, L.O.: Policy imperatives for diverting construction waste from landfill: experts' recommendations for UK policy expansion. J. Clean. Prod. **147**, 57–65 (2017)
26. Akinade, O.O., et al.: Designing out construction waste using BIM technology: Stakeholders' expectations for industry deployment. J. Clean. Prod. **180**, 375–385 (2018)
27. Li, J., Zuo, J., Cai, H., Zillante, G.: Construction waste reduction behavior of contractor employees: an extended theory of planned behavior model approach. J. Clean. Prod. **172**, 1399–1408 (2018)
28. Getahun, M.A., Shitote, S.M., Gariy, Z.C.A.: Artificial neural network based modelling approach for strength prediction of concrete incorporating agricultural and construction wastes. Constr. Build. Mater. **190**, 517–525 (2018)
29. Ding, Z., Zhu, M., Tam, V.W., Yi, G., Tran, C.N.: A system dynamics-based environmental benefit assessment model of construction waste reduction management at the design and construction stages. J. Clean. Prod. **176**, 676–692 (2018)
30. Liu, J., Yi, Y., Wang, X.: Exploring factors influencing construction waste reduction: a structural equation modeling approach. J. Clean. Prod. **276**, 123185 (2020)
31. Adak, D., Sarkar, M., Maiti, M., Tamang, A., Mandal, S., Chattopadhyay, B.: Antimicrobial efficiency of nano silver-silica modified geopolymer mortar for eco-friendly green construction technology. RSC Adv. **5**(79), 64037–64045 (2015)
32. Mohammadi, S., Birgonul, M.T.: Preventing claims in green construction projects through investigating the components of contractual and legal risks. J. Clean. Prod. **139**, 1078–1084 (2016)
33. Ofek, S., Akron, S., Portnov, B.A.: Stimulating green construction by influencing the decision-making of main players. Sustain. Cities Soc. **40**, 165–173 (2018)
34. Sang, P., Liu, J., Zhang, L., Zheng, L., Yao, H., Wang, Y.: Effects of project manager competency on green construction performance: the Chinese context. Sustainability **10**(10), 3406 (2018)
35. Zhou, J., Tam, V.W., Qin, Y.: Gaps between awareness and activities on green construction in China: a perspective of on-site personnel. Sustainability **10**(7), 2266 (2018)
36. Almalkawi, A.T., Balchandra, A., Soroushian, P.: Potential of using industrial wastes for production of geopolymer binder as green construction materials. Constr. Build. Mater. **220**, 516–524 (2019)
37. Oh, B.K., Glisic, B., Lee, S.H., Cho, T., Park, H.S.: Comprehensive investigation of embodied carbon emissions, costs, design parameters, and serviceability in optimum green construction of two-way slabs in buildings. J. Clean. Prod. **222**, 111–128 (2019)
38. Cianciarullo, M.I.: Green construction–reduction in environmental impact through alternative pipeline water crossing installation. J. Clean. Prod. **223**, 1042–1049 (2019)
39. Jiang, S., Wu, Z., Zhang, B., Cha, H.S.: Combined MvdXML and semantic technologies for green construction code checking. Appl. Sci. **9**(7), 1463 (2019)
40. Keshavarz-Ghorabaee, M., Amiri, M., Hashemi-Tabatabaei, M., Zavadskas, E.K., Kaklauskas, A.: A new decision-making approach based on Fermatean fuzzy sets and WASPAS for green construction supplier evaluation. Mathematics **8**(12), 2202 (2020)
41. Zhao, X., Hwang, B.G., Lim, J.: Job satisfaction of project managers in green construction projects: constituents, barriers, and improvement strategies. J. Clean. Prod. **246**, 118968 (2020)
42. Onubi, H.O., Hassan, A.S.: Understanding the mechanism through which adoption of green construction site practices impacts economic performance. J. Clean. Prod. **254**, 120170 (2020)
43. Tian, W., Wang, M., Liu, Y., Wang, W.: Ohmic heating curing of high content fly ash blended cement-based composites towards sustainable green construction materials used in severe cold region. J. Clean. Prod. **276**, 123300 (2020)

44. Avotra, A.A.R.N., Chenyun, Y., Yongmin, W., Lijuan, Z., Nawaz, A.: Conceptualizing the state of the art of corporate social responsibility (CSR) in green construction and its nexus to sustainable development. Front. Environ. Sci. **541** (2021)
45. RezaHoseini, A., Noori, S., Ghannadpour, S.F.: Integrated scheduling of suppliers and multi-project activities for green construction supply chains under uncertainty. Autom. Constr. **122**, 103485 (2021)
46. Web of Science. https://www.webofscience.com/wos/woscc/basic-search. Accessed 16 May 2022

Examining the Influence of Various Factors that Affect Construction Professionals Lifestyle – A Case of Tamil Nadu and Kerala

S. Senthamizh Sankar ⬤, **K. S. Anandh** ⬤, **and M. Rama** ⬤

Abstract The construction sector has a low quality of lifestyle when compared to other occupations due to a variety of problems associated with their work. The work-life balance is also harmed as a result of the unhealthy lifestyle prevalent among construction professionals. The factors that contribute to the scarcity of construction personnel ready to work in their sector are investigated in this study. This study reveals several common factors affecting construction professionals' lifestyles to improve their quality of life. The first step was to conduct a literature study to identify and summarize significant lifestyle influencing factors. Then, hypotheses were given on the impact of five different factors (financial, organizational, quality-health and environmental, work-related, and social) on construction professionals' lifestyles. The information gathered from 180 construction professionals in Tamil Nadu and Kerala via questionnaires was statistically examined. The findings revealed that these five factors have a major impact on the lifestyle of construction professionals. The financial factor is the primary factor that influences the lifestyle of construction professionals by affecting their socio-economic position. This pioneering study presents a detailed overview of the current construction professional lifestyle and the essential factors that influence it. The association between each factor and the more relevant factors was discovered using statistical analysis, which will serve as a guide for researchers, policymakers, and construction professionals to conduct additional research and improve the current lifestyle. A healthier lifestyle will increase an employee's productivity and, as a result, the company's worth.

S. Senthamizh Sankar · K. S. Anandh (✉)
Department of Civil Engineering, College of Engineering and Technology, SRM Institute of Science and Technology, SRM Nagar, Kattankulathur, Tamil Nadu 603203, India
e-mail: anandhk@srmist.edu.in

S. Senthamizh Sankar
e-mail: ss3069@srmist.edu.in

M. Rama
Department of Civil Engineering, Government College of Technology, Coimbatore, Tamil Nadu 641013, India
e-mail: mrama@gct.ac.in

1 Introduction

In India, agriculture is the most important industry, followed by the construction industry (CI). India's CI contributes 7.74 percent of the country's total GDP (Ministry of Statistics and Programme Implementation Planning Commission, Government of India, 2017). The CI is a naturally stressful environment, with high employment demand and little job security [1–3]. The most stressful and health-damaging experience is that of social assistance [4, 5]. The industry employs a considerable number of people, and the government, through both the public and private sectors, supports numerous infrastructure investment programs [6]. While the CI provides a wide range of career opportunities across the country, due to a lot of factors, including financial factors (FF) [7], organizational factors (OF) [8, 9], quality, health, and environmental factors (QHEF) [10–12], work-related factors (WRF) [13–15] less civil engineers are willing to work in the same field. This reluctance could be attributed to work-related issues that influence construction engineers' lifestyles.

Due to the current shortage of construction professionals (CP) to work for construction companies, it is vital to determine the causes and critical aspects that are contributing to this problem [16]. Construction workers have a poor quality of life when compared to other occupations because of a variety of variables associated with their work [17–19]. The top-level management's leadership style is a crucial organizational factor that defines the lifestyle of professionals since it affects the superior-subordinate relationship. Therefore, due to this unhealthy lifestyle, work-life balance is failing [20]. As a result, this study is crucial in establishing the factors that contribute to a CP shortage in the construction industry. The purpose of this study is to find out what factors influence CPs' lifestyles and to recommend and suggest solutions to improve their quality of life.

2 Methodology

The following procedures make up the methodology for this paper: literature study, identification of multiple factors that influence CPs' lifestyle, designing of questionnaire, gathering of data and analysis, conclusion, and discussion.

The initial stage was to acquire and study all types of literature relating to the topic. Previous research has identified the factors that influence CP's way of life. Following the discovery of factors, the top-ranked factors were chosen for further investigation. The questionnaire was created based on the variables that were rated. A random sample method was used to conduct a questionnaire survey among CP from various construction organizations in Tamil Nadu (TN) and Kerala. The information

was gathered from some people working in the construction industry in the private sector. Construction professionals in construction organizations received 200 sets of questionnaires. 180 of the 200 samples reacted, and the data was examined using statistical methods. The data analysis and hypothesis testing was carried out by using the software IBM SPSS Statistics for Windows, version 28.0.1 (IBM Corp., Armonk, N.Y., USA).

3 Results and Discussions

3.1 Frequency Analysis of Demographic Profile

From the frequency analysis as shown in Fig. 1 (Figs. 1a to h), most of the sampled respondents are male, which accounted for nearly 64, and 42.20% of the respondents fall under the age group of 18 to 25 years. Regarding the educational qualification, it is found that 76% of them are undergraduates in construction-related engineering disciplines and that 70.60% of the respondents are working as site engineers. Likewise, 54% of the respondents are from the state of Kerala, and 46% of the respondents are from TN. The majority of the sampled respondents have one to five years of working experience, which accounts for nearly 85%. Similarly, 58.30% of respondents are daily working for eight to ten hours and 92.20% of respondents are working six days a week.

3.2 Reliability Analysis

The instrument's dependability was evaluated by Cronbach's Alpha's coefficient of reliability. Cronbach's Alpha is a number ranges from 0 to 1. If the Cronbach's alpha nearer to 1, the better the inner reliability and thus the trustworthy of the questionnaire's items is justified. Generally, if the Cronbach's alpha value is more than 0.7, the questionnaire is regarded as reliable in accurately examining the constructs [15]. The reliability analysis shows that the FF has the Cronbach's alpha value of 0.898; OF has the coefficient value of 0.766; QHEF has the reliability coefficient value of 0.798; similarly, the WRF has the Cronbach's alpha value of 0.842 and SF has the coefficient value of 0.754. Accordingly, the questionnaire used in this study is reliable and can be administered to the respondents.

3.3 Independent Sample t-Test

Hypothesis 1

Hypothesis 1: There is no significant difference in the perception of employees based on gender toward various lifestyle factors in the construction industry.
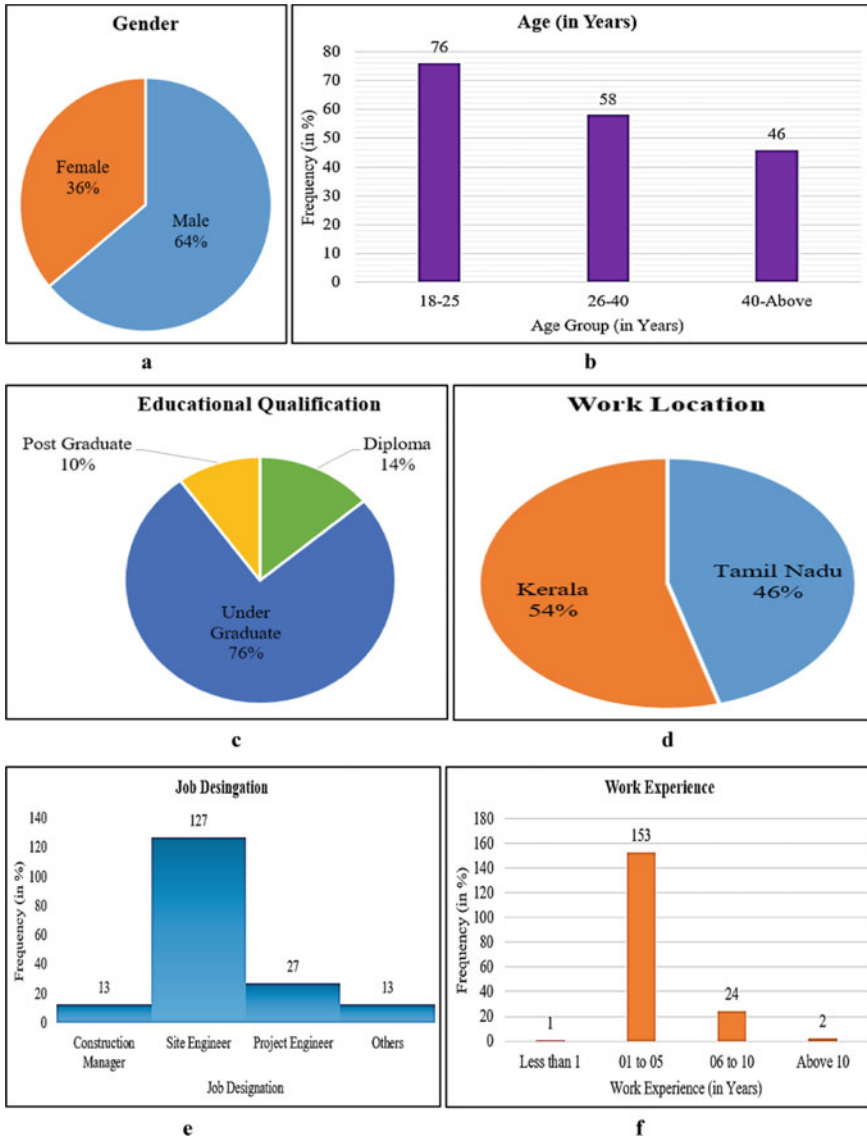
Fig. 1 Demographic profile of the respondents

g

h
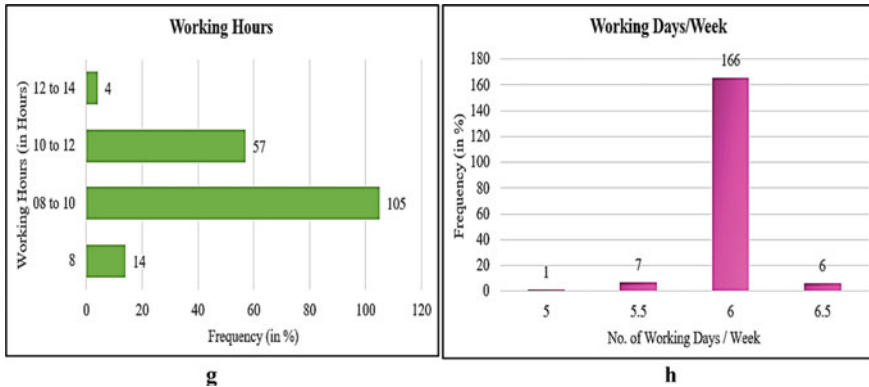
Fig. 1 (continued)

Table 1 Independent sample t-test: Gender vs Employee lifestyle factors in the construction industry

Time spent on the activities	Gender	N	Mean	Std. deviation	t-value	p-value
Financial factors	Male	115	3.94	0.59	2.8634	0.004**
	Female	65	3.71	0.51		
Organizational factors	Male	115	3.80	0.46	2.9224	0.003**
	Female	65	3.90	0.43		
Quality, health and environment factors	Male	115	3.57	0.92	1.05	0.295
	Female	65	3.72	0.87		
Work related factors	Male	115	3.84	0.65	1.036	0.302
	Female	65	3.73	0.84		
Social factors	Male	115	3.65	0.24	2.4444	0.015*
	Female	65	3.64	0.24		

Gender was used as the independent variable, and employee lifestyle factors such as FF, OF, QHEF, WRF, and SF were used as the dependent variables in an independent sample t-test. Since the p-value is less than 0.05 as shown in Table 1, infers that male and female participants of the study vary notably on the mean ranking for lifestyle aspects such as FF, OF, and SF. In the study's lifestyle factors, such as QHEF, and WRF, however, there was no remarkable difference in the mean ratings of male and female respondents.

Therefore, the hypothesis that "There is no significant difference in the perception of employees based on the gender toward various lifestyle factors in the construction industry" was rejected for the factors like FF (1% level), OF (1% level), and SF (5% level). However, the hypothesis was accepted for the factors like QHEF and WRF.

Table 2 Independent sample t-test: State vs Lifestyle factors in the construction industry

Time spent on the activities	State	N	Mean	Std. deviation	t-value	p-value
Financial factors	Kerala	98	3.94	0.60	2.6399	0.009**
	Tamilnadu	82	3.71	0.56		
Organizational factors	Kerala	98	3.80	0.65	2.0408	0.0428*
	Tamilnadu	82	3.59	0.73		
Quality, health and environment factors	Kerala	98	3.69	0.93	1.093	0.276
	Tamilnadu	82	3.55	0.87		
Work related factors	Kerala	98	3.94	0.64	2.804	0.006**
	Tamilnadu	82	3.64	0.79		
Social factors	Kerala	98	3.75	0.66	2.2893	0.0232*
	Tamilnadu	82	3.53	0.62		

Hypothesis 2

Hypothesis 2: There is no significant difference in the perception of employees based on their state of residence toward various lifestyle factors in the construction industry.

This hypothesis was tested using an Independent sample t-test with the state that the respondents represent as the independent variable and employee lifestyle factors like FF, OF, QHEF, WRF, and SF as the dependent variables. Since the p-value for the lifestyle categories FF, OF, WRF, and SF is less than 0.05 as shown in Table 2, it is obvious that the respondents from Kerala and TN differ significantly on the mean ranking. The mean ranking of respondents from Kerala and TN for the lifestyle factor "QHEF" did not differ significantly.

Therefore, the hypothesis that "There is no significant difference in the perception of employees based on the state of residence toward various lifestyle factors in the construction industry" was rejected for the factors like FF (1% level), OF (1% level), and WRF (1% level) and SF (5% level). However, the hypothesis was accepted for the factor namely QHEF.

3.4 One Way ANOVA

Hypothesis 1

Hypothesis 1: There is no significant difference in the perception of respondents based on the educational qualification toward employee lifestyle factors in the construction industry.

The significance of the variation in respondents' perceptions of employee lifestyle factors in the construction sector depending on educational qualification was tested using a one-way ANOVA. The educational qualification of respondents categorized as Diploma, BE/Btech, ME/Mtech, and Others was used as the independent variable.

Table 3 One way ANOVA test for testing the significance of difference on the lifestyle factors of construction engineers based on qualification

Time spent on the activities	Diploma (N = 25)		BE/Btech (N = 137)		ME/Mtech (N = 16)		F – value	p-value
	Mean	SD	Mean	SD	Mean	SD		
Financial factors	3.27	0.24	3.27	0.25	3.05	0.32	5.921	0.003**
Organizational factors	3.32	0.37	3.29	0.37	3.34	0.49	0.160	0.852
Quality, health and environment factors	3.75	0.71	3.60	0.88	3.59	0.85	0.303	0.739
Work related factors	3.76	0.70	3.79	0.69	3.72	0.55	0.109	0.897
Social factors	3.74	0.33	3.64	0.27	3.48	0.51	3.793	0.02*

The employee lifestyle factors like FF, OF, QHEF, WRF, and SF were taken as the dependent variable.

Table 3 displays the average ranking of responders with various educational backgrounds. As the p-value is more than 0.05, it is obvious that there was no remarkable difference in the mean evaluation between participants with different qualifications on criteria such as OF, QHEF, and WRF. However, since the p-value is smaller than 0.05, notable changes in the mean evaluation across respondents with various degrees were identified for factors such as FF and SF.

Thus, the null hypothesis that "There is no significant difference in the perception of respondents based on the educational qualification toward employee lifestyle factors in the construction industry" was accepted for the employee lifestyle factors like OF, QHEF, and WRF. However, the hypothesis was rejected for the factors like FF and SF at a 1% level of significance.

Hypothesis 2

Hypothesis 2: There is no significant difference in the perception of respondents based on the age group toward employee lifestyle factors in the construction industry.

The significance of the difference in respondents' perceptions of employee lifestyle factors in the construction industry based on their age group was tested using a one-way ANOVA. The age group of respondents categorized as 18–25, 25–35, and 35–45 years used as the independent variable. The dependent variable is employee lifestyle factors such as FF, OF, QHEF, WRF, and SF.

Table 4 shows the mean rating of respondents from different age groups. Since the p-value is less than 0.05, it is apparent that there was a significant difference in the mean rating between respondents with various qualifications on all factors such as FF, OF, QHEF, and WRF. However, because the p-value was greater than 0.05, the study identified no significant variations in mean ratings between respondents of different age groups for the category SF.

Table 4 One Way ANOVA test for testing the significance of difference on the Lifestyle Factors of Construction Engineers based on Age Group

Time spent on the activities	18–25 Years (N = 76)		25–35 Years (N = 58)		35–45 years (N = 46)		F – value	p-value
	Mean	SD	Mean	SD	Mean	SD		
Financial factors	3.30	0.26	3.19	0.19	3.22	0.32	3.112	0.047*
Organizational factors	3.43	0.41	3.27	0.37	3.25	0.39	3.492	0.033*
Quality, health and environment factors	3.80	0.82	3.55	0.88	3.43	0.85	3.118	0.047*
Work related factors	3.87	0.66	3.86	0.66	3.55	0.72	3.649	0.028*
Social factors	3.65	0.28	3.65	0.30	3.60	0.38	0.350	0.705

Thus, the null hypothesis that "There is no significant difference in the perception of respondents based on the age group toward employee lifestyle factors in the construction industry" was rejected for the employee lifestyle factors like FF, OF, QHEF, and WRF at 5% level. However, the hypothesis accepted for the factor namely SF.

4 Conclusion

FF, OF, QHEF, WRF, and SF are the five factors identified in the study, and they are all vital in guaranteeing the quality of life of construction employees. The results of the questionnaire survey show that the discussed issues have a significant impact on a construction professional's lifestyle. As a result, by anticipating the causes and making positive changes in one's life, a construction professional can live a better life. Employee productivity and organizational value will increase as a result of a healthier lifestyle. As a result, it is suggested that a CP's lifestyle can be enhanced if the factors (FF, OF, QHEF, WRF, and SF) are correctly examined. Few unique solutions are being offered to combat the unhealthy lifestyle of construction professionals in the building business, such as the Just-In-Time (JIT) concept, which is a globally emerging production technique that overcomes many challenges in the construction sector [21]. Future research could look into the role of leadership styles and safety management in the construction sector, as well as their relationship to construction professionals' lifestyles. Currently investigating a portion of this work in the Indian context is in progress, and it can be expanded to the global construction forum.

References

1. Vicknayson, T., Mawdesly, M.: Perception of human risk factors in construction projects. an exploratory study. Int. J. Proj. Manag. **22**(2), 131–137 (2004)
2. Sankar, S.S., Anandh, K.S., Pandian, S.R., Aravinth, K.S.: Investigating the ways to optimize the production of ready mix concrete plants. Lect. Notes Civ. Eng. **191**, 369–380 (2022)
3. Al-Mohammad, M.S., et al.: Factors affecting BIM implementation: evidence from countries with different income levels. Constr. Innov. (2022). https://doi.org/10.1108/ci-11-2021-0217
4. Anandh, K.S., Gunasekaran, K.: An investigation on stress among the professionals in the Indian construction industry. In: Construction Research Congress 2018 Safety Disaster Management - Selected Papers from Construction Research Congress 2018, vol. 2018, pp. 1–7 (2018) https://doi.org/10.1061/9780784481288.001
5. King, S.S., Rahman, R.A., Fauzi, M.A., Haron, A.T.: Critical analysis of pandemic impact on AEC organizations: the COVID-19 case. J. Eng. Des. Technol. (2021). https://doi.org/10.1108/JEDT-04-2021-0225
6. Thomas, N., Saud, S.J.: Disruption of construction industry during COVID-19 pandemic—a case study from Ernakulam, Kerala, India. In: Proceedings of SECON 2021, 2021, pp. 151–163. https://doi.org/10.1007/978-3-030-80312-4_13
7. Pheng, L.S., Chuan, Q.T.: Environmental factors and work performance of project managers in the construction industry. Int. J. Proj. Manag. **24**(1), 24–37 (2006). https://doi.org/10.1016/j.ijproman.2005.06.001
8. Anin, E.K., Ofori, I., Okyere, S.: Factors affecting job satisfaction of employees in the construction supply chain in the ashanti region of Ghana. Eur. J. Bus. Manag. **7**(6), 2222–2839 (2015)
9. Francis, V.: Supportive organisational cultures and their effect on male civil engineers. Aust. J. Constr. Econ. Build. **4**(1), 1–10 (2004)
10. Takim, R., Talib, I.F.A., Nawawi, A.H.: Quality of life: psychosocial environment factors (PEF) in the event of disasters to private construction firms. Procedia Soc. Behav. Sci. **234**, 28–35 (2016). https://doi.org/10.1016/j.sbspro.2016.10.216
11. Ratnawat, R., Jha, D.P.: Impact of job related stress on employee performance: a review and research agenda. IOSR J. Bus. Manag. **16**(11), 01–06 (2014). https://doi.org/10.9790/487x-161150106
12. Love, P.E.D., Edwards, D.J., Irani, Z.: Work stress, support, and mental health in construction. J. Constr. Eng. Manag. **136**(6), 650–658 (2010). https://doi.org/10.1061/(asce)co.1943-7862.0000165
13. Shujat, S., Cheema, F.-E.-A., Bhutto, F.: Impact of work life balance on employee job satisfaction in private banking sector of Karachi. J. Manag. Soc. Sci. **7**(2), 8–15 (2011). https://doi.org/10.46745/ilma.jbs.2011.07.02.02
14. Poulose, S., Sudharsan, N.: Work- life balance: a conceptual review. Int. J. Adv. Manag. Econ. **3**(2), 1–17 (2014)
15. Adams, G.A., King, L.A., King, D.W.: Relationships of job and family involvement, family social support, and work-family conflict with job and life satisfaction. J. Appl. Psychol. **81**(4), 411–420 (1996). https://doi.org/10.1037/0021-9010.81.4.411
16. Lingard, H., Francis, V., Lingard, H., Francis, V.: The work - life experiences of office and site - based employees in the Australian construction industry the work-life experiences of office and site-based employees in the Australian construction industry. Constr. Manag. Econ. **22**, 991–1002 (2004). https://doi.org/10.1080/0144619042000241444
17. Priya, M.G.S., Anandh, K.S., Prasanna, K.: A quantitative study on construction job safety analysis and occupational safety and health management. Lect. Notes Civil Eng. **191**, 355–368 (2022). https://doi.org/10.1007/978-981-16-5839-6_31
18. Anandh, K.S., Prasanna, K., Joseph, H.: Investigation employee retention in Indian construction industry. J. Adv. Res. Dyn. Control Syst. **10**(8), 1089–1094 (2018)

19. Anandh, K.S., Gunasekaran, K., Mannan, M.A.: Investigation on the factors affecting lifestyle of professionals in the construction industries (Kerala and Tamil Nadu). Int. J. Integr. Eng. **12**(9), 246–252 (2020). https://doi.org/10.30880/ijie.2020.12.09.029
20. Anandh, K.S., Gunasekaran, K., Sankar, S.S.: An envisage on emotional intelligence among superior-subordinate in construction sector of Chennai City, India. In: AIP Conference Proceedings, vol. 2277, pp. 1–8 (2020). https://doi.org/10.1063/5.0025223
21. Anandh, K.S., Prasanna, K., Priya, M.G.S., Simon, S.M.: An industrial study of just in time (JIT) management in precast construction projects. In: AIP Conference Proceedings, vol. 2277, no. November, p. 240011 (2020). https://doi.org/10.1063/5.0025220

Assessing Quality of Working Life (QWL) Among Construction Professionals in Private Sectors in Chennai

M. G. Soundarya Priya ⓘ **, K. S. Anandh** ⓘ **, S. Kamal** ⓘ **, and S. Shanmuga Priya** ⓘ

Abstract The construction industry is necessary for the socio-economic development of a nation. It provides ample job opportunities. It is next to agriculture in terms of employment. In this industry, the potential and performance of construction professionals play a vital role in developing and recuperating the sector. The potential of the construction personnel is affected by personal, organizational, societal, and other miscellaneous factors. Among these discrete factors, this study focused on the working environment, work culture, management, career growth, and personal satisfaction of construction professionals because these factors significantly impact the construction industry and thus affect the country's economy. This study was conducted to identify the organizational factors influencing the potential and performance of construction personnel to ensure quality work-life outcomes. A pilot study was conducted to determine the key parameters and structured questionnaire framed. Data was collected by distributing the questionnaire to the construction professionals at various management levels, and data analysis was performed. Findings say that work outcomes, organizational climate, insecure career growth, lesser payments, and lack of personal time affect employee productivity. In addition, a lack of good formal relationships with colleagues and superiors creates more work complexity. From the study discussion, recommendations are made.

M. G. Soundarya Priya · K. S. Anandh (✉)
Department of Civil Engineering, College of Engineering and Technology, SRM Institute of Science and Technology, SRM Nagar, Kattankulathur 603 203, Tamil Nadu, India
e-mail: anandhk@srmist.edu.in

M. G. Soundarya Priya
e-mail: sm0295@srmist.edu.in

S. Kamal
Department of Civil and Structural Engineering, Annamalai University, Chidambaram 608 001, Tamil Nadu, India
e-mail: kamalselva21@gmail.com

S. Shanmuga Priya
Department of Civil Engineering, Coimbatore Institute of Technology, Coimbatore 641 014, Tamil Nadu, India
e-mail: shanmugapriya@cit.edu.in

1 Introduction

The construction industry engages professional's skilled, well-trained working personnel and unskilled people from various parts of the country. Each day, 27 km of highway is being built in India, and it is evident that the fastest development is in infrastructure projects. Looking broadly into the construction industry, the performance of all professionals is the primary concern of human resources (HR) management. Their performance is monitored in terms of better productivity and the excellent quality of work they contribute. Projects can become quite complex and challenging; hence, managers in the industry face unprecedented changes [1]. However, human factors are neglected in many construction sites, leading to vulnerable risk in construction [2–4]. Engineering professionals' productivity depends on organizational, societal, personal or individual, and external factors. The importance of organizational factors and their impact on project success is unclear. The perception of the workplace environment is crucial and can differ from project to project the objectives, vision, and mission of management influence the engineers' performance. The importance of career growth opportunities and personal job satisfaction are vitally important. The performance of an employee is depicted in Fig. 1. The study's main objectives are to identify various factors influencing the efficiency of construction engineers and examine the impact of those factors on all management levels of construction professionals. And in addition to that, factor analysis is also done.
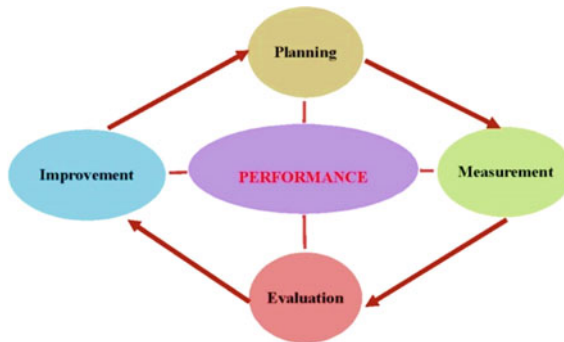
Fig. 1 Performance cycle of engineers

2 Literature Review

The impact of authority on a construction site manager's efficiency is determined by examining 30 site managers' meeting structures and their candid comments. The amount of protection provided (i.e., calamity level) was used with the website

managers' supervisors [5]. Personal burnout can lead to psychological distress, anxiety, depression, reduced self-esteem, and substance abuse. In the workplace, burnout leads to absenteeism, reduced turnover and productivity, and lower levels of job satisfaction and organizational commitment. The results indicate that efforts to address burnout should focus on work-family interface problems [6]. In addition, a lack of idea on work-life stability is harmful to workers regarding their job approval and efficiency. The counterproductive factors for workers are work stress, nonattendance, high abrasion rate, burnout, job control, work pressure, and fitness issues. The significance of work-life equilibrium is that it provides enthusiasm, job happiness, efficiency to an employee, and it decreases attrition and enhances retention rates while reducing malingering. It also increases competence and shows great promise to change some work situations that, presently, negatively interfere in the family lives of workers. There are vast differences in terms of gender, the job site, and the organization's structure. An excellent work-life balance will result in job satisfaction for employees and will create managerial achievement [7, 8].

Meanwhile, the critical issue is examining the work-life equilibrium of IT experts in terms of the built-in managerial structure, allocation of ability, central administrative beliefs, credibility, communication, income, job approval, operational hours, ease of use, and scheme surroundings. The main factors affecting the performance of engineers included physical stress, administrator support, and unintentional risk [9]. The following solutions to these problems: job preparation, stress decrease programs, employment policies, and the enhancement of safety measures. Furthermore, temporary issues are addressed and provide a basis for several changes relating to stress management for Asian construction organizations [10].

The work-life balance of engineers is measured in terms of workplace pressure, delays, job management, and the conflicts between work and family commitments. Employers need to manage and promote more-helpful work surroundings. The factors involved are demographic issues, job command, control features, delays, managerial issues, and job pressure. Employers would benefit from looking for early-warning signs of work-life conflict among employees and creating ways by which these signs can be efficiently noticed and addressed through the HR organization [9, 11]. Management actions can enhance employee job happiness. In a period of change, benefits and education will lead the organization to address employees' issues [12]. Costs of a lack of work-life equilibrium are reduced job happiness, reduced efficiency, fewer managerial promises, reduced vocation objectives and achievement, increased malingering, worker exhaustion, job pressure, reduced physical and emotional fitness, and employees are making less of a contribution to their family life. These problems involve personality factors (character, health, cleverness), directorial features (work preparation, laws, programs, work stress, knowledge, position factors), and communal issues. Equilibrium leads to job happiness. The company keeps valuable expertise by increasing employee retention. Throughout this study, all the features of work–life stability with job happiness are built. It presents various factors that can exaggerate certain issues and must be considered. Formerly, these factors were scrutinized from the viewpoint of engineering and business-oriented management [13–15].

In two studies, it was observed that each employee spends a considerable part of life working to earn enough to meet their needs. Because of this significant quantity of time spent in employment, the work environment can significantly affect an employee's quality of life. The work-life balance contributes to the holistic well-being of an employee more than other workplace characteristics. This alters previous views on the quality of the work-life balance, and organizations will benefit from a superior method of achieving a balance. The damage between the specialized professionals inside the Indian construction industry, recognize the cause of the pressure is due to workload in the construction job site, and they need a strategy that has an effect on the efficiency of employees' occupations, the work-life equilibrium in the construction industry, and their stability and role within the industry. This article addresses the stress between the expansions of specialization, methodically examines different studies and looks for connections. The statistical analysis results show that relationship examination, behavior, and consequences were also scrutinized. The survey indicated that women in specialized jobs are more stressed than men. Overall, it was found that construction professionals experience high stress [16–18]. The relationship between superiors and subordinates always plays a key role in the performance of engineers working in the construction industry. Various factors are considered in this personnel, and family roles play a major role [19]. The Superior-subordinate relationship is the primary working relationship in the construction industry that directly forces productivity [20].

The performance of engineers should be addressed by management seriously, as it is directly related to time and cost and quality of work. Performance was generally examined for construction project management, and it is shown in the model in Fig. 1. Engineer performance is a complex issue because of the interaction in the working environment, organizational factors, personal satisfaction, and career growth. The organizational factors include several variables, such as working time, management policies for the employees, management support, supervisor support, colleague support, work overload, and modern technology. Hence, the factors that influence the performance of engineers identified in the literature review are working environment, work culture, management, career growth, productivity, remuneration and fringe benefits and personal satisfaction, as shown in Fig. 2.
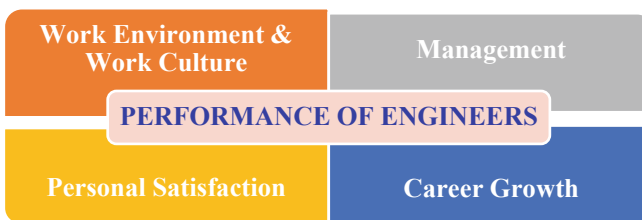
Fig. 2 Factors influencing the performance of engineers

3   Methodology

The identified factors influence the effectiveness and performance of engineers in accomplishing commitments and ensuring the best quality. The impact of the factors on the engineers is studied with the help of statistical tools after data collection to develop a conceptual model for the representation of those parameters. The questionnaire adopted in the study was initially a pilot with a small circle of respondents as a sample. The respondents were selected based on the management categories of senior, middle, and junior levels. This pilot study was conducted at the initial stage, before the commencement of collecting the data, to assess the response rate and the effect on the size, validity, and suitability with respect to the questionnaire without compromises in terms of ambiguity. In the end, based on the experts' suggestions questionnaire was modified. Data collection was carried out as per convenience sampling with the help of a well-structured questionnaire which was framed and distributed to various construction personnel: senior, middle and junior management personnel in Chennai city. In the questionnaire, the satisfaction levels were mentioned: Highly Dissatisfied (HDS), Dissatisfied (DS), Somewhat Satisfied (SS), Satisfied (S), and Highly Satisfied (HS). Valid responses from 510 professionals have been collected for this study. The collected responses were ranked to obtain statistical data. As an ordinal scale was adopted, rank 1 represented "little effect," rank 2 represented "some effect," rank 3 represented "average effect," rank 4 represented "high effect," and rank 5 represented "very high effect." Data taken were normalized for data analysis.

4   Data Analysis

4.1   Questionnaire Validation

The questionnaire was first validated by reliability analysis with the help of IBM SPSS Statistics for Windows, version 28.0.1 (IBM Corp., Armonk, N. Y., USA) software. The reliability value after analysis is tabulated in Table 1.

The relative importance index (RII) was adopted to analyse the collected data. Equation (1) uses the following formula to calculate the RII.

Table 1 Reliability analysis

Management level	Reliability value
Senior	0.957
Middle	0.740
Junior	0.944

Table 2 Ranking as for RII

Parameters	Senior level	Middle level	Junior level
Career growth	Promotion rate	Opportunity	Opportunity
	Recognition	Job environment	Job environment
	Personal growth	Personal growth	Personal growth
	Working hours	Promotion rate	Promotion rate
Management	Training	Superior support	Training
		Training	Working hours
		Working hours	Travel distance
		Travel distance	Work environment
		Work environment	Discussion of issues
Work culture	Employee equality	Discussion of issues	Management transparency
			Authority
Productivity	Self-appraisal	Goal clarity	Performance review
		Self-analysis	Self-analysis
Remuneration & fringe benefits	Incentive schemes	Compensation	Compensation
	Financial assistance	Employee benefit scheme	Employee benefit scheme
	Employee benefit scheme	Personal health care schemes	Personal health care schemes

$$(RII) = \frac{\left(5n^5 + 4n^4 + 3n^3 + 2n^2 + n^1\right) * 100}{5(n^1 + n^2 + n^3 + n^4 + n^5)} \tag{1}$$

where n^1, n^2, n^3, n^4, and n^5 are the numbers of respondents answering ranks 1, 2, 3, 4, and 5, respectively.

The RII was found for all factors, and ranking of the various parameters was then undertaken. Finally, the ranking was used to find the construction personnel's level of satisfaction concerning the selected factors. After the analysis, the various parameters ranked at a higher level are listed in Table 2.

4.2 Demographic Details

The demographic details from the data were gathered through the questionnaire. The basic details of the respondents were collected like gender, experiences, qualification, etc. Hence, there is always a relationship between the demographics in this study. The frequency analysis performed is described in Tables 3, 4 and 5.

This study was conducted to learn the individual satisfaction levels of construction professionals among various management levels. As a result, the factors showing a

Table 3 Category of the respondent based on gender

Category	Male		Female	
	N	%	N	%
Senior level	57	11	96	19
Middle level	111	22	30	06
Junior level	170	33	46	09

Table 4 Frequency analysis based on qualifications of respondents

Qualification	Diploma		Under graduate		Post graduate engineering		Post graduate management		Others
	N	%	N	%	N	%	N	%	
Senior level	15	3	46	9	92	18	17	03	0
Middle level	0	0	68	13	94	18	08	02	0
Junior level	19	4	132	26	07	01	12	03	0

Table 5 Frequency analysis based on the experiences of the respondents

Experiences (Yrs.)	0–5		06–10		11–15		>15	
	N	%	N	%	N	%	N	%
Senior level	0	0	30	06	30	06	110	22
Middle level	59	12	77	14	34	07	0	0
Junior level	94	18	76	15	0	0	0	0

significant influence were identified: career growth factors, management factors and remuneration and fringe benefits factors and the difference in satisfaction levels among the professionals of various management levels is shown in Fig. 3 (Fig. 3a to c).
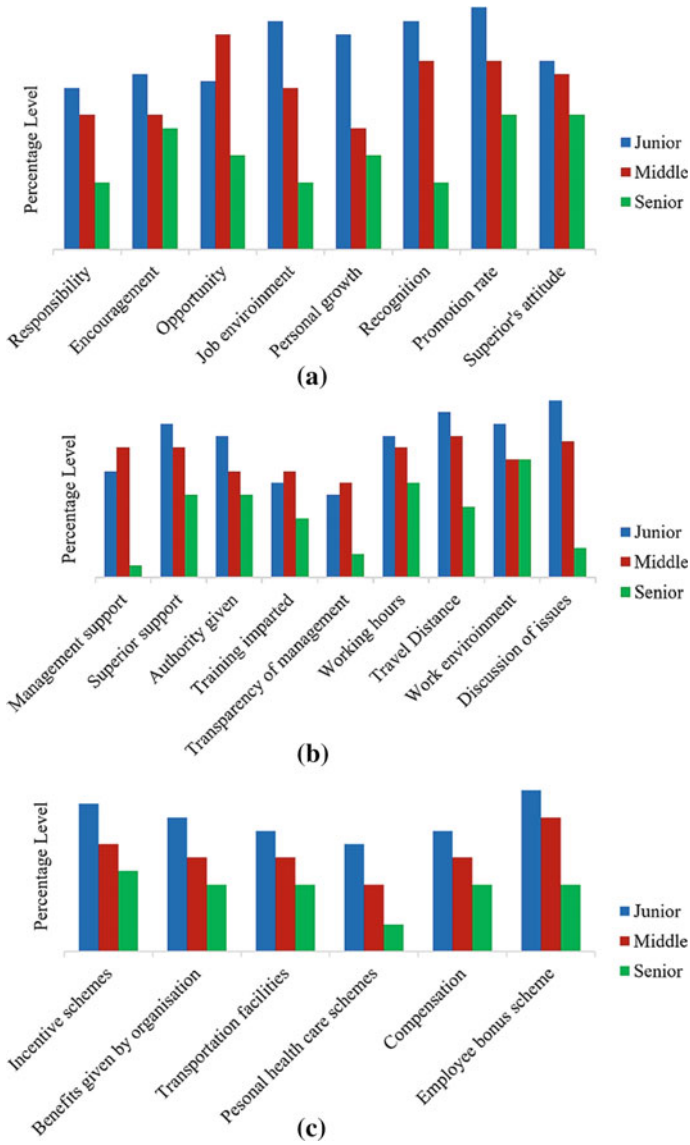
Fig. 3 Comparative studies of satisfaction levels for all management levels **a** Career growth **b** Management factors **c** Remuneration and fringe benefits
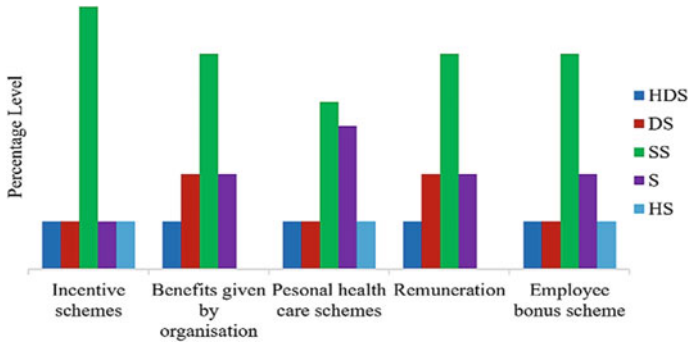
Fig. 4 Responses of senior-level management

4.3　Senior Management Level

The senior management professionals were found to have dissatisfaction with the remuneration and fringe benefits given to them, which is shown in Fig. 4.

4.4　Middle Management Level

The middle management professionals were found to have dissatisfaction with career growth, management factor, and the remuneration and fringe benefits given to them are shown in Fig. 5 (Fig. 5a to c).

4.5　Junior Management Level

The junior management professionals were found to have dissatisfaction with the work culture, and remuneration and fringe benefits are shown in Fig. 6 (Fig. 6a and b).
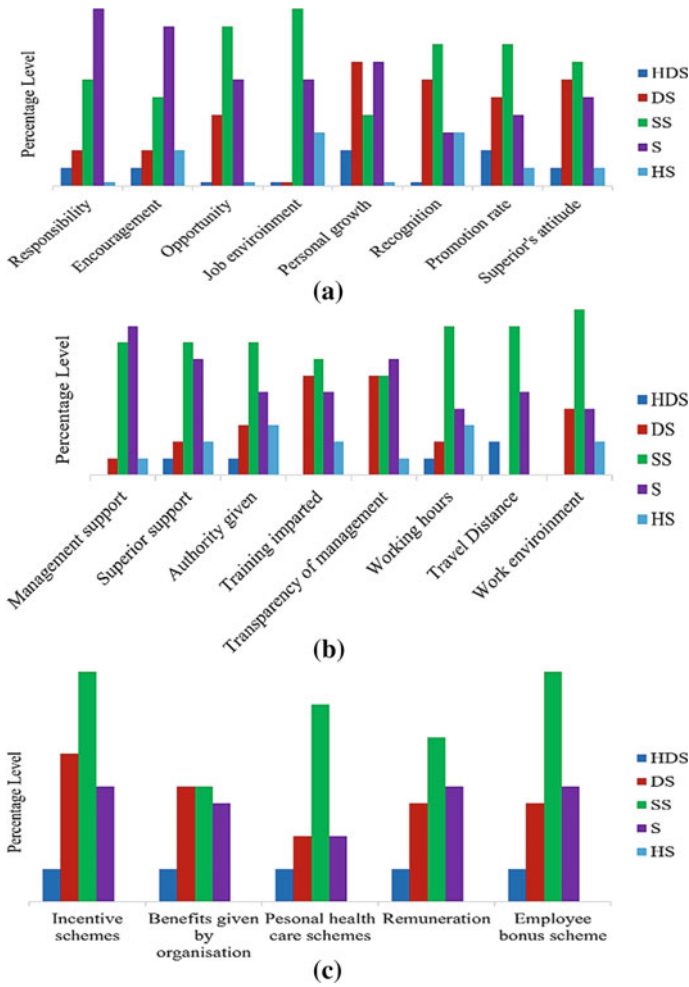
Fig. 5 Comparative studies of middle management level **a** Career growth **b** Management factor **c** Remuneration and fringe benefits

The factor analysis for all the different management levels senior management level, middle management level, and junior management level was carried out separately and is shown in Table 6.
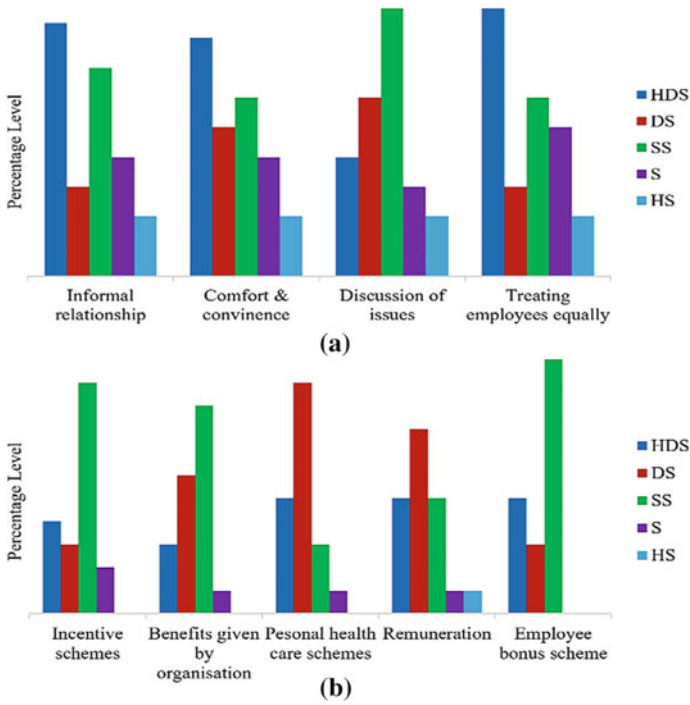
Fig. 6 Comparative studies of junior level **a** Work culture **b** Remuneration and fringe benefits

Table 6 Factor analysis for different management level

Particulars	Senior level	Middle level	Junior level
Total components	101	101	101
Components extracted	5	9	8
Deficient areas	Dormant professional growth	Work environment	Career insecurity
	Job complexities	Job clarity	Organizational assistance
	Formal relationships	Personal time	Work challenges
	Emoluments	Performance appraisal	Self-appraisal
	Personal time	Work complication	Job environment
	Social commitments	Financial assistance	Emoluments
	Family commitments		Personal time
			Job complexities
			Formal relationship

5 Conclusion

Related to this research, objective data were collected, analyzed and thoroughly studied to find significant factors affecting the performance of construction professionals. The key parameters are categorized into six groups: management, career growth, work culture, work commitment, productivity, and remuneration and fringe benefits. The conclusion is that organizational climate, insecure career growth, inadequate compensation and lack of personal time affect employees' productivity rates. A lack of good relationships with colleagues and superiors creates more stress at work. Demographic analysis shows that 18% of junior-level employees have less than five years of experience and lack clarity in work assignments and associated complications for mid-level engineers. In addition, it is observed that professionals have no time or very little time for themselves or their families; this causes dissatisfaction in employees. Finally, senior professional employees are experiencing stagnant professional growth and more job complications owing to project requirements. Salary increases and rates of promotion are slow. These employees lack personal time and time for social and family commitments.

The various recommendations based on this study are listed below: The organization should provide a convenient job environment and reliable or flexible working hours. The management should perform a "performance appraisal" for each employee at regular intervals and should impart training to its employees at specific intervals. Career development practices should be engaged and designed to meet the requirements of different levels of employees. Since annual income influences the employees' productivity, it is suggested that the policies used by other income groups be offered accordingly to benefit the employees. Organizations should motivate employees to do higher studies and give stress relief and motivation counselling classes. Special data on work-life policies should be stored. Further research can be focused on the relationship between the employer and employee which is termed as "Psychological Contract" (PC) to improve the quality of work life. The author of this study is currently working in this to bridge this knowledge gap, which will probably give fruitful outcomes.

References

1. Zamani, S.H., Rahman, R.A., Fauzi, M.A., Mohamed Yusof, L.: Government pandemic response strategies for AEC enterprises: lessons from COVID-19. J. Eng. Des. Technol. (2022). Pre-Print. https://doi.org/10.1108/jedt-10-2021-0540
2. Anandh, K.S., Prasanna, K., Priya, M.G.S., Simon, S.M.: An industrial study of just in time (JIT) management in precast construction projects. In: AIP Conference Proceedings, vol. 2277, p. 240011 (2020). https://doi.org/10.1063/5.0025220
3. Priya, M.G.S., Anandh, K.S., Prasanna, K.: A quantitative study on construction job safety analysis and occupational safety and health management. In: Lecture Notes in Civil Engineering, vol. 191, pp. 355–368 (2022). https://doi.org/10.1007/978-981-16-5839-6_31

4. Sankar, K.S.A., Senthamizh, S., Anandh, K.S., Raja Pandian, S.: Investigating the ways to optimize the production of ready mix concrete plant. In: Lect. Notes Civ. Eng., vol. 191, pp. 369–380 (2022). https://doi.org/10.1007/978-981-16-5839-6_32

5. Mustapha, F.H., Naoum, S.: Factors influencing the effectiveness of construction site managers. Int. J. Proj. Manag. **16**(1), 1–8 (1998). https://doi.org/10.1016/S0263-7863(97)00025-2

6. Lingard, H.: Work and family sources of burnout in the Australian engineering profession: comparison of respondents in dual- and single-earner couples, parents, and nonparents. J. Constr. Eng. Manag. **130**(2), 290–298 (2004). https://doi.org/10.1061/(asce)0733-9364(2004)130:2(290)

7. Larsson, J., Eriksson, P.E., Olofsson, T., Simonsson, P.: Leadership in civil engineering: effects of project managers' leadership styles on project performance. J. Manag. Eng. **31**(6), 04015011 (2015). https://doi.org/10.1061/(asce)me.1943-5479.0000367

8. Chandrasekar, K.S., Suma, S.R., Nair, R.S., Anu, S.R.: Study on work-life balance among the executives in it industry with special reference to Technopark, Trivandrum, Kerala. Asian J. Multidimens. Res. **2**(3), 2278–4853 (2013)

9. Bowen, P., Govender, R., Edwards, P.: Structural equation modeling of occupational stress in the construction industry. J. Constr. Eng. Manag. **140**(9), 04014042 (2014). https://doi.org/10.1061/(asce)co.1943-7862.0000877

10. Leung, M.-Y., Liang, Q., Olomolaiye, P.: Impact of job stressors and stress on the safety behavior and accidents of construction workers. J. Manag. Eng. **32**(1), 04015019 (2016). https://doi.org/10.1061/(asce)me.1943-5479.0000373

11. Bowen, P., Edwards, P., Lingard, H., Cattell, K.: Predictive modeling of workplace stress among construction professionals. J. Constr. Eng. Manag. **140**(3), 04013055 (2014). https://doi.org/10.1061/(asce)co.1943-7862.0000806

12. Caldwell, S.D., Liu, Y.: Further investigating the influence of personality in employee response to organisational change: the moderating role of change-related factors. Hum. Resour. Manag. J. **21**(1), 74–89 (2011). https://doi.org/10.1111/j.1748-8583.2010.00127.x

13. Shujat, S.: Impact of work life balance on employee job satisfaction in private banking sector of Karachi. IBT J. Bus. Stud. **7**(2), 7–15 (2011). https://doi.org/10.46745/ilma.jbs.2011.07.02.02

14. Poulose, S., Susdarsan, N.: Work-life balance: a conceptual review. Int. J. Adv. Manag. Econ. **3**(2), 1–17 (2014)

15. Hopkins, B.W.E.: Integrated in such a way that allows them to formulate corporate strategy, which results in some level of organization performance. Implied in this model is that the level of organization performance is directly related to the level of commitment and AC, vol. 7, no. 2, pp. 213–222 (1991)

16. Anandh, K.S., Gunasekaran, K.: An investigation on stress among the professionals in the Indian construction industry. In: Construction Research Congress 2018: Safety and Disaster Management - Selected Papers from the Construction Research Congress 2018, pp. 1–7 (2018). https://doi.org/10.1061/9780784481288.001

17. Anandh, K.S., Gunasekaran, K.: Constructing a model to examine the influence of quality of work-life on work-life balance - discernment of civil engineers from construction industry in Chennai. Indian J. Sci. Technol. **9**(40) (2016). https://doi.org/10.17485/ijst/2016/v9i40/100760

18. Anandh, K.S., Gunasekaran, K., Mannan, M.A.: Investigation on the factors affecting lifestyle of professionals in the construction industries (Kerala and Tamil Nadu). Int. J. Integr. Eng. **12**(9), 246–252 (2020). https://doi.org/10.30880/ijie.2020.12.09.029

19. Harish, N., Anandh, K.S., Antony, S.: Envisage on superior-subordinate in construction engineers pertaining to Indian context. Int. J. Innov. Technol. Explor. Eng. **8**(6), 894–897 (2019)

20. Anandh, K.S., Gunasekaran, K., Sankar, S.S.: An envisage on emotional intelligence among superior-subordinate in construction sector of Chennai City, India. In: AIP Conference Proceedings, vol. 2277, p. 240012 (2020). https://doi.org/10.1063/5.0025223

Response Analysis of Multi-layer Foundation System Supported by Soft Subgrade Subjected to Moving Load

Avneet Lahariya and Ashutosh Trivedi

Abstract The development of transportation networks on soft subgrade is potentially active interest among researchers, engineers, and practitioners due to the rapid urbanization of human civilizations. In the present study, a finite element model is developed to examine the dynamic response of a multi-layer foundation system supported by soft subgrade. The reduced integration technique is adopted to investigate the response of subgrade with varied load and velocity. For the set of specified parameters in the study, the elastoplastic displacement response of soft-subgrade is calculated. After 150 kN of moving load, the soft-subgrade exhibits plastic behaviour. The estimation of subgrade plasticity with varying loading magnitude and velocity yields significant results in the analysis of the soft-subgrade-supported transportation network.

Keywords Soft subgrade · Finite element modeling · Subgrade plasticity · Pavement dynamics

1 Introduction

The engineering structures like the transportation network of highways and railways involve the interaction of pavement-subgrade material subjected to moving loads. The dynamic responses of the pavement under moving load conditions are significantly different from the static responses. To ensure the safety and durability of pavement that is subjected to moving vehicular load during its service, an adequate model for simulation and parametric analyses should be developed [1]. In traditional road analysis, constant moving loads were frequently used. A pavement's dynamic response is mainly due to repeated actions under moving vehicle loads [2, 3]. A non-linear anisotropic pavement finite-element (FE) model was used to examine the

A. Lahariya (✉) · A. Trivedi
Department of Civil Engineering, Delhi Technological University, Delhi 110042, India
e-mail: avneetlahariya_2k20gte06@dtu.ac.in

A. Trivedi
e-mail: atrivedi@dce.ac.in

mechanical behavior of visco-elastic pavement under the effect of moving load [4, 5]. The contact forces on the interface of tire-road surface are being used as input to pavement modelling by a number of studies [4, 6]. A 3-dimensional road model and a tire model can be used to extract the 3D contact stress to evaluate the response and damage to the pavement [7, 8]. The vehicle speed and frictional property of tire/terrain interface on the road are crucial factors for the finite element tire/terrain interaction model to evaluate the soil compaction [9]. It is vital to anticipate cumulative deformation of fine-grained soils under moving loads in order to plan efficient road building and maintenance. A soil's stress history, drainage conditions, and continuous loading all have a role in determining its strength and deformation resistance [10]. The plastic deformations that occur in granular materials when subjected to repeated traffic loads can be evaluated by using the Mohr–coulomb model [11–13].

Practically the problem of finding exact values of displacement for moving load is very difficult in the field as it involves various field complexities. In the present study, velocity-induced loading, displacements, stress and strain response of pavement subjected to moving mass are captured using a numerical program. An implicit integration approach is used to solve this problem numerically using the commercial software tool Abaqus.

2 Numerical Model

2.1 Finite Element Simulation

The numerical analysis of the multi-layer foundation model is analyzed using the commercially available finite element software ABAQUS [14]. The ballasts, sub-ballasts, and subgrade are simulated using dynamic implicit method with biased hexahedral meshed elements. From top to bottom, zero-thickness interface elements are used to represent different layer interfaces: load block-ballast, ballast-sub ballast, and sub-ballast-subgrade. The recoverable strain field modeling approach has been adopted for load block, ballast, and sub ballast in which strain recovers after passage of moving load and for soft sub-grade, Mohr–Coulomb constitutive model has been used.

2.2 Pavement Structure and Material Parameters

A multi-layer road is modeled in Abaqus, namely as ballast, sub-ballast and soft subgrade. All layers of pavement are of same length as 10 m and same width as 4 m. The thickness of ballast, sub-ballast and subgrade are of 120 mm, 200 mm and 500 mm respectively. The ballast and sub-ballast are modeled as elastic materials because the functions of ballast and sub-ballast include transfer of the imposed

Table 1 Material properties of the model

Components	Density (Kg/m^3)	Modulus of elasticity (MPa)	Poisson ratio
Load block	1100	100	0.4
Ballast	1670	6.24	0.35
Sub-ballast	1630	2.87	0.32
Subgrade	1830	1.25	0.4

moving load uniformly to the subgrade soil and to provide uniform support with the necessary degree of elasticity and resilience to absorb vibrations and shock [15, 16]. The soft subgrade is considered as a cohesive soil with cohesion yield strength of 8 kPa with negligible frictional strength [10]. For numerical stability of the algorithm in the software, the soil's friction angle and dilation angle are considered as 1° and 0.85° respectively [17]. The permeability of subgrade is taken as 3.24×10^{-10} m/s [10]. Table 1 lists the material parameters utilized in the dynamic implicit condition analysis using a three-dimensional FEM model.

2.3   FE Meshing and Boundary Condition

C3D8R elements are used to mesh the ballast, sub-ballast, and subgrade (3D Plane Stress Reduced-Integration Brick Elements). A total of 7500 elements constitute the multi-layer road model. The model incorporates biased meshing to concentrate finer elements beneath the load block and pavement interface.

For time-history analysis on the bottom sides of the subgrade, absorbent boundaries are utilized to absorb incoming waves and approximate infinite boundary conditions. The absorbent border condition is accounted for using the spring-dashpot support. The spring constant is taken as 2.71×10^7 N/m and dashpot coefficient is taken as 197,500 N.s/m. However, fixed boundary support is used for the lateral and longitudinal vertical face of the road layers (Figs. 1 and 2).

2.4   Loading Procedure

The load distribution zones of tire-road surface contact are typically simplified into a circular shape. The tire-road surface interaction is quite complicated. A surface made of rectangles with length and breadth disparities is used to simplify radial tire-road surface contact regions. In this analysis, a single axle load is considered which is moving with velocity of 10 to 40 m/s and loading intensity of 150 to 250 kN in the direction of pavement [18, 19].
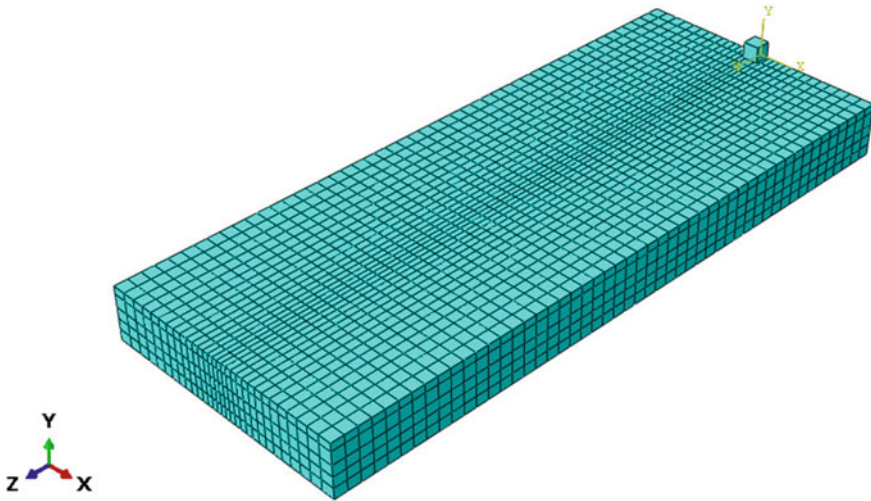
Fig. 1 The meshing of the finite element model
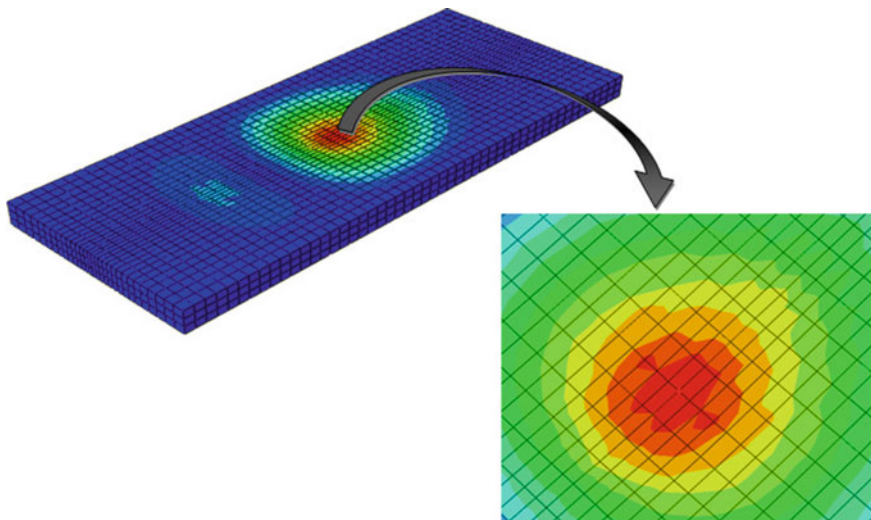
Fig. 2 Reference node in the subgrade layer

2.5 *Layer Interface Modeling*

The interface condition in a multi-layer pavement has a significant impact on road performance. The surface-to-surface interaction is used between ballast and loading block. The penalty friction algorithm is used to represent them with "hard" normal contact and for the tangential contact, a friction coefficient is to be taken as 0.2. The

general contact interaction is used for the subsequent road layers, with "hard" normal contact and for tangential contact, friction coefficient is taken as 0.3.

3   Results and Analysis

3.1   Displacement Response

The Fig. 3 shows that the displacement of the pavement when the load is moving with the constant velocity of 10 m/s and the loading intensity is increased from 150 to 250 kN. The maximum deflection can be seen of 80.8 mm at the loading intensity at 250 kN. It has been observed that the plastic behavior of soil is initialized beyond 150 kN of load moving with 10 m/s velocity. Further, deformation in the subgrade layer gets stored, which can't be recovered and is referred to as the plasticity of the subgrade. The plasticity or the stored deflection of the pavement is increased with the increment of the loading intensity. The load–displacement curve is plotted that shows the region of elastic, initial yield and plastic of the subgrade layer [20].

The further displacement response of the pavement at 20, 30 and 40 m/s is shown in the Fig. 4. The displacement of subgrade is reduced with increasing velocity of moving vehicle but it is increased with increasing in the loading intensity at same velocity. This is because of the small interaction time of moving vehicle with the road.
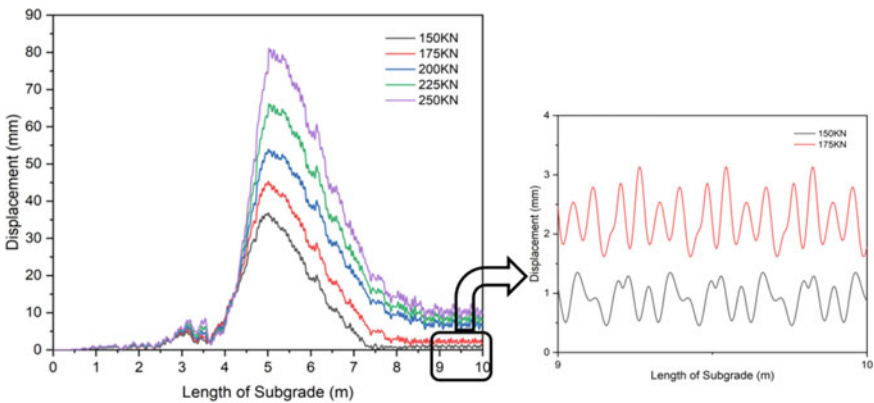
Fig. 3   Displacement response of the subgrade layer
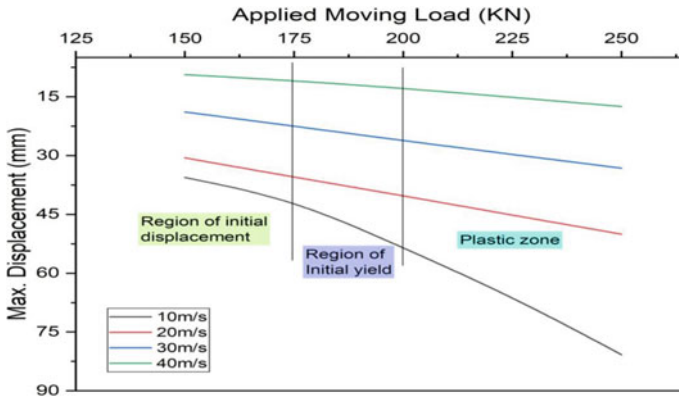
Fig. 4 Maximum displacement of subgrade layer

3.2 Stress Response

The Fig. 5 shows the stress response of the subgrade when 250 kN load is moving with velocity of 10 m/s. This is the nodal stress of subgrade layer at the mid length of the soil subgrade. Initially, the reference node start to show gradual stress increment when the load move along the road. But when the load reaches at the mid length and coincide the reference node, the stress in the subgrade layer reaches its peak value of 226 kPa.

Simultaneously, the Fig. 6 shows the maximum stress that have been found when variable load is moving with the velocity of 10, 20, 30 and 40 m/s. The stress in the subgrade layer (at reference point) is increased with increasing the loading intensity but it is decreasing with increasing the velocity of moving load. Due to the higher velocity of moving load, the interaction time between the contact surfaces is reduces,
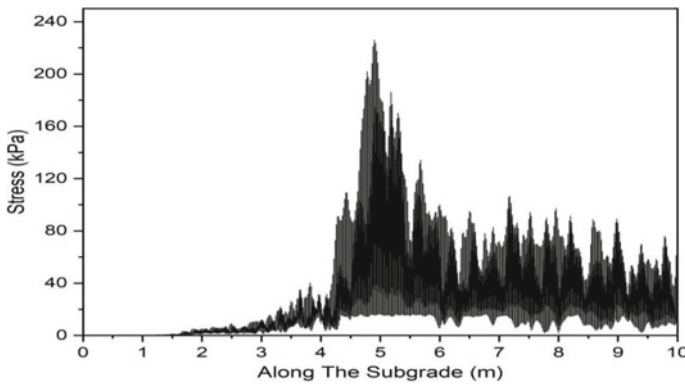
Fig. 5 Stress response on the subgrade layer
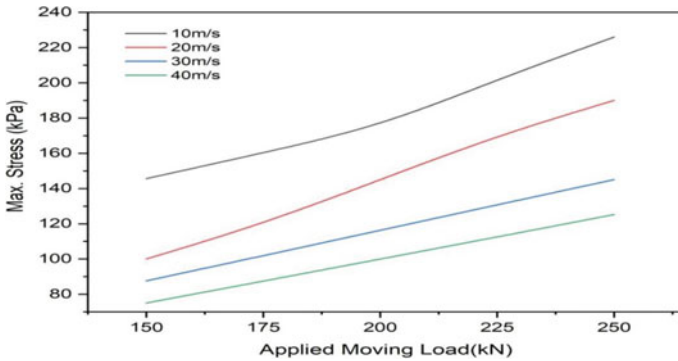
Fig. 6 Maximum stress on the subgrade layer

which causes the less stress at higher velocity as compare to higher stress at low velocity.

3.3 Strain Response

The Fig. 7 Shows the maximum strain value of subgrade layer (at reference point), when the variable loading intensity is moving with the variable velocities. The strain is increased with increasing the loading intensity but it decreases with increasing the velocity of moving load. The maximum strain in the subgrade layer is found to be 0.0785 at 250 kN load moving with the 10 m/s.

The initial strain of all the curve are seen to be similar, but with increasing the load, it can be seen that the rate of increasing of strain at 10 m/s velocity curve is higher than the velocity curve of 20, 30 and 40 m/s respectively.
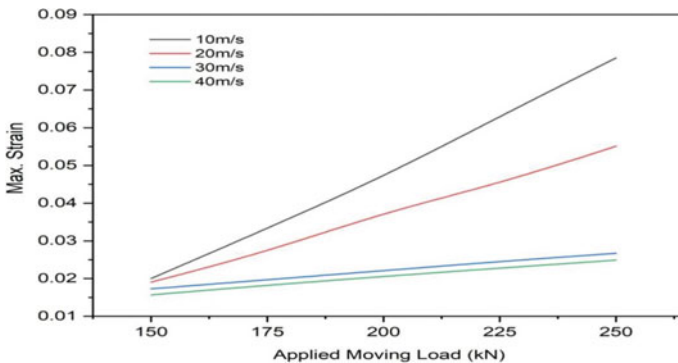
Fig. 7 Maximum strain in the subgrade layer

4   Conclusions

This paper presents a numerical model of a multi-layer foundation system supported by a soft subgrade subjected to moving load. The mechanical responses of the subgrade under moving load are computed, and the regularities of displacement, stress, and strain variation of the subgrade at reference node are studied. It can be demonstrated that after reaching the threshold velocity, the interaction time between the layers and moving load is decreases with further increase in the velocity which results in decrement of displacement, stress and strain response. Based on the findings of this study, the following conclusions can be drawn:

1. The plasticity of the soft subgrade increases with increasing the loading intensity. The plasticity behavior of the soft subgrade is initialized after 150 kN load with velocity of moving load at 10 m/s.
2. The subgrade reaches the threshold value of velocity and further increase in the velocity of moving load leads to the decrementing response of displacement, stress, and strain.
3. The maximum reduction of displacement in the subgrade layer varies from 73 to 78% for the selected inputs of moving load velocities.
4. The maximum reduction of stress in the subgrade layer for varied velocity parameters ranges from 50 to 80% of the velocity induced stresses.
5. The maximum reduction of strain in the subgrade layer is observed as 22 to 68% with variation in the velocity of moving load.

References

1. Liu, Z., Niu, J., Jia, R.: Dynamic analysis of arbitrarily restrained stiffened plate under moving loads. Int. J. Mech. Sci. **200**, 106414 (2021)
2. Zhao, Y.X., Qiu, Y.J., Cao, P., Ai, C.F.: Research on dynamic response of pavement under moving vehicle loading using three dimensional finite element method. Appl. Mech. Mater. **444–445**, 1197–1203 (2013)
3. Singh, M., Trivedi, A., Shukla, S.K.: Influence of geosynthetic reinforcement on unpaved roads based on CBR and static and dynamic cone penetration tests. Int. J. Geosynth. Ground Eng. **6**(2), 1–13 (2020)
4. Wang, Y., Wang, L.J., Lu, Y.J., C.D.: Simulation on viscoelastic behavior of asphalt pavement under complex moving wheel load. J. Vibr. Shock **36**(15), 181–186 (2017)
5. Mehra, S., Trivedi, A.: Pile groups subjected to axial and torsional loads in flow-controlled geomaterial. Int. J. Geomech. **21**(3), 04021002 (2021)
6. Han, F., Wang, H., Dan, D.H.: Dynamic response of a bridge deck pavement. In: Proceedings of the Institution of Civil Engineers-Transport, vol. 172, no. 4, pp. 221–232 (2019)
7. Al-Qadi, I.L., Wang, H.: Prediction of tire pavement contact stresses and analysis of asphalt pavement responses: a decoupled approach. Asphalt Paving Technol. Proc. Assoc. Asphalt Technol. **80**, 289 (2011)
8. Kumar, Y.: Dynamic analysis of constrained rigid pavement subjected to moving load (Doctoral dissertation) (2020)

9. Xia, K.: Finite element modeling of tire/terrain interaction: application to predicting soil compaction and tire mobility. J. Terrramech. **48**(2), 113–123 (2011)
10. Chawla, S., Shahu, J.T.: Analysis of cyclic deformation and post-cyclic strength of reinforced railway tracks on soft subgrade. Transp. Geotech. **28**, 100535 (2021)
11. Wolff, H., Visser, A.T.: Incorporating elasto-plasticity in granular layer pavement design. Proc. Ice Transp. **105**(4), 259–272 (1994)
12. Trivedi, A., Singh, S.: Cone resistance of compacted ash fills. J. Test. Eval. **32**(6), 429–437 (2004)
13. Shahu, J.T., Hayashi, S.: Cumulative plastic strain and threshold stress of a Quasi-saturated compacted silty clay. Lowland Technol. Int. **10**, 10–20 (2008)
14. Liu, L., Hao, P.: ABAQUS program-based numerical analysis on U-shaped cracking of asphalt pavement. In: 2011 International Conference on Remote Sensing, Environment and Transportation Engineering, pp. 2861–2864 (2011)
15. Wang, G.C.: Unbound slag aggregate use in construction. In: The Utilization of Slag in Civil Infrastructure Construction, pp. 155–184 (2016)
16. Burmister, D.M.: The general theory of stresses and displacements in layered systems. I J. Appl. Phys. **16**(2), 89–94 (1945)
17. Satyal, S.R., Leshchinsky, B., Han, J., Neupane, M.: Use of cellular confinement for improved railway performance on soft subgrades. Geotext. Geomembr. **46**(2), 190–205 (2018)
18. Zhao, H.Y., Indraratna, B., Ngo, T.: Numerical simulation of the effect of moving loads on saturated subgrade soil. Comput. Geotech. **131**, 103930 (2021)
19. Zhao, J., Wang, H.: Dynamic pavement response analysis under moving truck loads with random amplitudes. J. Transp. Eng. Part B Pavements **146**(2), 04020020 (2020)
20. Trivedi, A., Shukla, S.K.: Testing and technology for load carrying capacity of deep foundations (2019)

Analysis of Steel Dual Ring Damper in a Braced Steel Frames

Anju Raju and N. Neeraja

Abstract Over the past few decades, world has experienced increased loss of human life and severe structural damages due to numerous devastating earthquakes. In order to reduce these damages, different dampers can be effectively used in building to control earthquake induced vibration as it can absorb and dissipate energy of seismic waves moving through building structure. The Steel Dual-Ring Damper (SDRDs) is a metallic damper composed of two concentric steel rings connected by a gusset plate which restrict buckling of braced frames and yield more in tension and compression due to its circular shape compared to other dampers. The work mainly focuses on determining the effect of cyclic behavior of an energy dissipation system with SDRDs in the brace to brace connection using ANSYS software. Parameters like stiffness, ductility and total dissipated energy of SDRDs were evaluated. Studies indicate that the SDRDs can be used as ductility member in concentrically braced frame systems.

Keywords Cyclic loading · Energy dissipation · Steel Dual-Ring Damper (SDRDs) · ANSYS

1 Introduction

During an earthquake, severe damages occur in the building structures due to the low strengthening effects. The concentrically braced frames (CBFs) have high stiffness and less ductility, because of that, seismic performance of concentrically braced frames is low. [6] One of the methods to strengthening the structures is by using energy absorbing systems. It also increases the ductility of the concentrically braced frames. Previous studies were investigated the energy dissipation capacity of steel ring damper and dual—ring damper by cyclic loading, analytically and numerically. The Steel dual ring damper (SDRD) proposed as a ductile element and is responsible for energy absorption and energy dissipation. The SDRD is made up of two concentric rings which are connected to each other by steel plates. [3] Thus, the steel ring must

---

A. Raju (✉) · N. Neeraja
Department of Civil Engineering, FISAT, Angamaly, India
e-mail: rajuanju805@gmail.com

be designed such that it has good ductility and strength. It has the ability to be easily installed and replaced in the bracing system. [2] More studies only focusing on metallic damper and the investigation of steel dual ring damper on a braced steel frame is not done.

This study aims to evaluate the energy dissipation capacity of a steel dual ring damper (SDRD) on a braced steel frames. To compare the performance of with and without damper in braced steel frame. Cyclic loading is carried on the steel frame and its performance is studied by changing the parameters like thickness and diameter of the inner and outer ring, and length of the ring. Also, find the performance of SDRD in a different bracing system.

2   Finite Element Formulation

In order to investigate the energy dissipation capacity of steel dual ring damper on braced steel frames, finite element analysis was done by using ANSYS 16.2.

2.1   Geometric Description

A single storey braced steel frame with SDRD damper was modeled. The model and its specifications are chosen as per the details provided on the paper "The influence of moment resisting beam to column connections on seismic behavior of chevron concentrically braced frames" by Costanzo et al. [5]. The height of the frame taken for the analysis was 4000 mm. The width of the frame was 8000 mm. As per EN1998-1 code (European standard), dimensions of I section of the steel frame was selected. The S355 grade of steel was used for modeling. The column section and beam section adopted as HEM 280 and IPE 600 respectively. The geometry of the braces is a circular shape. The size of bracing was taken as 193.7 × 8 mm. Figures 1 and 2 shows geometry of braced steel frame with and without SDRD damper. Table 1 shows dimensions of beam and column I section. The SDRD damper is placed in between the bottom end of the brace and column. The dimensions of the SDRD damper are shown in Table 2.

2.2   Material Properties

The material properties of steel used for the study is shown in Table 3.
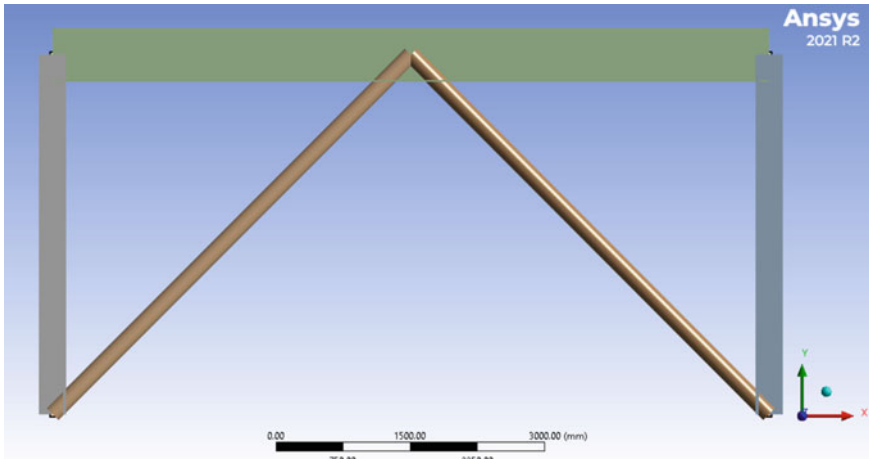
Fig. 1 Geometry of braced steel frame
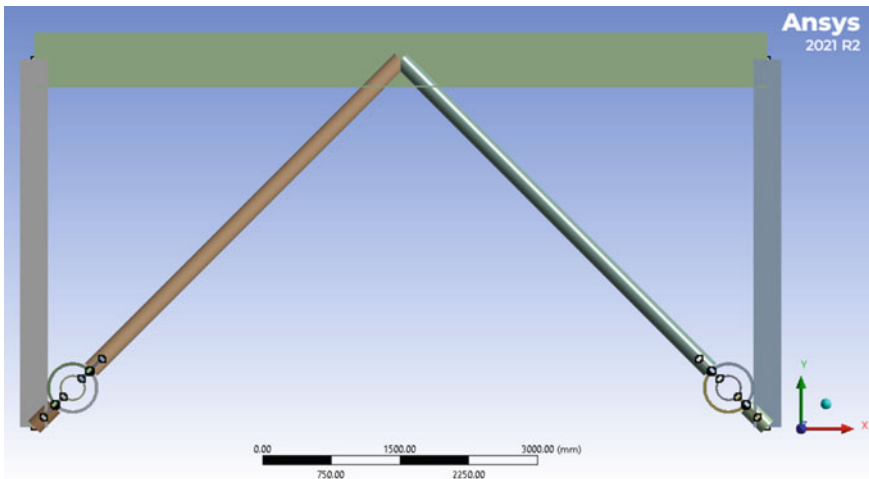
Fig. 2 Geometry of braced steel frame with SDRD

Table 1 Dimensions of beam and column I section

Dimension	Height of the section, h (mm)	Width of the flange, b (mm)	Thickness of web, t_w (mm)	Thickness of flange, t_f (mm)
HEM 280	310	288	18.5	33
IPE 600	600	220	12	19

Table 2 Dimensions of the SDRD damper

SDRD	Dimensions (mm)
Diameter of the outer ring, Do	500
Diameter of the inner ring, Di	250
Thickness of the outer ring, to	25
Thickness of the inner ring, ti	12.5
Length of the ring, L	250

Table 3 Material properties of steel

Properties of steel	Value
Young's modulus, (GPa)	200
Yield strength, fy (MPa)	355
Poisson's ratio	0.3

2.3   Finite Element Modeling

The model consists of SDRD damper and braced steel frame. The SOLID 186 is a 20-node solid element with quadratic displacement characteristics. The element is made up of 20 nodes with three degrees of freedom in each node and translations in the x, y, and z dimensions. The shape of meshing was Hexahedron (Fig. 3).
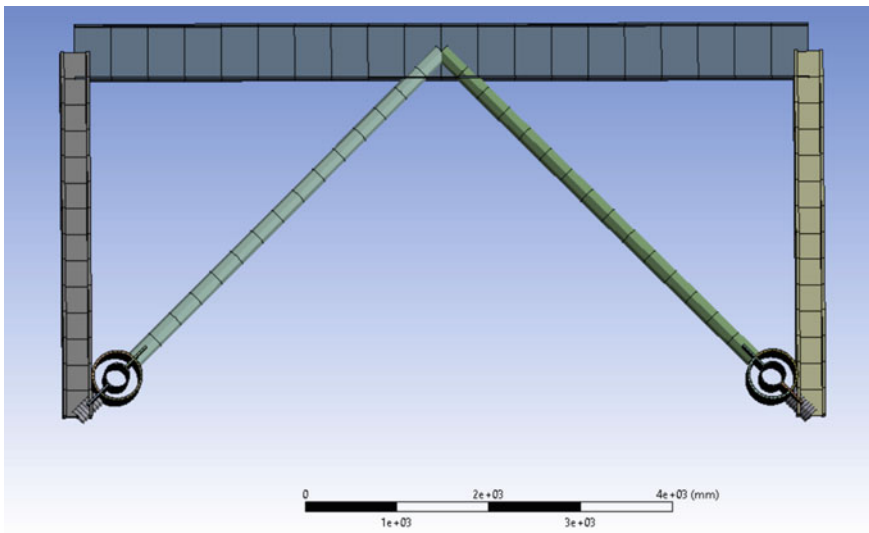
Fig. 3 Meshing model
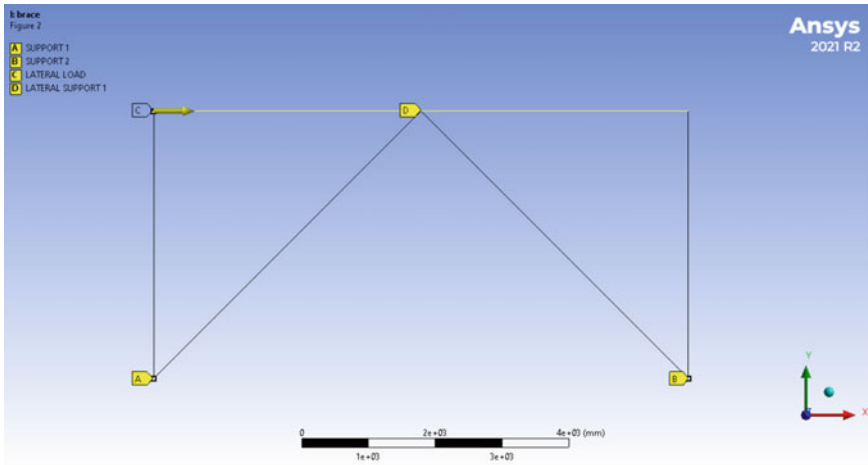
Fig. 4 Support condition of braced frame

2.3.1 Support condition and Loading

The braced steel frame was modeled in the XY plane in which the bottom end of the column was provided with pinned support by preventing translation in all directions and permitting rotation along the z direction as shown in Fig. 4. A lateral load was provided at the top interface of the frame.

3 Results and Discussions

The braced frame with and without damper was modeled and analysed. The load and deformation were noted. The ultimate load of braces w/o damper was obtained as 2322 KN. The deformation of the frame w/o damper was 15.365 mm. The braced frame with damper (Damper size: Do = 500 mm, Di = 250 mm, to = 25 mm, ti = 12.5 mm) was analysed. The ultimate load capacity and deformation of the braced frame was 2203.1 KN and 190 mm, respectively. Figure 5 shows total deformation of braced frame with SDRD damper.

The four models of SDRD with varying length of the ring damper were analysed. The effect of varying the length of ring were investigated by comparing the maximum load carrying capacity obtained from the static structural analysis of the braced steel frame with SDRD. The length of the ring adopted as 250, 200, 150 and 100 respectively. The force reaction and corresponding deformation of the 4 models were noted and load—deformation curve were also plotted. Figure 6 shows load v/s deflection curve of the braced frame with and without damper.
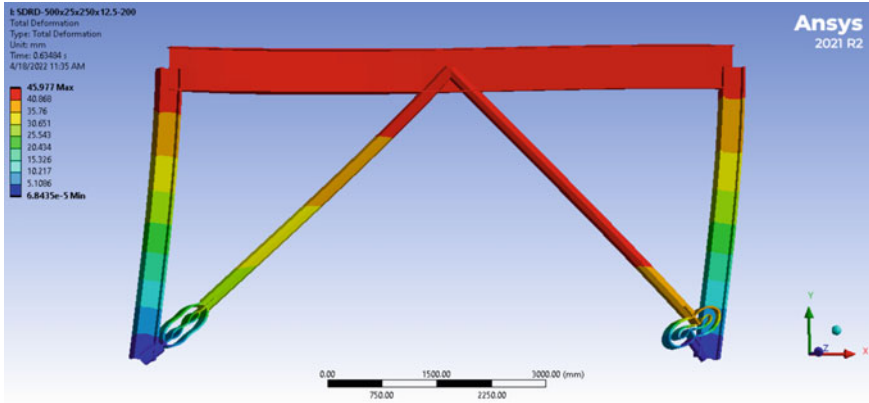
Fig. 5 Total deformation of braced frame with SDRD
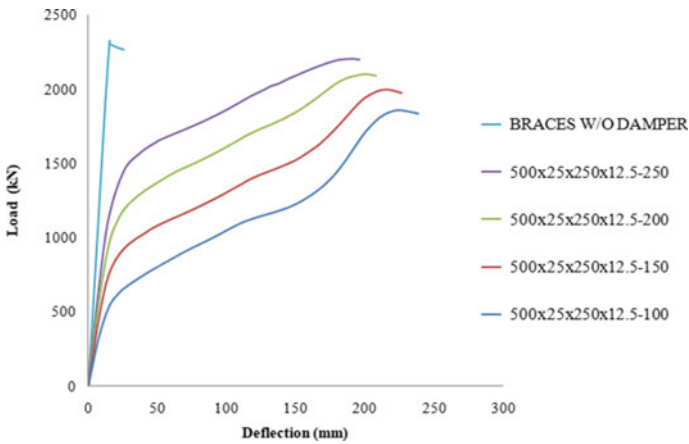
Fig. 6 Load-deflection graph with varying the length of ring

3.1 Ductility variation

The models of braced steel frame with SDRD damper with varying length of the ring was analysed. Stiffness is the ratio of load to displacement. Ductility (μ) is ratio of the maximum load, Δu to the yield displacement, Δy. Table 3 shown ductility variation of the braced frame with and without damper (Table 4).

Table 4 Stiffness and ductility value of braced frame with and without SDRD by varying the ring length

Models	Deflection (mm)	Ultimate load Δu (KN)	% Decrease in load	Yield displacement, Δy (mm)	Stiffness, Ko (KN/mm)	Ductility
Braces W/O Damper	15.365	**2322**	1.0	3.6188	151.12	4.25
500X25X250X12.5-250	190	2203.1	5.1	7.3799	11.60	25.75
500X25X250X12.5-200	199.74	2100.1	9.6	7.3795	10.51	27.07
500X25X250X12.5-150	214.12	1993.3	14.2	7.3789	9.31	29.02
500X25X250X12.5-100	224.42	1854	20.2	7.3783	8.26	30.42

4 Conclusion

In this study, braced frame with and w/o SDRD damper was modeled and analysed. The effects of varying the length of SDRD damper were investigated.

- Comparing the braced frame with and w/o damper, it was observed that model without damper showed higher load carrying capacity. The value of ultimate load was 2322 KN and corresponding deflection was 15.365 mm.
- The length of the ring (L) adopted as 250, 200, 150 and 100 mm respectively. A continuous decrease in load carrying capacity is observed while decreasing the length of the ring.
- It was observed that the stiffness of the braced steel frame with SDRD damper decreases when compared to the braced steel frame without damper.
- Comparing to the braced frame without damper, it was observed that the ductility of the braced frame with damper increases.
- Length variation does not give any sufficient improvement in load carrying capacity of the damper. Further studies have to be done by changing the parameters such as diameter and thickness of the inner and outer ring in order to study whether there is any improvement in strength.

References

1. Behzadfar, B., Maleki, A., Lotfollahi Yaghin, M.A.: Improved seismic performance of chevron brace frames using multi-pipe yield dampers. J. Rehabil. Civil Eng. **8-4** (2020)
2. Azandariani, M.G., Azandariani, A.G., Abdolmaleki, H.: Cyclic behavior of an energy dissipation system with steel dual-ring dampers (SDRDs). J. Constr. Steel Res. **172** (2020)
3. Azandariani, M.G., Abdolmaleki, H., Azandariani, A.G.: Numerical and analytical investigation of cyclic behavior of steel ring dampers (SRDs). Thin-Walled Struct. **151** (2020)
4. Costanzo, S., D'Aniello, M.: The influence of moment resisting beam to column connections on seismic behavior of chevron concentrically braced frames. Soil Dyn. Earthq. Eng. **113** (2018)
5. Peng, X.-T., Lin, C., Cao, Y.-M., Duan, W.-X.: Seismic behaviors of the composite central brace with steel ring damper. Adv. Eng. Res. **170** (2018)

6. Sahoo, D.R., Singhal, T., Taraithia, S.S., Saini, A.: Cyclic behavior of shear and flexural yielding metallic dampers. J. Constr. Steel Res. **114** (2015)
7. Andalib, Z., Bazzaz, M., Kafi, M.A., Kheyroddin, A.: Experimental investigation of the ductility and performance of steel rings constructed from steel plates. J. Constr. Steel Res. **103** (2014)

Experimental Study on Pervious Concrete with Silicafume as Cement Replacement

Liya Mary Denny and S. Sreerath

Abstract Permeable concrete is such a concrete in which the void ratio is suitably increased such that the structural member allows water to percolate it through, making the water, which is supposed to get lost as run off, percolate to the immediate ground. The voids are affected by many factors such as size and quantity of aggregates, amount of fine particles in the concrete, changing the porosity while designing the concrete etc. The modern concepts of structural engineering promoted the use of alternative materials as replacement cement as well as natural aggregate. Present study focuses on the effect of silica fume as replacement for cement in pervious concrete. Different porosities (8, 10, 12%) were considered to find out the nominal mix. The mix with highest strength value is selected as the nominal mix. The cement content in the nominal mix is then replaced with silica fume for 3, 4, 5, 6, 7%. Based on the strength results obtained, the optimum mix of silica fume based pervious concrete is selected. Cement can be replaced with 5% of silica fume for effective strength gain.

Keywords Pervious concrete · Recycled aggregate · Silica fume

1 Introduction

Today, demolition of old structures and waste concrete from new structures has increased the availability of crushed concrete in huge amounts. Annual rate of generation of construction waste is expected to be 3 million tonnes by 2050. Thus recycling construction waste has gained more importance, both in order to reduce the amount of open land required for landfilling and to protect the environment through resource conservation. Thus from the aspect of sustainable and green building technologies recycled aggregate in construction has increased globally. Recycled aggregate concrete is a kind of new concrete made from recycled aggregate which is crushed and processed from waste concrete and replaces natural aggregate partly or totally.

L. M. Denny (✉) · S. Sreerath
Department of Civil Engineering, Federal Institute of Science and Technology (FISAT), Ernakulam 683577, India
e-mail: liyamarydenny1998@gmail.com

In order to resolve the problems such as runoff of rainwater, spoliation of ecology, the concept of pervious concrete has gained more importance. Pervious concrete also possess many other advantages including sound absorption and skid resistances. However, the existence of air voids result in low strength, so pervious concrete is not effective for heavy traffic loadings, so that they can be used in parking lots.

A decrease in the mechanical properties was generally observed in all concrete in which the natural coarse aggregate was replaced with recycled aggregate prepared by the crushing of old concrete. This may be attributed to the fact that the microstructure of recycled concrete has an adverse effect when subjecting it to a new environment. Incorporation of fine aggregate from crushed concrete in the production of new concrete leads to an even greater decrease in the mechanical properties. RILEM Technical Committee 121-DRG (1994) recommended that only 20% of the natural aggregate can be replaced with recycled coarse aggregate in the preparation of new concrete of all strength classes, and limited the concrete classes when 100% recycled construction waste is used [3].

1.1 *Objectives*

1. To find the optimum percentage of cement replacement with silica fume for pervious concrete.
2. To find the optimum percentage of natural aggregate replacement with recycled concrete aggregate for pervious concrete containing optimum percentage of silica fume.
3. To evaluate the performance of silica fume pervious concrete containing recycled aggregate as coarse aggregate.

1.2 *Scope*

1. Only 12 mm size aggregate was used as coarse aggregate for pervious concrete.
2. No fine aggregate is added, in order to make the concrete more porous.
3. Silica fume is used as the replacement for cement.

2 Experimental Program

2.1 *Materials*

Cement
Portland Pozzolana Cement (PPC) of grade 53 conforming to IS 8112-1989 is used in the study. The physical properties of cement are listed in Table 1.

Table 1 Physical properties of cement

Experiment	Result	Standard method as per Indian Standard Code
Fineness	6.5%	IS:4031-1988 Part-IV
Specific gravity	2.69	IS:4031-1988 Part-XI
Initial setting time	85 min	IS:1489 (Part 1):1991
Consistency	33%	IS:4031-1988 Part-IV

Table 2 Physical properties of coarse aggregates

Sl. no.	Properties	Test results
1	Specific gravity	2.85
2	Water absorption	0.101%
3	Bulk density	1.33 kg/L

Coarse Aggregate

Crushed granite angular aggregate from a local source, having a maximum size of 12.5 mm, was used for the present study. Test results on coarse aggregate conformed to IS 2386-1963 (Part 3). Physical properties of coarse aggregates are shown in Table 2.

Silica Fume

Silica fume, commonly known as microsilica, is an amorphous (non-crystalline) polymorph of silicon dioxide. It's an ultrafine powder made up of spherical particles with an average particle diameter of 150 nm that's collected as a by-product of silicon and ferrosilicon alloy manufacture. The most common use is as a pozzolanic substance in high-performance concrete.

Water

Water is the most important material which is used for mix up of all the ingredients in concrete. Potable water has to be used for this purpose. The presence of sulphates & salts can reduce the concrete strength and have to be avoided.

2.2 Mix Proportions

Two mix proportioning methods were adopted to obtain the control mix for the experiment. One was based on NRMCA method and the other was based on porosity of porous concrete adopted from the study conducted by Cui X et al. 2017. The mix design was done for three porosity values, 8, 10 and 12% and water cement ratio was taken as 0.36. A total of 36 samples were prepared and the 7th, 28th days compressive strength of each sample for both methods were evaluated. Since strength

is considered as the primary factor for this work, the mix with highest strength value will be chosen as the control mix for this work.

NRMCA Method
I. TRIAL MIX 1-Design void content $= 8\%$

1. Determine the dry roded unit weight of the aggregate and calculate the void content

$$\text{Void content} = 38.7\%$$

2. Estimate the approximate percentage and the volume of paste (V_p) needed. The paste volume is then estimated as follows

$$V_p(\%) = Aggregate\ Void\ Content(\%) + CI(\%) - Vvoid(\%)$$

   CI = Compaction Index = 5.
   Vvoid = Design void content of the pervious concrete mix = 10%
   Vp = 35.7%
   The value of CI can be varied based on the anticipated consolidation to be used in the field. For greater consolidation effort a compaction index value of 1 to 2% may be more reasonable. For lighter level of consolidation, a value of 7 to 8% can be used. NRMCA used a value of 5% to get a similar value between measured fresh pervious concrete void content (ASTM C1688) and design the void content. Using a smaller value for CI (%) will reduce the paste volume.

3. Calculate the paste volume, (V_p) in ft^3 per cubic yard of pervious concrete:

$$Vp = Vp(\%) \times 27$$
$$= 9.639\ ft^3$$

4. w/c ratio $= 0.36$
5. Calculate the absolute volume of cement (Vc) ft^3

$$Vc = Vp/(1 + w/c \times RDc)$$

   RDc = Specific gravity of cement = 2.72.
   Vc = 4.87 ft³
6. Calculate the volume of water, (Vc) ft^3

$$Vw = Vp - Vc = 4.769\ ft^3$$

7. Calculate the volume of SSD aggregate (Vagg),

$$Vagg = 27 - (Vp + Vvoid)$$

Vvoid = design void content for the pervious concrete mix = 10%,
Vagg = 17.281 ft^3

8. Convert the volumes to weight of ingredients per cubic yard and for trial batches:

$$Cement(lb/yd3) = Vc \times RDc \times 62.4 = 826.601 \text{ lb/yd}^3$$
$$= 490.27 \text{ kg/m}^3$$

$$Water(lb/yd3) = Vw \times 62.4 = 297.586 \text{ lb/yd}^3$$
$$= 176.504 \text{ kg/m}^3$$

$$Aggregate(lb/yd3) = Vagg \times RDagg. \times 62.4 = 2868.37 \text{ lb/yd}^3$$
$$= 1701.28 \text{ kg/m}^3$$

MIX RATIO = 1: 3.5
Similarly mix was designed for void content 10, 12, 15%

Porosity Method
I. TRIAL MIX 4-Design void content = 8%

1. Selection of target porosity (P) = 8%
2. The mass of the coarse aggregate per cubic meter of concrete is determined by the density of aggregate,
   Density of aggregate, (ρa) = 1.62 kg/l
   Mass of aggregate, (ma) = 1620 kg
   Multiplying the mass with a reduction factor = mass $\times$ 0.98 = 1587.6 kg
3. Void content (V) of aggregate = 38.7%
4. Selection w/c ratio (Rw$_c$) = 0.36
5. Calculating the quantities of cement (mc) and water (mw)

$$m_c = 421.09 \text{ kg}$$
$$mw = mc \times Rwc = 151.88 \text{ kg}$$

RATIO: 1: 3.7

Mix Designation
See Table 5.

3 Results and Discussions

3.1 Compressive Strength

Compressive strength test results of the prepared mixes at different ages are presented in Table 3. MMm$_1$.

From the test results it has been observed that MN8S0R0 mix has greater strength. MN8S0R0 mix was selected as the control mix. In the control mix cement was replaced by silica fume in varying percentage of 3, 4, 5, 6, 7%. As shown in Table 4. It has been observed that greater strength results for mixes where cement is replaced by silica fume by 5% (Tables 6, 7 and Figs. 1, 2).

Table 3 Mix proportion of trial mix using NRMCA method

Trail mix	Mix designation	Void content (%)	Mix proportion
1	MN8S0R0	8	1: 3.5
2	MN10S0R0	10	1: 3.8
3	MN12S0R0	12	1: 4.14

Table 4 Mix proportion of trial mix using porosity method

Trail mix	Mix designation	Porosity (%)	Mix proportion
1	MP8S0R0	8	1: 3.77
2	MP10S0R0	10	1: 4
3	MP12S0R0	12	1:4.32

Table 5 Mix designation of trial mix

Mix designation	Mix design (%)	
	NRMCA	Porosity
MN8S0R0	8	0
MN10S0R0	10	0
MN12S0R0	12	0
MP8S0R0	0	8
MP10S0R0	0	10
MP12S0R0	0	12

Table 6 7 and 28 days compressive strength pervious concrete

Mix ID	Compressive strength at 7 days (MPa)	Compressive strength at 28 days (MPa)
MN8S0R0	11.6	15.98
MN10S0R0	6.27	9.58
MN12S0R0	10.25	14.25
MP8S0R0	5.62	8.64
MP10S0R0	9.44	11.57
MP12S0R0	8.17	12.47

Table 7 7 and 28 days compressive strength of pervious concrete with cement replacement

Mix ID	Compressive strength at 7 days (MPa)	Compressive strength at 28 days (MPa)
MN8S3R0	3.6	4.9
MN8S4R0	3	3.8
MN8S5R0	4.2	5.4
MN8S6R0	3.2	4.1
MN8S7R0	2	2.5
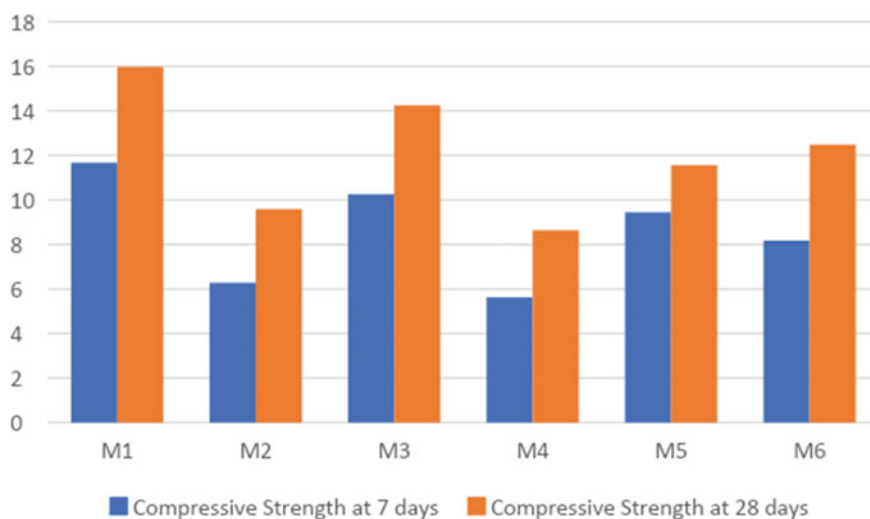
Fig. 1 7 day and 28 day compressive strength (MPa) of pervious concrete

3.2 Water Absorption Test

Water absorption of pervious concrete was determined as per IS: 13,630 (Part-2).
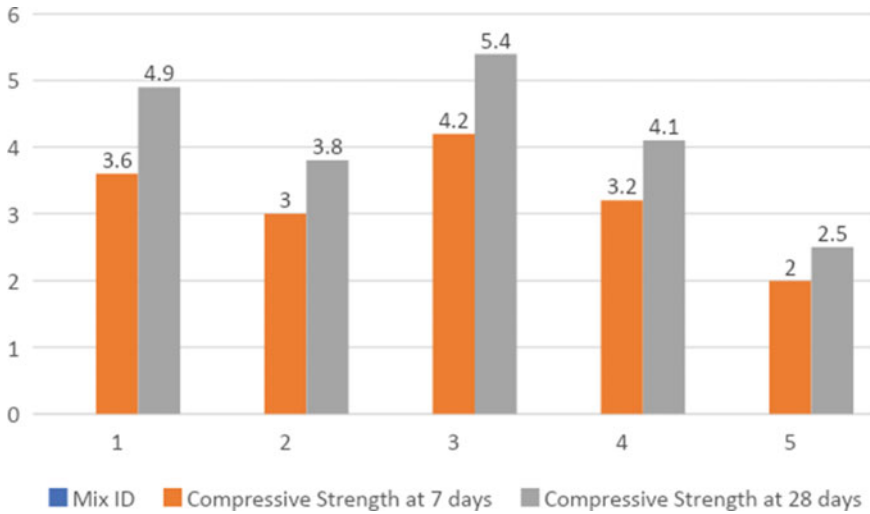
Fig. 2 7 day and 28 day compressive strength (MPa) of pervious concrete with cement replacement

$$\text{Water absorption}(\%) = \frac{m2 - m1}{m1} \times 100 = \frac{7.2 - 6.9}{6.9} \times 100 = 4.34\%$$

4 Conclusions

- With the increase in porosity from 8–12%, 28 days compressive strength was within the range of 10–20 MPa.
- Incorporation of silica fume decreased the initial strength, due to slower pozzolanic action of silica fume. With the increase in ages, compressive strength increased.
- The highest strength value was observed for samples with 5% silica fume replacement. The reason for this increase may be due to the pozzolanic and filler effect of silica fume.
- But compressive strength decreased at 6% replacement and this can be due to due to in partial replacement of cement with silica fume.
- The pervious concrete mix containing silicafume replacement achieved an average water absorption of 4.34%
- In all five replacement levels of silica fume, 28 days compressive strength values were either close to or greater than that of control mix.

References

1. Lee, M.G., Chiu, C.T., Kan, Y., Yen, T.: Experimental study of pervious concrete on parking lot. ASCE Geotech. Spec. Publ. **193**, 125–131 (2009)
2. Lee, M.-G., Huang, Y.-S., Chang, T.-K., Pao, C.-H.: Experimental Study of Pervious Concrete Pavement. Geotechnical Special Publication No. 218 © ASCE 2011
3. Kou, S.C., Poon, C.S., Chan, D.: Influence of fly ash as cement replacement on the properties of recycled aggregate concrete. J. Mater. Civ. Eng., 709–717 (2007). https://doi.org/10.1061/(ASCE)0899-1561(2007)19:9(709)
4. IRC58-2015: Guidelines for the Design of Plain Jointed Rigid Pavements for Highways - 4th Revision. 25. IRC74-1979, Tentative Guidelines for Lean-Cement Concrete and Lean Cement Fly Ash Concrete as a Pavement Base or Sub Base
5. Sumanasooriya, M.S., Neithalath, N.: Pore structure features of pervious concretes proportioned for desired porosities and their performance prediction. Cement Concr. Compos. **33**, 778–787 (2011)
6. Tamura, M., et al.: Life cycle design based on complete recycling of concrete. In: Proc., 1st Fib Congress, Europe (2002)

Seismic Performance of Braced Ductile Shear Panel

Anaswara Hareendran and B. R. Beena

Abstract Bracing is important as it gives a structure adequate architectural aesthetics and mechanical flexibility compared to wall systems. These bracings also provide better performance during an earthquake. The addition of shear panels to these bracings can prevent damage to neighbouring steel columns or beams, improve the performance of traditional concentric steel braces under compression and buckling, and eliminate fracture failure of steel braces subjected to multiple loads. As a result, the entire buckling of the bracing system is transmitted to the shear panel's plastic shear deformation. This thin shear panel and concentric X-braces combine to form the braced ductile shear panel (BDSP) system. To enhance the structure's lateral strength and energy dissipation capacity stiffening ribs are also attached to the shear panel. This BDSP system is connected to the surrounding steel parts using plate hinges, which can be removed after a strong earthquake if it gets damaged. This removable BDSP component provides lateral rigidity to the structure and thus restricts lateral inter-storey drift and maintains reasonable energy dissipation. This study focus on the performance of braced ductile shear panel systems with a different arrangement of stiffening ribs keeping the material density constant. The performance is evaluated by pushover analysis using the ANSYS software. The test results of the study showed the BDSP system with stiffening ribs located at multiple positions is better than that provided at a single position.

Keywords Shear panel · Buckling · Braces · BDSP · Stiffening ribs · Energy dissipation · Pushover analysis

1 Introduction

Structures in areas associated with high seismic activity are required to resist strong lateral forces resulting from earthquake-triggered ground accelerations. Usually, a building or any other structure rising above ground must resist smaller, frequent

A. Hareendran (✉) · B. R. Beena
Department of Civil Engineering, FISAT, Angamaly, India
e-mail: anaswarahareendran98@gamil.com

earthquakes as well as large, less frequent earthquakes [1]. The structure must have not only enough strength and stiffness to resist frequent events, but also should have adequate ductility or another form of damping to economically and efficiently ensure stability and safety during major events. In today's steel buildings the most frequently used steel structural systems for resisting lateral forces are the moment-resisting frame (MRF) and the concentrically braced frame (CBF). An appealing alternative to withstand the lateral forces and regulate the dynamic response of structures will be the introduction of shear panels in concentrically braced systems [2]. Shear panels can be utilized as a seismic resistance framework under moderate and strong seismic tremor loads due to their high stiffness and strength. They can also be employed for seismic protection of the primary structure when designed as dissipative elements, due to the substantial energy dissipation capacity where plastic deformations occur.

Researchers have conducted various investigations on different types of materials such as aluminium, and low yield steel which can be used as shear panels. Steel plates with different opening shapes such as auxetic [3], ring [4], and circle [5] shapes were also studied. Masayoshi Nakashima [6], conducted an experimental investigation on the hysteretic behaviour of low-yield steel shear panels and it was found that strain hardening behaviour during loading influenced the hysteric behaviour. Natalia Egorova et al. [4] conducted a study on a new type of steel plate shear wall in which a steel web plate was cut in the form of ring holes to resist out-of-plane buckling. Inorder to determine the energy dissipation in frame structures Li Zhengying et al. [7] yielding shear panel device (YSPD) was modelled and its effectiveness in the structural response and pinching behaviour was investigated based on this. Li-Yan Xu et al. [8] used a metallic shear panel damper device BLY160 made of a new low-yield-point steel to determine the seismic behaviour of the dampers. The influences of the width-thickness ratio and corner perforation of the panel, size of the stiffening ribs, and the cyclic load history were also analyzed. A study on perforated plates with periodic auxetic-shaped cellular forms to reduce the amount of out-of-plane buckling, having a negative Poisson's ratio was also conducted [3]. Based on various studies it was observed that thin steel exhibits high lateral-load carrying capacity.

The present study focused on a Braced ductile shear panel (BDSP) component having a thin shear panel, concentric X-braces, and a flange plate. Stiffeners of varying thickness and various patterns are also attached to the shear panel having thicknesses 3, 4, 6, and 12 mm, and were provided in horizontal and vertical directions. This removable BDSP component provides sufficient lateral stiffness thus limiting the lateral inter-storey drift. Monotonic loading is applied to each specimen by the push-over analysis method and the buckling behaviour, load-carrying capacity, ductility and energy dissipation are analyzed for the same.

2 Finite Element Formulation

A lot of studies were carried out to evaluate the performance of shear panel. V. Broujerdian et al. carried out numerical investigations on the impact of a crack and its progression on the seismic behaviour of steel shear walls by using finite element programs of ANSYS and ABAQUS [10]. Mohammad Meghdadaian et al. conducted a study on the influence of openings on the performance of composite steel plate shear walls systems. In order to get accurate results, the experimental results were verified using ABAQUS software [11]. Therefore, inorder to study the seismic performance of braced ductile shear panels, the finite element modeling was done in the ANSYS workbench. The model and configurations were chosen as per the details provided in the prior research paper [9].

2.1 Geometry of the Component

The total height of the specimen was 840 mm and the two bottom pinned connections were separated by a center-to-center distance of 1400 mm. The details of the specimen are illustrated in Table 1. It is made up of two parts: a central region shear panel with a 120 mm wide flange and four individual brace components with a cross-section of 150 150 10 10 mm that can be reused [9]. The dimension of the shear panel adopted was 450×350 mm. A total of 4 BDSP specimens were designed and labeled as H4V4S-3, H3V3S-4, H2V2S-6, and H1V1S-12 in such a way that the stiffeners in each of the model have the same quantity of material. The stiffeners are attached to the shear panel by bonded connection. The number nearer to H and V represents the number of stiffening ribs in the horizontal and vertical direction and the number nearer to S represent the thickness of ribs. The stiffening ribs were arranged in such a way that ribs are equally spaced in the horizontal and vertical directions. Figure 1 shows the specimen details.

Table 1 Details of specimen

Model	Size of the shear panel (mm)	Thickness of shear panel (mm)	Thickness of flange (mm)	Thickness of stiffening ribs (mm)
H4V4S-3	450×350	3	6	3
H3V3S-4	450×350	3	6	4
H4V4S-6	450×350	3	6	6
H1V1S-12	450×350	3	6	12
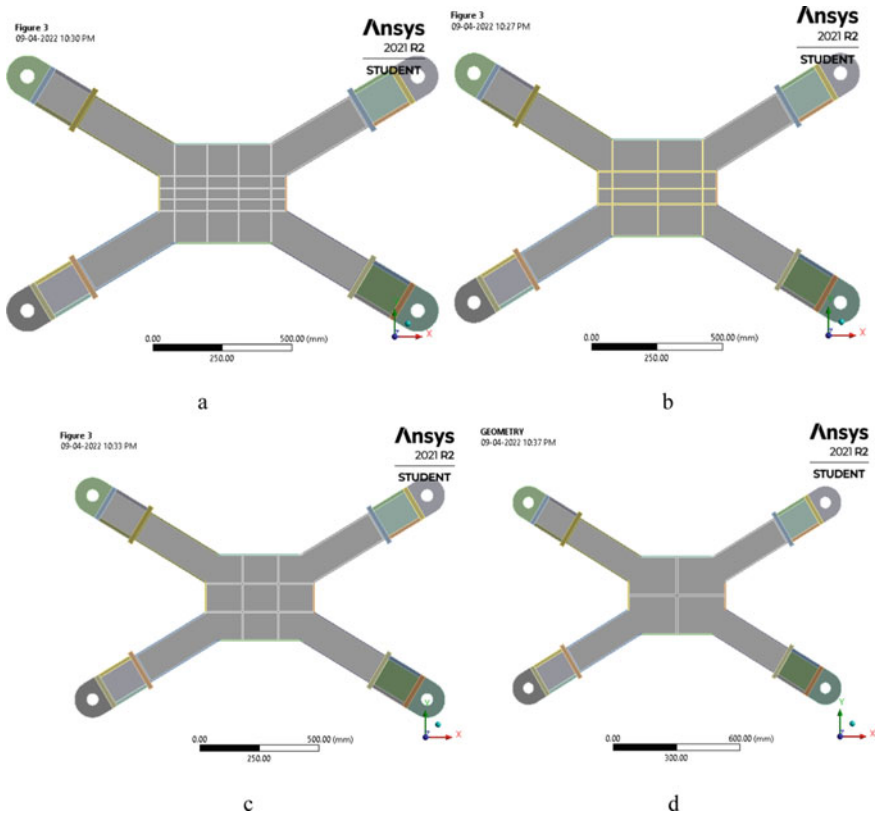
Fig. 1 Geometry of specimens: **a** H4V4S-3, **b** H3V3S-4, **c** H2V2S-6, **d** H1V1S-12

2.2 Material Properties

A bilinear stress–strain curve was assumed for modeling the component. The material property of 3 mm thick panel used for the study is shown in Table 2. The modulus of elasticity E for the steel used in shear panel 2×10^5 MPa. The bracings were fabricated based on Chinese standard conformant Q345B having an elasticity of 2×10^5 MPa and yield strength of 345 MPa [9].

Table 2 Material properties

Properties	Value
Young's modulus, (MPa)	2×10^5
Yield strength, f_y (MPa)	331
Poisson's ratio, (MPa)	0.3

2.3 Finite Element Modeling

The Analytical study of the BDSP components was done to study the post-buckling behaviour and the load-carrying capacity under push-over analysis. 4 finite element models H4V4S-3, H3V3S-4, H2V2S-6, and H1V1S-12 were developed to evaluate the influence of the various patterns of stiffeners on the seismic performance of braced ductile shear panel. Stiffeners are modelled using the required profile pattern, connected to the shear panel by bonded connections and then extruded. The model consists of a shear panel and concentric X braces which provides that provide a combined effect along with and stiffeners. The SOLID 186 element was used to model the elements. SOLID 186 is a 20-node solid element with quadratic displacement characteristics. The element is made up of 20 nodes, each with three degrees of freedom: translations in the x, y, and z dimensions. The mesh size adopted was 20 mm and the shape of meshing was Hexahedron.

Condition and Loading. The specimen was modeled in the XY plane in which the bottom of the two braces was provided with pinned support by preventing translation in all directions and permitting rotation along the Z-direction as shown in Fig. 2. A lateral displacement of 25 mm was provided at the top interface in the form of load which was obtained by the trial-and-error method.
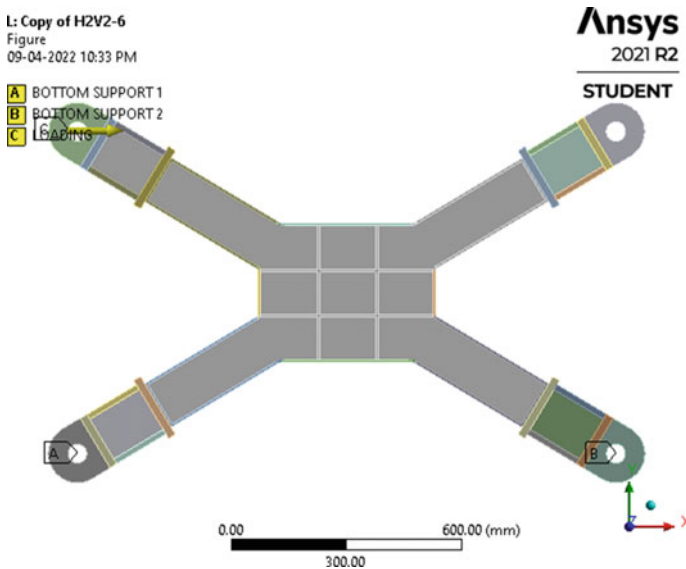
Fig. 2 Boundary condition of H2V2S-6

3 Results and Discussion

3.1 Load Carrying Capacity

The 4 models H4V4S-3, H3V3S-4, H2V2S-6, and H1V1S-12 with different patterns of stiffening ribs were analyzed and failure patterns were obtained for all the models. Force reaction and corresponding deformation were noted for all 4 models and load-deformation curves were also plotted for the same. The model H2V2S-6 exhibited the highest deformation with a value of 23.55 mm and the lowest deformation of 7.9772 mm was exhibited by the model H1V1-12 The deformation value obtained for the models H3V3S-4 and H4V4S-3 were 20.969 mm and 19.099 mm respectively. The deformation pattern of the H2V2S-6 under loading is shown in Fig. 3.

Figure 4 indicates the load v/s deformation curve obtained from the analysis. The graph clearly indicates that the model with a larger number of stiffeners i.e. H2V2S-6, H3V3S-4, H4V4S-3 has a higher load-carrying capacity than H1V1S-12. Even though the thickness of the stiffener for the model H1V1S-12 is 12 mm, it does not increase the load-carrying capacity of the specimen. There is no clear-cut idea of the effect of thickness on the load-carrying capacity so a detailed study needs to be carried out to find the influence of thickness. The load-carrying capacity for the specimen H2V2S-6 obtained was 280.11 kN and for the specimen, H4V4S3-4 was 284.17 kN.

H3V3S-4 model having stiffeners of the thickness of 4 mm has the highest load-carrying capacity of 286.93 kN compared to the H1V1S-12 model having a load-carrying capacity of 226.06 kN. Since the models, H2V2S-6, H3V3S-4, and H4V4S-3 have only 0.8–2.3% variations in their load-carrying capacities. H2V2S-6 model with 6 mm thick stiffeners is considered to perform better due to their lesser number of connections and thereby reduced amount of work as compared to H3V3S-4 and H4V4S-3. The performance comparison chart shown in Fig. 5 indicates that the
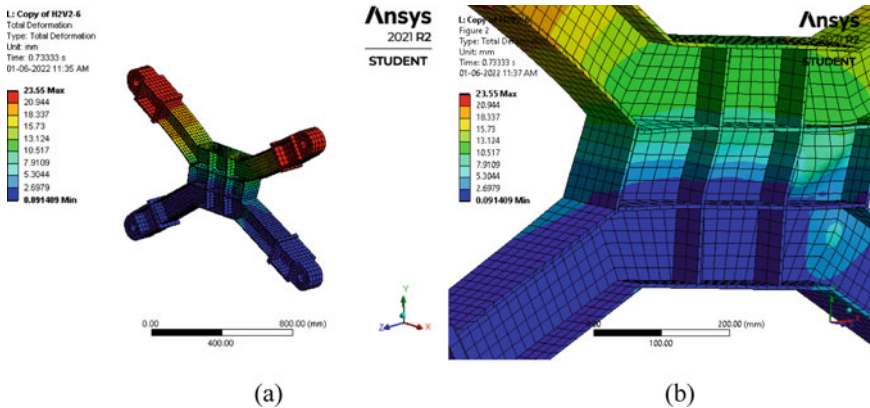
Fig. 3 Deformation of H2V2S-6 specimen
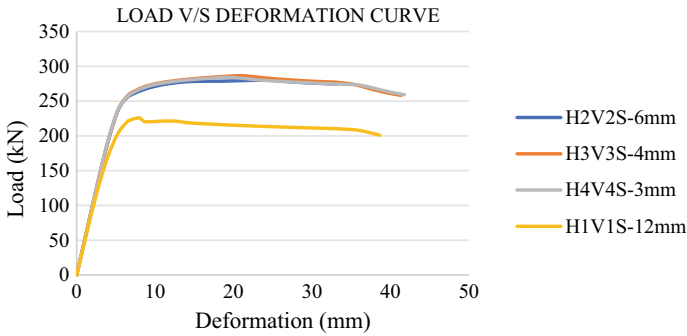
Fig. 4 Load v/s deformation curve
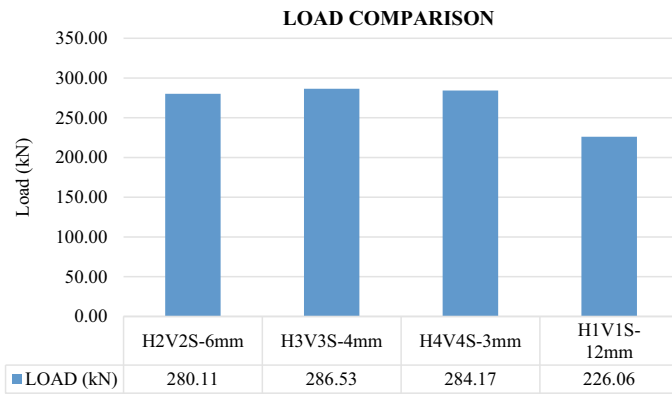
Fig. 5 Load comparison chart

load-carrying capacity of H2V2S-6 is 19% more than the specimen H1V1S-12. The buckling phenomena was reduced with the adoption of stiffening ribs therefore by distributing the stiffeners over the entire shear panel, the local buckling of the panel got limited to the sub-regions bounded by the stiffeners, and thus load carrying capacity of the component also increased.

3.2 Ductility

Table 3 summarizes the ductility μ obtained from the models which is the ratio of ultimate displacement (δ_u) to the displacement corresponding to that of the yield point (δ_y). Ultimate displacement is the maximum displacement at which the specimen fails.

Table 3 Ductility

Models	δ_u (mm)	δ_y (mm)	μ
H2V2S-6	23.55	1.345	17.64
H3V3S-4	20.97	1.331	15.75
H4V4S-3	19.09	1.330	12.84
HIVIS-12	7.97	1.330	5.99

The table above shows that the specimen with two number of stiffeners i.e. H1V1S-12 has the least amount of ductility with a value of 5.99, while the other three models H2V2S-6, H3V3S-4 and H4V4S-3 have higher ductility values compared to H1V1S-12 among which H2V2S-6 have the highest ductility with a value of 17.64.

3.3 Energy Dissipation

Figure 6 shows the energy dissipated by each of the models. All the models dissipated a significant amount of energy among which the model H2V2S-6 has the highest energy dissipation with a value of 2357.64 J. The least amount of energy dissipation was seen in the model H1V1S-12. The model H2V2S-6 has 87.76% higher energy dissipation as compared to the model H1V1S-12.

	H2V2S-6mm	H3V3S-4mm	H4V4S-3mm	H1V1S-12mm
Energy Dissipation (kJ)	2.3577643	1.999227	1.740017	0.28852
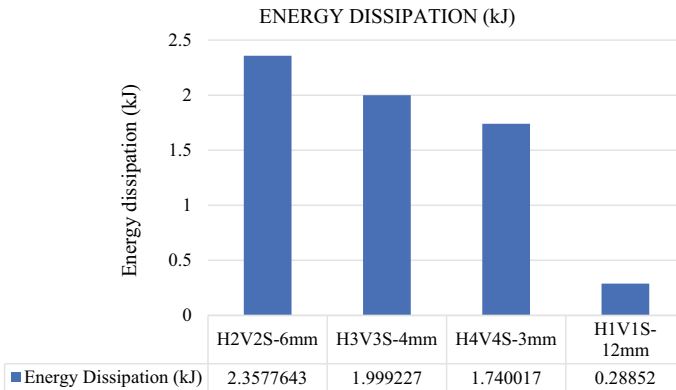
Fig. 6 Energy dissipation chart

4 Conclusion

BDSP component exhibits an excellent lateral load-resisting capacity for newly built steel structures or damaged reinforced concrete structure buildings. They also provide sufficient lateral stiffness to limit the lateral inter-storey drift. Stiffeners were introduced of the same material quantity but varying thickness and pattern.

- Nonlinear static analysis was carried out for each of the BDSP specimens to determine the influence of various stiffener patterns on the load-carrying capacity of the Braced ductile shear panel.
- The test results of the study showed that the model with a larger number of stiffeners exhibited better load carrying capacity.
- Among the models H2V2S-6, H3V3S-4, and H4V4S-3 the specimen H2V2S-6 with 6 mm thick stiffener is selected as it is considered to work better compared to the specimen H1V1S-12 with 12 mm thick stiffeners because of easiness in connections.
- The load-carrying capacity of H2V2S-6 increased by a percentage of 19% by introducing more stiffeners.
- Ductility and energy dissipation capacity was computed for all the models and it was seen that the model H2V2S-6 showed higher ductility and energy dissipation values.
- The energy dissipation was 87.72% more by introducing stiffeners
- Therefore, by distributing the stiffeners over the entire shear panel, the buckling of the panel can be reduced, and thus load carrying capacity can also be increased.

References

1. De Matteis, G., Landolfo, R., Mazzolani, F.M.: Seismic response of MR steel frames with low-yield steel shear panels. Eng. Struct. **25**(2), 155–168 (2003)
2. Jain, S., Rai, D.C., Sahoo, D.R.: Postyield cyclic buckling criteria for aluminum shear panels. J. Appl. Mech. **75**(2) (2008)
3. Hamed, A.A., Asl, R.B., Rahimzadeh, H.: Experimental and numerical study on the structural performance of auxetic-shaped, ring-shaped and unstiffened steel plate shear walls. J. Build. Eng. **34**, 101939 (2021)
4. Egorova, N., Eatherton, M.R., Maurya, A.: Experimental study of ring-shaped steel plate shear walls. J. Constr. Steel Res. **103**, 179–189 (2014)
5. Valizadeh, H., Sheidaii, M., Showkati, H.: Experimental investigation on cyclic behavior of perforated steel plate shear walls. J. Constr. Steel Res. **70**, 308–316 (2012)
6. Nakashima, M., Akazawa, T., Tsuji, B.: Strain-hardening behavior of shear panels made of low-yield steel. II: model. J. Struct. Eng. **121**(12), 1750–1757 (1995)
7. Li, Z., Albermani, F., Chan, R.W., Kitipornchai, S.: Pinching hysteretic response of yielding shear panel device. Eng. Struct. **33**(3), 993–1000 (2011)
8. Chen, S.J., Jhang, C.: Cyclic behavior of low yield point steel shear walls. Thin-Walled Struct. **44**(7), 730–738 (2006)
9. Sun, G., Bao, C., Liu, W., Fang, Y.: Cyclic behavior of an innovative braced ductile thin shear panel. Structures **32**, 973–986 (2021)

10. Broujerdian, V., Ghamari, A., Ghadami, A.: An investigation into crack and its growth on the seismic behavior of steel shear walls. Thin-Walled Struct. **101**, 205–212 (2016)
11. Meghdadaian, M., Ghalehnovi, M.: Improving seismic performance of composite steel plate shear walls containing openings. J. Build. Eng. **21**, 336–342 (2019)

Structural Behavior of Non-prismatic Dual Tubular Steel Long Columns

Gayathri Sarkar and M. Preethi

Abstract Tapered Concrete-Filled Dual Steel Tubular (CFDST) columns have been commonly used in structures like transmission tower, wind turbine support column, sub way platform and offshore platform columns. Non-prismatic concrete filled dual tubular steel column members consist of the outer steel tube, the inner steel tube and the concrete filled in their interspace having varying cross section in longitudinal direction. It has been widely recognized for their good structural performance. This work focuses on the analysis of axial compressive behavior of different combined inner and outer cross-sections of tapered concrete filled dual steel tubular long columns. The complete analytical modeling and extensive parametric studies are carried out using ANSYS software.

Keywords Tapering · Ductility · Buckling behavior · CFST · CFDST · ANSYS

1 Introduction

Concrete filled dual tubular steel (CFDST) member inherits similar behavior from the Concrete-Filled Steel Tubular (CFST) member including high bearing capacity, large stiffness, greater axial, flexural and torsional strengths as well as improved strength-to-weight ratios and good ductility, while it possesses additional advantages due to its particular sectional properties i.e., the self-weight of CFDST members is lighter than that of CFST. A partial fire and corrosion resistance can be gained due to the concrete protection of the inner tube. The usage of composite steel-concrete columns combines the best features of both materials. Steel-concrete is the most often utilized composite. The composite columns are closer to steel or reinforced concrete columns depending on the amount, shape, placement, and utilization rate of the steel or concrete. The composite steel-concrete structures utilize high compressive strength of concrete and high tensile resistance of the structural steel.

G. Sarkar (✉) · M. Preethi
Department of Civil Engineering, FISAT, Angamaly, India
e-mail: gayathrisarkar1998@gmail.com

Concrete filled dual tubular steel columns are extensively used in construction of high-rise buildings, factories, bridges. It provides with higher construction efficiency and provision of high stiffness and strength. Being economical, faster construction and composite action of steel and concrete are the major advantages of concrete filled steel tube columns over reinforced concrete conventional columns. The study includes the analysis of buckling behavior of CFDST long columns with four different cross-sectional shapes under axial loading. The shapes are Circle-Circle (CC), Square-Square (SS), Inner Square-Outer Circle (CS), Outer circle-Inner square (SC).

2   Finite Element Formulation

In order to determine the buckling behavior of concrete filled dual skin steel tubular long columns of different cross-sections. Finite element analysis is done using ANSYS 16.0. The model and its configurations are chosen as per the details provided in the prior research paper. The method adopted for loading is displacement control method in which the displacement changes incrementally while the reaction force results depend on the stiffness of the structure. The axial force in the form of axial displacement is applied until the specimen fails and the ultimate strength of the specimens are determined.

2.1   Geometric Description

Tapered concrete filled dual tubular steel long column consist of two steel concentric members infilled with concrete with cross-sectional dimension varying in longitudinal direction. The specimens used for the test are of varied cross-sections which are; (i) Inner and Outer circles, (ii) Inner and Outer squares, (iii) Inner Square and Outer Circle, (iv) Inner Circle and Outer Square. The L/D ratio chosen for the analysis is 14. According to IS456:2000, long columns are those with L/D ratio more than 12. Keeping the L/D ratio and diameter of the column specimen (Base diameter(398 mm) with reference to prior base journal) constant; The, length of the column is 5572 mm. The thickness of concrete infill is kept as 50 mm. Circle-Circle specimen is taken as benchmark specimen as per the research paper. For L/D ratio 14, the ultimate load, P_u was 2327.6 kN for a maximum deformation of 23.450 mm for Circle-circle section [1] (Fig. 1).
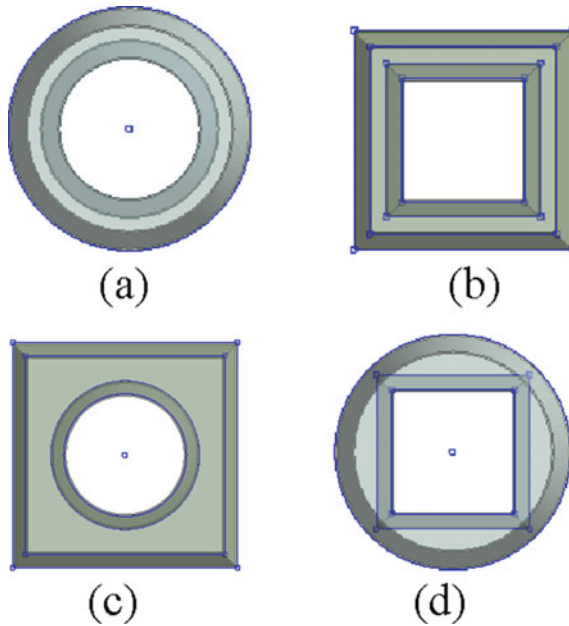
Fig. 1 Different test specimen geometry; **a** Circle-Circle (CC) **b** Square-Square (SS) **c** Square-Circle (SC) **d** Circle-Square (CS) [*Source* ANSYS Workbench]

Table 1 Material properties of steel tubes

No.	Thickness (mm)	Yield strength (f$_y$) MPa	Ultimate strength (f$_u$) MPa	Young's modulus (E) MPa	Poisson's ratio (μ)
1	3.0	326.67	445.00	2.15×10^5	0.30
2	2.5	336.67	461.67	2.10×10^5	0.29

2.2 Material Properties

Concrete mixture used to fill in between the steel tubes is of characteristic compressive strength (f$_{ck}$ = 0.67f$_{cu}$), where f$_{cu}$ is the cubic compressive strength of concrete. The average cubic compressive strength of the concrete (f$_{cu}$) at the time of the tests was 37.64 MPa. The inner and outer steel tubes are of varied thickness conforming to IS code, IS456:2000. The thickness, yield strength (f$_y$), ultimate strength (f$_u$), Poisson's ratio (μ) of steel tubes used are given in Table 1. The specifications of the specimens are defined in Table 2.

Table 2 Specifications of specimens analyzed

Specimen	Dimension of the specimens (mm)				Length of specimen (mm)	Area of concrete (mm²)	
	Outer		Inner			Top	Bottom
	Top	Bottom	Top	Bottom			
CC	340	398	234	292	5572	44,611	53,721
SS	340 × 340	398 × 398	234	292	5572	44,556	53,768
SC	261 × 261	340 × 340	234	292	5572	44,667	53,656
CS	340	398	208 × 208	259 × 259	5572	44,352	53,606
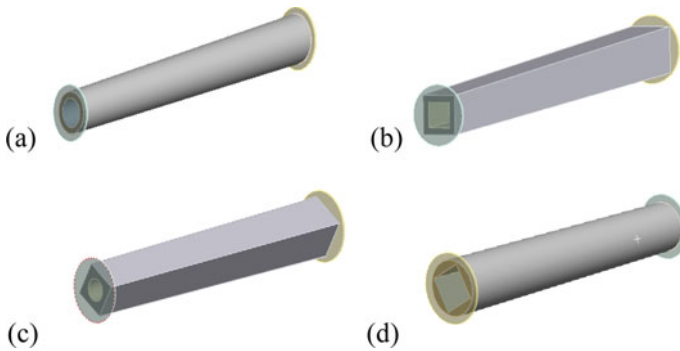
Fig. 2 Different test specimen models; **a** Circle-Circle (CC) **b** Square-Square (SS) **c** Square-Circle (SC) **d** Circle-Square (CS) [*Source* ANSYS Workbench]

2.3 Finite Element Modeling

Modeling in ANSYS includes defining geometry, providing appropriate elements, and assigning suitable material models. The column is modeled using SOLID 185 in 3-D, 8-node hexahedron solid element that exhibits quadratic displacement behavior for both steel and concrete, with three degrees of freedom at each node. The mesh size chosen after trial and error is 40 mm. The modelled specimens are shown in the Fig. 2.

2.4 Support Condition and Loading

The geometry is modelled in ZX plane. Pinned supports are provided on both ends with rotational motion in X-direction. Load is applied axially downward in Y direction as an enforced displacement using trial and error method until the specimen fails. The load is applied on a plate attached to the column ends in order to distribute the load uniformly over the column. Along with total deformation and force reaction,
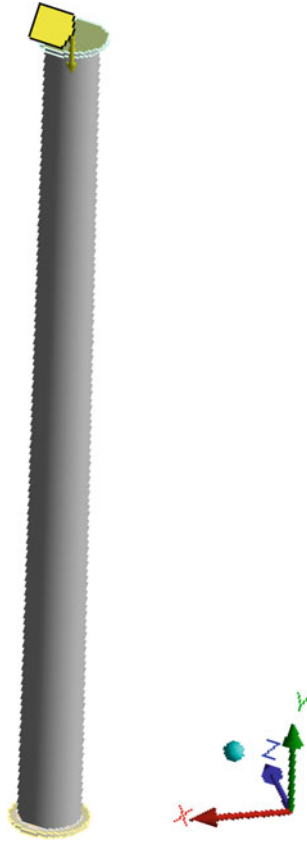
Fig. 3 Axial loading of Circle-Circle (CC) column [*Source* ANSYS Workbench]

Equivalent plastic strain of inner tube, outer tube and infilled concrete is obtained. Axial loading is shown in Fig. 3.

3 Results and Discussions

Concrete filled dual steel tubular columns are made into four different cross-sectional shapes and are analyzed for buckling behavior under axial loading. 20 mm displacement is axially applied downwards at the top end of the column over the plate as axial force. The load deformation curve of four specimens is shown in Fig. 4. Initially the load carrying capacity of the specimen increased and then decreased indicating the failure of specimen. The maximum value of force reaction is taken as the ultimate load carrying capacity of the specimen and the corresponding deformation is taken

as the maximum total deformation. Table 3 shows the variation of ultimate load of different shapes corresponding to different deformation values.

It is observed that the maximum load carrying capacity of 2831.40 kN is observed for circle-circle section with a maximum deformation of 16.012 mm and minimum value of 2032.10 kN is observed for square-circle section with a maximum deformation of 31.12 mm. Square-Square section and circle-square section lies in between circle-circle and square-circle sections.

The ultimate load carrying capacity of Square-square section is 2339.50 kN with a maximum total deformation of 21.639 mm and Circle-square section has a maximum force reaction of 2532.50 kN corresponding to 15.216 mm total deformation. The variation of deformation and load of four specimens are shown in Fig. 5 and Fig. 6 respectively.

About 28.22% increased strength is shown by Circle-Circle section than Square-Circle section. Circle-Circle section has 17.37% increased strength than Square-Square section and 10.57% increased strength than Circle-Square section.
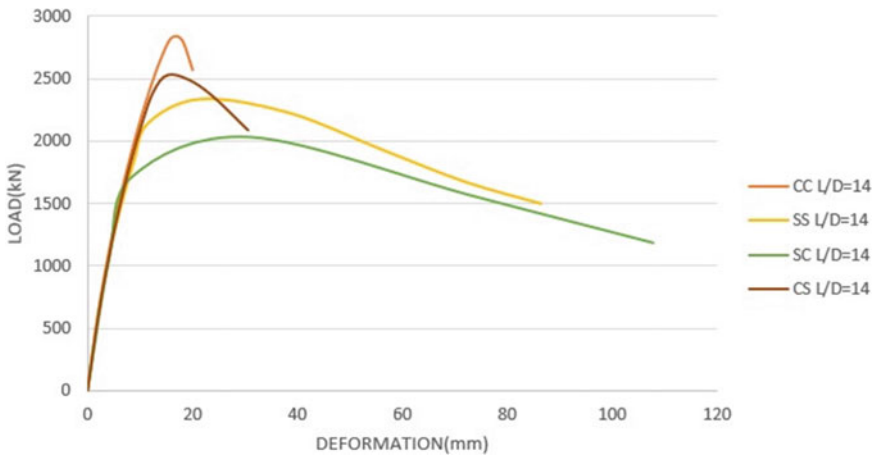
Fig. 4   Load versus deformation curve of four specimens

Table 3   Ultimate load and corresponding maximum deformations of four specimens

Specimen	Deformation (mm)	Ultimate load (kN)
CC	16.012	2831.40
SS	21.639	2339.50
SC	31.12	2032.10
CS	15.216	2532.50
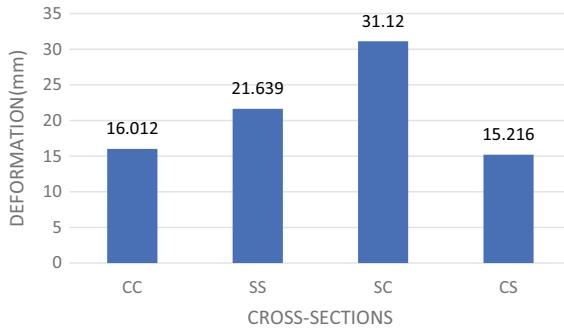
Fig. 5 Deformation comparison of tapered CFDST long column under axial loading
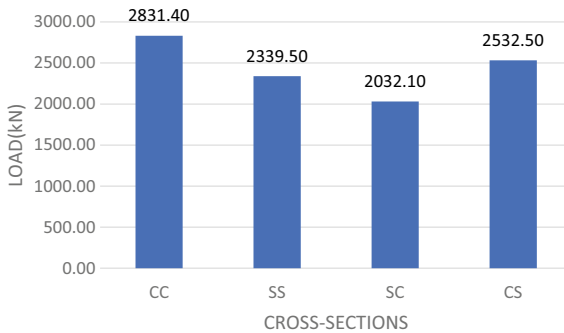
Fig. 6 Load comparison of tapered CFDST long column axial loading

4 Conclusions

In the analysis of buckling behavior under axial loading of concrete filled dual steel tubular columns it was observed that, about 28.22% increased strength is shown by Circle-Circle section than Square-Circle section. Since, Circle-Circle section has 17.37% increased strength than Square-Square section and 10.57% increased strength than Circle-Square section; Circle-Circle section behaves better than all other three cross-sections (SS, CS, SC) during axial loading where tapered concrete filled dual tubular steel columns with lateral dimensions quite small as compared with the length of the column is required. Comparatively Circle-circle is easy to cast, it lacks corners and are designed keeping in mind that eccentric load from beam may also need to be carried.

References

1. Deng, R.: Compressive behavior of tapered concrete-filled double skin steel tubular stub columns
2. Li, W.: Behavior of tapered concrete-filled double skin steel tubular (CFDST) stub columns. Thin-Walled Struct.
3. Vernardos, S.: Experimental behavior of concrete-filled double-skin steel tubular (CFDST) stub members under axial compression
4. Yang, Y.-F.: Axial compressive behavior of CFDST stub columns with large void ratio
5. Zhang, Y.-B.: Analytical behavior of tapered CFDST stub columns under axially partial compression. Constr. Steel Res.
6. Huang, H.: Analytical behavior of concrete-filled double skin steel tubular (CFDST) stub columns. J. Constr. Steel Res.
7. Zhao, X.-L.: CFDST stub columns subjected to large deformation axial loading. Eng. Struct.
8. Bahrami, A.: Performance of axially loaded tapered concrete-filled steel composite slender columns. J. Civil Eng. Manage.
9. Sulthana, U.M.: Axial compression behavior of long concrete filled double skinned steel tubular columns. Structures
10. Farajpourbonab, E.: Effective parameters on the behavior of CFDST columns
11. Sasi, S.: Compression & bending performance of non-prismatic circular tubed steel reinforced concrete columns. Int. Res. J. Eng. Technol.
12. Wang, Z.-B.: Strength, stiffness and ductility of concrete-filled steel columns under axial compression. Eng. Struct.
13. Wang, W.-D.: Research on mechanical behaviour of tapered concrete-filled double skin steel tubular members with large hollow ratio subjected to bending. J. Constr. Steel Res.

Development of Artificial Neural Network for the Fatigue Life Assessment of Self Compacting Concrete

B. Rabin Gani, Keerthy M. Simon, and J. Bharati Raj

Abstract Modern infrastructure needs to endure repeated loading for quick and sustainable development. Highway pavements, offshore supporting structures, bridge decks, machine foundations etc. are subjected to repeated loadings. This type of concrete structure deteriorates when subjected to cyclic loading. The heterogeneous nature of concrete combined with varying parameters of fatigue loading make the analysis complex and thereby produce approximate solution. As a result, a probabilistic approach is more suitable to this type of problem than a deterministic approach since variations and uncertainties exist. An Artificial Neural Network (ANN) can be used as a powerful computational tool that uses a probabilistic approach. The purpose of this study is to develop a generalized artificial neural network, which can predict the fatigue life of special concrete like Self Compacting Concrete (SCC). Several parameters affecting concrete fatigue life, such as material and fracture mechanics properties, are identified and are provided as input into the system. The created neural network is then trained using the available experimental data and validated. This developed model can therefore be used to assess the fatigue life of concrete with considerable accuracy.

Keywords Fatigue life · Artificial Neural Network (ANN) · Cyclic loading · Probabilistic approach

1 Introduction

1.1 General

The fatigue phenomenon is the result of gradual and permanent changes occurring within a material under cyclic or repeated loading. This fatigue loading results in crack formation due to internal flaws that exist within the material [1]. Fracture is the action of breaking an object or material into two or more pieces under stress.

B. Rabin Gani (✉) · K. M. Simon · J. Bharati Raj
Department of Civil Engineering, NSS College of Engineering, Palakkad, Kerala, India
e-mail: rabinganib@gmail.com

Many infrastructures such as highway and airport pavements, railway sleepers, bridge decks and offshore windmill supporting structures must withstand a large number of repeated cyclic loadings of varying amplitudes [2]. The service life of these infrastructures could be shortened due to fatigue fracture in the material. As a result, it's crucial to think about crack formation in fatigue-prone structural components. Materials can be classified as brittle, quasi-brittle, or ductile depending on the nature of their fracture. These ductile materials like metals, brittle materials like ceramics are homogeneous in nature and their fracture occurrence is much more predictable. Due to its homogeneous nature, these materials have undergone extensive fatigue studies using various methods and their fatigue fracture prediction is less variable. Whereas the fatigue properties of cementitious material are more complex due to the heterogeneities in it and therefore not much studies are conducted [6].

1.2   Fatigue Behaviour of Concrete

Concrete is heterogeneous in nature, even if it appears to be homogeneous from a design standpoint. Concrete is made up of 3 main components: aggregate, matrix-aggregate interface and cement matrix. Since concrete is heterogeneous in nature, numerous internal flaws form, triggering crack initiation even before loading is applied. The three zones of fatigue crack growth in concrete are the initiation zone, the propagation zone and the unstable crack growth zone. The crack will propagate through the concrete matrix's weakest path [5]. Microcracks form in a distributed manner at the location of these pre-existing flaws during loading and eventually localise to form a major crack. This crack propagates in a stable way after reaching the peak stress and an inelastic zone called the fracture process zone (FPZ) forms ahead of the crack tip [3]. The post-peak softening response in tension, as well as the size effect behaviour, are both attributed to this FPZ development. The size-effect transition from nominal strength to linear elastic fracture mechanics determines the brittleness characteristic of concrete. Even before the maximal monotonic load is attained, structures or materials exposed to repeated loading will fail. Despite this, concrete's quasi-brittle nature makes fatigue failure prediction more difficult and it is rarely taken into account.

1.3   Self Compacting Concrete

Self Compacting Concrete (SCC) is a type of civil engineering material that can compact itself using gravity alone. To vibrate concrete during the placing process, no external force is required. The concrete can completely fill the formwork and achieve good homogeneity even if there is a lot of rebar. Okamura, a Japanese scholar, was the first to suggest SCC. SCC offers superior fluidity, homogeneity and stability as compared to regular concrete [1]. SCC can be prepared to reduce early faults,

increase pouring quality, lower costs, improve durability and mechanical qualities. It is a high-performance type of concrete. Currently most SCC research mainly focuses on combined design, performance and fundamental mechanical qualities with little research on SCC fatigue behaviour. In addition to static stress, concrete structures can be affected by reciprocating forces such as vehicle rolling, rain washing, and so on. Long-term cyclic loads cause concrete to gradually accumulate fatigue damage, resulting in a reduction in local failure or structural resistance. Plain concrete is currently being used extensively in the study of concrete fatigue behaviour. Because SCC differs from plain concrete in terms of composition, it is required to investigate its fatigue performance and calibrate the previous fatigue damage model in order to create a fatigue damage model that is appropriate for SCC.

In plain concrete, there are detrimental pores, ITZ, other imperfections and internal problems reduce fatigue resistance. SCC has superior fatigue performance than plain normal concrete, has more powder content and has better workability and fluidity. The powder content has the ability to plug pores and SCC has a lower porosity than plain concrete because of this. As a result, SCC has fewer early faults and a more homogenous and thick internal structure, allowing it to withstand fatigue better.

The objective of this study is to create a neural network model to predict the fatigue life of Self Compacting Concrete. The parameters that affect the fatigue life of SCC are studied and selected appropriately for the ANN model. The proposed model will be able to predict the fatigue life of SCC with certain level of precision and accuracy.

2 Artificial Neural Network Modelling

2.1 General

The input, hidden and output layers make up the artificial neural network architecture. The data is received by the input layer. The hidden layer then perceives and analyses the data and the output layer eventually provides the result. Input data as well as output data will be represented by the number of input nodes and output nodes. The no. of hidden layers and the no. of units in these layers are critical components of the neural network architecture [7]. After selecting the number of layers and units in each layer, the network's weights and thresholds must be adjusted to reduce the network's prediction error and this job will be effectively performed by selecting appropriate training techniques. The number of different of input data will affect the no. of neurons and hidden layers, which is critical to the model's efficiency. There are several rules for determining the critical number of neurons, but none of them are universal. However, the model's structure and complexity will decide the number of hidden layers and neurons. If the number of neurons in the network is insufficient, the learning process will be blocked or underfitting will occur, which occurs when the network is unable to provide correct predictions on the training data set. Also, if

an excessive number of hidden neurons is utilised, overfitting occurs, which means that the neural network will be very good at learning its training set but will not be able to generalise beyond it, resulting in the generalisation problem.

2.2 Data Collection

The data was gathered based on fatigue loading of Self Compacting Concrete experiments. The experimental data from the work of Lu Feng et al. [1] is used to validate the neural network. The beam is subjected to three-point loading in this project. These data were gathered based on several geometrical and fracture mechanics factors that account for Self Compacting Concrete fatigue life prediction. These data were taken from fatigue test performed on Self Compacting Concrete beams that were subjected to three-point loads at various loading ratios.

2.3 Model Training Methodology

The ANN model is developed and training is done using neural network toolbox in MATLAB R2021a software. The procedures involved in creating a neural network are listed below.

Collection of Data

Create the network

Initialise the weights and biases

Train the network

Validate the network

Use the network
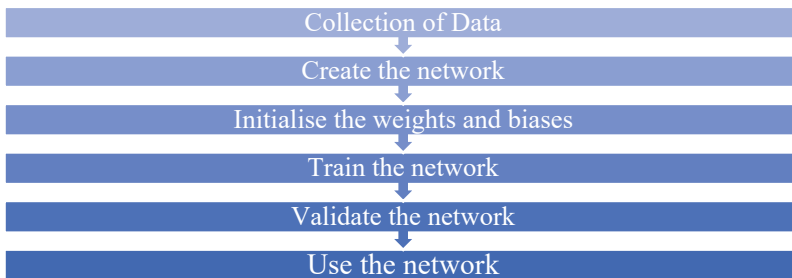
Although data collecting and organisation takes place outside of the ANN environment, it is the most crucial phase in network modelling. Any inaccuracy in the data will have an impact on the model's efficiency. The model is configured after the first phase by providing sufficient input and output data. The input and output neuron numbers will be the same as the input and output parameters. Following that, the network is built using the proper training technique, learning function, activation function, and number of hidden layers and neurons. The network is trained after selecting correct training parameters, which are dependent on the training and learning function and the weights and biases values are randomised according to the input parameters. If the error between the target and predicted output is not acceptable

after training, the model must be retrained. If the training error is in an unacceptable range, the model must be verified using a different set of data. After satisfactory validation of the model performance, the ANN model will be ready for prediction; if not, the network architecture should be remodelled.

2.4 Neural Network

For the current study, the experimental data reported by Lu Feng et al. [1] is used for the validation of neural network model. The model was created using NN (Neural Network) toolbox of MATLAB2021a. More than 100 data points were fed into the system for training of the network.

2.5 Description of the Developed Model

Multilayer perceptron network (MLPN) or multilayer feed-forward back propagation network is the basis for the developed neural network architecture. For the training algorithm, the Levenberg–Marquardt back propagation algorithm was utilised since it produces accurate results in less time and is more dependable for complicated modelling issues. The input parameters are set based on the material and fracture mechanics qualities required for crack propagation to occur and is given in Table 1.

As output data, the relative crack depth (a/d) at which failure occurs is chosen. The data sets were randomly divided into three groups for modelling, with 70% being utilised for training, 15% is used for validation and 15% used for testing. The network configuration adopted are given in Table 2.

Mean Squared Error (MSE) and regression value (R) were used as performance metrics to determine the optimal number of hidden neurons for the best performing neural network model. The model with the lowest MSE value and a R value near to 1 was chosen as the best ANN architecture and in this study a network with seven neurons in the hidden layer performed better than others. Thus, the optimal

Table 1 Details of input parameter

Input neuron no	Input parameter
1	Load ratio (R)
2	Maximum load (P_u)
3	Width (b)
4	Depth (d)
5	Stress intensity factor (K)
6	No. of load cycles (N)

Table 2 Neural network configuration

Parameter	Specification
Number of neurons in input layer	6
Number of neurons in hidden layer	2–10
Number of neurons in output layer	1
Training function	Levenberg–Marquardt (trainlm)
Activation function	Tan-sigmoid
Performance function	Mean squared error (MSE) Regression value
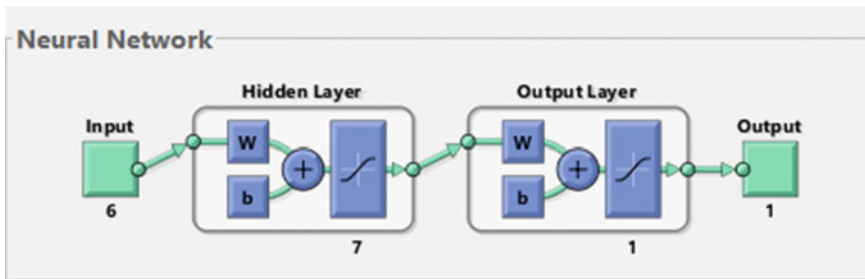
Fig. 1 Neural network configuration

architecture obtained has an MSE of .000011379 and a R of 0.99453, as well as six input neurons, seven hidden neurons, and one output neuron as shown in Fig. 1.

To find the best solution, the Mean Squared Error (MSE) and Regression Value (R) are used to evaluate the neural network's performance. The model with the lowest Mean Squared Error and the Regression value closest to 1 is picked as the best. To get the best network architecture, the number of neurons in the hidden layer must be determined. In the hidden layer, the number of neurons was changed from 2 to 10. Below and above this range, the number of neurons does not provide sufficient performance. This could be the result of insufficient training or data overfitting.

The training performance of eight ANN models, as well as their related MSE and R, are shown in Table 3. Figure 2 shows an MSE value plot with varied numbers of hidden neurons. The rise in the number of hidden neurons is not directly proportional to the training procedure, as seen in Table 3 and Fig. 2. The ANN model with 7 neurons in the hidden layer performed the best.

Table 3 R and MSE values of all the models considered

Model non	No of neurons in hidden layer	R value	MSE
1	2	0.97746	0.000091702
2	3	0.95875	0.0000091432
3	4	0.97286	0.00022352
4	5	0.96453	0.00027425
5	6	0.99336	0.000020471
6	**7**	**0.99453**	**0.000011379**
7	8	0.95648	0.000024554
8	9	0.9739	0.000085149
9	10	0.99127	0.000014914
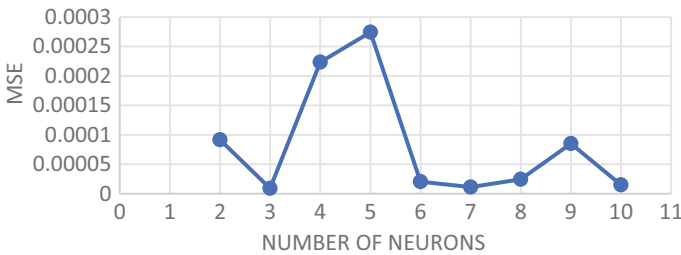
Fig. 2 MSE vs number of neurons plot

2.6 *Evaluation of ANN Model*

The Regression value is used to evaluate the performance of the constructed neural network. The model with the R value closest to 1 is the best. In order to achieve the best network architecture, the number of neurons in the hidden layer must also be decided. The R value can be used to find the best neural network (Fig. 3).

3 Results

Figure 4 shows the accuracy of the neural network model in predicting relative crack depth (a/d) at failure for data sets of Self Compacting Concrete beams with a R value of 0.99453. The anticipated output is largely accurate, reflecting the ANN tool's prediction accuracy. The graph displays the relationship between relative crack depth and no. of cycles of the samples taken, it shows the experimental data output and the output data obtained from the created neural network model. The experimental
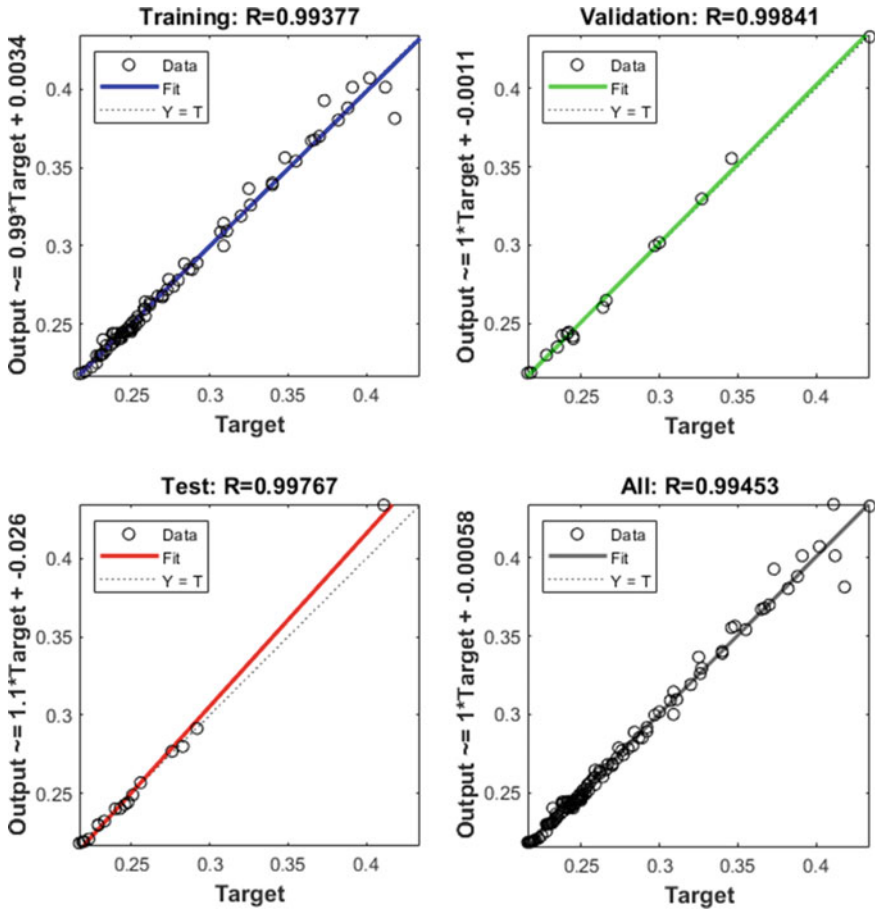
Fig. 3 Regression plots for training, validation, testing and overall data in MATLAB R2021a

results and the expected model output are in good accord. Because the validation results are within acceptable bounds, the created model can accurately and precisely forecast the fatigue life of Self Compacting Concrete.
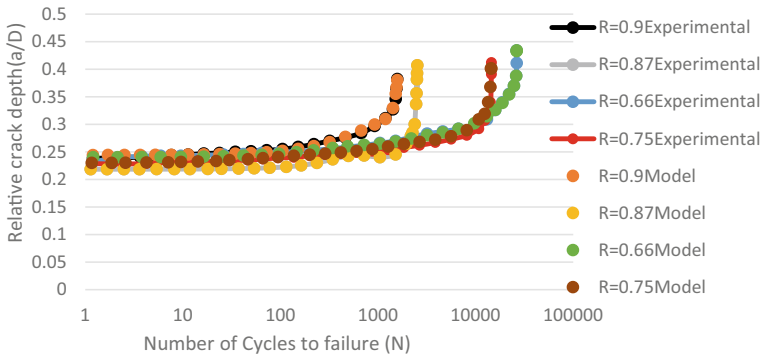
Fig. 4 Comparison of relative crack depth with number of cycles

4 Conclusions

- This work mainly deals with the validation of fatigue life prediction model for self-compacting concrete using ANN.
- Artificial Neural Network was found to be a reliable when dealing with problems consisting of uncertainties and variations.
- Optimum neural network was found to be model 6 with 7 number of neurons in the hidden layer.
- This model has the least MSE value close to 0 and R value close to 1. The neural network was able to reproduce the same output data as in the experimental setup with certain level of accuracy and precision.
- ANN was found to be a reliable tool to predict the fatigue life of SCC.

References

1. Feng, L., Chen, X., Zhang, J., Yuan, J., Dong, W.: Fatigue behaviour and prediction model of self-compacting concrete under constant amplitude load and incremental amplitude load. Int. J. Fatigue **145** (2021)
2. Ray, S., Jeshnaa, C.C., Gupta, N.: Fatigue life assessment of concrete members under variable amplitude loading: an analytical approach. Eng. Fract. Mech. **223** (2020)
3. Simon, K.M., Chandra Kishen, J.M.: Influence of aggregate bridging on fatigue behaviour of concrete. Int. J. Fatigue **90** (2016)
4. Ray, S., Chandra Kishen, J.M.: Analysis of fatigue crack growth in reinforced concrete beams. Mater. Struct. **1;47**(1–2), 183–198 (2014)
5. Ray, S., Chandra Kishen, J.M.: Fatigue crack propagation model and size effect in concrete using dimensional analysis. Mech. Mater. **43**(129), 75–86 (2011)

6. Sain, T., Chandra Kishen, J.M.: Probabilistic assessment of fatigue crack growth in concrete. Int. J. Fatigue **30** (2008)
7. Antony Jeyasehar, C., Sumangala, K.: Damage assessment of prestressed concrete beams using artificial neural network (ANN) approach. Comput. Struct. **84**, 1709–1718 (2006)

Structural Performance of Innovative CFS Integrated Ultra-Light Weight Composite Beams

M. Shreya and Nincy Jose

Abstract This paper investigates the performance of double channel CFS sections placed in front-to-front and back-to-back position. An ultra-light weight concrete was used to infill the section to reduce the newly suggested composite beam's self-weight and cost. A total of 7 specimens were analytically tested including a conventional RCC beam using finite element software, ANSYS. The conducted failure modes, load and deformation comparison are presented and discussed. The results confirmed that fully filled CFS composite sections showed the maximum performance and the back or front placement had only a slight impact. Moreover, infilling with ultra-light weight cement concrete increased the moment capacity of CFS structure and had the capability to be used as a primary structure.

Keywords CFS · Ultra-light weight cement concrete · Buckling resistance · ANSYS

1 Introduction

The use of cold-formed steel (CFS) load-bearing elements has grown in popularity over the last few decades, and CFS portal frames are being used in industrial and agricultural structures all over the world. This development can be due to CFS's multiple advantages, including high strength-to-weight and stiffness-to-weight ratios, easy handling, transportation, and stacking, and a fast production speed especially when combined with a modular approach [2]. However, CFS members are often governed by cross-sectional instabilities such as local and distortional buckling, which may occur in combination with global buckling. The increased structural demands placed on CFS members as a result of their frequent use as key structural members are fundamentally incompatible. As a result, when individual sections are unable to carry the load or span the requisite span, built-up members are a popular option in current practice.

M. Shreya (✉) · N. Jose
Department of Civil Engineering, FISAT, Angamaly, India
e-mail: shreyanair633@gmail.com

The ultra-lightweight cement composite (ULCC) is a new form of composite with low densities of less than 1500 kg/m^3, high compressive strengths of more than 60 MPa, and a specific strength of up to 47 kPa/(kg/m^3). ULCC's low unit weight and high strength are obtained by adding cenospheres with densities ranging from 600 kg/m^3 to 900 kg/m^3 as micro-lightweight aggregates in a dense cement paste matrix. Also, ultra-light weight cement composite (ULCC) has attracted extensive research interests due to its high specific strengths and low unit weights [3].

2   Finite Element Formulation
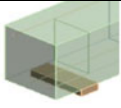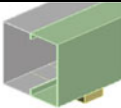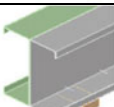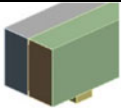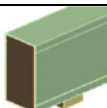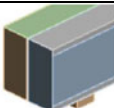
In order to investigate the performance of CFS built-up sections and CFS integrated ultra-light weight concrete sections, Finite element analysis of 7 models including a conventional reinforced concrete beam section was done using ANSYS software.

First two models were such that two CFS channel sections placed front-to-front manner, one in which limb to limb were bolted and second in which flanges were overlapped and then the limbs were bolted with web of other and both fully filled with ultra-light weight concrete. Next two models were such that CFS channel sections were placed in same manner as above, but without any concrete filling, and last two models were such that two channel sections placed in back-to-back manner, one with ultra-light weight concrete and one without it. Then these models were compared with a conventional concrete model.

2.1   Model Geometry

The composite beams are modelled using SOLID 185. SOLID185 is used for 3-D modelling of solid structures. It is defined by eight nodes having three degrees of freedom at each node: translations in the nodal x, y, and z directions. The element has plasticity, hyper-elasticity, stress stiffening, creep, large deflection, and large strain capabilities. It also has mixed formulation capability for simulating deformations of nearly incompressible elastoplastic materials, and fully incompressible hyper-elastic materials. Hexahedron meshing is done and element size is 25 mm. Length and height of different models are 3000 mm and 200 mm respectively, and thickness of plate used is 1.5 mm (Table 1).

Table 1 Different specimen models in ANSYS and their properties

MODEL	FIGURE	BREADTH (mm)	CROSS SECTIONAL-AREA (mm²)
RCC		150	30000
FULLY STEEL SECTIONS			
S-F2F		150	28848
S-F2F-OVERLAPPED		75	14424
S-B2B		150	28848
FULLY FILLED SECTIONS			
FF-F2F		150	28848
FF-F2F-OVERLAPPED		75	14424
FF-B2B		150	28848

NB: RCC: Reinforced Cement Concrete, F2F: Face-to-face, B2B: Back-to-back, FF: Fully filled, S: Fully steel

Table 2 Material properties assigned in ANSYS software

Material	Density (kg/m^3)	Young's modulus (Pa)	Poisson's ratio
CFS	7850	2×10^{11}	0.3
Ultra-light weight concrete	1250	1.079×10^{10}	0.12

A SIMPLY SUPPORTED 1
B SIMPLY SUPPORTED 2
C LOAD
D LOAD 2

Fig. 1 Loading diagram of in ANSYS

2.2 Material Properties

Structural quality sheet steel that are formed into C-sections of 1.5 mm thickness by roll-forming the steel through a series of dies (CFS) are designed. Ultra-light weight concrete of density less than 1500 kg/m^3. Both steel and concrete used are of high strength. ULCC's low unit weight and high strength are achieved by using "cenospheres" as micro light weight aggregates in a dense cement paste matrix (Table 2).

2.3 Support and Loading

Simply supported conditions were created for the beam specimens, the beam is inhibited from any vertical movement at both ends whereas it is allowed to rotate freely. A load of 60 mm was provided at center in the form of load in negative Y-direction (Figs. 1 and 2).
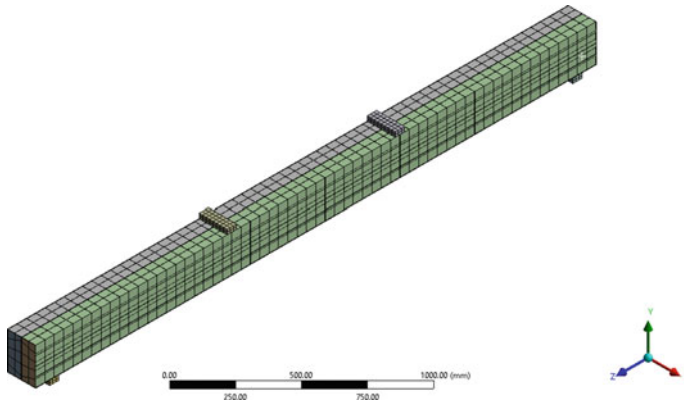
Fig. 2 Meshed model
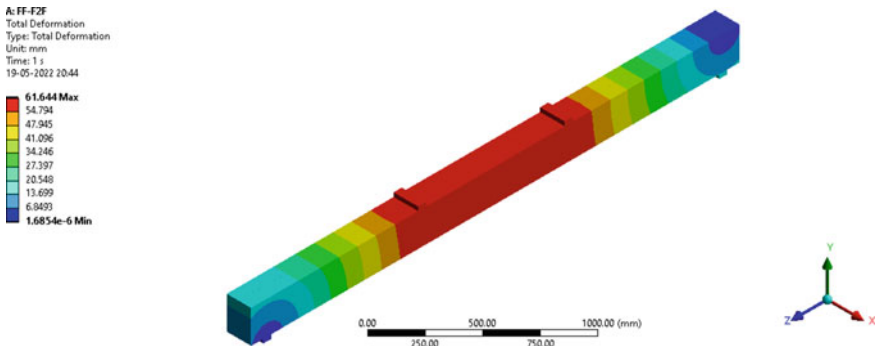
Fig. 3 Total deflection of FF-F2F model

3 Results and Discussion

The test results of the analysis showed that the model FF-B2B showed maximum deflection value indicating better yielding capacity and can take more deflection before failure. Figures 3 and 4 shows the total deformation and strain diagram obtained from software of FF-F2F model after analysis. All the models showed similar patterns in the analysis result (Table 3).

From the study of full steel CFS section, the load bearing capacity is ranging from 75.365 to 93.746 kN and its maximum value of 93.746 kN is of the channel section placed front-to-front in overlapped manner while that of fully filled CFS section range from 99.247 to 103.3 kN and its maximum value of 103.3 kN is of channel section placed back-to-back manner. The load bearing capacity of conventional concrete was found to be 84.61 kN.
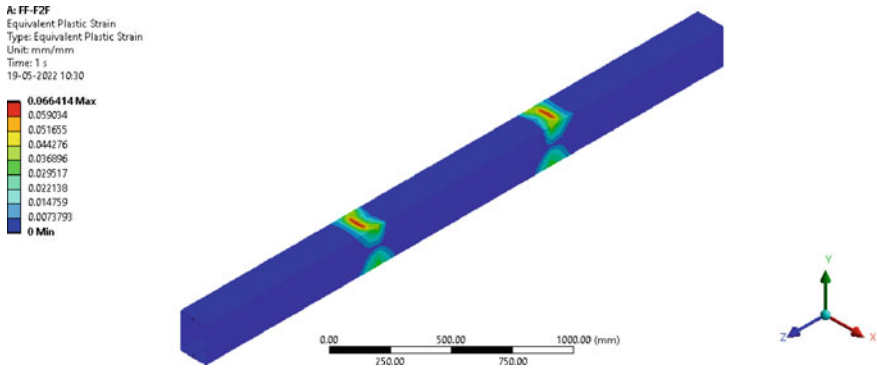
Fig. 4 Total strain of FF-F2F model

Table 3 Maximum load and corresponding deflection values of different models

Model	Load (kN) (Maximum)	Deflection (mm)
RCC	84.61	17.491
S-F2F	75.365	14.484
S-F2F-Overlapped	93.746	28.032
S-B2B	93.428	34.761
FF-F2F	102.38	45.578
FF-F2F-Overlapped	99.247	48.11
FF-B2B	103.3	53.579

When compared with conventional RCC beam, only one model of full steel CFS section had load capacity less than that of RCC, while the other two models had greater value. When compared with RCC, fully filled CFS gives better load bearing capacity. A percentage increase of 35.84 and 10.56 was found when full steel sections were infilled with ULCC of front-to-front and back-to-back placed sections respectively which also improves the buckling resistance of steel only CFS sections. Load deflection curves of 7 models are shown in Fig. 5.

From Figs. 6 and 7 it is clear that values of both maximum deflection and ultimate load are maximum for FF-B2B section, thus indicating maximum load bearing and moment resisting capacity.
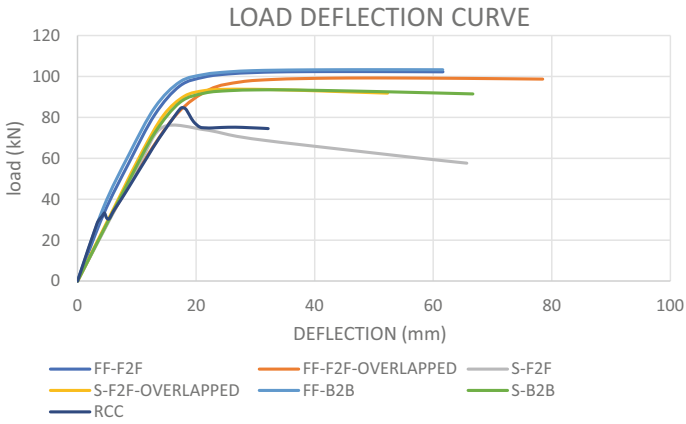
Fig. 5 Load deflection curve of all models
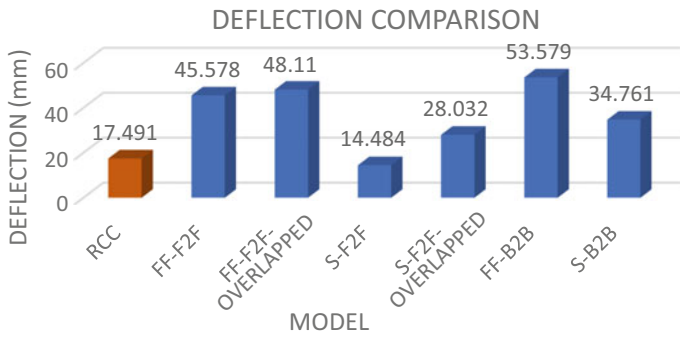
Fig. 6 Deflection at failure comparison chart of different models
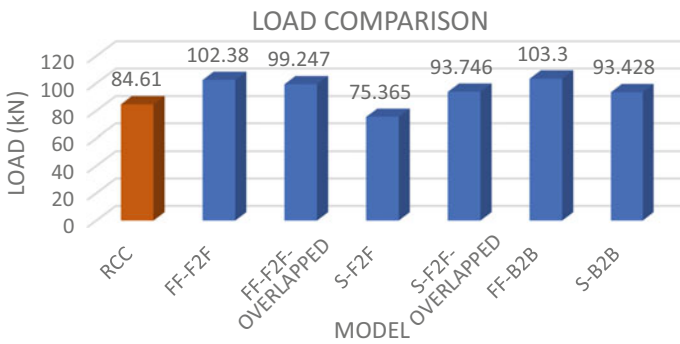
Fig. 7 Ultimate load comparison chart of different models

4 Conclusion

This study investigated the performance of CFS channel sections placed in back-to-back and front-to-front manner with only steel and fully filled with ULCC. The conclusion obtained from the analysis results are summarized as follows:

- Among all the models, FF-B2B showed the maximum load bearing capacity and deformation resistance
- Among steel only CFS sections, S-F2F Overlapped showed maximum load bearing capacity
- Among the fully filled CFS sections, FF-B2B showed maximum load bearing capacity
- Steel only CFS sections when infilled with ULCC, improved the load carrying behavior and also improved the moment resistance
- When compared to conventional RCC beam of same size, CFS integrated ultra-light weight concrete beams showed better performance (about 22%) and can be better replacement option as it is light weight and can be cost effective

References

1. Al Zand, A.W., Hosseinpour, E., Badaruzzaman, W.H.W., Ali, M.M., Yaseen, Z.M., Hanoon, A.N.: Performance of the novel C-purlin tubular beams filled with recycled-lightweight concrete strengthened with CFRP sheet. J. Build. Eng. **43**, 102532 (2021). https://doi.org/10.1016/j.jobe.2021.102532
2. Meza, F.J., Becque, J., Hajirasouliha, I.: Experimental study of cold-formed steel built-up beams. J. Struct. Eng. **146**(7), 04020126 (2020). https://doi.org/10.1061/(ASCE)ST.1943-541X.0002677
3. Wang, J.Y., Wanga, J.-Y., Gao, X.-L., Yan, J.-B., et al.: Developments and mechanical behaviours of steel fibre reinforced ultra-lightweight cement composite with different densities. Constr. Build. Mater. **171**, 643–653 (2018)
4. Liao, F., Wu, H., Wang, R., Zhou, T.: Compression test and analysis of multi-limbs built-up cold-formed steel stub columns
5. Meza, F.J.: The behaviour of cold-formed steel built-up structural members. Ph.D. thesis, Dept. of Civil and Structural Engineering, Univ. of Sheffield (2018)
6. Zhang, X., Rasmussen, K.: Tests of cold-formed steel portal frames with slender sections. Steel Constr. **7**(3), 199–203 (2014). https://doi.org/10.1002/stco.201410030
7. Wang, J.Y., Chia, K.S., Liew, J.Y.R., Zhang, M.H.: Flexural performance of fibre reinforced ultra-lightweight cement composites with low fibre content. Cem. Concr. Compos. **43**, 39–47 (2013)
8. Chia, K.S., Zhang, M.H., Liew, J.Y.R.: High-strength ultra-lightweight cement composite-material properties. In: 9th International Symposium on High Performance Concrete-Design, Verification & Utility, Rotorua, New Zealand, 9–11 August 2011

Development and Performance Evaluation of Geopolymer Based Self Compacting Earthen Concrete

P. R. Krishna Raj, K. B. Anand ⓘ, and Anil Kumar Sharma ⓘ

Abstract Alkali activation of earthen mixture capable of self-consolidation was investigated. Influential factors such as the concentration of activator, additive substitution, and the curing process are studied, keeping the mix workable. A reliable mix proportion with 75% dry weight as soil and 25% dry weight as fly ash (both class C and class F types) with an optimized curing temperature and duration is achieved. The role of curing temperature and duration in strength development is studied and optimum value is obtained. These mixes were then added with a minor proportion of OPC, and its response to two curing methods, viz., moist curing and ambient curing, is also investigated. The end products are microstructurally studied through SEM and XRD.

Keywords Soil geopolymer · Soil activation · OPC-Geopolymer · Earthen concrete

1 Introduction

Earth is an eco-friendly building material that has a reduced impact on the environment. Manufactured bricks are not sustainable options as they involve enormous energy consumption, increasing the carbon footprint. Unfired clay brick is environmentally friendly, but it lacks the essential fundamental property of strength, and they are also vulnerable to seasonal changes. Adding stabilizers can improve their strength and other properties, but these stabilising agents like cement and lime are associated with large-scale carbon dioxide emissions while being manufactured. Unfired bricks attract more research as it involves lesser energy resulting in a reduction in CO_2 emission and impact on the environment.

P. R. Krishna Raj · K. B. Anand (✉)
Department of Civil Engineering, Amrita School of Engineering, Coimbatore, Amrita Vishwa Vidyapeetham, Coimbatore, India
e-mail: kb_anand@amrita.edu

A. K. Sharma
Department of Civil Engineering, National Institute of Technology Patna, Patna, Bihar, India

The ease of working and its economics makes concrete favourite construction material. One of its integral properties is the rheology of fresh concrete to take the shape of the formwork and its ability to pass through the service tubes/reinforcement. When used as a construction material, earth lacks this property and is typically used by ramming using manual or hydraulic pressure (also known as Rammed earth construction). This technique involves the addition of a stabilizer like lime (L) or ordinary Portland cement (OPC) to sieved soil and then ramming at optimum moisture content to achieve high dry density [19]. Although the strength can be improved by varying the quantity of stabilizers [15], one disadvantage of rammed earth is its labour intensiveness. Developing a self-consolidating mixture of earth with the right ingredients capable of giving good workability and strength can be one more step in sustainable construction practices.

A flowable mix with ingredients such as soil, cement and water was proposed and attempted by Arooz and Halwatura [1] for making mud block. As more pore volume resulted from the escape of excess moisture content during the drying process, this technique could only yield blocks of low strength. It has been reported [5] that the French firm CEMATERRE specializes in building stabilised earth walls (with additives like lime, cement and flax fibre) by pumping the earthen mix capable of self-compaction into the formwork.

Ever since the innovation of Geopolymer technology in the '1970s [3], other researchers have focused on applying geopolymerization in building technology. Geopolymers are inorganic Si-O-Al-O networks in polymeric layers formed by the dispersion of silica and alumina in an alkaline medium. Industrial waste such as Class F fly ash (FFA), Class C fly ash (CFA), Metakaolin, and Ground granulated blast furnace slag contain amorphous silica, calcium and alumina. These constituents are utilised in geopolymer technology [2, 11, 19].

Geopolymerisation has been successfully implemented in producing bricks. Silica-rich materials such as clay, kaolin and fly ash [4, 6, 7, 14, 17, 18] have been utilized as a pozzolanic material to react with activator solution. Geopolymer technology brought about by a combination of clay and FFA was studied by Sukmak et al. [17, 18]. The main parameters studied were the ratio of alkalis, alkali to precursor material ratio (L/FA), fly ash to clay ratio (FA/Clay) and heat curing conditions on compressive strength.

The practical difficulty in providing heat for on-field applications can probably justify the inclusion of a minor quantity of OPC in alkali-activated soil mixture to eliminate heat curing. The addition of OPC in activated soil mixture is an area yet to be explored. Nevertheless, few attempts have been made with geopolymer concrete to eliminate heat curing through OPC addition.

Suwan and Fan [20] have studied the setting time and early age strength of geopolymer paste by replacing 5 to 70% of fly ash with OPC. Adding OPC improved the mechanical property and microstructure and eliminated the necessity for heat curing for samples with larger OPC% as heat released during hydration of OPC aided the polymerisation reaction taking place. Nath and Sarkar [12] analysed workability, setting time, strength behaviour, and microstructural modification with the addition of 5% OPC as a replacement for low calcium fly ash in geopolymer concrete.

Table 1 General properties of CFA and FFA

Properties	CFA	FFA
Specific gravity	2.61	2.18
Colour	Grey	Light grey
Particle size distribution	9–400 μm	10–300 μm
Median particle size	34 μm	38 μm
Oxide proportion $CaO/SiO_2/Al_2O_3$	32.8/21.2/25.1	10.2/56.5/22.5

This paper presents the study on the properties of heat-cured self-compacting Soil fly ash Geopolymer (SFGP). The influence of temperature and duration of heat curing is studied and optimum value is reported. Properties are compared for OPC added in moist and ambient cured Soil fly ash Geopolymer (OPC-SFGP). Microstructural studies are also compared for the two types of geopolymers through XRD and SEM.

2 Materials and Methodology

2.1 Materials

Locally available soil collected from a depth of 2 m was used. The particle size distribution confirmed that the soil mainly consists of sand to silt-sized particles. Flyash is used as additive in the geopolymerisation process and the properties of both class C flyash (CFA) and class F flyash (FFA) are given in Table 1.

2.2 Methodology

The initial phase was devoted to finding various factors affecting soil alkali activation, gradually progressing towards a reliable mix composition. The compressive strength of samples (5 × 5 × 5 cm cubes) is taken as an indicator during the progress of the study. Strength variation with heat curing at different temperature levels and duration is recorded to identify the best combinations of materials leading to a mix articulated in the study as SFGP (Soil Flyash Geo Polymer). On the contrary, heat curing was avoided by doing tests under wet and ambient temperature curing with the minor addition of OPC in SFGP (SFGP-OPC). The microstructural changes were compared for both heat-cured SFGP samples and SFGP-OPC samples.

3　Experiments, Results and Discussions

3.1　Feasibility of Alkali Activation for Soil

Various trials were performed to check for the feasibility of local soil in Geopolymerisation.

Selection of Mix Proportion and Activator.　The details of the trials made to choose the activators and mix proportions are given in Table 2. Trial 1 differs from trial 2 in mix ratio, type of activators used, the concentration of activator used, curing temperature and curing duration. The samples were cast to determine the potential strength and hence duration of curing was kept longer for these trials. The second trial with NaOH & Na_2SiO_3 as activators was much more workable mix then trial 1.

　　This trial produced satisfactory strength results and hence the mix proportion is adopted as a base for all future trials. Water has been added only through the activator solution. The flowchart (Fig. 1) represents the base mix proportion details formulated based on the literature review and the preliminary trials.

Table 2　Selection of activators

Stabilizer	FFA	
Activators	NaOH, NaCl	NaOH, Na_2SiO_3
Conc. of activator (Molal)	6	7.5
Curing temperature (°C) & Duration (days)	100 & 3	60 & 5
Compressive strength (MPa)	6.4	4.7
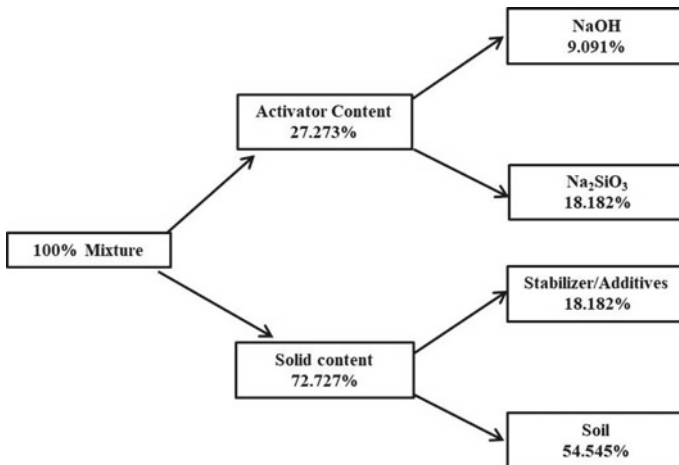
Fig. 1　Base mix proportion
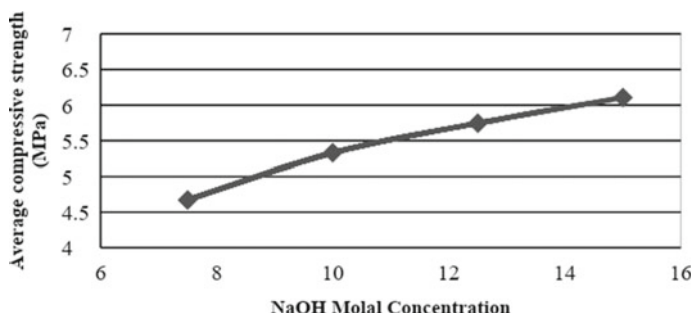
Fig. 2 Influence of activator concentration

Influence of Activator Concentration. The influence of activator concentration on compressive strength by varying the molality of NaOH solution was performed on the same mix design formulated. The graph showing the variation is represented in Fig. 2. A higher concentration can dissolve the stabilizer rapidly, forming a polymeric matrix and attaining short time strength but a further dissolution of silica stops preventing long-time gains. There was a noticeable decrease in workability with higher activator concentration. The flow table test was performed to identify the mix that meets the rheology of cementitious pastes capable of self-consolidation by their mass. From trials 12.5 molal mix which gave a flow value of 105% was adopted as an optimum activator concentration for further trials. Higher concentration achieved higher compressive strength but the resultant mix became non workable.

Influence of Curing Process. The samples were cast in $5 \times 5 \times 5$ cm mould. The significant water content in the ~~soil~~ mixes ~~~~ causes volume change and it lead to shrinkage cracks while heat curing the sample alongside mould was also tried. A curing process after demoulding in which specimens are subjected to heat all around could prevent crack formation. However, when FFA used as a stabilizer, it did not set at ambient temperatures and took several days for the sample to be demoudable. By using CFA instead of FFA in the mix enabled early setting and the specimen was demouldable after one day of casting. Curing duration was shortened to 1 day. The sample was subjected to a heat curing at temperature of 60 °C for 22 h, followed by 2 h at 100 °C. The compressive strength achieved was 6.7 MPa, thus favoring the curing process adopted.

Influence of Additive Combinations. The additives selected were industrial by-products. They contain sufficient amounts of lime, silica, and alumina to help in chemical activation, and also bring down the demoulding time. The mix proportion adopted in this stage is slightly different from the base general mixture—with the additive part (18.182%) substituted by two different additives. The combinations of additives examined are shown in Table 3.

All combinations of tested samples showed improved compressive strengths in the range of 8 to 12 MPa. Although the strength of the Metakaolin combination was satisfactory, it was not considered for further study considering their higher cost.

Table 3 Influence of additive

Additive combination	FFA(50%)-GGBS(50%)	GGBS(50%)-Metakoalin(50%)	FFA(60%)-CFA(40%)
Compressive strength (Mpa)	12.2	11.7	8.9

Table 4 Influence of additive proportions

Stabilizer	FFA				FFA		
Additive	GGBS				CFA		
Additive mixture %	5	7.5	10	12.5	40	30	20
Demoulding (days)	3				2	3	5
Curing temperature (°C) & Duration (hours)	60 & 22 followed by 100 & 2						
Compressive strength (MPa)	12.6	12.5	12.9	12.2	8.9	10.2	10.8

Influence of Additive Proportions. The addition of fly ash may prove to be economically better; hence FFA-GGBS and FFA-CFA mixes have also been studied to be optimized further. The details of the trials are shown in Table 4.

FFA-GGBS mixes did not show a significant variation in compressive strength with varying GGBS percentages. Mixes involving FFA-CFA perform better at 20% because of the more significant portion of FFA, which is better suited for activation. However, the setting time for this mix is more prolonged, whereas the 40% combination makes the mix less workable. Hence 30% is considered optimum from considerations of economy, adequate strength, good workability and faster setting characteristics.

3.2   Soil Fly Ash Geopolymer (SFGP)

Influence of Temperature and Duration on Strength: Samples of SFGP optimized with 30% CFA and 70% FFA combination were further studied for its strength variation with respect to curing temperature and duration. Figure 3 shows the compressive strength variation after 24, 48, and 72 h of curing at 65, 75 and 85 °C.

The results show that the strength is reduced with the curing time for the same curing temperature. However, samples cured at 75 °C showed increased strength with curing time. For all the trials, the temperature exposure of 24 h gives the maximum strength values. At all temperatures, a further increase in duration causes a reduction in strength. 75 °C heating temperature meets the objective of being optimum to achieve higher strength in SFGP. Similar results were observed by Sukmak et al. [18]. It has been experimentally shown that there is a decrease in strength after the
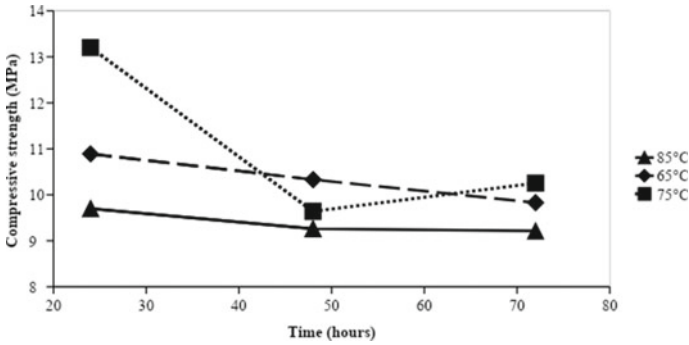
Fig. 3 Influence of heat curing temperature & duration on strength

optimum curing duration for a specific temperature: the specimen shrinks and cracks beyond this duration due to loss of pore water.

Studies on SFGP—OPC Mixes: Hydration of ordinary Portland cement can generate heat which can aid in the geopolymerisation reaction. SFGP-OPC mixes were also studied to understand the self-curing capability and determine the extent to which OPC could be advantageous compared to samples subjected to heating. SFGP-OPC samples follow a similar mix as base mix given in Fig. 2. In these mixes, to the 18.18% additive portion of FFA, OPC is added in small replacements of 5, 7.5, and 10%. These mixes are designated as SFGP-OPC (5/7.5/10). Two curing methods were attempted, viz., wet and ambient temperature.

Wet Curing: Figure 4(a) denotes the 7, 14, and 28 day strengths of wet cured samples in water. As expected, the strength results were better and as the percentage of OPC increased, there was a slight loss of workability. There was an increase in strength as the curing period increased from 7 to 28 days. Adding just 5% OPC can eliminate heat curing and achieve moderate strength gain with time.

Ambient Curing: Figure 4(b) shows the effect of curing at ambient temperature with 10% OPC as it showed the highest strength during wet curing. The ambient
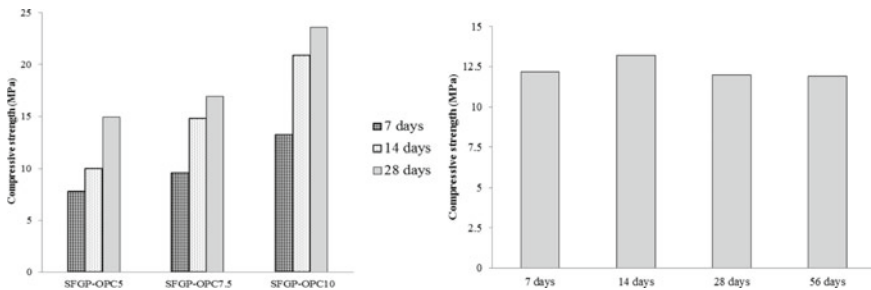
Fig. 4 Strength of SFGP-OPC **a** with moist curing; and **b** under ambient curing

temperature curing may achieve strength during the initial setting period, during which more heat from OPC hydration can aid geopolymerization. Hence curing (~25 °C) was done on SFGP-OPC10 and was compared with wet cured SFGP-OPC10 samples. The strength achieved was almost constant (~12 MPa) and did not vary with different curing periods. Ambient cured samples could achieve similar strength to wet cured samples after seven days of curing and is satisfactory for load-bearing application.

3.3 Comparison of SFGP and SFGP-OPC

OPC-SFGP samples cured under ambient temperature seem to be less efficient under a small dosage of OPC addition. Samples that are wet cured (SFGP-OPC) showed higher strengths than heat-cured SFGP samples. 75 °C, 24 h heat-cured SFGP sample and SFGP-OPC5 28 days wet cured samples have attained similar strength in the range of 13 to 15 MPa; and microstructure comparison is made of these samples.

Microstructural Studies Using SEM. SEM micrographs of SFGP sample (75 °C, 24 h cured) and OPC-SFGP5 are shown in Fig. 5(a) and (b) respectively.

The figures show that fly ash particles were spherical, whereas soil particles were irregular in shape [13]. Geopolymerised aluminosilicate polymer products are very dense. SEM micrographs have identified the precipitation process on the surface of fly ash particles Fig. 5b. The assemblage of dense spherical flocs makes its presence on the surface of fly ash. Heat cured samples develop micro cracking on the surface of fly ash and these cracks affect strength. Hence optimum temperature and curing duration prevent these microcracks from scattering from the fly ash particles.

Such microcracks were identified and plotted in Fig. 6. SFGP developed a homogenous structure of amorphous alumina silicate acting as a bonding agent between
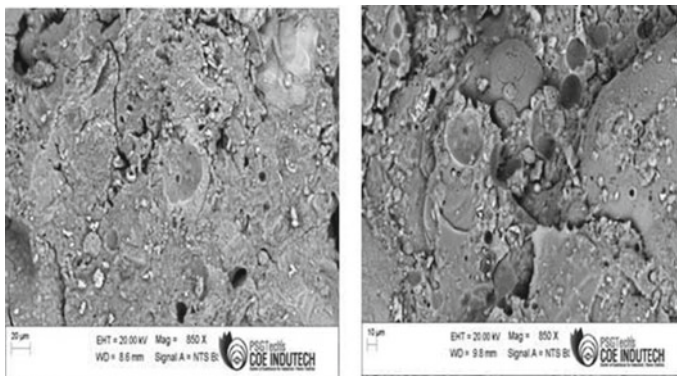
Fig. 5 SEM micrographs of **a** SFGP sample and **b** SFGP-OPC5
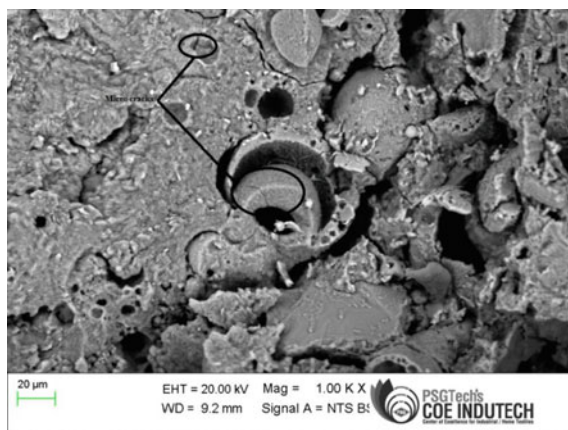
Fig. 6 SEM micrographs showing microcracks in SFGP sample

mixtures with almost complete reaction. In contrast, OPC-SFGP showed large amounts of unreacted elements caused due to inadequate geopolymeric gel to cover all surfaces.

4 Conclusion

The strength development of alkali-activated soil has been studied, and, in the process, self-consolidating Soil fly ash Geopolymer (SFGP) with a suitable mix proportion has been developed. Major conclusions are:

1. Mix capable of self-consolidation achieving good strength by including 75% of their solid content as the soil makes this study practically effective.
2. The optimum curing temperature for the SFGP mix was found to be 75 °C.
3. 5% OPC substitution with moist curing eliminates the necessity of heat curing as the samples achieve similar strength.
4. Ambient temperature cured SFGP samples with 10% OPC achieved a strength of 12 MPa in 7 days and could be practically viable.

References

1. Arooz, F.R., Halwatura, R.U.: Mud-concrete block (MCB): mix design and durability characteristics. Case studies in construction materials **8**, 39–50 (2018)
2. Arulrajah, A., Kua, T.A., Horpibulsuk, S., Phetchuay, C., Suksiripattanapong, C., Du, Y.J.: Strength and microstructure evaluation of recycled glass-fly ash geopolymer. Constr. Build. Mater. **114**, 400–406 (2016)
3. Davidovits, J.: Geopolymer Chemistry and Applications. Geopolymer Institute, Saint-Quentin (2015)
4. Douiri, H., Louati, S., Baklouti, S., Arous, M., Fakhfakh, Z.: Structural and dielectric comparative studies of geopolymers prepared with metakaolin and Tunisian natural clay. Appl. Clay Sci. **139**, 40–44 (2017)
5. Eid, J., Taibi, S., Fleureau, J.M., Hattab, M.: Drying, cracks and shrinkage evolution of a natural silt intended for a new earth building material. Impact of reinforcement. Constr. Build. Mater. **86**, 120–132 (2015)
6. Ferone, C., Liguori, B., Capasso, I., Colangelo, F., Cioffi, R., Cappelletto, E., Di Maggio, R.: Thermally treated clay sediments as geopolymer source material. Appl. Clay Sci. **107**, 195–204 (2015)
7. Hwang, C.L., Huynh, T.P.: Investigation into the use of unground rice husk ash to produce eco-friendly construction bricks. Constr. Build. Mater. **93**, 335–341 (2015)
8. IS 1727: Method of Test for Pozzolanic Materials. Bureau of Indian Standards (BIS), New Delhi, India (1967)
9. IS 2720 Part 4: Methods of test for soils: Grain size analysis. Bureau of Indian Standards (BIS), New Delhi, India (1985)
10. IS 12269: Ordinary Portland Cement, 53 Grade – Specifications. Bureau of Indian Standards (BIS), New Delhi, India (2013)
11. Karuppuchamy, Ananthkumar, K.M., Raghavapriya, S.M.: Effect of alkaline solution with varying mix proportion on geopolymer mortar In: IOP Conference Series: Materials Science and Engineering, vol. 310, no. 1, p. 012039. IOP Publishing (2018)
12. Nath, P., Sarker, P.K.: Use of OPC to improve setting and early strength properties of low calcium fly ash geopolymer concrete cured at room temperature. Cem. Concr. Compos. **55**, 205–214 (2015)
13. Paloma, A., Grutzeck, M.W., Blanco, M.T.: Alkali-activated fly ashes: a cement for the future. Cem. Concr. Res. **29**, 1323–1329 (1999)
14. Peyne, J., Joussein, E., Gautron, J., Doudeau, J., Rossignol, S.: Feasibility of producing geopolymer binder based on a brick clay mixture. Ceram. Int. **43**(13), 9860–9871 (2017)
15. Raj, S., Sharma, A.K., Anand, K.B.: Performance appraisal of coal ash stabilized rammed earth. J. Build. Eng. **18**, 51–57 (2018)
16. Sethu Parvathy, S., Sharma, A.K., Anand, K.B.: Comparative study on synthesis and properties of geopolymer fine aggregate from fly ashes. Constr. Build. Mater. **198**, 359–367 (2019)
17. Sukmak, P., Horpibulsuk, S., Shen, S.L.: Strength development in clay–fly ash geopolymer. Constr. Build. Mater. **40**, 566–574 (2013a)
18. Sukmak, P., Horpibulsuk, S., Shen, S.L., Chindaprasirt, P., Suksiripattanapong, C.: Factors influencing strength development in clay-fly ash geopolymer. Constr. Build. Mater. **47**, 1125–1136 (2013b)
19. Suresh, A., Anand, K.B.: Strength and durability of rammed earth for walling. J. Archit. Eng. **23**(4), 06017004 (2017)
20. Suwan, T., Fan, M.: Influence of OPC replacement and manufacturing procedures on the properties of self-cured geopolymer. Constr. Build. Mater. **73**, 551–561 (2014)

Optimisation of Artificial Neural Network Using Cuckoo Search Algorithm for Damage Detection

A. Fida, Prince Thankachan, and T. M. Madhavan Pillai

Abstract Artificial Neural Network is a tool of Structural Health Monitoring based on non-destructive methods for finding damage detection. ANN is a parallel distributed network inspired by the biological nervous system and has the potential to learn and identify from experience to improve its performance. Therefore, a trained network can be utilised to classify and examine new data sets that show similar characteristics as that of trained data sets. By virtue of the potential capability of ANN, it can be used to solve both simple linear and complex nonlinear functions. But due to the gradient descent nature of the backpropagation algorithm, the problem of local minima arises and which acts as a great hindrance to the best solution. To overcome this, various evolutionary algorithms based on global minima were used in conjunction with ANN such as Particle Swarm Optimisation, Genetic Algorithm, Cuckoo Search (CS), etc. Cuckoo Search is a powerful meta-heuristic search algorithm derived from the reproduction strategy of the Cuckoo bird. The lesser number of parameters in CS makes it simple and potentially more genetic. This paper presents a method for damage detection in structures by amalgamating a flexible combination of Artificial Neural Network and Cuckoo Search algorithm. CS is employed with ANN to improve the training parameters (weight and bias) by minimising the difference between the real and desired output and these parameters were used for generating the network. For the study, a lattice structure is used to assess the robustness of the created network and this will be compared with efficiency in damage location and identification of the network created using ANN alone. The Study proved that ANN-CS outperforms ANN alone in damage identification, localisation, and quantification.

Keywords Structural Health Monitoring · Artificial Neural Network · Cuckoo Search · Back-propagation · Damage Detection · Evolutionary Algorithm

A. Fida (✉) · P. Thankachan · T. M. M. Pillai
Department of Civil Engineering, National Institute of Technology Calicut, Kozhikode, India
e-mail: fidaabdurahiman@gmail.com

1 Introduction

Periodic health monitoring is essential for any engineering structure. It can be either destructive methods or non-destructive methods. The process of establishing a damage identification and characterisation strategy for engineering structures is called structural health monitoring. Different technologies have evolved in the field of structural health monitoring. Idichandy et al. [1] suggested the use of modal vectors for structural health monitoring. This paper used an analytical model and a scale down physical model of the structure. Experiments are conducted on the model by stimulating damage through removing the members and varying deck load. Results showed variation in frequency if the damage is influencing the stiffness of the structure. Later advancement in SHM results in the introduction of machine learning in damage detection. Artificial Neural Network has the capability to do pattern recognition, image processing, it can create linear as well as non-linear modelling. A trained network is capable of understanding reliable and precise information from an unreliable, imprecise and a noise polluted data and it will train the network in such a way that it can provide a better output matching with the target data. There are different kinds of inputs are available for training ANN such as frequency, mode shapes, modal flexibility, modal strain energy etc. X Wu et al. [2] studied the learning capability of neural networks in structural damage identification. Wherein the authors selected a simple neural network and trained it for the undamaged and damaged cases with various possibilities of damage. The study showed that neural networks can learn the behaviour of the undamaged and damaged structures and it can also identify the damage, extent of damage, etc. But the training of data's using ANN results in problems of local minima which is a great hindrance to the search for the best solution. Xin-She Yang [3] proposed a new algorithm for optimisation called a cuckoo search algorithm evolved from the reproduction strategy of cuckoo bird. The new algorithm is compared with existing optimisation algorithms such as genetic algorithm and particle swarm optimisation, Studies indicate that cuckoo search algorithm outperforms other optimisation algorithms. Anuja S Joshi et al. [4] described the working principle of Cuckoo search algorithm. Later this optimisation algorithm was combined with artificial neural network for minimising the problem of local minima. Vedanshu et al. [5] introduced multi-objective cuckoo search algorithm for weights and biases initialization. Which results in a lesser convergence time as compared Gaussian distribution generally used in ANN. Hoa Tran-Ngoc et al. [6] proposed a flexible combination of artificial neural network combined with cuckoo search algorithm. ANN is a powerful tool amalgamating artificial intelligence but the problem of local minima is a great hindrance the searching for the best solution. So here cuckoo search is combined with ANN which can reduce the difference between actual and desired output. The method has been demonstrated in a beam made of steel and a large-scale truss bridge. The study proved the higher efficiency of the method in damage localisation and identification compared with other evolutionary algorithms combined with ANN such as PSO, GA, or ANN alone.

2 Theoretical Background

Artificial Neural Network is a parallelized structure influenced by the biological nervous system that can learn and improve its performance by identifying patterns in data. This can train classify and examine new data sets that are similar in character to the trained data sets. ANN can be used to solve complex non-linear functions which cannot be solved using common methods. Applications of ANN consist of identification, classification, and pattern recognition in image processing and control systems.

The structure of ANN consists of layers; the input layer and output layer are interconnected by one or more hidden layers. Input data is given through the input layers and output data is taken from output layers. Each layer has a set of neurons and these layers are connected by connection parameters such as weights and biases. Each neuron contains a synaptic processing unit depending on the number of inputs and outputs. Figure 1 represents the transmission of signals between neurons in layers. The input layer collects signal (*P1, P2, …. , Pn*) and afterward communicates the signal pattern to hidden layer. This hidden layer is an intermediate between first and last layer. The signal transmission process is grounded on some equations, the first equation is a summation function calculated as the sum of weight ratios, output signals, and biases of previous layers.

$$input_t = \sum_{i,t-1}^{n,m} w_{it} * xi + b_t; i = (1 : n); t = (1 : m) \tag{1}$$
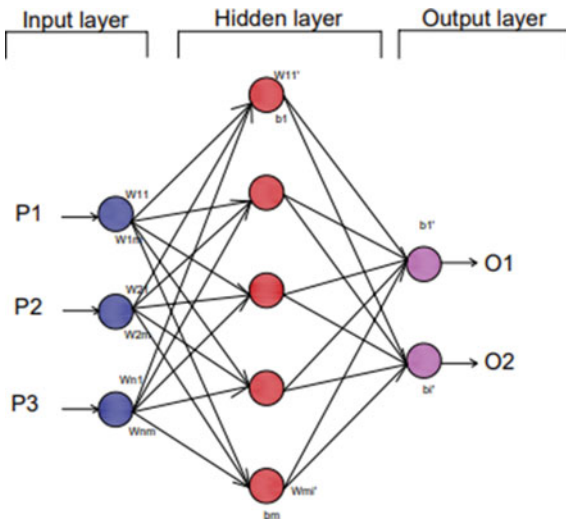
Fig. 1 Structure of neural network

where,

x_i = outcome of the ith neuron of the input layer,
w_{it} = weight ratios that link i^{th} and t^{th} neuron,
b_t = bias ratios connecting input and hidden layers,
$input_t$ = input of tth neuron of the hidden layer,

Processing neurons denoted in input layer is i and hidden layer is t, number of the neurons in the input and hidden layers are represented by n and m.

Subsequently an activation function is used to define the range of value of output nodes. To study non-linearity, a sigmoid activation function is incorporated. Finally output results are obtained from input result as follows

$$output_l = \frac{1}{1 + e^{-input_q}}; q = (1 : m); l = (1 : 1) \tag{2}$$

where,

$input_q$ = input of the qth neuron in output layer,
$output_j$ = output of the lth neuron of the output layer.

Even though ANN can learn, identify and predict the results the problem of local minima makes complex errors with too many local bests. So, in recent decades an evolutionary algorithm called Cuckoo Search algorithm developed by Xin-She Yang and Suash Deb [7] is used along with ANN. This technique based on global search helps to search the best solution avoiding the problem of local minima. The lesser parameters in CS algorithms make it less complex. CS replaces the back propagation algorithm for training the parameters such as biases and weights by minimising the variation between the real and desired outcome.

CS is a metaheuristic algorithm motivated by the reproduction strategy of cuckoo bird. Cuckoo birds keep their eggs in the nest of another bird. If these birds find the cuckoo eggs, they either throw their eggs or they may abandon their nests. CS is based on mainly three ideologies.

1. Cuckoo keep their eggs in a random nest one at a time
2. The nest will pass to the next generation only if it has high-quality eggs
3. The number of host nests is specified and eggs prawn by cuckoos is identified by the host will have a probability between 0 and 1.

An objective function based on relative minima provides the optimum solution in cuckoo search. The latest solution $X(i + 1)$ is found out by

$$PX_{i+1} = X'_i + a * levy(\lambda) \tag{3}$$

where,

X'_i = previous solution
a = step size of scale of problems of interest (mostly a = 1 is applied).

levy(λ) = step length.

The *levy(λ)* gives a random walk. Step length is taken from leavy distribution using the equation below.

$$levy\ u = t^{-\lambda}, (1 \leq \lambda \leq 3) \tag{4}$$

3 Application on a Lattice Structure

Validation of the method is done using undamaged and damaged conditions of a lattice structure. Lattice structure is an important offshore structure used commonly in oil platforms, offshore wind turbine generators, etc. The finite element model of the experimental lattice structure [1] is formulated in SAP2000 software which is shown in Fig. 2. The model has four main legs and four skirt legs rigidly fixed to the base. Main leg of the structure has an internal diameter of 40 mm and wall thickness of 1.5 mm, inclined bracing has an internal diameter of 20 and 1.2 mm thick, and horizontal bracing has an internal diameter of 16 mm diameter and 1 mm thick. Perspex sheets were placed on the main and cellar deck. A uniform load of 10 kg is uniformly distributed over the main deck. Model has 50 nodes and 124 beam elements. The nodes were located at the intersection of longitudinal members of the structure.

The input and output data from finite element software SAP2000 are given to a neural network created in MATLAB. Input data is the natural frequency in the first five modes and output data is the centroid of removed members. Both single and multiple damages are simulated. Single damage is made by the removal of one member at a time. Multiple damages are simulated in two different ways (1) By removing two members at different heights and (2) By reducing the cross-sectional area from 50 to 10% with a step size of 10%. To evaluate the efficiency of the method, ANN-CS is compared with a network created using ANN alone by the algorithms created in MATLAB. Results from two networks are compared in terms of damage prediction, RMSE, and damage location in terms of height.

3.1 Lattice Structure in Single Damage Condition

Damage scenario is formulated by removing one member at a time in chronological order. 78 damage cases were modelled out of these 6 cases are used for testing and remaining cases for training and validation. A 2-layer neural network having 35 number of neurons are used for training of neural network in ANN and ANN-CS method. Table 1 shows the results of testing data obtained from ANN and ANN-CS
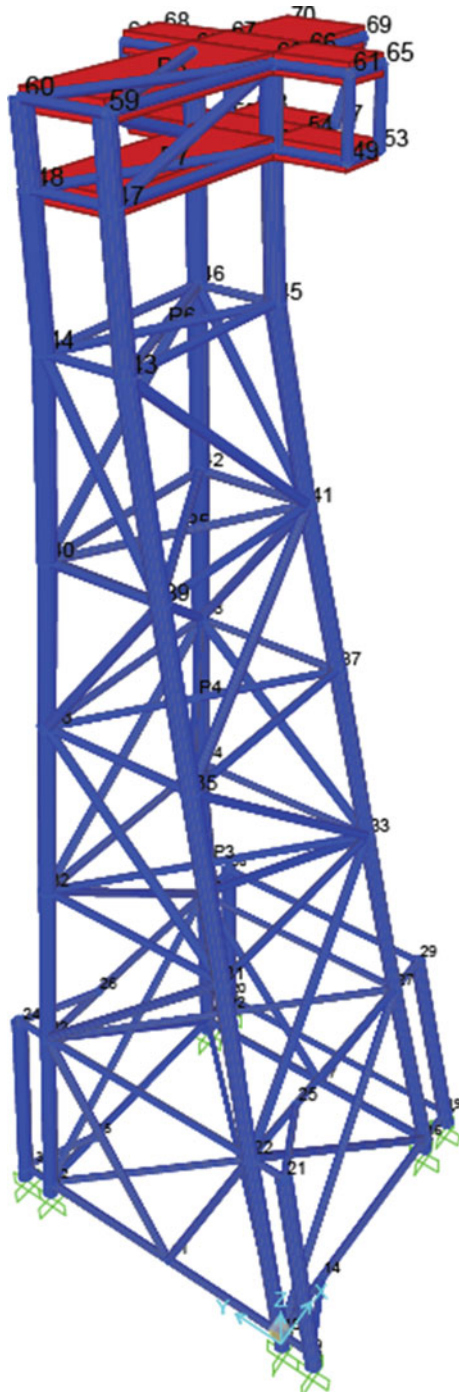
Fig. 2 Lattice structure modelled in SAP2000

networks. These results from trained networks are used to evaluate the effectiveness of the method.

The correlation connecting the calculated and desired results for training, testing, and validation line falls along a 45-degree straight line, the regression coefficient is higher than 0.94 in both cases, all this indicates the close correspondence of target results with the output. The RMSE results of test data in Fig. 3 show that RMSE values are the least in ANN-CS in almost all test cases, which results in the least error data from the ANN-CS network. Figure 4 compares the damage location in terms of height. The results show that ANN-CS is predicting the damage with the least variation from the actual damage location as compared to ANN network. Predicting the height of damage with lesser error means locating the damage precisely.

Table 1 Results from ANN & ANN-CS networks in single damage condition

Actual			ANN				ANN-CS			
X (m)	Y (m)	Z (m)	X (m)	Y (m)	Z (m)	RMSE	X (m)	Y (m)	Z (m)	RMSE
0.3405	0.792	0.368	0.323	0.474	0.787	0.303859	0.282	0.427	0.994	0.419731
0.305	0.157	1.309	0.199	0.292	1.75	0.273217	0.35	0.349	1.53	0.171007
0.273	0.222	1.823	0.179	0.402	2.189	0.241655	0.299	0.395	2.09	0.184295
0.273	0.587	2.038	0.289	0.44	1.27	0.451549	0.282	0.415	1.557	0.294972
0.2465	0.3	2.46	0.223	0.458	1.841	0.369088	0.269	0.418	1.918	0.320517
0.444	0.418	2.67	0.215	0.427	2.34	0.231964	0.238	0.441	2.477	0.163518
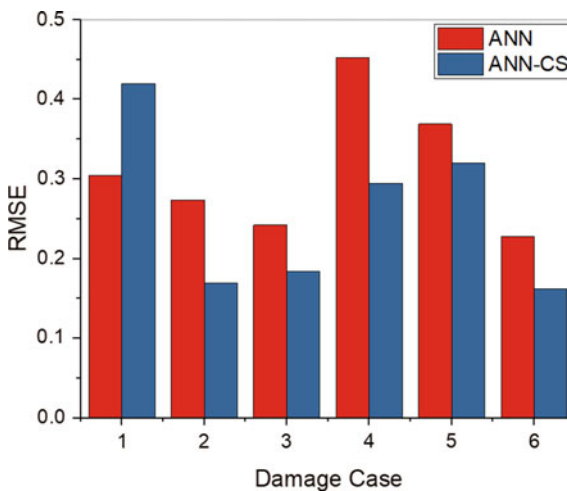
Fig. 3 RMSE value from single damage condition
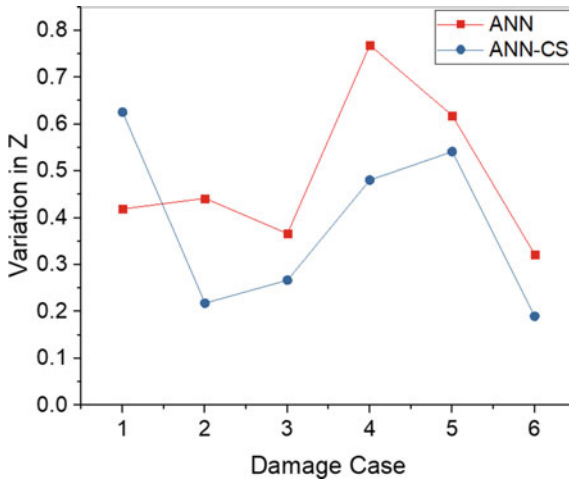
Fig. 4 Variations of Z value in single damage condition

3.2 Removal of Two Members at Different Height

Damage to structure is formulated by removing two members at different height (RTDH). A total of 320 cases were formed of which 10 cases shown in Table 2 are used for testing and the remaining are used for training and validation. A two-layer neural network having 35 number of neurons are used to create the network, Results of test data from ANN and ANN-CS are shown in Tables 3 and 4 respectively.

The regression coefficient value is above 0.9 and which lies along a 45-degree line. The RMSE values in Fig. 5 are the least for ANN-CS as compared to ANN

Table 2 Cartesian coordinates of removed members in RTDH case

Damage case	Members removed		X1 (m)	Y1 (m)	Z1 (m)	X2 (m)	Y2 (m)	Z2 (m)
R1	4	22	0	0.792	0.368	0.305	0.121	1.023
R2	9	65	0.727	0.043	0.368	0.247	0.3	2.46
R3	19	8	0	0.121	1.023	0.387	0.792	0.368
R4	26	50	0.646	0.714	1.023	0.247	0.248	2.038
R5	33	53	0	0.189	1.566	0.52	0.391	2.038
R6	38	62	0.578	0.189	1.566	0	0.442	2.46
R7	49	25	0	0.587	2.038	0.646	0.382	1.023
R8	52	64	0.52	0.248	2.038	0.222	0.536	2.46
R9	61	39	0	0.3	2.46	0.578	0.45	1.566
R10	68	7	0.469	0.536	2.46	0.387	0.043	0.368

Table 3 Results from ANN network in RTDH case

Damage case	X1 (m)	Y1 (m)	Z1 (m)	X2 (m)	Y2 (m)	Z2 (m)	RMSE
R1	0.35	0.52	0.119	0.381	0.368	1.517	0.308
R2	0.395	0.484	0.374	0.343	0.381	1.707	0.385
R3	0.349	0.362	1.099	0.293	0.464	1.464	0.501
R4	0.366	0.414	0.784	0.285	0.474	1.488	0.311
R5	0.391	0.383	1.344	0.281	0.438	1.508	0.311
R6	0.317	0.315	1.39	0.221	0.425	1.364	0.477
R7	0.23	0.308	2.293	0.358	0.378	0.985	0.216
R8	0.313	0.444	1.741	0.327	0.427	1.281	0.513
R9	0.258	0.395	2.373	0.312	0.485	1.215	0.215
R10	0.286	0.444	2.111	0.289	0.365	1.027	0.344

Table 4 Results from ANN-CS network in RTDH case

Damage case	X1 (m)	Y1 (m)	Z1 (m)	X2 (m)	Y2 (m)	Z2 (m)	RMSE
R1	0.386	0.527	0.411	0.287	0.409	0.876	0.233
R2	0.391	0.428	0.404	0.247	0.383	2.589	0.218
R3	0.284	0.266	1.24	0.301	0.446	1.112	0.372
R4	0.41	0.38	1.054	0.309	0.365	2.018	0.176
R5	0.12	0.164	1.485	0.353	0.433	2.239	0.123
R6	0.323	0.154	1.518	0.163	0.478	2.6102	0.141
R7	0.219	0.496	1.816	0.664	0.291	1.109	0.142
R8	0.296	0.397	2.034	0.239	0.411	2.445	0.121
R9	0.269	0.342	2.547	0.196	0.512	1.115	0.269
R10	0.282	0.417	2.504	0.321	0.391	0.8745	0.269

alone. The variation in damage prediction represented as the height of the damaged member in Figs. 6 and 7 is lesser in ANN-CS as compared to ANN alone. Thus ANN-CS can locate the damage accurately compared to ANN alone.

3.3 Stiffness Reduction of Three Members

This is simulated by the stiffness reduction of three members (SRT) at a time. The order of member selection is shown in Fig. 8. The stiffness reduction was carried out by decreasing the cross sectional area of the members between 10 to 50% with an increment of 10%. A total of 80 damage cases were modelled by the reduction in cross section sequentially, out of which 6 cases in Table 5 were used for testing and the remaining cases were used for training the neural network. Tables 6 and 7
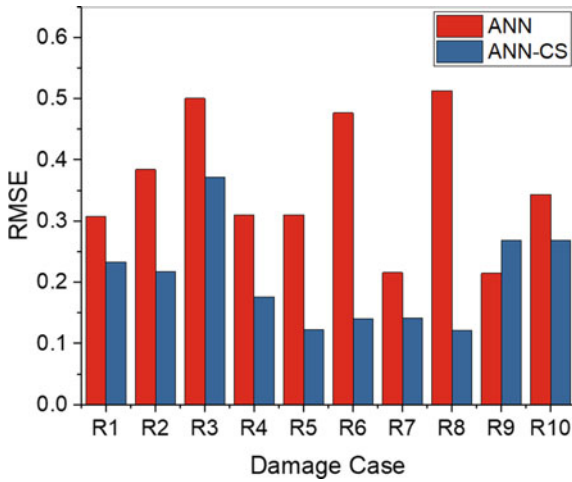
Fig. 5 RMSE value from RTDH case
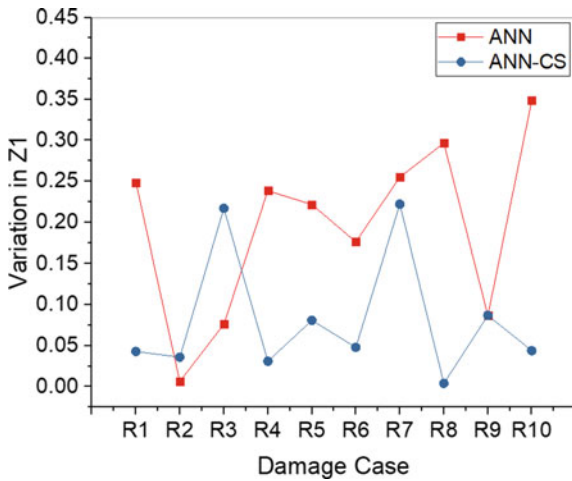
Fig. 6 Variations of *Z1* value in RTDH case

show the result from test data in ANN and ANN-CS networks. The damage case regression coefficient value is more than 0.99. A regression value close to 1 means it shows mutual agreement between target results and output. RMSE value represented in Fig. 9 is close to zero in ANN-CS as compared to ANN alone, So ANN-CS predicts the damage more accurately than ANN alone. In damage prediction damage localisation is compared in terms of the height of damaged members in Figs. 10, 11, and 12, which shows that ANN-CS has a lesser deviation from the actual value.
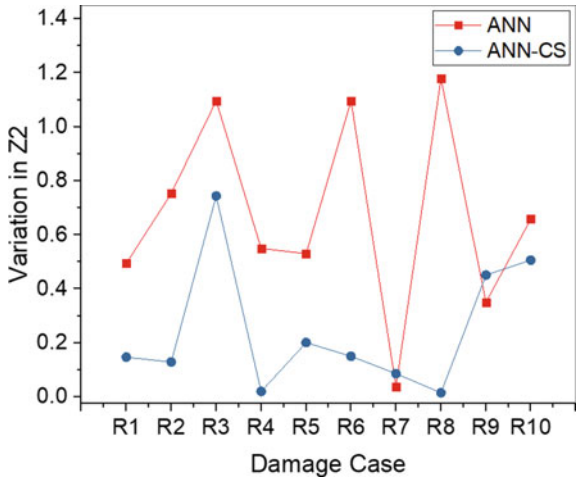
Fig. 7 Variations of *Z2* value in RTDH case
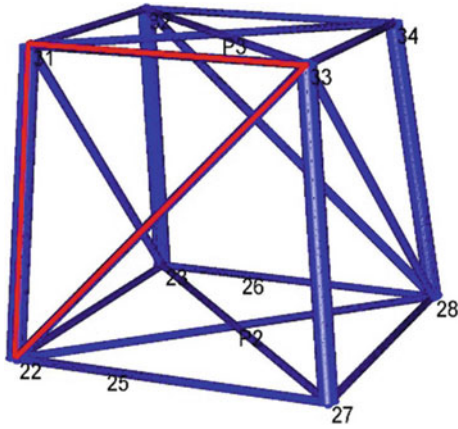
Fig. 8 Triangular damage pattern in SRT case

Table 5 Cartesian coordinates of removed members in SRT case

Damage case	Members removed	% of damage	X1, Y1, Z1 (m)	X2, Y2, Z2 (m)	X3, Y3, Z3 (m)
S1	19,22,28	50	0, 0.123, 1.023	0.305, 0.121, 1.023	0.305, 0.157, 1.309
S2	26,23,31	20	0.646, 0.714, 1.023	0.341, 0.714, 1.023	0.305, 0.678, 1.309
S3	38,37,42	30	0.578, 0.189, 1.566	0.305, 0.189, 1.566	0.273, 0.22, 1.823
S4	47,50,56	20	0, 0.248, 2.038	0.247, 0.248, 2.038	0.247, 0.275, 2.252
S5	54,51,59	30	0.520, 0.587, 2.038	0.273, 0.587, 2.038	0.247, 0.56, 2.252
S6	63,64,73	40	0, 0.536, 2.46	0.222, 0.536, 2.46	0.222, 0.511, 2.667

Table 6 Neural network outcome from ANN alone in SRT case

Damage case	% of damage	X1 (m)	Y1 (m)	Z1 (m)	X2 (m)	Y2 (m)	Z2 (m)	X3 (m)	Y3 (m)	Z3 (m)	RMSE
S1	50.035	0.312	0.344	0.841	0.327	0.337	0.842	0.368	0.158	1.26	0.358
S2	19.69	0.24	0.422	1.23	0.297	0.36	1.221	0.337	0.342	1.928	0.296
S3	29.978	0.323	0.385	1.619	0.253	0.257	1.56	0.249	0.289	1.942	0.338
S4	19.858	0.142	0.318	1.977	0.199	0.4	2	0.213	0.282	2.147	0.270
S5	29.898	0.17	0.307	1.913	0.262	0.403	1.926	0.277	0.277	2.22	0.380
S6	40.779	0.359	0.408	2.425	0.248	0.444	2.391	0.247	0.42	2.507	0.294

Table 7 Neural network outcome from ANN-CS in SRT case

Damage case	% of damage	X1 (m)	Y1 (m)	Z1 (m)	X2 (m)	Y2 (m)	Z2 (m)	X3 (m)	Y3 (m)	Z3 (m)	RMSE
S1	50.0389	0.321	0.192	1.047	0.38	0.161	1.055	0.375	0.209	1.339	0.119
S2	19.684	0.164	0.497	1.053	0.291	0.491	1.055	0.275	0.481	1.338	0.266
S3	30.1	0.36	0.255	1.489	0.222	0.262	1.502	0.205	0.285	1.772	0.103
S4	19.553	0.187	0.337	2.025	0.245	0.405	2.032	0.235	0.424	2.248	0.179
S5	28.498	0.317	0.569	2.11	0.317	0.56	2.13	0.302	0.553	2.33	0.515
S6	40.463	0.165	0.574	2.468	0.133	0.535	2.472	0.124	0.512	2.675	0.170
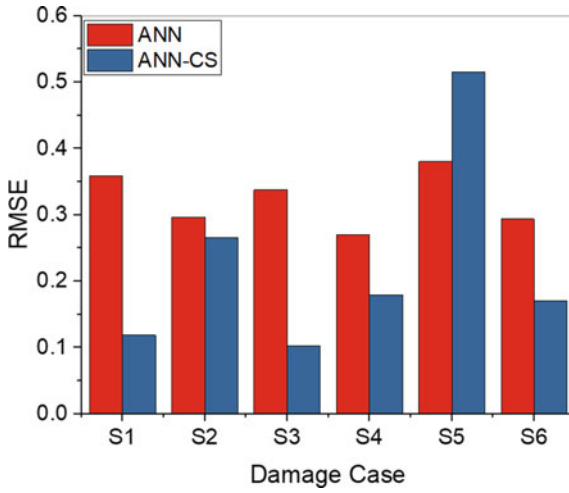
Fig. 9 RMSE value from SRT case
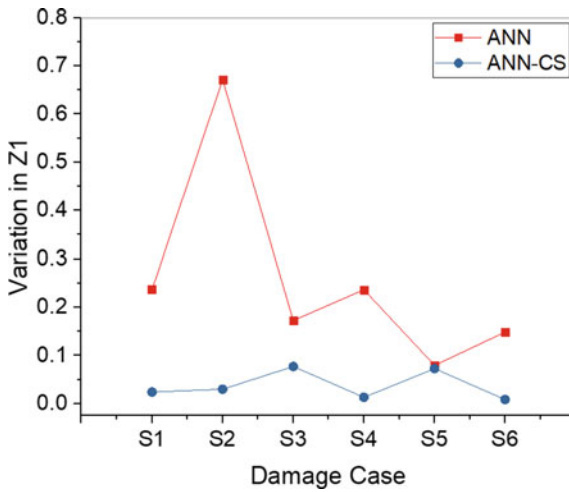
Fig. 10 Variations of *Z1* value in SRT case
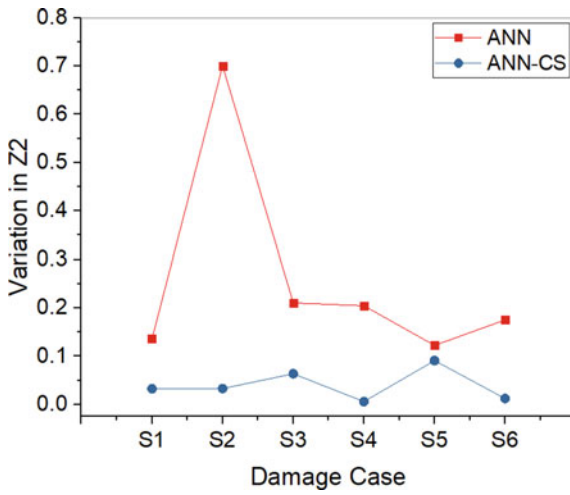
Fig. 11 Variations of *Z2* value in SRT case
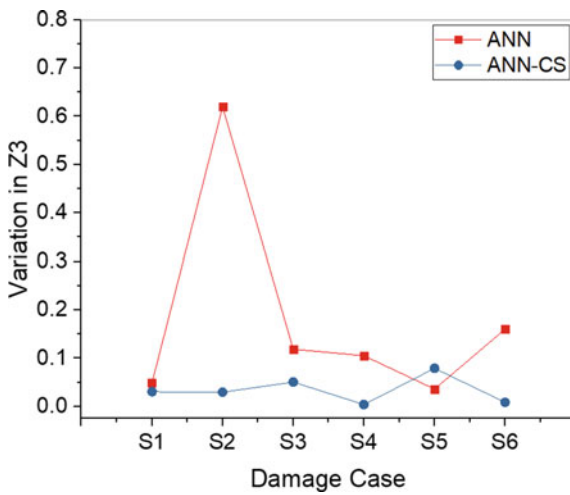
Fig. 12 Variations of *Z3* value in SRT case

4 Conclusion

In all the above-mentioned scenarios, ANN combined with CS shows better performance in terms of accuracy than ANN alone. Major findings from the study are.

1. ANN-CS can locate the damage precisely. It can identify the damage scenario and its severity accurately than ANN alone. This was verified with the Z-coordinate of the actual damage location.
2. Though ANN can identify the damage and severity, the prediction gets trapped in local minima, so the result becomes less accurate.
3. It was observed that ANN-CS produced more converged results by lower RMSE value as compared to ANN alone.
4. ANN-CS can learn and classify similar data and the network can predict the damage condition that do not belong to the data set.
5. Since training of the neural network depends only on the data set and the method, this approach can be used for other lattice structures like truss bridges.
6. Further studies needed to be conducted for more real structures to check the capability of the approach.

References

1. Idichandy, V.G., Ganapathy, C.: Modal parameters for structural integrity monitoring of fixed offshore platforms. Exp. Mech. (1990)
2. Wu, X., Ghaboussi, J., Garret Jr., J.H.: Use of neural networks in detection of structural damage **41**(4), 649–659 (1992). Department of Civil Engineering, University of Illinois at Urbana-Champaign, U.S.A
3. Yang, X.-S.: Nature-Inspired Metaheuristic Algorithms, Second Edition University of Cambridge, United Kingdom (2010)
4. Anuja, S.J., Kulkarni, O., Kakandikar, G.M., Nandedkar, V.M.: Cuckoo search optimization-a review. Mater. Today Proc. **4**, 7262–7269 (2017)
5. Vedanshu, Tripathi, M.M.: Weight and bias initialization of ANN for load forecasting using cuckoo search algorithm. IEEE (2019). 978-1-7281-0627
6. Tran-Ngoca, H., Khatira, S., De Roeckc, G., Bui-Tienb, T., Abdel Wahabd, M.: An efficient artificial neural network for damage detection in bridges and beam-like structures by improving training parameters using cuckoo search algorithm. Eng. Struct. **199**, 10963 (2019)
7. Yang, X.-S., Deb, S.: Cuckoo search via Lévy flights. 2009 World congress on nature & biologically inspired computing (NaBIC). IEEE (2009)

Comparison of Structural Performance of U-Shaped Concrete Composite Beam having Steel Encasing with Corrugated Profiles

V. Athira and Reshma Prasad

Abstract Composite U-shaped reinforced concrete beams are commonly used in the construction of long span beams for high-rise buildings. In the present study, a U-shaped steel-encased concrete composite beam with straight sides (SUSCCB) in which the U-shaped steel plates are fully encased in the concrete flange is modelled. Composite action of the steel-encased concrete composite beam is developed with the help of reinforcing bars that are passed through perforations provided in the steel plates at the top region. In this research, a U-shaped steel-encased concrete composite beam with straight sides is proposed with various improvements to reduce buckling of plates by introducing the profiled cross section and therefore improvement in its load carrying capacity is developed. This work focuses on increasing load carrying capacity in cold form steel plates by incorporating various profile shapes like trapezium and rectangular. The complete analytical model and extensive parametric studies have been carried out using a non-linear finite element method in ANSYS 2021 R2. When the load deflection curves of the U-shaped beam with various shapes were compared to the that with normal steel plate, it was found that the trapezoidal profile had a 59.62% increase in load carrying capacity and the rectangular profile had a 73.07% increase in load carrying capacity.

Keywords SUSCCB · Profiles · Thin walled · Steel encased

1 Introduction

Excellent characteristics like high bearing capacity, great stiffness and good ductility performance makes steel reinforced concrete structures more suitable in large-span or high-rise structures. When steel and reinforced concrete are combined, more safer structures can be developed than the structures which are made with either of the material alone. In case of tall structures and bridges, U-shaped concrete

V. Athira (✉) · R. Prasad
Department of Civil Engineering, FISAT, Angamaly, India
e-mail: athirabalachandran33@gmail.com

composite beams with steel encasing are used so that the efficiency of the structure can be increased [5]. Cold-formed U-shaped steel–concrete composite beam (CUCB) consists of a U-shaped steel plate that is completely filled with concrete which makes the concrete slab and bottom part function together [6]. Since the CUCB has several benefits over the steel–concrete composite beam with H shape and reinforced concrete beam, it is frequently utilised in prefabricated residential projects. Shear connection connecting the bottom steel plate and the concrete flange has an important role in governing the overall behaviour of composite beams.

A new U-shaped steel-encased concrete composite beam with straight sides having steel encasing with normal and profiled steel plate was analysed [4]. Figure 1 shows the details of SUSCCB model with normal steel plates. In this model, the U-shaped steel plates are totally encased in the concrete flange. A row of holes (perforations) is provided at the top of U-shaped steel plate. The model has reinforcing bars that are passed through the perforations which results in a proper composite action. The straight sides at the top of the U-shaped steel plate strengthen the web's contact with the flange and provide stability throughout the beam's construction phase. The perfobond connectors used here to connect the upper and lower part have sufficient strength to prevent slipping [1]. From the analytical study it was found that the structural performance of steel encased beam with normal steel plates is satisfactory and has a comparable load carrying capacity with the conventional steel encased beam like varus type [5, 6] and valgus type [2, 3] top flanges.

In this study, the performance of SUSCCB with different profile shapes of cold formed steel like rectangle, trapezoid of the beam is studied by using non-linear static analysis. The load carrying capacity of the SUSCCB with different profile shapes is compared to that of the U-shaped steel-encased concrete composite beam having normal shaped steel plate.
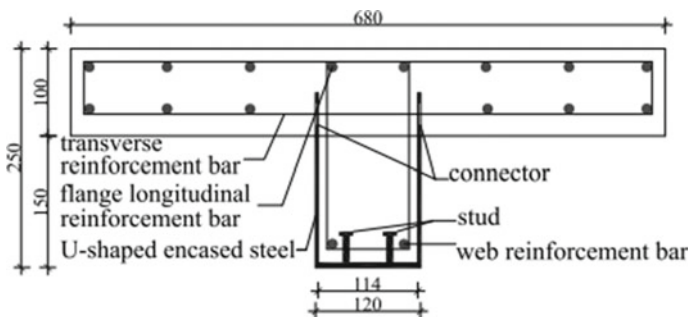
Fig. 1 Details of the model with normal steel plate [4]

2   Finite Element Formulation

To study the performance of the U-shaped steel encased concrete composite beam with straight sides, finite element analysis was performed in ANSYS workbench 2021 R2. The model is chosen based on the information in the earlier studies work [4]. Figure 2 shows the finite element model.

2.1   Geometric Description

The beams are of size 150×120 mm. The model is provided with 14, 6 mm diameter reinforcement bars in the flange and two 6 mm diameter reinforcement bars in the web. The perforations on the U-shaped steel plate are 25 mm in diameter and 160 mm apart in the longitudinal direction. Headed studs are provided in the steel plate for the proper connection between U-shaped steel and concrete web. The studs are 50 mm long and 16 mm in diameter, with a spacing of 160 mm. Concrete has a compressive strength of 50.8 MPa. Cross section of the plate with corrugations is shown in Fig. 3. All measurements are in mm. Two different shapes of cold formed steel i.e., rectangle and trapezoid shape are provided in the bottom steel plate as the bottom of beam is subjected to tension. In each shape, number of corrugations is varied by keeping the depth of corrugation constant.

2.2   Material Properties

Concrete has a compressive strength of 50.8 MPa. The properties of the material used in ANSYS modelling are described in Tables 1 and 2.

Fig. 2 Finite element model of SUSCCB with normal steel plate
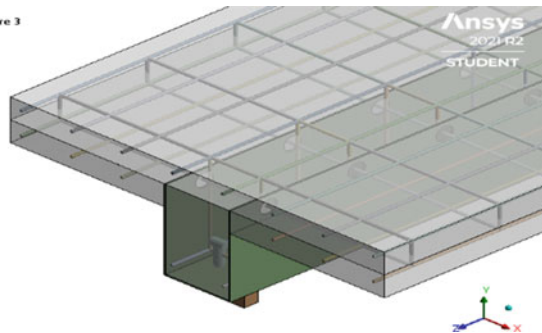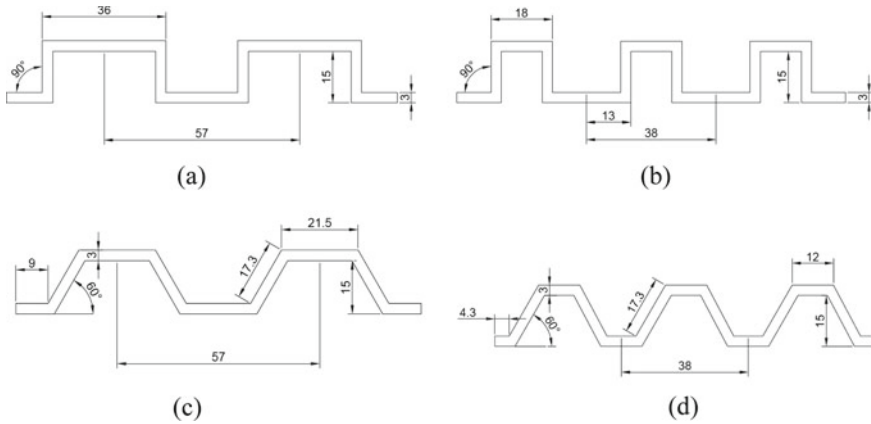
Fig. 3 Corrugated steel plate cross section **a** rectangular profiled steel plate with 2 corrugations **b** rectangular profiled steel plate with 3 corrugations **c** trapezoid profiled steel plate with 2 corrugations **d** trapezoid profiled steel plate with 3 corrugations

Table 1 Material properties of steel

Material	Diameter/Thickness (mm)	Poisson's ratio	Yield strength (MPa)	Young's modulus (MPa)
Steel	3	0.3	466	2×10^5
Rebar	6	0.3	390	2×10^5

Table 2 Material properties of concrete

Material	Compressive strength (MPa)	Poisson's ratio	Young's modulus (MPa)
Concrete	50.8	0.2	33,575

2.3 Finite Element Modelling

All engineering data was used to develop the geometry. All the model comprises of a beam, slab, steel plates, and shear studs. Five U-shaped steel encased concrete composite beams were investigated. One model with normal steel plate were developed. Two different shapes of cold formed steel i.e.; rectangle and trapezoid shape are provided in the bottom steel plate. In each shape two models were created by varying number of corrugations. Each model has two 3000 mm spans with a total length of 6000 mm and different profile shapes of cold formed steel are provided. Element shape of meshing is hexahedron and element size is 25 mm. Concrete and steel plates are modelled using SOLID185 element. SOLID185 is an element for modelling solid structures in three dimensions. It consists of eight nodes each with three degrees of freedom: translations in the nodal x, y, and z directions. The REINF 264 element is used for rebar. The element can be used to simulate reinforcing fibres

Figure

■ Symmetry Region
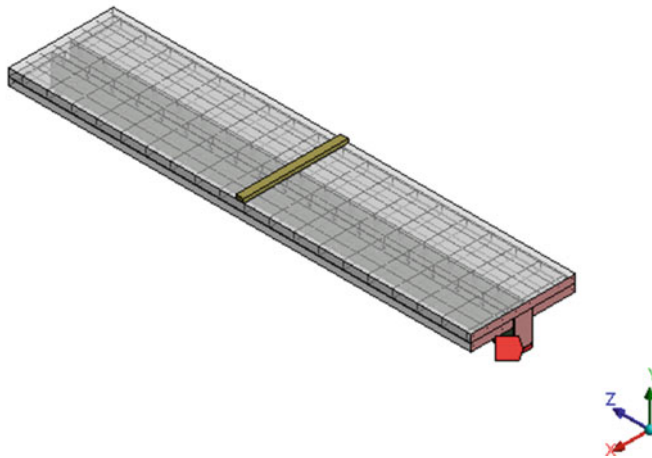
Fig. 4 Model considered as half symmetry

of any orientation. For simplicity, only half of the model was considered in the modelling due to symmetry geometry (Fig. 4). Models were varied by providing different shapes of bottom steel plate and number of corrugations at bottom of the beam. Steel plate of 3 mm thickness were adopted. Figure 5 shows various SUSCCB with different profile shaped steel plates.

2.3.1 Support and Loading

The model was given simply support conditions at the bottom of the beam. A vertical displacement of 100 mm was provided at the top surface as point load at the centre of the span. For determining load carrying capacity of model with normal steel plate, RC2-t3, RC3-t3, RC3-t3, TC2-t3 and TC3-t3, displacement-controlled method was applied. Figure 6 depicts the loading and support conditions.

3   Results and Discussions

The failure patterns for all types of SUSCCB are investigated. For each model, force reaction and deformation were calculated, and load deformation curves were plotted. Figure 7 shows the deformation pattern under loading for the model with normal steel plate. The load carrying capacity for the models TC2-T3 and TC3-t3 were 454.96 kN and 479.24 kN respectively. Model having trapezoidal shape steel plate with three corrugations (TC3-t3) has the highest load carrying capacity of 479.24kN compared to the model having normal steel plate having a value of 300.22
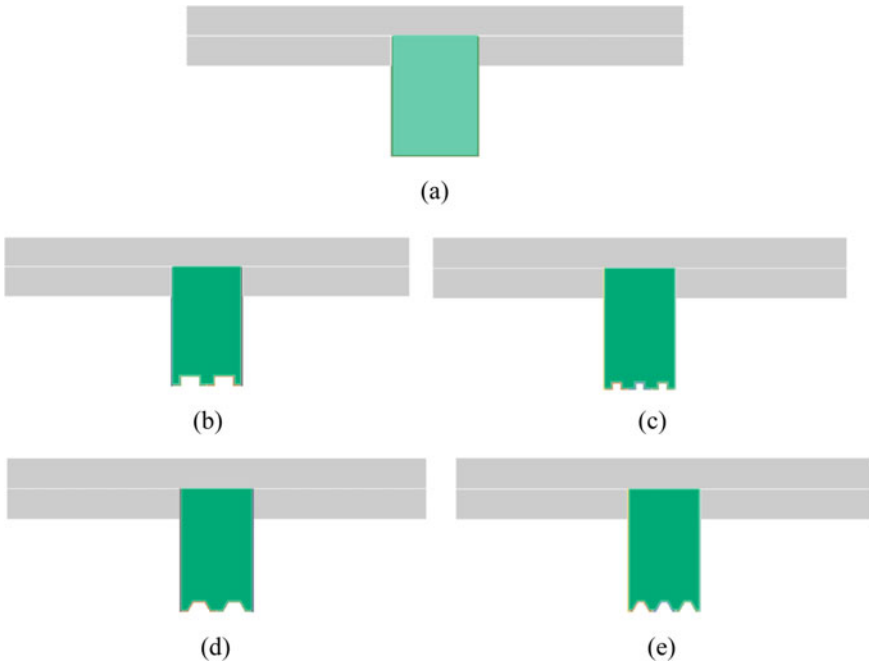
Fig. 5 Front view of SUSCCB models with **a** normal shaped steel plate at bottom **b** rectangular shaped steel plate at bottom with two corrugations (RC2-t3) **c** rectangular shaped steel plate at bottom with three corrugations (RC3-t3) **d** trapezoid shaped steel plate at bottom with two corrugations (TC2-t3) **e** trapezoid shaped steel plate at bottom with three corrugations (TC3-t3)
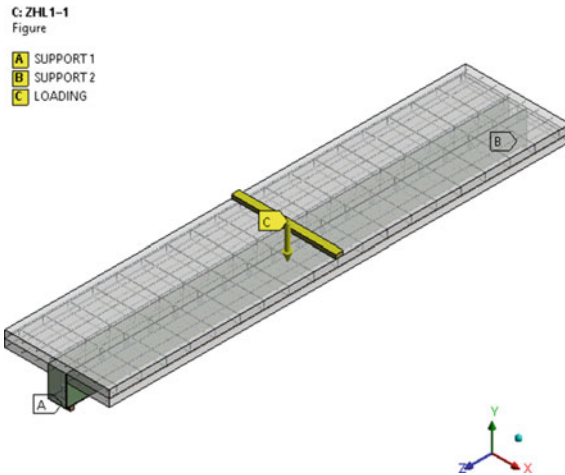
Fig. 6 Loading and support condition

kN (Fig. 8). Comparing the model having normal steel plate and rectangular profile steel plate, highest load carrying capacity of 519.60 kN is obtained for rectangular steel plate with 3 corrugations (Fig. 9). Of all the models, rectangular shape with three corrugations has the highest load carrying capacity. The reason for increased load carrying capacity may be due to the profiled shape of the steel plate that holds the concrete properly. Also, from various previously conducted studies it is obtained that presence of corrugations will increase the beam's stability against local buckling and also against lateral-torsional buckling. Figure 10 depicts the load comparison results of all the models.
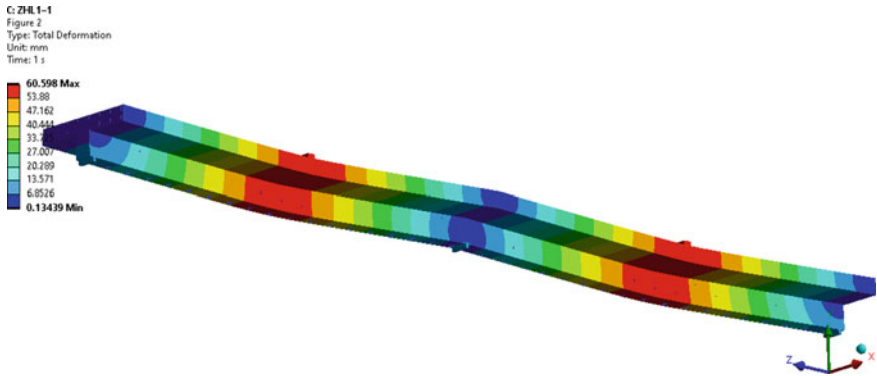
Fig. 7 Total deformation of model with normal steel plate
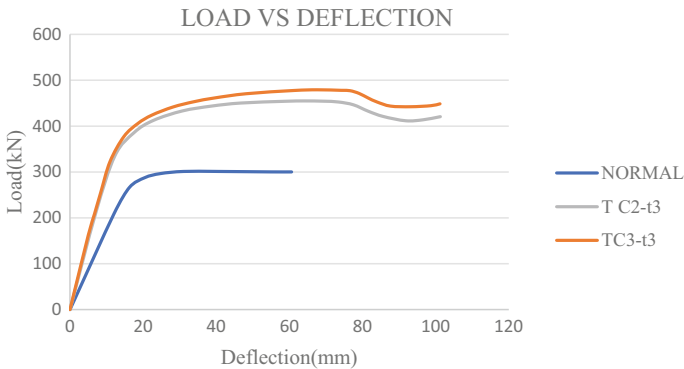
Fig. 8 Load vs deformation comparison between normal steel plate and trapezoidal profiled steel plate
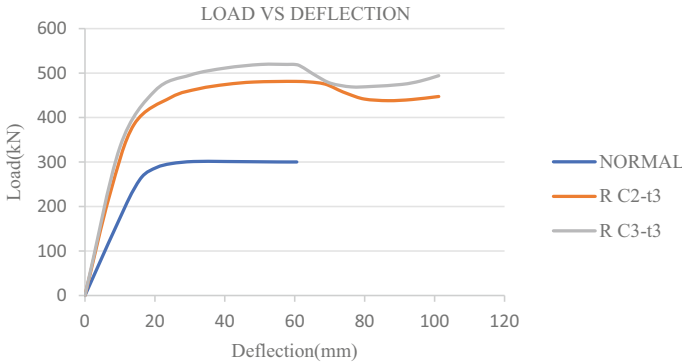
Fig. 9 Load vs deformation comparison between normal steel shape and rectangular profiled steel plate
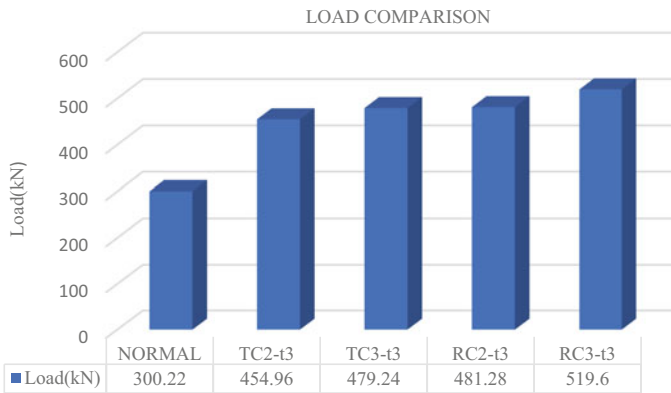
Fig. 10 Load comparison

4 Conclusion

In SUSCCB, the U-shaped steel plates are fully encased in the concrete flange. Composite action of the beam is developed with the help of reinforcing bars that are passed through perforations provided in the steel plates at the top region. The U section's upper straight sides strengthen the web's contact to the flange and provide stability throughout the beam's building phase and also the perfobond connectors have adequate capacities against uplifting and slipping between the concrete flange and the lower section that includes the U-shaped steel plate, encased concrete, and web reinforcement bars. Using ANSYS Workbench, an analytical study was conducted on SUSCCB with profiled shaped steel plates by varying the number of corrugations. Corrugated shapes have a high resistance to shear buckling, a significant load carrying capacity, and the ability to adjust the member's bending moment.

Corrugated web profiles are less expensive than traditional plates and have a better structure. Based on the load deflection results, it is obtained that the bottom steel plate of the beam with profile shapes has more load carrying capacity than with normal steel plate. Compared against normal SUSCCBs: for similar area of steel plate, load carrying capacity are higher. It can be seen that compared to the normal U-shaped steel encased concrete composite beam with straight sides, the load carrying capacity of TC3-t3 increased by a percentage of 59.62% and of TC2-t3 increased by 51.54%. The load carrying capacity of RC3-t3 increased by a percentage of 73.07% and of RC2-t3 increased by 60.3%. Thus, it is concluded that by increasing number of corrugations of profile shapes, the load carrying capacity increases. Also, by comparing the load carrying capacity of normal, rectangular and trapezoid, rectangular with three corrugations has high load carrying capacity of 519. 60 kN. According to the study's test results, the model with more number of corrugations had a higher load carrying capacity. It can be concluded that by providing profile shapes to the steel plate of the beam, load carrying capacity can be increased and they are also competitive with normal SUSCCB of similar strength and coverage area.

References

1. Liu, Y., Xin, H., Liu, Y.: Experimental and analytical study on shear mechanism of rubber-ring perfobond connector. Eng. Struct. **197**, 109382 (2019)
2. Nakamura, S.I.: Bending behaviour of composite girders with cold formed steel U section. J. Struct. Eng. **128**(9), 1169–1176 (2002)
3. Nakamura, S.I.: New structural forms for steel/concrete composite bridges. Struct. Eng. Int. **10**(1), 45–50 (2000)
4. Yan, Q., Zhang, Z., Yan, J., Laflamme, S.: Analysis of flexural capacity of a novel straight-side U-shaped steel-encased concrete composite beam. Eng. Struct. **242**, 112447 (2021)
5. Zhao, Y., Zhou, X., Yang, Y., Liu, J., Chen, Y.F.: Shear behaviour of a novel cold-formed U-shaped steel and concrete composite beam. Eng. Struct. **200**, 109745 (2019)
6. Zhou, X., Zhao, Y., Liu, J., Chen, Y.F., Yang, Y.: Bending experiment on a novel configuration of cold-formed U-shaped steel-concrete composite beams. Eng. Struct. **180**, 124–133 (2019)

Structural Behaviour of Tapered Piles Under Imperfection Scenario

Nithya Baby and P. E. Kavitha

Abstract Piles are those long structures constructed of concrete, steel, wood, or polymer that are used to carry structural stresses from soft clays or loose sands to deeper rock or hard soil layers. Tapered piles are found to be a cost-effective alternative to cylindrical piles. So it is vital to establish the structural performance of tapered piles. During manufacturing, transporting, or installation processes geometric imperfections may occur and these imperfections are unavoidable in the piles. Thus buckling analyses of tapered piles with nonlinear pile-soil interactions and geometric imperfections is an important factor to be considered. This study focuses on structural behaviour of tapered piles under imperfection scenario. In order to investigate the buckling response of straight and initially bent, i.e., geometrically imperfect, end-bearing piles in soil subjected to axial load, 3D Finite Element analyses have been performed herein for steel piles using ANSYS software. Test results of the study shows that tapered piles outperform standard cylindrical piles in terms of axial and lateral load resistance. The analyses results also show that the load-carrying capacity of the piles decreases with increasing pile curvature.

Keywords Tapered pile · Curved pile · Elastic–Plastic material · Finite-Element (FE) analysis · Geometric imperfections · Nonlinear buckling

1 Introduction

Pile foundations are extensively used in many civil structures to support vertical and lateral loads. Piles are long, slender elements constructed of concrete, steel, wood, or polymer that are used to carry structural stresses from shallow depths where soft clays or loose sands exist into deeper rock or hard soil layers. Classical bearing capacity failure, i.e., plunging of the pile into soil due to loss of bearing capacity, structural failure, i.e., crushing or yielding of the pile cross section upon loading, movement of a pile foundation under eccentric axial loading, shear and bending failure of a

N. Baby (✉) · P. E. Kavitha
Department of Civil Engineering, FISAT, Angamaly, India
e-mail: nithyababy11@gmail.com

pile, overall stability failure of a pile due to the development of a failure mechanism enveloping the pile foundations are the major causes of failure for a pile under axial loading [1]. Buckling is one of the most common types of failure for lengthy piles. Buckling failure of thin piles can occur due to the effect of axial stress on the pile and the loss of surrounding confining pressure provided by the earth, or due to severe corrosion. Slope movement and seismic loading create lateral loading and cause an increase in the lateral deflections of the pile, which can lead to buckling failure even at low axial loads. Out-of-line straightness in the pile, which can occur as a result of the pile-driving technique employed during pile installation or the presence of boulders beneath the pile, increases lateral deflection and the chance of pile buckling. Plastic hinges in the pile may also fail due to buckling failure, resulting in the structure collapsing [1].

Efficiency of driving a pile in field is not only affected by soil parameters, but also by pile geometry including the pile shape and taper angle [4]. Jian-Hong Wan present a non-prismatic beam-column element for nonlinear buckling analysis, considering nonlinear pile-soil interactions and combined external loads to robustly and efficiently simulate the buckling response of tapered piles [5]. Joon Kyu Lee presents a novel unified model to analyze the free vibration and buckling of partially embedded end-bearing piles subjected to axial compressive load. Consideration is given to the tapered piles of variable cross-sectional shape with constant volume [6]. Joon Kyu Leea, developed an analytical model to estimate the buckling behavior of tapered friction piles fully embedded in inhomogeneous soil. In frictional grounds, tapered piles with a greater cross-section at the pile head than at the tip are usually used to attain high compressive bearing capabilities [7]. The process and efficiency of pile driving are influenced not only by soil characteristics, but also by pile geometry, such as pile shape and taper angle. Hammer blow counts, penetration, and pile velocity developed during driving are all significant effective elements in pile driving [4].

2 FE Model Validation

Mohammad Nadeem [1] conducted a study on nonlinear buckling analysis of straight cylindrical piles with geometric imperfections. 3D-FE analyses have been performed herein for steel piles of 10 m length. In the analysis three different initial bent amplitudes 'a', e.g., 50, 100, and 150 mm were used. In order to validate the results a model have been developed and the results were compared. The model selected for the validation is having a quarter-sine profile and is having an initial bent of 50 mm. The results obtained from analysis shows that the maximum axial load is slightly higher for the model developed (372t, 1t = 9.96 kN) than the study conducted by Nadeem (360t) [1]. The difference between these two curves is 3.22% which is less than 10% and is acceptable. Figure 1 shows the deformation pattern and the load comparison.

(a)   (b)
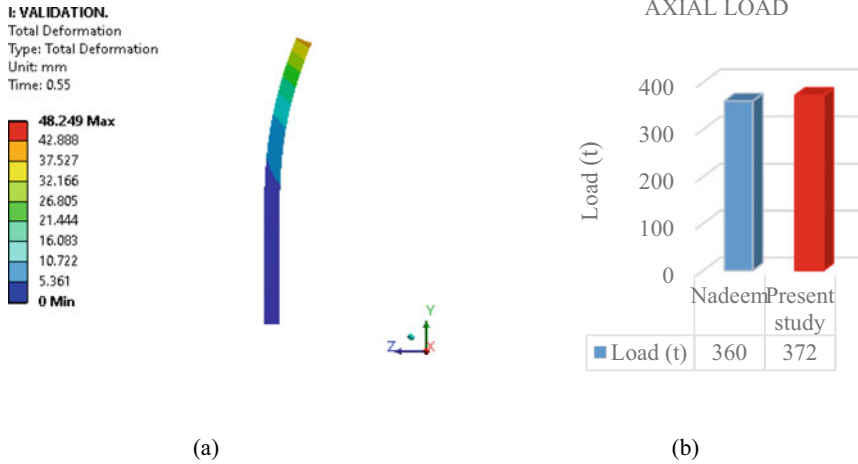
Fig. 1 a Deformation of QS 50 mm and b Axial load comparison

3 Comparison of Cylindrical and Tapered Piles

Structural behaviour of cylindrical and tapered piles have been studied using a linear buckling analysis. 3D-FE analyses have been performed herein for steel piles of 2.5 m length. The cylindrical pile taken for analysis is having a diameter of 162 mm [4]. The volume of the pile is thus 0.051 m^3. The volume of the tapered pile is taken as the same and thus the top and bottom diameter of the pile is calculated as 202 and 115 mm respectively. Two types of soils were considered, i.e. very loose sandy soil and soft clayey soil. The material property of the soil is as obtained from the Lassaad Hazzar and Mahmoud N. Hussein [8]. Density of both soil is taken as same and friction angle is taken as 26 and 0 respectively. Thus four models have been developed, i.e. cylindrical (C) and tapered pile (T) with each soil condition. Analysis results shows that tapered piles have more resistance to axial load, with a percentage load increment of 3.83% and 3.56% for the clayey and sandy soil condition respectively (Fig. 2).
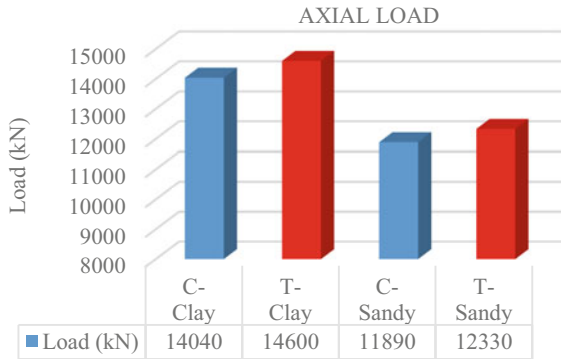
Fig. 2 Axial load comparison of piles

4   Finite Element Formulation

A lot of studies were carried out to evaluate buckling analysis of piles. Since tapered pile have superior benefit over the cylindrical pile it is necessary to conduct analyses on tapered pile. In order to investigate the buckling response of straight and initially bent, i.e., geometrically imperfect, end-bearing piles in soil subjected to axial load, FE modelling was done in ANSYS workbench.

4.1   Geometric Description

Three-dimensional Finite Element analyses have been performed herein for tapered steel piles of 10 m in length. A tapered pile with a top diameter of 0.8 m and a bottom diameter of 0.5 m was evaluated. The pile taken for the analysis is partially embedded in the soil as shown in Fig. 3. The top 2 m of the pile is above the soil. The next 4 m of the pile is inside the SAND 1, i.e. brown medium fine, loose with some fine gravel and traces of silt. The next 2 m of the pile is embedded in SAND 2, i.e. brown, fine grained, medium dense, silty with some gravel. And the bottom 2 m of the pile is surrounded by SAND 3, i.e. gray, fine grained, medium dense, silty with some gravel [2].

In reality, piles are not perfectly straight. So while calculating the critical buckling load of piles, geometric imperfections must be taken into account. As reported by Nadeem [1] there are mainly two typical initially bent profiles while considering the geometric imperfections, i.e., quarter sine profile (QS), as represented by (Fig. 4a), and half sine profile (HS) (Fig. 4b) [3]. These two initially bent profiles can be characterized numerically by defining the pile node coordinates, and the x-coordinate can be determined using "Eqs. (1) and (2)" as follows:
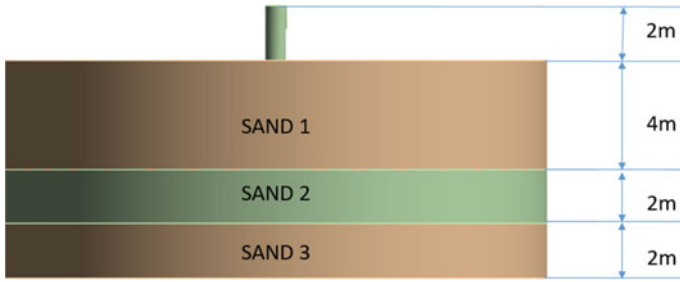
Fig. 3 Soil layers at different depths

(a) Quarter sine profile   (b) Half sine profile
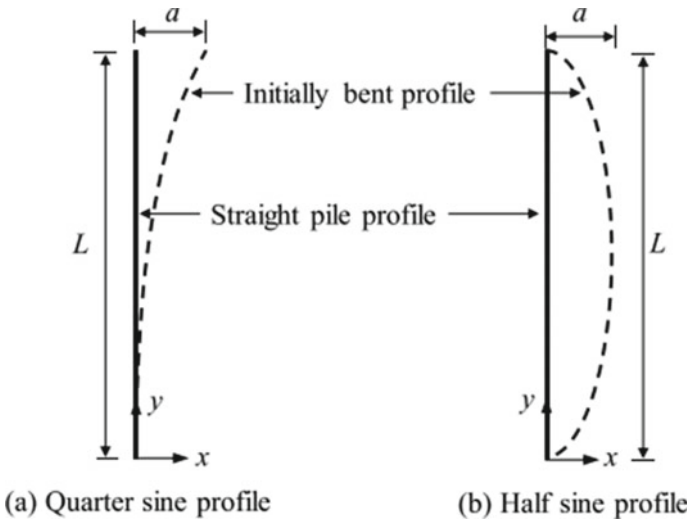
Fig. 4 Two typical initially bent pile profiles: **a** Quarter-sine profile; and **b** Half-sine profile [3]

$$x = a\,sin\frac{\pi y}{2L}\,(\text{For quarter} - \text{sine profile}) \tag{1}$$

$$x = a\,sin\frac{\pi y}{L}\,(\text{For half} - \text{sine profile}) \tag{2}$$

where 'a' is the initial imperfection amplitude, L is the length of pile (Fig. 4) [3].
Three alternative initial bent amplitudes e.g., 50, 100, and 150 mm (considered as
being practically possible to occur) were used in this here. Table 1 gives x and y
values. Five points were taken along the length of the pile and the respective y values
were calculated using the equation for both QS and HS profiles.

Table 1 Node coordinates of pile

y (m)	x (mm)					
	Half-sine (50 mm)	Half-sine (100 mm)	Half-sine (150 mm)	Quarter-sine (50 mm)	Quarter-sine (100 mm)	Quarter-sine (150 mm)
0	0	0	0	0	0	0
2.5	35.35	70.71	106.06	19.13	38.26	57.4
5	50	100	150	35.35	70.71	106.06
7.5	35.35	70.71	106.06	46.19	92.38	138.58
10	0	0	0	50	100	150

Table 2 Material properties of pile used in the proposed model [1]

Material	Density of pile ρ (kg/m^3)	Young's modulus E (GPa)	Poisson's ratio v	yield stress σ_y (MPa)
Steel pile	7850	200	0:3	200

Table 3 Material properties of sands used in the proposed model [2]

Property	SAND 1	SAND 2	SAND 3
Young's modulus, E (MPa)	9.32	15.20	18.12
Poisson's ratio, v	0.29	0.29	0.29
Cohesion (MPa)	0.1	0.1	0.1
Angle of friction, φ (deg)	34	38	42

4.2 Material Properties

A multilinear stress strain curve was assumed for modeling the materials. Tables 2 and 3 gives the material property of the pile and the soil used in the present study.

Herein, both the soil and the pile have been considered as linear elastic perfectly plastic materials. The Mohr–Coulomb material model was used to simulate the stress–strain behaviour of soil.

4.3 Finite Element Modeling

Modeling in ANSYS includes providing appropriate elements, defining geometry and assigning suitable material models. A total of seven finite element models were created. The models with two type of bent profile such as quarter sine and half sine bent profiles were analysed. In each case three different initial bent amplitudes 'a', e.g., 50, 100, and 150 mm were developed and also a straight tapered steel pile was modelled. Figure 5 shows the model of QS and HS with a = 150 mm.
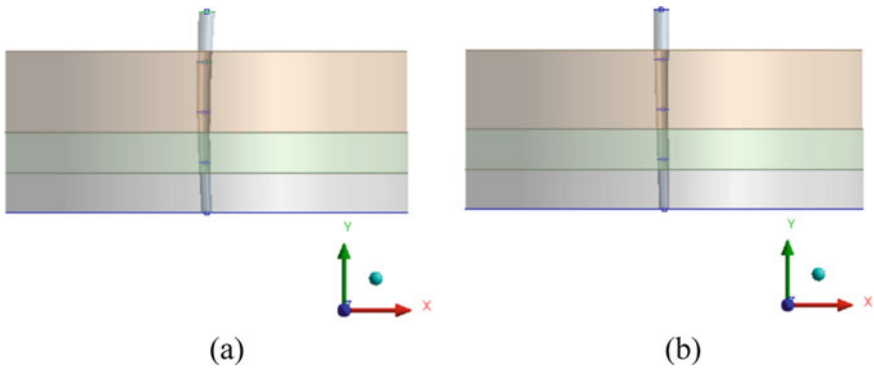
Fig. 5 Models **a** HS 150 mm and **b** QS 150 mm

The proposed models consist of tapered steel pile and 3 layers of soil. The elements are modeled using SOLID 186 element. SOLID 186 is a 3-D 20-node solid element that exhibits quadratic displacement behavior. The element is made up of 20 nodes, each of which has three degrees of freedom: translations in the nodal x, y, and z dimensions. It is well suited to model irregular meshes. Shape of meshing was hexahedron.

4.4 Support Condition and Loading

The model was made in the ZX plane. Fixed support is provided at the bottom end and thus all the motions are restricted. In the top end of the pile as shown in Fig. 6, load is applied axially downward in Y direction and translation is allowed in the X and Y direction. Rotational motion along X direction is permitted and it is restrained in the Y and Z direction. A displacement of 100 mm was provided at the tip of the pile in the form of load. The displacement value provided is obtained by trial –and-error method.

5 Results and Discussion

The models with two type of bent profile such as QS and HS profiles with three different initial bent amplitudes 'a', e.g., 50, 100, and 150 mm were analysed and failure patterns were obtained for all the models. Force reaction and corresponding deformation were noted for all the models. Load–deformation curves were also plotted for the same. The deformation pattern of HS 50 mm under axial loading is as shown in the Fig. 7.

H: STRAIGHT PILE
load
Time: 1. s

load
Components: Free,-200.,Free mm
Rotation: Free, 0., 0. °
Location: 50., 10000., 2.6015e-015 mm
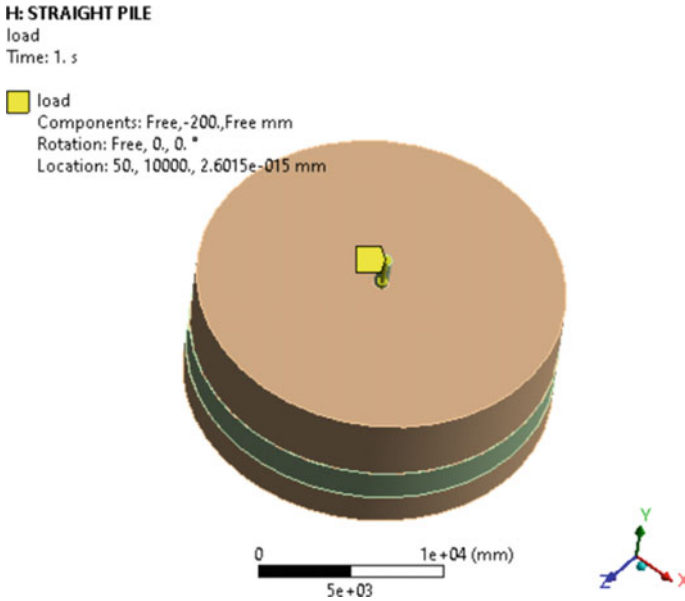
Fig. 6 Boundary condition of models

(a)   (b)
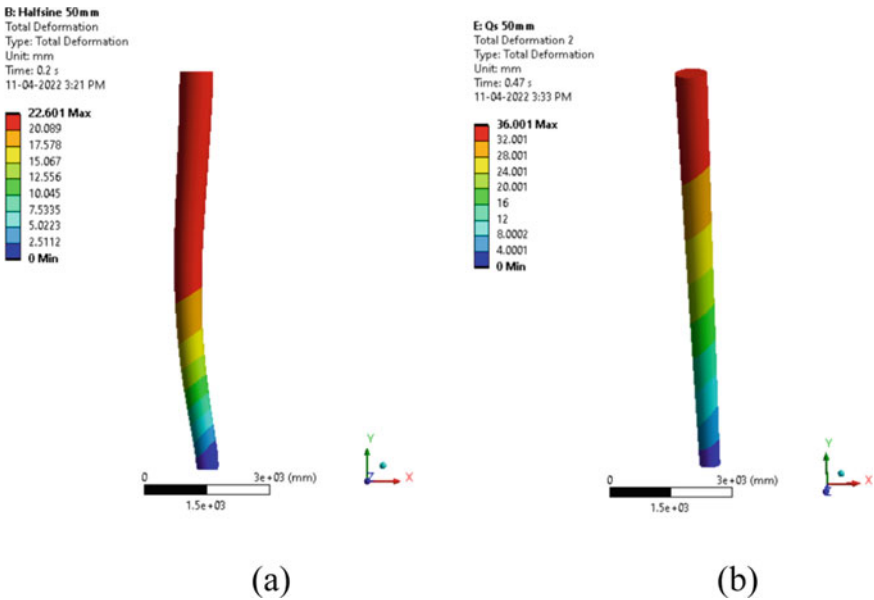
Fig. 7 Deformation of **a** HS-50 mm and **b** QS-50 mm
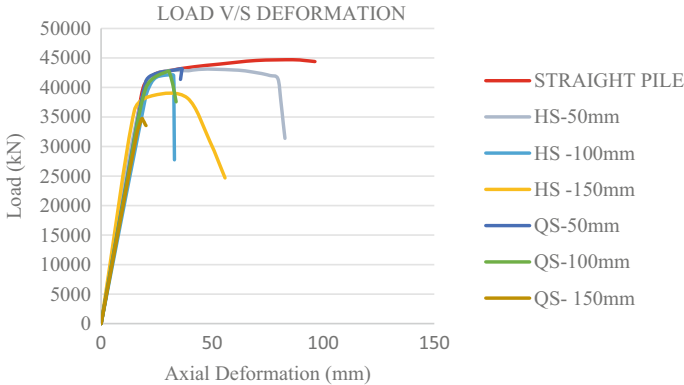
Fig. 8 Load v/s axial pile head deformation

The straight pile model exhibited highest deformation with a value of 86.22 mm and lowest deformation of 18.36 mm was exhibited by the model QS-150 mm. The deformation patterns obtained for the models shows that it decreases with the increase of pile curvature for both QS and HS.

The load vs. deformation curve for an axial pile head deformation produced from the analysis is shown in Fig. 8. The graph clearly indicates that model without initial bent have higher load carrying capacity and piles with a half-sine bent show lower load-carrying capacity as compared with that for quarter-sine bent piles for 50 and 100 mm analyses. A percentage decrease in the axial load carrying capacity of about 3.9%, 5.78% and 13.51% is obtained for HS and of 3.44%, 4.35% and 22.2% for QS with initial bent of 50,100 and 150 mm respectively. Figure 9 indicates load v/s deformation curve for a lateral pile head deformation obtained from the analysis and similar results are obtained. Figure 10 shows the load comparison of various models. Tapered pile without initial bent has the highest load carrying capacity when compared to all other models having initial bent. Results shows that the load-carrying capacity of the piles decreases with increasing pile curvature.
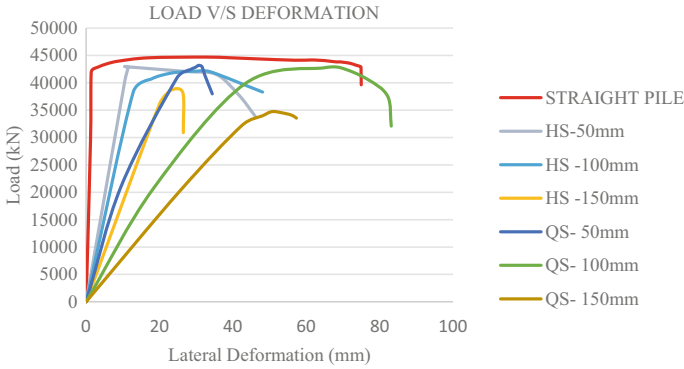
Fig. 9 Load v/s lateral pile head deformation
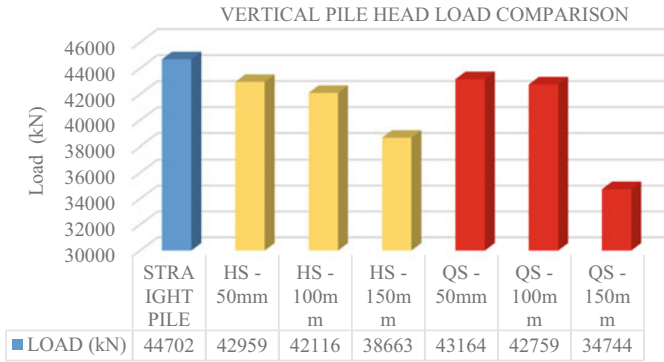
Fig. 10 Load comparison

6 Conclusion

Structural behaviour of partially embedded tapered steel pile under axial loading is investigated analytically in this paper. One of the goal was to check whether tapered piles outperform standard cylindrical piles in terms of axial load resistance. Another goal was to analyze the structural behaviour of tapered pile with and without an initial bent. According to the findings, tapered piles are more resistant to axial load than cylindrical piles. It is also found that the load-carrying capacity of the straight piles is always higher than the pile with the initial bent regardless of how small the initial bent is. Based on the analytical results obtained, the conclusion can be summarized as follows:

1. In the analysis of cylindrical and tapered pile under clayey and sandy soil condition, it is observed that tapered piles have more resistance to axial load, with a percentage load increment of 3.83 and 3.56% for the clayey and sandy soil condition respectively.

2. In the analysis of tapered piles with and without initial bent, it is observed that the load carrying capacity of the straight piles is always higher than the pile with the initial bent regardless of how small the initial bent is.
3. From the analysis it is inferred that by increasing amount of initial bent, the axial ultimate load-carrying capacity of piles decreases considerably.
4. The result shows that percentage decrease in the load carrying capacity of a pile with half sine profile is 3.9, 5.78 and 13.51% for 50, 100 and 150 mm initial bent respectively when compared to the straight tapered pile (i.e. without bent).
5. The result shows that percentage decrease in the load carrying capacity of a pile with quarter sine profile is 3.44, 4.35 and 22.28% for 50, 100 and 150 mm initial bent respectively when compared with the straight tapered pile.
6. Piles with a bent show a smaller load-carrying capacity compared with that for a quarter-sine bent pile for 50 and 100 mm analysis.
7. The results shows that the percentage increase in the load-carrying capacity of quarter sine when compared to half sine bent for 50 and 100 mm initial bent is 0.47 and 1.5% respectively.

References

1. Nadeem, M., Chakraborty, T., Matsagar, V.: Nonlinear buckling analysis of slender piles with geometric imperfections. J. Geotech. Geoenviron. Eng. **141**(1), 06014014 (2015)
2. Abyaneh, M.J., El Naggar, H., Sadeghian, P.: Numerical modeling of the lateral behavior of concrete-filled FRP tube piles in sand. Int. J. Geomech. **20**(8), 04020108 (2020)
3. Zhang, X., Tang, L., Ling, X., Chan, A.: Critical buckling load of pile in liquefied soil. Soil Dyn. Earthq. Eng. **135**, 106197 (2020)
4. Tavasoli, O., Ghazavi, M.: Effect of tapered and semi-tapered geometry on the offshore piles driving performance. Ocean Eng. **201**, 107147 (2020)
5. Wan, J.H., Liu, S.W., Li, X.Y., Zhang, L.M., Zhao, H.P.: Buckling analysis of tapered piles using non-prismatic beam-column element model. Comput. Geotech. **139**, 104370 (2021)
6. Lee, J.K.: A unified model for analyzing free vibration and buckling of end-bearing piles. Ocean Eng. **152**, 17–25 (2018)
7. Lee, J.K., Jeong, S., Kim, Y.: Buckling of tapered friction piles in inhomogeneous soil. Comput. Geotech. **97**, 1–6 (2018)
8. Hazzar, L., Hussien, M.N., Karray, M.: Influence of vertical loads on lateral response of pile foundations in sands and clays. J. Rock Mech. Geotech. Eng. **9**(2), 291–304 (2017)

Study on Structural Behaviour of Fully Bolted Beam Column Joints in Modular Steel Buildings

M. Thamis, Keerthy M. Simon, and J. Bharati Raj

Abstract The importance of modularized pre-fabricated steel buildings has been rising in construction due to its high speed of construction, degree of industrialization, low labour intensity etc. Joints are the most critical sections in a pre-fabricated modular steel structure. Conventionally used joints are welded connection or a combination of welded connections and bolts. The main advantage of steel over concrete in small buildings is it can be re-assembled and can be reused, but the use of welded connections in joints makes the dismantling process a heavy task and it may even lead to change the properties of the section. This has led to the use of a fully bolted connection at these joint. Beam through joint is considered for analysis, the columns are attached to beam at these joints by a base plate and stiffeners. This study focuses in identifying the improvement in bearing capacity and seismic performance of these bolted joint. Bearing capacity is improved by stiffening methods that is by using external stiffeners in both web and flange of the beam and column and seismic performance is improved by introducing reduced beam section concept. Various models are modelled and analysed analytically using ANSYS 2021 R2.

1 Introduction

Steel is one of the most regularly used building materials. Steel constructions are vulnerable to a variety of environmental factors. Steel is increasingly being used in development projects and civil engineering-related fields all around the world. The use of steel in developing structures has become common practice. Quick coupling and good seismic performance are important features of column joints in steel structures. Compared with web-bolted flange joints, no welding is required in the area, and can be used in multi-storey buildings. Therefore, the study was conducted on the need for a joint development of a fully integrated bolt column, aimed at providing pre-built multi-storey buildings without compromising on their beauty, service, strength, stability, and earthquake performance. The main objective of this work is to improve

M. Thamis (✉) · K. M. Simon · J. Bharati Raj
Department of Civil Engineering, NSS College of Engineering, Palakkad, India
e-mail: thamiskvk@gmail.com

Fig. 1 Beam through joint
[4]
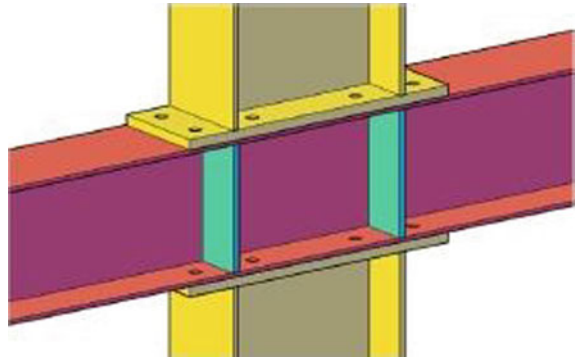
the bearing capacity and seismic performance of joint by parametric study of beam through joints by various strengthening methods like varying plate thickness or by adding stiffeners or endplates or by introducing reduced beam section (RBS).

2 Structure of the Joint

Structure consists of H-steel column and beam, column bottom plate (base plate), and stiffener, etc. The diagram of joints is shown in Fig. 1. The column bottom plate is a rectangular steel plate with bolt holes as per the standard size. In this beam-through joint (JD2) the beam is continuous and columns are attached to the beam using column bottom plate. Dimension of panel zone is same as that of the web of the beam.

3 Numerical Analysis of Beam Through Joint

Modelling is done using ANSYS 2021 R2. Beam column elements are modelled and the material properties are assigned to the sections. Solid 186 is assigned for flange, web and stiffeners and beam 188 is given for bolts. Mesh size of 40 mm is adopted. Hexahedron is the element shape used for modelling.

Tables 1 and 2 shows the details of model geometry and material properties. Figure 2 shows the ANSYS model.

Table 1 Dimensions of joint [4]

Joint	Column (mm)	Beam (mm)	Form of the panel zone	Web thickness in the panel zone (mm)
JD2	$300 \times 150 \times 6.5 \times 9$	$200 \times 150 \times 6.5 \times 9$	Beam through	6.5

Table 2 Material properties of specimen [4]

Component	t (mm)	f_y (N/mm^2)	f_u (N/mm^2)	E_s (Gpa)
Flange	6.5	372.35	541.03	204.9
Web	9	368.73	537.87	204.7
Column bottom plate	15	385.52	539.36	205
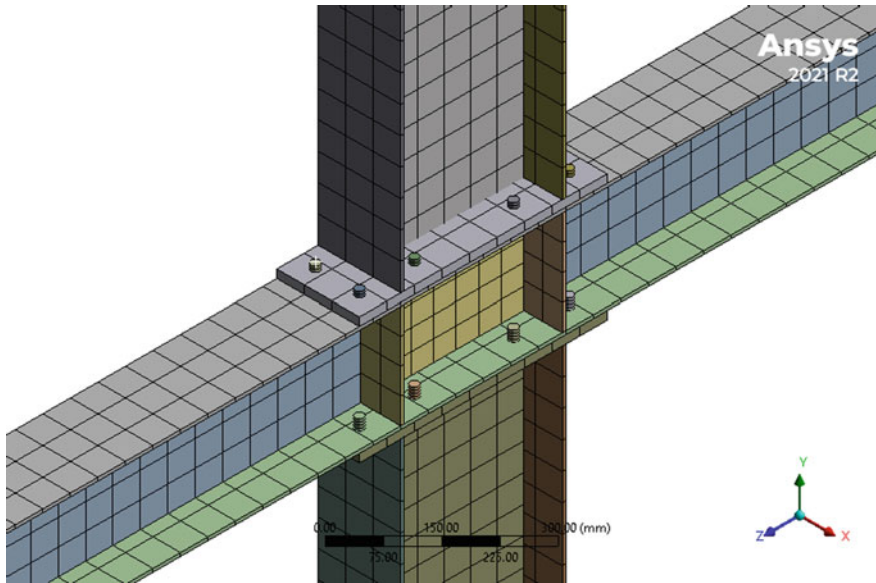
Fig. 2 ANSYS model

The material properties and dimensions of the joint is taken from Zhihua Chen et al. [4].

Boundary conditions are given to the model as bottom of the column is hinged while top of the column is fixed. For the beam cyclic load is given at both the ends as per FEMA 350 (Fig. 3).

A: JD - 2
Figure

A COL-BOTTOM - HINGED
B COL-TOP SUPPORT
C R B CYCLIC LOADING
D L B CYCLIC LOADING
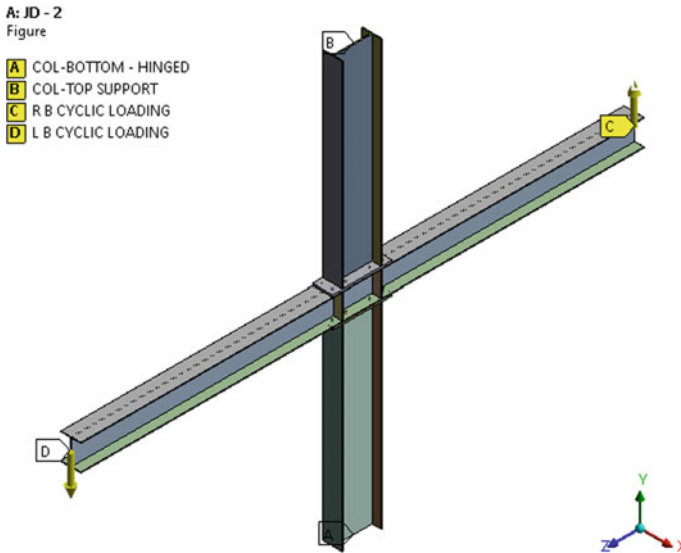
Fig. 3 Support condition

4 Results

The model is analyzed and it is observed that maximum stress concentration is found in panel zone and in the flange of the beam as shown in Fig. 4. Then load-deflection curve of the joint JD2 is plotted and ultimate load is obtained as 22.33 kN and the corresponding deflection is 61.10 mm (Figs. 5 and 6).

5 Parametric Study on Beam Through Joint

Web stiffeners are employed to resist lateral loading of the plate and to prevent plate buckling. The occurrence of web post buckling close to the support region in beams with thin webs subjected to uniformly distributed load is caused by the interaction of normal and shear stresses in this region. If the beam is too short and the applied load approaches its maximum capacity, buckling might occur due to compression of the web post towards the centre of the span. The presence of a web stiffener in the support region has a positive effect in these cases and preventing the web from buckling close to the supports.
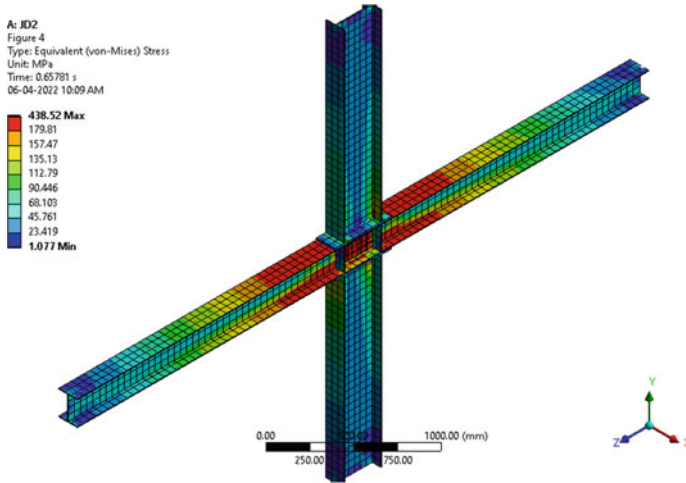
Fig. 4 Stress diagram
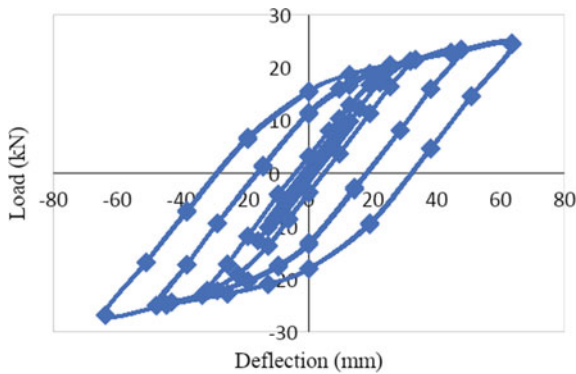
Fig. 5 Hysteretic curve of beam through joint (JD 2)

Further study is carried out for improving the performance on beam through joint by adding web stiffeners in different locations and these structures and modelled and analysed (Table 3 and Fig. 7).

The load–deflection curve is plotted for all models and it is observed that there is increase in deflection when compared with the beam through joint (JD2) and ultimate load is only increased by 10% (Figs. 8, 9, 10 and Table 4).
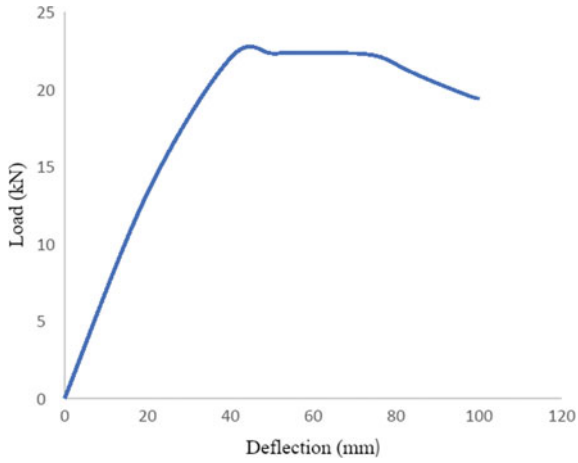
Fig. 6 Skelton curve of beam through joint (JD2)

Table 3 Model details

Model no.	Model name
1	Two vertical stiffeners outside of the panel zone of thickness 6 mm (VS-2-OUT-T6)
2	Inclined stiffeners in the panel zone of thickness 6 mm (IS-IN-T6)
3	Both vertical and inclined stiffeners (VS-2-OUT+IS-IN)
4	Four vertical stiffeners of thickness 6 at 75 mm spacing (VS-4-T6-75)
5	Four vertical stiffeners of thickness 6 at 50 mm spacing (VS-4-T6-50)
6	Four vertical stiffeners of thickness 6 at 25 mm spacing (VS-4-T6-25)
7	Eight vertical stiffeners of thickness 3 at 50 mm spacing (VS-8-T3-50)
8	Eight vertical stiffeners of thickness 3 at 25 mm spacing (VS-8-T3-25)
9	Eight vertical stiffeners of thickness 3 at 75 mm spacing (VS-8-T3-75)
10	Twelve vertical stiffeners of thickness 3 at 75 mm spacing (VS-12-T3-75)
11	Twelve vertical stiffeners of thickness 3 at 50 mm spacing (VS-12-T3-50)
12	Twelve vertical stiffeners of thickness 3 at 25 mm spacing (VS-12-T3-25)
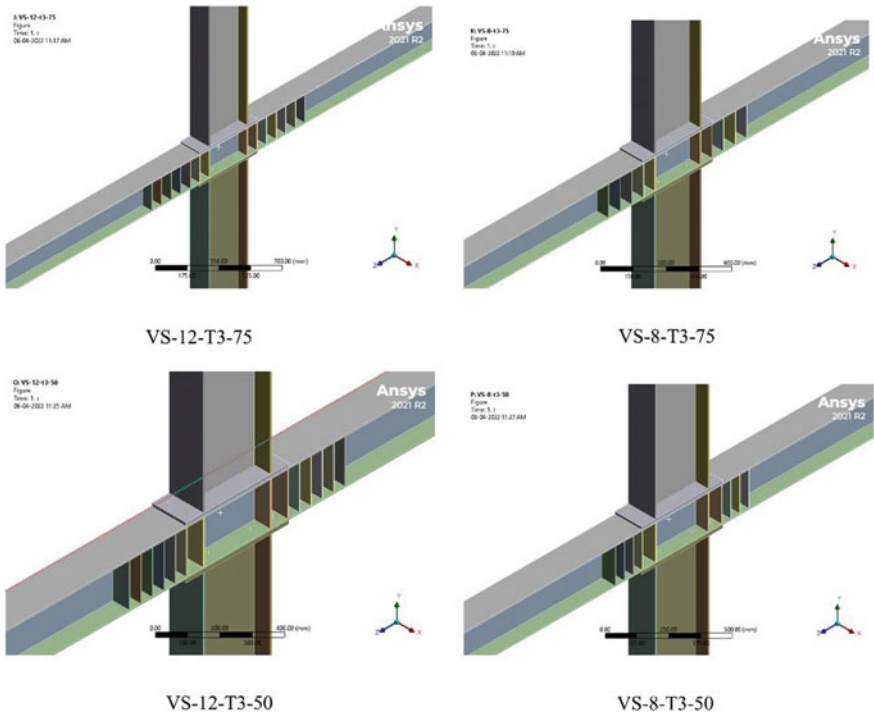
Fig. 7 Figure of models
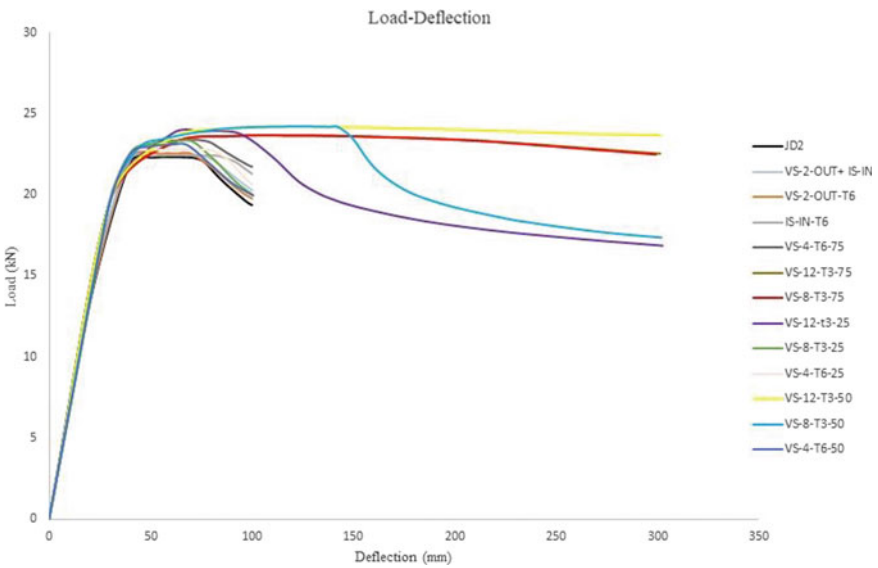
Fig. 8 Skelton curve of all models
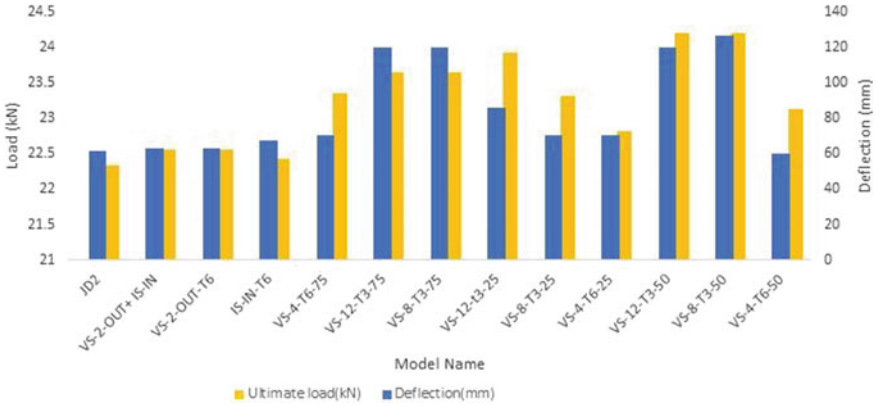
Fig. 9 Maximum deflection and ultimate Load for all models
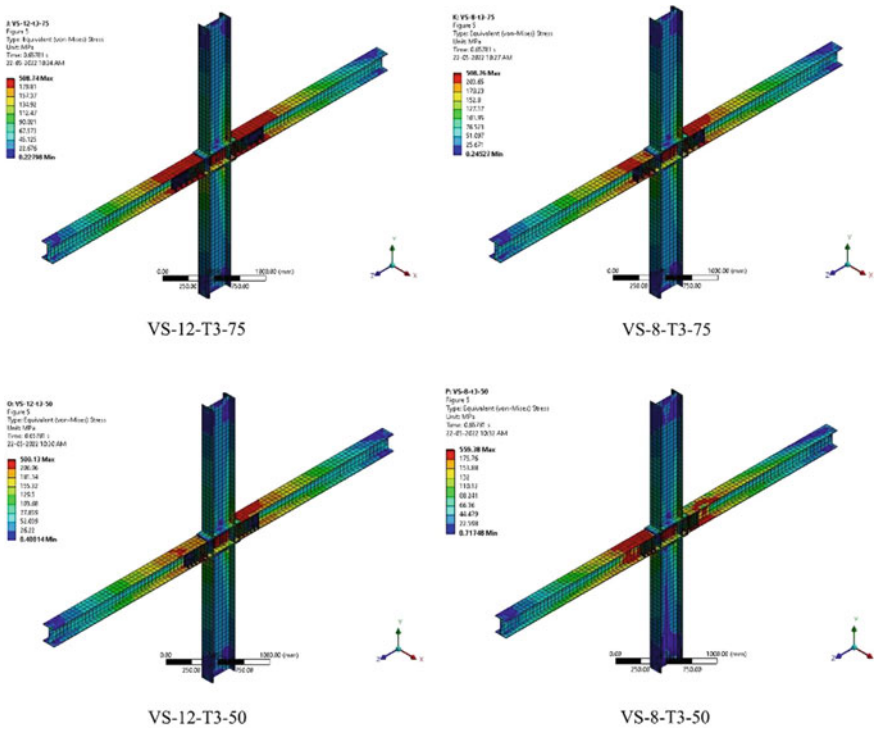
Fig. 10 Stress diagram of models

Table 4 Maximum deflection and ultimate load

Model	Ultimate load (kN)	Ductility index
JD2	22.336	3.050
VS-2-OUT+IS-IN	22.548	3.125
VS-2-OUT-T6	22.553	3.125
IS-IN-T6	22.427	3.337
VS-4-T6-75	23.356	7.000
VS-12-T3-75	23.649	4.001
VS-8-T3-75	23.641	3.996
VS-12-t3-25	23.929	2.850
VS-8-T3-25	23.312	7.000
VS-4-T6-25	22.806	7.000
VS-12-T3-50	24.202	4.001
VS-8-T3-50	24.201	4.225
VS-4-T6-50	23.130	6.000

6   Conclusions

From this study the following conclusions are made;

- Addition of web stiffeners at different locations increases the ratio of ultimate displacement to yield displacement of the joint that is the ductility of the joint is improved.
- The bearing capacity of the joint increased by 10% when compared with beam through joint (JD2).
- The stress diagram of these joints shows that failure first occurs in the flange of the beam, so to increase the bearing capacity of the structure it is required to strengthen the flange of the beam. Further study is to be done for the improvement of flange so that the bearing capacity and seismic performance of the whole structure will be improved.

References

1. William, A., et al.: Lateral behaviour of modular steel building with simplified models of new inter-module connections. Eng. Struct. **236**, 112103 (2021)
2. Mou, B., Liu, X., Sun, Z.: Seismic behavior of a novel beam to reinforced concrete-filled steel tube column joint. J. Constr. Steel Res. **187**, 106931 (2021)

3. Lian, J.-Y., et al.: Numerical analysis on seismic performance of corner fitting connection in modular steel building. Structures **33**, 1659–1676 (2021)
4. Chen, Z., et al.: Seismic study on an innovative fully-bolted beam-column joint in prefabricated modular steel buildings. Eng. Struct. **234**, 111875 (2021)
5. Liu, X.C., Cui, F.Y., Zhan, X.X., Yu, C., Jiang, Z.Q.: Seismic performance of bolted connection of H-beam to HSS-column with web endplate. J. Constr. Steel Res. **156**, 167–181 (2019)
6. Chen, C.-C., Lin, C.-C.: Seismic performance of steel beam-to-column moment connections with tapered beam flanges. Eng. Struct. **48**, 588–601 (2013)
7. Lee, J., Goldsworthy, H.M., Gad, E.F.: Blind bolted moment connection to unfilled hollow section columns using extended T-stub with back face support. Eng. Struct. **33**, 1710–1722 (2011)
8. Gerami, M., Saberi, H., Saberi, V., Saedi, D.A.: Cyclic behavior of bolted connections with different arrangement of bolts. J. Constr. Steel Res. **67**, 690–705 (2011)

Comparative Study on the Modal Parameter of Cracked Beams

Amala Rose James and Sneha M. Varghese

Abstract Crack occurrence is a crucial factor that affects the lifespan of civil structures. Cracks present on the surface of the structural element like beams, accounts changes in stiffness, flexibility and consequently their static and dynamic behaviour is affected. The influence of natural frequencies and modes of vibration of structures have been the subject of many investigations. The damage detection studies contain forward approach and inverse approach. The forward approach involves the determination of dynamic characteristics while inverse approach deals with detecting damage with the help of those characteristics. Forward approach is used in this study. The effect of crack location, crack depth, material and fixity conditions on the changes in natural frequencies of the beam are studied. The finite element analysis of different cases of cracked beam is done using the software Ansys Workbench and the results obtained are compared.

Keywords Damage detection · Mode shape · Modal analysis · Natural frequency

1 Introduction

Nowadays structural health monitoring has high importance for damage assessment and safety evaluation of structures. The objective of structural health monitoring is to detect structural damage at earlier stage to avoid catastrophic failures. Engineering structures when subjected to repeated loading conditions undergoes cracks or damages in overstressed regions. Cracks can be described as unintended discontinuities in structural components [1]. They may occur due to various reasons. Cracks present on the surface of the structural element like beam, causes changes in stiffness, significantly depending upon the characteristics of cracks. Since the behavior of the structures are affected by cracks, it is necessary to detect them.

As the presence of cracks affects the vibration parameters like modal natural frequencies, mode shapes, etc., vibration based crack detection approaches [4] has

A. R. James (✉) · S. M. Varghese
Saintgits College of Engineering (Autonomous), Kottayam, India
e-mail: amalarosejames1998@gmail.com

been discovered by a lot of investigators. The advantages of vibration based technique over other methods are they are quick, non-destructive, economical, identifies more cracks and also detects internal cracks which are not visible to naked eye. Basically crack detection consists of forward problem and backward problem. The forward problem involves determination of various vibrational characteristics while the backward problem focuses on detection of cracks using these vibrational characteristics. So by identifying the changes in natural frequency and mode shapes of structure having cracks, it is possible to detect the cracks in a structure.

Modal analysis refers to the study of the dynamic properties of structures subjected to vibration. The natural frequency and mode shape of a beam like structure is determined by modal analysis. When the structures are subjected to vibration loads, the dynamic response of structures like natural frequencies, mode shape and damping are affected.

The main objective is to study and compare the changes in natural frequency of beams with cracks at different locations, depth, materials and fixity conditions. The study is limited to mode 1 vibration.

2   Validation

Natural Frequencies (NF) and mode shapes of a slender steel beam in healthy condition and beam with cracks at different location and depth were determined by modal analysis. Modal Analysis of Cracked Cantilever Beam was carried out using the software Abaqus by Mia et al. The validation was done using the finite element analysis software Ansys Workbench R19.2. The validation was conducted for 6 cases of beam without crack and beams with crack at different locations and depths. The crack was modelled as a triangular shape. The opening width of the crack provided was 2 mm. Crack was given at the top surface throughout along the width of the beam. The mesh size given for the study was 30 mm. The mode 1 Natural Frequencies of different cases were obtained. These values were compared with the values from Mia et al. and percentage error was also calculated. Table 1 gives the properties of beam used for the validation. Table 2 shows the different cases considered for validation, values of NF of mode 1 obtained from the analysis and from Mia et al. and percentage error for all the 6 cases. The percentage error obtained was comparatively less for all the cases considered for validation.

Table 1 Properties of specimen used for validation [1]

Property	Value
Length (L)	3 m
Width (w)	0.25 m
Depth (t)	0.2 m
Material	Mild steel
Elastic modulus (E)	210×10^6 N/m^2
Density	7860 kg/m^3
Poisson's ratio	0.3

Table 2 Summary of validation

Cases	Location of crack (m)	Depth of crack (m)	Obtained values of NF	Values of NF from Mia et al. [1]	% Error
Case 1	0	0	18.561	18.622	0.328
Case 2	1	0.1	16.621	16.936	1.86
Case 3	1	0.075	17.587	17.733	0.823
Case 4	1	0.125	14.983	15.471	3.154
Case 5	1.5	0.1	17.73	17.917	1.044
Case 6	2	0.1	18.353	18.437	0.456

3 Numerical Study on Different Types of Beams

3.1 General

The NF of Reinforced Cement Concrete (RCC) beams, Plain Cement Concrete (PCC) beams and Steel–Concrete (SC) Composite beams with and without cracks for both cantilever and fixed end boundary conditions were determined by modal analysis. Crack was provided at different locations of 0.2L, 0.4L, 0.6L and 0.8L from the fixed end of cantilever beam and left end of fixed end beams, where L is the total length of beam and for each of these locations the crack depth varied by 5, 10, 20 and 40 mm. Table 3 shows different cases considered for the study. The study was conducted using the finite element analysis software Ansys Workbench R19.2. For all the cases the crack was modelled as a triangular notch with an opening size of 5 mm extending throughout the width of beam considered.

Table 3 Different cases considered for modal analysis

Cases	Location	Depth (mm)	Cases	Location	Depth (mm)
Case 1	0	0	Case 10	0.6L	5
Case 2	0.2L	5	Case 11	0.6L	10
Case 3	0.2L	10	Case 12	0.6L	20
Case 4	0.2L	20	Case 13	0.6L	40
Case 5	0.2L	40	Case 14	0.8L	5
Case 6	0.4L	5	Case 15	0.8L	10
Case 7	0.4L	10	Case 16	0.8L	20
Case 8	0.4L	20	Case 17	0.8L	40
Case 9	0.4L	40			

3.2 Modal Analysis of Different Types of Beams for Different Cases

Modal analysis was conducted on RCC, PCC and SC Composite beams for 17 cases. The beams were modelled in Ansys Workbench R19.2. For RCC, the concrete was modelled by SOLID 65 and reinforcement by Link 180 finite elements and for PCC, the concrete was modelled by solid element. For SC Composite beam also, the materials were modelled by solid elements and different materials added with the help of modelling feature 'Add Frozen'. The study was conducted on 2 boundary conditions, cantilever and fixed end conditions. The analysis was done under the loading condition of self weight only. The mesh sizing given was 25 mm for RCC and PCC beams while for SC Composite beams it was given as 20 mm. For RCC and PCC beams, the crack locations given were 0.2, 0.4. 0.6 and 0.8 m and they were provided at top surface. For SC Composite beams, crack was given at 0.1, 0.2, 0.3 and 0.4 m at bottom surface. For all the cases, the depth varied as 5, 10, 20 and 40 mm. The specimen details of RCC, PCC and SC Composite beams are given in Tables 4, 5 and 6 respectively. Figure 1 shows the model of SC Composite beam.

3.3 Natural Frequencies Obtained for Different Cases

Natural Frequencies of different modes of vibration were obtained by modal analysis. Modal analysis was conducted on RCC, PCC and SC Composite beams for both cantilever and fixed end boundary conditions. For each type, a total of 17 cases were considered on the basis of location and depth of cracks. The mode 1 NF obtained for all the cases for all types of beams for both cantilever and fixed conditions are given in Table 7. Figures 2 and 3 shows the mode shape of mode 1 vibration of RCC cantilever beam of case 9 and PCC fixed beam of case 12 respectively.

Table 4 Details of RCC beam [2]

Particulars	Property	Value
Dimension	Length	1 m
	Width	0.25 m
	Depth	0.4 m
Reinforcement	Top bar	2# 20 mm dia
	Bottom bar	2# 8 mm dia
	Stirrups	8 mm dia @ 83.33 mm c/c
Concrete cover	Cover to reinforcement	40 mm
Concrete properties	Strength	25 MPa
	Young's modulus	3×10^7 kN/m^2
	Poisson's ratio	0.2
Reinforcement steel properties	Strength	500 N/mm^2
	Young's modulus	2×10^8 kN/m^2
	Poisson's ratio	0.3

Table 5 Details of PCC beam

Particulars	Property	Value
Dimension	Length	1 m
	Width	0.15 m
	Depth	0.15 m
Concrete properties	Density	2348.65 kg/m^3
	Young's modulus	2.58×10^7 kN/m^2
	Poisson's ratio	0.3

Table 6 Details of SC composite beam [3]

Property	Steel	Adhesive	Concrete
Length	500 mm	500 mm	500 mm
Width	100 mm	100 mm	100 mm
Depth	6 mm	2 mm	100 mm
Density	7579.0 kg/m^3	1611.8 kg/m^3	2364.4 kg/m^3
Young's modulus	12.5 GPa	200.3 GPa	48 GPa
Poisson's ratio	0.16	0.3	0.3

4 Results and Discussions

The NF obtained for different cases of all types of beams were compared. The comparison study was done for mode 1 vibration. The variation of NF keeping the
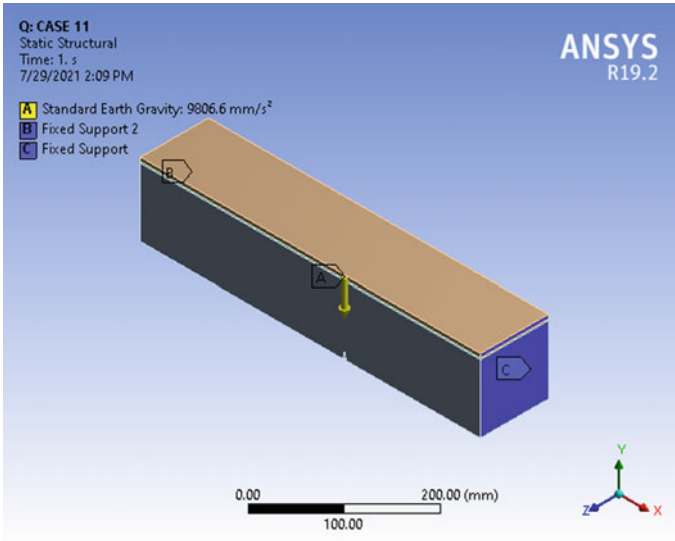
Fig. 1 Geometry of SC composite fixed beam with crack at 0.6 m and 10 mm depth (case 11)

Table 7 NF obtained for different cases

Cases	RCC beam		PCC beam		SC composite beam	
	Cantilever	Fixed	Cantilever	Fixed	Cantilever	Fixed
Case 1	139.09	697.67	79.245	453.88	282.45	1530.4
Case 2	139.08	697.66	79.127	453.86	282.13	1530.2
Case 3	139.02	697.61	78.787	453.80	281.16	1529.4
Case 4	138.80	697.44	77.400	453.53	277.15	1525.9
Case 5	137.73	696.31	71.882	452.22	255.59	1507.8
Case 6	139.08	697.68	79.191	453.58	282.33	1530.0
Case 7	139.06	697.60	79.062	452.85	281.91	1528.0
Case 8	138.96	697.27	78.515	449.75	280.36	1520.4
Case 9	138.48	695.50	76.111	437.84	274.81	1493.1
Case 10	139.09	697.69	79.233	453.58	282.44	1530.0
Case 11	139.08	697.62	79.204	452.81	282.36	1528.4
Case 12	139.06	697.29	79.064	449.56	281.97	1520.8
Case 13	138.93	695.51	78.421	437.44	280.43	1494.5
Case 14	139.09	697.66	79.250	453.86	282.51	1530.2
Case 15	139.10	697.63	79.255	453.80	282.55	1529.4
Case 16	139.10	697.43	79.257	453.54	282.63	1525.9
Case 17	139.10	696.31	79.233	452.29	282.67	1508.6
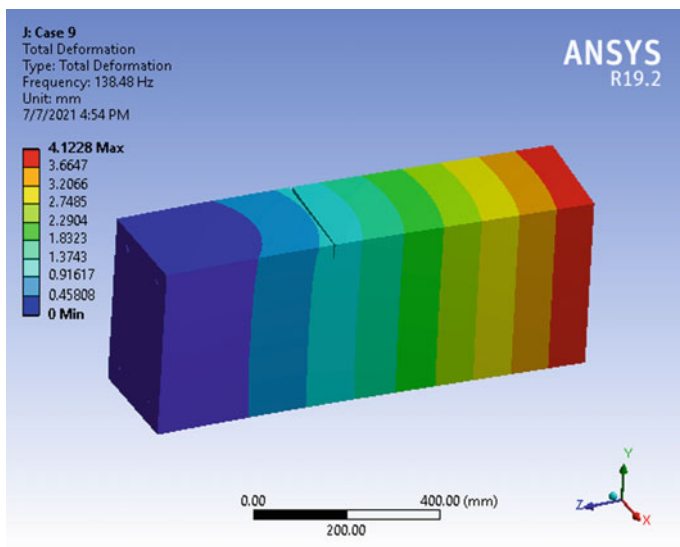
Fig. 2 Mode shape of mode 1 vibration of RCC cantilever beam of case 9
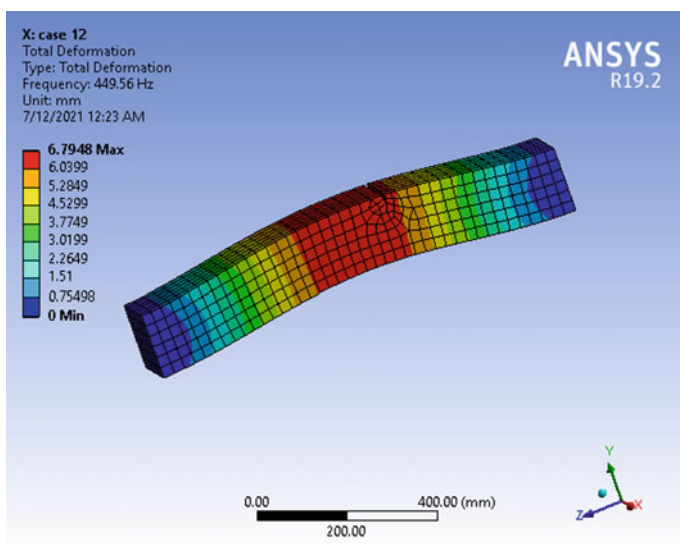
Fig. 3 Mode shape of mode 1 vibration of PCC fixed beam of case 12

location of crack as constant and varying the depth of crack as well as variation of NF keeping the depth of crack as constant and varying the location of cracks were found out. Comparison study was carried out by creating comparison charts in which crack depth or crack location is plotted along x- axis while NF is plotted along y-axis. Figure 4a and b shows the graph depicting variation in NF of RCC cantilever beam for mode 1 vibration with respect to location and depth of crack respectively. Figure 5a and b shows the graph depicting variation in NF of RCC fixed beam with respect to location and depth respectively.

From the study of cantilever beams, it is found that NF decreases as crack depth increases. The variation in NF is more for cracks having higher depths. For a constant depth, the variation reduces as the crack position moves from fixed end to free end of the beam. NF increases as crack position moves to free end at constant depths for mode 1 vibration. From the study of fixed beams, it is also found that NF decreases as crack depth increases. The variation in NF is more for cracks having higher depths. The variation in NF shows a symmetric pattern. The reduction in NF is more at the
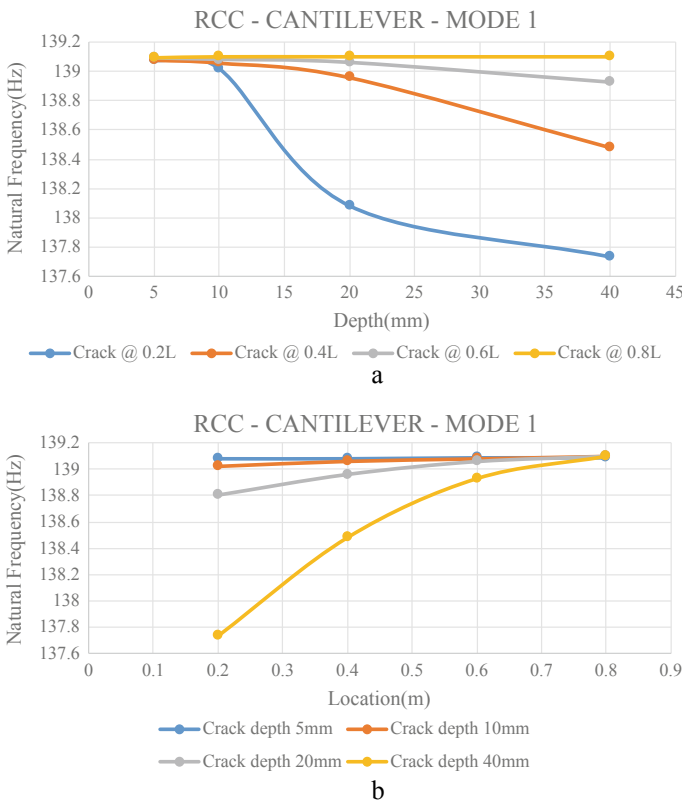
Fig. 4 **a** Variation in NF of RCC Cantilever beam with respect to location **b** Variation in NF of RCC Cantilever beam with respect to depth

a

b
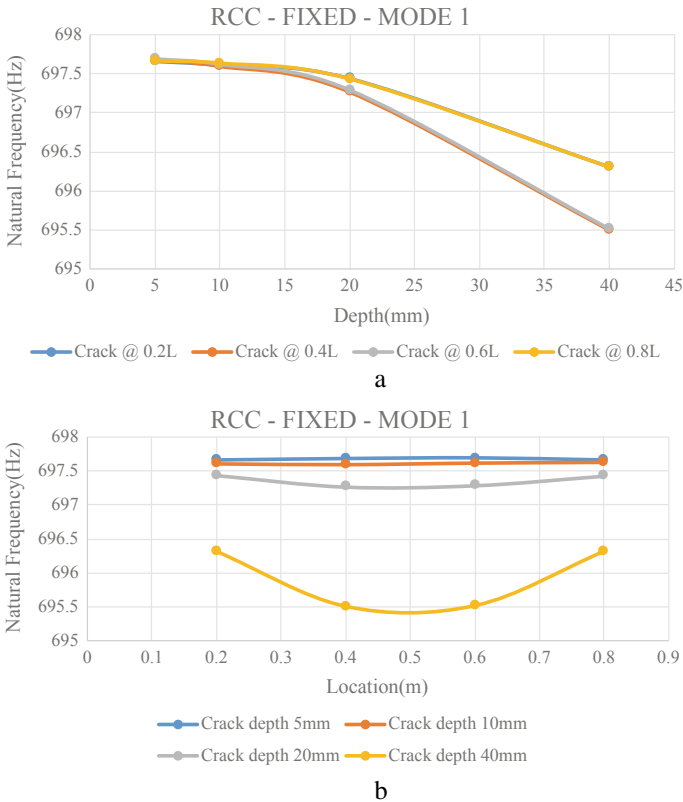
Fig. 5 a. Variation in NF of RCC Fixed beam with respect to location. **b.** Variation in NF of RCC Fixed beam with respect to depth

mid span than far ends i.e., NF decreases as crack position moves towards center and then increases. For both cantilever and fixed cases all the three types of beams i.e., RCC, PCC and SC Composite beams showed similar results.

5 Conclusion

The forward approach of crack detection is focused in this study. The study was conducted on different types of concrete beams. Beams with and without cracks were modelled in Ansys Workbench and modal analysis was done to obtain Natural Frequency and Mode Shapes. The Natural Frequencies of different cases were compared to identify the pattern of variation in Natural Frequency in the presence of cracks. From the study the following conclusions are made.

1. In all types of concrete beams considered, for both cantilever and fixed beams, as depth of crack increases, the Natural Frequency decreases.
2. In cantilever beams, the effect of crack is more at cantilever end.
3. In fixed beams, the effect of crack is more at mid spans for mode 1 vibration.
4. There is much greater difference in the values of Natural Frequency between cantilever and fixed beams for each cases.
5. The variations in Natural Frequency is very less for lower depth cracks.

So it is clear that the modal parameters can be used for the purpose of damage identification. By measuring these modal parameters, we can detect and quantify the damages in a structural member with the help of suitable crack detection strategies.

References

1. Mia, S., Islam, S., Ghosh, U.: Modal analysis of cracked cantilever beam by finite element simulation. Procedia Eng. **194**, 509–516 (2017)
2. Stoynova, I., Christov, T.: Response of a reinforced concrete cantilever beam subject to impulse impact loads. IOP Conf. Ser. Mater. Sci. Eng. **951**, 012015 (2020)
3. Knak, M., Wojtczak, E., Rucka, M.: Non-destructive diagnostics of concrete beams strengthened with steel plates using modal analysis and wavelet transform. Materials **14**, 3014 (2021)
4. Karmaker, R., Deb, U., Das, A.: Modeling and simulation of a cracked beam with different location using FEM. Comput. Water Energy Environ. Eng. **9**, 145–158 (2020)
5. Kumar, S.A., Velmurugan, V., Paramasivam, V., Thanikaikarasan, S.: Mesh8 Modal analysis of stainless steel cantilever beam crack dynamics using finite element method. Mater. Today Proc., 2214–7853 (2019)
6. Orhan, S.: Analysis of free and forced vibration of a cracked cantilever beam. NDT&E Int. **40**, 443–450 (2007)
7. Ramachandra, C., Ponnudurai, R.: Finite element analysis of beam having crack at various locations. Int. J. Sci. Res. Publ. **6**(12) (2017)
8. Sawant, S.U., Chauhan, S.J., Deshmukh, N.N.: Effect of crack on natural frequency for beam type of structures. AIP Conf. Proc. **1859**, 020056 (2017)
9. Viola, E., Nobile, L., Federici, L.: Formulation of cracked beam element for structural analysis. J. Eng. Mech. **128**(2), 220–230 (2002)

Numerical Investigation of Wave Structure Interaction Over a Vertical Wall Using OpenFOAM

N. R. Reshma, D. Anu, Beena Mary John, and P. A. Akram

Abstract The complex interactions between nearshore waves and coastal structures are widely modelled using numerical methods. This paper presents the results of a numerical study on interaction of nearshore waves on a vertical wall, by modelling a two-dimensional numerical wave tank generating regular waves using OpenFOAM, an open source CFD software capable of simulating a wide range of CFD problems. The dynamic behavior of the incompressible fluid is governed by solving the Navier Stokes equation by combining the continuity equation and momentum balance equation. Volume of fluid (VOF) method is used to track two phase fluid that determine the air–water interface. The wave structure interaction of near shore structures and modelling of wave breaking over a vertical sea wall structure placed for different wave heights and periods are addressed with the aid of numerical simulations.

Keywords Coastal structures · Numerical wave tank · Wave structure interaction · Wave breaking

1 Introduction

Vulnerable coastal regions subjected to severe coastal erosion, increase in tide and storm events, coastal flooding, the gradual rise in sea levels, increase in the frequency of storms, are indeed a common occurrence around the globe in the present day. Coastal regions are also economically developed, being important as centres of commerce, shipping, trade and recreation activities. Therefore, the design and construction of coastal infrastructure is at an all-time high and is expected to increase in the coming years. Physical model studies and numerical modelling approaches in coastal engineering are becoming more refined in the present day. With the rapid development of computational capabilities, large scale numerical studies for simulating coastal structures and the wave–structure interaction studies are very viable and less expensive. Apart from being time-effective and cost-saving, numerical models

N. R. Reshma (✉) · D. Anu · B. M. John · P. A. Akram
Department of Ship Technology, Cochin University of Science and Technology, Kochi, India
e-mail: reshma180ramesh@gmail.com

could also be used for full-scale simulations, as opposed to limitations of reduced-scale physical modelling facilities (scale effects) and is therefore a powerful and reliable method for studying the dynamic behavior of physical systems.

The use of numerical modelling techniques in coastal engineering is gaining direct applications in complex coastal processes and wave-structure interaction problems. The impact forces induced by wave breaking phenomena on coastal and maritime structures are regarded as one of the complex and least known and their effect on structures needs to be clearly understood [1]. Attempts to study this effect of breaking waves on structures has been investigated using experimental facilities since a long time and during the last few years, the capability of numerically modelling the breaking phenomena is widely being used [2–5]. The transient hydrodynamic disturbances at the surface caused by breaking waves shows that it is highly non-linear, and as a consequence, two-phase flows which are highly rotational and turbulent are generated near the breaking crests [6]. Recent studies have also shown the capability of OpenFOAM in accurately modelling the nonlinear wave interaction and breaking phenomena over coastal and offshore structures [7–10]. In the present study, it is attempted to model a numerical wave tank which can produce monochromatic waves, using the computational fluid dynamics (CFD) software—OpenFOAM, and to demonstrate its capability to study the wave structure interaction over a vertical wall for different ranges of incident wave conditions.

2 Methodology

2.1 Governing Equations of the Numerical Model

In this study, the open-source CFD package OpenFOAM, with InterFoam solver for incompressible fluids is used for all the simulations. It uses the Finite Volume Method (FVM) for discretization of governing equations and the VOF method for the capturing the interface. The Navier–Stokes equations for an incompressible, constant viscosity fluid [11] in cartesian coordinates are:

$$\rho\left(\frac{\partial u}{\partial t} + u\frac{\partial u}{\partial x} + v\frac{\partial u}{\partial y} + w\frac{\partial u}{\partial z}\right) = -\frac{\partial p}{\partial x} + \mu\left(\frac{\partial^2 u}{\partial x^2} + \frac{\partial^2 u}{\partial y^2} + \frac{\partial^2 u}{\partial z^2}\right) + \rho g_x \quad (1)$$

$$\rho\left(\frac{\partial v}{\partial t} + u\frac{\partial v}{\partial x} + v\frac{\partial v}{\partial y} + w\frac{\partial v}{\partial z}\right) = -\frac{\partial p}{\partial y} + \mu\left(\frac{\partial^2 v}{\partial x^2} + \frac{\partial^2 v}{\partial y^2} + \frac{\partial^2 v}{\partial z^2}\right) + \rho g_y \quad (2)$$

$$\rho\left(\frac{\partial w}{\partial t} + u\frac{\partial w}{\partial x} + v\frac{\partial w}{\partial y} + w\frac{\partial w}{\partial z}\right) = -\frac{\partial p}{\partial z} + \mu\left(\frac{\partial^2 w}{\partial x^2} + \frac{\partial^2 w}{\partial y^2} + \frac{\partial^2 w}{\partial z^2}\right) + \rho g_z$$
$$(3)$$

where ρ is the density of the fluid (kg/m^3), u, v and w are the velocity components of the x, y and z axes, respectively, t is the time (s), μ is the dynamic viscosity of the fluid (Pa s), p is the pressure (Pa), g is the acceleration due to gravity (m/s^2).

The following form of the continuity equation is satisfied, since the flow is assumed as incompressible (density is constant):

$$\frac{\partial u}{\partial x} + \frac{\partial v}{\partial y} + \frac{\partial w}{\partial z} = 0 \tag{4}$$

To capture the free-surface, the position and the development of the free surface between the air and water phase of the computational domain is computed. The tracking of the movement of the free surface is captured using the interFoam solver of the OpenFOAM, which uses the Volume of Fluid method (VOF). The volume fraction, that is, the fraction of each fluid that exists in each cell of the computation mesh, follows the equation:

$$\frac{\partial \alpha}{\partial t} + \nabla.(\alpha U) = 0 \tag{5}$$

where, α represents the volume fraction of water and U represents the velocity field.

2.2 Wave Generation and Absorption

The methods commonly employed to replicate waves which are dynamic in nature, and the experimental wave generation mechanism are: internal wave generation, static wave generation and absorption using Dirichlet-type boundary conditions, and the moving-boundary wave generation [12]. In the numerical methods, the moving boundary is used to replicate the movement of physical wave-maker paddles, that is, piston-type or flap-type wave-makers. In the physical models, the movement of paddles creates horizontal displacement of water and thus generates waves [13]. [14] adopted the relaxation zone method in the waves2Foam code to generate and absorb waves.

The modelling of waves in a numerical wave tank which emulates the physical wave flumes or tanks involves dealing with the wave reflections at the end or the boundary of the wave tank. So, the study of wave absorption theory is necessary [15] and the property of the boundary ensures good and efficient wave generation and absorption [16]. The main approaches used to achieve this is classified into two: passive and active absorption. The passive method involves creating a dissipative beach, sponge layers or damping zones, relaxation zones at the boundaries of the tank. In the active wave absorption, the incident and reflected wave signals can be separated using or applying digital filters. The reflected waves are cancelled out by generating a wave opposite to the reflected wave at the boundary.
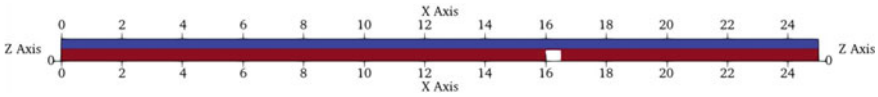
Fig. 1 Snapshot of the numerical wave tank of length 25 m used in the present study
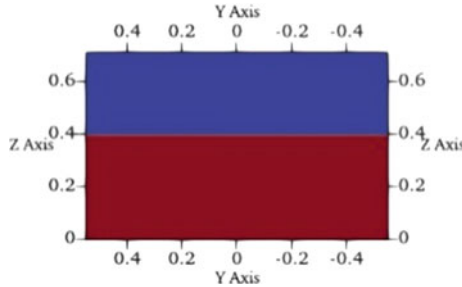
Fig. 2 Water depth of NWT

2.3 *Model Description*

The Numerical Wave Tank (NWT) and geometry of the vertical wall is created with the OpenFoam utility BlockMeshDict. A mesh is created then with the OpenFOAM utility called BlockMesh, and all the geometries are placed in the computational domain. Motivated by the authors' previous experimental investigations with artificial coastal vegetation in the wave flume at the Department of Water Resources and Ocean Engineering (formerly known as Department of Applied Mechanics and Hydraulics) at National Institute of Technology Karnataka (NITK Surathkal), Mangaluru, India [17], a scaled NWT with length, width and height of 25 m, 0.71 m, and 1.1 m respectively, is developed. The vertical wall with breadth, width and height of 0.5, 0.55 and 0.35 m is placed at a distance of 16 m from the left wall, as seen in Fig. 1.

In NWT, waves are generated at the left end (inlet) of the tank and absorbed at the other end i.e., outlet. The simulations are conducted for different wave periods and heights to study the wave-structure interaction especially the wave breaking phenomena. For all the simulations water depth is taken as constant of 0.4 m as shown in Fig. 2.

2.4 *Boundary Conditions*

Wave generation is activated at the inlet. Wave absorption activated at the outlet, is created based on shallow water theory to prevent the impact of the reflected waves in the wave propagation direction. The dynamic pressure P_rgh is defined at the

Table 1 Boundary conditions used in all simulation cases

	Inlet (left wall)	Outlet (right wall)	Bottom 1	Vertical wall	Sides (frontAndBack)	Top
U	moving WallVelocity	waveVelocity	fixedValue	fixedValue	Empty	pressureInletOutletVelocity
P_rgh	fixedFluxPressure	fixedFlux Pressure	fixedFlux Pressure	fixedFlux Pressure	Empty	totalPressure
pointDisplacement	waveMaker	fixedValue	fixedValue	fixedValue	Empty	zeroGradient
Alpha.water	zeroGradient	zeroGradient	zeroGradient	zeroGradient	Empty	inletOutlet

outlet region (normal zero-gradient boundary condition). A fixed value for velocity (0 m/s in the three directions) and zero-gradient for volume fraction is defined [16]. The FixedFluxPressure boundary condition related to the zeroGradient is used for all boundaries except the top one.

For the top boundary, the totalPressure boundary condition is set for pressure, pressureInletOutletVelocity boundary condition is set for velocity, and inletOutlet boundary condition is set for the volume fraction. The details of the boundary conditions used for the simulation are shown in Table 1.

2.5 Mesh Generation

It is well known that the accuracy of numerical results can be improved by the refinement of free-surface meshes. In this numerical study, the meshes are generated using *blockMesh*, which is a built-in utility for mesh generation in OpenFOAM. The number of cells in the mesh and grading of cells in a given direction is specified. So, the geometry of the NWT is created in *blockMeshDict*. Tables 2 and 3 shows the mesh size and block limits of each block cells of modelled NWT respectively.

The 2D NWT is meshed in *blockMeshDict* and the appropriate boundary conditions are set in 0.orig directory. The *setFields* utility is used to set the volume and initial position of the two fluid phases, air and water.

Table 2 Mesh size of each block cells of modelled NWT

Mesh	Block 0	Block 1	Block 2	Block 3	Block 4
Cell size in x-direction	0.00516667	0.00666667	0.006	0.006	0.00583333
Cell size in y-direction	1.1	1.1	1.1	1.1	1.1
Cell size in z-direction	0.16	0.160001	0.005	0.085	0.0850015

Table 3 Block limits of block cells of NWT

blockID	xmin	xmax	ymin	ymax	zmin	zmax
block0	0	16	−0.55	0.55	0.4	0.71
block1	0	16	−0.55	0.55	0	0.4
block2	16	16.5	−0.55	0.55	0.35	0.71
block3	16.5	25	−0.55	0.55	0.4	0.71
block4	16.5	25	−0.55	0.55	0	0.4

Table 4 Wave characteristics of different cases

Cases	Water depth (h) [m]	Period (T) [s]	Wave height (H) [m]	Wave length (L) in [m]	Steepness (H/L)
Case 1	0.4	1.2	0.08	1.938	0.04
Case 2	0.4	1.4	0.10	2.4003	0.041
Case 3	0.4	1.6	0.12	2.824	0.042
Case 4	0.4	1.8	0.14	3.376	0.042

2.6 Wave Characteristics

For all the simulations, water depth is taken as 0.40 m. The values of wave height and period for each of the simulated runs are shown in Table 4.

2.7 Physical Properties

The simulations ignored turbulence effects. The *simulationType* laminar is used for the simulations. The value of surface tension, properties of the fluids, such as their density and viscosity (*transportProperties* file, located in the constant folder) and other physical properties are summarized in Table 5. The turbulence settings are set in the *turbulentProperties* file located in the constant folder [16].

Table 5 Wave characteristics

Property		Value	Unit
Acceleration gravity (g)		9.81	m/s^2
Surface tension (σ)		0.07	N/m
Density (ρ)	Air	1	Kg/m^3
	Water	1000	
Kinematic viscosity (μ)	Air	$1.48 * 10^{-5}$	m^2/s
	Water	$1 * 10^{-6}$	

3 Results and Discussion

The waves generated in the 2-D numerical wave tank of length 25 m, height is 1.1 m, by moving flap paddles, for different wave characteristics of heights 0.08, 0.10, 0.12 , 0.14 m, and periods 1.2, 1.4, 1.6, 1.8 s are analyzed theoretically and numerically. In this paper, the model of the numerical wave tank without structure is validated by comparing the values of free surface elevation at locations 1.7, 3.2, 6.3, 10.1, and 13.7 m from the left wall by plotting along a probe line, by considering alpha.water equal to 0.5 as the free surface or air–water interface, with the theoretical values of free surface elevation.

Waves are then generated in the numerical wave tank with the vertical wall in place, at a distance of 16 m from the left wall, with different wave characteristics. The generated profiles for different cases are illustrated in Fig. 3, which shows that interFoam simulates propagation of a regular wave within the numerical wave tank. All the simulations are run for 25 s.

The Fig. 4a and b depicts the deformation of the free surface and the evolution of waves over the vertical wall. Four different cases are defined in order to simulate breaking waves.

The characteristics of the breaking wave varies with the incident wave characteristics as seen from the various profiles obtained. The results show that *interFoam* is able to properly simulate different wave breaking types. Among these four cases, the wave breaking phenomenon is considerably higher in the last case, with incident wave characteristics of wave height 0.14 m and period 1.8 s.

Figure 5 demonstrates the velocity fluctuations at various locations around the vertical wall over time. In these figures, it is clearly seen that the maximum velocity of NWT in the x-direction is nearly 3 m/s. At first, when the wavefield hits the vertical wall, the speed of the water particles decreased to zero. This location is called the contact point or stagnation point. As the wave flows from the vertical wall, the velocity field increases along the sides. As the wave continues to flow around the rear side of the vertical wall, the velocity decreases and form another stagnation

H = 0.08 m and T = 1.2 s *(t =20 s)*

H = 0.10 m and T = 1.4 s *(t =20 s)*

H = 0.12 m and T = 1.6 s *(t =20 s)*

H = 0.14 m and T = 1.8 s *(t =20 s)*
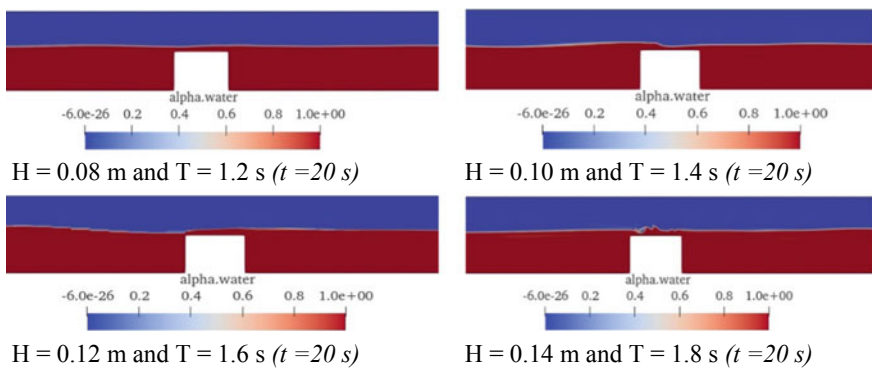
Fig. 3 NWT showing profiles for different wave heights and wave periods at $t = 20$ s

CASE 1   **CASE 2**

H = 0.08 m and T = 1.2 s   H = 0.10 m and T = 1.4 s

t = 5 s

H = 0.08 m and T = 1.2 s   H = 0.10 m and T = 1.4 s

t = 15 s

H = 0.08 m and T = 1.2 s   H = 0.10 m and T = 1.4 s

t = 25 s

a

CASE 3   **CASE 4**

H = 0.12 m and T = 1.6 s   H = 0.14 m and T = 1.8 s

t = 5 s

H = 0.12 m and T = 1.6 s   H = 0.14 m and T = 1.8 s

t = 15 s

H = 0.12 m and T = 1.6 s   H = 0.14 m and T = 1.8 s

t = 25 s

b
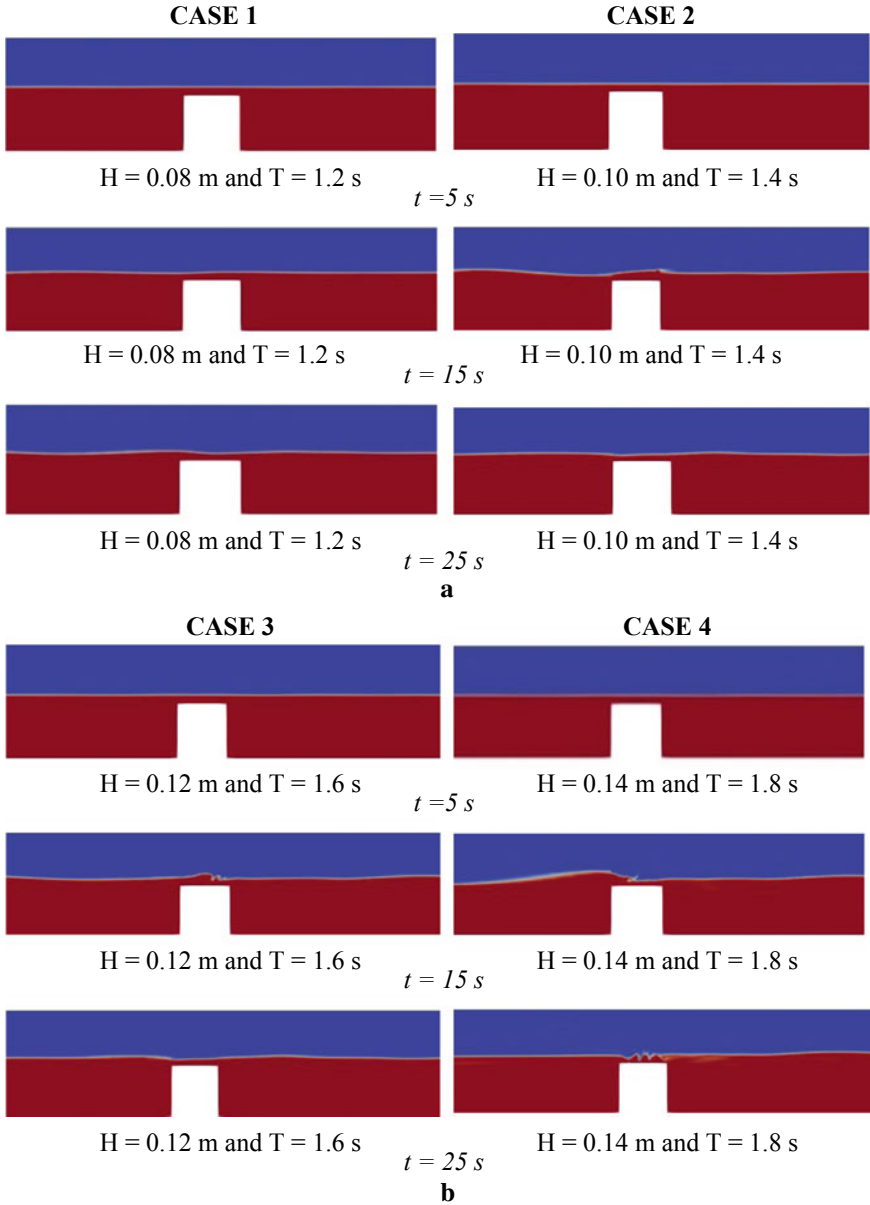
Fig. 4 **a** Wave profiles corresponding to the incident wave characteristics (H = 0.08 m and T = 1.2 s; H = 0.10 m and T = 1.4 s) **b** Wave profiles corresponding to the incident wave characteristics (H = 0.12 m and T = 1.6 s; H = 0.14 m and T = 1.8 s)

point. The model is also validated against theoretical velocity and is found to be in good agreement with the theoretical results.

Figure 6 demonstrates the maximum pressure fluctuations at locations around the vertical wall over time. The pressure variations around the structure are similar to that of velocity distribution. When the wave hits the structure, the dynamic pressure reaches its peak value along the front surface of the structure. The wave moves from the high-pressure to the low-pressure region, where the movement of water particles along the substructure gradually decreases.
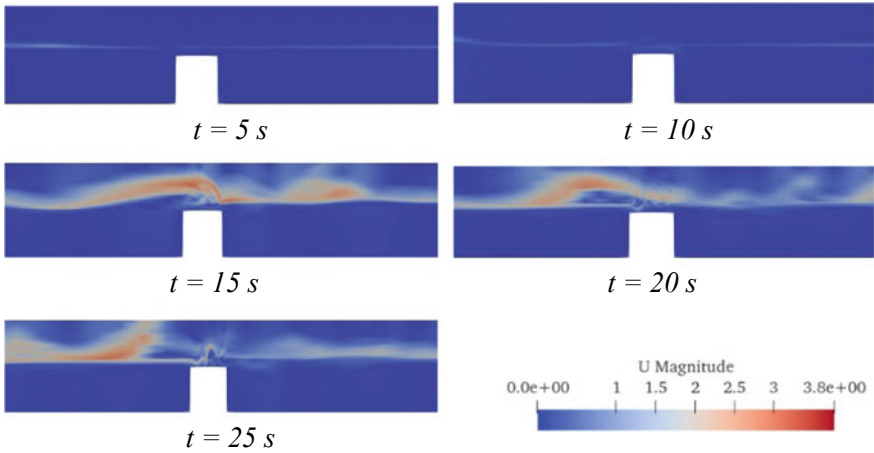
Fig. 5 Velocity fluctuations at locations around the vertical wall over time
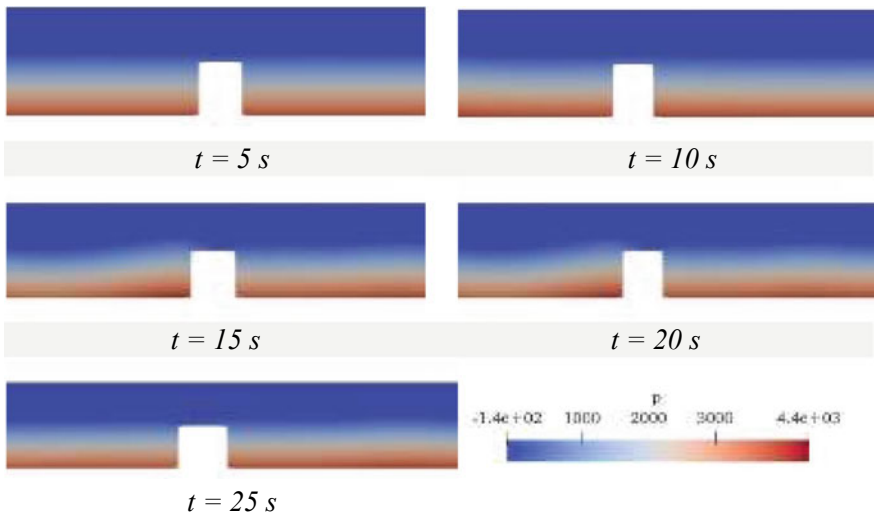
Fig. 6 Pressure distribution of NWT having wave height of 0.14 m and wave period 1.8 s

4   Conclusions

This study presents OpenFOAM as powerful software which can be used in wave structure interaction problems related to coastal and ocean engineering. This work also shows that *interFoam* has the capability of correctly modelling regular wave propagation both in generation and absorption of the waves as well as simulating the wave behaviour interaction with the structure.

References

1. Oumeraci, H., Klammer, P., Partenscky, H.W.: Classification of breaking wave loads on vertical structures. J. Waterw. Port Coast. Ocean Eng. **119**(4), 381–397 (1993)
2. Bullock, G.N., Obhrai, C., Peregrine, D.H., Bredmose, H.: Violent breaking wave impacts. Part 1: results from large-scale regular wave tests on vertical and sloping walls. Coast. Eng. **54**(8), 602–617 (2007)
3. Wang, Z., Zou, Q., Reeve, D.: Simulation of spilling breaking waves using a two phase flow CFD model. Comput. Fluids **38**(10), 1995–2005 (2009)
4. Kamath, A., Chella, M.A., Bihs, H., Arntsen, Ø.A.: Breaking wave interaction with a vertical cylinder and the effect of breaker location. Ocean Eng. **128**, 105–115 (2016)
5. Liu, S., Gatin, I., Obhrai, C., Ong, M.C., Jasak, H.: CFD simulations of violent breaking wave impacts on a vertical wall using a two-phase compressible solver. Coast. Eng. **154**, 103564 (2019)
6. Reul, N., Branger, H., Giovanangeli, J.P.: Air flow structure over short-gravity breaking water waves. Bound.-Layer Meteorol. **126**(3), 477–505 (2008)
7. Higuera, P., Lara, J.L., Losada, I.J.: Simulating coastal engineering processes with Open-FOAM®. Coast. Eng. **71**, 119–134 (2013)
8. Chen, L.F., Zang, J., Hillis, A.J., Morgan, G.C., Plummer, A.R.: Numerical investigation of wave–structure interaction using OpenFOAM. Ocean Eng. **88**, 91–109 (2014)
9. Hu, Z.Z., Greaves, D., Raby, A.: Numerical wave tank study of extreme waves and wave-structure interaction using OpenFoam®. Ocean Eng. **126**, 329–342 (2016)
10. Chen, W., Warmink, J., van Gent, M., Hulscher, S.: Modelling of wave overtopping at dikes using OpenFOAM. Coast. Eng. Proc. (36v), 27 (2020)
11. Lambert, R.J.: Development of a numerical wave tank using OpenFOAM (Doctoral dissertation) (2012)
12. Higuera, P., Losada, I.J., Lara, J.L.: Three-dimensional numerical wave generation with moving boundaries. Coast. Eng. **101**, 35–47 (2015)
13. Dao, M.H., Chew, L.W., Zhang, Y.: Modelling physical wave tank with flap paddle and porous beach in OpenFOAM. Ocean Eng. **154**, 204–215 (2018)
14. Jacobsen, N.G., Fuhrman, D.R., Fredsøe, J.: A wave generation toolbox for the open-source CFD library: OpenFoam®. Int. J. Numer. Meth. Fluids **70**(9), 1073–1088 (2012)
15. Miquel, A.M., Kamath, A., Alagan Chella, M., Archetti, R., Bihs, H.: Analysis of different methods for wave generation and absorption in a CFD-based numerical wave tank. J. Marine Sci. Eng. **6**(2), 73 (2018)
16. OpenFOAM: User Guide v2112
17. John, B.M., Shirlal, K.G., Rao, S.: Wave attenuation characteristics of simulated heterogeneous vegetation. Curr. Sci. **119**(8), 1322 (2020)

Numerical Investigation of 'Ogrid' Bracing System

M. S. Muhammed Salih and Jiji Antony

Abstract This study presents cyclic performance of a new bracing scheme using elliptical bracing elements on OGrid bracing systems for damage mitigation in structures subjected to earthquake excitations. To evaluate the seismic properties of this bracing system, a finite element method (FEM) analysis was performed on the Moment Resisting Frame (MRF) with an elliptical OGrid bracing subjected to cyclic loading. Also, the cyclic performance of forward and angle bracing systems with different cross-sectional orientations are analysed and compared with Elliptical OGrid.

Keywords OGrid · Finite element method

1 Introduction

Advancements in construction technology and material technology have given rise to the increase in the number of tall structures. Lateral loads like wind loads and seismic loads play an important role in the stability of a tall structure. Seismic loads are instantaneous loads which are unpredicted and cannot be quantified before their occurrence. These loads should be considered with utmost importance during the design process of a structure. These lateral loads are resisted by the exterior structural system. An important standpoint in building design is changing the form of buildings to provide more rigidity and more stability to the structure [2]. It may include adoption of various geometries for the lateral load resisting members in the structure.

An advancement in the lateral load resisting methods of high-rise buildings is a new bracing system called OGrid [1]. OGrid has intermediate rigidity and ductility characteristics unlike other bracing systems which are highly rigid [1]. Hence, it helps the system to perform efficiently under earthquake excitations without causing major damages to the population inside the building. OGrid is formed by connecting the beams and columns of a moment resisting frame (MRF) by a circular element.

M. S. M. Salih (✉) · J. Antony
Department of Civil Engineering, FISAT, Angamaly, India
e-mail: swalih21@gmail.com

This paper focuses on the study of performance of a modified OGrid called elliptical OGrid under earthquake excitations. It is not a perfectly circular OGrid but with different diameters along its circumference [3, 4]. Also, other bracing systems like angle [5] and forward bracings are also studied with different cross-section geometry orientations for performing the comparison.

2 Finite Element Formulation

To investigate the performance of elliptical OGrid bracings with different cross-sectional orientations, ANSYS 2021 R2 software is used. The behaviour of the elliptical OGrid with different cross-sectional area orientations were studied using this software. Also for comparison, other bracing systems like forward and angle bracings with different cross-sectional area orientations were modelled and studied. The analysis has been done under controlled displacement conditions by providing displacement of a default value in equal intervals.

2.1 Validation Study

The work done by Maryam Boostani *et. al.* proposed a new bracing system called 'OGrid' which is a circular bracing connected to the four members of a moment resisting frame. The work proved that circular OGrid bracings have high energy absorption capacity. An energy absorption of 27.72 and 20.07 were observed for the H and I orientations of bracings respectively. The maximum ultimate load obtained in the study is 116.2 kN and by validation the obtained value is 117.25 kN. The percentage error obtained is 0.991% which is within the acceptable limit (<10%). The result obtained in validation was approximately nearer to the result obtained in the reference and therefore the model is valid and can be extended for further studies.

2.2 Geometric Description

The moment resisting frame consists of two columns and a beam with interior dimensions as 1680 × 1820 mm which is the same as mentioned in the previous research journals. The cross section details of the columns and beam are given in Fig. 1(a) and (b).

The connections are made as fixed welded connections [6, 7]. In the elliptical OGrid, length of the outer major axis and outer minor axis are 1820 and 1680 mm respectively. Figure 2 shows the model of the elliptical OGrid bracing.
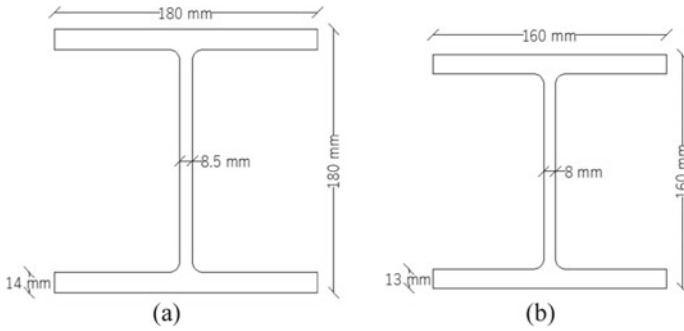
Fig. 1 Sectional properties of beam and column
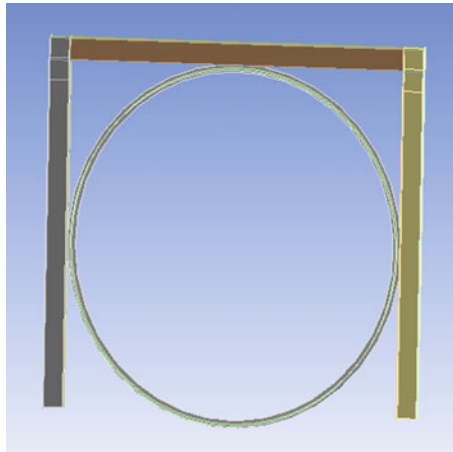
Fig. 2 Elliptical OGrid bracing system

As mentioned earlier, forward and angle bracings are also modelled for comparison. The length and breadth of the moment resisting frame is the same as that for elliptical OGrid. The length and breadth of the moment resisting frame are 1820 and 1680 mm respectively. In the case of angle bracings, the length of both the diagonal bracings are 2193 mm and the diagonal members are connected at a distance of 1410 mm from the bottom of the column. For forward bracings, the length of the diagonal member is 2477 mm and is connected between the bottom of one column and the beam column junction of the opposite column. The model geometries of angle and forward bracings are shown in Figs. 3(a) and (b).

For all the bracing systems chosen, three different cross-section orientations are also applied instead of following a single cross-section orientations. Three cross-section orientations which are H, I & C are chosen considering the real-time practicality in mind. These are named in such a way that the cross-section orientation has similarity to these alphabets. The three cross-section orientations are shown in
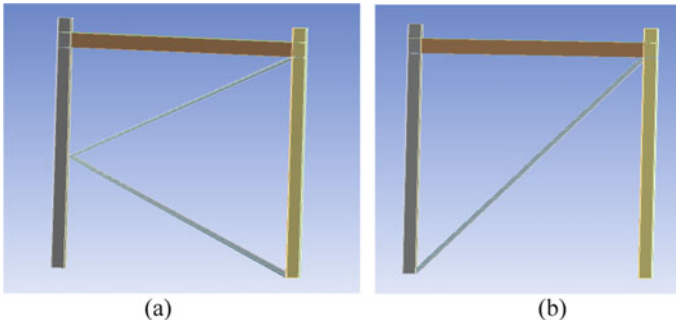
Fig. 3 Angle and forward bracing system
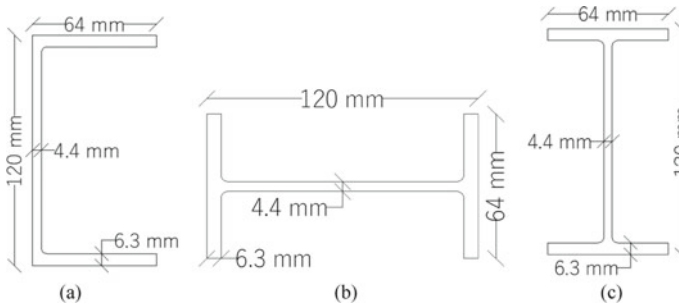
Fig. 4 C, H and I cross-section orientations

Figs. 4(a), (b) and (c). With three types of cross-section orientations for each three bracing systems, a total of nine samples were modelled.

2.3 Material Properties

The material used is structural steel with a yield strength of 480 MPa and Young's Modulus of 200 GPa. The density of the material is 7850 kg/m^3 and has a poisson's ratio of 0.3.

2.4 Finite Element Modelling

Modelling in ANSYS includes defining geometry, providing appropriate elements, and assigning suitable material models. The column is modelled using SOLID 186 in 3-D, 20-node hexahedron solid element that exhibits quadratic displacement behaviour for steel. The mesh size chosen after trial and error is 40 mm [8].
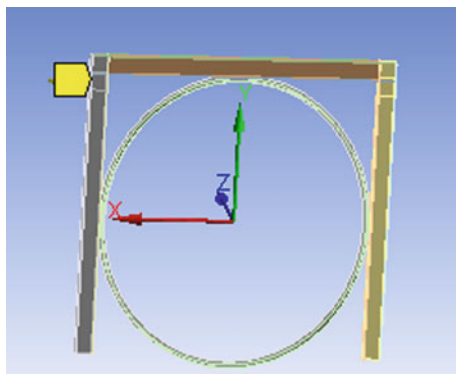
Fig. 5 Loading of the structure

2.5   Support Condition and Loading

The geometry is modelled in the ZX plane. The bottom end of the columns are provided as fixed supports with no provisions for rotation. Load is applied axially along the X-direction in such a way to obtain a certain deflection at a certain time [9].

Loading is applied in a way to obtain 25 mm deflection in each cycle. After reaching a deflection of 100 mm, the loading is withdrawn by reducing the deflection by 25 mm in each cycle. The time period of each cycle of loading is 0.001 s. Loads corresponding to different deflection values are obtained and plotted with deflection along X-axis and load among Y-axis. Area of the Load vs. Deflection graph is found which gives the value of absorbed energy by the structure under the loading. Figure 5 shows the loading mechanism of the structure.

3   Results and Discussions

Lateral load resisting bracing systems of three types with three different cross-section orientation were made and were analysed for energy absorption characteristics under lateral loading. Lateral load is applied at the top of the moment resisting frame (MRF). The load–deflection curve of the elliptical OGrid with C, H and I orientations is shown in Figs. 6, 7 and 8. In the initial cycles of the loading, the structure remained in the elastic state and in the succeeding cycles, the structure transformed into the plastic state and also showed improvement in load carrying characteristics. The C orientation of the bracing showed more energy absorption characteristics than other orientations, with I orientation having the least energy absorption characteristics. This is due to the fact that C orientation had the least moment of inertia along the cross-section because of its geometry and hence showed more ductility than other cross-section orientations.
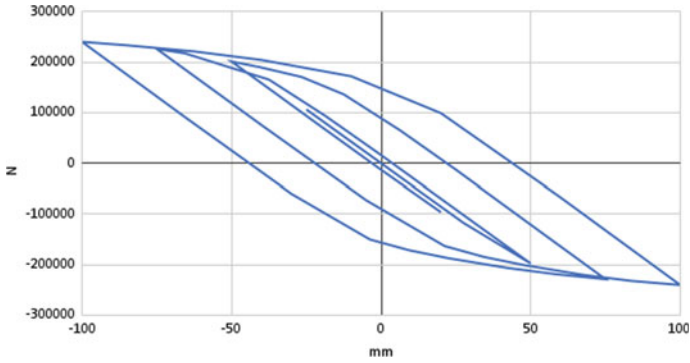
Fig. 6 Load vs. Deflection curve of Elliptical OGrid-C
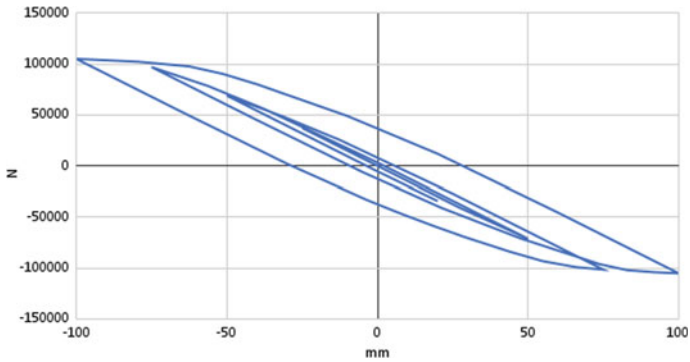
Fig. 7 Load vs. Deflection curve of Elliptical OGrid-H

The I-section had the maximum moment of inertia and hence the bracing was more rigid and showed lower ductility characteristics compared to the other orientations. The load vs deflection graphs of the other two models are shown in Figs. 9, 10, 11, 12, 13 and 14

The maximum value of absorbed energy is found out by calculating the area under the outer loop of the hysteresis loop formed by plotting load against deflection in each loading cycle. The maximum absorbed energy values of all the tested specimens are mentioned in Table 1. The length of steel used in each type of bracing is mentioned in Table 2.
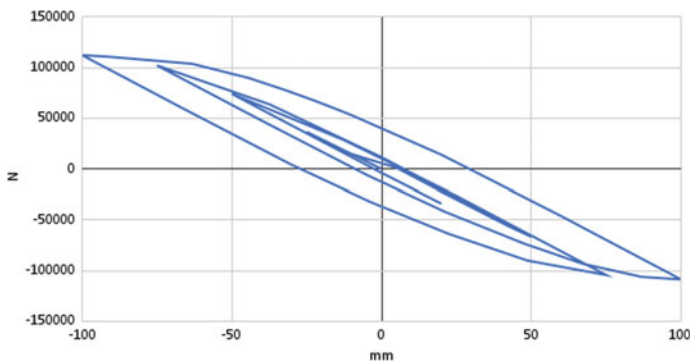
Fig. 8 Load vs. Deflection curve of Elliptical OGrid-I
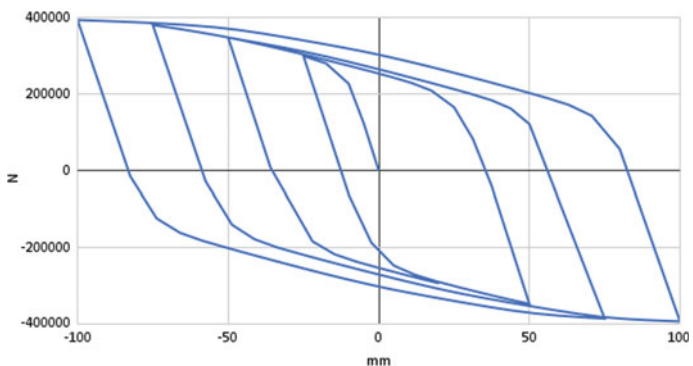
Fig. 9 Load vs. Deflection curve of Forward-C
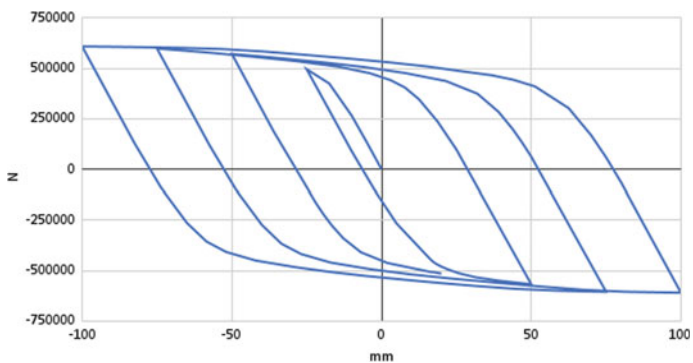
Fig. 10 Load vs. Deflection curve of Forward-H
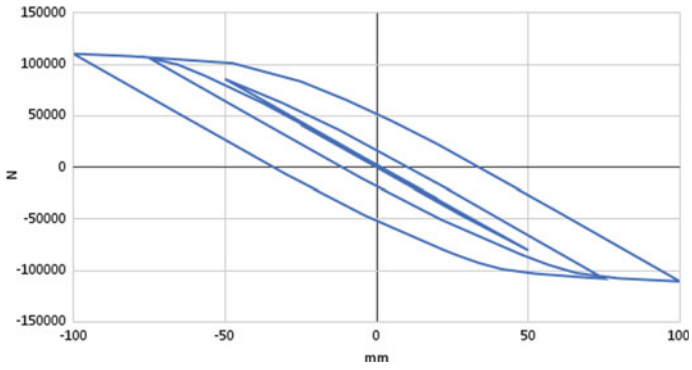
Fig. 11 Load vs. Deflection curve of Forward-I
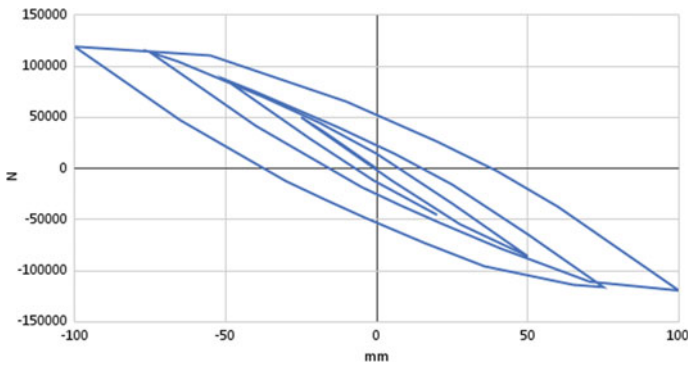
Fig. 12 Load vs. Deflection curve of Angle-C
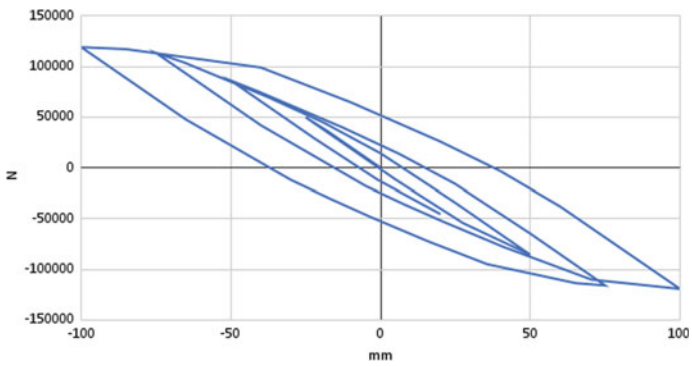
Fig. 13 Load vs. Deflection curve of Angle-H
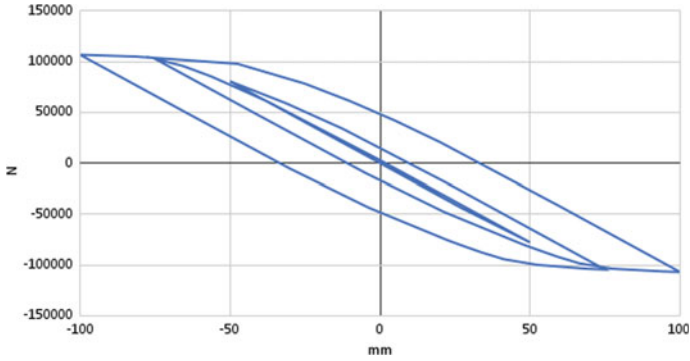
Fig. 14 Load vs. Deflection curve of Angle-I

Table 1 Maximum absorbed energy by each bracings

Energy Absorption Values for different bracings (kJ)					
Elliptical		Angle		Forward	
C	20.74	C	21	C	21.34
H	13.41	H	20.73	H	19.71
I	12.76	I	16.18	I	17.1

Table 2 Total length of steel used in each bracing

Name of bracing	Length of steel (m)
Elliptical OGrid	10.68
Angle	4.386
Forward	2.4

From the analysis, it is observed that the C orientation of forward bracing has the highest energy absorption capacity. The C and H orientation of angle bracing also showed similar energy absorption capacity. The least energy absorption capacity was exhibited by I orientation of the elliptical bracing system. It is clear that Elliptical OGrid bracing did not exhibit distinguishable energy absorption characteristics than other bracing systems. Also, the only Elliptical OGrid which had similar energy absorption characteristics was the C-orientation. From the previous research, it is observed that circular OGrid bracing showed a higher energy dissipation of *43.88*, *27.72* and *20.07* kJ respectively for C, H and I orientations.

4 Conclusions

Elliptical OGrid, Angle and Forward bracings with C, I and H orientations were modelled in ANSYS and were tested for cyclic loading to determine their energy absorption capacities. A total of nine specimens were modelled and tested for the same. The conclusions from the study are:

- For all bracings which were analysed in this study, the C-orientation showed the highest energy absorption characteristics among them because of its cross-section geometry.
- For all the bracing models, maximum energy absorption was shown by forward bracings
- Among the three models, forward bracings require the least length for bracings while elliptical bracings required the most length
- Elliptical bracings can be very useful if used in places where openings are to be provided.
- Elliptical OGrid has good aesthetics and energy absorption characteristics which makes it suitable to use in situations where aesthetics of the project is a concern.

References

1. Boostani, M., Rezaifar, O., Gholhaki, M.: Introduction and seismic performance investigation of the proposed lateral bracing system called "OGrid." Arch. Civil Mech. Eng. **18**(4), 1024–1041 (2018)
2. Al-Safi, S., Alameri, I., Wasel, W.A., Al-kadasi, A.B.: Linear and nonlinear behaviour of steel buildings with different bracing systems. Int. J. Steel Struct. **21**(2), 475–486 (2021)
3. Shamivand, A., Akbari, J.: Ring-shaped lateral bracing system for steel structures. Int. J. Steel Struct. **20**(2), 493–503 (2020)
4. Bazzaz, M., Kafi, M.A., Kheyroddin, A., Andalib, Z., Esmaeili, H.: Evaluating the seismic performance of off-center bracing systems with circular elements in optimum place. Int. J. Steel Struct. **14**(2), 293–304 (2014)
5. Fukuta, T., Nishiyama, I., Yamanouchi, H., Kato, B.: Seismic performance of steel frames with inverted V braces. J. Struct. Eng. **115**(8), 2016–2028 (1989)
6. Yoo, J.H., Lehman, D.E., Roeder, C.W.: Influence of connection design parameters on the seismic performance of braced frames. J. Constr. Steel Res. **64**(6), 607–623 (2008)
7. Jin, J., El-Tawil, S.: Seismic performance of steel frames with reduced beam section connections. J. Constr. Steel Res. **61**(4), 453–471 (2005)
8. Montuori, R., Nastri, E., Piluso, V., Todisco, P.: A simplified performance based approach for the evaluation of seismic performances of steel frames. Eng. Struct. **224**, 111222 (2020)
9. Mojtabaei, S.M., Kabir, M.Z., Hajirasouliha, I., Kargar, M.: Analytical and experimental study on the seismic performance of cold-formed steel frames. J. Constr. Steel Res. **143**, 18–31 (2018)

Effect of Plastic Hinge Length in Column Reinforced with Iron Based SMA

Gisha George, Roshan Joseph, and K. R. Bindhu

Abstract Failure of the columns occurs due to earthquakes. Hence, it demands performance improvement and post- earthquake functionality of the columns. The use of innovative material like Shape Memory Alloy (SMA) provides significant promises in performance improvement of columns. SMAs are unique materials that have the ability to undergo large inelastic deformations, make the structure reusable after strong earthquake. It is assumed that maximum seismic damage occurs at plastic hinge regions which necessitate the prediction of plastic hinge length for columns. The use of SMA as reinforcement in plastic hinge regions undergoes large elastic deformations with less permanent deformation. In the present study, two iron based SMAs namely, FeNCATB and FeMnAlNi are provided in varying lengths as longitudinal reinforcements for different column models. The numerical analyses of the columns are done using finite element software SeismoStruct. The effect of varying critical regions on load carrying capacity, maximum displacement, residual displacement and ductility of the columns are evaluated under reverse cyclic loading with constant axial load. Plastic hinge length of each model is obtained from their respective strain profiles.

Keywords Iron based SMA · Plastic hinge length · Rebar strain profile · Inelastic deformation · Reverse cyclic lateral loading

1 Introduction

Building columns are subjected to inelastic deformations during earthquakes. It is assumed that maximum damage occurs in plastic hinge zone i.e., area of concentrated damage. During seismic excitations, the column experiences excessive cracking, crushing and peeling of concrete and buckling of longitudinal rebars in these regions. Superelastic Shape Memory Alloys (SMAs) have the capacity to undergo large elastic deformation known as super elasticity in the range of 4–13%. The shape

G. George (✉) · R. Joseph · K. R. Bindhu
College of Engineering Trivandrum, APJ Abdul Kalam Technological Universitry,
Thiruvananthapuram, India
e-mail: geo.gisha@gmail.com

recovery property of nickel based SMA has proven its efficiency in improving the seismic performance of the columns in terms of higher displacement capacity with less permanent deformation. So, the replacement of longitudinal steel rebars with SMA in critical region facilitates the reduction in damage level. This mandates the determination of length of the column for which SMA needs to be incorporated in the critical region or plastic hinge length. This can be done by varying the length of critical regions of the column and incorporating SMAs as longitudinal reinforcement in those regions to evaluate the column performances.

Only few studies have been carried out on the iron based SMAs compared to other types for reinforced concrete columns subjected to seismic loads. Also, only little research has been done towards determining plastic hinge regions of columns consisting of SMA in critical regions. So, the current study makes use of two iron based SMAs such as FeNCATB and FeMnAlNi as reinforcement instead of steel reinforcement for RC columns in the critical region to evaluate their seismic performances.

2 Literature Review

[11] conducted shake table experiments to understand the effectiveness of using the nickel based SMA bars at plastic hinge regions of the column specimens. The results show that the residual displacements in SMA reinforced columns were minimal and columns can remain functional after earthquakes. [8] predicted the length of the plastic hinge, crack width, crack spacing, and bond-slip relationship for super elastic SMA as reinforcement in RC structural elements. The authors concluded that SMA can be used for seismic design and reduces repair cost. [1] conducted experiments on concrete frame with SMA bars in critical region using inelastic dynamic time-history analysis and pushover analysis. The results indicate that SMA-RC frames were able to recover most of its post-yield deformation, even after a strong seismic load. [10] investigated the behaviour of columns incorporated with Ni–Ti SMA and ECC in critical region. The authors studied three columns viz., conventional RC column, RC column with Ni–Ti SMA in critical region and column with SMA-ECC in critical region. The SMA-ECC column experienced least damage and highest drift capacity compared to the other two specimens. [12] evaluated the dynamic performance of the bridge pier with copper based SMA and ECC in the plastic hinge regions. They found that it would be a feasible alternative to keep bridges functional after strong seismic excitations. [4] derived numerical expression for plastic hinge length of SMA reinforced concrete bridge pier considering various parameters like yield strength of SMA, compressive strength of concrete, axial load ratio, longitudinal and transverse reinforcement ratio. [13] conducted seismic fragility analysis on bridge pier with different ratios of NiTi SMA and steel reinforcement, which was compared with conventional bridge piers. It shows low vulnerability and high resilience against earthquakes.

3 Geometry of the Model

In order to avoid shear dominated failure, full scale column having an aspect ratio of 5 is modeled. 12 numbers of 25 mm diameter steel bars (longitudinal reinforcement ratio of 2%) having yield strength of 415 N/mm^2 is used in normal reinforced column (NRC). 12 mm diameter bars are provided as transverse reinforcement at a spacing of 300 mm with special confining reinforcement at 100 mm spacing for a length of 300 mmm from base. Two iron based SMAs viz., FeNCATB (Fe–Ni-Co-Al-Ta-B) and FeMnAlNi are provided in varying lengths taken as 0.5, 1, 2 times diameter of the column [3, 9]. These two iron based SMA's were produced with different metals. The columns are modeled using displacement-based non-linear beam–column elements in SeismoStruct (see Fig. 1).

The material properties of confined and unconfined concrete are modeled using [6] model. The steel rebar and SMA's are modeled using [7] steel model and [2] respectively. The properties of SMA like austenite to martensite starting stress (f_y), austenite to martensite finishing stress (f_{p1}), martensite to austenite starting stress (f_{T1}), and martensite to austenite finishing stress (f_{T2}) are shown in Table 1. An axial load is applied at the top of the pier. The SMA's are connected to the steel reinforcement using mechanical couplers. The slippage of SMA rebar inside the coupler is modelled by incorporating a bond–slip model. The bond-slip inside the coupler is modeled using Takeda model (1970).
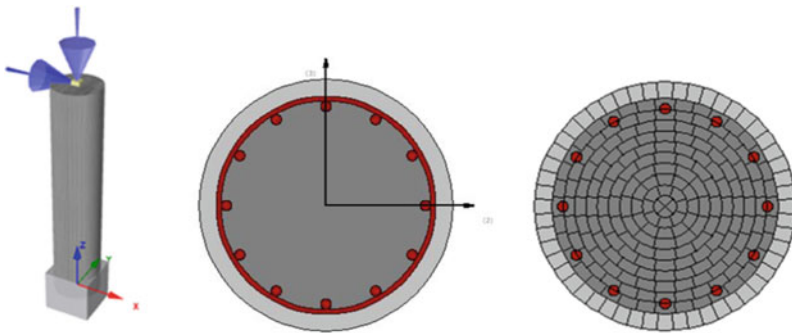
Fig. 1 Numerical model of the column with cross-section discretization

Table 1 Properties of iron based SMA

Alloy	E (GPa)	ε_s (%)	f_y (MPa)	f_{p1} (MPa)	f_{T1} (MPa)	f_{T2} (MPa)	Rebar strain
FeNCATB	46.9	13.5	750	1200	300	200	0.0159
FeMnAlNi	98.5	6.13	320	442.5	210.8	122	0.00325

Table 2 Specimen details

Designation	SMA used	Lp/d
CC	–	1
CF1-0.5	FeNCATB	0.5
CF1-1	FeNCATB	1
CF1-2	FeNCATB	2
CF2-0.5	FeMnAlNi	0.5
CF2-1	FeMnAlNi	1
CF2-2	FeMnAlNi	2

4 Analysis of the Column Models

Circular cantilever columns of 3 m height and 0.6 m diameter are used and SMA is provided in the critical region. Three types of models are considered. The first model considered is a conventional concrete column with steel reinforcement and is designated as CC. The second type of model consists of conventional concrete column with FeNCATB SMA in the critical region and steel reinforcement in the rest of the column. They are designated as CF1-x. The third type of model consists of FeMnAlNi SMA in the critical region and steel reinforcement in the rest of the column and is designated as CF2-x. Here, 'x' denotes the ratio between critical length (Lp) up to which a particular SMA is incorporated and diameter (d) of the column. The value of 'x' is taken as 0.5, 1 and 2 And the specifications of other column models are summarized in Table 2. The reverse cyclic horizontal load was provided with an increment of 1% of two consecutive cycle upto 20% drop in maximum strength.

5 Results and Discussions

The load versus displacement hysteresis loops of the various column models are obtained using finite element analysis (see Fig. 2a, b and c).

5.1 Ultimate Load Capacity

The ultimate load is obtained from envelope curve of the columns where the curve reaches the maximum load value. Figure 3 shows the envelope curves corresponding to maximum load in each cycle. From the results obtained for the CF1-x, it is observed that SMA reinforcement in critical region of RC column increase its peak load capacity. The maximum peak load is obtained for CF1-2. This is due to the elastic strain limit of FeNCATB alloy. In the case of CF2-x, the ultimate load capacity is
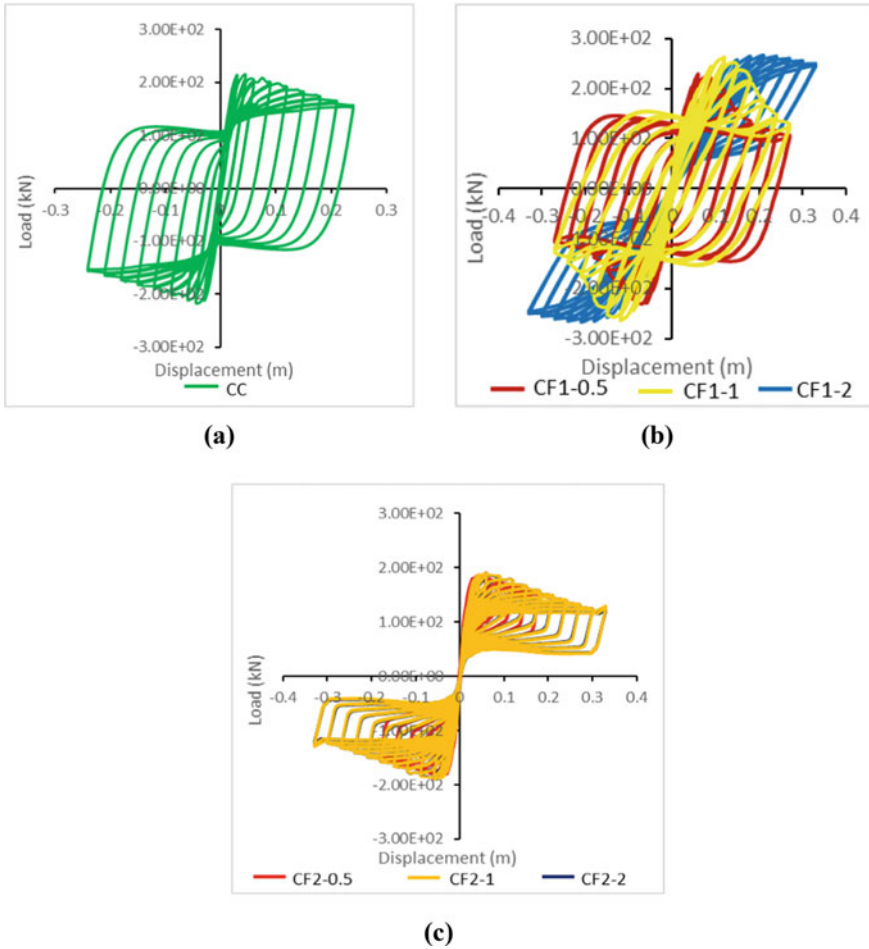
Fig. 2 Hysteresis curve of the columns

lower than normal column for all values of critical length it is provided, and there is no significant variation in its ultimate load. The ultimate load obtained for different column specimen is shown in Table 3.

5.2 Maximum and Residual Displacements

Maximum displacement and permanent deformation/residual displacement are the important parameters to be considered in the seismic design of structures. Maximum
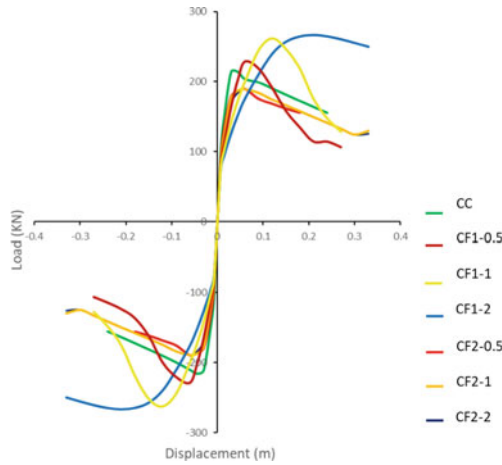
Fig. 3 Envelope curve of the columns

Table 3 Ultimate load of the different specimen

Designation	Lp/d	Ultimate load (kN)
CC	1	214.7919
CF1-0.5	0.5	228.6892
CF1-1	1	262.0924
CF1-2	2	266.5629
CF2-0.5	0.5	189.6013
CF2-1	1	189.06025
CF2-2	2	189.06025

displacement is taken as 0.8 times the specimen's ultimate load carrying capacity. Residual displacement is taken as the displacement corresponds to zero load of the hysteresis curve at the last load cycle provided. The maximum and residual displacements of the columns are summarized in Table 4.

The maximum displacement exhibited by CF1-0.5 is less than that of CC. But, as the critical length increases, the maximum displacements of the CF1-x specimens are increased. The same trend is also shown by CF2-x models. In the case of residual displacement, CF1-0.5 shows greater residual displacement than CC model. Even then, as the critical length for which FeNCATB SMA is provided increases, the residual displacement reduces. In the case of CF2-x, for all values of critical length, they exhibit zero residual displacement.

Table 4 Maximum and residual displacements of the columns

Designation	Lp/d	Maximum displacement (m)	Residual displacement (m)
CC	1	0.182	0.213
CF1-0.5	0.5	0.13	0.24
CF1-1	1	0.186	0.21
CF1-2	2	0.21	0
CF2-0.5	0.5	0.18	0
CF2-1	1	0.204	0
CF2-2	2	0.2036	0

Table 5 Ductility of the columns

Designation	Lp/d	Yield displacement (m)	Ultimate displacement (m)	Ductility
CC	1	0.02027	0.182	8.98
CF1-0.5	0.5	0.0389	0.13	3.34
CF1-1	1	0.066	0.186	2.8
CF1-2	2	0.089	0.21	2.36
CF2-0.5	0.5	0.0202	0.18	8.91
CF2-1	1	0.023	0.204	8.87
CF2-2	2	0.0257	0.2036	7.92

5.3 Ductility

Ductility means the ability of element to undergo large inelastic displacement. It is the ratio of ultimate displacement to the yield displacement [5]. Table 5 shows the ductility of different column models.

CF1-x columns exhibit lower ductility than CC. This is because, even though FeNCATB alloy has the highest strain plateau and post-yield stiffness among other alloys, it is found that with larger bar diameter, the displacement ductility decreases. In the case of CF2-x columns, FeMnAlNi alloy has very low yield strength to elastic modulus ratio (0.0033) and consequently, yields at lower displacement. Hence, these columns exhibit comparatively higher ductility than columns having FeNCATB.

5.4 Determination of Plastic Hinge Region

During a seismic event, plastic hinges form in the region of the columns, where inelastic rotation takes place. This causes increased strain in members under compression side and reaches a critical value leads to the spalling of concrete cover. This is followed by yielding of longitudinal bars and crushing of concrete cover. More
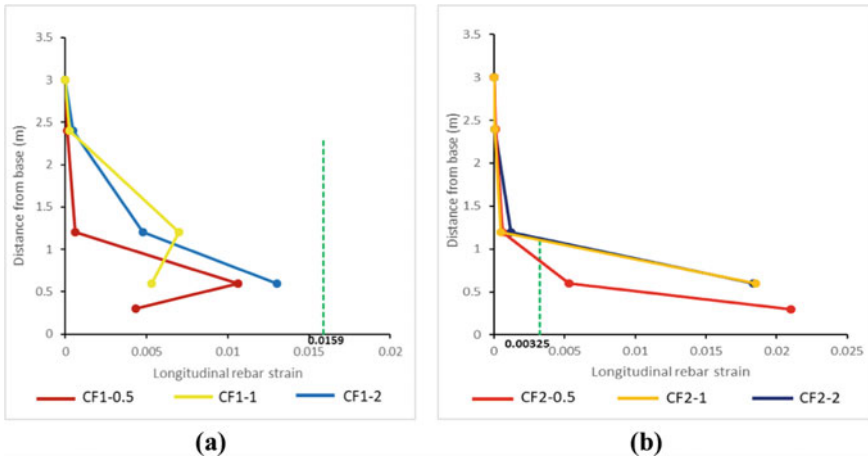
Fig. 4 Rebar strain profile of the column models **a** CF1-x models **b** CF2-x models

damage happens when this condition goes on and forms plastic hinges till compressive strain in the longitudinal rebar equals compressive strain in the outer core concrete fiber. So, the formation of plastic hinge can be determined using rebar compressive strain profile along the height of the column. Figure 4 shows the rebar strain profiles of the column models.

Here, CF1-x columns failed due to some other reason (e.g. Spalling and cracking of concrete) other than straining of rebars. Hence accurate computation of plastic hinge zone is difficult. Even then, the portion of the column approaching close to yield strain of FeNCATB (0.0159) can be considered as plastic hinge region.

In the case of CF2-x, the yield strain of FeMnAlNi is 0.00325. The portion of the column where the rebar reaches this value is its plastic hinge zone. When FeMnAlNi is provided for greater lengths of critical region, the plastic hinge length obtained from rebar strain profile also increases. The location of plastic hinge zone of the columns obtained from their respective strain profiles are shown in Table 6.

Table 6 Plastic hinge length of the column models

Designation	Lp/d	Rebar strain	Plastic hinge length obtained from strain profile (m)
CC	1	0.002	0.59
CF1-0.5	0.5	0.0159	0.6
CF1-1	1	0.0159	1.2
CF1-2	2	0.0159	0.6
CF2-0.5	0.5	0.00325	0.87
CF2-1	1	0.00325	1.109
CF2-2	2	0.00325	1.12

6   Conclusions

The load Following are the conclusions drawn based on the numerical study of column specimens having iron based SMAs in critical region:

- FeNCATB SMA when reinforced in critical region of RC column increase its ultimate load carrying capacity. Higher load carrying capacity is obtained when FeNCATB is provided for greater critical lengths due to its higher yield strength. The use of FeMnAlNi shows lower load carrying capacity than control column.
- Both category of columns having FeNCATB and FeMnAlNi SMA exhibits improvement in maximum displacement with increase in critical region, even though the value for columns having Lp/d = 0.5 is only slightly less than that of normal column.
- The FeNCATB SMA reinforced columns exhibits reduced residual displacement with increase in critical length. In the case of FeMnAlNi, zero residual displacement is achieved for all critical lengths.
- The displacement ductility is observed to be lower for both the SMAs compared to normal column for all critical lengths. FeMnAlNi exhibits comparatively greater ductility than FeNCATB. This is because FeMnAlNi alloy has very low elastic strain limit consequently, yields at lower displacement.
- The failure of columns due to reasons other than straining of FeNCATB bar resulted in slightly vague prediction of plastic hinge length. But for columns having FeMnAlNi, plastic hinge length was computed from strain profile and it was observed that when SMA is provided for greater lengths of critical region, the location of plastic hinge also increases from column base.
- Considering the ultimate load capacity, rate of increase in maximum displacement with increase in critical length and appreciable performance in reduction of residual displacement, FeNCATB SMA in critical region exhibits better seismic performance.

References

1. Alam, M.S., Nehdi, M., Youssef, M.: Seismic performance of concrete frame structures reinforced with superelastic shape memory alloys. Smart Struct. Syst. **5**, 565–585 (2009)
2. Auricchio, F., Sacco, E.: A superelastic shape-memory-alloy beam. J. Intell. Mater. Struct. **8**, 489–501 (1997)
3. Billah, A.H.M., Alam, M.S.: Probabilistic seismic risk assessment of concrete bridge piers reinforced with different types of shape memory alloys. Eng. Struct. **162**, 97–108 (2018)
4. Billah, A.H.M., Alam, M.S.: Plastic hinge length of shape memory alloy (SMA) reinforced bridge pier. Eng. Struct. **117**, 321–331 (2018)
5. Elshamandy, M.G., Farghaly, A.S., Benmokrane, B.: Experimental behaviour of glass fiber-reinforced polymer-reinforced concrete columns under lateral cyclic load. ACI Struct. J. **115**, 337–349 (2018)
6. Mander, J.B., Priestley, M.J.N., Park, R.: Theoretical stress-strain model for confined concrete. J. Struct. Eng. **114**, 1804–1826 (1988)

7. Menegotto, M., Pinto, P.E.: Method of analysis for cyclically loaded R.C. plane frames including changes in geometry and non-elastic behaviour of elements under combined normal force and bending. In: Symposium on the Resistance and Ultimate Deformability of Structures Acted on by Well Defined Repeated Loads, International Association for Bridge and Structural Engineering, Zurich, Switzerland, pp. 15–22 (1973)
8. Nehdi, M., Alam, M.S., Youssef, M.: Analytical prediction of the seismic behaviour of superelastic shape memory alloy reinforced concrete elements. Eng. Struct. **30**, 3399–3411 (2008)
9. Omori, T., Ando, K., Okano, M., Tanaka, Y., et al.: Superelastic effect in polycrystalline ferrous alloys. Science **333**, 68–71 (2011)
10. Saiidi, M.S., O'Brien, M., Zadeh, M.S.: Cyclic response of concrete bridge columns using superelastic Nitinol and bendable concrete. ACI Struct. J. **106**, 69–77 (2009)
11. Saiidi, M., Wang, H.: An exploratory study of seismic response of concrete columns with shape memory alloys reinforcement. ACI Struct. J. **103**, 436–443 (2006)
12. Varela, S., Saiidi, M.S.: Dynamic performance of novel bridge columns with superelastic CuAlMn shape memory alloy and ECC. J. Intell. Mater. Syst. Struct. **2**, 29–58 (2014). https://doi.org/10.1177/1045389X16679285
13. Xiang, N., Chen, X., Alam, M.S.: Probabilistic seismic fragility and loss analysis of concrete bridge piers with superelastic shape memory alloy-steel coupled reinforcing bars. Eng. Struct. **207**, 110229 (2020). https://doi.org/10.1016/j.engstruct.2020.110229

Occupancy Rights and Building Defects: Public Understanding and Challenges in Malaysia

Amira Munirah Abd Razak, Mohammad S. Al-Mohammad, Saffuan Wan Ahmad, and Rahimi A. Rahman

Abstract Building occupancy rights are crucial in defective buildings, especially in unforeseen circumstances. However, occupants face several challenges in practicing their rights in defective buildings. This study aims to identify the public understanding of occupancy rights in the event of building defects and the challenges to practicing those rights in Malaysia. Face-to-face and online interviews were carried out with twenty residents. Thematic analysis was then used to analyze the data collected from the interviews. The results demonstrate that occupancy rights can be categorized into two themes: legal and social. The challenges to practicing the rights can also be categorized into two themes: regulations and information. The findings provide an understanding of the current occupancy rights issues in Malaysia.

Keywords Occupancy rights · Building defects · Public understanding · Challenges

A. M. A. Razak (✉) · S. W. Ahmad
Department of Civil Engineering, College of Engineering, Universiti Malaysia Pahang, Gambang, Malaysia
e-mail: nengmuniraa@gmail.com

S. W. Ahmad
e-mail: saffuan@ump.edu.my

M. S. Al-Mohammad · R. A. Rahman
Faculty of Civil Engineering Technology, Universiti Malaysia Pahang, Gambang, Malaysia
e-mail: PAP20002@stdmail.ump.edu.my

R. A. Rahman
e-mail: arahimirahman@ump.edu.my

R. A. Rahman
General Educational Development, Daffodil International University, Dhaka, Bangladesh

1   Introduction

Construction represents activities of creating a structure with different elements for a certain location [1]. This structure can mainly be divided into three main categories: buildings and houses, public works, and industrial-type structures [2]. Buildings provide a comfortable and healthy environment for activities and businesses. However, building defects remain a critical issue due to hairline fractures in beams, design defects, poor construction materials, and structural flaws in walls [3]. Also, the exposure to sunshine and precipitation produces rusted reinforcement bars, causing construction rework. As a result, project parties are required to make extra payments incurred from rework-related activities. According to the Construction Industry Institute, the direct expenditures incurred from rework account for 5% of construction costs [4]. Therefore, this study aims to identify the public understanding of occupancy rights in the event of building defects and the challenges to practicing those rights in Malaysia. In this study, a new building is defined as constructed during the defect liability period (DLP). DLP in Malaysia is between 12 and 24 months and 1 to and years [1]. After this period, a structure is considered new, and DLP is no longer considered [1].

2   Literature Review

2.1   Defect Liability Period

DLP is a rectification term in Joint Contracts Tribunal (JCT) contracts that starts after practical completion is certified and lasts for six to twelve months [5]. During this time, the homebuyer can submit any problems to the contract administrator to determine faults or maintenance concerns. The contractor is then given a reasonable amount of time to correct them. At the end of the defect responsibility period, the contract administrator develops a schedule of defects and lists the issues that have yet to be rectified. This is done in the presence of the contractor. The contractor should commit to resolving those defects within a reasonable timeframe. The contract administrator then issues a certificate when all defects are rectified. This releases the balance of any detention and issues the final certificate. However, DLP is not a chance to correct the defects arising after completing the project. Rather, it is a timeframe during which the contractor can be summoned back to fix any surface flaws. If any flaws emerge before project completion, they must be corrected before being awarded a practical completion certificate [6].

2.2 Homeowner and Developer Relationship: Cordiality Factor

The stronger the relationship between the developer and the homeowner, the more satisfied the homeowner is with the developer's services [7]. The developers' neglect and disregard for occupants' requests negatively affect their relationship. This is especially true when building defects are serious. However, there is still room for improvement. Aggressive and proactive monitoring procedures can be developed to maintain a good relationship between the developer and the homeowner [8]. On the contrary, providing high-quality services and products enhances homeowner satisfaction. Service is the most critical component for contentment the homebuyers. The happiness of homebuyers is influenced by three separate dimensions: house design, house quality, and homebuilder service. Good relationships can be fostered by providing exceptional aftercare service.

2.3 Homeowner and Developer Relationship: Formal and Legal Conditions

Faults in windows and door joinery, moisture, scratches on walls, and balconies and terraces are less frequent in the first six months after the building is commissioned. Those defects continue to increase during the warranty period. However, electrical installation defects are most common during the first year of warranty but become less common. Legislation demands the homebuyer's acceptance before transferring the title to the homebuyer. The inspection is usually carried out during the acceptance meeting. The homebuyer develops an acceptance procedure and rectifies any issues or flaws detected during the meeting. The homebuyer has the authority to pick which defects are included in the acceptance protocol as the receiving party. The occupants have the right to report any items, including minor ones [9].

3 Methodology

3.1 Interviews and Data Collection

Data collection was carried out using interviews with twenty residents of Gambang Damai because the area was hit by building collapse issues in 2021. Residents include permanent residents and renters. The purpose of the interviews was to collect opinions about the occupancy rights. Interviews are adequate to capture in-depth information about a subject. This approach has been used to identify emerging variables in other aspects of construction management [10–12]. Three open-ended questions

Table 1 Respondent profile

No	Gender	Interview duration (min)	Status	No	Gender	Interview duration (min)	Status
1	Male	10	Renter	11	Female	13	Permanent
2	Male	12	Permanent	12	Female	15	Permanent
3	Female	15	Renter	13	Male	12	Permanent
4	Male	16	Renter	14	Male	18	Permanent
5	Female	14	Permanent	15	Female	13	Renter
6	Female	13	Permanent	16	Female	14	Renter
7	Male	11	Permanent	17	Male	12	Permanent
8	Male	14	Permanent	18	Female	11	Permanent
9	Male	12	Permanent	19	Female	12	Permanent
10	Male	13	Permanent	20	Female	8	Permanent

were asked during the interviews: (1) What are your rights if your house collapses? (2) What are the procedures involved in exercising those rights? and (3) What challenges that you might face in exercising those rights? Table 1 presents the respondents' gender, the interview duration, and residency status.

3.2 Data Analysis

Data analysis was carried out using thematic analysis. The thematic analysis allows structuring the data systematically to find patterns associated with the phenomenon being investigated. Thematic analysis was deemed adequate to contextualize the responses collected from the interviews [13]. Other construction management works have used this method to examine qualitative data [14, 15]. The first step includes reading, transcribing, and identifying ideas in the data set. The second phase entails identifying potential codes and collecting ideas relevant to each code. The third phase combines the codes into a common theme. The fourth phase includes going back and forth through themes to check whether a theme represents the identified codes. The fifth phase requires naming a theme based on the data captured. Finally, the sixth phase includes reporting the output of the analysis.

4   Results and Discussion

4.1   Occupancy Rights in Defective Buildings

The analysis results show that occupancy rights can be divided into two themes: legal and social. The two themes include four subthemes: tribunal, developer, insurance, and social welfare. Figure 1 shows the thematic analysis results.

Legal
Tribunal
If the developer fails to respond to the homebuyers' request, a claim can be submitted to the Housing Tribunal. This is to protect the homebuyers for the first time [16]. The Homebuyer's Tribunal provides the homeowner with a speedy judicial process when the developer fails to seek remedies. Examples of the collected responses include:

> *"Claim compensation to the Consumer Tribunal. The tribunal is the alternative facility that can help the occupancies to get their right." (Respondent 2)*

> *"In addition, the occupant might seek relief from a home tribunal at the same period (homebuyers claims)." (Respondent 19)*

Developer
If the building functions are not adequate during the DLP of 24 months, a report containing errors can be issued to the contractor [15]. Occupants can complain about defects that have emerged during DLP. Some comments from the interviews include:

> *"Claim the right to the developer which is there still has a warranty or over the warranty – the developer is the person that responds for the house." (Respondent 5).*

> *"Claim to the developer, in this case, the developer is the person that responsible for the house if it has any defects or collapses." (Respondent 6)*
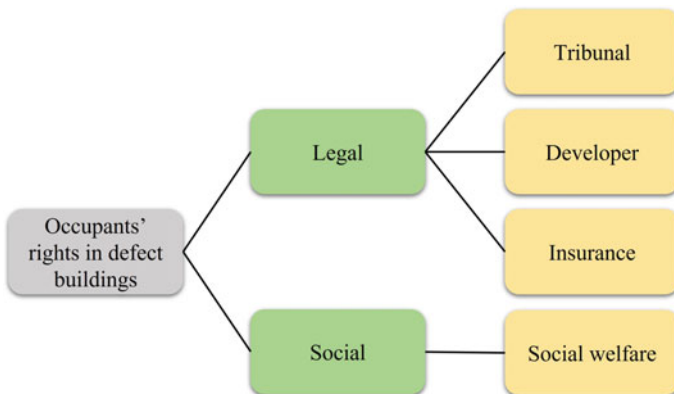
Fig. 1   Public understanding of occupancy rights for defective buildings

Insurance

Insurance is an alternative by which occupants can protect their rights against building defects. Although insurance companies look after their interests, providing latent defects insurance cause a deluge of claims from occupants. Some comments are:

> *"The costs of repairing the building defect can be reduced or completely covered by insurance. Furthermore, the insurance policies will protect their right to occupy." (Respondent 1)*

> *"The respondent has insurance that can cover the defects/collapses that occurs in his house. There are a few common insurance policies; basic fire and house policies. Most of the insurance have rights for each policy." (Respondent 4)*

Social

Social Welfare

If any damage occurs to the social welfare buildings, the elected representatives help provide temporary shelter, free home repairs, and consolation. Some respondents declared that:

> *"Besides, get the charity from the government, from local representatives, or the person that is responsible for that area." (Respondent 14)*

> *"Raise funds from the organization that manages the welfare of the local community." (Respondent 15)*

4.2   Challenges to Occupancy Rights in Defective Buildings

The analysis results suggest that occupancy rights challenges can be divided into two themes: regulations and information. Five subthemes emerged during the analysis: requirements, laws, knowledge, time constraints, and neglect. Figure 2 shows the thematic analysis results on the challenges to occupancy rights in defective buildings.

Regulation

Certain parties develop regulations for occupants when claiming building defects. This calls the occupants to prepare the right documents and completing some arrangements. Regulation is categorized into two subthemes: requirements and laws.

Requirements

Some respondents argued that there are several forms, agreements, and documents to fill in. Examples of the comments received from the interviews include:

> *"Because there are many requirements, the chances of getting it right are slim. The occupancies should have strong reasons and details to get the right." (Respondent 2)*

> *"Many forms should be filled up, and there are many agreements to complete." (Respondent 9)*
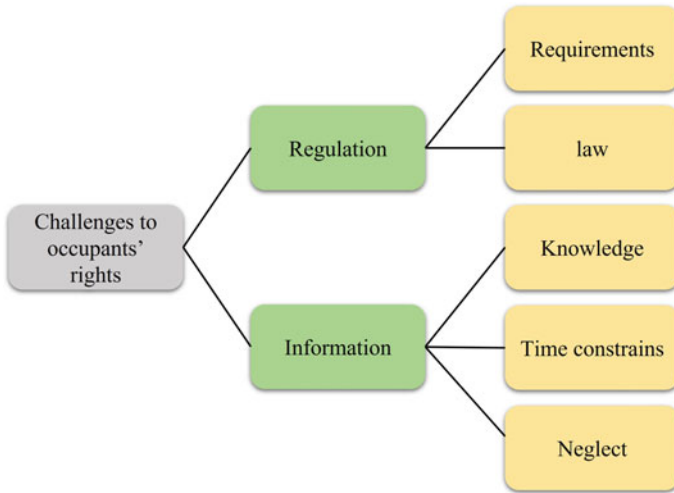
Fig. 2 Challenges to occupancy rights on defective buildings

Laws

The occupants must send a written notification or complaint to the developer and management office. The developer must correct the faults within 30 days after receiving the notice. If the developer fails to remedy the deficiencies adequately, the occupants have the right to solve the defect by choosing his or her contractor and seeking a quote for the repairs. Two respondents stated that:

> *"To get back the overview of the building and geographical area in their house." (Respondent 14)*

> *"Act of bribery may occur within the lawsuit if the defendant is connected with the court."* (Respondent 17)

Information

Information is divided into three subthemes: knowledge, time constraints, and neglect.

Knowledge

Occupants may lack knowledge of housing and the skills of replying when claiming rights. Also, some occupants may lack the rights actions when a building defect occurs. Some respondents declared that:

> *"To understand the architecture drawing respond the actual building so that the construction engineering is facing." (Respondent 14)*

> *"Lack of knowledge from jurisdictional authorities regarding the issue." (Respondent 17)*

Time Constraints

Processing the documents when claiming rights might be time-consuming. Therefore, occupants may use their own money to solve the defect. Some respondents pointed out that:

> *"The time duration to settle on the documentation and needs more appointments since it will relate to many sides." (Respondent 3)*
>
> *"Duration took a longer time. There is more chance for the repairing work to delay and take months or maybe years to settle down with all parties involved." (Respondent 3)*

Neglect

Occupants may lack communications and experienced individuals who can help claim their rights. Conversely, some parties discard the claims by occupants. Therefore, occupants prefer to neglect their rights. Some respondents stated that:

> *"While waiting for the process to get the rights, the occupancies need to use their own money to cover up the defects." (Respondents 5)*
>
> *"The process to get the approval takes la longer time and needs to use its own money to cover up the defects of the house." (Respondent 6)*

5   Conclusion

This study aims to identify occupancy rights and the challenges to exercising their rights in defective buildings. Face-to-face and online interviews were carried out with 20 occupants. Thematic analysis was then used to analyze the data.

The results illustrate that occupancy rights in defective buildings can be categorized into two themes: legal and social. Legal includes three subthemes: tribunal, developer, and insurance. Social includes social welfare. This indicates that understanding and awareness of the occupants of their rights is vital when any defect emerges. Also, an emphasis should be put in place on raising funds from the entities that manage the welfare of the community. Furthermore, the challenges to occupancy rights in defective buildings can be categorized into two themes: regulations and information. Regulations contain two subthemes: requirements and laws. At the same time, information contains three subthemes: knowledge, time constraints, and neglect. To overcome these challenges, occupants should be aware of the developed regulations to ensure they fulfill the requirements needed to claim their rights (e.g., strong justification for claiming the right). Also, occupants should prepare alternatives since claiming the right may not be done in a reasonable time.

The findings are beneficial in understanding the occupancy rights and the challenges of protecting their right in defective buildings. Future works can develop solutions to help overcome the challenges of practicing occupancy rights in defective buildings. However, this study has some limitations. The results are based on the opinions of individuals residing in Malaysia. Focusing on different contexts can be a future research direction. Furthermore, future works can explore the issues faced by improper risk assessment leading to fatalities.

References

1. Hang, H.C.: Investigation of defects in new buildings in Malaysia. Petaling Jaya (2016)
2. Lateef, O.A.: Building maintenance management in Malaysia. J. Build. Apprais. **4**, 207–214 (2009)
3. Hasan, M.M.I., Razak, N.N.A., Endut, I.R., Samah, A.S.A., Ridzuan, A.R.M., Saaidin, S.: Minimizing defects in building construction project. Jurnal Teknologi **78**, 79–84 (2015)
4. Hwang, B.-G., Stephen, R., Thomas, M., Carl, T., Haas, M., Carlos, H., Caldas, M.: Measuring the impact of rework on construction cost performance. J. Constr. Eng. Manag. **135**(3), 187–198 (2009)
5. Institute of Civil Engineering: designing buildings. https://www.designingbuildings.co.uk/wiki/Defects_liability_period_DLP
6. Glover, J.: Liability for Defects in Construction Contracts - Who Pays and How Much? 1st ed, Fenwick Elliot, London (2008)
7. Milion, R.N., Alves, T.D.C.L., Paliari, J.C., Liboni, L.H.B.: CBA-Based evaluation method of the impact of defects in residential buildings: assessing risks towards making sustainable decisions on continuous improvement activities. Sustainability **13**, 6597 (2021)
8. Nahmens, I., Ikuma, L.H.: Discovering the variables that influence new homebuyer service satisfaction. Int. J. Consum. Stud. **33**(5), 581–590 (2009)
9. Plebankiewicz, E., Malara, J.: Analysis of defects in residential buildings reported during the warranty period. Formal Legal Cond. **10**(17), 6123 (2020)
10. Badraddin, A.K., Radzi, A.R., Almutairi, S., Rahman, R.A.: Critical success factors for concrete recycling in construction projects. Sustainability **14**(5), 3102 (2022)
11. Radzi, A.R., Rahman, R.A., Doh, S.I., Esa, M.: Construction readiness for highway projects: key decision criteria. J. Constr. Eng. Manag. **148**(2), 04021196 (2022)
12. Munianday, P., Radzi, A.R., Esa, M., Rahman, R.A.: Optimal strategies for improving organizational BIM capabilities: PLS-SEM approach. J. Manag. Eng. **38**(3), 04022015 (2022)
13. Kiger, Michelle E., Varpio, Lara: Thematic analysis of qualitative data: AMEE Guide No. 131. Med. Teach. **42**(8), 846–854 (2020)
14. Asnor, A.S., Al-Mohammad, M.S., Ahmad, S.W., Almutairi, S., Rahman, R.A.: Challenges for implementing environmental management plans in construction projects: the case of Malaysia. Sustainability **14**(10), 6231 (2022)
15. Ng, C.C., Rahman, R.A., Ahmad, S.W.: Factors affecting the enforcement of environmental regulation: the case of erosion and sediment control plan. IOP Conf. Ser. Earth Environ. Sci. **682**(1), 012046 (2021)
16. Sudhar, T.S.: Challenging an award of the tribunal for homebuyer claims. https://www.stsp.my/challenging-an-award-of-the-tribunal-for-homebuyer-claims/

Fuzzy Logic-Based Inference System for Structural Health Monitoring of a Cantilever Beam

Amitesh Sharma, Prince Thankachan, and T. M. Madhavan Pillai

Abstract The presence of fault in a structure may lead to catastrophic failure if it remains undetected. So the damage diagnosis is an essential part in health monitoring of structures. Damage in a structure leads to change in the dynamic response which will be helpful for diagnosis of the structure. The relation between modal response and damage vector is in such a way that there exist unique change in response for unique damage. So damage detection is an inverse problem where it is required to relate the modal response to the damage state.

Problems of damage detection are too intricate and the distinct boundary between crisp values cannot be identified for expressing the damage level and measurement deltas. Thus, mapping technique like Fuzzy Logic Inference System (FLIS) can be used for such problems. A fuzzy logic will operate on linguistic variables and associate the data (structural response) with the damage conditions and provide output as level of damage and damage location.

In this study, the change of modal response due to damage in a cantilever beam is investigated and a FLIS is designed for the structural health monitoring purpose. The change in natural frequency is the measurement delta. FLIS is designed using data pool obtained from Finite Element (FE) analysis of different damaged scenarios of the specimen. The FLIS is tested with noise up to 20% and it is found to be robust against small contamination in measurement deltas.

Keywords Structural health monitoring · Fuzzy logic · Modal response · Damage detection

1 Introduction

Damage detection is an essential part of structural health monitoring. Damage can be defined as "a deficiency or deterioration in the strength of a structure caused by external loads, environmental conditions, or human errors" [1]. Detection of

A. Sharma (✉) · P. Thankachan · T. M. M. Pillai
Department of Civil Engineering, National Institute of Technology Calicut, Kozhikode, India
e-mail: sharma.amitesh.04@gmail.com

fault characteristics are necessary that too in non-destructive way so that the down time can be minimized resulting in low cost structural health monitoring [2]. The Damage detection methodologies based on their nature has been classified into classical method, Finite element method, AI method and other miscellaneous methods [3]. The fuzzy inference system is an AI based scheme useful in predicting damages. The fuzzy logic is an inference system which works on predefined rules on fuzzy sets. The fuzzy sets include members of set with continuously graded membership ranging from 0 to 1. [4].

Presence of fault in a structure consequently results in changes of its performance. This changes can be quantified by studying the changes in frequency, mode shapes and maximum extent of free vibration and so on [5]. There exist substantial changes in natural frequency when there is increase in flexibility due to fault. In beams maximum changes are observed at location of higher bending moment [6], also the magnified view of mode shapes are useful in identification of crack location [5]. Sazonov et. al. [7] detected damage by mode shapes and curvature of mode shape by forming fuzzy logic to mimic human like decision making process. The inverse problem of damage detection was studied by Vestroni and Capecchi [8], they related the amount and quality of data required for damage detection and showed the process of finding the optimum number of natural frequency required to locate and quantify the damage uniquely. The use of natural frequency is popular because it is simple to determine [1]. Das and Pahri [9] formulated fuzzy logic based crack detection system and compared its performance with experimental results, the fuzzy logic system show quick response within nanoseconds. Pawar and Ganguli [1] have given detail procedure to use genetic fuzzy logic inference system for fault diagnosis in various type of structures like beam, composite tube etc. Ashigbi et. al. [10] provided crack in beam like structure by saw cut and fuzzy logic was designed by comparing the modal frequency in damaged and undamaged condition measured from experiment as well as with the analytical method. The study concluded that more clustered data pairs will be helpful in better prediction by fuzzy rule base.

The present study include the design of fuzzy logic for a steel cantilever beam on the basis of the change in modal responses, calculated numerically by FE analysis of beam in undamaged and damaged condition, there after forming the fuzzy logic. Fuzzy logic with artificial neural network based supervised learning was used for automatic forming of membership function and rule by Wenning Yu et. al. [11]. To determine the health status of a structure or machine Swayer et al. [12] used the principle of continuum damage mechanics to identify the location and extent of the damage, fuzzy logic was formulated by monitoring the static, eigenvalue, and dynamic responses. Angelov and Filev [13] designed fuzzy logic first with limited information and then modifying the existing rule base, this evolving approach provided summarized rule base and compact fuzzy logic. Pawar and Ganguli [14] related the damage, in composite tube, in the form of matrix cracking with the changes in natural frequency and a robust genetic fuzzy inference system was designed by incorporating the effect of noise in measurement deltas. Chandrasekhar and Ganguli [15] provided details of probabilistic variation of measurement deltas due to various uncertainty and discussed its implication on fuzzy logic damage detection scheme

and fuzzy logic architecture was created and tested for contaminated measurements due to the uncertainties involved. Ganguli [1] developed fuzzy logic system for structural health monitoring of helicopter rotor blade, fuzzy logic system showed 100% correct prediction of four damage cases for noise level up to 15%. The present study utilizes C++ codes for reading the measurement deltas and writing command for forming fuzzy logic system using the fuzzy logic tool box in MATLAB.

Vimal et. al. [16] provide the damage as decrease in mass and detection of crack was done by first four natural frequencies. Ganguli [15] provided the damage by changing the Young's modulus of elasticity of the elements in finite element model. Das and Parhi [17] provide the damage as a cut of various relative depth. In the present study damage parameter is defined as various cut depth as percentage of overall depth of 2 mm wide cut at five different locations along the longitudinal direction of the cantilever beam. The dynamic response of the cantilever beam is evaluated by finite element analysis in ABAQUS. Fuzzy logic deals with partial truth. Fuzzy logic is a logic which maps the given numerical input to a linguistic output (a word or a group of words). This property is useful in classifications of the data in such a manner that output is not affected by the uncertainty of data. Thus, in present study the output has been tested with contaminated measurement deltas.

2 Theoretical Background

A FLIS is an inference scheme which maps the input and output of a problem. In other words it is an inference engine which evaluates and executes a set of predefined rules connecting the input and output of a problem. Fuzzy means vague. It is different from Boolean logic which understand only true and false. Fuzzy logic deals with partial truth.

In FLIS, the system reads measured structural responses (numerical or crisp values) and then convert them into the fuzzy sets (linguistic variables). The inference scheme processes the damage implication through reading and implementing the related rules in the knowledge base and the supplied fuzzy states. The output of this implication procedure is a fuzzy vector, which can also be defuzzified with different methods to get numerical value, describing possible damage levels of predefined regions in the structure.

2.1 Terminologies

Input and Output. For damage detection problems change in any structural response which is occurred as the consequence of the change in the stiffness of the structure or part of the structure because of prevailing damage, can be used. Natural frequencies are the input and the output are damage location and severity.

Fuzzy Set. A set in which every member has a degree of membership. A fuzzy set is a set in the form of ordered pairs.

Fuzzy Rules. The fuzzy rules are usually of the form of "if–then" statements. The '*If'* part is the antecedent part and **then** part is known as the consequent part. The two fuzzy parts are connected with words like AND, OR, NOT, etc.

For example,

"If X is A_1 and Y is B_1, then Z is C_1"

Fuzzifier. It performs the fuzzification and maps numbers into fuzzy sets. This number-to-word transformation is very important in fuzzy logic, as all further operations such as rules are performed on the words. If the input is relative change in first natural frequency, it can be fuzzified as linguistic measures '$F1R1$', '$F1R2$' for two different measurements of first frequency. The appropriate choices of linguistic variable and associated range of measurement deltas depend on the problem and can be different for different problems.

Defuzzifier. In some case if the output is required as numerical value, then defuzzifier is used. Defuzzifier maps the linguistic term (output) into a numerical or crisp value. For our problem we can either get the output as a linguistic variable indicating a portion (or range of length) of structure where fault is present or as a crisp value indicating the location of fault. The former has more significance as the latter one is subjected to accuracy of defuzzification methods.

There are several methods of defuzzification presented by Ross T.J. [18] in the present study centroid method is used. In this method the centroid of the output area is calculated and the crisp value corresponding to the same is called the output of the fuzzy logic. This method is more appealing because it takes into consideration of whole area. It doesn't give higher weightage to the part of output area with relatively higher membership value.

It can be expressed as given in Eq. (1),

$$y^* = \frac{\int \mu(y)y\,dy}{\int \mu(y)\,dy} \tag{1}$$

where, y^* is the defuzzified value and $\int$ signifies the algebraic integration.

3   Problem Formulation

A steel cantilever beam is taken for forming FLIS based SHM scheme for detection of presence of fault along the span. The problem is solved by earlier researchers also. The basic problem of cantilever beam for genetic fuzzy logic formation was done by Pawar et.al [1]. The geometric and material properties of the beam has been

taken from Chandrupatla and Belegundu [19]. The cantilever beam is as shown in the Fig. 1.

The beam has been indicated with the distance from the fixed end as the fraction of the span length (L). The SHM scheme is designed to provide the damage parameter and the location of the fault. In the present study the damage is provided in five different locations marked in Fig. 1. The information about the beam's material and geometric properties is as shown in the Table 1 (Chandrupatla and Belegundu [19]).

For damage detection, the reference baseline can be formed with numerically obtaining the first eight natural frequencies of cantilever beam in bending. For numerical simulation the beam behavior can be depicted as an Euler–Bernoulli beam. In Fig. 1 reference coordinate system can be assumed x as 0 at the fixed end and x equals to L at the tip. The natural frequencies of the beam can be numerically calculated by solving the partial differential equation given in Eq. (2),

$$\frac{\partial^2}{\partial x^2}\left(EI\frac{\partial^2 y}{\partial x^2}\right) + m\frac{\partial^2 y}{\partial t^2} = 0 \tag{2}$$

Here, E is the Young's modulus of elasticity, and I is the moment of inertia. The above equation has no exact solution, it can be solved by using finite element method. The problem can be expressed as an eigenvalue problem involving Global Stiffness Matrix $[K]$ and Global Mass Matrix $[M]$ stated as in Eq. (3),

$$K\phi = \omega^2 M\phi \tag{3}$$
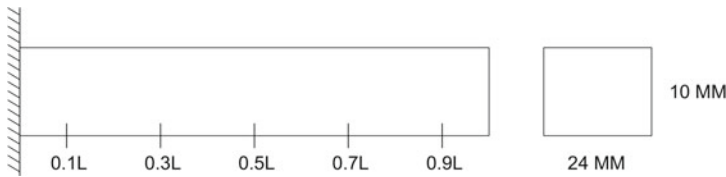
Fig. 1 Steel cantilever beam

Table 1 Geometric and material properties of cantilever beam

Material and Geometric properties	Values
Material	Steel
Young's modulus of elasticity (E)	2.00×10^5 N/mm^2
Poisson's ratio (ν)	0.3
Cross sectional area (A)	240 mm^2
Moment of inertia (I)	2000 mm^4
Mass density (ρ)	7840×10^{-9} kg/ mm^3
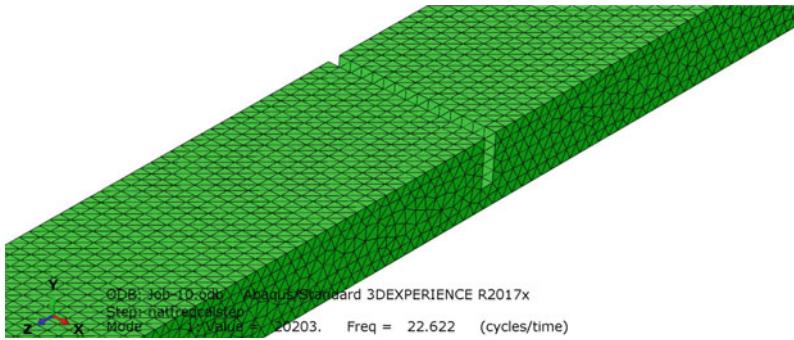
Fig. 2 Steel cantilever beam with damage provided as 2 mm wide cut

In the above equation, ϕ and ω are the eigenvector (mode shape) and eigenvalue (natural frequency).

The cantilever beam is modelled in ABAQUS, was meshed for a size of 1.75 mm for both undamaged and damaged beam. Based on the computing limitations, the mesh size as well as the cut width (2 mm) is decided, the cut width is chosen slightly greater than the mesh size. The element used in the finite element analysis is a 10-nodded quadratic Tetrahedron element designated as $C3D10$. The eight different damage cases were introduced at five location namely, 0.1L, 0.3L, 0.5L, 0.7L & 0.9L from the fixed end of cantilever beam as shown in the Fig. 2. Thus, forty finite element models were created and modal analysis was performed. The values of first eight natural frequency was found for all the models.

The steel beam has to be damaged at various location, since a crack or a cut will better represent the damage. So in the present study, cut of various depth d_{cut} was made in the beam for inducing damage. The cut was provided on the top side of the cantilever beam throughout the width of the beam. The depth of cut varies in the proportion of the actual depth of beam, $d_{undamaged}$ as its percentage like 10%, 20%, up to 80%. For example, if the damage parameter is $D3$ then the depth of cut is 3 mm. The damage parameter used in the present study, is mathematically shown in Eq. (4),

$$Din\% = 100\frac{d_{cut}}{d_{undamaged}} \tag{4}$$

The damage D is discretized into eight different linguistic variables shown in Fig. 3. It can be expressed by the following representation,

$$T(Din\%) = \{D1, D2, D3, D4, D5, D6, D7, D8\}$$

For fuzzification of measurement deltas, the whole universe discourse was classified into different sets in the form of $F(N)R(n)$, where linguistic terms F and R indicate the frequency and range, N and n are the indices representing N^{th} frequency
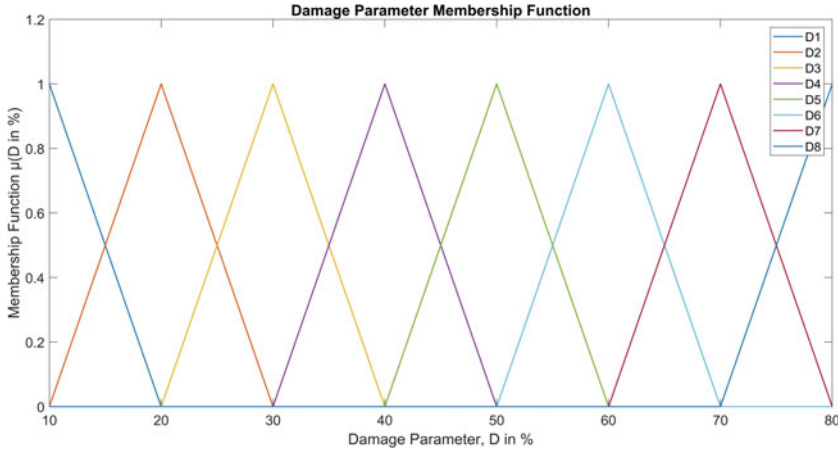
Fig. 3 Membership functions for damage parameter in D (%)

and n^{th} range respectively. Gaussian membership function with a standard deviation (σ) of 15% of the measurement delta is used for fuzzification.

The membership function (μ) used here is as follows in Eq. (5),

$$\mu(\Delta z) = \mu(100 * (\Delta\omega/\omega)in\%) = e^{-0.5(\frac{x-m}{\sigma})^2} \tag{5}$$

where ω and $\Delta\omega$ are frequency and change in frequency, m is the mid-point of fuzzy sets.

The membership function plots for measurement delta corresponding to the first and eighth mode focused in the range 0 to 200 is shown in Fig. 4. Table 2 gives the midpoint of the fuzzy sets used for fuzzification of measurement deltas.

The above plot shows only a part of the universe discourse for better visualization of the membership plot; for example, the actual plot of the eighth measurement delta is in the universe discourse of 0 to 982.143. The first and eighth measurement deltas can be expressed in 25 discretized linguistic variables as follows,

$T(\Delta Z_1) = \{F1R1, F1R2, F1R3, F1R4, F1R5, F1R6, F1R7, F1R8, F1R9,$
$F1R10, F1R11, F1R12, F1R13, F1R14, F1R15, F1R16, F1R17, F1R18,$
$F1R19, F1R20, F1R21, F1R22, F1R23, F1R24, F1R25\}.$

$T(\Delta Z_8) = \{F8R1, F8R2, F8R3, F8R4, F8R5, F8R6, F8R7, F8R8, F8R9,$
$F8R10, F8R11, F8R12, F8R13, F8R14, F8R15, F8R16, F8R17, F8R18,$
$F8R19, F8R20, F8R21, F8R22, F8R23, F8R24, F8R25\}.$

The C++ codes are made in such a way that the overlapping ΔZ ranges within $\pm 2\sigma$ are discarded and unique ΔZ ranges have been retained. It automatically provides the standard deviation of the plot as the absolute value of 15% of the ΔZ. Thus
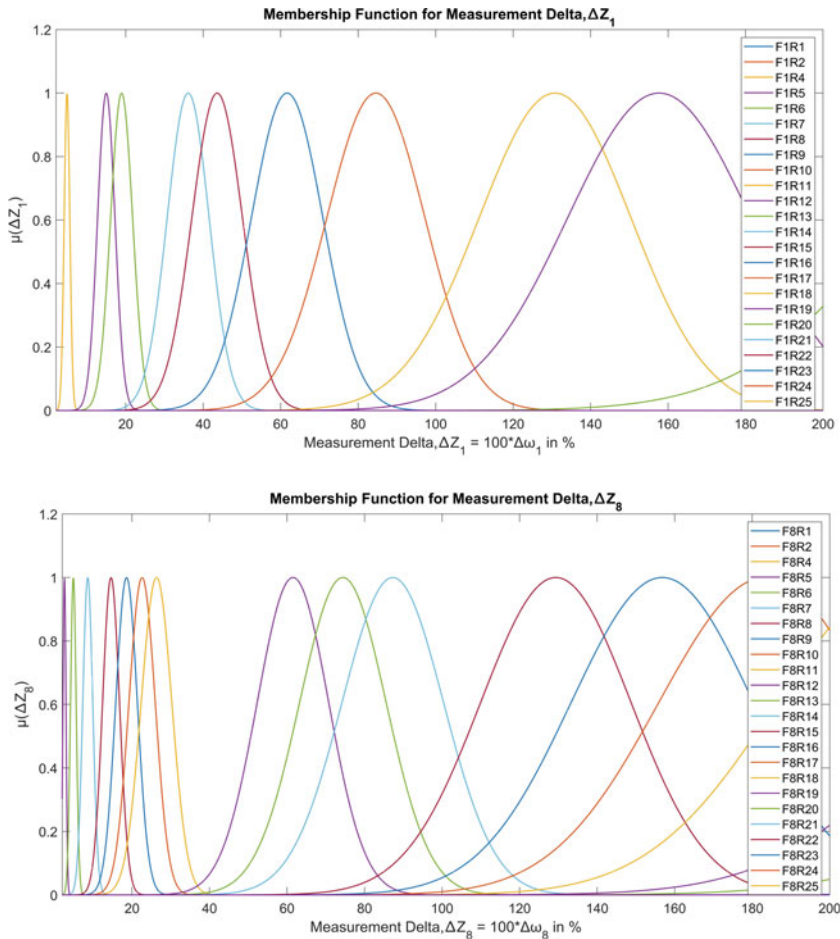
Fig. 4 Memberships function for (a) ΔZ_1 (b) ΔZ_8

the specified linguistic variable will easily cover variation of measurement deltas. The above Gaussian variation of memberships of measurement deltas are chosen so that the small changes in measurement deltas can be incorporated and the results obtained are robust against the contamination. The effect of noise in the form of random deviation in the measurement deltas was introduced in the data pool. The effect can be mathematically expressed as,

$$\Delta Z_{noisy} = \Delta Z (1 \pm \varepsilon * \alpha) \tag{6}$$

where, ΔZ_{noisy} is the changed measurement delta, α is the noise level say 10%, 15% etc. and ε is the random number between 0 to 1.

Table 2 Linguistic Notation for ΔZ_8

Linguistic notation	F8R1	F8R2	F8R3	F8R4	F8R5	F8R6	F8R7	F8R8	F8R9	F8R10	F8R11	F8R12	F8R13
Mid-point	0	0.2862	1.1447	2.5756	4.8649	8.5852	14.5948	18.6012	22.6076	26.3278	61.5270	74.4048	87.2825
Linguistic notation	F8R14	F8R15	F8R16	F8R17	F8R18	F8R19	F8R20	F8R21	F8R22	F8R23	F8R24	F8R25	
Mid-point	129.35	156.822	183.436	219.208	270.719	316.506	418.956	485.634	567.193	668.784	844.494	982.143	

4   Numerical Results

4.1   Frequencies in Undamaged Condition

The first eight natural frequencies for the beam is as shown in Table 3,

Using the above reference frequencies, the percentage change in frequencies due to various damages was calculated, and the same was scaled up by multiplying a constant 100 so that small damage cases are also identified uniquely. This constitutes eight measurement deltas. The changes in the dynamic response are obtained as expected. The first measurement delta is plotted against the changing damage parameter for damage at different locations in Fig. 5.

Table 3   Natural frequencies in the translation (y direction)

Natural frequency	Calculated value (Hz)
First	22.702
Second	142.09
Third	397.06
Fourth	775.84
Fifth	1277.8
Sixth	1900.4
Seventh	2640.4
Eighth	3494.5

Fig. 5   Damage parameter, D (%) versus measurement delta 1, ΔZ_1 due to damage at various locations from the fixed end of the cantilever beam

Table 4 Fuzzy rules

Rule no.	Measurement deltas								Damage	Location
1	$F1R14$	$F2R7$	$F3R6$	$F4R2$	$F5R12$	$F6R1$	$F7R7$	$F8R8$	$D1$	$0.1L$
2	$F1R17$	$F2R11$	$F3R9$	$F4R1$	$F5R9$	$F6R3$	$F7R10$	$F8R11$	$D2$	$0.1L$
3	$F1R19$	$F2R14$	$F3R10$	$F4R1$	$F5R12$	$F6R5$	$F7R12$	$F8R14$	$D3$	$0.1L$
4	$F1R21$	$F2R16$	$F3R12$	$F4R4$	$F5R15$	$F6R6$	$F7R14$	$F8R17$	$D4$	$0.1L$
5	$F1R22$	$F2R17$	$F3R13$	$F4R2$	$F5R17$	$F6R8$	$F7R16$	$F8R19$	$D5$	$0.1L$
6	$F1R23$	$F2R19$	$F3R15$	$F4R3$	$F5R19$	$F6R11$	$F7R17$	$F8R20$	$D6$	$0.1L$

The plot shows that the value of measurement delta is higher corresponding to the presence of fault near the fixed end and negligible when fault is near to the free end.

4.2 Fuzzy Logic Rule Base

The measurement deltas were fuzzified into linguistic form, thus written as fuzzy rules. There are a total of unique forty rules, from which six rules for damage at location $0.1L$ are shown in Table 4 as follows,

On the basis of the above rules, fuzzy logic inference system will be able to predict the damage cases. For example, the fuzzy logic inference system will interpret rule no. 1 as,

If
ΔZ_1 *is* **F1R14** *and* ΔZ_2 *is* **F2R7** *and* ΔZ_3 *is* **F3R6** *and* ΔZ_4 *is* **F4R2** *and* ΔZ_5 *is* **F5R12** *and* ΔZ_6 *is* **F6R1** *and* ΔZ_7 *is* **F7R7** *and* ΔZ_8 *is* **F8R8**
Then,
Damage is **D1** at *location* **0.1L**

4.3 Test with Noisy Data

The presence of noise in the data may lead to the failure of the damage detection scheme. The FLIS is robust to these noises because of its spread of inputs in the form of Gaussian membership function. 40 rules stated above were tested with two different level of noises. The noises were introduced in the measurement deltas as stated in Eq. (6). The values of some results showing the prediction by FLIS are mentioned in Table 5. It shows the damage prediction by the Rule no. 1 and 13 with random noises for $\alpha = 15\%$.

Table 5 Prediction of damages by the FLIS

Rule no.	Measurement deltas								Damage %	Location
Rule 1	40.53	14.78	2.52	−0.9	26.61	9.47	15.53	18.60	10	0.1L
Contaminated measurements	42.62	12.97	2.54	−1.01	28.71	8.61	13.24	16.43	10	0.1L
	41.16	15.84	2.28	−0.94	28.07	8.37	13.66	19.15	10	0.1L
	44.29	15.36	2.35	−0.88	23.48	10.42	15.55	17.51	10	0.1L
	45.92	14.56	2.53	−0.90	27.96	10.73	14.01	18.78	10	0.1L
Rule 13	464.30	118.24	490.38	170.53	62.61	586.22	235.20	4.86	50	0.3L
Contaminated measurements	430.10	115.03	441.47	185.91	66.41	538.69	231.80	5.30	50.10	0.3L
	396.07	135.02	514.85	187.13	64.54	656.38	228.35	4.76	50.00	0.3L
	400.59	133.82	526.50	147.43	67.02	531.26	214.88	4.56	50.00	0.3L
	485.71	113.64	555.02	162.68	59.58	669.36	225.39	5.57	50.20	0.3L

Table 6 Success rate S_R for different value of α

α in %	No. of rules checked	No. of acceptable prediction	S_R (%)
15	320	319	99.68
20	320	319	99.68

The noises are made in a random fashion and for each level of noises 320 trial have been performed. The success rate (S_R) can be defined as the ratio of number of trial in which a rule is giving correct results to the total number of trials. The Table 6 shows the success rate FLIS for two values of α.

5 Conclusion

A fuzzy logic rule base has been formulated for the prediction of location of damage, which is very useful for SHM. The procedure has been demonstrated by its application in a steel cantilever beam. It is observed that the fuzzy rules were capable of detection damages cases which were provided as the rules.

To check the reliability of the prediction, random noises within 20% was introduced in the measurement deltas and the working of fuzzy logic was checked. It is noted that the success rate of the prediction is as high as 99.68%. It shows the robustness of the fuzzy logic against uncertainty dues to material properties and modeling. More robustness can be achieved with more data and more number of damage location.

C++ codes prepared are capable of handling large data, thus by creating FE model of the other structures with choosing appropriate damage parameter and measurement deltas, FLIS can be used for other structures also.

References

1. Pawar, P., Ganguli, R.: Structural Heath Monitoring using Genetic Fuzzy System, 1st edn. Springer, London (2011)
2. Nayak, B.B., Sahu, S., Roy, S.: Damage detection in structural elements: using optimization of fuzzified rules. Mater. Today Proc. **44**, 797–800 (2021)
3. Parhi, D.R.K., Kumar, D.A.: Analysis of methodologies applied for diagnosis of fault in vibrating structures. Int. J. Veh. Noise Vib. **5**(4), 271–286 (2009)
4. Zadeh, L.A.: Information and control. Fuzzy sets **8**(3), 338–353 (1965)
5. Agarwalla, D.K., Parhi, D.R.: Effect of crack on modal parameters of a cantilever beam subjected to vibration. Procedia Eng. **51**, 665–669 (2013)
6. Quila, M., Mondal, S.C., Sarkar, S.: Free vibration analysis of an un-cracked & cracked fixed beam. J. Mech. Civil Eng. **11**(3), 76–83 (2014)
7. Sazonov, E.S., Klinkhachorn, P., Gangarao, H.V., Halabe, U.B.: Fuzzy logic expert system for automated damage detection from changes in strain energy mode shapes. Nondestruct. Test. Eval. **18**(1), 1–20 (2002)

8. Vestroni, F., Capecchi, D.: Damage detection in beam structures based on frequency measurements. J. Eng. Mech. **126**(7), 761–768 (2000)
9. Das, H.C., Parhi, D.R.: Online fuzzy logic crack detection of a cantilever beam. Int. J. Knowl.-Based Intell. Eng. Syst. **12**(2), 157–171 (2008)
10. Ashigbi, D.M., Sackey, M.N., Fiagbe, Y.A., Quaye-Ballard, J.: Vibration response based crack diagnosis in beam-like structures using fuzzy inference system. Sci. Afr. **14**, e01051 (2021)
11. Yu, W., Wang, Y., Gui, W., Yang, C.: A vibration fault diagnosis system of HGS based on FNN. IFAC Proc. Vol. **39**(13), 252–257 (2006)
12. Sawyer, J.P., Rao, S.S.: Structural damage detection and identification using fuzzy logic. AIAA J. **38**(12), 2328–2335 (2000)
13. Angelov, P.P., Filev, D.P.: An approach to online identification of Takagi-Sugeno fuzzy models. IEEE Trans. Syst. Man Cybern. Part B (Cybern.) **34**(1), 484–498 (2004)
14. Pawar, P.M., Ganguli, R.: Matrix crack detection in thin-walled composite beam using genetic fuzzy system. J. Intell. Mater. Syst. Struct. **16**(5), 395–409 (2005)
15. Chandrashekhar, M., Ganguli, R.: Uncertainty handling in structural damage detection using fuzzy logic and probabilistic simulation. Mech. Syst. Signal Process. **23**(2), 384–404 (2009)
16. Mohan, V., Parivallal, S., Kesavan, K., Arunsundaram, B., Ahmed, A.F., Ravisankar, K.: Studies on damage detection using frequency change correlation approach for health assessment. Procedia Eng. **86**, 503–510 (2014)
17. Das, H.C., Parhi, D.R.: Detection of the crack in cantilever structures using fuzzy Gaussian inference technique. AIAA J. **47**(1), 105–115 (2009)
18. Ross, T.J.: Fuzzy Logic With Engineering Applications, 3rd edn. John Wiley & Sons, United Kingdom (2005)
19. Chandrupatla, T.R., Belegundu, A.D.: Introduction to Finite Elements in Engineering. Prentice Hall, Englewood Cliffs (2001)

Challenges in Adhering to Earthquake Design Regulations: Consultant Perspective

Chu Zin Kai, Afiqah R. Radzi, Saffuan Wan Ahmad, and Rahimi A. Rahman

Abstract Malaysia is surrounded by earthquake-prone countries such as Indonesia and the Philippines. Throughout the years, earthquakes have caused disasters to our land. Two major earthquake-related events in Malaysia are the 5.9 magnitude earthquake in Ranau and the tsunami that struck Perlis, Kedah, Penang, and Perak due to the 8.9 magnitude earthquake in Acheh. These incidents had caused numbers of casualties and millions in property losses. This study aims to determine the challenges and solutions in adhering to earthquake design regulations from consultants' perspectives. The data is collected from consultants through open-ended interviews and analyzed using thematic analysis. The study findings suggest that the challenges in adhering to earthquake design regulations are increased cost to projects, the reluctance of key personnel to the regulation, and enforcement. On the other hand, the potential solutions for these challenges are reviewing the current earthquake design regulation, mandating the regulation, and increasing the exposure of the regulation. Local authorities can use these findings to foresee the challenges and solutions to improve the implementation of earthquake design regulations in Malaysia.

Keywords Earthquake design regulation · Cost increase · Reluctancy of key personnel · Enforcement of the regulation

C. Z. Kai (✉) · S. W. Ahmad
Department of Civil Engineering, College of Engineering, Universiti Malaysia Pahang, Gambang, Malaysia
e-mail: zinkaibryan@gmail.com

A. R. Radzi
Faculty of Built Environment, University of Malaya, Kuala Lumpur, Malaysia

R. A. Rahman
Faculty of Civil Engineering Technology, Universiti Malaysia Pahang, Gambang, Malaysia

General Educational Development, Daffodil International University, Dhaka, Bangladesh

1 Introduction

Large earthquake events can cause the overlying water to move suddenly, resulting in a disastrous tsunami. In 2004, Acheh, Indonesia, was struck by an 8.9 magnitude earthquake, causing an aftershock, and generating the Indian Ocean tsunami with high tidal. The tsunami resulted in 68 deaths, 299 people injured, and nearly MYR 80 million in property losses in Malaysia [1]. In 2015, a 6.0 magnitude earthquake caused 18 deaths at Mount Kinabalu and substantial damage to buildings and utility infrastructure. Following the earthquake, concerns about the structural stability and integrity of existing building structures in Malaysia have been raised. This incident has gained attention from many researchers as this is no more far-field effect from the other active seismic fault zone. According to [2], non-ductile detailing was observed in almost 90% of the surveyed reinforced concrete buildings. Damage due to the low quality of construction materials and unconfined infill walls were observed in 25 and 15% of the surveyed reinforced concrete buildings. The column undergoes spalling of concrete cover and buckling of reinforcement. At the same time, the beams only experience hairline cracks and spalling of plaster [3]. In other words, the reinforced concrete building in Malaysia is not up to seismic standards. The effects of earthquakes on structures that were not designed based on the earthquake design code are inevitable. Problems such as cracking, column buckling, and shear failure are the most common destruction observed from the buildings in the disaster area. These integrity issues are questionable if an earthquake strikes again.

Malaysia has an established building code, namely the Uniform Building By-Laws 1984 (UBBL 1984). UBBL 1984 is enforced by local authorities and applicable to all building types constructed in an area [4]. According to UBBL 1984, clause 55, part 2, the load due to the seismic forces is provision to the dead and imposed loads. These laws will be sent to local authorities for adoption and enforcement. One of the main functions of a local authority is development control in concurrence with its statutory role as a planning authority. Local authorities have jurisdiction over all buildings, including buildings owned by the federal government, and UBBL applies to all buildings in Peninsular Malaysia. The earthquake in Sabah has shown poor compliance with the building code. With inadequate construction practice and a low level of preparedness, buildings in Sabah will be vulnerable when an earthquake strikes again. The challenges and potential solutions from both sides can be compared to capture a general concept of the study.

From the incident timeline, two earthquake design codes have been released following the event of the earthquake. In 2017, Malaysia's Public Service Department (JKR) drafted the "Handbook on Seismic Design Guidelines for Concrete Buildings in Malaysia" after the Acheh earthquake [5]. In late 2017, Malaysia enacted its first national code of practice for the seismic design of buildings following the release of the Malaysian National Annex (NA) of Eurocode 8 (EC8) [6]. This study investigates whether these design codes are being adopted in Malaysia. Not only safeguard the integrity of the structure, but the lives in the building are also more worthy than the effort paid to enforce the regulation. Thus, this study highlights the challenges

in adhering to the earthquake design regulation for structures and infrastructures in Malaysia, as well as the solutions to overcome the challenges.

2   Methodology

The data were collected through open-ended interviews with industry professionals working in the construction industry. The collected data is analyzed using qualitative methods. The methods for collecting and analyzing the data are discussed in the following subsections.

2.1   Data Collection

In this qualitative study, an open-ended interview method is adopted for the data collection. Open-ended questions can be used to obtain aspects that stand out from the answers and thus could be interpreted as facts, behaviors, and reactions, typical to a defined panel of respondents. This approach has been used in other works in construction management research, including identifying success factors [7, 8] and decision criteria [9, 10]. The target population is consultants with at least five years of experience in the construction industry. The interviewer needs to give respondents a framework when using open-ended questions. After determining the target population, the researcher developed an interview protocol with a series of questions to conduct the interview. The interview questions are: (1) What challenges do you face in adhering to the earthquake design regulations? And (2) What are the solutions to overcome the challenges?

   The open-ended interviews are conducted via phone call or teleconference application. After the interview session ended, an interview summary was sent to the respondent as consent. If there is no comment from the respondent, the interview session is completed. As there are many consultants firm and engineers in Malaysia, it is impossible to include every professional opinion in this study. This study limitation may be anticipated, but this is the most suitable approach for qualitative study in the current situation. Finally, twenty open-ended interviews with industry professionals were conducted. All respondents have five or more years of experience in the construction industry. Therefore, the data from the interviews can be considered as reliable.

2.2   Data Analysis

Thematic analysis is adopted because it allows researchers to derive new concepts and insight from the data collected. The thematic analysis involves reading, familiarizing,

identifying, organizing, and offering insight into patterns or themes through a set of data. This is an inductive approach to data coding and analysis whereby the researcher maps the concept, and ideas derived are not necessarily linked to the semantic data content [11]. Other construction management research has used this method to identify parameters and success factors for implementing environmental management plans [12, 13].

The first phase of thematic analysis starts with the researcher familiarizing with the data. Next, preliminary codes are generated. These initial codes act as points that are ready to form lines. In phase 3, searching for themes is carried out. The analysis begins to form shape when the codes are grouped to see a theme emerging from the data. When generating themes and subthemes, the codes can be clustered when they propose the same meaning and pattern in the data. In the fifth phase, potential theme reviewing is involved. The themes developed shall work with the code extracted. This phase requires the researcher to define and name the themes. In the final phase, the final analysis and report writing was done.

3   Result and Discussion

3.1   Challenges in Adhering to Earthquake Design Regulations

Resources. Resources refer to all sorts of materials available to achieve something. Some of the common yet essential resources in a construction project include money, key personnel, construction material, and equipment. In complying with the earthquake design regulation, the availability of resources has played a major role, especially in an unorthodox field. From the data analysis, the challenges from resources involved in the study are cost, knowledge, experience, and technology.

Cost. In a construction project, the cost can consist of various items and parties such as consultation, legal and labor fees and material and machinery costs. The cost of a project also determines the profit of a project. Cost control and estimation play important roles in a construction project. Project cost will increase when the earthquake design regulation is implemented. One significant hike is the material cost, such as implementing high ductile reinforcement. The significant increase has resulted in consultants not following the earthquake design regulation.

Knowledge and Experience. Knowledge in the engineering field will be utilized to solve a problem professionally. In contrast, experience in the engineering field draws a picture of decisions. These two elements are crucial throughout the project cycle. As most regions in Malaysia are not affected by earthquakes, many engineers are not familiar with earthquake design. Also, earthquake engineering is not a compulsory subject in the Malaysian university syllabus. This shows that the knowledge of earthquake design in Malaysia is very limited compared to other countries such

as Indonesia, India, and Japan. On the other hand, the information and statistics on earthquake incidents in Malaysia are insufficient to serve as a reference for the whole nation. In other words, there is a lack of knowledge and experience in earthquake design in Malaysia.

Technology. The Malaysian Meteorology Department can detect earthquakes. However, the building nearby the region is still threatened. When an earthquake or an aftershock hits Malaysia, the safety of the buildings will be the main concern. While implementing the earthquake regulation to all structures in Malaysia is impractical, limited technology to identify earthquake hazards is the larger constraint. As a result, the regulation cannot be implemented in regions more prone to earthquakes.

Authority. In Malaysia, the federal government establishes the building regulations while local authorities such as PWD, Construction Industry Development Board (CIDB), and the local town council enforce the regulation. These are the regulatory agency responsible for ensuring that all construction projects in Malaysia abide by the rules and regulations. The local town council controls the development in concurrence with its statutory role as a planning authority. The guidelines and standards might be the best practice, but they are not embodied in the regulation. While projects are under the responsibility of different town councils, it is very hard to standardize the jurisdiction over all buildings.

Enforcement. Most regions in Malaysia are not affected by earthquakes. Therefore, some town councils are not requesting consultants to implement the earthquake design for a project. The lenient enforcement of the regulation might be happening in most town councils. However, the process of considering the implementation is yet to be acknowledged. The decision made by the town council is subject to the discussion and experience of the relevant department. The uncertainty of the enforcement between the town councils had directly caused communication problems between all parties, including consultants, contractors, and clients.

Implementation in Practice. The implementation rate of the earthquake design regulation is relatively low in Malaysia. Most projects in Malaysia are designed according to BS8110 without considering the earthquake loading to the structure. In addition, many town councils do not request the project adhere to the earthquake design regulation. As the risk of earthquakes is relatively low, local authorities only imply the mandatory regulation on certain projects that are more exposed to the damage of earthquakes. The uncertainty in the application of the earthquake regulation has confused industry practitioners.

Regulation Laws are formulated by the Federal Government and passed down to State Government to be gazette. The local authority is responsible for development control in concurrence with its statutory role as a planning authority. These roles are governed by the relevant laws, bylaws, and standards. Local authorities have jurisdiction over all buildings, including buildings owned by the federal government, and UBBL legal applies to all buildings in Peninsular Malaysia.

Reluctancy of Regulation. During the interview, the reluctance toward the regulation was shown when most respondents were not aware that earthquake design

regulation was being implemented in Malaysia. Many engineers are not familiar with the earthquake design regulation, and some do not know the existence of the regulation in Malaysia. Therefore, the reluctance of the earthquake design regulation is an obvious answer throughout the data collection period.

Uncertainty of Regulation. The regulation and standard both serve as standalone elements in Malaysia. There is no mandatory earthquake design regulation which leads to confusion in the industry. The standard remains useless if they are not adopted into practice. Without the mandatory compliance to these guidelines neither in the UBBL nor the federal laws, the regulation serves nothing.

3.2 Solutions to Overcome the Challenges

Resources. To resolve the challenges directly, it is best to provide a relevant solution. When the challenges lack resources, it is best to provide more resources or solve the problem with limited resources. As mentioned in the earlier theme, the challenges faced by the industry in terms of resources include cost, knowledge and experience, and technology. Hence, the potential solutions will be based on these directions.

Provide Funding. Adopting earthquake design will directly increase the project cost. The price surge behind an earthquake design project is the construction material Therefore, controlling the cost would help resolve this challenge. Local authorities can allocate money to encourage the industry to practice earthquake design regulations, including incentives to cost control on reinforcement bars, bonuses for companies that adhere to the earthquake design regulation, and tax exemptions to projects that complies with the regulation. Consultants may convince clients to adopt the earthquake design if such funding aids exist.

Education. Education is fundamental to every skill and work. However, the industry currently lacks exposure and education on earthquake design. Webinars and courses can also be held from university to industry level to promote the implementation of the earthquake design regulation. The earthquake engineering subject can also be included in the course structure for engineers, especially structural engineering. These initiatives can increase the exposure and knowledge of future engineers in related areas.

Skill Personnel. Local authorities can propose conferences or idea exchange forums with earthquake experts such as Indonesia and Japan. As Malaysia has a geographical advantage and is less prone to earthquakes, the experience brought by experts is more than enough. Besides, the government also can hire experts as advisors in terms of regulation review, standard review, and others. Their skill and knowledge in earthquake design can be fully utilized.

Role of Authorities
Authorities also serve as a regulator and are responsible for enforcing the regulation. As a law enforcer, the role is clear to ensure everyone abide-by the rules and

regulations. There are plenty of initiatives that the authorities can do to ensure the earthquake <u>regulation</u> implementation. When the regulation is bounded in the grey areas in legislation, this can become a sentiment of abuse by practitioners in the industry. A review shall be done of the implementation system to identify what is not right.

Regulation Review. The earthquake regulation stated in UBBL 1984 refers to the provision of dead load, and live load shall include loads due to seismic forces. The unclear regulation shall be revised and updated to cater to the current situation in Malaysia. With the enactment of the National Annex, the regulation shall serve more standards for different types of projects or regions required to adhere to the earthquake design regulation. The regulation review is best to involve the related department from the federal government, local authorities, industry representatives, and experts from the experienced country. A more systematic and dynamic regulation can persuade the industry to practice according to the risk and threat level. A good regulation that consists of all parties will contribute effectively to the nation and people in terms of good practice and safeguarding the building integrities.

Mandatory Regulation. Mandatory regulation prevents the industry from not adhering to earthquake-related codes and standards. However, the mandatory works even better after the regulation review is done. The synergy between two solutions can improve the earthquake-resistant building in Malaysia, resulting in one plus one greater than two. Instead of blindly adhering to the regulation, which can result in unnecessary overdesign, identifying a more dynamic regulation that can balance the safety of the buildings and the benefits of the clients is vital.

Identification of Earthquake Hazards. Despite not being in the Pacific Ring of Fire, Malaysia is still surrounded by earthquake-prone regions. Malaysia has been heavily affected twice due to the far-field earthquake attacks, including the 8.9 magnitude Acheh earthquake in 2004 and the 5.9 magnitude Ranau earthquake in 2015. Malaysia should learn from history and take the initiative to minimize earthquake damages. The soil type classification or regional boundary method can be adapted to determine the required levels of earthquake design. The hazard prediction will determine the degree to implementing the earthquake design regulation.

4 Conclusion

The study aims to determine the challenges in adhering to earthquake design regulations as well as the potential solutions from a consultant perspective in Malaysia. After conducting interviews with 20 representatives from consultants, the interview data were analyzed using thematic analysis.

The study findings on the challenges can be summarized into three themes: resources, the role of authorities, and regulation. The resources can be divided into three subthemes: cost, technology, knowledge, and experience. The implementation

of the earthquake design regulation can increase project costs. Also, the availability of technology to measure the risk of earthquakes is questionable. Engineers might lack knowledge and experience in handling earthquake design as Malaysia is not affected by earthquakes. Another challenge to the implementation is the role of authorities. The enforcement of the regulation in Malaysia is lenient, and it directly affects the implementation of the earthquake design regulation. Also, the local authorities only request selective projects to adhere to the earthquake design regulation leading to a low adoption rate in the construction industry. Another major challenge is regulation. Engineers in Malaysia are hesitant to implement the earthquake design because there are unfamiliar with the earthquake design and regulation.

References

1. Abd Razak, S.M.S., Adnan, A., Abas, M.C., Lin, W.S., Zainol, N.Z., Yahya, N., Mohamad, M.E.: A historical review of significant earthquakes in region surrounding Malaysia. In Proceeding of International Conference on Durability of Building and Infrastructures, pp. 242–245 (2018)
2. Alih, S.C., Vafaei, M.: Performance of reinforced concrete buildings and wooden structures during the 2015 Mw 6.0 Sabah earthquake in Malaysia. Eng. Fail. Anal. **102**, 351–368 (2019)
3. Ganasan, R., Tan, C.G., Ibrahim, Z., Nazri, F.M., Wong, Y.H.: A case study on structural failure of reinforced concrete beam-column joint after the first significant earthquake impact in Malaysia. Int. J. Integr. Eng. **12**(8), 288–302 (2020)
4. Uniform Building By-Laws (UBBL) 1984. Laws of Malaysia (2015)
5. Chiang, J., Hee, M.C.: Technical review of JKR's handbook on seismic design guidelines for concrete buildings in Malaysia. Bull. Inst. Eng. Malaysia (2008)
6. Looi, D.T.W., Tsang, H.H., Lam, N.T.K.: The Malaysian seismic design code: Lessons learnt. In: Proceedings of the 2019 Pacific Conference on Earthquake Engineering (2019)
7. Munianday, P., Radzi, A.R., Esa, M., Rahman, R.A.: Optimal strategies for improving organizational BIM Capabilities: PLS-SEM approach. J. Manag. Eng. **38**(3), 04022015 (2022)
8. Badraddin, A.K., Radzi, A.R., Almutairi, S., Rahman, R.A.: Critical success factors for concrete recycling in construction projects. Sustainability **14**(5), 3102 (2022)
9. Radzi, A.R., Rahman, R.A., Doh, S.I., Esa, M.: Construction readiness for highway projects: key decision criteria. J. Constr. Eng. Manag. **148**(2), 04021196 (2022)
10. Radzi, A.R., Rahman, R.A., Doh, S.I., Esa, M.: A comparative study on the readiness parameters of highway construction projects. IOP Conf. Ser. Earth Environ. Sci. **641**(1), 012008 (2021)
11. Braun, V., Clarke, V.: Using thematic analysis in psychology. Qual. Res. Psychol. **3**(2), 77–101 (2006)
12. Ng, C.C., Rahman, R.A., Ahmad, S.W.: Factors affecting the enforcement of environmental regulation: the case of erosion and sediment control plan. IOP Conf. Ser. Earth Environ. Sci. **682**(1), 012046 (2021)
13. Asnor, A.S., Al-Mohammad, M.S., Ahmad, S.W., Almutairi, S., Rahman, R.A.: Challenges for implementing environmental management plans in construction projects: the case of malaysia. Sustainability **14**(10), 6231 (2022)

The Development of Structural Health Monitoring System (SHMS) for Special Bridges in Indonesia: To Improve the Monitoring of Special Bridges Using the Integration of SHMS

Vebry Puspitasari

Abstract Special bridges are infrastructures for land connectivity that require special treatment in their maintenance. The number of bridges in the operational services period is 140. Maintenance is necessary to maintain the durability of bridges and to ensure any low condition can return to the durable condition as per requirements. However, before maintenance inspection and monitoring should be done to avoid accidents or collapses, such was the case with Kutai Kartanegara (Kukar) bridge in East Kalimantan, Indonesia. Currently, monitoring of Special Bridges is still lacking, especially for bridges far from city centers. Moreover, monitoring is usually done by visual inspection of the bridges' condition and thus unable to determine whether the structures are still safe according to their planning age. In recent years, there have been several Special Bridges with SHMS, such as the Soekarno bridge, Merah Putih bridge, etc. Unfortunately, on those bridges, the local SHMS is not functioning well, likewise with the integrated central SHMS. Therefore, there is a need to conduct, first, parameter or component analysis that is necessary for the development of integrated SHMS, and second, development of the integration and management of local and central SHMS. With the working system, the bridges' condition can be monitored in real-time and can become the basis for decision making by stakeholders to conduct maintenance or repair when there are damages or accidents or any force majeure and unforeseen conditions.

Keywords Infrastructures · Special bridge · Health of structure · Monitoring · Data · Integration · SHMS

V. Puspitasari (✉)
University of Indonesia, Depok City, Indonesia
e-mail: vebry.widya@gmail.com

843

1 Introduction

1.1 General

Bridges are one of the infrastructures for land connectivity, namely roads located above the water surface and/or above ground level. Bridges are divided into standard and non-standard bridges/special bridges. They are called special bridges because they require special handling in the design and implementation of their construction (Ministry of Public Works and Housing of The Republic of Indonesia, 2015). The following are the criteria for special bridges:

1. Bridges with a span of at least 100 m,
2. Arch bridges with a span of at least 60 m, suspension bridges, and cable-tested bridges,
3. Bridges with a total length of at least 3,000 m,
4. Bridges with a pillar height above 40 m,
5. Bridges that have high structural complexity or have high strategic value or are designed using new technology.

Bridges that are outside these criteria are called normal or standard bridges.

The number of special bridges in Indonesia is 213 bridges consisting of 30 in stages of preparation (design), 43 in stages of construction, and 140 in stages of service (operational and under maintenance). These bridges include bridges on toll roads, busway roads, as well as railroads such as the Light Rapid Transit (LRT) and the Jakarta Bandung Fast Train [1].

Bridges that are in the service stage require maintenance work to maintain the condition of the bridge remains stable and ensure that the deterioration of the condition can be returned to a steady state according to the required performance.

Currently, the condition of some bridges has not been properly monitored during the operational and maintenance/preservation periods. One of them is the Kutai Kartanegara (Kukar) Bridge in East Kalimantan which collapsed during maintenance work on November 26, 2011.

The impact of unmonitored bridges is that the performance of the bridges is not monitored, the condition of the bridge is not known, and the maintenance or preservation program is hampered.

Several special bridges in Indonesia have implemented a structural health monitoring system (SHMS), including the Suramadu Bridge in East Java, the Musi VI Bridge in South Sumatra, the Rumpiang Bridge in South Kalimantan, Merah Putih Bridge in Ambon, and the Soekarno Bridge in Manado. Monitoring is done by placing sensors on the bridge structure without changing the behavior of the structure. Sensors used include accelerometer, ATRH (Ambient Temperature and Relative Humidity) tiltmeter, strain transducer, electromagnetic, DMM (vertical displacement), and DSS (horizontal displacement).

Bridges that have been installed with SHMS have problems displaying data in real-time, especially for the benefit of central management in making decisions for

repair and or maintenance (Suhendro, 2020). The existing integration system that is in the central office (Directorate General of Highways, Ministry of Public Works and Housing) for monitoring the condition of all the bridges in each region is not functioning.

The cause of the problem must be immediately addressed or improved so that the SHMS integration system runs well and smoothly and data on special bridges throughout Indonesia can be monitored in real-time at the Ministry of Public Works and Housing Headquarters by the direction of the Minister of Public Works and Housing. Thus, it is necessary to develop the existing SHMS integration by first looking at the troubleshooting in each local SHMS, then re-planning systems integration and making management that is clearly in operates/manage integration SHMS by making guidelines or SOP (Standard Operational Procedure) including the structure of his organization. System integration can be used as a basis for making decisions for the repair and or maintenance of special bridges.

1.2 Objectives

- Analyze the parameters or components needed for the development of the Special Bridge SHMS integration system in Indonesia.
- Develop integrated SHMS management to improve monitoring of specific bridges in Indonesia.

So, both SHMS analysis was conducted in each bridge (Local SHMS) and system integration in Central.

1. Local SHMS

    - Check system SHMS
    - Check contract vendor SHMS
    - Check the person in charge or SHMS management organization

2. Integrated Monitoring Center

    - Check software for integration
    - Check database system
    - Check the person in charge or SHMS management organization

From the display in an integrated monitoring center, stakeholders can monitor, report, action, and recommendation.

2 Case Study

This study analyzes the case studies of special bridges that have used SHMS to identify the problems in the operation of SHMS and can thus find solutions for the development of SHMS integration systems in Indonesia.

SHMS data of the bridges that will be analyzed are the Suramadu Bridge in Surabaya, the Soekarno Bridge in Manado, and the Merah Putih Bridge in Ambon.

2.1 Suramadu Bridge

The Suramadu Bridge has been installed with SHMS since 2012, using 514 sensors that are useful for maintenance, and monitoring traffic density, wind speed, and earthquakes. But over time due to weather conditions, the surrounding environment, and others, some sensors are damaged or not working properly.

In detail, a review of the existing literature related to the examination of SHMS at the Suramadu Bridge results as follows:

- There are several sensors or SHMS elements that are damaged so that they must be replaced, such as tiltmeter, nozzle wire sensor, DAU (Data Acquisition Unit), ethernet switch, GPS receiver, and others.
- Some sensors or SHMS elements are unmaintained, such as loose cable connections
- GPS sensor data acquisition software and windows operating system have been discontinued so data acquisition stops.
- Some sensors have to be recalibrated due to anomalous data.
- Lack of bandwidth capacity so that data does not reach the Suramadu Bridge SHMS network.
- Suramadu Bridge SHMS data is not included in the SHMS integration system at the Center.
- There is no clear management of SHMS at the project level to the Balai (representative offices of the Directorate General of Highways in each region throughout Indonesia) level. It means no organizational structure in the management of SHMS

2.2 Soekarno Bridge

Soekarno Bridge SHMS has been installed since 2015. Currently, there are several problems in its operation, including:

- Malfunction of sensors and SHMS elements.
- Monitoring room that is less resistant to water and weather around the bridge
- Unmaintained sensors and other elements for SHMS.

- Suramadu Bridge SHMS data is not included in the SHMS integration system at the Center.
- Inadequate internet network
- Lack of human resources due to the absence of clear SHMS management at the project level to the Balai level.

2.3 Merah Putih Bridge

The Merah Putih Bridge has also been installed with SHMS, but currently, the data from the sensor cannot be read on the local server. In detail, the problem is as follows:

- Non-functioning sensors and SHMS elements installed with wireless connections, as well as wired connections, almost all of them do not work.
- Internet network is still inadequate.
- There is no clear management of SHMS at the project level to the Balai level.

2.4 Problems with Local SHMS on Bridges

Judging from the 3 (three) bridges that have been installed with SHMS, there are several problems in common, including:

- Damage to the sensor and SHMS element so that it must be replaced or repaired.
- There is no system for the maintenance of sensors and SHMS elements.
- Software for data retrieval and display is not updated and is not well integrated with the integration system.
- Inadequate internet network, especially for wireless connection.
- There is no clear management of SHMS either at the project level to the Balai level, let alone the Central level.

The problems above are components or parameters of the importance of solutions for the development of local SHMS and well-integrated systems at the Center.

The problem that will be the focus of this research is the improvement of SHMS management, because as its stance, in terms of management, whether it is monitoring or maintaining SHMS, there is no clear organizational structure and reporting system at the Balai level and the Central level (Directorate General of Highways, Ministry of Public Works and Housing).

There are some of the challenges of the SHMS in Indonesia among them are:

- Maintenance
- Implementing Simple SHMS
- Improvement of Data Transfer
- Improvement Software SHMS
- Managed Service Contract
- SHMS management responsibility

The effectiveness of developing the SHMS integration system has been documented in other countries, for example in South Korea. They have developed a continuous SHMS integration system from inspection to how to maintain equipment, data, and the SHMS system itself from each bridge such as Jindo Bridge, Cheonsa bridge, and others, as well as an integrated system to monitor all bridges, including the organizational structure in managing them [2]. The integrated system has allowed for early alert in case of abnormalities or disasters such as an earthquake.

3   The Development of SHMS Integration System

The repair of SHMS on each bridge is different depending on the needs of each bridge, moreover, the types of bridges are also different. However, in general, the main problem can be solved even though the bridge types vary.

The system integration flow can be described as follows (Fig. 1):

3.1   Maintenance of Sensors and SHMS Elements According to the Needs of Bridges

Sensors and elements in the SHMS must be maintained so that they can continue to function according to the lifetime of the sensor, especially if the sensor is placed without protection against rain, wind, vandalism, and others. Therefore, a manual is made for each sensor and element in the SHMS. These sensors and elements are guaranteed at least 5 (five) years from the time they are installed and the service provider must fulfill a service life of 10 years.

The following are maintenance sensors to be done among others:
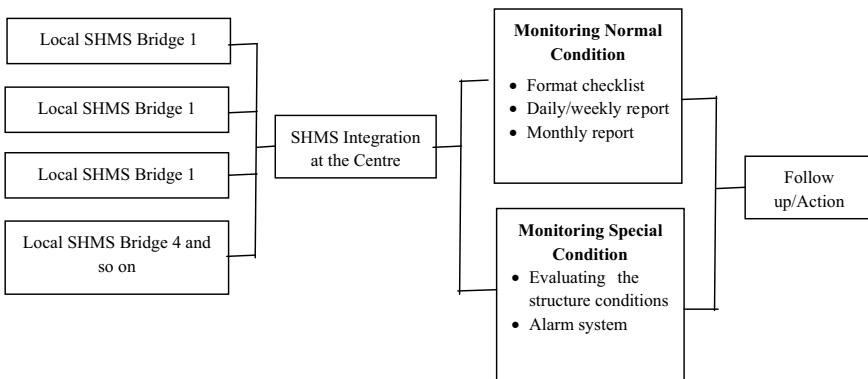
Fig. 1 System integration flow

Table 1 Categorized components of SHMS

Section		Component of SHMS	Remarks
Bridge site	Hardware	Sensor, DAQ Server, Storage Data, Emergency generator, UPS, Power Redundancy, Equipment of server	Unified Remote Monitoring System including seismic measurement
	Software	DAU, application system of SHMS	
	Network	VPN, data logger	
Integrated monitoring center	Hardware	Storage for Database, Web server	
	Software	Application for Integration	
	Network	VPN	

1. Categorized components of SHMS to be examined and repaired (Table 1).
2. Made performance index for each group of the sensor (essential and supported), among others.

   - **Operation Rate**
       Index to evaluate long-term operation condition of SHMS
   - **Threshold Setting Rate**
       The criterion for determining the long-term integrity level of monitoring data
   - **Service Life Score**
       The score of SHMS Aging Effect

3. Inspection and Maintenance sensors based on report data of SHMS (by weekly/monthly) and regularly visual inspection of sensors (by monthly).
4. These sensors and elements are guaranteed at least 5 (five) years from the time they are installed and the service provider must fulfill a service life of 10 years

3.2 Installation of Sensors and SHMS Elements According to the Needs of Bridges

Sensors and installed elements should match the data required in monitoring the health of the bridge structure against traffic and environmental conditions. Based on the modeling of designs in the determination of critical location on structure.

After construction, check the condition bridge by loading test. Then, the result of the loading test becomes the base threshold (strain, structural differential settlement, vibration, displacement) bridge condition along with operational and maintenance Thus, the installation of sensors will be simpler and more targeted. At least the installed sensors can determine dynamic properties (vibration) and static properties (vertical displacement, strain, structural differential settlement), as well as

monitoring temperature which is useful for monitoring other sensors if there are anomalies.

For bridges in sea areas or where there are strong winds, sensors are needed to determine wind speed for the safety of road users. Besides those, it required the addition of servers and data storage capacity.

The installation of the sensor so that it is accurate is carried out by modeling the structure of the results of the planning consultant or the results of the last loading test.

3.3   Software Usage for Local and Central SHMS

Software used for both Local and Central SHMS must be able to synchronize with each other. Software in Local SHMS must be open source, which means that it can be accessed by stakeholders in the project without having to depend on the software service provider. As with sensors, the service period for software is at least 10 years, replacement may be carried out because it is assumed that after 10 years there is the latest technology in SHMS software.

The software at the Center to integrate Local SHMS needs to be improved, especially regarding the protocols that burden the server in retrieving data from each local SHMS. Alternative protocols that can be used later include real-time databases such as firebase (a Google product) so that data from each local SHMS can be real-time.

The development of Local SHMS software and system integration in Central among others:

- Take the data with passing over the bridge and easily move the sensor to another bridge for temporary monitoring
- Increase the speed of data transfer to obtain a reliable SHMS
- Improving the SHMS to automatically detect the problem and able to diagnose the health of the bridge from model
- Endeavor to implement big data analysis into the SHMS to support further data processing and the provision of complete information
- Software in Local SHMS must be open source, which means that it can be accessed by stakeholders in the project without having to depend on the software service provider/vendor.
- Software used for both Local and Central SHMS must be able to synchronize with each other.
- The service period for software is at least 10 years, reconstruction of SHMS may be carried out because it is assumed that after 10 years there is the latest technology in SHMS software (Figs. 2 and 3).

The following is a screenshot of the SHMS integrated system at the Central:

Fig. 2 SHMS integrated system application
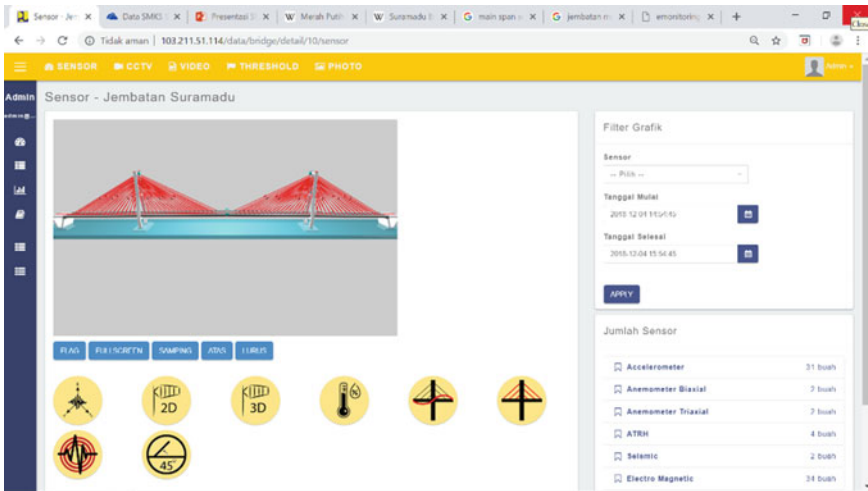
Fig. 3 Example of SHMS dashboard for Suramadu Bridge

3.4 The Organization of SHMS Management

In the operation of SHMS, there is a need for management, namely the need for a clear organizational structure that will be responsible for each process of analysis, reporting, and maintenance of the SHMS.

With the organizational structure, the party responsible for each process can make a list of human resource needs. For example, in the development of local SHMS and integration systems at the Center, other techniques are needed besides Civil Engineering, namely System Analysts and System Architects. Then, for SHMS operators,
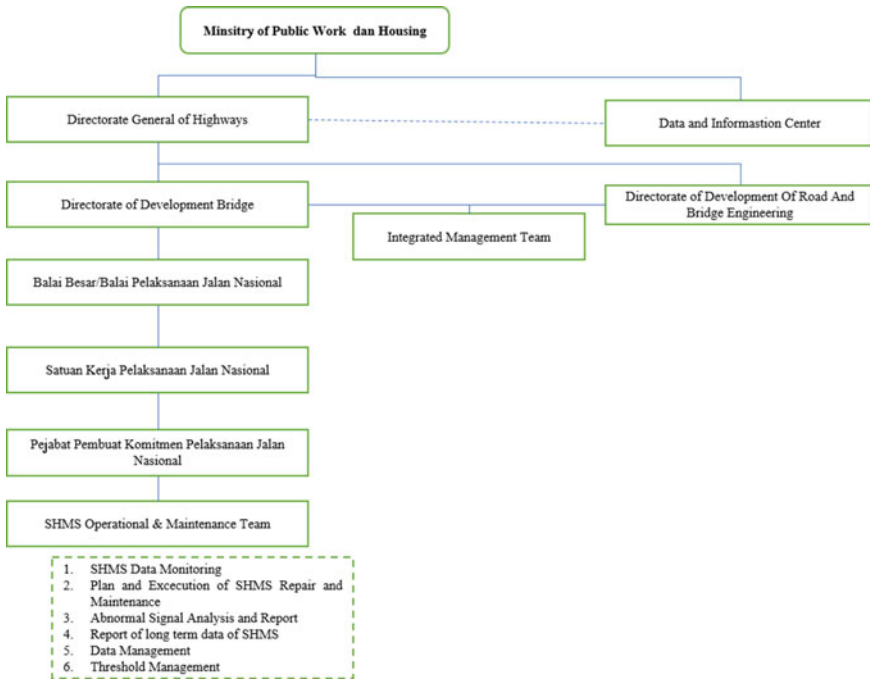
Fig. 4 Structure organization of SHMS

Civil Engineering is needed who understands the application or software so that they can read the sensor results and can find out if there are data anomalies.

In the reporting process, SOP (Standard Operating Procedures) are made so that each section knows its authorities and responsibilities as well as the reporting flow so that stakeholders can follow up.

The description of the organizational structure of SHMS in the Ministry of Public Works and Housing is as follows (Fig. 4):

4 Conclusion

Bridges are one of the important means of connecting land connectivity that is separated by rivers, seas, plains, or other traffic crossings, so a Structural Health Monitoring System (SHMS) is needed to monitor the health of the bridge structure and can detect damage early and can be followed up quickly by contractors. stakeholders both at the local/each bridge level and at the central level. Therefore, it is necessary to have an integrated system that runs well from each local SHMS. However, currently, the existing integration system is not running, so it is necessary to develop a local

and central SHMS system, which can later be handled more quickly and precisely if something happens that interferes with the health of the bridge.

So, SHMS integration system development to increase the number of special bridges that can be monitored and good management in SHMS can accelerate the handling of the repair and programming maintenance for a special bridge.

References

1. Balai Jembatan. Laporan data jembatan khusus di Indonesia. Direktorat Jenderal Bina Marga, Jakarta (2021)
2. KALIS & EJtech. Integrated Management System. Dipresentasikan pada 5th Workshop Structural Health Monitoring System (SHMS) Hibah Korea, Jakarta (2022)

Parameters Comparison of Green Building and Healthy Building

Nanda Wardhana, Mohammed Ali Berawi, and Mustika Sari

Abstract The Green building (GB) concept has been widely adopted by practitioners from the building and construction industry in the last few decades as an effort to reduce the negative environment al impacts caused by the development of the built environment. GB concept emphasizes resource usage efficiency, which focuses on conserving the natural resources to preserve the climate and environment through innovations in building design, construction methods, and materials. Awareness and surge of attention to the healthy building (HB) concept, which focuses on the quality of life and well-being in buildings, has increased lately due to the pandemic. However, minimal evidence was found regarding the implementation of healthy buildings. Therefore, this study aims to identify the building variables and elements that construct the HB concept and determine its differences from GB. Archive analysis and comparative study were performed to obtain this objective, taking into account the GB guideline practiced in Indonesia and several HB parameters derived from the literature. The results of this study indicated that there are elements that overlap, particularly in the indoor environmental quality factor, but there are fundamental differences between the two concepts.

Keywords Green building · Healthy building · Indoor environmental quality · Comparative study

1 Introduction

Environmental issues and climate change are important and interesting issues to discuss. Researchers are also trying to find a solution regarding this issue, including its relation to the building. One of the efforts to overcome this is by developing an

N. Wardhana (✉) · M. A. Berawi · M. Sari
Department of Civil and Environmental Engineering, Faculty of Engineering, Universitas Indonesia, Kampus UI Depok, Depok 16424, Indonesia
e-mail: nanda.wardhana@ui.ac.id

M. Sari
Center for Sustainable Infrastructure Development, Faculty of Engineering, Universitas Indonesia, Kampus UI Depok, Depok 16424, Indonesia

innovative building concept that minimizes the impact on the environment, which in its development is known as a Green Building (GB).

GB focuses on the environmental aspect; however, the occupants' health and convenience should also be considered in the building design [1]. This topic is important to discuss because of the necessity of dealing with the possible health consequences of the built environment and move beyond the concept of GB towards Healthy Building (HB) with not only focuses on the environment, but also to occupants' health and wellbeing which in the end affects performance and productivity [2]. The pandemic also makes this discussion even more important. To accelerate the understanding of the transformation of the concept, it is necessary to conduct a comparative study between GB and HB.

Therefore, the development of the HB concept began in the US in the 1990s [3] and has been implemented in various countries in the last decade [4]. Despite its development, the concept of HB has not been considered in several countries. In Indonesia, located in South-East Asia, the HB concept has not been widely discussed yet, since it is still focusing on implementing the GB concept in its building and construction sector. This study is expected to contribute to the advancement of building construction in countries that have not been familiar with the HB concept, especially Indonesia.

The method used in this paper is a qualitative review with the data used are those from published journals, building codes, standards and guidelines related to green building and healthy building. Comparison analysis is a method with two or more objects that aims to discover the differences and similarities as well as the causal relation between them [5]. This method is used to determine and analyze the parameters of HB and compare them to GB parameters and discover the differences and relationships between them.

2 Green Building

2.1 Green Building Concept and Certification

In the modern GB movement raised in the 1980s, the Montreal Protocol restricted the application of chlorinated fluorocarbons, which were harmful to the ozone layer that is so vital for human life. A group of far-sighted architects formed the Committee on the Environment within the American Institute of Architects (AIA) in the late 1980s. This starts the process of steering the profession towards sustainable design. Two important events occurred in the early 1990s that influenced the formation of the U.S. Green Building Council (USGBC). In the United States, the 20th anniversary of the original Earth Day occurred in 1990; in Brazil, the United Nations Conference on Environment and Development, known as the Earth Summit, was held in Rio de Janeiro in 1992. These two events led the formation of the USGBC in 1993 [6].

Furthermore, to accommodate the Green Building Council in all countries worldwide, the World Green Building Council (WGBC) was formed in 2002 with eight initial members, namely USA, Canada, Brazil, Japan, India, Australia, Mexico, and Spain. Until now, WGBC has more than 70 Green Building Council Members worldwide, including Green Building Council Indonesia (GBCI) [7].

According to Yudelson [6], a GB is a high-performance property that reduces and considers its impact on the environment and human health. A GB is designed to use less energy, water, and minimize the life-cycle environmental effects of the materials used. WGBC defines a GB as a building that reduces or eliminates negative impacts and can positively affect our climate and natural environment in its design, construction, or operation. GB preserve precious natural resources and improve our quality of life. [8]

According to previous studies, about 600 national and international Green Building Rating Systems (GBRS) have been developed around the world [9, 10]. Among these methods, the most famous and most widely applied are the Building Research Establishment Assessment Method (BREEAM), organized by Building Research Establishment (BRE) in the United Kingdom, and the Leadership in Energy and Environmental Design (LEED), organized by the United States Green Building Council (USGBC) from USA [11]. Indonesia also has its GBRS called Greenship, organized by the Green Building Council Indonesia (GBCI). This certification has been held since 2010 and lastest updated in 2013 [12, 13]. This paper will focus on analyzing these three GBRS to get the whole GB features and parameters.

2.2 Green Building Parameters

Each organization develops different parameters, methods, approaches, and features, but there are similarities that we can elaborate on from them. For that purpose, we analyze each of the detailed assessments of BREEAM, LEED, and Greenship. The standards we study are the latest editions of each GBRS and are used for new buildings. We find the GB parameters as shown in Table 1.

In the analyzing process, we merge some areas of focus & parameters that have a similar concept to simplify the composition of the whole GB parameters. For example, in the "Commissioning and Handover" parameter, the sentence is written in the BREEAM standard, while in the Greenship standard, it says, "Proper Commissioning", and in LEED, it says, "Fundamental Commissioning and Verification". Due to the similarity of objectives, we simplify it in one parameter derived from the three references. We also do the same process on other parameters to get the whole GB parameter.

Table 1 The green building parameters

Area of focus	Parameters	Reference
Management	Project brief & universal design	[14]
	Life cycle cost & service life plan	[14]
	Responsible construction practices	[14]
	Commissioning and handover	[13–15]
	Aftercare & occupant survey	[13, 14]
Indoor environmental quality	Visual comfort	[13–15]
	Indoor air quality management	[14, 15]
	Thermal comfort	[13–15]
	Acoustic performance	[13–15]
	Tobacco smoke control	[13, 15]
	Low-emitting material & monitoring	[13–15]
	Ventilation	[13]
	Hazards	[14]
	Private space	[14]
Energy	Energy metering & monitoring	[13–15]
	Energy efficiency performance	[13–15]
	Natural/external lighting	[13, 14]
	Renewable energy	[13, 15]
	Adaptation to climate change impact	[13, 14]
Location & transportation	Public transport accessibility	[13–15]
	Amenities & community accessibility	[13, 14]
	Bicycle facility	[13–15]
	Reduced parking	[14, 15]
	Site selection & equitable development	[13, 15]
	Electric vehicles	[15]
Sustainable site development & ecology	Basic green & open space area	[13–15]
	Site selection & assessment	[13–15]
	Site landscaping	[13]
	Reduction of light pollution	[14, 15]
	Protect or restore existing ecology	[14, 15]
Water	Water quality	[14]
	Water metering & calculation	[13, 15]

<div align="right">(continued)</div>

Table 1 (continued)

Area of focus	Parameters	Reference
	Water use reduction	[13, 15]
	Water recycling	[13]
	Water efficiency landscaping & protection	[13, 14]
	Rainwater management	[13, 15]
	Responsible water resources	[13, 14]
Material & resouces	Refrigerant management	[13–15]
	Safe & environmentally friendly material	[13–15]
	Regional source of material	[13, 15]
	Recycled material	[14, 15]
Waste	Construction waste management	[13–15]
	Operational waste management	[13, 14]

3 Healthy Building

3.1 Healthy Building Concept and Certification

A healthy building (HB) is a concept that aims to minimize the negative impact on the environment, as well as to maximize the positive effect on the health and well-being that a building has on its occupants. With urbanization increasing health costs and other social consequences, we must also consider the positive impact it can have on humans as well as reduce the negative impacts on our environment. According to a study conducted by Spengler & Chen [16] it is still unclear whether HB are just part of a GB due to widely defined criteria that did not exist at the time.

According to Levin [3] a HB is one whose building design concepts affect the welfare of users or a more significant environmental impact. Indoor air quality is one of the issues that should be addressed to avoid unfriendly effects on the occupants' well-being and health. HB not only considers using healthy materials (with consideration of acoustic comfort, thermal comfort, etc.) but also promotes healthy living by educating them about living healthy [17].

In contrast to the Green Building Rating System, which is already mature and developed over the last two decades, systems to specifically recognize HB are more recent arrivals to the global scene. And there is no transparent rating system that states that the system is the Healthy Building Rating System, but several researchers have identified that some rating systems focus on health; among them are the WELL and Fitwel rating systems [4, 18].

WELL has been operated by International WELL Building Institute (IWBI) since 2014 [4]. WELL standard focuses exclusively on impacts on human health and well-being through several factors: water, air, light, nourishment, movement, thermal comfort, materials, sound, mind, and community [19].

Fitwel was formed in 2017 by US Center for Disease Control (CDC) and Prevention and the US General Services Administration (GSA) and operated by the Center for Active Design (CfAD) [20]. Fitwel was designed for single-tenant, commercial interior, and multi-tenant buildings and encouraged certification without necessarily engaging a consultant [4]. Its focus is on twelve sections: building access, location, outdoor spaces, entrances and ground floor, stairs, workspaces, indoor environments, shared spaces, water supply, emergency procedures, vending machines and snack bars and food services [21].

3.2 Healthy Building Parameters

In the same way as elaborating the green building parameters above, we also do it to get HB parameters. We analyze each detailed assessment of WELL and Fitwel. The standards studied are the latest WELL Building Standard and Fitwell building standard for Multi-Tenant Whole Building. The results we found are shown in Table 2.

The WELL building standard has 122 parameters in its ten sections. Several Parameters with a close meaning and purpose were combined to create a more straightforward list. In addition to referring to the WELL and Fitwel standards, we also refer to one reference that is quite a lot referred to by healthy building researchers, namely the nine foundations of healthy building written by J. Allen et al. [22]. In the paper, some factors have not been included in the WELL and Fitwel standards, namely the Safety and Security factors. So, we add these parameters to form the concept of healthy building.

4   Discussion

As has been known and widely used as a background for research on green building, buildings are responsible for 50% of all extracted materials and almost 40% of global energy-related carbon emissions [23]. On the other hand, a fact behind many studies on HB; humans spend about 90% of their time in buildings [24, 25]. Therefore, protecting the environment and supporting human health are essential goals that should be achieved in every building design, construction, as well as during its operational period.

GB is a building concept that minimizes the impact on the environment caused by its construction and use. Generally, it includes energy efficiency measures, while HB focuses on protecting the health of occupants as the core concept. It minimizes not

Table 2 The healthy building parameters

Area of focus	Parameters	Reference
Location & building access	Walkability	[21]
	Incentivizing & proximity to transit	[21]
	Pedestrian route to transit	[21]
	Commuter access	[21]
	Bicycle parking	[21]
	Efficiency parking	[21]
Indoor environmental quality	Indoor air quality management	[19, 21, 22]
	Tobacco and smoke-free environment	[19, 21]
	Enhanced operable windows/shading	[19, 21]
	Thermal comfort monitoring & control	[19, 21, 22]
	Enhanced ventilation design	[19, 21, 22]
	Microbe & mold control	[19]
	Moisture management	[19, 22]
	Air filtration	[19]
	Sound/acoustic performance	[17, 22]
	Light/visual comfort	[17, 21, 22]
Water	Water quality	[19, 21, 22]
	Drinking-water quality	[19]
	Water bottle refilling station	[19, 21]
	Drinking-water promotion	[19]
	Easy water access	[21]
Materials	Hazardous material restrictions & management	[19]
	Material transparency & optimization	[19]
	Cleaning product & protocols	[19]
	VOC restrictions	[19]
Waste and pest	Waste management	[19]
	Integrated pest management & pesticide use	[19, 21, 22]
Movement	Ergonomic workstation design	[19]
	Circulation network	[19]
	Facilities for active occupants	[19, 21]
	Site planning and selection	[19]
	Physical activity spaces, equipment, and promotion	[19]
	Self-monitoring	[19]
	Stair design, access & safety	[21]
Mind	Mental health services, education & promotion	[19]
	Stress management	[19]

Table 2 (continued)

Area of focus	Parameters	Reference
	Restorative opportunities, spaces & programming	[19]
	Enhanced access to nature/open space	[19]
	Substance use services	[19]
Community & shared spaces	Health and well-being promotion	[19, 21]
	Integrative & universal design	[19]
	Occupant survey	[19, 21]
	Family support	[19]
	Diversity and inclusion	[19]
	Responsible labor practices	[19]
	Hand-washing signage	[21]
	Bathroom cleaning protocol	[21]
	Lactation room & stations	[19, 21]
	Active pedestrian areas	[21]
Food & nourishment	Fruits and vegetables	[19]
	Nutritional transparency & education	[19]
	Refined & artificial ingredients	[19]
	Mindful eating, special diets & portion sizes	[19]
	Food source, production & preparation	[19]
	Healthy vending machine & snack bars	[21]
Safety & security	Emergency preparedness & management	[19, 21]
	Safety & security system	[22]

only the negative impact on the environment but also maximizes the positive impact on health that the building can give to the building occupants [26]. The comparison of the green and HB is shown in Fig. 1. The overlapping parameters are dominated by the element of Indoor Environmental Quality (IEQ).

From Fig. 1, we can see that there are some GB parameters which are not HB parameters, or we can name it "GB-only parameters". Among these parameters are those related to direct impacts on the environment, such as the issue of climate change. This parameter requires the calculation of the reduction in CO_2 emissions obtained from the difference in energy requirements between the design and baseline data. This feature is also related to the requirements for the use of low-emitting materials, and refrigerant management which requires the prevention of the use of materials that have a high potential to damage ozone, such as chlorofluorocarbons (CFCs) and hydro chlorofluorocarbons (HCFCs) [13, 27, 28]. GB also gives points to construction that uses local or regional source of material, recycled material and performs good construction waste management. In order to maintain and preserve natural conditions prior to building construction, GB also requires to protect and restore existing ecology, also conduct site landscaping to improve the quality of the
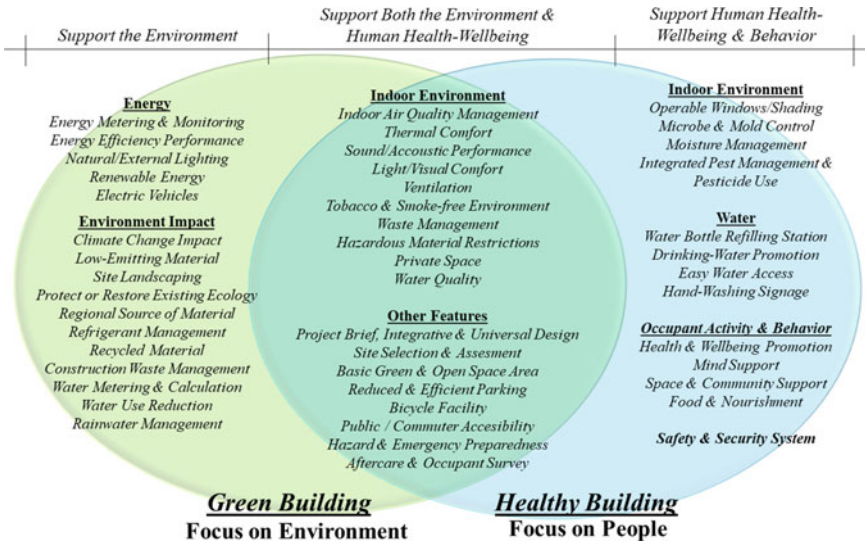
Fig. 1 Comparison of green and healthy building parameters

microclimate, reduce the burden of the drainage system, prevent soil erosion, as well as maintain the balance of groundwater sources [13, 14].

Furthermore, the energy aspect is in the GB parameters but not in the HB parameter. Since there are energy consequences for many IEQ features, indoor air quality, thermal comfort, and ventilation are parameters that significantly affect the energy consumption in a building. Heating, ventilation, and air conditioning (HVAC) systems aim to satisfy these parameters, which represent between 40 and 60% of the energy consumption of a building [29]. Because of these consequences, it is crucial to consider energy consumption in the design process, although the building will implement the HB concept.

GB places great emphasis on the importance of energy efficiency in a building and gives significant points on this aspect. GB encourage the installation of energy sub-metering to allow monitoring of operational energy consumption and requires buildings to perform energy efficiency that can be achieved with design strategies that consider energy saving and efficiency, such as building envelope design, lighting design that prioritizes natural or external light, design of heating and cooling in HVAC systems, and using energy-efficient equipment and appliances. GB also encourages the use of renewable energy, preferably from on-site renewable energy generation, and also promotes the use of electric vehicles. Implementing energy efficiency in buildings will require additional investment costs but will reduce energy costs during the operational period and will eventually result in lower life-cycle costs [30].

In the subsequent discussion, HB parameters that are not present in GB are features related to occupant activity and behavior, such as health and wellbeing promotion,

mind support, space and community support, and even arranging the food and nourishment. HB's mind concept promotes mental health through policies, programs and design strategies that seek to address the diverse factors that affect cognitive and emotional well-being. HB provides mental health services and education, restorative spaces and opportunities, which aim to encourage a healthy work-life balance and stress management. HB's community concept aims to support access to essential health care, build a health culture that accommodates the needs of diverse populations and build an inclusive and engaged community of people. And HB's food and nourishment concept requires the availability of fruits and vegetables and nutritional transparency. It encourages the creation of food environments, where the healthiest choice is the easiest choice [19].

Other parameters required by HB are those related to the indoor environment, such as operable windows, microbe and mold control, moisture management, pesticide use, and pest control. Excessive accumulation of moisture in buildings creates favorable conditions for mold growth, which, if left unchecked, can damage the surfaces on which mold grows [31]. HB requires projects to utilize Ultraviolet Germicidal Irradiation (UVGI) systems and/or conduct regular inspections on components of the cooling system to reduce or eliminate growth of mold and microbes [19]. Biological or chemical pesticides should only be used when necessary. Pesticide use, and associated risks, can be reduced through the application of Integrated Pest Management (IPM) [32]. Safety and security is one of the foundations of HB, because feeling unsafe and insecure can affect health. Worry about crime is implicated in a cycle of decreased health, increased vulnerability, and further insecurities about crime [33]. We can achieve it by providing adequate lighting in common areas, be situationally aware through video monitoring, interactive patrols and report of incident, maintain an emergency action plan and how to communication to building occupants [22].

Both GB and HB require the proper water quality on the water aspect. This parameter aims to minimize the risk of water contamination in buildings and ensure the provision of clean and fresh water sources for building occupants [14, 19, 21]. However, HB has stricter requirements, up to the level of water quality that is safe and healthy to drink and requires regular water quality testing. Apart from water quality, there are other parameters that each GB and HB require different things. GB emphasizes the importance of reducing water use, water metering and calculation, and also gives more points to buildings with rainwater management. It can be understood as protecting the environment that provides water supply. This is not required or given additional points by HB. On this water aspect, HB also has parameters that GB does not have. HB provides convenience for its users' easy access to water and has a bottled water refilling station, drinking water promotion, and hand-washing signage. This requirement is certainly made to improve the health of its occupants.

As previously mentioned, IEQ dominates the intersection between GB and HB. IEQ has the greatest effect on human health, physical and psychological, and also has a major impact on the environment. Based on research conducted by Dunleavy et al. [34] on the IEQ, particularly the thermal comfort, indoor air quality, visual comfort, and acoustic comfort that have been associated with psychological distress. Aboveground and underground workspaces were found to have a higher negative

psychological impact when thermal comfort, indoor air quality, acoustic comfort, and visual comfort were of lower quality. Building design that focuses on these parameters can help in countering the negative effects.

Both GB and HB stress the importance of bringing stakeholders into the design process starting from the pre-design stage, the aim of this integrative process is to engage parties to start thinking about building systems as interconnected networks and not separate entities, leading to better performance and more cost-effective. to maintain cleanliness and health, both require the management of waste generated by occupant activities, however GB adds an obligation to manage waste during the construction period. On the transportation aspect, both encourage reduced car parking, bicycle facility and easy public transport accessibility.

A building certified as a GB can more easily adopt and implement an HB compared to the other way around because the HB parameters that are not present in the GB are dominated by occupant activity and behavior. This can still be fulfilled in the post-construction period or during the operational period of the building. However, on the other hand, the GB parameter, which is not an HB requirement, is dominated by energy and environmental protection aspects, which require more significant effort to fulfill. However, the ideal condition is a building that maximizes support for the occupants' health and minimizes the impact on the environment by meeting the criteria of GB and HB, which may result in a new concept of Green Healthy Building.

5   Conclusion

Protecting the environment and promoting health are agreed as the goals of a development in the built environment. Therefore, these two objectives should be combines by considering the two features of the GB concept and the HB concept in the design, construction, and operational period of the building.

In this comparative study, as shown in Fig. 1, we found 16 parameters of GB-only, 13 parameters of HB-only, and 18 parameters of intersections or overlapping between GB and HB. These findings indicate that although GB and HB have different fundamental focus, namely the environment and occupants' health, both have many relationships.

Research on GB has been around for decades, but research on HB is a recent development. This paper is expected to help GB researchers who want to develop their research towards HB research so that we can advance not only focusing on the environment but also on human health and wellbeing. This study also expected to contribute to the advancement of building construction research in countries that familiar with the GB concept but not with HB concept.

References

1. Awada, M., et al.: Occupant health in buildings: impact of the COVID-19 pandemic on the opinions of building professionals and implications on research. Build. Environ. **207**, 108440 (2022). https://doi.org/10.1016/J.BUILDENV.2021.108440
2. Xie, H., Clements-Croome, D., Wang, Q.: Move beyond green building: a focus on healthy, comfortable, sustainable and aesthetical architecture. Intell. Build. Int. **9**(2), 88–96 (2017). https://doi.org/10.1080/17508975.2016.1139536
3. Levin, H., et al.: Building ecology: an architect's perspective on healthy buildings (1995)
4. Sadikin, N., Turan, I., Chegut, A.: The Financial Impact of Healthy Buildings: Rental Prices and Market Dynamics in Commercial Office (2021). https://doi.org/10.2139/ssrn.3784779
5. Pickvance, C.G.: Four varieties of comparative analysis. J. Hous. Built Environ. **16**(1), 7–28 (2001). https://doi.org/10.1023/A:1011533211521
6. Yudelson, J.: The Green Building Revolution. Island Press (2010)
7. World Green Building Council, "Our Story." https://www.worldgbc.org/our-story. Accessed 20 Mar 2022
8. World Green Building Council, "About Green Building." https://www.worldgbc.org/what-green-building. Accessed 20 Mar 2022
9. Ferrari, S., Zoghi, M., Blázquez, T., Dall'o, O.: New Level(s) framework: assessing the affinity between the main international Green Building Rating Systems and the european scheme. Renew. Sustain. Energy Reviews **155**, 111924 (2022). https://doi.org/10.1016/j.rser.2021.111924
10. Vierra, S.: Green building standards and certification systems. Whole Build. Des. Guid. (2016)
11. Doan, D.T., Ghaffarianhoseini, A., Naismith, N., Zhang, T., Ghaffarianhoseini, A., Tookey, J.: A critical comparison of green building rating systems. Build. Environ. **123**, 243–260 (2017). https://doi.org/10.1016/J.BUILDENV.2017.07.007
12. Naning, S., Adiwoso, P.A., Perdana, S.: Towards Indonesia Sustainable Future through Sustainable Building and Construction. Jakarta (2010)
13. Green Building Council Indonesia, Greenship Rating Tools for New Building Version 1.2. Divisi Rating dan Teknologi GBCI (2013)
14. Building Research Establishment, BREEAM International New Construction - Technical Manual (2021)
15. US Green Building Council, "LEED - Scorecard," (2021). https://www.usgbc.org/leed-tools/scorecard. Accessed 27 Feb 2022
16. Spengler, J.D., Chen, Q.: Indoor air quality factors in designing a healthy building. Ann. Rev. Energy Environ. 25, 567–600 (2000). Accessed 30 Mar 2022. www.annualreviews.org
17. Jutraz, A., Stimac, S.: How to design healthy building for healthy living? Complex network of health (2015)
18. McArthur, J.J., Powell, C.: Health and wellness in commercial buildings: systematic review of sustainable building rating systems and alignment with contemporary research. Build. Environ. **171**, 106635 (2020). https://doi.org/10.1016/J.BUILDENV.2019.106635
19. International Well Building Institute, "WELL Certification." https://www.wellcertified.com/certification/v2. Accessed 13 Mar 2022
20. Center for Active Design, "Fitwel." https://www.fitwel.org/. Accessed 15 Mar 2022
21. Center for Active Design, Reference Guide for the Fitwel Certification System. New York (2019)
22. Allen, J., et al.: Building Evidence for Health. The 9 Foundations of a Healthy Building. Harvard TH Chan School of Public Health Boston, MA, USA (2017)
23. World Green Building Council, "WBGC Annual Report 2021," London (2021)
24. D'Amico, A., Pini, A., Zazzini, S., D'Alessandro, D., Leuzzi, G., Currà, E.: Modelling voc emissions from building materials for healthy building design. Sustainability **13**(1), 184 (2020). https://doi.org/10.3390/su13010184

25. Klepeis, N.E., et al.: The National Human Activity Pattern Survey (NHAPS): a resource for assessing exposure to environmental pollutants. J. Expo. Sci. Environ. Epidemiol. **11**(3), 231–252 (2001). https://doi.org/10.1038/sj.jea.7500165
26. Mark, A.: The Difference Between Green, Sustainable and Healthy Buildings. Saint Gobain (2016). https://multicomfort.saint-gobain.co.uk/the-difference-between-green-sustainable-and-healthy-buildings. Accessed 22 Feb 2022
27. US Green Building Council, LEED v4.1 Building Design & Construction - Guide (2021)
28. Dong, Y., Coleman, M., Miller, S.A.: Greenhouse gas emissions from air conditioning and refrigeration service expansion in developing countries. Ann. Rev. Environ. Res. **46**(1), 59–83 (2021). https://doi.org/10.1146/annurev-environ-012220-034103
29. Solano, J.C., Caamaño-Martín, E., Olivieri, L., Almeida-Galárraga, D.: HVAC systems and thermal comfort in buildings climate control: an experimental case study. Energy Rep. **7**, 269–277 (2021). https://doi.org/10.1016/J.EGYR.2021.06.045
30. Hajare, A., Elwakil, E.: Integration of life cycle cost analysis and energy simulation for building energy-efficient strategies assessment. Sustain. Cities Soc. **61**, 102293 (2020). https://doi.org/10.1016/j.scs.2020.102293
31. Occupational Safety and Health Administration, Preventing Mold-Related Problems in the Indoor Workplace: A Guide for Building Owners, Managers, and Occupants. Washington DC (2006)
32. Kass, D., et al.: Effectiveness of an integrated pest management intervention in controlling cockroaches, mice, and allergens in New York City public housing. Environ. Health Perspect. **117**(8), 1219–1225 (2009). https://doi.org/10.1289/EHP.0800149
33. Jackson, J., Stafford, M.: Public health and fear of crime: a prospective cohort study. Br. J. Criminol. **49**(6), 832–847 (2009). https://doi.org/10.1093/BJC/AZP033
34. Dunleavy, G., et al.: Prevalence of psychological distress and its association with perceived indoor environmental quality and workplace factors in under and aboveground workplaces. Build. Environ. **175**, 106799 (2020). https://doi.org/10.1016/J.BUILDENV.2020.106799

Analysis of Self Healing Microcapsule in Asphalt Binder Using Finite Element Method

Jishma Alex, Padmakumar Radhakrishnan, and Vignesh Dhurai

Abstract Self-healing materials are those that have a potential to repair mechanical damages and cracks, without the need for human interference and restore their original set of properties. Incorporating self healing property of bitumen into road design process helps to extend the life of asphalt pavements. Traffic load repetition and ageing causes microcracks in the pavement which gradually leads to pavement failure. This necessitates frequent pavement maintenance procedures. Self healing property of bitumen can automatically repair damage and recover strength. By reducing premature ageing of asphalt pavements, self healing asphalt can reduce amount of natural resources used in road maintenance and reduce environmental pollution by decreasing CO_2 emission in maintenance process. Addition of rejuvenator to asphalt material is the widely used method for achieving self healing of bitumen. A comprehensive understanding of the self healing properties of bitumen such as its ability to heal, factors affecting healing property can considerably help in the development of durable and sustainable asphalt pavements. ABAQUS is 3D finite element analysis software used for predicting mechanical behavior and pavement performance subjected to various traffic factors. In this study, modeling of bituminous material modified with rejuvenator is done using ABAQUS software in which model dimensions, element types and meshing strategies are taken by successive trial and error to achieve desired accuracy and convergence of the study. Analysis of self healing asphalt modified with microcapsule containing rejuvenator shows that there is a reduction of stress around the microcapsule region.

Keywords Self healing · Finite element method · Microcapsules

J. Alex (✉) · P. Radhakrishnan · V. Dhurai
Department of Civil Engineering, College of Engineering Trivandrum, APJ Abdul Kalam
Technological University, Thiruvananthapuram, Kerala, India
e-mail: jishmaalex@gmail.com

P. Radhakrishnan
e-mail: rpk@cet.ac.in

V. Dhurai
e-mail: dvignesh005@gmail.com

1 Introduction

Bitumen is the commonly used binder in the construction of flexible pavement. It is a visco-elastic substance that occurs naturally. The asphalt behaves like a viscous fluid at high temperatures or low frequencies, with little ability to recover when the load is removed. The asphalt binder behaves like an elastic solid at very low temperatures or high frequencies, regaining its previous shape after deformation. Bituminous materials have the ability to regain their strength and stiffness by repairing microcraks that form when bituminous pavement is subjected to varying wheel loads in varying environmental conditions This intrinsic property of bitumen is known as self healing However, after several years of use, bitumen's ability to self-heal diminishes. When bitumen is subjected to years of mechanical and thermal forces, as well as environmental factors, it becomes brittle. This causes microcracks to form, which eventually cause irreversible damage to the asphalt pavement. The addition of a rejuvenator is an effective way for restoring self-healing properties.

By incorporating bitumen's self-healing characteristics into the construction of flexible pavement, microcracks caused by wheel load can be healed. This reduces the need for routine maintenance and extends the life of pavements. By adding diverse material properties, finite element analysis can be utilised to analyse pavement for varied wheel loads and tyre pressures. Finite element analysis (FEA) demonstrates how materials respond to real-world stresses, vibrations, and other physical impacts. This also indicates if a product may fail, break, or wear out. Modeling bitumen modified with rejuvenators and analysing the performance of microcapsule containing rejuvenator in asphalt can be done using the finite element method of analysis.

Microcracks in the asphalt binder can pierce microcapsules holding rejuvenators, and the encapsulated rejuvenators can fill the cracks to start the self-healing process [1]. The tensile strength of bitumen samples enhanced with rejuvenator was found to be higher than that of pure bitumen [2]. Nanoparticle addition, induction heating, and rejuvenation are examples of self-healing technologies for asphalt pavement design that have the ability to cure distressed asphalt pavement. This improves the pavement's durability and reliability, as well as reducing maintenance work and lowering the overall cost of asphalt pavements. By including self-healing asphalt material into the pavement construction, the material cost of construction and typical overdesign of material can be avoided [3]. Bitumen's self-healing capacity is determined by calculating self-healing efficiency, which is defined as the ratio of shear modulus after a rest interval to the original shear modulus. Bitumen microcapsules have greater rheological characteristics than untreated bitumen. Following resting for a period of time after a microcrack, encapsulated asphalt demonstrated progressive recovery in terms of shear strength [4]. Healing test carried on bituminous specimen modified with rejuvenator at different crack opening displacement values showed that microcapsules could resist the thermal effects of asphalt and could only broken by microcrack [5].

The aim of this study is to analyse the property of asphalt modified with rejuvenators with the help of finite element analysis.

2 Methodology

2.1 Material Modeling

Bituminous material was modeled as square shaped particle. Oil rejuvenator for modifying the bitumen was modeled in spherical shape and distributed randomly in the bituminous matrix. Bituminous matrix and rejuvenator particle was created separately and material properties was assigned to both. Figure 1(a) and (b) shows the bitumen and rejuvenator that was modeled separately. It was them assembled and merged together suppressing their original instances. Merged bituminous and rejuvenator assembly is shown in Fig. 2. ABAQUS then consider this as a single composite material with combined property. Mesh was generated for the modified bituminous-rejuvenator material. Mesh size was decided so as to obtain simulation responses with optimum accuracy. Meshed model is shown in Fig. 4. A reference point set was also generated along the x axis. Each face of the modified bituminous material in the shape of cube was selected and named as a different set (Fig. 3).

2.2 Material Characterisation

Asphalt is natural viscoelastic material so viscoelastic properties was assigned to bituminous matrix and for rejuvenator linear elastic behavior was assumed. In ABAQUS viscoelastic material is defined by Prony series expansion of dimensionless relaxation modulus. Properties of bitumen and rejuvenator used for material modelling are given in (Tables 1 and 2).

2.3 Load and Boundary Conditions

The front face of the bituminous material along x direction was linked to the reference point set so that when a load is given to the reference point, the front face translate along with it. Other faces of the bituminous model was constrained against displacement and rotation. Loading step was created after the initial step and the loading was given as cyclic with a loading time with an increment of one second. A tensile deformation was given in the loading step to the reference point along the x direction as shown in Fig. 5 and the front face moves along with the reference point.

(a)

(b)
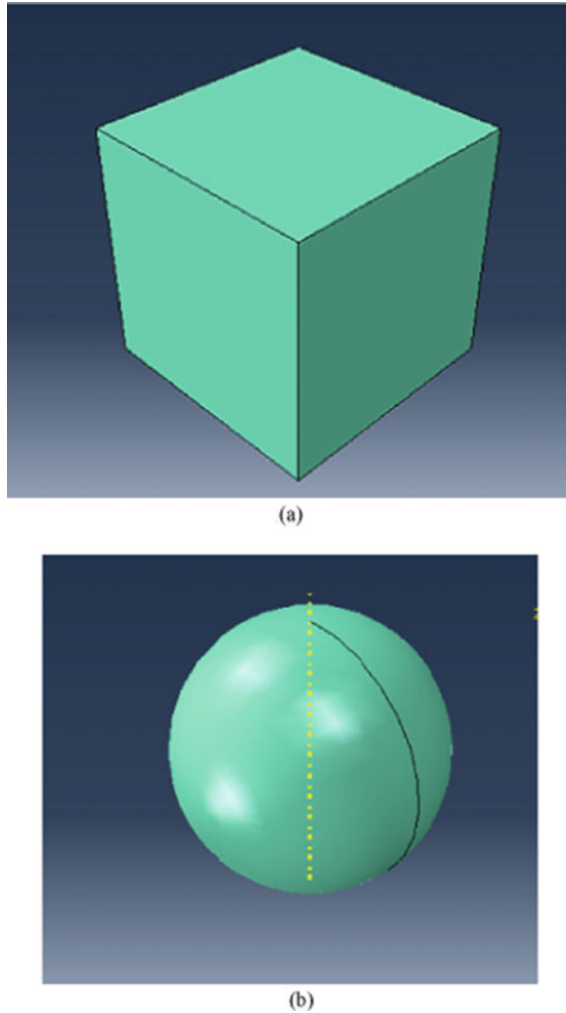
Fig. 1 **a** Bituminous matrix **b** Rejuvenator particle

3 Results and Discussion

Stress and strain values in unmodified bitumen was found to have uniform value along the entire model. As the unmodified bitumen does not contain any modifier particle stress and strain is distributed equally throughout the material.

The stress and strain values of bitumen modified with rejuvenator shows a less value than unmodified bitumen. Stress and strain variation in modified bituminous material is shown in Fig. 6 and 7.
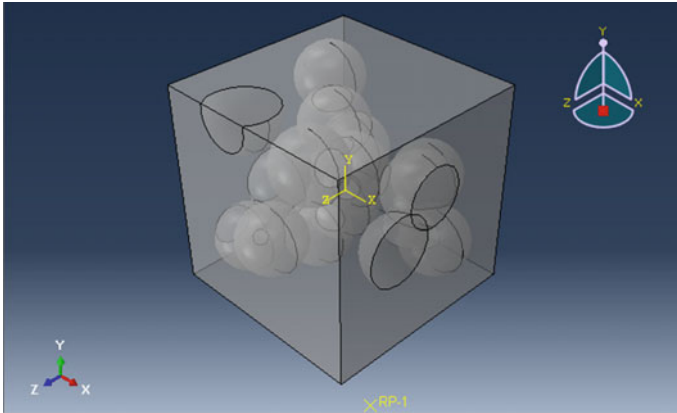
Fig. 2 Merged bituminous and rejuvenator particle
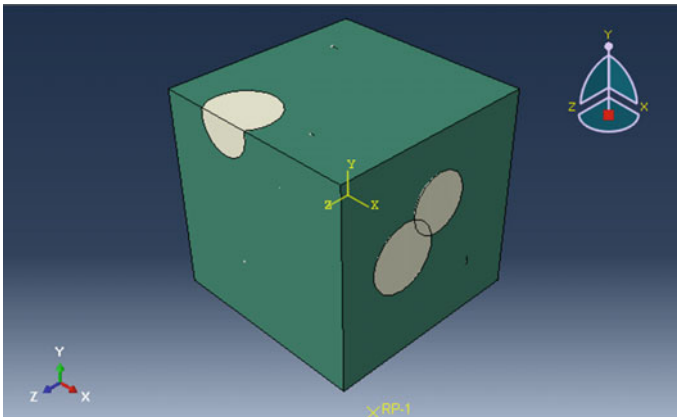
Fig. 3 Composite bitumen-rejuvenator model showing different included materials

Stress variation in bitumen modified with rejuvenator shows a lower value compared to that of unmodified bitumen. This shows that addition of rejuvenator to bituminous material improved the strength of the material. Increased strength of the bituminous material enables it to carry more wheel load which means the durability of the pavement constructed with bitumen modified with rejuvenator is more.

The stress values observed in modified bitumen is particularly low around the rejuvenator particle added. On the surface of bituminous material where the stress values are found to be lower than rest of the part, when it was cut open, rejuvenator particles was found beneath it. Rejuvenator particles hold the bitumen around it from undergoing deformation. Bitumen was found more vulnerable on places where rejuvenator was not added.
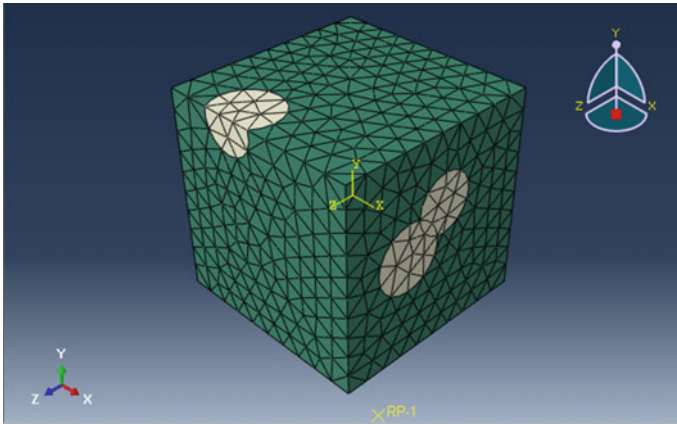
Fig. 4 Meshed model of modified bituminous material

Table 1 Properties of bitumen

Elastic modulus (MPa)	150
Viscosity (Pa s)	240
Poisson's ratio	0.35

Table 2 Properties of rejuvenator

Elastic modulus (MPa)	10
Viscosity (Pa s)	4.33
Density (g/cm^3)	0.922
Poisson's ratio	0.3
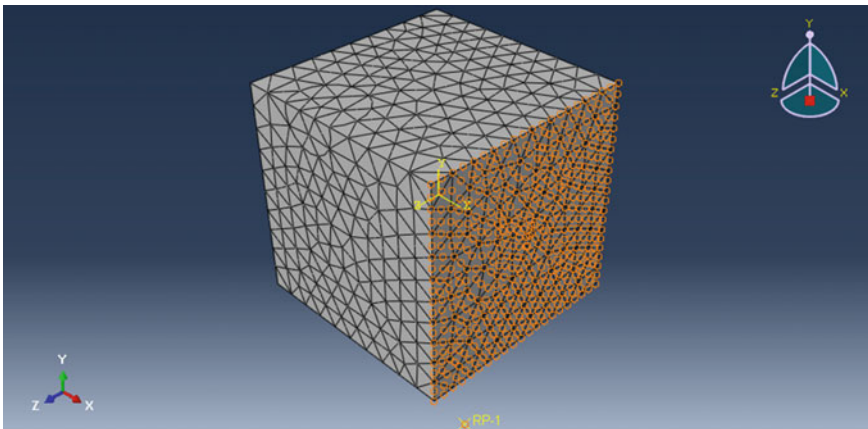
Fig. 5 Tensile deformation along x axis
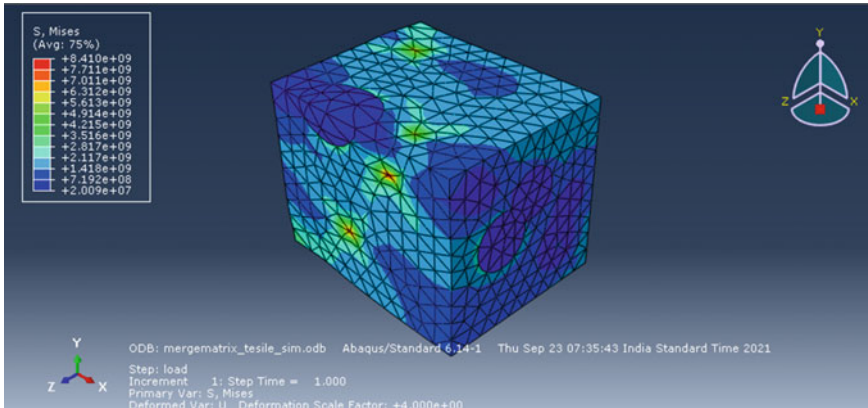
Fig. 6 Stress variation of bitumen modified with rejuvenator
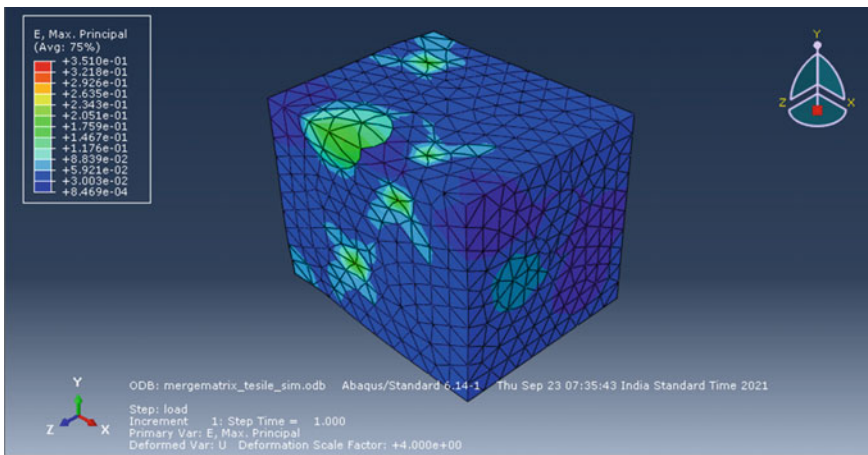
Fig. 7 Strain variation of bitumen modified with bitumen

4 Conclusion

Application of finite element analysis software ABAQUS for the analysis of pavement and pavement is quite useful and reasonable and it can be used to find out the performance of pavement under different loading conditions. This work analyses the performance of asphalt material modified with rejuvenator using finite element analysis software. The study done on the micro level can be used for finding the response of the material at macrolevel.

Addition of rejuvenator to bitumen improved the properties of bitumen. The stress value of bitumen decreased by the addition of rejuvenator. Reduction in stress values

improves the strength of bituminous material which increases the durability of pavement. Further studies has to be done for modeling and analyzing the relationship between the self-healing behaviors of bitumen and mean size, contents of rejuvenator, resting time and temperature. More researches and studies are needed in this field to study the performance and responses of asphalt modified with rejuvenator under real pavement conditions.

References

1. Su, J.F., et al.: Experimental observation of the self-healing microcapsules containing rejuvenator states in asphalt binder. Constr. Build. Mater. **147**, 533–542 (2017). https://doi.org/10.1016/j.conbuildmat.2017.04.190
2. Su, J.F., Yang, P., Wang, Y.Y., Han, S., Han, N.X., Li, W.: Investigation of the self-healing behaviors of microcapsules/bitumen composites by a repetitive direct tension test. Materials (Basel) **9**(7), 600 (2016). https://doi.org/10.3390/MA9070600
3. Tabaković, A., Schlangen, E.: Self-healing technology for asphalt pavements. Adv. Polym. Sci. **273**, 285–306 (2016). https://doi.org/10.1007/12_2015_335
4. Chung, K., Lee, S., Cho, W., Seo, J., Hong, Y.: Rheological analysis of self-healing property of microcapsule-containing asphalt. J. Ind. Eng. Chem. **64**, 284–291 (2018). https://doi.org/10.1016/j.jiec.2018.03.026
5. Su, J.F., Qiu, J., Schlangen, E., Wang, Y.Y.: Experimental investigation of self-healing behavior of bitumen/microcapsule composites by a modified beam on elastic foundation method. Mater. Struct. Constr. **48**(12), 4067–4076 (2015). https://doi.org/10.1617/s11527-014-0466-5

Crack Detection in Concrete Using Artificial Neural Networks

T. Palanisamy, Rajat Shakya, Sudeepthi Nalla, and Sai Shruti Prakhya

Abstract This paper aims to explore the possibility of using machine learning (ML) algorithms and image processing to determine cracks in concrete and classify them as Cracked and Uncracked. This is a very current field of study with a lot of research currently taking place. In particular, neural network algorithms such as VGG16, ResNet50, Xception and MobileNet, were used to name a few. Two datasets were used to detect the presence of cracks in concrete. The first two datasets were taken from the Kaggle website. The first dataset is generated from 458 high-resolution images (4032 × 3024 pixels). This dataset consists of 40,000 images, 20,000 with and 20,000 without cracks. The second dataset had pictures of cracked and uncracked decks on a bridge from a dataset called SDNET2018 (2018). VGG16 Architecture based artificial neural network performed the best while MobileNet performed the worst. As the scope for the project expanded, an effort was made to determine crack properties, specifically crack width as an automated system for the same would be much more useful than a manual one. It was done using morphological transformations and concepts of Euclidean distance.

Keywords Structural health monitoring · Crack detection · Machine learning · Neural networks · Image processing · Non-destructive testing

1 Introduction

Structural performance of various infrastructure such as buildings, bridges, dams etc., deteriorate over time and sometimes natural disasters such as landslides, earthquakes and storms can speeden the process. Hence, structural health monitoring is extremely important in predicting the lifespan of buildings and extending that if possible. Cracks not only degrade the aesthetics of a structure but also decrease its load carrying capacity [1].

T. Palanisamy (✉) · R. Shakya · S. Nalla · S. S. Prakhya
National Institute of Technology Karnataka, Surathkal, Mangalore, India
e-mail: tpalanisamycivil@nitk.edu.in

It is possible to manually study these cracks but such studies require a specialist to prepare the sketch of the crack, note the irregularities and go forward to study the width and depth of cracks. This is not only a time consuming process but also requires a specialist to come on board. Requirement of an expert leads to a lacking of objectivity in an otherwise specialised process [2].

Hence image processing has proven as a promising alternative to manual crack detection. Some of the difficulties faced in the image based detection are due to the random shape and irregular size of cracks and various noises such as irregularly illuminated conditions, shading, blemishes and concrete spall in the acquired images [2]. Many of the image processing based detection methods have been proposed owing to their simplicity in processing. These methods are classified into four categories, namely integrated algorithm, morphological approach, percolation-based method, and practical technique [3].

Finding the width of the crack is necessary for estimating the serviceability and durability of Reinforced Concrete. Manually finding the width of an image is time consuming and not always effective in large scale scenarios. The code used will also be finding the width of the cracks in terms of pixels.

This paper makes use of image processing to find the presence of a crack and classifies them as Cracked and Uncracked. Further, the images with cracks are used to find the width of the crack automatically. Sensors and photogrammetric methods (e.g. via drones) can be used for collecting these necessary images.

2 Literature Review

In the paper, *Image-based Retrieval of Concrete Crack Properties* [1] cracks are not only detected but a method for the retrieval of the properties of these cracks from the images is presented. It has defined a crack by its end points. These can be either simple or split. The cracks are then marked by stars and the length is the length between end points or split points and the width is calculated using a natural object in the image as reference.

One of the studies [3], provided the collective survey of the different image processing techniques that are used for the detection of the cracks in the engineering structures. Objective based analysis showed that the majority of the papers (from the 50 papers they've reviewed) had the objective to analyse the surface of the crack, with length, width and depth of the crack coming close second. Accuracy based analysis showed that the accuracy was above 90% for the majority of the papers. Some researchers summarise crack detection techniques. It is subdivided into four categories, namely integrated algorithm, practical technique, percolation-based method, and morphological approach. Integrated algorithm, morphological approach, and percolation-based method are all automatic in crack detection, while practical technique based on route-finder algorithm is semi-automatic.

Another paper [4], compared fuzzy logic and neural network methods in crack detection. The accuracies of the models have been measured in five ways: the

number of images detected correctly (image-wise accuracy), specificity, sensitivity, the number of objects detected correctly (objectwise accuracy), and precision.

There is a lot of literature available on using deep learning methods in order to detect cracks. ImageNet is an image database organised according to the WordNet hierarchy, in which each node of the hierarchy is depicted by hundreds and thousands of images. This project has been instrumental in advancing computer vision and deep learning research.

The data is available for free to researchers for non-commercial use. One of the major challenges in deep learning is the greater difficulty of training very deep neural networks [5]. The above paper presents a methodology for the same using the ImageNet data set. It proposes the use of a residual learning framework to make this process easier. Deep networks naturally integrate low/mid/high level features and classifiers in an end to end multilayer fashion, and the "levels" of features can be enriched by the number of stacked layers. The literature on crack width calculation ws also extensively studied, particularly the ones that used morphological transformations involving the concepts of Euclidean distance.

3 Methodology

3.1 Dataset

The datasets contain images of different types of concrete surfaces that have and do not have cracks. There are two folders in this dataset: negative (without cracks) and positive (with cracks). Each of these folders contain 20,000 images with RGB channels and 227×227 pixels. Four hundred and fifty eight high resolution images have generated the dataset. This has been done according to the method proposed by Zhang et al. (2016) [6]. Data augmentation has not been applied.

3.2 Convolutional Neural Network

Convolutional Neural Networks (CNN) are a subset of Artificial Neural Networks with characteristic high depth, and specialised ability to handle 2D grid data. This makes it ideal for its use in Image Processing and Analysis. The working of CNN can be divided into three types of layers: i) Convolutional Layer, ii) Pooling Layer, and iii) Fully Connected Layer [7]. The Convolutional layer applies some linear mathematical operation on the subset of image data, and produces an output which is passed to the next layer. The Pooling layer reduces the grid size of the input by applying some mathematical function, such as max function, over a subset of image data. The Convolutional and Pooling layers work together to perform feature extraction, wherein the network identifies key features that distinguish the various

output classes (in our case two classes, cracked and non-cracked). This mapping of features to the classes is done by the Fully Connected Layers.

3.3 CNN Architectures

VGG16 Architecture. VGGNet is a Convolutional Neural Network architecture proposed by Karen Simonyan and Andrew Zisserman from the University of Oxford in 2014. VGG based convNet takes in a 224 * 224 RGB image as its input. The preprocessing layer takes the RGB image with pixel values in the range of 0–255 and subtracts the mean image values calculated over the entire ImageNet training set. After preprocessing, the input images are passed through these weight layers. The training images are passed through a stack of convolution layers. There are a total of 13 convolutional layers and 3 fully connected layers in VGG16 architecture. VGG has smaller filters (3 * 3) with more depth instead of having large filters.

The output of the VGG16 Network is a 1D array of size 512. These values are then passed on to 2 sets of 64 noded Fully Connected or Dense layers with ReLU activation function, followed by an Output Layer of 2 classes with SoftMax activation function. The network illustration after the VGG16 architecture is shown below, where the Input Layer is a 512 nodded layer that contains the output of the VGG16 convolution network. The 2 classes in the Output layer correspond to Positive or Negative class, with the Positive class corresponding to images of cracked concrete, and the Negative class corresponding to images of non-cracked concrete.

ResNet50 Architecture. ResNet50 is a variant of the ResNet model which has 48 Convolution layers along with 1 MaxPool and 1 Average Pool layer. It has 3.8×10^9 Floating points operations. It is a widely used ResNet model and ResNet50 architecture was explored in depth.

Xception Architecture. The concepts of Inception are taken further in Xception. It basically means Xtreme Inception. Inception takes the help of convolutions of the size 1×1 which leads to the original input being compressed, and various filters were used on individual depth spaces from each input space. Xception is the reverse of the step.. It starts with the application of filters on individual depth maps. Post this, the input space is compressed with the help of 1×1 convolution. This convolution is applied across the depth. Xception is very similar to an old design of neural networks known as a depth wise separable convolution. Another difference between Inception and Xception is the fact that in the former the operation is succeeded with a ReLU non-linearity while the same does not apply to the latter.

MobileNet Architecture. This model is curated to be used in various mobile applications. It is the first mobile computer vision model by TensorFlow. It uses depth convolutions that are depth-wise separable. This leads to a reduction in the quantity of parameters when weighed against any other network that has convolutions

(regular) with depth equal to that of nets. The final result is a deep neural network that is light in weight.

3.4 Algorithm

First, the dataset is built by classifying the images manually, and they are labelled either "Negative" for uncracked images, and "Positive" for cracked images. The images are then preprocessed according to the needs of the architecture used for training. These preprocessing settings are used from the inbuilt-libraries. After the images have been pre-processed, they need to be split into three sets namely, the training set, the testing set and the validation set. In this study, the dataset was split into training and testing in 80–20 ratio. The training dataset was further split with an 80–20 ratio into training and validation sets. With the training, validating and testing dataset ready, the CNN models were then trained. Four different CNN architectures were used in this study, namely VGG16, ResNet50, Xception and MobileNet. The accuracy metric is used to determine the effectiveness of each of the models. Once the training is over, the model can then be used to predict if a given image is cracked or not.

If an image of concrete is classified as being cracked, the image can then be further processed to find the average width of the detected crack. For this phase, the images have to be preprocessed once again. This preprocessing involves the use of morphological operations. These operations convert the colored image into a binary image where the area of cracks are highlighted in white and everything else is in black. To do this, firstly the image is converted to a grayscale image. This step converts the three channels of RGB image into a single channel image. Next, the morphological operation of thresholding is employed. Thresholding operation converts a grayscale image into a binary image (i.e., each pixel will either have 1 or 0 as its value), based on a certain thresholding value. The Adaptive Gaussian Filter was used for thresholding. The result of thresholding is an image where the darker pixels are colored white and lighter pixels are colored black. This leads to cracks and other dark spots being highlighted white in the binary image. This binary image will often have noise in it, especially if the concrete is an older specimen. Therefore after thresholding, the morphological operations of opening and closing are used to remove any straggler noise pixels, and to smoothen the pixels corresponding to cracks respectively. With the preprocessing done, the average crack width is then calculated using the Euclidean Distance Transformation function in Matlab. Matlab is used over python owing to its mathematical and technical computing superiority. The entire algorithm has been encapsulated in the form of a flowchart in Fig. 1.
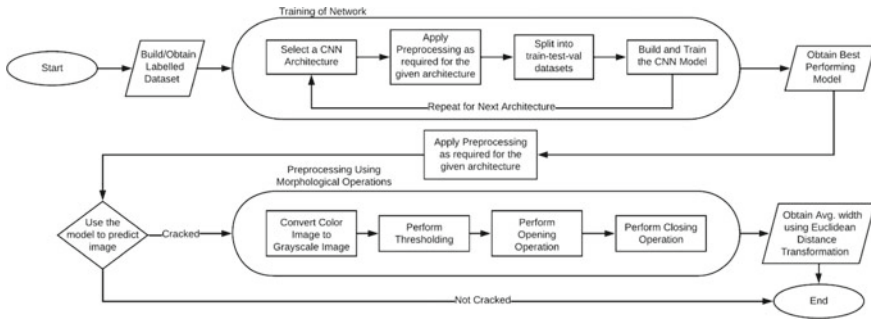
Fig. 1 Flowchart of the algorithm

4　Result

Each model was trained with 5 epochs and it was found that all four models were able to learn and classify the images into cracked or non-cracked. Of the four architectures used, VGG16 showed the best performance with an accuracy score of 0.998000 while MobileNet showed the worst performance with 0.997150. The full result of Architectures with their accuracy is depicted in Table 1. Figure 2 depicts the same in the form of a bar chart. It was also observed that MobileNet and Xception were more prone to overfitting as compared to VGG16 and ResNet50 architectures.

Figure 3 shows the results of the morphological operations at every step. Noise was removed from the picture, and the crack feature was isolated from the original image, without losing too much information of the crack width and shape.

Figure 4 depicts the input and the output of the Euclidean Distance Transformation function in Matlab. The image shown in the figure corresponds to img_1.jpg, which has an average crack width of 3.1421 pixels. Upon closer inspection of the original image, it was found that the significant portions of the original crack have the width between 4 and 2 pixels.

The size of the width can be converted from pixels to standard units if the conversion scale (image : physical measurement) is known.

Table 1 Accuracy of different architectures of CNN model

S.No	Model	Accuracy
1	VGG16	0.998000
2	ResNet50	0.997375
3	Xception	0.997250
4	MobileNet	0.997150
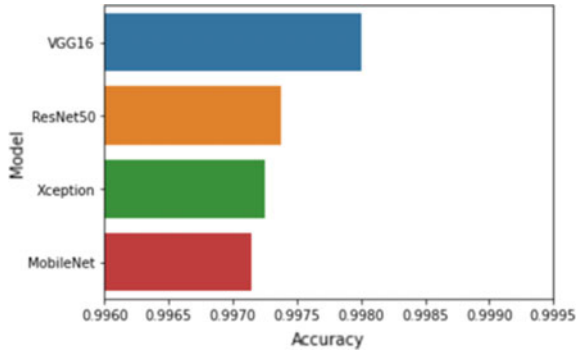
Fig. 2 Bar graph of accuracy of different architectures of CNN model
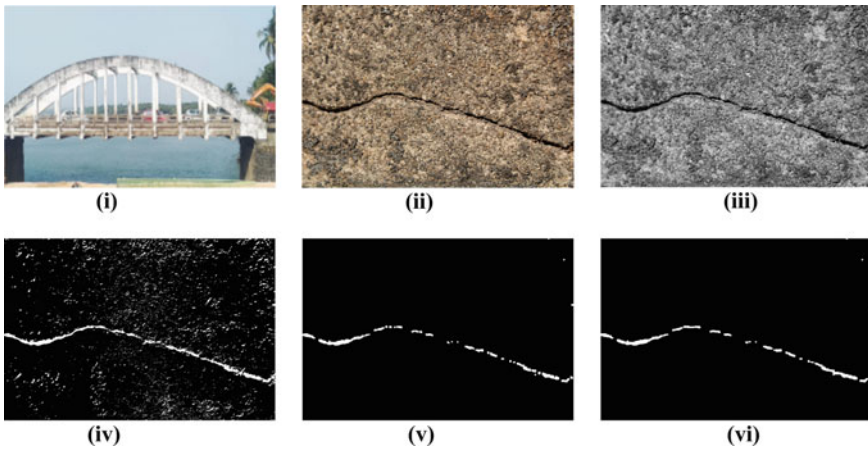
Fig. 3 **i** Image of site **ii** Original image of crack **iii** Greyscaled image **iv** Binary image after applying adaptive gaussian filter for thresholding **v** Binary image after applying opening operation **vi** binary image after applying closing operation
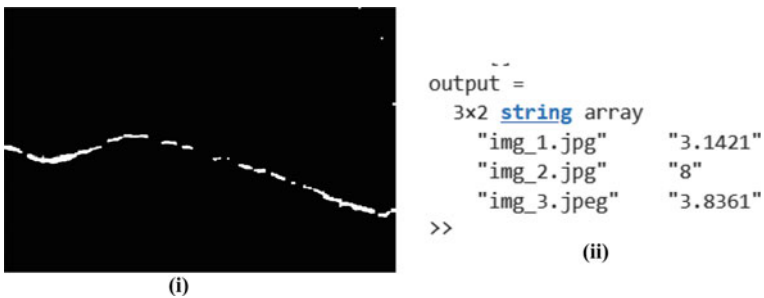
Fig. 4 **i** Preprocessed input image for crack width detection for "img_1.jpg" **ii** Average crack width for the image

5   Conclusion

It can be successfully concluded that the VGG 16 is simple and intuitive and hence adopted as a pretrained model for classification of images over the other models. The designed model was able to train and classify the images of concrete into either "Cracked" or "Uncracked" categories. The VGG16 model reported an accuracy of 99.80% during testing whereas Xception and MobileNet were not able to predict the status of cracks as accurately. Hence, VGG16 model and ResNet50 can be adopted to sort any new images into cracked and uncracked classes over the others. Matlab has higher efficiency for mathematical computation and therefore a matlab code is used for calculating the width of the crack and the crack width in pixels is accurate when compared with the one measured using scale.

6   Future Scope

What has been done is the use of ANN's to identify the cracks in concrete. Many studies have shown its usage in steel structures as well. Hence, the model can be upgraded to meet both Steel and concrete cracks.

The work can also be expanded from image processing to video analysis, which would pave the way for real-time crack detection. To further monitor the propagation of cracks, the code can be edited to give accurate location/placement of the crack on the structure. The length of the cracks, along with the knowledge of the toughness of the concrete, stress level being applied on the concrete enables us to know if a crack is detrimental to the structure or not.

References

1. Adhikari, R.S., Moselhi, O., Bagchi, A.: Image-based retrieval of concrete crack properties. In: ISARC. Proceedings of the International Symposium on Automation and Robotics in Construction, vol. 29. IAARC Publications (2012)
2. Mohan, A., Poobal, S.: Crack detection using image processing: a critical review and analysis. Alex. Eng. J. **57**(2), 787–798 (2018)
3. Wang, P., Huang, H.: Comparison analysis on present image-based crack detection methods in concrete structures. In: 2010 3rd International Congress on Image and Signal Processing, vol. 5. IEEE (2010)
4. Choudhary, G.K., Dey, S.: Crack detection in concrete surfaces using image processing, fuzzy logic, and neural networks. In: 2012 IEEE Fifth International Conference on Advanced Computational Intelligence (ICACI). IEEE (2012)
5. He, K., et al.: Deep residual learning for image recognition. In: Proceedings of the IEEE Conference on Computer Vision and Pattern Recognition (2016)

6. Lei, Z., Yang, F., Zhang, Y.D., Zhu, Y.J., Zhang, L., Yang, F., Zhang, Y.D., Zhu, Y.J.: Road crack detection using deep convolutional neural network. In: 2016 IEEE International Conference on Image Processing (ICIP) (2016)
7. Yamashita, R., et al.: Convolutional neural networks: an overview and application in radiology. Insights Imag. **9**, 611–629 (2018)

Response of Reinforced Concrete Bridge Subjected to Blast Loading

Roouf Un Nabi Dar and P. Alagappan

Abstract Bridges are key components of transportation network, especially in strategic border areas in a country, and consequently are susceptible to subversive blast attacks. Hence in this study, dynamic response of a reinforced concrete (RC) bridge (single span) consisting of a deck slab supported on longitudinal girders along with transverse ones placed symmetrically has been numerically investigated when subjected to blast loading using ABAQUS/CAE 2020. The effects of an explosive charge of 226.8 kg (TNT) at 1 m standoff distance have been analyzed using the CONWEP algorithm. Three different locations of the bursting charge along the cross section at mid span of the bridge above the deck, such as on the central girder, between two adjacent longitudinal girders, and on the cantilever part, have been considered. Concrete damage distribution in terms of concrete spalling and cracking has been studied with concrete damage plasticity (CDP) model. Also, the response in terms of damage dissipation energy, maximum displacements, and stresses has been compared for the blast scenarios. Furthermore, AASHTO: LRFD Bridge Design Specifications (2017) provisions have been used to compare obtained maximum displacement values.

Keywords CONWEP · Blast · Finite element analysis · RCC bridge · Damage · Concrete · CDP model

1 Introduction

Blast-related issues are becoming critical for civil infrastructure these days. Few recent events like the Beirut explosion, the 9/11World Trade centre event etc. prove

R. U. N. Dar (✉) · P. Alagappan
Structural Engineering Division, Department of Civil Engineering, Indian Institute of Technology Madras, Sardar Patel Road, Adyar, Chennai, Tamil Nadu 600036, India
e-mail: roufunnabi16@gmail.com

P. Alagappan
e-mail: alagappan@civil.iitm.ac.in

that they cannot be limited to military facilities only. Blast events can result in critical injuries and mass casualties in addition to structural damage, all of which have negative economic and societal consequences. Bridges are an important part of the transportation system because they provide quick and convenient access to destined locations separated by topography and other artificially created obstructions. Furthermore, because they are built with cutting-edge technology having an appealing look and act as landmarks these become a vulnerable target for subversive attacks, resulting in massive economic and social losses. Additionally, the vulnerability of bridges to accidental explosions cannot be overlooked due to the diversity of their users. Blast engineering for infrastructure such as bridges has attracted structural engineers' attention in recent years. More research is being carried out to improve the understanding of blast implications on critical infrastructures. Nonetheless, many parts of this area, particularly the majority of bridge-related issues, still require intensive research. This study is a step in that direction.

Various experimental and numerical studies were carried out to study the dynamic behavior of bridges under impulse loadings including blast loading. *(Winget, D. G.* et al. *2005* [15]*; Ray, J. C. 2006* [11]*; Son, 2008* [13]*; Yi, Z. 2009* [14]*; Fujikura and Bruneau, 2011* [7]*; Coffer W. F.* et al. *2012* [3]*; Simon E. and Sirajuddin M. 2017* [12]*; Dar R.U.N et.al., 2021* [4]*). Winget, D. G.* et al. *2005* [15] numerically studied the response of a simply-supported concrete girder bridge (4-Span prestressed) when subjected to explosion using SPAn32. Cross sectional area got reduced due to localized failure/damage and same was calculated from the empirical equations. The deck detached from the girders due to the absence of a shear fastener when the blast occurred below the deck. Detonations simultaneously occurring at the opposite sides of a column resulted in much greater damage than the equivalent explosion impacting a single face only. *Ray, J. C. 2006* [11] devised an investigation program that included a series of 1/2-scale blast experiments and also ran parallel numerical simulations involving steel bridge towers, with the following parameters: charge weight, steel plate span, compressibility of retrofit material, steel quality, axial load intensity, and fastener type. The actual explosive charge weights could not be found as same was not revealed for security reasons. The elements of interest were displayed in blast trials, which is fine as long as enough details are provided to completely capture the effects of interest and get boundary conditions simulating field conditions from reaction frames. There were no results to disclose and this study merely gave a high-level description of the research strategy. According to the report, the test series would provide valuable insight into the advantages and drawbacks of the current analytical tools available to scientists. *Yi, Z. 2009* [14] used LS-DYNA to study a simply-supported composite girder bridge (three-span). The blast pressures calculated using ConWep were directly applied to the receiving faces of the ambient elements without the need to model the explosive. Magnusson and Hallgren's test data were used to determine the mesh sizes that would be used (2004). Compressive crushing was reported to have occurred in the deck, according to the findings. The deck got separated from the girders during a below-deck explosive event. *Son, 2008* [13] modeled an orthotropic steel deck with a composite girder using MSC. Dytran to simulate the various situations in the earth-anchored suspension bridge, cable-stayed bridge,

and self-anchored suspension bridge, different degrees of axial loads were imposed. The nodal displacements measured away from the explosion impact were used to describe the deck and girder's overall behavior. An explosion above the deck caused local damage to the deck, which fractured and experienced plastic deformation due to the close proximity to the explosive. Results revealed the massive axial forces on the cable supported bridge along the girder system would show poor blast performance. *W. F. Coffer* et al*., 2012* [3] reported two full-scale prestressed concrete girder explosion tests. ABAQUS was used to model a singly spanned simply-supported prestressed concrete girder bridge, experimental results were numerically validated. The parts closest to the supports were believed to be elastic and two empirical tests were used to validate finite element model of a precast, prestressed girder. Analytical and empirical results for an explosive event above or below the girder were found to be in agreement. The girder model was then extended to a four-girder- single-span bridge. 250 pounds of TNT at a standoff distance of four feet above the deck was investigated, resulting in localized damage but making it possible that other sections (undamaged) of the bridge are immediately reopened after the blast. For other load cases from below the deck, 500 pounds of TNT at a standoff distance of ten feet was studied, and it was found that the slab was heavily damaged and rendered the bridge unserviceable. *Fujikura and Bruneau, 2011* [7] tested two non ductile steel jacketed reinforced concrete piers and seismically designed two ductile reinforced concrete piers built under blast loading. To avoid blast wave interference, enough spacing between the piers along the reaction frame was provided. This led to the conclusion that an explosive placed close to the column base had a high potential for causing shear failure, the most common type of failure in various blast scenarios. *Simon, E. and Sirajuddin, M. 2017* [12] studied the RC Bridge performance at different standoff distances under blast loading using numerical technique. A finite element model of a RC bridge was analyzed for an explosive charge of 10 kg TNT at varying standoff distances. This was concluded that increasing standoff distance reduced maximum displacements and stresses considerably. Results revealed that the reduction in peak displacement value was approximately 50% when the explosive charge standoff distance was increased to 5 m from 1 m. Moreover, below deck location of the blast proved to be the critical blast scenario on the bridge. *Dar, R.U.N and Alam, M.2021* [4] numerically investigated the effects of the location of blast on RC bridge deck supported on three longitudinal girders placed symmetrically. Blast pressure wave was applied as pressure–time history which was obtained from the modified Friedlander equation. An explosive charge of 1000 kg (TNT) and standoff distance of 0.5 and 1 m were considered. The four locations of these explosives considered were 1) on the central girder above the deck, 2) between two adjacent girders above the deck, 3) cantilever portion above the deck, and 4) below the central girder. The crack pattern was observed and concrete damage in terms of percentage of elements damaged have been calculated using damage evolution and element removal technique of ABAQUS software. Concrete elements have been modeled using Concrete damage plasticity (CDP) model. It was observed that the explosive location below the girder proved to be the critical blast location inflicting maximum damage in the bridge model.

The literature review presented shows that detonating explosive charges at different locations significantly influence the RC bridge response. Stresses and displacements had been studied in the past. However, damage study in conventional RC bridges was not thoroughly done. Moreover, the actual blast load effects can be considered using the CONWEP algorithm, which can be compared with some experimental investigations of close-in blast scenarios. Hence in this study, the behavior of a single span reinforced concrete (RC) bridge deck supported on girders placed symmetrically along both longitudinal and transverse directions under blast loading has been numerically investigated using ABAQUS/CAE 2020. Various blast scenarios above the deck with an explosive charge of 226.8 kg (TNT) at 1 m standoff distance have been studied. Three different locations of the explosive charge along the mid span section of the bridge above the deck, such as on the central girder, between two adjacent longitudinal girders, and on the cantilever part, have been considered.

2 Three Dimensional Finite Element Modeling

In this study, dynamic explicit analyses of a three-dimensional reinforced concrete (RC) bridge under blast loading have been performed using software called ABAQUS [2]. The concrete damage plasticity model in the software has been used to model the stress-strain response of concrete. Blast load is simulated using the CONWEP feature, which uses the Kingery-Bulmash equation [8].

2.1 The Finite Element Model

The developed FE model of the RC Bridge consists of a deck supported by three longitudinal girders and four transverse girders placed symmetrically is shown in Fig. 1. The single span RC bridge considered in the study has deck slab of dimensions $12 \times 9 \times 0.25$ m which is supported on three longitudinal RC girders symmetrically spaced at 3 m c/c and transverse girders spaced 4 m c/c cast monolithically with the slab. Furthermore, deck slab is cantilevered with clear projection measuring 1.275 m beyond longitudinal side girders as shown in Fig. 2. The dimensions of the girders along with reinforcement details are presented in Fig. 3. Reinforcement in the deck slab comprises of 12 mm diameter bars at a spacing of 125 mm c/c as sagging (positive) and hogging (negative) reinforcement along both directions. Material constants such as concrete density, modulus of elasticity and Poisson's ratio used are 24 KN/m^3, 30 GPa, and 0.20 respectively [10]. Also, modulus of elasticity of 200 GPa and yield strength of 415 MPa have been used for steel re-bars.
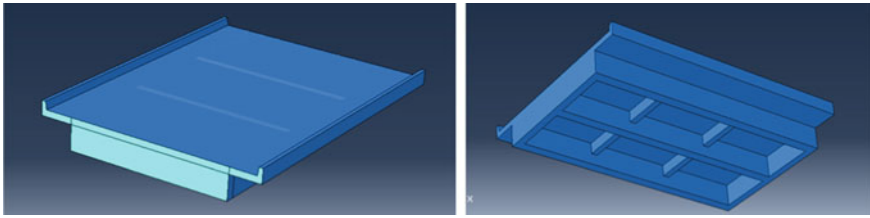
Fig. 1 Three dimensional finite element bridge model
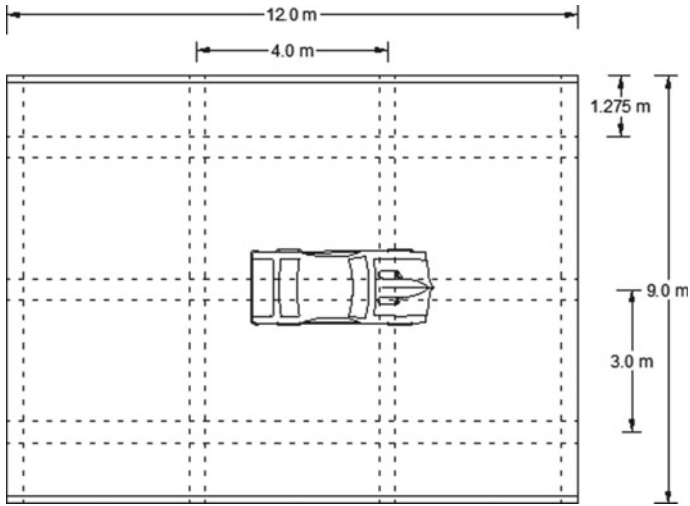
Fig. 2 Plan view of the bridge model

a)Longitudinal girder   b) End cross girder   c) Intermediate cross girder
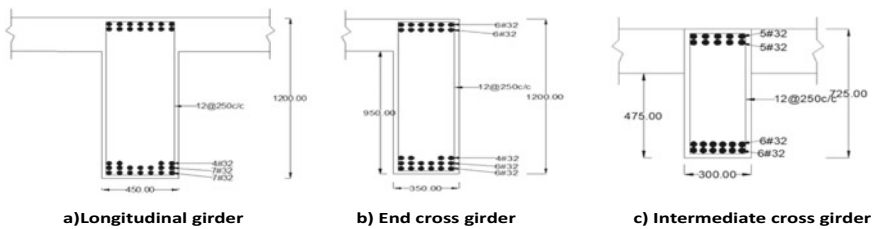
Fig. 3 Girders, their dimensions (mm) and reinforcement details

2.2 Blast Modeling

In this study, the CONWEP model has been used to simulate blast, which uses the modified Kingery-Bulmash Eq. (1) [8]. This equation applies to both free-air along with surface blasts and is used for the evaluation of all the parameters of the

blast pressure–time history curve. Also, this equation applies to UFC 3-340-02, U.S. Department of Defence published report, and softwares developed by the U.S. Army Corps of Engineers. Scaled distances should satisfy the range criterion of 0.05 to 40 m/kg$^{1/3}$ for free-airblast and 0.06 to 40 m/kg$^{1/3}$ for surface blast. Not more than five number of constants are used for the modified equation with as many significant figures. Different constants used are obtained from the work of Jeon, D. et al. [8]. The modified Kingery-Bulmash equation [8] is given as,

$$Y = 10^{(C_0 + C_1 \times \log Z + C_2 \times (\log Z)^2 + C_3 \times (\log Z)^3 + C_4 \times (\log Z)^4} \tag{1}$$

$$Z = \frac{R}{W^{\frac{1}{3}}}, \tag{2}$$

where, Y = Parameter of interest (Peak incident pressure, Positive phase duration etc.); C_0, C_1, C_2, C_3 and C_4 = Constants to be obtained from the work of Jeon, D. et al. [8]; Z = scaled distance (m/kg$^{1/3}$), R = standoff distance (m), and W = amount of TNT (kg).

The pressure–time history of the blast used in CONWEP is based on the Friedlander's equation [5] given below:

$$P(t) = P_s \times \left(1 - \frac{t}{t_d}\right) e^{-b\frac{t}{t_d}} \tag{3}$$

where P_S is peak incident overpressure; t_d is positive phase duration; and b is decay constant.

Here, 226.8 kg of TNT at a standoff distance of 1 m equivalent to a scaled distance of 0.164 m/kg$^{1/3}$ has been used. This blast scenario is a realistic scenario and can be attributed to explosive material in a car having 0.8 m ground clearance plying on a bridge [9].

2.3 CDP Model and Meshing

The concrete damage plasticity (CDP) model is a well known damage model for concrete, assuming its failure mechanisms as tensile cracking for failure in tension and compressive crushing for compression. CDP model used for the current study is for M 40 grade of concrete and is referred to the experimental results given in the paper by Milad, H. et al. [10]. To visualize concrete cracking (damage), CDP assumes that the cracking starts at points where equivalent tensile plastic strain attains some non zero value. Also, crack direction which is taken parallel to the direction of plastic strain can be perceived in visualization mode of the software. Furthermore, compression damage state and tension damage state are characterized by two damage variables, tensile damage variable (d_t) and compressive damage variable

a) Meshed Model   b) Rendered view of reinforcement
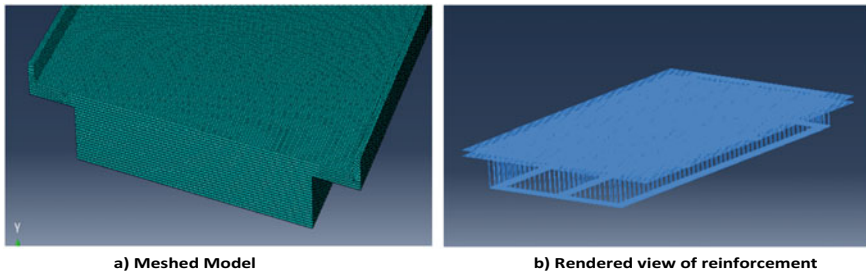
Fig. 4 a Meshed model **b** Reinforcement

(d_c) respectively, and plastic strains by tensile plastic strain ($\in_{tpl,}$) and compressive plastic strain *($\in_{cpl}$)* respectively.

A C3D8R element, 8-noded brick element (linear) has been considered for modeling concrete and the reinforcement bars have been modeled using two-node (3-D) truss element called T3D2 [2]. The extent of meshing of the structure in a finite element program is essential in achieving the accuracy of results. Mesh sizes of 150, 125,100, 75, 50, and 25 mm are studied for mesh convergence. Less than 5% result change is observed for reduction of mesh size from 50 to 25 mm, and consequently 50 mm size is adopted in the current study. Furthermore, support conditions at abutments have been assumed as pinned to simulate realistic bridge support conditions (Fig. 4).

3 Results and Discussion

Table 1 shown below summarizes the responses of the RC bridge for different locations of the bursting charge of magnitude 226.8 kg (TNT) used in this study. The distributions of von Mises stress, tensile and compressive concrete damage at a scaled distance of 0.164 m/kg$^{1/3}$ are shown in Figs. 5, 6 and 7, respectively. The maximum permissible displacement considering traffic and pedestrian load according to *AASHTO: LRFD Bridge design specifications, 8th edition(2017)* [1] is L/1000, where "L" is the span of the deck slab hence is 12 mm for the considered bridge model. Three considered locations of the blast of magnitude 226.8 kg (TNT) at 1 m standoff distance along the cross section at mid span of bridge above the deck were considered, i.e., on the central girder (Case 1), between two longitudinal adjacent girders (Case 2), and on the cantilever portion (Case 3) have been considered. Maximum resultant displacements of 49, 78, and 90 mm have been recorded for blast locations in Case1, Case2, and Case3, respectively. These displacements are greater than the allowable displacement of 12 mm. Hence, this RC bridge is regarded to be unsafe for the three blast scenarios from a deflection point of view. The values of maximum recorded von Mises stress for three locations of the blast are shown in Table 1, and contours are in Fig. 5. Damage results of one of the blast scenarios

from numerical analyses are compared with the experimental work of Foglar, M. and Kovar, M. [6] for validation purpose. Numerical and experimental studies are consistent with each other, as shown in Fig. 8.

Damage pattern can be described as below:

Tensile Damage: The explosive charge on the central longitudinal girder above the deck produced tension cracks at the top, as shown in Fig. 6. These cracks are a result of the large hogging moment along girders. Moreover, there is spalling of concrete on the bottom side of the central longitudinal girder and deck slab on either side. The explosion when considered between two adjacent girders above the deck slab yielded damage tensile in nature in the form of cracks at the top face of the deck slab due to the excessive hogging moment developed along girders. There is large tensile cracking at the bottom of the deck portion confined by girders and spread of cracks to the overhanging portion and nearby girders that are flexural in nature. Lastly, the explosive charge located above the cantilever projection damaged the kerb and deck
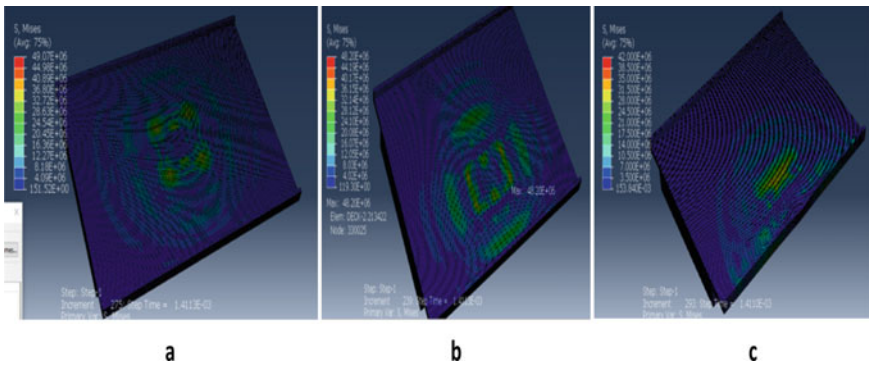
Fig. 5 Von Mises distribution contours for blast locations **a** Above central longitudinal girder **b** Between two longitudinal girders **c** Above overhang portion
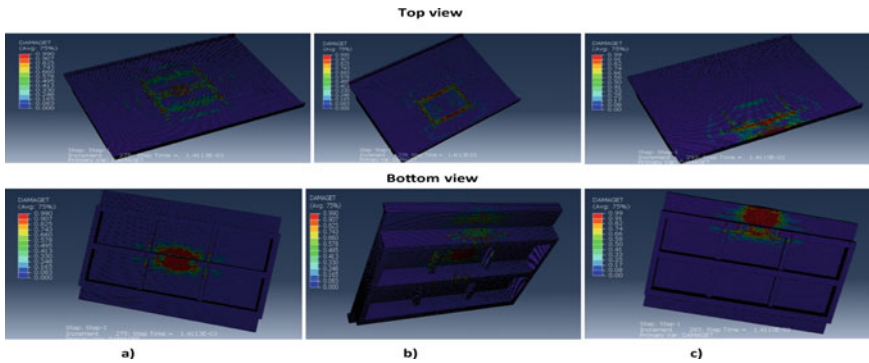
Fig. 6 Tensile damage distribution contours for blast locations **a** Above central longitudinal girder **b** Between two longitudinal girders **c** Above overhang portion
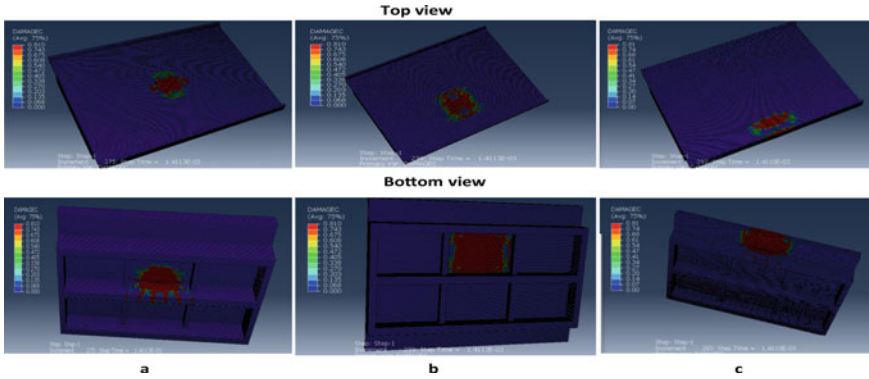
Fig. 7 Compressive damage distribution contours for blast locations **a** Above central longitudinal girder **b** Between two longitudinal girders **c** Above overhang portion

Table 1 Dynamic responses for the different locations of explosive charge conidered

Explosive charge location	Scaled distance (m/Kg$^{1/3}$)	Maximum resultant displacement in the deck (mm)	Maximum von Mises stress (MPa)	Maximum damage dissipation energy (Joules)
Case1 (Above the longitudinal central girder)	0.164	49	92.5	71
Case1 (Between two longitudinal girders above deck)	0.164	78	94.9	32
Case3 (At the end of cantilever projection above deck)	0.164	90	101	38
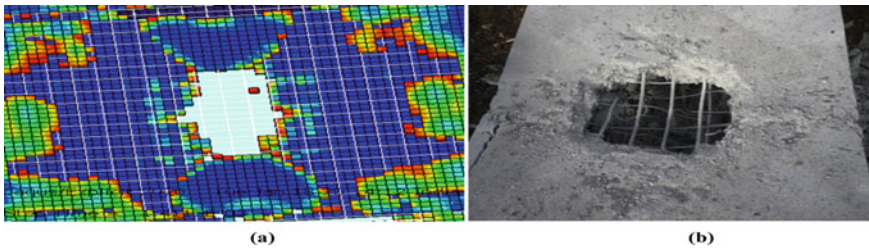
Fig. 8 Validation of **a** numerical simulation with the **b** experimental work of Foglar, M. and Kovar, M. [6]

slab, as shown in Fig. 6c. Some flexural cracks are also seen in the flexural zone of the end girder.

Compressive Damage: Figure 7 shows compressive damage distribution for different blast scenarios considered. All the blast scenarios resulted in highly localized damage in the bridge model. For explosion above central longitudinal girder i.e. case1, a high magnitude of peak overpressure resulting from the explosive charge of 226.8 kg punched holes in deck slab on either side of central longitudinal girder rendering the bridge unserviceable. Moreover, deep and wide flexural cracks along with shear cracks are reported at the bottom of the central girder. However, in case2 i.e. blast between two longitudinal girders above deck results in a large crater confined by girders on four sides. The bridge may not be immediately serviceable at the damaged location, but traffic can be restored along one lane. Girders remained relatively undamaged. For blast located above the overhanging region of the bridge deck i.e. case3, damage remained confined to the overhanging region only. Localized damage in the deck along with kerb for a flexural zone of around 3 m can be seen. Flexural shear cracks and spalling at the end longitudinal girder were also observed. Traffic can be restored immediately in such a scenario as the bridge is expected to remain standing after the blast.

4   Conclusion

In this study, reinforced concrete (RC) bridge deck supported on longitudinal and transverse girders placed symmetrically was created as a finite element model and analyzed for different locations of blast above the deck. Three different locations of the bursting charge of magnitude 226.8 kg (TNT) at 1 m standoff distance along the cross section at mid span of a bridge above the deck were considered, such as on the central girder (case1), between two adjacent longitudinal girders (case2), and on the cantilever portion (case3).The summary of the current study is as follows:

The primary modes of failure for all blast scenarios were seen as localized damage in the deck and predominantly shear failure in girders. The bridge model is unsafe for all blast scenarios based on the allowable deflection. When the explosive charge was located on the central girder (case1), the pressure punched holes through the deck slab on either side of girders along with large concrete spalling in longitudinal girder. This case makes it highly unlikely to restore traffic on the bridge immediately. When the explosive charge was located between two adjacent longitudinal girders (case2), highly localized failure in concrete slab confined by girders occurred along with minor damage in girders. However, the bridge can be immediately restored for traffic on an alternate lane. When the explosive charge was located on the cantilever portion of the deck (case3), localized damage in the deck along with kerb for a flexural zone of around 3 m length can be seen. Flexural shear cracks and spalling at the end longitudinal girder were also observed. After immediate retrofitting of the girder, the bridge can be restored for traffic.

References

1. AASHTO, Load Resistance and Factor Design: Bridge Design Specifications, 8th edn.American Association of State Highway and Transportation Officials, Washington D.C. (2017)
2. ABAQUS 6.14. User Documentation, Dessault Systems (2014)
3. Coffer, W.F., Debra, S., David, I.: Effects of blast loading on prestressed girder bridge. Shock Vibr. **19**, 1–18 (2012)
4. Dar, R.U.N., Alam, M.: Damage evaluation of reinforced concrete bridge subjected to blast loading. recent advances in structural engineering. In: Lecture Notes in Civil Engineering, vol. 135 (2021)
5. Dewey, J.: The Friedlander Equations (2018)
6. Foglar, M., Kovar, M.: Conclusions from experimental testing of blast resistance of FRC and RC bridge decks. Int. J. Impact Eng **59**, 18–28 (2013)
7. Fujikura, S., Bruneau, M.: Experimental investigation of seismically resistant bridge piers under blast loading. J. Bridg. Eng. **16**(1), 63–71 (2011)
8. Jeon, D., Kim, K., Han, S.: Modified equation of shock wave parameters. Computation **5**(3), 41 (2017)
9. Lee, J., Choi, K., Chung, C.: Numerical analysis-based blast resistance performance assessment of cable-stayed bridge components subjected to blast loads. Appl. Sci. **10**(23), 8511 (2020)
10. Milad, H., Hijazi, F., Vaghei, R., Jaafar, M.S.: Simplified damage plasticity model for concrete. Struct. Eng. Int. **27**(1), 68–78 (2017)
11. Ray, J.C.: Validation of numerical modeling and analysis of steel bridge towers subjected to blast loadings. In: Proceedings of the 2006 Structures Congress. St. Louis, Missouri (2006)
12. Simon, E., Sirajuddin, M.: Parametric study of stand-off distance on a bridge under blast loading. Int. J. Adv. Res. Eng. Technol. **8**(2), 01–07 (2017)
13. Son, J.: Performance of cable supported bridge decks subjected to blast loads. The University of California, Berkeley, California (2008)
14. Yi, Z.: Blast Load Effects on Highway Bridges. The City University of New York, New York (2009)
15. Winget, D.G., Marchand, K.A., Williamson, E.B.: Analysis and design of critical bridges subjected to blastloads. J. Struct. Eng. **131**(8), 1243–1255 (2005)

Comparative Study of Prying Effect in T-stub Steel Connections

Theertha Deljit, Vishnumoorthi Acharya, and M. Ramesh Kannan

Abstract In the era of digitalization and rapidly increasing urbanization; Safety, Quality and Fast construction is a need of the day. Steel structures are ideal proposals to cater this increasing demand. Optimum connection design plays a major role in the design of steel structures and hence, it is very important to understand and appreciate the significance of each governing failure modes and existing approaches for its evaluation.

Prying effect is one of the detrimental phenomena in the design of bolted connections subjected to tension and/or moment. In majority of the cases, thickness of base plate/anchor plate and size/number of bolts in these types of connections is determined by the prying effect. Prying effect cannot be overlooked; besides, connections cannot be over designed due to the limitation of existing empirical expressions. Hence, a comparative study of prying effect with respect to Indian Standard, European Standard and British Standard has been done amongst which IS code was observed to be more accurate. Hence IS code was used for further study. Parametric study on IS code equation has been done and results has been compared with that of Finite Element approach. Considering the variation between them, an effort is made to understand the gap and a way forward.

Keywords Bolt force · Prying force · Idea Statica · Hilti Profis Engineering

T. Deljit (✉) · M. R. Kannan
Vellore Institute of Technology, Chennai, India
e-mail: theerthadeljit.td@gmail.com

V. Acharya
Larsen and Toubro Construction, Mumbai, India

1 Introduction

1.1 *General*

Prying force is an additional force developed in the bolts due to flexibility of the connected part. It occurs when the bolts are subjected to tension. In the below given figure (Fig. 1), as the force (2T) is applied on the web, it is distributed in the bolts.

Further, since the flange is flexible, it deforms leaving the contact pressure between the middle portion of the flange and base as zero. This leads to the edge of the flange pushing the base and for equilibrium the base gives the push back. This pushing force is additional to the already existing contact pressure between the edges of flange and base. This additional force is called the prying force, represented by Q. The force Q induces a tension in the bolt and is added on to the direct tension on the bolt summing up to the bolt force. In certain practical cases, the prying force could be large enough to cause failure of the connection if not considered in design [3]. Hence it is very important to design the bolt/anchor or plate including prying force. It is a common culture to increase the thickness of the base plate to compensate for the prying force generated. As per Indian Standard, IS 800:2007, clause 10.4.7 provides formula for calculation of prying force and suggests to be added to tension in the bolt. Seismic designs require ductility as one of the major considerations. Thick plates are not advisable, since it leads to low ductility. Hence thin plates are used. Thickness of the plate has a great influence on the prying effect. Prying force is inversely related to the thickness of the plate; upto a limit beyond which the higher thickness cannot reduce the prying force considerably [2]. Prying force has the potential to reduce the fatigue strength as well as ultimate capacity of the bolt connection [1]. Equations and provisions have been included in many standard codes to consider this effect
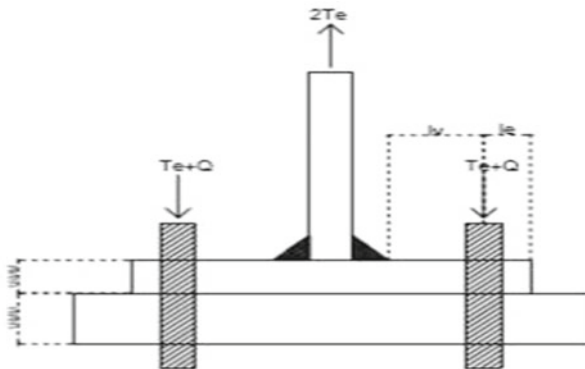
Fig. 1 Connection under direct tensile load
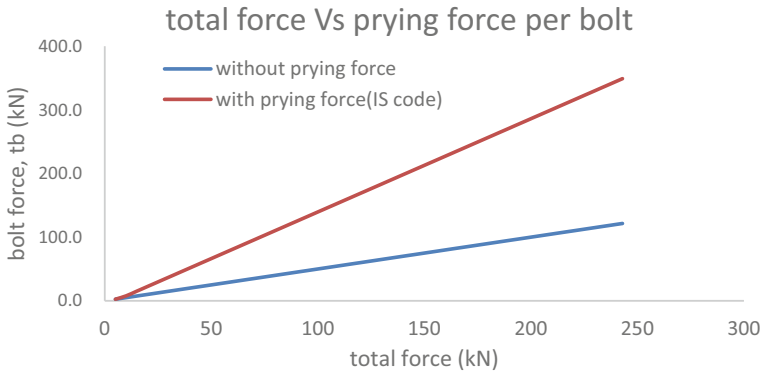
Fig. 2 Comparison plot of numerical calculations with and without prying inclusion

during design. The Indian Standard code has provided an equation to calculate the prying force generated on a system, which; at times, happens to give over designed sections in real time scenarios. This leads to uneconomical design of sections. This paper majorly focuses on identifying the gap of the equation from FE analysis and other calculations. Finite Element Analysis tools such as Idea Statica and Hilti Profis Engineering shall be used for a more accurate explanation.

1.2 Significance of Prying Force

Bolt forces were calculated considering into account two cases; one of which considering prying force (as per IS 800: 2007, Clause10.4.7) and the other neglecting prying force. It was observed that the bolt forces considering prying has shown huge variation as compared to that of the plot without considering prying force. This contributed to the thought that prying force is an important parameter that could not be ignored. Figure 2 shows the variation in plot.

The inclusion of prying force in calculation leads to a bolt force which is 187.27% (at the extreme load) of the initial bolt force which is considerably high. Hence it is very important to study and research for improvement of this force.

1.3 Abbreviations

be   Effective width of base plate/end plate per pair of bolts
e   End distance
FE   Finite Element
fo   Proof stress

Le   Distance of resultant prying force from bolt centreline
Lv   Distance of bolt centreline to the toe of fillet weld
M   Moment
Md   Design bending moment
Mmax   Maximum bending moment
n   Number of bolts
nq   Total prying force in n number of bolts
Q   Prying force per bolt
t or d   Thickness of end plate/base plate
tb   Bolt force
T or Te Tension force applied
W250   Maximum allowable load for plate of fy 250
W240   Maximum allowable load for plate of fy 240
W230   Maximum allowable load for plate of fy 230
Ze   Elastic section modulus
Zp   Plastic section modulus

2 Methodology

2.1 Understanding Global Standard Codes and FE Approach

Prying force was calculated for a specific connection using Indian code, British code and Euro code [7–10]. To further understand the proximity of the results with realistic scenarios, finite element approach which is considered very much close to reality has been chosen. A comparison plot of results from FEA tool Hilti Profis Engineering as well as the International standard codes has been projected below (Fig. 3) for better understanding. It has been observed that calculation using IS code best matches with FEA results (Fig. 3). Total tension to be considered for design is plotted as per IS code equation, British code and European code. With the same connection, FE analysis is also carried out (using Hilti Profis Engineering software). FE analysis is considered as the reference. IS code has a nearer value to FEA. Hence IS code is used for further study.

2.2 Idea Statica and Hilti Profis Engineering

Idea Statica and Hilti Profis Engineering are two commonly used softwares in the industry. Idea Statica, been used widely across industries has been validated with advanced finite element tool, ANSYS. Hilti Profis Engineering, similar to Idea Statica has been validated using ANSYS. Through further study and calculations carried out, it has been observed that Hilti Profis Engineering and Idea Statica follow almost
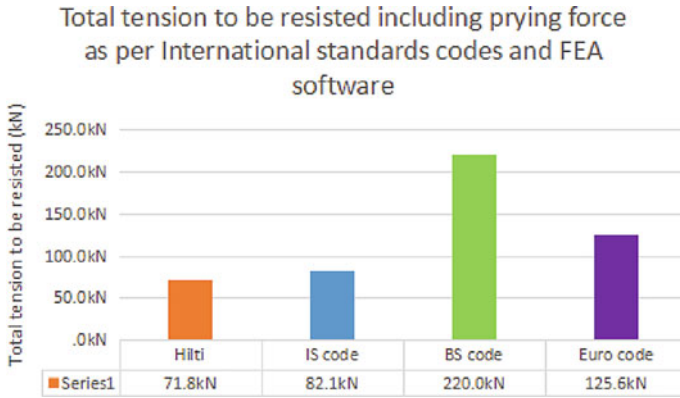
Fig. 3 Result comparison of FEM and global standard codes

similar trends, except for slight variation in the plastic region. Since Idea Statica produced more detailed results regarding prying force, it has been chosen as the prior study tool.

2.3 Equations

The equations used in the further study are from IS code, mostly from the part of, 'General Construction in Steel - Code of Practice', IS 800:2007. Equation for prying force is mentioned in Clause 10.4.7 of IS 800:2007:

$$Q = \frac{L_v}{2L_e}\left[T_e - \frac{\beta \eta f_o b_e t^4}{27 L_e L_v^{\,2}}\right] \tag{1}$$

Detailed study has been conducted based on the parameters in the above equation (Eq. 1). Parameters such as load applied, thickness of the plate etc. were considered case by case and each of the parameter was varied keeping all other factors constant. Further, the results were plotted in the form of graph for ease to compare it with the results of FEA. Few loading and connection cases (biaxial prying, double curvature bending, tension due to moment etc.) are also studied using the same methodology. FEM tool used for most of the above cases is Idea Statica. Hence for validation of Idea Statica, comparison of few cases was done in Idea Statica as well as Hilti Profis. Conclusions were made based on the results obtained.

3   Comparison of FEM and Numerical Results

3.1   Comparison of Prying Force with Varying Tensile Load

The column was loaded axially with tensile forces of 5 to 243 kN. The fracture load was chosen to fix the extreme loading condition. Interestingly, the trend of the graph obtained from the software results was different from the graph obtained through numerical calculations. The plot from software involves several points, which could be marked as the onset or offset of behavioral change in the connection. Extreme loading condition provided as input can be defined as the 'fracture load'. This condition is based on a criterion where the plastic strain crosses its limiting value of 5%. The immediate previous load is considered as the 'ultimate load'.

Yielding of the plate starts way earlier. This is reflected in the graph through loss of linearity. Beyond a specific point the plot does not show linear progress. This is marked as offset of linearity or 'proportionality limit'. This point also marks the onset of plastic strain. The prying force in the bolt increases and reaches a point beyond which it starts to drop. The upper limit of the prying force in this region can be termed as upper yield point. The drop in the prying force reaches a minimum value beyond which it again tend to increase. This minimum value is termed as lower yield point. The further increase in the prying force is drastic where the slop of the plot is comparably higher than that of the linear region. The plot trend resembles to that of the stress-strain curve of mild steel and can be well explained using the yielding of the plate. Through further observations, it was clear that the curve goes well with the plastic strain values (%) obtained from the software. The plastic strain until the proportionality limit is 0 which suggests that the plate is within the elastic limit. Along all these paths, the results from numerical analysis remain perfectly linear. There is no limiting load unless the capacity of the elements are applied.

The comparison also shows the huge gap diverging gap between the finite element results and result from equation suggested by IS code. This clearly confirms that numerical approach is conservative (Fig. 4).

The stress in the setup increases until the proportionality limit and settles down for a nearly constant maximum level farther side.

In case of strain, the figure above provides information regarding the zero plastic strain until proportionality limit (Fig. 5). This simulation goes with the values of plastic strain obtained and the loading vs prying force graphical diagram (Fig. 6).

The shaded region in the above graph resembles modulus of resilience. The slope of the plot above this region provides a ratio of prying force to load. This can be termed as Modulus of prying, denoted by Pm.

$$Modulus\ of\ prying\ =\ Prying\ force/Load$$

$$Pm\ =\ Q/Te \tag{2}$$
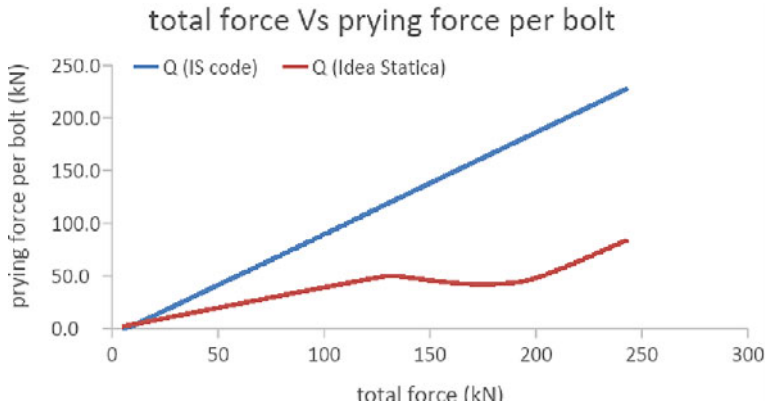
Fig. 4 Result comparison of software and numerical calculations
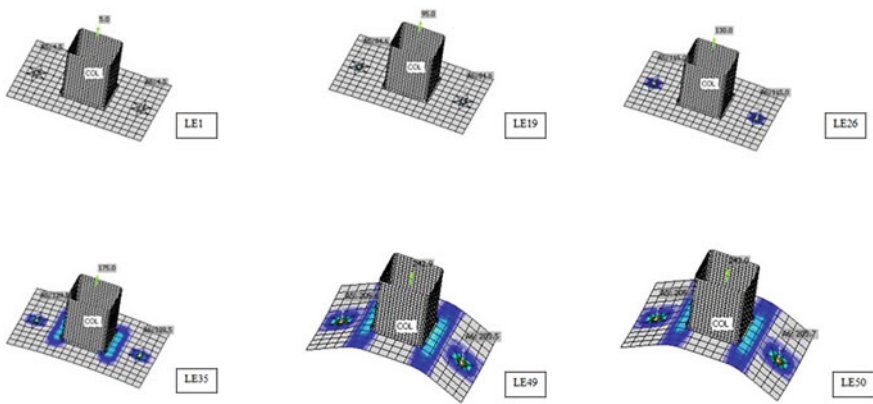
Fig. 5 Representation of plastic strain in connection
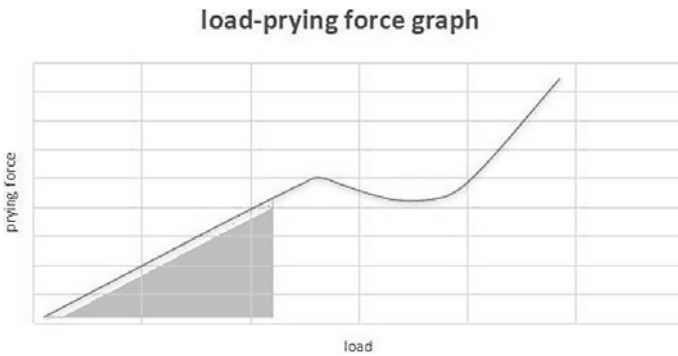
Fig. 6 Modulus of prying

Pm is constant for a particular connection setup. When prying force is calculated for one particular load, Pm could be formulated and with this value, prying force under any load can be calculated within the proportionality limit.

3.2 Comparison of Prying Force with Varying Plate Thickness

In this case, the load is kept constant for carrying out the analysis while varying the thickness of the plate alone. The thickness is varied from 18 to 120 as per the available plate section details in market. As expected, the increase in the thickness beyond a certain limit has brought down the prying force in the plate to zero. Although until the connection attained zero value for prying in both connection, the point of attainment is different for software results as well as numerical results. Finite element analysis value attains zero prying first. The difference in the point of attainment of zero is lesser compared to the gap in initial case (lesser thick sections). The trend remains same for both numerical and finite element analysis, while there is a convergence. The gap between the results becomes a matter of discussion only when the thickness is lesser. As the thickness increases, the gap lessens further leading negligible difference. This also points toward the fact that, for a prying of 29 kN the equation in IS800: 2007 suggests the use of 50 mm plate, while the actual requirement is less than 25 mm. Similarly, an 18 mm plate is opted considering to satisfy the need of 204.5 kN, whereas in reality, the prying force is only 69.1 kN. The requirement is just 33.79 % of the expected value. This lead to huge uneconomical sections. Hence revising the roots of this dilemma is vital (Fig. 7).
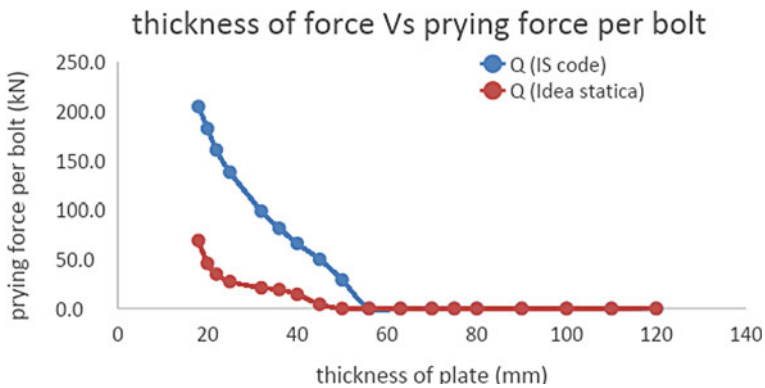
Fig. 7 Effect of thickness variation as per IS code and FEM tool
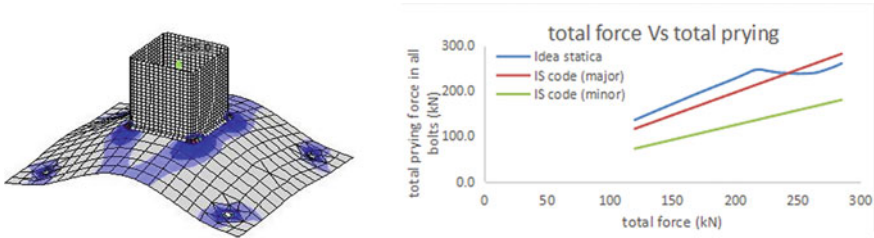
Fig. 8 Biaxial prying in 4 bolted connections

3.3 Four Bolted Connections and Bi-Axial Prying

The consideration of cases in this section shows that there is a major drawback that the actual prying is underestimated by the codal equation. This could lead to uneconomical design. The reasons for this could be the ones explained before and more. It is also observed that bi-axial prying becomes more prominent when the number of bolts used are located more towards the corner of the plates (Fig. 8).

3.4 Four Bolted Configuration with Stiffeners

In this category, there are two cases studied. One being the stiffener given along single axis alone and the other being the stiffener provided in both directions. For each case, rectangular as well as chamfered stiffeners are used. After the calculations, it has been observed that, there are no significant changes in prying forces between cases of chamfered and rectangular stiffeners. Hence a take away can be done from this study that chamfered stiffeners give economical section in terms of prying force consideration. Alongside, stiffeners only on one axis as well as stiffeners along both axes give comparably different values for prying force. Single axis stiffener gives slightly higher value than double axes stiffeners. Even though, the values do not produce much variation, both axes stiffeners cannot be taken for granted due to it's significant contribution in increasing the stiffness of the section. The results are plotted below. In the plot, R1 refers to rectangular stiffener in one axis. R2, rectangular stiffener in 2 axes. C1 and C1 are for corresponding chamfered cases (Figs. 9 and 10).

In the plot above, the section with no stiffeners give highest prying force undoubtedly. But the codal equation does not take care of this prying. It takes care of a prying slightly higher than the one with C1 stiffeners. This could be taken as a re-establishment and can be interpreted as: The codal equation is limited to the case in which stiffness is expected along the major direction. The stiffness could be extended as a plate longing across the width of the plate, which gives stiffness as in case of C2 setup. This gives a scope to think in new aspects.
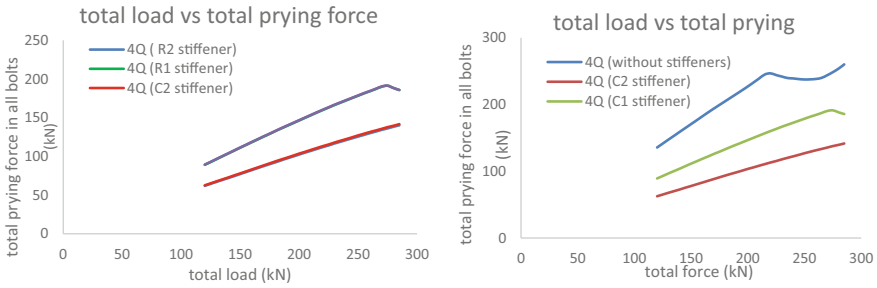
Fig. 9 Prying force comparison under the effect of stiffeners
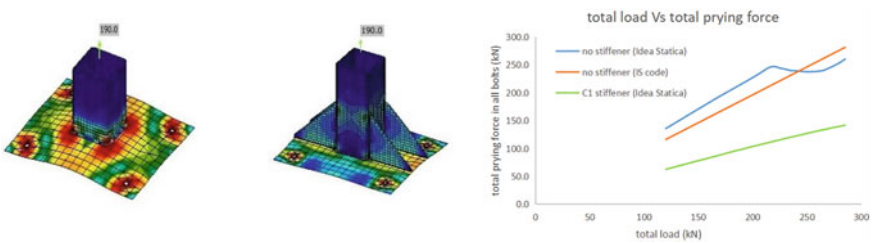
Fig. 10 Representation of usage of stiffeners

3.5 Varying End Distance of the Plate

The end distance of the plate is varied while keeping the load, thickness, bolt-to-to distance and other parameters constant. The dimension of the plate alone is varied to achieve this. In this study, four- bolted connection is used. The end distance is varied from 40 to 120 mm. The results break the conventional concept that end distance beyond a certain limit does not contribute to the effect. Though the effect spreads gradually, it is not nil (Fig. 11).

3.6 Comparison of Prying Force with Varying Moment

The equation in IS code discuss only about direct tensile load, while in real time cases, that is not the only load that leads to prying force. In many scenarios, moment governs the load. Hence, connection subjected to moment is studied here. Same values of moments were used to study the behavior in major and minor directions. It was observed that prying develops only on the tension side of the setup. This result merges well with the concepts. The image snipped from Idea Statica software is shown below (Fig. 12).
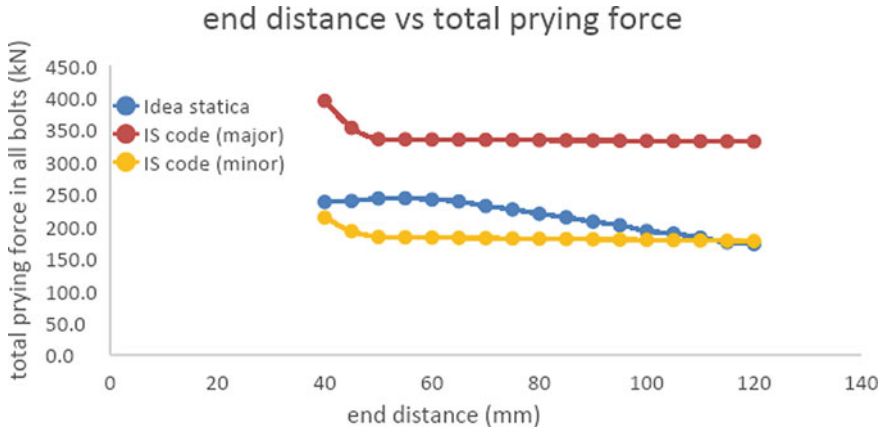
Fig. 11 Prying force comparison of FEM and numerical calculations

(a)

(b)
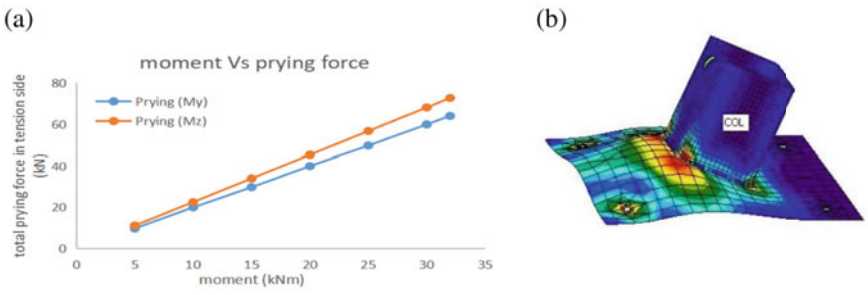
Fig. 12 a Comparison of prying force in different axes with application of moment b Prying dominant in tension side of setup

Further, study has been done to extend the concept to meet the requirement of parameters in IS code equation. Moment has been converted to an equivalent load. Prying force by equivalent loads were calculated for respective directions in which prying with moment is concerned. The values of equivalent load for the same moment along the two directions were different. Hence, the results are plotted separately as follows (Fig. 13):

Both the above graphs conveys that the prying occurring when load is applied as moment is much higher than when equivalent tensile load is applied. This could be due to the splitting of equivalent tensile load to either side of the stub equally, which is not true while moment is applied. It gets clustered in the tension side of the setup.
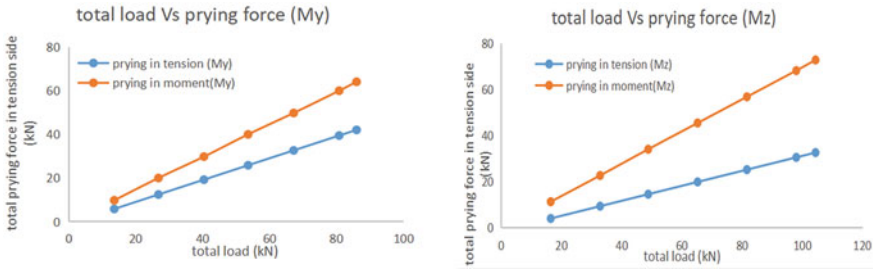
Fig. 13 Comparison of prying forces for moment and equivalent tension

3.7 Prying Force in Steel-To-Steel Connection

Bolted connection was done connecting stubs using two base plates. As the load was applied, it was observed that unlike anchor connection, the prying occurred in both the sections. Double curvature bend was formed. This effect seems to be neglected in the IS code (Fig. 14).

As the plot above shows, the curve with double curvature undergoes more prying force and yields at an initial stage.

The comparison plot of software and numerical results very clearly shows that the equation in IS code has under estimated the double curvature bending. The graphical plot has been provided below.
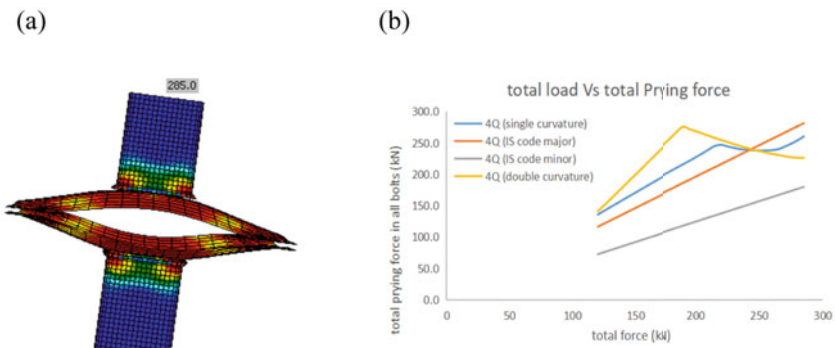
Fig. 14 a Double curvature prying in steel-to-steel connection **b** Result comparison of software and numerical calculations
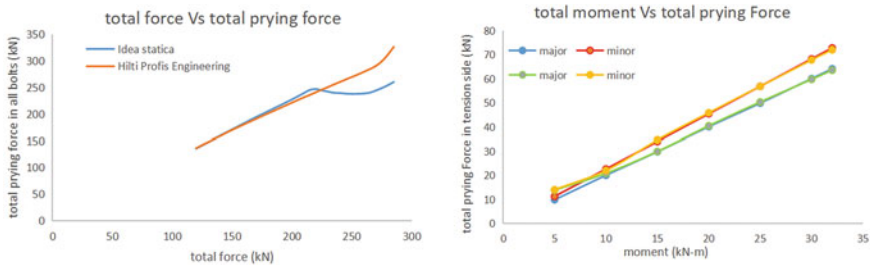
Fig. 15 Comparison of results under **a** tension **b** moment

3.8 Comparison of Idea Statica and Hilti Profis Engineering

Few cases were studied using Idea Statica as well as Hilti Profis Engineering to compare the two softwares. The cases include, varying the load as well as varying the moment (Fig. 15).

Varying the load, as shown in the above plot, yields prying force that are relatively similar for both Idea Statica as well as Hilti Profis Engineering upto the proportionality limit. Beyond this, the dip due to yielding of the plate is not predominant in Hilti Profis Engineering.

When comparison is made with moment as the parameter, results from Idea Statica overlaps results from Hilti Profis Engineering. Both the major axis results overlap as well as both the minor axis result overlap. All the results in this case are before strain hardening. The study could not be proceeded with higher moment values due to the restriction of moment enforced by the softwares.

3.9 Observations

a) It has been observed that the bolt reaction is depended on the grade of concrete used in the base. Variations in bolt reactions have been noted with varying grade of concrete.

b) An effort has been made to provide an approximate approach to use thinner base plate with reduced prying force. The equation for moment as per IS code has been used to calculate the Ze of the section.

c) The maximum load applied is 1810 kN to base plate of 50 mm thickness. A new base plate of reduced thickness (36 mm) is chosen such that the Ze of the new plate is atleast half of the Ze of 50 mm plate. Stiffener dimensions are chosen such that the Ze of combined stiffener and plate is greater than the Ze of 50 mm plate.

d) Equivalent depth of the 36 mm plate with stiffener is found out using the Ze value. This value was around 49.811 mm. This depth is used as input to the prying force equation in IS code.

(a)　　　　　　　　　　　　　(b)　　　　　　　　　　　　　(c)
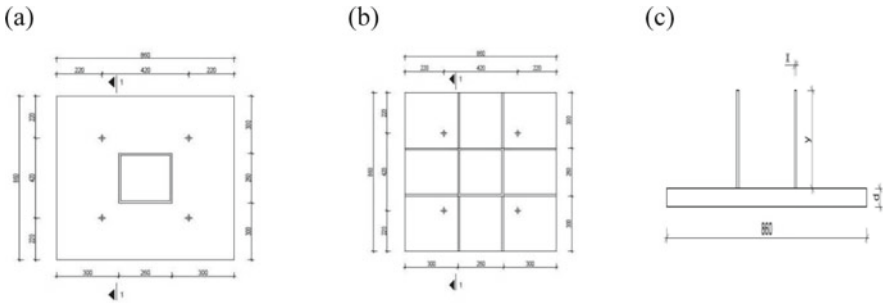
Fig. 16 **a** Thick plate without stiffener **b**, **c** equivalent thin plate with stiffener

Table 1 Usage of stiffener and total bolt reactions

Case	Use of stiffener	Total bolt reactions (kN)
36 mm plate	no	2237
50 mm plate	no	1810
36 mm plate	yes	1810

e) The results have shown that prying force on plate (36 mm) has come down by 63.7% by using stiffener. Or, in other terms, 36 mm plate can take the optimum load of 50 mm thick plate when adequate stiffeners are provided with the prying force corresponding to only 50 mm thickness (provided the other parameters remain constant). Relevant diagrams are shown in Fig. 16(a), (b) and (c).

The values obtained for bolt reactions (FEM) for the above mentioned cases are briefed in the below table (Table 1):

Rectangular stiffener of 10×191.7 mm has been used that extends to the end of the plate.

4　Conclusion

i. To understand the significance of prying, tension loads were plotted against bolt reaction with and without the effect of prying force. It has been found that inclusion of prying effect has increased the bolt force by 187.27% in the study. This emphasizes on the requirement of prying consideration in the bolt design. Further, in-depth study on prying force and its related parameters are performed to understand the existent design procedures.

ii. Several global standard codes such as British standard code BS 5950–1-2000 and Euro code EN were used to compare the equation of prying force. Indian Standard 800:2007 has found to give better results among those studied, in terms of the parameters considered and closeness to FEA.

iii. To study the results and closeness of prying force equation specified in IS code, Finite Element approach is utilized. Industrially renowned softwares such as Idea Statica and Hilti Profis Engineering are explored to serve this purpose.

iv. Comparison of results from Hilti Profis Engineering and Idea Statica were done for certain cases. Idea Statica proves to be a decent and reliable approach for the study. Infact, it includes more precise details like the yielding of the plate. Hence, Idea Statica has been used further for comparison between FEM and IS code.

v. The output obtained from Idea Statica software shows that, yielding and strain hardening of the plate is reflected in prying force. Linear behaviour of the prying force changes when plastic strain starts in the plate. This will give useful information for the designer in plastic analysis.

vi. The values obtained through IS code equation seems to be highly conservative with respect to Idea Statica results when two bolted connections are used (prying force calculated using IS code equation is 2.7 times higher than that found using Idea Statica; when the applied force is maximum). The conservative approach is always true only for such two bolted connections under direct tensile loading.

vii. Four bolted connection leads to a phenomena of bi-axial prying, which is not defined well in IS code. Due to this, the codal equation may lead to unsafe design. This pulls back the effectiveness of equation in bi-axial prying cases.

viii. Varying Lv, keeping the plate dimensions and load (tensile) as constant; yield similar trend of graph as varying load in two bolted connection. This once again points towards the observation that, the results from IS code is much conservative. Moreover, the divergence in this case provide a much larger gap than in case of varying load.

ix. According to the study, when end distance was varied, the conventional concept that increment in end distance beyond a point does not contribute to the effect was proven obsolete with the software results, which has shown that the prying force further keeps decreasing with increase in end distance, even though not linearly.

x. Introduction of stiffener is yet another scenario. It was observed that, the prying force reduces considerably under direct tension load with the use of stiffeners (53.96% reduction in total prying force with use of stiffeners). The plot obtained from codal equation is slightly above the plot of Idea Statica results. This re-establishes that IS code considers the section which is stiff along one of the axes. However, there is no defined approach in IS code to evaluate prying force in case of four side stiffeners.

xi. The usage of rectangular stiffener and chamfered stiffener yields almost the same results. This can suggest the designer to use a chamfered stiffener for optimum design.

xii. The provision of obtaining prying force when moment is the input, is not discussed in the IS code equation. Through FE analysis, it has been understood that the effect of moment on prying is neither negligible, nor equal to the prying obtained with equivalent tensile load. Prying from moment, in real scenario

occurs on tension side of the setup, whereas equivalent load gives prying on both sides of the stub.

xiii. Double curvature bending is an inevitable phenomenon occurring in steel-to-steel connection. As per results from Idea Statica software, the prying force in such a connection is very high as compared with IS code results (difference of 47.9% between results from Idea statica and IS code). Hence usage of IS code equation for such connection without detailed FEM analysis may lead to unsafe design.

References

1. Katzeff, S.E.M.: An investigation into prying models in tension clips. Thin-Walled Struct. **145**, 10639 (2019)
2. Huang, F., Zhang, D., Hong, W., Li, B.: Mechanism and calculation theory of prying force for flexible flange connection. J. Constr. Steel Res. **132**, 97–107 (2017)
3. Bai, R., Chan, S.L., Hao, J.P.: Improved design of extended end-plate connection allowing for prying effects. J. Constr. Steel Res. **113**, 13–27 (2015). https://doi.org/10.1016/j.jcsr.2015.05.008
4. Prinz, G.S., Nussbaumer, A., Borges, L., Khadka, S.: Experimental testing and simulation of bolted beam-column connections having thick extended endplates and multiple bolts per row. Eng. Struct. **59**, 434–447 (2014). https://doi.org/10.1016/j.engstruct.2013.10.042
5. Yang, J.G., Park, J.H., Kim, H.K., Back, M.C.: A prying action force and contact force estimation model for a t-stub connection with high-strength bolts. J. Asian Arch. Build. Eng. **12**(2), 309–316 (2013)
6. Katula, L., Márai, P.: Study the prying effect on bolted base-plate connections. Civil Eng. **57/2**, 157–172 (2013). https://doi.org/10.3311/PPci.7171, http://periodicapolytechnica.org/ci
7. IS 800: General Construction in Steel - Code of Practice [CED 7: Structural Engineering and Structural Sections] (2007)
8. Chapter No. 33, Bolted Connections, teaching resource material, The Institute for Steel Development & Growth (INSDAG)
9. EN 1993-1-8 (English): Eurocode 3: Design of steel structures - Part 1–8: Design of joints [Authority: The European Union Per Regulation 305/11, Directive 98/34/EC, Directive 2004/18/EC] (2005)
10. BS 5950–1: Structural Use of Steelwork in Building, Part-1: Code of Practice for Design - Rolled and Welded sections (2000)

Size Optimization of Truss Structures Using Real-Coded Genetic Algorithm with a Novel Constraint Handling Method

George John Joseph, Govind Mohan, V. Harikrishna, M. V. Sandra, and A. S. Sajith

Abstract Minimum weight design has been increasingly important in the twenty-first century due to rising concerns about reducing the carbon footprint of structures. Further, it also reduces the cost by better utilization of the materials. The advances of metaheuristic algorithms have resulted in the ability to attain global optimum even for highly non-linear, non-convex problems such as structural size optimization of complex structures. However, the computational time for the optimization process could increase drastically with the complexity of the problem. Therefore, the requirement for reducing the computational time of the process is essential. This research aims to do weight minimization for truss structures by size optimization using a real-coded genetic algorithm. A new constraint handling technique called the 'corner bounding fly-back mechanism' is proposed in this work. The proposed method enables a feasible set of solutions during each iteration and produces a higher convergence rate than other traditional methods. A series of well-known benchmark examples in the literature are optimized using the proposed method, coded in MATLAB. The numerical results obtained indicate that the convergence rate for the proposed method is about four to ten times when compared to other conventional constraint handling methods in the literature.

Keywords Structural optimization · Size optimization · Constraint handling · Genetic algorithm · Truss structures

1 Introduction

The optimal design concept has become increasingly relevant in recent times considering how urgent the need to conserve and protect our resources and environment has become, as it can produce economic designs while lowering the overall environmental

G. J. Joseph (✉) · G. Mohan · V. Harikrishna · M. V. Sandra · A. S. Sajith
Department of Civil Engineering, National Institute of Technology Calicut, Kozhikode, India
e-mail: georgejohnjoseph2k@gmail.com

A. S. Sajith
e-mail: sajithas@nitc.ac.in

impact. The fact that the building construction industry alone is responsible for 38% of the total global energy-related carbon dioxide emissions manifests this. Structural optimisation involves finding the optimal design of the structural systems by minimising (or maximising) one or more objective functions mathematically based on the given constraints. Minimising the weight of the structure can minimize the materials required for construction thereby playing a direct role in cost and carbon footprint minimisation [1].

Metaheuristic algorithms have become increasingly popular for optimization problems due to their efficiency in finding the global optimum [1]. But the high complexity and the inadequacy of high-dimensional problems call for more research to enhance its performance. All metaheuristic algorithms involve exploitation and exploration, a good combination of which helps achieve the global optimum solution. Genetic algorithm has become one of the most popular metaheuristic techniques used for structural optimization problems [2]. The genetic algorithm can handle discrete search spaces with great efficiency and can produce mathematically and practically feasible solutions. This research aims to do a weight minimisation of truss structures by size optimization using a real-coded genetic algorithm.

2   Real-Coded Genetic Algorithm

Genetic Algorithm (GA), a technique that has been widely used for various optimization problems, can be both real coded and binary-coded. Two major components of the real-coded GA that makes it closely resemble the evolutionary principle in nature are SBX (Simulated Binary) crossover and polynomial mutation [3]. Figure 1 shows the flowchart of the structural optimization program using real-coded GA. The number of parents or children and the number of loops which are indicated in the flowchart by 'n' and 'm' respectively are user-defined parameters in the program.

3   Corner-Bounding Fly-Back Mechanism

Most works in repairing infeasible solutions have been proposed based on the past explored feasible space. Unlike many conventional constraint handling techniques such as the penalty function method where a near-optimal solution could be lost due to constraint handling, the fly-back mechanism, proposed using the particle swarm optimization technique, restores the solution to its previous position and thereby helps in retaining the near-optimal solutions [4, 5]. However, in optimization problems involving the summation of a discrete set (weight of individual elements) to determine the overall fitness such as in the case of truss weight optimization, there exists a possibility to repair each discrete part with the maximum possible fitness value. This thereby increases the overall fitness of the repaired solution. The repair process will attain a local minimum for the parent in the highly nonlinear search
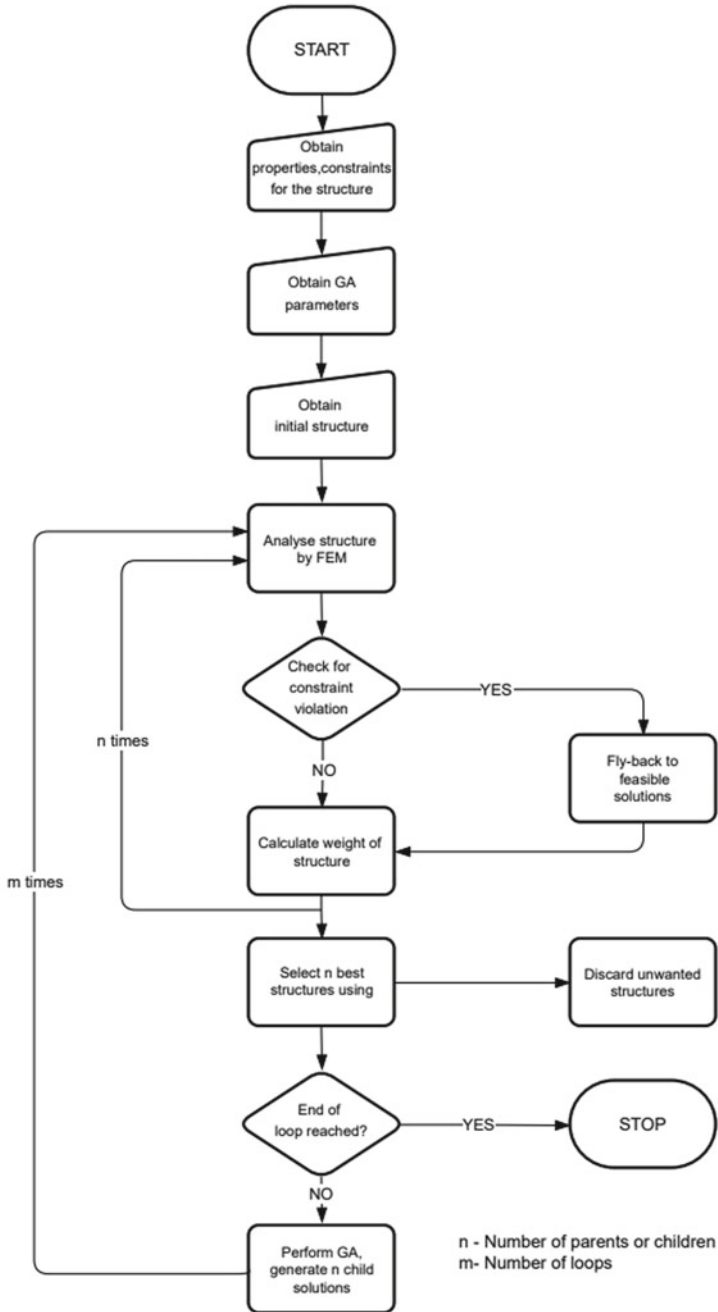
Fig. 1 Flow chart of the structural optimization program

space. Therefore, the repair will result not only in the preservation of a near-optimal solution but also in the convergence of the child solution to the local minimum. However, due to the crossover and mutation processes in GA being independent of the repair, the global search for the optimal solution is not compromised. Hence, the convergence to the global optimum is accelerated through enhanced local search aided by the repair of infeasible solutions.

4 Optimization Problem Formulation

This work aims to achieve the maximum possible weight reduction for the truss structures without violating any prescribed axial stress constraint. This can be formulated as the objective function given by Eq. 1 and the constraint function given by Eq. 2.

$$\text{Minimize}: W = \sum \gamma \, A_i L_i g \tag{1}$$

$$\text{Subject to}: \sigma_{\min} \leq \sigma_i \leq \sigma_{\max} \tag{2}$$

where, W_i = weight of the i$^{\text{th}}$ element, γ = density of the material, A_i = cross-sectional area of element i, L_i = length of element i, g = acceleration due to gravity, σ_i = axial stress in member i, $\sigma_{\min}$ = minimum axial stress under compression, $\sigma_{\max}$ = maximum axial stress under tension.

5 Numerical Examples

For validation of the proposed method, a few selected benchmark problems will be solved in this section. The number of iterations required for the convergence of the solution to the optimal solution and some given values of total weights is compared.

All the numerical examples are coded in MATLAB while the finite element method is used in the determination of forces, stresses and displacement in the structures [6]. For the real-coded genetic algorithm, 50 parent solutions are taken. In the following numerical examples, the probability of crossover is 0.8 and that of mutation is 0.2, while the distribution index for both crossover and mutation is assigned as 20.

5.1 10-Bar Plane Truss

The 10-bar plane truss shown in Fig. 2. is a very popular benchmark example that researchers have been using in truss optimization problems. The optimal design

problem has the properties such as material density of 2767.99 kg/m^3, modulus of elasticity of 68,647.59 MPa, and stress limits [−172.25, 172.25 MPa]. The cross-sectional areas of the ten truss members are the ten design variables for the optimization problem. The loading P_1 applied on the structure is at nodes 2 and 4, which has a value of 444.822 kN. The optimal cross-sectional areas and optimal weights obtained in the present study are compared with that obtained by earlier works in the literature as shown in Table 1 [7]. The plot of the minimum weight (N) vs the number of iterations obtained is given in Fig. 3.
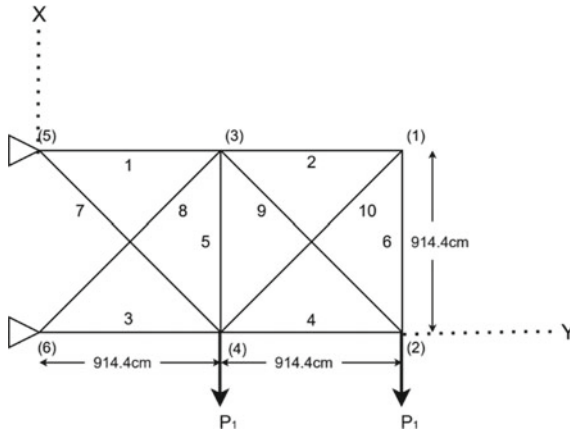
Fig. 2 Ten bar planar truss

Table 1 Optimal mass (kg) and cross-sectional area (mm^2) comparison for 10-bar planar truss by various studies with the present study

Study	Mass	A_1	A_2	A_3	A_4	A_5	A_6	A_7	A_8	A_9	A_{10}
Galante [8]	2475.88	21,613	1045	14,194	9161	1045	1045	5142	14,774	14,194	1045
Nanakorn et al. [9]	2494.48	21,613	1045	14,774	10,000	1045	1045	4658	14,774	14,194	1045
Coello et al. [10]	2534.08	19,355	1045	14,774	8710	1045	1045	8968	14,194	14,194	1045
Sivakumar et al. [11]	2540.06	19,355	1045	12,839	10,903	1045	1045	5142	17,097	14,774	1284
Rajeev et al. [2]	2546.44	21,613	1045	14,194	10,000	1045	1045	9161	12,839	12,839	1690
Present Study	**2472.98**	**19,554**	**1114**	**15,120**	**10,004**	**3985**	**1114**	**4798**	**13,600**	**13,697**	**1045**
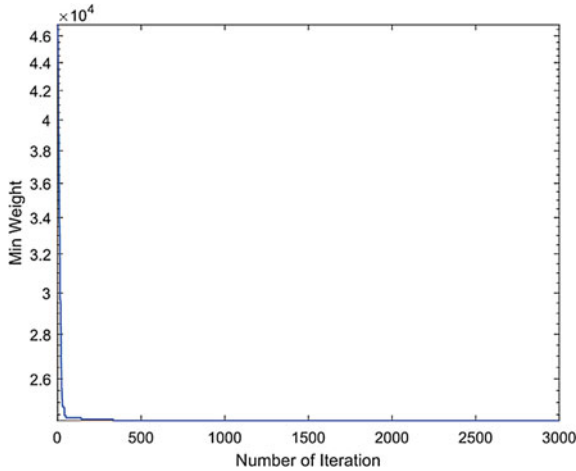
Fig. 3 Minimum weight (N) vs Number of iterations plot for 10-bar planar truss

5.2   25-Bar Space Truss

The 25- bar space truss shown in Fig. 4 is also another popular benchmark problem that has been used by researchers in the 3-dimensional truss optimization problems. This optimal design problem has the following properties which include the material density of 2767.99 kg/m^3, modulus of elasticity of 68,647.59 MPa, and stress limits [-275.79, 275.79 MPa]. The design variables for this example are reduced to eight considering the symmetry of the structure. The loading applied on the structure is at nodes 1 and 2, which has a value of -444.822 kN along both the X and Y axes. The results are compared with that obtained by some of the well-established papers in the literature as indicated in Table 2 [1]. The plot of the minimum weight (N) vs the number of iterations obtained for this example is as indicated in Fig. 5.

6   Discussions

The results obtained for the two numerical examples highlight the superiority of the proposed method. The convergence obtained is almost more than four to ten times faster than that obtained in the other works compared in case-1. The present study takes only 26 iterations to cross the total weight of 2600 kg for the 10-bar planar truss, while other studies take roughly 80 to 300 iterations to reach the same value despite starting from a lower initial weight. Also, in the case of the 25-bar space truss, the present study takes just 13 iterations to cross the total weight of 250 kg, while other studies take roughly 50 to 150. The main reason for the accelerated convergence is due to the combined advantage of accelerating the local search using
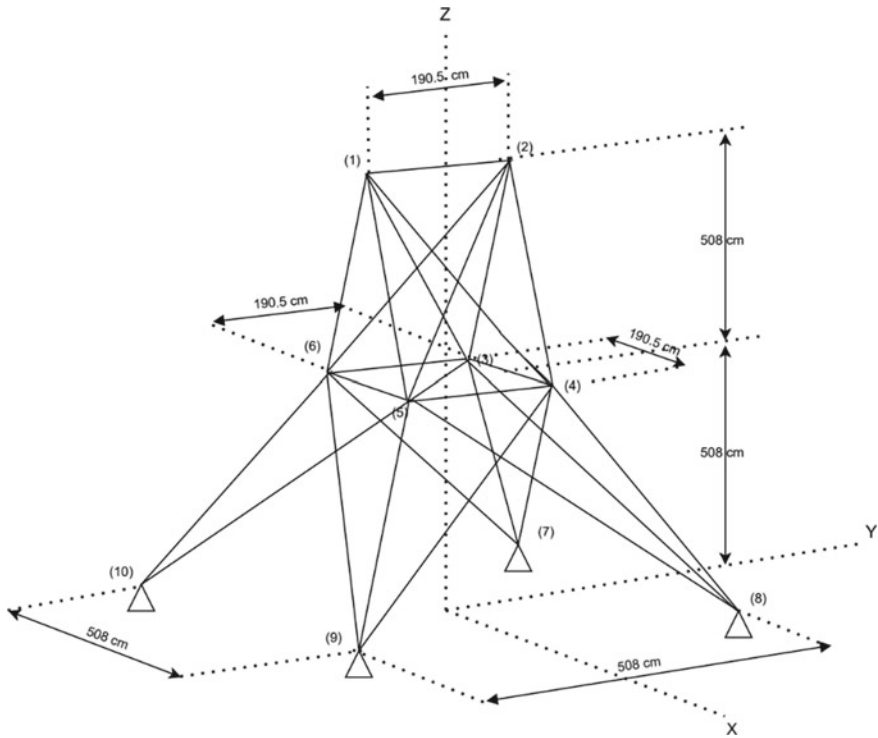
Fig. 4 Twenty-five bar space truss

Table 2 Optimal mass (kg) and cross-sectional area (mm^2) comparison for 25-bar space truss by various studies with the present study

Study	Mass	A_1	A_2	A_3	A_4	A_5	A_6	A_7	A_8
Togan et al. [12]	219.25	65	194	2194	65	1290	645	323	2194
Coello et al. [10]	224.05	65	452	2065	65	903	710	323	2194
Erbatur et al.[13]	233.60	65	645	2194	129	387	710	581	1935
Flager et al. [14]	238.96	65	65	2194	65	65	516	1613	1613
Rajeev et al. [12]	247.67	65	1161	1484	129	65	516	1161	1935
Present Study	**248.62**	**65**	**1302**	**1941**	**65**	**65**	**4381**	**1039**	**1728**

the corner-bounding and preservation of solutions that violate the constraints using the fly-back mechanism.

The major limitation of the proposed technique is the involvement of an additional computation of the cross-sectional area of the elements which violates the specified constraints leading to a maximum of twice the computational effort for each iteration as compared to the conventional techniques. However, this limitation is overcome by
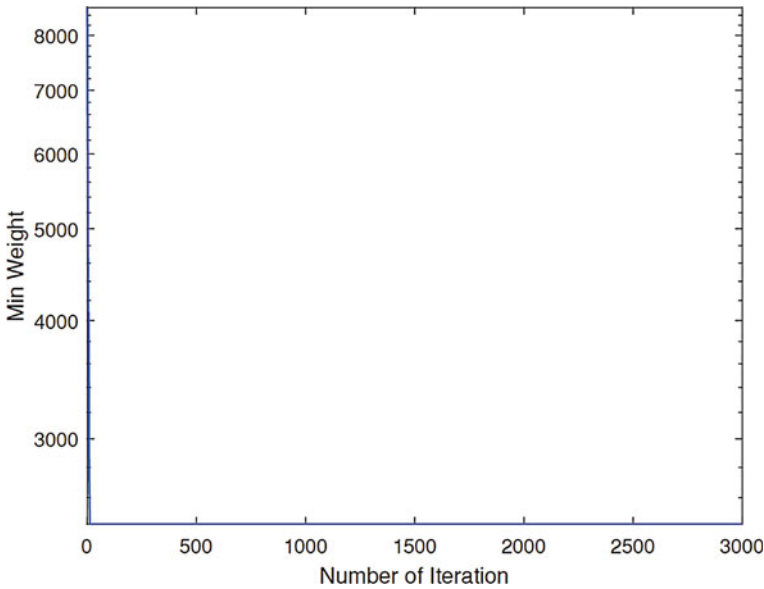
Fig. 5 Minimum weight (N) vs Number of iterations plot for 25-bar space truss

the higher convergence rate which allows the technique to attain the optimal solution with a reduced overall computational effort.

The work was aimed to achieve the maximum possible weight reduction for the truss structures without violating any prescribed axial stress constraint for each element using the novel corner-bounding flyback mechanism. The application of the proposed technique to shape, topology and layout optimization along with the addition of the buckling and nodal displacement constraint handling techniques in the size optimization problem could be further improvement to the proposed work.

7   Conclusion

The paper presents a novel constraint handling technique, the corner-bounding flyback mechanism for structural size optimization using a real-coded genetic algorithm. The proposed method possesses the advantage of an increased convergence rate of about four to ten times more than when other conventional constraint handling techniques are used. This advantage is also credited to the generation of multiple varying parent solutions within the feasible search space from an initial solution, as it activates the crossover function from the initial solution.

Future works on the proposed techniques may include the application of the proposed technique to shape, topology and layout optimization. The addition of the

buckling and nodal displacement constraint handling techniques using the proposed technique could be another improvement to the proposed work.

References

1. Mei, L., Wang, Q.: Structural optimization in civil engineering: a literature review. Buildings **11**(2), 66–92 (2021)
2. Rajeev, S., Krishnamoorthy, C.S.: Discrete optimization of structures using genetic algorithms. J. Struct. Eng. **118**(5), 1233–1250 (1992)
3. Deb, K.: Multi-Objective Optimization Using Evolutionary Algorithms. Wiley, Chichester (2001)
4. He, S., Prempain, E., Wu, Q.H.: An improved particle swarm optimizer for mechanical design optimization problems. Eng. Optim. **36**(5), 585–605 (2004)
5. Kaveh, A., Talatahari, S.: Particle swarm optimizer, ant colony strategy and harmony search scheme hybridized for optimization of truss structures. Comput. Struct. **87**(44352), 267–283 (2009)
6. Kattan, P.: Matlab Guide to Finite Elements: An Interactive Approach, 2nd edn. Springer, Heidelberg (2008)
7. Appelo, S.A.: Structural Optimisation via Genetic Algorithms. MSc Eng(Civil) Thesis paper, Department of Structural Engineering, University of Stellenbosch, South Africa (2012)
8. Galante, M.: Genetic algorithms as an approach to optimize real world trusses. Int. J. Numer. Meth. Eng. **39**, 361–382 (1996)
9. Nanakorn, P., Meesomklin, K.: An adaptive penalty function in genetic algorithms for structural design optimization. Comput. Struct. **79**, 2527–2539 (2001)
10. Coello, C.A., Rudnick, M. and Christiansen, A.D. (1994) Using genetic algorithms for optimal design of trusses. IEEE, 88–94.
11. Sivakumar, P., Rajaraman, A., Knight, G.M.S., Ramachandramurthy, D.: Object-oriented optimization approach using genetic algorithms for lattice towers. J. Comput. Civil Eng. **18**, 162–171 (2004)
12. Togan, V. and Daloglu, A.T. (2008) An improved genetic algorithm with initial population strategy and self-adaptive member grouping, *Computers and Structures*, 1204–1218.
13. Erbatur, F., Hasancebi, O., Tütüncü, I., Kilic, H.: Optimal design of planar and space structures with genetic algorithms. Comput. Struct. **75**, 209–224 (2000)
14. Flager, F., Soremekun, G., Shea, K., Fischer, M., Haymaker, J.: Fully constrained design: a scalable method for discrete member sizing optimization of steel frames structures. Technical Report, Stanford University. Center for Integrated Facility Engineering (2011)

Evaluation of Geopolymer Concrete with Crumb Rubber: A Review

P. K. Arjun Raj, Praveen Nagarajan, and A. P. Shashikala

Abstract Cement is a major source of CO_2 emissions, which has negative consequences for the environment. Geopolymer concrete is found to be a promising substitute for Portland cement. Rubberized concrete provides a suitable way for tire waste disposal by replacing aggregates in concrete with crumb rubber. There have been several studies conducted on both geopolymer concrete as well as rubberized concrete. A combination of both these to form a rubberized geopolymer concrete promises to be sustainable construction material, which has been a hot topic among researchers recently. Important aspects such as constituents, mixing and curing aspects, physical and fresh properties, durability properties, and mechanical properties of RuGPC conducted on previous works are reviewed. The effect of crumb rubber addition, alkali, binder type, the alkali to binder ratio, and curing type on the above-mentioned aspects are reviewed. From the review of literature, it was found that durability in terms of wear depth is only 0.8 mm even with 30% replacement of fine aggregates by crumb rubber. New treatments that can be given to crumb rubber for improving the bonding between geopolymer matrix and rubber is also highlighted in this work.

Keywords Geopolymer concrete · Rubberized concrete · Rubberized geopolymer concrete · Crumb rubber

1 Introduction

After water, concrete is the most frequently utilised substance on the globe [1]. Its vast usage has many reasons, such as simplicity of handling, durability, capability to transform the concrete into various shapes, impressive mechanical properties, fresh properties, etc. Concrete is made of natural fine and coarse aggregates, water and binder [2]. Ordinary Portland cement (OPC) has been used as a binder for many years, but it generates a large amount of CO_2 during the manufacturing process and uses a lot

P. K. A. Raj (✉) · P. Nagarajan · A. P. Shashikala
National Institute of Technology Calicut, Kozhikode, India
e-mail: arjunraj_p200045ce@nitc.ac.in

P. Nagarajan
e-mail: praveen@nitc.ac.in

A. P. Shashikala
e-mail: apska@nitc.ac.in

of natural resources. For output of 1 ton of ordinary Portland cement, approximately 1.8 tons of raw materials are required of which 70% is constituted by limestone [3–5]. Fuel combustion in the kiln produces a temperature of about 1450°Cwhich is a highly energy-intensive process [6]. Other harmful gases like nitrogen dioxides and Sulphur trioxides are also created enormously during cement manufacturing, which boosts global warming and acid rains [7].

One of the effective and viable replacements of conventional concrete is geopolymer concrete, which uses aluminosilicate-based materials activated by an alkali. Ground granulated blast furnace slag (GGBS), Fly ash (FA), Metakaolin (MK), Red mud, Rice husk ash, waste wood ash, and other aluminosilicate materials are used for geopolymer [4–10]. Sodium hydroxide (NaOH), sodium silicate (Na_2SiO_3), potassium hydroxide (KOH), and potassium silicate (K_2SiO_3) are alkaline solutions used for geopolymer [11, 12]. Geopolymer concrete is a newly developed material that is impressive due to its ease of manufacture, notable performance, and low carbon footprint than conventional concrete [13].

Sudden development in population and transportation has led to considerable growth in the automotive industry, which in turn led to significant rubber waste from tyre disposal. According to the data from 2017, tyre production has increased to 2.9 billion units per year throughout the world, while tyre waste is about comparable to tyre production [47]. The gases expelled from fuel-burning can cause deleterious effects on the environment and if proper landfilling methods are not adopted in this case, serious environmental wastes will be created [17].

A considerable quantity of literature is already available on geopolymer concrete and rubberized concrete but only a piece of limited knowledge is available on rubberized geopolymer concrete. RuGPC (Rubberized geopolymer concrete) is having advantages over both geopolymer concrete and rubcrete [4]. The alkaline solution used in the geopolymer construction is also used to treat rubber particles to have the proper bond between geopolymer mix and crumb rubber [19]. This work reviews the constituents of rubberized geopolymer concrete including alumino-silicate base materials, natural aggregates, rubber aggregates, alkaline solution and admixtures. This is a brief review of fresh properties, physical properties, durability, and mechanical properties like compressive strength, split tensile strength, flexural strength, and elastic modulus of Rubberized geopolymer concrete.

2 Constituents of RuGPC

2.1 Aluminosilicate Base Materials

Aluminosilicate rich materials used to construct geopolymer concrete include Fly ash, GGBS, rice husk ash, wood ash, metakaolin, silica fume etc. Geopolymer gels are formed when these base materials react with the alkaline solution [20]. The nature of the reaction of aluminosilicate base material is relying to a large extent on the

Table 1 Chemical constituents of aluminosilicate base materials

Ref	SiO_2	Al_2O_3	CaO	Fe_2O_3	K_2O	TiO_2	SO_3
Fly ash							
Zhang, Baifa, et al. [21]	51.2	22.8	6.5	10.7	4.5	2.5	1.3
Park et al. [4]	54.7	29	1.29	6.74	–	–	0.1
Osama et al. [22]	51.1	18.1	5.8	9.7	1.84	0.8	1
Aslani et al. [18]	50.4	31.5	3.3	10.4	0.5	1.9	0.10
Azmi et al. [11]	50	23.4	5.06	17.29	1.41	1.60	0.08
Avg	51.48	24.96	4.39	10.96	2.06	1.7	0.516
GGBS							
Zhang, Baifa, et al. [21]	21.2	8.1	63.3	0.6	0.5	2.6	2.5
Osama et al. [22]	32.8	13.4	43.1	0.4	0.3	0.6	1.9
Aslani et al. [18]	32.92	13.8	42.13	0.58	0.32	0.57	3.33
Nguyen et al. [23]	36.5	11.60	39.46	0.43	0.68	0.84	0.73
Kishore et al. [24]	34.5	12.36	35.4	1.8	0.28	0.5	0.5
Avg	31.58	11.85	44.67	0.762	0.416	1.022	1.792

mineral and chemical constituents of materials [12]. The chemical composition of aluminosilicate base materials is shown in Table 1. Fly ash is a waste product of coal-fired power plants that have sufficient pozzolanic characteristics. FA production is reported to be approximately 375–400 million tonnes per year globally [13]. Fly ash is made up of small, powdery particles that are generally, solid or hollow, spherical and amorphous in composition. Coal ashes have a specific gravity of almost 2.0, but it varies greatly, ranging from 1.6 to 3.1.

Particle form, gradation, and chemical composition are all elements that contribute to this variance [25]. According to IS 3812 (Part 1): 2013, the sum of the percentage by mass of aluminium oxide (Al_2O_3), silicon dioxide (SiO_2) and Iron oxide (Fe_2O_3) should be greater than 70% for Siliceous fly ash and 50% for calcareous fly ash [26]. As per ASTM C618-19, low calcium fly ash has a calcium oxide content of less than 18%. From Table 1, almost all the experiments are done using class F fly ash which can be effectively used to find out the optimum binder properties [7]. The problem with the class C fly ash is that the flash setting can only be used where early strength attainment is important [27].

Ground Granulated Blast Furnace Slag is a cementitious material that is mostly exploited in geopolymer concrete and it is a waste material from iron blast furnaces [28]. GGBS has a specific gravity ranging from 2.7 to 2.9 [29]. Due to the significant Calcium oxide content of GGBS (greater than 30% from table 1), it has flash setting properties and high shrinkage [7, 30]. The aluminosilicate material GGBS is often used as the base material for developing geopolymers. From Table 2, the combination of Class F fly ash and GGBS is used to make rubberized geopolymer mostly due to its proper workability, setting time and strength development under ambient conditions [2].

Table 2 Aluminosilicate base materials, alkaline solutions, curing methods, admixtures

Ref	Aluminosilicate base materials	Alkaline solutions	Alkali/binder ratio	Admixture type and dose	Curing type and duration
Luhar et al. [13]	Class F fly ash	NaOH-flakes-14 M Na_2SiO_3-n r Na_2SiO_3/NaOH-2.5	0.4	Naphthalene based-2%	Oven-90 °C-48 h
Aslani et al. [18]	Class F fly ash GGBS	NaOH-pellets-14 M Na_2SiO_3- n r Na_2SiO_3/NaOH-2.5	0.4–0.6	Polycarboxylate based and VMA	Ambient-23 °C-7-28 days
Azmi et al. [11]	Class F fly ash	NaOH-12 M Na_2SiO_3- 3.2 MS Na_2SiO_3/NaOH-2	0.4	nr	Ambient-20–22 °C-until testing
Wongsa et al. [31]	Class C fly ash	NaOH-10 M,15 M, 20 M Na_2SiO_3-2.41 M.S Na_2SiO_3/NaOH-	0.65, 0.75,0.85	nr	Oven-60 °C 90 °C- 48 h
Luhar et al. [8]	Class F fly ash	NaOH-14 M Na_2SiO_3- nr Na_2SiO_3/NaOH-2.5	0.4	Naphthalene based-2%	Oven-90 °C-48 h
Aly et al. [3]	GGBS	NaOH-nr Na_2SiO_3-3.39 M S Na_2SiO_3/NaOH-0.39	0.54	nr	Ambient-until testing
Ali et al. [32]	Class F fly ash	NaOH-10 M Na_2SiO_3-nr	0.45	Naphthalene based	Hot water curing-60 °C
Yahya et al. [33]	Class F fly ash	NaOH-12 M Na_2SiO_3-nr Na_2SiO_3/NaOH-2.5	0.5	nr	Seawater- until testing
Rashad et al. [34]	GGBS	NaOH-nr Na_2SiO_3-3.39 MS Na_2SiO_3/NaOH-nr	0.3	nr	Heat curing 45 °C-28 days
Zaetang et al. [10]	Class C fly Ash	NaOH-10 M Na_2SiO_3-2.41 MS Na_2SiO_3/NaOH-1	0.75	nr	Oven-60 °C-48 h

2.2 Alkalies

In most of the studies, NaOH and Na_2SiO_3 are the alkalies used in the making of RuGPC. Through the action of hydroxide ions, alkaline activators help in the dissolution of Si and Al atoms from the source material [38] and the solution is prepared one day before mixing [9]. The NaOH is available in different forms and can be bought as pellets and flakes. It is highly soluble in water and dissolution generates heat. It is white in colour also [11]. The NaOH solution's concentration is expressed as a molarity number. Molarity is the concentration of a solution measured as the number of moles of solute per litre of the solution [4]. As per Table 2, the molar concentration of NaOH varies from 10 to 20 M for the preparation of RuGPC but a variation of 12 to 14 M is encountered mostly. The molarity change affects the compressive strength of the RuGPC mix [4, 39].

The other part of the alkaline activator is Na_2SiO_3 and it is known as water glass. In most studies, it is used as a highly viscous liquid [3]. The constituents of Na_2SiO_3 are sodium oxide (Na_2O) and SiO_2. The ratio of SiO_2/Na_2O is known as the Modulus of silicate and it affects the compressive strength of geopolymer mixes as well as the reaction kinetics and Geopolymerization reaction [40]. The value of the Modulus of silicate used in the preparation of RuGPC varies from 2 to 3.39 in Table 2 with optimal values ranging from 2 to 2.5 [4, 7, 13]. From the studies of RuGPC indicated in Table 2, the value of $Na_2SiO_3/NaOH$ ranges from 0.39 to 2.9 and most of the studies adopted a range of 2 to 2.5. One of the key parameters which affect almost all the characteristics of RuGPC is the alkali to binder ratio and it varies from 0.4–0.85. The optimum value range used in these studies is from 0.4 to 0.5.

2.3 Rubber Particles and Pre-treatments

Rubber particles are used in the form of Rubber fibres, crumb rubber, waste rubber powder etc. [8, 35, 31, 33]. These are used to replace the aggregate portion of the mix. From Table 3 The specific gravity of rubber particles ranges from 0.38 to 1.16. Shredded rubber particles are employed to replace coarse aggregates, whereas crumb rubber is used to replace fine aggregates. Some research [8, 13, 33, 34] used rubber particles to replace aggregates by weight, whereas others used rubber particles to replace aggregates by volume [3, 11, 18, 32].

Common pre-treatment methods for rubber particles include water treatment, Pre-treatment with NaOH, pre-treatment with cement paste, and pre-treatment using ultra-fine slag [42]. The objective of rubber particle treatment is to eliminate contaminants from the surface to improve the bonding between rubber particles and paste [36]. High workability and compressive strength are obtained for rubberized geopolymer mixes processed with NaOH treatment and ultra-fine slag treatment, according to Saloni et al. [42]. Lazorenko et al. [41] treated the rubber with some more methods like H_2SO_4 treatment, UV treatment, $(CH_3)_2CO$ treatment, and $KMnO_4$ treatment and they found that the treatments of NaOH, H_2SO_4, $(CH_3)_2CO$, and UV waves on crumb rubber particles have been discovered to not affect the mechanical characteristics of rubberized GP composites. When compared to GeoPC with untreated rubber, treatment with a 5% $KMnO_4$ aqueous solution improved geopolymerization and helped build strong hydrogen connections between geopolymer and rubber, resulting in a 21% improvement in compressive strength [41].

2.4 Admixtures

Admixtures used in the formation of rubberized GeoPC include Naphthalene based superplasticizers, Polycarboxylate based superplasticizers, VMA (Viscosity modifying agents), lignosulfonates, melamine-based SPs and naphthalene-based SPs. In

Table 3 Sizes, specific gravities and treatment of aggregates and rubber particles

Ref	Fine aggregates	Coarse aggregates	Rubber particles
Luhar et al. [13]	River sand-Zone 2. Sp gravity: 2.61 FM: 2.56, Water absorption: 0.5%	Crushed basalt Size 20 mm, Sp gravity: 2.59, FM: 2.7, water absorption: 0.5%	Rubber fibre: 2–4 mm width and 22 mm long and sp gravity: 1.09 Replacement: 10% by weight of fine aggregates
Aslani et al. [18]	Quarry sand- Size: < 4 mm	Quarry aggregate- Size: 7 mm, 10 mm	Crumb rubber: CR1-2–5 mm, CR2-5–10 mm Replacement: 10% and 20% by volume replacement for both CR1 and CR 2. Treatment: water soaking method
Azmi et al. [11]	nr	nr	Crumb rubber: 73 μm to 375 μm. Replacement: 5, 10, 15, 20% by volume of fine aggregates
Wongsa et al. [31]	River sand-Sp gravity: 2.63, bulk density: 1671 kg/m^3, Water absorption:0.35%, FM:3.30	nr	Crumb rubber: Sp gravity: 1.16, bulk density: 487 kg/m^3, Water absorption: 3.27%, FM:3
Luhar et al. [8]	River Sand-zone 2 Sp gravity: 2.61, Water absorption:0.5%, FM:2.56	Size: 10 mm,20 mm	Rubber tyre fibres: Sp gravity: 1.09, length: 2-4 mm width, 22 mm length and aspect ratio: 8–10 Replacement: 10, 20 and 30% by weight of fine aggregates
Aly et al. [3]	Natural clean (35% by weight) sand: Size less than 0.5 mm. Sp. gravity of sand:2.65 g/cc. FM:2.25	Clean Crushed dolomite (65% by weight) max size:12 mm and specific gravity: 2.96 g/cc	Crumb rubber of mesh 40 sizes and 1–4 mm size. Sp gravity of crumb rubber: 0.45. Replacement: 10, 20, 30% by volume of both types of aggregates
Ali et al. [32]	River sand- with 2- and 4-mm size	Crushed gravel of 10 mm maximum size	Recycled chopped tyre rubber: 2 mm and 4 mm size. Replacement: 10%, 20%, 30% by volume with two sizes 2 and 4 mm

the majority of studies, Naphthalene based and Polycarboxylate based superplasticizers are used [8, 13, 18, 32]. Naphthalene-based SPs improved the workability and compressive strength of alkali-activated GGBS depending on the activator type and concentration, whereas Sika Viscocrete-3430, a modified polycarboxylate, was recommended for FA-based geopolymer [43]. Nguyen et al. [23] concluded that the slump of the Geopolymer concrete was improved by both naphthalene and polycarboxylate superplasticizers. A superplasticizer like Glenium 51, on the other hand, maybe useful for both compressive strength and water absorption [23].

2.5 Curing Methods

Table 2 shows the main curing methods used for RuGPC: ambient curing, oven/heat curing, steam curing, and water curing. Because the activator ingredients will be leached out through pores, generating chemical instability of the mix, water curing is not a frequent procedure for geopolymer concrete [44]. Heat curing or oven curing involves placing the specimen at a temperature range of 45–90 °C for 48 h in the majority of studies [8, 13, 31, 34, 10] after that, the specimens are left at room temperature until they are tested. Steam curing, on the other hand, includes placing specimens in an autoclave for seven days at a temperature of around 46 degrees Celsius, then leaving them out in the open until testing [4].

Hassan et al. [45] studied the effect of ambient curing and heat curing at 75 °C for 26 h on a fly ash-based geopolymer mix, concluding that heat-cured specimens have higher compressive and flexural strength. When exposed to temperatures of 100, 200, 400, 600, 800, and 1000 °C, Zhang et al. [46] reported that ambient-cured geopolymer concretes lost more mass than heat-cured specimens for the same composition.

3 Fresh and Physical and Durability Properties

3.1 Workability

When crumb rubber replacement levels increased, workability in terms of flow value reduced [18, 31, 10, 36]. When 5, 10, and 15% of fine aggregate were replaced with crumb rubber, the flow was reduced by 14, 29, and 50%, respectively when compared to the control mix [36]. Similarly, increasing the size of crumb rubber particles reduced the slump of rubberized geopolymer. When 2 to 5 mm size crumb rubber is used in the mix with percentage replacement of 10 and 20%, obtained slump flow values are 650 and 640 mm, but when 5–10 mm size is used, slump flow values decreased to 622 and 610 mm respectively [18]. Apart from % replacement and size of crumb rubber particles, other factors affecting the workability of rubberized geopolymer include treatment of rubber, alkali to binder ratio, the molarity of sodium

hydroxide solution, sodium silicate to sodium hydroxide ratio [19, 36]. Dong et al. [19] reported that when the percentage replacement of sand by crumb rubber increases from 0 to 15%, the slump slightly increased because of additional adsorbed water during water treatment. But at a 30% replacement level, contact between rubber particles increased, causing friction decreases the workability [19]. Because soaking rubber in NaOH roughens the surface of rubber, resulting in increased rubber to paste adhesion and flow resistance, pre-treatment of crumb rubber for 1 and 24 h reduces flow by 57 and 71%, respectively, compared to the control mix for a replacement of 15% of fine aggregates by rubber [36]. The alkali to binder ratio was increased, which improved the flow value of the crumb rubber geopolymer mix. With the increase of molarity of NaOH solution from 10 to 15 M, workability was slightly reduced because it increases the stiffness of the solution. Because of the high viscosity of sodium silicate solution, the workability of the crumb rubber geopolymer mix decreases as the ratio of sodium silicate to sodium hydroxide increases [31].

3.2 Density

Due to the decreased density of rubber particles compared to fine aggregate, the densities of rubberized geopolymer specimens were lower than the control geopolymer specimens [13, 18, 19, 31]. Wongsa et al., for example, found that when 100% of the sand was replaced with crumb rubber, the density was 42% lower than the control geopolymer mix. The bulk density of the mix with 15% rubber replacement of fine aggregates was around 1900–2000 kg/m^3 at 28 days, according to Dong et al. [19], whereas the value dropped to 1700 kg/m^3 for the mix with 30% replacement. Another factor for RuGPC's lower density is their non-polar nature and tendency to trap air in their rough surfaces [37]. Dong et al. [19] observed that for geopolymer mix with 15% replacement by rubber, compressive strength was proportional to bulk density throughout the curing process. Wongsa et al. [31] discovered that as the alkaline solution to binder ratio increases, the density of crumb rubber geopolymer mix reduces slightly, but increases slightly as the sodium hydroxide concentration increases. The ultrasonic pulse velocity value (UPV) and thermal conductivity of the control geopolymer specimen are lower due to the large porosity and low density [31].

3.3 Durability Parameters

As a measure of durability, Luhar et al. conducted an abrasion resistance test. Abrasion is measured on the basis of wear depth. As more rubber fibres are added to the mix, abrasion resistance improves [8]. They observed that when there are no rubber fibres in the mix, maximum depth occurs. For example, at 28 days, the reported wear

depth was 1.2 and 0.8 mm, respectively, with 0 and 30% crumb rubber addition by weight of fine aggregates [8].

Rashad et al. [34] investigated the effects of multiple cycles of immersion in sulphate and drying at 80 °C on various specimens using compressive strength measurements. They observed that the addition of rubber crumbs in the mix decreases the strength reduction ratio [34]. For instance, after 15 and 20 cycles, the reference specimen has lost 16.9 and 30.3% of its initial compressive strength, respectively, whereas the mix with 1% crumb rubber replacement of alkali-activated slag has lost 14.1 and 23.14%. After 15 and 20 cycles, the mix with 2.5% crumb rubber replacement of alkali-activated slag has lost 12.5 and 19.7% of its original compressive strength, respectively and this finding confirmed the high durability of the specimen with waste rubber powder [34].

4 Mechanical Properties

4.1 Compressive Strength

A higher percentage of crumb rubber particles in RuGPC reduces the compressive strength of the specimen regardless of the kind of aluminosilicate precursor, alkali, or curing [3, 7, 11]. According to the literature [3], 28-day strengths for both 20 and 30% aggregate substitution were 28.3 and 24.8 MPa, respectively, losing 24 and 34% compared to the control mixture's compressive strength. They observed that for 10% aggregate replacement, 7% gaining of compressive strength is obtained [3]. The inclusion of NaOH may change the surface roughness of rubber particles, generating an increase in paste adhesion and thus compressive strength. Azmi et al. [11] noticed a decrease in compressive strength up to 60% for fly ash based RuGPC with 15% CR substitution by volume of fine aggregates.

The type of treatment method of crumb rubber also influences the strength of RuGPC [41]. For instance, when potassium permanganate-treated crumb rubber is added to the geopolymer binder, the compressive strength value rises to 15.5 MPa, which is about 21% greater than that of the control specimen [41].

4.2 Split Tensile Strength

The 28-day split tensile strength of the control specimen decreased from 3.6 MPa to 2.355 MPa, according to Aly et al. [3] (34.65 percent reduction). When crumb rubber replacement was increased to 20% and subsequently 30%, splitting tensile strengths declined by 23 and 35.5% respectively [3]. At 10 and 20% rubber replacement of aggregate, Aslani et al. [18] found that split tensile strength reduced from 2.26 MPa

for the control specimen to 1.84 MPa (18.6% reduction) and 1.82 MPa (19.5% reduction). Lower Crumb rubber particle adherence to the geopolymer mix owing to rubber's hydrophobic nature, as well as the establishment of a weaker interfacial transition zone around the CR particles, are the possible reasons for this decrease [18].

4.3 Flexural Strength

Like other mechanical properties, the flexural strength of RuGPC also decreases with respect to the increase in crumb rubber content. When compared to the control specimen, Aly et al. [3] found that increasing the fraction of aggregate replacement by crumb rubber to 10% caused in a 20% fall in flexure strength with a flexure force of 2.00 kN. For 20 and 30% replacement by crumb rubber, flexural strength decreased by 30% compared to the control specimen [3] Zaetang et al. [10] experienced a decrement of 61.4 and 77.3% in flexural strength with CR replacement of aggregates by 50 and 100%. Flexure strength loss is on the rise, which could be due to the same reasons that impact compressive and tensile strength [10].

5 Conclusions

- For the preparation of RuGPC, the molarity of NaOH varies from 10 to 20 M, but the most common range is 12 to 14 M. The compressive strength of the RuGPC mix is affected by molarity variations.
- The value of the Modulus of silicate used in the preparation of RuGPC varies from 2 to 3.39 with optimal values ranging from 2 to 2.5 and the adopted value of $Na_2SO_4/NaOH$ in most of the studies varies from 2 to 2.5.
- Crumb rubber can be treated with NaOH solution, water soaking, and $KMnO_4$ to increase rubber particle adherence to the surrounding geopolymer mix, which leads to improved mechanical characteristics.
- For RuGPC mixes, heat curing is found to be more effective than ambient curing. When compared to heat-cured specimens, the mass loss rate for ambient cured specimens is greater.
- Concrete slump/flow is reduced when a high CR replacement of aggregate is used in RuGPC. With 15% CR replacement, this might result in a 50% reduction in slump.
- Density of specimen is reduced when a high CR replacement of aggregate is used in RuGPC. With 100% CR replacement, this might result in a 42% reduction in density.
- Abrasion resistance which is a measure of durability in terms of wear depth increases as the percentage of crumb rubber increases. At 28 days, the depth

of wear was 1.2 and 0.8 mm, respectively, with 0% and 30% rubber crumb substitution by weight of fine aggregates.

- Compressive strength of RuGPC is low compared to the corresponding control specimens generally. With 15% CR substitution of fine aggregates, compressive strength is reduced by as much as 60%.
- Similar to all mechanical properties, elastic modulus reduce with higher rubber content.

References

1. https://www.theguardian.com/cities/2019/feb/25/concrete-the-most-destructive-material-on-earth
2. World Business Council for Sustainable Development, The Cement Sustainability Initiative: Recycling Concrete, Washington, D.C. (2009)
3. Aly, A.M., El-Feky, M.S., Kohail, M., Nasr, E.S.A.R.: Performance of geopolymer concrete containing recycled rubber. Constr. Build. Mater. **207**, 136–144 (2019)
4. Park, Y., Abolmaali, A., Kim, Y.H., Ghahremannejad, M.: Compressive strength of fly ash-based geopolymer concrete with crumb rubber partially replacing sand. Constr. Build. Mater. **118**, 43–51 (2016)
5. Kumar, S., Bishnoi, M.: The fabrication of geo-polymer concrete using rice husk, crumb rubber and GGBS. J. Xidian Univ. **14**, 1–15 (2020)
6. Sorrentino, F.: Chemistry and engineering of the production process: state of the art. Cem. Concr. Res. **41**, 616–623 (2011)
7. Rajendran, M., Akasi, M.: Performance of crumb rubber and nano fly ash based ferro-geopolymer panels under impact load. KSCE J. Civ. Eng. **24**, 1810–1820 (2020)
8. Luhar, S., Chaudhary, S., Luhar, I.: Development of rubberized geopolymer concrete: Strength and durability studies. Constr. Build. Mater. **204**, 740–753 (2019)
9. Amran, Y.H.M., Alyousef, R., Alabduljabbar, H., El-Zeadani, M.: Clean production and properties of geopolymer concrete: a review. J. Clean. Prod. **251**, 119679 (2020)
10. Zaetang, Y., et al.: Utilization of crumb rubber as aggregate in high. Int. J. GEOMATE **17**, 158–165 (2019)
11. Azmi, A.A., Abdullah, M.M.A.B., Ghazali, C.M.R., Victor Sandu, A., Hussin, K.: Effect of crumb rubber on compressive strength of fly ash based geopolymer concrete. MATEC Web Conf. **78**, 4–8 (2016)
12. Yeluri, S.C., Yadav, N.: Mechanical properties of rubber aggregates based geopolymer concrete - a review. IOP Conf. Ser. Mater. Sci. Eng. **989**, 012204 (2020)
13. Luhar, S., Chaudhary, S., Luhar, I.: Thermal resistance of fly ash based rubberized geopolymer concrete. J. Build. Eng. **19**, 420–428 (2018)
14. Rangan, B., Hardjito, D.: Studies on fly ash-based geopolymer concrete. In: Proceedings of 4th World Congress Geopolymer (2005)
15. Azmi, A.A., et al.: A review on fly ash based geopolymer rubberized concrete. Key Eng. Mater. **700**, 183–196 (2016)
16. Raffoul, S., et al.: Behaviour of unconfined and FRP-confined rubberised concrete in axial compression. Constr. Build. Mater. **147**, 388–397 (2017)
17. Shu, X., Huang, B.: Recycling of waste tire rubber in asphalt and portland cement concrete: an overview. Constr. Build. Mater. **67**, 217–224 (2014)
18. Aslani, F., Deghani, A., Asif, Z.: Development of lightweight rubberized geopolymer concrete by using polystyrene and recycled crumb-rubber aggregates. J. Mater. Civ. Eng. **32**, 04019345 (2020)

19. Dong, M., Elchalakani, M., Karrech, A., Yang, B.: Strength and durability of geopolymer concrete with high volume rubber replacement. Constr. Build. Mater. **274**, 121783 (2021)
20. Singh, B., Ishwarya, G., Gupta, M., Bhattacharyya, S.K.: Geopolymer concrete: a review of some recent developments. Constr. Build. Mater. **85**, 78–90 (2015)
21. Zhang, B., et al.: Rubberized geopolymer concrete: Dependence of mechanical properties and freeze-thaw resistance on replacement ratio of crumb rubber. Constr. Build. Mater. **310**, 125248 (2021)
22. Youssf, O., et al.: Mechanical performance and durability of geopolymer lightweight rubber concrete. J. Build. Eng. **45**, 103608 (2022)
23. Nguyen, T.T., Goodier, C.I., Austin, S.A.: Factors affecting the slump and strength development of geopolymer concrete. Constr. Build. Mater. **261**, 119945 (2020)
24. Kishore, K., Gupta, N.: Mechanical characterization and assessment of composite geopolymer concrete. Mater. Today Proc. **44**, 58–62 (2021)
25. Bhatt, A., et al.: Physical, chemical, and geotechnical properties of coal fly ash: a global review. Case Stud. Constr. Mater. **11**, e00263 (2019)
26. Standard, BoI. IS 3812 (Part-1): 2013 Pulverized Fuel Ash-Specification (2017)
27. Luga, E., Duran, C.: Optimization of heat cured fly ash/slag blend geopolymer mortars designed by "Combined Design" method : Part 1. Constr. Build. Mater. **178**, 393–404 (2018)
28. Shi, C., Qian, J.: High performance cementing materials from industrial slags - a review. Resour. Conserv. Recycl. **29**, 195–207 (2000)
29. Saraya, M.E.S.I.: Study physico-chemical properties of blended cements containing fixed amount of silica fume, blast furnace slag, basalt and limestone, a comparative study. Constr. Build. Mater. **72**, 104–112 (2014)
30. Zhong, H., Poon, E.W., Chen, K., Zhang, M.: Engineering properties of crumb rubber alkali-activated mortar reinforced with recycled steel fibres. J. Clean. Prod. **238**, 117950 (2019)
31. Wongsa, A., Sata, V., Nematollahi, B., Sanjayan, J., Chindaprasirt, P.: Mechanical and thermal properties of lightweight geopolymer mortar incorporating crumb rubber. J. Clean. Prod. **195**, 1069–1080 (2018)
32. Ali, I.M., Naje, A.S., Nasr, M.S.: Eco-friendly chopped tire rubber as reinforcements in fly ash based geopolymer concrete. Glob. Nest J. **22**, 342–347 (2020)
33. Yahya, Z., Abdullah, M.M.A.B., Ramli, S.N.H., Minciuna, M.G., Abd Razak, R.: Durability of fly ash based geopolymer concrete infilled with rubber crumb in seawater exposure. IOP Conf. Ser. Mater. Sci. Eng. **374**, 012069 (2018)
34. Rashad, A.M., Sadek, D.M.: Behavior of alkali-activated slag pastes blended with waste rubber powder under the effect of freeze/thaw cycles and severe sulfate attack. Constr. Build. Mater. **265**, 120716 (2020)
35. Gandoman, M., Kokabi, M.: Sound barrier properties of sustainable waste rubber/geopolymer concretes. Iran. Polym. J. English Ed. **24**, 105–112 (2015)
36. Ameri, F., Shoaei, P., Reza Musaeei, H., Alireza Zareei, S., Cheah, C.B.: Partial replacement of copper slag with treated crumb rubber aggregates in alkali-activated slag mortar. Constr. Build. Mater. **256**, 119468 (2020)
37. Toufigh, V., et al.: Mechanical properties and environmental impact of rubberized fly ash- and red mud-based geopolymer concrete. Eur. J. Environ. Civ. Eng., 1–24 (2021)
38. Dar, T.A., Azam, F.: Development of fly ash based geo-polymer concrete. Int. J. Sci. Res. **6**, 1539–1560 (2015)
39. Luhar, S., Chaudhary, S., Dave, U.: Effect of different parameters on the compressive strength of rubberized geopolymer concrete. Multi-Disc. Sustain. Eng. Curr. Futur. Trends., 77–86 (2016). https://doi.org/10.1201/b20013-13
40. Firdous, R., Stephan, D.: Effect of silica modulus on the geopolymerization activity of natural pozzolans. Constr. Build. Mater. **219**, 31–43 (2019)
41. Lazorenko, G., Kasprzhitskii, A., Mischinenko, V.: Rubberized geopolymer composites: Effect of filler surface treatment. J. Environ. Chem. Eng. **9**, 105601 (2021)
42. Saloni, P., Pham, T.M., Lim, Y.Y., Malekzadeh, M.: Effect of pre-treatment methods of crumb rubber on strength, permeability and acid attack resistance of rubberised geopolymer concrete. J. Build. Eng. **41**, 1–12 (2021)

43. Rashad, A.M.: A comprehensive overview about the influence of different admixtures and additives on the properties of alkali-activated fly ash. Mater. Des. **53**, 1005–1025 (2014)
44. Dong, M., Elchalakani, M., Karrech, A.: Development of high strength one-part geopolymer mortar using sodium metasilicate. Constr. Build. Mater. **236**, 117611 (2020)
45. Hassan, A., Arif, M., Shariq, M.: Effect of curing condition on the mechanical properties of fly ash-based geopolymer concrete. SN Appl. Sci. **1**, 1–9 (2019)
46. Zhang, H., et al.: Deterioration of ambient-cured and heat-cured fly ash geopolymer concrete by high temperature exposure and prediction of its residual compressive strength. Constr. Build. Mater. **262**, 120924 (2020)
47. Raffoul, S., Garcia, R., Escolano-Margarit, D., Guadagnini, M., Hajirasouliha, I., Pilakoutas, K.: Behaviour of unconfined and FRP-confined rubberised concrete inaxial compression. Constr. Build. Mater. **147**, 388–397 (2017)

Effect of Superabsorbent Polymer (SAP) and Nano Silica on the Durability Properties of Blended Cement Paste

S. Loknath, S. M. Renuka, and C. Umarani

Abstract Superabsorbent polymer (SAP), which has absorption and desorption capabilities, promotes the internal curing effect when incorporated in cement mortar. The strength in cement mortar/concrete improved with the addition of Nano-silica. Hence, this study aims to examine the combined effect of SAP and Nano-silica on the durability properties of blended cement paste. Experimental investigations were performed to assess the durability were water absorption, Acid and sulfate attack test. The mix combination contains SAP 0.2 and 0.3% of cement content, and Nano silica ranging from 0.5 to 2% of cement content for each quantity of SAP was studied. The compressive strength showed a decrease in the increasing dosage of Nano-silica since an increase in Nano-silica reduced the workability and demanded more water. The durability test results show minimum weight loss after a long-term study. The results of the water absorption test for samples were assessed to be within the permissible limit. The results of compressive strength after the durability test show that there is a 30% loss of strength after the acid resistance test and 22.2% strength gain after sulfate attack.

Keywords Durability test on cement mortar · SAP · Nano Silica · Microstructural study in cement mortar · Change in strength in a different environment

1 Introduction

Various studies in concrete technology are leaning towards the improvement of durability in high strength concrete. High strength concrete has many capillary pores that create capillary tensile stress inside the matrix which leads to the development of surface cracks. The durability of high strength concrete is improved by using blended

S. Loknath (✉) · S. M. Renuka · C. Umarani
Division of Structural Engineering, Department of Civil Engineering, College of Engineering Guindy Campus, Anna University, Chennai 600025, India
e-mail: loknathce@gmail.com

S. M. Renuka
e-mail: renuka@annauniv.edu

C. Umarani
e-mail: umarani@annauniv.edu

cement and by using nano materials. Blended cement is made by adding supplementary cementitious material along with ordinary Portland cement-like fly ash, GGBS, etc. which helps in reducing the permeability of the concrete thereby durability against penetration of harmful elements is improved. An internal curing agent such as a super absorbent polymer (SAP) is used to improve the internal structure of the matrix thereby improvement in durability is achieved. Past studies shown that super absorbent polymer (SAP) has reduced autogenous shrinkage significantly compared to light weight aggregates [1–4, 6, 7]. Eventhough SAP was effective in reducing autogenous shrinkage. It has some negative impact in compressive strength when the SAP dosage is higher [5, 8, 9].

The addition of Nano-silica improved the mechanical properties but an increase in the dosage of Nano-silica demanded more SP and agglomeration of the particle may develop. Optimum dosage of 1–2% improved the mechanical properties [10]. SAP addition causes a decrease in compressive strength due to pore formation while Nano-silica addition compensated for the strength loss [11–14]. In this study combination of Nano silica and SAP is varied in blended cement mortar then their durability performance is assessed through various experimental investigations.

2   Sample Preparation and Mix Combination

Mortar cubes samples with a 1:3 ratio confining to IS 4031-PART-VI [15] were prepared by altering Nano silica and SAP dosage in the percentage of cement in the matrix. The cement used in this study was Portland pozzolana cement (PPC) of grade 53 and M-Sand as fine aggregate. SAP was added in the wet state i.e., for every mix 25 ml of water was added for pre-wetting of SAP measured through the power model. These mortar cubes were tested for durability criteria [3] after that those samples were assessed for change in compressive strength using the compressive strength test. The Mix combination chosen was listed in Table 1.

Table 1 Details of mix combination

Mix id	Nano silica dosage in the percentage of cement	SAP dosage in the percentage of cement	Cement (g)	M-sand (g)
P1	2.0	0.3	200	600
P2	1.5	0.3	200	600
P3	1.0	0.3	200	600
P4	0.5	0.3	200	600
P5	2.0	0.2	200	600
P6	1.5	0.2	200	600
P7	1.0	0.2	200	600
P8	0.5	0.2	200	600

Table 2 Compressive strength test

Mix id	Compressive strength (MPa)			
	3rd day	7th day	14th day	28th day
P1	12.13	15.87	20.73	26.20
P2	12.07	16.47	23.27	29.53
P3	10.03	22.67	31.50	37.20
P4	09.60	13.13	22.93	29.87
P5	13.07	15.80	21.33	25.27
P6	9.73	12.47	21.40	25.27
P7	11.07	18.73	32.27	36.30
P8	09.73	13.08	24.27	29.87

3 Experimental Investigations

3.1 Compressive Strength Test

Mortar cubes of standard size $70.7 \times 70.7 \times 70.7$ mm were prepared with a 1:3 ratio as per IS standard and placed in a curing tank then their compressive strength is calculated by observing the failure load on the 3rd day, 7th day, 14th day and 28 days respectively in the compressive testing machine. The compressive strength for the respective days in Mpa was tabulated in Table 2.

3.2 Durability Test and Their Effect on Compressive Strength

Water Absorption Test. Mortar cubes prepared was exposed to the atmosphere after 28 days of curing for about 60 days by this process constant weight is attained. The initial weight of the samples was weighed and immersed in water for 24 h. The final weights of the samples were weighed after the samples dried in the atmosphere and then the percentage of water absorption is calculated. The observation and the results were tabulated in Table 3.

From Table 4 it is observed that SAP of 0.3% dosage has minimum water absorption and among the mix combination Nano silica with 1% dosage shows minimum water absorption.

Impact on Compressive Strength After Water Absorption Test. The water absorption is observed to be in the range of 3–5.5%. The same sample was now tested for compressive strength in CTM and their results were tabulated in Table 4. The change in compressive strength is represented in the form of a graph in Fig. 1.

The comparison between the water absorption and change in compressive strength is shown in Fig. 2.

Table 3 Water absorption test

Mix id	Initial weight (g)	Final weight (g)	Water absorption (%)
P1	780	820	5.12
P2	770	810	5.19
P3	770	800	3.80
P4	760	795	4.60
P5	780	820	5.13
P6	760	800	5.26
P7	730	767	5.06
P8	740	780	5.40

Table 4 Impact on compressive strength after water absorption

Mix id	Compressive strength after water absorption (MPa)	Change in compressive strength in percentage
P1	25.20	3.81
P2	28.60	3.15
P3	35.21	5.34
P4	28.75	3.75
P5	30.45	4.07
P6	27.80	6.76
P7	33.40	7.98
P8	25.23	15.5
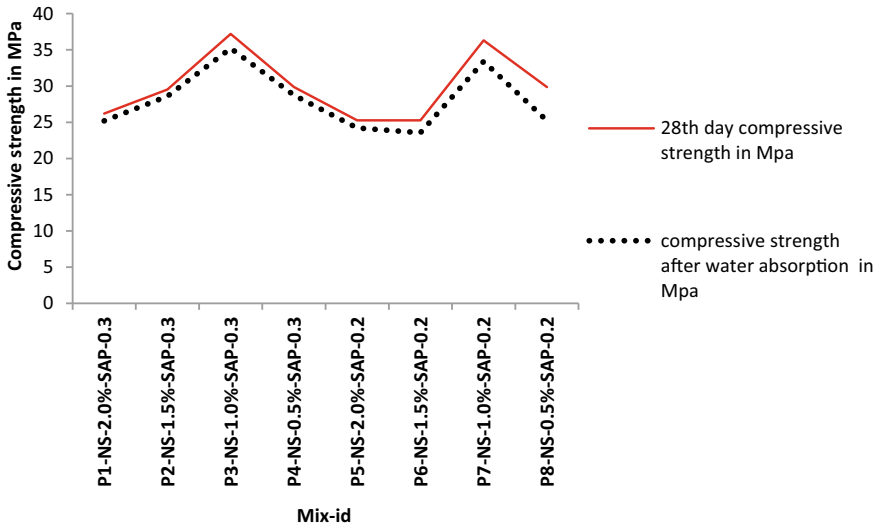
Fig. 1 Compressive strength comparison after water absorption test
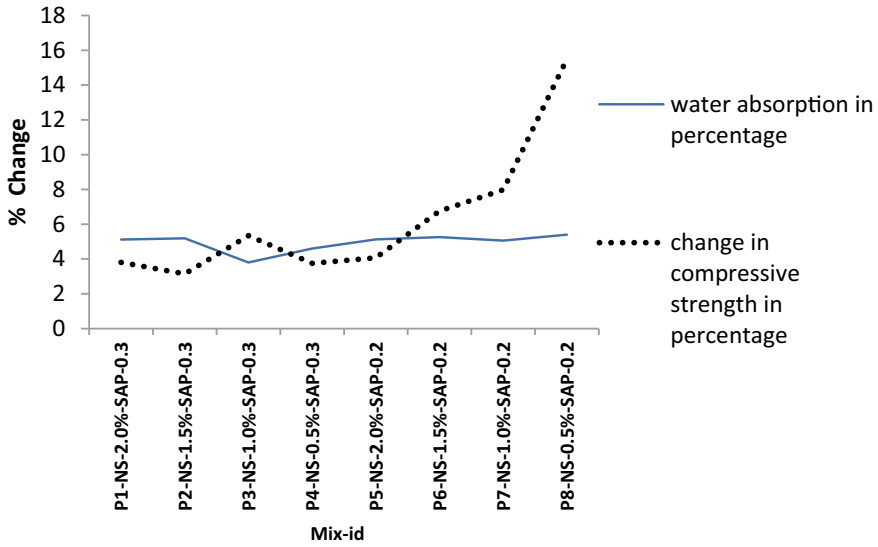
Fig. 2 Comparison between changes in compressive stress and water absorption in percentage

Acid Resistance Test. Resistance against acid is improved by making the matrix impermeable. Detrition takes in concrete when it comes in contact with the environment with a PH level of less than 6.5 by chemical reaction. The calcium compounds formed during chemical reactions get washed off thus microstructure becomes weak. Therefore mortar cube samples were tested for acid attack and weight loss is assessed. The initial weight of the specimen is taken after 28 days of curing. The mortar cubes were immersed in 5% H_2So_4 for 28 days. Then these samples were kept at room temperature for 2 days for the attainment of constant weight. The weight loss assessed is tabulated in Table 5.

Impact on Compressive Strength After Acid Resistance Test. Compressive strength test is performed for samples tested for acid resistance. The change in compressive

Table 5 Acid resistance test

Mix id	Percentage loss in weight on 28th day
P1	4.53
P2	4.72
P3	4.32
P4	4.49
P5	5.13
P6	4.98
P7	5.38
P8	5.54

strength is calculated and the results were tabulated in Table 6. The comparison between compressive strength on the 28th day and compressive strength of samples used for the acid resistance test is shown in Fig. 3.

The variation in compressive strength due to the acid resistance test is represented in Fig. 4 which shows the change in compressive strength in percentage compared to the change in mass due to acid resistance.

Sulfate Attack Test. Mortar cube specimen after 28 days of curing taken out and kept at room temperature for attaining constant weight. After finding the initial weight,

Table 6 Impact on compressive strength after acid resistance test

Mix id	Compressive strength after acid resistance test (MPa)	Change in compressive strength in percentage
P1	12.70	51.53
P2	17.90	39.38
P3	21.60	44.90
P4	20.40	31.70
P5	18.90	25.21
P6	19.90	21.25
P7	23.40	35.54
P8	20.40	31.70
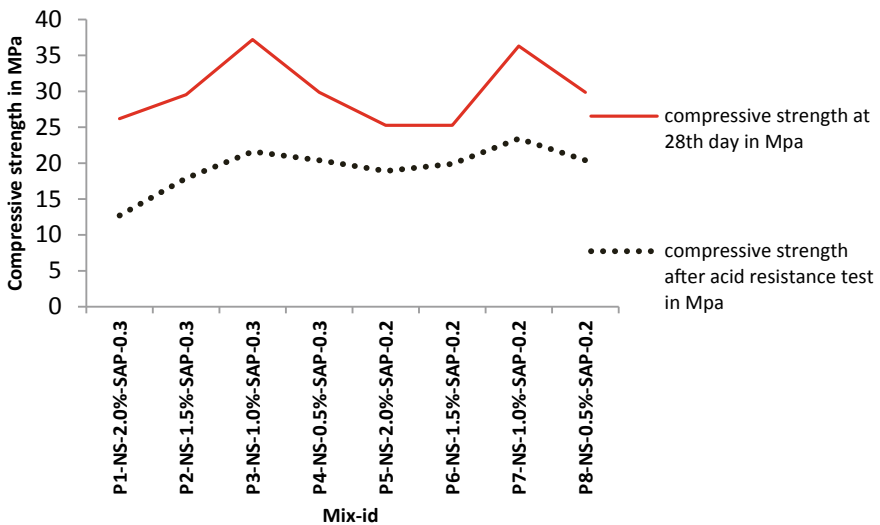
Fig. 3 Compressive strength comparison after acid resistance test
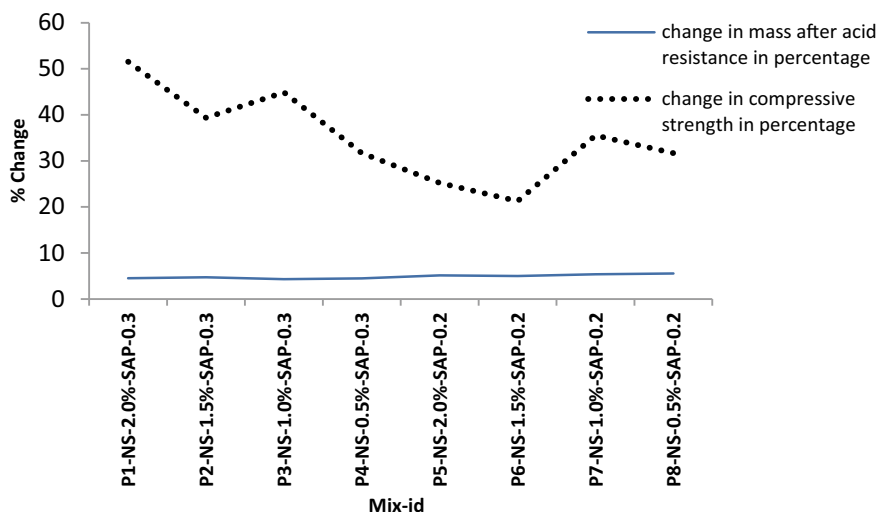
Fig. 4 Change in compressive strength compared to change in weight due to acid resistance

samples were immersed in Na_2So_4 solution for 28 days and a weight change is noted. Weight gain is noted instead of weight loss therefore the sample was immersed for another 30 days. After 30 days, samples were kept at room temperature for 2 days and a weight change is noted. Marginal weight loss noted at 60th day shown in Table 7.

Impact on Compressive Strength After Sulfate Attack. Weight gain after 28 days of immersion in Na_2So_4 is unexpected and it had a significant impact on compressive strength. An improvement in compressive strength is noted after the alkaline resistance test is noted after 60 days when the compressive strength was performed after weight loss is assessed after 60 days. The improvement in compressive strength observed is tabulated in Table 8 (Figs. 5 and 6).

Table 7 Change in weight of the sample after sulfate attack test

Mix id	Percentage weight gain from initial weight at 28[h] day	Percentage weight loss from initial weight at 60th day
P1	2.70	2.08
P2	2.70	2.44
P3	2.43	1.13
P4	2.33	1.12
P5	3.51	1.08
P6	2.74	0.15
P7	2.40	1.96
P8	2.54	1.71

Table 8 Impact on compressive strength after sulfate attack test

Mix id	Compressive strength after sulfate attack test (MPa)	Change in compressive strength in percentage
P1	30.91	17.98
P2	35.57	20.25
P3	40.57	03.34
P4	40.81	36.62
P5	28.80	13.96
P6	35.31	39.73
P7	41.81	15.18
P8	41.01	37.30
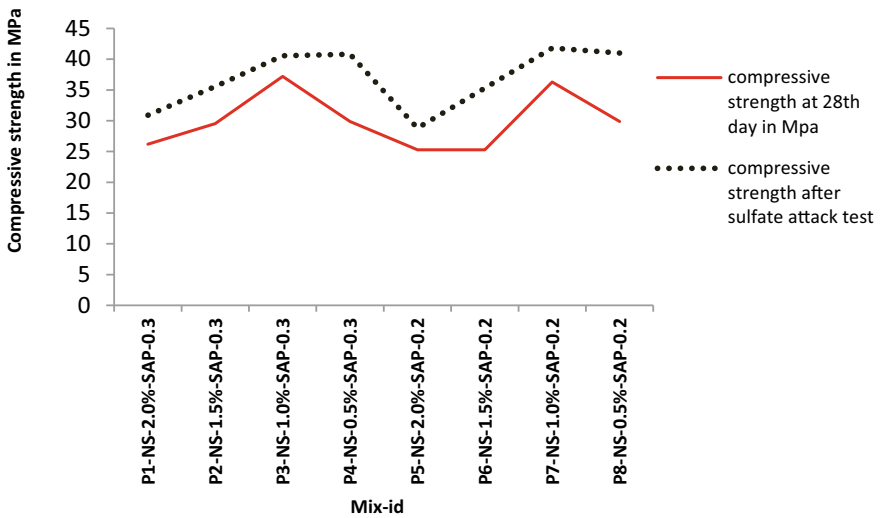
Fig. 5 Compressive strength comparison after sulfate attack test

Microstructural Characteristics. The microstructure of the sample tested for sulfate attack is studied to examine the reason for weight gain and compressive strength improvement using SEM analysis. Reorganization of internal structure is noted in the sample tested for sulfate attack compared to the sample not tested for alkaline resistance, in the SEM image and it is shown in Fig. 7a & b. The reorganization is due to the chemical reaction forming the N–C bond it is interpreted using FTIR peak analysis shown in Fig. 8.
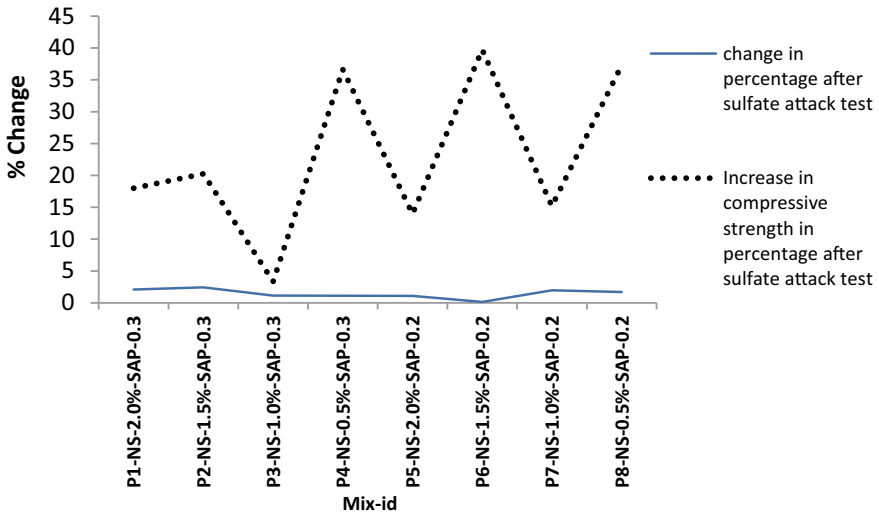
Fig. 6 Change in compressive strength compared to change in weight due to sulfate attack

4   Results and Discussions

- The peak compressive strength obtained for the mix combination chosen was 29.80% less than the target strength. This is due to the addition of SAP in the mix combination since SAP creates larger voids greater than capillary pores.
- Water absorption observed to be in the range of 3–6% accounts for 3.8–16% strength loss. Compressive strength loss is indirectly proportional to the water absorption was noted.
- The acid resistance test shows weight loss in the sample in the range of 4%-6% accounts for about 25–52% strength loss which indicates the mix combination chosen was not suitable for a harmful acidic environment.
- The sulfate attack test showed weight gain on the 28th day and weight loss on the 60th day. The weight loss is in the range of 1–3% and unexpectedly strength gain was observed in the range of 3–38%. Therefore, the internal structure was studied using SEM analysis where the internal structure was observed to be reorganized and large formation nitriles carbenes triple bond is identified using FTIR peak analysis.
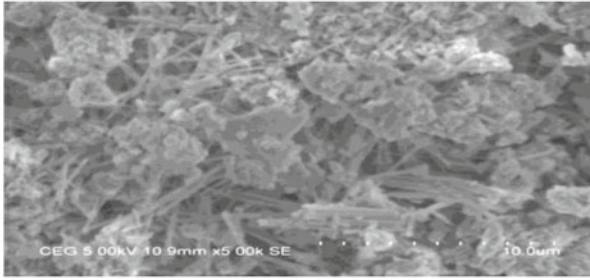
a. SEM image of sample P3 before sulfate attack test.
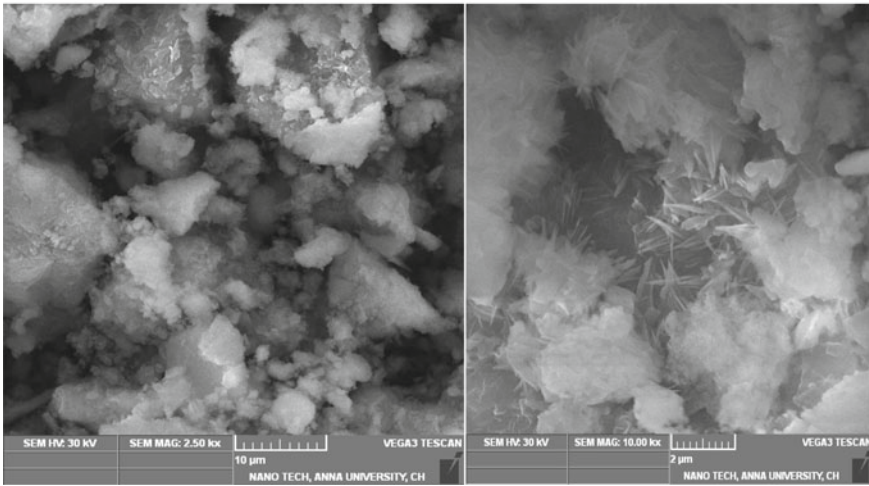
b. SEM image of sample P3 after tested for sulfate attack test.

Fig. 7 a SEM image of sample P3 before sulfate attack test. **b** SEM image of sample P3 after tested for sulfate attack test
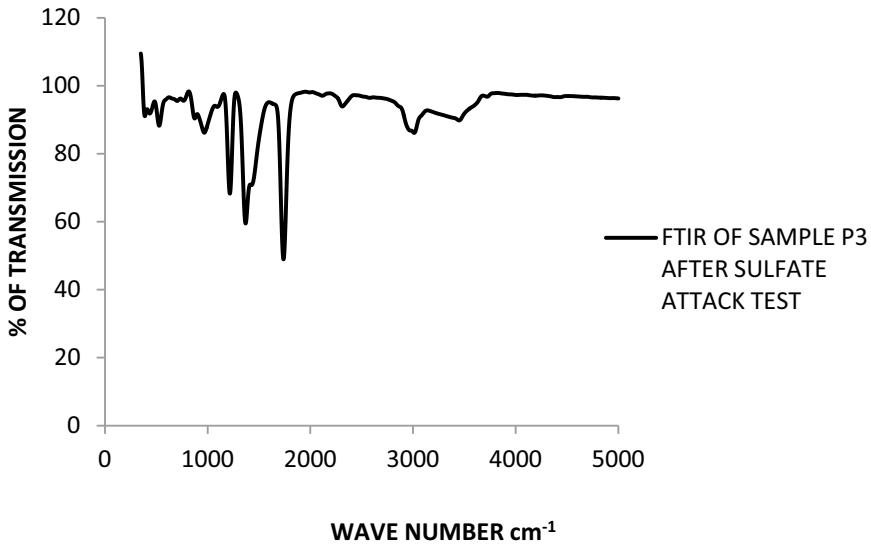
Fig. 8 FTIR of sample P3 used for sulfate attack test

5   Conclusions

Compressive strength reduction is noted due to the presence of SAP and an increase in nano-silica dosage. A higher dosage of nano-silica resulted in a decrease in workability of the mix thus ultimately leading to a reduction in compressive strength. Further studies with the addition of superplasticizers may increase the compressive strength from that we can find the optimum dosage of nano-silica in the mix containing SAP. The durability performance for the mix proportion chosen is studied with different experiments. Sulfate attack led to an increase in solid volume assessed through microstructural studies and an increase in compressive strength after the sulfate attack test is noted. The performance in other durability tests is not satisfactory therefore further study is required to improve the durability of the matrix.

References

1. Li, H., Xiao, H.G., Yuan, J., Ou, J.: Microstructure of cement mortar with nano-particles. Compos. B Eng. **35**(2), 185–189 (2004). https://doi.org/10.1016/S1359-8368(03)00052-0
2. Justs, J., Wyrzykowski, M., Bajare, D., Lura, P.: Internal curing by superabsorbent polymers in ultra-high-performance concrete. Cem. Concr. Res. **76**, 82–90 (2015). https://doi.org/10.1016/j.cemconres.2015.05.005
3. Tang, S.W., Yao, Y., Andrade, C., Li, Z.J.: Recent durability studies on concrete structure. Cement Conc. Res. **78**, 143–154 (2015). https://doi.org/10.1016/j.cemconres.2015.05.021

4. Yang, J., Wang, F.Z., Liu, Y.P.: Comparison of ordinary pores with internal cured pores produced by superabsorbent polymers. Adv. Mater. Res. **1129**, 315–322 (2015). https://doi.org/10.4028/www.scientific.net/amr.1129.315

5. Mechtcherine, V.: Use of superabsorbent polymers (SAP) as a concrete additive. RILEM Tech. Lett. **81** (2016). https://doi.org/10.21809/rilemtechlett.2016.18.

6. Wang, F., Yang, J., Hu, S., Li, X., Cheng, H.: Influence of superabsorbent polymers on the surrounding cement paste. Cem. Concr. Res. **81**, 112–121 (2016). https://doi.org/10.1016/j.cemconres.2015.12.004

7. Lee, H.X.D., Wong, H.S., Buenfeld, N.R.: Self-sealing of cracks in concrete using superabsorbent polymers. Cement Conc. Res. **79**, 194–208 (2016)

8. Olivier, G., Combrinck, R., Kayondo, M., Boshoff, W.P.: Combined effect of nano-silica, super absorbent polymers, and synthetic fibres on plastic shrinkage cracking in concrete. Constr. Build. Mater. **192**, 85–98 (2018)

9. Park, Y., Choi, Y.C.: Self-healing capability of cementitious materials with crystalline admixtures and super absorbent polymers (SAPs). Constr. Build. Mater. **189**, 1054–1066 (2018)

10. Baloch, H., Usman, M., Rizwan, S.A., Hanif, A.: Properties enhancement of super absorbent polymer (SAP) incorporated self-compacting cement pastes modified by nano-silica (NS)addition. Constr. Build. Mater. **203**, 18–26 (2019)

11. Lefever, G., Tsangouri, E., Snoeck, D., Ageless, D.G., De Belie, N., Van Vlierberghe, S., Van Hemelrijck, D.: Combined use of superabsorbent polymers and nano-silica for reduction of restrained shrinkage and strength compensation in cementitious mortars. Constr. Build. Mater. **251**, 118966–118975 (2020)

12. Lyu, Z., Shen, A., Mo, S., Chen, Z., He, Z., Li, D., Qin, X.: Life-cycle crack resistance and micro characteristics of internally cured concrete with superabsorbent polymers. Constr. Build. Mater. **259**, 119794 (2020). https://doi.org/10.1016/j.conbuildmat.2020.119794

13. Abhilash, P.P., Nayak, D.K., Sangoju, B., Kumar, R., Kumar, V.: Effect of nano-silica in concrete; a review. Constr. Build. Mater. **278**, 122347 (2021). https://doi.org/10.1016/j.conbuildmat.2021.122347

14. Kim, I.S., Choi, S.Y., Choi, Y.S., Yang, E.I.: An experimental study on absorptivity measurement of superabsorbent polymers (SAP) and the effect of SAP on freeze-thaw resistance in mortar specimens. Constr. Build. Mater. **267**, 120974 (2021). https://doi.org/10.1016/j.conbuildmat.2020.120974

15. IS 4031 (PART VI)-1988. Methods of physical tests for hydraulic cement

Quantification of Seismic Damage of Reinforced Concrete Bridge Under Near-Field Ground Motions

Md Shafquat Izhar [ID]**, Mohammad Umair** [ID]**, and Md. Imteyaz Ansari** [ID]

Abstract   Bridges are important structures which play a key role in transportation of goods and people from one place to another. Its accessibility is hindered during natural hazards such as earthquakes. This phenomenon necessitates the seismic assessment of reinforced concrete bridges. While conducting the seismic vulnerability assessment of such structure, keen attention is required to the characteristics and intensity of ground motions. In light of the above statement, the present study focuses on quantification of seismic damage of bridge, designed as per Indian standard codes under near field ground motions. Some of the inherent characteristics of near field ground motions such as PGV, pulse indicator, pulse period, impulsivity index, etc. are influencing factors in vulnerability assessment are also considered in the study. A nonlinear concentrated hinge based finite element model is used for seismic vulnerability assessment. Responses obtained from the analyses show that severe damage occurs in the structure when it is subjected to near fault ground motions specifically when it is inbred with certain characteristics. The study also reveals that before conducting the seismic vulnerability assessment of structures, it is significant that all characteristics of ground motions should be closely characterized.

Keywords   Reinforced concrete bridge · Near field ground motions · Seismic damage assessment

1   Inroduction

Earthquakes are natural events which may result in considerable damage to structures. When it occurs, critical structures like bridge get damaged causing unfavorable effect on human life [1]. To mitigate this disaster, seismic vulnerability assessment of such critical structures is of utmost importance. Severity of damage increases when structures are subjected to near field ground motions. For identification of near field ground motions many studies are being carried out since last decade [2–4]. A few

M. S. Izhar (✉) · M. Umair · Md. I. Ansari
Department of Civil Engineering, Jamia Millia Islamia, New Delhi 110025, India
e-mail: mdshafquatizhar@gmail.com

studies are performed regarding seismic damage assessment of RC bridges under near field ground motions. A hysteresis model is proposed to capture the residual displacement under the near field ground motions [5]. Studies show that which structural response (isolation period) of seismic isolated bridge is strongly related to its intensity measure (IMs) under the pulse like ground motions [6]. For modification in current design guidelines, fragility analysis and seismic damage assessment of RC bridge under the near fault ground motions are performed [7]. Seismic vulnerability assessment of cable stayed bridge is performed by considering the near field ground motions [8]. In continuation of above, Priestley first introduced the term as "performance based design" [9]. This tool is used to design the structures for future earthquakes, based on displacement capacity of structures. Apart from this, some studies are available to account for the seismic damage of bridge. Some damage models are proposed to quantify the damage in bridge or bridge piers by considering the different structural parameters [10–13]. By considering near source to site conditions, responses of bridge are assessed [14]. Also, some tools are available for seismic damage assessment or health monitoring of RC bridges. Fragility analysis is a versatile tool which is used for seismic vulnerability assessment [15–17].

The above studies show that all existing damage parameters do not holds good for near field ground motions. Hence the present study is framed for seismic vulnerability assessment of RC bridge under the near field ground motion by considering different ground motion parameters such as PGV (Peak Ground Velocity), Tp (Velocity Pulse Period), and IP index (Impulsivity Index). Also in this study a new damage model is proposed. All the parameters used in proposed damage model are closely monitored with characteristics of pulse like or near field ground motions.

2　Structural Modeling

2.1　Description of Bridge

A four span RCC bridge, which is simply supported with 108 m longitudinal length, 7.5 m in width, and 6.19 m height, is taken in this study. The span length is 27 m. Precast I-girder of height 1.65 m is used and designed as per the Indian Standard. Three I girders with spacing of 2.65 m center-to-center are used in modeling. Thickness of deck slab is 0.22 m. Pier cap is modeled as concrete element with depths varying between 0.75 to 1.50 m. Bridge is modeled in SAP2000 with pier of diameter 1.2 m (as shown in Fig. 1). Concentrated plastic hinge (interacting P-M2-M3) is assigned at possible hinge location of pier [18, 19]. M-40 concrete is used having material nonlinearity defined as per Mander Model. 31 bars of diameter 32 mm of grade Fe-500 is consider in this study. Yield and ultimate rotation is calculated as per EUROCODE [20].
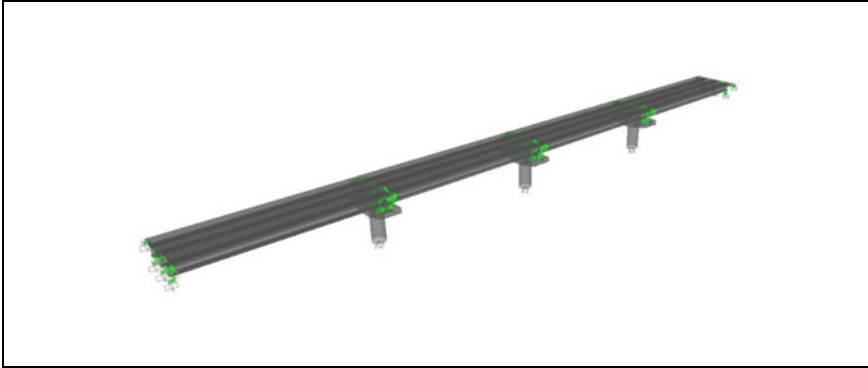
Fig. 1 Finite element model

Bearing Modeling. Superstructure and sub-structure are connected by means of bearings. Height of elastomers is 100 mm having dimension of 500 × 500 mm. Parameters such as elastic stiffness (6250 kN/m), characteristics strength (42 kN) and shear force deformation are used for designing of bearings [21, 22]. Movement of bearing is free in traffic direction and fixed in transverse direction.

3   Selection, Normalization and Scaling of Ground Motions

The characteristic of selected ground motions depends on site to source distance. Near-fault ground motions cause severe damage in region near to seismic source. Near field ground motions are impulsive in nature in terms of velocity at low frequency, velocity pulse period, and displacement. In light of above statement, input parameters for selection of near field ground motions are- ruptures distance less than 10 km [23–25], PGV greater than 30 cm/s [3, 26], and impulsivity index less than 12 [26]. A set of six near field ground motions is selected and extracted from PEER NGA-WEST 2 [27] ground data base, for incremental dynamic analysis by considering above parameters as tabulated in Table 1. Impulsivity Index (IP Index) is defined as the ratio of development length to PGV of ground motions. The development length is the length between two successive points at interval $t_{(i+1)}$-$t_{(i)}$ corresponding to velocity increments from time $t_{(i)}$ to $t_{(i+1)}$ [26].

Scaling and normalization of considered ground motions are performed according to P695 without disturbing frequency content of original ground motions. IS-1893 (Zone-V) response spectrum is used as target spectrum for scaling.

Table 1 Selected ground motions

Earthquake name	Record sequence number	Mag	Rjb (km)	PGA (g)	PGV (cm/s)	Velocity pulse period (Tp)	IP Index
San Salvador	569	5.8	3.71	0.40	56.37	1.127	10.41
Northridge-01	982	6.69	0	0.41	111.47	3.157	11.48
Northridge-01	1063	6.69	0	0.87	147.99	1.246	12.00
Chi-Chi_Taiwan	1505	7.62	0	0.51	249.59	12.285	7.10
Loma Prieta	3548	6.93	3.22	0.44	85.69	1.568	10.10
Cape Mendocino	3744	7.01	8.49	0.17	67.89	5.362	9.30

4 Definition of Damage States and Damage Index

Damage index is a tool which is used for seismic damage quantification. The damage model is defined on the basis of structural responses. Many researchers have given different damage models to quantify the different damage states [10, 12, 28–32].

In this study, a new damage model is proposed based on cumulative and yield energy dissipation as shown in Eq. (1). During seismic event, structures subjected to reversal loading result in dissipation of seismic energy and damage is initiated when cumulative dissipation energy crosses the yield energy dissipation. Structure collapses when it attains ultimate value in terms of cumulative energy dissipation. Between these values of energy dissipation there are several stages of damage. Keeping in mind the above statement, damage index is defined as the ratio of any intermediate value of cumulative energy dissipation beyond the yield point to the total cumulative energy dissipations by excluding the cumulative yield energy.

Proposed damage model has been validated by referring the experimental results [11]. Monotonic pushover load was applied at top of the pier cap. Analytical results show that at 0.15% drift, first crack in cover concrete and yielding in longitudinal bars occurred. In experiment [11], first cracking was observed at drift 0.2 to 0.4%. At the same stage, value of proposed damage index is 0.07.In analytical result at drift ratio 4.4%, plastic rotation at hinge location is 50% of ultimate rotation, which shows extensive damage in the pier. At this stage the value of DI is 0.41. In experiments, significant spalling was occurred at drift ratio 4.4%, which indicates extensive damage in the pier. By considering above comparisons of analytical and experimental results, a new damage model is proposed in this paper as shown in Eq. (1).

$$DI = \frac{E_i - E_y}{E_T - E_y} \qquad (1)$$

where, DI = Damage Index.
E_i = Cumulative Energy Dissipation at any i[th] cycle.
E_y = Cumulative Energy Dissipation up to yield point.
E_T = Total Cumulative Energy Dissipation up to the collapse point.

When value of DI is equal to 1 it means that the structure is totally collapsed and when its value is zero, there is no damage in the structure. Value of DI between 0 and 1 indicates the intermediate damage that may be categorized in slight, moderate and extensive damage states.

5 Results and Discussion

In the present study seismic damage quantification is carried out in terms of cumulative energy dissipation and proposed damage index on the reinforced concrete bridge. Analytical modeling and analysis is carried out in SAP 2000 for assessment of damage and incremental dynamic analysis. The RC bridge consists of three piers. It has been observed that the middle pier has collapsed at low value of ultimate point in terms of displacements and dissipated energy. Also damage index of middle pier achieved the value 1, prior to the three piers in pushover analysis. Hence, middle pier is considered to be the most vulnerable during seismic events. Obtained structural responses and IDA curves are presented and plotted below.

In Fig. 2, IDA curve for PGA Vs cumulative energy dissipation is plotted. The figure shows that structure has yielded close to 0.12 g PGA and corresponding cumulative energy is 42 kN-m. Further it is observed that minimum cumulative energy is 11.5 kN-m and corresponding top displacement of pier is 9 mm. Similarly, maximum value of cumulative energy dissipation is 9500 kN-m and corresponding top displacement at pier cap is 339 mm. Also it is depicted from figure, that the structure has dissipated a small amount of energy in short range of PGA against Chi-Chi_Taiwan earthquake as compared with other ground motions. Main causes of this earthquake are: 1.very high PGV among all considered earthquake, 2.very high velocity pulse period, 3.high value of ratio of PGV to PGA among the selected ground motions and 4) IP index (less than 12 which is very small). It shows that it is very high impulsive ground motions. Similar trends are followed by rest of the ground motions in Fig. 2.

In Fig. 3, DI is plotted against IM(PGA). Figure shows that value of DI at yield point, i.e. at 0.12 g, is 0.015. Structure has collapsed at PGA 0.6 g against four considered ground motions. Value of DI at this stage is 1.

Further, structure has collapsed at PGA 0.7 g against two ground motions. The reason for this is the value of ratio of PGV to PGA which are lower among the considered earthquakes. Also the value of Tp of earthquake San Salvador (569) and Northridge-01 (1063) are 1.127 s and 1.246 s respectively, which are also lower among the six ground motions. The mean response in terms of DI of the bridge is found to be lying near the response of the Chi-Chi_Taiwan ground motion. As we know that the Chi-Chi_Taiwan ground motion is highly destructive, therefore it can be deduced that the considered ground motions would also be destructive.
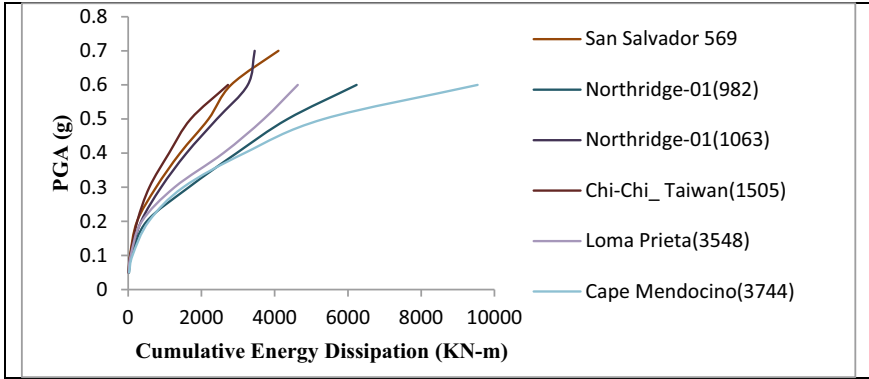
Fig. 2 IDA curve for cumulative energy dissipation
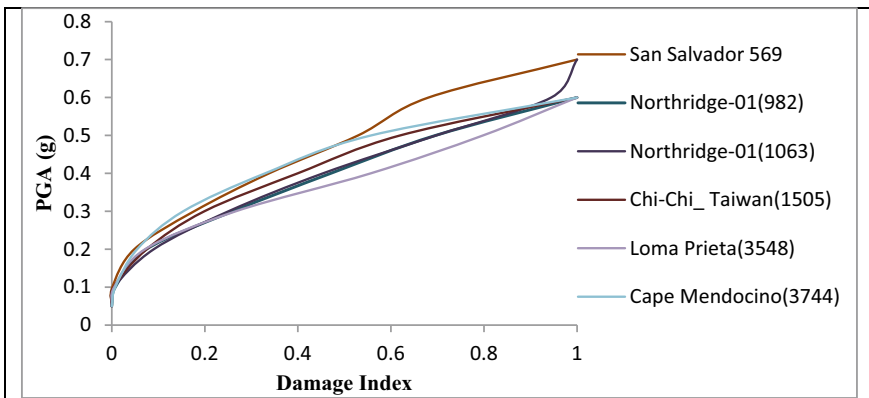
Fig. 3 IDA curve for PGA vs DI

Figure 4 depicts that structure has yielded at PGV greater than 30 cm/s, at this stage, average value of yield energy is 40 kN-m. As value of PGV increases the cumulative energy dissipation also increases. The bridge collapses earlier when it is subjected to the Chi-Chi_Taiwan earthquake, due to its high PGV value and high impulsiveness nature. Also plot shows that moving up the graph, velocity pulse period (Tp) of ground motions increases.

Figure 5 shows the trends of DI with PGV. As PGV increases, DI increases. For Chi-Chi_Taiwan earthquake the PGV value (raw earthquake data) is 249.59 cm/s, and corresponding value of DI is about 0.6 which is the highest value among the six considered earthquakes. Hence Chi-Chi_Taiwan ground motion has the highest PGV value, ratio of PGV to PGA value and velocity time period value (Tp), confirming that it is the highest impulsive ground motion.

From Fig. 6, as the cumulative energy dissipation increases the values of IP index decrease. This IDA curve again shows that the Chi-Chi_Taiwan is highly vulnerable
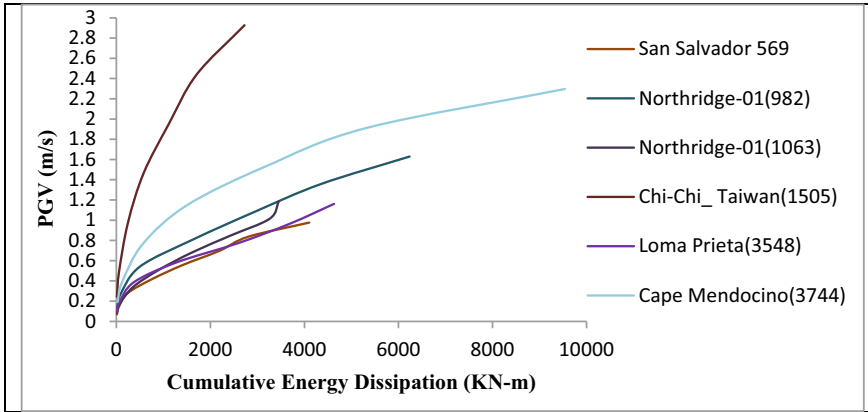
Fig. 4 IDA curve for PGV vs cumulative enegy dissipation
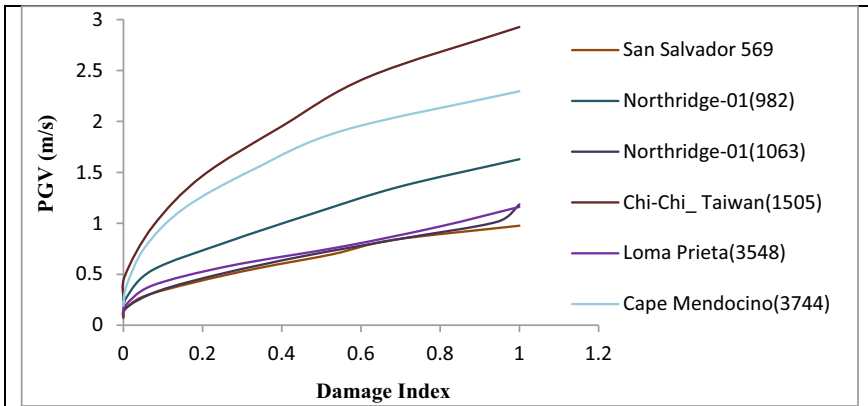
Fig. 5 IDA curve for PGV vs DI

to the structure. Structure has dissipated its total energy within a short range and collapsed early.

In Fig. 7, IP index decreases with the increase in DI. In order to classify the ground motions whether it is impulsive in nature or not, it is important to analyze the wave of velocity time series. It has been seen that lower frequency wave with low development length shows impulsive wave. Also many researchers concluded that the high wave amplitude/PGV show the impulsive nature of ground motions. By considering above discussion, lower value of development length and higher value of PGV gives high impulsive pulse ground motions. Also high PGV and low development length values lead small IP index values. Here in the Fig. 7, the IP index decreases with the increase in value of PGV and impulsiveness of ground motions [26]. Hence, from the IDA curve, IP index of Chi-Chi Taiwan ground motion is the lowest among the six ground
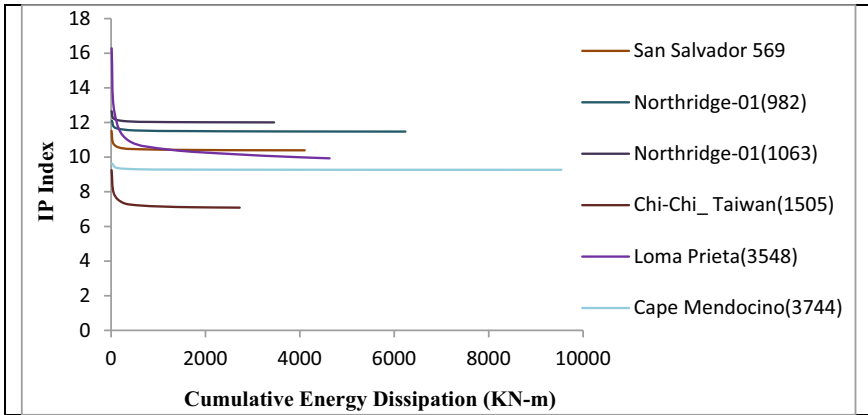
Fig. 6 IDA curve for IP index vs cumulative energy dissipation
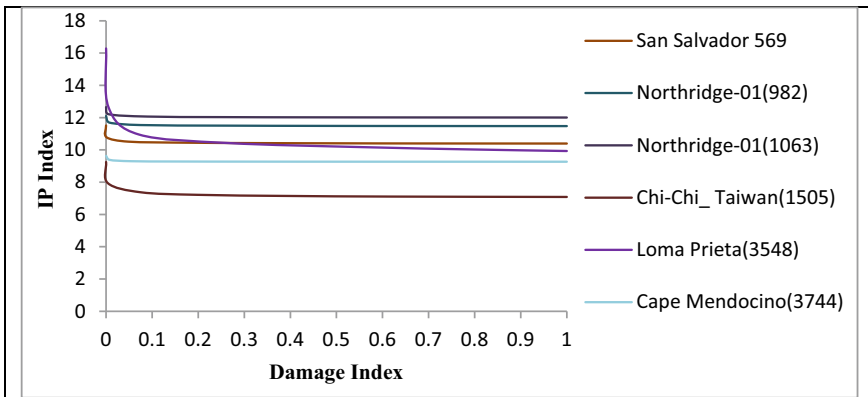
Fig. 7 IDA curve for IP index vs DI

motions (due to high PGV value) which indicates, bridge is more vulnerable against Chi-Chi Taiwan ground motion among the considered earthquake.

The range between DI = 0.005 to DI = 0.2, the IP index value of Loma Prieta (3548) is aberrant during IDA analysis. Between this ranges, the value of IP index is slightly greater than the IP index of raw ground motion. Due to this reason, impulsiveness of said ground is less among the top three ground motions as depicted in the Fig.

6 Conclusion

This analytical study is performed on the RC Bridge using incremental dynamic analysis for seismic vulnerability assessment in SAP 2000. Main conclusions are below:

Among the six ground motions, structure is found to be most vulnerable against Chi-Chi_Taiwan earthquake due to: high PGV value; high pulse period; higher PGV to PGA ratio; and lower value of IP Index (IP index < 12).

Considering the IP index of the selected ground motions (ranging from 7.1 to 12), the structure is observed to be more vulnerable against the ground motions bearing lesser value of IP index.

While conducting the seismic damage assessment under near field ground motions, keen attention is required for the selection of ground motions. Its characteristics or intensity measures should be closely monitored.

The present study also reveals that the role of PGV, velocity pulse information-such as velocity pulse period and its development length, and IP index, play key role in vulnerability assessment of the structures subjected to near field ground motions.

The damage model proposed in the present study has been compared with the experimental results obtained by Kunnath et al. [11] and the damage model is found to be in close agreement with experimental values.

References

1. Berry, M.P., Eberhard, M.O.: Performance modeling strategies for modern reinforced concrete bridge columns (2007)
2. Bertero, V.V., Mahin, S.A., Herrera, R.A.: Aseismic design implications of near-fault san fernando earthquake records. Earthq. Eng. Struct. Dyn. **6**, 31–42 (1978). https://doi.org/10.1002/eqe.4290060105
3. Baker, J.W.: Quantitative classification of near-fault ground motions using wavelet analysis. Bull. Seismol. Soc. Am. **97**, 1486–1501 (2007). https://doi.org/10.1785/0120060255
4. Shahi, S.K., Baker, J.W.: An efficient algorithm to identify strong-velocity pulses in multicomponent ground motions. Bull. Seismol. Soc. Am. **104**, 2456–2466 (2014). https://doi.org/10.1785/0120130191
5. Phan, V., Saiidi, M.S., Anderson, J., Ghasemi, H.: Near-fault ground motion effects on reinforced concrete bridge columns. J. Struct. Eng. **133**, 982–989 (2007). https://doi.org/10.1061/(ASCE)0733-9445(2007)133:7(982)
6. Avşar, Ö., Özdemir, G.: Response of seismic-isolated bridges in relation to intensity measures of ordinary and pulselike ground motions. J. Bridg. Eng. **18**, 250–260 (2013). https://doi.org/10.1061/(ASCE)BE.1943-5592.0000340
7. Todorov, B., Billah, A.H.M.M.: Seismic fragility and damage assessment of reinforced concrete bridge pier under long-duration, near-fault, and far-field ground motions. Structures **31**, 671–685 (2021). https://doi.org/10.1016/j.istruc.2021.02.019
8. Tochaei, E.N., Taylor, T., Ansari, F.: Effects of near-field ground motions and soil-structure interaction on dynamic response of a cable-stayed bridge. Soil Dyn. Earthq. Eng. **133**, 106115 (2020). https://doi.org/10.1016/j.soildyn.2020.106115
9. Priestley, M.J.N., Calvi, G.M., Kowalsky, M.J.: Displacement-Based Seismic Design of Structures. IUSS Press, Pavia (2007).(in press)

10. Park, Y., Ang, A.H.-S.: Mechanistic seismic damage model for reinforced concrete. J. Struct. Eng. **111**, 722–739 (1985). https://doi.org/10.1061/(ASCE)0733-9445(1985)111:4(722)

11. Kunnath, S.K., El-Bahy, A.W.T.A., Stone, W.C.: Cumulative seismic damage of reinforced concrete bridge piers. Buffalo. State Univ. of New York at Buffalo, National Center for Earthquake Engineering Research, NY (1997)

12. Mahboubi, S., Shiravand, M.R.: Proposed input energy-based damage index for RC bridge piers. J. Bridg. Eng. **24**, 04018103 (2019). https://doi.org/10.1061/(ASCE)BE.1943-5592.0001326

13. Newmark, N.M., Rosenblueth, E.: Fundamentals of Earthquake Engineering. Prentice-Hall, Englewood Cliffs (1971)

14. Rodriguez-Marek, A., Cofer, W.: Dynamic Response of Bridges to Near-fault, forward Directivity Ground Motions (Report No. WA-RD 689.1). United States; Federal Highway Administration: Washington, DC, USA, 2007 (2007)

15. ATC-13, Earthquake damage evaluation data for California," Applied Technology Council, Report. No. 13. Redwood City (1985)

16. HAZUS, Earthquake loss estimation methodology-Technical manual," Federal Emergency Management Agency and National Institute of Building Science, Washington, DC (1999)

17. Porter, K., Kennedy, R., Bachman, R.: Creating fragility functions for performance-based earthquake engineering. Earthq. Spectra. **23**, 471–489 (2007). https://doi.org/10.1193/1.2720892

18. FEMA-356, Prestandard and commentary for the seismic rehabilitation of buildings. Prepared by American Society of Civil Engineers for the Federal Emergency Management Agency, Washington, D.C. (2000)

19. ATC-40, Seismic Evaluation and Retrofit of Concrete Buildings Volume-1 by APPLIED TECHNOLOGY COUNCIL 555 Twin Dolphin Drive, Suite 550 Redwood City, California 94065 (1996)

20. Eurocode-8-Part 3, Assessment and retrofitting of buildings. Pinto P.E. and Franchin P., University of Rome, La Sapienza (2004)

21. Naeim, F., Kelly, J.M.: Design of Seismic Isolated Structures: From Theory to Practice. John Wiley & Sons Inc., New York (1999)

22. Roeder, C.W., Stanton, J.F., Taylor, A.W.: Performance of elastomeric bearings (1987)

23. Spudich, P., Bayless, J.R., Baker, J., Chiou, B.S.J., Rowshandel, B., Shahi, S., Somerville, P.: Final report of the NGA-West2 directivity working group. Pacific Eng. Res. Cent. Rep. **162**, 1199–1221 (2013)

24. Somerville, P.G., Smith, N.F., Graves, R.W., Abrahamson, N.A.: Modification of empirical strong ground motion attenuation relations to include the amplitude and duration effects of rupture directivity. Seismol. Res. Lett. **68**, 199–222 (1997). https://doi.org/10.1785/gssrl.68.1.199

25. Tarbali, K., Bradley, B.A., Baker, J.W.: Ground motion selection in the near-fault region considering directivity-induced pulse effects. Earthq. Spectra. **35**, 759–786 (2019). https://doi.org/10.1193/102517EQS223M

26. Panella, D.S., Tornello, M.E., Frau, C.D.: A simple and intuitive procedure to identify pulse-like ground motions. Soil Dyn. Earthq. Eng. **94,** 234–243 (2017). https://doi.org/10.1016/j.soildyn.2017.01.020

27. PEER., Pacific earthquake engineering research center, strong motion database. https://ngawest2.berkeley.edu/

28. A. Ghobarah, H. Abou-Elfath, A. Biddah, Response-based damage assessment of structures, Earthq. Eng. Struct. Dyn. 28 (1999). https://doi.org/10.1002/(SICI)1096-9845(199901)28:1<79::AID-EQE805>3.0.CO;2-J

29. Powell, G.H., Allahabadi, R.: Seismic damage prediction by deterministic methods: concepts and procedures. Earthq. Eng. Struct. Dyn. **16**, 719–734 (1988). https://doi.org/10.1002/eqe.4290160507

30. Jung, D., Andrawes, B.: Seismic damage assessment of SMA-retrofitted multiple-frame bridge subjected to strong main shock-aftershock excitations. J. Bridg. Eng. **23**, 04017113-1-04017113–12 (2018). https://doi.org/10.1061/(ASCE)BE.1943-5592.0001164

31. Bassam, A., Iranmanesh, A., Ansari, F.: A simple quantitative approach for post earthquake damage assessment of flexure dominant reinforced concrete bridges. Eng. Struct. **33**, 3218–3225 (2011). https://doi.org/10.1016/J.ENGSTRUCT.2011.06.024
32. Diaz, S.A., Pujades, L.G., Barbat, A.H., Vargas, Y.F., Hidalgo-Leiva, D.A.: Energy damage index based on capacity and response spectra. Eng. Struct. **152**, 424–436 (2017). https://doi.org/10.1016/J.ENGSTRUCT.2017.09.019

Traffic Signal Violation Behavior of Pedestrian at Urban Intersections—A Case Study of New Delhi

Faizanul Haque and **Farhan Ahmad Kidwai**

Abstract Accidents involving pedestrian at signalized intersections are major safety issue in developing countries such as India. A significant proportion of pedestrian accidents reported at intersections are primarily due to violation behavior of pedestrians. The objective of this study is to analyze pedestrian road crossing behavior and factors affecting their signal violation propensity at urban signalized intersections. Data is collected through video recording technique in New Delhi, India. Chi-square and t-test are performed to identify statistically significant explanatory variables. Pedestrian signal violation behavior is modelled using binomial logistic regression. Pedestrian personal attributes and situational factors are found to have significant association with signal violation behavior and the model has significant predictive capability. Interventions focusing on behavioral modifications, such as increasing pedestrian safety awareness would be most effective in reducing violation, though engineering measures might also be useful. The findings would certainly help city planners, policy makers and designers in deeper understanding of pedestrian behavior to improve safety at urban signalized intersections.

Keywords Pedestrian safety · Signal violation · Binary logit regression · Pedestrian crossing behavior · Signalized intersection

1 Introduction

Road accidents involving pedestrians are of grave concern globally and particularly in developing countries. Every year about 1.35 million fatalities occur worldwide due to road accidents [1]. India is not an exception to this global trend as the country reported the occurrence rate of road accident at 53 per hour and on an average 17 lives are lost per hour. Delhi reported the highest number of accidental deaths followed by Chennai [2]. Pedestrians are the most vulnerable road users and ultimate sufferers of road accidents. Road accident deaths involving pedestrians accounts for about 22%

F. Haque (✉) · F. A. Kidwai
Department of Civil Engineering, Jamia Millia Islamia, New Delhi 110025, India
e-mail: faizanul26@gmail.com

of the total fatalities worldwide [3]. Pedestrian fatalities due to traffic accidents in China are as high as 30% [4]. The share of fatal pedestrian road crashes in India was 13.8% in 2017 which is 3.4% more than previous year whereas for Delhi it is almost 40% [2].

The probability of pedestrian accidents is high at intersections during road crossing due to shared signal phases. In Delhi about 62% of accidents occurred at intersections resulting in 60% of fatalities [2]. Several studies have reported signal violation behavior by pedestrians as the leading cause for pedestrian vehicular conflicts which turns fatal mostly for pedestrians [5–7]. As compared to other road users, the behavior of pedestrians is often unpredictable and difficult to generalize as it varies according to situation and location. They have higher freedom to choose their path, cross the road along random paths and are bounded by fewer laws. In the past researchers have tried to understand and analyze pedestrian's road crossing behavior with specific focus on signal violation to assess their safety.

Pedestrians' gender, age group and group size were found to be significantly related with signal violation behavior in previous studies. Male pedestrians have increased violation and risk taking propensity than females. Contrary to this, female pedestrians are more sensitive to risk and prefer to cross the road during pedestrian phase [8–10]. Females also wait more for safer crossing opportunity to cross the road as their mean waiting time is about 27% more than males [11]. Older pedestrians are found to be most law abiding whereas young adults commit frequent violations [12, 13]. Increase in number of pedestrian crossing together decreases the odds of signal violation [14]. Pedestrians are also influenced by others behavior and are more likely to infringe upon signal if others are doing the same. Contrary to this, presence of children and other pedestrians who wait for walk sign, increases the signal compliance behaviour [15, 16].

Pedestrian crossing speed is a crucial parameter for designing of pedestrian facilities. It had been found that average crossing speed varies largely between 1.2–1.4 m/s. Results also suggest that crossing speed is mostly related to age, gender and group size of pedestrians. Higher crossing speed was reported for pedestrians with violation behavior, males, young and smaller groups as compared to their counter parts [7, 14, 17]. Higher levels of education significantly reduces the signal violation tendency [18]. Other factors such as trip purpose and technological distractions are also found to be significantly related with unsafe crossing behaviors [8, 19, 20].

Pedestrian attitude pertaining to road crossing decisions are complex and are predominantly governed by comfort, convenience and safety [21]. Properly designed and placed pedestrian facilities encourage users to cross at a certain location. Signalized intersection with crosswalk helps to channelize pedestrian traffic [22]. Presence of refuge island increase safety perception of pedestrians [4].

Pedestrian behavior and attitude are very stochastic in nature. It often changes according to the surroundings. Despite an outspread variety of studies on pedestrian behavior at signalized intersection in developed countries, few studies have been conducted in developing countries such as India. Moreover behavior of pedestrian at some location is not entirely similar with other location hence it requires regular and location specific understanding. Therefore the present study aims at understanding pedestrian signal violation behavior at urban signalized intersections located in New Delhi.

2 Methodology

The research methodology is broadly divided into data collection; analysis and modeling.

2.1 Data

Data was collected at two signalized intersections located in New Delhi, India on weekdays and normal weather conditions. Both locations have substantial pedestrian and vehicular traffic volume. Site 1 is 4-legged and has mixed land use patterns consisting of college, offices, commercial establishment and open spaces. Site 2 is 3-legged and predominantly industrial area with few residential dwellings. Figure 1 shows study site pictures. Video recordings were done to capture pedestrians' behavior while crossing the road at the selected intersections. Two or more cameras were installed as per the site conditions to cover entire study section. The height and field of view (FOV) of the cameras were adjusted as per the prevailing site conditions so as to cover the ends of the road, crosswalk and signals. Video recordings were carried out for one hour in morning (9–10 AM) and evening (5–6 PM), without disturbing the normal flow of traffic. Pedestrian movements were recorded without their realization so as to get their naturalistic behavior. The data from recordings were extracted by using AVS video editor software. Recordings were played in ultra slow motion and frame by frame images were watched to extract the required data. The data was further coded and entered into excel formats by trained volunteers. Complete information pertaining to 552 pedestrians was extracted.

2.2 Analysis and Modeling

Descriptive statistics are performed for the variables from video data to have general understanding of the pedestrian behavior. Chi-square and t-test are performed to identify variables which are significantly related with signal violation behavior (SVB)

Fig. 1 **a** Broad view of location 1 **b** SVB by group crossing at location 1 **c** Broad view of location 2 **d** SVB by male pedestrian at location 2

using IBM SPSS Statistics 22. If p-value is less than 0.05 then it supports the alternate hypothesis that significant difference exist within groups in terms of SVB. To have a comprehensive understanding of factors affecting SVB a binary logistic regression (BLR) model is developed using statistically significant variables. A pedestrian have only two choices while crossing the road- SVB YES or NO. Therefore, binary logistic regression model is used to predict binary responses from categorical predictor variables.

The probability of selecting an alternative (compliance/non compliance) is based on a linear combination function (utility function) expressed as:

$$U_i = \beta_0 + \beta_1 x_{1,i} + \beta_2 x_{2,i} + \beta_3 x_{3,i} + \ldots \beta_N x_{N,i} \tag{1}$$

$$P(i) = \frac{e^{U_i}}{1 + e^{U_i}} \tag{2}$$

where U_i = the utility of choosing alternative i, i = the alternative (SVB-Yes/SVB-No), N = number of independent variables, β_0 = model constant, and β_N = coefficients of predictor variables, x = predictor variables that determine the probability of outcome of alternatives and $P(i)$ = probability of signal violation.

3   Results and Discussion

The descriptive statistics, variables details, description and coding of significant variables are given in Table 1. It is found that 14.1% of pedestrians violated signal while crossing the road. It can be seen the majority of pedestrians are young and walked at normal pace to cross the road. A significant proportion of pedestrians crossed along straight path and from far end of the road. About 12% of pedestrians showed distracted behavior. The mean waiting time of pedestrians before crossing the road is found to be 6.265 s.

Subsequently these statistically significant variables are used to develop BLR model pertaining to pedestrian signal violation behavior (SVB). From the total data 80% is used for model development and the remaining for validation. The model outcomes are shown in Table 2. The model result show that age group is positively related with SVB suggesting that as the age of pedestrian increases the violation tendency also increases. Middle aged pedestrian violated the signal most followed by old and young. The result is contrary to previous findings [12, 13]. The odd of SVB of those pedestrians who ran to cross the road is about three times more than the walking pedestrians. It can be attributed to the fact that these pedestrians crossed the road during vehicle phase and hence they ran and cross the road to avoid collision with the oncoming vehicles. Pedestrian crossing along oblique path have higher propensity for signal violation. Oblique crossing pedestrians enter the intersection from random directions thus failing to notice the signal and exhibiting SVB.

Table 1 Descriptive statistics of significant variables

Pedestrian characteristics and behavior		Description (Coding)	Value
Age group	Young	Since the exact age of a pedestrian cannot be found from video, it is estimated by grouping them into Young (0), Middle (1) and Old (2)	57.6%
	Middle		36.6%
	Old		5.8%
Walking pace	Walk	Walking (0), Running (1)	90.2%
	Run		9.8%
Crossing path	Straight	Pedestrian crossing path Straight (0), Oblique (1)	61.4%
	Oblique		38.6%
Crossing direction	Near end	Pedestrian starts crossing from sidewalk Near end (0), from median Far end (1)	38.6%
	Far end		61.4%
Carrying object	No	Pedestrian carrying any luggage, backpack or hand bags Yes (1), No (0)	44.4%
	Yes		55.6%
Distraction	No	If pedestrian is not attentive while crossing, talking with others, not gazing for oncoming traffic and other casual behavior Yes (1), No (0)	88.0%
	Yes		12.0%
Waiting time	Waiting time	Mean waiting time of pedestrian before crossing (sec)	6.265 s

Table 2 BLR model outcomes for SVB

Variables	B	Std. Error	Exp(B)	p-value
Constant	−2.352	0.368	0.095	0.000***
Age group	0.562	0.232	1.754	0.015**
Walking pace	1.125	0.395	3.079	0.004***
Crossing path	0.986	0.288	2.680	0.001***
Crossing direction	−0.419	0.297	0.658	0.069*
Carrying object	−0.557	0.285	0.573	0.051*
Distraction	1.016	0.400	2.761	0.011**
Waiting time	0.015	0.032	1.015	0.001***
Model summary				
Sample	Model Development – 444 Validation - 108			
Log likelihood	330.024			
Cox & Snell Pseudo R^2	0.078			
Nagelkerke Pseudo R^2	0.139			
Hosmer and Lemeshow Test χ^2	8.631 (p-value = 0.374)			
Model accuracy	Development - 86.3% Validation - 86.1%			

Significant at: * 90% CL, ** 95% CL and *** 99% CL.

Crossing direction and carrying any object are negatively related with SVB, thus suggesting that pedestrian crossing from near end of road and not carrying any object violate signal more often as compared to their counterparts. As compared to pedestrians crossing from near end, pedestrians crossing from medians to sidewalks (far end) have arrived at median after crossing an approach. Since the traffic on the other approach is still moving so they wait on median and cross only when traffic phase is red.

A very crucial finding of this research is that distracted pedestrians are about 2.7 times more likely to violate signal than the non distracted pedestrians. The result compliments the findings from previous studies [20]. Waiting time is an important factor related to SVB. Mean waiting time of signal violating pedestrian is 1.295 s and for signal compliance pedestrian is 13.662 s. Pedestrian having strong violation tendency prefer to wait less for the pedestrian's phase whereas signal compliant pedestrian wait for longer duration and only cross the road during pedestrian's green phase. The results are consistent with previous findings with states that, pedestrians with violation intentions does not prefer to wait longer [8, 23, 24]. Once pedestrians reach their threshold value of waiting time they would become impatient and exhibit dangerous behavior by crossing against the red light. Contrary to previous finding mean waiting time of males is found to be slightly more than females [11]. Young pedestrians have most waiting time followed by middle and old age pedestrians. Distracted pedestrians prefer to wait less as compared to non distracted pedestrians.

The model has predictive accuracy of more than 86%. Hosmer and Lemeshow test is used to assess the model goodness of fit, and is found to be insignificant (p = 0.374). An insignificant values suggest that our model has significant data fitting [25].

4 Conclusions

The present study analyzed pedestrian signal violation behavior at signalized intersections in New Delhi, India. Data was collected by means of video recordings. SVB was modeled using BLR technique. The following important conclusions are made from this research.

- Pedestrians' demographics, road crossing behavior and waiting time are found to be significant predictors of SVB.
- Signal violating pedestrians are inherently impatient and do not prefer to wait more for safe opportunity to cross the road.
- Binary logistic regression technique is well suited to model pedestrian SVB and has excellent predictive accuracy.

Since most of the signal violating pedestrians ran to cross the road and have lesser waiting time, pedestrian countdown signal (PCS) should be installed at intersections in order to facilitate them in road crossing decisions. Medians or refuge islands should be properly designed and wider so as to encourage the pedestrians to wait

for safe crossing opportunity. Finally awareness should be created about the safety implications of signal compliance and the danger of distracted road crossings at signalized intersections.

The present study has limited sample size collected from two signalized intersections only. Pedestrians' personal attributes and behavior were only considered to model SVB. In future more intersections might be included while considering the impact of location specific factors as well.

References

1. World Health Organization: Global status report on road safety, Geneva (2018)
2. Transport Research Wing: Road accidents in India-2017, New Delhi, India (2018)
3. Zhang, W., Wang, K., Wang, L., Feng, Z., Du, Y.: Exploring factors affecting pedestrians' red-light running behaviors at intersections in China. Accid. Anal. Prev. **96**, 71–78 (2016). https://doi.org/10.1016/j.aap.2016.07.038
4. Ni, Y., Cao, Y., Li, K.: Pedestrians' safety perception at signalized intersections in shanghai. Transp. Res. Procedia 1955–1963. Elsevier B.V. (2017). https://doi.org/10.1016/j.trpro.2017.05.222.
5. Gupta, U., Tiwari, G., Chatterjee, N., FAzio, J.: Case study of pedestrian risk behavior and survival analysis. In: Proceedings of the Eastern Asia Society for Transportation Studies, pp. 389–389 (2009)
6. Ashur, S.A., Kroeker, K.J., Baaj, M.H.: A study of factors contributing to pedestrian crashes in El Paso County, Texas. In: Proceedings of the Transportation Research Board 82nd Annual Meeting, Washington, D.C., pp. 1–20 (2003)
7. Zaki, M.H., Sayed, T.: Automated analysis of pedestrians' nonconforming behavior and data collection at an urban crossing. Transp. Res. Rec. J. Transp. Res. Board **2443**, 123–133 (2014). https://doi.org/10.3141/2443-14
8. Guo, H., Wang, W., Guo, W., Jiang, X., Bubb, H.: Reliability analysis of pedestrian safety crossing in urban traffic environment. Saf. Sci. **50**, 968–973 (2012). https://doi.org/10.1016/J.SSCI.2011.12.027
9. Aghabayk, K., Esmailpour, J., Jafari, A., Shiwakoti, N.: Observational-based study to explore pedestrian crossing behaviors at signalized and unsignalized crosswalks. Accid. Anal. Prev. **151**, 105990 (2021). https://doi.org/10.1016/j.aap.2021.105990
10. Mukherjee, D., Mitra, S.: A comprehensive study on factors influencing pedestrian signal violation behaviour: experience from Kolkata City, India. Saf. Sci. **124** (2020). https://doi.org/10.1016/j.ssci.2020.104610
11. Tiwari, G., Bangdiwala, S., Saraswat, A., Gaurav, S.: Survival analysis: pedestrian risk exposure at signalized intersections. Transp. Res. Part F Traffic Psychol. Behav. **10**, 77–89 (2007). https://doi.org/10.1016/j.trf.2006.06.002
12. Ren, G., Zhou, Z., Wang, W., Zhang, Y., Wang, W.: Crossing behaviors of pedestrians at signalized intersections: observational study and survey in China. Transp. Res. Rec. **2264**, 65–73 (2011). https://doi.org/10.3141/2264-08
13. Holland, C., Hill, R.: The effect of age, gender and driver status on pedestrians' intentions to cross the road in risky situations. Accid. Anal. Prev. **39**, 224–237 (2007). https://doi.org/10.1016/j.aap.2006.07.003
14. Marisamynathan, S., Perumal, V.: Study on pedestrian crossing behavior at signalized intersections. J. Traffic Transp. Eng. (Engl. Ed.) **1**, 103–110 (2014). https://doi.org/10.1016/S2095-7564(15)30094-5
15. Yagil, D.: Beliefs, motives and situational factors related to pedestrians' self-reported behavior at signal-controlled crossings. Transp. Res. Part F Traffic Psychol. Behav. **3**, 1–13 (2000). https://doi.org/10.1016/S1369-8478(00)00004-8

16. Zhou, R., Horrey, W.J., Yu, R.: The effect of conformity tendency on pedestrians' road-crossing intentions in China: An application of the theory of planned behavior. Accid. Anal. Prev. **41**, 491–497 (2009). https://doi.org/10.1016/j.aap.2009.01.007

17. Muley, D., Kharbeche, M., Alhajyaseen, W., Al-Salem, M.: Pedestrians' crossing behavior at marked crosswalks on channelized right-turn lanes at intersections. Procedia Comput. Sci. 233–240. Elsevier B.V. (2017). https://doi.org/10.1016/j.procs.2017.05.339

18. Marisamynathan, S., Vedagiri, P.: Modeling pedestrian crossing behavior and safety at signalized intersections. J. Transp. Res. Board. **2672**, 76–86 (2018). https://doi.org/10.1177/036119 8118759075

19. Hatfield, J., Murphy, S.: The effects of mobile phone use on pedestrian crossing behaviour at signalised and unsignalised intersections. Accid. Anal. Prev. **39**, 197–205 (2007). https://doi. org/10.1016/j.aap.2006.07.001

20. Russo, B.J., James, E., Aguilar, C.Y., Smaglik, E.J.: Pedestrian behavior at signalized intersection crosswalks: observational study of factors associated with distracted walking, pedestrian violations, and walking speed. Transp. Res. Rec. **2672**, 1–12 (2018). https://doi.org/10.1177/ 0361198118759949

21. Al Bargi, W.A., David Daniel, B., Prasetijo, J., Md Rohani, M., Mohamad Nor, S.N.: Crossing behaviour of pedestrians along urban streets in Malaysia. In: MATEC Web Conference, pp. 1–10 (2017). https://doi.org/10.1051/matecconf/201710308003

22. Sisiopiku, V.P., Akin, D.: Pedestrian behaviors at and perceptions towards various pedestrian facilities: an examination based on observation and survey data. Transp. Res. Part F Traffic Psychol. Behav. **6**, 249–274 (2003). https://doi.org/10.1016/j.trf.2003.06.001

23. Wang, W., Guo, H., Gao, Z., Bubb, H.: Individual differences of pedestrian behaviour in midblock crosswalk and intersection. Int. J. Crashworthiness **16**, 1–9 (2011). https://doi.org/ 10.1080/13588265.2010.491715

24. Brosseau, M., Zangenehpour, S., Saunier, N., Miranda-Moreno, L.: The impact of waiting time and other factors on dangerous pedestrian crossings and violations at signalized intersections: a case study in Montreal. Transp. Res. Part F Traffic Psychol. Behav. **21**, 159–172 (2013). https:// doi.org/10.1016/j.trf.2013.09.010

25. Hosmer, D.W., Lemeshow, S.A., Sturdivant, R.X.: Applied Logistic Regression, 3rd edn. Wiley, New York (2013)

Hyper-parameter Optimised Artificial Neural Network Model for Failure Mode Identification of RC Shear Wall

A. Aswin Vishnu, Aswin Suresh, Ritu Anne Koshy, S. Sanjna, and P. Robin Davis

Abstract A reinforced concrete (RC) shear wall is a popular lateral-force-resisting element in high-rising structures for better seismic performance and damage reduction. Hence, it is essential to predict the shear wall's failure modes and collapse resistance. The mechanics-based approach is very involved and time-consuming to accurately predict failure modes of RC shear walls subjected to seismic loading. Neural networks can describe complex input–output functional relationships with their general nonlinear mapping capacity. This study investigates the efficiency of the Artificial Neural Network (ANN) model to predict the failure modes of RC shear walls employing a limited experimental dataset. The dataset consists of 393 one-story, one-bay reinforced concrete shear walls with sliding shear failure, shear failure, flexure-shear failure, and sliding shear flexural failure as the four classes of failure modes. For each data sample in the database, nine input parameters are considered as the input features, including the wall configuration, reinforcement index, and cross-section shape. The study also optimises the performance of the model by investigating the hyper-parameters. Various hyper-parameter optimisation methods such as random search, grid search, hyperband, genetic algorithm (GA), Bayesian Optimization (BO), and particle swarm optimisation (PSO) are considered to improve the baseline model. These hyper-parameter tuned models are evaluated and compared using various performance parameters such as accuracy and f1 score. This study can contribute to developing improved ANN models by effectively identifying the proper hyper-parameter configurations and their subsequent optimisation.

Keywords RC shear wall · Failure modes · Artificial neural networks · Hyperparameter optimization

A. A. Vishnu (✉) · A. Suresh · R. A. Koshy · S. Sanjna · P. R. Davis
Department of Civil Engineering, National Institute of Technology Calicut, Kozhikode, India
e-mail: aswinvishnuaaswinam@gmail.com

P. R. Davis
e-mail: robin@nitc.ac.in

1 Introduction

Over the course of human history, earthquakes have been the greatest natural hazard, causing damage to property and life. The damage to reinforced concrete (RC) buildings caused by earthquakes is a result of improper structural design, poor construction, and maintenance. It is important for a structure to be able to resist lateral forces like seismic forces and wind force. Since the 1960s, more efficient systems for resisting lateral forces have been developed for multistorey buildings by including shear walls. A shear wall is a lateral force resisting structural member reinforced concrete framed structures that keep structures safe from lateral forces.

It has been observed that buildings containing shear walls have shown better performance during any seismic event. [1] Shear walls were usually reinforced in a conventional manner for gravity and overturning but did not consider details for ductility [2] So, for proper designing, failure modes of shear walls have to be known. Using data-driven approaches instead of computationally thorough numerical models provides a feasible substitute for risk and vulnerability assessments. In this work, data-driven hyper-parameter optimised ANN models are suggested for the identification of failure modes of shear walls.

1.1 Research Significance

There have been several studies in the field of earthquake and structural engineering which have demonstrated the importance and benefits of shear walls in reinforced concrete structures. Even though shear walls play an important role in overall structural integrity, safety margins aren't properly addressed. Like any structure, shear walls can fail under certain circumstances. By knowing which failure modes an RC shear wall is susceptible to, engineers are able to complete structural performance analyses and come up with appropriate retrofit strategies. A convenient failure mode prediction tool is crucial to provide rapid retrofitting decision strategies, damage assessments, and seismic risk assessments. Experimental efforts in the past decades have not proven efficient in properly identifying the failure modes of shear walls. Since these areas haven't been explored extensively, there aren't many efficient mechanics-based or empirical methods for the rapid identification of shear wall failure modes.

Machine learning models have proved to be more efficient in providing the desired level of accuracy in the analysis process when compared to traditional analytical and finite element models. A machine learning approach is the best choice for problems involving complex interactions. It can efficiently uncover hidden relationships between data inputs. Mangalathu et al. (2020) [3] have used eight machine learning models such as K-Nearest Neighbours, Decision Tree, Naïve Bayes, XGBoost, AdaBoost, LightGBM, Random Forest, and CatBoost to find the best among them for shear wall failure mode prediction. Out of which, the random forest method gave

an accuracy of 86% in identifying the failure modes. But in that study, an ANN model is not developed and evaluated to predict the same. So, in the present study, a Hyper-parameter Optimised Artificial Neural Network Model is suggested and evaluated for rapid identification of failure modes of reinforced concrete shear walls.

Initially, an Artificial Neural Network was developed as the baseline model for failure mode prediction. The model's performance is then optimised by investigating the hyper-parameters. Activation function, batch size, number of neurons, number of hidden layers, and optimiser are considered hyperparameters. Since the available experimental dataset size is limited, the chance of overfitting the trained model is high. So, to reduce the overfitting of the model, the dropout rate is also chosen as one of the hyperparameters. Studies have been done for the classification of RC panel damage modes using ANN model in which the model hyperparameters were optimised when a small set of data was learned [4]. Yang et al. [5] suggest various hyper-parameter optimisation techniques for both classification and regression. In the current study. Hyper-parameter optimisation methods such as random search, grid search, hyperband, genetic algorithm (GA), Bayesian Optimization (BO), and particle swarm optimisation (PSO) are considered to improve the baseline ANN model in the current study.

2 Failure Modes of RC Shear Walls

In building systems, RC shear walls are subjected to bending moments, shear forces, axial loads, and cyclic loads. They exhibit more noticeable shear effects than columns, are more susceptible to cyclic shear, and fail in distinct ways when subjected to cyclic stress. Failure modes of reinforced concrete shear walls depend mainly on the configuration of the wall and reinforcement index. On the basis of their shear span length to wall-length ratio, shear walls are categorised as squat (low-rise) or slender (high-rise). [6] In slender walls, flexural yielding towards the base characterises the ductile failure mechanism. Squat walls feature shear-controlled failure mechanisms as a result of their geometry and are more prone to produce an unpredicted shear failure, which may be defined as an abrupt loss in strength and stiffness under seismic loads.

Mangalathu et al. [3] classified the failure modes of RC shear walls based on the available experimental data as,

- **Flexural failure**: Flexural failure occurs in the plastic hinge zone owing to the fracture in the longitudinal reinforcement or concrete crushing.
- **Sliding shear failure**: Sliding shear failure occurs due to huge cracks at the wall base, concrete crushing, and rebar buckling throughout a narrow band along the base of the wall.
- **Flexure shear failure**: Flexure shear failure is the corner-to-corner cracks due to diagonal compression or tension.
- **Shear failure**: The special case of squat walls failing in shear.

3 Dataset

Experimental data that consist of 393 single-story, single-bay reinforced concrete shear walls with cross sections as non-rectangular or rectangular are used in this study. This dataset is adopted from Mangalathu et al. [3]. The study was compiled from related RC shear wall performance studies published between 1975 and 2022, including 60 flanged specimens, 95 barbell-cross sections, and 238 rectangular specimens.

3.1 *Input Parameters*

For each data sample in the database, there are 9 parameters of the experiment considered as input features, including the configuration of the wall, reinforcement index, and cross-section shape. Table 1 presents the feature description-

According to the design parameters, all input features in the database are dimensionless. Input features, namely, l_w/t_w, M/Vl_w, and A_b/A_g are utilised to account for the design of shear walls. Further, the input features include four reinforcement indices, namely $(\rho_{vw}f_{y,vw}/f_c')$, $(\rho_{hw}f_{y,hw}/f_c')$, $(\rho_{vc}f_{y,vc}/f_c')$, and $(\rho_{hc}f_{y,hc}/f_c')$. These indices are defined as the strength ratio based on the quantity and strength of materials incorporated. Moreover, the shear walls' cross-sectional shape is an additional input parameter. Three different cross-sectional shapes are considered here: the barbell (B), the flanged (Fl), and the rectangular (R).

Table 1 Input parameters

Features	Description
F_1	Aspect ratio (M/Vl_w)
F_2	Ratio of Wall length to wall thickness (l_w/t_w)
F_3	Area of boundary element to area of gross sectional area of wall (A_b/A_g)
F_4	Axial load ratio ($P/f_c'A_g$)
F_5	Web vertical reinforcement index ($\rho_{vw}f_{y,vw}/f_c'$)
F_6	Web horizontal reinforcement index ($\rho_{hw}f_{y,hw}/f_c'$)
F_7	Boundary element vertical reinforcement index ($\rho_{vc}f_{y,vc}/f_c'$)
F_8	Boundary element horizontal reinforcement index ($\rho_{hc}f_{y,hc}/f_c'$)
F_9	Shape of cross section

3.2 Output Class

The dataset contains four classes of failure, namely flexural failure (F), flexure-shear failure (FS), failure due to shear (S), and sliding shear failure (SL). These are assigned as classes 0,1,2, and 3 respectively. There were 152, 96, 122, and 23 specimens in the database that showed flexural failure, flexure-shear failure, shear failure, and sliding shear failure, respectively.

4 Theoretical Background of Methods Used

4.1 Artificial Neural Network (ANN)

Artificial Neural Networks is a deep learning technique that mimics the neurons in the brain. It's commonly used to solve regression and classification problems. A neural network mainly consists of three layers: an input layer, a hidden layer, and an output layer. Neurons are the building blocks of each layer. The inputs can be feature values. In our study, each data sample contains the nine values, which consist of configuration, reinforcement index, and cross-section shape of the RC shear wall, and are taken as the feature values. The outputs of the output neurons of the network indicate to which class the feature values belong. Since Artificial Neural Network is a supervised learning technique, the dataset must contain the feature values and the labels (targets). Neural networks are trained by processing these data samples. The training process takes the error between the predicted output and target output. And then, the network optimises its weighted associations between the neurons to get a minimum error.

4.2 Hyperparameter Optimisation Strategies

- **Grid Search**-Grid search works on the principle of Cartesian products. For a given subset of hyper-parameter configuration space of a learning algorithm, it gauges all hyper-parameter combinations and thus can be deemed an exhaustive search method. However, it is inefficient for use in high-dimensional hyper-parameter configuration spaces.
- **Random search**-Random Search, though similar to Grid search, replaces the exhaustive enumeration of all hyperparameter combinations by randomly selecting them. RS can explore a more extensive search space than GS with a limited budget. Random Search's major pro is that it is resource-allocated and parallelised effortlessly since evaluations are not dependent.

- **Hyperband**-The Hyperband method, by dynamically selecting a fair number of configurations, is purported to resolve the problem of sequential halving algorithms. By splitting the whole budget (B) into n parts and assigning each part to each configuration (b = B/n), an optimal balance can be achieved between the number of configurations of hyper-parameters (n) and their allotted budgets. Each group of random configurations is subjected to successive halving, disregarding the inadequately performing configurations of hyper-parameter and enhancing efficiency.
- **Bayesian optimisation**-bayesian optimisation creates a probabilistic model of the function translating from hyperparameter values to the objective as measured on a validation set [7]. A potential hyperparameter configuration is repeatedly assessed using an existing model and updated based on observations that provide as much information about this function as possible. In Bayesian optimisation models, the exploitation and exploration processes are balanced to discover the currently optimised regions and improved configurations in the unexplored regions.
- **Particle Swarm Optimization (PSO)**-Particle swarm optimisation (PSO) is a collection of evolutionarily inspired algorithms that allow a cluster of particles (swarm) to move through a search space in a semi-random approach [8]. By communicating information and cooperation among different particles in a group, the Particle swarm optimisation algorithms identify the optimal solution. In Particle swarm optimisation, only data on the global best particle and the individual best particle is shared so that the complete optimisation procedure trails the direction of the current optimal solution.
- **Genetic algorithm (GA)**-Genetic algorithm (GA) [9] is a metaheuristic algorithm based on the theory of evolution-, which means those with the best survival capacity and the ability to adapt to their surroundings are much more likely to live on and pass those traits and characteristics onto their progeny. Each generation will inherit traits from their parents and produce superior and worse individuals. The superior progeny will persist and have more competent offspring in the long run, while the worse ones will progressively perish. The most adaptable entity will emerge as the global optimum after several generations.

5 Hyper-parameter Optimised ANN Models and Results

The data is split into testing and training data using a train-test split of 0.3. This training data is used to train, and k fold cross-validation and testing data are utilised for testing. This data is normalised by using a min–max scaler in scikit learn. Further, the categorical variables are one hot encoded for passing it to the input layer of ANN. A model function was created considering various hyperparameters like the number of hidden layers, the number of neurons in each hidden layer, the activation function in these layers, the batch size, the dropout rate, and the optimisation algorithm. The number of neurons in the input layer and output layer is fixed to be 11 and 4, respectively. In order to receive probability values at the output layer, we have used the SoftMax activation function.

Table 2 Optimum hyperparameters obtained from various optimisation techniques

Method of hyperparameter optimisation	Hyper parameters					
	Activation	Batch size	Number of neurons	Number of hidden layers	Optimiser	Dropout
GridSearchCV	Relu	16	64	3	Adam	0.1
RandomSearchCV	Relu	16	64	1	Rmsprop	0.2
HyperBandCV	Relu	16	64	2	Adam	0.1
BayesSearchCV	Relu	64	64	2	Rmsprop	0.4
Particle swarm optimisation	Relu	16	72	2	Adam	0.2
Genetic algorithm	Relu	32	71	2	Rmsprop	0.2

One of the major problems of ANN, along with small datasets, is overfitting. To solve this issue, we decided to create a dropout layer after each hidden layer that is defined. After model definition, the model compilation is done by taking categorical cross-entropy as the loss function and accuracy as the metric. In order to maximise the performance of the model, various hyperparameter optimisation methods are used which include grid-searchCV, random-searchCV, Hyperband, BayesSearchCV, Particle Swarm Optimisation and Genetic Algorithm.

For grid-search, random search, hyperband, and Bayes search methods, an initial search space is defined for each hyperparameter that is under consideration. The search space of activation contains two values that are ReLU and tanh. Since the number of hidden layers is more than three, it would cause the model to overfit the small dataset available; the search space includes at least one hidden layer and the utmost three layers. Here the number of neurons in each hidden layer is considered to be the same, and this is taken as a hyperparameter. For the grid search method, there are three values for the number of neurons; 16, 32, and 64.Search space for batch size includes four values that are 16, 32, 64, and 128.The value of dropout can vary from 0.1 to 0.4 with an increment of 0.1.

The Optimization Algorithm is fixed between Adam and RMSprop using the hyperparameter optimisation methods. Since the grid search method considers all the possible combinations, the computational cost is high compared to other methods. For PSO and GA-based hyperparameter optimisation methods, the number of neurons, batch size, and dropout are taken as continuous variables. The number of Neurons for PSO based hyperparameter optimisation method is varied between 10 and 100. The number of evals for the PSO is taken as 20. For hyperparameter optimisation using genetic algorithms, various parameters, including population size, gene mutation probability, gene crossover probability, tournament size, and the number of generations are to be fixed. Here population size is taken as 10, gene mutation probability as 0.10, gene crossover probability as 0.5, tournament size as three, and the number of generations is taken as 5. Once the search space is fixed, the best parameter is found based on the cross-validation score. Table 2 shows the various hyperparameters fixed

Table 3 Metrics of each HPO method

Method of hyperparameter optimisation	Metrics		
	Mean CV score	Mean test loss	Mean test accuracy
GridSearchCV	0.9307	0.6335	0.8503
RandomSearchCV	0.8471	0.4990	0.8446
HyperBandCV	0.9054	0.5613	0.8588
BayesSearchCV	0.7999	0.5712	0.8079
Particle swarm optimisation	0.9054	0.5527	0.8559
Genetic algorithm	0.8582	0.5128	0.8531

using the above hyperparameter optimisation methods. Using these hyperparameters, the model is redefined, and a three-fold cross-validation score for the model is found. For each fold, the performance of the model is evaluated with test data. The mean cross-validation score, mean test loss, and mean test accuracy for the redefined model are found Re (Table 3).

Confusion matrix corresponding to various hyperparameter optimization methods is made for each fold Re (Fig. 1a, b, c). Micro F1 score is a single value metric that balances the precision and recall for a given multiclass classification problem. From the Confusion matrix, micro f1 scores are found for all three folds corresponding to all hyperparameter optimisation methods. The micro f1 scores for each fold in these methods are visualised. Figure 2 shows a comparison of mean micro f1 scores. From this figure, it is evident that the model defined using the hyperparameter set obtained from the hyperband method resulted in the highest mean micro f1 score of 0.8587. The model derived from the hyperparameter set fixed using the Bayes search method resulted in a mean micro f1 score of 0.8079, which is the lowest among all the methods.

GridSearchCV

RandomSearch CV

Fold 1 :   (i)   (iv)

Fold 2 :   (ii)   (v)

Fold 3 :   (iii)   (vi)
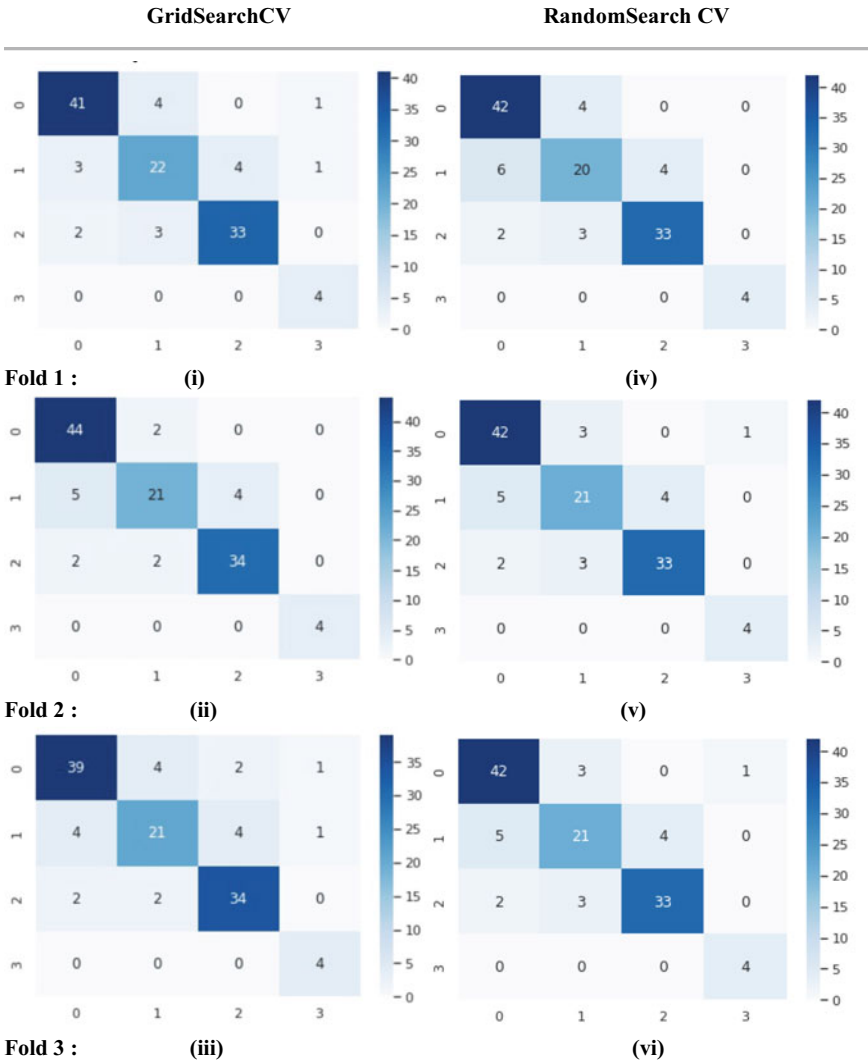
Fig. 1 The confusion matrix of the present models: (i)–(iii): GridSearchCV; (iv)–(vi): Random-SearchCV; (vii)–(ix): HyperBandCV; (x)–(xii): BayesSearchCV; (xiii)–(xv): Particle Swarm Optimisation; (xvi)–(xviii): Genetic Algorithm

HyperBandCV   BayesSearchCV

Fold 1 :   (vii)   (x)

Fold 2 :   (viii)   (xi)

Fold 3 :   (ix)   (xii)

Fig. 1 (continued)

Particle Swarm Optimisation   **Genetic Algorithm**

Fold 1 :   (xiii)   (xvi)

Fold 2 :   (xiv)   (xvii)

Fold 3 :   (xv)   (xviii)
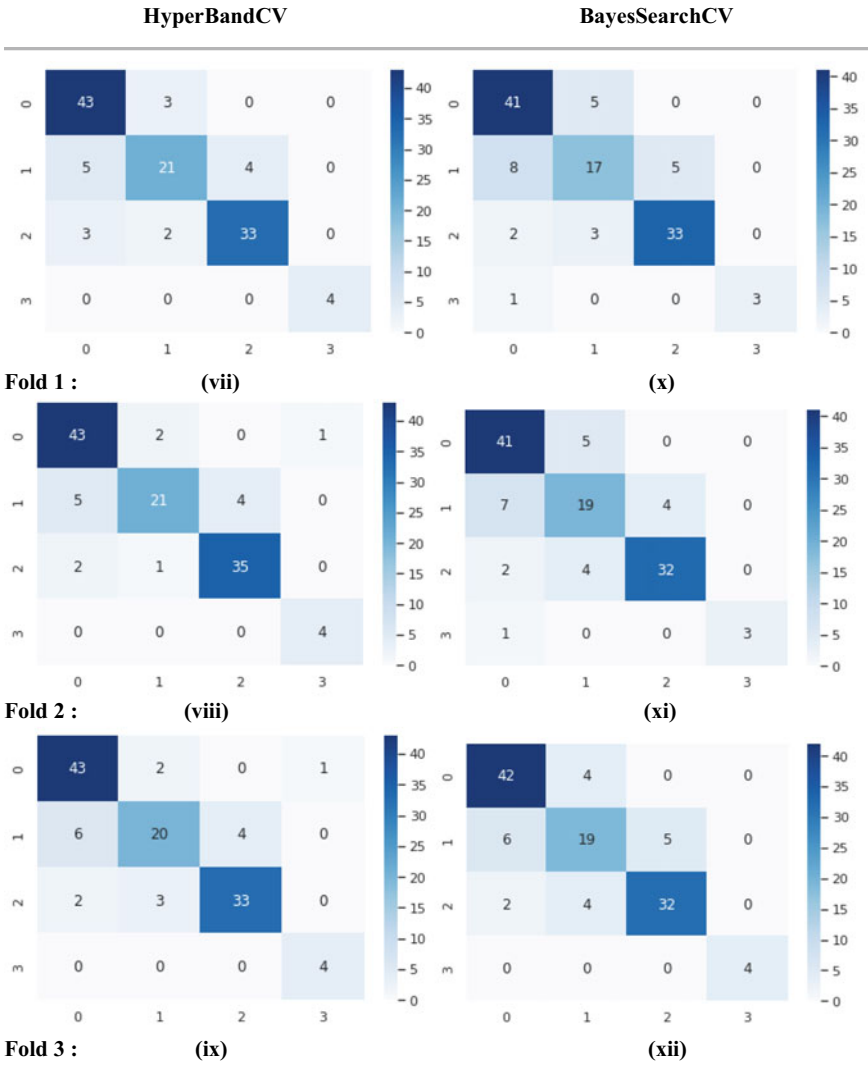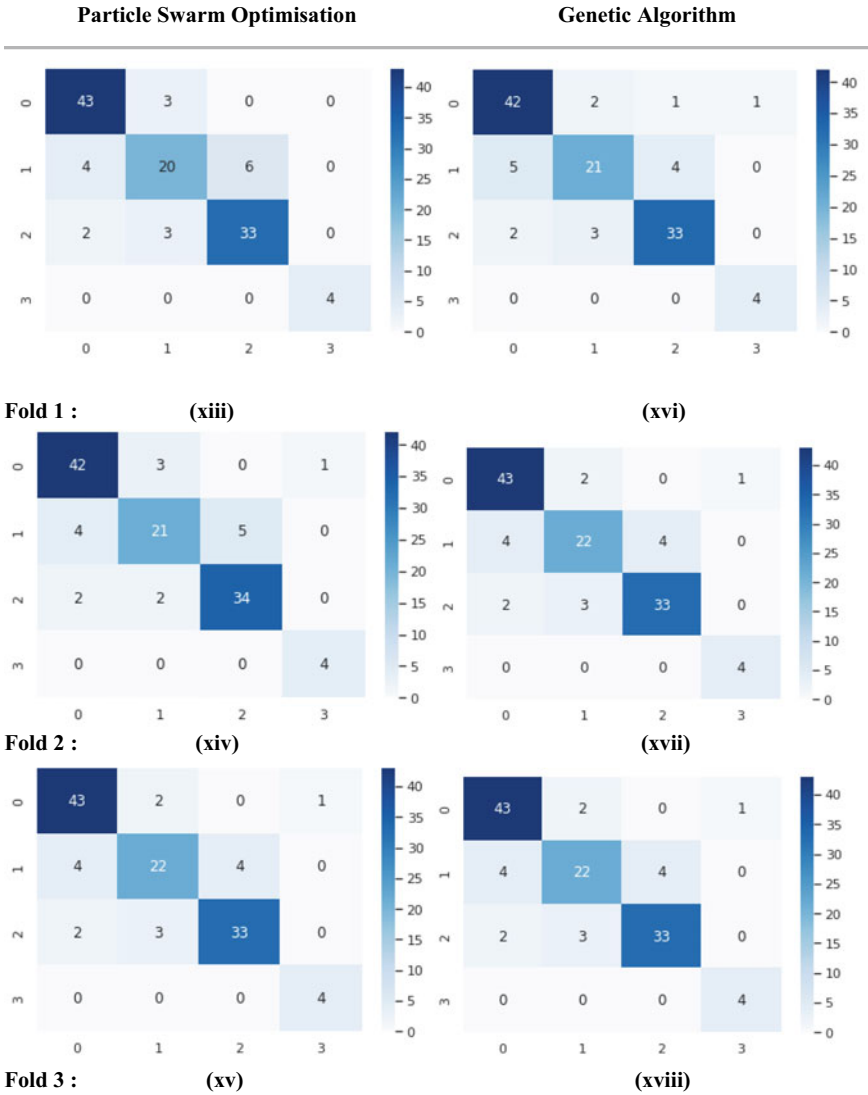
Fig. 1 (continued)
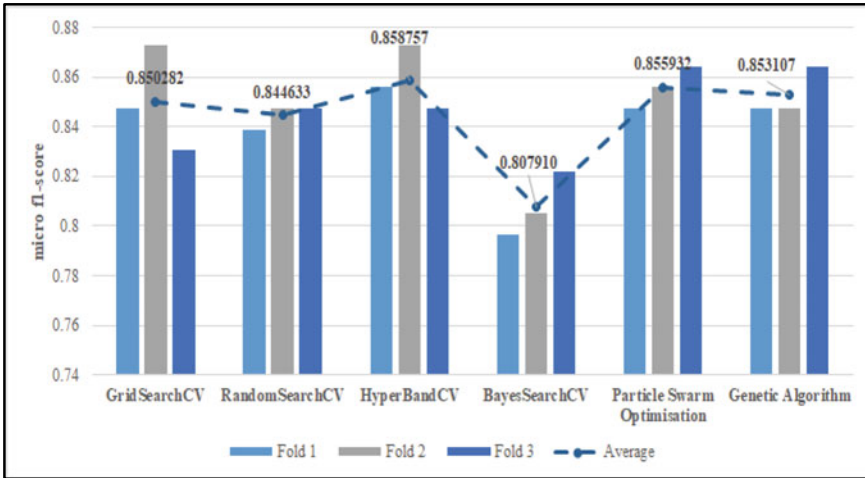
Fig. 2 The comparison of micro-average f1-scores

6 Conclusions

Shear walls provide lateral force resistance during earthquakes and wind. Shear walls can fail in flexure-shear, shear, sliding, or flexure, depending on the geometric, material, and loading configurations. Despite extensive experiments and earthquake reconnaissance examining the behaviour of walls in different configurations, there is no empirical or physics-based method to predict the failure mode of shear walls. A convenient failure mode prediction tool is crucial to provide rapid retrofitting decision strategies, damage assessments, and seismic risk assessments. This paper explores the capability of various hyperparameter-optimised artificial neural networks in failure mode prediction of RC shear walls.

Initially, a baseline ANN model was developed for the RC shear wall failure mode prediction, and then various hyperparameter optimisation methods were utilised to improve the performance. The database consists of 393 one-story, one-bay reinforced concrete shear walls with rectangular or non-rectangular (barbell (I-) or flanged) sections. In the database, the number of specimens with flexural failure, flexure-shear failure, shear failure, and sliding shear failure is 152, 96, 122, and 23, respectively. The hyperparameter is fixed using hyperparameter optimisation methods, including Grid Search, Random search, Hyperband, Bayes search, Particle swarm optimisation, and genetic algorithm. Experimental data obtained from previous studies were used. The entire data is divided into training and testing using a train-test split of 0.3. Models obtained using the hyperparameter optimisation methods are cross-validated on the training data and evaluated on test data. Confusion matrices on test data for each of these models are found. The performances of these models are compared using the mean micro f1 score. It is found that the model hyperparameter set obtained using hyperband performed best based on the mean micro f1 score found on the test data.

The present study demonstrates how ANN can predict failure modes in shear walls and how to develop a hyperparameter optimised ANN using a limited experimental database to get good results. This technique can be used for predicting failure modes of other structural components. At present, the failure mode is only predicted without reason for the failure being identified. Further studies and data are necessary to determine how damage progression patterns differ based on failure modes.

References

1. Fintel, M.: Performance of buildings with shear walls in earthquakes of last thirty years (1995). P.E
2. Paulay, T.: Design aspects of shear walls for seismic areas. Can. J. Civ. Eng. **2**(3), 321–344 (1975)
3. Mangalathu, S., Jang, H., Hwang, S.H., Jeon, J.S.: Data-driven machine-learning-based seismic failure mode identification of reinforced concrete shear walls. Eng. Struct. **208** (2020)
4. Doan, Q.H., Le, T., Thai, D.K.: Optimisation strategies of neural networks for impact damage classification of RC panels in a small dataset. Appl. Soft Comput. J. **102** (2021)
5. Yang, L., Shami, A.: On hyperparameter optimisation of machine learning algorithms: theory and practice. Neurocomputing **415**, 295–316 (2020)
6. American Society of Civil Engineers. (2017) ASCE standard ASCE/SEI 41-17: Seismic Evaluation and Retrofit of Existing Buildings
7. Talaat, F.M., Gamel, S.A.: RL-based hyper-parameters optimisation algorithm (ROA) for convolutional neural network. J. Ambient Intell. Humaniz. Comput. (2022)
8. Eberhart, R., Kennedy, J.: A new optimiser using particle swarm theory. In: MHS1995. Proceedings of the Sixth International Symposium on Micro Machine and Human Science, pp. 39–43. IEEE (1995)
9. John, H.: Holland- Adaptation in Natural and Artificial Systems: An Introductory Analysis with Applications To Biology, Control, and Artificial Intelligence. The MIT Press, Cambridge, England (1975)

Finite Element Modeling of Flexible Pavement Reinforced with Geogrid

Aswathy Santhosh, Padmakumar Radhakrishnan, and Vignesh Dhurai

Abstract The necessity to extend road service life and improve performance has increased the usage of pavement reinforcements in recent times. Geogrids are progressively being employed as a reinforcement in a wide range of engineering disciplines. The flexible pavement is among the core area, where enhancement in performance of pavement service life is needed. The purpose of this modelling is to study how geogrids in pavement work using the finite element method using ABAQUS software. This research evaluates the effectiveness of geogrid-reinforced pavement in terms to reduction in rutting under load. The finite element system was used to do analysis on models of unreinforced and reinforced roads. The findings of the finite element study demonstrate that adding geogrids between the pavement layers lowered surface distortion. The findings attained show that the grids are frequently widely utilized enhance the effectiveness of flexible pavements and may contribute significantly to crack resistance and the prevention of permanent deformation.

Keywords Geogrid · Finite element modelling · Reinforcement · Deformation

1 Introduction

Pavement surface deterioration is a condition when cracks form in the road as a result of the cumulative impacts of traffic and environmental conditions. It has a significant impact on the quality and safety of the road. The road surface is sensitive to several types of distresses over the course of its life. Cracking and rutting are the most typical

---

A. Santhosh (✉) · P. Radhakrishnan · V. Dhurai
Department of Civil Engineering, College of Engineering Trivandrum, APJ Abdul Kalam
Technological University, Thiruvananthapuram, Kerala, India
e-mail: aswathyss98@gmail.com

P. Radhakrishnan
e-mail: rpk@cet.ac.in

V. Dhurai
e-mail: dvignesh005@gmail.com

987

types of flexible pavement distress mechanisms. Rutting is due to the increase of tire pressure and axle loads. It is described as the permanent longitudinal deformation of the pavement caused by repeated loadings over the wheel path.

Geogrid, a geosynthetic made of polymers, was chosen for this study to improve performance of roads. Geogrids perform two key functions: separation and reinforcement.

The notion behind reinforcing paved roads is that if the bitumen surface is strong in compression but has low tensile strength, reinforcements can be added to give the required tensile stress resistance. Geogrid reinforcements can be placed between the layers of the pavement to improve fatigue resistance, reduce rutting, and restrict reflective cracking.

Using PLAXIS 2D software, Ahirwar [1] analysed vertical surface deformation upon the upper layer of pavement with response to change in thickness under the same conditions with and without geogrid reinforcement. Installing geogrid at one-third from bottom of the base layer increases the performance of the pavement [2]. Glass-fiber related geogrids have been effectively employed as interlayers on air terminal runways to prolong the serviceability of black-top asphalt pavements [3]. In aggregate surfaced pavement and flexible pavement road construction, there are a number of design procedures for using geosynthetic reinforcement [4]. Numerical investigation was done using 3-D FEM to analyse the effectiveness of an unpaved road network strengthened by a geogrid in terms of rutting minimization during continuous traffic loading [5]. The inclusion of grid reinforcement at the lower part of the black-top layer increased the pavement's stiffness and bearing capacity. The restraining effects was aided by its firmness and interlocking with the asphalt surface [6]. Vertical pavement deflection is reduced most when reinforcement is installed there at bottom of an asphalt concrete layer [7].

It's been discovered that incorporating geogrid strengthening there at base-bituminous concrete interface reduces fatigue strain the most. When the reinforcement is positioned at the interface of the base and subgrade layers, the vertical strain is reduced the most [8]. Another study used a FEM simulation to investigate how installing a geosynthetic membrane at the base-subgrade interface of a flexible pavement layer decreased rut depth [9].

ABAQUS is a finite element model (FEM) tool designed to analyse different varieties of structures. The objectives of the study are the modelling of pavement with and without geogrid using ABAQUS and to evaluate the variation in surface deformation after reinforcing with geogrid.

2 Methodology

2.1 Material Behavior

Unreinforced Section

The materials data used during the simulations was believed to be as real as possible, based on recent literature research and IRC 37-2018. Flexible pavement section includes 4 layers, surface, base, sub base, subgrade. The layer thickness is selected according to the requirements given in [10]. Table 1 lists the material parameters of the pavement used for the study.

Reinforced Section

Type of material used as reinforcement is Geogrid. Apertures of the grids are big enough to permit soil strike through from one face to the other. They are located between adjoining pairs of longitudinal and transverse ribs. Geogrid properties utilized in the analysis are shown in the Table 2.

Table 1 Mechanical materials data for each flexible pavement layer

Pavement layer	Layer thickness (mm)	Elastic modulus (MPa)	Poisson's ratio (μ)
Bituminous layer with VG30	80	2000	0.35
Unbound granular layer over CTSB sub-base	100	300	0.35
Cement treated sub-base (CTSB)	150	600	0.25
Subgrade	500	76.827	0.35

Table 2 Properties of geogrid [6]

Material model	Linear elastic
Axial stiffness	200–1000 KN/m
Aperture size	33 × 33 mm
Shape of aperture opening	Square
Ultimate tensile strength	20 KN/m
Mass density	2440 kg/m^3
Elastic modulus (E)	400 MPa
Poisson's ratio	0.30
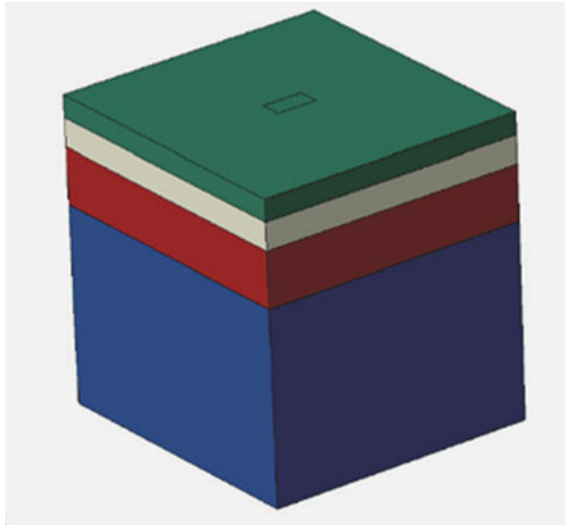
Fig. 1 FEM model of typical pavement section

2.2 Pavement Model Using ABAQUS

Two stretches of pavement were created. The first is unreinforced, and the second is reinforced with a geogrid positioned at the surface-base contact.

Figure 1 shows a three-dimensional representation of a FEM model used in ABAQUS for a typical pavement structure. It is made up of four layers: a bituminous surface layer, a base layer, a sub-base layer, and a subgrade layer. A three-dimensional model with thickness 0.003 m and open lattices was used to model the grid at the Surface-Base interface in the reinforced section, as shown in Fig. 3. A configuration of geogrid section modelled in ABAQUS software is represented in Fig. 2. The pavement surface was designed about 1×1 m dimension and having a total thickens of 0.83 m. The layers have thickness respectively as bituminous layer (80 mm), base (100 mm), subbase (150 mm) and subgrade (500 mm).

All pavement layers were considered to have a linear elastic model. The contact at the surface-geogrid and the geogrid-base interface in the reinforced section is due to a tangential and a normal component. A hard contact type and a penalty type behaviour is applied for the normal and tangential component respectively.
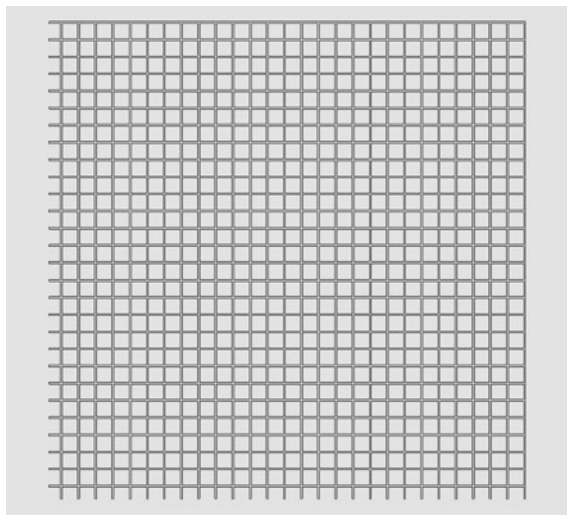
Fig. 2 Configuration of geogrid
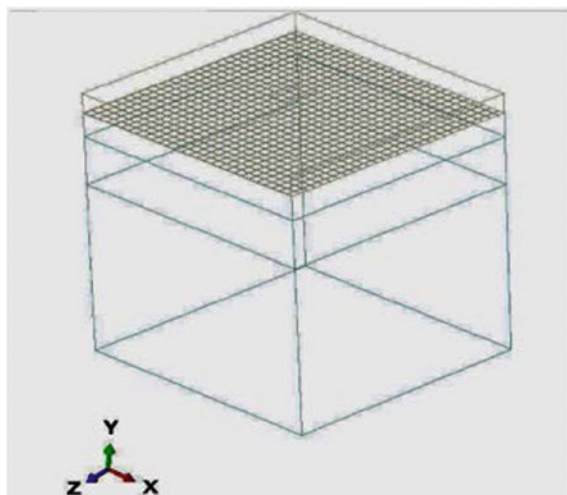
Fig. 3 FEM Model of reinforced section

2.3 *Load and Boundary Conditions*

A load equivalent to one-half of axle load (PAxle = 80 kN, therefore P = 40 kN) was provided as automobile traffic, results in a pavement pressure of 3.55 MPa. It was applied to a 150 × 75 mm rectangular tyre contact area. To minimize the influence of stress distribution, boundary conditions were chosen. Model is constrained at

the bottom and on other faces movements except the normal directions are fully restrained.

Since mesh refinement has been the most essential aspect in calculating accurate results in the pavement section, the densest mesh is necessary for top layer, that's where the load applied. Pavement layers were meshed with eight-node linear brick elements, while the grid layer was meshed with four-node quadrilateral membrane elements.

3 Results

A series of simulations have been carried out to examine the benefits provided by the usage of a geogrid against permanent deformation and rutting in a pavement system reinforced by geogrid at the Surface-Base interface.

3.1 Analysis of Unreinforced Paved Section

Unreinforced pavement section is analysed and results are compared with behaviour of reinforced flexible pavement. The total deformation, stress values are shown in Figs. 4 and 5 respectively.
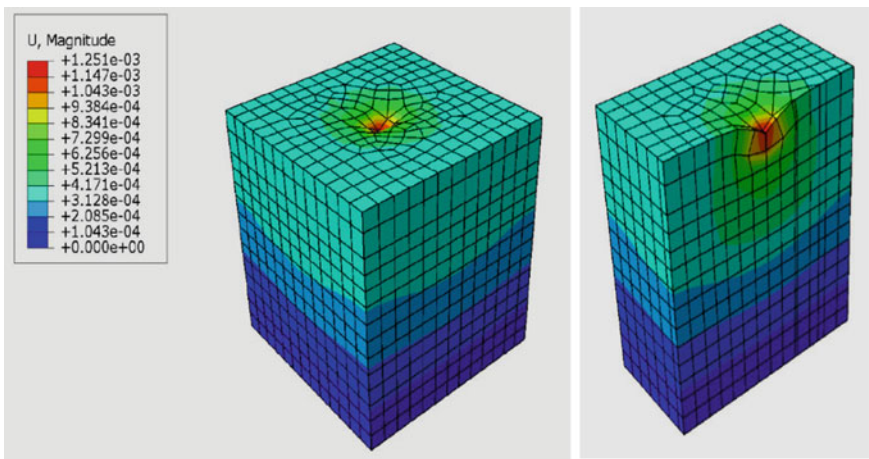
Fig. 4 Total permanent displacements in unreinforced section
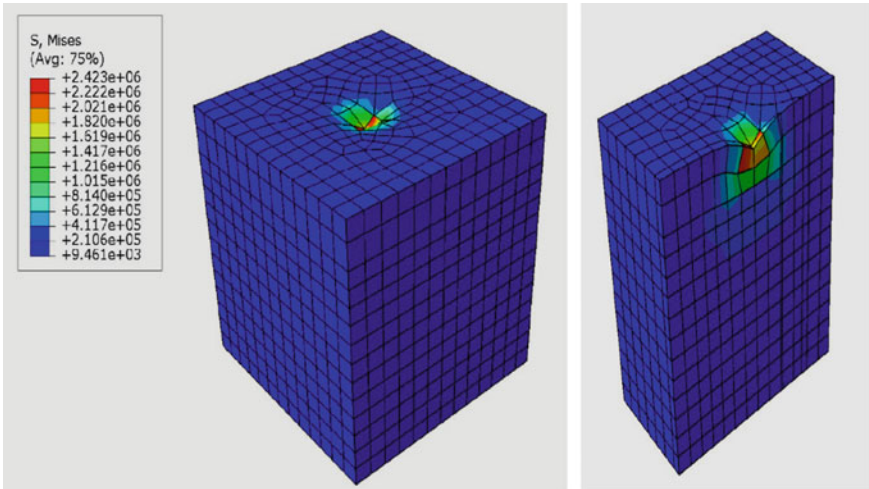
Fig. 5 Stress in unreinforced section
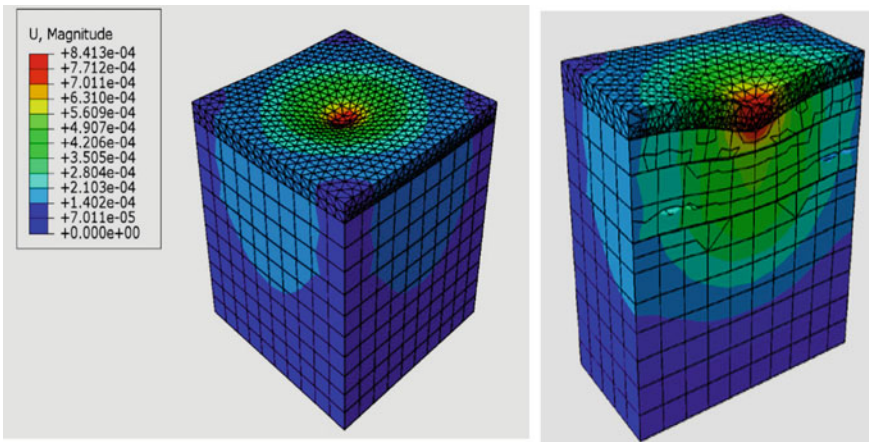
Fig. 6 Total permanent displacements in reinforced section

3.2 Analysis of Paved Section Reinforced with Geogrid

The final vertical surface displacements after loading, are about 0.00125 and 0.000841 m for unreinforced and reinforced section respectively. The magnitude of stress is reduced by 48.9%. The total deformation and stress values are shown in Figs. 6 and 7 respectively.
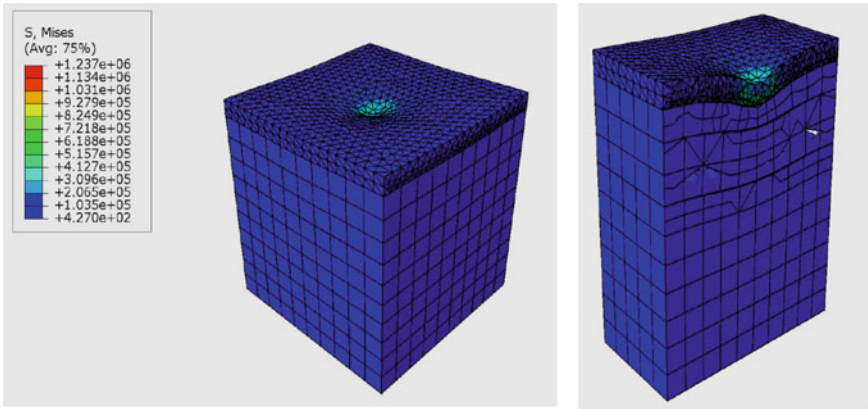
Fig. 7 Stresses in reinforced section
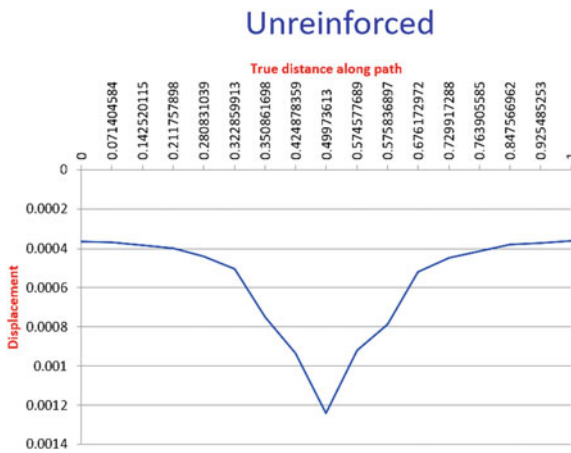
Fig. 8 Unreinforced section

3.3 Pavement Surface Deformation Profiles

Surface deformation profiles for sections with and without geogrid reinforcement are shown in Figs. 8 and 9 respectively.

These results obtained clearly demonstrate the benefits of flexible pavement reinforcement. When geogrid is placed in the surface-base contact, it results in a 32 percent decrease in surface rutting.
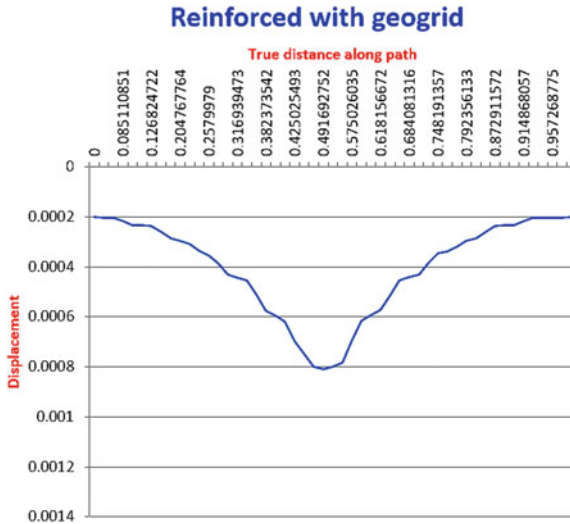
Fig. 9 Reinforced section

4 Conclusion

In the study, FEM is used to study the advantageous impact of reinforcement in pavement layer. According to the FEM simulation performed in ABAQUS on road sections, unreinforced and reinforced, each subjected to the identical wheel loading, adding Geogrid at the Surface-Base interface results in a substantial change in pavement behavior.

For the same thickness and load circumstances, the FEM analysis revealed that geogrid-reinforced pavement has less deformation than unreinforced flexible pavement. The inclusion of geogrid reduces surface deformation by around 32%, resulting in a significantly longer road life. The reason for this is that the application of reinforcement, which strengthens the asphalt layer's tensile strength and decreases vertical stresses on the underlying layers, resulting in less surface deformation under repeated traffic.

The interlocking effect, which increases the tensile strength of the pavement surface, lowers the vertical stresses on the underlying layers, resulting in less surface deformation.

References

1. Ahirwar, S.K., Mandal, J.N.: Finite element analysis of flexible pavement with Geogrids. Procedia Eng. **189**, 411–416. Saint Petersburg (2017). Transportation Geotechnics and Geoecology, TGG 2017

2. Deshmukh, R., Patel, S., Shahu, J.T.: Finite element modeling of geogrid-reinforced unpaved road. Adv. Water Resour. Transp. Eng. **149**, 205–213 (2021)
3. Hook, K., Penman, J.: The Use of Geogrids to Retard Reflective Cracking on Airport Runways, Taxiways and Aprons. CRC Press, Pavement Cracking (2008)
4. Kumar, R., Ali, M., Singh, U.: A study review on geosynthetics use on flexible pavement design. Int. J. Eng. Res. Technol. **9**(6), 886–888 (2020)
5. Leonardi, G., Bosco, D.L., Palamara, R., Suraci, F.: Finite element analysis of geogrid–stabilized unpaved roads. Sustainability **12**(5), 1929 (2020)
6. Ling, H.I., Liu, Z.: Performance of geosynthetic-reinforced asphalt pavements. J. Geotech. Geoenviron. Eng. **127**(2), 177–184 (2001)
7. Moayedi, H., Kazemian, S., Prasad, A., Huat, B.K.: Effect of geogrid reinforcement location in paved road improvement. J. EJGE **14**, 3313–3329 (2009)
8. Pandey, S., Rao, K.R., Tiwari, D.: Effect of geogrid reinforcement on critical responses of bituminous pavements. In: Proceedings of the 25th ARRB Conference; Shaping the Future: Linking Policy, Research and Outcomes, Perth, Australia (2012)
9. Wathugala, G.W., Huang, B., Pal, S.: Numerical simulation of geogrid reinforced flexible pavements. Transp. Res. Rec. **1534**(1), 58–65. Washington, D.C. (1996)
10. IRC: 37-2018 Guidelines for the Design of Flexible Pavements, Indian Road Congress, New Delhi

A Study on Geopolymer Mortar Containing Fly Ash and Dredged Clay

Sreedevi Lekshmi and J. Sudhakumar

Abstract In this study, an effort is made to experimentally evaluate the durability properties of fly ash-dredged clay based geopolymer mortar. Low calcium fly ash was used in the study as source material for geopolymer. The fly ash was replaced with low grade waste clay dumped by dredging. The dredged waste clay was collected from Koilandy, Calicut, Kerala. The geopolymer mortar was synthesized using 7 M NaOH solution with sodium silicate to sodium hydroxide ratio of 2.5 and percentage of dredged clay used was 25% at 75 °C of oven curing temperature. The durability performances in terms of water absorption, abrasion resistance acid attack resistance and sulfate attack resistance were evaluated.

Keywords Geopolymer · Dredged clay · Durability · Fly ash

1 Introduction

1.1 General

The need for concrete as a construction material is mushrooming the demand for Portland cement. The extensive demand for cement over the globe results in drastic climatic change due to global warming and hence environmental protection has become a major concern for mankind. Many researches were conducted to find an alternate material that could be used by partial or full replacement of cement so as to reduce the carbon dioxide emission due to cement production. This led to the invention of an alternate binder by Davidovits which make use of industrial or agricultural waste which are of rich source of aluminates and silicates activated by an alkaline medium which results in the formation of a non-cementitious binder called geopolymer. This method eliminates the usage of cement to the fullest.

Geopolymerization is the chemical process that rapidly transforms the aluminosilicate source material partially or fully into the three dimentional polymeric network.

S. Lekshmi (✉) · J. Sudhakumar
Civil Engineering Department, National Institute of Technology Calicut, Kozhikode, India
e-mail: sreeevilekshminair@gmail.com

Geopolymerization is an exothermic reaction which occur in multistep which takes place simultaneously as follows [1].

  i.   Dissolution of aluminosilicate source in alkaline activator solution.
 ii.   Rearrangement and diffusion of dissolved ions to small coagulated formations.
iii.   Polycondensation to form aluminosilicate gel phase.
 iv.   Setting and hardening to develop hardened geopolymer specimens.

The commonly used alumina silicate rich source materials in geopolymerization are fly ash, ground granulated blast furnace slag, metakaoline, etc. The chemical formula of clay is $Al_2O_3.2SiO_2.2H_2O$ [2]. Hence as apparent from literature that clays are good source of aluminates and silicates, it possesses the peculiar property of source material in geopolymers. Priyadharshini et al. (2017) reported that the unutilized excavated clay obtained from construction activities such as excavations, tunnelling, mining, dredging, etc. are referred as waste clay or soil waste, causes health and environmental issues due to dumping in open spaces [3].

1.2 Research Significance

In the present study, the feasibility of using dredged clay as source material in class F fly ash based geopolymer mortar has been investigated in terms of compressive strength and durability properties. From the observations, the GPM developed can be utilized as insulating material, blocks, etc. and hence the environmental impacts related with the dumping of dredged clay can be rectified to some extent.

2 Materials and Methods

2.1 Materials

The dredged clay was collected from Calicut, Kerala (Fig. 1a). The low calcium fly ash or class F fly ash used in the study was collected from Mettur, Tamil Nadu, India (Fig. 1b). The locally available silica rich sand collected from river bed was used in the study as fine aggregate (Fig. 1c). The alkaline solutions used were sodium hydroxide (Fig. 1d) and sodium silicate (Fig. 1e). For performing the study, the parameters such as molarity of NaOH solution, ratio of sodium silicate to sodium hydroxide (S/N), percentage of dredged clay and temperature oven curing was taken from the existing literature. 7 M NaOH solution was prepared by dissolving NaOH pellets of 97% purity in distilled water. The ratio of S/N was taken as 2.5. Percentage of dredged clay was taken as 25% and the temperature of oven curing was taken as 75 °C [4].
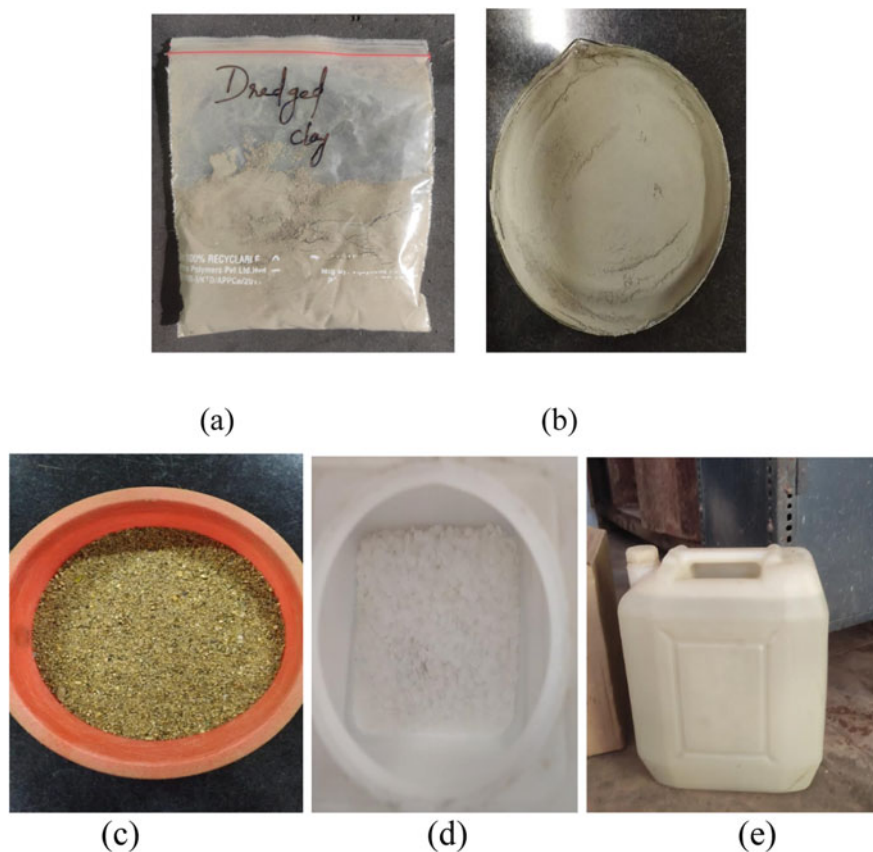
Fig. 1 Various materials used in the study **a** dredged clay **b** fly ash **c** river sand **d** NaOH pellets **e** sodium hydroxide solution

2.2 Experiments

Workability

The workability was performed based on ASTM C1437-15 [5]. The workability for all design trials were maintained as $110 \pm 5\%$. The following equation was used for determining the mortar flow (1).

$$\text{Flow} = (D_{avg} - D_0)(100/D_0) \tag{1}$$

where D_{avg} is the average base diameter and D_0 is the actual base diameter.

Compressive Strength

The compressive strength (CS) of geopolymer mortar (GPM) cube specimens was determined as per ASTM C109 [6]. The cube specimens (6 number) of 5 cm size were used for the study and the calculation were based on Eq. (2).

$$f_m = P/A \tag{2}$$

where, f_m is the CS in MPa, P is the maximum load in N and A is the area of loaded face of the specimen in mm^2.

Water Absorption

The water absorption was tested using ASTM C 642 [7]. The cube specimens (3 number) of 5 cm size were used for the study. The weight of the specimen (W_1) after taken from water and the weight of the dry specimen (W_0) was observed. The water absorption was calculated using the Eq. (3).

$$W_A = (W_1 - W_0)(100/W_0) \tag{3}$$

Abrasion Resistance

The abrasion resistance was tested based on IS 15658: 2006 [8]. 4 cube specimens were tested and averaged. The calculation was based on Eq. (4)

$$\Delta V = \Delta m/PR \tag{4}$$

where, ΔV is the volume reduction after sixteen cycles in cm^3, Δm is the mass reduction after sixteen cycles in grams and PR is the specimen density in g/mm^3.

Chemical Attack Resistance in Terms of Acid and Sulfate Attack

ASTM C1898-20 and ASTM C 267-20, respectively was used to study the acid and sulfate attack resistance of GPM cube specimens. GPM specimens were immersed in 3% H_2SO_4 and sulfate solution for a duration of 3 months. Solutions were changed frequently on monthly basis to maintain the concentration uniform throughout the duration. The specimen weight (3 specimens) and compressive strength (6 specimens) was noted before and after exposing to the solutions [9, 10].

Fourier Transform Infrared Spectroscopy (FTIR Analysis)

Microstructural characterization in terms of FTIR analysis was performed to identify the effect of addition of dredged clay on the reordering of the structural functional group of fly ash based geopolymer mortar.

3 Results and Discussion

3.1 Microstructural Characterization of Dredged Clay

Microstructural characterization of dredged clay using scanning electron microscopy (SEM) and thermogravimetric analysis (TGA) was performed. Morphological aspects of dredged clay were revealed by SEM analysis. SEM photographs revealed the presence of organic deposits with rounded and flakey particles (Fig. 2a). Loss of mass by removal of water and organic matter on heating is given by the TG curve for dredged clay as shown in Fig. 2b. DTA curve shows the exothermic and endothermic behaviour of marine clay upon heating. The upward slope from 90 to 209 °C is associated with the exothermic behaviour in relation with the combustion of organic matter present in dredged clay. The tendency of the specimens towards an exothermic effect around 400 °C in DTA is attributed to the structural change in the clay.

Dredged clay had a grey colour with plastic limit, liquid limit and shrinkage limit of 8%, 51% and 17%, respectively. The specific gravity, pH and electrical conductivity of the dredged clay was obtained as 2.42 mV, 7.3 mV and 159.5 mV, respectively. The oxide composition of dredged clay used in the study is reported in Table 1 [11]. The fine aggregate used was river sand having specific gravity, fineness modulus and pH of 2.67, 3.39 and 7.2, respectively.

3.2 Workability

The liquid alkaline to binder ratio obtained to maintain a workability between 105 to 115% was 0.75 for the mix. 1:1 mortar mix was used in the study [1, 4].

3.3 Compressive Strength, Water Absorption and Abrasion Resistance

The CS, water absorption and abrasion resistance of GPM specimens containing dredged clay in raw state is reported in Table 2. The specimens were tested on the 7th day after 24 h of oven curing. Ogundiran et al., 2015 stated that the CS increased with increase in concentration of NaOH solution which is attributed to polycondensation of alumina and silica species after its dissolution in the alkaline medium. Increased NaOH concentration in the alkaline solution accelerates the polymerization process and the polymerization products of reactive ingredients filled up the pores of specimen which reduce the porosity and hence water absorption. It was reported by Mo et al., 2014 that at higher curing temperature the porosity of the matrix increases which resulted in increase in water absorption (Fig. 3).
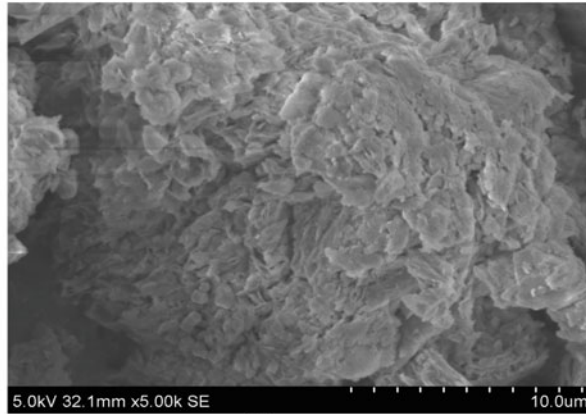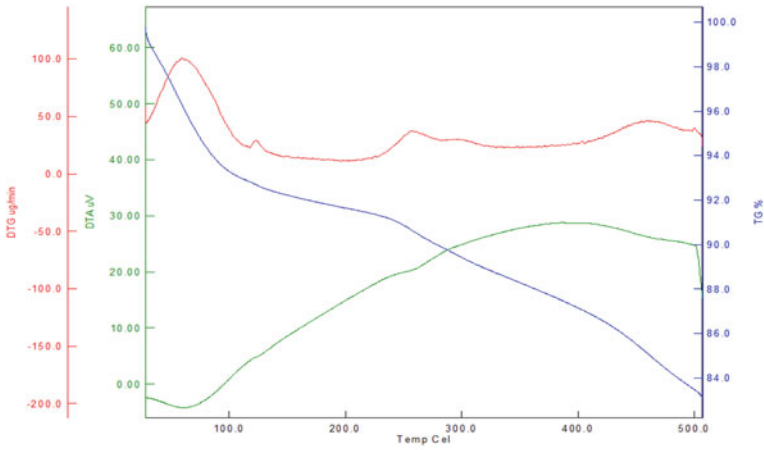
Fig. 2 **a** SEM micrograph **b** TGA of dredged waste

Table 1 Chemical oxide composition of dredged clay

Oxides	SiO_2	Al_2O_3	CaO	MgO
First	51.81	21.97	0.87	1.91

Table 2 Test results of GPM specimens

Properties	Compressive strength (MPa)	Water absorption (%)	Abrasion resistance (cm^3)
GPM	7.18	12.83	16.05

Fig. 3 Test setup for abrasion testing

3.4 Chemical Attack Resistance in Terms of Acid and Sulfate Attack

The loss in weight and loss in compressive strength of dredged clay-based GPM was observed as 4.28% and 34.53%, respectively in acid medium. Again, the loss in weight and loss in compressive strength of dredged clay-based GPM in sulfate medium was observed as 6.67% and 34.58%, respectively.

The study was performed by exposing cube specimens to chemical attack and evaluating the change in compressive strength before and after exposure for 3 months. The breakage of Si-O-Si and Si-O-Al bonds due to depolymerization resulted in the reduction in CS. The formation of pores with the leaching of aluminosilicate gel and its enlargement with the duration of exposure also reduced the compressive strength [12–15].

3.5 FTIR Analysis

The FTIR spectra in the infrared region between 350 to 4000 cm^{-1} are shown in Fig. 4. The characteristic band between 441 to 462 cm^{-1} represents the bending vibration of Si-O bond. The band between 450 to 500 cm^{-1} and 950 to 1250 cm^{-1} represents the Si-O-Si and Si-O-Al bonds. The symmetric stretching of Si-O-Si and Si-O-Al bond was represented by the characteristic band between 1028 to 1049 cm^{-1}. At 1000 cm^{-1}, the stretching vibration of Si-O/Al-O was observed. The shifting vibration from 900 to 990 cm^{-1} showed the formation of calcium alumina silicate hydrate.

Fig. 4 FTIR analysis of GPM
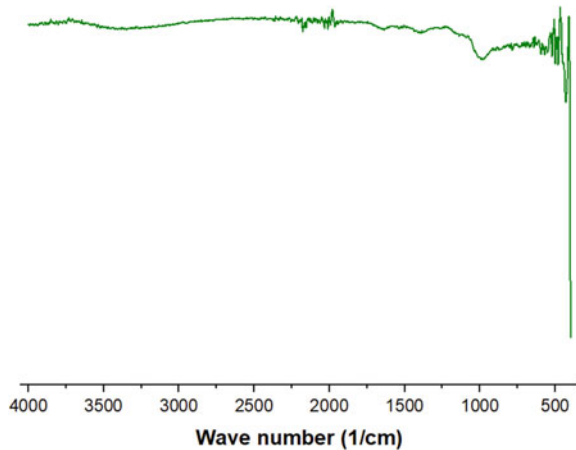
4 Conclusion

The synthesis of geopolymer mortar using class F fly ash and dredged clay was performed in the study. The study was performed on GPM specimens containing dredged clay in raw state. A compressive strength of 7.18 MPa with a water absorption of 12.83% was obtained. The performance of GPM in terms of strength and durability, can be improved by adopting treatment methods such as calcining or thermally treating the dredged clay, mixing the clay with lime, ground granulated blast furnace slag, etc. It can be concluded from the test results that the GPM containing 25% dredged waste, 75% class F fly ash with 7 M NaOH solution and sodium silicate to sodium hydroxide ratio of 2.5 at 75°C of oven curing temperature can be utilized in developing pre-fabricated blocks of low strength. The presence of C-S-H was revealed by FTIR analysis.

References

1. Liew, Y.M.; Heah, C.Y.; Mohd Mustafa, A.B.; Kamarudin, H.: Structure and properties of clay-based geopolymer cements: a review. Prog. Mater. Sci. **83**, 595–629 (2016). https://doi.org/10.1016/j.pmatsci.2016.08.002
2. Ogundiran, M.B., Kumar, S.: Synthesis and characterization of geopolymer from Nigerian Clay. Appl. Clay Sci. **108**, 173–181 (2015). https://doi.org/10.1016/j.clay.2015.02.022
3. Priyadharshini, P., Ramamurthy, K., Robinson, R.G.: Excavated soil waste as fine aggregate in fly ash based geopolymer mortar. Appl. Clay Sci. **146**, 81–91 (2017). https://doi.org/10.1016/j.clay.2017.05.038
4. Lekshmi, S., Sudhakumar, J.: Engineering and durability performances of fly ash based geopolymer mortar containing aluminosilicate rich flood soil waste with and without lime treatment. Silicon. https://doi.org/10.1007/s12633-021-01391-y
5. ASTM, C1437–Standard test method for flow of hydraulic cement mortar, ASTM International, West Conshohocken, PA, pp. 1–2

6. ASTM C109/109M-16a, Standard test method for compressive strength of hydraulic cement mortars (Using 2-in. or cube specimens), ASTM International, West Conshohocken, PA, pp. 1–10

7. ASTM C 642: Standard Test Method for Rate of Water Absorption, ASTM International, West Conshohocken, PA, pp. 1–4

8. IS:15658-2006: Indian Standard Precast Concrete Block for Paving-Specification, Bur. Indian Stand.. New Delhi, India, pp. 1–27

9. ASTM C1898: Standard Test Methods for Determining the Chemical Resistance of Concrete Products to Acid Attack, ASTM International, West Conshohocken, PA, pp. 9–10. https://doi.org/10.1520/D1898-20.1

10. ASTM C267-20 Standard Test Methods for Chemical Resistance of Mortars, Grouts, and Monolithic, Current, ASTM International, West Conshohocken, PA, pp. 1–6. https://doi.org/10.1520/C0267-20.2

11. Benjamin, B., Lekshmi, S., Zachriah, S., Sudhakumar, J., Suchithra, T.V.: A study on marine clay as fine aggregate in microbial cement mortar mix. In: Materials Today Proceedings, April 2022.https://doi.org/10.1016/j.matpr.2022.04.132

12. Guo, L.: Sulfate resistance of hybrid fiber reinforced metakaolin geopolymer composites. Compos. Part B **183**, 107689 (2020). https://doi.org/10.1016/j.compositesb.2019.107689

13. Jin, M., Zheng, Z., Sun, Y., Chen, L., Jin, Z.: Resistance of metakaolin-MSWI fly ash based geopolymer to acid and alkaline environments. J. Non. Cryst. Solids **450**, 116–122 (2016). https://doi.org/10.1016/j.jnoncrysol.2016.07.036

14. Saranya, P., Nagarajan, P., Shashikala, A.P.: Performance studies on steel fiber-reinforced ggbs-dolomite geopolymer concrete. J. Mater. Civ. Eng. **33**(2), 04020447 (2021). https://doi.org/10.1061/(asce)mt.1943-5533.0003530

15. Saranya, P., Nagarajan, P., Shashikala, A.P.: Development of ground-granulated blast-furnace slag-dolomite geopolymer concrete. ACI Mater. J. **116**(6), 235–243 (2019). https://doi.org/10.14359/51716981

Utilisation of Nano Titanium Dioxide as a Soil Stabiliser

Ashima J Catherine, K Athulya, S Chandrakaran, and N Sankar

Abstract Recent advancements in nanotechnology show great potential in addressing many challenges. Nanoparticles in cementitious materials have been extensively documented due to its low cost, safety, and chemical stability; nevertheless, few studies have been undertaken to explore the impacts of nanoparticles on the stabilisation of soils. In the present study, the ability of a nanoparticle to act as a soil stabiliser is investigated. The strength properties of three cohesive soils combined with a nanoparticle were studied. The nanoparticle used in this study is nano titanium dioxide (N-TiO$_2$). Nano titanium dioxide in the range of $0.5-1.2$ per cent was shown to have an effect on the behaviour of three cohesive soils. The cohesive soils selected for the study were marine soil, paddy soil and laterite soil. At various curing times, a series of consistency limits and unconfined compression tests were performed. The experimental results indicate a decrease in the liquid limit and plasticity index of soils with the increase in N-TiO$_2$. The addition of nano titanium dioxide has brought about an improvement in the strength of the cohesive soils. The lowering of the plasticity index was unaffected by the curing time. The study implies that even trace levels of N-TiO$_2$ can affect soil properties. Hence N-TiO$_2$ could be used as an effective agent in stabilising cohesive soils.

Keywords Cohesive soils · Nano titanium dioxide · Plasticity index · Soil stabilisation · Unconfined compressive strength

1 Introduction

In recent times, in most civil engineering projects, ground improvement has become a critical stage. There are, at present, an extensive collection of ground improvement techniques to choose from for application to various types of ground [1]. As sustainable development is a crucial factor in any work, selecting a sustainable, eco-friendly method for ground improvement is often a complex task.

A. J. Catherine (✉) · K. Athulya · S. Chandrakaran · N. Sankar
Department of Civil Engineering, National Institute of Technology Calicut, Calicut, India
e-mail: ashima0811@gmail.com

However, of all the ground improvement techniques, integration of admixtures into the soil is the ancient and extensive method adopted [2, 3]. Chemical stabilisation is a general term for all those methods in which chemical rather than physicochemical and physical interactions play a vital role. It covers how one or more chemical compounds are introduced to the soil for treatment [4]. The traditionally used additives are lime, cement, bitumen, fly ash, silica fume. Some of the primary reactions between soil and additives are hydration, ion exchange, pozzolanic reaction (cementation), flocculation, precipitation, polymerisation, oxidation, and carbonation [4].

In recent years, nanoparticles have piqued scientists' curiosity in a variety of civil engineering applications. The smallest particles found in soil are nanoparticles, which range in size from 1 to 100 nm. In this paper, an attempt is made to study the effect of nanoparticle addition on the plasticity behaviour and strength characteristics of cohesive soils.

The compressive strength of clay soil was found to improve using nanosilica [5]. Lime was added at a rate of 5% by weight, and the nanosilica levels of the clayey soil–lime mixture was 1, 3, and 5% by weight. The findings revealed that adding nanosilica to the soil–lime mixture improves the UCS significantly. The optimum amount of nanosilica was determined to be 3% based on the findings.

The types of nanoparticles that are most commonly used in cementitous composites are SiO_2, TiO_2, Al_2O_3, and carbon nanotube. In a study the effect of nanosilica on the Atterberg limits, hydraulic conductivity and the compressive strength of cement-treated residual soil was evaluated [6]. The specimens were prepared using kaolinite clay with cement and nanosilica. The results indicate that the addition of nanosilica reduced PI and exhibited a significant (80%) increase in its compressive strength. The lowest conductivity among the specimens occurred when 0.4% nanosilica was added [7].

A study was conducted to exhibit the effect of nano TiO2 on the characteristics of Shanghai clayey silt - alluvial soil in the Yangtze River Estuary [8]. The Shanghai clayey silt was combined with nano TiO2 of various size groups and content. The findings demonstrate that nano TiO2 significantly enhance the acid resistance of sample while lowering the plasticity index to some extent.

In a study conducted to evaluate the effect of nano sized particles of titanium dioxide, it was inferred that addition of it lowers the plasticity characteristics of soft soil. The presence of nano titanium dioxide promotes the improvement of shear strength thus causing reduction in consolidation settlement [9].

This study attempts to cover the effect of Nano Titanium dioxide as stabilising agent on three cohesive soil samples namely, marine soil, paddy soil and laterite soil. While numerous investigations are and have been carried out to understand the behaviour of cohesive soil treated with organic and inorganic additives, minimal work has been reported on the use of nano sized titanium dioxide for the stabilisation of soil, in general. However, several studies have been reported [7, 10], stating that nanoparticles by themselves improve soil properties.

2 Materials

The present study utilizes three types of natural soils namely, marine soil, paddy soil and laterite soil. The marine soil was procured from Thevara, which marks the southwest boundary of Kochi, Kerala. The paddy soil was collected from Mavoor, Calicut. The third type, laterite soil, was procured from the premises of NITC campus. Sufficient amount of soil was acquired from two metre depths below the ground level leaving the top layer of soil. After being transferred to the laboratory, the soil specimens were air-dried, pulverised manually, sieved through a 0.420 mm sieve and stored in large containers for subsequent use as part of the process. The soil samples used have been characterized to determine the selected properties, given in Table 1. All the specimens in this study were prepared and tested, conforming to the standard testing procedures approved by the Bureau of Indian Standards.

The nanoparticle used in this study is Nano Titanium dioxide(N-TiO$_2$). It was collected from KMML, Kollam. It is a white coloured powder. The properties of Nano Titanium dioxide used are given in Table 2.

The current work scope is focused on the changes in the plasticity behaviour and unconfined compressive strength of nanoparticle treated soil systems. The use of nanoparticles in a soil mixture increases strength, decreases plasticity index, permeability, settlement, and volumetric strains. The optimum dosage of nanoparticle in the selected cohesive soil samples are determined.

Table 1 Properties of soil samples

Properties	Marine soil	Paddy soil	Laterite soil
Specific gravity	2.53	2.44	2.63
Sand(%)	19.0	22	20
Silt and clay(%)	81.0	78	80
Soil classification	MH	CH	CI
Liquid limit(%)	111	97	46
Plastic limit(%)	58	39	27
Plasticity index(%)	53	52	19
Unconfined compressive Strength(kPa)	47	78	166

Table 2 Properties of Nano Titanium dioxide

Composition	98% rutile
Particle size	30–40 nm
Specific surface area	10–45 m^2/g
Appearance	White powder
Bulk density	0.46 g/ml
pH	5.5–6.0

3   Methodology

The collected soil samples were transferred to the laboratory where they were air-dried, pulverized to 0.420 mm size. They were kept at room temperature, in large containers. In the first phase of this study, the properties of the three types of cohesive soil samples selected were determined. The plasticity and strength characteristics of cohesive soils mixed with N-TiO2 were determined in the second phase. The samples were mixed in dry form to ensure the uniform distribution of the stabilizing agent. The treated samples were mixed with optimum moisture content ($\pm 5\%$) at maximum dry density ($\pm 5\%$). The prepared samples were subjected to curing for 1,7,14, and 28 days. All tests were performed conforming to the standard procedures.

4   Results and Discussion

4.1   Plasticity Characteristics

The liquid limit and plastic limits of marine soil, paddy soil and laterite soil stabilised with N-TiO$_2$ were determined. The liquid limit test values of the three treated cohesive soils determined after the curing period of 7 and 28 days is represented in Figs. 1 and 2. The values of plastic limit and plasticity index of the stabilised soils after 7 and 28 days curing period are represented graphically from Figs. 3, 4, 5 and 6.

At the end of the curing period, a marked decrease in the liquid limit of soils treated with N-TiO$_2$ is observed. The results of marine soil and paddy soil showed a drop in the liquid limit from 111 to 61% and 97 to 56%. In the case of laterite soil, the decrease in liquid limit is comparatively less. The plastic limit and the plasticity

Fig. 1 Liquid limit after 7 days curing period
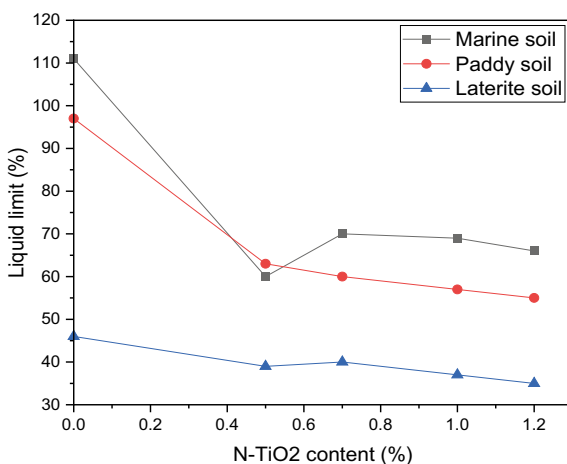
Fig. 2 Liquid limit after
28 days curing period
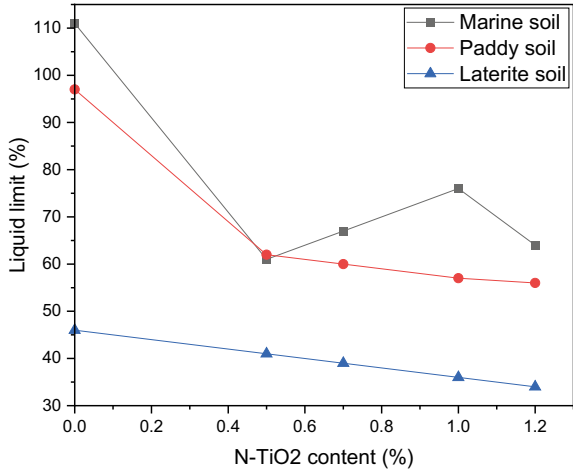
Fig. 3 Plastic limit after
7 days curing period
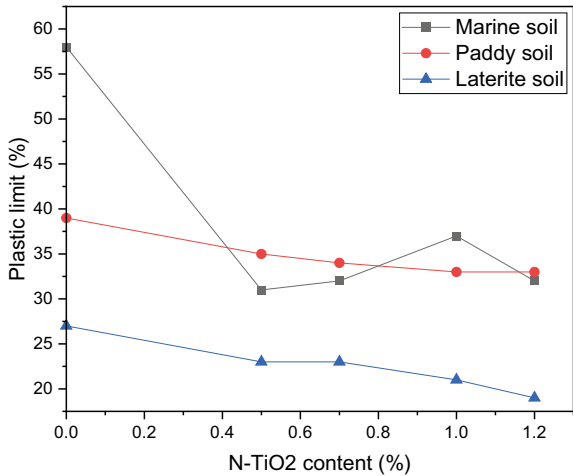
indices of treated marine soil suffers a reduction to 32% and 29%, respectively. The maximum decline being observed at 0.5% N-TiO$_2$ content. In the presence of increasing amount of N-TiO$_2$, the plastic limits and plasticity indices of paddy soil and laterite soil are found to decrease. It is worth noting that the plasticity behaviour of the soil samples is unaffected by the curing period.

The diffuse double layer is paramount in affecting soil plasticity, as it significantly controls the amount of water attracted to the surface of clay minerals. The formation of diffuse double layer occurs only on the external surface of clay particles. The volume of attracted water depends on the effective surface area of the soil and the thickness of the diffuse double layer [11]. The reduction in soil plasticity in the presence of N-TiO$_2$ may be attributed to the formation of an outer layer by the

Fig. 4 Plastic limit after
28 days curing period
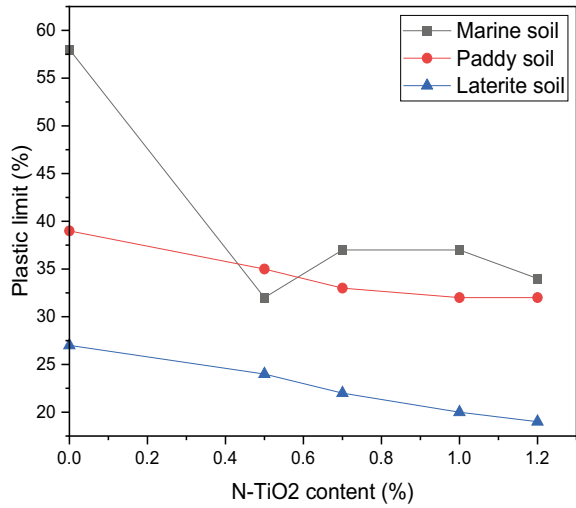
Fig. 5 Plasticity index after
7 days curing
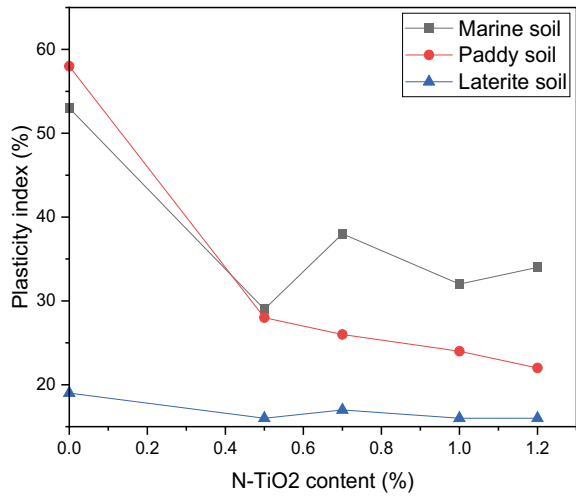
nanoparticle on the soil particles [10, 11]. This hinders the formation of double layer
leading to low values of plasticity.

4.2 Compressive Strength

The soils were mixed at varying proportions of N-TiO$_2$ by the dry weight of the soil.
The unconfined compression test was performed on soil samples prepared at their

Fig. 6 Plasticity index after 28 days period curing period
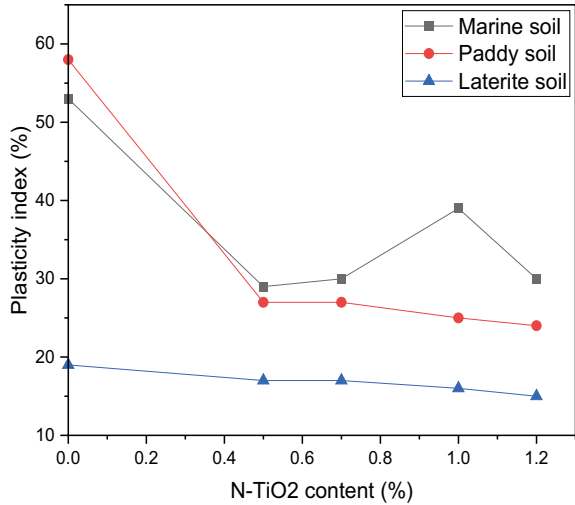
Fig. 7 Unconfined compressive strength after 7 days curing period
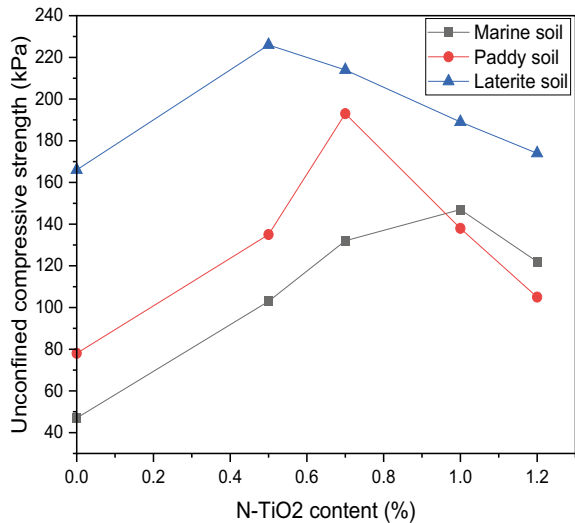
maximum dry densities after a curing period of 1,7,14, and 28 days. The results after 7 and 28 days curing period are plotted graphically in Figs. 7 and 8.

In the case of nanoparticle treated marine soil, the maximum strength gain of 164 kPa to 166 kPa is observed at 0.7–1% nanoparticle content. From the above results, the strength of paddy soil is also found to increase from 78 to 306 kPa at 0.7% N-TiO$_2$. It is observed that presence of N-TiO$_2$ contributes to the compressive strength of laterite soil from 166 to 234 kPa at a lower amount of 0.5% N-TiO$_2$. At increasing amount of nanoparticle there is a reduction in the increase in compressive strength of soils. However, ageing is found to have enhanced the compressive strength of soils.
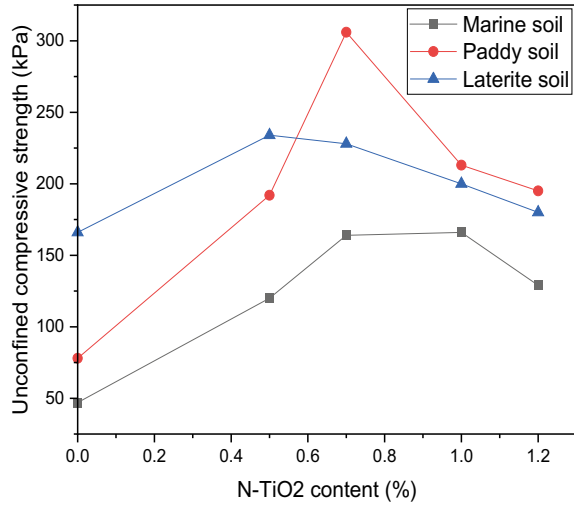
The larger specific surface area of nanoparticles may be the reason for the strength
improvement in soils [7].

5   Conclusions

In this study, liquid and plastic limit, and unconfined compression tests on N-TiO$_2$-
modified cohesive soils under different content of N-TiO$_2$ have been carried out. The
following conclusions may be drawn:

- N-TiO2 is an effective soil additive in improving the plasticity behaviour of
  cohesive soils.
- The liquid and plastic limits of N-TiO$_2$ stabilised cohesive soils decreased. The
  increasing amount of N-TiO$_2$ has contributed to the decline in the values of paddy
  and laterite soils. Similar effect is traced in the values of plasticity index.
- From this study, the curing period has not been pivotal in the improvement of
  plasticity behaviour of cohesive soils.
- The large specific surface area of N-TiO2 has benefitted in improving the strength
  of marine soil, paddy soil and laterite soil.
- In the case of marine and paddy soils, there has been a strength increase of more
  than 250 at 0.7% N-TiO$_2$ compared to nano-free soil samples. Nevertheless, the
  presence of 0.5% N-TiO$_2$ has contributed to the improvement by 40% in the case
  of N-TiO$_2$ modified laterite soils.
- The study implies that even trace levels of N-TiO$_2$ can bring about pronounced
  effect in soil properties.

References

1. Evans, J., et al.: Introduction to ground improvement engineering (2021)
2. Afrin, H.: A review on different types soil stabilization techniques. Int. J. Trans. Eng. Technol. **3**(2), 19–24 (2017)
3. Zhu, Z., Liu, S.: Eng. Geol. **97**(3–4), 192–198 (2008)
4. Winterkorn, H.F., Pamukcu, S.: Soil Stabilization and Grouting. In: Fang, H.Y. (ed.) Foundation Engineering Handbook. Springer, Boston (1991)
5. Mamaghanian, J., Gelsefidi, S., Alireza, S., Jaber, M.: Stabilization of a weak low plasticity clay soil using nanomaterial. In: 5iYGEC, Paris (2018)
6. Bahmani, S., Huat, B., Asadi, A., et al.: Constr. Build. Mater. **64**, 350–359 (2014)
7. Ghasabkolaei, N., Janalizadeh, A., Roshan, N.: Archiv. Civ. Mech. Eng. **17**(3), 639–650 (2017). https://doi.org/10.1016/j.acme.2017.01.010
8. Jili, Q., Yawen, Z., et al.: Sci. Eng. Compos. Mater. **28**, 169–179 (2021)
9. Babu, S., Joseph, S.: Effect of nano materials on properties of soft soil. Int. J. Sci. Res. (IJSR) **5**(8), 634–637 (2016)
10. Zhang, G.: Soil nanoparticles and their influence on engineering properties of soils. In: Advances in Measurement and Modeling of Soil Behavior, Geo-Denver 2007, pp. 1–13. Geotechnical Special Publication (2007)
11. Zhang, G., Germaine, J., et al.: Index properties of a highly weathered old alluvium. Geotechnique **54**(7), 441–451 (2004)

Structural Performance of Stone Prism Encased Composite Columns as Environment Friendly Structures

M. M. Jamshiya and S. Usha

Abstract Concrete with cement as binder is the most common construction material used in building industry. Carbon dioxide, a potent greenhouse gas produced during cement manufacture causes environmental pollutions. In the present study, granite waste from quarry industry is utilized to reduce cement concrete in concrete filled steel tube columns. Large amount of natural stone wastes is spawned from various activities in the quarry and industries. Major part of granite waste is dumped in open lands. A modified type of square concrete-steel tube structural member with waste granite square stone prism in central portion of the infilled concrete is investigated by utilizing stone waste. The structural behavior of the square stone prism encased square cross-sectional concrete-filled steel tube (SCFST) members under axial and eccentric loading conditions are studied using ANSYS software with different height specimens. The primary parameters considered were the size of the stone prism ($s = 75$, 100 or 125 mm), wall-thickness of the steel tube ($t = 6.0, 8.0$ or 12 mm), and concrete strength ($fcu = 62.3$ or 107.0 MPa) [1]. The effect of the parameters on the failure mechanism, load-carrying capacity, load versus deformation response, and ductility of the SCFST specimens are investigated. Then the analytically obtained results of each square cross sectional SCFST specimen will be compared with conventional CFST columns.

Keywords Square granite stone prism · Composite columns · Environment friendly structures · ANSYS

M. M. Jamshiya (✉) · S. Usha
Sree Narayana Gurukulam College of Engineering, Cochin, India
e-mail: Jemshiyas123@gmail.com

1 Introduction

Concrete with cement as binder is the most popular construction material used in building industry. During cement manufacture carbon dioxide is emitted which causes environmental pollutions. 900 kg of CO_2 is released during one ton of cement production. Utilization of waste materials reduces the production cost and environmental pollution. Large amount of natural stone wastes is spawned from various activities in the quarry and industries. Out of this huge quantity of waste, a little recycled and rest is dumped in open lands.

Stone is an essential and more permanent building material in construction than other natural building materials. It can be used in building for flooring, masonry, dams etc., depends on availability. Building stones has possess high strength and durability. Stone have been considered as one of the popular building materials from olden days due to its strength and economy. A large number of residential buildings have been constructed with natural stone blocks since ancient times, especially in China, where hard, tough and durable natural stones were readily available.

A new type of square concrete filled steel tube structural member is proposed by replacing the central portion of the infilled concrete with waste granite square stone prism [1]. The mechanical behaviors of the square stone prism of different height, encased in square cross-sectional concrete-filled steel tube (SCFST) members under axial compression loading performance are studied through ANSYS 2021 R2 software. The effect of the parameters on the failure mechanism, load-carrying capacity, load versus deformation response of the SCFST specimens are investigated.

2 Literature Review

Several experimental and analytical investigations were done on columns with different materials such as concrete-filled steel tubes (CFST), concrete filled bimetallic tubular (CFBT) columns etc. The review on the previous works are summarized below.

Concrete-filled steel tubes are being used effectively in the construction industry as columns of mid-rise and high rise buildings, in bridge as piers and piles, submarine pipelines, and other engineering structures. CFST are known for their high ductility, high stiffness, greater energy absorption and, greater seismic and fire resistance. Bearing capacity of the CFST columns increases with increase in compressive strength of concrete [1–3, 7]. Stone is a natural material that possess relatively high compressive strength and durability. Embedding polymer based mortar and steel bars in to the bed joints is an effective method to improve the lateral load carrying capacity and stiffness of stone masonry walls. The prestressed NSM CFRP reinforcing technique could be considered as an effective method for improving the flexural behavior of the stone beams [6, 8, 9]. CFSST columns generally show improved ductility, higher energy dissipation ability, and superior fire performance compared

with conventional CFST with carbon steel. The bond strength between the stainless steel tube and core concrete in a CFSST column is 32–69% lower than that in a CFST column due to the smoother surface of the stainless steel. Compared with the CFST column specimens, more bulges appear in CFBT columns [4].

3　Numerical Analysis

The numerical model created in finite element software is validated using available input data [7]. Numerical analysis is reciprocated using model dimensions and other input parameters from the journal. The model named as c62-t8-s75 was taken for the validation purpose. Circular cross sectional concrete-filled steel tube with square stone prism encased were modelled using Solid 186 as Element type and hexahedron mesh shape with 10 mm mesh size. The primary parameters considered were the size of the stone prisms as 75 mm, wall-thickness of the steel tube as 8.0 mm and concrete strength as 62.3 MPa. The outer diameter of the steel tube as 219 mm, length of the tube as 600 mm, the characteristic ultimate stress of the steel as 504 MPa, yield stress of steel as 335 MPa, poisons ratio of steel as 0.31 µs, Young's modulus as 214 GPa are taken for modelling. After analysis, the maximum strength index and load corresponding to maximum displacement are obtained as 1.33 and 5464.20 kN respectively, corresponding to the Journal values of 1.43 and 52,654 kN. The observed percentage error is less than 5%.

3.1　Modelling of SCFST Columns

A special type of square concrete-filled steel tube structural member was modelled by replacing the central portion of the infilled concrete with square stone prism. ANSYS 2021 R2 WORKBENCH was used to model the column specimens. The model's material property was assigned in the engineering data section of the ANSYS software. The engineering data section of the software consists of pre-assigned values for each material. The material properties are shown in Table 1.

Table 1 Material properties of base model

Material	Concrete	Steel tube	Stone prism
Youngs modulus	37,386 MPa	2.14E + 0.5 MPa	45,000 MPa
Poisson's ratio	0.2	0.3	0.18
Bulk modulus	2.077E + 10 Pa	1.7833E + 11 Pa	2.3438E + 10 Pa
Shear modulus	1.5578E + 10 Pa	8.2308E + 10 Pa	1.9068E + 10 Pa

Table 2 Description of specimens

Specimen ID	Description
C62-t8-s75	Convectional model-circular cross sectional SCFST Column
SQ-T1	Square cross sectional SCFST Column with normal position of prism
SQ-T2	Square cross sectional SCFST column with 45 degree inclined position of prism
SQ-3	Square cross sectional SCFST column with intermittent position of 3 number of prisms
SQ-2	Intermittent position of 2 number of prisms

A total of four square cross-sectional SCFST columns were prepared and analyzed to study the effects of different position of stone prism. The volume of these models is same as that of convectional model. The dimension of steel tube is $219 \times 219 \times 8$ mm and the length is 600 mm. The dimension of stone prism is 75 mm and cube compressive strength of the concrete fcu $= 62.3$ MPa. The description of specimens is shown in Table 2.

3.2 Support and Loading of Test Specimen

Bottom end of the specimen is fixed and load is applied axially on top end. Figure 1 (a to e) represents the loading and support diagram of conventional model (circular cross sectional SCFCT columns C62-t8-s7), proposed model with square cross-sectional prism (SQ-T1), proposed model with 45° inclined position of square cross-sectional prism (SQ-T2), proposed model with intermittent position of three numbers of square cross-sectional prism (SQ-3) and propose model with intermittent position of two numbers of square cross-sectional prism (SQ-2) respectively. The gap between the prism in each model is 50 mm. The volume of steel tube and stone prism is same as that of conventional model.
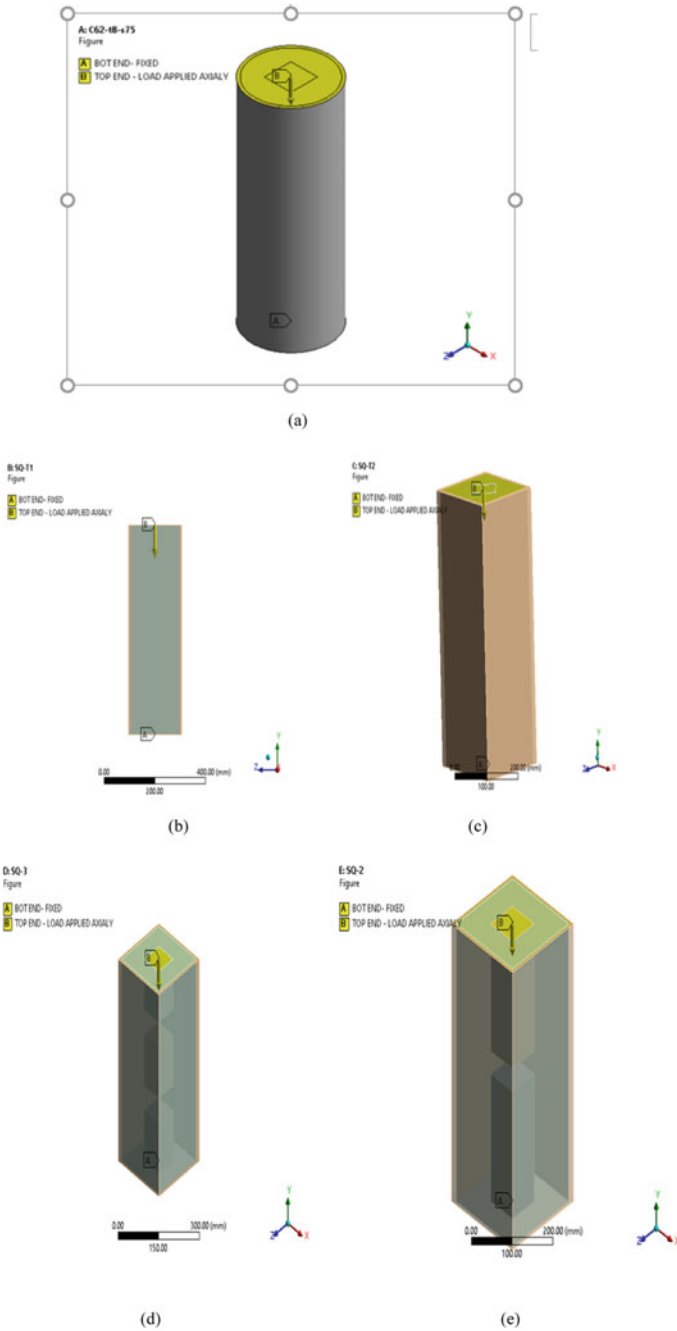
Fig. 1 Load and support diagram of **a** C62-t8-s7 **b** SQ-T1 **c** SQ-T2 **d** SQ-3 **e** SQ-2, loading condition is cantilever. Bottom end is fixed and load applied axially on top end

4   Results and Discussion

The concrete was modelled with Solid 186 three dimensional element for capturing total deformation, plastic strain and force reaction. FE analysis has been carried out using ANSYS WORKBENCH 2021 R2 for each specimen. Figure 2 shows the deformation diagram of specimens.
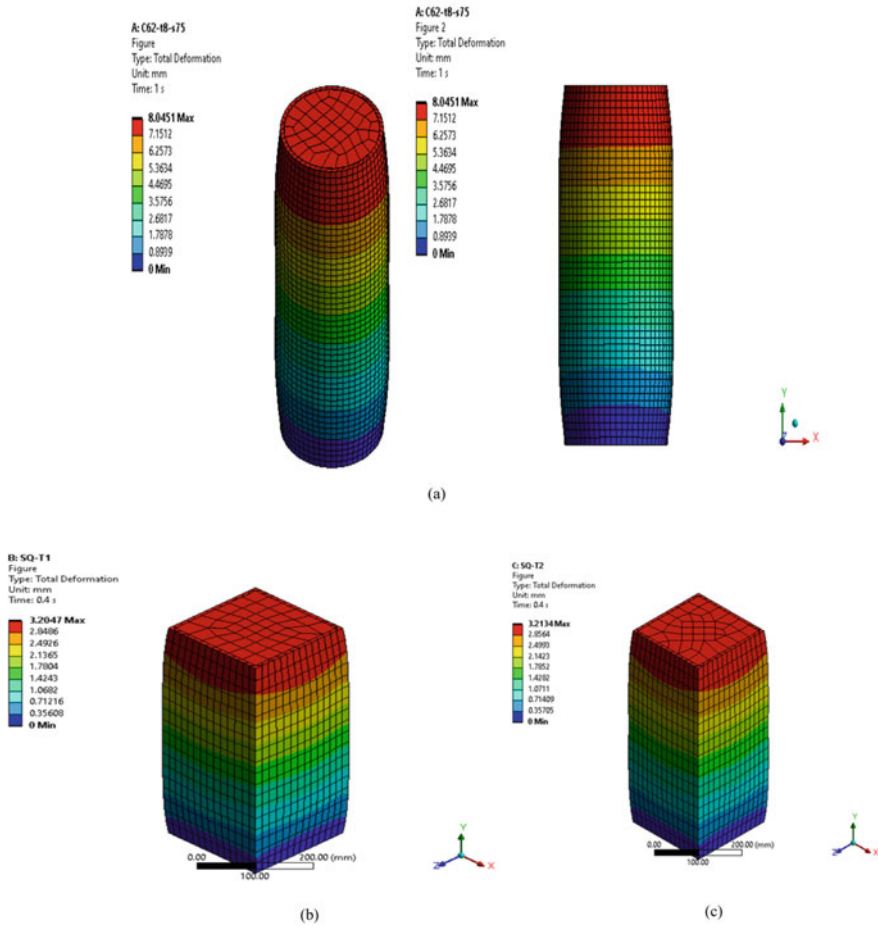
Fig. 2 Deformation diagram of **a** C62-t8-s7 **b** SQ-T1 **c** SQ-T2 **d** SQ-3 **e** SQ-2
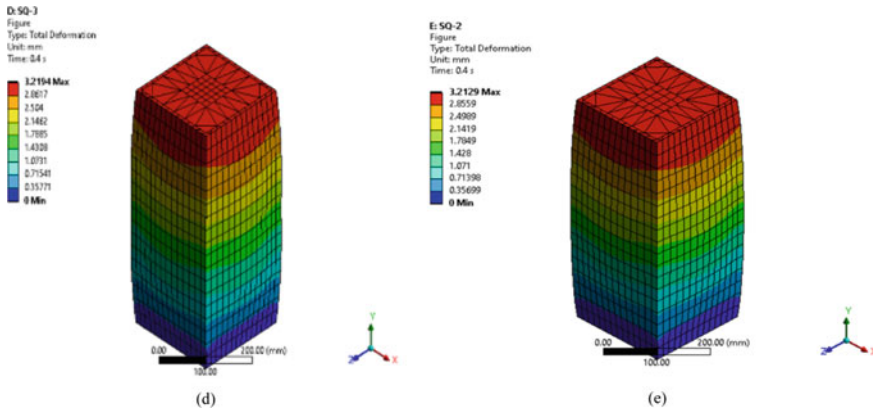
Fig. 2 (continued)

The deformation of each specimen under axial loading was compared and shown in Fig. 3. Compared with convectional model, SQ-T1 column show minimum deformation. The deformation of SQ-T1 is 3.2035 mm.

Figure 4 depicts the load carrying capacity of different column specimens. From the above analysis SQ-T1 and SQ-T2 shows more load carrying capacity than other positions of prism. The load carrying capacity of SQ-T1 is 6341.4 kN and SQ-T2 is 6361.8 kN. The load carrying capacity of SQ-T2 is slightly more than that of SQ-T1, whereas the deformation of SQ-T2 large compared to that of SQ-T1. Specimen
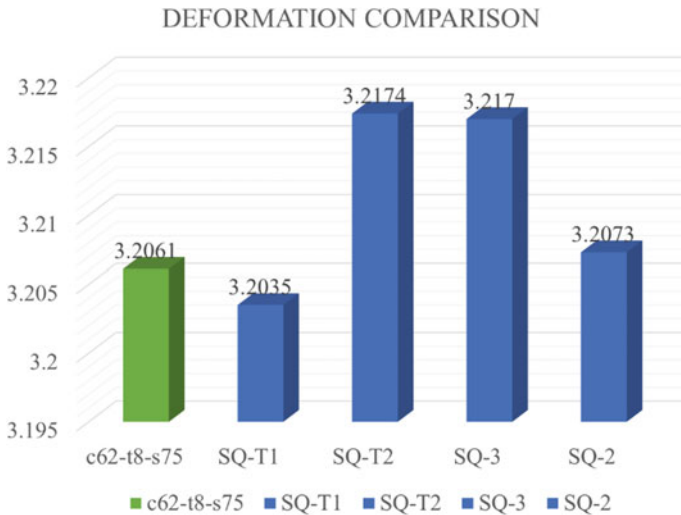
Fig. 3 Deformation comparison
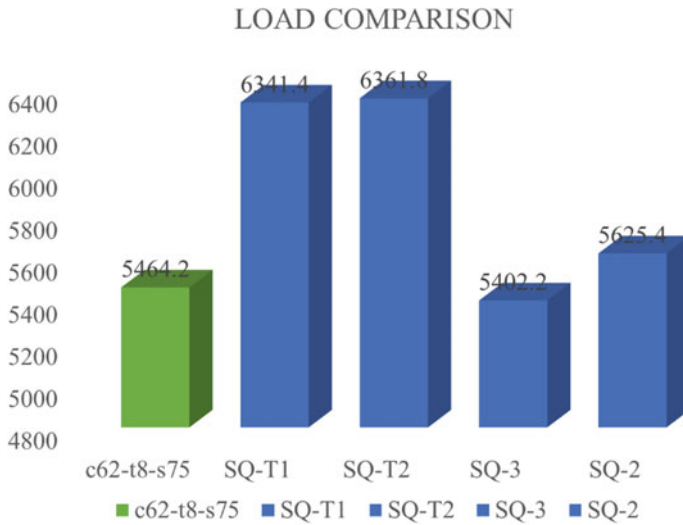
LOAD COMPARISON

Fig. 4 Load comparison

SQ-T1 shows 1.16 time load capacity than the convectional model with minimum deformation.

5 Conclusion

FE analysis has been carried out using ANSYS WORKBENCH 2021 R2 for each square cross sectional SCFST column with different stone prism position encasing. From the present study, the following observations are listed below;

- Column specimens SQ-T1 and SQ-T2 shows more load carrying capacity than convectional model. The maximum load carrying capacity of a SQ-T2 is 6361.8kN and that of SQ-T1is 6341.4 kN.
- Compared with convectional model, SQ-T1 column show minimum deformation.
- The specimen with square cross sectional prism (SQ-T1) shows slightly less load carrying capacity than specimen with 45 degree inclined position of square cross sectional prism (SQ-T2), whereas the deformation under loading of SQ-T1 is very less compared to that of SQ-T2.
- Considering the overall performance, SQ-T1 is better than SQ-T2.
- Concrete volume is reduced due to the replacement of cement concrete with granite stone and thus reducing the CO_2 emission.

References

1. Xu, F., Wang, J., Chen, J., Wang, Y.H.: Load-transfer mechanism in angle-encased CFST members under axial tension. Eng. Struct. **178**(2019), 162–178 (2019)
2. Ilanthalir, A., Regin, J.J., Maheswaran, J.: Concrete-filled steel tube columns of different cross-sectional shapes under axial compression: a review. Mater. Sci. Eng. **983**(2020), 012007 (2020)
3. Han, L.H., Li, W., Bjorhovde, R.: Developments and advanced application of concrete-filled steel tubular (CFST) structures: members. J. Constr. Steel Res. **100**(2014), 211–228 (2014)
4. Lin-Hai Han, Chuan-Yang Xu & Zhong Tao(2018), " Performance of concrete filled stainless steel tubular (CFSST) columns and joints: Summary of recent research", journal of construction steel research, vol xxx (2017)
5. Ren, Q.X., Zhou, K., Hou, C., Tao, Z., Han, L.H.: Dune sand concrete-filled steel tubular (CFST) stub columns under axial compression, thin walled structures, vol. 124 (2018)
6. Liu, X.J., et al.: Seismic behaviour of ashlar stone masonry walls with enhanced mortar joint, accepted manuscript format (2018)
7. Ye, Y., Liu, Y., Guo, Z.X., Chicchi, R.: Stone prism encased concrete filled steel tube columns subjected to axial compression. Structures **33**(2021), 1853–1867 (2021)
8. Ye, Y., Zhang, S.J., Han, L.H., Liu, Y.: Square concrete-filled stainless steel/carbon steel bimetallic tubular stub columns under axial compression. J. Constr. Steel Res. **146**(2018), 49–62 (2018)
9. Ye, Y., Guo, Z., Liu, Y., Wang, L.: Flexural behavior of stone beams reinforced with prestressed NSM CFRP bars. Constr. Build. Mater. **54**(2014), 466–476 (2014)

Response of Underground Tunnel Against Seismic Loading

Mulayam Singh, Kasilingam Senthil, and Shailja Bawa

Abstract From past earthquakes, it is evident that underground structures found more vulnerable to seismic activities which lead to the collapse of whole structure. Therefore, the study is focused to investigate the behavior of underground tunnel against seismic loading, considering static and dynamic scenarios using two-dimensional finite element software ABAQUS CAE. In static analysis, effects of gravity load and geostatic load on the soil domain was considered whereas time history data of earthquake was used to study the seismic response in case of dynamic analysis. The tunnel liner behavior is modeled using elastic model whereas elastic–plastic behavior of soil is incorporated using Mohr Coulomb Plasticity model readily available in ABAQUS library. The predicted numerical results were presented in terms of displacements and compared with Uttarkashi earthquake data and found that the results were in close proximity using both static (4.83 mm) as well as dynamic (96.36 mm) analysis. Further, the response of tunnels under two different earthquake data such as El Centro and Kobe ground motion time history in soil domain were studied in order to estimate the response of tunnels under severe conditions. It was observed that the maximum displacement for Uttarkashi, Kobe and El-Centro earthquake was found to be 96.36, 185.36 and 281.56 mm, respectively. It was also observed that the variation of displacement along y- direction in El- Centro and Kobe earthquake is found to be 36% however; the magnitude of displacement is very less as compare to x-direction.

Keywords Underground structures · Static analysis · Dynamic analysis · Time history data · RC liner

M. Singh · K. Senthil (✉) · S. Bawa
Department of Civil Engineering, Dr B R Ambedkar National Institute of Technology, G.T. Road, Amritsar Bypass, Jalandhar, Punjab 144011, India
e-mail: kasilingams@nitj.ac.in

M. Singh
e-mail: mulayams.ce.20@nitj.ac.in

S. Bawa
e-mail: bawas@nitj.ac.in

1 Introduction

Nowadays tunnel construction is widely used for transportation and maintaining connectivity between the places especially in hilly areas where it helps to shorten the distance. Tunnels constructed underground are also useful in highly populated metro cities as these do not hamper with the pre constructed infrastructure and helps in proper utilization of space. Earlier, it was believed that underground structures are safe against seismic load as they suffer lesser damage as compared to the surface structures. However, recent earthquakes such as Kobe earthquake (1995), Loma Prieta earthquake (1989), Niigata earthquake (2004), Wenchuan earthquake (2008), Chi-Chi earthquake (1999), Tohoku earthquake (2011), Duzce earthquake (1999) have shown serious damage to underground structures and have proved the vulnerability of underground structures to earthquake [1]. Hence it is necessary to study the effects of these tunnels against seismic loading in order to mitigate the risk of injury caused by their damage. Although thorough studies conducted in the past suggests that resistant against seismic response of underground tunnels are better than that of surface based structures, yet severe earthquakes might lead to its failure and loss of life [2].

Sharma et al. [3] taken from 192 cases, involving 85 different earthquake. Based on six criteria it was investigated to correlate the venerability of tunnel under seismic loading with different factors such as maximum ground acceleration, subsoil condition, tunnel cover, earthquake magnitude, epicenter distance and different supporting system. It was found that 60% of the damage is found in shallow tunnel less than 100 m depth and among that 42% are to be found in unlined tunnel rock. It was concluded that, as overburden depth of underground structure increases, the damage of the structure reduces. Rowe et al. [4] Studied the effects due to earthquake wave, fault, hard rock and liquefaction on a 500 m deep tunnel. Where it was concluded that safety index of tunnel increases with the depth and when the waves passes through fault unequal displacement is generated which might cause severe damage. The degree of damage is function of displacement of fault, tunnel lining and quality of rock. Tunnels in soft soil and soft rock layers are more vulnerable to damage. Youssef Hashasg et al. [5, 6] studied about seismic analysis and design of underground structure and engineer's methods for determining the seismic damage on a structure. Probabilistic and deterministic approaches are used for seismic hazard analysis. Free field ground motion deformation due to this hazard is estimated for given level of earthquake shaking. Asheghabadi et al. [7] considered different two sandy soil condition having loose and dense sand are created using ABAQUS software. Seismic effect of soil in both the condition was studied based on amplification, strain and stress propagation and response of acceleration in each seismic ground motion record. It was concluded that presence of tunnel amplifies the wave propagation on surface of soil-tunnel interaction. Singh et al. [8] studied the seismic response of an underground tunnel, it was concluded that damping is an integral part of seismic analysis as the forces generated in RC liners decreases with increase in damping. Fuxue Sun et al. [9] studied about tunnel passing below the metro station and dynamic interaction due to seismic hazard. It was observed that underground

structure influences with depth of structure with the relation to a soil response. It was also observed that the effect of underground structure against seismic loading was influenced up to 5 times the width of station and significant response was observed within this distance. Tsinidis et al. [10] conducted a set of centrifuge model tests and investigated the effects of input ground motion and depth on seismic behavior of tunnels in dry sand.

Based on the literature survey it was observed that the study conducted in the past focusing on the seismic analysis of underground tunnel is found to be limited. Also, it is vital to study the interaction between tunnel liner and soil, found to be limited. Therefore, this paper focuses to investigate the behavior of tunnel in alluvial soil against seismic loading. Section 2 deals with the constitutive behavior and numerical of the model using Mohr Coulomb plasticity model for soil and elastic model for RC liner using ABAQUS/ CAE software. Section 3 deals with the validation of the numerical analysis under static and dynamic conditions. Section 4 deals with the seismic response of the tunnel against El Centro and Kobe Earthquake. Section 5 deals with the results in terms of maximum displacement and acceleration on the tunnel under dynamic analysis.

2 Constitute Behavior and Numerical Modelling

Underground tunnel was modeled in ABAQUS software [11], and validation studies were conducted on the research conducted by Singh et al. [8]. Model was validated using time history data of Uttarkashi earthquake; see Fig. 1, however, the Kobe and El-Centro earthquake data is presented as these data is considered in Sect. 5. Rayleigh's damping of soil and RC liner was considered. Rayleigh coefficient for RC liner and soil layers is shown in Table 2. Alluvial soil deposit having saturated unit weight γ_{sat} and bulk unit weight γ_{bulk} were taken to be 20 and 18 kN/m^3, excavated soil is locally known as Delhi silt, is considered and variation of its young's modulus with depth shown in Table 1 and Fig. 2. Geotechnical investigations concluded the soil to be cohesion less with dilation (ψ) and friction (ϕ) angle as 5 and 35° respectively [12]. Two dimensional soil-tunnel model was created, with soil domain of 140 × 60 m^2 and tunnel diameter of 6.26 m and placed at 20 m depth from natural ground surface. The reinforced concrete liner of 0.28 m thickness was considered with poison's ratio of 0.15, modulus of elasticity of RC liner as E_c as 3.16 × 10^7 kPa.

Tunnel liner was modeled as beam (B21) element and soil surrounding the tunnel were considered as 2D plane strain continuum element (CPE4R) around the tunnel and infinite boundary (Lysmer viscous absorbent boundary) element (CINPE4) is used in order to prevent wave return after getting reflected. Figure 3 shows the modeling of soil layer and RC liner in ABAQUS. Rayleigh damping is calculated using Eq. (1)

$$C = \alpha M + \beta k \tag{1}$$
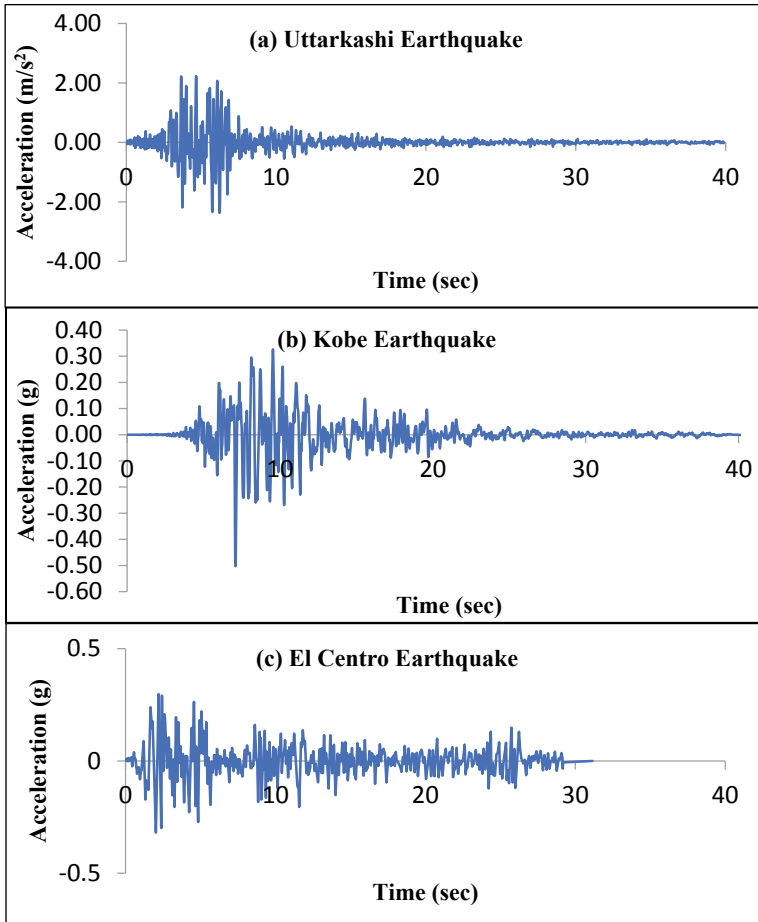
Fig. 1 Earthquake data during **a** Uttarkashi **b** Kobe and **c** El-Centro

Table 1 Elastic modulus variation with the depth of Soil [8]

Depth of Soil (m)	Young modulus of elasticity (MPa)
0–10	7.5
10–20	15
20–35	30
35–50	40
50–60	50

Table 2 Rayleigh damping coefficient for Soil and RC liner

Rayleigh damping coefficient	Soil (5%)	Soil (10%)	RC liner (2%)
α	0.171	0.397	0.084
β	0.016	0.028	0.005

where α and β are Rayleigh damping coefficient determined using Table 2 and M and K are mass and stiffness matrix which is given by below equation

$$\begin{Bmatrix} \alpha \\ \beta \end{Bmatrix} = \frac{2\xi}{\omega_m + \omega_n} \begin{Bmatrix} \omega_n \omega_m \\ 1 \end{Bmatrix} \tag{2}$$

where m, n are the different mode shapes for which natural frequency (ω) in terms of rad/sec is determined using ABAQUS for ground response analysis which came out to be 0.4157 and 0.9023 Hz for mode 1 and 2 respectively. ξ is the damping ratio, for soil it is considered at 5 and 10%, whereas RC liner is taken as 2%. Vibration of soil and structure is assumed at different modes for this case the soil-tunnel system is vibrating in mode 1 and 2. Hence, the value of m and n are consider as 1 and 2
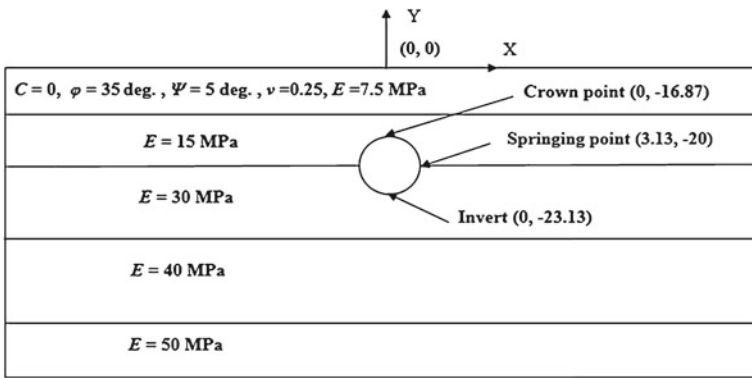
Fig. 2 Geometry of physical model [8]
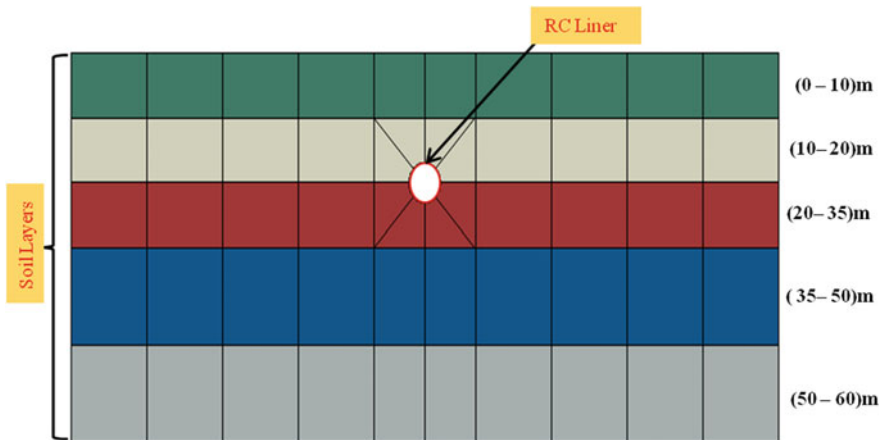
Fig. 3 Modeling of soil layers and RC liner in ABAQUS
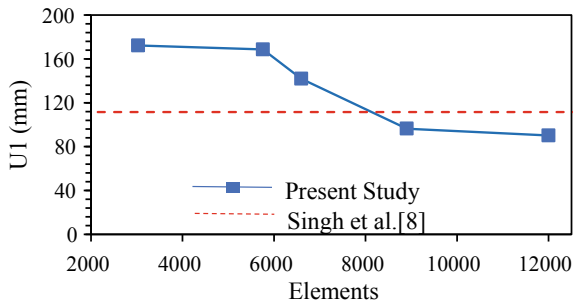
Fig. 4 Displacement of tunnel as comparison of present study with Singh et al. [8]

respectively. α and β are the Rayleigh damping coefficients (see Table 2) determined for RC liners and soil surrounding it using Eq. 2.

3 Validation

In this section validation of static and dynamic result is validated using ABAQUS software. This section also deals with comparison of response of the model under static and dynamic conditions.

3.1 Mesh Convergence Study

Mesh convergence study is adopted to obtain the most efficient model. A circular tunnel is analyzed by varying the number of element of the soil and RC liner. Thorough mesh converge study was conducted by varying mesh size of RC liner by 0.05, 0.1, 0.15, 0.2 and 0.25 m and soil by 0.5, 1, 1.5, 2 and 2.5 m the results were shown in terms of displacement of the element present at the top most point of RC liner inside the tunnel. It was concluded that the most optimum results are generated using size of soil and RC liner as 1 and 0.1 is 96.36 mm which is closest with the results obtained in the Singh et al. see Fig. 4.
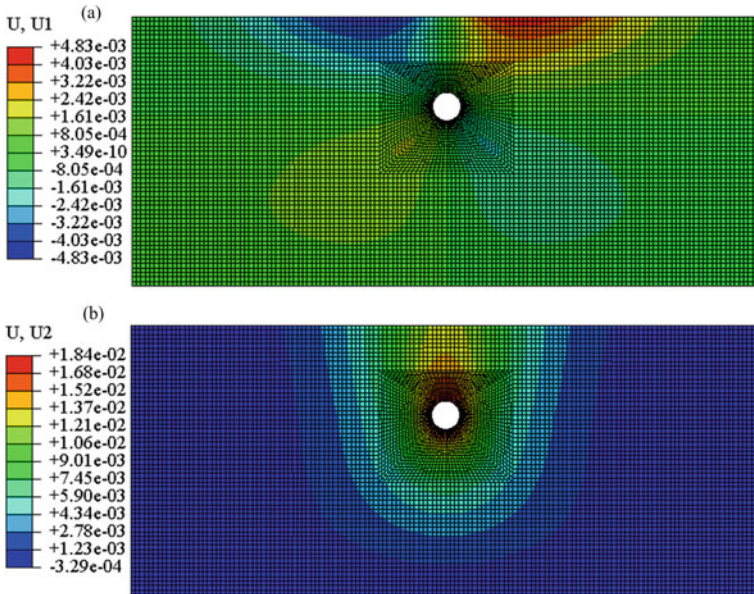
Fig. 5 Displacement of soil along **a** U1 and **b** U2 direction

3.2 Static Analysis

In this Model, for soil having size of mesh for analysis has been taken as one and two dimensional plane strain continuum element CPE4R is used. Elastic 2D beam element B21 having approximate meshing size 0.1 for RC liner is also be taken into consideration. Figure 5 (a-b) shows static validation results in terms of displacement for soil; Fig. 6 (a-b) shows the static validation results in terms of displacement for RC liner and Table 3 shows comparison of results obtained from Singh et al. [8] result and simulated result. For validation of static test along U1 direction for both soil and RC liner, percentage variation was found to be 25.05 and 22.9%, respectively. Along U2 direction, the same was found to be 18.09 and 16.52%, respectively.

3.3 Dynamic Validation

Dynamic validation was conducted by simulating a 2-D model of soil tunnel system with Uttarkashi Earthquake time history data. Soil having same meshing size as that for static validation with element type as CPE4R in whole region and type CINPE4 at the ends to create similar conditions as that of infinite viscous absorbent boundary. RC Liner having B21 is considered having mesh size as 0.1. Figure 7 shows the comparison between displacement in x direction obtained from Singh
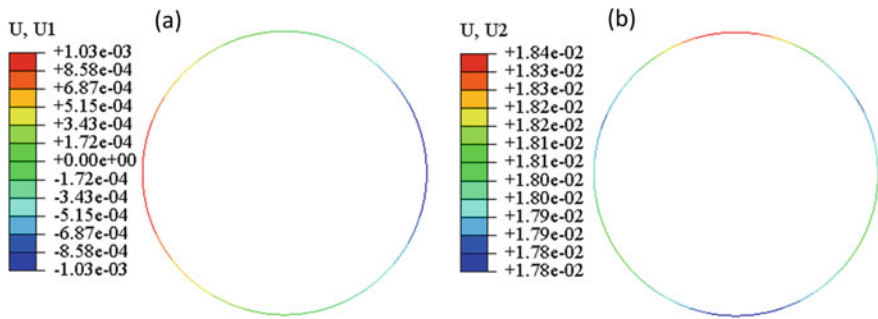
Fig. 6 Displacement in RC Liner along **a** U1; **b** U2 direction

Table 3 Comparison of results from Singh et al. with ABAQUS

Maximum displacement (mm)	Static results[8]		Static simulation		Percentage variation	
	Soil	RC Liner	Soil	RC Liner	Soil	RC Liner
Ux	3.62	0.794	4.83	1.1	25.05	22.9
Uy	15.07	15.36	18.4	18.4	18.09	16.52
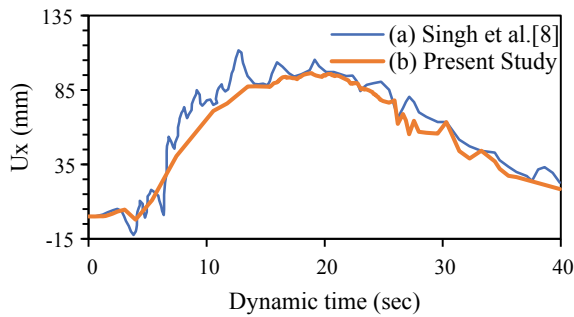
Fig. 7 Comparison of displacement between **a** Singh et al. [8] and **b** Present study

et al. [8] and simulation. It was observed that the displacement measured from the present study and Singh et al. as 96.36 and 112.43 mm, respectively. It was observed that along U1 direction, percentage variation was found to be 13.65% which are in close approximation with the Singh et al. [8].

4 Methodology

Two predefined fields were created at which the initial step was considered for geostatic stress calculated using Eq. 3 and void ratio was considered as 1.

$$S = \rho\, gh \tag{3}$$

where ρ is density of soil (taken as 1835 kg/m^3), g is the acceleration due to gravity (9.81 m/s^2) and h is the height (in meters) from ground level to center of tunnel. Time period of geostatic step was taken as 1 s to allow the geostatic load to settle. The soil was restrained against translation in X and Y direction at the base and only restrained against translation in X direction at the sides. Another step was created for static loading for gravity load having time period of $1e^{-10}$ s. Third step was created using dynamic implicit solver for 40 s duration in order to simulate the time history data of Kobe and El Centro earthquake at the base, amplitude of 9.81 m/s^2 was taken. Tie constraints were assigned between tie and RC liner [13].

5 Results and Discussion

As discussed previously, a typical section of tunnel has been considered for analysis. Loading, boundary condition and constraints were kept similar to as that used for validation whereas only time history data has been changed. The dynamic time history analysis has been carried out to obtain the response of El-Cento and Kobe earthquake.

5.1 Response of Soil Tunnel System Due to El-Centro Earthquake

The analysis of soil tunnel system has been carried out on El-Centro earthquake considering 5% damping for soil mass and 2% damping for RC liner. From Fig. 8 (a-i), it is observed, that for first 2.5 s the displacement along length (U_x) is mobilized and 2.5–15 s soil stats to oscillate with increasing amplitude having peak at 4.1 s and maximum value of 281.56 mm. After peak value it was also observed that displacement of soil start to decrease and comes to rest due to damping. From Fig. 8 (a-ii) it is observed, that total displacement (U) is mobilized for 2.5 s and start to oscillate its value is increases up to 4.2 s and maximum value obtained as 282.28 mm and for after 4.2 s its value drastically decreases due to damping. In the interval of 10–15 s, the response increases up to 221.56 mm due as intensity of loading of earthquake increase. After 15 s the response starts to decrease and then it comes to rest. Figure 8 (b-i) shows the ground surface have maximum horizontal acceleration of 1.75 m/s^2
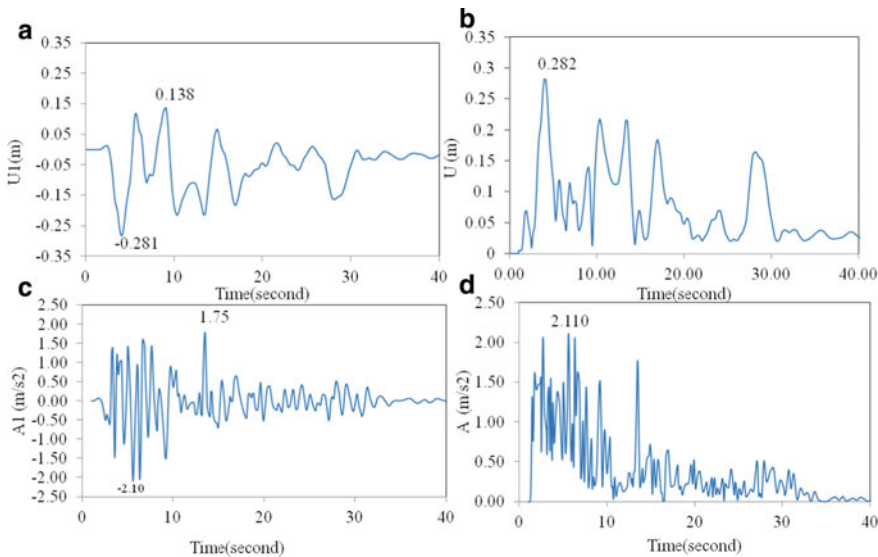
Fig. 8 Simulation results of El-Centro earthquake in terms of **a** displacement and **b** acceleration in (i) along the length and (ii) total displacement

which is equivalent to 0.18 g or 62.1% of maximum applied acceleration. Figure 8 (b-ii) shows the total acceleration of earthquake 2.12 m/s^2 which is equivalent to 0.21 g or 73.8% of maximum acceleration applied. The maximum displacement of the tunnel along y direction is found 34.35 mm which is very less as compared to the response in x-direction. From Fig. 10 (a-b) it was observed that at t = 4.2 s the maximum displacement under El-Centro earthquake along U1 direction and total displacement is found to be 286.36 and 290.57 mm, respectively.

5.2 Response of Soil Tunnel System Due to Kobe Earthquake

The analysis of soil tunnel system has been carried out on Kobe earthquake considering 5% damping for soil mass and 2% damping for RC liner. From Fig. 9 (a-i), it is observed, that for first 5 s the horizontal displacement (U_x) is mobilized and 5–15 s soil stats to oscillate with increasing amplitude having peak at 13.8 s and maximum value of 185.36 mm. After 13.8 s it was also observed that displacement of soil starts to decrease and comes to rest at 40 s due to damping. From Fig. 9 (a-ii) it is observed, that total displacement (U) is mobilized for 5 s and its value is increases up to 10–13 s and maximum value obtained as 197.58 mm and for next 13–16 s its value drastically decreases due to damping. In the interval of 13–16 s, the response increases up to 187.89 mm due as intensity of loading of earthquake increase. After 16 s the response starts to decrease up to 40 s then it comes to rest. Figure 9 (b-i)
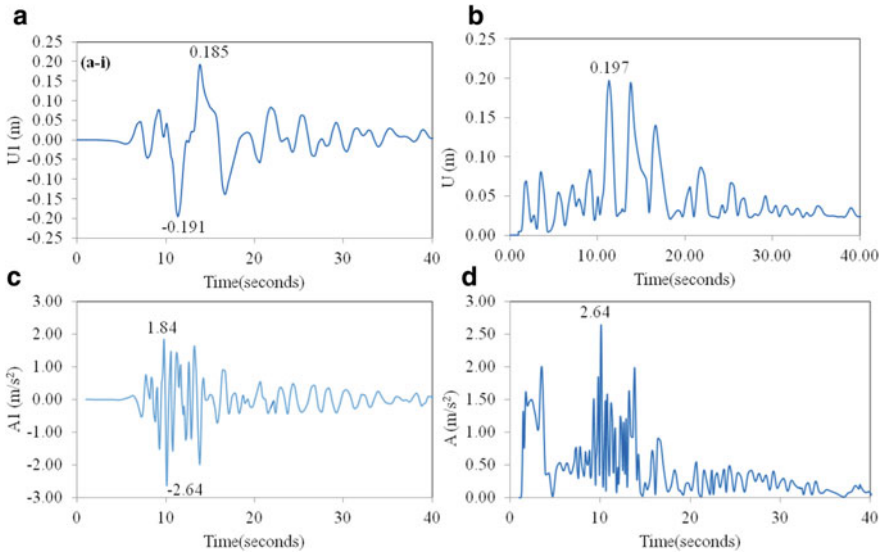
Fig. 9 Simulation results of Kobe earthquake in terms of **a** displacement and **b** acceleration in (i) along the length and (ii) total displacement
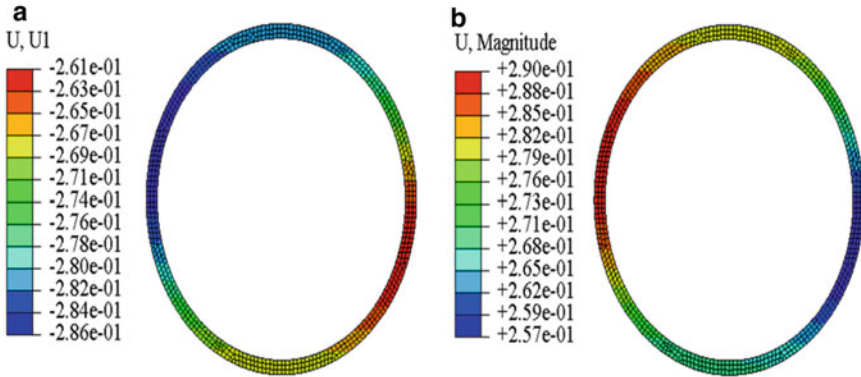
Fig. 10 Maximum displacement under El-Centro earthquake **a** Along U1 direction; **b** Total displacement at t = 4.2 s

shows the ground surface have maximum horizontal acceleration of 1.84 m/s^2 which is equivalent to 0.18 g or 57.53% of maximum applied acceleration. Figure 8(b-ii) shows the total acceleration of earthquake 2.64 m/s^2 which is equivalent to 0.26 g or 82.14% of maximum acceleration applied. The maximum displacement of the tunnel along y direction is found 25.87 mm which is very less as compared to the response in x-direction. Figure 11(a-b) it was observed that at t = 13.8 s the maximum
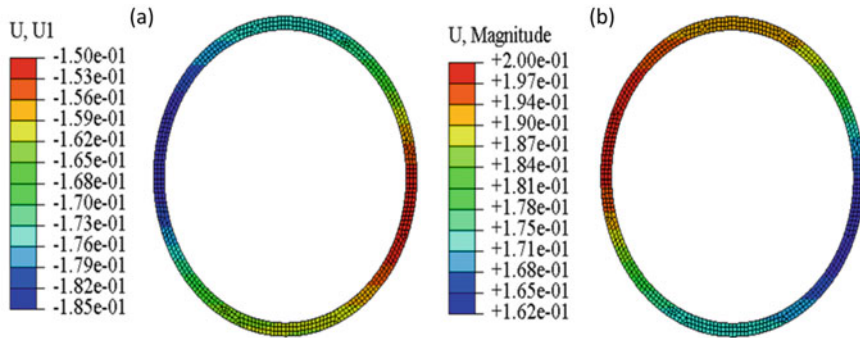
Fig. 11 Maximum displacement under Kobe Earthquake **a** Along U1 direction; **b** Total displacement at t = 13.8 s

displacement under El-Centro earthquake along U1 direction and total displacement is found to be 185.16 and 200.67 mm, respectively.

6 Conclusion

In this study, dynamic study of seismic load was conducted through time history analysis and following are the conclusions that were drawn:

- It was observed that the percentage variation was found to be 25.05 and 22.9%, respectively in terms of displacement U1 direction on both soil and RC liner under static test. Along U2 direction, the same was found to be 18.09 and 16.52%, respectively. In dynamic simulations, along U1 direction, percentage variation was found to be 13.65% which are in close approximation with the literature.
- It was observed that the maximum displacement along the length for Uttarkashi data, Kobe earthquake El-Centro is found to be 96.361, 185.36 and 281.56 mm respectively. The maximum acceleration along the length on Uttarkashi data found to be 1.36 m/s^2 whereas Kobe earthquake and El-Centro is found to be almost same as 1.84 and 1.57 m/s^2 respectively.
- Variation of displacement along y-direction in El-Centro and Kobe earthquake is found to be 36%. However, the magnitude of displacement is very less as compared to x-direction.

References

1. Patil, M., Choudhury, D., Ranjith, P.G., Zhao, J.: Behavior of shallow tunnel in soft soil under seismic conditions. Tunn. Undergr. Sp. Technol. **82**, 30–38 (2018). https://doi.org/10.1016/j.tust.2018.04.040
2. Pitilakis, K., Tsinidis, G.: Performance and seismic design of underground structures. Soil Dyn. Geotech. Earthq. Eng. (2013)
3. Sharma, S.W.R.: Underground opening damage from earthquake. J. Eng. Geol. **30**(3–4), 263–275 (1991)
4. Rowe, R.: Tunnel engineering in earthquake area. J. Tunn Tunn. 41–4 (1992)
5. Hashash, Y.M.A., Park, D., Yao, J.I.C.: Ovaling deformations of circular tunnels under seismic loading, an update on seismic design and analysis of underground structures. Tunn. Undergr. Sp. Technol. **20**, 435–441 (2005). https://doi.org/10.1016/j.tust.2005.02.004
6. Hashash, Y.M.A., Hook, J.J., Schmidt, B., I-Chiang Yao, J.: Seismic design and analysis of underground structures. Tunn. Undergr. Sp. Technol. **16**, 247–93 (2001). https://doi.org/10.1016/S0886-7798(01)00051-7
7. Asheghabadi, M.S., Matinmanesh, H.: Finite element seismic analysis of cylindrical tunnel in sandy soils with consideration of soil-tunnel interaction. Procedia Eng. **14**, 3162–3169 (2011). https://doi.org/10.1016/j.proeng.2011.07.399
8. Singh, M., Viladkar, M.N., Samadhiya, N.K.: Seismic analysis of Delhi metro underground tunnels. Indian Geotech. J. **47**, 67–83 (2017). https://doi.org/10.1007/s40098-016-0203-9
9. Sun, F., Wang, G.B., Peng, X.J., Jin, Z.Z., Li, X.C., Zhao, J.L.: Seismic response study of tunnels running underneath a subway station in parallel. Shock Vib. **2020** (2020). https://doi.org/10.1155/2020/8822981
10. Tsinidis, G., et al.: Seismic behaviour of tunnels: from experiments to analysis. Tunn. Undergr. Sp. Technol. **99**, 103334 (2020). https://doi.org/10.1016/j.tust.2020.103334
11. System D. Abaqus/Standard–User's Manual. Dassault Systems Simulia Corp. n.d.
12. Yadav, H.R.: Geotechnical evalution of Delhi Metro Tunnels. Ph. D. Geotech Evalution Delhi Metro TunnelsPhD Thesis Dep Civ Ngineering, IIT Delhi, India (2005)
13. Nariman, N.A., Hussain, R.R., Msekh, M.A., Karampour, P.: Prediction meta-models for the responses of a circular tunnel during. Undergr. Sp. (2018). https://doi.org/10.1016/j.undsp.2018.06.003

Experimental Investigation on the Mechanical and Durability Properties of Bacterial Mortar

Meyyappan Palaniappan [ID] **, Anita Selva Sofia** [ID] **, M. Aparna, L. R. Puja Shree, M. Dhivya Prabha, and G. Muthu Selvi**

Abstract Improvement of reasonable structure has turned out to be progressively imperative as of late for ecological contemplations. Use of reused materials will be an approach under such condition. Due to external loading and chemical reactions, microcrack spreads, causing harmful species to enter the concrete causing durability of the concrete to deteriorate. In this study, the precipitations of bacillus cereus were introduced in the mortar as a strategy to repair cracks on their own to cultivate the self healing property. In this study, 10, 20 and 30 ml of bacillus cereus were introduced in the mortar. Mechanical (such as compressive) and durability properties (Sorptivity, RCPT and Water absorption) were studied on this self healing mortar. In this experimental study, it is understood that, the optimum level of replacement of bacillus cereus in mortar around 20 ml shows better result in terms of compressive strength of the mortar specimen at the age of 28 days curing.

Keywords Bacterial mortar · Self healing property · Cracks bacillus cereus

1 Introduction

Bacterial-based self-healing concrete is relatively new technology whichcan be used in larger-scale applications in the sector of construction industries [1, 7, 11]. In the past literatures, the varieties of bacteria found in concrete and how they are used as healing agents are discussed and it is in the inception level [2–6]. Inherently the concrete is having micro-cracks and thus it leads to the level of decay, allowing toxic substances to enter the concrete and causing structural damage etc [8–12]. Self-healing characteristics are applied recently to overcome these circumstances. Calcite and calcium sources are created by adding bacteria to concrete, which causes

M. Palaniappan (✉) · M. Aparna · L. R. P. Shree · M. D. Prabha · G. M. Selvi
Centre for Building Materials, Kalasalingam Academy of Research and Education, Krishnankoil, Tamil Nadu 626126, India
e-mail: meyyappan@klu.ac.in

A. S. Sofia
Sri Ramakrishna Engineering College, Coimbatore, Tamil Nadu 641114, India

1041

calcite to precipitate. Thus the use of bio-mineralization technology to seal tiny fissures/cracks in concrete has shown to be effective. In the past literatures is also indicating that, the freshly formed micro cracks can also be sealed by a permanent hydration process in the concrete along with growth of bacterial concentration [6, 9, 11]. Biomineralization is a method of chemically altering an environment through microbial activity, which results in mineral precipitation. Biocementation is a crack-repair process that is clean, long-lasting, and environmentally benign. It has been used for sand, ground improvement, and the construction of low-energy buildings [13–16]. Surface cracks and fissures in various structural formations can be remedied using biocementation, as can surface soil consolidation and the strength and durability of mortar and bricks [2, 4, 10]. So based on the past researches, an attempt is made to investigate the behavior of cement mortar with and without the bacterial concentration in terms of strength and durability characteristics.

2 Material Used

The following concrete making materials are used in this study:

2.1 Cement

For this study, ordinary Portland cement (OPC) of 43 grade is used as per the standards of IS:8112 code. The specific gravity is found as 3.09.

2.2 Fine Aggregate

The river sand which is obtained locally passing through IS sieve 2.36 mm is considered for this study. The fine aggregates is obtained to be 2.53 which is confirming zone II grading as per the standards of IS:382 code.

2.3 Seed Culture and Bacterial Inoculum

The Seed culture was prepared using Luria–Bertani media and bacterial inoculum to be used for remediation of cracks in mortar was prepared using urea broth as shown in Fig. 1.
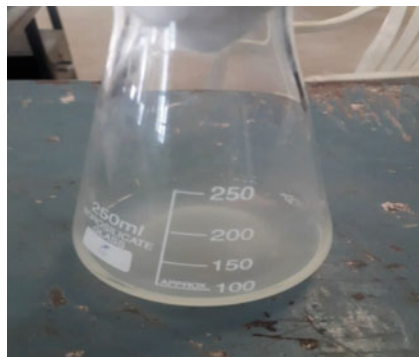
Fig. 1 Preparation of bacterial culture

The isolate KLUVAA was inoculated in urea broth and incubated at 37 °C, 150 rpm for the period of 24 h. Calcium chloride (CaCl2) is added which is acting as a catalyst and supplying the food to support the growth of the bacteria. After 24 h, the culture was used for mixing the cement mortar for self healing process.

3 Mix Design and Specimen Details

The mix ratio taken for the study is 1:3 with a water cement ratio of 0.50. The W/c ratio was taken based on the flow table test conducted with the flow value 104.6. Cement and fine aggregates were mixed thoroughly in dry state of form (Fig. 2). Then the required amount of water is added to prepare the wet mix (Fig. 3). For this experimental study, the prepared bacterial culture is added to the cement mortar in the varying proportions of bacteria such as 10, 20 and 30 ml to the cement mortar. Cube specimens of size 70.6 × 70.6 mm were used to determine the compressive strength and sorptivity of the bacterial mortar specimen. Cylindrical disc specimens of size 100 mm (height) × 50 mm (diameter) were used to determine the water absorption and rapid chloride penetration test. Ensure proper oil coating is applied on the moulds before casting the specimens for easy demoulding process. After placing of cement mortar into moulds, proper compaction is ensured in 3 levels. Then casted specimens were demoulded after a period of 24 h and allowed to place on the water curing tank for a period of 28 days. For this experimental study, 6 cube specimens (3 for compression test and 3 for sorptivity test) and 6 disc specimens (3 for water absorption and 3 for RCPT) were casted against each of the test. Out of total 48 specimens, 24 cube specimens and 24 disc specimens were casted as shown in Table 1 against each of the mix proportions.

Fig. 2 Dry mixing of mortar

Fig. 3 Wet mixing of mortar

Table 1 Bacteria concentration and Specimen details

S. No	Mix ID	Amount of bacteria (ml)	Cube specimens	Disc specimens
1	BC00	0	6	6
2	BC10	10	6	6
3	BC20	20	6	6
4	BC30	30	6	6
Total specimens			24	24

4 Experimental Investigation

After 28 days, the specimens were allowed for natural drying and then it was placed on the compression testing machine (CTM) as shown in Fig. 4.

The axial compressive load is applied gradually on the specimen until it gets ruptured. The readings were noted down and the compressive strength of the specimens were calculated by the ratio of failure load to the cross sectional area of the

Fig. 4 Specimen placed under CTM

specimen. It was expressed in terms of N/mm^2. Water absorption test was carried out on the cube specimens to find the porosity (P) values. The weight of the specimen is taken as W1 and allowed to place in the hot air oven for the period of 24 h at 120° temperature. After 24 h, the specimen is taken out of the oven and taken the weight as W2. The porosity (volume of pores in percentage) can be estimated by the given formula:

$$P = \frac{W_1 - W_2}{W_1} \times 100$$

In Sorptivity, the rate of water penetration into the pores in mortar due to capillary action is measured. This test was conducted in a cube specimen. The specimens were dried for 24 h and then cooled for 24 h. With the coating of insulation paint, sides of the cubes were sealed. After taking initial weight, the specimen was kept immersed into the water to a depth of 5 to 10 mm. The weight increased has to be noted at every regular interval of 30 min over a period of duration 4 h. The cumulative volume of water that has penetrated per unit surface of exposure is plotted against the square root of time of exposure. The resulting graph could be approximated by the straight line. The slope of the straight line is the representation of the measure of movement of water through capillary pores and it is called sorptivity.

The rapid chloride penetration test (RCPT) method determines the electrical conductance of cement mortar. The cylindrical disc specimen is considered for this test. The experimental setup of RCPT carried out with the help of pipe having diameter 4 in. Two halves of the pipes were taken and both ends have been sealed with the aid of couplers. So it was ensured that, the solution is tightly protected without any possibility of leakage issues. A hole is made in both the halves and wire mesh has been inserted to represent the cathode and anode ends as shown in Fig. 5. After 28 days of curing, the specimen has made dry and clamped in between the pipes and tightly packed with M-seal agent. The specimen was clamped between two cells and a potential difference (60 V DC) was retained in a crossways. For performing RCPT test, the mortar sample is placed into the two reservoirs (cells). One of the

reservoirs is filled with NaCl solution (upstream cell) and another one with NaOH solution (downstream cell). The quantity of these NaCl and NaOH solutions used in the respective reservoirs were 3% and 0.1 M respectively. 3% of NaCl solutions were prepared by diluting 30 g of NaCl per litre of water and 0.1 M of NaOH were prepared by diluting 4 g of NaOH per litre of water. The preparation of solution was shown in Fig. 6. In each of the periodic intervals (30 min), the passing current was noted down. The total charge passed, was recorded in the duration of 6 h in terms of coulombs.

Fig. 5 RCPT set up

Fig. 6 Preparation of NaOH solution

5 Results and Discussions

5.1 Compressive and Porosity Test

The compressive strength and porosity test results were shown in Table 2 against the various amount of bacteria concentration level 0, 10, 20 and 30 ml respectively for the age of 28 days curing.

From the test result is it observed that the compressive strength for the conventional mortar specimen is 21.14 N/ mm^2. The compressive strength is increased by 10.87 and 18.88% for 10 and 20 ml bacterial concentration in compared with the conventional mortar. But if the bacteria concentration is increased further to 30 ml, the compressive strength seems to be in detrimental as shown in Fig. 7. For upto 20 ml of bacterial concentration, the compressive strength is increased due to the precipitation of calcium carbonate. These filled the micro pores and thus boost up the concrete microstructure as indicated by Hasaan Amer Algaifi (2021). This property is self healing and it is attained due to the presence of bacterial concentration. For higher amount of bacterial concentration, the effectiveness of self healing property is getting declined.

The pore in the conventional mortar specimens is estimated as 14.43%. The porosity values are 12.87, 10.79 and 12.08% for the bacterial concentration 10 ml, 20 ml and 30 ml respectively. For 10 and 20 ml bacterial concentration, the pores were reduced by 10.08 and 25.23%. This clearly indicates that arresting of pores has

Table 2 Compressive strength and porosity test results

S. No.	Mix ID	Amount of bacteria (ml)	Compressive strength (N/mm^2)	Porosity (%)
1	BC00	0	21.14	14.43
2	BC10	10	23.72	12.87
3	BC20	20	26.06	10.79
4	BC30	30	22.84	12.08
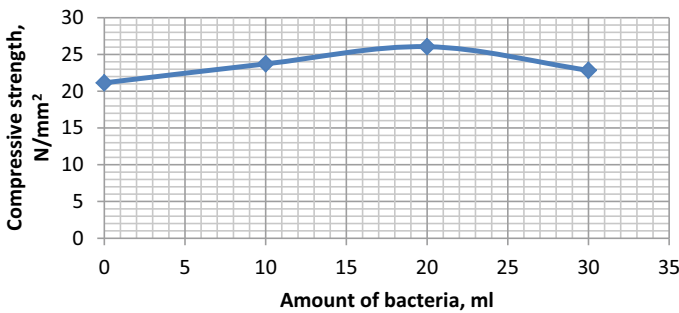
Fig. 7 Compressive strength Vs amount of bacterial concentration
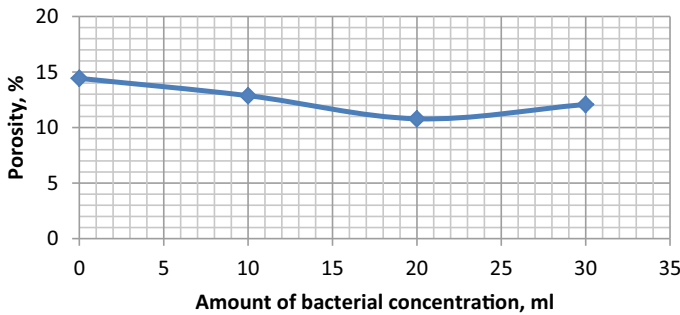
Fig. 8 Porosity Vs amount of bacterial concentration

Table 3 Sorptivity test results

Sl. No.	Mix ID	Amount of bacteria (ml)	Minutes						
			0	15	30	45	60	75	90
1	BC00	0	0	0.103	0.129	0.258	0.284	0.309	0.387
2	BC10	10	0	0.077	0.114	0.206	0.258	0.284	0.335
3	BC20	20	0	0.068	0.104	0.186	0.232	0.249	0.309
4	BC30	30	0	0.076	0.114	0.207	0.249	0.256	0.331

done by the self healing property of the presence of the activeness of the bacterial compound as shown in Fig. 8.

The continuous decrease in the pore size due to the presence of this bacterial compound upto 20 ml. After 20 ml concentration, the efficiency level of self healing property is seems less due to the reduction of active metabolism conversion of calcium nutrients into the pores.

5.2 Sorptivity Test

The sorptivity test results are shown in Table 3 for the bacterial concentration 0 to 30 ml.

The results were tabulated on each 15 min interval with respect to volume of water penetration. It seems that the conventional mortar specimen has more water penetration than the presence of bacterial concentration. In the graph as shown in Fig. 9, 13.44 and 20.16% of reduction in the penetration of water in to the specimen because of the reduction of the pore due to its self healing property that activated within the specimen. There is some decreasing trend in the reduction of penetration of water, as the bacterial concentration increased to 30 ml as shown in Fig. 9. For lower amount of bacterial concentration, the self healing property is better in terms of less water penetration than the higher amount of concentration.
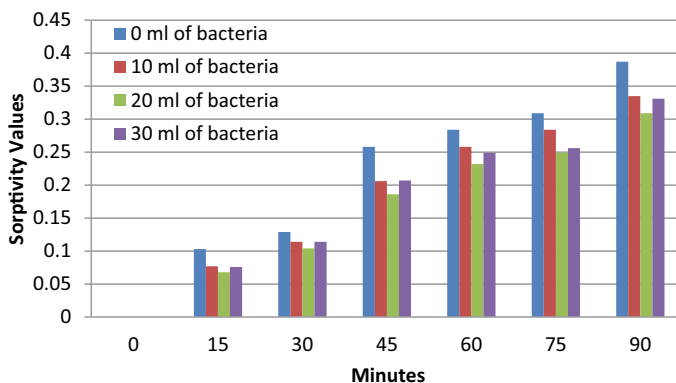
Fig. 9 Sorptivity Vs amount of bacterial concentration

Table 4 Rapid chloride penetration test results

S. No.	Mix ID	Amount of bacteria (ml)	Cumulative charge	Total charge passed	Chloride ion permeability
1	BC00	0	0.646	1162.8	Low
2	BC10	10	0.984	1771.2	Low
3	BC20	20	1.071	1927.8	Low
4	BC30	30	1.277	2298.6	Moderate

5.3 Rapid Chloride Penetration Test

Table 4 shows the experimental test results for RCPT. The result table shows the cumulative charge, total charge passed and category of chloride ion permeability.

The total charges passing into the conventional mortar specimen is 1162.8 coulombs and it is lying in the low category of chloride ion permeability. For the specimens prepared from 10 and 20 ml of bacterial concentration has the total charge of 1771.2 and 1927.8 coulombs respectively. Even though the presence of 10 and 20 ml, has more than the conventional mortar, but they are lying in the low category of chloride ion permeability. If the bacterial concentration is increased to 30 ml, the total charge passed is estimated as 2298.6 coulombs and the same is lying in moderate category of chloride ion permeability. For higher bacterial concentration, chloride ion permeability is also moving to higher level as shown in Fig. 10.

In overall, it is observed that, the 20 ml of bacterial concentration is better and improvement is clearly seen in terms of strength and durability characteristics of the mortar which is a clear evidence that lively nature of self healing property due to the presence of bacterial concentration.
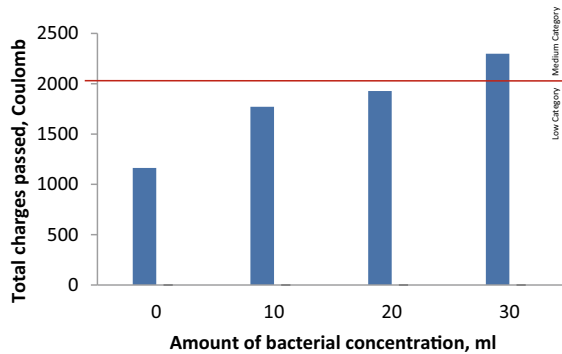
Fig. 10 Total charges Vs amount of bacterial concentration

6 Conclusions

Based on the experimental investigation conducted on the cement mortar with and without bacterial concentrations, the following conclusions were arrived. They are:

(a) The compressive strength of the cement mortar with bacterial concentration is more than the conventional cement mortar. For 20 ml of bacterial concentration, the compressive strength achieved is 26.06 N/ mm^2 which is 18.18% higher than the conventional mortar. For more than 20 ml bacterial concentration (30 ml), the rate of increase in the compressive strength is getting declined.

(b) For 20 ml of bacterial concentration, there is a reduction of pores on the pororsity test upto 25.23% and penetration of water on the sorptivity test is upto 20.16%. This is due to the reduction of the pore due to its self healing property that activated within the specimen. This clearly indicates that the pores are getting arrested by the activeness of the self healing property due to the presence of bacterial concentration.

(c) It is found that, the specimen with bacterial concentration of 10, 20 ml and conventional mortar are in the category of low chloride ion permeability whereas the specimen with 30 ml bacterial concentration is falling under medium category of chloride ion permeability.

(d) 20 ml of bacterial concentration on the cement mortar is found to be optimum in terms of both strength and durability aspects.

References

1. Damena, A., Fekadu, Y., Shah, D.: Critical literature review on improvement of concrete properties by bacterial solution (2017)
2. Ling, H., Qian, C.: Effects of self-healing cracks in bacterial concrete on the transmission of chloride during electromigration. Constr. Build. Mater. **144**, 406–411 (2017)

3. Khade, S.G., Mane, S.J., Student, M.E.: Investigation of bacterial activity on compressive strength of cement concrete. Int. J. Eng. Sci. **7**(9), 14880 (2017)
4. Maheswaran, S., et al.: Strength improvement studies using new type wild strain Bacillus cereus on cement mortar. Current Sci. **106**(1), 50–57 (2014)
5. Shaikh, A., John, R.: Self healing concrete by bacterial and chemical admixtures. Int. J. Sci. Eng. Res. **8**(3), 145–151 (2017)
6. Naqash, J.A., Masoodi, M.A.A., Chakraborty, P.: Bacteria impregnated concrete-effects on strength parameters (2018)
7. Irwan, J.M., Teddy, T.: An overview of bacterial concrete on concrete durability in aggressive environment. Pertanika J. Sci. Technol. **25**, 259–264 (2017)
8. Vijay, K., Murmu, M., Deo, S.V.: Bacteria based self healing concrete–a review. Constr. Build. Mater. **152**, 1008–1014 (2017)
9. Mondal, S., Ghosh, A.D.: Investigation into the optimal bacterial concentration for compressive strength enhancement of microbial concrete. Constr. Build. Mater. **183**, 202–214 (2018)
10. Ramakrishnan, V., Panchalan, R.K., Bang, S.S., City, R.: Improvement of concrete durability by bacterial mineral precipitation. In: Proceedings of the 11th International Conference on Fracture, pp. 20–25, March 2005
11. Jonkers, H.M., Thijssen, A., Muyzer, G., Copuroglu, O., Schlangen, E.: Application of bacteria as self-healing agent for the development of sustainable concrete. Ecol. Eng. **36**(2), 230–235 (2010)
12. Ahn, T.H., Kishi, T.: Crack self-healing behavior of cementitious composites incorporating various mineral admixtures. J. Adv. Concr. Technol. **8**(2), 171–186 (2010)
13. Meyyappan, P., Carmichael, M.J.: An effective replacement of granite and marble powder on cement mortar subjected to chloride ion penetration test. In: Dasgupta, K., Sudheesh, T.K., Praseeda, K.I., Unni Kartha, G., Kavitha, P.E., Jawahar Saud, S. (eds.) Proceedings of SECON 2020. SECON 2020. LNCE, vol. 97. Springer, Cham (2021). https://doi.org/10.1007/978-3-030-55115-5_49
14. Meyyappan, P., Carmichael, M.J.: A comparative investigation on the utilization of marble dust and granite dust in the cement mortar against the sulphate resistance. In: Dasgupta, K., Sudheesh, T.K., Praseeda, K.I., Unni Kartha, G., Kavitha, P.E., Jawahar Saud, S. (eds.) Proceedings of SECON 2020. SECON 2020. LNCE, vol. 97. Springer, Cham (2021). https://doi.org/10.1007/978-3-030-55115-5_48
15. Meyyappan, P.L.: Effect of glass fibers, fly ash, quarry dust on strength and durability of aspects of concrete–an experimental study. In: IOP Conference Series: Materials Science and Engineering, vol. 396 (2018). https://doi.org/10.1088/1757-899X/396/1/012001.
16. Meyyappan, P.L., Amuthakannan, P., Sutharsan, R., Ali, M.A.: Utilization of M-sand & basalt fibre in concrete: an experimental study on strength and durability properties. In: IOP Conference Series: Materials Science and Engineering, vol. 561 (2019). https://doi.org/10.1088/1757-899X/561/1/012035

Evaluation of Sensitive Parameters in the Design of Deeper Manhole

N. K. Yadav, K. Senthil, Shailja Bawa, and Ankush Thakur

Abstract Manholes are critical sections in the design of underground construction. Concrete manholes have become mainstream in the recent decades due to its durability and are widely used for cleaning sewer lines. Therefore, the manuscript focused to study the influential parameters such as depth of manhole, grade of concrete and thickness of wall in the design of concrete manholes using Staad Pro, finite element software and a total of 240 simulations were performed on the manhole of 15 different depths (2.4 to 30 m), four different grade of concretes (M25-M40) and four different thickness of walls (125–200 mm). Also, two different diameters (1.5 and 1.8 m) of manhole were taken in the simulation as per the existing design code. The most critical loading conditions that exert pressure on the manhole outer surface from different directions were identified from the simulations and the results were presented in terms of displacement, moments and stresses. The validation on 1.5 and 1.8 m top slanting portions was performed as it is most vulnerable to overturning due to comparatively lesser self- weight by applying stability check against overturning. The predicted results in terms of safety factor against overturning found about 1.7 whereas recommended as 1.4 as per IS code. It is concluded that the deflection found to increases with increase in depth. It was also concluded that the deflection found to decreases with increase in grade of concrete, however it was observed that the moment and stress remained same for all the grades of concrete.

Keywords Manhole · Diameter of manhole · Deeper Manhole · Grade of concrete · Simulation

1 Introduction

Manholes are the openings having removable cover by which a person may get into a sewer for inspection, cleaning and other maintenance and such structure may also sustain the imposed load above it [1]. They are suitably provided when the gradient,

N. K. Yadav · K. Senthil (✉) · S. Bawa · A. Thakur
Department of Civil Engineering, Dr B.R. Ambedkar National Institute of Technology, Jalandhar, Punjab, India
e-mail: kasilingams@nitj.ac.in

alignment or diameter of the drainage is changed [2]. The dearth of technical literature available on concrete manhole has often caused insufficient design or over design of this important utility. In India, the ministry of housing and urban affairs has stated the need for the formulation of a national manual containing various aspects of storm water drainage system that also include detailed engineering of facilities [3]. A few studies based on concrete manholes as well as other material manholes from various parts of the world was available and discussed in this Section.

Saleem and Langdon [4] proposed the design parameters for precast concrete manhole and its components. The study investigates the construction condition, stability, loading, lateral load on the manhole walls, durability as well as soil bearing pressure. In addition, the author stated service conditions, proposed reference standards and summarised the specifications of manhole components in this study. Further, experimental investigations and mathematical modelling of manholes was conducted by **Sabouni and Naggar** [5, 6], presents the comparative details between the different configuration (1200 and 1500 mm diameter) of concrete manholes. The design parameters considered in the experiment was surrounding soil, soil compaction, water table elevation and trench width. It was observed that in both the configurations, pressure profiles underneath the manhole base was maximum at centre and decreased towards edge of the base. Also, it was observed that the critical contact pressure at the manhole base was mostly due to presence of water table at the top of the manhole. **Abbas et al.** [7] conducted experimental and analytical studies to propose a new design of manholes to be used in separate sewage systems. The improved design helps in easier installation of one manhole instead of two separate manholes that does not allows foul flow and storm flow to mix. The study is conducted using mathematical model and validated by. It was found that the proposed design has improved resistance to live loads of higher magnitude. **Kim and Park** [8] presented manhole with gear-shaped stairs to adjust its height. To determine the optimal dimension of gear shaped stairs, mechanical design has been adopted by using stress formula considering the shear and fatigue forces. It was concluded that by using height adjustable manholes there is reduction in human effort, elimination of reconstruction, improved remediation and rehabilitation.

A detailed literature survey revealed that a very few attempts in finite-element simulation of manholes by varying different parameters have been conducted. It is also being observed that a detailed investigation on deep manholes against various load combinations found to be limited. The requirement to fill this gap was motivated to provide valuable data that may be used to design the concrete manhole. This study is focussed on to investigate the basic design features of deep manholes that are not included in any design aid heretofore. In the present study, the influence of depth on deep manhole, diameter, grade of concrete and wall thickness has been studied. Also, this paper focused on studying the influence of depth beyond the range present in the existing design manual. A detailed numerical investigation of simulation, material properties and validation has been discussed in Sect. 2. The approach has been validated against applied earth pressure loading conditions with earth on one side and checked for safety against overturning. The response of the manhole was studied in terms of stresses, moments and displacements and compared in Sect. 3.

2 Numerical Investigation

The numerical investigation was carried out using finite element model in STAAD. Pro connect edition [9]. The model of the manhole has been made in accordance with the geometries employed in **IS SP 7 (Group 5): 2005** [1] and **IS 4111-1:1986** [10]. A total of 240 simulations were performed for manhole models at 15 different depths ranging from 2.4 to 30 m. At each depth, four different thicknesses of wall 125, 150, 175 and 200 mm were used to study the effect of moment and stress. At each depth and each thickness, four different grades of concrete M25, M30, M35, and M40 were used to study the effect on displacement.

2.1 Modelling of Manhole

The initial depth was considered at 2.4 m and was increased subsequently such that the plate element is standardised at 0.9 m for next simulation model each to reach 30 m depth. The wall of the manhole was modelled as plate elements and the base was set as fixed support. The design as per the Indian Standard for circular manhole was followed for modelling manhole that includes straight down in lower portion and slanting in top portion which narrow down the top opening that is equal to the internal diameter of manhole cover [1, 10]. Figure 1 represents a typical manhole model in 2D front elevation and 3D isometric rendered view prepared from STAAD. Pro. The internal diameter of circular manhole was used as specified in Indian standards [1, 10] up to 14.0 m depth (see Table 1). Beyond the depth of 14 m; no codal provisions are available in Indian standards and therefore 1800 mm internal diameter was continued up to 30 m depth.

The top portion that narrow down was modelled for internal diameter same as in straight lower portion for bottom end and was provided 560 mm internal diameter at the top opening as proposed by the Indian standard for minimum clear opening exceeding 0.9 m depth [10], and therefore for bottom internal diameter 1500 and 1800 mm, the maximum tapering angle of slanting portion was 32.07 and 34.56° with respect to vertical respectively.

The properties of concrete used throughout the analysis are given in Table 2. The value for characteristic compressive strength was provided in IS 456:2000, Table 2. The value of young's modulus of elasticity was calculated using Eq. (1) as per IS 456:2000 [11]. Further, the value of shear modulus of elasticity was calculated using Eq. (2) as per the theory of elasticity [12].

$$E_c = 5000\sqrt{f_{ck}} \tag{1}$$

$$G = \frac{E}{2(1 + \mu)} \tag{2}$$
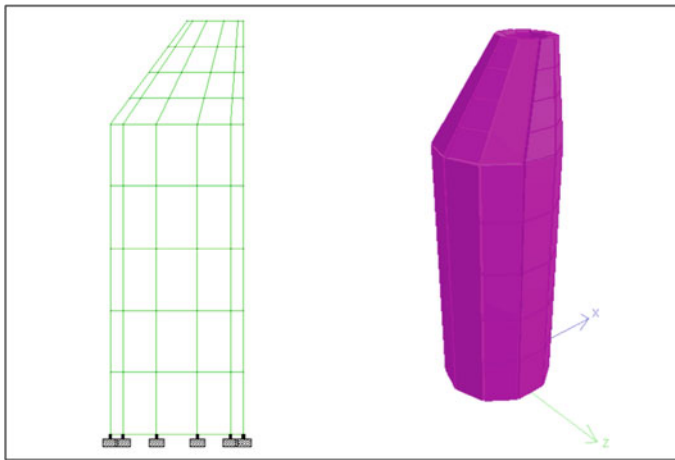
Fig. 1. Representation of a typical manhole model in 2D front elevation view and 3D isometric view of manhole prepared from STAAD.Pro

Table 1 Internal diameter of circular manholes for varying depths as per Indian standards

Depth above (m)	Depth Upto (m)	Diameter (m)
0.90	1.65	0.9
1.65	2.30	1.2
2.30	9.00	1.5
9.00	14.00	1.8

Table 2 Elastic properties of various grade of concrete

Grade of concrete	Characteristic compressive strength (N/mm^2)	Concrete density (kN/m^3)	Poisson's ratio, μ	Young's modulus of elasticity, E_c (N/mm^2)	Shear modulus of elasticity, G (N/mm^2)
M25	25	24.00	0.20	25,000.00	10,416.67
M30	30	24.00	0.20	27,386.12	11,410.88
M35	35	24.00	0.20	29,580.39	12,325.16
M40	40	24.00	0.20	31,622.77	13,176.15

2.2 Application of Loads and Combinations

The required load cases were applied onto the simulation models that include dead load, earth pressure, surcharge and IRC load. Further the load combination was also applied as per the Indian standard [13, 14].

Table 3 Parameters considered to calculate hydrostatic pressure and earth pressure

Description	Notation	Value
Unit weight of water	Υ_w (kN/m^3)	10
Unit weight of soil	Υ (kN/m^3)	20
Poisson's ratio of soil	η	1/3
Coefficient of earth pressure at rest	K_o	0.5
Surcharge Load	w_1(kN/m^2)	25

Hydrostatic Pressure and Earth Pressure. The hydrostatic and earth pressure were applied on the wall as proposed by IS 875-5: 1987 [14] including surcharge loads. Uniform horizontal pressure due to surcharge was applied that was calculated using Eq. (3) and the lateral earth pressure was calculated by using Eq. (4). Various parameters that were considered to calculate the hydrostatic pressure and earth pressure are given in Table 3.

$$P_h = K_o w_1 \tag{3}$$

$$P_e = \gamma k h + \left(\frac{1}{2}\right)\gamma_w h \tag{4}$$

IRC Loads. The traffic load was considered as imposed load. Axle load as proposed by IRC, class A loading was considered that specifies class A loading axle load of 114 kN [15]. Wheel load of 57 kN is multiplied by an impact factor of 1.25 that is approximately 72 kN which is applied on the nodes of the top portion at the narrow end of manhole model.

2.3 Validation of Slanting Portion of Manhole

The validation study on slanting portion of manhole was performed by applying stability check against overturning. The overturning and restoring moments were calculated for the 1.5 and 1.8 m top slanting portions at 125 and 150 mm wall thickness of manhole as it is most vulnerable to overturning due to less self- weight. The forces required for the calculation of moments were derived from the results obtained from STAAD. Pro as well as manual calculation using Ms-Excel. The stability check was applied against overturning of the manhole to interpret the actual adverse condition as, when the section is surrounded by soil from one side only and occurrence of surcharge condition is found negligible. The factor of safety against overturning was calculated as 0.9 times restoring moment by overturning moment, considered as per IS code [11]. The overturning moment and restoring moment were

calculated about the point located at the base of slanting sections near the outer edge on the farther side where no horizontal load was applied. It was found that the overturning moment due to earth pressure was 9.0 and 13.9 kN-m for 1.5 and 1.8 m top slanting sections, respectively having wall thickness 125 mm. It was observed that at 150 mm wall thickness, the overturning moment was 9.2 and 14.1 kN-m for 1.5 and 1.8 m slanting sections, respectively. It was also found that the restoring moment due to dead load at 125 mm thickness of wall for 1.5 and 1.8 m slanting portion was 17.3 and 28.7 kN-m, respectively. The restoring moment due to dead load at 150 mm wall thickness for 1.5 and 1.8 m slanting section was observed as 21.2 and 35.1 kN-m, respectively. It was concluded that the calculated factor of safety against overturning found satisfactory as about 1.7 found higher as compared to recommended value 1.4 by the IS 456:2000 code [11].

3   Result and Discussion

The analysis of the manhole was carried out against lateral earth pressure, hydrostatic pressure, surcharge load and vertical traffic load. Varying sensitive parameters such as depth and thickness, the manhole models were simulated against these loads and combination and the behaviour was studied. The actual moments and stresses were generated due to different loading conditions that can be estimated accurately by the use of software simulations only. Although a large number of stresses, moments and displacement were considered to study the results however, only critical value have been discussed. The results obtained by varying thickness or depth, one at a time were compared and discussed in this section.

3.1   *Influence of Thickness of Wall*

The simulation was carried out at different depths by varying thickness of wall as 125, 150, 175 and 200 mm. It was found that the moment (M_x and M_y) were maximum for 200 mm thickness at each depth. The percentage increase in moment (M_y) for 150, 175 and 200 mm wall thickness was compared against 125 mm thick wall and has been represented in Fig. 2. Overall, it was observed that the moment found to decrease with decrease of the manhole wall thickness. The reason may be due to the fact that the self-weight of the wall increased on increasing thickness of manhole's wall. It was found that the stresses (S_x and S_y) were maximum for 125 mm thick wall at each depth. The stresses were observed to be minimum for 200 mm thickness of wall. The percentage decrease in stresses (S_x) for 150, 175 and 200 mm thick wall against 125 mm thickness is shown in Fig. 3.
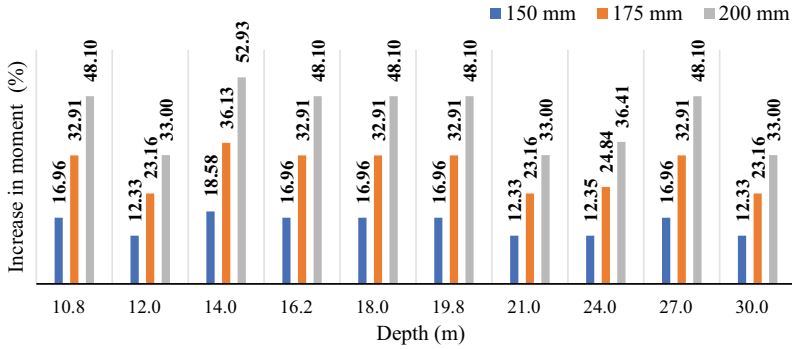
Fig. 2 Percentage increment in moment in comparison to 125 mm thick wall
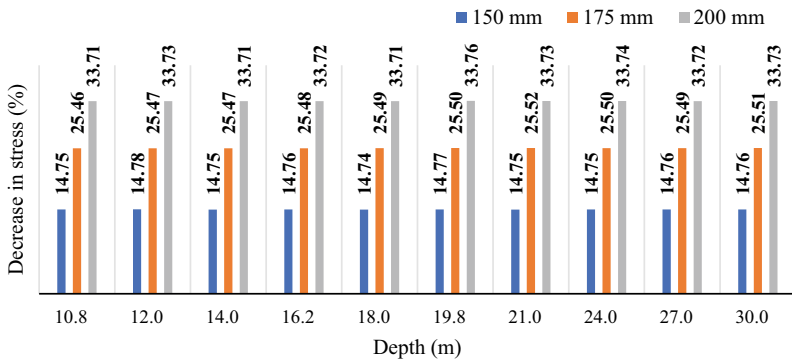
Fig. 3 Percentage decrement in stress in comparison to 125 mm thick wall

3.2 Influence of Varying Depth

The simulations were carried out to study the influence of change in depth at constant thickness and diameter of a manhole. The diameter was changed as per the IS code provision after 9 m depth only. The simulation results for displacement at each depth considered were plotted, see Figs. 4 and 5. It was found that as the depth was increased; the magnitude of the displacement found increased in principle directions against the load combination. It was also found that the maximum increase in displacement was due to displacement in principle directions with the increase in depth. Figures 4 and 5 represents increase in displacement for increase in depth at 125 mm thick wall for different concrete grade for range of depth 2.4 to 9 m and 10.8 to 30 m, respectively. The position of maximum displacement along the depth was observed in the simulation models and it was found that the maximum displacement occurred near the top node in the slanting portion at the narrow opening.
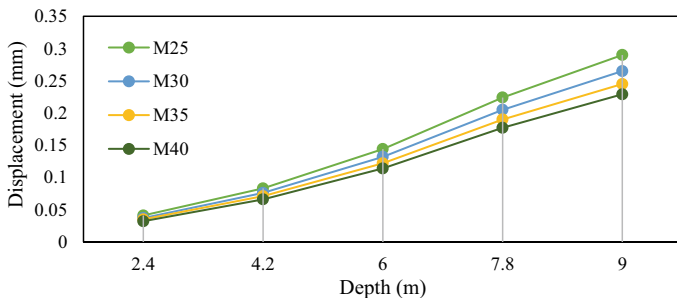
Fig. 4 Displacement for 2.4 to 9.0 m depth range at 1.5 m diameter and 125 mm thick wall
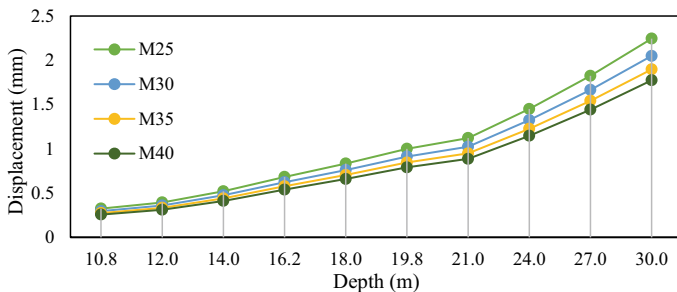
Fig. 5 Displacement for 10.8 m to 30.0 m depth range at 1.8 m diameter and 125 mm thick wall

3.3 Effect of Grade of Concrete

The analysis was carried out for four different grades of concrete to study the effect of material on analysis results. Simulations were performed for M25, M30, M35 and M40 grade of concrete and the results were found to remain same for all grade of concrete for moments and stresses. This may be due to the fact that the stress and moment are influenced by the loads applied but not by the grade of concrete.

However, the grade of concrete influenced the displacement of the manhole. The resultant displacement values were found to be maximum in each case in comparison to principle directions. It was found from the analysis that using higher grade of concrete decreased the displacement at same diameter and thickness of wall compared to the lower grade of concrete. The comparison of decrease in displacement in percentage between two simultaneous grades of concrete was conducted at various depths and has been expressed at two different depth for same thickness of wall and diameter (see Table 4); and the results were observed to be in close proximity of each other. The plotted results for resultant displacement against different grade of concrete shows decrease in displacement for increase in grade of concrete at 14 and 30 m depth as shown in Figs. 6 and 7, respectively.

Table 4 Percentage decrease in displacement by using relatively next higher grade of concrete

Depth (m)	Thickness of manhole wall (mm)	M25 to M30 (%)	M30 to M35 (%)	M35 to M40 (%)
14	125	8.65	7.37	6.59
	150	8.64	7.42	6.35
	175	8.79	7.23	5.52
	200	8.54	7.61	6.37
30	125	8.69	7.42	6.48
	150	8.75	7.38	6.49
	175	8.73	7.39	5.78
	200	8.75	7.40	6.50
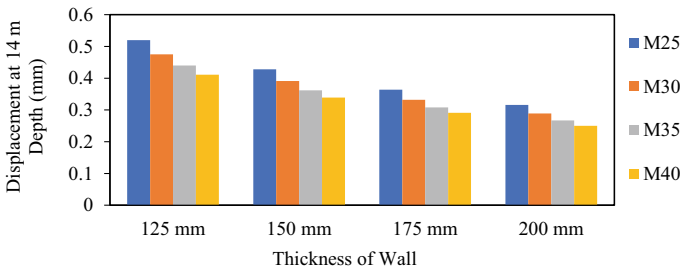
Fig. 6 Comparison of displacement on different grades of concrete and varying thickness of wall manhole at 14 m depth
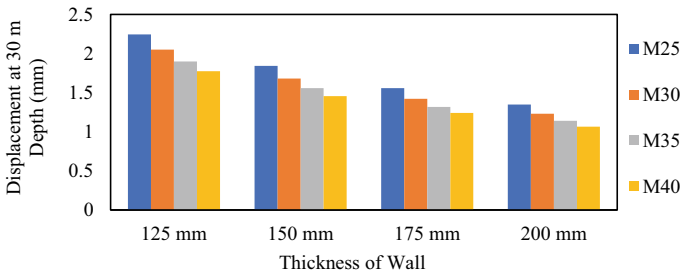
Fig. 7 Comparison of displacement on different grades of concrete and varying thickness of wall manhole at 30 m depth

4   Conclusion

The manuscript focused on studying the influential parameters such as depth of manhole, grade of concrete and thickness of wall in the design of concrete manholes using finite element software and a total of 240 simulations were performed for

manhole models of varying depths, thickness of wall and grade of concrete. The most critical loading conditions that exert pressure on manhole outer surface from different directions were considered for the simulations. The results were presented in terms of displacement, moments and stresses and the following conclusions were drawn;

- The simulations were carried out to study the influence of thickness of manhole wall and it was observed that moment found to increase with increase in the thickness of manhole wall. It is concluded that the moment is maximum for 200 mm thickness of wall at each depth.
- The validation has been performed on 1.5 and 1.8 m top slanting portions of 125 and 150 mm manhole wall thickness since it is more susceptible to overturning due to less self-weight under adverse condition. It was concluded that the calculated factor of safety against overturning found satisfactory as about 1.7 found higher as compared to recommended value 1.4 by the IS code.
- The simulations were carried out to study the influence of varying depth of manhole and depth was in the range of 2.4 to 30 m. It is concluded that the deflection increases with increase in depth.
- The simulations were carried out for four different grades of concrete and it was concluded that the deflection decreased with increase in grade of concrete. However, it is proposed to use M35 or higher grade of concrete due to the nature of work involved such as concrete in direct contact with corrosive fumes and corrosive water retained in it up to certain depth, as per recommendation for exposure condition 'very severe' in IS 456:2000. In light of reaction forces, it is also concluded that the moment and stress remained same for all the grades of concrete.
- The simulations were carried out to study the influence of parameters in the design of manhole. In light of slanting portion of manhole, the modelling was carried out for 1500 and 1800 mm depth such that the depth and bottom inner diameter are equal and top inner diameter is 560 mm that provides satisfactory slope to the tapering portion. It was concluded that for the above geometric configurations the maximum tapering angle was approximately 32 and 34° with respect to vertical for 1500 and 1800 mm depth respectively and thus the angle values in this close proximity may be used for design of the slanting portion under similar geometric configurations.

References

1. SP 7: Group 5:2005, National Building Code of India 2005 GROUP 5 (2005)
2. IS 1742:1983, Code of practice for building drainage (1983)
3. Manual on Storm water Drainage Systems, vol. I, Part: A 1st Edition, pp.14–16, May 2019
4. Al-saleem, H.I., Langdon, W.: Precast concrete manholes–a review and upgrade of current (2016)

5. Sabouni, R., El Naggar, M.H.: Circular precast concrete manholes: experimental investigation. Can. J. Civ. Eng. **38**(3), 319–330 (2011). https://doi.org/10.1139/L10-135
6. Sabouni, R., El Naggar, M.H.: Circular precast concrete manholes: numerical modeling. Can. J. Civ. Eng. **38**(8), 909–920 (2011). https://doi.org/10.1139/l11-059
7. Abbas, A., Ruddock, F., Alkhaddar, R., Rothwell, G., Andoh, R.: Improving the geometry of manholes designed for separate sewer systems. Can. J. Civ. Eng. **46**(1), 13–25 (2018). https://doi.org/10.1139/cjce-2018-0057
8. Kim, C.H., Park, J.H.: Development of a height-adjustable manhole, vol. 14, no. 1, pp. 21–25 (2006)
9. STAAD.Pro. https://docs.bentley.com/LiveContent/web/STAAD.Pro%20Help-v14/en/GUID-CEBB5436-47CA-487E-AD06-E5C67F8496AC.html
10. IS 4111-1 (1986): Code of practice for ancillary structures in sewerage system, Part I: Manholes (1986)
11. IS 456:2000: Plain and Reinforced Concrete Code of Practice, Bureau of Indian Standard, New Delhi (2000)
12. Landau, L.D., Lifshitz, E.M.: Theory of Elasticity, vol. 7. Course of Theoretical Physics, p. 14, 2nd Edn. Pergamon, Oxford (1970)
13. IS 875 Part 1:1987, Code of Practice for Design Loads for Building and Structures Part 1: Dead Loads–Unit Weights of Building Material and Stored Materials (1987)
14. IS 875 Part 5: 1987, Code of Practice for Design Loads for Building and Structures Part 5: Special Loads and Combinations (1987)
15. IRC 6:2017: Standard specifications and code of Practice for road bridges–Section: 2, Loads and load combinations (2017)

Neural Network and AELH Based Efficient Aerodynamic Forecasting of 'Y' Plan Shaped Tall Building

Prasenjit Sanyal and **Sujit Kumar Dalui**

Abstract Y plan-shaped tall buildings are ubiquitous and architecturally efficient for residential and commercial purposes. The side ratio (SR) of these buildings can be altered based on the ventilation need and availability of the total plot area. Aerodynamic coefficients of Y plan-shaped tall buildings for various SRs are measured by varying the Wind incidence angle (WIA). The design parameters and outputs of the CFD analysis are utilized for training Artificial Neural Networks (ANN). Audze—Eglais Uniform Latin Hypercube (AELH) sampling method and Genetic Algorithm (GA) optimization approach are blended for selecting some most efficient sample points. Computational Fluid Dynamics (CFD) study is done on ANSYS CFX for these particular data points. The very good predictabilities of ANN suggest the efficiency of the AELH sampling method. This type of combined efficient approach can be used in the future for various aerodynamic studies, and it will significantly decrease the total computational cost without compromising the forecasting error.

Keywords Artificial neural network · Computational fluid dynamics · Audze—Eglais uniform Latin hypercube sampling · Aerodynamic coefficients · Wind structure interaction

1 Introduction

With the continuous upgrade in modern analysis tools and construction technologies, the number of skyscrapers is increasing day by day. Artificial intelligence (AI) is further easing the design procedure and motivating the construction industries to focus on irregular and unconventional buildings. These irregular buildings are sometimes highly vulnerable to wind-induced hazards. On the other hand, proper guidelines for irregular plan-shaped buildings are not available in different international codes. Furthermore, the interfering effects of different tall towers also create local high-velocity zones. This may be proved to be thermally comfortable for normal

P. Sanyal (✉) · S. K. Dalui
Indian Institute of Engineering Science and Technology, Howrah, India
e-mail: prasenjit.sanya14@gmail.com

atmospheric conditions, but it can be disastrous for a critical cyclonic condition. These problems can be overcome by proper wind tunnel analysis of the building models in appropriate environmental conditions. But wind tunnels are not always accessible, and the model creation process is time-consuming. These can be overcome by computational Fluid Dynamics (CFD) analysis. Nowadays, high computation setups are easily accessible. These CFD studies are quite fast and easily configurable, and the results are also highly acceptable. Previously some experimental and CFD studies have been done on irregular plan-shaped tall buildings [1–5]. Different types of shape modified Y plan-shaped tall buildings were also previously studied [6–9]. For the present study, the analysis has been done on a triaxial symmetrical Y plan-shaped tall building by blending the AELH sampling method, CFD and ANN.

2 Description of the Model

For performing the CFD analysis, a scale factor of 1:300 is used. The height (H) of the model is taken as 500 mm. The length (L) and width (W) of the primary building model are taken as 100 and 50 mm. Now the L/W of the building model is varied by keeping the total plan area same. Now as the building is triaxially symmetrical so the range of studied WIA is taken from 0 to 60°. The studied cases are selected as per the AELH sampling method as discussed in Sect. 4 (Figs. 1 and 2).

3 CFD Setup

The domain shown in Fig. 3 is constructed as per the suggestion of Franke et al. [10]. A clearance of 5H is provided along the side faces, top face and inlet of the domain. The clearance along the outlet is 15 H. Here H is the height of the studied building model. This much size of the domain is at least required for the proper occurrence of corner flow separation and leeward side wake. A scaling ratio of 1:300 is used for both model and domain as per the recommendation of Taranath [11].
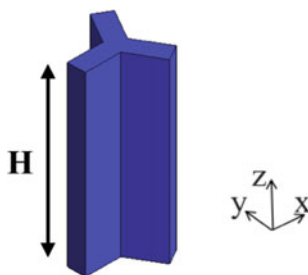
Fig. 1 Building model
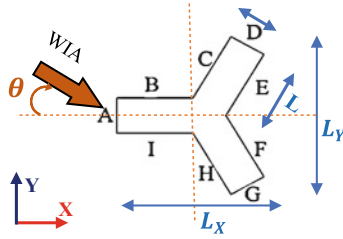
Fig. 2 Plan view
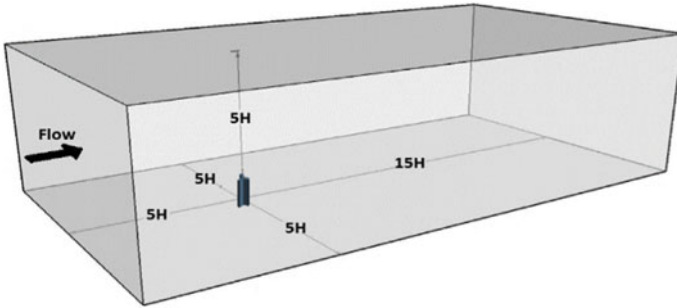
Fig. 3 Domain used for numerical simulation
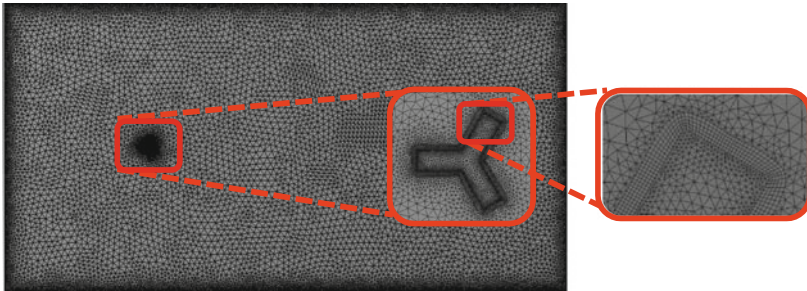
Fig. 4 Meshing details near the building model

The meshing is done with tetrahedral elements. Mesh near the building model is finer for adequately capturing the wind parameters. Biased edge sizing is used along the walls. Inflation is provided around the building model for proper separation of boundary layered flow (Fig. 4).

The flow environment generated in this CFD simulation is similar to what was used by Mukherjee et al. [6]. Inlet velocity is assigned as per the Power Law.

$$U(z) = U_0(Z/Z_0)^\alpha \tag{1}$$

Here U_z is the velocity at height Z. U_0 and Z_0 are the boundary layer velocity and depth. α is the power law exponent This value (0.133) is considered according to the terrain category II (open terrain with well-scattered obstruction) of IS 875 (part 3) 2015. U_0 is taken as 10 m/s. Building facets and the bottom of the domain are assigned as no-slip walls. Top and side faces are characterized by symmetry. The relative pressure difference between the inlet and outlet is taken as 0 Pa. The basic domain pressure is taken as 1 atm i.e., 101,325 Pa.

4 AELH Sampling Method

Forecasting is mainly incorporated to minimize the number of response evaluations and to eliminate the noise. For expensive analysis, the choice of point of evaluation is very important. The methodologies incorporated for the formulation of sample data points are collectively termed as Design of Experiments (DoE). Latin Hypercube (LH) sampling method has no dependency on the mathematical model of a problem. Normally LH method can be classified as Random Latin Hypercube (RLH) sampling and more structured AELH sampling. The LH DoE is taken so that all variables are placed into P at different and equal levels. Figure 5 shows some DoEs when there are two variables (N = 2) and three sample points (P = 3). For impermissible combinations, some points come in the same level, and some levels remain empty. For permissible combination, all the levels are utilized for different data points. RLH method uses random sampling for getting the permissible DoE. AELH method uses the analogy of minimum potential energy/minimum repulsive force among similarly charged particles.

Suppose P number of charged particles are released in a design space. In that case, every particle will give repulsive force to the other particles, and it will come to equilibrium when the repulsion among them is minimum. As per Coulomb's law, the repulsive force is inversely proportional to the distance square. Then by minimizing Eq. 2 we will get the AELH DoE

$$F_{\min} = \text{Min} \sum_{p=1}^{p} \sum_{q=p+1}^{p} \frac{1}{L_{pq}^2} \tag{2}$$
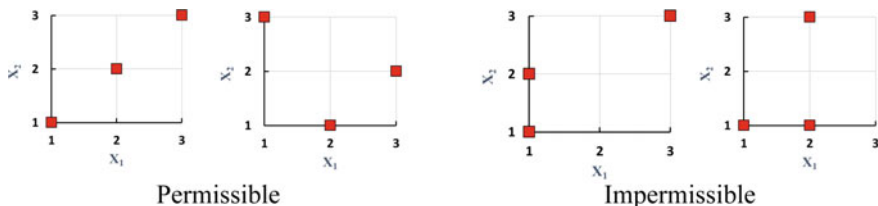
Fig. 5 Permissible and Impermissible LH DoE for N = 2, P = 3
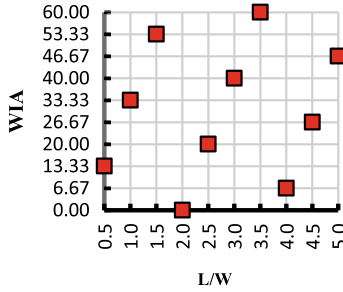
Fig. 6 Scaled.DoE as per AELH method

where L_{pq} is the distance between among charges having numbers p and q (p $\neq$ q).

For a LH DoE with P number of points and N number of design variables, the possible position of first point can be P^N, and the total number of combinations can be $P^N(P-1)^N(P-2)^N \ldots \ldots \ldots 3^N 2^N 1^N$. For P = 3 and N = 2 (Fig. 5) the possible position of first point can be 9 and the total number of combinations can be 36. Among these 36 combinations, the DoE with least repulsive force will be termed as AELH DoE. If P = 10 and N = 5, then the number of possible solutions is 6.3×10^{32}. If it takes at least one nano second for performing each evaluation then total 2 years $\times 10^{16}$ is required for getting the AELH DoE. This is practically impossible and optimization process is required for finding out the minimum repulsion points.

Bates et al. [12] has compared different optimization techniques and concluded that the Genetic Algorithm is the best approach to finding out the best sampling points. For the present AELH DoE, N = 2 (Side Ratio and WIA) and P = 10. Proper Scaling is done for fitting the variables in our studied range.

5 Results

The Aerodynamic Coefficients are calculated [13] using the following expressions

$$C_{Fx} = \frac{F_x}{0.5\rho U_H^2 \cdot L_Y.H} = \frac{\sum_i C_{pi} A_i cos\alpha_i}{\sum_i A_i cos\alpha_i} \tag{3}$$

$$C_{Fy} = \frac{F_y}{0.5\rho U_H^2 \cdot L_X.H} = \frac{\sum_i C_{pi} A_i sin\alpha_i}{\sum_i A_i sin\alpha_i} \tag{4}$$

$$C_F = \sqrt{C_{Fx}^2 + C_{Fy}^2} \tag{5}$$

C_F is the global force coefficient of the whole building; C_{Fx} and C_{Fy} are the force coefficients along X and Y axis; F_x and F_y are total effective force in the x and y-direction,, Cpi is the pressure coefficient of point i, 'A_i' is the subsidiary area of
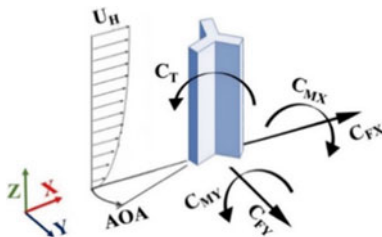
Fig. 7 Studied Aerodynamic coefficients

point i; $\cos \alpha$ and $\sin \alpha$ are the direction vector of point i along X and Y axis.

$$C_{Mx} = \frac{M_x}{0.5\rho U_H^2 \cdot L_X \cdot H^2} = \frac{\sum_i C_{pi} A_i z_i \sin\alpha_i}{H . \sum_i A_i \sin\alpha_i} \tag{6}$$

$$C_{My} = \frac{M_y}{1/2\rho U_H^2 \cdot L_Y \cdot H^2} = \frac{\sum_i C_{pi} A_i z_i \cos\alpha_i}{H . \sum_i A_i \cos\alpha_i} \tag{7}$$

$$C_M = \sqrt{C_{Mx}^2 + C_{My}^2} \tag{8}$$

C_M is the global moment coefficient of the whole building; C_{Mx} and C_{My} are the moment coefficients along X and Y axis; M_x and M_y are the total effective moments along X and Y-direction. Zi is the distance from point i to moment calculation point; H is the height of whole building.

$$C_T = \frac{M_Z}{0.5\rho U_H^2 \cdot L_X \cdot L_Y \cdot H} = \frac{\sum_i C_{pi} A_i y_i \cos\alpha_i + \sum_i C_{pi} A_i x_i \sin\alpha_i}{\frac{1}{H} . \sum_i A_i \cos\alpha_i . \sum_i A_i \sin\alpha_i} \tag{9}$$

C_T is the global torsional coefficient; M_z is the value of torsional moment along Z direction. x_i and y_i is the distance of point i from the mass centre of the building model (Figs. 6 and 7).

5.1 ANN Prediction

ANNs are used in different aerodynamic forecasting studies. Training algorithm, architecture, neuron number and training pattern play a vital role and a rational approach should be adopted in the selection process [14]. Selection totally depends on the nature and volume of the study. Researchers usually tend to use a large number of neurons which effectively decreases the prediction error. However, Huter and Yo [15] have suggested using lesser neurons and sufficient training patterns. They observed that this type of training can be actually suitable for patterns other than what is used for training. In this study, the Feed Forward Back Propagation (FFBP) method with

an architecture of Multilayer perception (MLP) is used. Levenberg–Marquardt (LM) method is used as

The second-order ANN. The data set is very limited in the present study so a network with one input, hidden (3 neurons) and output layer is used [Fig. 8]. The used input and output data used in the ANN is tabulated in Table 1. The flowchart of the analysis process is shown in Fig. 9. The training is done with 70% data and rests are used for validation and testing.

The regression plots are checked for training, validation and testing, and training is continued till all these values overtake 0.99 [Fig. 10]. The error histogram is shown in Fig. 11 and the error is actually less than 1% for most of the cases, and actually never larger than 5%. Results for all the design points are compared in Fig. 12 and it can be concluded that ANN prediction is highly admissible.
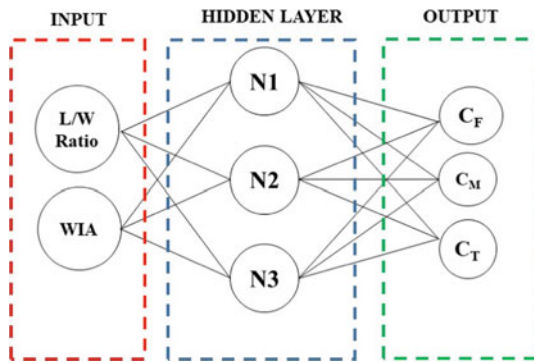
Fig. 8 Input, hidden and output layer of the ANN

Table 1 Force, moment and torsional coefficient data for the sample points (P = 10, N = 2)

WIA	L/W	L	W	C_F	C_M	C_T
0	2	100.00	50.00	0.73	0.41	0.00
6.67	4	143.86	35.97	0.82	0.45	0.04
13.33	0.5	45.61	91.21	0.80	0.44	0.12
20	2.5	112.56	45.03	1.22	0.65	0.10
26.67	4.5	152.89	33.98	1.35	0.71	0.12
33.33	1	68.44	68.45	1.01	0.54	0.15
40	3	123.87	41.29	1.13	0.59	0.16
46.67	5	161.41	32.28	1.18	0.60	0.17
53.33	1.5	85.65	57.10	0.83	0.44	0.09
60	3.5	134.24	38.35	1.13	0.57	0.02
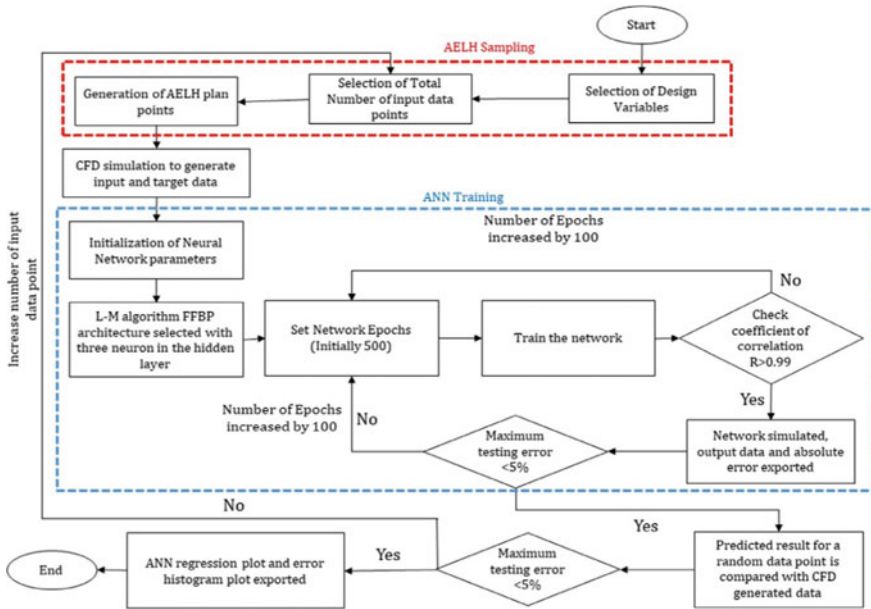
Fig. 9 Flowchart of the present problem
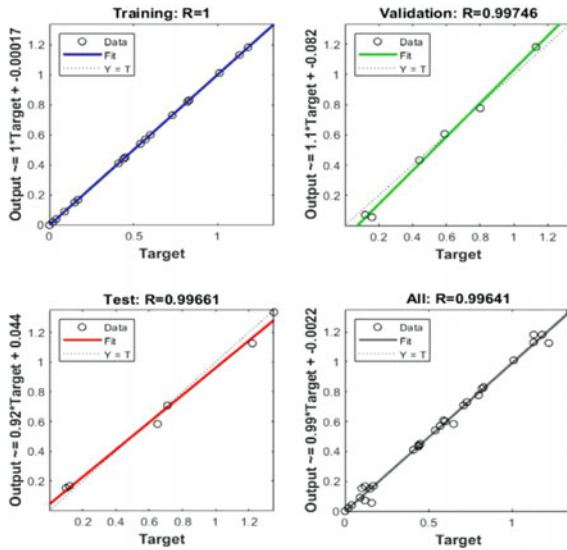
Fig. 10 Regression plots of the developed ANN model

Fig. 11 Error histogram of ANN
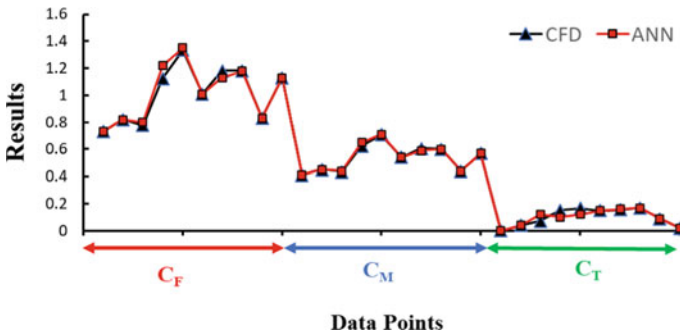
Fig. 12 Comparative analysis of different aerodynamic coefficients for various data points

6 Conclusion

The present study focuses on forecasting of aerodynamic coefficients of Y plan shaped building by blending Audze—Eglais Uniform Latin Hypercube (AELH) sampling method, Computational Fluid Dynamics (CFD) and Artificial Neural Network (ANN). The significant outcomes from the present study are

- Genetic Algorithm (GA) based optimized AELH sampling method is very efficient and it actually decreases the number of required sample points by distributing Design of experiments throughout the domain.
- ANN is highly efficient in predicting the aerodynamic coefficients with a maximum forecasting error of less than 5%.
- Total computational time can be significantly decreased by using a blended method of AELH, CFD and ANN. Here the studied range of L/W ratio is 0.5–5. If only direct CFD analysis is done then huge computational time is required since many random CFD runs are to be undertaken for studying the huge range of L/W ratio for various Wind Incidence Angles.

References

1. Gomes, M.G., Rodrigues, A.M., Mendes, P.: Experimental and numerical study of wind pressures on irregular-plan shapes. J. Wind Eng. Ind. Aerodyn. **93**(10), 741–756 (2005)
2. Chakraborty, S.K., Dalui, A.K.: Ahuja, Wind load on irregular plan shaped tall building–a case study. Wind Struct. **19**(1), 59–73 (2014)
3. Bhattacharjee, S., Banerjee, S., Majumdar, S.G., Dey, A., Sanyal, P.: Effects of irregularity on a butterfly plan-shaped tall building under wind load. J. Inst. Eng. (India) Ser. A **102**(2), 451–467 (2021)
4. Paul, R., Dalui, S.K.: Wind effects on 'Z' plan-shaped tall building: a case study. Int. J. Adv. Struct. Eng. **8**(3), 319–335 (2016)
5. Li, Y., Li, Q.S., Chen, F.: Wind tunnel study of wind-induced torques on L-shaped tall buildings. J. Wind Eng. Ind. Aerodyn. **167**, 41–50 (2017)
6. Mukherjee, S., Chakraborty, S., Dalui, S.K., Ahuja, A.K.: Wind induced pressure on 'Y' plan shape tall building. Wind Struct. **19**(5), 523–540 (2014)
7. Sanyal, P., Dalui, S.K.: Effects of internal angle between limbs of "Y" plan shaped tall building under wind load. J. Build. Eng. 33(2021), 101843 (2021)
8. Sanyal, P., Dalui, S.K.: Forecasting of aerodynamic coefficients of tri-axially symmetrical 'Y' plan shaped tall building based on CFD data trained ANN. J. Build. Eng. **47**, 103889 (2022)
9. Sanyal, P., Dalui, S.K.: Effects of side ratio for 'Y' plan shaped tall building under wind load. In: Building Simulation, vol. 14, no. 4, pp. 1221–1236. Tsinghua University Press (2021)
10. Franke, J., et al.: Recommendations on the use of CFD in wind engineering. Cost Action C (January), pp. 1–11 (2004)
11. Taranath, B.S.: Tall Building Design: Steel, Concrete and Composite Systems. CRC Press, United States of America (2016)
12. Bates, S.J., Sienz, J., Langley, D.S.: Formulation of the Audze—Eglais uniform Latin hypercube design of experiments. Adv. Eng. Softw. **34**(8), 493–506 (2003)
13. Sun, X., Liu, H., Su, N., Wu, Y.: Investigation on wind tunnel tests of the Kilometer skyscraper. Eng. Struct. **148**, 340–356 (2017)
14. Karsoliya, S.: Approximating number of hidden layer neurons in multiple hidden layer BPNN architecture. Int. J. Eng. Trends Technol. **3**(6), 714–717 (2012)
15. Hunter, D., et al.: Selection of proper neural network sizes and architectures—a comparative study. IEEE Trans. Ind. Inform. **8**(2), 228–240 (2012)

Estimation of Willingness to Pay for Reducing Road Accident Risk Using Route Choice Model

P. H. Sumayya Naznin, V. G. Anandu, Leena Samuel Panackel, and A. U. Ravishankar

Abstract The proportionality of road accidents with urbanization triggers road accident cost analysis, as a prime component in the planning and designing of road projects. However, proper quantification of accidents and analyzing every parameter associated with it is a tedious task and requires expert approaches. This study deals with the cost of road accidents in Thiruvananthapuram city as it houses the most critical accident spots in the state of Kerala. Essential stretches of roads to be analyzed were identified using Accident Severity Index (ASI). A Stated Preference (SP) survey was conducted to estimate the trip-wise mean willingness to pay value (WTP) of road users of the selected road stretches based on logit models. Travel time, travel costs, and accident rates were taken as the attributes. The behavior of individual users was interpreted from the coefficients estimated from the models. The mode-specific variables showed relations consistent with the expectations. The willingness to pay value to avoid a critical accident estimated from the final model was found higher for short trip setting (Rs.1.08/trip), which indicates the importance of safety of the short frequent trips among the road users compared to the longer trip setting (Rs. 0.72/trip).

Keywords Willingness to pay (WTP) · Logit models · Stated Preference (SP) survey

P. H. S. Naznin (✉) · A. U. Ravishankar
Department of Civil Engineering, National Institute of Technology, Mangaluru, Karnataka, India
e-mail: sumayyanazninph.187cv506@nitk.edu

V. G. Anandu
Department of Civil Engineering, TKM College of Engineering, Kollam, Kerala, India

L. S. Panackel
Department of Civil Engineering, Federal Institute of Science and Technology, Angamaly, Kerala, India

1 Introduction

The tremendous rise in road accidents across the Globe in the past few years drives the significance of sustainable transportation. The need for sustainable transportation systems is increasing day by day and requires efficient resource allocation. This process needs proper quantification of the associated costs and benefits. Valuation of road accidents [16], one of the negative impacts of road transport, is a challenging task apart from congestion, environmental and noise pollution.

According to the World Health Organization, low-income countries now have the highest annual road traffic fatality rates. About 80,000 people get killed in road crashes every year in India, which is 13% of the total fatality worldwide. The man behind the wheel plays a vital role in most of the crashes. In most cases, crashes occur either due to carelessness or due to a lack of road safety awareness of the road user. Hence, road safety education is as essential as any other necessary skills of survival (MoRTH).

The value of safety, usually represented as the Value of a Statistical Life (VSL) or the value of reducing risk, is a central element in the social evaluation of road projects. As transport safety is a non-market good whose price cannot be directly observed, developing promising methodologies to assess this value is necessary. The costs of road accidents can be subdivided into three components: Direct economic cost, indirect economic costs, and intangible costs. While the first two components constitute monetary amounts, the valuation of the intangible losses is complicated. Consequently, early research ignored this component, focusing instead on indirect economic costs. The Damage-cost approach and willingness to pay approach are the two essential methods for costing road accidents. The human capital approach is the basis of all damage-cost approaches. It relies on the assumption that the VSL is directly related to an individual's future production potential, usually represented through the gross income a person can earn over their entire working life.

Due to the shortcomings of the damage-cost approaches [13], several researchers [10,15] turned their attention to the newly developed Willingness to Pay (WTP) approach. This method is based on the willingness of individuals to pay an amount of money for the up-gradation of safety conditions (WTP). In this way, the value society assigns to a particular good is considered equal to market demand.

Most of the willingness to pay estimation methods are survey-based approaches, and survey-based approaches are criticized for fluctuating results. Hence there shall be adequate methods for the proper conduction of the survey to simulate the actual conditions in the willingness to pay estimation. Furthermore, accurate assessment of the value of risk reduction requires advanced modeling techniques with limited errors.

2   Methodology

The evaluation of willingness to pay is strictly a survey procedure where the respondents are asked how much they are willing to pay to reduce the risk of getting injured in a road accident [1]. Stated choice experiments deal with the indirect measurement of WTP value from the user behavior [9,17]. The estimation of the value of accidents involves Accident analysis and Sample selection, Perception survey, Experimental design, Questionnaire design, Primary data collection and Analysis, Stated choice survey. Development of models and Estimation of mean WTP.

Since this study concentrated on accident costing, the places where the accidents are concentrated need to be identified. This involves the analysis of accident data from various government sources. The population to be studied was selected based on the accident rates.

2.1   Site Selection

In this study, aggregated black spots in Thiruvananthapuram city were identified based on the district-wise Accident Severity Index (ASI) values as shown in Table 1. To incorporate complete exposure of the risk, two trip settings (a short one–1 km and a long one–3.5 km) were fixed for the two roads, considering the average values of the attributes involving two-wheelers and passenger vehicles.

Table 1 High-risk road segments

Critical stretches	Landmark	Road Type	ASI
Killippalam Junction-Pappanamcode (3.5 km)	Pappanamcode Mosque - Kerala Gramin Bank	NH 66	366
	Tax Towers - Karamana Junction	NH 66	314
	Killipalam Junction - Bharat Petroleum Petrol Pump	NH 66	234
	BSNL RTTC - 50 m before Pappanamcode Mosque	NH 66	183
Overbridge Junction-Attakulangara Junction (1 km)	Overbridge Junction - East Fort KSRTC Depot Junction	MG Road	241
	East Fort KSRTC Depo Junction - Attakulangara Junction	MG Road	250

2.2 Preliminary Survey

A preliminary survey form was created to understand the population characteristics, including inquiries related to the contingent valuation approach [8,18], stated choice methods, and socio-economic factors to the population of road users. Face to face interviews were carried out involving 12 people, of different categories of age, occupation, income and other factors considered for the survey [6,7,11]. Based on preliminary survey results, asking respondents directly how much they are willing to pay for a particular percent of risk reduction was removed as chances of partial protest responses are high, and a stated choice approach that was found easy for them to respond to was chosen. In addition, to reduce the complexity of design, binary alternatives [12] were selected as attributes cannot be compromised.

2.3 Stated Choice Survey

A Stated Choice (SC) experiment involving two alternatives was designed. Attributes chosen for the design were Travel Time (TT), Travel Cost (TC), and Critical Accident rate (CA), as these factors play a significant role in the decision-making process in selecting a route for travel [3,4,14]. To make a balanced design, equal levels of two each were chosen for all the attributes. The initial levels of attributes chosen were revised based on pilot studies. Since the accident rates are comparatively high, a higher difference level was chosen for the travel time and travel costs to prevent the complete neglecting of attributes fixed for the study. The most compact orthogonal design was generated using statistical analysis software. Out of the eight generated alternatives, the choices showing all values lower than the reference level, leading to the complete dominance of choices should be eliminated.

Finally, questionnaire was designed using four categories of questions, i.e., general socio-demographic characteristics, means of transport, Accident history, and the choice experiment part. Since the difference levels were not directly perceivable to the people, a trip condition showing the travel time, travel cost and the accident rates was used. The target population of road users was selected randomly with different age groups, including people who were victims of road accidents that resulted in personal injury and comprising a wide range of factors that affect the route choice behavior of people. They were provided a questionnaire with a total of 6 choice sets (each), separately stating the attribute values corresponding to the two stretches of study (six choice sets for Overbridge-Attakulangara Stretch and six for Killipplam-Pappanamcode stretch) as shown in Fig. 1. Alternatives were created based on the reference values of attributes associated with the trip.

In order to estimate the cost component, the capital cost per unit distance was calculated by taking the average service life of vehicles (in kilometers) into account, which was obtained from the previous studies [2,5] along with the cost data obtained from the questionnaire surveys among the vehicle users of Thiruvananthapuram city.

Fig. 1 Sample
representation of choice sets
in the questionnaire
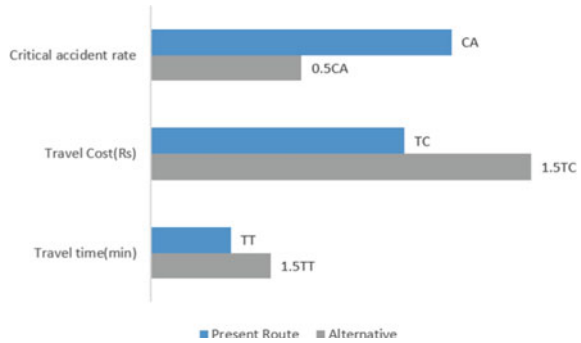
The values of the cost of travel for public vehicles were used as per the rates fixed by the Motor vehicle department, Government of Kerala, and the Kerala state road transport Corporation. Travel time was fixed based on the data obtained from the latest available Comprehensive mobility plan (CMP) for Thiruvananthapuram city.

The annual average accident rate was obtained from the combined analysis of District Crime Records Bureau (DCRB) data and the FIR reports collected from THUNA (a website managed by Kerala police). Since the area under study is high-risk road accident spots, only the accidents involving fatalities and severe injuries were taken for presenting the risk to the respondents.

3   Results and Discussions

3.1   *Data Analysis*

As the present study focus on generating a random effects model, even small sample sizes can give reliable results [2]. After removing the inconsistent responses, 160 samples were obtained from the users of Overbridge-Attakulangara road segment. About 34% of the respondents were females. Among the respondents, most were singles (66.25%). The samples show a dominance of graduates (68.75%). The average household size was four members. 27.5% of the respondents were students. Most of them do private jobs for a living (36.25%). Monthly household income was below 30,000 rupees for 33% of the users. This may be because of the soft pay scales for private jobs. About 41% of road users have an accident history. 68.75% of respondents have a household size of four. Most respondents prefer Two-wheelers (51.25%) and Cars (36.25%) compared to public means. About 26% of the respondents use the stretch for work trips, 16% for educational trips, and 58% for other trips as shown in Table 2.

Based on the data collected from 139 users of Killippalam - Pappanamcode road segment, it can be inferred that the socio-demographic characteristics of the second

Table 2 Socio-economic characteristics of Road Segment I and Road Segment II

Variables	Label	Road segment I	Road segment II
Gender	Female	34.38	33.10
	Male	65.62	66.90
Marital status	Married	33.75	30.20
	Single	66.25	69.80
Accident history	Yes	41.25	37.40
	No	58.75	52.60
Education	12th and below	14.38	12.94
	Graduate	68.75	70.50
	PG and above	16.88	16.56
Occupation	Student	27.50	28.05
	Unemployed	13.75	14.38
	Private job	36.25	33.81
	Government job	10.00	8.630
	Other	12.50	15.13
Age (Years)	18–25	58.75	59.71
	26–30	11.25	10.07
	31–40	9.38	15.10
	41–60	18.13	11.51
	Above 60	2.50	3.610
Monthly household income (Rupees in thousands)	Below 30	33.13	35.97
	31–50	19.38	22.30
	51–70	13.13	12.23
	71–90	6.88	7.910
	91–100	10.00	10.07
	101–200	11.25	6.470
	Above 200	6.25	5.050

road segment users don't show much difference as users of both of these segments were given the scenarios for both the segments.

For others, an option for choosing the stretches was given. Among the users, 33.1% were females and 66.9% were males. The respondents with accident history (37.40%) are less when compared to the road segment-I (41.25%). The education and occupational distribution show identical values in both segments. The users showed a higher proportion of age group between 31–40 years (15.10%) than the previous segment (9.375%), while the age group between 41–60 years is more (18.125%) for the latter segment than the former (11.51%). Also, the first segment has a greater number of respondents (17.5%) with household income above one lakh than the second segment (11.52%). More people prefer public transports in the second road

segment (17.98%) when compared with the first (12.5%). On the other hand, work and educational trips were high for the users of the second road segment.

3.2 Route Choice Model

Based on the perception survey, a Stated Choice (SC) experiment involving two alternatives was designed.

The selected attributes play a significant role in the decision-making process in selecting a route for travel. In route choice model, two routes with varying attributes were presented to the respondents to choose, based on their attitude towards the road safety. The NLOGIT developed by Econometric. Inc. was used for generating models for the estimations of detailed user behaviors. The parameter estimates of each road segments are given in Tables 3 and 4.

For Overbridge –Attakulanagara segment, 960 observations collected from 160 individuals were used for model formation. All attributes used are significant at a 95% confidence interval in both the initial and the final models. Apart from the attributes, marital status and accident history became significant at 95% in the initial model, but accident history became significant at 90% interval in the simulated model. The final model gives better R squared values (0.213 and 0.207) compared to the initial model. McFadden recommends a value between 0.2 and 0.4 for better fitness of the model. The probability of exceeding the chi-squared value is less than the significance levels, i.e., the alternate hypothesis that the addition of independent variables improves the model is accepted. The Akaike and Bayesian criterion values are lower for the final model, indicating low prediction error than the constant only and the multinomial logit models. The random parameters model gives the standard

Table 3 Parameter estimates for Overbridge–Attakulanagara road segment

Variable	Coefficient		t-value		p-value	
	MNL model	RPL model	MNL model	RPL model	MNL model	RPL model
Constant	0.2510	0.3830	1.089	1.002	0.2760	0.316
Travel time	−0.1560	−0.2547	−4.646	−5.703	0.0000	0.000
Travel cost	−0.1159	−0.1884	−8.121	−9.326	0.0000	0.000
Critical accident	−0.1261	−0.2047	−2.309	−2.914	0.0209	0.003
Married	−0.6787	−1.1065	−4.647	−2.713	0.0000	0.006
Accident history	0.4443	0.7070	3.170	1.817	0.0015	0.069
Standard deviation	–	2.0977	–	9.197	–	0.000

Table 4 Parameter estimates for Killippalam – Pappanamcode road segment

Variable	Coefficient		t-value		p-value	
	MNL model	RPL model	MNL model	RPL model	MNL model	RPL model
Constant	0.2282	0.3840	0.996	0.947	0.3195	0.3435
Travel time	−0.0514	−0.1040	−2.507	−3.483	0.0122	0.0005
Travel cost	−0.0367	−0.0734	−5.642	−7.262	0.0000	0.0000
Critical accident	−0.0264	−0.0527	−1.487	−2.087	0.1371	0.0369
Standard deviation	–	2.7744	–	8.811	–	0.0000

deviation of the estimates, which is an essential factor for analyzing the individual's characteristics. The standard deviation is significant with a t-value of 9.197 in the final model, confirming unobserved heterogeneity among the individuals. Hence, the random-effects model gives better estimates than the base models.

The 834 observations collected from 139 individuals were used for model formation. The start values based on the current sample were estimated by the software. The start value for critical accidents was not significant, but they became significant in the improved final model. In addition, all the attributes or generic variables became significant in the final model. All attributes used are significant at a 95% confidence interval in the final model. The critical accident values, which were insignificant, got improved in the final one. The final model gives better pseudo-R squared and adjusted R squared values. McFadden recommends a value between 0.2 and 0.4 for the model to be a good fit. The goodness of fit measures of the final model are given in Table 5.

The probability of exceeding the chi-squared value is less than the significance levels, i.e., the null hypothesis that the constant only model is equal to models with predictor variables is rejected. The random parameters model gives the standard deviation of the estimates, which is an essential factor for analyzing the individual's characteristics. The standard deviation is also significant with a t-value of 8.811 in the final model, confirming that there is unobserved heterogeneity among the individuals here also and a random-effects model gives better estimates than the base models. The log-likelihood values (absolute) of the final model are lesser than the initial ones, i.e., the final random-effects models provide a better fit to the data. The AIC and BIC values are lower for the final model (1.04 and 1.07), indicating low prediction error than the multinomial regression models.

Table 5 Goodness of fit measures

Measures of goodness of fit	Overbridge-Attakulangara			Killippalam-Pappanamcode		
	Constant-only model	MNL model (Start)	RPL model (Final)	Constant-only model	MNL model (Start)	RPL model (Final)
Log-likelihood function	−664.587	−613.362	−523.834	−575.924	−558.348	−429.395
Info. Criterion: AIC	–	1.29034	1.10590	–	1.34856	1.04172
Info. Criterion: BIC	–	1.32076	1.14139	–	1.37122	1.07005
Chi squared	–	–	283.174	–	–	297.378
Prob. [Chi-Squared. > value]	–	–	0.00000	–	–	0.00000
McFadden pseudo-R-squared	–	0.07708	0.21179	–	0.03052	0.25442
McFadden adjusted R-squared	–	0.07030	0.20600	–	0.02467	0.24993
Restricted Log-likelihood (RLL) (No Coefficients)	–	–	−665.421	–	–	−578.084
McFadden pseudo-R-squared*	–	–	0.21278	–	–	0.25721
McFadden adjusted R-squared*	–	–	0.20700	–	–	0.25273

3.3 Model Interpretation

It is imperative to understand the model results and the trend associated with the generic and the alternative specific variables. The final model for the users of the Overbridge-Attakulangara segment, gives significant estimates for travel time, travel cost, critical accidents, marital status and accident history. The variables gender, age and income, which usually show significance in choice decisions, became insignificant in the model. This might be because of the negative tendency of the respondents to disclose the actual values especially, in the case of online surveys. The attributes or mode-specific variables show parameters consistent with the expectations. The travel time (-0.254), travel cost (-0.188) and critical accidents (-0.204) show negative utility as the increase in these variables decreases the utility. The parameter estimate of marital status shows that the married people show negative utility (-1.106) towards riskier ones. It might be because of the assurance of the safety of the family as a responsible person. The respondents with accident history show a positive coefficient (0.707) for riskier roads, which is consistent with the results obtained by [2]. Even after experiencing accidents, their attitude towards the safer alternative is low, which might be because of the misinterpretation of the risk associated with the alternative routes or the confidence in their driving skills.

While in the Killippalam-Pappanamcode part, only attributes travel time (-0.104), travel cost (-0.073) and critical accidents (-0.052) were significant in the final model, which might be the same reason as in the first part, i.e., the discrepancy in the socio-economic factors given by the respondents. The attributes or the generic variables show negative signs, which is consistent with the expectations.

3.4 Willingness to Pay Estimation

The willingness to pay values to avoid a critical accident obtained from the coefficients of predictor variables (using marginal rate of substitution) are 1.08 and 0.72 rupees per person trip, i.e., to avoid an accident involving a fatality/severe injury, a road user is willing to pay an average value of 1.08 and 0.72 rupees for the short and the long trip settings respectively.

The common factors in both the trip settings are that both the road segments comes under urban category and have identical traffic condition. The main difference is the risk associated with the trips. The first segment was a short stretch with high risk and the second segment was a longer one with higher risk. The WTP values of the first one came out as a higher value than the second one. The Overbridge-Attakulangara road segment where the short trip setting was used is one of the most important roads in Thiruvananthapuram city and is very close to the central bus terminal, central railway station, Chalai Market, Govt. Ayurveda College, malls and many recreational centers. People use a small portion of roads frequently for daily purposes apart from work or educational trips, so the risk exposure is high for short stretches with comparatively

high risk. Usually, long trips are less frequent trips than short trips for the people living near those areas. Also, the road users may not be willing to compromise the quick high-speed travel ensured by the Killippalam–Pappanamcode National highway for safety, compared to the other road.

4 Conclusions

The preliminary analysis shows that the majority of the city population was familiar with both stretches. From the user characteristics of both the road segments, it can be concluded that the socio-demographic characteristics express identical values as the users of both the roads were given the scenarios for both the trip settings. The first segment has higher respondents with a household income of above one lakh. Preference for the public transport vehicles in the second segment is more when compared with the first one.

Separate models were developed for the road users of short and long trip settings. The random-effects model was chosen over the base model as the standard deviation of the random effect was significant. The final model expressed better statistical fitness criteria. The model for both the trip conditions gave robust estimates for the attributes (travel time, travel cost and accident rates) showing disutility. However, an accurate depiction of socio-demographic characteristics could not be obtained due to the inconsistency of the data provided by the respondents. Unlike the long trip setting, the short one showed reasonable estimates for marital status and the accident history, exhibiting estimates consistent with the patterns followed in previous works related to accident analysis. The willingness to pay values to avoid a critical accident were obtained as 1.08 and 0.72 rupees per person trip for the short and the long trip settings respectively. This willingness to pay values determined by the marginal rate of substitution between risk and the monetary parameter rendered higher value for short trip setting. This was consistent with the expectations as the users have given more importance to safety in short frequent trips with high risk than the longer ones. Using this willingness to pay values, the cost of road accidents in similar high-risk areas can be estimated which may in turn be used in the cost–benefit analysis of various safety infrastructures.

References

1. Ainy, E., Soori, H., Ganjali, M., Le, H., Baghfalaki, T.: Estimating cost of road traffic injuries in Iran using willingness to pay (WTP) method. PLoS ONE **9**(12), 1–16 (2014)
2. Antoniou, C.: A stated-preference study of the willingness-to-pay to reduce traffic risk in urban vs. rural roads. Eur. Transp. Res. Rev. **6**(1), 31–42 (2014)
3. Balakrishnan, S., Karuppanagounder, K.: Cost of two-wheeler road accidents in India. Int. J. Inj. Control Saf. Promot. **26**(2), 185–191 (2019)

4. Balakrishnan, S., Karuppanagounder, K.: Estimating the cost of two-wheeler road accident injuries in India using the willingness to pay method. Aust. J. Civ. Eng. **18**(1), 65–72 (2020)
5. Bansal, P., Kockelman, K.M.: Indian vehicle ownership: insights from literature review, expert interviews, and state-level model. J. Transp. Res. Forum **56**(2), 45–59 (2017)
6. Beattie, J., et al.: On the contingent valuation of safety and the safety of contingent valuation: part 1-caveat investigator. J. Risk Uncertain. **17**(1), 5–26 (1998)
7. Bhattacharya, S., Alberini, A., Cropper, M.L.: The value of mortality risk reductions in Delhi, India. J. Risk Uncertain. **34**(1), 21–47 (2007)
8. Chaturabong, P., Kanitpong, K., Jiwattanakulpaisarn, P.: Analysis of costs of motorcycle accidents in Thailand by willingness-to-pay method. Transp. Res. Rec. **2239**, 56–63 (2011)
9. Dissanayake, D.: Stated preference discrete choice model to investigate the determinants of public willingness to pay for road casualty risk reduction in Thailand. Asian Transp. Stud. **1**(2), 137–152 (2010)
10. Elvik, R.: An analysis of official economic valuations of traffic accident fatalities in 20 motorized countries. Accid. Anal. Prev. **27**(2), 237–247 (1995)
11. Haddak, M.M., Lefèvre, M., Havet, N.: Willingness-to-pay for road safety improvement. Transp. Res. Part A Policy Pract. **87**, 1–10 (2016)
12. Hensher, D.A., Rose, J.M., De Ortúzar, J.D., Rizzi, L.I.: Estimating the willingness to pay and value of risk reduction for car occupants in the road environment. Transp. Res. Part A Policy Pract. **43**(7), 692–707 (2009)
13. Jacobs. G.D,T.R.L.: (TRL) Costing Road Accident in Developing Countries: Overseas Road Note, p. 10 (1995)
14. Le, H., Geldermalsen, T., Van, Lim, W.L., Murphy, P.: Deriving Accident Costs using Willingness-to-Pay Approaches–A Case Study for Deriving Accident Costs using Willingness-to-Pay Approaches–A Case Study for Singapore, January 2014
15. Mon, E.E., Jomnonkwao, S., Khampirat, B., Satiennam, W., Ratanavaraha, V.: Willingness to pay for mortality risk reduction for traffic accidents in Myanmar. Accid. Anal. Prev. **118**(May), 18–28 (2018)
16. Hills, P.J.M.W.J.-L.: The costs of traffic accidents and valuation of accident prevention in developing counties, p. 240 (1983)
17. Rizzi, L.I., De Ortúzar, J.D.: Stated preference in the valuation of interurban road safety. Accid. Anal. Prev. **35**(1), 9–22 (2003)
18. Whittington, D.: Administering contingent valuation surveys in developing countries. World Dev. **26**(1), 21–30 (1998)

A Potential Review on Self-healing Material – Bacterial Concrete Methods and Its Benefits

M. L. Likhit and Jacob Alex

Abstract Building plays an important role for survival of human being in a safe place to live and store basic requirements. The building can be constructed for any purpose and the architecture of each building (official, residential) differs according to the plan. Beyond the plan for a building, it is also significant in designing plans for the construction of bridges, dams, canals, etc. In all the construction, the key goal is the strength of a building which completely depends on the materials that are chosen for each work. Hence, it is essential to prefer high quality materials for the construction of a building and the major materials are such as cement, concrete, steel, bricks, and sand. Among these materials, the concrete is often used for construction which enables to harden the building by combining cement, sand, and water. The concrete looks like a paste that reinforce to prolong life of the building. In this paper, we discuss a review on the use of bacteria in concrete that has the ability of self-healing cracks in the building. The procedural process behind the activation and reaction of bacteria into concrete is studied with the benefits of this process. This bacterial concrete usage assures to enhance the property of durability and but still it is yet to be introduced in the industries. Hereby, we review the recent research works undergone in concrete using bacteria.

Keywords Building construction · Bacterial concrete · Self-healing

1 Introduction

Advance growth in the field of Civil Engineering presents construction of long-life buildings using suitable materials. The professionals of this field are Civil Engineers who works on designing, constructing, operating and maintenance of the built work. The construction of any public or private sector infrastructure, requires preparation

M. L. Likhit (✉) · J. Alex
Department of Civil Engineering, Christ (Deemed to Be University), Bengaluru, India
e-mail: lihkit.ml@res.christuniversity.in

J. Alex
e-mail: jacob.alex@christuniversity.in

of a proper plan. In general, the prepared fair sketch is executed by levelling the ground, constructing foundation, then proceeding to plastering, pluming and final finishing [1–4]. The construction of a building needs a variety of materials as cement, concrete, steels and so on. Some materials are used as a mixture in a specified ratio and composition. To improve the stability of building, concrete is used [5–8]. There are many combinations of concrete is used and hence the decision making plays a vital role. As a development multi-criteria decision making (MCDM) algorithm is involved. This type of algorithms considers multiple factors for finalizing a decision regarding concrete. For instance, a Consistent Fuzzy Preference Relation (CFPR) method determines the concrete priority weight. However, it can be used only for system-based architecture construction. Still, the best option to define the quality of the building is the utilization of materials in the construction. However, the building is about the preference of materials, the quality and ratio of material mixtures leads to the issue of cracks. For solving this challenge, concrete is used whereas the climatic conditions are also important to utilize concrete for any type of building crack. The advantage of using concrete is that it is water resistant, ability to define any shape, less maintenance, and thermal expansion. As an advance development in concrete usage, 3D printing, bacteria use is presented [9–11]. The advantage of bacterial concrete is its property of self-healing. The process of self-healing is to fix up the damage caused in the constructed building. The self-healing techniques includes chemical encapsulation, microorganism's encapsulation, admixtures, glass tubing and intrinsic healing. To ignite the self-healing technique, three mechanisms are involved as ingress gasses, cracking, and heat action. This self-healing by concrete is classified into two ways as follows [12–14]. The working mechanism of self-healing is depicted in Fig. 1. As shown in this figure, the combined bacteria particles are either activated or breaks the capsule to release the healing agent while the crack occurred.

The main reason for cracks is environmental issues such as climatic changes and natural hazards [35–38]. Also, the architecture design of the building is a reason to cause crack on the walls within a short duration. The concrete can be generated into any adjustable shape at any size. The use of concrete can survive from cracks, acid
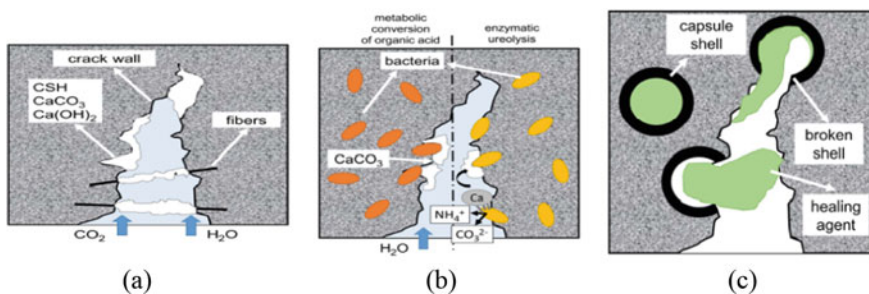
Fig. 1. **a** Autogenous Self-healing, **b** Autonomous Bacteria-Based Self-healing and **c** Autonomous Capsule-Based Self-healing [12]

rain, etc. The idea of self-healing works without the intervention of human, i.e., the cracks are repaired by itself. A study results measured of 32 mm crack is filled using microencapsulation, 27.2 mm crack by bacteria respectively [15, 16, 48]. Here are the types of healing that are performed.

(i) Autogenous healing: The autogenous healing works by combining a set of optimized products. This self-healing takes places in physical or chemical or mechanical. In physical-based process, the cement matrix present in the crack is used, whereas in chemical-based process uses Portland cement and creates calcium carbonate, then the mechanical-based process solves the crack issues using fine particles. This healing operates on two phases such as surface-controlled phase that uses calcium ions and diffusion-controlled phase is carried out on diffusion of ions. The important requirement of this autogenous healing is the water that is serious in some extreme environmental conditions. This healing process can get rid of smaller cracks, and it is able to heal crack width ranging 200 to 300 μm.

(ii) Autonomous healing: In this type of self-healing the damage is fixed using some add-on element such as healing agent or bacteria. This self-healing method is sub-categorized as bacteria-based and capsule-based. The autonomic healing takes place in two types as chemical self-healing and biological self-healing.

The process of chemical self-healing in autonomous is performed by encapsulation method, hollow pipette method and so on. Then the two modes in this process are active and passive. Whereas the biological self-healing performs using the participation of microorganisms (Bacteria, Fungus and Virus) that has the capability to live alive on a variety of materials. While it rises, he microorganism that depends on environmental features as moisture, temperature, PH value, etc. Encapsulation is one of the popular methods involved in this type of self-healing.

The self-healing is efficient, and it has been actively supported for some of the applications.

- Achieves good results for the buildings constructed in the poor climatic conditions of freezing and thawing.
- Suitable to be used for constructing building that are in vicinity to the irrigation fields.
- The dams, marine buildings that have direct contact with water also uses bacterial concrete for self-healing.
- The major damage on roadways is rectified using construction of sustainable roads and eventually it minimizes traffic jam due to good road conditions.

The materials that are available in the bacteria are Ceram site, Silica gel, Melamine, Hydrogel, Geopolymer, Iron Oxide and so on [29–31]. According to the characteristics of the elements, it is employed into the concrete as a specified composition. The bacterial culture plays a vital role for treating with the concrete [52]. There are some types of bacteria that are used in concrete and the bacteria are Bacillus cohnii, Bacillus subtilis, Bacilius sphaericus, Bacillius balodurans, etc. [32–34, 54, 61, 72, 75]. The main reason behind this metabolic activity when combination of

bacteria and concrete is the calcium carbonate component [71, 89, 90]. In general, the concrete is economical and hence it is chosen as a major material for building, but still the energy consumption is higher.

The major contributions of this paper are listed in the following.

- A detailed review about the building material concrete and the process performed to handle cracks using bacteria.
- Study on the advantages and disadvantages of the use of bacterial concrete is illustrated from most recent previous author's work.

This paper is organized into following sections as, Sect. 2 discusses about the utilization of concrete for the construction of a building, Sect. 3 illustrates the capsule-based bacterial concrete methods, then Sect. 4 deals with the details about the effect of using bacterial concrete, Sect. 5 demonstrates the risks that have been identified while using bacterial concrete and finally Sect. 6 concludes the review paper in the topic of bacterial concrete.

2 Concrete – A Construction Material

Concrete is defined as a stone-like mass that helps to strengthen the building when it is used at perfect proportions. In simple, it gels with cement, aggregate, sand, rock, and water is pre-defined ratio. The level of pH plays a vital role while performing mixing of concrete [21, 22, 39–41]. An ideal mixing of concrete results to improve performance in durability [94]. The level of pH in the concrete defined the alkalinity level which is the major reason to cause crack when the specified level decreases.

Hereby, the major problem while using concrete is the cracks on walls and floor structures due to the environmental or human activities. To solve this issue, bacterial concrete is introduced to recover cracks [17, 18, 47, 78, 91]. In general, the Bacillus Pasteurii and Sporosarcina bacteria is used in composition of cement mortar along with sand to rectify cracks. Hereby this combination reacts as urea and $CaCl_2$.

These bacteria are activated only when there occurs a damage on the concrete. It is efficient to obtain results, on the other hand it does not cause any harm to human beings [19, 20, 79, 80]. The microscopic images of Bacillus Subtilis and Bacillus Sphaericusare depicted in Fig. 2. These bacteria in concrete acts as urea, thereby transfers into carbon dioxide and ammonium hydroxide to improve ph.

The equation for pH trigger is given in the following,

$$Ca^{++} + HCO_3^- + OH^- \rightarrow CaCO_3 \downarrow + H_2O \tag{1}$$

$$Ca^{++} + 2HCO_3^- \leftrightarrow CaCO_3 \downarrow + CO_2 + H_2O \tag{2}$$
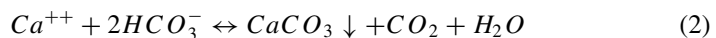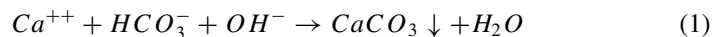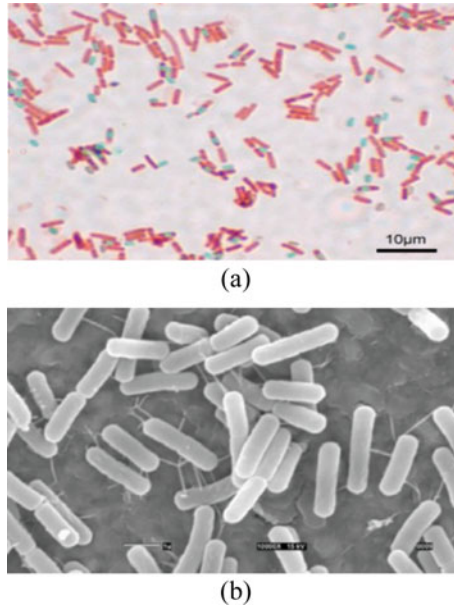
Fig. 2 Microscopic images **a** Bacillus Subtilis and **b** Bacillus Sphaericus [20]

The component $CaCO_3$ is calcium carbonate, H_2O is water, HCO_3^- is the biocarbonate, OH^- is hydroxy and CO_2 is carbon dioxide. A higher the level of pH is attained by the presence of bacteria. In Bacillus Subtilis, the self-healing takes place by the decomposition of $C_6H_{10}CaO_6$, whereas in Bacillus Sphaericus it is $Ca(NO_3)_2$ Ureolytic precipitation. Apart from these bacteria, Bacillus cohnii can also be used by the transformation of $C_6H_{10}CaO_6$.

Self-Curing Technology (SCT) using concrete for construction is involved in practice by civil engineers. A survey says that 43.1% of construction professional are aware about the concept of SCT [23, 24]. The utilization of effective microorganisms with optimal water, cement assures to achieve high performance in concrete.

3 Capsule-Based Self-healing Methods

The process of encapsulation based on capsule holding bacteria composed along concrete is called the capsule-based self-healing method. This method is carried out based on seven stages as illustrated in Fig. 3. The bacteria in self-healing mechanism performs metabolizing process according to the bacteria components in it.

The commonly occurred concrete crack and method of self-healing is shown in Figs. 4 and 5. The chemical component Carbon dioxide in the bacteria will perform metabolism while the crack occurs and the reaction of chemical components is depicted below.
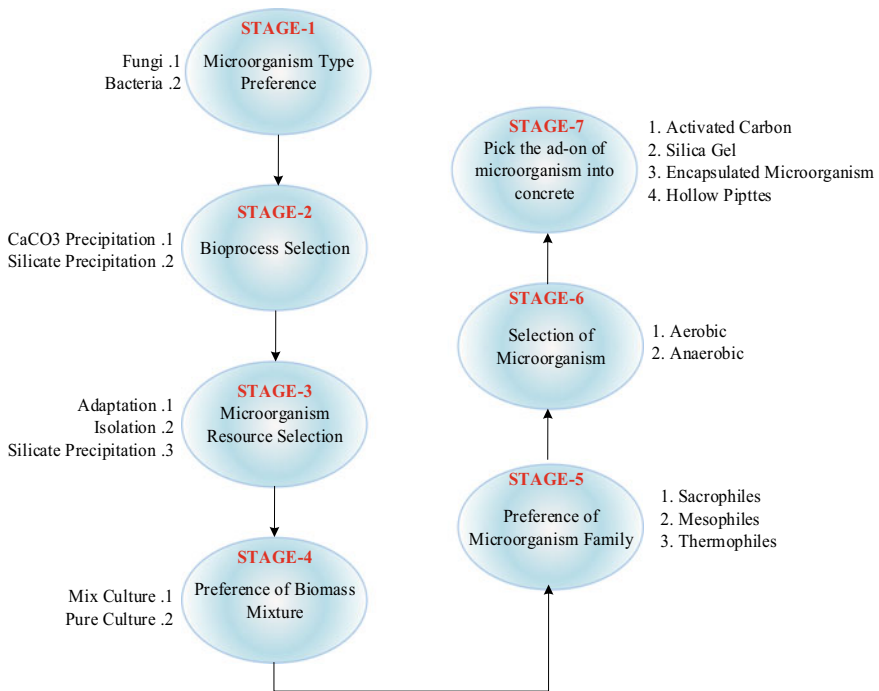
Fig. 3 Sequential stages of the encapsulated bacterial concrete
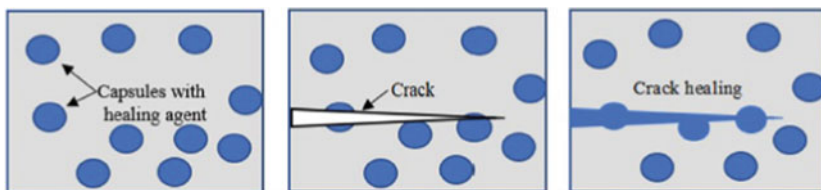
Fig. 4 Capsule-based self-healing mechanism [25]
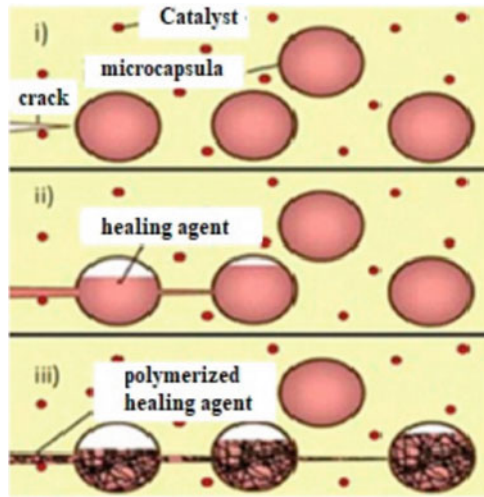
Fig. 5 Basic method in capsule-based self-healing [49]

$$Ca(C_3H_5O_2)_2 + 7O_2 \rightarrow CaCO_3 + 5CO_2 + 5H_2O \tag{3}$$
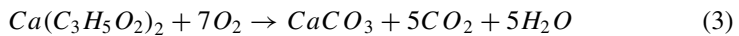
At first, the crack on the concrete starts to crush the mixed capsules and releases the healing agent from it. Then capillary action takes place which the agent is in contact to the catalyst present on concrete, then the polymerization or chemical reactions happens to rectify the crack. In this type of capsule based self-healing, the chemical reaction is conventional according to the nutrients that are available in the bacteria. In [25], the maximum crack depth of 1.2 mm is healed using Bacillus subtilis, whereas the Bacteria Cohnii heals crack of 1.24 mm. The Table 1 demonstrates the use of different type of bacteria in self-healing. One of the promising self-healing methods is the production of calcium carbonate and calcium hydroxide based on the microorganism activity and hereby the chemical reaction is depicted as follows.

$$H_2O + CO_2 \leftrightarrow H_2CO_3 \leftrightarrow H^+ + HCO_3^- \leftrightarrow 2H^+ + CO_3^{2-} \tag{4}$$

$$Ca^{2+} + CO_3^{2-} \leftrightarrow CaCO_3 \tag{5}$$

$$Ca^{2+} + HCO_3^- \leftrightarrow CaCO_3 + H^+ \tag{6}$$
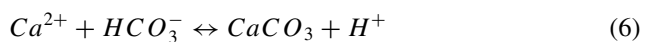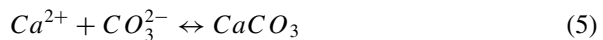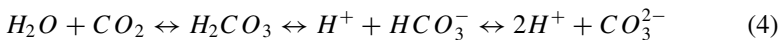
According to the above equations, the chemical reaction takes place when the CO_2 is in contact with water. In [26, 42, 43, 50] the authors have discussed about

Table 1 Types of bacteria and performances [25, 44]

Bacteria	Material	Concentration	Increase in compressive strength (%)	Increase in tensile strength	Depth of crack healed
Bacillus Megaterium	Concrete/Cement	30×10^2 cells/ml	24	36%	–
Bacillus Cereus	Concrete	10^6 cells/ml	38	–	–
Bacillus Sphaericus	Mortar/Concrete	10^5 cells/ml	50	29.37%	550–700 µm
Bacillus Aerius		10^5 cells/ml	8	–	–
Bacillus Subtilis	Mortar/Concrete	10^5 cells/ml	42	14%	–
Shewanella		10^5 cells/ml	25	–	
Sporosarcina pasteurii	Mortar/Concrete	10^5 cells/ml	29	29%	417 µm
Bacillus Cohnii	Cement Mortar	10^7 cells/ml	44	13%	1.24 mn
Bacillus Halodurans	Concrete	10^8 cells/ml	7	–	80–270 µm
Bacillus Licheniformis	Cement Mortar	10^5 cells/ml	11	–	–
Enterrobacer sp.M2	Cement Mortar	–	44	56.44%	–
Bacillus Flexus	Concrete	–	18	–	–
Enterococcus sp.	Cement Mortar	–	45	–	–

strength and durability on using bacterial concrete. The mixture is prepared from fine aggregate, Portland cement, Bacillus Subtilis bacteria, basalt fiber and calcium lactate. The calcium lactate is present in Bacillus cohnii, Bacillus Subtils, Bacillus pseudofirmus Bacillus Megaterium, and Bacillus pasteurii. This component is soluble in water, and it is a powder in white color. As per the ratio of this work, 10^5 cfu/ml measurement of bacteria is used for testing. The bacteria are measured in specified cell concentrations of 10^5, 10^7, 10^9 cells/ml respectively [27, 81]. The bacteria culture is important in improving the performance of bacterial concrete.

In [28] this bacterial concrete is tested in two different cement such as Portland Pozzolanic Cement (PPC) and Portland Cement type 2(PC2). This manufacturing process is carried only under room temperature, the materials used are washed sand, crushed sand of 1.5 cm and PPC, PC2. A measure of 5% to the weight of cement is the number of bacteria introduced into the concrete. This concrete is validating on

catalase test, pH test and urease test. The evaluation takes a couple of days for the reaction in it.

The compressive strength for 7 days using bacteria is 19.4 N/mm^2 for PPC and 18.3 N/mm^2 for PC2 respectively. On the other hand, the testing result for 28-days using bacteria is 27.48 N/mm^2 for PPC and 30.94 N/mm^2 for PC2 respectively. As per the increase in the number of days, the compressive strength also increases in bacterial concrete.

The bacterial concentration of 10^5 cells/ml results with higher efficiency in resolving the issue of concrete cracks [44]. The bacteria, Bacillus Cohniiis used in this level of concentration and tested for 28 days [45]. This preparation of bacterial concrete from the initial stage to the final mixing and casting for a building, these stages are demonstrated in the Fig. 6. On the other hand, the bacterial concrete also uses fiber in self-healing [68–70].

The Bacillus Cohnii is added as a solution for 5% in the concrete and nutrient solution of 95%. This mixture is tested on a concrete crack of width around 0.2 to 0.6 mm. The mathematical formula for determining the degree of crack healing is given as,

$$DCH = \frac{C_i - C_o}{C_o} \times 100 \tag{7}$$

DCH represents the degree of crack healing, C_i is the crack width measured initially and C_o is the width of crack measured after healing. Then the compressive strength of bacterial concrete is measured using the equation given below,

$$CS = \frac{f_r - f_b}{f_r} \times 100 \tag{8}$$

The compressive strength is denoted as CS, then f_r is the compressive strength of reference and f_b is the compressive strength of bacteria in the specimen respectively.

In [46], Sporosarcina pasteurii is a type of bacteria used in this work for preparation of self-healing concrete. A Latent Dirichlet Allocation (LDA) algorithm is used for analyzing the developed self-healing mechanism. However, this work was tested using a software i.e., MATLAB. The encapsulation of bacterial spores in concrete activates the nutrient particles in it. Hereby the reaction of a self-healing concrete is illustrated in [51], the equations are,

$$CaO + H_2O \rightarrow Ca(OH)_2 \tag{9}$$

$$Ca(OH)_2 + CO_2 \rightarrow CaCO_3 + H_2O \tag{10}$$
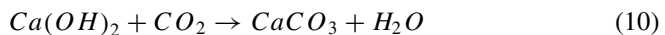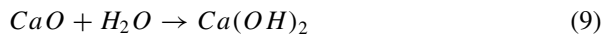
where CaO is the Calcium oxide with water forms Calcium hydroxide. Later this Calcium hydroxide reacts with carbon dioxide when the crack occurs and forms calcium carbonate which is an important mineral to heal the crack as shown in
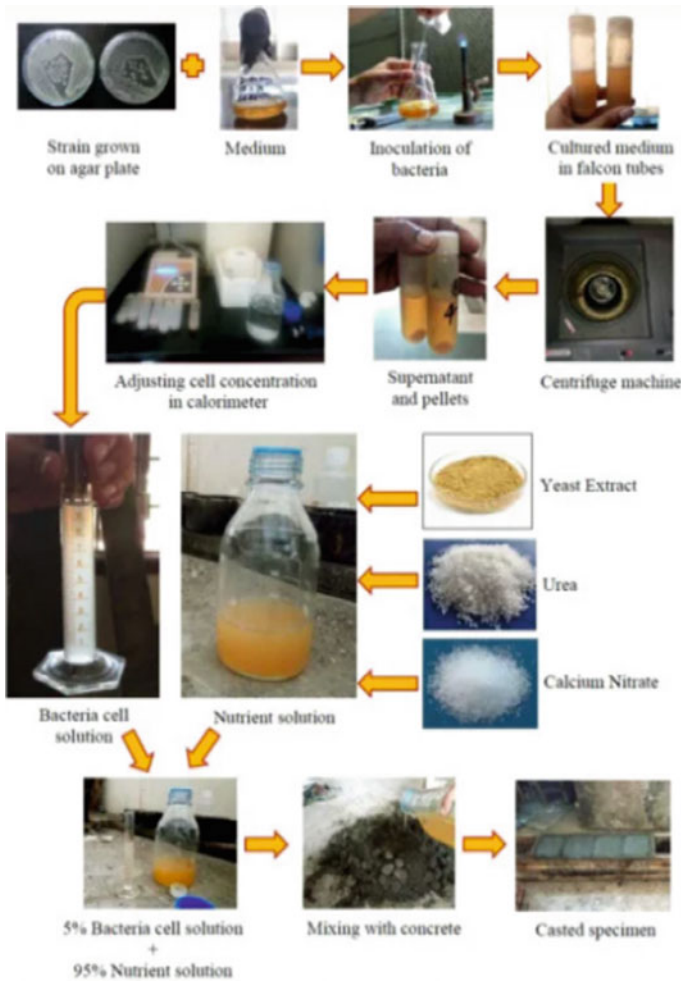
Fig. 6 Bacterial concrete preparation [45]

Fig. 7. Then the analysis of the resulted chemical components is measured in terms of the following formulations [57].

$$Ca(OH)_2 = WL_{ca(OH)_2} \times \frac{m_{ca(OH)_2}}{m_{H_2O}} \tag{11}$$

$$CaCO_3 = WL_{caCO_3} \times \frac{m_{caCO_3}}{m_{CO_2}} \tag{12}$$

The individual terms in the above mathematical equations are $WL_{ca(OH)_2}$ denotes the mass losses while decomposition of the component $Ca(OH)_2$, WL_{caCO_3} denotes
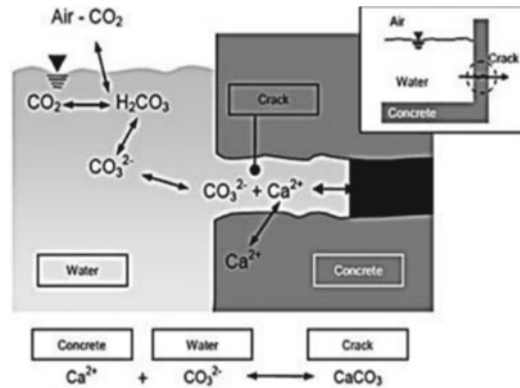
Fig. 7 Encapsulation self-healing using calcite [51]

the mass losses while decomposition of the component $CaCO_3$, the value of molecular masses are given as 74, 18, 100 and 44 g/mol for $m_{ca(OH)_2}$, m_{H_2O}, m_{caCO_3} and m_{CO_2}. The utilization of bacteria in cement improves the sustainability, whereas the ion components in the building material must be retained throughout. The viability of bacteria and the nutrient in the mixture is significant for improvements in bacterial concrete.

The bacteria used in concrete has different nutrients that enables to heal crack. The materials in bacteria are Silica gel, Hydrogel, Melamine and so on [56]. Hereby the components that are involved in the bacteria culture plays an important role to enhance the process of self-healing. There are different methods that are developed for evaluating the effect of self-healing using bacterial concrete.

Microbiological Induced Calcite Precipitation (MICP) is defined as a better method for healing crack [53, 59, 73, 74, 86, 87]. This calcite precipitation brings urease bacteria that is Bacillus Pasteurii, Bacillus Subtilis when it combines calcium. The same procedure is followed to heal cracks, while the pores in concrete are closed, then provisioning of nutrients and oxygen will be at hold state. If the cell in bacteria is damaged and dead, then the process of bacteria activation is stopped. In this work, the bacteria concrete is compared with control specimens and the results shows better for bacteria concrete by enhancing the compressive strength in 16, 13 and 9%.

Sulfate attack commonly occurs in a bacterial concrete based building [55]. A Negative Pressure Method (NPM) is presented to evaluate the durability. The sulfate attack aims to degrade the metabolic activity of the bacteria which is undergone for self-healing. According to this NPM test method the negative pressure is created, and the air is removed for the immobilization materials. In this testing, as per the increase in the immobilizing time, the bacterial count is also higher in counts.

In [58, 60], the authors have illustrated that every bacterium has ability to generate calcite which acts as a repairing agent to heal cracks. The formation is calcite is based on the equations depicted in the following.

$$CO(NH_2)_2 + H_2O \rightarrow NH_2COOH + NH_3 \tag{13}$$

$$NH_2COOH + H_2O \rightarrow NH_3 + H_2CO_3 \tag{14}$$

$$H_2CO_3 \rightarrow HCO^{3-} + H^+ \tag{15}$$

$$2NH_3 + 2H_2O \rightarrow 2NH^{4+} + 2OH^- \tag{16}$$

$$HCO^{3-} + H^+ + 2OH^- \rightarrow CO_3^{2-} + 2H_2O \tag{17}$$

$$CO(NH_2)_2 + 2H_2O + Ca^{2+} \rightarrow 2NH^{4+} + CaCO_3 \tag{18}$$
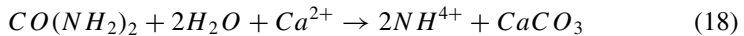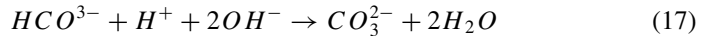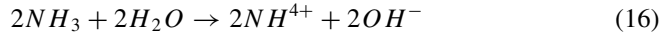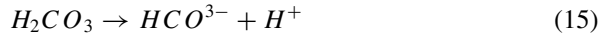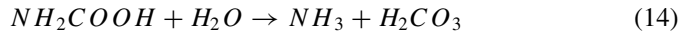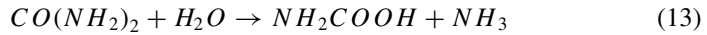
Above all the common chemical reactions, urease enzyme is present in all the micro-organism [76]. Most of the previous works have discussed that the bacterial concrete is able to perform self-healing using the bacteria and the components that are present in it.

4 Effect of Bacterial on Concrete

In this section, the effects of using bacterial concrete are discussed. Table 2 demonstrates the research works the studies on the bacterial concrete. The culture of bacteria also has impact on achieving high performance on the use of concrete. The temperature, environmental conditions, and number of days for the bacteria results in high strength [63, 64, 66, 67].

Bacterial concrete requires perfect bacteria culture that takes a time of 7, 14, 28 and 56 days. The performance of this concrete is measured in terms of compressive strength.

The compressive strength is determined based on the concrete capacity up to the ability to sustain the load [41, 82, 83, 88]. The effect of using bacteria results urea hydrolysis based on ammonia concentration is measured using the following formula.

$$CO(NH_2)_2 + H_2O \rightarrow CO_3^{-2} + 2NH_4^+ + 2H_2O \tag{19}$$
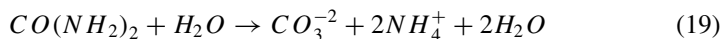
$$UH_{(mg/L)} = \frac{NH_{4(mg/L)}^+ \times 60_{(g/mole)}}{2 \times 18_{(g/mole)}} \tag{20}$$

The Eq. (20) gives urea hydrolysis occur from the process of decompose. The chemical reaction produces ammonia which results higher pH and generates alkaline condition [97]. On the other hand, the construction cost while using this bacterial

Table 2 Comparison of bacteria usage

Existing literature	Control samples	Type of bacteria	# Of days	Tests for measurement	Compressive strength	Concrete preparation
[18]	✗	B. Subtilis	7, 14 and 28 days	Scanning Electron microscope (SEM)	14.25 N/mm^2	Use 30 ml bacteria in M20 grade
[19]	✗	B. Subtilis	–	Ultrasonic pulse velocity test	27.5 N/mm^2	Uses MICP in M20 grade
[20]	✓	B. Sphaericus and B. Subtilis	7, 14 and 28 days	Carl Zeis-SEM and X-ray diffraction	30.33 N/mm^2	Use water cement ratio 0.42 in M25 grade
[26]	✗	B. Subtilis	7, 28 and 56 days	X-ray diffraction	>20 MPa	Mix 1 – Water ratio 0.45 with basalt fiber reinforced Mix 2 – Water ratio 0.4 with bacteria Mix 3 – Water ratio 0.35 with 10^5 cfu/ml bacteria and 0.5% cement Mix 4 – Harden concrete
[27]	✗	B. Subtilis	7, 14, 28 and 56 days	Urease test and Bio-chemical test	>15 MPa	Use 840 ml water, 5.019 kg coarse aggregate, 2.209 kg fine aggregate and 1.292 kg cement and bacteria concentration
[28]	✓	Aerobic bacteria	7 and 28 days	SEM	30.94 N/mm^2	Use 190 ml water, 1200 kg sand, and 375 kg cement
[31]	✗	Bacillus species	20, 40, 70 and 100 days	–	–	Use 192 g water, cement 384 g, fine aggregates 929 g, W/C ratio 0.5 g
[33]	✗	Bacillus Subtilis	44 days	Rapid chloride permeability test	–	Bacteria and Nutrients

(continued)

Table 2 (continued)

Existing literature	Control samples	Type of bacteria	# Of days	Tests for measurement	Compressive strength	Concrete preparation
[34]	✕	Bacillus cohnii	90 days	SEM	28.3%	Water, Bacteria and cement
[37]	✕	Bacillus family	7 and 28 days	Standard test	38.95 N/mm^2	Water, bacteria, and clay
[38]	✓	Modified Bacillus halodurans	–	Image analysis - X-ray computed tomography and MICP	–	Bacteria spray
[45]	✕	Bacillus cohnii	3, 7, 14 and 28 days	SEM and CX-ray Diffraction	97%	Use 95% nutrient solution, 5% bacterial cell solutions, 219 kg/m^3 water, 710 kg/m^3 fine aggregate and 438 kg/m^3

concrete is large range of 2.3 to 3.9 times than the use of traditional building material i.e. concrete. The bacteria specimen is tested on different grades of concrete and water ratio [84, 85, 92, 93]. The bacteria can compose of chlorides, sulphate, alkaline and so on. Based on the components in bacteria the crack is healed. The performance of this bacterial concrete is tested in real, while it is also measured using microscopic images to undergo depth view on pixels and then validate self-healing in consecutive stages. The measurements of cement, fine aggregate and coarse aggregate is essential. Since each material compose multiple elements in it whose value should be optimum for improving the performance. This composition also effects on the growth of the performance in bacterial concrete. A perfect mixing of concrete composition and exact incubation of bacteria culture obtains better compressive strength.

Compressive strength and durability are an important parameter measured to predict the performance of bacterial concrete [95, 96, 98]. This parameter is graphically plotted based on the time and the cell concentration of the bacteria. The results are shown in Figs. 7 and 8, for different cell concentration and increasing time. Then the performance of commonly used bacteria is depicted in Fig. 9, with respect to the healing width. The healing width is defined as the depth of crack on building. The healing process takes a couple of days, so the testing is validated for 28 days, and 56 days is performed.

The different types of bacteria used for self-healing concrete is depicted in Table 3 based on 7, 14 and 28 days. Among all the bacteria, Bacillus Subtilis is commonly used in most of the works, and it attains better performance result.
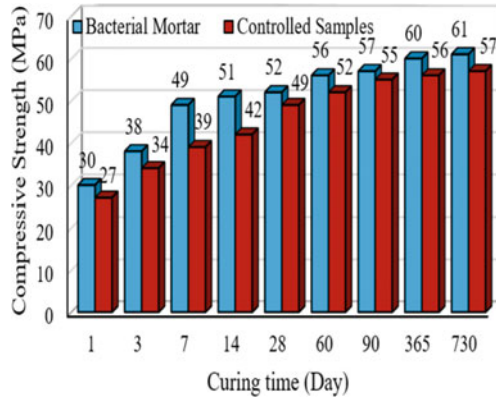
Fig. 8 Calcite matrix compressive strength [51]
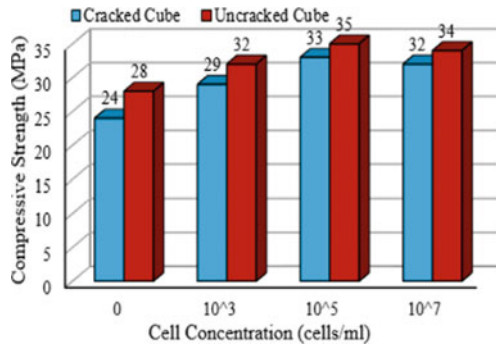
Fig. 9 Compressive strength in 21 days self-healing [62]

Table 3 Comparison on compressive strength for bacillus family [72]

Concrete Cube Samples 4″ × 4″ × 4″	Compressive Strength (MPa)		
	7 days	14 days	28 days
Control Sample	22.54	32.30	34.75
BS-1 (B. Specie)	19.85	28.10	30.55
BS-2 (B. Pasturii)	21.68	30.47	33.61
BS-3 (B. Anthracis)	22.46	31.14	35.38
BS-4 (B. Anthracis)	23.87	33.71	36.73
BS-5 (B. Specie)	20.43	28.88	31.44
BS-6 (B. Subtilis)	23.66	32.79	37.26
BS-7 (B. Subtilis)	25.48	35.32	40.13

5   Rapid Chloride Permeability Test

The Rapid Chloride Permeability Test (RCPT) is conducted in two scenarios of using bacteria and plain concrete mixture without bacteria [101]. The concrete is casted in cylindrical at the diameter and height of 200 and 100 mm respectively. The number of days of 91 is cured using water and solution of urea and $CaCl_2$. In Table 2 the 90 days maintenance of specimen is depicted. The bacteria Sporosarcina pasteurii PTCC 1645 is used to act as calcium carbonate precipitating agent which is mixed with calcium source and urea in 25 mm of $CaCl_2$ and 2% respectively. In this ratio, the bacteria culture is inaugurated and incubated for 2 days in 37 °C in the speed of 150 rpm. Before harvesting the bacterial cells, the process of centrifuging takes place for 10 min.

The experimental setup for this RCPT analysis is depicted in Fig. 10. The corrosion is a main constraint that is arouses in the concrete due to the presence of chloride ions [100]. The cell is tested for 6 h to calculate the number of coulombs passed. The charge passed ranges between 100 to 4000 coulombs. The measurements are noted for every 1/2 an hour and the chloride permeability with respect to the charge passed is given in Table 4. The prediction of chloride permeability denotes the ability of the chloride ions to penetrate the developed concrete. This helps to analyze the concrete's durability which is one of the important aspects in achieving higher performances (Table 5).
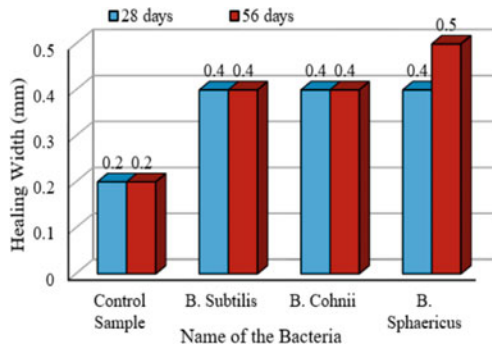
Fig. 10 Self-healing of crack in 28 days [65]

Table 4 Chloride permeability

Charge passed (Coulombs)	Chloride permeability
>4000	High
2000–4000	Moderate
1000–2000	Low
100–1000	Very low
<100	Negligible

Table 5 Specimen specification for RCPT [101]

Test	Shape	Curing condition	90 Days (Specimen's Label)
RCPT	Disc (Height – 50 mm and Diameter – 200 mm)	Urea-CaCl$_2$	(YN-UD-2)
		Urea-CaCl$_2$	(YN-UD-2)
		Urea-CaCl$_2$	(NY-UD-2)
		Urea-CaCl$_2$	(NN-UD-2)
		Water	(YN-WD-2)
		Water	(NN-WD-2)

YN – Cured in the presence of Urea-CaCl$_2$ using bacteria solution i.e., mixing preparation before concrete.
YY – Bacteria before mixing with concrete and water specimen.
NY – Absence of bacteria in concrete in the mixture of water and bacteria.
NN – Aggregate curing in fresh water in prior to the concrete mixture in control specimen.

In RCPT, the specimens are kept into vacuum desiccator without air for 3 h. This specimen is submerged into water and then the 1 h of vacuum is maintained. Still, the specimen is left over for 18 h in desiccator and then it is shifted to gasket. The supply of power is 60 v i.e., denoted as I_0 which is current measurement. The flow of current is noted for the time of 30 min for the total 6 h. To predict the current for each cell, trapezoidal rule is followed, and the equation is given as below.

$$Q = 900 \times (I_0 + 2I_{30} + 2I_{60} + \cdots + 2I_{330} + I_{360})$$ (21)

From the above equation, the current flow Q in terms Coulombs, then I_0 denotes immediate current recording voltage in amperes, I_t denotes the current recording of voltage during time t. The test results of RCPT are shown in Fig. 11 for the specimen that is tested in the presence and absence of bacteria (Fig. 12).

The four types of specimens are RCPT test is conducted in the presence and absence of bacteria. The treatment of surface concrete is performed in the cylindrical
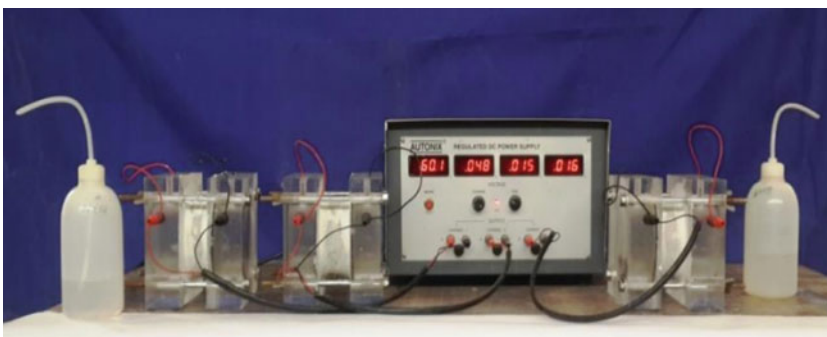
Fig. 11 RCPT analysis experimental setup
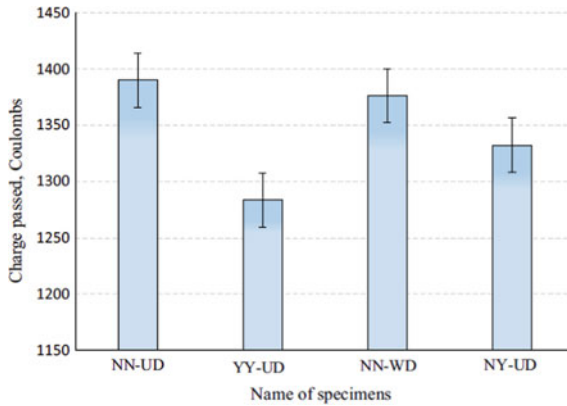
Fig. 12 RCPT test result for with and without bacteria

specimens that follows ASTM C 1202 and the height is 50 mm. Then, the curing condition based on this RCPT test on the temperature of 20 ℃ and the curing takes place for a week. The specimen constructed is dipped and on completion of 1 h.

Further, the cell is filled up to 3% of the NaCl solution and a software-based temperature and current maintenance for every 5 min over a time 6 h [21]. The RCPT test is efficient for the building applications of vehicle parking lots, bridges, and other. The charge pass is mathematically computed using the following equation,

$$Q = \int I(t)dt \tag{22}$$

The terms in equations are $I(t)$ denotes the time-dependent total electrical current for the time t determined for all the Q mixes. Then the chloride profile is determined using nonlinear regression analysis from the formulation as below,

$$C = C_s.\exp(-ax^2) \tag{23}$$

The C and C_s represent chloride content and surface chloride content respectively, a is the constant used according to the experiments based on the concrete specimens that are developed.

The RCPT have multiple advantages and disadvantages in measuring the performances of bacterial concrete. The major points in this testing are illustrated in the following,

- This test analysis gives quality result.
- RCPT analysis of self-Compacting Concrete (SCC) that is low will assure to mitigate the cracks that are raised due to the voids on the concrete.
- In case of increase in the mineral admixture, the RCPT will decrease in charges that indicates lesser presence of chloride ion.

- The measurements are not efficient when performed in prior in steady state.
- This testing has possibilities to induce variation on the specimen in terms of both physical and chemical. By this means, it leads to produce unrealistic values.
- This RCPT is not apt to be used for analyzing with the steel or carbon fibers that are used in the specimen.

6 Risks of Bacterial Concrete

In this section, the risks on using bacteria concrete are enlisted [77]. A bacterial concrete is used to heal cracks while, it is also challenging to prepare bacteria culture and composition of concrete. The risk in the bacterial concrete is given below.

- The sustainability of the alkaline level in the concrete at varying environmental factors.
- The blending of multiple materials may cause damage to the encapsulated bacteria.
- The increase in pore diameter on the concrete surfaces will break out bacteria when processing hydration to heal the cracks.
- In the most of bacterial concrete, calcium carbonate precipitation is produced, which also generates ammonia from the chemical reaction. Due to this reaction, it is harmful when used by human in construction.
- The survival days of the bacteria is essential to be assured, if bacteria are not at proper mixture, then the bacteria may get dead and not able to process self-healing.

7 Conclusion

This paper reviews the bacterial concrete that is used for self-healing. The cracks on building are healed using the bacteria's encapsulated along with the concrete mixture. The key goal of the encapsulated bacterial concrete is to improve durability and strength. The bacteria in capsules are released when crack occurs and then it is healed based on the chemical activity. The nutrient calcium is importantly used in bacteria as one of the major components to solve the cracks on the building. Most of the research works use Bacillus Subtilis for self-healing while other bacteria from the family of Bacillus can be used for this application of self-healing bacterial concrete. According to the width of the crack, it takes time to heal with respect to the density of alive bacteria. The preparation of bacterial concrete in previous research work is discussed and the performance of compressive strength is depicted.

The outcome on the use of each type of bacteria is measured and it is illustrated from the estimation of compressive strength with the increase in number of days. This paper gives a full review on recent research works that are studied on bacterial concrete and its measurements.

References

1. Zavadskas, E.K., Antucheviciene, J., Vilutiene, T., Adeli, H.: Sustainable decision-making in civil engineering construction and building technology. Sustainability MDPI **10**(1), 14 (2017)
2. Mei, L., Wang, Q.: Structural optimization in civil engineering: a literature review. Buildings MDPI **11**(2), 66 (2021)
3. Nusen, P., Boonyung, W., Nusen, S., Panuwatwanich, K., Champrasert, P., Kaewmoracharoen, M.: Construction planning and scheduling of a renovation project using BIM-based multi-objective genetic algorithm. Appl. Sci. MDPI **11**(11) (2021)
4. Yudina, A.: Enhancing technological processes in building construction and reconstruction by means of new technologies. Asian J. Civ. Eng. **20**, 727–732 (2019)
5. Sangiorgio, V., Iacobellis, G., Adam, J.M., Uva, G., Fatiguso, F.: User-reporting based decision support system for reinforced concrete building monitoring. In: IEEE International Conference on Systems, Man, and Cybernetics (SMC) (2018)
6. Wójcik, R., Tunkiewicz, M.: Problems using foam concrete substructure building foundations in irrigated soils. In: Baltic Geodetic Congress (BGC Geomatics) (2017)
7. Chatterjee, K., Zavadskas, E.K., Tamošaitienė, J., Adhikary, K., Kar, S.: A hybrid MCDM technique for risk management in construction projects. Symmetry MDPI **10**(2) (2017)
8. Dzwierzynska, J., Prokopska, A.: Pre-rationalized parametric designing of roof shells formed by repetitive modules of Catalan surfaces. Symmetry MDPI **10**(4) (2018)
9. Meurer, M., Classen, M.: Mechanical properties of hardened 3D printed concretes and mortars-development of a consistent experimental characterization strategy. Materials MDPI **14**(4), 752 (2021)
10. Stanaszek-Tomal, E.: Bacterial concrete as a sustainable building material? Sustainability MDPI **12**(2) (2020)
11. Lucas, S.S., Moxham, C., Tziviloglou, E., Jonkers, H.: Study of self-healing properties in concrete with Bactria encapsulated in expanded clay. Sci. Technol. Mater. Sciencedirect **30**, 93–98 (2018)
12. Rajczakowska, M., Habermehl-Cwirzen, K., Hedlund, H., Cwirzen, A.: Autogenous self-healing: a better solution for concrete. J. Mater. Civ. Eng. **31**(9) (2019)
13. Danish, A., Mosaberpanah, M.A., Salim, M.U.: Past and present techniques of self-healing in cementitious materials: a critical review on efficiency of implemented treatments. J. Mater. Res. Technol. **9**(3), 6883–6899. Elsevier (2020)
14. Snoeck, D., Pel, L., De Belie, N.: Autogenous healing in cementitious materials with superabsorbent polymers quantified by means of NMR, Scientific Reports, No. 642 (2020)
15. Muhammad, N.Z., et al.: Tests and methods of evaluating the self-helaing efficiency of concrete: a review. Constr. Build. Mater. Elsevier **112**, 1123–1132 (2016)
16. Bekas, D.G., Tsirka, K., Baltzis, D., Paipetis, A.S.: Self-healing materials: a review of advances in materials, evaluation, characterization and monitoring techniques. Compos. Part B Eng. Elsevier **87**, 92–119 (2016)
17. Ramakrishnan, V., Ramesh, K.P., Bang, S.S.: Bacterial concrete. SPIE Digital Library (2001)
18. Saradha, P., Vidhya, K., Visali, S.: Experimental investigation on bacterial concrete using bacillus subtitles. Int. Res. J. Multidiscip. Technovation **1**(6), 207–219 (2019)
19. Srinivasan, G., Saravanan, J.: A study on strength characters of bacterial concrete. In: IOP Conference Series Materials Science and Engineering (2020)
20. Chithambar Ganesh, A., Muthukannan, M., Malathy, R., Ramesh Babu, C.: An experimental study on effects of bacterial strain combination in fibre concrete and self-healing efficiency. KSCE J. Civ. Eng. 4368–4377 (2019)
21. Stojanović, G., Radovanović, M., Krstić, D., Ignjatović, I., Dragaš, J., Carević, V.: Determination of pH in powdered concrete samples or in suspension. Appl. Sci. MPDI **9**(16), 3257 (2019)
22. Behnood, A., Van Tittelboom, K., De Belie, N.: Methods for measuring pH in concrete: a review. Constr. Build. Mater. Elsevier **105**, 176–188 (2016)

23. Nduka, D.O., Ameh, J.O., Joshua, O., Ojelabi, R.: Awareness and benefits of self-curing concrete in construction projects: builders and civil engineers perceptions. Buildings MDPI **8**(8) (2019)

24. Memon, R.P., Mohd, A.R.B., Awang, A.Z., Huseien, G.F., Memon, U.: A review: mechanism, materials and properties of self-curing concrete. ARPN J. Eng. Appl. Sci. **13**(24) (2018)

25. Dinarvand, P., Rashno, A.: Review of the potential application of bacteria in self-healing and the improving properties of concrete/mortar. J. Sustain. Cement-Based Mater. (2021)

26. Vijay, K., Murmu, M.: Self-repairing of concrete cracks by using bacteria and basalt fiber. SN Appl. Sci. (2019)

27. Akindahunsi, A.A., Adeyemo, S.M., Adeoye, A.: The use of bacteria (Bacillu subtilis) in improving the mechanical properties of concrete. J. Build. Pathol. Rehabil. (2021)

28. Pourfallahi, M., Nohegoo-Shahvari, A., Salimizadeh, M.: Effect of direct addition of two different bacteria in concrete as self-healing agent. Structures Elsevier **28**, 2646–2660 (2020)

29. Griño, A.A., Daly, M., Klarissa, M., Ongpeng, J.M.C.: Bio-influenced self-healing mechanism in concrete and it testing: a review. Appl. Sci. **10**(15) (2020)

30. Zhang, W., Zheng, Q., Ashour, A., Han, B.: Self-healing cement concrete composites for resilient infrastructures: a review. Compos. Part B Eng. **189**. Elsevier (2020)

31. Wiktor, V., Jonkers, H.M.: Quantification of crack-healing in novel bacteria-based self-healing concrete. Cement Concr. Compos. Elsevier **33**(7), 763–770 (2011)

32. Sharma, T.K., Alazhari, M., Heath, A., Paine, K., Cooper, R.M.: Alkaliphilic bacillus species show potential application in concrete crack repair by virtue of rapid spore production and germination then extracellular calcite formation. J. Appl. Microbiol. Online Wiley **122**(5), 1233–1244 (2017)

33. Nguyen, T.H., Ghorbel, E., Fares, H., Cousture, A.: Bacterial self-healing of concrete and durability assessment. Cement Concr. Compos. **104**. Elsevier (2019)

34. Wangui, N.R., Karanja Thiong'o, J., Wachira, J.M.: Effect of bacillus cohnii on some physi-comechanical and microstructural properties of ordinary Portland cement. J. Chem. Hindawi (2020)

35. Safiuddin, M.D., Kaish, A.A., Woon, C.O., Raman, S.N.: Early-age cracking in concrete: causes, consequences, remedial measures, and recommendations. Appl. Sci. **8**(10) (2018)

36. Shah, K.W., Huseien, G.F.: Biomimetric self-healing cementitious construction materials for smart buildings. Biomimetics **5**(4) (2020)

37. Gautam, B.R.: Bacteria based self-healing concrete–a bacterial approach. Int. J. Eng. Sci. (IJES) 57–61 (2018)

38. Zhang, Z., Weng, Y., Ding, Y., Qian, S.: Use of genetically modified bacteria to repair cracks in concrete. Mater. Struct. MDPI (2019)

39. Hulimka, J., Kałuża, M.: Basic chemical tests of concrete during the assessment of structure suitability–discussion on selected industrial structure. Appl. Sci. MDPI **10**(1) (2020)

40. Esaker, M., Hamza, O., Souid, A., Elliott, D.: Self-healing of bio-cementitious mortar incubated within neutral and acidic soil. Mater. Struct. **54**, 96 (2021)

41. Krishnapriya, S., Babu, D.V., Arulraj, G.P.: Isolation and identification of bacteria to improve the strength of concrete. Microbiol. Res. **174**, 48–55. Elsevier (2015)

42. Su, Y., Qian, C., Rui, Y., Feng, J.: Exploring the couple mechanism of fibers and bacteria on self-healing concrete from bacterial extracellular polymeric substances (EPS). Cement and Concr. Compos. **116**. Elsevier (2021)

43. Akindahunsi, A.A., Uzoegbo, H.C.: Strength and durability properties of concrete with starch admixture. Int. J. Concr. Struct. Mater. **9**, 323–335 (2015)

44. Parashar, A.K., Gupta, A.: Effects of the concentration of various bacillus family bacteria on the strength and durability properties of concrete: a review. In: IOP Conference Series: Materials Science and Engineering (2020)

45. Sumathi, A., et al.: Development of bacterium for crack healing and improving properties of concrete under wet-dry and full-wet curing. Sustainability MDPI **12**(24), 10346 (2020)

46. Chen, H.J., Chen, M.C., Tang, C.W.: Research on improving concrete durability by biomineralization technology. Sustainability MDPI **12**(3), 1242 (2020)

47. Sangadji, S.: Can self-healing mechanism helps concrete structures sustainable? Procedia Eng. **171**, 238–249. Elsevier (2017)
48. Abo Sabah, S.H., et al.: The use of calcium lactate to enhance the durability and engineering properties of bioconcrete. Sustainability MDPI **13**(16), 9269 (2021)
49. Toader, T.P., Mircea, A.C.: Self-healing concrete mix-design based on engineered cementitious composites principles. In: Proceedings, MDPI, vol. 63, no. 1 (2020)
50. Chambua, S.T., Jande, Y.A.C., Machunda, R.L.: Strength and durability properties of concrete containing pumice and scoria as supplementary cementitious material. Adv. Mater. Sci. Eng. Hindawi (2021)
51. Morsali, S., Yucel Isildar, G., Tahni, A.: The application of bacteria as a main factor in self-healing concrete technology. J. Build. Pathol. Rehabil. (7) (2019)
52. Durga, C.S.S., Ruben, N., Chand, M.S.R., Indira, M., Venkatesh, C.: Comprehensive microbiological studies on screening bacteria for self-healing concrete. Materialia **15**. Elsevier (2021)
53. Jogi, P.K., Lakshmi, T.V.: Self heling concrete based on different bacteria: a review. Mater. Today Proc. Scienedirect **43**, 1246–1252 (2021)
54. Chen, H.J., Peng, C.F., Tang, C.W., Chen, Y.T.: Self-healing concrete by biological substrate. Materials MDPI **12**(24), (2019)
55. Yang, K.H., Kwon, S.J., Yoon, H.S.: Enhancement of strength and resistance to sulfate attack in bio-coating material through negative pressure method for bacteria immobilization. Appl. Sci. MDPI **11**(19) (2021)
56. Reddy, P.Y., Ramesh, B., Kumar, L.P.: Influence of bacteria in self healing of concrete–a review. Mater. Today Proc. Sciencedirect **33**, 4212–4218 (2020)
57. Skevi, L., Reeksting, B.J., Hoffmann, T.D., Gebhard, S., Paine, K.: Incorporation of bacteria in concrete: the case against MICP as a means for strength improvement. Cement Concr. Compos. **120**. Elsevier (2021)
58. Vashisht, R., Shukla, A.: Potential application of bacteria to improve the self-healing and strength of concrete. J. Build. Pathol. Rehabil. (10) (2020)
59. Rao, P.P., Asadi, S.S., Krishna, M.R., Babu, A.S., Alla, S.: An experimental investigation of bacteria impact on compressive strength of cement mortar and concrete. Mater. Today Proc. Sciencedirect **43**, 1949–1955 (2021)
60. Mors, R.M., Jonkers, H.M.: Towards a bacteria-based agent to make concrete self-healing. MRS Online Proc. Libr. **1488**, 75–80 (2012)
61. Rohini, I., Padmapriya, R.: Effect of bacteria subtilis on e-waste concrete. Mater. Today Proc. Sciencedirect **42**, 465–474 (2021)
62. Singh Wani, I.Y., Singh, K.:Effect of encapsulated bacteria on concrete properties: a review. Mater. Today Proc. Sciencedirect **33**, 1706–1712 (2020)
63. Wedatalla, A.M., Jia, Y. and Ahmed, A.A.: Curing effects on high-strength concrete properties. Adv. Civ. Eng. Hindawi (2018)
64. Mitrofanova, O., Mardanova, A., Evtugyn, V., Bogomolnaya, L., Sharipova, M.: Effects of bacillus serine proteases on the bacterial biofilms. In: BioMed Research International, Hindawi (2017)
65. Rauf, M., Khaliq, W., Khushnood, R.A., Ahmed, I.: Comparative performance of different bacteria immobilized in natural fibers for self-healing in concrete. Constr. Build. Mater. **258**. Elsevier (2020)
66. Abdullah, M.A.H., Abdullah, N.A.H., Tompang, M.F.: Development and performance of bacterial self-healing concrete–a review. In: IOP Conference Series: Materials Science and Engineering, vol. 431, no. 6 (2018)
67. Abishek Kumar, A.A, Stephen, E., George, M., Muhammad, A., Naveen, C.: Evaluation of strength and durability properties for various amount of bacillus subtilis bacteria in concrete, vol. 9, no. 6 (2020)
68. Karimi, N., Mostofinejad, D.: Bacillus subtilis bacteria used in fiber reinforced concrete and their effects on concrete penetrability. Constr. Build. Mater. **230**. Elsevier (2020)

69. Kumar, M.M., Ganapathy, D.V., Devi, V.S., Iswarya, N.: Experimental investigation on fibre reinforced bacterial concrete. In: Materials Today: Proceedings, vol. 22, pp. 2779–2790 (2020)

70. Salmasi, F., Mostofinejad, D.: Investigating the effects of bacterial activity on compressive strength and durability of natural lightweight aggregate concrete reinforced with steel fibers. Constr. Build. Mater. **251**. Elsevier (2020)

71. Alonso, M.J.C., et al.: Improved strength and durability of concrete through metabolic activity of ureolytic bacteria. Environ. Sci. Pollut. Res. Int. 21451–21458 (2018)

72. Shahid, S., Aslam, M.A., Ali, S., Zameer, M., Faisal, M.: Self-healing of crack in concrete using bacillus strains encapsulated in sodium alginate beads. Chem. Sel. **5**(1), 312–323 (2020)

73. Fahimizadeh, M., Diane Abeyratne, A., Mae, L.S., Singh, R.R., Pasbakhsh, P.: Biological Self-Healing of Cement Paste and Mortarby Non-Ureolytic Bacteria Encapsulated in Alginate Hydrogel Capsules. Materials, MDPI (2020)

74. Van Der Bergh, J.M., et al.: Comparion of microbially induced healing solutions for cracks repairs of cement-based infrastructure. Sustainability **13**(8) (2021)

75. Priya, T.S., Ramesh, N., Agarwal, A., Bhusnur, S., Chaudhary, K.: Strength and durability characteristics of concrete made by micronized biomass silica and Bacteria-Bacillus sphaericus. Constr. Build. Mater. 827–83. Elsevier (2019)

76. Xu, J., Wang, X., Zuo, J., Liu, X.: Self-healing of concrete cracks by ceramsite-loaded microorganism. Adv. Mater. Sci. Eng. Hindawi (2018)

77. Lee, Y.S., Park, W.: Current challenges and future directions for bacterial self-healing concrete. Appl. Microbiol. Biotechnol. (2018)

78. Girish, S., Soumya, T., Girish, S.: An experimental study on self-remediating bacterial concrete. In: Narasimhan, M.C., George, V., Udayakumar, G., Kumar, A. (eds.) Trends in Civil Engineering and Challenges for Sustainability. LNCE, vol. 99, pp. 283–293. Springer, Singapore (2021). https://doi.org/10.1007/978-981-15-6828-2_22

79. Vats, R., Duggal, P., Singh, N., Tyagi, A., Tomar, R.K., Bhardwaj, U.: Analysis of physical changes due to bacterial remediation in LECA LWA concrete. In: Proceedings of the 2nd International Conference on Intelligent Engineering and Management (ICIEM), 2021.

80. Insaurralde, C.C., Rahman, P.K., Ramegowda, M., Vemury, C.M.: Follow-up methods for autonomic repairing process. In: IEEE International Conference on Systems, Man, and Cybernetics (SMC) (2017)

81. Durga, C.S.S., Ruben, N., Chand, M.S.R., Venkatesh, C.: Evaluation of mechanical parameters of bacterial concrete. Int. Inf. Eng. Technol. Assoc. **43**(6), 395–399 (2019)

82. Siddique, R., Nanda, V., Kadri, E.H., Khan, M.I., Singh, M., Rajor, A.: Influence of bacteria on compressive strength and permeation properties of concrete made with cement baghouse filter dust. Constr. Build. Mater. **106**, 461–469 (2016)

83. Algaifi, A.H. et al.: Mathematical prediction of the compressive strength of bacterial concrete using gene expression programming. Ain Shams Eng. J. (2021)

84. Rao, M.V., Reddy, V.S., Sasikala, C.: Performance of microbial concrete developed using bacillus subtilus JC3. J. Inst. Eng. 501–510 (2017)

85. Kumar, M.M., Ganapathy, D.V., Devi, V.S., Iswarya, N.: Experimental investigation on fibre reinforced bacterial concrete. In: Materials Today: Proceedings, Elsevier, vol. 22, pp. 2779–2790 (2020)

86. Zhang, J.L., Wu, R.S., Li, Y.M., Zhong, J.Y.: Screening of bacteria for self-healing of concrete cracks and optimization of the microbial calcium precipitation process. Appl. Microbiol. Biotechnol. (2016)

87. Joshi, S., Goyal, S., Mukherjee, A., Reddy, M.S.: Microbial healing of cracks in concrete: a review. J. Ind. Microbiol. Biotechnol. 1511–1525 (2017)

88. Nain, N., Surabhi, R., Yathish, N.V., Krishnamurthy, V., Deepa, T., Tharannum, S.: Enhancement in strength parameters of concrete by application of bacillus bacteria. Constr. Build. Mater. **202**, 904–908. Elsevier (2019)

89. Xu, J., Yao, W.: Multiscale mechanical quantification of self-healing concrete incorporating non-ureolytic bacteria-based healing agent. Cement Concrete Res. **64**, 1–10. Elsevier

90. Seifan, M., Ebrahiminezhad, A., Ghasemi, Y., Berenjian, A.: Microbial calcium carbonate precipitation with high affinity to fill the concrete pore space: nanobiotechnological approach. Bioprocess Biosyst. Eng. 37–46 (2019)
91. Luo, M., Qian, C.X., Li, R.Y. Factors affecting crack repairing capacity of bacteria-based self-healing concrete. Constr. Build. Mater. Elsevier **87** (2015)
92. Tziviloglou, E., Wiktor, V., Jonkers, H.M., Schlangen, E.: Bacteria-based self-healing concrete to increase liquid tightness of cracks. Constr. Build. Mater. **122**, 18–125 (2016)
93. Jafarnia, M.S., Saryazdi, M.K., Moshtaghioun, S.M.,: Used of bacteria for repairing cracks and improving properties of concrete containing limestone powder and natural zeolite. Constr. Build. Mater. **242**. Elsevier (2020)
94. Parmar, A., Patel, A., Shah, P.: Improvement of the concrete cracks by using bacillus sphaericus. Int. J. Eng. Dev. Res. (2013)
95. Jakubovskis, R., Jankutė, A., Urbonavičius, J., Gribniak, V.: Analysis of mechanical performance and durability of self-healing biological concrete. Constr. Build. Mater. **260**. Elsevier (2020)
96. Jonkers, H.M., Thijssen, A., Muyzer, G., Copuroglu, O., Schlangen, E.: Application of bacteria as self-helaing agent for the development of sustainable concrete. Ecol. Eng. **36**, 230–235. Elsevier (2010)
97. Xu, J., Wang, X., Wang, B.: Biochemical process of ureolysis-based microbial $CaCO_3$ precipitation and its application in self-healing concrete. Appl. Microbiol. Biotechnol. 3121–3132 (2018)
98. Vijay, K., Murmu, M.: Effect of calcium lactate on compressive strength and self-healing of cracks in microbial concrete. Front. Struct. Civ. Eng. 515–525 (2019)
99. Xue, C., Li, W., Li, J., Tam, V.W., Ye, G.: A review study on encapsulation-based self-healing for cementitious materials. Wiley Online Library (2018)
100. Tayebani, B., Mostofinejad, D.: Penetrability, corrosion potential, and electrical resistivity of bacterial concrete. J. Mater. Civ. Eng. **31**(3) (2019)
101. Balam, N.H., Mostofinejad, D., Eftekhar, M.: Effects of bacterial remediation on compressive strength, water absorption, and chloride permeability of lightweight aggregate concrete. Constr. Build. Mater. **145**, 107–116. Elsevier (2017)

Seismic Evaluation of Reinforced Structure Using Pushover Analysis for Different Soil Types

Passang Diki Sherpa and **Greegar George**

Abstract India belongs to seismically active regions and many existing structures that were built are often found vulnerable to earthquake damage. This paper focuses on the seismic performance of Reinforced Concrete Special Moment Resisting Frame (RC SMRF) with and without foundation soil behaviour by performing a pushover analysis for G + 2 storey, G + 5 storey, and G + 9 storey buildings located in seismic Zone IV. The response reduction factor is also evaluated for the buildings with the fixed-base and flexible-base condition. It is always economical to design the building for design base shear as the design base shear is always lower than the actual base shear. The response reduction factor is the factor that is used to obtain the design base shear from the actual base shear. The response reduction factor depends upon ductility, overstrength, and redundancy of the structure. SAP2000 has been used to generate a model of G + 2 storey, G + 5 storey, and G + 9 storey reinforced concrete buildings to perform non-linear pushover analysis.

Keywords Pushover analysis · Soil-structure interaction · Response reduction factor

1 Introduction

The interaction between the soil and structure is an important factor which needs to be considered during the design of structures. The soil-structure interaction (SSI) can affect the actual behaviour and design of structures. When SSI is taken into account, the building's damage index rises before a threshold period is reached, which is generally equal to the predominant period of the ground motion [1]. It

P. D. Sherpa (✉) · G. George
Department of Civil Engineering, National Institute of Technology, Tiruchirappalli, India
e-mail: 203220019@nitt.edu

G. George
e-mail: greegar@nitt.edu

implies that the fixed-base method underestimates the damages sustained by structures having periods shorter than this threshold period. The SSI, in particular, significantly increases the damage index of short-period buildings on soft soils. It has also been observed that the effect due to SSI increases as the aspect ratio (width to height ratio) increases, due to which the damage index also increases [1].

The pushover analysis is a nonlinear technique for assessing the strength and deformation demand of the structure in design earthquakes. By comparing these demands to available capacities, the desired performance level of the structures can be achieved. Pushover analysis is used to assess factors such as global drift, interstorey drift, element deformation, and element and connection forces that cannot sustain plastic deformation [2]. The key concept in this technique is that the response of a multi-degree of freedom structure is regulated by an equivalent single degree of freedom system. The reaction of the structure is dominated by the first mode of vibration and the first mode shape. The pushover analysis involves subjecting structures to monotonically increasing patterns of lateral loads which represent the inertial forces that the structure would experience if it is subjected to ground shaking. The pushover analysis is generally performed for fixed-base conditions. The parts of structural components may yield consecutively under steadily increasing loads. As a result, the structure loses its rigidity as the yielding occurs [3].

The base shear, displacement, and time period of the structure increase gradually as the seismic zone progresses from II to V. The hinge formation starts in the beams of the ground floor and slowly propagates upwards. Ultimately, it forms in columns to validate the strong column-weak beam concept [4]. An increased fundamental natural period of a structure due to SSI does not always result in a smaller response. The widely held belief in structural engineering that SSI is always beneficial is sometimes a misrepresentation that can lead to unsafe design [5].

The soil-structure interaction can be done by two methods namely, the direct method and the sub-structure method. In the direct method, soil, structure, and foundation are all modelled and analysed in one step using finite element models. Freefield motion is used to describe the ground motion. The substructure method is computationally more efficient than the direct method. This method is helpful as it allows the complex soil-structure system to be broken down into more manageable sections that can then be solved and verified in an ease manner [6]. The nonlinear SSI is shown to increase the displacement demand of the structure as compared to the equivalent linear soil model [7]. The base shear reduces at the performance point and lateral drift increases due to the increase in flexibility of structure when SSI is considered [8].

In this paper, the response reduction factor is also evaluated for the buildings with different soil types. The overstrength factor, ductility factor, damping factor, and redundancy factor are all used to compute the response reduction factor [9]. Equation (1) defines the response reduction factor where R_s denotes the overstrength factor, R_μ denotes the ductility factor, R_ξ denotes the damping factor, and R_R denotes the redundancy factor.

$$R = R_S R_\mu R_R R_\xi \tag{1}$$

Researchers have come up with many expressions to determine the ductility factor. The widely used expressions are given by Miranda and Bertero [10], Krawinkler and Nassar [11], and Riddel et al. [12]. The equations given by Miranda and Bertero [10] are used in this study to find out the response reduction factor. The strength reduction factor was derived by considering 5% damping. The influence of local site conditions on the ductility factor was investigated by Miranda and Bertero by considering different ground motions recorded during earthquakes in various types of soil conditions [10]. The sites at which the ground motion was recorded are classified into three groups, namely rock, alluvium, and soft soil sites. Equation (2) represents the ductility factor.

$$R_\mu = \frac{\mu - 1}{\varnothing} + 1 \tag{2}$$

Here, ϕ is a function of μ, T, and soil conditions at the site. Equations (3) to (5) represent the effect of the site conditions on $\varnothing$ when, rock, alluvium, and soft sites are considered.

$$\text{For rock sites :} \quad \varnothing = 1 + \frac{1}{10T - \mu\,T} - \frac{1}{2T}\exp\left[-\frac{3}{2}\left(\ln\,T - \frac{3}{5}\right)^2\right] \tag{3}$$

$$\text{For alluvium sites :} \quad \varnothing = 1 + \frac{1}{12T - \mu\,T} - \frac{2}{5T}\exp\left[-2\left(\ln\,T - \frac{1}{5}\right)^2\right] \tag{4}$$

$$\text{For soft sites :} \quad \varnothing = 1 + \frac{T_g}{3T} - \frac{3T_g}{4T}\exp\left[-3\left(\ln\frac{T}{T_g} - \frac{1}{4}\right)^2\right] \tag{5}$$

Here, T_g denotes the predominant period of ground motion. In this paper, the pushover analysis of buildings considering the interaction between the structure and the soil is carried out. The target displacements are determined for the buildings and the response reduction factor is calculated for the buildings with the fixed-base and flexible-condition.

2 Description of the Structural System

The study considers three different buildings; model 1 (G + 2), model 2 (G + 5), and model 3 (G + 9) storey buildings resting on three different soil types (hard, medium, and soft).

The regular and symmetric structures having a constant storey height of 3 m are considered in this study. The building heights of model 1 (G + 2), model 2 (G + 5) storey, and model 3 (G + 9) storey buildings are 9, 18, and 30 m respectively. Two bays are considered each with a width of 4 m. The elevations of the buildings
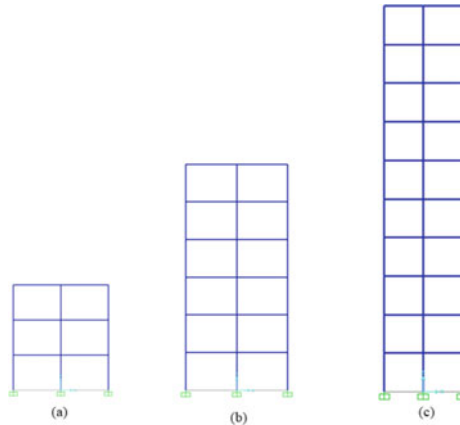
Fig. 1 Elevations of the structures for **(a)** model 1 (G + 2) storey, **(b)** model 2 (G + 5) storey, and **(c)** model 3 (G + 9) storey considering fixed-base condition

are shown in Fig. 1. The building is assumed to be situated in Zone IV as per Indian Standard (IS) code [13]. IS 1893 (Part-1):2002 has been used to analyse the structure, assuming a fixed and flexible base with damping of 5% and a response reduction factor of 5. IS 875 Part 1 and Part 2 are used to determine the design dead and live loads [14, 15].

3 Pushover Analysis with Soil-Structure Interaction

For modelling the soil-structure interaction, the multilinear plastic link element is used at each support of the building modelled in SAP2000 [16]. The sizes of the isolated foundation considered for model 1 (G + 2), model 2 (G + 5), and model 3 (G + 9) storey buildings are 1.5 m × 1.5 m, 2.1 m × 2.1 m, and 2.5 m × 2.5 m respectively, each with a depth of 500 mm. This is modelled using the shell element. The foundation is built on three different types of soil: hard, medium, and soft. The values of the elastic moduli for hard, medium, and soft soil are assumed to be 65000 kN/m², 35000 kN/m², and 15000 kN/m² respectively [17]. The model considering the SSI is shown in Fig. 2. The equations given by George Gazetas (1991) are used to determine the stiffness for different vibration modes [18]. The stiffnesses used are as follows:

$$\left(\frac{2GL}{1-\nu}\right)(0.73 + 1.54\chi^{0.75}) \tag{6}$$

$$\left(\frac{2GL}{2-\nu}\right)(2 + 2.50\chi^{0.85}) \tag{7}$$
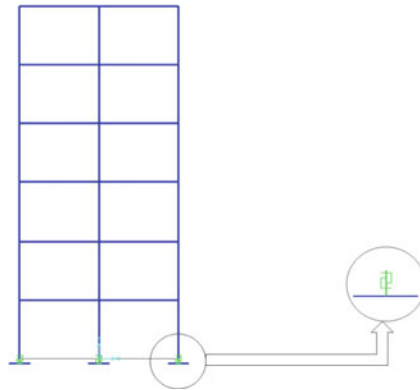
Fig. 2 Model 3 (G + 9) storey structure showing soil-structure interaction

$$\left(\frac{G}{1-\nu}\right){I_{by}}^{0.75}\left(\frac{L}{B}\right)^{0.15} \tag{8}$$

Here, Eq. (6) represents the static stiffness for the vertical direction, Eq. (7) represents the stiffness for the lateral direction and Eq. (8) represents the stiffness for the rotation along the lateral axis. Also, I_{by} denotes the area moments of inertia about the y-axis of actual soil-foundation contact surface, B and L denote the half-width and half-length of the circumscribed rectangle, G is the shear modulus, and ν is the Poisson's ratio. The quantity, χ can be evaluated as,

$$\chi = \left(\frac{A_b}{4L^2}\right) \tag{9}$$

where, A_b denotes the base area of the foundation.

4 Results and Discussions

The pushover analysis has been performed on three different models with hard, medium, and soft soil using SAP2000 software. Figures 3, 4 and 5 shows the hinge distribution of these models. It can be seen that the formation of the hinge starts from the bottom and ends at the top of the structure.

Table 1 shows the pushover parameters obtained for hard, medium, and soft soil. Here, V_d is the design base shear, V_u is the ultimate base shear, Δy is the yield displacement, Δu is the ultimate displacement, and μ is the ductility factor.

The response reduction factor obtained for hard, medium, and soft soil by considering fixed- base are shown in Table 2.
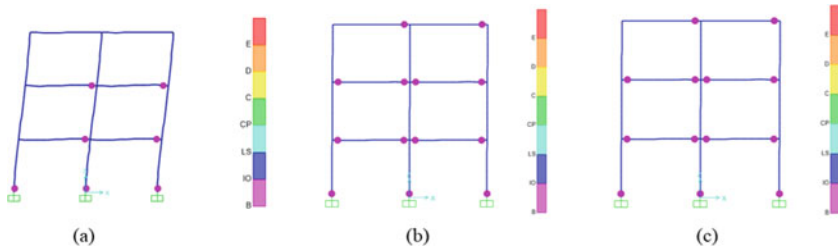
Fig. 3 Plastic hinge distribution for a model 1 (G + 2) storey building resting on **(a)** hard soil, **(b)** medium soil, and **(c)** soft soil
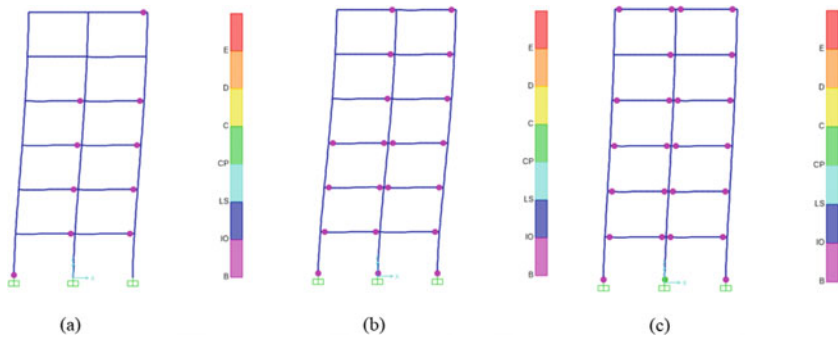
Fig. 4 Plastic hinge distribution for a model 2 (G + 5) storey building resting on **(a)** hard soil, **(b)** medium soil, and **(c)** soft soil
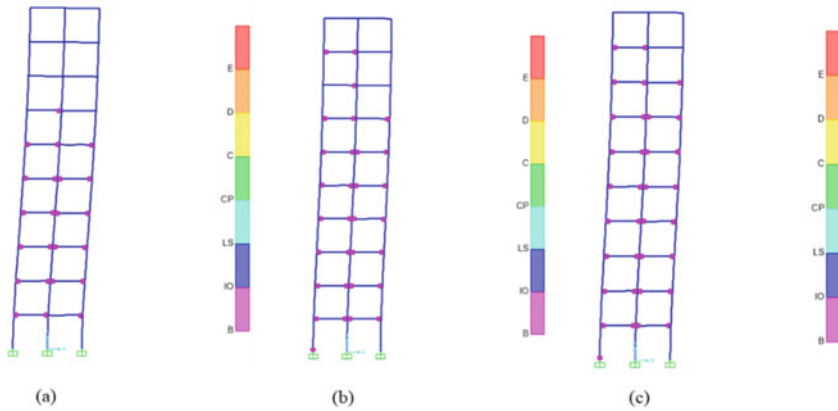
Fig. 5 Plastic hinge distribution for a model 3 (G + 9) storey building resting on **(a)** hard soil, **(b)** medium soil, and **(c)** soft soil

Table 1 Pushover parameters

Type of soil	Type of structure		Design base shear	Ultimate base shear	Yield displac-ement	Ultimate displacement	Ductility factor
	Notation		V_d	V_u	Δy	Δu	μ
	Unit		kN	kN	mm	mm	–
Hard	Model 1	(G + 2) Storey	32.64	179.20	27.08	124.11	4.58
	Model 2	(G + 5) Storey	51.61	340.07	66.70	263.22	3.94
	Model 3	(G + 9) Storey	50.57	452.23	40.83	275.93	6.75
Medium	Model 1	(G + 2) Storey	48.97	179.20	27.10	124.10	4.57
	Model 2	(G + 5) Storey	70.19	340.07	66.70	263.22	3.94
	Model 3	(G + 9) Storey	113.96	452.20	59.17	595.97	10.07
Soft	Model 1	(G + 2) Storey	32.64	179.01	27.09	124.23	4.58
	Model 2	(G + 5) Storey	73.81	345.65	60.71	281.36	4.63
	Model 3	(G + 9) Storey	84.45	452.20	59.08	595.97	10.08

Table 2 Response reduction factor for fixed-base condition

Type of soil	Type of structure	R_S	R_μ	R_R	R
Hard	Model 1 (G + 2) Storey	5.48	3.18	1	8.75
	Model 2 (G + 5) Storey	6.58	3.51	1	11.56
	Model 3 (G + 9) Storey	5.45	6.51	1	17.77
Medium	Model 1 (G + 2) Storey	3.66	2.85	1	5.22
	Model 2 (G + 5) Storey	4.84	5.45	1	13.18
	Model 3 (G + 9) Storey	4.89	3.2	1	6.33
Soft	Model 1 (G + 2) Storey	5.483	3.79	1	10.39
	Model 2 (G + 5) Storey	4.68	5.29	1	12.38
	Model 3 (G + 9) Storey	5.35	14.29	1	38.25

By considering the flexible base condition, the values of response reduction factor are evaluated for hard, medium, and soft soils and are tabulated in Table 3.

The target displacements are evaluated as per FEMA 356 [19]. Table 4 shows the values of target displacements for different structures by considering the fixed and flexible base condition.

Table 3 Response reduction factor for flexible-base condition

Type of soil	Type of structure	R_S	R_μ	R_R	R
Hard	Model 1 (G + 2) Storey	3.06	3.51	1	10.76
	Model 2 (G + 5) Storey	3.94	3.86	1	15.2
	Model 3 (G + 9) Storey	4.89	3.97	1	19.44
Medium	Model 1 (G + 2) Storey	3.22	3.59	1	11.56
	Model 2 (G + 5) Storey	3.21	3.94	1	12.66
	Model 3 (G + 9) Storey	4.65	3.87	1	18.04
Soft	Model 1 (G + 2) Storey	3.06	3.59	1	11
	Model 2 (G + 5) Storey	3.42	3.94	1	13.5
	Model 3 (G + 9) Storey	5.35	4.37	1	25.34

Table 4 Target displacements

Type of soil	Type of structure	For fixed base	For flexible base
	Unit	mm	mm
Hard	Model 1 (G + 2) Storey	36	57
	Model 2 (G + 5) Storey	55	88
	Model 3 (G + 9) Storey	75	201
Medium	Model 1 (G + 2) Storey	41	75
	Model 2 (G + 5) Storey	65	118
	Model 3 (G + 9) Storey	85	273
Soft	Model 1 (G + 2) Storey	70	97
	Model 2 (G + 5) Storey	101	144
	Model 3 (G + 9) Storey	124	335

5 Conclusions

The present study has focused on the pushover analysis of three different buildings with a regular plan; namely model 1 (G + 2), model 2 (G + 5), and model 3 (G + 9) storey buildings with and without the soil-structure interaction. The buildings are assumed to be supported by three types of soil, namely, hard, medium, and soft soil. The seismic Zone IV with critical damping of 5% has been assumed in the analysis. From the analysis, it can be concluded that the number of hinges in the structure increases as the soil type goes from hard to soft soil. This indicates that the structure suffers more damage as the stiffness of the soil is reduced. By considering the soil-structure interaction, the target displacement is found to be more than that of the fixed base structure. It is also found that as the storey height increases, the target displacement increases. The response reduction factor obtained in this study exceeds the recommended IS code values, indicating that the models under consideration are ductile and safe. The response reduction factor increases as the storey height increases

and also with the soil type from hard to medium to soft soil. The response reduction factor obtained for the same buildings considering the soil- structure interaction is found to be higher than the fixed-base condition.

References

1. Nakhaei, M., Ghannad, M.A.: The effect of soil-structure interaction on damage index of buildings. Eng. Struct. **30**, 1491–1499 (2008)
2. Krawinkler, H., Seneviratna, G.D.P.K.: Pros and cons analysis of seismic evaluation. Eng. Struct. **20**, 452–464 (1998)
3. Applied Technology Council, ATC-40: Seismic evaluation and retrofit of concrete buildings, vols. 1 and 2, California (1996)
4. Deep, V.M., Raju, P.: Pushover analysis of RC building: comparative study on seismic Zones of India. Int. J. Civ. Eng. Technol. **8**(4), 567–578 (2017)
5. Gazetas, G., Mylonakis, G.: Seismic soil-structure interaction: beneficial or detrimental? J. Earthq. Eng. **4**(3), 277–301 (2000)
6. Wolf, J.P.: Dynamic Soil-structure Interaction. Prentice-Hall, New Jersey (1985)
7. Ghoozhdi, H.A., Attarnejad, R.: A winkler-based model for inelastic response of soil-structure systems with embedded foundation considering kinematic and inertial interaction effects. Eng. Struct. **28**, 589–603 (2020)
8. Liu, L., Gou, W., Xie, Q., Bi, L., Li, Y., Wu, Y.: Analysis of elasto-plastic soil-structure interaction system using pushover method. In: Proceedings of the 15th World Conference on Earthquake Engineering, Lisbon (2012)
9. ATC: Structural response modification factors. ATC-19. Appl. Technol. Counc, 1-69. Redwood City, California (1995)
10. Miranda, E., Bertero, V.V.: Evaluation of strength reduction factor for earthquake-resistance design. Earthq. Spectra **10**(2), 357–379 (1994)
11. Krawinkler, H., Nassar, A.A.: Seismic demand for SDOF and MDOF Systems. Report No. 95, The John A. Blume Earthquake Engineering Center, Stanford University (1991)
12. Riddell, R., Hidalgo, P., Cruz, E.: Response modification factors for earthquake resistant design of short period buildings. Earthq. Spectra **5**(3), 571–590 (1989)
13. IS 1893-1: Criteria for Earthquake Resistant Design of Structures, Part 1: General Provisions and Buildings [CED 39: Earthquake Engineering] (2002)
14. IS 875 (Part 1)- 1987: Indian standard code of practice for design loads (other than earthquake) for buildings and structures, Part I: dead loads–unit weights of building materials and stored materials (1987)
15. IS 875 (Part 2)-1987: Code of practice for design loads (other than earthquake) for buildings and structures, Part 2: Imposed loads (1987)
16. SAP2000: Integrated software for structural analysis and design. Computers and Structures Inc., Berkeley, CA, USA
17. Bowles, J.E.: Foundation Analysis and Design, 5th edn. McGraw Hills, New York (1998)
18. Gazetas, G.: Formulas and charts for impedances of surface and embedded foundations. J. Geotech. Eng. 117(9), 1363–1381 (1991)
19. F.E.M.A.: Pre-standard and Commentary for Seismic Rehabilitation of Buildings. FEMA-356. American Society of Civil Engineers, Washington DC (2000)

Accident Prediction Modelling and Crash Scene Investigation

P. H. Sumayya Naznin, Leena Samuel Panackel, Sowmya Zaviar, and Shiya Babu

Abstract In recent years, traffic incidents have been a major cause of deaths, injuries, and property damage in India. By definition, an accident is "an unforeseen and unplanned incident that causes harm or injury"; nevertheless, in most circumstances, accidents can be avoided by taking specific precautions. Understanding the primary and contributing factors may combat road traffic accident severity. This research uncovered new information as well as the most important target-specific contributing elements to the severity of road accidents. The goal of this study was to analyse accident data from Koratty and Angamaly towns in Kerala's Ernakulam district, and to identify and classify black spots into first, second, third, fourth, and fifth orders based on the ASI value and the crash scenes were investigated in order to analyze the causes. An attempt was made to design collision and condition diagrams, as well as develop an accident prediction model for these dangerous areas, using the information acquired thus far. The collision diagrams for various places also revealed the pattern of road accidents that occurred over a two-year period, while the condition diagrams revealed the precise site of the accident. Using this knowledge, certain short-term corrective measures/solutions for the crash studied sites were offered.

Keywords Accident prediction model · Collision diagram · Condition diagram · Crash scene investigation · Multiple linear regression

P. H. Sumayya Naznin (✉)
National Institute of Technology, Mangalore, Karnataka, India
e-mail: sumayyanaznin@gmail.com

L. S. Panackel
Department of Civil Engineering, Federal Institute of Science and Technology, Angamaly, Kerala, India

S. Zaviar
Transportation Engineering, National Institute of Technology, Mangalore, Karnataka, India

S. Babu
Transportation Engineering, Federal Institute of Science and Technology, Angamaly, Kerala, India

1   Introduction

1.1   *General Background*

The number of road traffic deaths is steadily increasing, reaching 1.35 million in 2016. However, the rate of death relative to the size of the world's population has remained constant. When considered in the context of the increasing global population and rapid motorization that has taken place over the same period, this suggests that existing road safety efforts may have mitigated the situation from getting worse. However, it also indicates that progress to realize Sustainable Development Goal (SDG) target calls for a 50% reduction in the number of road traffic deaths by 2020 remains far from sufficient, [9]. There has also been more progress in reducing the number of road traffic deaths among middle- and high-income countries than low-income countries. Between 2013 and 2016, no reductions in the number of road traffic deaths were observed in any low-income country, while some reductions were observed in 48 middle and high-income countries. The global rate of road traffic death is 18.2 per 100,000 population. This rate varies across the world's regions, where the rate of death ranges from 9.3 to 26.6 per 100,000 population. Regional rates of road traffic deaths in Africa and South-East Asia are highest at 26.6 and 20.7 deaths per 100,000 population respectively. This is followed by the Eastern Mediterranean and Western Pacific regions, which have rates comparable to the global rate with 18 and 16.9 deaths per 100,000 population respectively [9]. The status of India according to WHO is as follows: About 1,50,785 road traffic fatalities were reported in India, 85% of which were males, and the rest were females. The number of deaths per 1,00,000 population reached a peak in 2011 which reduced for the next 3 years but since then has been increasing.

Road traffic deaths also vary according to the type of vehicles and road user category. Since Indian traffic is mixed this plays a major role. According to WHO, about 40% of road traffic deaths are witnessed by riders of motorized 2 and 3 wheelers, followed by passengers of 4 wheeled cars and light vehicles contributing 12% to the total number of fatalities [9]. The trend of road accidents in Kerala is as shown in 40,181 accidents, 4303 deaths and 45,458 injuries were reported in the year 2018 alone emphasizing the seriousness of the situation, (Kerala Road Safety Authority). Evaluation of road safety measures appears happens to be one of the weakest components of road safety management systems. To improve safety on roads, road authorities and designers use prediction tools, commonly known as Accident Prediction Models (APMs), allowing them to understand the potential safety issues, to identify safety improvements and to estimate the potential effect of these improvements in terms of crash reduction [5]. Causes of accidents and related injury severity are of special concern to researchers in traffic safety since such research would be aimed not only at prevention of accidents but also at reduction of their severity, (Highway Safety Manual, 2010). One way to accomplish this is to predict accident frequency or accident severity by using this statistical technique. The causes of traffic accidents are usually complex and involve several factors. The main factors can be divided into

four categories: the driver, the vehicle, the roadway, and the environment. Human factors account wholly or partly to 93% of all traffic accidents, [1]. Drivers are the primary cause of those accidents. The main cause of traffic accidents is disobeying the traffic safety laws, which include speeding, driver distraction, driving under the influence of drugs or alcohol, close following between the running vehicles, etc.

1.2 Scope and Objective

The scope of this research was to collect and analyse accident data of Koratty & Angamaly police station boundaries and to identify the locations with maximum accident rate. The study also included investigation of crash scenes in these locations to analyse the causes. Finally, an attempt was made to draw the collision & condition diagrams which was used to identify the precise cause of accident at the site and to develop an accident prediction model.

2 Methodology

2.1 Primary Data Collection

For accident data collection, the nearby police stations of Angamaly and Koratty was approached. The accident data of the past 5 years ie., 2014–2018 were collected from these stations which include information regarding type of vehicles involved, the vehicle registration number, place of collision, date, time, details of injuries and the FIR details.

2.2 Analysis of Primary Data

According to NATPAC, Ernakulam district ranks first in terms of number of accidents black spots. National highway authority of India (NHAI) identifies hazardous locations based on Accident Severity Index (ASI). Depending on the ASI value the black spots are classified into first order, second order, third order, fourth order and fifth order black spots. Angamaly, Karukutty, Karayamparambu and Vengoor were identified as first order black spots and these locations come under the jurisdiction of Angamaly Police Station. Similarly, Koratty (NH544) has also been named a first order black spot which comes under the jurisdiction of Koratty Police Station. Analysing the data collected from the police stations, it was clear that these locations witness the greatest number of accidents. From the FIR details, the causes and type

of collision can be identified. This helps in developing collision diagrams of the hazardous locations.

2.3 Crash Scene Investigation

Accident reconstruction is an important tool to study the causes of accidents in detail. Crash Scene Investigation aids in identifying the causes using photographic documentation, measurements, and diagrams etc., [7]. These techniques will be made use of in the investigation of live crash scenes in the black spots identified in the previous step. The photographs will be taken from all major directions to record the general scene. This includes all sides of the vehicles and their position at rest, the approach path of each vehicle or moving object, possible skid marks, their positions at rest and the deformations on the vehicles. From the investigation details collision and condition diagrams can be drawn.

2.4 Developing Accident Prediction Model

Accident prediction models have been extensively used in the domain of road infrastructure for the estimation of the expected number of accidents on road segments and junctions as well as for the estimation of safety benefits. Using the data collected, an attempt will be made to develop a prediction model using the multiple linear regression model. In this approach modelling is carried between a scalar dependent variable y and one or more explanatory variables (or independent variable) denoted as X.

$$Y = \beta 0 + \sum \beta_i X_i \tag{1}$$

where, X_i is explanatory variables and β_i is regression coefficients of the respective independent variables and $\beta 0$ is the regression constant, [8]. The SPSS (Statistical Package for Social Sciences) software will be used in developing the Regression Models.

3 Analysis of Data

3.1 General Background
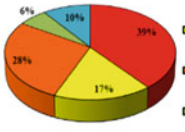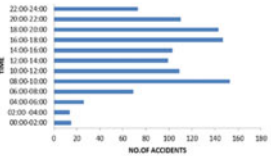
The status in terms of road accidents and numbers of fatalities during the last five years is given in Table 1 below.

Table 1 Road accidents & number of fatalities in the last five years (2014–2018)

3.1.1 Classification Based on Accident Severity	 In both Angamaly and Koratty, major accidents are more frequent (68% and 73% respectively) followed by minor accidents (21% and 15% respectively)
3.1.2 Based on the Type of Vehicles Involved The level of vulnerability of road users to accidents is high, as the same road space is being shared along wide variety of motorized, non-motorized vehicles and pedestrians	 As observed, two wheelers cause the greatest number of accidents, followed by four wheelers and then heavy vehicles. A small number of accidents also involve cycles and electric scooters.
3.1.3 Based on the Type of Collision Collisions can be of different kinds: vehicle to vehicle, vehicle to pedestrian, vehicle to non-motorized vehicle and others which include vehicle skidding, overturning and vehicles going out of control due to vehicle defects.	 Mostly, rear-end collisions and sideswipes occur. The analysis of the data also revealed that even though head on collisions are less frequent than rear end collisions, these categories of accidents are more severe and sometimes fatal.

Table 1 (continued)

3.1.4 Based on the Causes of Road Accidents Road accidents are multi – causal and are resulted by an interplay of various factors. These can broadly be categorized into those related to (i) human error (ii) road environment and (iii) vehicular condition	 According to this classification, a major share of accidents was caused due over speeding, and a few were due to violations like lack of indicator, red light violation, etc.
3.1.5 Based on Monthly distribution of accidents	 The month wise data on road accidents presented in graphs reveals that, over the period of last five years (2014-2018), the month in which the maximum number of accidents occur is January and the minimum number occur in December.
3.1.6 Time interval-wise distribution of accidents The traffic is denser during the morning and evening peak hours when more vehicles travel to/from the city centres or areas of major economic activity.	 Most of the accidents take place during the peak hours. The peak traffic hours of 8:00am-10:00am and 4:00pm-6:00pm recorded maximum of number of accidents.

3.2 Introduction

The first step of crash scene investigation is the identification of study areas. After analysing the data, the top five accident spots (with respect to the total number of accidents) were plotted onto a map.

4   Crash Scene Investigation

4.1   Introduction

The first step of crash scene investigation is the identification of study areas. After analysing the data, the top five accident spots (with respect to the total number of accidents) were plotted onto a map.

4.1.1   Pongam

Accident Location:	Pongam
Name of Road:	NH544 Salem-Kochi Highway
Date of Accident:	12–10-2019
Time:	10:15am
Vehicles Involved:	Trailer x Car
IPC Section:	279, 337
Type of Crash:	Minor
Type of Collision:	Sideswipe
Description of Location:	The Fig. 1 shown below are the collision and condition diagrams. The scene is located at Pongam in NH544, which is a four-lane divided carriageway with a median of 5.4m width. The number of accidents is very high owing to the high travel speeds on the highway. Majority of the fatalities involve accidents involving pedestrians. The remaining accidents are either of the minor or major category.
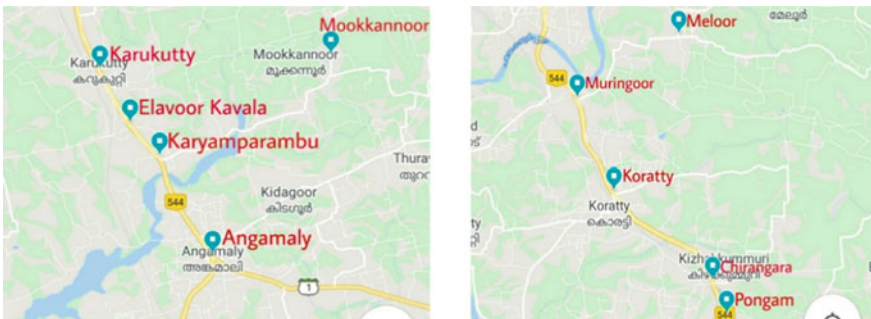
Fig. 1 Top five accident prone areas within Angamaly and Koratty Police Station respectively
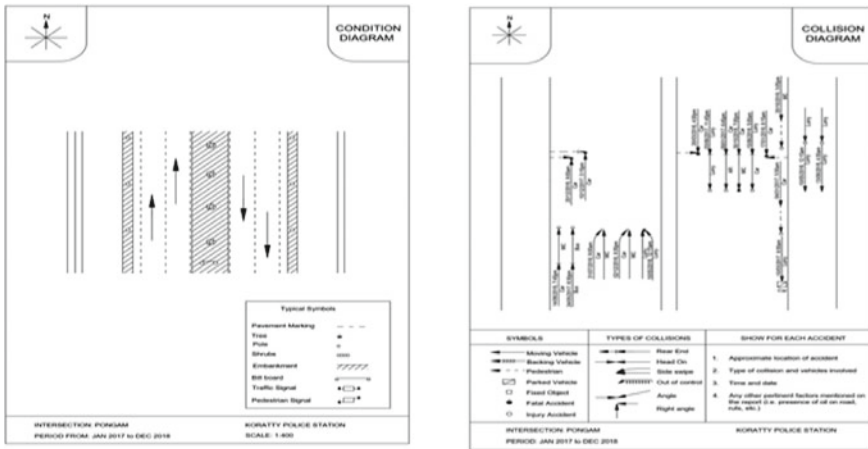
Fig. 2 Collision and condition diagram of Pongam

4.1.2 Angamaly Bank Junction Accident

Accident Location:	Angamaly Bank Junction
Name of Road:	NH544 Salem-Kochi Highway
Date of Accident:	25–11-2019
Time:	7:30 am
Vehicles Involved:	Bus x Auto rickshaw
IPC Section:	304(A)
Type of Crash:	Fatal
Type of Collision:	Angle
Description of Location:	The Fig. 2 shown above are the collision and condition diagrams. From the collision diagram it is clear that, even though the number of accidents are comparatively less, the severity of accidents is more (either fatal or major accidents).

4.1.3 Nayathode Accident

Accident Location:	Nayathode
Name of Road:	M C Road, State Highway
Date of Accident:	12–12-2019
Time:	4:30 am
Vehicles Involved:	Lorry x Car
IPC Section:	279, 338
Type of Crash:	Major
Type of Collision:	Head-on
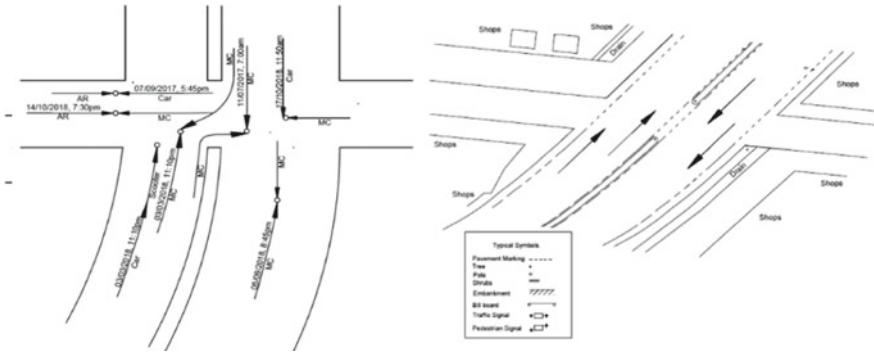
Fig. 3 Collision and condition diagram of Angamaly Bank Junction

Description of Location: The Fig. 3 shown above are the collision and condition diagrams. A huge number of accidents are observed in this location due to the high travel speeds and due to the carriageway being undivided.

4.1.4 Karukutty Accident

Accident Location: Karukutty
Name of Road: NH544, Salem-Kochi Highway
Date of Accident: 29–01-2020
Time: 12:00 am
Vehicles Involved: Lorry x Crane
IPC Section: 279, 337
Type of Crash: Minor
Type of Collision: Side-swipe
Description of Location: The collision and condition diagrams are given in Fig. 4. From the collision diagram it can be observed that the number of accidents are very high due to the high travel speeds of vehicles on the highway (Fig. 5).
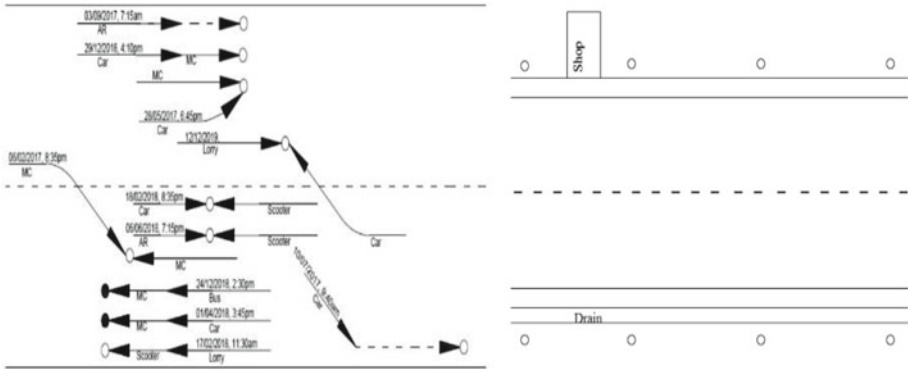
Fig. 4 Collision and condition diagram of Nayathode
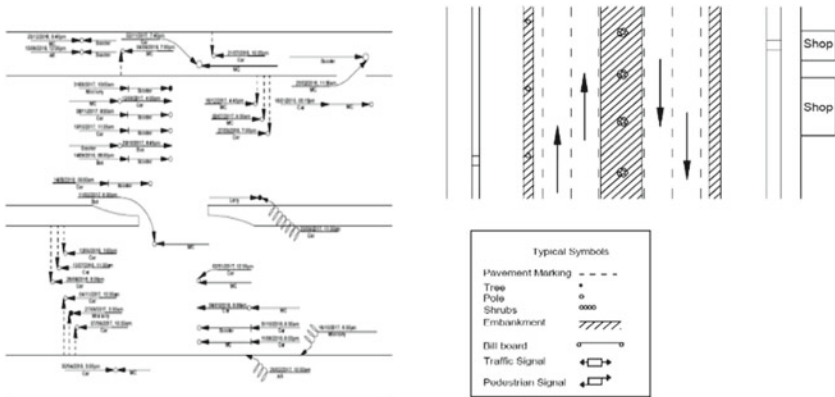
Fig. 5 Collision and condition diagram of Karukutty

5 Crash Scene Investigation

5.1 Introduction

Accident prediction models (APMs) are extremely important tools for estimating the expected number of accidents on entities such as intersections and street segments. These estimates are generally used in the identification of sites for possible safety treatment and their evaluation. An APM is, principally, a mathematical equation that expresses the average accident frequency of a site as a function of several explanatory variables. Models can be of different kinds like Multiple Linear Regression, Poisson Regression, Negative Binomial Models, Random Parameter Model, Logit Models, Probit Models etc. Our objective was to develop prediction models using suitable regression technique. As we attempted to predict the number of accidents, the negative binomial model cannot be used as the first assumption of this model is that the dependent variable (the variable that we are predicting) should be measured on a dichotomous scale. Examples of dichotomous variables include gender (two groups: "males" and "females"), presence of heart disease (two groups: "yes" and "no"), personality type (two groups: "introversion" or "extroversion"), body composition (two groups: "obese" or "not obese"), and so forth. However, if the dependent variable is not measured on a dichotomous scale, but a continuous scale instead, multiple regression and Poisson regression models are preferred. In order to carry out Poisson regression, the mean and variance must be equal and the value of the dependent variable should be less than 10. Since the data collected did not satisfy both of these conditions, Poisson regression could not be carried out and hence, multiple regression technique was adopted for developing the APM.

5.2 Multiple Linear Regression

Early models of traffic accident models were based on the simple multiple linear regression approach assuming normally distributed errors. The general form of the linear crash pr β_i ediction model can be expressed as follows:

$$Y\,|\Theta \sim Dist(\Theta)\,with\,\Theta\,=\,f(X, \beta, \varepsilon) \qquad (2)$$

where,

Y: the dependent variable (i.e. crash frequency),
θ: the crash dataset,
Dist(θ): the model distribution,
X: a vector representing different independent variables (i.e. risk factors),
β: a vector of regression coefficients,
f(.): link function that relates X and Y together,
ε: the disturbance or error terms of the model.

In this approach, modelling is carried between a scalar dependent variable Y and one or more explanatory variables (or independent variable) denoted as X.

$$Y = \beta 0 + \sum \beta_i X_i + e \tag{3}$$

where, X_i is explanatory variables and β_i is regression coefficients of the respective independent variables, β_0 is regression constant and e is the error.

5.3 SPSS Software

SPSS (Statistical Package for Social Sciences) software was used in developing the Regression Models in this study. SPSS is considered one of the most frequently used program for researchers in many fields such as engineering, science, art, education, and psychology.

5.4 Development of APM

In order to develop a multiple linear regression model, the sample size required is at least ten. Hence, the yearly data that was collected was divided into quarters so that the sample size was 20. The aim was to develop a model that predicted the total number of accidents for 2019 relating the accident frequency to their causes. In order to run the analysis, the data must be entered into the SPSS software. Firstly the variables must be entered in the variable view of the software. The selected variables were the total number of accidents and their causes. Since the data is of count nature, it must be inputted as scalar and the time frame is inputted as nominal.

Then, in the data view, the data collected was organised and entered. Once this was complete, a multiple linear regression analysis was run keeping the total number of accidents as the dependent variable and the various causes as the independent variables. Stepwise regression method was selected so that only statistically significant variables entered the regression equation.

5.4.1 Development of APM for Angamaly

The correlations between the dependent variable and the independent variables are found to be positive which implies that if the number of any of the causes increases it will directly affect the total number of accidents. It is also seen that not all the independent variables entered the regression. Only those that were statistically significant entered the equation.

Table 2 Model Summary of Angamaly APM

Model	R	R Square	Adjusted R Square	Std. Error of the Estimate	Durbin-Watson
1	0.807[a]	0.652	0.632	8.596	
2	0.876[b]	0.767	0.740	7.231	
3	0.973[c]	0.947	0.937	3.547	
4	0.993[d]	0.987	0.983	1.852	
5	0.996[e]	0.992	0.989	1.497	
6	0.997[f]	0.994	0.992	1.289	1.738

a. Predictors: (Constant), Carelessness
b. Predictors: (Constant), Carelessness, Overspeed
c. Predictors: (Constant), Carelessness, Overspeed, Rash driving
d. Predictors: (Constant), Carelessness, Overspeed, Rash driving, Violations
e. Predictors: (Constant), Carelessness, Overspeed, Rash driving, Violations, Pavement condition
f. Predictors: (Constant), Carelessness, Overspeed, Rash driving, Violations, Pavement condition, Driver condition
g. Dependent Variable: Total accidents

Table 2 shows the summary of the model. For a model to be valid the R2 value needs to be as close to 1 as possible. The analysis results are based on iterations and checks the goodness of fit of the model by adding the variables one by one. The iterations stop when the R2 value is close to 1, suggesting that the last iteration is the most valid. Since the R2 value of the sixth model is 0.997, that model is chosen as the most appropriate. Using the coefficients obtained, an equation was developed as follows:

$$Y = -3.128 + 1.311X1 + 0.884X2 + 1.151X3 + 1.456X4 + 0.485X5 + 0.935X6 \qquad (4)$$

where,
    Y = Total no. of accidents
    X1 = Careless driving X4 = Violations
    X2 = Over speeding X5 = Pavement condition
    X3 = Rash driving X6 = Driver condition

Table 3 Model Summary for Koratty APM

Model	R	R Square	Adjusted R Square	Std. Error of the Estimate	Durbin-Watson
1	0.802[a]	0.644	0.624	3.203	
2	0.902[b]	0.814	0.792	2.383	
3	0.943[c]	0.890	0.869	1.888	
4	0.965[d]	0.931	0.912	1.546	
5	0.982[e]	0.965	0.952	1.142	
6	0.988[f]	0.976	0.965	0.975	2.277

a. Predictors: (Constant), Carelessness
b. Predictors: (Constant), Carelessness, Rash Driving
c. Predictors: (Constant), Carelessness, Rash Driving, Overspeed
d. Predictors: (Constant), Carelessness, Rash Driving, Overspeed, Violations
e. Predictors: (Constant), Carelessness, Rash Driving, Overspeed, Violations, Vehicle Defect
f. Predictors: (Constant), Carelessness, Rash Driving, Overspeed, Violations, Vehicle Defect, Pavement Condition
g. Dependent Variable: Total Accidents

5.4.2 Development of APM for Koratty.

The correlations are similar to that of the model developed for Angamaly i.e., all positive correlations. From model summary (Table 3), the R2 is closest to 1 for the last model and hence that is chosen as the model for Koratty police station jurisdiction. Using the coefficients obtained, an equation was developed as follows:

$$Y = -0.09 + 1.087X1 + 0.888X2 + 1.022X3 + 1.173X4 + 1.179X5 + 0.795X6 \quad (5)$$

Where,
　　Y = Total no. of accidents
　　$X1$ = Careless driving $X4$ = Violations
　　$X2$ = Rash driving $X5$ = Vehicle defect
　　$X3$ = Over speeding $X6$ = Pavement condition

6 Results and Discussions

6.1 Summary of Collected Data

From the accident data collected, the trend of road accidents was deeply analysed. After analysis it was found that, even though the number of accidents decreased in the first few years, it increased again in the subsequent years. Most of these accidents were major. Two wheelers contributed a huge share in the number of accidents in

Table 4 Trend of road accidents during lockdown (State Crime Records Bureau, Kerala)

Period of Lockdown: 25–03-2020 to 03–05-2020			Corresponding period in 2019		
No. of Accidents	No. of Fatalities	No. of Injuries	No. of Accidents	No. of Fatalities	No. of Injuries
483	64	482	4437	565	5005

both the jurisdictions. Vehicle to vehicle collisions are more frequent and among them rear end collisions and side swipes are common. This is followed by vehicle to pedestrian collisions. Most of the accidents are caused due to driver's faults, some due to violation of traffic rules and others due to vehicle defects and various other reasons. January recorded the most number of accidents and December recorded minimum number of accidents. It was also found that time plays a major role in the frequency of road accidents, i.e., peak hours recorded most number of accidents owing to the high traffic during those hours.

With the increase in population, number of automobiles and modes of transport have also increased. The entire world was affected during the outbreak of Corona Virus (Covid-19) which broke out during December 2019 by posing a major threat to human beings. People were forced to stay at homes and not travel much, except for important needs and emergencies, in order to contain the pandemic. The impact of this lockdown not only affected the lives of human beings but also the environment. Studies revealed that due to less traffic on roads the pollution levels came down alarmingly. It also brought down the number of road accidents and fatalities. The data corresponding to accident statistics in Kerala during this lockdown period has been given below in Table 4. Number of accidents found a decrease of about 89% and the number of fatalities reduced by 88.7% during this lockdown phase.

6.2 Results of Crash Scene Investigation

The collision diagrams of the different locations also gave the pattern of road accidents that occurred within a two year period and the condition diagrams gave an information about the exact location of accident. Using these information, certain short term remedial measures /solutions proposed for the crash investigated sites of Pongam, Angamly Bank Junction, Nayathode and Karukkuty have been suggested in Table 5.

Based on the current road condition, countermeasures /remedial measures for improving the safety performance like sign boards, caution boards, warning boards, road marking, etc. can be suggested for Pongam, Nayathode and Karukkutty. Long term improvements like flyover or intersection can be avoided by closing the crossing road in Angamaly Bank Junction.

Table 5 Short Term Remedial Measures/Solutions

Sl. no	Crash site	Cause of accident	Remedial Measures/ Suggested solutions
1	Pongam -1	Careless driving and high speed	• Sign Boards • Caution Boards
2	Angamaly Bank Junction	Lack of indicator and high speed	• Close/Avoid Crossing • Caution Signal
3	Pongam -2	High speed	• Awareness class • Warning Board
4	Nayathode	High speed	• Road marking • Caution Signal
5	Karukkuty	Careless driving	• Caution Signal • Awareness class

6.3 Validation of APM

Validation of APM for Angamaly. The model was validated using the accident data of the year 2019.

$$Y1 = -3.128 + 1.311*28 + 0.884*20 + 1.151*15 + 1.456*2 + 0.485*1 + 0.935*1 = 72.857.$$

$$Y2 = -3.128 + 1.311*26 + 0.884*12 + 1.151*10 + 1.456*4 + 0.485*2 + 0.935*0 = 59.87.$$

$$Y3 = -3.128 + 1.311*22 + 0.884*13 + 1.151*10 + 1.456*0 + 0.485*1 + 0.935*2 = 51.071.$$

$$Y4 = -3.128 + 1.311*24 + 0.884*15 + 1.151*13 + 1.456*2 + 0.485*2 + 0.935*1 = 61.376.$$

$$\therefore Y = Y1 + Y2 + Y3 + Y4 = 72.857 + 59.87 + 51.071 + 61.376 = 245.174.$$

The actual number of accidents that occurred in the year 2019 in the Angamaly police station jurisdiction was 242. The predicted number of accidents is only 1.3% more and therefore the model is valid.

Validation of APM for Koratty. The model was validated using the accident data of the year 2019.

$$Y1 = -0.09 + 1.087*12 + 0.888*3 + 1.022*9 + 1.173*4 + 1.179*1 + 0.795*2 = 32.277.$$

$$Y2 = -0.09 + 1.087*11 + 0.888*9 + 1.022*6 + 1.173*2 + 1.179*1 + 0.795*1 = 30.311.$$

$$Y3 = -0.09 + 1.087*9 + 0.888*6 + 1.022*6 + 1.173*2 + 1.179*1 + 0.795*1 = 25.473.$$

$$Y4 = -0.09 + 1.087*8 + 0.888*10 + 1.022*9 + 1.173*5 + 1.179*1 + 0.795*3 = 36.113.$$

$$\therefore Y = Y1 + Y2 + Y3 + Y4 = 32.277 + 30.311 + 25.473 + 36.113 = 124.174.$$

The actual number of accidents that occurred in the year 2019 in the Koratty police station jurisdiction was 125. The predicted number of accidents is only 0.66% less and therefore the model is valid.

7 Conclusions

The various modes of transport, narrower and overcrowded roads coupled with fast growing population and urbanization has made people vulnerable to frequent road accidents resulting in loss of life and property. Most of the road accidents are mainly caused by the carelessness of drivers and their ignorance and negligence of traffic rules and sometimes also due to errors in design of pavements. The crash scene investigation gave an idea about the main causal factors of road accidents in the selected study areas. The major factor that contributed to most of the accidents that were studied was careless driving. This can only be avoided by providing proper awareness to the drivers about safety on roads. Road safety awareness classes plays a major role in increasing the knowledge on road safety and thus helps to avoid road accidents. The collision and condition diagrams give an outline of the type of collisions that occurred, along with information about the location.

The density of traffic plays a very important role in contributing to road accidents. When the number of vehicles on the roads increase, there is a rise in number of road accidents. This fact has been discussed with an example of lockdown during Covid-19 outbreak. Even so, once traffic resumes, the earlier trends are likely to return and thus tools like APMs, which uses present data, are required to the predict the future trends.

The purpose of the project was to formulate APMs which would predict the expected number of accidents as accurately as possible by identifying the factors affecting safety, with the help of explanatory variables in the models. The multiple linear regression models developed were validated and found to be accurate. The selected model coefficients were significant and thus can be used for the prediction of the number of road accidents in future.

References

1. Wang, D., Liu, Q., Ma, L., Zhang, Y., Cong, H.: Road traffic accident severity analysis: a census-based study in China. J. Safety Res. **70**, 135–147 (2019)
2. Abojaradeh, M.: Development of traffic accident prediction models to improve traffic safety and to reduce traffic accident severity and rate in Jordan. J. Biol. Agric. Healthc. **5**, 2 (2015)
3. Niveditha, V., Ramesh, A., Kumar, M.: Development of models for crash prediction and collision estimation- a case study for Hyderabad City. Int. J. Trans. Eng. **3**, 2 (2016)
4. Greibe, P.: Accident prediction models for urban roads. Accid. Anal. Prev. **35**, 273–285 (2003)
5. Ackaah, W., Salifu, M.: Crash prediction model for two-lane rural highways in the Ashanti region of Ghana. IATSS Res. **35**, 34–40 (2011)

6. Dhamaniya, A.: Development of accident prediction model under mixed traffic conditions: a case study. In: Third International Conference on Urban Public Transportation Systems, Urban Public Transportation Systems (2013)
7. Peters, G.A., Peters, B.J.: Automotive Vehicle Safety. Taylor and Francis, London (2003)
8. Mathew, T. V.: Accident studies. In: Transportation Systems Engineering (2014)
9. The global status report 2018. World Health Organisation (2018)
10. Highway Safety Manual, 1st Edition. American Association of State Highway and Transportation Officials, Washington (2010)
11. Road Accidents in India, Ministry of Road Transport and Highways Transport Research Wing, New Delhi (2018)

Landslide Hazard Zonation of Peerumedu Taluk Using ArcGIS

C. T. Ahammed Thanveer, Hidash Mohammed, Althaf Ibrahim Puthuvathara, P. M. Dilruba, and T. R. Rajalakshmi

Abstract Landslides are the instant event of mass movement of the earth's surface down a slope, causing loss of life and property. Neotectonic movements, earthquakes, high precipitation, and those triggered by land-use changes such as tree felling, agriculture, mining, and road cutting in hilly terrain are the most common causes. Landslide hazard zonation mapping is a critical phase in the planning, managing, and mitigating landslides.

This paper uses a multi-criteria analysis technique for landslide hazard zonation mapping for Peerumedu Taluk of Idukki district of Kerala. The methodology incorporates factors in seven thematic layers such as slope, drainage density, geomorphology, soil, geology, lineament density and land use/land cover into a GIS platform. The land hazard zonation was done using a weighted rating system based on the relative importance of numerous causative elements gathered from remotely sensed data and other thematic maps. This technique produces a hazard zonation map that divides the area into relative hazard classes, with high hazard zones corresponding to high landslide frequency. The landslide hazard zonation map was then validated using the landslide incidence spots based on field investigation and Kerala's natural hazard zonation map, prepared by the Kerala Disaster Management Authority. The landslide hazard zonation map is utilized for prevention, correct infrastructure planning, and regional environmental development.

Keywords ArcGIS · Landslide · Landslide Hazard Zonation

1 Introduction

Landslides are natural disasters that can significantly lose lives and property. It is defined as the downward movement of a pile of rock, rubble, or a slope under gravity's effect. Due to human intervention, landslides have become a real concern. Deforestation, mining, landfilling, and other non-scientific development activities have led to

C. T. A. Thanveer (✉) · H. Mohammed · A. I. Puthuvathara · P. M. Dilruba · T. R. Rajalakshmi
Federal Institute of Science and Technology (FISAT), Hormis Nagar, Mookkannoor, Angamaly,
Kerala 683577, India
e-mail: thanveerahammad@gmail.com

an increase in the size and frequency of landslides. In addition, the inherent structure and composition of some places predispose them to landslides. The evolution of increased landslide hazards has drawn the attention of geologists, engineers, local people, and all levels of government in many countries. Susceptibility assessment of probability mapping has traditionally been challenging and time-consuming due to the time and effort necessary for human data management and processing. GIS has recently become an essential tool for assessing avalanche danger.

Kerala experiences extreme rainfall every year; this results in flooding and landslide hazards leading to deaths and severe destruction of property. Floods and landslides have caused extensive damage to houses, roads, railways, bridges, power supplies, communications networks, and other infrastructure; washed away crops and livestock and affected the lives and livelihoods of millions of people in the state. Kerala experienced its worst-ever floods since 1924, between June 1 and August 18, 2018. During this period, the state received more than 2428.9 mm of rain which was 42% more than the normal average. The torrential rains triggered several landslides. Idukki, the worst-hit district, was affected by 143 landslides. The magnitude of the floods and landslides has underscored the need for research and knowledge generation activities. The current work demonstrates how to construct a landslide hazard zonation map for Peerumedu Taluk of Idukki district in Kerala, India, using a weighted overlay analysis method based on Remote Sensing and GIS techniques. Peerumedu Taluk is prone to landslides and has been devastated by landslides in the past. The findings of this study can assist residents, planners, and engineers in preventing and mitigating damages caused by existing and future landslides.

1.1 Study Area

In recent years, landslides of disastrous nature have been common in the hill ranges of the Idukki district. The present study area, Peerumedu Taluk of Idukki district, Kerala, is located at 9.55°0'0" N latitudes and 77.03°0'0" E longitude. It covers a total area of 1280 km^2 with slopes ranging up to 77.978°; drainage density varies from 0.489–6.289 km/km^2, and lineament density from 0.087–0.968 km^2. The soil nature varies from clay, loam, gravelly loam and gravelly clay soils. The geomorphological features of the study area include water bodies, denudational structural hills, piedmont zone rock exposures, pediplain, denudational hills and flood plain. The land cover includes agricultural plantation, barren rocky, forest, fallow land, grassland, industrial area, water bodies, mining, rural and scrub. The rock types found include acidic, basic, migmatite complex, khondalites, charnockites and pegmatite rocks. The study area map is shown in Fig. 1.
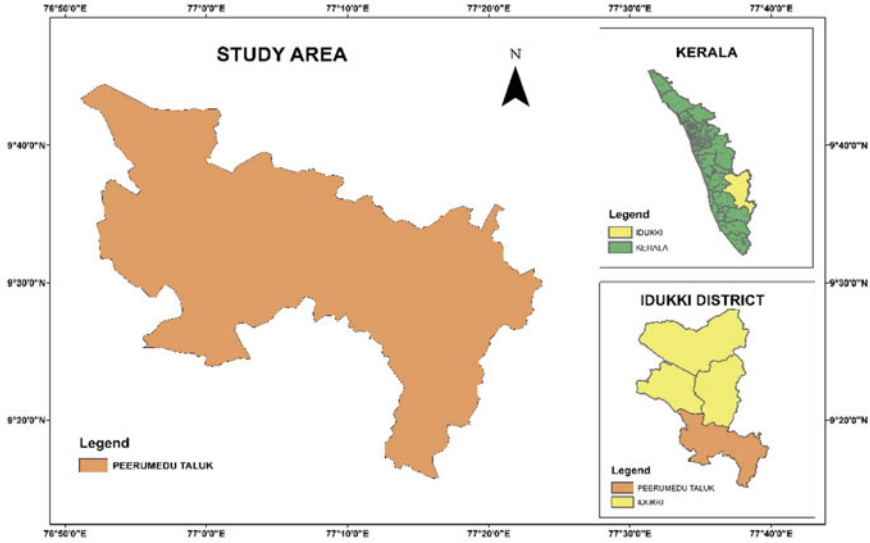
Fig. 1 Study area

2 Methodology

The Kerala State Remote Sensing and Environment Center in Thiruvananthapuram provided thematic maps for geology, soil type, geomorphology, land use/land cover, lineament, and density map for the region. Thematic maps were made by digitizing them using the polygon to raster tool in ArcGIS 10.3. The Natural breaks (Jenks) approach reclassified the thematic map layers. The slope map was created using DEM data obtained from opentopography.org. The line density tool in ArcGIS 10.3 was used to create the drainage density map and the lineament density map. The weightage for each influencing element was supplied using Multi-Criteria Analysis to generate the study area's hazard zonation map. Multi-Criteria Analysis is a method for systematically ranking adaptation choices based on a set of decision criteria. It emphasizes each factor causing landslides, and this method is most widely used as it is easier and faster than other methods. The weightage of the various criteria can be adjusted to reflect their relative importance. The factors were given a distinct rank and weightage depending on their influence on landslide occurrence on a scale of 1–5. Weighted Overlay Analysis is used to create the landslide hazard zonation map. The landslide incidence spots based on field investigation and Kerala's natural hazard zonation map were prepared by the Kerala State Disaster Management Authority to validate the LHZ map. The methodology flowchart is shown in Fig 2.
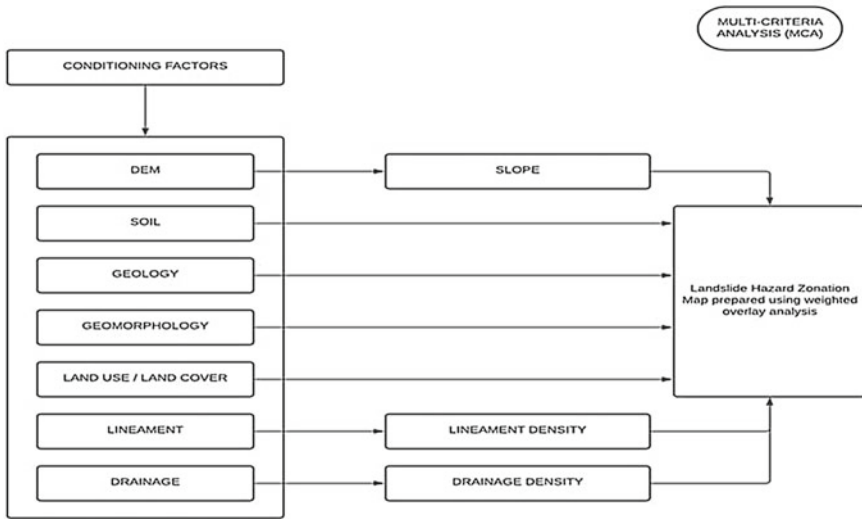
Fig. 2 Methodology flow chart

3 Results and Discussion

3.1 Slope

A slope is the most crucial natural component that triggers landslides. The landslide probability is directly related to this component, given as a percentage or degree. Since the slope angle increases the shear stress of the soil, it increases the possibility of a landslide. Many elements influence the stability of a slope phase, including slope angle, slope form, slope length, soil, and moisture content. As the slope value rises, the likelihood of a landslide also increases. Nevertheless, even a mild slope might be prone to landslides due to the influence of other factors. The slope of this study area is grouped into five classes 0–8.68, 8.868–15.901, 15.901–22.934, 22.934–30.885, and 30.885–77.978°. The DEM data collected is shown in Fig. 3. The slope map is shown in Fig. 4.
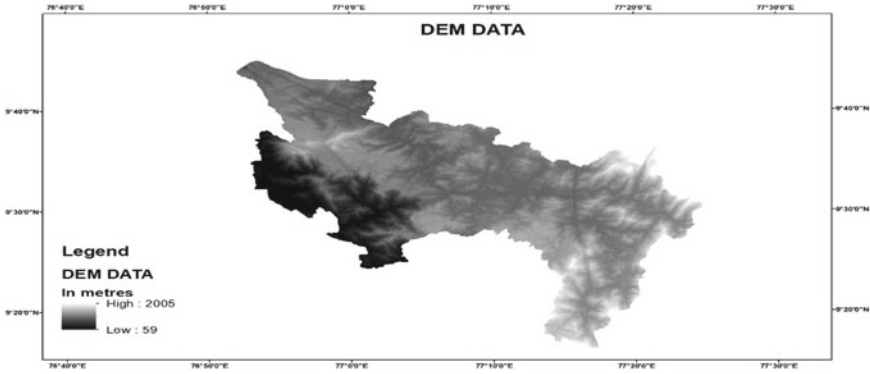
Fig. 3 DEM data
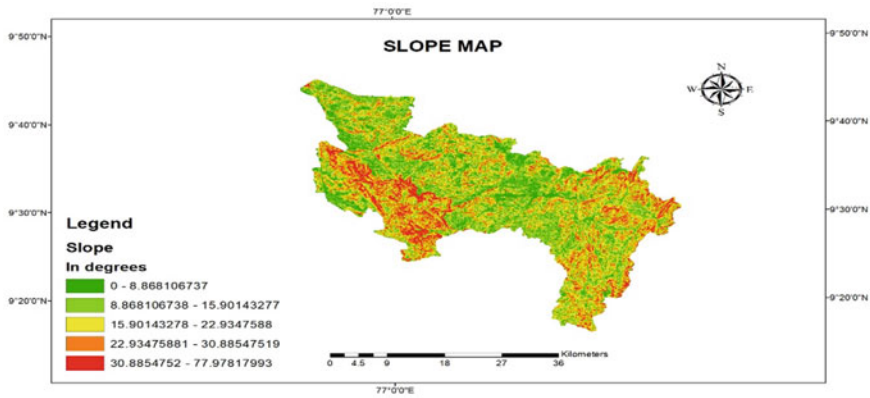
Fig. 4 Slope map

3.2 Drainage Density

Drainage density is a metric that measures stratum perviousness, rainfall, vegetation, and stream incision. The density of the drainage system has a considerable impact on the occurrence of landslides. Hydrological elements such as streams or rivers might compromise slope stability. Slope stability can be harmed by stream erosion and undercutting at the foot of slopes. As a result, slopes are more susceptible to landslides during periods of excessive rainfall, or they may cause catastrophic failure along joints, bedding, and exfoliation plains [1]. This area's drainage density is divided into five categories: 0.489–2.357, 2.357–3.177, 3.177–3.815, 3.815–4.499, 4.499–6.298, and 4.499–6.298 km/km^2. Figure 5 depicts the drainage density map.
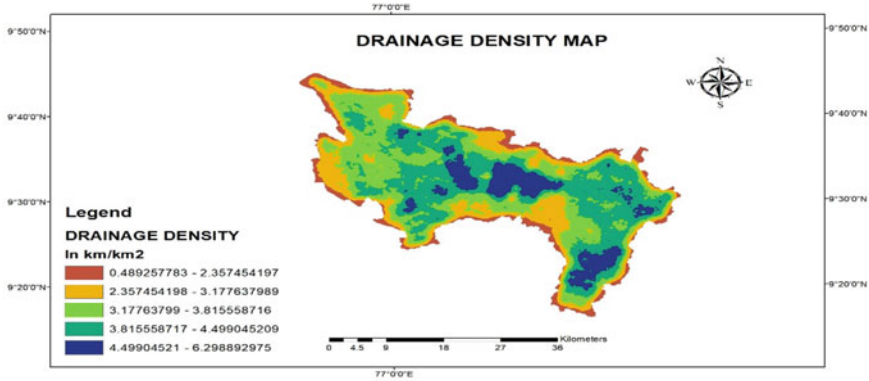
Fig. 5 Drainage density map

3.3 Geomorphology

Geomorphology is the study of the earth's surface characteristics, including interpretive descriptions of landforms, their origin, development, and the nature and mechanism of geomorphological processes that evolve landforms. The main geomorphological features of the study area include structured origin-moderately dissected hills and valleys, structural origin-highly dissected hills and valleys, denudational origin-highly dissected hills and valleys, and anthropogenic origin [2, 3]. Surface features of denudational origin are more prone to landslides than structural origin. Waterbody, Denundational structural hills, Piedmont zone, Rock exposure, Pedi plain, Denundational hills, and Flood plain are the different classifications. Figure 6 depicts a theme geomorphology map.
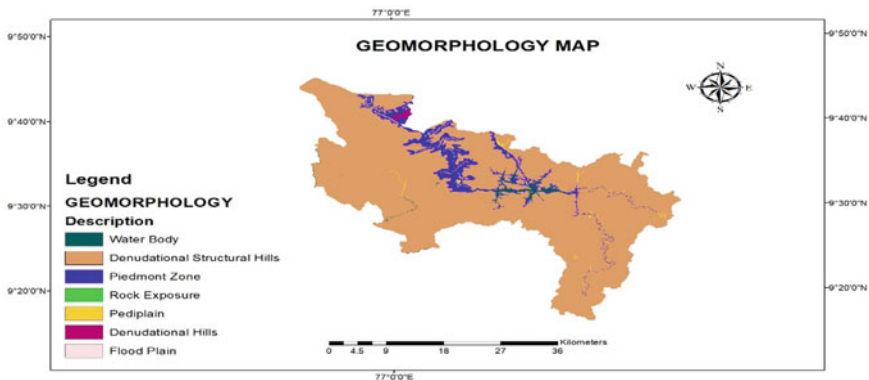
Fig. 6 Geomorphology map
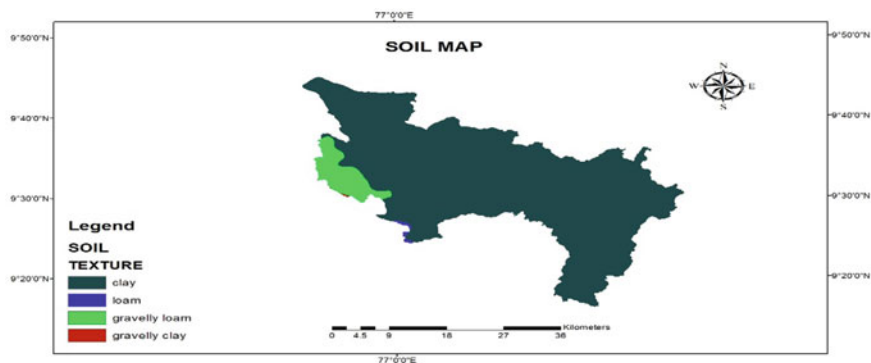
Fig. 7 Soil map

3.4 Soil

The soil map could be a map or a geographical drawing displaying various soil types and features within the research area. The soil qualities in a given area significantly impact landslide occurrence. Sandy soil creates a place vulnerable to landslides because it reacts quickly to rainfall, causing it to slip. The soil column thickness is extremely sensitive and vital. The soil column's shear strength due to downward gravity pull is critical, and the shear strength of the soil is reduced by increased infiltrated pore water pressure. The buildup of water at depths due to soil permeability and percolating rains increases pore water pressure [1]. Clay, loam, gravelly loam, and gravelly clay are the distinct types of soil found in the research region. These soil types were evaluated and ranked according to their impact on landslides. Figure 7 depicts the thematic soil map.

3.5 Geology

Landslides are influenced by lithology in a variety of ways. Landslides are most common in loose and inadequately cemented slopes above the bedrock. A weak and inept rock is more likely to tumble than one that is robust and skilled. Rocks are often more stable than unconsolidated materials [4]. Several factors influence the inherent strength of rock, including the rock's genetic type, the existence and nature of discontinuities such as joints or other cracks, and the level of weathering. The greater the number of discontinuities in a rock type, the greater the risk of rock instability. Igneous and metamorphic rocks are often rigid and large, increasing erosion resistance. On the other hand, Sedimentary rocks are prone to erosion and cause instability. Acidic, basic, Migmatite complex, Khondalites, Charnockites, and Pegmatite are the rock types found in this study region. Figure 6 depicts the geology
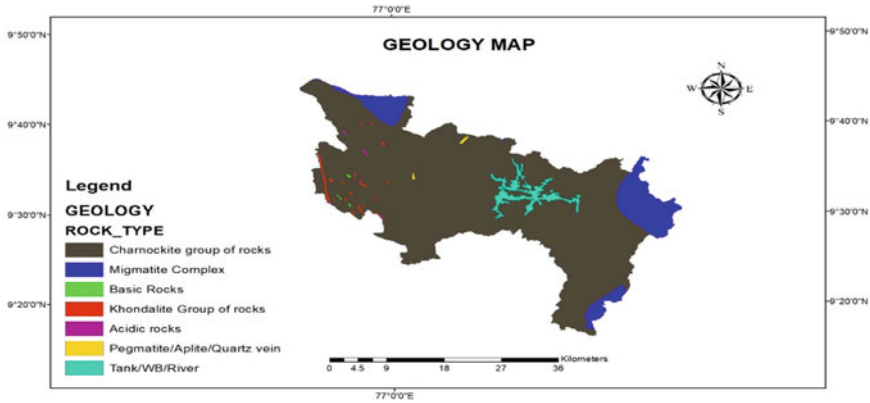
Fig. 8 Geology map

map. Because of their weathering qualities, the khondalite groups are particularly prone to landslides. Figure 8 depicts a thematic geology map.

3.6 Lineament Density

Landslides are likely in areas with high lineament density. Lineament zones are areas of relative crustal movement that are tectonically active. Water pours through the fractures, forcing the ground to slip down this lineament, generating a landslide. As a result, landslides can occur when fault or shear movements are released, especially in high-slope sites with solidified materials [5]. Faults, fractures, and joints destabilize the area by deteriorating the rock's strength and hastening the weathering process. This area's lineament density is divided into five categories: 0–0.087, 0.087–0.235, 0.235–0.387, 0.387–0.588, 0.588–0.968, and 0.588–0.968 km/km^2. Figure 9 depicts the lineament density map.

3.7 Land Use/Landcover

Land cover is another critical component that contributes to the occurrence of landslides. Deforestation, improper agriculture techniques, urbanization, and land reclamation, among other things, all have an impact on landslides. Due to increased erosion, sparsely vegetated areas are more prone to landslides than densely vegetated areas. The amount of water that penetrates geomorphologically unstable slopes with loose soil and weak rocks determines the possibility of a landslide [6, 7]. The excess soil erosion can be avoided if adequate slope management strategies are implemented in land use patterns. The use of land has a considerable impact on slope behaviour.
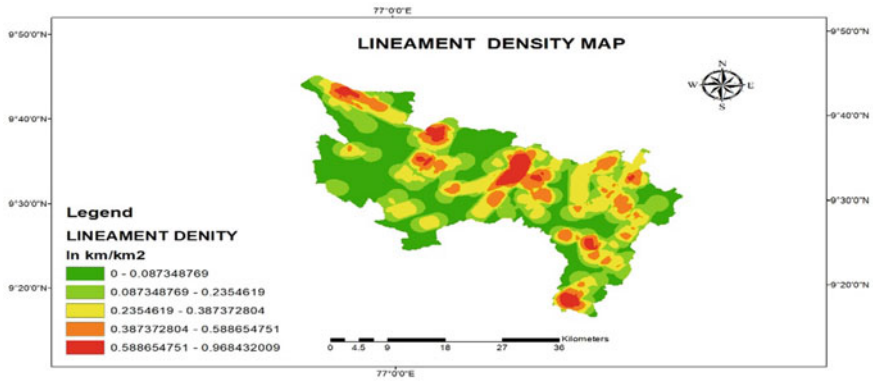
Fig. 9 Lineament density map

During the rainy season, land use and agriculture patterns substantially affect the rate of surface water infiltration. When the topsoil is loosened during cultivation, the rate of water infiltration increases. The amount of water penetrating geomorphologically unstable slopes with loose soils and rocks determines the likelihood of a landslide. Agriculture plantation, barren rocky, forest, fallow land, grassland, industrial area, waterbody, mining/quarry area, rural, and scrub are the land use/land cover types. Mining, barren rocky, and agricultural regions are more prone to landslides in the research area. Figure 10 depicts the land use/land cover map.
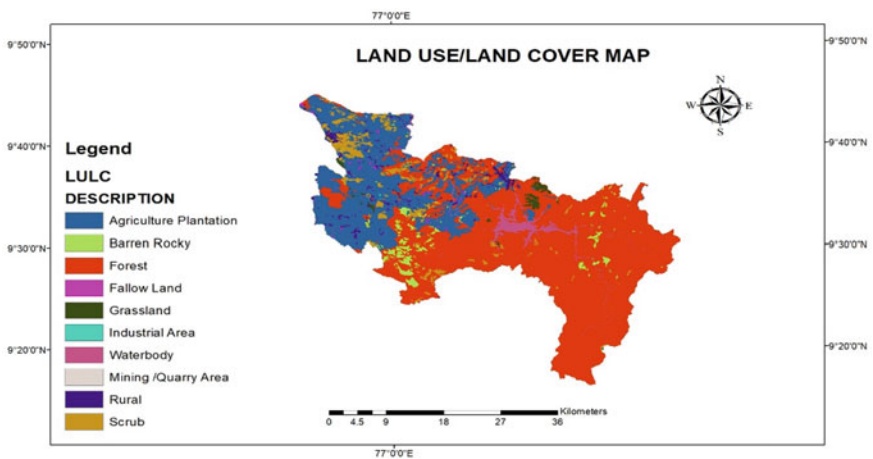
Fig. 10 Land use/Land cover map
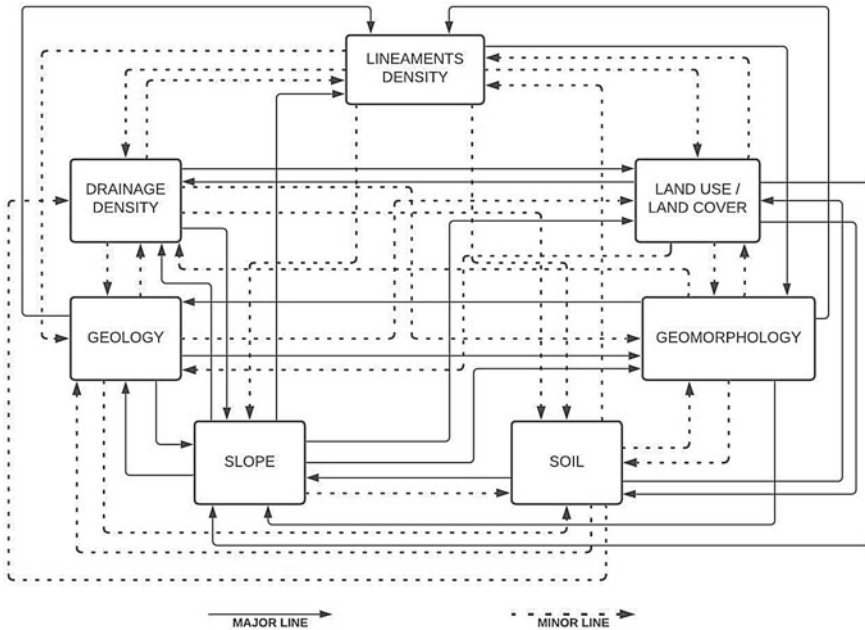
Fig. 11 Inter-relationship of multi-influencing factors

3.8 Multi-criteria Analysis

"Multi-criteria analysis establishes preferences between options by referencing an explicit set of objectives identified by the decision-making body. It has established measurable criteria to assess the objectives extent to achieved objectives" [8]. MCA is a method for systematically ranking adaptation choices based on a set of decision criteria. MCA emphasizes each factor causing landslides, and this method is most widely used as it is easier and faster than other methods. The weightage of the various criteria can be adjusted to reflect their relative importance. The weighted sum of the various standards is employed to rank the possibilities. The different factors were given weights using the multi-influencing factor technique. The interdependency of the different factors is shown in Fig. 11. The factors having a major impact on the other were indicated using straight lines, and the ones having minor impact were highlighted with dotted lines. The major impact was given weightage of 1.0, and the minor impact was given a weightage of 0.5. For example, drainage density has a major effect on a slope. The presence of hydrological elements such as streams or rivers might compromise slope stability. Slope stability can be harmed by stream erosion and undercutting at the foot of slopes [1]. So, their inter-relationship was weighed as 1. On the other hand, lineament density and drainage density have no direct impact. So their inter-relationship was ranked 0. The same method was carried

Table 1 Weightage using MCA

Factors	Major effect (A)	Minor effect (B)	A + B	Percentage (%)
Slope	1 + 1 + 1 + 1 + 1	0.5	5.5	18
Soil	1 + 1 + 1	0.5 + 0.5 + 0.5	4.5	15
Geology	1 + 1 + 1	0.5 + 0.5 + 0.5	4.5	14
Geomorphology	1 + 1 + 1	0.5 + 0.5 + 0.5	4.5	14
Land use/Land Cover	1 + 1	0.5 + 0.5 + 0.5 + 0.5	4	14
Drainage Density	1 + 1	0.5 + 0.5 + 0.5 + 0.5	4	13
Lineament Density	1	0.5 + 0.5 + 0.5 + 0.5 + 0.5	3.5	12
		Total	30.5	100

out to determine the factor with the highest effect in causing a landslide, as shown in Table 1. The equation determined the proposed score for each influencing factor,

$$\% = \frac{(A + B) * 100}{\sum_a^b (A + B)}$$

where A denotes a major interrelationship between two components and B represents a minor interrelationship. A higher weightage number indicates a more significant impact, whereas a lower weightage value suggests a more negligible effect in generating landslides [9]. Slope received the highest weighting (18 points), followed by soil (15 points), geology, geomorphology, LULC (14 points), drainage density (13 points), and lineament density (12 points). Weighted overlay analysis in ArcGIS was used to calculate the integration of these elements and their potential weights.

Table 2 shows how the concerned score for each influencing component is divided and assigned to each reclassified factor based on their potential to trigger landslides. Slope has been classified into 5 categories as 0–8.868, 8.868–15.901, 15.901–22.934, 22.934–30.885 and 30.885–77.978°. Since the slope angle increases the shear stress of the soil, it increases the likelihood of a landslide. Since the likelihood of landslide increases as the slope value increases, the slope with the steepest angle (30.885–77.978°) is assigned an influence rank of 5, indicating that it is more susceptible to landslide occurrence on a scale of 1 to 5. Drainage density has been classified into 5 categories as 0.489–2.357, 2.357–3.177, 3.177–3.815, 3.815–4.499 and 4.499–6.298 km/km². Slope stability can be affected by proximity to hydrological features such as streams or rivers. Higher drainage densities indicate a higher probability of landslide. Geomorphology has been classified into seven categories: Waterbody, Denudational structural hills, Piedmont zone, Rock exposure, Pedi plain, Denundational hills, and Flood plain. Surface features of denudational origin are more prone to landslides than structural origin. Soil has been classified into clay, loam, gravelly loam, and gravelly clay. It has been seen that landslides are more

Table 2 Ranking of the influence factor

Sl no.	Factor	Class	Rank	Percentage influence
1	Slope (in degrees)	0–8.868	1	18
		8.868–15.901	2	
		15.901–22.934	3	
		22.934–30.885	4	
		30.885–77.978	5	
2	Drainage Density (in km/km2)	0.489–2.357	1	13
		2.357–3.177	2	
		3.177–3.815	3	
		3.815–4.499	4	
		4.499–6.298	5	
3	Geomorphology	Water Body	1	14
		Denudational Structural Hills	3	
		Piedmont Zone	2	
		Rock Exposure	3	
		Pedi plain	1	
		Denudational Hills	4	
		Flood Plain	1	
4	Soil	Clay	5	14
		Loam	2	
		Gravelly Loam	3	
		Gravelly Clay	4	
5	Geology	Charnockite Group	4	15
		Migmatite Complex	3	
		Basic Rocks	2	
		Khondalite Group	5	
		Acidic Rocks	1	
		Pegmatite/Aplite/Quartz Vein	1	
		Tank/WB/River	1	
6	Lineament Density (in km/km2)	0–0.087	1	12
		0.087–0.235	2	
		0.235–0.387	3	
		0.387–0.588	4	
		0.588–0.968	5	
7	Land Use/Land Cover	Agriculture Plantation	4	14
		Barren Rocky	4	

Table 2 (continued)

Sl no.	Factor	Class	Rank	Percentage influence
		Forest	1	
		Fallow Land	4	
		Grassland	1	
		Industrial Area	2	
		Waterbodies	1	
		Mining and Quarry	5	
		Rural	1	
		Scrub	1	

prone to occur in clayey soil. Geology has been classified into seven categories: Charnockite group, Migmatite complex, Basic rocks, Khondalite group, Acidic rocks, pegmatite/aplite/quartz vein, and tank/WB/river. Rocks are often more stable than unconsolidated materials. Because of their weathering qualities, the khondalite groups are particularly prone to landslides. Igneous and metamorphic rocks are often hard and large, increasing erosion resistance. On the other hand, Sedimentary rocks are prone to erosion and cause instability. Lineament density has been classified into 5 categories as 0–0.087, 0.087–0.235, 0.235–0.387, 0.387–0.588 and 0.588–0.968 km/km^2. Landslides are likely in areas with high lineament density. Land use/Land cover has been classified into agriculture plantation, barren rocky, forest, fallow land, grassland, industrial area, water bodies, mining, quarry, rural, and scrub. Due to higher erosion, places with sparse vegetation are more prone to landslides than areas with thick vegetation.

3.9 Landslide Hazard Zonation Map

The study area's landslide hazard zonation map is created by considering seven key factors: slope, soil, geology, drainage density, land use/land cover, geomorphology, and lineament density. The weights were assigned to each factor based on Multi-Criteria Analysis. The landslide hazard zonation map is prepared using weighted overlay analysis in ArcGIS 10.3. The map's area is divided into three different vulnerability zones: low, moderate, and high. The incidence spots were overlaid on the landslide-prone zones to validate the results. Eight landslide incidents were recorded in the research region during the field survey. Most of the eight landslide incidence points are spatially distributed throughout the high and moderately susceptible zones. Table 3 shows the area and percentage of landslide-prone zones that have been calculated. The research region comprises 12.95% (1040.63 km^2) of high vulnerable zones. In places with high slopes and elevations, landslides are more common due to the terrain's direct relationship with stability. Due to the erosional

Table 3 Landslide susceptibility area

Susceptibility class	Area (km^2)	Area percentage (%)
Low	71.00	5.56
Moderate	1040.63	81.49
High	165.34	12.95
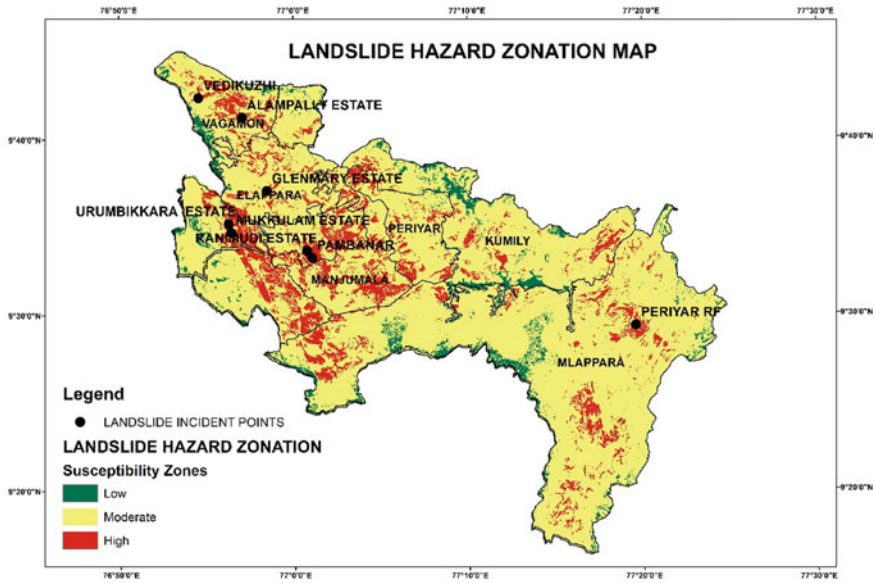
Fig. 12 Landslide hazard zonation map

actions of streams, regions with high drainage density are more prone to landslides. Built-up areas have seen the most slope failures, followed by agricultural terrain. Figure 12 depicts the LSZ map.

4 Conclusion

Landslide susceptibility analysis identifies the main factors affecting landslides, and the landslide hazard zonation map of Peerumedu Taluk was developed using Multi-criteria analysis. The study region has been classified into three landslide-prone zones, ranging from "low" to "high". The high susceptible zones constitute 12.95% (165.34 sq. km) of the study area. Landslides are likely in areas with higher slopes and elevations due to their direct relationship to terrain stability. According to this study, the north and north-western portions of Peerumedu Taluk are more prone to landslides. The provided landslide hazard zonation map was validated using the Kerala

State Disaster Management Authority's landslide hazard zonation map. Planners and developers may find the provided landslide hazard zonation map helpful in selecting good sites for future developments and land use planning and locating constructions in unsafe zones. The highly susceptible areas identified can be carried out with slope stability analysis. Slopes having stability issues could be dealt with appropriate landslide mitigation measures like anchors, soil nails and anti-slide piles to strengthen and stabilize the slope. It could be helpful to local authorities in guaranteeing the safety of residents in affected areas.

References

1. Ajin, R.S., Loghin, A., Vinod, P.G., Jacob, M.K., Krishnamurthy, R.R.: Landslide susceptible zone mapping using ARS and GIS techniques in selected taluks of Kottayam district, Kerala, India. Int. J. Appl. Remote Sens. GIS **3**(1), 16–25 (2016)
2. Kailas, A., Shajan, G., Joy, S., George, G.K.: Landslide hazard zonation (LHZ) Mapping of Attappady, Kerala using GIS. Int. Res. J. Eng. Technol. **05**(03), 3808–3812 (2018)
3. Swetha, T.V., Gopinath, G.: Landslides susceptibility assessment by analytical network process: a case study for Kuttiyadi river basin (Western Ghats, southern India). SN Appl. Sci. **2**(11), 1–12 (2020). https://doi.org/10.1007/s42452-020-03574-5
4. Sreekumar, S., Aslam, A.: Geospatial approach for landslide disaster management: a case study from India. Int. J. Appl. Adv. Sci. Res. Impact **5**(2), 120–127 (2017). www.dvpublication.com
5. Lakshmi, S.V.: M. H. H, A. Final, and C. Engineering, Identification of Landslide Hazard Zonation in Iddiki Using Remote Sensing, vol. 119, no. 17, pp. 3211–3221 (2018)
6. Acharya, T.D., Yang, I.T.: Landslide hazard zonation using GIS: a case study from Sindhupalchowk, Nepal. Int. J. Appl. Eng. Res. **10**(7), 18385–18394 (2015)
7. Khanlari, G.R., Abdi, Y., Babazadeh, R.: Geotechnical Geology, no. January (2014)
8. Bagherzadeh, A., Mansouri Daneshvar, M.R.: Mapping of landslide hazard zonation using GIS at Golestan watershed, northeast of Iran. Arab. J. Geosci. **6**(9), 3377–3388 (2013). https://doi.org/10.1007/s12517-012-0583-9
9. Bera, A., Mukhopadhyay, B.P., Das, D.: Landslide hazard zonation mapping using multi-criteria analysis with the help of GIS techniques: a case study from Eastern Himalayas, Namchi, South Sikkim. Nat. Hazards **96**(2), 935–959 (2019). https://doi.org/10.1007/s11069-019-03580-w

Evaluation of Response Reduction Factor of Bamboo Reinforced Building

Vrutik Patel and **V. R. Panchal**

Abstract When it comes to constructing structures, most seismic design standards take into consideration and anticipate the non-linear response of components to an earthquake's magnitude. The response reduction factor provides a comprehensible perspective that is critical in the design of building structures. Seismic analysis is regarded to be a significant factor in the design of structural elements. In seismic design, the strength and ductility of frame components are primarily determined by the response reduction factor (R). In this study a bamboo reinforced concrete structure is constructed and analysed and then subsequently a non-linear static analysis of the same building was done for the different earthquake zone. It is proposed in this work to evaluate the response reduction factor of a bamboo reinforced concrete structure in various earthquake zones (Z). The findings are generated by using a non-linear static analysis technique known as push-over analysis, which is implemented in software known as E-TABS. Thus, we analysed that bamboo reinforced buildings can be constructed, although with significant limitations. This kind of bamboo reinforced structure may be used in lower-story buildings as well. Non-linear static analysis or pushover analysis also reveals that a response reduction factor's value varies between zones. Basis of the analysis, we determine that the values of the response reduction factor in all zones lies in between 4.0 to around 5.20.

Keywords Response reduction factor · Bamboo reinforced building · Non-linear static analysis · Push-over analysis

V. Patel (✉) · V. R. Panchal
M. S. Patel Department of Civil Engineering, Chandubhai S. Patel Institute of Technology, Charotar University of Science and Technology, Changa, India
e-mail: patelvrutik227@gmail.com

V. R. Panchal
e-mail: Vijaypanchal.cv@charusat.ac.in

V. Patel
Changa, India

1 Introduction

Material selection has been more influenced by cost and ease of manufacture or processing. Industrial materials like OPC and steel are used in every industry and every country. Advanced materials, such as Nylon, Kevlar, new alloy metals were created and imported in regions where regionally manufactured resources are abundant, particularly in developing nations. In light of the educational system's preoccupation on developed countries, there is currently no systematic teaching or research programme addressing traditional and locally accessible materials and technology in developing countries. People and experts utilise manufactured materials because they have trustworthy technical knowledge about them [1].

In tropical and subtropical regions, bamboo has long been used as a building material. It is frequently employed in various types of building, especially rural dwellings. Bamboo is a renewable and adaptable material that is easy to use with basic equipment. As one of the most significant non-timber forest resources, Bamboo items have economic value. In 14.5 million hectares, 1200 species are expected to exist. Asia, Africa, and Latin America produce them. Bamboo is the world's fastest growing tree. It grows 7.5–40 cm each day, including a world record of 1.2 m in 24 h in Japan. Others can't keep up with bamboo's three-fold Bamboo matures in four or five years, following which it may be harvested every second year for up to 120 years in certain species and forever in others. Bamboo produces 40 tonnes or more of biomass per hectare per year in controlled stands. It produces around a quarter of the tropical and subtropical biomass. Used to restore soil ravaged by brick manufacturing in India and abandoned tin mines in Malaysia. A micro-climate for forest regeneration and watershed preservation, it protects the top soil from tropical downpours. Bamboo's tightly matted roots may bind up to six cubic metres of soil, so it's often planted along banks, streams, and other susceptible regions [2].

As a kind of giant grass, bamboo has a large economic and cultural impact in many countries of the world, particularly China and Japan. Aside from being utilised as a food source, a cosmetic, and a fertiliser, it has also been used in the production of pulp, paper, and textiles, as well as in the production of oil, gas, and charcoal. As a result, bamboo is readily available and is still used in several nations. Civil construction materials such as concrete take almost twice as much energy to produce a cubic metre of volume as bamboo. Steel is 50 times more energy-intensive than bamboo. Steel produces two tonnes of CO_2 each tonne. Bamboo, unlike other plants, sucks CO_2 from the air. In several Asian and Latin American countries, bamboo has been utilised for centuries to create bridges, rural homes, and water channels. Despite its high strength-to-weight ratio, bamboo has been mostly used in rural homes because of a lack of construction regulations. As a result, bamboo's utilisation has been limited in contrast to more traditional building materials like concrete, steel, brick, and wood. Bamboo's utilisation will be affected in the near future by research-based knowledge of bamboo's behaviour, the launch of new products (laminated products and fibre composites), and the establishment of testing and structural standards (building codes). Prefabricated constructions may benefit from bamboo's reduced

weight. Reduced handling loads are achieved by using precast beams. The weight of a structure may be reduced by using bamboo instead of steel. A reinforced concrete beam does not need much strength in the area where it is subjected to stress. It is possible that bamboo will play a significant part in the construction industry due to the material's important sustainability qualities including rapid growth, renewable and biodegradable nature, and carbon sequestration.

As a matter of fact, certain bamboo species may have a utilisation rate four times greater than that of wood [3, 4].

A study of bamboo culm anatomy, physical and mechanical features, alternative preservation measures, and fire performance will also be conducted based on the most current research. In addition, structural design requirements and construction laws, as well as bamboo testing, will be covered. According to the Colombian Building Code, NSR-10, the design of elements subjected to bending, axial, and combination forces will be covered in this chapter (AIS, 2010). We'll go through the many ways bamboo members may be connected, as well as the dowel-type connections that can be used. It will also be described how bamboo buildings may be manufactured and built-in certain countries, such as those detailed in the NSR-10 (AIS, 2010) [3].

1.1 Applications of Bamboo

One of the fastest-growing plants on the planet, bamboo. Rhizome-subordinate design allows them to grow at a rate that is many times that of most other plants. They are a long-term, versatile asset that can be used for a variety of purposes. Among the diverse applications of bamboo, housing is one of the most crucial, particularly in light of global private shortages.

Bamboo may be used to make all structural and non-structural components of tiny houses, with the exception of fireplaces and chimneys. However, it is commonly combined with other materials.

As we are all familiar with bamboo as a building material, some of its applications are Bamboo Trusses, Bamboo Roofs Skeleton, Bamboo walling, Bamboo ceiling, Bamboo as Scaffolding, Bamboo Strip as walls, Bamboo Strip as roofing material.

2 Properties of Bamboo

2.1 Tensile Strength

The fibres of bamboo are axial. Several vascular bundles with high tensile strength are seen in the outer zone. These fibres have a tensile strength greater than steel, but they cannot be used to convey that strength. Here, too, shorter tubes outperform wider ones. The silicate skin contains axial parallel elastic fibres with tensile strengths of

up to 400 N/mm^2. Super-strong wood fibres, on the other hand, can endure tension of 50 N/mm^2 [5, 6].

2.2 Compressive Strength

Compressive strength is better in slimmer tubes than in bigger tubes. Due to the little amount of outer skin that is especially resistant to stress in bigger tubes, smaller tubes provide higher material properties. Bamboo textiles are mostly made up of lignin-rich culms, which may cause the fabric to buckle and lose its tensile strength [2].

2.3 Elastic Modulus

As with tension, shear, and bending strength, the aggregation of strong fibres in the tube wall's outer regions is beneficial to the elastic modulus. The elastic modulus indicates the bamboo's quality. Its extreme flexibility makes it a great construction material in earthquake-prone locations [2].

3 Response Reduction Factor (*R*)

In many developing countries, the seismic design regulations of the United States and Europe are used as a guide. When assessing the structure's ability to absorb energy via inelastic behavior, the "Response Reduction" (Modification) Factor," also known as the "Force Reduction Factor," is the single most important quantity. During an earthquake, a huge quantity of horizontal and overturning forces is created, which have a significant impact on the mass of the structure. The real earthquake force is greater than that for which the structure was built, and we cannot build the structure for the actual severity of the earthquake while keeping cost in mind. As a consequence, the factor *'R'* was introduced to IS codes, lowering the base shear and increasing efficiency [7, 8].

"Response reduction factor" is defined in IS 1893 as "the factor by which the actual base shear force that would be generated if the structure remained elastic during its response to the Design Basis earthquake (DBE) shaking is lowered to get the design lateral force." When a structure is in a seismic zone, as mentioned before in this article, a base shear is always greater than the actual structural reaction. As a result, it has a certain degree of reserve strength. Because a structure's maximum lateral strength is always more than its design strength, reserve strength or excess strength develops. As a result, once the structure reaches the inelastic phase, it is capable of absorbing a considerable quantity of seismic energy. As a result, seismic

codes reduce design loads in order to take advantage of the structure's over-strength and ductility. Response Reduction Factor is the name given to this force reduction factor (*R*) [9].

Over-strength, energy absorption, and dissipation, as well as structural ability to transfer stresses from inelastic highly strained areas to less stressed locations in the structure are all taken into account by the Response reduction Factor (*R*). This component is unique and varies depending on the kind of construction and materials utilised. As a result, categorising response modification factors for diverse structural systems is critical in order to perform evaluations based on demand (seismic ground motion) and structure capacity.

According to ATC-19, *R* is made of following components:

- Over strength factor (R_s)
- Ductility factor (R_μ)
- Structural redundancy (R_R)
- Damping factor (R_ξ)

It may be expressed as an equation:

$$R = R_S \times R_\mu \times R_R \times R_\xi \tag{1}$$

3.1 Over Strength Factor (**R**$_s$)

The nonlinear static analysis approach may be used to evaluate the structure's strength. Create the structure's base shear-roof displacement connection by practicing pushover analysis. Calculate the base shear force V_u (i.e., from the curve) in the structure at the limiting roof displacement. The reserve strength of the structure is determined by subtracting the design base shear V_d from the design base shear V_u [7].

Use the following expression to get the strength factor.

$$\underline{R_s} = (V_u/V_d) \tag{2}$$

3.2 Ductility Factor (**R**$_\mu$)

Based on a study of 124 ground motions, Miranda and Bertero (1994) developed a formula for the value of *R,* which is often employed. Alluvium and rock soils were the most common, although there were also a few kinds of exceptionally soft soils.

Table 1 Structural redundancy (Atc-19)

Lines of vertical seismic framing	Draft redundancy factor
2	0.71
3	0.86

It was anticipated that a critical damping of 5% was in place. These are the formulae for calculating the period-dependent force reduction factors R.

$$R\mu = \frac{\mu - 1}{\Phi} + 1 \tag{3}$$

where Φ is determined using formula for rock, alluvium, and soft sites

3.3 Structural Redundancy Factor ($\mathbf{R}_r$)

Frame should be designed and defined to convey seismic-induced inertia to the foundation through several vertical lines of framing, each of which should be built and described. ATC-19 specifies a redundancy factor, which is shown in Table 1

It should also be mentioned that, according to ATC-19, the upwards values are recommended just to show a possible trend, generate discussion among design experts and scholars, and foster research and study activity. These values lack a technical foundation and are not intended for inclusion in seismic regulations or recommendations [7].

3.4 Damping Factor ($\mathbf{R}_\xi$)

The damping factor, R, balances the impact of supplemental viscous damping and is most commonly used in constructions with additional energy dissipation devices. In the absence of such devices, the damping factor is considered to be 1.0. As a result, it is frequently overlooked. As a result, the response reduction factor might primarily consist of two factors: Over Strength Factor (RS) and Ductility Factor ($R\mu$). The graph in Fig. 1 clearly illustrates the connection between R, Rs, and R. Figure 1 shows the concept of R [7].
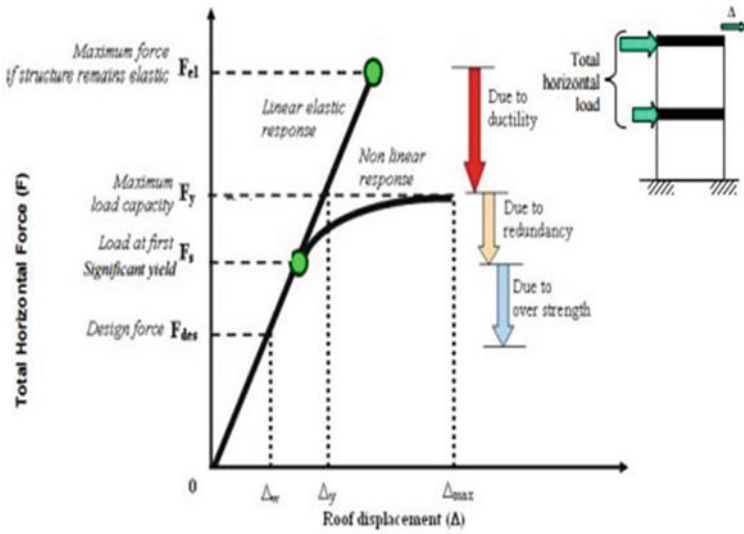
Fig. 1 Concept of *R* [Is 1893 Part-1 (Draft Code)] [10]

4   Non-linear Static Analysis

Pushover analysis is another name for nonlinear static analysis. The earthquake stresses are progressively applied to the structure in this approach, allowing a succession of plastic hinges to form until the structure reaches the collapse mechanism. There are several load patterns for pushover analysis, but the most typical is to apply the lateral force proportionately to the narrative mass.

The pushover analysis is a helpful and effective method for assessing the various performance levels of a structure subjected to lateral loadings. The pushover study is a significant step in addressing the structure's inelastic response and allows us to properly comprehend the structure during strong earthquakes. As a result, we may use this approach to assess the structure's inelastic reaction. It is crucial to remember, however, that the pushover technique is an approximation of deformation needs [7, 8].

5   Fundamental of Non-linear Static Analysis

It is a nonlinear way to studying a structure's seismic performance, in which lateral movement is applied until a required displacement or a collapse mechanism is found, as seen in the figure below. The gravitational loads are maintained constant throughout the study. It is pushed until enough hinges are created and a pushover curve of base shear vs corresponding roof displacement is formed. Based on Pushover

curve calculations, one may determine how much base shear and corresponding horizontal displacement can be sustained. The Pushover curve (ATC-40) and lateral load distribution are shown in Fig. 2 [7].

6 Design and Analysis

In this research, bamboo reinforced buildings were taken into account for several zones of design and analysis. Different seismic zones and their corresponding maximum velocities are anticipated for the structure's design. E-TABS software is used to develop and assess the models. A typical building plan is shown in the diagram below. ETABS software is used to simulate this. ETABS's grid format makes it easier to put together simulations (Fig. 3).

Figure depicts an ETABS model of a typical reinforced concrete three-dimensional building. It has slabs, columns, beams, and footings.
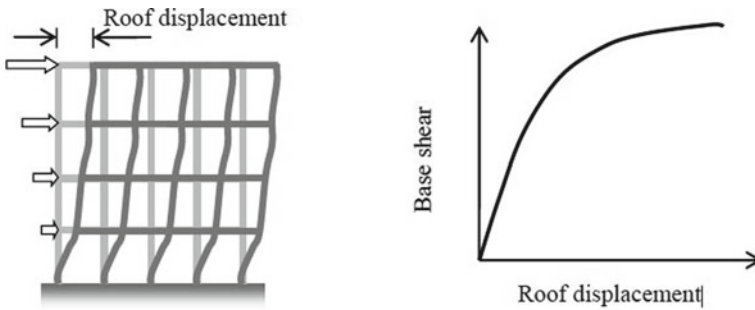
Fig. 2 Lateral load distribution and pushover curve (Atc-40) [7]
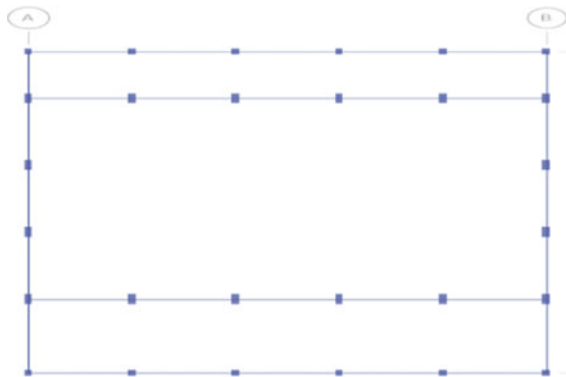
Fig. 3 Plan of bamboo reinforced building

Fig. 4 3D model of bamboo
reinforced building
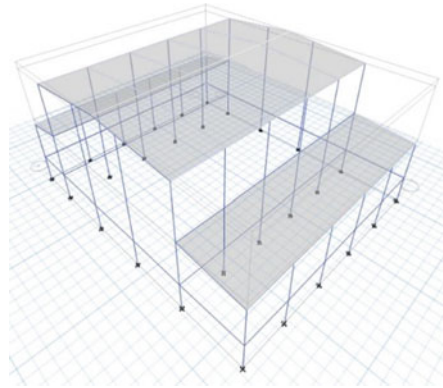
Table 2 Geometry data

	Geometry Details
Height of the building	9.3 m
Height of the floor	1.8, 3.5, 4.0 m

Table 3 Details of material

	Materials
Grade of concrete	M20
Grade of steel	Fe500 & Fe 450

The components are addressed for horizontal loads such as earthquake loads as well as gravity loads. In order to represent the limit state in flexure, the maximum (positive and negative) bending moment is necessary for the most factored loads and rebar area major RCC and Bamboo buildings. Table 2 and 3 indicate model geometry and material description. While Table 4 shows building description (Table 5).

For the building, distinct zones and situations of earthquakes are allocated to it in order to distribute the loads.

6.1 Design Results

6.2 Column Results

Column Size: (750 × 300) MM
Table 6 compares column findings from analysis. Figure 5 shows the comparison column. The findings show that bamboo reinforcement delivers more rebar area than steel bar. But it may also impact the column sizes as the rebar area is close to 4%.

To accommodate the bamboo as a support in certain circumstances, a larger column is required for suitable paving work.

Table 4 Building description

Description	Steel		Bamboo
Material Name	HYSD500	HYSD415	Bamboo bar
Material/type	Rebar	Rebar	Rebar
Weight per Unit Volume (kN/m^3)	76.9729	76.9729	7.5511
Modulus of Elasticity, E (MPa)	200,000	200,000	6500
Coefficient of Thermal Expansion, A (1/°C) & (1/°F)	0.0000117	0.0000117	0.00003607
Minimum Yield Strength, Fy (MPa)	500	415	105
Minimum Tensile Strength, Fu (MPa)	545	485	370
Expected Yield Strength, Fye (MPa)	550	456.5	105
Expected Tensile Strength, Fue (MPa)	599.5	533.5	370

Table 5 Types of loads

Types of loads	Elements	Loads (kN/m^3)
Dead load	RCC	25
Dead load	Brick masonry	19
Dead load	Floor finish	1.5
Dead load	Wall load	12
Live load	Single story building	2.5

Table 6 Results of column

Description	Bamboo	RCC
Design load (Pu)	523.9509 KN	524.7725
Design moment (Mu)	40.1455 KN-m	61.215
Rebar area (mm^2)	8440	2602
Rebar (%)	3.75	1.16
Moment Ma (KN-m)	29.67	50.7195

Fig. 5 Design results of beam
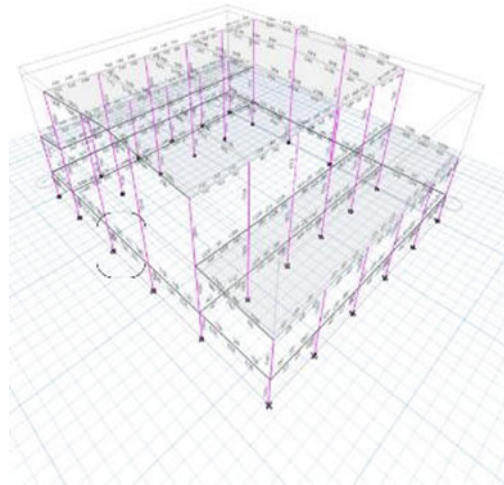
Table 7 Results of beam

Description	Bamboo	RCC
Length	5000	5000
Factored moment (KN-m)	−82.14	−119.1363
Rebar area top (mm^2)	999	210
Rebar area bottom (mm^2)	934	296

6.3 Beam Results

Beam Size: (600 × 230) MM

Table 7 compares the analytical findings of beams. Figure 7 depicts the comparison beam. The beam design behaves like the column design. However, Bamboo-reinforced beams have lower estimated moments than RCC-reinforced beams.

The building's columns and beams meet design specifications and are safe due to the use of bamboo as rebar instead of steel. We cannot completely replace the bamboo with steel since bamboo cannot be bent. Bamboo may be used as a principal reinforcement in beams and columns. Steel bar is recommended for shear reinforcement.

Bamboo has a lower yield strength than HYSD bar, giving a larger rebar area. Higher rebar area may increase beam and column size. Bamboo is not recommended for high-rise buildings but may be used for one to Buildings with two stories.

Table 8 Value of response reduction factor in different zones

SR no	ZONE	RS	Rμ	RR	Rξ	R
1	II	1.71	4.27	0.71	1	5.18
2	III	1.692	4.07	0.71	1	4.88
3	IV	1.11	6.01	0.71	1	4.73
4	V	1.35	4.28	0.71	1	4.10

7 Push-Over Analysis of Bamboo Reinforced Building

The structures are examined using non-linear static pushover analysis. It is necessary to calculate the structures' push-over curve by first computing them under gravity loads, and then progressively applying lateral loads whose magnitudes grow over time according to a predetermined load pattern. These are the hinge properties for P-M2-M3 and M3 columns, respectively, according to FEMA 356: In accordance with ASCE 41-13, the seismic performance of a building may be assessed on a variety of levels. Instant occupancy (IO), life safety (LS), and collapse prevention (CP) are all taken into consideration. The degree of hinge growth, cracking, and deterioration determines these classes. An earthquake zone's reaction reduction factor values are calculated using the static pushover graph's recorded values for each structure in the earthquake zone.

8 Results of Pushover Analysis

Table 8 shows the results disclaimer value of the response reduction factor in different zones for bamboo reinforced concrete buildings, which are different from one another.

9 Pushover Curve

The pushover curve, also known as the capacity curve due to the fact that it indicates the structural ability to withstand lateral loads, is sometimes referred to as the capacity curve. There is a load-deformation curve that depicts the base shear force of the building as a function of the horizontal roof displacement. This curve is used to describe the nonlinear behaviour of the structure. It is possible to determine the maximum displacement at the roof and the base reaction of the structure during a displacement-controlled study by referring to the pushover curve. The capacity curve is a useful predictor of the inelastic stage, and displacement-controlled pushover analysis was used to analyse the pushover curve for a bamboo reinforced structure.in Figs. 4, 5, 6and7 we can see different pushover curve for a different zone by the

pushover curve we can easily predict about base shear and roof displacement (Figs. 8, 9 and 10).
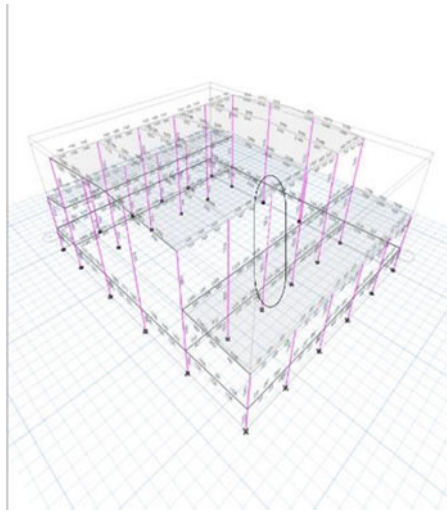
Fig. 6 Design results of column
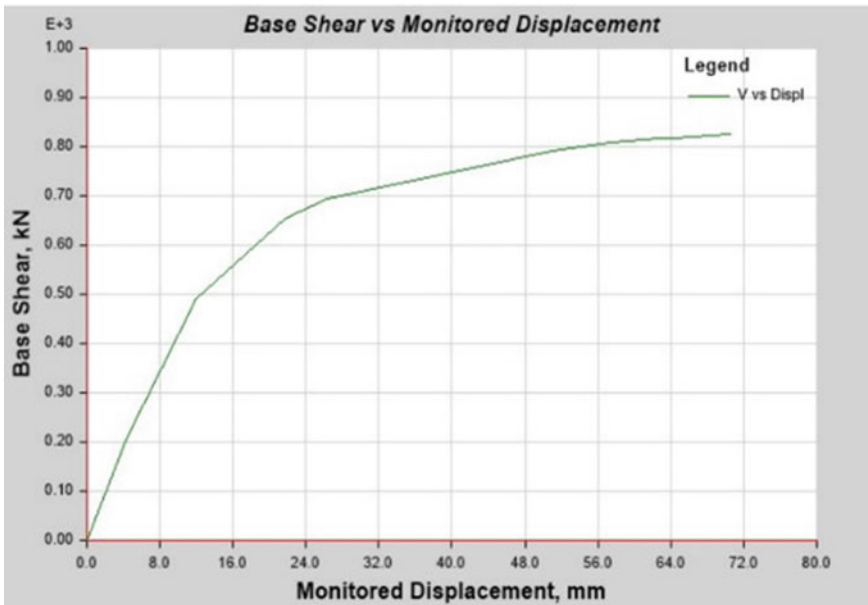
Fig. 7 Pushover curve in zone V
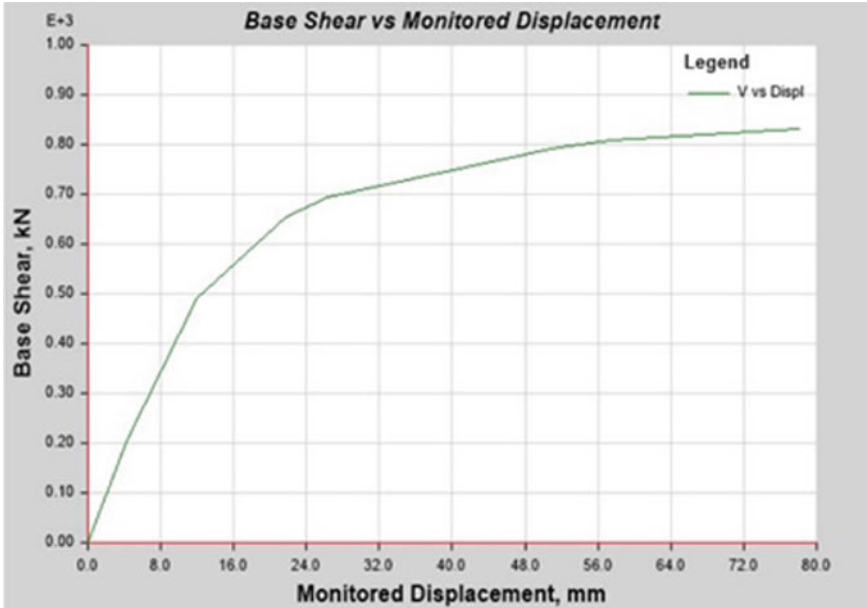
Fig. 8 Pushover curve in zone IV
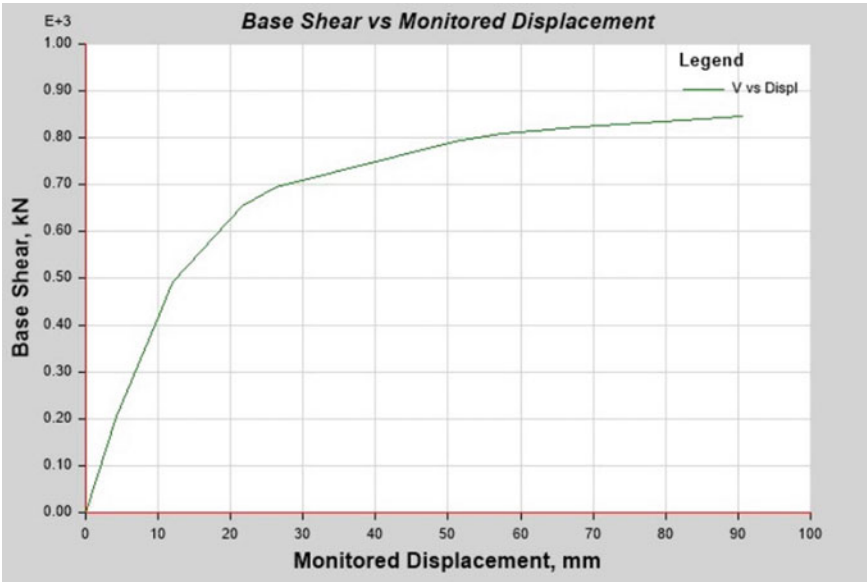
Fig. 9 Pushover curve in zone III
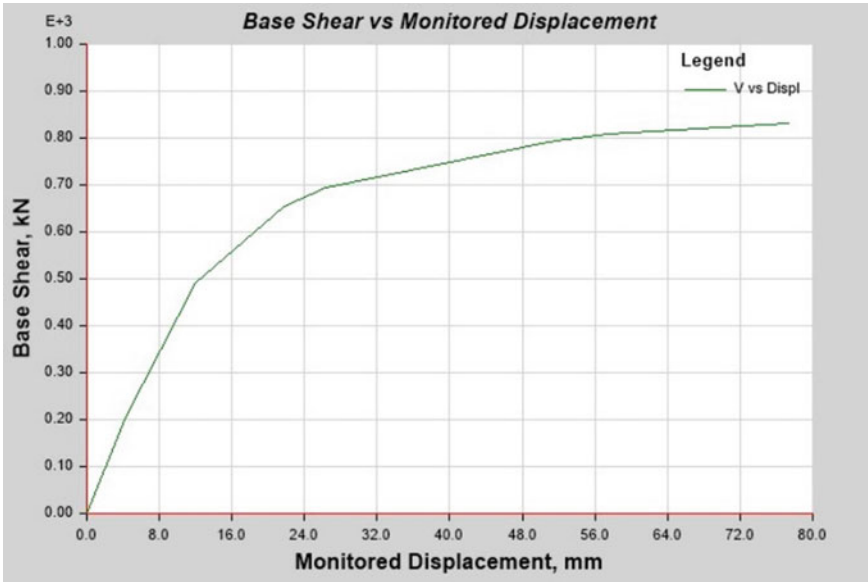
Fig. 10 Pushover curve in zone II

10 Conclusions

- Height has an effect on response reduction values in the ductility equation, as shown above in the ductility equation.
- Different earthquake zones need a different response reduction factor value.
- Soil stratum also affects the response reduction factor's value.
- The results of the analysis show that the value of *R* varies depending on the zone.
- As the intensity of an earthquake rises, the value of *R* drops.
- The response reduction factor reaches its maximum value of 5.18 in the lower intensity zone.
- In the higher intensity zone, the response reduction factor decreases in comparison to lower intensity zone.
- The value of the response reduction factor decreases as the intensity of the earthquake increases.

References

1. Xiao, Y., Inoue, F., Paudel, S.: Proceedings of 1st International Conference on Modern Bamboo Structures, ICBS-2007: Preface (2008)
2. Kumar, M.N., Utkarsh Mathur, M., Phulwari, M.B., Choudhary, M.A.: BAMBOO as a construction material (2017). www.ijariie.com343

3. Correal, F.F.: Bamboo design and construction. Elsevier Ltd. (2019)
4. Bamboo Reinforced Concrete: MATEC Web Conference, vol. 103 (2017). https://doi.org/10.1051/matecconf/201710302001
5. Vengala, J., Mohanthy, B.N., Raghunath, S.: Seismic performance of Bamboo housing–an overview, no. 2273
6. Akeju, T.A.I., Falade, F.: Utilization of Bamboo as reinforcement in concrete for low-cost housing. Struct. Eng. Mech. Comput. **2**, 1463–1470 (2001). https://doi.org/10.1016/b978-008043948-8/50164-8
7. ATC 19: Structural Response Modifictaion factors, Applied Technology Council (ATC), pp. 1–69 (1995)
8. Bureau of Indian Standards: IS 1893:Part-I-2016 Criteria for Earthquake resistant design of structures, Part 1:General Provisions and buildings, Bur. Indian Stand. New Delhi, vol. 1893, no. December, pp. 1–44 (2016)
9. Bureau of Indian Standards New Delhi: Criteria for Earthquake Resistant Design of Structures–General Provisions and Buildings Part-1, Bur. Indian Stand. New Delhi, vol. Part 1, pp. 1–39 (2002)

Investigation on Fire Induced Damages of RCC Building

K. P. Megha, S. Karthiyaini, and Deepak

Abstract Fire is one of the most hazardous loads that can affect a concrete structure. The amount of damage that happened in the structure depends on the temperature range and duration of exposure of heat to the structure. An RCC structure can withstand the temperature up to 200 °F. After 200 °F the concrete will begin to show some damages that can be either noticed by visual inspection or by tests like destructive and non- destructive tests. Repair and rehabilitation method is preferred for such buildings than demolition. So many retrofitting methods are used to repair the damaged structural members based on the deteriorated effects that happened. In this paper a fire damaged building situated at Ernakulam, Kerala is studied. As of the first stage of assessment visual inspection followed by non- destructive tests are carried out to find out the damages on the structural member. Analysis is done for the structure before and after fire exposure and adequate retrofitting methods have been suggested for damaged structural member.

Keywords Fire · Concrete · Retrofitting methods · Non-destructive tests · Jacketing

1 Introduction

Fire is one of the most dangerous loads that can damage a structure. The number of damages will depend on the structural configuration, range of temperature exposure and duration of fire. Concrete has higher resistance to fire but if it exceeds the limit damage can happen. The damage can be spotted by visual inspection and laboratory tests. Non-destructive tests like Core test, rebound hammer test, Ultrasonic Pulse velocity test and corrosion tests are commonly used. Currently, Repair and rehabilitation method is preferred over demolition of the building. The damaged structural

K. P. Megha (✉) · S. Karthiyaini
Department of Civil Engineering, VIT Chennai, Chennai, Tamilnadu, India
e-mail: megha.kp2020@vitstudent.ac.in

Deepak
Principal Structural Consultant, Kozhikode, Kerala, India

member can be retrofitted by using many retrofitting techniques. Based on the deteriorated effects occurred on the structure, adequate retrofitting method is selected. In this paper a fire damaged building situated at Eranakulam, Kerala is studied. The building is a G + 6 storied mercantile building used to stack foot wears, bags and briefcases etc. The fire happened on 20th February 2019 around 11.00 am and the fire effectively started at 11.45 am. The firefighting agencies reached and controlled the fire at 6.00 pm in the evening due to heavy traffic in the city Centre due to the metro rail construction. That means almost 7 h of duration in effectively the fire had full control on the structure. Fire initiation might have been caused from a short circuit in the generator room. Foot wears is made of polyurethane which is a highly exothermic material which can emit the range of temperature of 600–1000 °C. The building is ventilated well which had provided enough support to the fire intensity.

2 Literature Review

M. Usman et al., in their paper explained that when a structure made of concrete is exposed to fire its strength in compression and member stiffness will be affected even when there is no any noticeable cracks. To increase the strength Carbon Fiber Reinforced polymer composite wrapping system is chosen. In the paper published by R. Folic et al., a fire damaged university building is chosen for study. Almost 73% of the structure is splits or cracked. The crack depth ranges from 6–12 cm from the column surface. Reinforced concrete walls had cracks in transverse direction on a depth up to 7 cm from surface. Concrete honey combing occurred because of insufficient concrete cover reinforcement visible on the surface. Uneven dimensions and imperfections at the sides due to loosening of formwork. Net-like cracks are visible on the concrete cover. Separation, falling and spalling off of the cover occurs. Crumbled and broken grains with changed color are noticed. Broken off edges of columns are also noticed. Changes in aggregate grain color from light pink to dark red due to the intensity of heat are found. Piotr Knyziak et al., did an inspection on fire exposure at a shopping center and reported that concrete temperature exceeding 500–600 °C damaged noticeably that it is not suitable for future use. Aleksandra Zawadoska et al., explained that heating concrete will evaporate free water at a range of 100–140 °C and concrete contraction is noticed in the whole heating phase. Larger strength reduction at higher temperature noticed in tests conducted on concrete. Ashok. R. et al., explained that at higher temperature RCC structure would lose its stability and if the temperature increased around 750 °C it would require rapid cooling and 11 retrofitting after proper evaluation and the quenched samples took 10% greater load to failure. Naila Qadir mentioned that the changes in color appeared on the member is considered as the first impact to the fire if the color of beam changes to dark black and grey, damages found all the surfaces. Metri Shankar mentioned that modulus of elasticity decreases with increase in temperature. When finite element analysis has been done, it is noted that temperature decreases with increase in depth and fixed-fixed boundary condition have the higher safe temperature followed by

pinned-pinned, fixed-rolled then pinned-rolled. Alwyn Varghese mentioned about fiber reinforced polymer that the fibers have very negligible influence on compressive concrete strength when exposed to higher temperature. Deepesh Majumdar explained about a fire exposed building that fire exposed moderately on the surfaces showed dusty feeling when touched with fingers. By using jacketing methodology, RCC beams and columns can be retrofitted. Cracks can be sealed using epoxy resins. Exposed reinforcement should be cleaned by gentle hammering. Rust can be removed by corrosion removing gel. Abhijith Mastri et al., reported that loss of strength under fire depends on many factors such as exposure conditions, concrete type, loading tec. The damage level count on age of the structure, duration and intensity of fire, clear cover amount, cooling method etc. Chandrahar et al., experimentally proved that the strength in flexure of beam was lowered when in higher temperature range and the beam be seen in flexural crack in the region of pure bending for higher temperature. And the increased load carrying capacity is noticed when the structure retrofitted with GFRP.

3 Methodology

Various journals which discuss fire damaged buildings and retrofitting methods have been collected and a literature review have been made to study the effect on material properties of the building and also the vital NDT tests performed for the fire damaged building. As an initial reconnaissance visual inspection has been done by identifying the damage caused by fire with the help of collected literature and the photographs taken from the site. Nondestructive tests like rebound hammer test, corrosion test, Ultrasonic Pulse Velocity etc. have been done to identify the changes in material properties after the fire on the affected members. A structural frame modelled asper the relevant IS standards to find the deforming forces in the building frame. Design check is done both manually and by using software to cross verify the entire structural system then compared the results of before and after fire analysis. The software used for analysis is ETABS. The analysis done by defining the material and section properties and various loads to the structure as per IS code provisions. After identifying the structural weakness of the structural members, an adequate retrofitting method has been recommended and a manual retrofitting design has been done as per IS 15988:2013 and concluded the work with recommendations on structural design if any while designing a mercantile and storage building.

4 Initial Reconnaissance

An existing structure situated at Ernakulam, Kerala which have G + 6 storeys was taken for the study. The height of each storey is 3 m. Grade of concrete taken is M25 and grade of steel is Fe415. Beam dimensions are 300 × 400 mm on X axis and 300

Fig. 1 Fire damaged building

× 650 mm on Y axis. Column dimension is 750 × 750 mm and a slab thickness of 150 mm (Fig. 1).

4.1 Visual Inspection

Significant strength damage has happened to concrete exposed to temperature above 600 to 1000 °C to a consistent exposure to 7h. Some damages are noticed from the photographs taken for initial reconnaissance which are damages in steel connections, flexural cracks on the beams, angular displacement of column, color changes, cracks and spalling. Some beams experience flexural cracks due to fire. Flexural cracks developed due to tensile stress developed on the member. Crack may appear on upper side joints and mid span of the beam. Mid span crack is due to the sagging moment at the mid portion and support cracks is due to the hogging moment. "Figure 2 shows the flexural crack on beam". Visible deflections spotted in beams of first, second and third floor. Extensive spalling and vertical cracks are also spotted. Leaching of calcium carbide is noticed on some slabs. Leaching is caused when a cement-based material subjected to humid condition for a prolonged period of time, water penetrates into the concrete material. Here leaching may happen because of the sudden quenching experienced on the structure Re (Fig. 3). Sudden Quenching had reversed thermal gradient resulting in surface cracks on the concrete. The fire water has corroded the calcium oxide released from fire damaged concrete at the hair line cracks on RCC slabs of the building.

Some columns experienced angular displacement Re (Fig. 4). The twist or angular displacement on a column occurs due to the torsional force and shear force. Torsional force will damage the longitudinal and shear reinforcement.

Fig. 2 Flexural cracks in beams

Fig. 3 Leaching of calcium carbide from slabs during water spray

Fig. 4 Angular displacement on column

In a section of core showed color change of whitish grey to a depth of 85 mm from the surface is noticed Re (Fig. 5a). So, the temperature affected on that surface maybe in the range of 600–900 °C. Some color column surface showed prominent color changes of normal grey to pink or red. So, the exposed on that surface maybe in the range of 300–600 °C Re (Figs. 5b and 6).

(a)   (b)
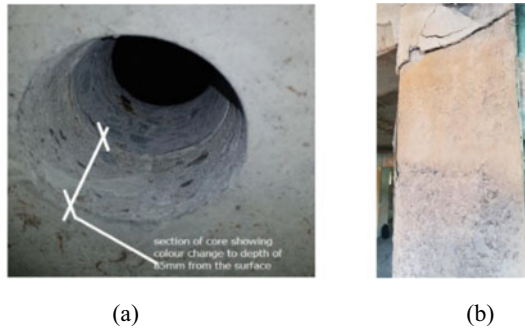
Fig. 5 Color changes noticed on the concrete surfaces

Fig. 6 Spalling of concrete on columns

Obvious spalling of concrete happened on some columns are identified from the photographs. Spalling is delamination of concrete which has cracked by external force from the substrate. It is caused due to higher temperature that is more than 800 °C. Most of the slab members also damaged that their deflection exceeded the limit of 20 mm.

4.2 Non-destructive Testing

Here in this study, core test and rebound hammer test is done for inspection. Core test is conducted to find out the compressive strength of concrete specimen. Columns are tested and. The strength over an average depth of 150 mm from the surface of the column members tested and noted that almost half of the columns are damaged under fire. The design strength chosen for concrete was M25 Grade but after the fire the strength reduced noticeably. Some columns are tested after removing a 45 mm depth of broken parts from the top surface and noted an adequate strength. It underlines that even though the concrete core strength beyond 45 mm depth from member surface seems unaffected, the temperature impact has crossed the steel reinforcement by damaging the bond strength and engineering properties of the reinforced steel in the column. Rebound hammer test also be done for reference and it is found that 2–22%

Table 1 Comparison of core test values and rebound hammer test values

Sl No.	Type of structural member	Location ID	Estimated strength of concrete (Mpa)	
			Core test	Rebound hammer test
1	Column	B2-2	10.5	23.3
2		D2-2	10.5	20.3
3		B1-2	24.5	16.2
4	Beams	D1-D2-2FR	10.5	13.7
5		D1-D2-3FR	15.5	18.9

variation on test result on column noted in rebound hammer test. when compared to core test result, a drastic variation in the result is noted. Both core test and rebound hammer test give lesser compressive strength value than actual value before fire. As the percentage accuracy of Rebound hammer test is within 25% and also considering the inefficiency in detecting fine cracks within the member it is more justifiable to rely on core values in case of variations. "Table 1 shows the compressive strength value results from core test and rebound hammer test".

Reinforcement steel taken from the damaged slab is tested which had spalling, reinforcement exposure to hot gases and smoke and the sudden quenching with water spray on to the hot specimen had disrupted the yield strength. The grade of steel provided throughout the building was Fe415 grade. But after the fire severe variation was noticed after testing the steel. The yield strength of steel reduced to 202 to 206 MPa. That means almost 50% yield strength is lost after the fire impact. This proves the prediction that the steel has been imparted with temperature more than 800 °C even in the presence of concrete cover. It also inferred that Steel might have recovered better under atmospheric cooling.

In initial reconnaissance all damaged members are identified and tested. The structure is damaged severely under the influence of temperature of 600–1000 °C for more than 6-h duration. The burning heat wave of polyurethane-based material have taken the atmospheric temperature sound enough to penetrate the concrete cross section of the column to a depth ranging from 60 to 150 mm in columns and 70 to 150 mm in beams. The damages extended when sudden quenching happened due to the water spray on hot surface which reversed the thermal stress variation resulted in hairline cracks on the surfaces. Damages occurred up to 150 mm depth from surface which includes the reinforcement area which may have weakened the bond stress between steel and concrete.

5 Modelling

Model has been created using Auto CAD (Computer Aided Design) and ETABS software. The structure analyzed for the conditions before and after fire. For before fire analysis, the grade of concrete and steel provided was M25 and Fe415 respectively
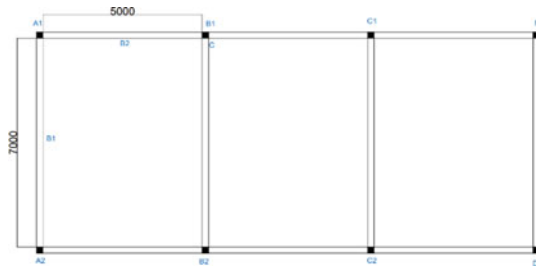
Fig. 7 Frame layout

and analyzed for the factored design load combinations as per IS standards, with the structural dimensions provided by structural drawing Re (Fig. 7). The analysis of the structure after fire has been done by assigning the grade of concrete and steel as M15 and Fe250 grade respectively. The structure designed as per IS456:2000, IS1893:2016 provisions and design load combinations also provided for analysis. Manual calculation for damaged column and beam is done as per IS456:2000, SP16 guidelines. Increased percentage reinforcement is calculated for both column and beam. Retrofitting design is done using IS15988:2013 guidelines.

6   Results and Discussion

The structure before fire is analyzed and corresponding member forces are obtained. The structure shows normal results after analysis before fire. Structure after fire is analyzed by revising the material strength properties to M15 for concrete and Fe 250 for steel and results showed some variations from the normal results. Shear force diagram and Bending moment values are changed even though the diagram seems normal. Axial forces increased in each storey when compared to before fire results. By choosing a damaged column, the design is done manually to find out how much percentage reinforcement should be increased for getting safe structural member. The building columns before fire were designed while assuming 2.9% percentage steel for M25 concrete and Fe 415 steel grades. By calculating with revised material properties which are M15 and Fe250, the percentage steel of 2.9% were not sufficient. By doing the manual calculation for one damaged column, the percentage steel increased to 3.41% is obtained to get safe design. A damaged beam also analyzed and resulted that shear reinforcement has to be redesigned.

In the beam design, the area of reinforcement required before fire was 1200 mm^2 when the strength of concrete and steel was M25 and Fe415 respectively. But now it is increased to 1618 mm^2. So, we have to provide 400 mm^2 extra reinforcement to the member. This 400 mm^2 is added to the member through retrofitting along with half percentage of reinforcement required before fire.

In the current situation the building should not be used for mercantile purpose as the imposed load for mercantile building is 6 KN/m^2 and the structure cannot withstand this load. If we reduced the imposed load to 3 KN/m^2 the building can be used for residential purpose. But if the repair of the damaged structural members by various retrofitting methods like Concrete jacketing, carbon fiber wrapping etc., the structure can be reused as a mercantile building itself. The retrofitting design is done by considering IS15988:2013 code provision. Concrete jacketing design and detailing of one column and beam is done manually for retrofitting. For beams only shear reinforcement design is done.

6.1 Concrete Jacketing Design of Column

Use of reinforced jacketing helps to improve the column flexural strength and ductility of the structure. As per IS 15988:2013, the jacketing of column of size 750×750 mm is done. The axial load P and Moment M is obtained from the analysis after fire is taken for the design procedure. According to IS 15988:2013 provisions, cl.8.5.1.2 "Concrete Strength shall be at least 5 MPa greater than the strength of concrete."

That is $15 + 5 = 20$ N/mm^2. Here fck = 25 N/mm^2 is taken for design.

By using the equation

$$P_u = 0.4f_{ck}A_c + 0.67f_yA_{sc} \tag{1}$$

New concrete area is calculated.

But as per IS 15988:2013; cl.8.5.1.1

$A_c = 1.5 A'_c$. so, A_c is again increased and corresponding B and D value is calculated.

According to IS 15988:2013,

"Minimum jacket thickness shall be 100 mm" Therefore, new size of column will be taken as 950×950 mm and according to cl.8.5.1.1

As = 4/3 A'$_s$.

So, the steel area again increased and diameter of reinforcement for jacketing is calculated. Which is 16 mmØ bars.

For the design of Lateral Ties, as per IS 15988:2013 cl.8.5.1.2,

"Minimum Diameter of ties shall be 8mm and not less than one third of longitudinal bar diameter."

Therefore, diameter of bar = $1/3 \times Ø_{longitudinl} = (1/3) \times 16 = 6$ mm ≈ 8 mm.

Spacing of ties,

As per IS 15988:2013, cl.8.5.1.1,

"Spacing of ties to be provided in the jacket in order to avoid flexural shear failure of column and provide adequate confinement to the longitudinal bar along jacket is,"

$$S = \frac{fy \times dh^2}{\sqrt{fck} \times tj} \tag{2}$$
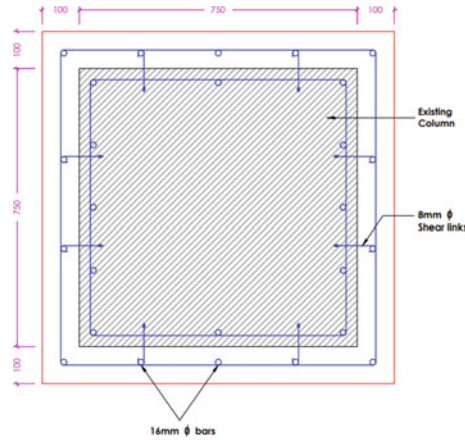
Fig. 8 Jacketing details of column

$S = \frac{450 \times 16^2}{\sqrt{25} \times 200} = 110 \, \text{mm}$

Provide 8 mm at 110 mm c/c.

"For columns where extra jacket is not required a minimum of 12Ø bars in 4 corners and ties 8Ø at 100 mm c/c should be provided with 135° bends and 10Ø leg lengths" (Fig. 8).

6.2 Concrete Jacketing Design of Beam

An increase of 400 mm^2 of reinforcement area occurred after fire check on beams. So we have to provide this extra reinforcement along with the half percentage reinforcement of the member before fire. So, total of 1000 mm^2 has to provide as a retrofit. Beam jacketing with thickness of 75 mm on both sides of beam section is considered. 5 no.of 16 mmØ bars provided at bottom and 3 no.s provided at top portion of the beam. 0.15% of side reinforcement also provided. Micro concrete is used for jacketing the section. Shear reinforcement should be redesigned for the member.

Size of beam $= 300 \times 650$ mm.

Design Shear Reinforcement.

Factored SF $= 80.6$ KN.

From IS 456:2000.

$\tau_v = 0.45$ and $P_t = 0.34$. Therefore, from IS 456:2000 Table 19, $\tau_c = 0.39$.

That means $\tau_v > \tau_c$

So, Shear reinforcement has to be provided.

Thickness of 75 mm can be taken instead of minimum thickness of 100 mm if we are using micro concrete.

Therefore, jacketed beam section size $= (650 + 150) \times (300 + 150) = 800 \times 450$ mm.
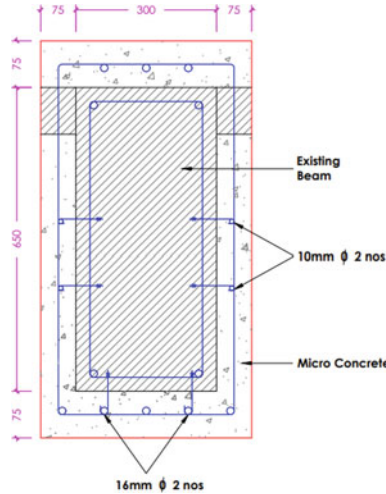
Fig. 9 Jacketing details of beam

Provide a shear reinforcement using two legged 8 mm Ø bars.
Spacing required,

1. $S_v = \frac{0.87 \times 415 \times 2 \times \left(\frac{\pi}{4}\right) \times 64 \times 270}{12155} = 806\,\text{mm}$
2. $0.75d = 202$ mm
3. 300 mm

Take minimum of the above values. That is two legged 8 mmØ stirrups at 200 mm c/c (Fig. 9).

7 Conclusions

Poly urethane is a highly exothermic material that can emit the temperature of 600–1000 °C. The effect of temperature affects the structural member very severely that the building cannot be used for current purpose in the future. Significant strength damages are noticed due to heavy exposure of fire which is more than 600 °C. Cracking and spalling of concrete is noted in most of the structural members and it is observed that the reinforcement strength also varied. Most of the slabs exceeded the limit of deflection criteria. 50% reduction in concrete and steel strength is observed after fire. Sudden quenching leads to reduction in yield strength as the thermal stress induced in the member. Comparison of results of before and after fire analysis showed noticeable variations. The feasibility of functional utility at present stage of analysis shall be used for residential purpose that means the imposed load of 3 kN/m^2 can be assigned instead of 6 kN/m^2. After manual calculation, percentage reinforcement that should be increased for members is found out to be 3.14%. Retrofitting methods

like concrete jacketing, concrete fiber wrapping can be used for repairing. Here, Concrete jacketing design of one column and beam have been done by using the IS 15988:2013 provisions and the increased size of column and beam with jacketing reinforcement has been calculated for making the building fully functional as before.

Inference

If the building is constructing for the usage of any highly exothermic material, then the concrete cover thickness of the structural components should be taken more because increased cover thickness can prevent fire approaching the reinforcement. High grade concrete should be preferred since the strength of the concrete will be more and can withstand fire to a limit. By using fire resistant paints on the surface will prevent the heat entering in to the concrete core. Sudden quenching should not be performed on the structure immediately after fire because it will reduce the yield strength as the thermal stress induced in the member. River sand is preferred for construction because M sand absorbs heat more than river sand.

References

1. Majumdar, D.: A case study for retrofitting scheme of a fire damaged RCC structure. Int. J. Eng. Sci. Technol. (IJEST) (2020)
2. Biondini, F.: Cellular finite beam element for nonlinear analysis of concrete structures under fire. J. Struct. Eng. **137**(5), 543–558 (2020)
3. Wang, L.: Repair of fire-exposed preloaded rectangular concrete columns by post compressed steel plates. J. Struct. Eng. **140**(3), 04013083 (2014)
4. Chang-Jiu, J.: Shear performance of fire-damaged reinforced concrete beams repaired by a bolted side-plating technique. J. Struct. Eng. **143**(5), 04017007 (2017)
5. Khaliq, W.: Effectiveness of polypropylene and steel fibers in enhancing fire resistance of high-strength concrete columns. J. Struct. Eng. **144**(3), 04017224 (2018)
6. Yang, O.: Bond performance between slightly corroded steel bar and concrete after exposure to high temperature. J. Struct. Eng. **144**(11), 04018209 (2018)
7. Liu, F.: Experimental and numerical studies of reinforced concrete columns confined by circular steel tubes exposed to fire. J. Struct. Eng. **145**(11), 04019130 (2019)
8. Chen, J.: Structural performance of reinforced concrete walls under fire conditions. J. Struct. Eng. **146**(3), 04020006 (2020)
9. Qureshi, R.: Probabilistic models for temperature-dependent strength of steel and concrete. J. Struct. Eng. **146**(6), 04020102 (2020)
10. Yu, Y.: Fire-resistance mechanism and residual bearing capacity of prestressed concrete beams after fire exposure. J. Struct. Eng. **147**(8), 04021109 (2021)
11. Yim, H.J.: Characterization of thermally damaged concrete using a nonlinear ultrasonic method. Cem. Concr. Res. **42**, 1438–1446 (2012)
12. Lin, Y.: The effect of post-fire-curing on strength-velocity relationship for nondestructive assessment of fire-damaged concrete strength. Fire Saf. J. **46**, 178–185 (2011)
13. Liu, Y.: Fire performance of axially ductile connections in composite construction. Fire Saf. J. **121**, 103311 (2021)

14. Short, N.R.: Assessment of fire damaged concrete using colour image analysis. Constr. Build. Mater. **15**, 9–15 (2001)
15. Felicetti, R.: The drilling resistance test for the assessment of fire damaged concrete. Cem. Concr. Compos. **28**, 321–329 (2006)
16. Ghan, Y.N.: Residual strength and pore structure of high-strength concrete and normal strength concrete after exposure to high temperatures. Cem. Concr. Compos. **21**, 23–27 (1999)

Experimental Study on Durability and Mechanical Properties of Lightweight Mortar with Encapsulated Spore Forming Bacteria

J. P. Akshay, Basil Baby, and T. Palanisamy

Abstract Concrete is a material that is used worldwide for centuries as a construction material. Increased consumption of concrete leads to vulnerability of structure physically, chemically and biologically. Exposure to extreme conditions and detrimental effects of corrosion of reinforcements leads to cracking of concrete. Compressive strength, Flexural strength, and permeability can be affected by these cracks consequently leading to shortening the useful life of the concrete. Repairing and maintenance of these infrastructures need higher cement consumption and expenses. The benefits of microbial concrete can reduce the consumption of cement for structural replacements and maintenance works. Self-healing concrete by microbially induced calcite precipitating bacteria is an economical and sustainable solution, as it autonomously repairs small cracks. In this paper, we discuss the mechanism and performance of bio-concrete along with the idea of microbially induced calcite precipitation (MICP). The Bacillus species is proven to be an effective microbial agent for self-healing concrete. Hence the sample preparation is done using encapsulated spore-forming Bacillus Subtilis bacteria species as a biological healing agent. Three concentrations of 10^5, 10^7, and 10^9 cells per millilitre are adopted for sample preparation. The mix proportion of cement mortar is 1:3, using expanded perlite as a replacement for the fine aggregate in the percentages 10% was done. The mechanical and durable properties of bio-mortar are evaluated to ascertain the possibility of the same as a resilient building material.

1 Introduction

Due to its numerous performance features, concrete remains as the most used materials in nowadays and it will undoubtedly remain as the most manufactured and consumed construction material in the long run, owing to the expanding urbanisation of developing countries and the growing global population [1]. Concrete is distinguished by numerous cracking behaviour because of low tensile strength and

J. P. Akshay (✉) · B. Baby · T. Palanisamy
Department of Civil Engineering, National Institute of Technology Karnataka, Mangaluru, India
e-mail: akshayjp.202cm004@nitk.edu.in; akshayjp4121996@gmail.com

brittleness. Cracks can weaken the integrity and beating capacity of structure. Due to volume instabilities or other external reasons such as excessive loads, severe strength environmental exposure, or design error, cracks can develop at any point of a concrete structure's service life [2, 12]. Micro-cracks in concrete allow water and contaminants to enter, causing matrix degradation and corrosion of embedded steel reinforcement, compromising the structure's strength and endurance [3].

Steel reinforcement is frequently used to avoid cracks, but it is quite expensive and requires a big amount of steel, which is never acceptable. As a result, new environmentally friendly and self-healing procedures must be developed to protect existing and future structures and increase their durability. For the improvisation of the strength and durability of concrete, a variety of approaches have been devised [4]. Microbiologically Induced Calcite Precipitation (MICP), a type of mineral precipitation induced by the metabolism of bacteria in concrete, it is recently discovered to increase the performance of concrete. Biomineralization is accomplished by a process known as Microbiologically Induced Calcite Precipitation (MICP). The microbial urease hydrolyses urea to form ammonia along with carbon dioxide. As a result of the ammonia released into the environment, the pH rises, causing a deposit of insoluble calcium carbonate [5]. MICP is a practical, sustainable alternative to traditional technologies as solutions to many problems in industries. These biomineralization concepts in concrete could lead to the creation of a novel material known as Bacterial Concrete [6, 13].

1.1 MICP - Microbially Induced Calcium Carbonate Precipitation

Microbially induced calcium carbonate precipitation (MICP) is a part of various geological habitats like soils, limestone caves. Calcium carbonate (CaCO3) crystals can be formed via biological mechanism in two ways: Autotrophic and heterotrophic pathways. Biotechnological approaches to innovation of a type of bio concrete have been proposed based on microorganisms' inherent ability to produce calcium carbonate precipitation [7]. When a crack forms, the bacteria imbedded within it are become active, and calcium carbonate minerals are produced and fills the cracks. In comparison to ordinary self-healing concrete, the MICP-based self-healing technique provides a long-term and ecologically sustainable solution to cracking. The number and quality of induced minerals have a significant impact on the MICP process efficiency [6, 8].

Ammonium and carbonate formed by hydrolysis of urea, catalysed by urease. One mole of carbamic acid is formed from hydrolysed ammonia and Carbamic acid, which further hydrolysed to ammonia and carbonic acid [9].

$$CO(NH_2)_2 + H_2O \rightarrow NH_2COOH + NH_3 \tag{1}$$

$$NH_2COOH + H_2O \rightarrow NH_3 + H_2CO_3 \qquad (2)$$
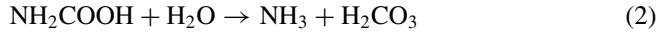
The products, Ammonia and Carbonic acid produces bicarbonate, and also ammonium and hydroxide ions. The carbonate ions formed by the shift in pH due to increased hydroxide ion concentration and pH. This change will then cause the precipitation of the metal ions. The formation of NH_4^+ and increases the local pH. The reaction continues to produce calcium carbonate [10].

$$H_2CO_3 \leftrightarrow HCO_3^- + H^+ \qquad (3)$$

$$2NH_3 + 2H_2O \leftrightarrow 2NH_4^+ + 2OH^- \qquad (4)$$

$$HCO_3^- + H^+ + 2OH^- \leftrightarrow CO_3^{2-} + 2H_2O \qquad (5)$$
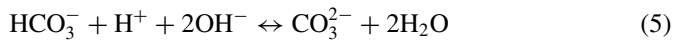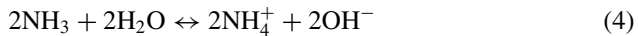
If there is enough concentration of Ca^{2+} and $CO_3{}^{2-}$ in solution. $CaCO_3$ is precipitated at the cell surface of bacteria [10].

$$Ca^{2+} + \text{Bacterial cell} \rightarrow \text{Cell} - Ca^{2+} \qquad (6)$$

$$\text{Cell} - Ca^{2+} + CO_3^{2-} \rightarrow \text{Cell} - CaCO_3 \qquad (7)$$
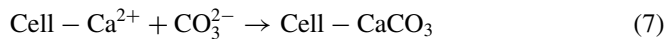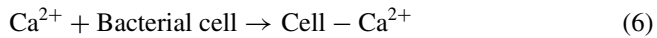
2 Materials and Methods

2.1 Ordinary Portland Cement – 53 Grade

Because of its outstanding crystalline structure and perfect particle size distribution, OPC 53 grade has a high strength and durability. OPC 53 Grade cement must meet BIS specification IS: 12,269-1987, having a specified strength of at least 53 MPa or 530) kg/cm^2 for 28 days. IS: 4031-1988 and IS 12269-2013 were used to test the cement's physical qualities.

The average specific gravity of the sample is determined to be 3.14 and consistency as 31.5%. Average 7 day compressive strength of the cement sample is determined as 39.07 N/mm^2 followed by 28th day strength of 55.27 N/mm^2.

2.2 Fine Aggregate

Fine aggregate should have a particle size range of 0.075 to 4.75 mm. Fine aggregate used in this study is river sand. The fine aggregate must meet the requirements of IS 2386-1963(R2016) and IS 383:2016 (Table 1).

2.3 Expanded Perlite

Perlite, is a glassy form of rhyolitic magma, which is made from pumice and contains 2–5% of water. The commercial product, named as expanded perlite, produced by heating the perlite to 760–1100 °C, which converts the material's native water to vapour and resulting in expansion of 4–20 times its original volume [14], the final product is lightweight and highly porous aggregates. The Expanded Perlite which should be used in this research must be in the range of 1 to 4 mm (Fig. 1).

It is necessary to understand, how the incorporation of lightweight porous expanded perlite aggregate (EPA) affects the strength of masonry mortar, when the

Table 1 Properties of fine aggregate sample

Number	Physical property	Values
1	Specific gravity	2.65
2	Fineness modulus	3.52
3	Water absorption	1.719%
4	Grading Zone	IV
5	Bulk density	1560 kg/m^3
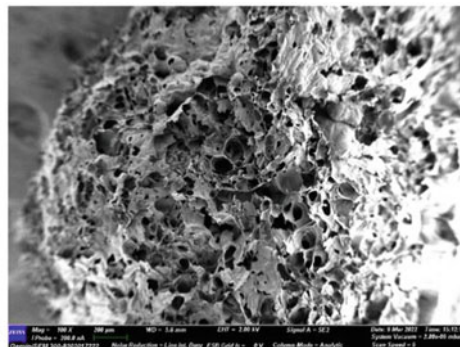
Fig. 1 100× scanning electron microscopy image of expanded perlite surface

Table 2 Bacterial strain details

Fields	Detailed information
NCMR Accession Number	MCC 2183
Taxonomic designation	Bacillus subtilis (Ehrenberg 1835) Cohn 1872
Source of Isolation	Lonar lake soil sample
Medium Name and Number	72a (Horikoshi and Akiba Agar and Broth medium (pH 120)
pH of Medium	12
Temperature of Growth in Degree Celcius	30
Incubation Period	1 d
Subculturing Period	3 months
Additional information	Efficient alkaline protease and amylase producer, alkalophilic and thermotolerent

dosage value increases. So that, the optimum amount of EPA can be used in bio-mortar, to act as a carrier for microbes. In this study percentage of EPA, as 10% was used, by replacing equivalent amount of fine aggregate from the mortar mix.

2.4 Sodium Silicate

Sodium silicates are colourless glassy or crystalline solids, or white powders. They are water soluble, with the exception of the silicon-rich ones, and produce alkaline solutions. In both neutral and alkaline fluids, sodium silicates are stable. To preserve the spores during mixing and putting, a two-layer covering of sodium silicate solution and silica fume is applied to the encapsulated expanded perlite [11] (Table 2).

2.5 Bacterial Strain

3 Experimental Methodology

3.1 Cultural Growth of Bacteria

For the preparation of bacterial solution of 1 L volume, Nutrient broth was mixed with 500 ml of distilled water and quantity of NB was measured as;

$$13 \text{ gm} = 1000 \text{ ml}, 6.5 \text{ gm} = 500 \text{ ml}$$

Therefore, 6.5 gm of NB was added in 500 ml distilled water and further the solution was then kept in autoclave for 1 h to remove any contamination present in it. Similarly, the $Ca(OH)_2$ which gives cementitious properties added in 500 ml of distilled water and quantity was taken as;

$$74.09 \text{ gm} = 1000 \text{ ml}, 37.045 \text{ gm} = 500 \text{ ml}$$

The required pH of complete 1000 ml solution, for the growth of bacteria, was in the range of 9 to 12 and then the solution is kept in shaker for 24 h at 30 °C. After 24 h urea, calcium acetate and inoculum were added to the solution [8, 15].

3.2 Bacterial Inoculum

Inoculum was added as 10% of the total solution so the quantity of inoculum for 1000 ml of solution is 10 ml. The whole bacterial culturing process was done under sterile condition so that the solution was not getting contaminated by the intrusion of other bacteria present in the environment. The solution was kept in BOD Incubator for at least 1 days for proper growth of bacteria.

3.3 Mix Proportion and Sample Preparation

The mix proportion of the mortar study was in the ratio Cement: Fine Aggregate for 1:3. CONPLAST SP 432 MS superplasticizer was used in various dosage levels to get a minimum flow value of 15 cm and w/c is 0.5. The proportion of mixes used for casting cube is given below (Table 3).

Casting of Bio mortar cubes is same method as followed for conventional cubes. Expanded perlite was immersed in the solutions of different concentrations and kept for 2 h under pressure. This will make the pores of expanded perlite filled with microbial spores then the immersed Expanded Perlite is taken out and is oven-dried for 24 h at 30 °C. The oven dried encapsulated expanded perlite is then immersed in

Table 3 Mix proportion of materials in EPA mortar

Sl. No.	ID	Cement (g)	Fine aggregate (g)	Expanded Perlite aggregate(g)	Bacterial concentration (cells/ml)
1	CS	1010	3264	0	0
2	C10P5B	1010	2940	24.8	10^5
3	C10P7B	1010	2610	49.59	10^7
4	C10P9B	1010	2290	74.38	10^9

sodium silicate solution and was readily taken out to roll over cement powder. This will impart a brittle coating to protect the encapsulated spores from deterioration during mixing and placing.

4 Experimental Tests

4.1 Water Absorption Test

The amount of water absorbed under specified conditions is calculated. It was calculated by measuring the dry and wet weight of the mortar cubes. Mortar cubes are oven dried at a temperature of 100 to 110 °C and weighed (W_1). Wet weight is measured by saturating the cubes in water for 24 h and the weight is taken as W_2. Low permeability is an important feature of a good quality mortar. A mortar with low permeability counter the ingress of water to it and is resistant to freezing and thawing. Water absorption is calculated by the formula, (Fig. 2)

$$\text{Percentage absorption} = \frac{W_2 - W_1}{W_1} * 100 \tag{8}$$
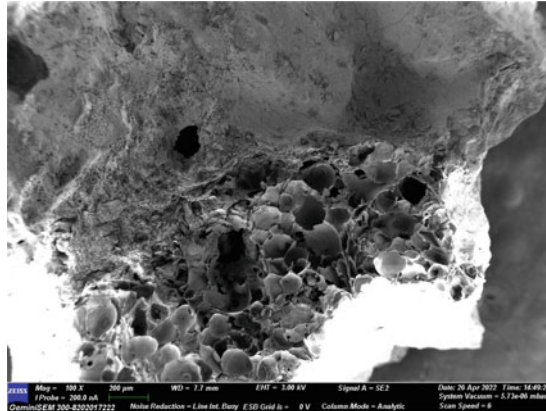
$$\text{Percentage absorption} = \frac{W_2 - W_1}{W_1} * 100 \qquad (\text{Eq.8})$$

Fig. 2 100× scanning electron microscopy image of light weight mortar with encapsulated bacteria

4.2 Compressive Strength Test

The hardness of mortar specimen is found out using compression test. The strength of a mortar specimen depends upon various factors such as cement, aggregate, water-cement ratio, curing temperature, and age and size of specimen. In the present experiment, Cubes of sizes 70.6 × 70.6 × 70.6 mm were prepared and entire sample specimen tested under compression testing machine. The load is applied gradually and continuously at the rate of 40 tons/minute till the specimen fails [18].

4.3 Split Tensile Strength Test

The porous nature of concrete makes it weak under tension and brittle to stress. So concrete easily cracks under tensile forces. As a result, the concrete tensile strength evaluation is a must in order to determine the maximum load the concrete member can yield. The splitting tensile strength is calculated as,

$$Tsp = \frac{2p}{\pi dl} \tag{9}$$

where, p = Load applied d = Diameter of cylinder l = Length of the cylinder.

4.4 Flexural Strength Test

Beam samples were cast and flexural test conducted on 3rd 7th and 28th day. The 160 × 40 × 40 mm size beam was subjected to two-point loading to discuss the behaviour of the RCC beam. The crack widens and extends all the way to the top of the beam as the weight increases. The tension zone yield stress cause flexure as the failure mode of the RCC beam.

4.5 pH Value Test

The pH value of a mortar determines if bacteria can have a negative impact on the passive layer that protects reinforcement bars from corrosion. The crushed mortar obtained after compressive strength testing was powdered to pass through a 300 μ sieve. The powdered material was mixed with water in a ratio of 1:9 and left for 12 h. The pH of the combination was determined the next day using a pH metre. Surface mortar samples were taken from the top surface for 3, 7, and 28 days, and the pH was recorded.

4.6 EDTA Test

The presence of calcium carbonate in the sample produced from crushed cubes is confirmed by this test. The solution was made by combining the mortar sample with sodium hydroxide and water. A drop of hydroxyl naphthol blue indicator was added to the resulting solution, giving it a bright pink colour. The coloured solution was titrated against EDTA. The pink colour solution was changed to violet hue at a specified time during the titration. The presence of calcium carbonate in the mortar sample is confirmed by the change in colour from pink to violet. The amount of EDTA used is proportional to the amount of $CaCO_3$ produced.

5 Experimental Results and Discussion

Due to the addition of bacteria the mortar, qualities have been improved and it is analysed here. The different tests results of both conventional and bio mortar are compared.

5.1 Water Absorption

Compared to the conventional mortar the water absorption decreased majorly by the presence of bacteria. Water absorption of Light weight mortar cubes has been found to be 3.6%.The water absorption was reduced after a coating of calcium carbonate crystals was deposited on the surface. As a result, undesirable material infiltration may be restricted. The deterioration of crystal surface of cementitious material has been improved by the presence of a layer of carbonate crystals by bacterial action.

5.2 Compressive Strength

On the 3rd, 7th, and 28th days, three cubes of ordinary mortar cubes were tested for compressive strength. 2.74, 5.97 and 8.6 N/mm^2 were found to be the average of the results. Table 4 shows that that bio mortar cubes have a higher compressive strength than conventional mortar.

Table 4 Comparison of results of compressive strength test

Compressive strength	3 day (N/mm^2)	7 day (N/mm^2)	28 day (N/mm^2)
CS	2.74	5.97	8.6
Bacterial mortar	3.57	7.11	11.65

Table 5 Comparison of results of split tensile strength

Split tensile strength	3 day (N/mm^2)	7 day (N/mm^2)	28 day (N/mm^2)
CS	1.6	2.5	2.86
Bacterial mortar	1.76	2.8	3.5

Table 6 Comparison of results of flexural strength test

Flexural strength	3 day (N/mm^2)	7 day (N/mm^2)	28 day (N/mm^2)
CS	1.98	2.61	3.22
Bacterial mortar	2.54	3.61	4.20

5.3 Split Tensile Strength

On the 3rd day, 7th day, and 28th days, three cubes of conventional mortar were carried under for split tensile strength. The results shows that bacterial mortar has a better tensile strength than regular mortar (Table 5).

5.4 Flexural Strength

On the 3rd day, 7 day, and 28 days, three beams of conventional mortar were tested for flexural strength. 3.15, 4.22, and 5.35 N/mm^2 were found to be the average of the test findings (Table 6).

Because live cells got good nourishment during the first curing phase while the cement was still porous, improvement in strength found starting at initial stage in almost all cases. It indicates that the bacteria activities were on peak on the initial days. Calcite would form on the cell surface as well as within the Portland cement sand matrix as the cell grew. As a result, the porous and permeable nature of Portland cement is reduced. It was observed when bacteria growth is properly adopted to atmosphere inside mortar cube, Compressive strength, Split tensile strength and Flexural strength has been increased. And it is due to formation of calcite layer.

5.5 pH Value Test

The growth of bacteria is checked by calcium hydroxide powder. The control specimens showed a pH of 12 on each day. Addition of bacteria does not have effect on pH of bio mortar. Therefore, it shows that pH for all the specimens were favourable to the bacterial growth condition (Table 7).

Table 7 pH values of samples

Days	CS	C10P5B	C10P7B	C10P9B
3	11.19	12.1	12.12	12.56
7	12.1	12.3	12.31	12.36
28	12.4	12.54	12.6	12.65

Table 8 EDTA measurement

Sample	EDTA change (ml)	EDTA used (ml)	$CaCo_3$ calculation (gm)	
			For 1 gm	For 0.5 gm
CS	41.4–42.2	1	5.006	2.503
C10P5B	36.3–41.2	4.9	24.52	12.26
C10P7B	45.2–50.4	5.2	26.04	13.01
C10P9B	31.9–36.5	4.6	23.02	11.51

5.6 EDTA Test

The amount of EDTA added and amount of $CaCO_3$ formed is depicted in the table. The test was done for 28 days of mortar cubes. Due to calcite precipitating property of Bacillus Subtillis bacteria, EDTA values for the sample is high at optimal concentration (Table 8).

6 Conclusion

This chapter summarises the results from the tests performed on conventional and bacterial test specimens.

- Bacillus subtilis is a soil bacterium with a safer bio safety value of 1 and it can be prepared in a laboratory. Calcite precipitation reduces as the number of bacteria increases. Bacterial mortar has a lower rate of water absorption than conventional mortar, this is due to the microorganism's action in forming calcium carbonate in the voids of the mortar, resulting in less void spaces and hence a low permeability value.
- The result of compressive strength indicates that the introduction of bacteria in mortar cubes increases the strength compared to conventional cubes. The 3rd day, 7th day and 28th day compressive strength after curing shows that the strength increased by 36.64, 18.89 and 35.46%. Like, the flexural strength results showed an increase of 28.02, 35.64 and 31.02%. Split tensile strength results has an increase of 10.93, 14.52 and 22.09%.
- pH of all the samples was observed approximately 12 at 3, 7 and 28 days. For every case, addition of bacteria in mortar does not affect the pH of mortar.

- Bacterial mortar shows very less water absorption in comparison with conventional mortar. The penetration of harmful substances are limited due to the carbonate crystal surface. And also due to the carbonate layer, the degradation of cementitious material has been shown to be increased.
- EDTA test with colour change from pink to violet indicates the presence of calcium carbonate precipitation.
- Porous materials is to be used in order to incorporate the bacterial colonies, expanded perlite possess the qualities for colonization of Bacillus Subtillis bacteria. And also the more pores in the mortar, the more bacteria spores can inhabit. Results in less permeable and strong mortar matrix.
- Using expanded perlite as a replacement for aggregate, extensive use of natural aggregate can be decreased, making it a sustainable alternative to natural aggregate scarcity.

The microbes used to make the mortar test specimens have been proven to be very effective in achieving high initial strength, so it is clear that some of the voids are filled with the precipitated calcium carbonate, resulting in less permeable and compact surface. Radical change in strength has been observed after 7 days. After 28 days the increase in strength was not considerable. Because after all the pores on surface were blocked, anaerobic condition arises and leads to slowing down of bacterial activity, results in spore formation of bacteria. OPC with developed bacteria is a viable alternate solution to environmental pollution. Passive layer formation due to bacteria culture will prevent corrosion of reinforcement bar, So bacterial mortar can also be used for construction because of it is corrosion resistant ability.

References

1. Van Tittelboom, K., De Belie, N., De Muynck, W., Verstraete, W.: Use of bacteria to repair cracks in concrete. Cem. Concr. Res. **40**(1), 157–166 (2010)
2. Kumari, C., Das, B., Jayabalan, R., Davis, R., Sarkar, P.: Effect of nonureolytic bacteria on engineering properties of cement mortar. J. Mater. Civ. Eng. **29**(6), 06016024-1–9 (2017)
3. Jonkers, H.M., Thijssen, A., Muyzer, G., Copuroglu, O., Schlangen, E.: Application of bacteria as self-healing agent for the development of sustainable concrete. Ecol. Eng. **36**(2), 230–235 (2010)
4. Seifan, M., Samani, A.K., Berenjian, A.: Bioconcrete: next generation of self-healing concrete. Appl. Microbiol. Biotechnol. 100(6), 2591–2602 (2016). https://doi.org/10.1007/s00253-016-7316-z
5. Douglas, S., Beveridge, T.J.: Mineral formation by bacteria in natural microbial communities. FEMS Microbiol. Ecol. **26**(2), 79–88 (1998)
6. Jongvivatsakul, P., Janprasit, K., Nuaklong, P., Pungrasmi, W., Likitlersuang, S.: Investigation of the crack healing performance in mortar using microbially induced calcium carbonate precipitation (MICP) method. Constr. Build. Mater. **212**, 737–744 (2019)
7. Manzur, T., Shams Huq, R., Hasan Efaz, I., Afroz, S., Rahman, F., Hossain, K.: Performance enhancement of brick aggregate concrete using microbiologically induced calcite precipitation. Case Stud. Constr. Mater. **11**, e00248 (2019)
8. Rong, H., et al.: Influence of bacterial concentration on crack self-healing of cement-based materials. Constr. Build. Mater. **244**, 118372 (2020)

9. Anbu, P., Kang, C.H., Shin, Y.J., So, J.S.: Formations of calcium carbonate minerals by bacteria and its multiple applications. Springerplus **5**(1), 1–26 (2016)
10. Mitchell, A.C., Espinosa-Ortiz, E.J., Parks, S.L., Phillips, A.J., Cunningham, A.B., Gerlach, R.: Kinetics of calcite precipitation by ureolytic bacteria under aerobic and anaerobic conditions. Biogeosciences **16**(10), 2147–2161 (2019)
11. Souradeep, G., Kua, H.W.: Encapsulation technology and techniques in self-healing concrete. J. Mater. Civ. Eng. ASCE **28**(12), 04016165-1–15 (2016)
12. Wani, I.Y., Singh, K.: Effect of encapsulated bacteria on concrete properties: a review. Mater. Today Proc. 1706–1712 (2019)
13. Wang, J.Y., Soens, H., Verstraete, W., De Belie, N.: Self-healing concrete by use of microencapsulated bacterial spores. Cem. Concr. Res. **56**, 139–152 (2014)
14. Zhang, J., et al.: Immobilizing bacteria in expanded perlite for the crack self-healing in concrete. Constr. Build. Mater. **148**, 610–617 (2017)
15. Xu, J., Yao, W., Jiang, Z.: Non-ureolytic bacterial carbonate precipitation as a surface treatment strategy on cementitious materials. J. Mater. Civ. Eng. ASCE **26**(5) (2014)
16. Mohammed, H., Ortoneda-Pedrola, M., Nakouti, I., Bras, A.: Experimental characterisation of non-encapsulated bio-based concrete with self-healing capacity. Constr. Build. Mater. **256**, 119411 (2020)
17. Wu, M., Hu, X., Zhang, Q., Cheng, W., Di, X., Zhao, Y.: Application of bacterial spores coated by a green inorganic cementitious material for the self-healing of concrete cracks. Cem. Concr. Compos. **113**(103718) (2020)
18. Mondal, S., Ghosh, A.: Investigation into the optimal bacterial concentration for compressive strength enhancement of microbial concrete. Constr. Build. Mater. **183**, 202–214 (2018)

Seismic Response of Liquid Storage Tank Isolated with Double Sliding Isolator with Variable Curvature (DSIVC)

J. P. Rathod , **V. R. Panchal** , **and D. P. Soni**

Abstract The paper describes the earthquake response of liquid storage tank that has been isolated with double sliding isolator with variable curvature (DSIVC). Under six near-fault bilateral earthquake ground excitations, a DSIVC isolated liquid storage tank is studied. A DSIVC isolator is made up of two sliding surfaces variable in curvature and slider positioned between the two sliding plates. A double sliding isolator has double isolator displacement capacity compared to single sliding isolator with same size therefore flexibility in designing. A geometric function formula is used to calculate the response quantities from a liquid storage tank that has been isolated with DSIVC. Newmark's step-by-step approach is used to solve a governing equation of motion. Convective, impulsive, and rigid masses are linked to a liquid storage tank detached using DSIVC. A DSIVC-isolated liquid storage tank has four response quantities: Convective, impulsive and isolator displacement, and base shear. For parametric study DSIVC isolator four design cases are considered for different geometry of sliding surfaces at the top and bottom and values of response quantities obtained. A liquid storage tank isolated using DSIVC isolator is compared to the identical liquid storage tank isolated with DVCFPS for a comparative research. It was observed that isolator displacement and convective displacement reduces after installation of DSIVC and base shear and impulsive displacement increases after installation of DSIVC as compared to DVCFP isolated liquid storage tank.

Keywords Double Sliding Isolator with Variable Curvature (DSIVC) · Double variable curvature friction pendulum system (DVCFPS) · Bilateral earthquake ground motion · Response quantities

J. P. Rathod (✉) · V. R. Panchal
M. S. Patel Department of Civil Engineering, Chandubhai S. Patel Institute of Technology, Charotar University of Science and Technology, Changa, Gujarat, India
e-mail: rathodjayrajsinh9@gmail.com

V. R. Panchal
e-mail: vijaypanchal.cv@charusat.ac.in

D. P. Soni
Civil Engineering Department, Sardar Vallabhbhai Patel Institute of Technology, Gujarat Technological University, Vasad, Gujarat, India

1 Introduction

In the past, many near-fault ground earthquakes occurred, which caused structural instability and damage to various utility structures like liquid storage tanks. Many essential liquids and gases are stored in liquid storage tanks, which are necessary in industry, power plants, and agriculture. The damage in the storage structure leads to utility loss, economic loss, and spilling liquids that should not come into direct contact with the atmosphere pollutes the ecosystem. Furthermore, tanks storing flammable substance might cause a large scale fire in the surrounding area, which could result in the loss of life [1].

The designing of structures under this type of ground motion makes construction very costly. Therefore, seismic isolation is demonstrated in numerous studies to be one of the most effective strategies for protecting structural or non-structural components from earthquakes. Seismic isolation is basically the separation of a superstructure from harmful earthquake excitation coming from the foundation of the structure by the insertion of an isolator between the superstructure and the foundation of the structure.

Presently there are many isolators available for the seismic isolation from which sliding type isolators are commonly used for the structure isolation under far-field and regular earthquake events. Pendulum isolators feature a spherical sliding surface with an uniform curvature, resulting in uniform isolation stiffness and vibration period. The advantages of an isolation system with friction pendulum isolators are as follows: (i) An invariant isolation period (ii) Lower eccentricity (iii) Higher buckling stability (iv) Higher vertical rigidity due to following advantages friction pendulum isolator was applied in many isolation systems of structures worldwide [2].

In past different isolation techniques are used and it was studied by Panchal and Soni [3] in 2013. VFPS isolates a liquid storage tank is investigated by Panchal and Jangid [4] in 2008. Behaviour of broad and slender under near fault earthquake ground motions, a liquid storage tank isolated by VCFPS is examined by Panchal and Jangid in 2012 [5]. DVFPI isolated liquid storage tank is examined under 20 far field ground motion is studied by Soni et al. in 2011 [1].

The author Lu et al. recently investigated the practicality of a passively adaptable isolator known as a double sliding isolator with variable curvature (DSIVC). A DSIVC is often constructed with an top and bottom sliding surfaces of varying circumference, as well as a slider in the between. Because a DSIVC contains two sliding plates with varying circumference, it also contains the majority of the benefits of ordinary sliding-type isolators, although it is adaptable and has double the displacement capabilities [2].
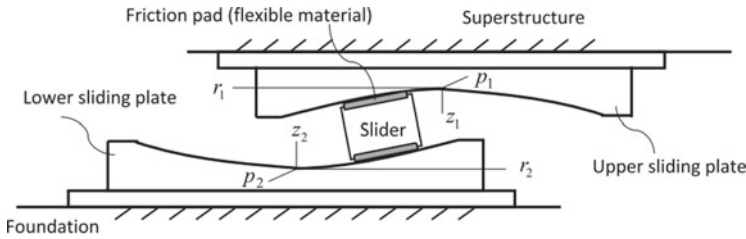
Fig. 1 Schematic diagram of variable curvature double sliding isolator [2]

2 Description of DSIVC

2.1 Geometry of DSIVC

A DSIVC isolator made up of a top and bottom two sliding surfaces having a slider sandwiched between both moving interfaces. In terms of physical properties, a DSIVC isolator is the same as a DVFPI. (Double variable friction pendulum isolator). It has two sliding surfaces; however they are not uniformly spherical and have a varied curvature. A DSIVC isolator the central axis of sliding surfaces is axially symmetrical axis z_1 and z_2 as shown in Fig. 1. But their curvature changes as they move along the radial coordinator r_1 and r_2. The geometric function $z_1 (r_1)$ and $z_2 (r_2)$ can be used to define the geometry of the two sliding surfaces and p_1, p_2 are the axis perpendicular to the r_1, r_2 and z_1, z_2 axis [2].

2.2 Restoring Force of DSIVC

As shown in Fig. 2 U_{r1} and U_{p1} are the component of lateral shear, exhibited by the DSIVC as well as perpendicular radial axes of the superstructure, The axial force acting on the DSIVC is denoted by W; r_1 represents the slider's sliding distance with reference to the top sliding plate's vertical centerline; The normal force of contact between both the slider as well as the top sliding plate is denoted by N_1. N_1's inclined vertical angle is represented by the symbol θ; $Fr1$ and $Fp1$ are the friction forces that are exerted in both the radial and perpendicular (circumferential) axes, $Fr1$ and $Fp1$ are both perpendicular to N1 [2].

$$U_{r1} + W tan\theta + \frac{F_{r1}}{\cos \theta} \tag{1}$$

$$N_1 = F_{r1} \tan \theta + \frac{W}{\cos \theta} \tag{2}$$
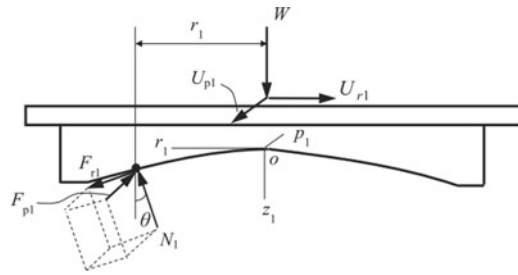
Fig. 2 Top sliding plate free body diagram (without considering moment effect) [2]

$$U_{p1} = F_{p1} \tag{3}$$

$$\tan \theta = z1'(r1) \ll 1 \tag{4}$$

$$U_{r1} = u_{r1}(r_2) + F_{r1} = W z_1'(r_2) + F_{r1} \tag{5}$$

$$U_{r2} = u_{r2}(r_2) + F_{r2} = W z_2'(r_2) + F_{r2} \tag{6}$$

$$U_{p2} = F_{p2} \tag{7}$$

In Fig. 3 it is shown DSIVC isolator mechanical property transists from softening behaviour to hardening behaviour
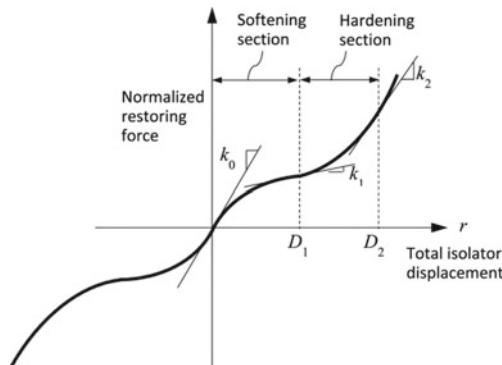
Fig. 3 Design specifications for the DSIVC's restoring force [2]

2.3 Effective Stiffness of DSIVC

Isolator stiffness for sliding surfaces at the top and bottom can be expressed as $k_{r1}(r_1)$ and $k_{r2}(r_2)$ [2].

$$k_{r1}(r_1) = \frac{u_{r1}(r_1)}{r_1}; \tag{8}$$

$$k_{r2}(r_2) = \frac{u_{r2}(r_2)}{r_2}; \tag{9}$$

Two sliding plates of isolator sliding surfaces at the top and bottom are in parallel as demonstrated in Fig. 1 so the restoring force acts as two springs are connected in series. The total displacement of top and bottom sliding surface of DSIVC r_1 and r_2 is equal to total displacement of DSIVC isolator $r = r_1 + r_2$. A DSIVC isolator effective stiffness k_{eff} is same as effective stiffness k_{eff} of the spring connected in series (1).

$$\frac{1}{k_{eff}(r)} = \frac{1}{k_{r1}(r1)} + \frac{1}{k_{r2}(r2)}; \tag{10}$$

$$k_{eff}(r) = \frac{k_{r1}(r1)k_{r2}(r2)}{k_{r1}(r1) + k_{r2}(r2)}; \tag{11}$$

2.4 Geometric Function of DSIVC Isolator

The axial load W is proportionate to the restoring force u_{r1} and u_{r2} of the DSIVC and the geometric function's first derivative $z_1(r_1)$ and $z_2(r_2)$ [2].

$$z_1'(r_1) = \frac{u_{r1}}{w} \tag{12}$$

$$z_2'(r_2) = \frac{u_{r2}}{w} \tag{13}$$

In this study, $z_1'(r_1)$ and $z_2'(r_2)$ are also referred to as the normalized restoring force.

$$z_1(r_1) = \frac{a_1}{8}r_1^8 + \frac{b_1}{6}r_1^6 + \frac{c_1}{4}r_1^4 + \frac{d_1}{2}r_1^2 \tag{14}$$

$$z_1'(r_1) = a_1 r_1^7 + b_1 r_1^5 + c_1 r_1^3 + d_1 r_1 \tag{15}$$

$$a_1 = -55361, b_1 = 7967.4, c_1 = -154.1, d_1 = 1.786 \tag{16}$$

So from the above equations we get normalized restoring force

$$z_1'(r_1) = -55361r_1^7 + 7967.4r_1^5 - 154.1r_1^3 + 1.786r_1 \tag{17}$$

$$z_2'(r_2) = -55361r_2^7 + 7967.4r_2^5 - 154.1r_2^3 + 1.786r_2 \tag{18}$$

$$u_{(r1)} = Wz_1'(r_1) \tag{19}$$

$$u_{(r2)} = Wz_2'(r_2) \tag{20}$$

$u_{(r1)}$ and $u_{(r2)}$ are the restoring force of top and bottom sliding surface of DSIVC isolator [2].

3 Modelled DSIVC Isolated Liquid Storage Tank

Haroun's [6] proposed base isolation modelling makes use of a liquid storage tank. Figure 4(a) depicts a liquid storage tank being isolated one at a time with the above-mentioned isolators. It is considered that the stored liquid is inviscid, incompressible, and has irrotational flow. The entire fluid mass of the tank shakes in three variations during an earthquake: Convective or sloshing, impulsive, and rigid mass. The modes of vibration of a convective and an impulsive mass are distinct, but for response assumption, the convective mode is used first, followed by the impulsive mode. The lumped masses in this case are the impulsive mass (mi), sloshing mass (mc), and rigid mass (mr).

For analysis, a three-degree-of-freedom system is used, with u_b, u_i, and u_c as illustrated in Fig. 4(b), indicating in the sequence of absolute rigid displacement of masses, the impulsive displacement of masses, and the displacement of masses caused by sloshing.

The system takes into account the following suppositions:

1. The storage tank own weight is neglected because it is so little.
2. The damping ratio is used to determine the damping coefficient of impulse and convection mass motion.
3. The relative velocity of sliding surfaces is unaffected by coefficient of friction of isolation system.
4. It is expected that the isolator's slider stays in connection with the sliding surfaces.

(a) DSIVC detached model of a fluid storage tank

(b) Mathematical modelling of fluid storage tank [1]
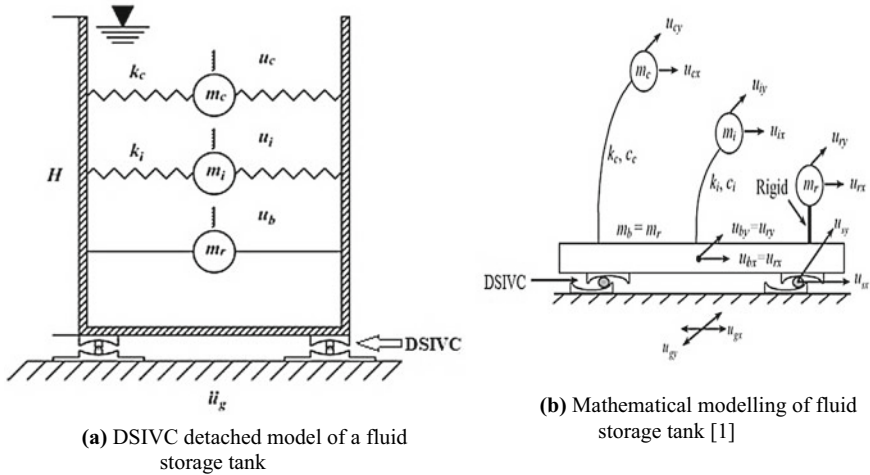
Fig. 4 **a** DSIVC detached model of a fluid storage tank **b** Mathematical modelling of fluid storage tank [1]

The following is a mathematical model of a ground resting fluid storage tank segregated by the isolators stated previously. The m_c, m_i and m_r in terms of fluid mass m, and different mass proportion for $t_h/R = 0.004$ are presented as follows:

$$m_c = Y_c m \tag{20}$$

$$m_i = Y_i m \tag{21}$$

$$m_r = Y_r m \tag{22}$$

$$m = \pi R^2 H \rho_w \tag{23}$$

$$Y_c = 1.01327 - 0.87578 * S + 0.35708 * S^2 0.06692 * S^3 + 0.00439 * S^4 \tag{24}$$

$$Y_i = -0.15467 + 1.21716 * S - 0.62839 * S^2 + 0.14434 * S^3 - 0.0125 * S^4 \tag{25}$$

$$Y_r = -0.01599 + 0.86356 * S - 0.30941 * S^2 + 0.04083 * S^3 \tag{26}$$

where Y_c, Y_i, and Y_r are the ratio of masses indicated before; Proportion of radius to height of tank, $S = H/R$; ρ_w represents retaining fluid's mass density; R is radius of tank; and H denotes the fluid's height.

Following formulaes expresses the convective and impulsive mass fundamental frequency, ω_c and ω_i, respectively:

$$\omega_c = \sqrt{1.84\left(\frac{g}{R}\right)\tanh(1.84S)} \tag{27}$$

$$\omega_i = \frac{P}{H}\sqrt{\frac{E}{\rho_s}} \tag{28}$$

where g is gravitational acceleration; E represents elasticity modulus, ρ_s represents density of tank wall and P would be calculated by:

$$P = 0.037085 + 0.084302 * S - 0.05088 * S^2 + 0.012523 * S^3 - 0.0012 * S^4 \tag{29}$$

The damping and stiffness, which are comparable to the impulsive and convective masses, are defined as follows:

$$c_c = 2\xi_c m_c \omega_c \tag{30}$$

$$c_i = 2\xi_i m_i \omega_i \tag{31}$$

$$k_c = m_c \omega_c^2 \tag{32}$$

$$k_i = m_i \omega_i^2 \tag{33}$$

where ξ_i and ξ_c represent the damping ratios of impulsive and sloshing mass, respectively.

4 Governing Equation of Motion

For a liquid holding tank with isolation, the equation determining the motion is represented in form of matrix as follows:

$$[m]\{\ddot{x}\} + [c]\{\dot{x}\} + [k]\{x\} + \{F\} = -[m]\{r\}\ddot{u}_g \tag{34}$$

where $[m]$ explicates mass matrix, $[c]$ explicates damping matrix and $[k]$ is the stiffness matrix; $\{x\} = \{x_c, x_i, x_b\}^T$; where $x_c = u_c - u_b$ is convective mass displacement, $x_i = u_i - u_b$ indicates the impulsive mass's displacement in proportion to the bearing's displacement and $x_b = u_b - u_g$ is bearing displacement as it relates to ground motion; $\{F\} = \{0, 0, F_x\}$ represents the vector of friction forces; $\{r\} = \{0, 0, 1\}^T$ represents influencing coefficient vector; F_x represents the isolators' friction force; and $\ddot{u}_g$ shows the ground acceleration caused by seismic activity. T signifies the transpose.

5 Numerical Study

The earthquake response of slender and broad water storage tank detached with DSIVC for six near-fault ground excitations are studied. The characteristics of the six near fault ground excitation are given as per Table 1. The various response quantities are base-shear *(Fb)*, isolator *(xb)*, impulsive *(xi)* and convective *(xc)* displacements. Parameters required to define for slender and broad tank are (i) damping ratio *(ξc and ξi)* are 0.5 and 2% for both slender and broad (ii) Elastic modulus *(E)* for slender and broad tank is 200GPa. (iii) Density of steel *(ρs)* for slender and broad tank is 7900 kg/m^3. (iv) Aspect ratio S *(H/R)* is 0.6 for broad and 1.85 for slender tank. (v) Height *(H)* is 14.6 for broad tank and 11.3 for slender tank. (vi) Radius of tank is 24.33 m for broad tank and 6.11 m for slender tank. (v) Thickness of tank wall is 97.32 mm for broad tank and 24.44 mm for slender tank. (vi) Natural frequency *(w_c and w_i)* is 0.123 and 3.944 Hz for broad tank and 0.273 and 5.963 Hz for slender tank. For comparative study double sliding isolator with variable curvature (DSIVC) and double variable curvature friction pendulum system (DVCFPS) isolators are used for four different design cases (A) $(T_1 < T_2$ and $\mu_1 < \mu_2)$ (B) $(T_1 = T_2$ and $\mu_1 = \mu_2)$ (C) $(T_1 = T_2$ and $\mu_1 < \mu_2)$ (D) $(T_1 < T_2$ and $\mu_1 = \mu_2)$ as given in Table 2. Tables 3 and 4 compares the maximum values of reaction quantities of slender and broad tanks isolated using DSIVC and DVCFP.

Table 1 Properties of six near fault ground excitations [4]

Near-Fault ground excitations	Normal component		
	PGD (cm)	PGV (cm/s)	PGA (g)
1979, Imperial Valley (El Centro Array #5)	76.5	98	0.37
1979, Imperial Valley (El Centro Array #7)	49.1	113	0.46
1994, Northridge (Newhall)	38.1	119	0.72
1992, Landers (Lucerne Valley)	230	136	0.71
1994, Northridge (Rinaldi)	39.1	175	0.89
1994, Northridge (Sylmar)	31.1	122	0.73

Table 2 DSIVC isolator four different design instances

Cases	T_1 (sec)	T_2 (sec)	T_{IC} (sec)	μ_1	μ_2	μ_c
A	2	2.5	3.202	0.05	0.07	0.062
B	2.264	2.264	3.202	0.062	0.062	0.062
C	2.264	2.264	3.202	0.05	0.05	0.062
D	2	2.5	3.202	0.062	0.062	0.062

Table 3 Maximum response quantities for slender water storage tank isolated with DSIVC and DVCFP

Earthquakes	Cases	x_c (mm)		x_i (mm)		x_b (mm)		F_b (W)	
		DSIVC	DVCFPS	DSIVC	DVCFPS	DSIVC	DVCFPS	DSIVC	DVCFPS
1979, Imperial Valley (El Centro Array #5)	A	1758.0	1976.5	3.03	1.55	425.92	382.56	0.38	0.16
	B	1634.1	1952.6	2.73	1.56	404.01	379.56	0.34	0.16
	C	1763.0	2027.3	3.07	1.58	427.49	392.68	0.39	0.17
	D	1640.5	1952.8	2.74	1.55	404.69	379.48	0.34	0.16
1979, Imperial Valley (El Centro Array #7)	A	2010.6	2156.3	3.36	1.75	443.58	374.86	0.40	0.17
	B	2018.7	2114.2	3.25	1.69	438.31	361.11	0.37	0.17
	C	2005.0	2188.2	3.55	1.76	446.99	386.04	0.42	0.17
	D	2013.7	2112.9	3.31	1.69	439.99	361.34	0.38	0.16
1994, Northridge (Newhall)	A	659.27	1052.9	1.47	1.48	331.40	270.20	0.16	0.15
	B	669.27	1058.5	1.39	1.49	317.85	257.69	0.14	0.14
	C	659.01	1057.4	1.45	1.50	330.47	273.05	0.16	0.15
	D	671.26	1059.3	1.39	1.48	317.25	257.82	0.14	0.14
1992, Landers (Lucerne valley)	A	439.29	1614.7	5.34	2.05	271.10	423.80	0.09	0.17
	B	585.38	1614.3	5.13	2.07	353.29	423.75	0.09	0.18
	C	439.03	1704.3	5.33	1.73	269.75	445.42	0.09	0.18
	D	433.29	1662.0	5.34	1.71	271.10	435.24	0.09	0.18

Table 3 (continued)

| Earthquakes	Cases	x_c (mm)		x_i (mm)		x_b (mm)		F_b (W)	
		DSIVC	DVCFPS	DSIVC	DVCFPS	DSIVC	DVCFPS	DSIVC	DVCFPS
1994, Northridge (Rinaldi)	A	913.83	929.14	4.34	2.03	464.82	429.13	0.48	0.18
	B	895	926.77	3.99	2.10	455.91	424.70	0.45	0.18
	C	913.84	934.64	4.33	2.04	465.13	434.02	0.48	0.18
	D	895	926.81	3.99	2.11	455.92	424.71	0.45	0.17
1994, Northridge (Sylmar)	A	1440.9	1519.1	4.26	2.18	461.72	471.13	0.49	0.18
	B	1157.5	1483.8	3.34	2.14	438.45	460.10	0.38	0.18
	C	1440.9	1549.7	4.26	2.25	461.72	477.27	0.49	0.19
	D	1157.5	1519.1	3.34	2.15	438.45	460.11	0.38	0.18

Table 4 Maximum response quantities for broad water storage tank isolated with DSIVC and DVCFP

Earthquakes	Cases	x_c (mm)		x_i (mm)		x_b (mm)		F_b (W)	
		DSIVC	DVCFP	DSIVC	DVCFP	DSIVC	DVCFP	DSIVC	DVCFP
1979, Imperial Valley (El Centro Array #5)	A	1310.6	1346.0	4.12	4.13	294.80	186.4	0.09	0.13
	B	1385.8	1351.8	4.51	4.08	277.0	183.5	0.09	0.12
	C	1347.5	1354.7	4.10	4.23	296.95	193.5	0.10	0.13
	D	1349.5	1351.9	4.48	4.08	273.94	183.6	0.09	0.12
1979, Imperial Valley (El Centro Array #7)	A	1163.6	1147.1	3.90	5.67	326.13	235.13	0.12	0.13
	B	1127.1	1168.7	3.98	5.16	320.16	227.17	0.12	0.13
	C	1116.1	1132.2	4.01	5.38	327.99	244.70	0.13	0.13
	D	1080.6	1167.6	4.11	5.11	322.12	227.63	0.12	0.12
1994, Northridge (Newhall)	A	447.21	685.3	4.46	7.09	260.0.21	617.24	0.08	0.19
	B	439.03	684.5	5.33	7.17	269.75	607.79	0.09	0.19
	C	444.34	683.4	4.46	7.08	259.83	621.33	0.08	0.20
	D	439.29	684.6	5.34	7.16	271.10	607.64	0.09	0.19
1992, Landers (Lucerne valley)	A	439.03	1955.7	5.34	4.55	269.75	183.23	0.09	0.12
	B	439.29	1955.0	5.33	5.07	271.10	170.86	0.09	0.12
	C	439.29	1958.2	5.34	4.70	271.10	191.71	0.09	0.12
	D	439.03	1955.3	5.33	5.06	269.75	170.99	0.09	0.11
1994, Northridge (Rinaldi)	A	702.26	660.93	8.36	7.64	398.32	425.58	0.25	0.18
	B	702.25	647.80	8.36	7.95	398.32	411.56	0.25	0.17
	C	702.22	662.72	8.36	7.76	398.32	423.20	0.25	0.18
	D	702.24	647.96	8.36	7.95	398.32	411.68	0.25	0.17
1994, Northridge (Sylmar)	A	588.14	686.73	3.99	5.81	354.32	370.38	0.15	0.15
	B	539.66	671.88	4.26	6.08	308.62	356.91	0.10	0.15
	C	585.38	692.42	3.34	5.94	353.29	379.12	0.15	0.16
	D	539.66	671.88	4.26	6.08	308.65	356.91	0.10	0.15
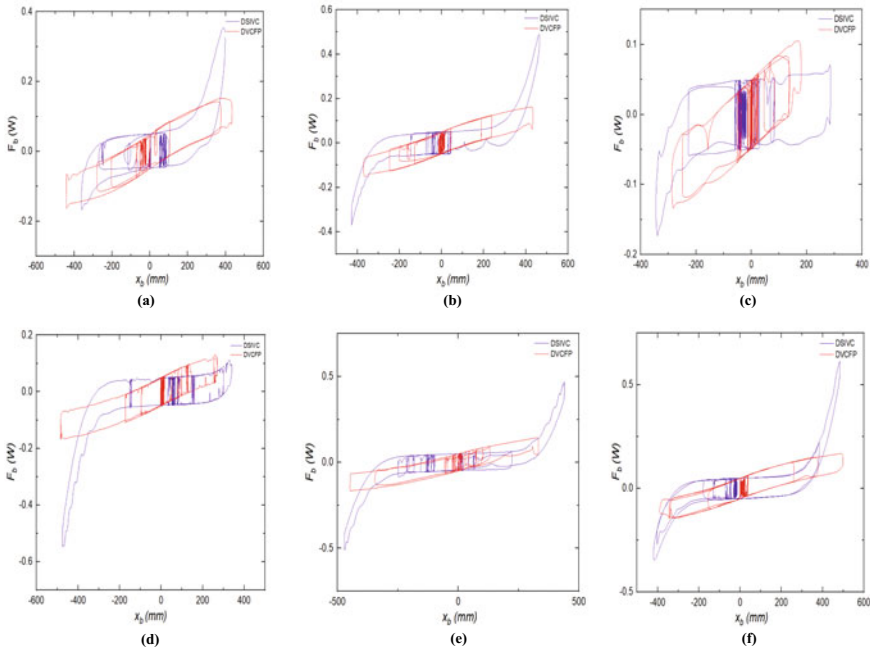
Fig. 5 Graph showing comparison of Isolator displacement vs Base shear (hysteresis loop) of slender water storage tank detached with DSIVC and DVCFP under six near fault bidirectional ground motions **a** 1979, Imperial Valley (EI Centro Array #5) **b** 1979, Imperial Valley (EI Centro #7) **c** 1994, Northridge (Newhall) **d** 1992, Northridge (Rinaldi) **e** 1994 Northridge (sylmar)

The variation of F_b with respect to x_b of slender and broad tank for near-fault ground motions are presented in graphical form (Figs. 5 and 6). The seismic responses (i.e., F_b, x_c, x_i and x_b) of slender liquid storage tank are determined for various near-field ground motion and presented in the form of graph (Figs. 7 and 8). From all the quantities of interest, relative isolator displacement is much important for designing of DSIVC. With a view to examine the efficiency of DSIVC, earthquake response of tank with DSIVC is compared with that of DVCFP. Tables 3 and 4 shows the comparison of peak value of F_b (Base shear), x_c (Convective displacement), x_i (Impulsive displacement) and x_b (Isolator displacement) of slender and broad liquid storage tank isolated with DSIVC and DVCFP.
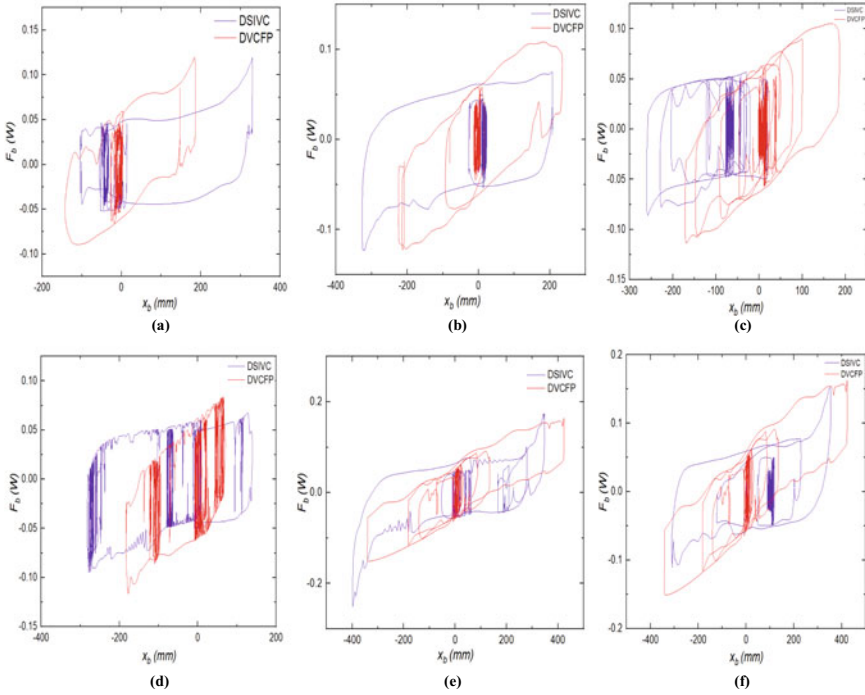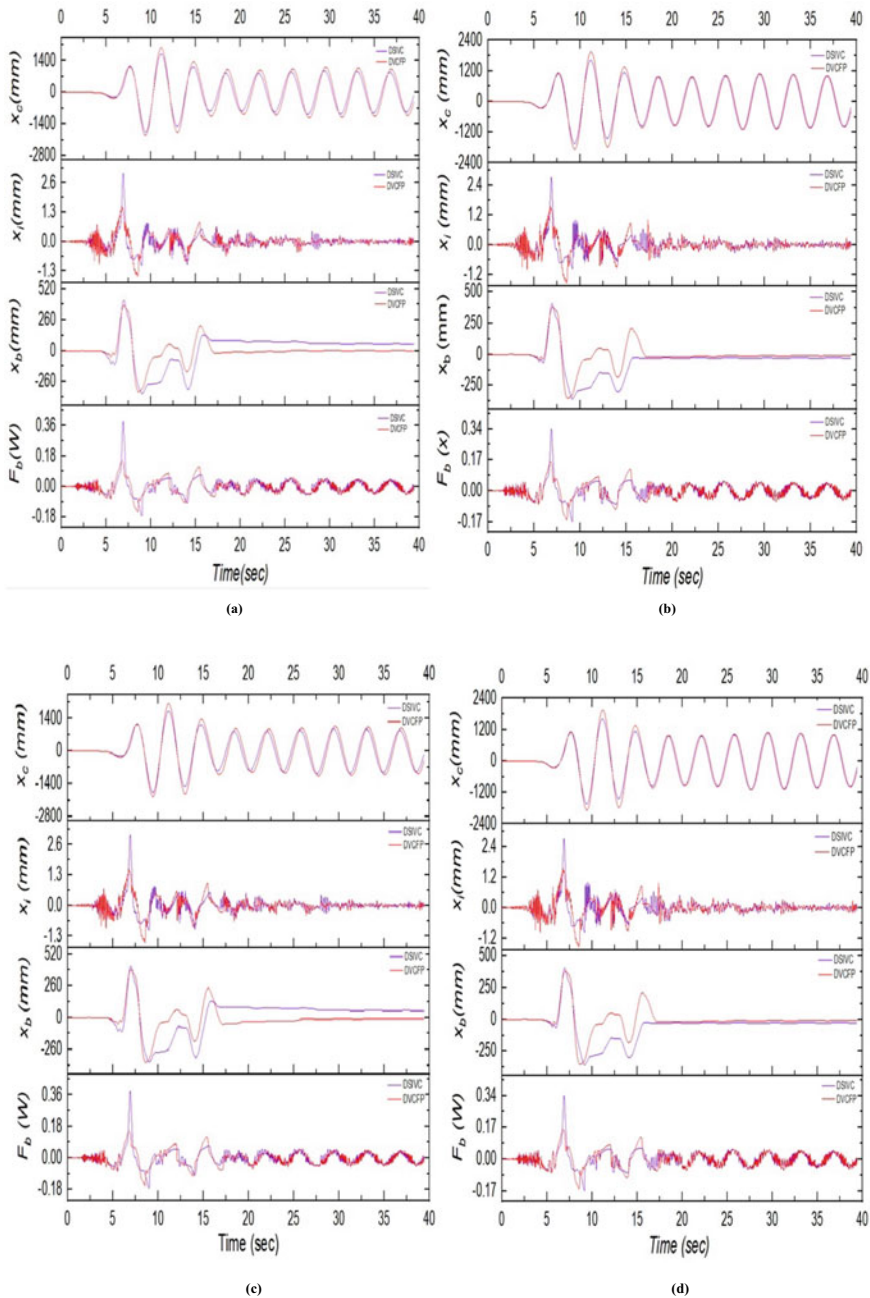
Fig. 6 Graph showing comparison of Isolator displacement vs Base shear (hysteresis loop) of broad water storage tank detached with DSIVC and DVCFP under six near fault bidirectional ground motions **a** 1979, Imperial Valley (EI Centro Array #5) **b** 1979, Imperial Valley (EI Centro #7) **c** 1994, Northridge (Newhall) **d** 1992, Northridge (Rinaldi) **e** 1994 Northridge (sylmar)

(a)

(b)

(c)

(d)

Fig. 7 Graph showing comparison of time variation of response quantities F_b, x_b, x_i, x_c of isolated slender water storage tank detached with DSIVC and DVCFP under 1979, Imperial Valley (El Centro Array #5) for different isolator design cases **a** Case A ($\mu_1 < \mu_2$ and $T_1 < T_2$); **b** Case B ($\mu_1 = \mu_2$ and $T_1 = T_2$); **c** Case C ($\mu_1 < \mu_2$ and $T_1 = T_2$); **d** Case D ($\mu_1 = \mu_2$ and $T_1 < T_2$)

(a)

(b)

(c)

(d)
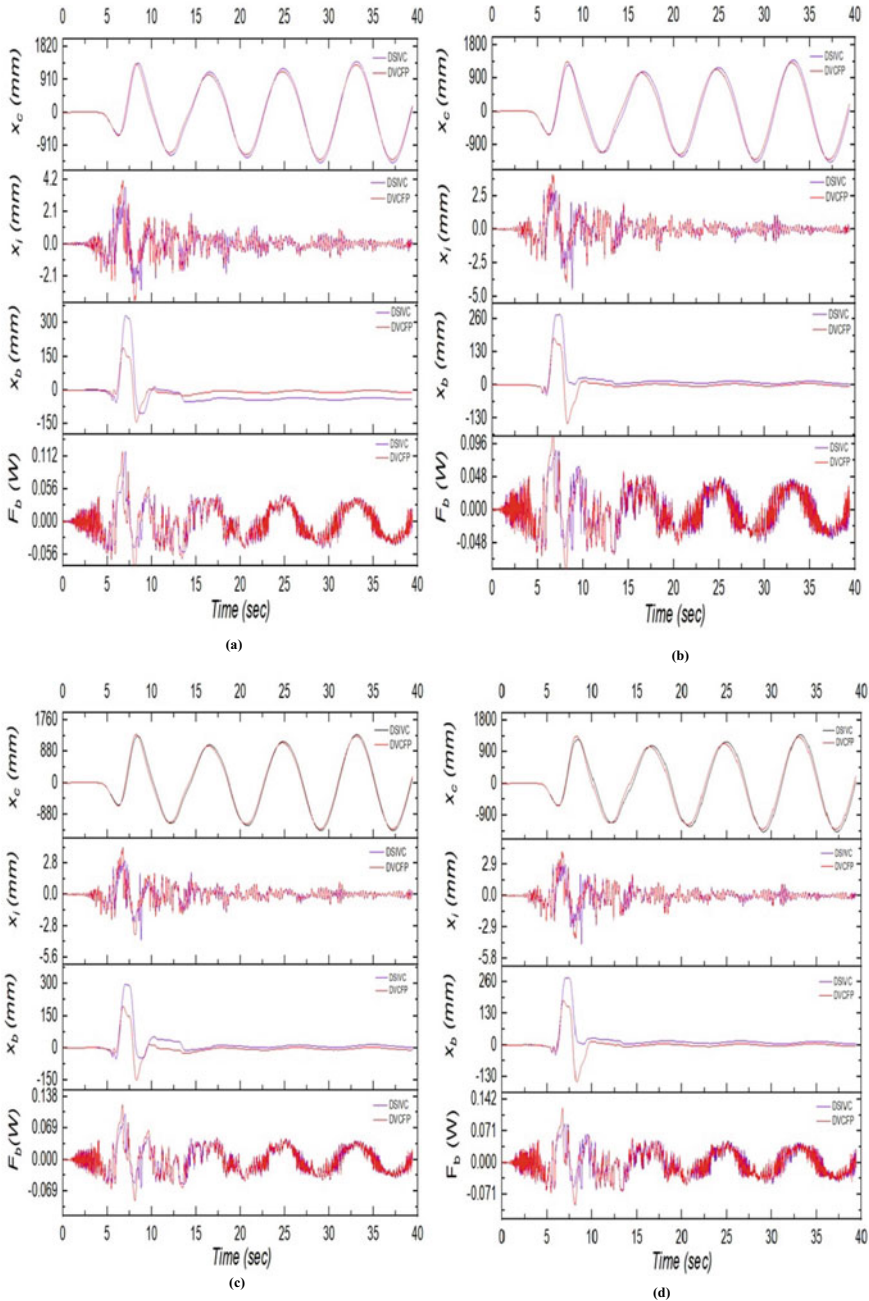
Fig. 8 Graph showing comparison of time variation of response quantities Fb, xb, xi, xc of isolated broad water storage tank detached with DSIVC and DVCFP under 1979, Imperial Valley (El Centro Array #5) for different isolator design cases **a** Case A ($\mu_1 < \mu_2$ and $T_1 < T_2$); **b** Case B ($\mu_1 = \mu_2$ and $T_1 = T_2$); **c** Case C ($\mu_1 < \mu_2$ and $T_1 = T_2$); **d** Case D ($\mu_1 = \mu_2$ and $T_1 < T_2$)

6 Conclusions

The earthquake response of slender and broad water storage tank under six bilateral near-fault earthquake ground excitations isolated with DSIVC and DVCFP isolator and value of response quantities compared and examined DSIVC isolator's efficiency. For comparative study, time variation of response quantities convective, impulsive, isolator displacements and base shear graph plotted and force-displacement hysteresis loop graph plotted and compared. For the parametric investigation, various isolator design instances with varying coefficients of friction and initial time periods are used.

1. The DSIVC is more efficient as compared to DVCFP in reducing the isolator displacement in broad tank, but in slender tank DVCFP is more efficient in reducing the isolator displacement than DSIVC.
2. Convective displacement reduces after installation of DSIVC isolator as compared to DVCFP isolator in slender and broad liquid storage tanks.
3. Impulsive displacement and base shear are increasing after installation of DSIVC isolator compared to DVCFP isolator in slender and broad liquid storage tanks.
4. From the force-displacement hysteresis loops, it can be noted that under six bilateral near fault ground motions, base shear and isolator displacement increase after installation of DSIVC isolator.

References

1. Soni, D.P., Mistry, B.B., Panchal, V.R.: Double variable frequency pendulum isolator for seismic isolation of liquid storage tanks. Nucl. Eng. Des. **241**(3), 700–713 (2011)
2. Lu, L.Y., Huang, H.W., Wu, Y., Wang, S.J.: Theory and experimental verification of a double sliding isolator with variable curvature. Eng. Struct. **238**, 112265 (2021)
3. Panchal, V.R., Jangid, R.S.: Variable friction pendulum system for near-fault ground motions. Struct. Control Health Monitoring Official J. Int. Assoc. Struct. Control Monitoring Eur. Assoc. Control Struct. **15**(4), 568–584 (2008)
4. Panchal, V.R., Jangid, R.S.: Behaviour of liquid storage tanks with VCFPS under near-fault ground motions. Struct. Infrastruct. Eng. **8**(1), 71–88 (2012)
5. Panchal, V.R., Soni, D.P.: Seismic behaviour of isolated fluid storage tanks: a-state-of-the-art review. KSCE J. Civ. Eng. **18**(4), 1097–1104 (2014)
6. Haroun, M.A.: Vibration studies and tests of liquid storage tanks. Earthq. Eng. Struct. Dyn. **11**(2), 179–206 (1983)

Monitoring and Analysis of Surface Cracks in Concrete Using Convolutional Neural Network

Harsh Kapadia, Nimit Soneji, Anirudha Rotti, Paresh V. Patel, and Jignesh B. Patel

Abstract Reinforced concrete is widely used for construction of infrastructure projects like bridges, buildings, highways, dams, and power plants etc. Monitoring structural health of infrastructure projects is essential for their uninterrupted functioning. Generally physical inspections are carried out to detect defects in structures for further rectification. With recent advancements in computational algorithms, machine vision based inspection is emerging as an efficient technique for monitoring structural health of structures. Surface cracks in concrete structures are one of the important indicators of its health and enable the assessment of serviceability of the structures. The present work aims to address the issue by developing a novel system using machine vision and deep learning. A convolutional neural network-based methodology is developed to detect surface cracks in concrete cube images. The implementation of proposed methodology is demonstrated through monitoring of crack development in concrete cubes of size $150 \times 150 \times 150$ mm with different compression strengths. The concrete cubes are subjected to compression loading in a standard compression testing machine. The analysis results in location, area, length, and number of cracks in synchronization with the applied compression load. The number of cracks, area of cracks, and length of cracks with respect to compression load are acquired using the developed system for different grades of concrete cubes. Results show that cracks detection and monitoring have been accurately performed with the developed system. The observations obtained from the crack load analysis can be very useful for improved understanding of concrete behaviour. The data acquired and observations can help professionals for improved structural health monitoring.

Keywords Structural health monitoring · Concrete structures · Crack detection · Convolutional neural network · Artificial intelligence

H. Kapadia (✉) · N. Soneji · A. Rotti · P. V. Patel · J. B. Patel
Institute of Technology, Nirma University, Ahmedabad 382481, Gujarat, India
e-mail: harsh.kapadia@nirmauni.ac.in

1   Introduction

Concrete is one of the most widely used materials in building infrastructures across the world. Annually, tons of concrete is used around the world for construction of various types of structures. Due to which there is immense potential of the structural health monitoring in the field for concrete structures [1]. Once the concrete infrastructures are built, engineers face a major issue related to the inspection of these structures and monitoring structural health for public safety. It is extremely challenging to inspect these huge structures manually by human experts. The problem can be addressed by automation, computer vision and artificial intelligence (AI) based advanced monitoring and damage assessment solutions. Conventionally the inspections and monitoring of structures are carried out manually and in a periodic manure [2]. The process is not only time consuming and costly, but it also requires a lot of intensive work in order to cover the huge structures. On the other hand, monitoring the health of these structures is crucial as many human lives and properties can be affected by their failure. In order to perform structural health monitoring and looking into the potential of the area, researchers have proposed different monitoring and assessment solutions using computer vision based intelligent methods. The methods cover a wide range of algorithms, methodologies, approaches using the domain like image processing, computer vision, artificial intelligence, unmanned aerial vehicles and advance sensor technologies. A semi-automatic computer vision tool was proposed by Gordan et al. [3], to inspect and analyse a Romanian hydro dam. The authors applied digital image enhancement on the features of the dam surface. The images were then used for expert analysis. Dinh et al. [4] used a machine vision based automatic crack detection method. The authors have proposed a peak detection algorithm for image segmentation using various image processing techniques. Additionally, researchers have also presented good work on real time monitoring of large concrete structures using deep learning [5].

The advancement of machine vision and artificial intelligence has made it simpler to address and solve real-world problems that were previously overlooked owing to a lack of understanding and technology. Machine vision is particularly useful for automated inspection owing to its efficiency, reliability and industrial performance. It also aids in the reduction of inspection time and expense for an application. Artificial Intelligence (AI) is used to drive the analysis component post the vision system. Recently, AI based solutions are proving useful in prediction, monitoring, and analysis-based applications. Due to which, experts are now working on artificial intelligence and machine vision-based systems for structural health monitoring of concrete structures. Majority of researchers utilized digital image enhancement/processing techniques as a solution to the problem of automated inspection. Colour map-based visualization, fuzzy sets, and computer image analysis were used to obtain the objective. An algorithm which is linked to a sophisticated system of hardware and software modules, measurement equipment, and a central database was deployed. Cracks were detected using gradient-based edge detection, then fuzzy edge enhancement methods and colour map-based visualization were applied. The

application required human assistance for analysis of extracted data. Pereira et al. [6] developed an embedded system for unmanned aerial vehicles (UAV) that employs image processing methods such as image segmentation using edge detection and crack detection using particle filters. The overall goal of the work was to deploy the solution in civil constructions in order to check building autonomously. A similar approach using UAV coupled with an additional ultrasonic distance sensors and Wi-Fi modules was proposed by Kim et al. [7]. The images were acquired using on-board camera, Raspberry Pi and processed in order to estimate the crack width. Dorafshan et al. [8] demonstrated an automated crack detection utilizing Otsu thresholding and morphological operations. A method was developed for faster detection of tiny to medium anomalies. Furthermore, some works demonstrated highly effective image processing-based techniques for a variety of applications, although the task at hand was to identify abnormalities like cracks on concrete. Chaudhuri et al. [9] demonstrated how blood vessels in the retina were detected using a specific image processing technique using two-dimensional matched filters. These approaches can be used in concrete crack detection applications since the images are tiny and the detection is extremely accurate. In another study conducted by Zhang et al. [10], pavement cracks were detected using a similar matched filter algorithm which was used for detection of blood vessels in retina. German et al. [11] proposed a novel approach to detect damage post earthquake automatically using local entropy-based thresholding algorithm, global adaptive thresholding algorithm, morphological operations and template matching. A visual based inspection technique for bridge inspection was proposed by Chul Min Yeum et al. [12]. The authors proposed a method to automatically process and analyze large number of images in order to detect crack near bolts.

Conventional image processing based techniques suffer from variety of limitations like blurred image, poor illumination, shadow, noise, dents, color variations, etc. Furthermore, image processing based solution may fail or be ineffective for materials and surface having high variation in size, shape, color, etc. In recent years, artificial intelligence has proven significant in solving the applications with inherent data variations. Various researchers have utilized the advantages of machine learning and deep learning-based approaches for different crack detection applications. Omar et al. [13] reported work to showcase the usage different machine learning approaches in structural health monitoring along with their compatibility. Żarski et al. [14] developed a software package that allows developers to create training data and detect cracks in infrastructure using a transfer learning technique. Furthermore, the European Union sponsored the work through the European Social Fund. Similarly, Zhang et al. [15] created an architecture based on Convolutional Neural Networks (CNN) called CrackNet specifically for crack detection. An automated pavement crack detection solution was developed using this architecture where 3D asphalt surface images were acquired using off-the-shelf 3D hardware and pixel perfect accurate solution was developed. An advanced and improved version of CrackNet was introduced by Zhang et al. [16]. The version has a deeper architecture with more hidden layers and removed the feature generator layers. These changes increased the efficiency of crack detection along with improvements in the speed of the inspection. In another

study proposed by Fan et al. [17], a deep learning model was developed. The authors focused on frequency relationship and space optimization of the image. The model was named as Residual Attention and Octave UNet (RAO-UNet). It splits image information into high frequency (thin cracks) and low frequency (rough cracks) components and detects sharp changes from one frequency domain into another. The concept was proposed by Yunpeng et al. [18] to store and process feature maps that vary spatially "slower" at a lower spatial resolution reducing both memory and computation cost. Cha et al. [19] developed a vision-based method using CNN for detecting concrete cracks. A sliding window technique was used to scan pictures and comparative analysis of crack detection performance using classic image processing approaches against CNN models was presented. Tayo et al. [20] developed a machine vision-based portable pavement crack width estimator. Raspberry pie was used to make the portable setup. Crack identification was carried out utilizing a variety of image processing techniques, followed by the development of a width calculation technique. A new approach in CNN called DeepCrack which does prediction using semantic segmentation where pixel-based labeling of cracks is applied was developed by Liu et al. [21].

Piyathilaka et al. [22] worked on real time concrete crack detection using transfer learning approach. Authors implemented an algorithm named YOLACT and trained it using transfer learning approach. The YOLACT model was pretrained on COCO dataset due to the low size of dataset. Another transfer learning based approach [23] was done by Su et al. where authors used various transfer learning approaches, among them inception-v3 had higher accuracy and lower training time. In another study authors detected concrete cracks using transfer learning approach and did comparative study between GoogLeNet and ResNet18 [24]. Sharma et al. concluded that these approaches were far more efficient than other methods and GoogLeNet had the highest accuracy.

From the literature work, it is evident that researches have utilized the advantages of latest AI techniques for crack detection of various surfaces. Also, deep learning-based approached were shown to be more effective, accurate and repeatable as compared to conventional image processing based techniques. Analysis of crack with respect to applied compression load post accurate crack-detection was less explored by the researchers. The paper demonstrates the use of computer vision technique for accurate crack detection in concrete structure. An integrated work of crack detection on concrete cubes and post crack-detection detailed crack-load analysis is presented. The methodology is presented for the laboratory scale concrete cubes subjected to compression testing. Crack detection is carried out using a convolutional neural network and transfer learning based approach. Number of cracks, crack length, and crack area of the detected cracks are monitored with respect to the applied compression load. Concrete cubes of different strengths are tested in a compression testing machine. The data acquisition is performed using an image and load acquisition setup. The information is captured synchronously during compression testing of a standard concrete cube of size $150 \times 150 \times 150$ mm. Detailed crack-load analysis is performed on the crack-load data and presented in the results section. Although the methodology is implemented for the crack detection and monitoring during the

compression testing of concrete cubes, the approach can be extended and used for other structural members as well as different types of loading.

2   Methodology

Conventionally, the concrete cubes of mix design and different strengths are casted in laboratory and various tests are carried out. Compression test provides the compressive strength of the concrete cube under observation. Peak load, strength of cube, rate of loading etc. can be obtained after the test is conducted in a conventional compression testing machine. The occurrence of first crack, load at initiation of first crack, total number of cracks occurred during the test, load at which the crack occurred, area of each crack, increase in crack area with respect to increase in applied load, crack length and increase in crack length with respect to increase in applied load etc. observation are unavailable in the standard compression tests. A methodology is developed in order to provide the crack-load analysis data during a standard compression test. The methodology involves an image and load acquisition setup. The data of concrete cube surface image and applied compression load are acquired in a synchronous manner using industrial machine vision setup, load cell and load cell controller. The vision system includes an industrial grade camera coupled with fixed focus lens and illuminations mounted on an adjustable aluminium section stand in front of the compression testing machine. The setup can be seen in Fig. 1. Concrete cube having mix design and ideal compression strength as 15 N/mm^2 was used for the study. An intelligent technique that uses deep learning method to detect the cracks from concrete cube images was developed. Inception v3 is a popular Convolutional Neural Network (CNN) model and was re-trained using large number of crack and non-crack contour image database. The model contains 42 layers architecture and was proven to be accurate on ImageNet database and efficient in terms of computation [25]. National Instruments NI Vision Assistant toolkit was used to investigate the crack parameters post accurate crack detection. Image processing techniques, such as thresholding and filters, were applied to the crack images. Particle analysis was used to carry out measurement of concrete crack parameters, including crack length and crack area. The obtained crack parameters were plotted with respect to applied compression load in order to study behaviour of concrete cube under compression loading. The work shows an integrated system for detecting cracks and analyzing the behaviour of crack parameters post detection. The outcomes of the work can be further developed and implemented to monitor concrete structures as the solution discussed the cracks behaviour under specific loading conditions. Multiple tests were carried out on standard laboratory concrete cubes with dimensions 150 × 150 × 150 mm and varying grades. A concrete compression machine was used to apply a load in on the cubes. Figure 1 shows the experiment setup comprising of compression testing machine, load cell, concrete cube, vision acquisition setup including camera, lights and mounting stand. The figure also show last image of concrete cube after the compression test is completed. Concrete cracks were accurately detected using the

Fig. 1 Data acquisition setup and sample concrete cube under compression load

re-trained CNN model. The number of cracks that occurred on the concrete block, the length of each crack, and the area of each crack were extracted and analyzed with respect to load.

A deep learning-based software application was used in the accurate detection of concrete cracks. Inception-V3 CNN model was in transfer learning mode in order to detect the crack occurring in the concrete cube images. Inception-V3 is a very popular pre-trained model used in machine vision applications as it is pre-trained on ImageNet database which has 1000 image categories. In transfer learning a pre-trained model is used and is retrained with the user dataset. More than 40,000 crack and non crack contours were used for training the pre-trained Inception-V3 model. The model has about 20 million parameters, large number of convolutional layers and takes fewest epochs to obtain good test scores. The model needed less time for single patch testing than most of the pre-trained models utilized and reported in the study. It is composed of symmetrical and asymmetrical blocks, each with different convolutional, average and max pooling, dropouts, and fully connected layers. The architecture also uses batch normalization in order to address the issue of co variate shift along with softmax activation function in the output layer.

Figure 2(a), (b) and (c) shows the overall crack detection methodology implemented in the present work. The dataset was prepared using the acquired images of different concrete cubes. A flowchart of dataset generation is depicted in Fig. 2(a). The acquired image of concrete cube surface is separated into crack and non-crack contours sub-images. Image pre-processing operations like median filter, intensity enhancement etc. were used. The extracted data is used to re-train the pre-trained Inception v3 CNN model. The flow diagram is shown in Fig. 2(b). Figure 2(c) show the flow diagram of the crack detection process. The retrained model is used for the real-time prediction of crack and non-crack contours. Bounding box on each contour are highlighted for better visualization and analysis.

(a)   (b)

(c)
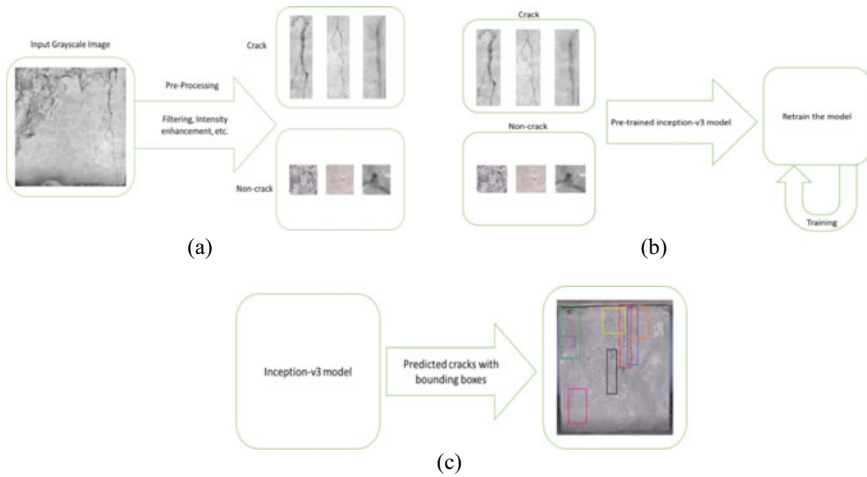
Fig. 2 **a** Dataset generation flow **b** Transfer learning **c** Crack detection flow

Cracks in concrete cubes were detected accurately using the transfer learning approach embedded in the Inception v3 CNN model. Later, the parameters associated with crack like crack length and crack area were extracted.

The extracted contours of each image were manually separated into the crack and non-crack classes with utmost care. A large number of images are used to prepare a large data set that covers the maximum possible variations and conditions. Figure 3 shows few of the extracted contours where sub-figures (a), (b), (c), and (d) are the crack contours images while (e), (f), (g), (h) are non-crack contour images. The contours were extracted from the grayscale prepossessed image. Vision Assistant is a tool provided by National Instruments (NI). It is utilized in the fields of machine vision and image processing. The concrete cube images captured during the compression test were transferred to the CNN model for accurate crack detection. The crack contours detected by the model analyzed in the tool to extract crack length and crack area. The grayscale images of crack were filtered using a 3 * 3 kernel and binarized using thresholding operation. The resultant binary image is analyzed for particle and particle length and area were extracted. The crack length and crack area extracted using the flow shown in Fig. 4 were in pixels. The parameters were calibrated to convert the results into mm and mm^2.

For crack length, the pixel coordinates of two corners were extracted to calculate the length of cube in pixel. The following formula shows the conversion factor which will help in converting pixels into mm.

$$Factor = \frac{Length\ of\ cube\ found\ using\ distance\ formula\ from\ the\ image(in\ pixel)}{150(cube\ length\ in\ mm)} \quad (1)$$

Fig. 3 Sample crack and
non-crack contour dataset

(a)　　(b)　　　(c)　　(d) (e)　　(f) (g) (h)
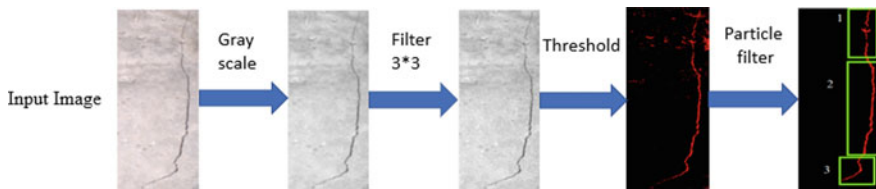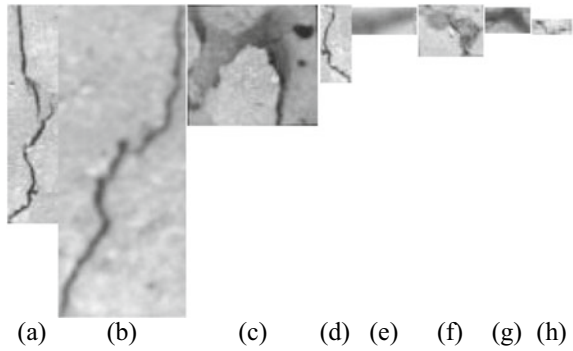
Fig. 4 Flow of crack analysis

Particle analysis measures the boundary of the crack, so the resultant measure
has to be halved to get the length of the crack. The following formula shows the
conversion.

$$Perimeter\,(mm) = \frac{Perimeter\,(in\,pixels)}{2 * Factor} \tag{2}$$

To get the crack area in mm^2 the Eqs. (3), (4) and (5) were used. First, the square
root of the area in pixel^2 was calculated and then it was divided by the factor found
in Eq. (2) and then the value found was squared to get the area in mm^2 using Eq. (5).

$$x = \sqrt{Area\,(in\,pixel^2)} \tag{3}$$

$$y = \frac{x}{Factor} \tag{4}$$

$$Area\,(in\,mm^2) = y^2 \tag{5}$$

By plotting the graphs of crack length in mm versus load in kN and crack area in
mm^2 versus load in kN, the crack-load analysis is performed.

3   Results and Discussion

The performance of the proposed methodology is carried out in terms of crack detection and crack-load analysis. M15 grade of concrete cube was casted in the Heavy structures laboratory of Nirma University and cured for 28 days to achieve 100% strength. Standard compression test was carried out on the cube and synchronous data of cube surface image and applied compression load were acquired. The images were used for accurate crack detection and crack-load analysis.

3.1   Concrete Crack Detection

The present work is evaluated in terms of crack detection performance and crack-load analysis results. The crack detection approach implemented using re-trained inception v3 model is evaluated for crack detection accuracy, precision and recall. Manual testing of the images which were not used for model training was carried out and presented in Table 1. For the study, crack is considered as the positive class whereas non-crack is considered as negative class. It presents the number of positive (P), number of negatives (N), number of true positive (TP), number of false-negative (FN), number of true negatives (TN), number of false-positive (FP), recall (R), precision (P), and accuracy (A). The parameter P (positives) show the number of contours which are crack where as parameter N (negatives) indicate the number of non-crack contours. The TP (True Positives) indicate the number of crack contours correctly predicted as crack by the model. The TN (True Negatives) shows the number of non-crack contours predicted as non-crack by the model during the testing. The parameter FP (False Positives) show the number of non-crack contours incorrectly classified as crack by the model whereas the FN (False Negatives) indicate the number of crack contours incorrectly classified as non-crack by the model. Ideal values of FP and FN for an accurate CNN model should be zero. Accuracy is represented by A and it indicates the overall effectiveness of the classifier.

Accuracy can be calculated by taking ratio of total number of crack and non-crack contours classified correctly to the total number of contours. The parameter precision and recall represented by P and R respectively shows the goodness of the network

Table 1   Crack detection performance

Image	P	N	TP	FP	TN	FN	R	P	A
1	7	197	5	3	194	2	0.71	0.62	97.55
2	13	355	11	3	352	2	1.00	0.81	98.64
3	6	253	4	1	252	2	1.00	0.85	98.84
4	11	146	7	0	146	4	1.00	1.00	97.45
5	9	164	6	1	163	3	1.00	0.90	97.69

to classify the classes in terms of sensitivity and specificity. Precision refers to the ratio of correctly classified number of crack contours to the total number of contours classified as cracks while Recall refers to the ratio of correctly classified number of crack contours to the total number of crack contours. For an ideal network, the values of precision and recall should be 1 and the value of FP and FN should be 0. From the performance of the CNN model reported in Table 1, it is evident that the model is not only accurate but also shows good precision and recall.

3.2   Crack-Load Analysis

Crack monitoring with respect to the applied compression load was performed on different concrete cubes. However, in order to limit the scope of the present work, crack-load analysis, observation and result image were carried out for M15 cube.

Table 2. shows the crack-load analysis of the studied M15 concrete cube. The table shows the data of crack number assigned in the order of their occurrence, steps of cracking i.e. initial and final, load in terms of kN, time in seconds, crack length in mm, crack area in mm^2 and location of crack on the cube surface. The location of crack is considered with reference to the four edges and four corners of the cube. No crack appeared on the concrete cube until 148 kN of compressive load. First crack was initiated at 155 kN with 3.41 mm crack length and 2.98 mm^2 crack area. The crack number 1 is removed from the concrete surface due to spalling of concrete. The final load of 243 kN along with 8.26 mm long crack and 9.96 mm^2 crack was reported. Crack number 2 and 3 occurred with progression in compressive load at 300 and 340 kN respectively. The crack number 2 was visually thin at the initiation. However, the crack expanded from 6.72 mm^2 till 56.18 mm^2 crack area. Crack number 3 occurred in right half of the cube and propagated vertically toward the bottom edge of the cube. Length of the crack number 3 was increased from 31.91 to 131.63 mm with respect to load. At 460 kN load, the fourth crack occurred quickly after the third crack had terminated. Initially the crack was visually thin and vertical which propagated from top edge to bottom edge till 480 kN load. The fifth crack occurred after the peak load of the cube and ended at 450 kN. The crack was diagonal in nature which was removed due to spalling of concrete. Crack number 6 appeared at a load of 463 kN and stopped at a load of 395 kN. Individual image of each crack initiation and terminated are shown in Fig. 5. Each crack is highlighted with a bounding box and numbered appropriately to match with the crack-load analysis reported in Table 2.

Figure 6(a) represents the graph of crack length in mm vs load in kN of M15 concrete cube while Fig. 6(b) shows the graph of crack area in mm^2 versus load in kN.

Table 2 Crack load analysis of M15 strength concrete cube

Crack No.	Steps of cracking	Load (kN)	Time (s)	Crack length (mm)	Crack area (mm^2)	Location
0	–	148	30	0	0	–
Remarks: No Cracks						
1	Initial	155	55	3.41	2.98	Top Right Corner
	Final	243	70	8.26	9.96	
Remarks: Visually small crack at the time of initiation and gets removed from the concrete cube with progressive load						
2	Initial	300	75	31.18	6.72	Top Left Corner
	Final	366	90	58.54	56.18	
Remarks: Visible crack at the time of initiation and the crack expands in length and area, which leads to spalling with progressive load						
3	Initial	340	84	31.91	13.5	Bottom left
	Final	460	107	131.63	106.16	
Remarks: Visible Diagonal Crack at the time of initiation, which increases in area with progressive load						
4	Initial	460	107	32.30	11.99	Top Right
	Final	480	118	67.75	59.85	
Remarks: Visible thin vertical crack which initiates from the top edge and propagates towards bottom with increase in length and area						
5	Initial	500	125	50.56	7.15	Right
	Final	450	138	116.35	189.94	
Remarks: Visible diagonal crack at the time of initiation, which leads to spalling with progressive load						
6	Initial	463	113	28.03	9.48	Centre
	Final	395	157	53.99	31.09	
Remarks: Visually thin diagonal crack at the centre of the cube, which increases in the length and area as the load propagates						

The graphs reported in the Fig. 6 depict the monitoring and analysis capability of the methodology. Propagation of individual cracks in terms of length and area can be studied with respect to applied load. Alternate grades of concrete cube and concrete cube with different materials may be studied in the future for research utilizing the implemented methodology.
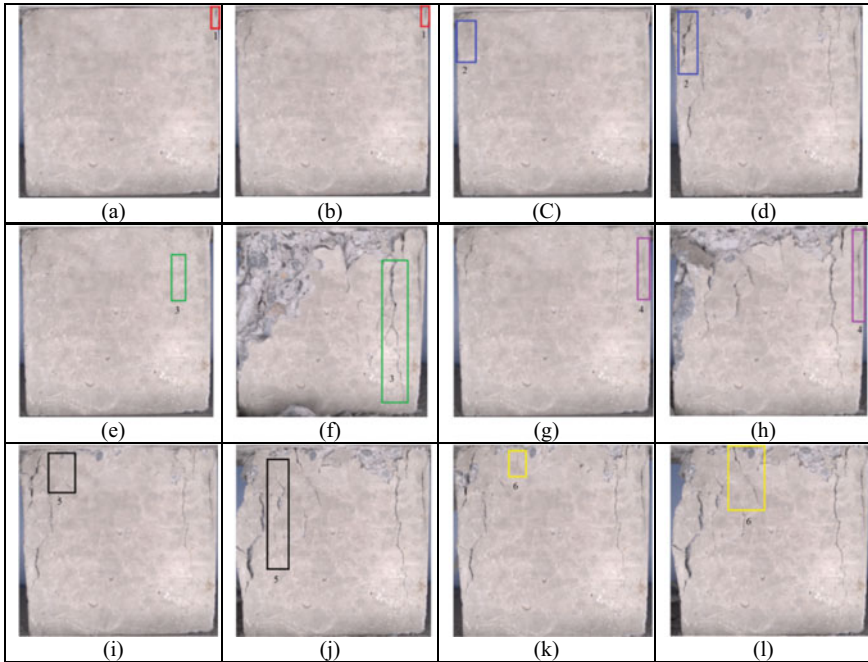
Fig. 5 M15 strength Concrete cube images showing initial crack and final crack
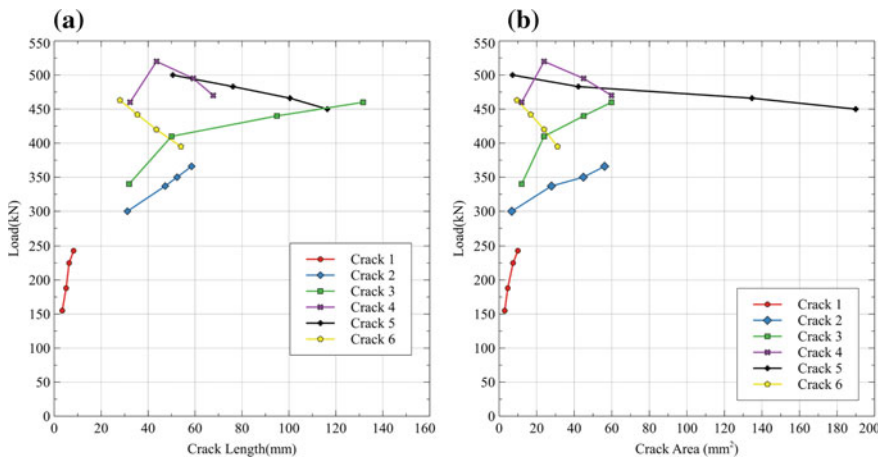
Fig. 6 **a** Crack length (mm) vs Load (kN) **b** Crack area (mm^2) vs Load (kN)

4   Conclusion

An automated, integrated and intelligent concrete structural health monitoring system is proposed in this study. An image and load data acquisition setup is developed to capture data in synchronous manner. The cracks occurring in concrete cubes under compressive load were detected accurately using a CNN based strategy. The Inception-v3 model was used in transfer learning mode to detect cracks on concrete cube images acquired using the developed setup. Furthermore, the detected cracks were analyzed using different image processing techniques and then parameters associated with crack were measured. These parameters were then analysed with respect to the applied compressive load. The study of concrete cube behaviour under compressive loading was presented. Engineers will benefit from the integrated solution of accurate crack detection and comparative crack-load analysis of different concrete grades in structural health monitoring. The implemented methodology can also be deployed to detect and monitor cracks in other concrete elements and real-life structures. Additionally, the concrete elements can be monitored for crack detection and propagation during different types of loading. The study if carried out can provide much more detailed information of concrete behaviour with respect to different types of loading.

References

1. Shanni, S.H., Girinivas, K.V.: Analytical investigation on reinforced concrete beams. Int. Res. J. Eng. Technol. **5**(12) (2018)
2. Ajagbe, W.O., Ojedele, O.S.: Structural investigation into the causes of cracks in building and solutions: a case study. Am. J. Eng. Res. (AJER) **7**(8), 152–160 (2018)
3. Gordan, M., Dancea, O., Vlaicu, A., Stoian, I., Tsatos, O.: Computer vision based decision support tool for hydro-dams surface deterioration assessment and visualization using fuzzy sets and pseudo-coloring. In: IEEE International Conference on Automation, Quality and Testing, Robotics (2008)
4. Dinh, T.H., Ha, Q.P., La, H.M.: Computer vision-based method for concrete crack detection. In: 14th International Conference on Control, Automation, Robotics and Vision (2016)
5. Kumar, P., Batchu, S., Narasimha Swamy, S., Kota, S.R.: Real-time concrete damage detection using deep learning for high rise structures. IEEE Access 9, 112312–112331 (2021)
6. Pereira, F.C., Pereira, C.E.: Embedded image processing systems for automatic recognition of cracks using UAVs. International Federation of Automatic Control (2015)
7. Kim, H., Sim, S.H., Cho, S.: Unmanned aerial vehicle (UAV)-powered concrete crack detection based on digital image processing. In: 6th International Conference on Advances in Experimental Structural Engineering (2015)
8. Dorafshan, S., Maguire, M., Qi, X.: Automatic surface crack detection in concrete structures using OTSU thresholding and morphological operations. Utah state university, UTC Report 01-2016 (2016)
9. Chaudhuri, S., Chatterjee, S., Katz, N., Nelson, M., Goldbaum, M.: Detection of blood vessels in retinal images using two-dimensional matched filters. IEEE Trans. Med. Imag. **8**(3), 263–269 (1989)
10. Zhang, A., Li, Q., Wang, K.C.P., Qiu, S.: Matched filtering algorithm for pavement cracking detection. J. Transp. Res. **2367**(1), 30–42 (2013)

11. German, S., Brilakis, I., DesRoches, R.: Rapid entropy-based detection and properties measurement of concrete spalling with machine vision for post-earthquake safety assessments. Adv. Eng. Inform. **26**(4), 846–858 (2012)
12. Yeum, C.M.: Vision-based automated crack detection for bridge inspection. Comput. Aided Civ. Infrastruct. Eng. **30**(10), 759–770 (2015)
13. Omar, I., Khan, M., Starr, A.: Compatibility and challenges in machine learning approach for structural crack assessment. Struct. Health Monitoring 1–22 (2022)
14. Żarski, M., Wójcik, B., Miszczak, J.A.: KrakN: transfer learning framework and dataset for infrastructure thin crack detection. Elsevier B.V (2021)
15. Zhang, A., et al.: Automated pixel-level pavement crack detection on 3D asphalt surfaces using a deep-learning network. Comput. Aided Civ. Infrastruct. Eng. **32**(10), 805–819 (2017)
16. Zhang, A., et al.: Deep learning–based fully automated pavement crack detection on 3D asphalt surfaces with an improved CrackNet. American Society of Civil Engineers (2018)
17. Fan, L., Zhao, H., Li, Y., Li, S., Zhou, R., Chu, W.: RAO-UNet: a residual attention and octave UNet for road crack detection via balance loss. The Institute of Engineering and Technology, Wiley (2021)
18. Chen, Y., et al.: Drop an octave: reducing spatial redundancy in convolutional neural networks with octave convolution. In: International Conference on Computer Vision (ICCV) (2019)
19. Cha, Y.-J., Choi, W., Oral, B.: Deep learning-based crack damage detection using convolutional neural networks. Comput. Aided Civ. Infrastruct. Eng. **32**(5), 361–378 (2017)
20. Tayo, C.O., Linsangan, N.B., Pellegrino, R.V.: Portable crack width calculation of concrete road pavement using machine vision. In: 2019 IEEE 11th International Conference on Humanoid, Nanotechnology, Information Technology, Communication and Control, Environment, and Management (HNICEM) (2019)
21. Liu, Y., Yao, J., Lu, X., Xie, R., Li, L.: DeepCrack: a deep hierarchical feature learning architecture for crack segmentation. Neurocomputing **338**, 139–153 (2019)
22. Piyathilaka, L., Preethichandra, D.M.G., Izar, U., Kahandawa, G.: Real-time concrete crack detection and instance segmentation using deep transfer learning. In: 7th Electronic Conference on Sensors and Applications, MDPI (2020)
23. Su, C., Wang, W.: Concrete cracks detection using convolutional neural network based on transfer learning. Math. Probl. Eng. **2020**, Article ID 7240129 (2020)
24. Sharma, N., Dhir, R., Rani, R.: Crack detection in concrete using transfer learning. Adv. Math. Sci. J. **9**(6), 3895–3906 (2020)
25. Szegedy, C., Vanhoucke, V., Ioffe, S., Shlens, J., Wojna, Z.: Rethinking the inception architecture for computer vision. In: 2016 IEEE Conference on Computer Vision and Pattern Recognition (CVPR) (2016)